JAHRBUCH

2019
BAND 159/1–4

Geologische Bundesanstalt

JAHRBUCH

2019

BAND 159/1–4

Geologische Bundesanstalt

www.geologie.ac.at

Die Geologische Bundesanstalt ist eine Forschungseinrichtung des Bundesministeriums für Bildung, Wissenschaft und Forschung.

Bundesministerium
Bildung, Wissenschaft
und Forschung

Medieninhaber, Herausgeber und Verleger: Geologische Bundesanstalt, Neulinggasse 38, 1030 Wien.
Redaktion: Christoph Janda
Lektorat: Christian Cermak
Verlagsort: Wien
Herstellungsort: Wien
Ziel des „Jahrbuches der Geologischen Bundesanstalt“
ist die Dokumentation und Verbreitung erdwissenschaftlicher Forschungsergebnisse.
Satz, Gestaltung und Druckvorbereitung: Jarmila Böhm im Auftrag der Geologischen Bundesanstalt.
Druck: Print Alliance HAV Produktions GmbH, Druckhausstraße 1, 2540 Bad Vöslau

JAHRBUCH DER GEOLOGISCHEN BUNDESANSTALT
Jb. Geol. B.-A. | ISSN 0016-7800 | Band 159 | Heft 1–4 | S. 1–423 | Wien, Dezember 2019

Inhalt

Contents

Berichte über Tätigkeiten zur Erstellung der Geologischen Karte der Republik Österreich 1 : 50.000 in den Jahren 2016–2019

Geological Mapping Reports for the 1 : 50,000 Scale Geological Map Series from the Years 2016–2019

Kartenwerk im BMN-System (Maps in BMN Map Projection)

Kartenwerk im UTM-System (Maps in UTM Map Projection)

Buchbesprechungen / Book Reviews

JAHRBUCH DER GEOLOGISCHEN BUNDESANSTALT
Jb. Geol. B.-A. | ISSN 0016–7800 | Band 159 | Heft 1–4 | S. 5–49 | Wien, Dezember 2019

Begriffskataloge der Geologischen Landesaufnahme für Quartär und Massenbewegungen in Österreich

Mathias Steinbichler[1], Jürgen M. Reitner[2], Michael Lotter[2] & Andrea Steinbichler[1]

4 Abbildungen, 6 Tabellen, 3 Anhänge

Geologische Kartierung
Standardisierung
Generallegende
Quartärgeologie
Gravitative Massenbewegungen
Lithogenetische Einheiten
Geomorphologische Einheiten

Inhalt

Zusammenfassung

Die „gleiche Terminologie“ im Sinne von gleich verstandenen und ebenso verwendeten Begriffen ist in den Geowissenschaften von essenzieller Bedeutung für die Erhebung, Auswertung und Darstellung von Geodaten. Die Geologische Bundesanstalt (GBA) betrachtet es als wesentliche Aufgabe, die dafür benötigten Standards zu definieren. Aufbauend auf der Generallegende für die pleistozänen und holozänen Sedimente des Periglazialraumes (Krenmayr et al., 2012) und auf den bisher in den GBA-Karten verwendeten Begriffen wurde eine Nomenklatur für Einheiten und Ablagerungsformen des Quartärs entwickelt. Diese werden in kartierbare Sedimentkörper (Lithogenetische Einheiten) und Reliefformen (Geomorphologische Einheiten) sowie zusätzliche für die Kartendarstellung relevante Informationen (Quartäre Phänomene) unter grundsätzlicher Berücksichtigung der etablierten prozessorientierten Klassifikation eingeteilt. Die Begriffe sind entsprechend thematisch zusammengefasst und folgen einer einfachen hierarchischen Ordnung. Durch die Hierarchisierung können die Begriffe in Aufnahmemaßstäben (1:10.000) bis hin zu Darstellungsmaßstäben (1:25.000, 1:50.000, 1:200.000) sowie auch in der Punktdatenaufnahme verwendet werden.

Terminology for geological mapping of Quaternary and mass movements in Austria

Abstract

An accepted terminology is a prerequisite for data acquisition, data analysis and evaluation as well as data production. Standardisation is an essential task of the Geological Survey of Austria. A nomenclature for Quaternary geological and geomorphological units including mass movements has been developed based on the existing terminology for the deposits of the periglacial environment (Krenmayr et al., 2012) and that of existing geological maps of Austria. These units are classified according to common understanding of geological processes into mapable deposits (Lithogenetic Units), landforms (Geomorphological Units) and additional forms (Quaternary Phenomena). The terms of classification are in hierarchical order. Hence, they can be used for different applications like data acquisition in various scales (e.g. 1:10,000, 1:25,000, 1:50,000, 1:200,000).

1 Mathias & Andrea Steinbichler: Münzgrubweg 17, 5550 Radstadt.
2 Jürgen M. Reitner, Michael Lotter: Geologische Bundesanstalt, Neulinggasse 38, 1030 Wien. juergen.reitner@geologie.ac.at, michael.lotter@geologie.ac.at

Einleitung

Aufgrund der Komplexität geologischer Informationen ist in den vergangenen Jahrzehnten eine große Anzahl verschiedener Begriffe in Form von Legendeneinträgen für quartäre Sedimente und Formen inklusive Massenbewegungen auf analogen und digitalen Kartenwerken der Geologischen Bundesanstalt (GBA) verwendet worden. Die Zahl aller Legendeneinträge, die jemals auf Landesaufnahme-Produkten der GBA für diesen Themenkomplex angewandt wurden, beläuft sich auf etwa **3.000**. Diese hohe Zahl lässt sich hauptsächlich auf zwei historisch gewachsene Faktoren zurückführen: a) Verschiedene Datenproduzenten, i.e. kartierende Geologen, verwendeten verschiedene Konzepte für die Gliederung des Quartärs (z.B. Lithogenetische Einheiten vs. Lithologie vs. Lithostratigrafie/Allostratigrafie/Morphostratigrafie; vgl. van Husen & Reitner, 2011) und b) Begriffe wurden geringfügig anders bezeichnet oder inhaltlich idente Legendeneinträge wurden unterschiedlich benannt. Letztlich ist eine gut durchdachte, fachlich geprüfte und konsequent eingehaltene Terminologie Grundvoraussetzung für eine moderne Datenverarbeitung an der GBA um a) einen Mindeststandard in der fachlichen Datenqualität zu sichern, b) homogene österreichweite Datensätze erzeugen zu können und c) den Anforderungen einer modernen Datenverarbeitung und Datenbereitstellung, die vernetzte Informationen fordert (z.B. INSPIRE), gerecht zu werden.

Zahlreiche Arbeiten legen bei der Gliederung quartärer Sedimente und Formen (inklusive Massenbewegungen) ihren Schwerpunkt auf einen faziellen und/oder prozessorientierten Bearbeitungsansatz (z.B. Lukas & Rother, 2016; Evans et al., 2006; Zangerl et al., 2008; Cruden & Varnes, 1996; Hungr et al., 2014). Im Bewusstsein dieser Ansätze beschäftigt sich der hier vorliegende Begriffskatalog mit einer Gliederung und Definition von Begriffen für die Aufnahme in qualitätsgesicherte, redaktionierte Datensätze und die Darstellung in geologischen Karten. Damit soll der Tradition der Klassifikation von Hinze et al. (1989) und von der Geologischen Landesaufnahme der Schweiz (Bundesamt für Wasser und Geologie, 2003) gefolgt werden.

Grundsätzlich wurde für die Definitionen der verwendeten Begriffe versucht, auf publizierte Standardwerke zurückzugreifen. Vielfach sind diese Definitionen für unsere Zwecke nicht direkt anwendbar (z.B. liegen Definitionen von Prozessen und nicht von den dazugehörigen Ablagerungen oder Formen vor) und wurden abgeändert oder neu definiert. Diese sind in der Quellenangabe zu jedem Begriff als „Diese Publikation“ gekennzeichnet.

Bezüglich der Bildung von Wortderivaten des Stammes *glazi-* folgen wir den Empfehlungen von Lukas & Rother (2016) und verwenden den Verbindungsvokal -o- für Wortbildungen (z.B. *glaziogen*, *glaziofluviatil* etc.).

Exkurs: Anwendung der Begriffskataloge in der Generallegende der GBA

Die in diesem Beitrag beschriebenen Begrifflichkeiten müssen unter Aufsicht einer GBA-internen Fachredaktion in Geografischen Informationssystemen (GIS) und Kartenanwendungen verwendet werden können. Daher wurde eine Generallegende Quartär aufbauend auf den drei Themen Lithogenetische Einheiten, Geomorphologische Einheiten und Quartäre Phänomene in Kombination mit GBA-intern abgestimmten und redaktionell geprüften Begriffskatalogen von Chronostratigrafie, Lithostratigrafie (inklusive Allo- und Morphostratigrafie) und Lithologie (inklusive Korngrößen) erstellt. Mit Hilfe dieser Generallegende ist es möglich, vordefinierte Begriffskombinationen in beispielsweise einem GIS-System anzubieten. Dadurch können während der gesamten Datenerstellung (Geländekarte bis fertiger Datensatz sowie abgeleitete Produkte wie digitale und auch analoge Karten) einheitliche Legendeneinträge und eine dementsprechend verwertbare Attribuierung gesichert werden.

Grundprinzipien der Klassifikation

Erfassung und Darstellung von Daten der Themen Quartär und Massenbewegungen

Entscheidend für die Akzeptanz eines Begriffsstandards ist neben einem logischen Aufbau auch die Anwendbarkeit in der Praxis. Die vordefinierten Begriffe wurden ausgehend von den Anforderungen bei der Datenerstellung für eine geologische Karte konzipiert. Folgende Grundprinzipien gelten für die Darstellung von Quartär und Massenbewegungen in einem modernen Datensatz und daraus generierter geologischer Karte.

Thematische Einteilung

Lithogenetische Einheiten: Quartäre Gesteinsvorkommen wie zum Beispiel Schwemmfächerablagerungen, die auf Grund ihrer Vielzahl nicht sinnvoll als einzelne Lithostratigrafische Einheiten formalisiert werden können (siehe auch Diskussion in van Husen & Reitner, 2011), werden in Lithogenetische Einheiten gegliedert. Unter einer Lithogenetischen Einheit versteht man nach dem GeoSciML Vokabular der „Commission for the Management and Application of Geoscience Information“ mit wenigen Ausnahmen (Sinterkalk, Alm, Hangbrekzie) einen kartierbaren Lockergesteinskörper, der durch seine Genese definiert ist (CGI, 2016: Lithogenetic Unit).

Geomorphologische Einheiten: Die oberflächlichen Ausprägungsformen von Gesteinsvorkommen jeder Art (Fest- oder Lockergestein) werden als Geomorphologische Einheiten beschrieben. Es gibt eine klare, sowohl begriffliche als auch kartentechnische Trennung zwischen der morphologischen Ausprägung und dem Sedimentinhalt von Lithogenetischen Einheiten. Die morphologische Ausprägung bestimmt demnach nicht die Zuteilung zu einer Lithogenetischen Einheit.

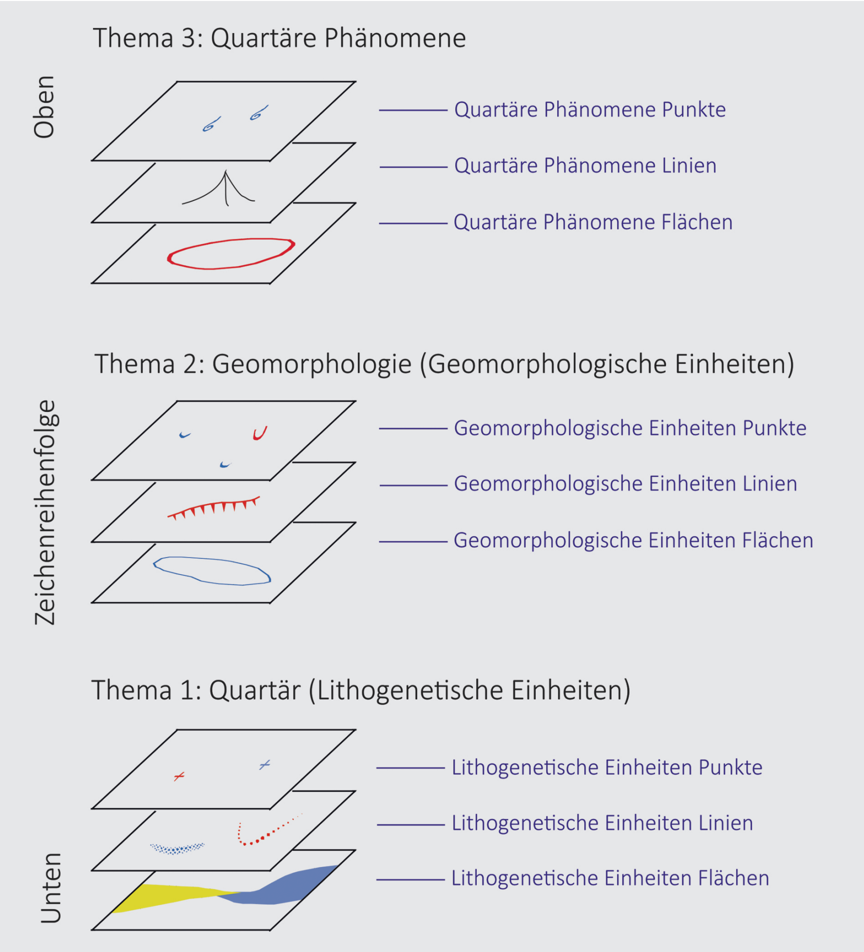

Abb. 1.
Zeichenreihenfolge der Geometrien innerhalb der Themen für Quartär und Massenbewegungen.

Quartäre Phänomene: Das Thema Quartäre Phänomene umfasst alle geologisch relevanten Objekte einer Karte, die nicht einer geologischen oder geomorphologischen Einheit zugewiesen werden können, aber dennoch wichtig für das Verständnis von quartären Prozessen sind (z.B. Umrandung einer Massenbewegung).

Diese drei Themen können miteinander in verschiedenen Geometrien kombiniert werden (Abb. 1, 2) und bilden somit einen logischen und anwendbaren Rahmen für die datenbanktechnische Erfassung als auch Darstellung von Quartär und Massenbewegungen.

Anwendung in der Kartierung und Darstellung

Grundsätzlich spiegeln die Begriffe Resultate abgeschlossener wie auch anhaltender geologischer Prozesse wider. Im Hinblick auf die Anwendbarkeit bei der Geländeaufnahme wurde ein pragmatischer Ansatz gewählt, der eine Begriffsfindung mit einfachen feldgeologischen Methoden ermöglicht.

Prinzip 1: Eine Lithogenetische Einheit beinhaltet nicht die Information über die geomorphologische Ausprägung eines Sedimentkörpers.

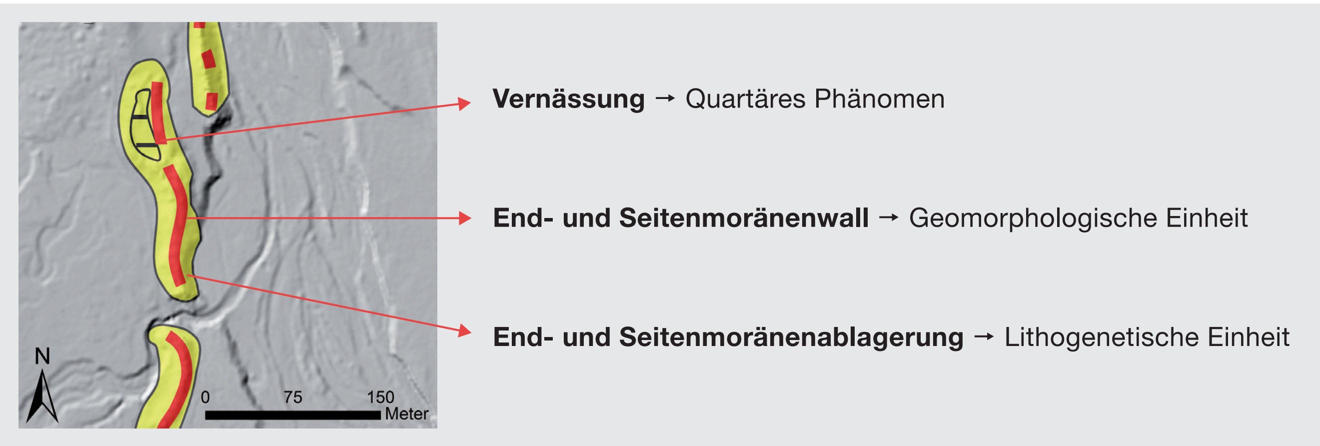

Abb. 2.
Beispiel für die Kombination von verschiedenen thematischen Ebenen anhand einer End- und Seitenmoränenablagerung mit Wall aus dem Egesen-Stadial.

Prinzip 2: Die geomorphologische Ausprägung eines Sedimentkörpers (z.B. End- und Seitenmoränenwall) und/ oder des Festgesteins (z.B. Zerrspalte) wird ausschließlich in einer eigenen Ebene (Thema Geomorphologie) gezeichnet und ist abhängig von der Kombination von mehreren thematischen Ebenen an eine Lithogenetische Einheit gebunden oder nicht.

Aus der kombinierten Darstellung von Prinzip 1 und 2 lassen sich im Kartenbild Informationen zu Prozessen und Prozessketten ableiten. Beispiele für diese Prinzipien wären:

- Eine End- und Seitenmoränenablagerung muss nicht zwangsläufig als Wall ausgebildet sein.
- Jedoch ist ein End- und Seitenmoränenwall an eine End- und Seitenmoränenablagerung gebunden.
- Hingegen kann ein „Ehemaliger Abfluss, Trockental“ über jede unterliegende Ebene gezeichnet werden.

Regelungen in Bezug zu Massenbewegungen

Die Klassifikation gravitativer Massenbewegungen erfolgt grundsätzlich mit einem prozessorientierten Bearbeitungsansatz, der auf deren Kinematik (Bewegungsmechanis-

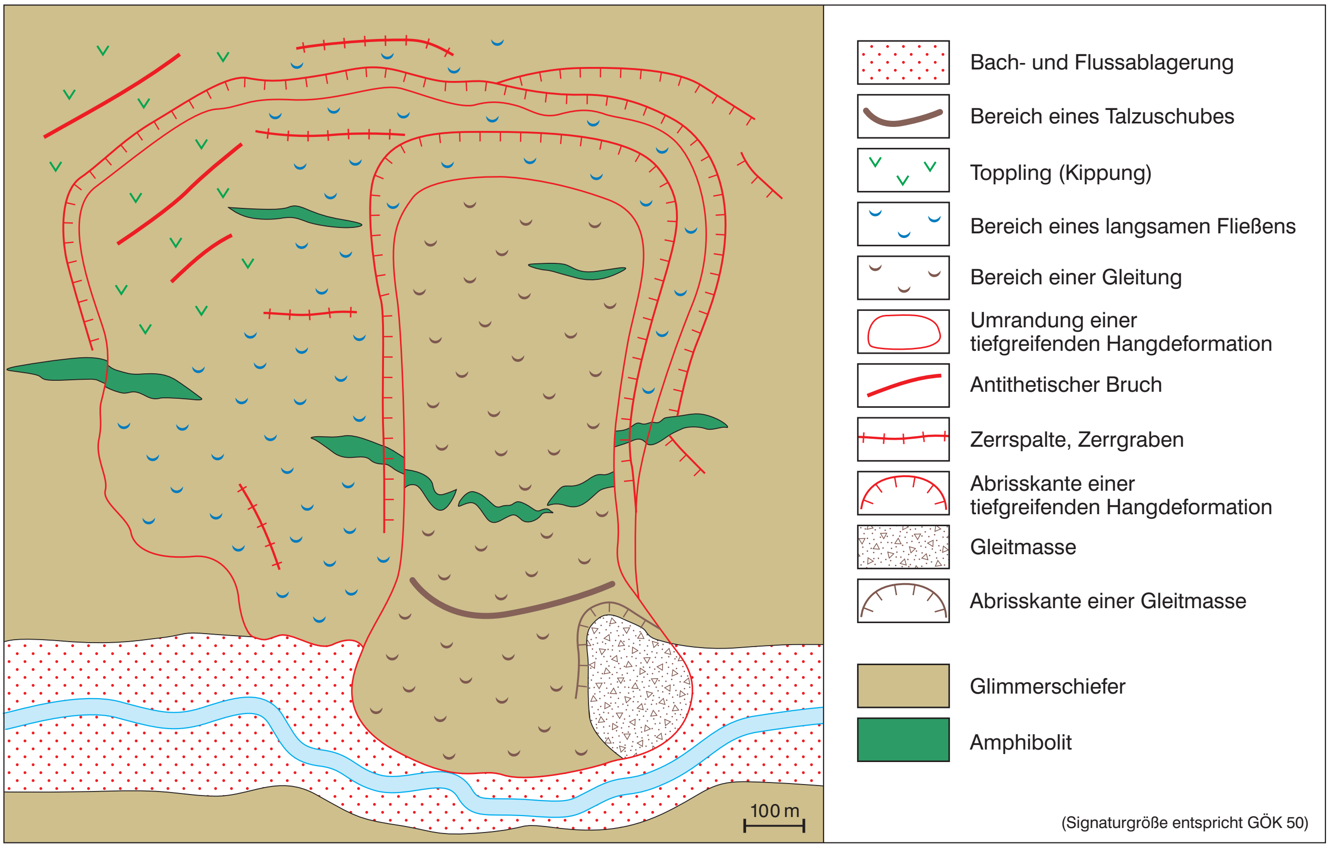

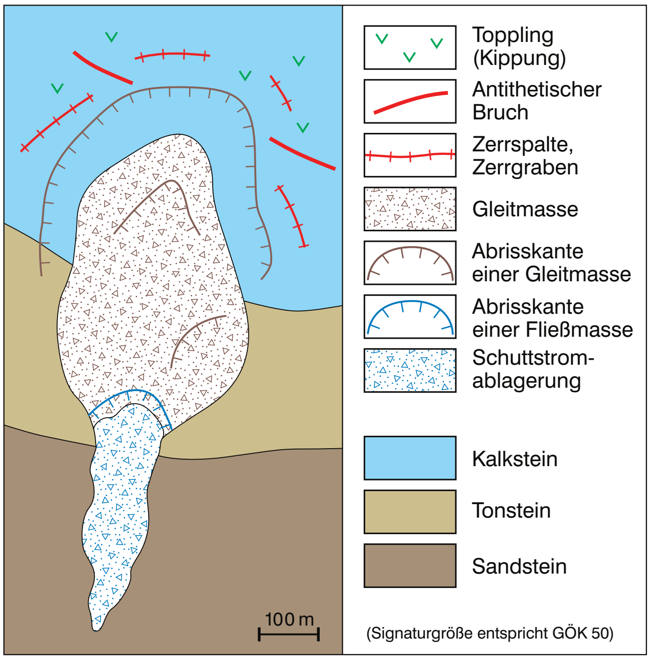

Abb. 3.
Beispiele (schematisiert) für die Darstellung von Massenbewegungen in mehreren thematischen Ebenen. Oberes Bild: Die Information über die Prozesse Gleiten, Fließen und Kippen wird hauptsächlich über Marker und Linien des Themenbereiches Geomorphologische Einheiten wiedergegeben. Der lithologische Verband der involvierten Gesteinsmassen ist trotz Auflockerung noch fast durchwegs vorhanden. Unteres Bild: Die Information über die Prozesse ist hier vor allem über die Lithogenetischen Einheiten (Gleitmasse, Schuttstromablagerung) als Sedimentneubildungen gegeben.

mus) und Materialzusammensetzung (Fest-, Lockergestein) basiert (ZANGERL et al., 2008 cum lit.). Aufgrund des generellen Bestrebens, möglichst viele lithologische Informationen und geologische Zusammenhänge in der Geologischen Landesaufnahme zu erheben, bedarf es für die Darstellung von Massenbewegungen einer Erklärung der anzuwendenden Regeln:

Regel 1: Eine Massenbewegung wird dann als Lithogenetische Einheit dargestellt, wenn die interne Zerlegung des Gesteinsverbandes dermaßen fortgeschritten ist, dass ein „neuer" kartierbarer (man beachte dabei die Maßstabsabhängigkeit!) Sedimentkörper entstanden ist. Die strukturellen Charakteristika des Ausgangsmaterials sind dabei derart überprägt, dass dessen Übergang vom Fest- zum Lockergestein bzw. vom anstehenden zum umgelagerten Material weitestgehend bis vollständig vollzogen ist (Abb. 3). Eine genaue Festlegung des Ausmaßes der Überprägung ist schwierig und situationsabhängig und wird schon in FÜRLINGER (1972) ausführlich diskutiert: So ist nach Trennflächen (Klüftung, Schichtung, Schieferung etc.) aufgelockerter Fels, das heißt „Geordnetes Blockwerk" nach HORNINGER (1958) noch keine eigene Lithogenetische Einheit. Dem gegenüber begründet die fortgeschrittene bis völlige Verbandsauflösung bei einem nach Klüften zerfallenen Fels bzw. „Anstehendes Blockwerk" nach ZISCHINSKY (1969) die Ausscheidung einer Lithogenetischen Einheit. Wir wollen als Faustregel die Zerlegung in mindestens Blockgröße und eine Verstellung der Kluftkörper, die ihre ursprüngliche Anordnung (Trennflächengefüge) zueinander nicht mehr erkennen lässt, mitgeben (Abb. 4).

Eine **Ausnahme** dieses Prinzips bilden **Bergsturzgleitmassen**, bei denen ein ursprünglicher geologischer Verband noch ersichtlich ist. Aufgrund der Dimension und der erheblichen Transportweite (ABELE, 1974) stellen diese ein hervorzuhebendes Element der Landschaftsentwicklung dar und werden in Anlehnung an bisherige Kartendarstellungen als Lithogenetische Einheit ausgeschieden.

Regel 2: Um einen Massenbewegungssedimentkörper als Lithogenetische Einheit ausscheiden zu können, muss die Zerlegung aus einem gravitativen Transportprozess resultieren (Stürzen, Fließen, Gleiten, Driften, Kippen). Dabei ist die Transportweite irrelevant.

Regel 3: Falls keine Lithogenetische Einheit gemäß Regel 1 ausgeschieden werden kann, sind die wichtigsten zu erhebenden Elemente geomorphologische Ausprägungen (Zerrspalten, Abrisskanten etc.) sowie die Abgrenzung von zusammenhängenden Gesteinsmassen mithilfe der Ausscheidung „Umrandung eines Massenbewegungskörpers" oder „Umrandung einer tiefgreifenden Hangdeformation" in der Themengruppe Quartäre Phänomene (Abb. 3).

Regel 4: Aufgelockertes Festgestein ohne erkennbare prozessbezogene Umlagerung (oft als „in situ" oder „subanstehend" bezeichnet) wird mit den Geomorphologischen Einheiten „Zerrspalten, Zerrgraben" (bevorzugt einzusetzen) und „Tiefgreifend aufgelockerter Fels" gekennzeichnet.

Regel 5: Geomorphologische Einheiten, die Prozesse beschreiben (z.B. „Bereich einer Gleitung" oder „Bereich eines langsamen Fließens"), können über jeden unterliegenden Layer (Festgestein, Quartär etc.) gezeichnet werden (Abb. 3).

Regel 6: Bestimmte Begriffe, die in der Literatur insbesondere hinsichtlich kinematischer und geomorphologischer Aspekte unterschiedlichen Ansichten unterliegen (siehe WEIDNER, 2000 cum lit.), werden nicht mehr verwendet oder werden bewusst in die Ebene Geomorphologie transferiert:

- Der Begriff „Sackung" wird nicht mehr verwendet.
- Der Begriff „Talzuschub" wird abgewandelt als „Bereich eines Talzuschubs" im Sinne einer rein geomorphologischen Ausprägung beibehalten.

Regel 7: Der Begriff „Hangschutt" wird nicht mehr verwendet, da in der Vergangenheit darunter häufig die gesamte Schuttbedeckung eines Hanges zusammengefasst wurde. Um die Differenzierung zwischen Verwitterungsprozessen und gravitativer Massenumlagerung zu betonen, wird der Begriff „Hangablagerung" nur für mittels Schwerkraft transportiertem Schutt verwendet. „Verwitterungsschutt" wird nicht mehr als Lithogenetische Einheit ausgeschieden, sondern die unterliegenden Ausgangsgesteine sind zu kartieren und gegebenenfalls mit den Quartären Phänomenen „Tiefgreifende Verwitterung" oder „Permafrostverwitterung" zu überlagern.

Hierarchie

Die Begriffe sind in maximal drei hierarchische Ebenen gegliedert (Tab. 1–3), die es erlauben, je nach Anwendung und Bedarf detaillierte oder gröbere Attribuierungen sowie systematische Abfragen vorzunehmen.

Begriffstabellen

Die Begriffe in den Tabellen 4 bis 6 spiegeln den derzeitigen Stand (Juni 2019) der Begriffskataloge für die Themen Lithogenetische Einheiten, Geomorphologische Einheiten und Quartäre Phänomene wider. Jeder Begriff hat eine englische Übersetzung, eine Definition, eine englische Definition, die Quelle der Definition sowie eine Darstellung der hierarchischen Zuteilung. In der Punktaufnahme und im Maßstab 1:10.000 sind alle diese Begriffe sinnvoll einsetzbar. Für kleinere Maßstäbe (1:25.000, 1:50.000, 1:200.000, 1:250.000) sind teilweise zu genaue Unterscheidungen nicht praktikabel und auch die Zusammenfassung von mehreren Begriffen notwendig (z.B. Gleit- und Fließmasse, Schutt- und Schwemmkegel etc.). Diese Maßstabsabhängigkeiten und benötigten Zusammenfassungen werden in der Generallegende für Quartär und Massenbewegungen (siehe Exkurs) abgebildet und im Anhang 1 bis 3 exemplarisch aufgelistet.

Symbolik

Die Symbole pro Begriff, die sich im Anhang (Gesamtübersicht) finden, sind Vorschläge seitens der Verfasser dieses Beitrages für die Darstellung der beschriebenen geologischen Einheiten und Formen sowohl für eine analoge Zeichnung, als auch für die digitale Darstellung. Basierend auf diesen Vorschlägen sind die Symboliken für die Generallegende Quartär und Massenbewegungen aufgebaut (siehe Exkurs). Diese können vor allem in der Farbgebung variieren, da beispielsweise eine chronologische Zuteilung von End- und Seitenmoränenwällen verschiedene Farben erfordert. Aufgrund der Limitation von gut unterscheidbaren (leserlichen) Symboliken und Schraffuren des Themenbereiches Quartär (z.B. begrenztes Farbenspektrum) wird

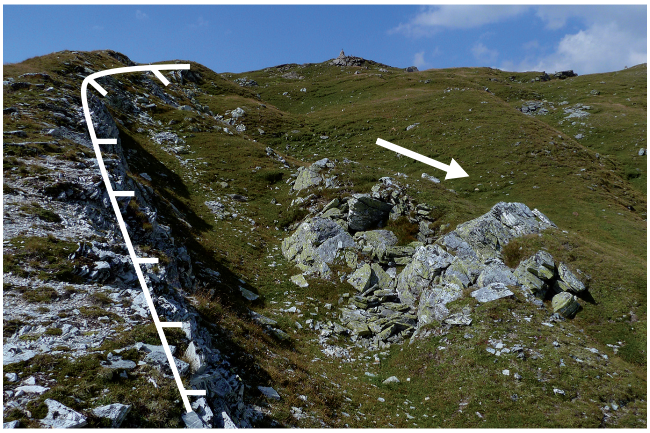

A. Abrisskante einer tiefgreifenden Hangdeformation mit anschließendem Bereich eines langsamen Fließens. Trotz Auflockerung und Verstellung der abgelösten plattigen Quarzite (Matreier Zone) sind die kaum dislozierten Festgesteine durchwegs im Verband kartierbar.

D. Gleitmasse, bei der ein aufgelockerter stratigraphischer Verband (Scheibelberg- über Kössen-Formation, Tirolikum) trotz einer Transportweite von über 200 m in Teilen erhalten ist: Sedimentneubildung neben dislozierten Ausgangsgesteinen (Bereich einer Gleitung) im gleichen Prozessraum (maßstabsabhängig differenzierbar).

B. Bereich einer initialen Gleitung in siliziklastischen Metasedimenten der Wustkogel-Formation (Subpenninikum) mit Verbandsauflockerung, Öffnung der Trennflächen und beginnender Verstellung der Kluftkörper.

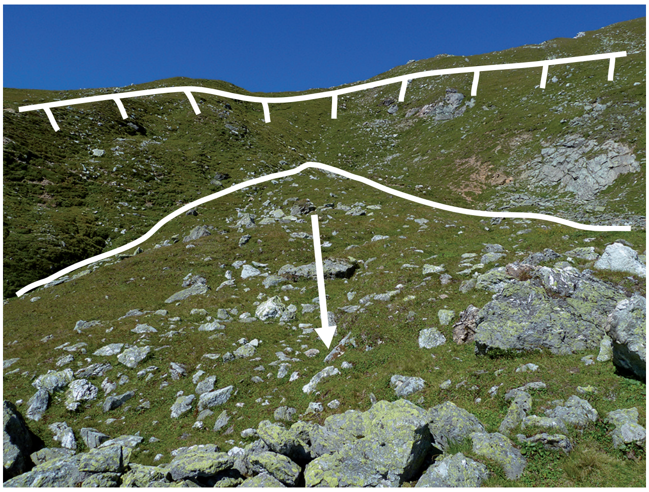

E. Ausbruchsnische einer Felsgleitung in Grünschiefern und Quarziten der Matreier Zone. Obwohl die Gleitmasse nach kurzem Transport im Abrissbereich verblieben ist, liegt nur mehr ein komponentengestütztes (Steine, Blöcke) Lockermaterial vor (lithogenetische Sedimentneubildung).

C. Bereich einer Gleitung in Paragneisen des oberostalpinen Schoberkristallins. Trotz starker Auflockerung und Verstellung ist die Anordnung der Kluftkörper nach dem Trennflächengefüge noch erkennbar und somit sind die Festgesteine kartierbar.

F. Schuttstromablagerung (Fließmasse mit matrixgestütztem Gefüge und Grobkomponenten), die sich aus der Prozesskette Kippen-Gleiten-Fließen in Phylliten der Löhnersbach-Formation (Grauwackenzone) entwickelt hat.

Abb. 4.
Beispiele für die Auflösung des Festgesteinsverbandes (A, B, C) hin zu einer Sedimentneubildung (D = Grenzfall, E, F) und folglich Ausscheidung als Lithogenetische Einheit (Regel 1 in Bezug zu Massenbewegungen). (Alle Abbildungen: M. Lotter)

für einige thematisch verwandte Begriffe die gleiche Symbolik vorgeschlagen. Sollten diese Begriffe auf der gleichen Karte (Darstellung) verwendet werden, steht es dem Bearbeitenden frei, ersatzweise ein geeignetes Symbol zu wählen. Aufgrund von Maßstabsabhängigkeiten der Geometrien einiger Begriffe können mehrere Symbolvorschläge pro jeweiliger Geometrie vorhanden sein.

Schlussfolgerungen und Ausblick

Mit diesem Dokument liegt eine Beschreibung für die strukturierte Datenerfassung und Kartierung im Gelände sowie für die Erstellung eines digitalen Datensatzes (inklusive Karten) vor. Damit ist eine zitierbare Grundlage für die geologische Landesaufnahme in den Themenbereichen Quartär und Geomorphologie, bestehend aus den hierarchischen Ebenen „Lithogenetische Einheiten", „Geomorphologische Einheiten" und „Quartäre Phänomene" einschließlich der dazugehörigen Begriffskataloge, gegeben.

Die Begriffskataloge spiegeln den derzeitigen Wissenstand wider und sind dementsprechend nach einer fachredaktionellen Prüfung modifizier- und erweiterbar.

Dank

Dieses Werk ist kein Produkt einer isolierten Wissenschaft im „Elfenbeinturm", sondern wurde im Hinblick auf größtmögliche Akzeptanz auch durch Diskussionen innerhalb der Kollegenschaft entwickelt. Besonderer Dank gilt Markus Palzer-Khomenko für die Unterstützung bei der Übersetzung der Fachbegriffe und Definitionen ins Englische sowie für fachliche Diskussionen. Zudem sind wir folgenden Kollegen zu Dank verpflichtet: Isabella Bayer und Horst Heger für die Mitarbeit an der Begriffsdatenbank; Dirk van Husen, Gerhard Doppler, Marc Ostermann, Christian Zangerl und Lukas Plan für ihre konstruktive Durchsicht und Verbesserungsvorschläge; Alfred Gruber, Hans-Georg Krenmayr, Gerhard Bryda, Michael Moser, Ralf Schuster und Manfred Linner für hilfreiche Anmerkungen.

Anmerkung zu Begriffstabellen (Tab. 1–6) und Symbolikvorschlägen (Anhänge 1–3)

Die Nummern (L1, etc.) sind nur zur besseren Orientierung in diesem Dokument gedacht und beziehen sich nicht auf eine allgemein gültige Nummer für den jeweiligen Begriff.

Nr.	Lithogenetische Einheit
L1	**Anthropogene Ablagerung**
L2	Anthropogene Ablagerung → Anthropogene Auffüllung
L3	Anthropogene Ablagerung → Anthropogene Aufschüttung
L4	Anthropogene Ablagerung → Anthropogene Aufschüttung → Dammbauwerk
L5	Anthropogene Ablagerung → Deponiekörper
L6	Anthropogene Ablagerung → Flugasche
L7	**Äolische Ablagerung**
L8	Äolische Ablagerung → Flugsand
L9	Äolische Ablagerung → Löss
L10	Äolische Ablagerung → Lösslehm
L11	Äolische Ablagerung → Vulkanische Aschenablagerung
L12	**Fluviatile Ablagerung**
L13	Fluviatile Ablagerung → Ablagerung in Talsohlen und Talkerben
L14	Fluviatile Ablagerung → Bach- und Flussablagerung
L15	Fluviatile Ablagerung → Bach- und Flussablagerung → Flussablagerung
L16	Fluviatile Ablagerung → Bach- und Flussablagerung → Flussbettablagerung
L17	Fluviatile Ablagerung → Bach- und Flussablagerung → Überschwemmungsablagerung
L18	Fluviatile Ablagerung → Wildbachablagerung
L19	Fluviatile Ablagerung → Murkegel
L20	Fluviatile Ablagerung → Schwemmkegel
L21	Fluviatile Ablagerung → Schwemmfächer
L22	**Glaziofluviatile Ablagerung**
L23	Glaziofluviatile Ablagerung → Sander
L24	Glaziofluviatile Ablagerung → Subglaziale Schmelzwasserablagerung
L25	Glaziofluviatile Ablagerung → Subglaziale Schmelzwasserablagerung → Eskerablagerung
L26	Glaziofluviatile Ablagerung → Eisrandablagerung
L27	Glaziofluviatile Ablagerung → Kameablagerung
L28	**Glaziogene Ablagerung**
L29	Glaziogene Ablagerung → Grundmoränenablagerung
L30	Glaziogene Ablagerung → Ablationsmoränenablagerung
L31	Glaziogene Ablagerung → Ablationsblock
L32	Glaziogene Ablagerung → Ablationsblock → Erratischer Block
L33	Glaziogene Ablagerung → End- und Seitenmoränenablagerung
L34	Glaziogene Ablagerung → Moränenstreu
L35	**Glaziolakustrine Ablagerung**
L36	Glaziolakustrine Ablagerung → Glaziolakustrine Beckenablagerung
L37	Glaziolakustrine Ablagerung → Subaquatische Moränenablagerung
L38	Glaziolakustrine Ablagerung → Dropstone Block
L39	**Gravitative Ablagerung**
L40	Gravitative Ablagerung → Bergsturzablagerung
L41	Gravitative Ablagerung → Bergsturzablagerung → Bergsturzgleitmasse
L42	Gravitative Ablagerung → Bergsturzablagerung → Sturzstromablagerung
L43	Gravitative Ablagerung → Felssturzablagerung
L44	Gravitative Ablagerung → Sturzblock
L45	Gravitative Ablagerung → Fließmasse
L46	Gravitative Ablagerung → Fließmasse → Erdstromablagerung
L47	Gravitative Ablagerung → Fließmasse → Murablagerung
L48	Gravitative Ablagerung → Fließmasse → Schuttstromablagerung

L49	Gravitative Ablagerung → Gleitmasse
L50	Gravitative Ablagerung → Hangablagerung
L51	Gravitative Ablagerung → Hangablagerung → Hangbrekzie
L52	Gravitative Ablagerung → Hangablagerung → Hangablagerung mit Moränenmaterial
L53	Gravitative Ablagerung → Hangablagerung → Schuttkegel
L54	Gravitative Ablagerung → Lawinenschuttablagerung
L55	Gravitative Ablagerung → Solifluktionsablagerung
L56	**Lakustrine Ablagerung**
L57	Lakustrine Ablagerung → Deltaablagerung
L58	Lakustrine Ablagerung → Rückstauablagerung
L59	Lakustrine Ablagerung → Seebeckenablagerung
L60	Lakustrine Ablagerung → Strandablagerung
L61	**Palustrische Ablagerung**
L62	Palustrische Ablagerung → Torfablagerung
L63	**Permafrostablagerung**
L64	Permafrostablagerung → Blockgletscher
L65	Permafrostablagerung → Blockgletscherablagerung
L66	Permafrostablagerung → Geli-Solifluktionsablagerung
L67	**Flächenspülungsablagerung**
L68	Flächenspülungsablagerung → Schwemmlöss
L69	Flächenspülungsablagerung → Verschwemmte Moränenablagerung
L70	**Chemische und Biochemische Ausfällungen**
L71	Chemische und Biochemische Ausfällungen → Sinterkalk
L72	Chemische und Biochemische Ausfällungen → Alm

Tab. 1.
Lithogenetische Einheiten – Hierarchie.

Nr.	Geomorphologische Einheit
G1	**Anthropogene Form**
G2	**Äolische Form**
G3	Äolische Form → Düne
G4	**Erosionsform**
G5	Erosionsform → Erdpyramide
G6	Erosionsform → Felsterrasse
G7	Erosionsform → Paläo-Kolk
G8	Erosionsform → Geländekante
G9	Erosionsform → Geländekante → Erosionskante
G10	Erosionsform → Geländekante → Terrassenkante
G11	Erosionsform → Verebnungsfläche
G12	Erosionsform → Yardang (Windhöcker)
G13	Erosionsform → Yardang (Windhöcker) → Windkanter
G14	**Glaziofluviatile Form**
G15	Glaziofluviatile Form → Übergangskegel (Sander)
G16	**Glaziogene Form**
G17	Glaziogene Form → Glaziogene Erosionsform
G18	Glaziogene Form → Glaziogene Erosionsform → Gletschermühle
G19	Glaziogene Form → Glaziogene Erosionsform → Gletscherschliff
G20	Glaziogene Form → Glaziogene Erosionsform → Muschelbruch

G21	Glaziogene Form → Glaziogene Erosionsform → Rat Tail
G22	Glaziogene Form → Glaziogene Erosionsform → Glaziale Striemungen
G23	Glaziogene Form → Glaziogene Erosionsform → Schliffgrenze
G24	Glaziogene Form → Glaziogene Erosionsform → Rundhöcker
G25	Glaziogene Form → Glaziogene Erosionsform → Whaleback
G26	Glaziogene Form → Glaziogene Erosionsform → Subglaziale Schmelzwasserrinne
G27	Glaziogene Form → End- und Seitenmoränenwall
G28	Glaziogene Form → Esker
G29	Glaziogene Form → Subglaziale Wallform
G30	Glaziogene Form → Subglaziale Wallform → Drumlin
G31	Glaziogene Form → Subglaziale Wallform → Flute
G32	Glaziogene Form → Toteisloch
G33	**Gravitative Form**
G34	Gravitative Form → Abrisskante einer Massenbewegung
G35	Gravitative Form → Abrisskante einer Massenbewegung → Abrisskante einer Fließmasse
G36	Gravitative Form → Abrisskante einer Massenbewegung → Abrisskante einer Gleitmasse
G37	Gravitative Form → Abrisskante einer Massenbewegung → Abrisskante einer Sturzmasse
G38	Gravitative Form → Abrisskante einer Massenbewegung → Abrisskante einer tiefgreifenden Hangdeformation
G39	Gravitative Form → Abrisskante einer Massenbewegung → Abrisskante eines Bergsturzes
G40	Gravitative Form → Antithetischer Bruch
G41	Gravitative Form → Zerrspalte, Zerrgraben
G42	Gravitative Form → Aufgelockerter Bereich durch Driften
G43	Gravitative Form → Bereich einer Gleitung
G44	Gravitative Form → Bereich eines langsamen Fließens
G45	Gravitative Form → Bereich einer tiefgreifenden Hangdeformation
G46	Gravitative Form → Toppling (Kippung)
G47	Gravitative Form → Bereich eines Talzuschubs
G48	Gravitative Form → Tiefgreifend aufgelockerter Fels
G49	Gravitative Form → Erdfall
G50	Gravitative Form → Tomahügel
G51	Gravitative Form → Massenbewegungswall
G52	Gravitative Form → Massenbewegungswall → Kompressionswall
G53	Gravitative Form → Massenbewegungswall → Randwall einer Massenbewegung
G54	Gravitative Form → Massenbewegungswall → Sturzstromwall
G55	**Fluviatile Form**
G56	Fluviatile Form → Ehemaliger Abfluss, Trockental
G57	Fluviatile Form → Natürlicher Damm (Levée)
G58	**Karsthohlform**
G59	Karsthohlform → Doline
G60	Karsthohlform → Doline → Einsturzdoline
G61	Karsthohlform → Dolinenfeld
G62	Karsthohlform → Polje
G63	**Oberflächliche Karstlösungsform**
G64	Oberflächliche Karstlösungsform → Karren
G65	Oberflächliche Karstlösungsform → Karren → Karrentisch
G66	**Höhle**
G67	Höhle → Halbhöhle
G68	Höhle → Erosionshöhle
G69	Höhle → Spalthöhle
G70	Höhle → Talushöhle

G71	**Permafrostform**
G72	Permafrostform → Blockgletscherwall
G73	Permafrostform → Wall einer Blockgletscherablagerung
G74	**Terrassenniveau**
G75	Terrassenniveau → Terrassen Niveau 1
G76	Terrassenniveau → Terrassen Niveau 2
G77	Terrassenniveau → Terrassen Niveau 3
G78	Terrassenniveau → Austufe
G79	Terrassenniveau → Austufe → Austufe Niveau 1
G80	Terrassenniveau → Austufe → Austufe Niveau 2

Tab. 2.
Geomorphologische Einheiten – Hierarchie.

Nr.	Quartäres Phänomen
P1	**Anthropogenes Phänomen**
P2	**Verwitterungsphänomen**
P3	Verwitterungsphänomen → Tiefgreifende Verwitterung
P4	Verwitterungsphänomen → Tiefgreifende Verwitterung → Tiefgreifende Verwitterung/Vergrusung
P5	Verwitterungsphänomen → Tiefgreifende Verwitterung → Tiefgreifende Verwitterung/Verlehmung
P6	Verwitterungsphänomen → Tiefgreifende Verwitterung → Wollsackverwitterung
P7	Verwitterungsphänomen → Tiefgreifende Verwitterung → Geologische Orgel
P8	Verwitterungsphänomen → Paläoboden
P9	**Gravitatives Phänomen**
P10	Gravitatives Phänomen → Umrandung eines Massenbewegungskörpers
P11	Gravitatives Phänomen → Umrandung eines Massenbewegungskörpers → Umrandung einer tiefgreifenden Hangdeformation
P12	**Hydrologisches Phänomen**
P13	Hydrologisches Phänomen → Abflusslose Senke
P14	Hydrologisches Phänomen → Moor
P15	Hydrologisches Phänomen → Moor → Hochmoor
P16	Hydrologisches Phänomen → Moor → Niedermoor
P17	Hydrologisches Phänomen → Anmoor
P18	Hydrologisches Phänomen → Vernässung
P19	Hydrologisches Phänomen → Schwinde
P20	Hydrologisches Phänomen → Schwinde → Ponor
P21	**Karstverwandtes Phänomen**
P22	Karstverwandtes Phänomen → Paläokarst
P23	**Permafrostphänomen**
P24	Permafrostphänomen → Permafrostverwitterung
P25	Permafrostphänomen → Eiskeil-Pseudomorphose
P26	Permafrostphänomen → Eiskeilnetz (fossil)
P27	Permafrostphänomen → Frostmusterboden
P28	Permafrostphänomen → Kryoturbation
P29	Permafrostphänomen → Unterkühlte Schutthalde

Tab. 3.
Quartäre Phänomene – Hierarchie.

Nr.		Deutsch	Englisch
L1	Name	**Anthropogene Ablagerung**	**Anthropogenic deposit**
	Definition	Ablagerung, die durch menschliche Tätigkeit (künstlich) erzeugt wurde.	A human-made (artificial) deposit.
	Quelle/source	Diese Publikation; verändert nach BWG (2003)	This publication; modified from BWG (2003)
	Hierarchie/hierarchy	Anthropogene Ablagerung	Anthropogenic deposit
L2	Name	Anthropogene Auffüllung	Fill
	Definition	Ablagerung, die durch menschliche Tätigkeit (künstlich) erzeugt wurde und einen Hohlraum füllt.	A deposit formed by human activity (artificially) to fill up a cavity.
	Quelle/source	Diese Publikation	This publication
	Hierarchie/hierarchy	Anthropogene Ablagerung → Anthropogene Auffüllung	Anthropogenic deposit → Fill
L3	Name	Anthropogene Aufschüttung	Embankment
	Definition	Ablagerung, die durch menschliche Tätigkeit (künstlich) erzeugt wurde und über das bisherige Niveau hinausragt.	A deposit formed by human activity (artificially), which rises a surface above the previous ground level.
	Quelle/source	Diese Publikation; verändert nach BWG (2003)	This publication; modified from BWG (2003)
	Hierarchie/hierarchy	Anthropogene Ablagerung → Anthropogene Aufschüttung	Anthropogenic deposit → Embankment
L4	Name	Dammbauwerk	Dam structure
	Definition	Aufschüttung in Wallform, die durch menschliche Tätigkeit (künstlich) erzeugt wurde und eine schützende oder stauende Funktion übernimmt.	A human-made (artificial) ridge-like embankment with a protecting or damming purpose.
	Quelle/source	Diese Publikation; verändert nach BWG (2003)	This publication; modified from BWG (2003)
	Hierarchie/hierarchy	Anthropogene Ablagerung → Anthropogene Aufschüttung → Dammbauwerk	Anthropogenic deposit → Embankment → Dam structure
L5	Name	Deponiekörper	Landfill
	Definition	Ablagerung die aus Aushub oder Abfall besteht.	A deposit consisting of excavation or rubbish.
	Quelle/source	Diese Publikation; verändert nach BWG (2003)	This publication; modified from BWG (2003)
	Hierarchie/hierarchy	Anthropogene Ablagerung → Deponiekörper	Anthropogenic deposit → Landfill
L6	Name	Flugasche	Fly ash
	Definition	Fester, disperser (teilchenförmiger, partikelförmiger, staubförmiger) Rückstand von Verbrennungen, der auf Grund seiner hohen Dispersität (Feinverteilung) mit Rauchgasen ausgetragen wird.	Coal combustion product composed of fine particles that are driven out of the boiler with the flue gases.
	Quelle/source	Diese Publikation	This publication
	Hierarchie/hierarchy	Anthropogene Ablagerung → Flugasche	Anthropogenic deposit → Fly ash
L7	Name	**Äolische Ablagerung**	**Aeolian deposit**
	Definition	Ablagerung, die durch Einwirkung von Wind gebildet wurde.	A deposit that has been transported by wind.
	Quelle/source	NEUENDORF et al. (2005)	NEUENDORF et al. (2005)
	Hierarchie/hierarchy	Äolische Ablagerung	Aeolian deposit
L8	Name	Flugsand	Cover sand
	Definition	Äolische Ablagerung von feinem bis sehr feinem Sand.	An Aeolian deposit of fine to very fine sand.
	Quelle/source	Diese Publikation; verändert nach NEUENDORF et al. (2005), HINZE et al. (1989)	This publication; modified from NEUENDORF et al. (2005), HINZE et al. (1989)
	Hierarchie/hierarchy	Äolische Ablagerung → Flugsand	Aeolian deposit → Cover sand
L9	Name	Löss	Loess
	Definition	Äolische Ablagerung, welche typischerweise aus Silt besteht und karbonathaltig, unverfestigt, porös und nicht geschichtet ist.	A wind-blown silty deposit that is commonly carbonate-bearing, friable, porous and unstratified.
	Quelle/source	NEUENDORF et al. (2005), HINZE et al. (1989)	NEUENDORF et al. (2005), HINZE et al. (1989)
	Hierarchie/hierarchy	Äolische Ablagerung → Löss	Aeolian deposit → Loess
L10	Name	Lösslehm	Loess loam
	Definition	Ablagerung, welche durch Verwitterungsvorgänge aus Löss entsteht, Tonmineralneubildungen enthält und karbonatfrei ist.	A clay-rich carbonate-free weathering product of loess.
	Quelle/source	Diese Publikation; verändert nach HINZE et al. (1989)	This publication; modified from HINZE et al. (1989)
	Hierarchie/hierarchy	Äolische Ablagerung → Lösslehm	Aeolian deposit → Loess loam

L11	Name	Vulkanische Aschenablagerung	Volcanic ash deposit
	Definition	Ablagerung, die aus pyroklastischen Teilchen < 2 mm besteht und bei einem explosiven Ausbruch eines Vulkans gebildet wurde.	A deposit consisting of pyroclastic particles < 2 mm, which were formed during a explosive volcanic eruption.
	Quelle/source	Diese Publikation	This publication
	Hierarchie/hierarchy	Äolische Ablagerung → Vulkanische Aschenablagerung	Aeolian deposit → Volcanic ash deposit
L12	Name	**Fluviatile Ablagerung**	**Fluvial deposit**
	Definition	Ablagerung eines Fließgewässers.	A deposit of a watercourse.
	Quelle/source	Diese Publikation; verändert nach NEUENDORF et al. (2005)	This publication; modified from NEUENDORF et al. (2005)
	Hierarchie/hierarchy	Fluviatile Ablagerung	Fluvial deposit
L13	Name	Ablagerung in Talsohlen und Talkerben	Valley fill
	Definition	Ablagerung in Tälern mit nicht ebenen Talsohlen (V-Täler), deren Genese nicht mehr eindeutig bestimmbar ist bzw. deren Genese eine Kombination verschiedener Prozesse ist (fluviatil, gravitativ, Solifluktion etc.).	The unconsolidated sediment deposited by any agent so as to fill or partly fill a valley.
	Quelle/source	Diese Publikation; verändert nach HINZE et al. (1989), NEUENDORF et al. (2005)	This publication; modified from HINZE et al. (1989), NEUENDORF et al. (2005)
	Hierarchie/hierarchy	Fluviatile Ablagerung → Ablagerung in Talsohlen und Talkerben	Fluvial deposit → Valley fill
L14	Name	Bach- und Flussablagerung	Creek and river deposit
	Definition	Ablagerung, welche die Kombination der verschiedenen Ablagerungsräume eines Baches oder Flusses beinhaltet.	A deposit formed in creeks or rivers.
	Quelle/source	Diese Publikation	This publication
	Hierarchie/hierarchy	Fluviatile Ablagerung → Bach- und Flussablagerung	Fluvial deposit → Creek and river deposit
L15	Name	Flussablagerung	River deposit
	Definition	Ablagerung, welche die Kombination der verschiedenen Ablagerungsräume eines Flusses beinhaltet.	A deposit formed in rivers.
	Quelle/source	Diese Publikation	This publication
	Hierarchie/hierarchy	Fluviatile Ablagerung → Bach- und Flussablagerung → Flussablagerung	Fluvial deposit → Creek and river deposit → River deposit
L16	Name	Flussbettablagerung	River-bed deposit
	Definition	Ablagerung, die im Bett eines Flusses abgelagert wurde und von der Größe des Fließgewässers abhängend aus meist gut sortierten und gerundeten Komponenten besteht.	A deposit formed within a river bed and consisting of mostly well sorted and rounded components.
	Quelle/source	Diese Publikation	This publication
	Hierarchie/hierarchy	Fluviatile Ablagerung → Bach- und Flussablagerung → Flussbettablagerung	Fluvial deposit → Creek and river deposit → River-bed deposit
L17	Name	Überschwemmungsablagerung	Overbank deposit
	Definition	Ablagerung, die während Überschwemmungsereignissen eines Fließgewässers entsteht, bei denen der normale Gewässerverlauf (Bach- oder Flussbett) überwunden wird. Das Korngrößenspektrum der Sedimente umfasst Ton-, Silt- und Feinsandfraktionen.	A deposit formed during a flooding event when flowing waters leave their bed. The sediments include clay, silt, and fine sand.
	Quelle/source	Diese Publikation; verändert nach HINZE et al. (1989)	This publication; modified from HINZE et al. (1989)
	Hierarchie/hierarchy	Fluviatile Ablagerung → Bach- und Flussablagerung → Überschwemmungsablagerung	Fluvial deposit → Creek and river deposit → Overbank deposit
L18	Name	Wildbachablagerung	Torrent deposit
	Definition	Ablagerung, die vor allem durch periodischen Oberflächenabfluss (Starkregen) in Wildbächen entsteht. Die Ablagerung besteht zumeist aus einer unsortierten Mischung mit Dominanz von Schutt und Blöcken.	A deposit formed mostly by periodic runoff (heavy rain) in torrents consisting mainly of unsorted debris and boulders.
	Quelle/source	Diese Publikation; verändert nach NEUENDORF et al. (2005)	This publication; modified from NEUENDORF et al. (2005)
	Hierarchie/hierarchy	Fluviatile Ablagerung → Wildbachablagerung	Fluvial deposit → Torrent deposit

L19	Name	Murkegel	Debris flood cone
	Definition	Ablagerung, die durch wiederholte Abgänge und Überlagerung von Muren in derselben Bahn entsteht und einen an den Hangfuß angelehnten Halbkegel ausbildet, dessen Spitze die Grenze zwischen der Transportbahn und dem Ablagerungskörper markiert.	A deposit formed by repeated debris floods following the same path and become superimposed to form a cone-like shape.
	Quelle/source	Diese Publikation; verändert nach AHNERT (2015)	This publication; modified from AHNERT (2015)
	Hierarchie/hierarchy	Fluviatile Ablagerung → Murkegel	Fluvial deposit → Debris flood cone
L20	Name	Schwemmkegel	Alluvial cone
	Definition	Unterform des Schwemmfächers, kegelförmig ausgebildet und im oberen Teil typischerweise steiler als ca. 20° ist.	Type of alluvial fan, which is shaped like a cone and typically steeper than 20° in its upper part.
	Quelle/source	Diese Publikation; verändert nach Busche et al. (2005), AHNERT (2015)	This publication; modified from BUSCHE et al. (2005), AHNERT (2015)
	Hierarchie/hierarchy	Fluviatile Ablagerung → Schwemmkegel	Fluvial deposit → Alluvial cone
L21	Name	Schwemmfächer	Alluvial fan
	Definition	Ablagerung, welche durch periodischen Oberflächenabfluss an Geländestufen, an denen sich die Fließgeschwindigkeit verringert, in Form von flachen fächerförmigen Körpern entsteht.	A deposit that has been formed by periodic run-off as a flat, fan-like body.
	Quelle/source	Diese Publikation; verändert nach NEUENDORF et al. (2005), HINZE et al. (1989)	This publication; modified from NEUENDORF et al. (2005), HINZE et al. (1989)
	Hierarchie/hierarchy	Fluviatile Ablagerung → Schwemmfächer	Fluvial deposit → Alluvial fan
L22	Name	**Glaziofluviatile Ablagerung**	**Glaciofluvial deposit**
	Definition	Ablagerung aus einem Gletscherschmelzwasser-gespeisten Fließgewässer.	Deposit of a glacial meltwater stream.
	Quelle/source	Diese Publikation; verändert nach NEUENDORF et al. (2005)	This publication; modified from NEUENDORF et al. (2005)
	Hierarchie/hierarchy	Glaziofluviatile Ablagerung	Glaciofluvial deposit
L23	Name	Sander	Outwash plain
	Definition	Breite, leicht abfallende, kegel- bis tafelförmige, glaziofluviatile Ablagerung (überwiegend Sand und Kies), welche durch Schmelzwasserströme aus Gletschertoren gebildet wurde.	A broad, gently sloping plain made up of sheet-like glaciofluvial deposits (mainly sand and gravel) formed by meltwater streams flowing in front of a glacier.
	Quelle/source	NEUENDORF et al. (2005)	NEUENDORF et al. (2005)
	Hierarchie/hierarchy	Glaziofluviatile Ablagerung → Sander	Glaciofluvial deposit → Outwash plain
L24	Name	Subglaziale Schmelzwasserablagerung	Subglacial meltwater deposit
	Definition	Glaziofluviatile Ablagerung, die durch Schmelzwasser unterhalb von Gletschern oder Inlandeis gebildet wurde.	A glaciofluvial deposit formed by melting water at the base of a glacier or ice-sheet.
	Quelle/source	Diese Publikation	This publication
	Hierarchie/hierarchy	Glaziofluviatile Ablagerung → Subglaziale Schmelzwasserablagerung	Glaciofluvial deposit → Subglacial meltwater deposit
L25	Name	Eskerablagerung	Esker deposit
	Definition	Glaziofluviatile Ablagerung meist in Wallform, die in ehemaligen Abflussbahnen auf, im oder an der Basis eines Gletschers von Schmelzwässern gebildet wurde.	A glaciofluvial ridge-like deposit formed in melt-water channels on top, within or at the base of a glacier.
	Quelle/source	HEINISCH et al. (2015)	HEINISCH et al. (2015)
	Hierarchie/hierarchy	Glaziofluviatile Ablagerung → Subglaziale Schmelzwasserablagerung → Eskerablagerung	Glaciofluvial deposit → Subglacial meltwater deposit → Esker deposit
L26	Name	Eisrandablagerung	Ice-marginal deposit
	Definition	Ablagerung, die in einer durch einen Gletscher verursachten Stausituation am Rand des Eises angelagert wurde. Aufgebaut wird die Ablagerung üblicherweise aus glaziofluviatilen und glaziolakustrinen Sedimenten.	A deposit formed in a glacier-dammed position at the glaciers limits. It‘s mostly composed of glaciofluvial to glaciolacustrine sediments.
	Quelle/source	Diese Publikation	This publication
	Hierarchie/hierarchy	Glaziofluviatile Ablagerung → Eisrandablagerung	Glaciofluvial deposit → Ice-marginal deposit

L27	Name	Kameablagerung	Kame deposit
	Definition	Ablagerung in Hohlräume, die auf oder zwischen Toteis eines zerfallenden Gletschers entstehen. Aufgebaut wird die Ablagerung üblicherweise aus glaziofluviatilen und glaziolakustrinen Sedimenten.	A deposit formed in cavities on, or between dead ice of a retreating glacier, usually consisting of glaciofluvial and glaciolacustrine sediments.
	Quelle/source	Diese Publikation; verändert nach HINZE et al. (1989)	This publication; modified from HINZE et al. (1989)
	Hierarchie/hierarchy	Glaziofluviatile Ablagerung → Kameablagerung	Glaciofluvial deposit → Kame deposit
L28	Name	**Glaziogene Ablagerung**	**Glaciogenic deposit**
	Definition	Direkt vom Gletscher oder Inlandeis abgeleitetes oder gebildetes Sediment.	A glacial deposit formed directly by, or derived from, glaciers or ice-sheets.
	Quelle/source	NEUENDORF et al. (2005)	NEUENDORF et al. (2005)
	Hierarchie/hierarchy	Glaziogene Ablagerung	Glaciogenic deposit
L29	Name	Grundmoränenablagerung	Subglacial traction till
	Definition	Subglaziale Sedimentablagerung eines Gletschers, der entweder aktiv über sein Bett gleitet und/oder dieses im Zuge der Bewegung durchgreifend deformiert.	Sediment deposited by a glacier sole either sliding over and/or deforming its bed.
	Quelle/source	Diese Publikation; verändert nach LUKAS & ROTHER (2016), EVANS et al. (2006)	This publication; modified from LUKAS & ROTHER (2016), EVANS et al. (2006)
	Hierarchie/hierarchy	Glaziogene Ablagerung → Grundmoränenablagerung	Glaciogenic deposit → Subglacial traction till
L30	Name	Ablationsmoränenablagerung	Melt-out till
	Definition	Ablagerung, die durch das Ausschmelzen von im oder auf dem Gletscher mitgeführtem Material entstanden ist.	A deposit formed by the melt out of material transported within or on top of a glacier.
	Quelle/source	Diese Publikation; verändert nach HINZE et al. (1989)	This publication; modified from HINZE et al. (1989)
	Hierarchie/hierarchy	Glaziogene Ablagerung → Ablationsmoränenablagerung	Glaciogenic deposit → Melt-out till
L31	Name	Ablationsblock	Melt-out block
	Definition	Räumlich isoliertes Gesteinsfragment (mindestens Blockgröße), welches nach einem Transport im oder auf dem Gletscher durch das Ausschmelzen abgelagert wurde.	A large rock fragment (min. boulder size) deposited by the melt out of material after a transport within or on top of a glacier.
	Quelle/source	Diese Publikation	This publication
	Hierarchie/hierarchy	Glaziogene Ablagerung → Ablationsblock	Glaciogenic deposit → Melt-out block
L32	Name	Erratischer Block	Erratic boulder
	Definition	Gesteinsfragment (mindestens Blockgröße), welches von Gletschern transportiert wurde und dessen lithologische Zusammensetzung nicht jener im Ablagerungsgebiet entspricht.	A large rock fragment (min. boulder size) carried by glacier and those lithological compositions do not fit the lithological composition of the deposition area.
	Quelle/source	Diese Publikation; verändert nach NEUENDORF et al. (2005)	This publication; modified from NEUENDORF et al. (2005)
	Hierarchie/hierarchy	Glaziogene Ablagerung → Ablationsblock → Erratischer Block	Glaciogenic deposit → Melt-out block → Erratic boulder
L33	Name	End- und Seitenmoränenablagerung	Till of a latero-frontal moraine
	Definition	Ablagerung, die am seitlichen oder frontalen aktiven Gletscherrand durch Ausschmelzen von Material aus dem Gletscher oder durch gletscherbedingten Zusammenschub von Material entsteht.	A deposit formed on the lateral margin or front of an active glacier as a result of melt-out of glacially transported material or material pushed by the glacier.
	Quelle/source	Diese Publikation; verändert nach HINZE et al. (1989)	This publication; modified from HINZE et al. (1989)
	Hierarchie/hierarchy	Glaziogene Ablagerung → End- und Seitenmoränenablagerung	Glaciogenic deposit → Till of a latero-frontal moraine
L34	Name	Moränenstreu	Patchy cover of till
	Definition	Lückenhafte Grund- und/oder Ablationsmoränendecke, die an vielen Stellen den Gesteinsuntergrund erkennen lässt.	Patchy cover of till where the underlying geological unit can be recognized.
	Quelle/source	Diese Publikation; verändert nach SCHUSTER et al. (2006)	This publication; modified from SCHUSTER et al. (2006)
	Hierarchie/hierarchy	Glaziogene Ablagerung → Moränenstreu	Glaciogenic deposit → Patchy cover of till

L35	Name	**Glaziolakustrine Ablagerung**	**Glaciolacustrine deposit**
	Definition	Direkt vom Gletscher beeinflusste Ablagerung in ein stehendes Gewässer (See).	A deposit in a lake formed under glacial influence.
	Quelle/source	Diese Publikation; verändert nach BWG (2003)	This publication; modified from BWG (2003)
	Hierarchie/hierarchy	Glaziolakustrine Ablagerung	Glaciolacustrine deposit
L36	Name	Glaziolakustrine Beckenablagerung	Glaciolacustrine basin deposit
	Definition	Direkt vom Gletscher beeinflusste feinkörnige Ablagerung aus einer Suspension in ein stehendes Gewässer (See).	A fine-grained deposit formed in a lake basin under glacial influence by suspension load.
	Quelle/source	Diese Publikation	This publication
	Hierarchie/hierarchy	Glaziolakustrine Ablagerung → Glaziolakustrine Beckenablagerung	Glaciolacustrine deposit → Glaciolacustrine basin deposit
L37	Name	Subaquatische Moränenablagerung	Waterlain till
	Definition	Glaziale Ablagerung, die durch Ausschmelzen an der Gletscherbasis direkt in ein stehendes Gewässer sedimentiert wurde.	A glacial deposit formed due to melt-out at the base of a glacier directly into a standing water body.
	Quelle/source	Diese Publikation; verändert nach Benn & Evans (2010)	This publication; modified from Benn & Evans (2010)
	Hierarchie/hierarchy	Glaziolakustrine Ablagerung → Subaquatische Moränenablagerung	Glaciolacustrine deposit → Waterlain till
L38	Name	Dropstone Block	Dropstone boulder
	Definition	Gesteinsfragment (mindestens Blockgröße), das aus Treibeis ausschmilzt und auf dem Seegrund abgelagert wird.	Isolated clast at least of boulder size dropped onto a lake bed from floating ice.
	Quelle/source	Diese Publikation; verändert nach Benn & Evans (2010)	This publication; modified from Benn & Evans (2010)
	Hierarchie/hierarchy	Glaziolakustrine Ablagerung → Dropstone Block	Glaciolacustrine deposit → Dropstone boulder
L39	Name	**Gravitative Ablagerung**	**Gravitational deposit**
	Definition	Ablagerung, die durch schwerkraftbedingte Umlagerung von Gesteinsmassen entstanden ist.	A deposit formed by mass wasting.
	Quelle/source	Diese Publikation	This publication
	Hierarchie/hierarchy	Gravitative Ablagerung	Gravitational deposit
L40	Name	Bergsturzablagerung	Deposit of a rapid landslide
	Definition	Ablagerung, die durch eine Massenbewegung mit hoher Geschwindigkeit (in Sekunden oder wenigen Minuten) entstanden ist und ein Volumen von über 1 Mio. m^3 oder eine Fläche von über 0,1 km^2 besitzt.	A deposit of a mass movement formed within seconds to minutes with a volume > 1 Mio. m^3 or a surface > 0.1 km^2.
	Quelle/source	Abele (1974)	Abele (1974)
	Hierarchie/hierarchy	Gravitative Ablagerung → Bergsturzablagerung	Gravitational deposit → Deposit of a rapid landslide
L41	Name	Bergsturzgleitmasse	Deposit of a rapid landslide with basal sliding plane
	Definition	Bergsturzablagerung, die durch extrem rasche Hangabwärtsbewegung von Locker- oder Festgestein entlang einer oder mehrerer diskreter Bewegungsflächen oder -zonen, in denen der Hauptanteil der Hangdeformation stattfindet (Gleiten), entstanden ist.	Rapid landslide deposit formed by extremely rapid downslope movement along one or more distinct displacement planes.
	Quelle/source	Diese Publikation; verändert nach Abele (1974), Zangerl et al. (2008)	This publication; modified from Abele (1974), Zangerl et al. (2008)
	Hierarchie/hierarchy	Gravitative Ablagerung → Bergsturzablagerung → Bergsturzgleitmasse	Gravitational deposit → Deposit of a rapid landslide → Deposit of a rapid landslide with basal sliding plane
L42	Name	Sturzstromablagerung	Rock avalanche deposit
	Definition	Bergsturzablagerung, die sich während des Bergsturzes durch dynamische Fragmentierung wie eine fluidisierte Masse verhalten hat.	Deposit of a rapid landslide, which was dynamically fragmented and behave like a fluid mass during the extremely rapid transport.
	Quelle/source	Pollet & Schneider (2004), Hsü (1975), Heim (1932)	Pollet & Schneider (2004), Hsü (1975), Heim (1932)
	Hierarchie/hierarchy	Gravitative Ablagerung → Bergsturzablagerung → Sturzstromablagerung	Gravitational deposit → Deposit of a rapid landslide → Rock avalanche deposit
L43	Name	Felssturzablagerung	Rockfall deposit
	Definition	Ablagerung von meist grobblockigem Material, die durch ein Sturzereignis entstanden ist und kleiner als ein Bergsturz ist.	A deposit of boulder-sized material formed by a rockfall event with a smaller dimension than a rapid landslide.
	Quelle/source	Diese Publikation; verändert nach Neuendorf et al. (2005), BWG (2003)	This publication; modified from Neuendorf et al. (2005), BWG (2003)
	Hierarchie/hierarchy	Gravitative Ablagerung → Felssturzablagerung	Gravitational deposit → Rockfall deposit

L44	Name	Sturzblock	Rockfall boulder
	Definition	Ablagerung, die aus einem Einzelblock oder einer kleinen Gruppe von Blöcken besteht und die durch einen Sturzprozess entstanden ist.	A deposit due to a rockfall consisting of a single boulder or a small number of boulders.
	Quelle/source	Diese Publikation; verändert nach BWG (2003)	This publication; modified from BWG (2003)
	Hierarchie/hierarchy	Gravitative Ablagerung → Sturzblock	Gravitational deposit → Rockfall boulder
L45	Name	Fließmasse	Mass flow deposit
	Definition	Ablagerung eines Fließprozesses. Aufgrund der hohen internen Teilbeweglichkeit der bewegten Gesteinsmasse treten potenzielle Gleitzonen nicht auf oder sind dicht angeordnet, kurzlebig und meist nicht erhalten.	A deposit formed by downslope movement without distinct displacement zones.
	Quelle/source	Diese Publikation; verändert nach ZANGERL et al. (2008), CRUDEN & VARNES (1996)	This publication; modified from ZANGERL et al. (2008), CRUDEN & VARNES (1996)
	Hierarchie/hierarchy	Gravitative Ablagerung → Fließmasse	Gravitational deposit → Mass flow deposit
L46	Name	Erdstromablagerung	Earth flow deposit
	Definition	Ablagerung eines Fließprozesses mit Dominanz der Feinanteile (Ton, Silt, Sand) gegenüber den Grobanteilen (Kies, Steine, Blöcke). Aufgrund der hohen internen Teilbeweglichkeit der bewegten Gesteinsmasse treten potenzielle Gleitzonen nicht auf oder sind dicht angeordnet, kurzlebig und meist nicht erhalten.	A deposit formed by downslope movement without distinct movement zones, where the fine grained portions (clay, silt, sand) prevail compared to coarse grained portions (gravel, cobbles, boulders).
	Quelle/source	Diese Publikation; verändert nach ZANGERL et al. (2008), LFU (2019a)	This publication; modified from ZANGERL et al. (2008), LFU (2019a)
	Hierarchie/hierarchy	Gravitative Ablagerung → Fließmasse → Erdstromablagerung	Gravitational deposit → Mass flow deposit → Earth flow deposit
L47	Name	Murablagerung	Debris flood deposit
	Definition	Ablagerung, die aus einer sehr rasch hangabwärts fließenden Mischung aus Wasser und Schutt gebildet wurde.	A deposit of a very rapid flow of water, heavily charged with debris traveling in a steep channel.
	Quelle/source	Diese Publikation; verändert nach HINZE et al. (1989), HUNGR et al. (2001)	This publication; modified from HINZE et al. (1989), HUNGR et al. (2001)
	Hierarchie/hierarchy	Gravitative Ablagerung → Fließmasse → Murablagerung	Gravitational deposit → Mass flow deposit → Debris flood deposit
L48	Name	Schuttstromablagerung	Debris flow deposit
	Definition	Ablagerung eines Fließprozesses mit Dominanz der Grobanteile (Kies, Steine, Blöcke) gegenüber den Feinanteilen (Ton, Silt, Sand). Aufgrund der hohen internen Teilbeweglichkeit der bewegten Gesteinsmasse treten potenzielle Gleitzonen nicht auf oder sind dicht angeordnet, kurzlebig und meist nicht erhalten.	A deposit formed by downslope movement without distinct movement zones, where the coarse grained portions (gravel, cobbles, boulders) prevail compared to fine grained portions (clay, silt, sand).
	Quelle/source	Diese Publikation; verändert nach ZANGERL et al. (2008), LFU (2019a).	This publication; modified from ZANGERL et al. (2008), LFU (2019a)
	Hierarchie/hierarchy	Gravitative Ablagerung → Fließmasse → Schuttstromablagerung	Gravitational deposit → Mass flow deposit → Debris flow deposit
L49	Name	Gleitmasse	Slide mass deposit
	Definition	Ablagerung, die durch die Hangabwärtsbewegung von Locker- oder Festgestein entlang einer oder mehrerer diskreter Bewegungsflächen oder -zonen, in denen der Hauptanteil der Hangdeformation stattfindet (Gleiten), entstanden ist.	A deposit formed by downslope movement where most of the deformation is localized on one or several distinct displacement horizon(s).
	Quelle/source	Diese Publikation; verändert nach ZANGERL et al. (2008), CRUDEN & VARNES (1996)	This publication; modified from ZANGERL et al. (2008), CRUDEN & VARNES (1996)
	Hierarchie/hierarchy	Gravitative Ablagerung → Gleitmasse	Gravitational deposit → Slide mass deposit
L50	Name	Hangablagerung	Talus
	Definition	Ablagerung, die infolge der Rückwitterung von Festgestein entstanden ist und durch Wirkung der Schwerkraft transportiert wurde.	A deposit formed below a weathering rock face and which was transported by gravitational processes.
	Quelle/source	Diese Publikation; verändert nach BWG (2003), NEUENDORF et al. (2005)	This publication; modified from BWG (2003), NEUENDORF et al. (2005)
	Hierarchie/hierarchy	Gravitative Ablagerung → Hangablagerung	Gravitational deposit → Talus

L51	Name	Hangbrekzie	Talus breccia
	Definition	Ablagerung, die aus gravitativ bewegtem Schutt (Hangschutt) besteht, der diagenetisch verfestigt wurde. Die Verfestigung steht häufig im Zusammenhang mit kalkreichen Hangwässern.	A deposit of gravitationally moved scree which was diagenetically solidified. The lithification is mostly associated to calcareous waters.
	Quelle/source	Diese Publikation; verändert nach NEUENDORF et al. (2005), HINZE et al. (1989)	This publication; modified from NEUENDORF et al. (2005), HINZE et al. (1989)
	Hierarchie/hierarchy	Gravitative Ablagerung → Hangablagerung → Hangbrekzie	Gravitational deposit → Talus → Talus breccia
L52	Name	Hangablagerung mit Moränenmaterial	Slope deposit with reworked till
	Definition	Mischung aus Hangablagerung und umgelagertem glazialem Material.	Mixture of slope deposit and reworked till.
	Quelle/source	Diese Publikation; verändert nach BWG (2003), NEUENDORF et al. (2005)	This publication; modified from BWG (2003), NEUENDORF et al. (2005)
	Hierarchie/hierarchy	Gravitative Ablagerung → Hangablagerung → Hangablagerung mit Moränenmaterial	Gravitational deposit → Talus → Slope deposit with reworked till
L53	Name	Schuttkegel	Talus cone
	Definition	Ablagerung, die infolge der Rückwitterung von Festgestein entstanden ist und durch Wirkung der Schwerkraft transportiert und in Kegelform ausgebildet wurde.	A cone-like deposit formed below a weathering rock face and which was transported by gravitational processes.
	Quelle/source	Diese Publikation; verändert nach BWG (2003)	This publication; modified from BWG (2003)
	Hierarchie/hierarchy	Gravitative Ablagerung → Hangablagerung → Schuttkegel	Gravitational deposit → Talus → Talus cone
L54	Name	Lawinenschuttablagerung	Avalanche talus
	Definition	Ablagerung aus (besonders im Hochgebirge auftretenden Grund-) Lawinen, welche nach Schmelzen des Schnees aus Bodenmaterial und Gesteinsschutt besteht.	Deposits formed by an avalanche (especially in high mountain areas, were the entire snow cover can be stripped off by the avalanche) consisting of soil and rock debris after snowmelt.
	Quelle/source	Diese Publikation; verändert nach AHNERT (2015)	This publication; modified from AHNERT (2015)
	Hierarchie/hierarchy	Gravitative Ablagerung → Lawinenschuttablagerung	Gravitational deposit → Avalanche talus
L55	Name	Solifluktionsablagerung	Solifluction deposit
	Definition	Ablagerung, die durch langsames viskoses Fließen von wassergesättigtem Lockermaterial (Boden und Verwitterungshorizont) entstanden ist.	A deposit formed by slow viscous downslope flow of water-logged soil and other unsorted and saturated surficial material.
	Quelle/source	Diese Publikation; verändert nach NEUENDORF et al. (2005)	This publication; modified from NEUENDORF et al. (2005)
	Hierarchie/hierarchy	Gravitative Ablagerung → Solifluktionsablagerung	Gravitational deposit → Solifluction deposit
L56	Name	**Lakustrine Ablagerung**	**Lacustrine deposit**
	Definition	Ablagerung, die am Grund oder am Rand eines Sees gebildet wurde.	A deposit formed within or along the margin of a lake.
	Quelle/source	NEUENDORF et al. (2005)	NEUENDORF et al. (2005)
	Hierarchie/hierarchy	Lakustrine Ablagerung	Lacustrine deposit
L57	Name	Deltaablagerung	Deltaic deposit
	Definition	Ablagerung, die sich am Mündungsbereich eines Baches oder Flusses in ein stehendes Gewässer (See) bildet und eine gesamte oder Teile einer Deltaabfolge (Bottomset, Foreset, Topset) enthält.	A deposit formed at the mouth of a stream or river into standing water including complete deltaic sequences (bottomset, foreset, topset) or parts of it.
	Quelle/source	Diese Publikation; verändert nach HINZE et al. (1989), BWG (2003)	This publication; modified from HINZE et al. (1989), BWG (2003)
	Hierarchie/hierarchy	Lakustrine Ablagerung → Deltaablagerung	Lacustrine deposit → Deltaic deposit
L58	Name	Rückstauablagerung	Backwater deposit
	Definition	Meist feinkörnige Ablagerung, die in ein durch Massenbewegungen oder Schwemmfächer aufgestautes Gewässer (See) sedimentiert wurde.	A mostly fine grained deposit formed in a standing water body, which was dammed by a mass movement or alluvial cone.
	Quelle/source	Diese Publikation	This publication
	Hierarchie/hierarchy	Lakustrine Ablagerung → Rückstauablagerung	Lacustrine deposit → Backwater deposit
L59	Name	Seebeckenablagerung	Lacustrine basin deposit
	Definition	Feinkörnige Ablagerung, die sich durch Sedimentation in den tieferen Beckenbereichen eines Gewässers (See) gebildet hat.	A fine grained deposit, which was formed in the deeper parts of a standing water body (lake).
	Quelle/source	Diese Publikation; verändert nach HINZE et al. (1989)	This publication; modified from HINZE et al. (1989)
	Hierarchie/hierarchy	Lakustrine Ablagerung → Seebeckenablagerung	Lacustrine deposit → Lacustrine basin deposit

L60	Name	Strandablagerung	Shoreline deposit
	Definition	Ablagerung, die am Ufer eines stehenden Gewässers (See) gebildet wurde.	A deposit which was formed at the shoreline of a standing water body (lake).
	Quelle/source	Diese Publikation	This publication
	Hierarchie/hierarchy	Lakustrine Ablagerung → Strandablagerung	Lacustrine deposit → Shoreline deposit
L61	Name	**Palustrische Ablagerung**	**Palustrin deposit**
	Definition	Ablagerung, die im Ablagerungsmilieu eines Feuchtgebietes (Sumpf, Moor, Marsch) entstanden ist und organisches Material enthält.	A deposit formed under wetland-conditions and which contains organic material.
	Quelle/source	Diese Publikation; verändert nach MARTIN & EIBLMAIER (2003)	This publication; modified from MARTIN & EIBLMAIER (2003)
	Hierarchie/hierarchy	Palustrische Ablagerung	Palustrin deposit
L62	Name	Torfablagerung	Peat
	Definition	Ablagerung, die im Ablagerungsmilieu eines Moores entstanden ist und mindestens 30 % Organik enthält.	A deposit formed in a bog-facies, which contains more than 30 % of organic material.
	Quelle/source	Diese Publikation; verändert nach MARTIN & EIBLMAIER (2003)	This publication; modified from MARTIN & EIBLMAIER (2003)
	Hierarchie/hierarchy	Palustrische Ablagerung → Torfablagerung	Palustrin deposit → Peat
L63	Name	**Permafrostablagerung**	**Permafrost deposit**
	Definition	Ablagerung, die durch (Perma-)Frost bedingte Prozesse gebildet wurde.	A deposit formed in an environment in which permafrost is an important agent.
	Quelle/source	Diese Publikation; verändert nach NEUENDORF et al. (2005)	This publication; modified from NEUENDORF et al. (2005)
	Hierarchie/hierarchy	Permafrostablagerung	Permafrost deposit
L64	Name	Blockgletscher	Rock glacier
	Definition	Ansammlung schlecht sortierter, eckiger Blöcke und feinen Materials, wobei ab etwa einem Meter unter der Oberfläche die Porenräume mit Eis gefüllt sind. Blockgletscher kommen in großen Höhen in Permafrost-Gebieten vor und bilden sich in Karen oder an steilen Bergflanken und bewegen sich durch Gravitation talwärts. Der distale Bereich ist durch eine Reihe von transversalen Wällen und einer typischen Rampen- und Wulst-Geometrie gekennzeichnet.	A mass of poorly sorted angular boulders and fine material with interstitial ice about one meter below the surface. Rock glaciers occur at high altitudes in permafrost areas and are derived from cirque walls or other steep cliffs and move gravitationally driven downslope.
	Quelle/source	Diese Publikation; verändert nach NEUENDORF et al. (2005)	This publication; modified from NEUENDORF et al. (2005)
	Hierarchie/hierarchy	Permafrostablagerung → Blockgletscher	Permafrost deposit → Rock glacier
L65	Name	Blockgletscherablagerung	Rock glacier deposit
	Definition	Ablagerung eines Blockgletschers nach Ausschmelzen des Eises (reliktischer Blockgletscher).	A deposit of a rock glacier after ice melt (relictic rock glacier).
	Quelle/source	Diese Publikation; verändert nach NEUENDORF et al. (2005)	This publication; modified from NEUENDORF et al. (2005)
	Hierarchie/hierarchy	Permafrostablagerung → Blockgletscherablagerung	Permafrost deposit → Rock glacier deposit
L66	Name	Geli-Solifluktionsablagerung	Geli-solifluction deposit
	Definition	Ablagerung, die durch langsames viskoses Fließen von wassergesättigtem Lockermaterial (Boden und Verwitterungshorizont) unter Permafrost-Bedingungen während Perioden des Auftauens entstanden ist.	A deposit formed by slow viscous downslope flow of water-logged soil and other unsorted and saturated surficial material under permafrost conditions during melting periods.
	Quelle/source	Diese Publikation; verändert nach NEUENDORF et al. (2005)	This publication; modified from NEUENDORF et al. (2005)
	Hierarchie/hierarchy	Permafrostablagerung → Geli-Solifluktionsablagerung	Permafrost deposit → Geli-solifluction deposit

L67	Name	**Flächenspülungsablagerung**	**Sheetwash deposit**
	Definition	Meist feinkörnige Ablagerung, die durch Flächenspülung (= flächenhafte, nicht kanalisierte Hangspülung bei Starkregenereignissen) entstanden ist.	A deposit (usually fine-grained) formed by an extensive down-slope surface-flow that is not confined to channels and is caused by heavy precipitation events.
	Quelle/source	Diese Publikation; verändert nach NEUENDORF et al. (2005), KRENMAYR et al. (2012)	This publication; modified from NEUENDORF et al. (2005), KRENMAYR et al. (2012)
	Hierarchie/hierarchy	Flächenspülungsablagerung	Sheetwash deposit
L68	Name	Schwemmlöss	Alluvial loess
	Definition	Durch Flächenspülung umgelagerter Löss.	Sheetwash deposit consisting of reworked loess.
	Quelle/source	Diese Publikation	This publication
	Hierarchie/hierarchy	Flächenspülungsablagerung → Schwemmlöss	Sheetwash deposit → Alluvial loess
L69	Name	Verschwemmte Moränenablagerung	Reworked till
	Definition	Durch Flächenspülung umgelagerte Grund- und/oder Ablationsmoränenablagerung.	Sheetwash deposit consisting of reworked till.
	Quelle/source	Diese Publikation	This publication
	Hierarchie/hierarchy	Flächenspülungsablagerung → Verschwemmte Moränenablagerung	Sheetwash deposit → Reworked till
L70	Name	**Chemische und Biochemische Ausfällungen**	**Chemical and biochemical precipitation**
	Definition	Ausfällungen, die durch direkte oder indirekte chemische Prozesse oder Aktivitäten von lebenden Organismen gebildet werden.	Precipitation formed by direct or indirect chemical processes or by living organism.
	Quelle/source	Diese Publikation; verändert nach NEUENDORF et al. (2005)	This publication; modified from NEUENDORF et al. (2005)
	Hierarchie/hierarchy	Chemische und Biochemische Ausfällungen	Chemical and biochemical precipitation
L71	Name	Sinterkalk	Calcareous sinter
	Definition	Meist zellig-poröses karbonatisches Locker- und/oder Festgestein (vorwiegend Calcit, seltener Aragonit), welches durch Ausfällung infolge von CO_2 Verlust an natürlichen oder künstlichen Grundwasseraustritten und Wasserfällen entsteht.	Usually a cellular/porous calcareous material and/or rock, formed by precipitation caused by CO_2 loss at natural or artificial groundwater outlets or waterfalls.
	Quelle/source	Diese Publikation; verändert nach HINZE et al. (1989), KRENMAYR et al. (2012)	This publication; modified from HINZE et al. (1989), KRENMAYR et al. (2012)
	Hierarchie/hierarchy	Chemische und Biochemische Ausfällungen → Sinterkalk.	Chemical and biochemical precipitation → Calcareous sinter
L72	Name	Alm	‘Alm’
	Definition	Helles, feinkörniges, ungeschichtetes Lockergestein aus Kalziumkarbonat, welches durch oberflächennahe Ausfällung z.B. nach zeitweiliger Überschwemmung oder Wasseraustritt entsteht.	A light, fine-grained, non-stratified sedimentary material consisting of calcium-carbonate formed by near-surface precipitation for example due to periodic flooding or surficial water discharge.
	Quelle/source	HINZE et al. (1989)	HINZE et al. (1989)
	Hierarchie/hierarchy	Chemische und Biochemische Ausfällungen → Alm	Chemical and biochemical precipitation → ‘Alm’

Tab. 4.
Lithogenetische Einheiten – Begriffserläuterung.

Nr.		Deutsch	Englisch
G1	Name	**Anthropogene Form**	**Anthropogenic feature**
	Definition	Durch menschliche Tätigkeit (künstlich) erzeugte geomorphologische Form.	A human-made (artificial) geomorphic feature.
	Quelle/source	Diese Publikation; verändert nach BWG (2003)	This publication; modified from BWG (2003)
	Hierarchie/hierarchy	Anthropogene Form	Anthropogenic feature
G2	Name	**Äolische Form**	**Aeolian feature**
	Definition	Geomorphologische Form, die durch Einwirkung von Wind gebildet wurde.	A geomorphological feature formed by wind.
	Quelle/source	Diese Publikation; verändert nach NEUENDORF et al. (2005)	This publication; modified from NEUENDORF et al. (2005)
	Hierarchie/hierarchy	Äolische Form	Aeolian feature
G3	Name	Düne	Dune
	Definition	Ansammlungen von windverfrachtetem Material (Flugsand, Löss) in Form eines Hügels oder Rückens.	An accumulation of wind-transported material (sand, loess) in the form of a mound or ridge.
	Quelle/source	Diese Publikation; verändert nach NEUENDORF et al. (2005)	This publication; modified from NEUENDORF et al. (2005)
	Hierarchie/hierarchy	Äolische Form → Düne	Aeolian feature → Dune
G4	Name	**Erosionsform**	**Erosional feature**
	Definition	Geomorphologische Form, die durch einen erosiven Prozess entstanden ist.	Geomorphological feature that has been formed by an erosive process.
	Quelle/source	Diese Publikation; verändert nach NEUENDORF et al. (2005)	This publication; modified from NEUENDORF et al. (2005)
	Hierarchie/hierarchy	Erosionsform	Erosional feature
G5	Name	Erdpyramide	Earth pyramid
	Definition	Säulen- bis kegelförmige Erosionsform, die aus Lockersediment besteht und meist von einem vorzugsweise plattigen Block aus relativ härterem Material gedeckelt ist. Dieser schützt das unterliegende, relativ weichere Material vor Erosion.	Pyramidal slim pillar of unconsolidated to poorly consolidated material mostly topped by a flat boulder of harder material protecting the underlying material against erosion.
	Quelle/source	Diese Publikation; verändert nach NEUENDORF et al. (2005)	This publication; modified from NEUENDORF et al. (2005)
	Hierarchie/hierarchy	Erosionsform → Erdpyramide	Erosional feature → Earth pyramid
G6	Name	Felsterrasse	Strath terrace
	Definition	In Fels entwickelte Erosionsform, die einen ehemaligen, breiten, flachen Talboden gebildet hat, der heute über dem Abfluss liegt und durch Einschneiden des Flusses aufgrund einer Änderung des Erosionsniveaus gebildet wurde.	A terrace formed in bedrock of a broad, flat, valley floor, which now stands above the present drainage as a result of down-cutting due to base-level change.
	Quelle/source	Diese Publikation; verändert nach NEUENDORF et al. (2005)	This publication; modified from NEUENDORF et al. (2005)
	Hierarchie/hierarchy	Erosionsform → Felsterrasse	Erosional feature → Strath terrace
G7	Name	Paläo-Kolk	Scour
	Definition	Örtlich begrenzte, durch Strömungsvorgänge verursachte Vertiefung in einem ehemaligen Gewässerbett.	A hollow in the bed or banks of a stream, caused by the erosive action of rapidly circulating water.
	Quelle/source	LOAT & MEIER (2003)	LOAT & MEIER (2003)
	Hierarchie/hierarchy	Erosionsform → Paläo-Kolk	Erosional feature → Scour
G8	Name	Geländekante	Terrane edge
	Definition	Relativ scharfe Hangkante, die durch geologische Prozesse gebildet wurde.	Sharp edge or crest formed by a geologic process.
	Quelle/source	Diese Publikation	This publication
	Hierarchie/hierarchy	Erosionsform → Geländekante	Erosional feature → Terrane edge
G9	Name	Erosionskante	Erosional edge
	Definition	Relativ scharfe Hangkante, die durch fluviatile Erosion gebildet wurde.	A relatively sharply pointed slope edge formed by erosion.
	Quelle/source	Diese Publikation; verändert nach NEUENDORF et al. (2005)	This publication; modified from NEUENDORF et al. (2005)
	Hierarchie/hierarchy	Erosionsform → Geländekante → Erosionskante	Erosional feature → Terrane edge → Erosional edge

G10	Name	Terrassenkante	Terrace edge
	Definition	Relativ scharfe Erosionskante, die den Abschluss einer Terrassenoberfläche bildet.	A sharp slope edge marking the termination of a terrace.
	Quelle/source	Diese Publikation; verändert nach BWG (2003)	This publication; modified from BWG (2003)
	Hierarchie/hierarchy	Erosionsform → Geländekante → Terrassenkante	Erosional feature → Terrane edge → Terrace edge
G11	Name	Verebnungsfläche	Peneplain
	Definition	Durch subaerische und fluviatile Abtragung in Zeiten tektonischer Ruhe bis zur Abschwächung jeglichen Landschaftsreliefs (bis zum base-level) entwickelte Ebene.	A relatively flat or gently undulating surface that formed by subaerial erosion and fluvial transport during quiet tectonic phases.
	Quelle/source	Diese Publikation; verändert nach NEUENDORF et al. (2005), MURAWSKI & MEYER (1998)	This publication; modified from NEUENDORF et al. (2005), MURAWSKI & MEYER (1998)
	Hierarchie/hierarchy	Erosionsform → Verebnungsfläche	Erosional feature → Peneplain
G12	Name	Yardang (Windhöcker)	Yardang
	Definition	Stromlinienförmiger und tafel- bis tropfenförmiger Körper aus Lockersedimenten, der durch Winderosion (Korrasion) entstanden und in Windrichtung ausgerichtet ist.	A yardang is a streamlined protuberance carved from consolidated or semi-consolidated material by wind erosion. It is orientated into the wind direction.
	Quelle/source	Diese Publikation; verändert nach NEUENDORF et al. (2005)	This publication; modified from NEUENDORF et al. (2005)
	Hierarchie/hierarchy	Erosionsform → Yardang (Windhöcker)	Erosional feature → Yardang
G13	Name	Windkanter	Ventifact
	Definition	Gesteinsfragment mit einer Oberfläche, die durch die abrasive Kraft von durch Wind transportiertem Sand geformt, zerschlissen, facettiert, geschnitten oder poliert wurde.	Rock surface shaped, worn, faceted, cut, or polished by the abrasive action of windblown sand.
	Quelle/source	Diese Publikation; verändert nach NEUENDORF et al. (2005)	This publication; modified from NEUENDORF et al. (2005)
	Hierarchie/hierarchy	Erosionsform → Yardang (Windhöcker) → Windkanter	Erosional feature → Ventifact
G14	Name	**Glaziofluviatile Form**	**Glaciofluvial feature**
	Definition	Geomorphologische Form, die durch den direkten Einfluss von Schmelzwasser aus Gletschern entstanden ist.	A geomorphological feature affected or created by glacial meltwater.
	Quelle/source	Diese Publikation	This publication
	Hierarchie/hierarchy	Glaziofluviatile Form	Glaciofluvial feature
G15	Name	Übergangskegel (Sander)	Outwash cone
	Definition	Kegelförmige Ausprägung glaziofluviatiler Sedimente, die von Schmelzwasserströmen ausgehend vom Gletschertor gebildet wurde.	Cone-like outwash deposit formed by glacial meltwater at the transition of a glacier to its fore field.
	Quelle/source	Diese Publikation; verändert nach NEUENDORF et al. (2005)	This publication; modified from NEUENDORF et al. (2005)
	Hierarchie/hierarchy	Glaziofluviatile Form → Übergangskegel (Sander)	Glaciofluvial feature → Outwash cone
G16	Name	**Glaziogene Form**	**Glacial feature**
	Definition	Geomorphologische Form, die durch direkten oder indirekten Einfluss von Gletschern oder Inlandeis entstanden ist.	A geomorphologic feature formed by the action of a glacier or ice-sheet.
	Quelle/source	Diese Publikation; verändert nach NEUENDORF et al. (2005)	This publication; modified from NEUENDORF et al. (2005)
	Hierarchie/hierarchy	Glaziogene Form	Glacial feature
G17	Name	Glaziogene Erosionsform	Glacial erosional feature
	Definition	Geomorphologische Form, die durch die erosive Wirkung von Gletschern oder Inlandeis entstanden ist.	A geomorphological feature formed by the erosion of a glacier or ice-sheet.
	Quelle/source	Diese Publikation	This publication
	Hierarchie/hierarchy	Glaziogene Form → Glaziogene Erosionsform	Glacial feature → Glacial erosional feature
G18	Name	Gletschermühle	Glacier mill
	Definition	Kolke, die an der Gletscherbasis durch die Wirkung subglazialer Schmelzwässer und deren mitgeführter Sedimentfracht entstanden sind.	Scour formed by the action of debris-laden meltwater at the base of a glacier.
	Quelle/source	Diese Publikation; verändert nach MARTIN & EIBLMAIER (2003)	This publication; modified from MARTIN & EIBLMAIER (2003)
	Hierarchie/hierarchy	Glaziogene Form → Glaziogene Erosionsform → Gletschermühle	Glacial feature → Glacial erosional feature → Glacier mill

G19	Name	Gletscherschliff	Polished surfaces
	Definition	Durch glaziale Erosion geschliffene und/ oder polierte Festgesteinsoberfläche, die Richtungsanzeiger (z.B. glaziale Striemung) enthalten kann.	Polished bedrock surface formed by subglacial erosion.
	Quelle/source	Diese Publikation	This publication
	Hierarchie/hierarchy	Glaziogene Form → Glaziogene Erosionsform → Gletscherschliff	Glacial feature → Glacial erosional feature → Polished surfaces
G20	Name	Muschelbruch	Muschelbruch
	Definition	Durch subglaziale Erosion entstandene sichel- oder muschelförmige Bruch-Hohlform in der Festgesteinsoberfläche. Die offene oder konkave Seite der Brüche zeigt dabei in Richtung des Eisflusses.	Mussel or sickle shaped depressions on the rock surface due to subglacial erosion. They have typically sharp convex up-flow rims and indistinct down-flow margins.
	Quelle/source	BENN & EVANS (2010)	BENN & EVANS (2010)
	Hierarchie/hierarchy	Glaziogene Form → Glaziogene Erosionsform → Muschelbruch	Glacial feature → Glacial erosional feature → Muschelbruch
G21	Name	Rat tail	Rat tail
	Definition	Kleine langgezogene Erhebung auf einer Festgesteinsoberfläche, die durch glaziale Erosion im Druckschatten von erosionsresistenterem Material entstanden ist. Zeigt die Eisflussrichtung an.	A small, elongated elevation formed by the shielding of bedrock to glacial erosion by a more competent zone. Shows the ice-flow direction.
	Quelle/source	Diese Publikation; verändert nach BENN & EVANS (2010)	This publication; modified from BENN & EVANS (2010)
	Hierarchie/hierarchy	Glaziogene Form → Glaziogene Erosionsform → Rat tail	Glacial feature → Glacial erosional feature → Rat tail
G22	Name	Glaziale Striemungen	Striae
	Definition	Serie von langen und parallelen Rillen oder Furchen, die durch glaziale Erosion auf Festgesteinsoberflächen entstehen und parallel zur Eisbewegung orientiert sind.	A series of long, commonly straight and parallel, furrows inscribed on a bedrock surface by glacial erosion. Usually oriented parallel to the direction of ice movement.
	Quelle/source	Diese Publikation; verändert nach NEUENDORF et al. (2005), BENN & EVANS (2010)	This publication; modified from NEUENDORF et al. (2005), BENN & EVANS (2010)
	Hierarchie/hierarchy	Glaziogene Form → Glaziogene Erosionsform → Glaziale Striemungen	Glacial feature → Glacial erosional feature → Striae
G23	Name	Schliffgrenze	Trimline
	Definition	Schliffkehlen zeigen die obere Grenze der glazialen Erosion in einem Tal an und sind somit auch die obere Grenze der Eisfüllung bzw. Eismächtigkeit in einem Tal.	Trimlines mark the highest limit of glacial erosion in a valley and therefore they mark the most recent highest extent of the glacier or ice in a valley.
	Quelle/source	Diese Publikation; verändert nach BENN & EVANS (2010)	This publication; modified from BENN & EVANS (2010)
	Hierarchie/hierarchy	Glaziogene Form → Glaziogene Erosionsform → Schliffgrenze	Glacial feature → Glacial erosional feature → Trimline
G24	Name	Rundhöcker	Roche moutonnée
	Definition	Mehr oder weniger stromlinienförmiger asymmetrischer Felshöcker, der durch glaziale Erosion modelliert wurde und poliert oder gekritzt sein kann. Die dem Eisfluss zugerichtete Seite ist flach (abradierte Luv-Seite) und die im Eisfluss orientierte Seite (Lee) ist steil.	Roches mountonées are asymmetric bedrock bumps or hills with abraded up-ice or stoss faces and quarried down-ice lee faces.
	Quelle/source	Diese Publikation; verändert nach BENN & EVANS (2010)	This publication; modified from BENN & EVANS (2010)
	Hierarchie/hierarchy	Glaziogene Form → Glaziogene Erosionsform → Rundhöcker	Glacial feature → Glacial erosional feature → Roche moutonnée
G25	Name	Whaleback	Whaleback
	Definition	Mehr oder weniger stromlinienförmiger symmetrischer Felshöcker, der durch glaziale Erosion modelliert wurde und poliert oder gekritzt sein kann.	A roughly streamlined symmetric bedrock elevation formed (polished and scratched) by glacial erosion.
	Quelle/source	Diese Publikation; verändert nach BENN & EVANS (2010)	This publication; modified from BENN & EVANS (2010)
	Hierarchie/hierarchy	Glaziogene Form → Glaziogene Erosionsform → Whaleback	Glacial feature → Glacial erosional feature → Whaleback

G26	Name	Subglaziale Schmelzwasserrinne	Subglacial meltwater channel
	Definition	Durch Schmelzwasser unter dem Gletscher erzeugte Rinne.	Channel formed by meltwater below a glacier.
	Quelle/source	Diese Publikation; verändert nach EMBLETON-HAMANN & WILHELMY (2007)	This publication; modified from EMBLETON-HAMANN & WILHELMY (2007)
	Hierarchie/hierarchy	Glaziogene Form → Glaziogene Erosionsform → Subglaziale Schmelzwasserrinne	Glacial feature → Glacial erosional feature → Subglacial meltwater channel
G27	Name	End- und Seitenmoränenwall	Ridge of a latero-frontal moraine
	Definition	Aus End- und Seitenmoränenmaterial bestehender Wall, der den aktiven Gletscherrand im Zungenbereich nachzeichnet.	Ridge of lateral and frontal moraine deposits formed at the glacier border of the glacial tongue.
	Quelle/source	Diese Publikation; verändert nach BWG (2003); BENN & EVANS (2010)	This publication; modified from BWG (2003); BENN & EVANS (2010)
	Hierarchie/hierarchy	Glaziogene Form → End- und Seitenmoränenwall	Glacial feature → Ridge of a latero-frontal moraine
G28	Name	Esker	Esker
	Definition	Langer, schmaler, gewundener Wall mit steilen Flanken, der von einem subglazialen Fließgewässer in Tunneln in oder unter dem Eis von stagnierenden oder zurückweichenden Gletschern gebildet wurde.	A long, narrow, sinuous, steep-sided ridge that was deposited by a subglacial stream flowing between ice walls or in an ice tunnel of a stagnant or retreating glacier.
	Quelle/source	Diese Publikation; verändert nach NEUENDORF et al. (2005)	This publication; modified from NEUENDORF et al. (2005)
	Hierarchie/hierarchy	Glaziogene Form → Esker	Glacial feature → Esker
G29	Name	Subglaziale Wallform	Subglacial ridge
	Definition	Geomorphologische Form, die durch Sedimentakkumulation an der Basis von Gletschern oder Inlandeis in Form eines Walls entstanden ist.	A geomorphological ridge-like feature formed by the accumulation of sediment at the base of a glacier or ice-sheet.
	Quelle/source	Diese Publikation	This publication
	Hierarchie/hierarchy	Glaziogene Form → Subglaziale Wallform	Glacial feature → Subglacial ridge
G30	Name	Drumlin	Drumlin
	Definition	Stromlinienförmige Wälle mit ovalem Grundriss, die aus subglazialen Ablagerungen aufgebaut und parallel zur ehemaligen Eisflussrichtung orientiert sind. Die dem Eisfluss zugerichtete Seite ist steil (Luv) und die im Eisfluss orientierte Seite (Lee) ist flacher.	Typically smooth, oval shaped hills of hillocks of glacial drift. Generally the steep, blunter end-points in the up-ice direction and the gentler sloping, pointed end faces in the down-ice direction.
	Quelle/source	Diese Publikation; verändert nach BENN & EVANS (2010), MENZIES (1979)	This publication; modified from BENN & EVANS (2010), MENZIES (1979)
	Hierarchie/hierarchy	Glaziogene Form → Subglaziale Wallform → Drumlin	Glacial feature → Subglacial ridge → Drumlin
G31	Name	Flute	Flute
	Definition	Elongierte stromlinienförmige Wälle, die aus subglazialen Ablagerungen aufgebaut und parallel zur ehemaligen Eisflussrichtung orientiert sind.	Elongated streamlined ridges oriented parallel to the paleo ice-current and consisting of subglacial material.
	Quelle/source	Diese Publikation; verändert nach BENN & EVANS (2010)	This publication; modified from BENN & EVANS (2010)
	Hierarchie/hierarchy	Glaziogene Form → Subglaziale Wallform → Flute	Glacial feature → Subglacial ridge → Flulte
G32	Name	Toteisloch	Kettle hole
	Definition	Beim Abschmelzen von Toteis, welches durch Lockersedimente bedeckt wurde, entstandene Senke.	A depression, formed by the melting of dead ice that was covered by deposits.
	Quelle/source	Diese Publikation; verändert nach BWG (2003)	This publication; modified from BWG (2003)
	Hierarchie/hierarchy	Glaziogene Form → Toteisloch	Glacial feature → Kettle hole
G33	Name	**Gravitative Form**	**Gravitative feature**
	Definition	Geomorphologische Ausbildung der Geländeoberfläche, die durch gravitative Prozesse entstanden ist.	A geological feature formed by a gravitative transport.
	Quelle/source	Diese Publikation; verändert nach NEUENDORF et al. (2005)	This publication; modified from NEUENDORF et al. (2005)
	Hierarchie/hierarchy	Gravitative Form	Gravitative feature
G34	Name	Abrisskante einer Massenbewegung	Scarp of a mass movement
	Definition	Morphologisch deutlich bis sehr undeutlich ausgebildete Hangkante, die den Herkunftsbereich einer gravitativ umgelagerten Gesteinsmasse begrenzt.	A morphologically sharp to fuzzy developed slope edge limiting the origin of a mass movement.
	Quelle/source	Diese Publikation; verändert nach CRUDEN & VARNES (1996), ZANGERL et al. (2008)	This publication; modified from CRUDEN & VARNES (1996), ZANGERL et al. (2008)
	Hierarchie/hierarchy	Gravitative Form → Abrisskante einer Massenbewegung	Gravitative feature → Scarp of a mass movement

G35	Name	Abrisskante einer Fließmasse	Scarp of a mass flow
	Definition	Morphologisch deutlich bis sehr undeutlich ausgebildete Hangkante, die den Herkunftsbereich einer Fließmasse begrenzt.	A morphologically sharp to fuzzy developed slope edge limiting the origin of a mass flow.
	Quelle/source	Diese Publikation; verändert nach CRUDEN & VARNES (1996), ZANGERL et al. (2008)	This publication; modified from CRUDEN & VARNES (1996), ZANGERL et al. (2008)
	Hierarchie/hierarchy	Gravitative Form → Abrisskante einer Massenbewegung → Abrisskante einer Fließmasse	Gravitative feature → Scarp of a mass movement → Scarp of a mass flow
G36	Name	Abrisskante einer Gleitmasse	Scarp of a slide mass
	Definition	Morphologisch deutlich bis sehr undeutlich ausgebildete Hangkante, die den Herkunftsbereich einer Gleitmasse begrenzt.	A morphologically sharp to fuzzy developed slope edge limiting the origin of a slide mass.
	Quelle/source	Diese Publikation; verändert nach CRUDEN & VARNES (1996), ZANGERL et al. (2008)	This publication; modified from CRUDEN & VARNES (1996), ZANGERL et al. (2008)
	Hierarchie/hierarchy	Gravitative Form → Abrisskante einer Massenbewegung → Abrisskante einer Gleitmasse	Gravitative feature → Scarp of a mass movement → Scarp of a slide mass
G37	Name	Abrisskante einer Sturzmasse	Scarp of a rock fall
	Definition	Morphologisch deutlich bis sehr undeutlich ausgebildete Hangkante, die den Herkunftsbereich einer Sturzmasse begrenzt.	A morphologic sharp to fuzzy developed slope edge limiting the origin of a rock fall.
	Quelle/source	Diese Publikation; verändert nach CRUDEN & VARNES (1996), ZANGERL et al. (2008)	This publication; modified from CRUDEN & VARNES (1996), ZANGERL et al. (2008)
	Hierarchie/hierarchy	Gravitative Form → Abrisskante einer Massenbewegung → Abrisskante einer Sturzmasse	Gravitative feature → Scarp of a mass movement → Scarp of a rock fall
G38	Name	Abrisskante einer tiefgreifenden Hangdeformation	Scarp of a deep seated gravitational slope deformation
	Definition	Morphologisch deutlich bis sehr undeutlich ausgebildete Hangkante, die den Herkunftsbereich einer tiefgreifenden Hangdeformation begrenzt.	Morphologically sharp to fuzzy developed slope edge limiting the origin of a deep-seated slope deformation.
	Quelle/source	Diese Publikation; verändert nach DRAMIS & SORRISO-VALVO (1994), WEIDNER (2000)	This publication; modified from DRAMIS & SORRISO-VALVO (1994), WEIDNER (2000)
	Hierarchie/hierarchy	Gravitative Form → Abrisskante einer Massenbewegung → Abrisskante einer tiefgreifenden Hangdeformation	Gravitative feature → Scarp of a mass movement → Scarp of a deep seated gravitational slope deformation
G39	Name	Abrisskante eines Bergsturzes	Scarp of a rapid landslide
	Definition	Morphologisch deutlich bis sehr undeutlich ausgebildete Hangkante, die den Herkunftsbereich einer Bergsturzmasse begrenzt.	Morphologically sharp to fuzzy developed slope edge limiting the origin of a rock avalanche.
	Quelle/source	Diese Publikation; verändert nach ABELE (1974), Heim (1932), ZANGERL et al. (2008)	This publication; modified from ABELE (1974), Heim (1932), ZANGERL et al. (2008)
	Hierarchie/hierarchy	Gravitative Form → Abrisskante einer Massenbewegung → Abrisskante eines Bergsturzes	Gravitative feature → Scarp of a mass movement → Scarp of a rapid landslide
G40	Name	Antithetischer Bruch	Antislope scarp
	Definition	Steil in den Hang einfallende Bewegungsfläche (Abschiebung), die aufgrund von Massenbewegungen entstanden ist. Die Ausbildung erfolgt unter Verwendung geeigneter prä-existenter Trennflächen.	Steep plane of displacement (normal fault) dipping into the slope due to mass movement along pre-existing planar fabric.
	Quelle/source	REITNER & LINNER (2009), BOVIS (1982)	REITNER & LINNER (2009), BOVIS (1982)
	Hierarchie/hierarchy	Gravitative Form → Antithetischer Bruch	Gravitative feature → Antislope scarp
G41	Name	Zerrspalte, Zerrgraben	Tension crack
	Definition	Gravitativ bedingte Extensionsstruktur. Die Ausbildung erfolgt unter Verwendung geeigneter prä-existenter Trennflächen.	Extensional structure due to gravitational processes, using pre-existing planar fabric to develop.
	Quelle/source	Diese Publikation; verändert nach HEINISCH et al. (2015), WEIDNER (2000), JAHN (1964), AMPFERER (1940)	This publication; modified from HEINISCH et al. (2015), WEIDNER (2000), JAHN (1964), AMPFERER (1940)
	Hierarchie/hierarchy	Gravitative Form → Zerrspalte, Zerrgraben	Gravitative feature → Tension crack
G42	Name	Aufgelockerter Bereich durch Driften	Area of rock spread
	Definition	Bereich gravitativ bedingter lateraler Extension mit bruchhafter Zerlegung einer spröden (relativ härteren) über einer duktilen (relativ weicheren) Gesteinsmasse.	Area of lateral extension features formed by gravitational processes due to loosening of competent bedrock overlying less competent bedrock.
	Quelle/source	Diese Publikation; verändert nach CRUDEN & VARNES (1996), ZÁRUBA & MENCL (1969), POISEL & EPPENSTEINER (1988, 1989)	This publication; modified from CRUDEN & VARNES (1996), ZÁRUBA & MENCL (1969), POISEL & EPPENSTEINER (1988, 1989)
	Hierarchie/hierarchy	Gravitative Form → Aufgelockerter Bereich durch Driften	Gravitative feature → Area of rock spread

G43	Name	Bereich einer Gleitung	Area affected by a slide
	Definition	Bereich, der durch die Hangabwärtsbewegung von Locker- oder Festgestein entlang einer oder mehrerer diskreter Bewegungsflächen oder Bewegungszonen, in denen der Hauptanteil der Hangdeformation stattfindet (Gleiten), gekennzeichnet ist. Eine Sedimentneubildung im Sinne einer Gleitmasse ist noch nicht erfolgt, sodass kein kartierbarer Sedimentkörper ausgeschieden werden kann.	Area of downslope movement along one or more distinct displacement planes.
	Quelle/source	Diese Publikation; verändert nach Zangerl et al. (2008), Cruden & Varnes (1996)	This publication; modified from Zangerl et al. (2008), Cruden & Varnes (1996)
	Hierarchie/hierarchy	Gravitative Form → Bereich einer Gleitung	Gravitative feature → Area affected by a slide
G44	Name	Bereich eines langsamen Fließens	Area of slow mass flow
	Definition	Bereich eines sehr langsamen Fließprozesses („Kriechen“) in Locker- oder Festgestein. Aufgrund der hohen internen Teilbeweglichkeit der bewegten Gesteinsmasse treten potenzielle Gleitzonen nicht auf oder sind dicht angeordnet, kurzlebig und meist nicht erhalten. Eine Sedimentneubildung im Sinne einer Fließmasse ist noch nicht erfolgt, sodass kein kartierbarer Sedimentkörper ausgeschieden werden kann.	Area affected by very slow mass flow.
	Quelle/source	Diese Publikation; verändert nach Zangerl et al. (2008), Poisel & Kieffer (2009), Nemcok et al. (1972)	This publication; modified from Zangerl et al. (2008), Poisel & Kieffer (2009), Nemcok et al. (1972)
	Hierarchie/hierarchy	Gravitative Form → Bereich eines langsamen Fließens	Gravitative feature → Area of slow mass flow
G45	Name	Bereich einer tiefgreifenden Hangdeformation	Area of deep-seated gravitational slope deformation
	Definition	Bereich einer sehr langsamen gravitativen Umlagerung einer nicht oder nur in Teilbereichen diskret begrenzbaren Gesteinsmasse. Der Zerlegungsgrad kann von Fels im Verband bis zur kompletten Zerlegung in Kluftkörper variieren.	Area affected by deep-seated gravitational movement processes, where a distinct body cannot be delimited.
	Quelle/source	Diese Publikation; verändert nach Dramis & Sorriso-Valvo (1994), Weidner (2000), Agliardi et al. (2001), Poisel & Kieffer (2009)	This publication; modified from Dramis & Sorriso-Valvo (1994), Weidner (2000), Agliardi et al. (2001), Poisel & Kieffer (2009)
	Hierarchie/hierarchy	Gravitative Form → Bereich einer tiefgreifenden Hangdeformation	Gravitative feature → Area of deep-seated gravitational slope deformation
G46	Name	Toppling (Kippung)	Toppling
	Definition	Bereich, wo sich eine Fest- oder Lockergesteinsmasse durch Rotation aus dem Hang herauslöst. Der Massenschwerpunkt der kippenden Gesteinsmasse liegt über der Rotationsachse.	Area of bedrock or sediments where parts of the mass are dislocated by a rotational process. The centre of gravity lies above the rotation axis.
	Quelle/source	Diese Publikation; verändert nach Zangerl et al. (2008), Reitner & Linner (2009), Goodman & Bray (1976), Prebble (1995), De Freitas & Watters (1973)	This publication; modified from Zangerl et al. (2008), Reitner & Linner (2009), Goodman & Bray (1976), Prebble (1995), De Freitas & Watters (1973)
	Hierarchie/hierarchy	Gravitative Form → Toppling (Kippung)	Gravitative feature → Toppling
G47	Name	Bereich eines Talzuschubs	Area of a ‚Talzuschub‘
	Definition	Bereich eines stark vorgewölbten Hangfußes (Talzuschubsstirn) aufgrund der langsamen gravitativen Umlagerung einer Gesteinsmasse. Charakteristisch für den Gesamthang ist die Ausbildung eines konvex-konkaven Hangprofils durch Massenverlust im Oberhang und Akkumulation im Unterhang. Dies resultiert in einer Verengung des Talquerschnittes.	A bulging toe of a slope due to slope deformation.
	Quelle/source	Diese Publikation; verändert nach Weidner (2000), Hermann (1996), Moser & Glumac (1982), Stini (1941), Zangerl et al. (2008)	This publication; modified from Weidner (2000), Hermann (1996), Moser & Glumac (1982), Stini (1941), Zangerl et al. (2008)
	Hierarchie/hierarchy	Gravitative Form → Bereich eines Talzuschubs	Gravitative feature → Area of a ‚Talzuschub‘
G48	Name	Tiefgreifend aufgelockerter Fels	Deep-seated loosened rock
	Definition	Großflächige, gravitativ bedingte Aufweitung des Trennflächengefüges im Festgestein. Der Fels befindet sich noch (weitgehend) im Verband und eine Dislozierung ist kaum oder nicht erkennbar (subanstehend).	A term covering non to slightly dislocated bedrock with loosening due to gravitational processes.
	Quelle/source	Diese Publikation	This publication
	Hierarchie/hierarchy	Gravitative Form → Tiefgreifend aufgelockerter Fels	Gravitative feature → Deep-seated loosened rock

G49	Name	Erdfall	Sinkhole
	Definition	Einbruch an der Erdoberfläche als Folge von natürlichen Hohlraumbildungen (durch Subrosion oder Suffosion) im Untergrund.	A depression in the earth's surface formed by the collapse of a subsurface cavity due to subrosion or suffosion.
	Quelle/source	Diese Publikation; verändert nach MARTIN & EIBLMAIER (2003)	This publication; modified from MARTIN & EIBLMAIER (2003)
	Hierarchie/hierarchy	Gravitative Form → Erdfall	Gravitative feature → Sinkhole
G50	Name	Tomahügel	Toma hill
	Definition	Eine isolierte kegel-, pyramiden- oder dachförmige Ausprägungsform von Sturzstromablagerungen.	An isolated cone-like, pyramidal or roof-like form of a rapid landslide body.
	Quelle/source	Diese Publikation; verändert nach ABELE (1974)	This publication; modified from ABELE (1974)
	Hierarchie/hierarchy	Gravitative Form → Tomahügel	Gravitative feature → Toma hill
G51	Name	Massenbewegungswall	Mass movement ridge
	Definition	Wallform, die durch eine gravitative Massenbewegung erzeugt wurde.	Ridge formed by a mass movement.
	Quelle/source	Diese Publikation	This publication
	Hierarchie/hierarchy	Gravitative Form → Massenbewegungswall	Gravitative feature → Mass movement ridge
G52	Name	Kompressionswall	Compressional ridge
	Definition	Durch Kompression (Stauchung) meist im Unterhang von gravitativen Massenbewegungen hervorgerufene Wälle oder Wülste.	A ridge caused by compression in the lower part of a mass movement.
	Quelle/source	Diese Publikation; verändert nach HINZE et al. (1989)	This publication; modified from HINZE et al. (1989)
	Hierarchie/hierarchy	Gravitative Form → Massenbewegungswall → Kompressionswall	Gravitative feature → Mass movement ridge → Compressional ridge
G53	Name	Randwall einer Massenbewegung	Ridge at the margin of a mass movement
	Definition	Wall, der am Rand einer gravitativen Massenbewegung zwischen bewegter und unbewegter Gesteinsmasse durch Transpression entsteht.	Ridge formed at the limits of a mass movement caused by transpression between moving and not moving material.
	Quelle/source	Diese Publikation	This publication
	Hierarchie/hierarchy	Gravitative Form → Massenbewegungswall → Randwall einer Massenbewegung	Gravitative feature → Mass movement ridge → Ridge at the margin of a mass movement
G54	Name	Sturzstromwall	Rock avalanche ridge
	Definition	Wall, der sich aufgrund des fluidartigen Verhaltens eines Sturzstromes gebildet hat.	Ridge formed by the fluid-like behaviour of a rock avalanche.
	Quelle/source	Diese Publikation	This publication
	Hierarchie/hierarchy	Gravitative Form → Massenbewegungswall → Sturzstromwall	Gravitative feature → Mass movement ridge → Rock avalanche ridge
G55	Name	**Fluviatile Form**	**Fluvial feature**
	Definition	Geomorphologische Form, die durch direkten oder indirekten Einfluss von fließenden Gewässern entstanden ist.	A geologic feature formed by the action of floating water.
	Quelle/source	NEUENDORF et al. (2005)	NEUENDORF et al. (2005)
	Hierarchie/hierarchy	Fluviatile Form	Fluvial feature
G56	Name	Ehemaliger Abfluss, Trockental	Dry valley
	Definition	Lineare Hohlform, die ursprünglich durch die Tiefenerosion eines Baches oder Flusses geschaffen wurde, aber heute kein Wasser mehr führt.	A linear depression formed by the erosion of a stream or river, but that no longer has an active streambed.
	Quelle/source	Diese Publikation; verändert nach AHNERT (2015)	This publication; modified from AHNERT (2015)
	Hierarchie/hierarchy	Fluviatile Form → Ehemaliger Abfluss, Trockental	Fluvial feature → Dry valley
G57	Name	Natürlicher Damm (Levée)	Levée
	Definition	Ein langer breiter Wall oder eine Anschüttung, der bzw. die von Fließgewässern an ihren Ufern gebildet wird, insbesondere während Hochflutereignissen, wenn das normale Fließbett überwunden wird und sich gröbere Kornfraktionen an den Ufern ablagern.	An elongated naturally occurring ridge or artificially constructed fill or wall, which regulates water levels. It is usually earthen and often parallel to the course of a river in its floodplain or along low-lying coastlines.
	Quelle/source	Diese Publikation; verändert nach NEUENDORF et al. (2005)	This publication; modified from NEUENDORF et al. (2005)
	Hierarchie/hierarchy	Fluviatile Form → Natürlicher Damm (Levée).	Fluvial feature → Levée

G58	Name	**Karsthohlform**	**Hollow pattern in karst**
	Definition	Hohlform in der Oberfläche, die durch Karstprozesse entstanden ist.	Hollow pattern in karst surface due to dissolution processes.
	Quelle/source	Diese Publikation	This publication
	Hierarchie/hierarchy	Karsthohlform	Hollow pattern in karst
G59	Name	Doline	Doline
	Definition	Durch Lösungsvorgänge und/oder Einsturz des Felsuntergrundes entstandene geschlossene Hohlform. Ihr Durchmesser variiert im Meter- bis Hundertmeterbereich.	A depression, formed by dissolution and/or collapse of a subsurface cavity. The diameter of such depressions can vary from a few meters to several hundred meters.
	Quelle/source	Diese Publikation; verändert nach BWG (2003)	This publication; modified from BWG (2003)
	Hierarchie/hierarchy	Karsthohlform → Doline	Hollow pattern in karst → Doline
G60	Name	Einsturzdoline	Collapse doline
	Definition	Hohlform in der Oberfläche, die durch den Versturz von oberflächennahen, durch Karstlösung gebildeten Hohlräumen, entstanden ist. Ist eine Unterform des Erdfalls.	Dolines formed by collapse of the surface into underlying voids produced by karstification. Special case of sinkhole.
	Quelle/source	Diese Publikation; verändert nach Ford & Williams (2007), Neuendorf et al. (2005)	This publication; modified from Ford & Williams (2007), Neuendorf et al. (2005)
	Hierarchie/hierarchy	Karsthohlform → Doline → Einsturzdoline	Hollow pattern in karst → Doline → Collapse doline
G61	Name	Dolinenfeld	Area of dolines
	Definition	Kartierbares Areal mit einer Anhäufung von isolierten Dolinen.	Mappable accumulation of isolated dolines.
	Quelle/source	Diese Publikation; verändert nach Ford & Williams (2007)	This publication; modified from Ford & Williams (2007)
	Hierarchie/hierarchy	Karsthohlform → Dolinenfeld	Hollow pattern in karst → Area of dolines
G62	Name	Polje	Polje
	Definition	Große geschlossene Senke mit flacher Sohle und steiler Randböschung auf zumindest einer Seite. Die Polje hat einen internen Karstabfluss und wird periodisch überflutet.	Large closed depression with steep margins and a flat bottom that is flooded periodically and which has a ‚karst' outflow.
	Quelle/source	Diese Publikation; verändert nach Ford & Williams (2007), Gams (1978), Goudie (2004), Neuendorf et al. (2005)	This publication; modified from Ford & Williams (2007), Gams (1978), Goudie (2004), Neuendorf et al. (2005)
	Hierarchie/hierarchy	Karsthohlform → Polje	Hollow pattern in karst → Polje
G63	Name	**Oberflächliche Karstlösungsform**	**Forms of karst dissolution on the surface**
	Definition	Oberflächliche, nicht weiter differenzierte Karstlösungsformen bilden das dominante geomorphologische Merkmal einer Landschaft.	Undifferentiated forms of karst dissolution are the dominant features in the area or landscape.
	Quelle/source	Diese Publikation	This publication
	Hierarchie/hierarchy	Oberflächliche Karstlösungsform	Forms of karst dissolution on the surface
G64	Name	Karren	Karren
	Definition	Lösungsbedingte Rillen, Kanäle oder Furchen sowie die Vollformen dazwischen auf der Oberfläche freiliegender verkarstungsfähiger Gesteine.	Grooves, channels or furrows caused by solution on massive bare limestone surfaces.
	Quelle/source	Diese Publikation; verändert nach EPA (2002), Ford & Williams (2007)	This publication; modified from EPA (2002), Ford & Williams (2007)
	Hierarchie/hierarchy	Oberflächliche Karstlösungsform → Karren	Forms of karst dissolution on the surface → Karren
G65	Name	Karrentisch	Pedestal
	Definition	Positivform in einer Oberfläche im Karstgestein, bedingt durch den lokalen Schutz vor Lösung aufgrund von aufliegenden Blöcken aus nicht verkarstungsfähigem Gestein.	Positive relief on a karst surface produced by shielding against solution by boulders of non-karstificable material.
	Quelle/source	Diese Publikation	This publication
	Hierarchie/hierarchy	Oberflächliche Karstlösungsform → Karren → Karrentisch	Forms of karst dissolution on the surface → Karren → Karrentisch

G66	Name	**Höhle**	**Cave**
	Definition	Natürlicher unterirdischer Hohlraum, der für den Menschen befahrbare Ausmaße hat (Kriterium für Aufnahme in den Österreichischen Höhlenkataster: Ganglänge > 5 m).	A natural subsurface cavity, which can be entered by man (A length of > 5 m is critical to the Austrian cave register).
	Quelle/source	Diese Publikation; verändert nach GUNN (2004), SPÖTL et al. (2016), FORD & WILLIAMS (2007)	This publication; modified from GUNN (2004), SPÖTL et al. (2016), FORD & WILLIAMS (2007)
	Hierarchie/hierarchy	Höhle	Cave
G67	Name	Halbhöhle	Shelter cave
	Definition	Meist durch Erosion entstandene Höhle, die in der Regel breiter ist als tief und keine lichtlosen Bereiche aufweist.	Cavity produced by erosion, usally broader than deep with no places without sunlight.
	Quelle/source	Diese Publikation	This publication
	Hierarchie/hierarchy	Höhle → Halbhöhle	Cave → Shelter cave
G68	Name	Erosionshöhle	Erosional cave
	Definition	Durch mechanische Erosion und/oder Verwitterung entstandene Höhle, die in jedem Gestein entstehen kann.	Cave formed by mechanical erosion or weathering.
	Quelle/source	Diese Publikation; verändert nach NEUENDORF et al. (2005)	This publication; modified from NEUENDORF et al. (2005)
	Hierarchie/hierarchy	Höhle → Erosionshöhle	Cave → Erosional cave
G69	Name	Spalthöhle	Crevice cave
	Definition	Durch gravitative Massenbewegung entstandene Höhle.	A cave developed due to gravitational mass movement.
	Quelle/source	Diese Publikation	This publication
	Hierarchie/hierarchy	Höhle → Spalthöhle	Cave → Crevice cave
G70	Name	Talushöhle	Talus cave
	Definition	Höhle, die in den Zwischenräumen von aneinandergrenzenden Blöcken einer Hangablagerung entwickelt ist.	A cave consisting of the interconnected spaces between boulders of talus.
	Quelle/source	Diese Publikation; verändert nach NEUENDORF et al. (2005)	This publication; modified from NEUENDORF et al. (2005)
	Hierarchie/hierarchy	Höhle → Talushöhle	Cave → Talus cave
G71	Name	**Permafrostform**	**Permafrost feature**
	Definition	Geomorphologische Form, die durch Einfluss von Permafrost entstanden ist.	A geological feature formed by the influence of permafrost.
	Quelle/source	Diese Publikation; verändert nach NEUENDORF et al. (2005)	This publication; modified from NEUENDORF et al. (2005)
	Hierarchie/hierarchy	Permafrostform	Permafrost feature
G72	Name	Blockgletscherwall	Ridge of a rock glacier
	Definition	Ein Rücken oder Wall eines Blockgletschers.	A ridge or wall of a rock glacier.
	Quelle/source	Diese Publikation; verändert nach NEUENDORF et al. (2005)	This publication; modified from NEUENDORF et al. (2005)
	Hierarchie/hierarchy	Permafrostform → Blockgletscherwall	Permafrost feature → Ridge of a rock glacier
G73	Name	Wall einer Blockgletscherablagerung	Ridge (rock glacier deposit)
	Definition	Aus Blockgletschermaterial (Schutt) bestehender Rücken/Wall eines nicht mehr existenten Blockgletschers (reliktischer Blockgletscher). Kommt meist in Gruppen von mehreren parallelen Wällen vor, wobei individuelle Wälle meist eine lobate bzw. zungenartige Form aufweisen.	A ridge consisting of deposits of a former rock glacier (relict rock glacier). In most cases, these ridges occur in groups where individual ridges show a lobate or tongue-like shape.
	Quelle/source	Diese Publikation; verändert nach NEUENDORF et al. (2005)	This publication; modified from NEUENDORF et al. (2005)
	Hierarchie/hierarchy	Permafrostform → Wall einer Blockgletscherablagerung	Permafrost feature → Ridge (rock glacier deposit)

G74	Name	**Terrassenniveau**	**Terrace level**
	Definition	Flacher horizontaler bis schwach geneigter Geländeteil, der jedenfalls an einer Seite mit einem steileren Hang gegen das benachbarte Gelände grenzt.	An elongated slightly inclined terrane surface with a steep slope on at least one side.
	Quelle/source	Diese Publikation; verändert nach MARTIN & EIBLMAIER (2003)	This publication; modified from MARTIN & EIBLMAIER (2003)
	Hierarchie/hierarchy	Terrassenniveau	Terrace level
G75	Name	Terrassenniveau 1	Terrace level 1
	Definition	Beim Vorkommen mehrerer Terrassenformen in unterschiedlicher Höhenlage die tiefste davon.	In case of several terrace levels, the lowermost terrace level.
	Quelle/source	Diese Publikation	This publication
	Hierarchie/hierarchy	Terrassenniveau → Terrassenniveau 1	Terrace level → Terrace level 1
G76	Name	Terrassenniveau 2	Terrace level 2
	Definition	Beim Vorkommen mehrerer Terrassenformen in unterschiedlicher Höhenlage die nächsthöhere über Terrassenniveau 1.	In case of several terrace levels, the one above the lowermost terrace level.
	Quelle/source	Diese Publikation	This publication
	Hierarchie/hierarchy	Terrassenniveau → Terrassenniveau 2	Terrace level → Terrace level 2
G77	Name	Terrassenniveau 3	Terrace level 3
	Definition	Beim Vorkommen mehrerer Terrassenformen in unterschiedlicher Höhenlage die nächsthöhere über Terrassenniveau 2.	In case of several terrace levels, the one above the second highest terrace level.
	Quelle/source	Diese Publikation	This publication
	Hierarchie/hierarchy	Terrassenniveau → Terrassenniveau 3	Terrace level → Terrace level 3
G78	Name	Austufe	Floodplain terrace
	Definition	Terrassenförmige Oberfläche in einer durch holozäne Flussdynamik (Überflutungen) geprägten Ebene.	Terrace-like surface developed as a flat floodplain.
	Quelle/source	Diese Publikation; verändert nach HINZE et al. (1989)	This publication; modified from HINZE et al. (1989)
	Hierarchie/hierarchy	Terrassenniveau → Austufe	Terrace level → Floodplain terrace
G79	Name	Austufe Niveau 1	Floodplain terrace level 1
	Definition	Beim Vorkommen mehrerer Austufen in unterschiedlicher Höhenlage die tiefste davon.	If more than one floodplain terrace exists, the lowermost one.
	Quelle/source	Diese Publikation; verändert nach HINZE et al. (1989)	This publication; modified from HINZE et al. (1989)
	Hierarchie/hierarchy	Terrassenniveau → Austufe → Austufe Niveau 1	Terrace level → Floodplain terrace → Floodplain terrace level 1
G80	Name	Austufe Niveau 2	Floodplain terrace level 2
	Definition	Die nächsthöhere Austufe über der Austufe Niveau 1.	If more than one floodplain terrace exists, the next one above the lowermost level.
	Quelle/source	Diese Publikation; verändert nach HINZE et al. (1989)	This publication; modified from HINZE et al. (1989)
	Hierarchie/hierarchy	Terrassenniveau → Austufe → Austufe Niveau 2	Terrace level → Floodplain terrace → Floodplain terrace level 2

Tab. 5.
Geomorphologische Einheiten – Begriffserläuterung.

Nr.		Deutsch	Englisch
P1	Name	**Anthropogenes Phänomen**	**Anthropogenic phenomenon**
	Definition	Durch menschliche Tätigkeit (künstlich) erzeugtes Phänomen.	A human-made (artificial) phenomenon.
	Quelle/source	Diese Publikation	This publication
	Hierarchie/hierarchy	Anthropogenes Phänomen	Anthropogenic phenomenon
P2	Name	**Verwitterungsphänomen**	**Weathering Phenomenon**
	Definition	Durch Verwitterungsprozesse erzeugtes Phänomen.	A phenomenon formed by weathering processes.
	Quelle/source	Diese Publikation	This publication
	Hierarchie/hierarchy	Verwitterungsphänomen	Weathering Phenomenon
P3	Name	Tiefgreifende Verwitterung	Deep seated weathering
	Definition	Bildungen, die durch in-situ-Verwitterungsprozesse ohne Umlagerung entstanden sind.	Features which were formed by deep seated in-situ weathering processes.
	Quelle/source	Diese Publikation	This publication
	Hierarchie/hierarchy	Verwitterungsphänomen → Tiefgreifende Verwitterung	Weathering Phenomenon → Deep seated weathering
P4	Name	Tiefgreifende Verwitterung/Vergrusung	Deep seated weathering/'Vergrusung'
	Definition	Bildungen, die durch in-situ-Verwitterungsprozesse ohne Umlagerung entstanden sind und eine Kornverkleinerung bis Sandgröße (Vergrusung) infolge haben können.	Features which were formed by deep seated in-situ weathering processes including a reduction in grain size down to sand.
	Quelle/source	Diese Publikation; verändert nach NEUENDORF et al. (2005), KRENMAYR et al. (2012)	This publication; modified from NEUENDORF et al. (2005), KRENMAYR et al. (2012)
	Hierarchie/hierarchy	Verwitterungsphänomen → Tiefgreifende Verwitterung → Tiefgreifende Verwitterung/ Vergrusung	Weathering Phenomenon → Deep seated weathering → Deep seated weathering/'Vergrusung'
P5	Name	Tiefgreifende Verwitterung/Verlehmung	Deep seated weathering/forming of loam
	Definition	Bildungen, die durch in-situ-Verwitterungsprozesse ohne Umlagerung entstanden sind und eine Kornverkleinerung bis Tongröße und Tonmineralneubildung (Verlehmung) infolge haben können.	Features which were formed by deep seated in-situ weathering processes including a reduction in grain size down to clay and genesis of clay minerals.
	Quelle/source	Diese Publikation; verändert nach NEUENDORF et al. (2005)	This publication; modified from NEUENDORF et al. (2005)
	Hierarchie/hierarchy	Verwitterungsphänomen → Tiefgreifende Verwitterung → Tiefgreifende Verwitterung/ Verlehmung	Weathering Phenomenon → Deep seated weathering → Deep seated weathering/forming of loam
P6	Name	Wollsackverwitterung	Spheroidal weathering
	Definition	Chemische Verwitterung, die am Trennflächensystem von Festgesteinen ansetzt und deren Oberfläche durch schalenförmiges Abplatzen von Gesteinsmaterial abrundet. Dadurch bilden sich sogenannte Wollsäcke.	Chemical weathering that affects jointed bedrock and results in the formation of concentric or spherical layers of decayed rock within weathered bedrock.
	Quelle/source	Diese Publikation; verändert nach NEUENDORF et al. (2005)	This publication; modified from NEUENDORF et al. (2005)
	Hierarchie/hierarchy	Verwitterungsphänomen → Tiefgreifende Verwitterung → Wollsackverwitterung	Weathering Phenomenon → Deep seated weathering → Spheroidal weathering
P7	Name	Geologische Orgel	Pipe-like weathering structure
	Definition	Durch intensive Lösungsverwitterung entlang von Wasserwegigkeiten entstandene Schlote oder Trichter in Karbonat führenden Lockergesteinen.	Pipe-like structure in carbonate bearing sediments due to weathering and dissolution along joints and cracks.
	Quelle/source	Diese Publikation; verändert nach LFU (2019b), VAN HUSEN (1999)	This publication; modified from LFU (2019b), VAN HUSEN (1999)
	Hierarchie/hierarchy	Verwitterungsphänomen → Tiefgreifende Verwitterung → Geologische Orgel	Weathering Phenomenon → Deep seated weathering → Pipe-like weathering structure
P8	Name	Paläoboden	Paleosol
	Definition	Boden und Reste von Böden, die in einem früheren geologischen Zeitraum entstanden sind.	A soil or remnants of a soil that was formed in an earlier geological period.
	Quelle/source	NEUENDORF et al. (2005)	NEUENDORF et al. (2005)
	Hierarchie/hierarchy	Verwitterungsphänomen → Paläoboden	Weathering Phenomenon → Paleosol

P9	Name	**Gravitatives Phänomen**	**Gravitative phenomenon**
	Definition	Phänomene, die aufgrund von Abtragungs-, Transport- und Ablagerungsvorgängen, überwiegend unter dem Einfluss der Schwerkraft (gravitative Massenbewegung) entstanden sind.	A phenomenon formed by gravitational mass wasting, transport and deposition.
	Quelle/source	Diese Publikation; verändert nach ZEPP (2002)	This publication; modified from ZEPP (2002)
	Hierarchie/hierarchy	Gravitatives Phänomen	Gravitative phenomenon
P10	Name	Umrandung eines Massenbewegungskörpers	Border of a mass movement
	Definition	Abgrenzung bzw. Umrandung eines zusammengehörigen Bereiches, dessen Morphologie und Inhalt auf gravitative Massenbewegung schließen lässt, aber dessen unvollständige und/oder komplexe Genese keine Zuordnung zu einer Lithogenetischen Einheit erlaubt.	Border of a body where morphology and composition indicate a gravitative mass movement and where the incompleteness or complexity of the genesis prevents a clear assignment to a certain lithogenetic unit.
	Quelle/source	Diese Publikation	This publication
	Hierarchie/hierarchy	Gravitatives Phänomen → Umrandung eines Massenbewegungskörpers	Gravitative phenomenon → Border of a mass movement
P11	Name	Umrandung einer tiefgreifenden Hangdeformation	Border of deep-seated gravitational slope deformation
	Definition	Abgrenzung bzw. Umrandung von gravitativ umgelagertem bzw. sich sehr langsam umlagernden Fest- und/oder Lockergestein meist sehr großer Kubatur und Fläche (gesamte Hangflanke) mit unterschiedlichstem Zerlegungsgrad (Fels im Verband bis komplett zerlegt in Kluftkörper).	Border of gravitational moved bedrock or sediments of large volume and expanse (full slope) of different degrees of disintegration.
	Quelle/source	Diese Publikation; verändert nach WEIDNER (2000), VARNES (1978), AGLIARDI et al. (2001)	This publication; modified from WEIDNER (2000), VARNES (1978), AGLIARDI et al. (2001)
	Hierarchie/hierarchy	Gravitatives Phänomen → Umrandung eines Massenbewegungskörpers → Umrandung einer tiefgreifenden Hangdeformation	Gravitative phenomenon → Border of a mass movement → Border of deep-seated gravitational slope deformation
P12	Name	**Hydrologisches Phänomen**	**Hydrological phenomenon**
	Definition	Phänomene, die mit dem Vorkommen, der Zirkulation, der Verteilung und den Eigenschaften von Wasser über, auf und unter der Erdoberfläche sowie deren Wechselwirkung mit der Umwelt in Zusammenhang stehen.	Any phenomenon related to the occurrence, circulation, distribution, and properties of water, whether above or below the land surface, and its interactions with the environment.
	Quelle/source	LOAT & MEIER (2003)	LOAT & MEIER (2003)
	Hierarchie/hierarchy	Hydrologisches Phänomen	Hydrological phenomenon
P13	Name	Abflusslose Senke	Drainless depression
	Definition	Einsenkung im Gelände ohne Abfluss.	Landscape depression without water-outflow.
	Quelle/source	Diese Publikation	This publication
	Hierarchie/hierarchy	Hydrologisches Phänomen → Abflusslose Senke	Hydrological phenomenon → Drainless depression
P14	Name	Moor	Bog
	Definition	Als Moore bezeichnet man die Entstehungsgebiete der Torfe (min. 0,3 m Torfmächtigkeit und min. 30 Gew.% organischen Anteil), die durch eine unvollständige Zersetzung aus bestimmten Pflanzengesellschaften entstehen. Die wichtigsten Bildungsbedingungen sind hoher Wasserüberschuss und damit verbundener Sauerstoffmangel.	Bogs are areas where peat is formed. Peat is formed by an incomplete disintegration of certain plant communities; the most important factor in its formation is the presence of excess water, resulting in a lack of oxygen.
	Quelle/source	HINZE et al. (1989), NEUENDORF et al. (2005)	HINZE et al. (1989), NEUENDORF et al. (2005)
	Hierarchie/hierarchy	Hydrologisches Phänomen → Moor	Hydrological phenomenon → Bog
P15	Name	Hochmoor	Highmoor bog
	Definition	Niederschlagsbedingte, vom Grundwasser unbeeinflusste Vermoorung. Im Hochmoor baut sich ein eigenständiger Wasserkörper auf. Die Nährstoffarmut des Niederschlagswassers und der geringe sonstige Eintrag an Nährstoffen bedingen eine extreme Nährstoffarmut und ein stark saures Milieu.	A bog formed by precipitation. A highmoor bog forms an enclosed water body. The lack of nutrients in water from precipitation and the absence of any nutrient input from other sources results in a sour environment.
	Quelle/source	HINZE et al. (1989), NEUENDORF et al. (2005)	HINZE et al. (1989), NEUENDORF et al. (2005)
	Hierarchie/hierarchy	Hydrologisches Phänomen → Moor → Hochmoor	Hydrological phenomenon → Bog → Highmoor bog

P16	Name	Niedermoor	Lowmoor bog
	Definition	Vermoorung unter dem Einfluss von Mineralbodenwasser. Entsprechend den unterschiedlichen örtlichen Bedingungen (Nässe, Chemismus) besteht hinsichtlich der Ausgangsvegetation und der Torfarten eine große Vielfalt.	A bog formed by groundwater in which different types of peat can form depending on the local conditions and vegetation.
	Quelle/source	HINZE et al. (1989)	HINZE et al. (1989)
	Hierarchie/hierarchy	Hydrologisches Phänomen → Moor → Niedermoor	Hydrological phenomenon → Bog → Lowmoor bog
P17	Name	Anmoor	Half-bog soil
	Definition	Als Anmoor bezeichnet man Gebiete mit einem Gemisch aus mineralischer und feinverteilter organischer Substanz (15–30 Gew.%) oder Torf, der weniger als 0,3 m mächtig ist.	Area with a mixture of mineral and dispersed organic matter (15–30 %) or peat of less than 0.3 m.
	Quelle/source	Diese Publikation; verändert nach HINZE et al. (1989), NEUENDORF et al. (2005)	This publication; modified from HINZE et al. (1989), NEUENDORF et al. (2005)
	Hierarchie/hierarchy	Hydrologisches Phänomen → Anmoor	Hydrological phenomenon → Half-bog soil
P18	Name	Vernässung	Wetland
	Definition	Gelegentlich durchnässtes bzw. dauerhaft feuchtes Gebiet.	A periodically or permanently wet area.
	Quelle/source	BWG (2003)	BWG (2003)
	Hierarchie/hierarchy	Hydrologisches Phänomen → Vernässung	Hydrological phenomenon → Wetland
P19	Name	Schwinde	Water sink
	Definition	Bereich, an der ein Oberflächengerinne teilweise oder zur Gänze versickert.	Area where water disappears in the ground.
	Quelle/source	Diese Publikation	This publication
	Hierarchie/hierarchy	Hydrologisches Phänomen → Schwinde	Hydrological phenomenon → Water sink
P20	Name	Ponor	Ponor
	Definition	Öffnung im Karst, in die oberflächliche Fließ- oder Stehgewässer teilweise oder zur Gänze, permanent oder temporär in ein Karstsystem eintreten und unterirdisch abfließen. Synonym für Schluckloch.	The opening through which a sinking stream loses its water to the subsurface into a karst system.
	Quelle/source	Diese Publikation; verändert nach GUNN (2004), NEUENDORF et al. (2005)	This publication; modified from GUNN (2004), NEUENDORF et al. (2005)
	Hierarchie/hierarchy	Hydrologisches Phänomen → Schwinde → Ponor	Hydrological phenomenon → Water sink → Ponor
P21	Name	**Karstverwandtes Phänomen**	**Karst like phenomenon**
	Definition	Überbegriff für Phänomene, die eine karstähnliche Genese besitzen.	Phenomenon formed by karst-like processes.
	Quelle/source	Diese Publikation	This publication
	Hierarchie/hierarchy	Karstverwandtes Phänomen	Karst like phenomenon
P22	Name	Paläokarst	Paleokarst
	Definition	Karst, der sich während eines früheren Erosionszyklus gebildet hat und konserviert wurde (Begraben oder durch Stilllegung der Verkarstungsprozesse).	A karst formed under an earlier erosion cycle, preserved by burial or suspension of karstification processes. Caves and sinkholes are usually filled with sediment.
	Quelle/source	NEUENDORF et al. (2005)	NEUENDORF et al. (2005)
	Hierarchie/hierarchy	Karstverwandtes Phänomen → Paläokarst	Karst like phenomenon → Paleokarst
P23	Name	**Permafrostphänomen**	**Permafrost phenomenon**
	Definition	Durch Permafrostprozesse entstandenes Phänomen.	A Phenomenon formed by periglacial processes.
	Quelle/source	Diese Publikation	This publication
	Hierarchie/hierarchy	Permafrostphänomen	Permafrost phenomenon
P24	Name	Permafrostverwitterung	Permafrost weathering
	Definition	Verwitterung aufgrund von Permafrost bedingten Prozessen (Frieren und Tauen).	Weathering due to processes related to permafrost conditions (freezing and melting).
	Quelle/source	Diese Publikation	This publication
	Hierarchie/hierarchy	Permafrostphänomen → Permafrostverwitterung	Permafrost phenomenon → Permafrost weathering

P25	Name	Eiskeil-Pseudomorphose	Ice wedge cast
	Definition	Keilförmige sedimentäre Struktur, die durch Frier- und Tauprozesse in Lockergesteinen während Permafrost-Bedingungen entstanden und mit Sediment verfüllt ist.	Wedge-shaped sedimentary structure, which formed by freezing and melting processes within unconsolidated sediments under permafrost conditions.
	Quelle/source	Diese Publikation; verändert nach NEUENDORF et al. (2005)	This publication; modified from NEUENDORF et al. (2005)
	Hierarchie/hierarchy	Permafrostphänomen → Eiskeil-Pseudomorphose	Permafrost phenomenon → Ice wedge cast
P26	Name	Eiskeilnetz (fossil)	Ice wedge polygon (fossil)
	Definition	Großflächige Verbreitung von Eiskeil-Pseudomorphosen.	Area with a high density of ice wedge casts.
	Quelle/source	Diese Publikation	This publication
	Hierarchie/hierarchy	Permafrostphänomen → Eiskeilnetz (fossil)	Permafrost phenomenon → Ice wedge polygon (fossil)
P27	Name	Frostmusterboden	Patterned ground
	Definition	Klar definierte, mehr oder weniger symmetrische Oberflächenformen (Polygone, Kreise, Streifen etc.), die aufgrund von Frier- und Tauprozessen in Permafrost-Regionen entstehen.	A clearly defined, more or less symmetrical surface feature (e.g. polygons, circles, strips) formed due to freezing and melting processes in regions of permafrost.
	Quelle/source	Diese Publikation; verändert nach NEUENDORF et al. (2005)	This publication; modified from NEUENDORF et al. (2005)
	Hierarchie/hierarchy	Permafrostphänomen → Frostmusterboden	Permafrost phenomenon → Patterned ground
P28	Name	Kryoturbation	Cryoturbation
	Definition	Durchmischung von Material in Lockergesteinen aus verschiedenen Horizonten aufgrund von Frier- und Tauprozessen während Permafrost-Bedingungen.	Mixing of loose sediment material of different horizons by freezing and melting.
	Quelle/source	Diese Publikation; verändert nach NEUENDORF et al. (2005)	This publication; modified from NEUENDORF et al. (2005)
	Hierarchie/hierarchy	Permafrostphänomen → Kryoturbation	Permafrost phenomenon → Cryoturbation
P29	Name	Unterkühlte Schutthalde	Undercooled talus
	Definition	Ablagerung aus grobem Material in Form einer Halde, die Temperaturen beträchtlich unter dem Jahresnormalwert der Lufttemperatur der unmittelbaren Umgebung aufweist. Ein derartiger Aufbau ermöglicht die Ausbildung eines Windröhrensystems mit Luftzirkulation, welche, je nach Temperaturdifferenz zur Außenluft, entweder aufsteigend (Winter- bzw. Nachtsituation) oder absteigend (Sommer bzw. Situation tagsüber) erfolgt.	Talus of coarse material with inside temperatures below the normal temperatures of the surroundings.
	Quelle/source	WAKONIGG (2006), SCHUSTER et al. (2006)	WAKONIGG (2006), SCHUSTER et al. (2006)
	Hierarchie/hierarchy	Permafrostphänomen → Unterkühlte Schutthalde	Permafrost phenomenon → Undercooled talus

Tab. 6.
Quartäre Phänomene – Begriffserläuterung.

Literatur

Abele, G. (1974): Bergstürze in den Alpen, ihre Verbreitung, Morphologie und Folgeerscheinungen. – Wissenschaftliche Alpenvereinshefte, **25**, 230 S., München.

Agliardi, F., Crosta, G. & Zanchi, A. (2001): Structural constraints on deep-seated slope deformation kinematics. – Engineering Geology, **59**, 83–102, Amsterdam.

Ahnert, F. (2015): Einführung in die Geomorphologie. – 5. Auflage, 458 S., Stuttgart.

Ampferer, O. (1940): Zum weiteren Ausbau der Lehre von den Bergzerreißungen. – Sitzungsberichte der mathematisch-naturwissenschaftlichen Klasse der Akademie der Wissenschaften in Wien, Abteilung I, **149**, 51–70, Wien.

Benn, D.I. & Evans, D.J.A. (2010): Glaciers and glaciation. – 2. Auflage, 802 S., London (Hodder Education).

Bovis, M.J. (1982): Uphill-facing (antislope) scarps in the Coast Mountains, southwest British Columbia. – Geological Society of America Bulletin, **93**, 804–812, Boulder.

Busche, D., Kempf, J. & Stengel, I. (2005): Landschaftsformen der Erde. Bildatlas der Geomorphologie. – 360 S., WBG, Darmstadt.

BWG – Bundesamt für Wasser und Geologie (2003): Anweisungen zur Darstellung des quartären Formenschatzes sowie weiterer Zeichen und Signaturen bei der Reinzeichnung der Manuskriptkarten des Geologischen Atlas der Schweiz 1:25.000. – 1 Ordner, 1 CD-ROM, BWG, Bern-Ittigen.

CGI (2016): Geoscience Vocabularies: Lithogenetic Unit. – http://resource.geosciml.org/classifier/cgi/geologicunittype/lithogenetic_unit (abgerufen am 17.12.2019).

Cruden, D.M. & Varnes, D.J. (1996): Landslide Types and Processes. – In: Turner, A.K. & Schuster, R.L. (Eds.): Landslides, Investigation and Mitigation. – National Research Council, Special Report, **247**, 36–75, Washington, D.C.

De Freitas, M.H. & Watters, R.J. (1973): Some field examples of toppling failure. – Géotechnique, **23**/4, 495–514, Paris.

Dramis, F. & Sorriso-Valvo, M. (1994): Deep-seated gravitational slope deformations, related landslides and tectonics. – Engineering Geology, **38**, 231–243, Amsterdam.

Embleton-Hamann, C. & Wilhelmy, H. (2007): Geomorphologie in Stichworten; III. Exogene Morphodynamik: Karstmorphologie – Glazialer Formenschatz – Küstenformen. – 6. neubearbeitete Auflage, 164 S., Stuttgart (Borntraeger).

EPA – United States Environmental Protection Agency (2002): A Lexicon of Cave and Karst Terminology with Special Reference to Environmental Karst Hydrology. – National Center for Environmental Assessment, Office of Research and Development, EPA/600/R-02/003, VI + 214 S., Washington, D.C.

Evans, D.J.A., Phillips, E.R., Hiemstra, J.F. & Auton, C.A. (2006): Subglacial till: Formation, sedimentary characteristics and classification. – Earth-Science Reviews, **78**, 115–176, Amsterdam.

Ford, D. & Williams, P. (2007): Karst Hydrogeology and Geomorphology. – 576 S., Chichester.

Fürlinger, W.L. (1972): Talzuschub und Wildbachverbauung. – Dissertation, Universität Wien, VI + 240 S., Wien.

Gams, I. (1978): The polje: the problem of definition. – Zeitschrift für Geomorphologie, **22**/2, 170–181, Stuttgart (Schweizerbart).

Goodman, R.E. & Bray, J.W. (1976): Toppling of rock slopes. – Proceedings of the Specialty Conference on Rock Engineering for Foundations and Slopes, ASCE Publications, **2**, 201–234, Boulder.

Goudie, A.S. (Ed.) (2004): Encyclopedia of Geomorphology. – Volume 1, XXX + 1–578, Volume 2, XIV + 579–1156, London–New York (Routledge).

Gunn, J. (Ed.) (2004): Encyclopedia of Caves and Karst Science. – XXIX + 1940 S., New York–London (Fitzroy Dearborn).

Heim, A. (1932): Bergsturz und Menschenleben. – Beiblatt zur Vierteljahresschrift der Naturforschenden Gesellschaft in Zürich, **77**/20, 218 S., Zürich (Fretz & Wasmuth).

Heinisch, H., Pestal, G. & Reitner, J.M. (2015): Geologische Karte der Republik Österreich 1:50.000, Erläuterungen zu Blatt 122 Kitzbühel. – 301 S., Geologische Bundesanstalt, Wien.

Hermann, S. (1996): Initiale Bergzerreißung als Gefahrenherd für Bergstürze, Nährgebiet für Muren und Großrutschungen. Beispiele aus dem Naturpark Sölktäler, Österreich. – Internationales Symposium Interpraevent, Band **1**, 409–418, Garmisch-Partenkirchen.

Hinze, C., Jerz, H., Menke, B. & Staude, H. (1989): Geogenetische Definitionen quartärer Lockergesteine für die Geologische Karte 1:25.000 (GK 25). – Geologisches Jahrbuch, A, **112**, 243 S., Stuttgart (Schweizerbart).

Horninger, G. (1958): Einiges über Talzuschübe und deren Vorzeichnung. – Geologie und Bauwesen, **24**/1, 37–54, Wien (Springer).

Hsü, K.J. (1975): Catastrophic debris streams (Sturzstroms) generated by rockfalls. – Geological Society of America Bulletin, **86**/1, 129–140, Boulder.

Hungr, O., Evans, S.G., Bovis, M.J. & Hutchinson, J.N. (2001): A Review of the Classification of Landslides of the Flow Type. – Environmental & Engineering Geoscience, **VII**/3, 221–238, Texas.

Hungr, O., Leroueil, S. & Picarelli, L. (2014): The Varnes classification of landslide types, an update. – Landslides, **11**, 167–194, Berlin–Heidelberg (Springer).

Jahn, A. (1964): Slopes morphological features resulting from gravitation. – Zeitschrift für Geomorphologie, Supplement **5**, 59–72, Berlin (Borntraeger).

Krenmayr, H.-G., Ćorić, S., Gebhardt, H., Iglseder, C., Linner, M., Mandl, G., Reitner, J., Rockenschaub, M., Roetzel, R. & Rupp, C. (2012): Generallegende der pleistozänen bis holozänen Sedimente und Verwitterungsprodukte des Periglazialraumes auf den geologischen Spezialkarten (1:50.000, 1:25.000) der Geologischen Bundesanstalt. – Jahrbuch der Geologischen Bundesanstalt, **152**, 57–66, Wien.

LfU (Bayerisches Landesamt für Umwelt) (2019a): Geologie-Massenbewegungen-Glossar, Definition Erd-/Schutt-/Blockstrom. – https://www.lfu.bayern.de/geologie/massenbewegungen/glossar/index.htm?action=show_def&tid=2043&dl=E&sl=1&tl=1 (abgerufen am 17.12.2019).

LfU (Bayerisches Landesamt für Umwelt) (2019b): Geologie-Bayerns schönste Geotope-82, Geologische Orgeln Oberschroffen. – https://www.lfu.bayern.de/geologie/bayerns_schoenste_geotope/82/index.htm (abgerufen am 17.12.2019).

Loat, R. & Meier, E. (2003): Wörterbuch Hochwasserschutz. – 424 S., Bundesamt für Wasser und Geologie/Schweizerische Bundeskanzlei, Bern (Haupt).

LUKAS, S. & ROTHER, H. (2016): Moränen versus Till: Empfehlungen für die Beschreibung, Interpretation und Klassifikation glazialer Landformen und Sedimente. – E&G Quaternary Science Journal, **65**/2, 95–112, Berlin.

MARTIN, C. & EIBLMAIER, M. (Hrsg.) (2003): Lexikon der Geowissenschaften. – Gesamtausgabe in 5 Bänden + 1 Registerband, 2840 S., Berlin–Heidelberg (Spektrum Akademischer Verlag).

MENZIES, J. (1979): The mechanics of drumlin formation with particular reference to the change in pore-water content of the till. – Journal of Glaciology, **22**/87, 373–384, IGS, Cambridge.

MOSER, M. & GLUMAC, S. (1982): Geotechnische Untersuchungen zum Massenkriechen in Fels am Beispiel des Talzuschubes Gradenbach (Kärnten). – Verhandlungen der Geologischen Bundesanstalt, **1982**/3, 209–241, Wien.

MURAWSKI, H. & MEYER, W. (1998): Geologisches Wörterbuch. – 10. Auflage, 278 S., Stuttgart (Enke).

NEMČOK, A., PAŠEK, J. & RYBÁŘ, J. (1972): Classification of landslides and other mass movements. – Rock Mechanics, **4**, 71–78, Wien (Springer).

NEUENDORF, K.K.E., MEHL, J.P. JR & JACKSON, J.A. (2005): Glossary of Geology. – 5. Auflage, XIII + 779 S., Berlin–Heidelberg–New York (Springer).

POISEL, R. & EPPENSTEINER, W. (1988): Gang und Gehwerk einer Massenbewegung Teil 1: Geomechanik des Systems „Hart auf Weich“. – Felsbau, **6**/4, 189–194, Essen (Glückauf).

POISEL, R. & EPPENSTEINER, W. (1989): Gang und Gehwerk einer Massenbewegung Teil 2: Massenbewegungen am Rand des Systems „Hart auf Weich“. – Felsbau, **7**/1, 16–20, Essen (Glückauf).

POISEL, R. & KIEFFER, S. (2009): Sackung – was ist das? – In: PFEILER, A. & AUGUSTIN-GYURTIS, K. (Eds.): Festschrift anlässlich des 80. Geburtstages von Univ. Doz. Dr. phil. Walter Eppensteiner, 33–38, Fachverband der Stein- und keramischen Industrie, Wien.

POLLET, N. & SCHNEIDER, J.-L.M. (2004): Dynamic disintegration processes accompanying transport of the Holocene Flims sturzstrom (Swiss Alps). – Earth and Planetary Science Letters, **221**, 433–448, Amsterdam (Elsevier).

PREBBLE, W.M. (1995): Landslides in tabular rock masses of an active convergent margin. – In: BELL, F.G. (Ed.): Proceedings of the 6th International Symposium on Landslides, 2145–2151, Rotterdam (Balkema).

REITNER, J. M. & LINNER, M. (2009): Formation and Preservation of large scale toppling related to Alpine tectonic structures – Eastern Alps. – Austrian Journal of Earth Sciences, **102**/2, 69–80, Vienna.

SCHUSTER, R., PESTAL, G. & REITNER, J.M. (2006): Geologische Karte der Republik Österreich 1:50.000, Erläuterungen zu Blatt 182 Spittal an der Drau. – 115 S., Geologische Bundesanstalt, Wien.

SPÖTL, C., PLAN, L. & ERHARD, C. (2016): Höhlen und Karst in Österreich. – 752 S., Oberösterreichisches Landesmuseum, Linz.

STINI, J. (1941): Unsere Täler wachsen zu. – Geologie und Bauwesen, **13**/3, 71–79, Wien (Springer).

VAN HUSEN, D. (1999): Geologisch-baugeologische Erfahrungen beim Bau des Eisenbahntunnels Lambach, OÖ. – Mitteilungen der Österreichischen Geologischen Gesellschaft, **90**, 137–154, Wien.

VAN HUSEN, D. & REITNER, J.M. (2011): An Outline of the Quaternary Stratigraphy of Austria. – E&G Quaternary Science Journal, **60**/2–3, 366–387, Berlin.

VARNES, D.J. (1978): Slope movement types and processes. – In: SCHUSTER, R.L. & KRIZEK, R.J. (Eds.): Landslides, analysis and control. – Transportation Research Board, Special Report, No. **176**, Chapter 2, 11–33, National Academy of Sciences, Washington, D.C.

WAKONIGG, H. (2006): Die unterkühlte Blockschutthalde beim Pflüglhof im Maltatal, Ergebnisse von Temperatur-Dauerregistrierungen von April 2001 bis Mai 2004. – Carinthia II, **196**/**116**, 501–518, Naturwissenschaftlicher Verein für Kärnten, Klagenfurt.

WEIDNER, S. (2000): Kinematik und Mechanismus tiefgreifender alpiner Hangdeformationen unter besonderer Berücksichtigung der hydrogeologischen Verhältnisse. – Dissertation Universität Erlangen-Nürnberg, X + 246 S., Erlangen.

ZANGERL, C., PRAGER, C., BRANDNER, R., BRÜCKL, E., EDER, S., FELLIN, W., TENTSCHERT, E., POSCHER, G. & SCHÖNLAUB, H. (2008): Methodischer Leitfaden zur prozessorientierten Bearbeitung von Massenbewegungen. – Geo.Alp, **5**, 1–51, Innsbruck–Bozen.

ZÁRUBA, Q. & MENCL, V. (1969): Landslides and their control. – 205 S., Amsterdam (Elsevier).

ZEPP, H. (2002): Geomorphologie: Eine Einführung. – 3. Auflage, UTB für Wissenschaft, **2164**, 354 S., Paderborn (Schöningh).

ZISCHINSKY, U. (1969): Über Sackungen. – Rock Mechanics, **1**, 30–52, Wien.

Eingelangt: 19. August 2019, angenommen: 3. Oktober 2019

Anhänge

Anmerkung zu den Anhängen

Mit den Symbolikvorschlägen in den Anhängen wird ein Grundgerüst für die Darstellung der in diesem Beitrag definierten Begriffe mitgegeben. Die Anhänge stellen einen Auszug aus der GBA-internen Generallegende dar und sind zu Gunsten der besseren Übersichtlichkeit auf die Attribute reduziert, die für Farb- und Symbolikgebung entscheidend sind. Außerdem sind beispielhaft wichtige kombinierte Legendenausscheidungen (z.B. Schwemmkegel, Murkegel) angeführt. Aufgeteilt sind die Symbole in drei Spalten mit den Maßstäben 1:10.000, 1:25.000 bzw. 1:50.000 und 1:200.000. Wenn kein Symbol in einer Spalte vorhanden ist, dann soll der betreffende Begriff in diesem Maßstab nicht verwendet werden.

Anhang 1: Symbolikvorschlag für Lithogenetische Einheiten

Nr.	Lithogenetische Einheiten	Kommentar	Symbol 1:10.000	Symbol 1:25.000/ 1:50.000	Symbol 1:200.000
L1	**Anthropogene Ablagerung**				
L2	Anthropogene Auffüllung				
L3	Anthropogene Aufschüttung				
L4	Dammbauwerk				
L5	Deponiekörper				
L6	Flugasche				
L7	**Äolische Ablagerung**				
L8	Flugsand				
L9	Löss				
L10	Lösslehm				
L9, L10	*Löss, Lösslehm*	Kombinationsbegriff			
L11	Vulkanische Aschenablagerung		A	A	
L12	**Fluviatile Ablagerung**				
L13	Ablagerung in Talsohlen und Talkerben				
L14	Bach- und Flussablagerung				
L15	Flussablagerung				
	Flussablagerung, Günz, Ältere Deckenschotter	Beispiel für Symboladaption aufgrund von Allostratigrafie			
	Flussablagerung, Mindel, Jüngere Deckenschotter	Beispiel für Symboladaption aufgrund von Allostratigrafie			
	Flussablagerung, Riß, Hochterrasse	Beispiel für Symboladaption aufgrund von Allostratigrafie			
	Flussablagerung, Würm, Niederterrasse	Beispiel für Symboladaption aufgrund von Allostratigrafie			
	Flussablagerung, Würm-Vorstoßphase	Beispiel für Symboladaption aufgrund von Chronologie			
L16	Flussbettablagerung				

L17	Überschwemmungsablagerung				
L18	Wildbachablagerung				
L19	Murkegel				
L20	Schwemmkegel				
L19, L20	*Schwemmkegel, Murkegel*	Kombinationsbegriff			
L21	Schwemmfächer				
	Linien für Murkegel, Schwemmkegel und Schwemmfächer nicht im digitalen Datensatz enthalten; nur für kartografische Nachbearbeitung				
L22	**Glaziofluviatile Ablagerung**				
	Glaziofluviatile Ablagerung, Günz, Ältere Deckenschotter	Beispiel für Symboladaption aufgrund von Allostratigrafie			
	Glaziofluviatile Ablagerung, Mindel, Jüngere Deckenschotter	Beispiel für Symboladaption aufgrund von Allostratigrafie			
	Glaziofluviatile Ablagerung, Riß, Hochterrasse	Beispiel für Symboladaption aufgrund von Allostratigrafie			
	Glaziofluviatile Ablagerung, Würm, Niederterrasse	Beispiel für Symboladaption aufgrund von Allostratigrafie			
L23	Sander				
	Sander, Günz, Ältere Deckenschotter	Beispiel für Symboladaption aufgrund von Allostratigrafie			
	Sander, Mindel, Jüngere Deckenschotter	Beispiel für Symboladaption aufgrund von Allostratigrafie			
	Sander, Riß, Hochterrasse	Beispiel für Symboladaption aufgrund von Allostratigrafie			
	Sander, Würm, Niederterrasse	Beispiel für Symboladaption aufgrund von Allostratigrafie			
L24	Subglaziale Schmelzwasserablagerung				
L25	Eskerablagerung				
L26	Eisrandablagerung				
L27	Kameablagerung				
L28	**Glaziogene Ablagerung**				
L29	Grundmoränenablagerung				
L30	Ablationsmoränenablagerung				
L29, L30	*Grundmoränenablagerung, Ablationsmoränenablagerung*	Kombinationsbegriff			
L31	Ablationsblock		×	×	
L32	Erratischer Block		×	×	

L33	End- und Seitenmoränenablagerung				
	End- und Seitenmoränenablagerung, Blöcke	Beispiel für Variation in litholo-gischer Zusammensetzung			
	End- und Seitenmoränenablagerung, Diamikt	Beispiel für Variation in litholo-gischer Zusammensetzung			
	End- und Seitenmoränenablagerung, Günz	Beispiel für Symboladaption aufgrund von Chronologie			
	End- und Seitenmoränenablagerung, Mindel	Beispiel für Symboladaption aufgrund von Chronologie			
	End- und Seitenmoränenablagerung, Riß	Beispiel für Symboladaption aufgrund von Chronologie			
	End- und Seitenmoränenablagerung, Würm	Beispiel für Symboladaption aufgrund von Chronologie			
	End- und Seitenmoränenablagerung, Diamikt mit End- und Seitenmoränenwall (Egesen)	Beispiel für Kombination von lithogenetischer und geomorphologischer Einheit			
L34	Moränenstreu	Punktsignatur			
	Moränenstreu	Flächensignatur			
L35	**Glaziolakustrine Ablagerung**				
L36	Glaziolakustrine Beckenablagerung				
L37	Subaquatische Moränenablagerung				
L38	Dropstone Block				
L39	**Gravitative Ablagerung**				
L40	Bergsturzablagerung				
L41	Bergsturzgleitmasse				
L42	Sturzstromablagerung				
L43	Felssturzablagerung				
L44	Sturzblock				
L45	Fließmasse				
L46	Erdstromablagerung				
L47	Murablagerung				
L48	Schuttstromablagerung				
L49	Gleitmasse				
L50	Hangablagerung				
L51	Hangbrekzie				
L52	Hangablagerung mit Moränenmaterial				
L53	Schuttkegel				
L20, L53	*Schuttkegel, Schwemmkegel*	Kombinationsbegriff			
		Linien für Schuttkegel und Schwemmkegel nicht im digitalen Datensatz enthalten; nur für kartografische Nachbearbeitung			

L54	Lawinenschuttablagerung				
L55	Solifluktionsablagerung				
L56	**Lakustrine Ablagerung**				
L57	Deltaablagerung				
L58	Rückstauablagerung				
L59	Seebeckenablagerung				
L60	Strandablagerung				
L61	**Palustrische Ablagerung**				
L62	Torf Ablagerung				
L63	**Permafrostablagerung**				
L64	Blockgletscher				
L65	Blockgletscherablagerung				
L66	Geli-Solifluktionsablagerung				
L67	**Flächenspülungsablagerung**				
L55, L67	*Solifluktionsablagerung, Flächenspülungsablagerung*	Kombinationsbegriff			
L68	Schwemmlöss				
L69	Verschwemmte Moränenablagerung				
L70	**Chemische und Biochemische Ausfällungen**				
L71	Sinterkalk				
L72	Alm				

Anhang 2: Symbolikvorschlag für Geomorphologische Einheiten

Nr.	Lithogenetische Einheiten	Kommentar	Symbol 1:10.000	Symbol 1:25.000/ 1:50.000	Symbol 1:200.000
G1	**Anthropogene Form**				
G2	**Äolische Form**				
G3	Düne				
G4	**Erosionsform**				
G5	Erdpyramide				
G6	Felsterrasse				
G7	Paläo-Kolk				
G8	Geländekante				
G9	Erosionskante				
G10	Terrassenkante				
G11	Verebnungsfläche				
G12	Yardang (Windhöcker)				
G13	Windkanter				
G14	**Glaziofluviatile Form**				
G15	Übergangskegel (Sander)				
G16	**Glaziogene Form**				
G17	Glaziogene Erosionsform				
G18	Gletschermühle				
G19	Gletscherschliff				
G20	Muschelbruch				
G21	Rat tail				
G22	Glaziale Striemungen				
G23	Schliffgrenze				
G24	Rundhöcker				
G25	Whaleback				
G26	Subglaziale Schmelzwasserrinne				

G27	End- und Seitenmoränenwall				
	End- und Seitenmoränenwall, Eiszerfallsphase	Beispiel für Symboladaption aufgrund von Chronologie			
	End- und Seitenmoränenwall, Gschnitz	Beispiel für Symboladaption aufgrund von Chronologie			
	End- und Seitenmoränenwall, Egesen	Beispiel für Symboladaption aufgrund von Chronologie			
	End- und Seitenmoränenwall, Kleine Eiszeit	Beispiel für Symboladaption aufgrund von Chronologie			
G28	Esker				
G29	Subglaziale Wallform				
G30	Drumlin				
G31	Flute				
G32	Toteisloch				
G33	**Gravitative Form**				
G34	Abrisskante einer Massenbewegung				
G35	Abrisskante einer Fließmasse				
G36	Abrisskante einer Gleitmasse				
G37	Abrisskante einer Sturzmasse				
G38	Abrisskante einer tiefgreifenden Hangdeformation				
G39	Abrisskante eines Bergsturzes				
G40	Antithetischer Bruch				
G41	Zerrspalte, Zerrgraben				
G42	Aufgelockerter Bereich durch Driften				
G43	Bereich einer Gleitung				
G44	Bereich eines langsamen Fließens				
G45	Bereich einer tiefgreifenden Hangdeformation				
G46	Toppling (Kippung)				
G47	Bereich eines Talzuschubs				
G48	Tiefgreifend aufgelockerter Fels				
G49	Erdfall				
G50	Tomahügel				
G51	Massenbewegungswall				
G52	Kompressionswall				
G53	Randwall einer Massenbewegung				

G54	Sturzstromwall				
G55	**Fluviatile Form**				
G56	Ehemaliger Abfluss, Trockental				
G57	Natürlicher Damm (Levée)				
G58	**Karsthohlform**				
G59	Doline				
G60	Einsturzdoline				
G61	Dolinenfeld				
G62	Polje				
G63	**Oberflächliche Karstlösungsform**				
G64	Karren				
G65	Karrentisch				
G66	**Höhle**				
G67	Halbhöhle				
G68	Erosionshöhle				
G69	Spalthöhle				
G70	Talushöhle				
G71	**Permafrostform**				
G72	Blockgletscherwall				
G73	Wall einer Blockgletscherablagerung				
G74	**Terrassenniveau**				
G75	Terrassenniveau 1				
G76	Terrassenniveau 2				
G77	Terrassenniveau 3				
G78	Austufe				
G79	Austufe Niveau 1				
G80	Austufe Niveau 2				

Anhang 3: Symbolikvorschlag für Quartäre Phänomene

Nr.	Lithogenetische Einheiten	Kommentar	Symbol 1:10.000	Symbol 1:25.000/ 1:50.000	Symbol 1:200.000
P1	**Anthropogenes Phänomen**		A	A	
P2	**Verwitterungsphänomen**				
P3	Tiefgreifende Verwitterung				
P4	Tiefgreifende Verwitterung/Vergrusung				
P5	Tiefgreifende Verwitterung/Verlehmung				
P6	Wollsackverwitterung				
P7	Geologische Orgel				
P8	Paläoboden				
P9	**Gravitatives Phänomen**				
P10	Umrandung eines Massenbewegungskörpers				
P11	Umrandung einer tiefgreifenden Hangdeformation				
	Umrandungen werden adaptiert als rote Polygongrenze gezeichnet, da farbliche Umrandungen derzeit im Arbeitsdatensatz nicht automatisch generierbar sind.				
P12	**Hydrologisches Phänomen**				
P13	Abflusslose Senke				
P14	Moor				
P15	Hochmoor				
P16	Niedermoor				
P17	Anmoor				
P18	Vernässung				
P17, P18	Vernässung_Anmoor	Beispiel kombinierter Begriff			
P19	Schwinde				
P20	Ponor				
P21	**Karstverwandtes Phänomen**				
P22	Paläokarst				
P23	**Permafrostphänomen**				
P24	Permafrostverwitterung				
P25	Eiskeil-Pseudomorphose				
P26	Eiskeilnetz (fossil)				

P27	Frostmusterboden		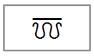	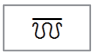	
P28	Kryoturbation		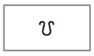	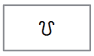	
P29	Unterkühlte Schutthalde, Holozän		❄	❄	

JAHRBUCH DER GEOLOGISCHEN BUNDESANSTALT

Jb. Geol. B.-A.	ISSN 0016–7800	Band 159	Heft 1–4	S. 51–65	Wien, Dezember 2019

Urban Hydrogeology of Vienna – Current state of knowledge

Sebastian Pfleiderer[1], Sabine Grupe[2] & Thomas Payer[2]

8 Text-Figures, 10 Tables

Österreichische Karte 1:50.000
BMN / UTM
40 Stockerau / NM 33-12-19 Tulln an der Donau
41 Deutsch Wagram / NM 33-12-20 Wien
58 Baden / NM 33-12-25 Baden
59 Wien / NM 33-12-26 Schwechat

aquifer properties
land use
groundwater use
groundwater residence times
groundwater chemistry

Contents

Abstract

This study describes the current knowledge of the hydrogeology of Vienna, Austria. It covers information on land use, conditions for groundwater recharge, geology, aquifer types as well as on the occurrence, yield and use of groundwater in the city. For each hydrogeological unit, it summarizes the available data on depth-to-groundwater, aquifer thickness, hydraulic conductivities, dynamics, residence times and groundwater chemistry. The study is based on data from online government portals, unpublished project reports as well as publicly available literature and identifies knowledge gaps for ongoing and future research.

Hydrogeological units in Vienna comprise the easternmost parts of the Austrian Calcareous Alps, the Flysch units of the Vienna Woods, Neogene marine sediments and Quaternary fluvial deposits. With regard to the hydrogeological properties of these units, information density is highest for fluvial deposits in the eastern half of the city area and decreases towards older units situated more to the west and/or at greater depth. In view of potential water supply backup systems and their protection, it is recommended to include those units known to a lesser extent, as for example coarse-grained Neogene sediments underlying the fluvial deposits, or karst aquifers at depth, in future monitoring and sampling networks.

Zur Hydrogeologie der Stadt Wien – gegenwärtiger Wissensstand

Zusammenfassung

Der Beitrag stellt den derzeitigen Wissensstand über die Hydrogeologie der Stadt Wien (Österreich) dar. Es werden Informationen über Landnutzung, Grundwasserneubildung, Geologie, Grundwasserleiter sowie über Grundwasservorkommen, Grundwasserergiebigkeit und Grundwassernutzung innerhalb des Stadtgebietes zusammengetragen. Für jede hydrogeologische Einheit werden verfügbare Daten zu Flurabstand, Grundwassermächtigkeit, hydraulische Durchlässigkeit, Grundwasserdynamik, Grundwasserverweilzeiten und Grundwasserchemie zusammengefasst. Die Basis bilden Daten von Onlineportalen, unveröffentlichten Projektberichten und veröffentlichter Literatur. Es werden Wissenslücken und mögliche zukünftige Forschungsthemen beschrieben.

1 Sebastian Pfleiderer: Geological Survey of Austria, Neulinggasse 38, 1030 Vienna, Austria. sebastian.pfleiderer@geologie.ac.at
2 Sabine Grupe, Thomas Payer: Wiener Gewässer Management, Heinrich-von-Buol-Gasse 6, 1210 Vienna, Austria.

Die hydrogeologischen Einheiten in Wien umfassen die östlichen Ausläufer der Kalkalpen, die Flyschzone im Wienerwald, Neogene marine Sedimente und quartäre Flussablagerungen. Bezüglich der hydrogeologischen Eigenschaften dieser Einheiten ist die Informationsdichte für die postglazialen Flussablagerungen der Donau in der östlichen Stadthälfte am höchsten, während sie für ältere Einheiten gegen Westen und in der Tiefe abnimmt. Im Hinblick auf mögliche Wasserversorgungsgebiete und deren Schutz wird empfohlen, bei zukünftigen Monitoring- und Beprobungskampagnen diese weniger gut erforschten Einheiten, wie zum Beispiel grobkörnige neogene Sedimente unterhalb quartärer Ablagerungen oder Karstaquifere in größerer Tiefe, mit zu berücksichtigen.

Introduction

The city of Vienna does not depend on urban groundwater for its drinking water supply. Since 1837, Vienna's drinking water is provided mainly by Alpine karst springs captured up to 120 km southwest of the city. Nonetheless, groundwater within the city area is widely used for irrigation, geothermal heat extraction and, to a lesser extent, for industrial and drinking water purposes. According to the Austrian Water Act, groundwater has to be protected to the extent that drinking water quality is ensured (BMNT, 2018, Wasserrechtsgesetz 1959 idgF.). Information on urban groundwater in Vienna is therefore important not only to secure a sustainable supply but also to protect its quality.

Numerous studies describe single aspects of Vienna's groundwater or cover parts of the city area or individual aquifers (e.g. Götzinger, 1951; Schuch, 1980; Schügerl et al., 1988; Erhart-Schippek & Niederbacher, 1995; Donauconsult, 1997; Grupe, 2011, 2012, 2013; Grupe & Payer, 2009, 2010, 2014, 2015, 2017, 2018; Grupe et al., 2016). A brief overview of hydrogeological units within the entire city area is given by the Municipal Department of Water Management (https://www.wien.gv.at/umwelt/gewaesser/schutz/hydrografie/grundwasser/hydrogeologie.html). However, detailed investigations including all aspects of urban hydrogeology and covering the entire city area date back to the 1980s (Lebeth at al., 1988; Lebeth, 1989).

The present review compiles hydrogeological data available from online government portals, unpublished project reports as well as from publicly available literature. It covers all relevant aspects of hydrogeology such as land use, conditions for groundwater recharge, geology, aquifer types as well as the occurrence, yield, use and quality of groundwater in the city. By collecting and analysing data on depth-to-groundwater, aquifer thickness, hydraulic conductivities, dynamics, residence times and groundwater chemistry separately for each hydrogeological unit, the paper takes an encompassing, holistic approach to, and presents the current knowledge of, Vienna's urban hydrogeology.

Data sources

Land use data for the city area of Vienna are available online as part of the EU Copernicus Urban Atlas (http://www.eea.europa.eu/data-and-maps/data/urban-atlas; EU Copernicus, 2016). This data set is based on a classification of multispectral satellite imagery with a 2.5 m spatial resolution and was published by the Copernicus Land Monitoring Service in 2012. Land use classes include urban fabric (five density classes), forests, parks, agricultural, industrial and traffic areas, and water bodies. A second data source constitutes the multi-purpose, digital city map issued as open government data by Vienna's Surveyors Department (https://www.wien.gv.at/stadtentwicklung/stadtvermessung/geodaten/mzk/index.html; MA 41, 2019). It is based on triangulation measurements with centimetre accuracy and distinguishes 51 land use classes. This data set was most recently updated in 2016. Both data sets allow for identification of sealed areas, which prevent rainwater infiltration, and, together with geological maps, to describe groundwater recharge.

Geological and lithological information was obtained from maps published by the Geological Survey of Austria at a scale of 1:200,000 (Schnabel et al., 2002) and 1:50,000 (Hofmann & Pfleiderer, 2003). Lithological descriptions of geological units were interpreted in terms of aquifer type. For maps and figures, the network of streams and rivers was downloaded as open government data from Vienna's Surveyors Department (https://www.wien.gv.at/ma41datenviewer/public).

The register of groundwater extraction licences, maintained by the Municipal Department of Water Management, was accessed in order to compile well location, types of groundwater use and abstraction limits. The latter were used to estimate groundwater yield of each hydrogeological unit. For deep aquifers, the depth information contained in the Water Rights Register was combined with a 3D geological model of Vienna's subsurface (Pfleiderer & Hofmann, 2004) to estimate groundwater yield. The register currently contains data for 3,127 extraction sites, however, no data exist within the area of the Calcareous Alps.

The depth-to-groundwater was obtained by querying the online data portal of the Hydrological Service (https://ehyd.gv.at). This portal contains the location of Austria's official groundwater monitoring stations and allows the download of time series of absolute heights of the uppermost water table including statistical parameters such as yearly maximum or minimum levels. The time series used here covered the period between 1996 and 2015. 38 monitoring stations were queried, all lying within Neogene and Quaternary sediment units. Together with the digital elevation model, provided by Vienna's Surveyors Department (https://www.wien.gv.at/ma41datenviewer/public), depth-to-groundwater was calculated. Combining the base level of aquifers, provided by the 3D geological model, with water table data enabled the calculation of groundwater thickness, albeit only for Quaternary deposits.

For Neogene and Quaternary sediments, 169 hydraulic conductivity data were derived by Pfleiderer & Hofmann (2004) using grain size distribution data (Beyer & Schweiger, 1969). In addition, 70 pumping test results were compiled from reports included in the Water Rights Register. Hydraulic gradients were extracted from groundwater table maps and groundwater flow velocities were calculated using the Darcy formula. Such groundwater table maps however only exist in the area east of the river Danube, and between the Danube River and the Danube canal (Blaschke et al., 1992; Pfleiderer & Hofmann, 2004; Gruppe Wasser, 2005; Pöyry, 2011).

Groundwater dynamics in porous aquifers were described by water table variations between 1996 and 2015 using 38 monitoring stations included in the data portal of the Hydrological Service. In fractured and karst aquifers, the ratio of maximum to minimum groundwater discharge of 12 springs monitored monthly during one year (Pfleiderer et al., 2010), were used to describe groundwater dynamics.

Groundwater residence times are published online by the Environment Agency Austria through an interactive map, which includes the results of all groundwater isotope studies performed in Austria (https://secure.umweltbundesamt.at/webgis-portal/isotopen/map.xhtml; Kralik et al., 2015). However, within Vienna's city area information on residence times is available only at 13 locations in the Danube plain and in younger terraces, and at one location for the deep thermal aquifers of the Calcareous Alps (Oberlaa).

Hydrochemical data were compiled for all hydrogeological units using three data sources. (1) Regular monitoring of groundwater quality is performed twice a year by the Municipal Department of Water Management at monitoring stations in the Danube plain, in alluvial deposits of tributary rivers and in younger terraces. Data can be viewed online via a portal hosted by the Environment Agency Austria (https://wasser.umweltbundesamt.at/h2odb). For this study, analyses of major ion and trace element concentrations, taken at 50 wells between 2015 and 2018, were used. (2) For the Flysch zone and the Calcareous Alps, hydrochemical analyses of major ion and trace element concentrations were sourced from a study commissioned by the Municipal Department of Water Management, which sampled 12 springs in monthly intervals during a period between October 2009 and September 2010 (Pfleiderer et al., 2010). (3) The archives of the Geological Survey of Austria contain additional hydrochemical analyses of groundwater samples from all hydrogeological units, taken between 1961 and 1994 and only include major ion concentrations. 42 of these analyses were considered reliable to describe groundwater chemistry.

Characteristics of hydrogeological units

The geological map 1:50,000 (Hofmann & Pfleiderer, 2003) forms the basis for identifying hydrogeological units. Geological units of this map were aggregated based on similar hydrological properties and aquifer type. Seven hydrogeological units were identified (Text-Fig. 1).

- The Calcareous Alps in the Southwest are made of limestones and dolomites and constitute karst aquifers.
- The Flysch zone in the western part of the city is made of sandstones, claystones and marlstones. Of these, the sandstone units yield groundwater in separate, partially confined, fractured aquifers.
- The Neogene sediments represent predominantly marine silt and clay deposits with sand and gravel intercalations. In particular near the Flysch zone (Badenian, Sarmatian), and in the Danube plain (Upper Pannonian), sandy gravel deposits are present. These form several, partially connected and partially artesian, porous aquifers. Locally, calcarenites occur within the Badenian and sandstones within the Sarmatian. These occurrences however do not constitute relevant groundwater bodies.
- Among the Pleistocene fluvial sediments, the older terraces (*Laaerberg*, *Wienerberg* and *Arsenal* terraces) represent sandy gravel deposits with a significant portion of sand and silt intercalations. Gravel components comprise rounded pebbles, predominantly consisting of quartz, crystalline and carbonate components, as well as platy sandstone pebbles. These terraces were deposited by the river Danube and constitute local, unconfined aquifers, partially covered by loess. Groundwater flows intermittently along subsurface channels prescribed by the morphology of the impermeable Neogene base.
- The younger Pleistocene sediments (*Stadt* terrace and *Liesingbach* gravel) also represent sandy gravel deposits, but with fewer sand and silt intercalations which form thin beds, sometimes of wide lateral extent. Gravel components comprise rounded pebbles, predominantly consisting of quartz, crystalline and carbonate components, as well as platy sandstone pebbles. The local, unconfined aquifers are partially covered by loess and hydraulically linked to the Danube plain aquifer.
- Postglacial sediments in the Danube plain consist of sandy gravel (rounded pebbles, predominantly consisting of quartz, crystalline and carbonate components) with thin silt intercalations of limited lateral extent. Locally, fine-grained flood plain deposits cover these sediments. Groundwater in the continuous, unconfined aquifer flows parallel to the Danube River. Where the underlying Pannonian sediments are fine-grained, these form the impermeable base of the aquifer. Where Pannonian sand or gravel deposits form the top of the Neogene, they are part of the Danube plain aquifer.
- Valley fill deposits along the tributary rivers from the West (e.g. the rivers Wien and Liesing) represent silt, sand and gravel (predominantly platy sandstone pebbles) deposits. Groundwater is linked, and flows parallel to these streams. Within the central part of the city area, the rivers are mostly channelled and flow underground.

Aquifer properties

Characteristic values for depth-to-groundwater are given for Neogene and Quaternary units in Table 1. In general, the interquartile ranges amount to 4–6 m, but can reach up to 11 m and 19 m within older terraces and the *Stadt* terrace, respectively. For Quaternary units, Table 1 also includes the interquartile range of values for groundwater thickness, ranging between 0.5 m and 2 m in older terraces and tributary valleys, and between 3 m and 10 m in younger terraces and in the Danube plain. The location of

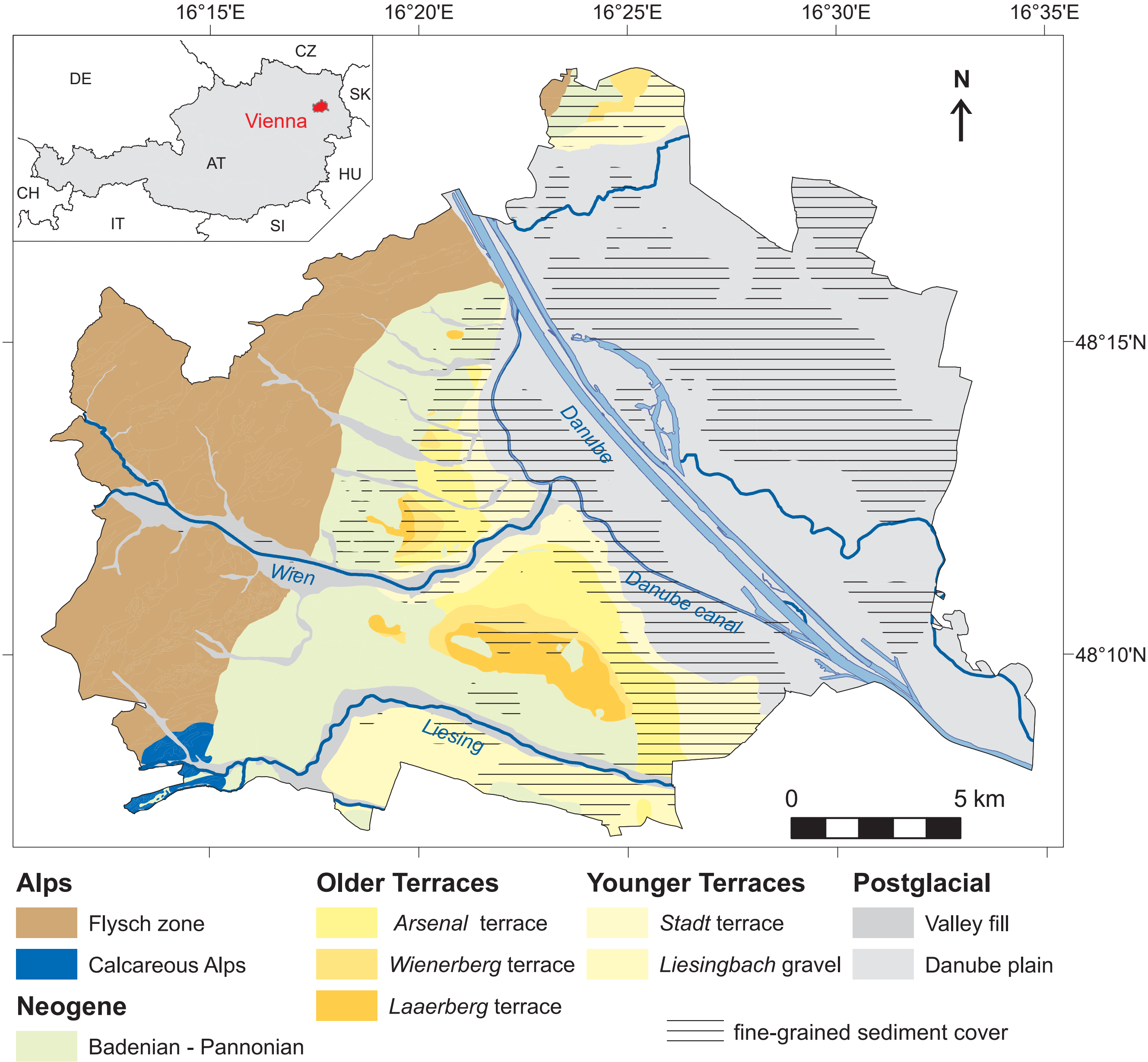

Text-Fig. 1.
Simplified geological map of Vienna (after HOFMANN & PFLEIDERER, 2003).

monitoring wells used to derive this information west of the Danube Canal is shown in Text-Figure 2. East of the Danube, and between the Danube River and the Danube canal, the information (Tabs. 1, 2) was derived from mean groundwater table maps (GRUPPE WASSER, 2005; PÖYRY, 2011).

The values cited for Neogene aquifers in Table 1 are representative for unconfined aquifers observed in wells where Neogene sediments appear at the surface east of the Flysch zone. For confined aquifers, no detailed information on hydraulic heads is publicly available. It is however known, that hydraulic heads often lie above ground (SCHUBERT, 2015). Text-Figure 2 shows the location of 80 artesian wells, compiled by SCHUBERT (2015). They represent groundwater levels in deeper layers of Neogene sediments, often overlain by Quaternary deposits. Concerning the groundwater thickness in Neogene sediments, information is available from cross-sections such as the one shown in Text-Figure 7 (NOWY et al., 2001), and from well

	Neogene (9)	**older terraces (10)**	**younger terraces (7)**	**Danube plain (derived from maps)**	**valley fill (11)**
depth-to-groundwater	4–6	5–11	*Stadt* terrace: 11–19 *Liesingbach* gravel: 5	4–6	4–5
groundwater thickness	no information	0.5–1.5	*Stadt* terrace: 3–6	4–10	1–2

Tab. 1.
Depth-to-groundwater and groundwater thickness of porous aquifers in Vienna (q_{25}–q_{75}) in Meter. Data count in brackets.

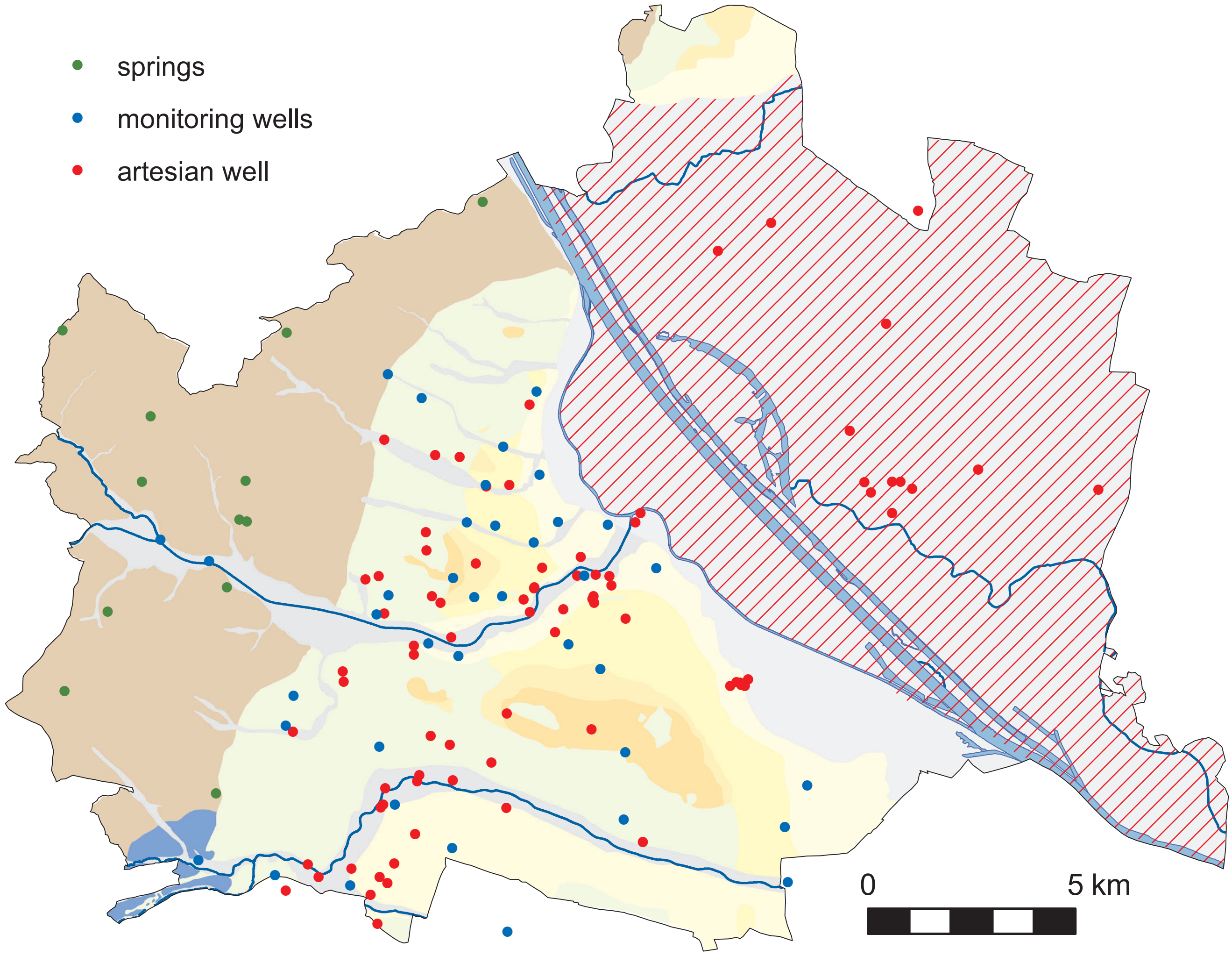

Text-Fig. 2.
Wells and springs used to derive depth-to-groundwater, groundwater thickness and dynamics; artesian wells in Vienna (SCHUBERT, 2015). Areas where mean groundwater table maps were used, are hatched in red.

logs. NIEDERBACHER et al. (1995) estimate the cumulative thickness of coarse-grained layers within the top 300 m of the Neogene in the Danube plain to be 80 m.

In porous aquifers, the water table variations over time give an indication of groundwater dynamics (Tab. 2). Interquartile ranges generally lie between 0.1 m and 1 m and show no significant differences between hydrogeological units. In the Danube plain east of the Danube River, the groundwater table is hydraulically linked to the river level, while the groundwater table between the Danube River and the Danube canal is uncoupled from the river and artificially controlled (DREHER & GUNATILAKA, 2008). In the other hydrogeological units, the groundwater table is free to vary according to recharge from precipitation.

To express the dynamics in fractured aquifers of the Flysch zone and in karst aquifers of the Calcareous Alps, the ratio of maximum to minimum groundwater discharge is listed in Table 2. The location of springs used to derive this information is shown in Text-Figure 2. A distinct difference is present between highly dynamic springs in the Flysch zone and more constant discharge of springs in the Calcareous Alps.

Characteristic values for hydraulic conductivities in the older terraces and the Danube plain (postglacial gravel and Neogene coarse-grained deposits, are listed in Table 3. For the Danube plain, the values agree with results from pumping test performed in previous studies (SCHUCH, 1980; SCHÜGERL et al., 1988; FÜRNKRANZ, 1990; VAN HUSEN,

	Calcareous Alps (1)	**Flysch zone (11)**	**Neogene (9)**	**older terraces (10)**	**younger terraces (7)**	**Danube plain (derived from maps)**	**valley fill (11)**
water table variation (m)			0.2–0.7	0.2–0.5	*Stadt* terrace: 0.1–0.5 *Liesingbach* gravel: 0.4–0.9	0.5–1	0.2–1
max/min groundwater discharge	4	13–39					

Tab. 2.
Groundwater dynamics of aquifers in Vienna (q_{25}–q_{75}). Data count in brackets.

	Neogene underlying Quaternary sediments	Danube plain
hydraulic conductivity (m/s) derived from grain size	5×10^{-5}–2×10^{-4}, 1×10^{-3} (120)	1×10^{-4}–1×10^{-3}, 2×10^{-3} (48)
hydraulic conductivity (m/s) derived from pumping test	6×10^{-5}–2×10^{-4}, 4×10^{-4} (4)	2×10^{-3}–8×10^{-3}, 7×10^{-2} (66)
groundwater flow velocity (m/day)		0.01–0.3, 4.6

Tab. 3.
Hydraulic conductivities and flow velocities of porous aquifers in Vienna (q_{25}–q_{75}, maximum). Data count in brackets.

1990). For Neogene, coarse-grained layers underlying Quaternary sediments, median hydraulic conductivity values are lower than Danube plain gravel by a factor of 40.

In the Danube plain, hydraulic gradients were derived from groundwater table maps. These gradients range from 0.4 ‰ to 0.8 ‰ and groundwater flow velocities were calculated to lie between 0.01 m/day and 0.3 m/day, with a maximum of 4.6 m/day (Tab. 3).

Land use

Due to their geographic position within the city area, the hydrogeological units display different percentages of land use classes according to the EU Copernicus Urban Atlas (Text-Fig. 3). While the Calcareous Alps and the Flysch zone in the West are covered mostly by forest, urban fabric dominates within the Neogene, the Pleistocene terraces and the valleys of tributary streams. In contrast, the Danube plain is characterised by large agricultural areas.

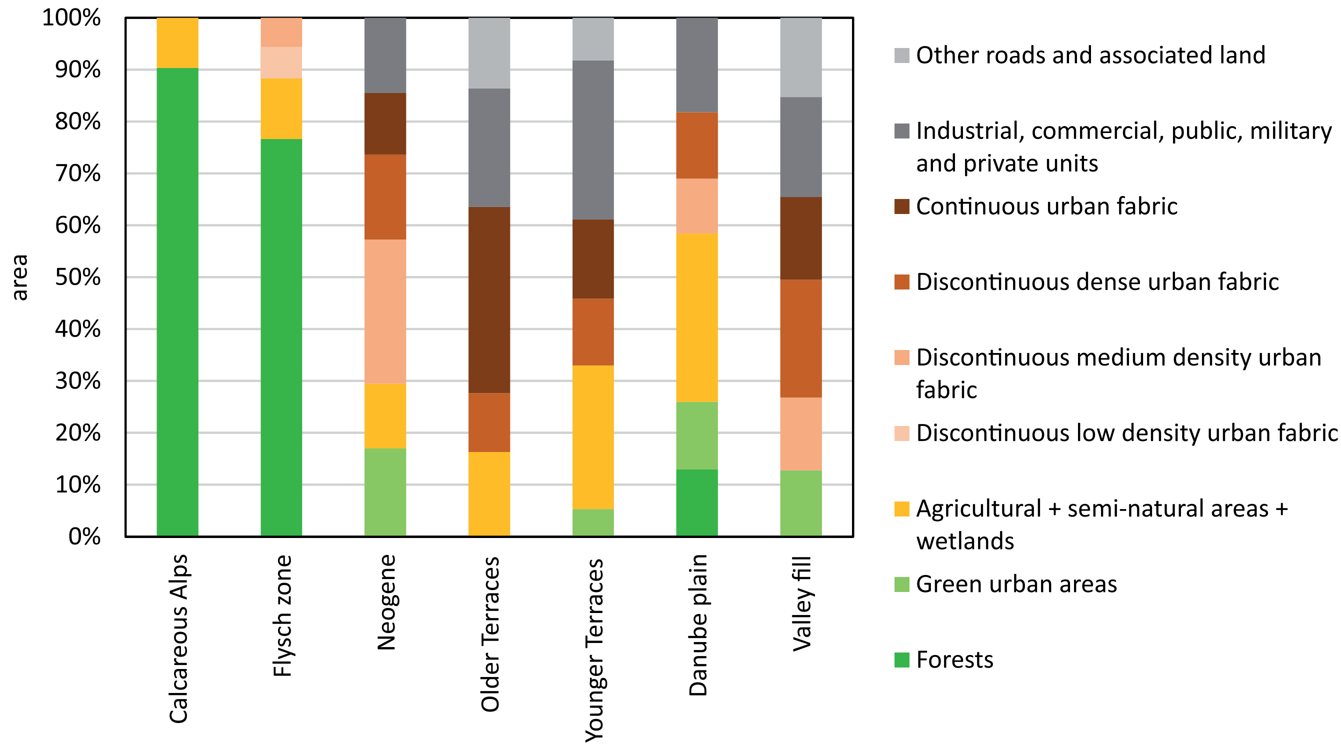

Text-Fig. 3.
Land use within hydrogeological units according to the Urban Atlas (EU Copernicus, 2016).

Hydrogeological unit	Recharge conditions	Percentage of sealed area
valley fill	Strongly reduced recharge due to sealing, possible infiltration from leaky sewage systems.	53
Danube plain	Reduced recharge due to sealing and loam cover, river filtrate of the Danube River east of the Danube, artificial infiltration of Danube River water into the groundwater between the Danube River and the Danube canal.	31
younger terraces	Strongly reduced recharge due to sealing and loess cover, possible infiltration from leaky sewage systems.	48
older terraces	Strongly reduced recharge due to sealing and loess cover, possible infiltration from leaky sewage systems.	56
Neogene	Strongly reduced recharge due to sealing and loess cover, possible infiltration from leaky sewage systems.	43
Flysch zone	High infiltration rates in sandstones, strongly reduced recharge in clay- and marlstones.	10
Calcareous Alps	High infiltration rates.	5

Tab. 4.
Conditions for groundwater recharge within hydrogeological units.

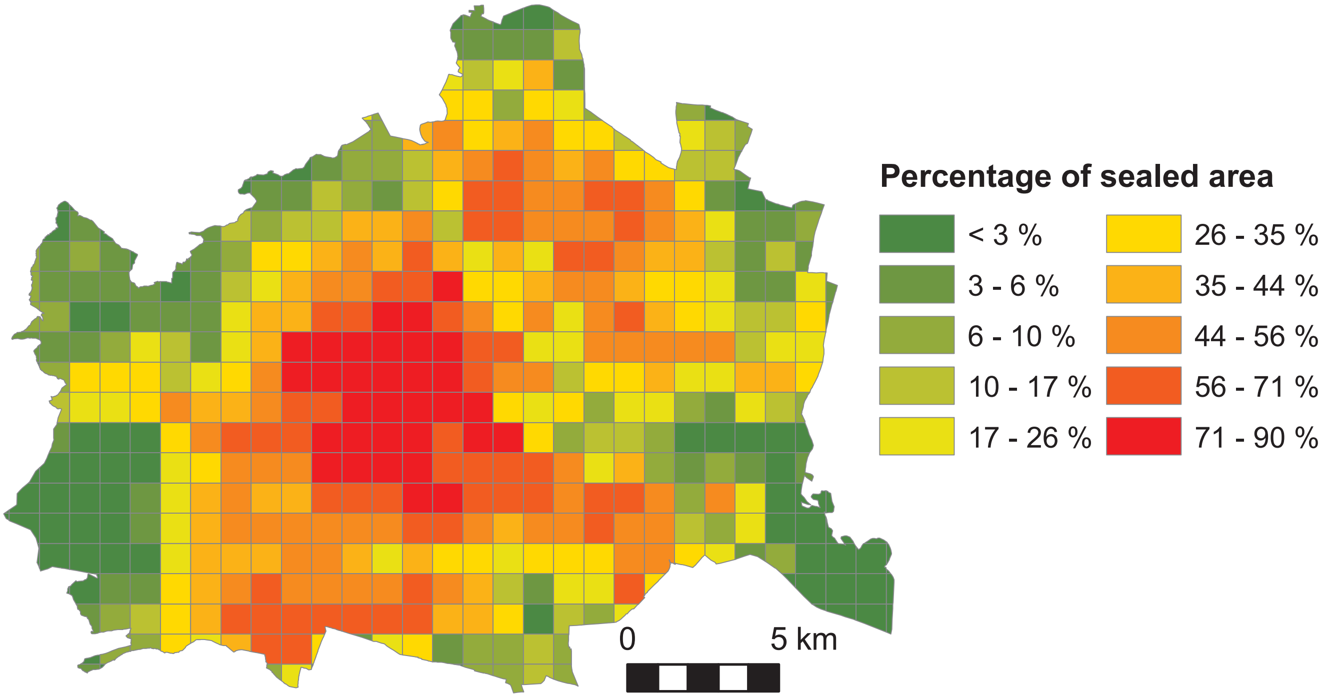

Text-Fig. 4.
Percentages of area sealed against rainwater infiltration as derived from Vienna's multi-purpose city map (MA 41, 2019).

The regional distribution of land use classes has implications not only for possible contamination sources for, but also for the recharge rate of, groundwater. The degree of sealing was derived from the multi-purpose city map by calculating percentages within regular cells of 1 x 1 km (Text-Fig. 4). Forest and agricultural areas located in the West and East show < 10 % sealed area, while in the city centre values increase up to 90 %. In the Neogene, the Pleistocene terraces and the valleys fill units, sealed areas amount to 44–57 % (Tab. 4).

In addition to surface sealing through infrastructure, fine-grained sediments such as loess or loam partially cover some of the hydrogeological units and restrict rainwater infiltration (Text-Fig. 1). On the other hand, some artificial groundwater recharge is assumed to take place through leaky sewage pipes and channels. With the currently available data sets, groundwater recharge rates cannot be calculated, nevertheless, Table 4 describes the condition for groundwater recharge within hydrogeological units.

Groundwater use

The most intensive use of groundwater takes place in postglacial gravel sediments of the Danube plain. In Vienna's Water Rights Register, 1,777 groundwater extraction sites are currently registered within this unit. The younger terraces (mostly the *Stadt* terrace) and the Neogene sediments (mostly Pannonian deposits underlying postglacial sediments in the Danube plain) are used at 57 and 46 sites, respectively. Distinctly less used is the groundwater in the Flysch zone, the older terraces and in valley fills (9, 10 and 8 sites, respectively). From carbonate aquifers of the Calcareous Alps, deep thermal groundwater is extracted at 2 wells for thermal use (spa Oberlaa). Text-Figure 5 shows the location, Text-Figure 6 the number of extraction sites for each hydrogeological unit, specifying the types of groundwater use.

Table 5 compares the abstraction limits, giving interquartile ranges and maxima of all wells within hydrogeological units. A clear grouping emerges with postglacial sediments of the Danube plain displaying the highest values (max. 16.9 m^3/s), followed by Neogene (particularly the Upper Pannonian and Sarmatian) layers underlying these

Flysch zone	Neogene	older terraces	younger terraces	Danube plain	valley fill
0.8–3, 3 (9)	Sarmatian: 1–2, 2.5 (4) Badenian: 5 (1)	23–25, 25 (10)	*Stadt* terrace: 2–6, 27 (53) *Liesingbach* gravel: 1 (4)	1–11, 16,948 (1,822)	2–8, 11 (9)
Calcareous Alps (deep geothermal aquifer)		**Neogene underlying Quaternary sediments**			
62 (2)		Upper Pannonian: 3–12, 81 (22) Middle Pannonian: 0.5–2, 6 (12) Sarmatian: 2–7, 40 (6) Badenian: 1–4, 7 (3)			

Tab. 5.
Abstraction limits of groundwater wells grouped by hydrogeological unit (q_{25}–q_{75}, maximum) in l/s. Data count in brackets.

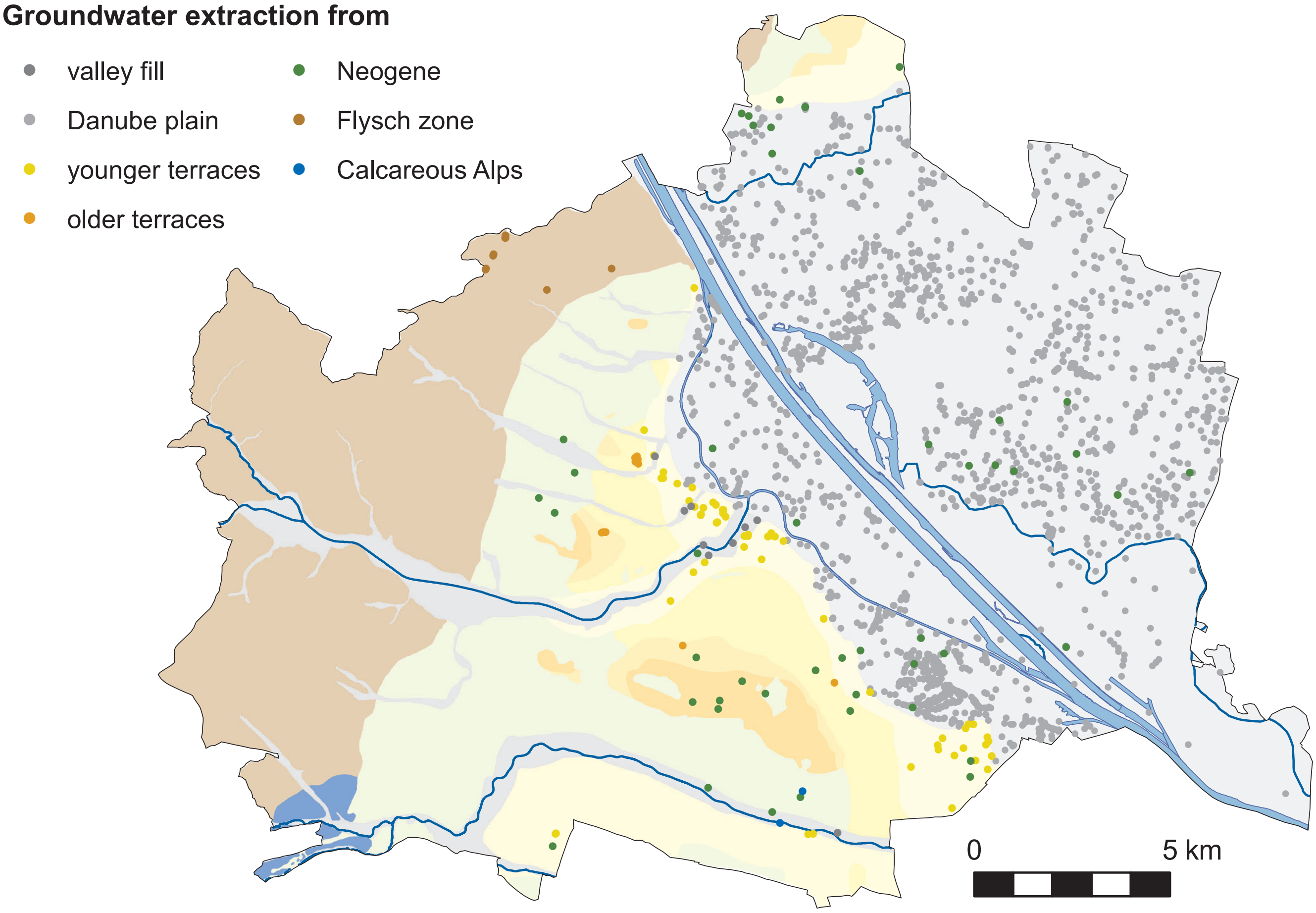

Text-Fig. 5.
Location of groundwater extraction sites grouped by hydrogeological unit.

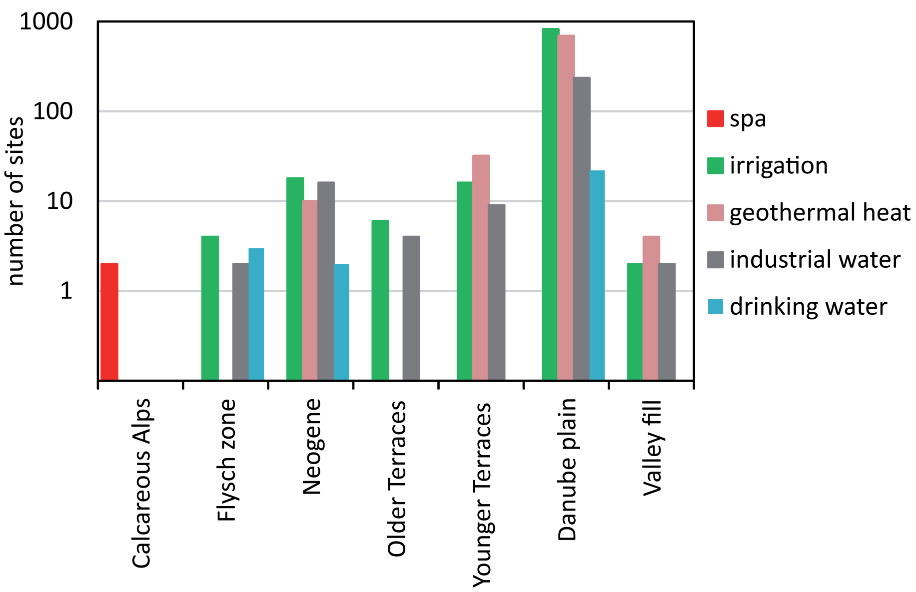

Text-Fig. 6.
Number of groundwater extraction sites and types of groundwater use, grouped by hydrogeological unit.

sediments in the Danube plain (max. 81 l/s). The terraces and valley fill take third place (max. 27 l/s and 11 l/s, respectively). Abstraction limits in the Flysch zone only reach a maximum of 3 l/s. As a special case, a total of 62 l/s are permitted to be extracted from 2 wells in the deep thermal carbonate aquifers at Oberlaa (Elster et al., 2016).

Although abstraction limits do not directly reflect groundwater yield, the data were used here as indicators to group aquifers according to their potential yield (Text-Fig. 7). At the surface, the Danube plain aquifer represents the only continuous, high yield, porous aquifer in Vienna. Discontinuous, porous aquifers with moderate yield include the younger and older terraces and the valley fill sediments. Even less yield is to be expected from Neogene units east of the Flysch zone although some important water supply sites here extract groundwater from coarse-grained lay-

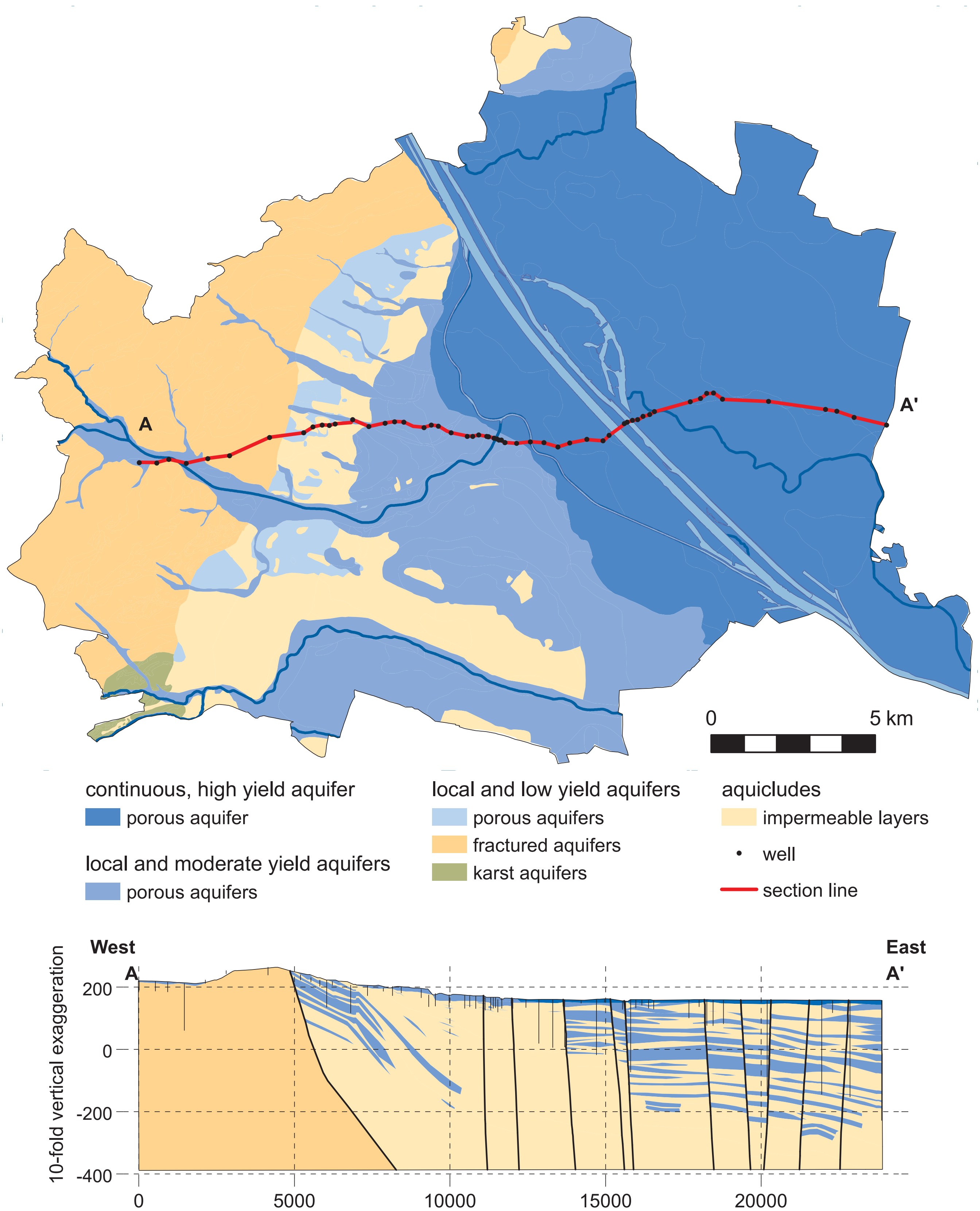

Text-Fig. 7.
Aquifer types in Vienna, grouped by relative yield, and cross-section (Nowy et al., 2001).

ers. Among the low yield aquifers, fractured aquifers of the Flysch zone and karst aquifers of the Calcareous Alps form separate groups due to their aquifer type. Text-Figure 7 includes a hydrogeological cross-section (modified from Nowy et al., 2001) showing coarse-grained layers within the Neogene which represent moderate to high yield, porous aquifers at depth.

Calcareous Alps (deep geothermal aquifer) (1)	younger terraces (3)	Danube plain (10)
> 10,000 years	< 5 years	< 5 years

Tab. 6.
Groundwater residence times in hydrogeological units (KRALIK et al., 2015; EICHINGER, 2009). Data count in brackets.

Groundwater residence times

Table 6 lists groundwater residence times derived from ^3H isotope data and published in the Austrian Water Isotope Map (KRALIK et al., 2015). The analyses in the Danube plain and in younger terraces show that the groundwater here infiltrated into the aquifer less than five years ago. This is not surprising in the light of high flow velocities, Danube river water infiltration and groundwater recharge through precipitation. The thermal groundwater at Oberlaa contains no tritium suggesting a residence time of > 60 years. The circulation system of this deep aquifer was explained by WESSELY (1983). According to EICHINGER et al. (2009), the thermal water entered the underground circulation system during the last ice age (> 10,000 years ago).

Groundwater chemistry

Text-Figure 8 shows the location of groundwater samples, Table 7 lists median values of major ion concentration in the samples, grouped by hydrogeological unit. In general, values are highest in the groundwater of postglacial deposits and decrease towards the Pleistocene and Neogene deposits, the Flysch zone and the Calcareous Alps, which show the lowest concentrations.

Some samples contain elevated concentrations of Fe, Mn, NO_2, NO_3 or SO_4. Table 8 shows the percentages of samples exceeding the Austrian National Guideline values for drinking water (TRINKWASSERVERORDNUNG 2001 idgF.). For example, 20 % of groundwater samples in the Flysch zone exceed Mn concentrations of 50 µg/l. These samples also show sporadically high Fe concentrations (> 200 µg/l). The natural chemical composition of Flysch rocks is the most likely cause for this (PFLEIDERER et al., 2010). The frequent exceedance of Fe, Mn and Na concentrations in groundwater within Neogene units may also have natural causes, as samples here were taken at great depth (100 m below ground on average) and are thus more highly mineralised.

On the other hand, 25 % of groundwater samples in the Danube plain, and 50 % of groundwater samples in the

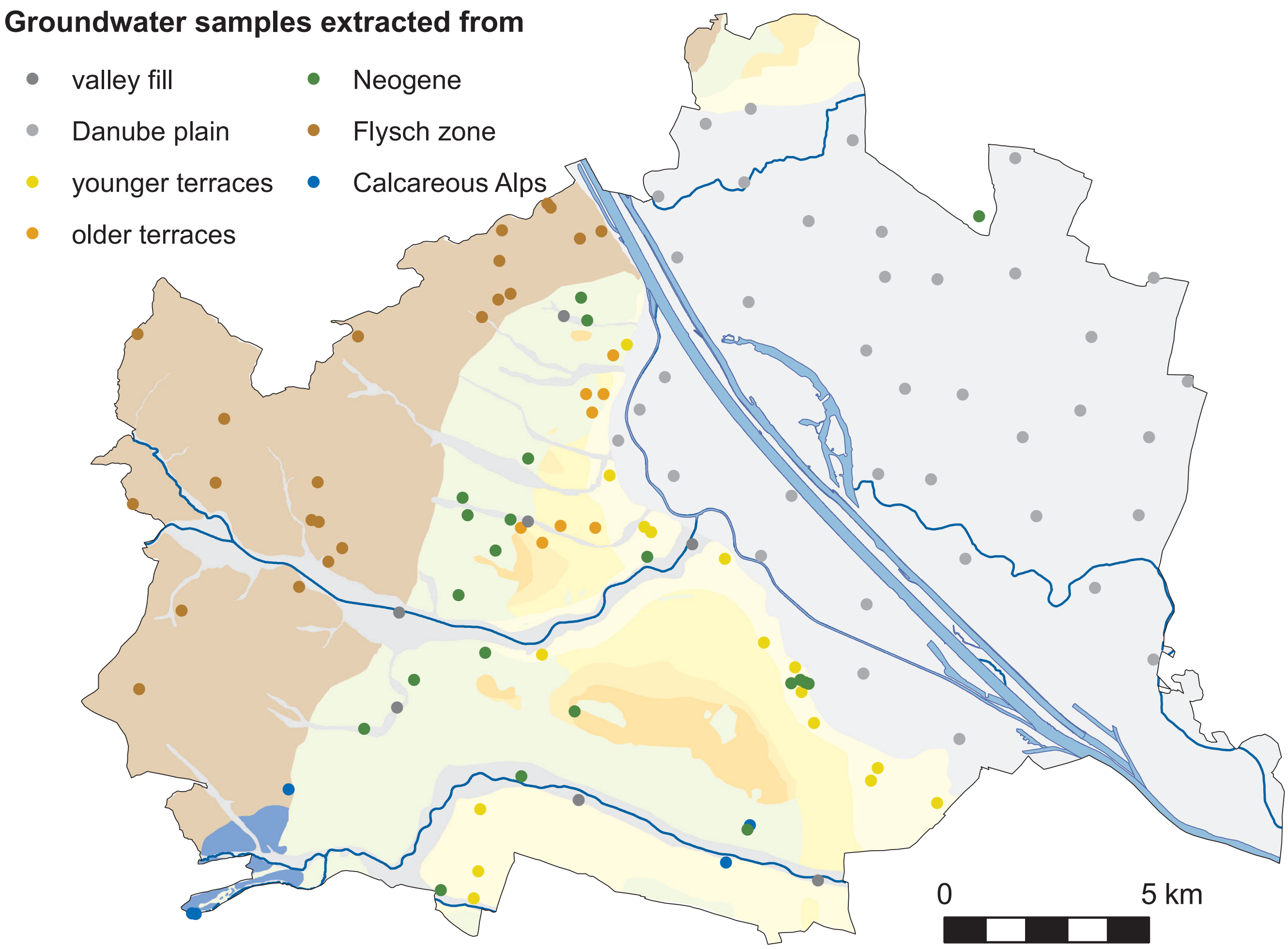

Text-Fig. 8.
Location of samples used for the description of groundwater chemistry.

Parameter	valley fill	Danube plain	younger terraces	older terraces	Neogene	Flysch zone	Calcareous Alps	Calcareous Alps (deep geothermal aquifer)
Number of analyses	2	284	57	6	18	129	13	3
Ca (mg/l)	165.1	116.5	112.25	112.21	96	143.84	92.288	446.6
Cl (mg/l)	40	100.745	51.9175	40	26	13.73	14.373	840
Fe (mg/l)	0.07	0.005	0.0075		0.135	0.014	0.025	< 0.015
H_2SiO_3 (mg/l)						18.36	8.955	42.9
HCO_3 (mg/l)	452	392	399.5	385.5	422	407	328.92	263.5
K (mg/l)		9.7175	6.515		2	2.3275	2.01	23.8
Mg (mg/l)	48.55	41.7	65.995	60.61	30.16	24.62	21.015	133
Mn (mg/l)	0.03	0.0015	0.0015		0.1	0.0023	0.0007	< 0.015
Na (mg/l)		48.825	51.5		27.56	11.245	9.01	531
NH_4((mg/l)		0.005	0.005		1	0.03	0.0275	1.31
NO_2 (mg/l)		0.0025	0.0025			0.011	0.0068	
NO_3 (mg/l)		39.805	28.835		0.5	12.453	4.53	< 0.35
PO_4 (mg/l)		0.0295	0.0325			0.08	0.1	
SO_4 (mg/l)	175	112.5	151.6	152	93.5	80	33.065	1302
Sr (mg/l)						1.385	0.565	13.9
TDS (mg/l)	881	856	951	770	738	727	483	3,700.89
Total hardness (dGH)	33.6	26.1	31.3	32.0	20.3	25.5	22.1	
Carbonate hardness	18.0	18.0	19.6	17.7	19.4	18.7	15.8	

Tab. 7.
Median values of major ion concentrations in groundwater, grouped by hydrogeological unit.

Parameter	valley fill	Danube plain	younger terraces	older terraces	Neogene	Flysch zone	Calcareous Alps
Cl	0	0	0	0	6	0	0
Fe	0	4	2	0	40	3	0
Mn	0	6	2	0	47	20	0
Na	0	0	0	0	13	0	0
NO_2	0	4	0	0	0	0	0
NO_3	0	25	50	0	0	0	0
SO_4	0	1	9	0	0	2	0

Tab. 8.
Percentages of groundwater samples exceeding Austrian National Drinking Water Guideline values.

younger terraces, exceed NO_3 concentrations of 50 mg/l. Here, anthropogenic activities, such as fertilization of agricultural land, are assumed to be the cause. Two springs in the Flysch zone consistently exhibit elevated Na and Cl concentrations, albeit not exceeding the Guideline values. The location of these springs' catchment areas near high traffic roads suggests road salt as the likely cause (Pfleiderer et al., 2010).

Analytical results from the deep geothermal aquifer at Oberlaa (Elster, 2016) are not compared to the guideline values as these waters are not considered as drinking water.

Within the Danube plain, the regional distribution of individual major ion concentrations shows a distinct pattern. Values for Ca, Mg, Na, SO_4, Cl and NO_3 are generally low near the Danube River and increase towards the East and West. In the East, this is due to river filtrate from the Danube, which is less mineralised and dilutes the groundwater near the river. In the West, the groundwater is artificially recharged with Danube river water, also diluting ion concentrations.

Median values of trace element concentrations in groundwater samples are grouped by hydrogeological unit in Table 9. None of the analyses shows concentrations in excess of National Guideline values. For groundwater in Quaternary units, maximum concentrations of Al, As, Cd, Cr, Cu, Hg, Ni, Pb and Zn are 2–50 times lower than the guideline values, in the Flysch zone and the Calcareous Alps even 6–104 times lower. Again, analytical results from the deep geothermal aquifer at Oberlaa are not compared to the guideline values, as these waters are not considered as drinking water.

Parameter	valley fill	Danube plain	younger terraces	Flysch zone	Calcareous Alps	Calcareous Alps (deep geo-thermal aquifer)
Number of analyses	2	145	26	114	12	1
Al (µg/l)		3.5	3.5	7.45	6.6	< 20
As (µg/l)	0.5	0.875	0.5	0.45	0.28	7
Cd (µg/l)	0.05	0.04	0.04		0.1	< 0.3
Cr (µg/l)	1	0.3	1.275	0.2	0.2	< 5
Cu (µg/l)		2.3	2.5	3.8	5.7	< 5
Hg (µg/l)	0.25	0.035	0.035			0.19
Ni (µg/l)		0.425	0.35			< 2
Pb (µg/l)	2.5	0.35	0.35	0.45	0.3	3
Zn (µg/l)		8.25	10	13	17.75	< 100

Tab. 9.
Median values of trace element concentrations in groundwater, grouped by hydrogeological unit.

In addition to major ion and trace element concentrations, analyses of groundwater quality performed by the Environment Agency Austria east of the Danube contain concentrations of chlorofluorocarbons, pesticides and their metabolites, per- and polyfluoroalkyl substances, polybrominated diphenyl ethers, polycyclic aromatic hydrocarbons, organotin compounds and mercury. The area east of the Danube is considered a prospective intervention area due to elevated concentrations of nitrate and desethyldesisopropyl atrazine. In 2016, analyses from 36 % of monitoring stations exceeded the alert threshold with respect to nitrate concentrations, 4 % with respect to nitrite, 5 % with respect to atrazine, 9 % with respect to desethyl atrazine and 44 % with respect to desethyldesisopropyl atrazine (Philippitsch & Grath, 2019).

Discussion

The derivation of depth-to-groundwater and groundwater thickness (Tab. 1), and of groundwater dynamics (Tab. 2) west of the Danube canal, rests on few data points, available online via the portal of the Hydrological Service. The values listed in Tables 1 and 2 therefore give only a first approximation. In addition to the wells included in the online portal, 600 more groundwater wells are monitored by Vienna's Municipal Department of Water Management. Ideally, maps of the groundwater table at high, medium and low levels should be used. Within Vienna's city area, such maps are however only available for the Danube plain east of the Danube River, and between the Danube River and the Danube canal. To derive thickness, the aquifer base was extracted from a 3D geological model, which bears uncertainties particularly at greater depths. For confined aquifers within the Neogene sediments, even hydraulic heads are largely unknown.

Hydraulic conductivities (Tab. 3) were derived from grain size distribution curves as well as from pumping tests. Within the Danube gravel, an equally large number of data exists for both methods. Comparing the results of two methods shows that values derived from grain size underestimate conductivities by a factor of 6–33. This is confirmed by pumping tests carried out in the Danube plain east of Vienna (Fürnkranz, 1990).

The quantification of areas sealed against rainwater infiltration (Text-Fig. 4) is based on the land use classes of Vienna's multi-purpose city map. Forests, meadows, parks, vineyards, cemeteries, sports fields, railway lines and gravel pits were considered as not sealed. For other classes, the interpretation in terms of surface sealing is less certain. For example, courtyards or construction sites may or may not be sealed. The surface area of these classes however amounts to 0.8 % of the city area and the uncertainties can be considered as negligible.

To identify the aquifers used for groundwater extraction (Text-Figs. 5, 6, Tab. 5), depth information was taken from well descriptions contained in the Water Rights Register. However, the location of screens is mostly given in meters below the well top, without specifying the height of the well top above ground. A digital elevation model was used for the translation into absolute depth assuming the well top at ground level, which can cause an error of up to approximately 1 m. Uncertainties in the 3D geological model add to the error. The identification of hydrogeological units from which water is extracted may therefore be false for individual sites and the data shown in Text-Figures 5, 6 and in Table 5 only give a general picture of groundwater use.

Abstraction limits are granted by the water authorities partly on the basis of groundwater availability but often on the basis of demand, which may be less than the actual yield. Therefore, abstraction limits can be used only as indicators of groundwater yield. The distinction of high, moderate and low yield in Text-Figure 7, based on maximum abstraction limits, reflects relative groundwater availability of Vienna's hydrogeological units. Yields, however, cannot be quantified with these data.

The median values of major ion concentrations in groundwater samples from older terraces and valley fill (Tab. 7) are based on very few hydrochemical analyses dating from 1961–1962 and are therefore not reliable. However, the high concentrations of Mn (and to a lesser extent Fe) in valley fill groundwater samples (10 times higher than samples from any other unit) agree with the fact that valley fill sediments consist mainly of sandstone components from the Flysch zone where groundwater samples also show high Mn concentrations (Tab. 8).

Ongoing research and knowledge gaps

The hydrogeology team of the Viennese Waters Management, a subsidiary company of the City of Vienna, has been investigating the extent, lithology and the base of Quaternary sediments in Vienna for the last 10 years, analysing > 60,000 drilling profiles in minute detail as a still ongoing project (GRUPE, 2011, 2012, 2013; GRUPE & PAYER, 2009, 2010, 2014, 2015, 2017, 2018; GRUPE et al., 2016). From this will emerge an updated geological map, more accurate than the map used here (HOFMANN & PFLEIDERER, 2003). In addition, a more accurate structural map of the Quaternary base will be produced. With groundwater table maps from the Municipal Department of Water Management, it will possible to develop a 3D model with better information on depth-to-groundwater, groundwater thickness and water table variations of the uppermost Quaternary aquifers. This will allow the revision of data in Tables 1 and 2.

The project "GeoPlasma" provides an online information system for shallow geothermal use of the topmost aquifer east of the Danube (https://portal.geoplasma-ce.eu/webgis/vienna) which includes important hydrogeological information such as aquifer productivity (STEINER et al., 2017).

The project "GeoTief Wien" currently investigates geothermal reservoirs underneath the city of Vienna at 2,500–6,500 m depth (SCHREILECHNER et al., in press). Both Neogene sediments and Triassic carbonates of the Calcareous Alps are studied. Results will include a geological model (3D structures) and a thermal-hydraulic model (reservoir properties).

From the present review and ongoing research, some knowledge gaps emerge (Tab. 10).

Future work could aim at linking the groundwater monitoring wells, residing at Vienna's Municipal Department of Water Management, and the groundwater extraction sites (Municipal Department of Water Rights) to the register of borehole logs (Municipal Department of Bridge Construction and Foundation Engineering, https://www.wien.gv.at/verkehr/grundbau/kataster.html) on a well-by-well basis. Defining the absolute heights of well screens would allow the correct identification of the aquifers, which are currently monitored for water table variations or used for groundwater extraction. Linked to the borehole logs, the site-specific description of the lithological characteristics of aquifers becomes possible. At the same time, it would allow the identification of areas where future monitoring and sampling sites should be installed to include hydrogeological units known to a lesser extent.

Conclusions

The present study describes the current knowledge of the urban hydrogeology of Vienna, Austria. It defines seven hydrogeological units based on similar geological and aquifer properties. Conditions for groundwater recharge were described on the basis of land use and fine-grained sediment cover. Aquifer type was interpreted from geological maps. Aquifer geometric properties (depth-to-groundwater, groundwater thickness) were derived from data on groundwater tables, from an elevation model and a 3D geological model. Aquifer material properties (hydraulic conductivity), groundwater residence times and groundwater chemistry were compiled from existing data sets. Groundwater use was derived from Vienna's Water Rights Register. Abstraction limits were used to infer relative groundwater availability, leading to a map of aquifer types grouped by yield.

The present study demonstrates that knowledge is scarce particularly for hydraulic aquifer properties, recharge rates, groundwater residence times and chemistry of aquifers in valley fill sediments and older terraces, for the Neogene confined aquifers and for the deep geothermal aquifer of the Calcareous Alps. Particularly in view of potential water supply backup systems and their protection, future investigations are recommended to focus on Neogene confined aquifers underlying Quaternary sediments in the Danube plain.

Acknowledgements

The authors thank GREGOR PESSENLEHNER (Vienna's Municipal Department of Water Management) for access to the Water Rights Register, GERALD SCHUBERTH-HLAVAC for programming, CHRISTOPH HOLUB, CORNELIA STEINER, ALEXANDER SCHRIEBL and WILFRIED PISTECKY for the compilation of the pumping test results and MARY GRACE WALLIS for improving the English language of this review.

Hydrogeological unit	geometric properties	hydraulic properties	recharge rates	residence times	chemistry
tributary valleys	~	x	x	x	x
Danube plain	~	√	x	√	√
younger terraces	~	x	x	x	√
older terraces	~	x	x	x	x
Neogene	x	x	x	x	x
Flysch zone	x	x	x	x	√
Calcareous Alps	~	~	x	x	x

Tab. 10.
Ongoing research and knowledge gaps (~: currently investigated, x: largely missing, √: largely known); Aquifer geometric properties include structural maps of the top and base of aquifers, of groundwater tables, depth-to-groundwater and groundwater thickness; hydraulic properties include porosity, conductivity, flow velocity, yield and storage.

References

BEYER, W. & SCHWEIGER, K.H. (1969): Zur Bestimmung des entwässerbaren Porenanteils der Grundwasserleiter. – WWT, **19**/2, Berlin.

BLASCHKE, A.P., SCHMALFUSS, R., KUPFERSBERGER, H. & ZHANG, W. (1992): Grundwasserströmungsmodell Stallingerfeld. – Endbericht Simulationen. – 31 S., 6 Anhänge, Institut für Hydraulik, Gewässerkunde & Wasserwirtschaft, TU Wien, Wien.

BMNT (2018): Wasserrechtsgesetz 1959 idF BGBl. I Nr. 73/2018. – 237 S., Bundesministerium für Nachhaltigkeit und Tourismus, Wien.

DONAUCONSULT ZOTTL & ERBER – ENVIROPLAN (1997): Grundwasserbewirtschaftungsplan Wien, Teil A. – Projektbericht der Stadt Wien, MA 45 – Wasserbau, 91 S., 30 Karten, Wien.

DREHER, J.E. & GUNATILAKA, A. (2008): Grundwassermanagement im städtischen Bereich am Beispiel 2. und 20. Bezirk in Wien. – Österreichische Wasser- und Abfallwirtschaft, **60**, 9–18, Wien.

EICHINGER, L., LORENZ, G. & WECHNER, S. (2009): Physikalisch-chemische und isotopische Untersuchungen des Thermalwassers der Tiefbohrungen Oberlaa TH1 und TH2. – Unveröffentlichter Bericht (Archiv der FA Hydrogeologie), 10 S., Hydroisotop GmbH, Schweitenkirchen.

ELSTER, D., GOLDBRUNNER, J., WESSELY, G., NIEDERBACHER, P., SCHUBERT, G., BERKA, R., PHILIPPITSCH, R. & HÖRHAN, T. (2016): Erläuterungen zur geologischen Themenkarte Thermalwässer in Österreich 1:500.000. – 296 S., Geologische Bundesanstalt, Wien.

ERHART-SCHIPPEK, W. & NIEDERBACHER, P. (1995): Tiefengrundwasservorkommen in Niederösterreich – Schwerpunkt Nördliches Inneralpines Wiener Becken – Hydrogeologische Grundlagen. – 42 S., 2 Beilagen, Amt der Niederösterreichischen Landesregierung, Abteilung B/9, St. Pölten.

EU COPERNICUS (2016): Mapping Guide for a European Urban Atlas. – http://www.eea.europa.eu/data-and-maps/data/urban-atlas (accessed: 2019-09-18)

FÜRNKRANZ, A. (1990): Hydrogeologische Erkundung 198/89 im Bereich der zukünftigen Versickerungsanlage. – 89 S. + Anhang, Marchfeldkanalgesellschaft.

GÖTZINGER, G. (1951): Zur Quellengeologie des Wienerwaldes (Flysch), Teil 1. – Anzeiger der mathematisch-naturwissenschaftlichen Klasse der Österreichischen Akademie der Wissenschaften, **88**/6, 150–158, Wien.

GRUPE, S. (2011): Angewandte hydrogeologische Forschung Stadtgebiet Wien – Teilgebiet Lobau. – 18 Präsentationsfolien. http://www.wgm.wien.at/Lobau.65.0.html (accessed: 2019-09-18)

GRUPE, S. (2012): Angewandte hydrogeologische Forschung Stadtgebiet Wien – Teilgebiet Wienerberg. – 31 Präsentationsfolien. http://www.wgm.wien.at/Wienerberg.79.0.html (accessed: 2019-09-18)

GRUPE, S. (2013): Angewandte hydrogeologische Forschung Stadtgebiet Wien – Teilgebiet Liesing. – 31 Präsentationsfolien. http://www.wgm.wien.at/Liesingtal.100.0.html (accessed: 2019-09-18)

GRUPE, S. & PAYER, T. (2009): Angewandte hydrogeologische Forschung Stadtgebiet Wien – Teilgebiet Hauptbahnhof, Aspanggründe, Arsenal, U1-Süd-Verlängerung, U2-Süd-Verlängerung. – 16 Präsentationsfolien. http://www.wgm.wien.at/Hauptbahnhof.90.0.html (accessed: 2019-09-18)

GRUPE, S. & PAYER, T. (2010): Angewandte hydrogeologische Forschung Stadtgebiet Wien – Teilgebiet Das Leopoldsdorfer Bruchsystem am Südrand von Wien. – 16 Präsentationsfolien. http://www.wgm.wien.at/Johannesberg.28.0.html (accessed: 2019-09-18)

GRUPE, S. & PAYER, T. (2014): Angewandte hydrogeologische Forschung Stadtgebiet Wien – Teilgebiet Simmering. – 32 Präsentationsfolien. http://www.wgm.wien.at/Simmering.123.0.html (accessed: 2019-09-18)

GRUPE, S. & PAYER, T. (2015): Angewandte hydrogeologische Forschung Stadtgebiet Wien – Teilgebiet Wienerberg bis Alsergrund. – 35 Präsentationsfolien. http://www.wgm.wien.at/U2-Verlaengerung.137.0.html (accessed: 2019-09-18)

GRUPE, S. & PAYER, T. (2017): Angewandte hydrogeologische Forschung Stadtgebiet Wien – Teilgebiet Wien östlich der Donau. – 35 Präsentationsfolien. http://www.wgm.wien.at/Floridsdorf.194.0.html (accessed: 2019-09-18)

GRUPE, S. & PAYER, T. (2018): Angewandte hydrogeologische Forschung Stadtgebiet Wien – Teilgebiet Wiental. – 73 Präsentationsfolien. http://www.wgm.wien.at/Wiental.205.0.html (accessed: 2019-09-18)

GRUPE, S., PAYER, T. & NEUBER, D. (2016): Angewandte hydrogeologische Forschung Stadtgebiet Wien – Teilgebiet Dornbach bis Alsergrund. – 45 Präsentationsfolien. http://www.wgm.wien.at/Geplante-U5.155.0.html (accessed: 2019-09-18)

GRUPPE WASSER (2005): Grundwasserspiegel Wien – linkes Donauufer. – https://www.wien.gv.at/umwelt/gewaesser/schutz/hydrografie/pdf/schichtenplan-2-20-mittlere.pdf (accessed: 2019-09-18)

HOFMANN, T. & PFLEIDERER, S. (2003): Digitaler angewandter Geo-Atlas der Stadt Wien – GEOModul. – Endbericht, Projekt WC 18, Teil 2, 29 S., 4 Beilagen, Geologische Bundesanstalt, Wien. [GBA, Wissenschaftliches Archiv, Nr. A 17118-R]

KRALIK, M., BENISCHKE, R. & WYHLIDAL, S. (2015): Erläuterungen zur Wasserisotopenkarte Österreichs. – Bundesministerium für Land- und Forstwirtschaft, Umwelt und Wasserwirtschaft, 30 S., Wien.

LEBETH. F. (Red.) (1989): Die Grundwassersituation in Wien. – 188 S., Magistratsabteilung 45, Wien.

LEBETH, F., PLACHY, H., JANAC, P., HIRHAGER, R. & SCHEMBOR, F. (1988): Erarbeitung von Grundlagen für einen langfristigen Plan zur Nutzung und zum Schutz des Grundwassers in Ballungszentren am Beispiel Wiens. – Endbericht, Projekt W-A-001c, 3 Teile mit Beilagen, 279 S., Wien.

MA 41 (2019): Digitale Mehrzweckkarte. – Magistratsabteilung 41 – Stadtvermessung Stadt Wien. https://www.wien.gv.at/stadtentwicklung/stadtvermessung/geodaten/mzk/index.html (accessed: 2019-09-18)

NIEDERBACHER, P., ERHARD-SCHIPPEK, W., WESSELY, G. & GOLDBRUNNER, J. (1995): Tiefengrundwasservorkommen in Niederösterreich. Schwerpunkt Nördliches Inneralpines Wiener Becken. – Unveröffentlichter Bericht, 74 S., Amt der Niederösterreichischen Landesregierung, Abteilung B/9, Wasser- und Abfallwirtschaft, Wien.

NOWY, W., TASCHKE, R., SCHIMANA, R. & STEPAN, C. (2001): Schutz von Tiefengrundwässern in Wien – Grundlagen für eine wasserwirtschaftliche Rahmenverfügung. – Endbericht, 58 S., Magistratsabteilung 45, Wien.

PFLEIDERER, S. & HOFMANN, T. (2004): Digitaler angewandter Geo-Atlas der Stadt Wien – HYDRO-Modul (Pilotphase). – Endbericht, Projekt WC 21, 26 S., 3 Beilagen, Geologische Bundesanstalt, Wien. [GBA, Wissenschaftliches Archiv, Nr. A 13534-R]

PFLEIDERER, S., SCHEDL, A., NEINAVAIE, H. & PIRKL, H. (2010): Umweltgeochemie Stadtgebiet Wien. – Endbericht, Projekt WC 26, 57 S., 4 Beilagen, Geologische Bundesanstalt, Wien. [GBA, Wissenschaftliches Archiv, Nr. A 16621-R]

PHILIPPITSCH, R. & GRATH, J. (2019): Wassergüte in Österreich. – 438 S., Bundesministerium für Nachhaltigkeit und Tourismus, Umweltbundesamt GmbH, Wien.

PÖYRY (2011): GW-Schichtenpläne 2. + 20. Bezirk. – https://www.wien.gv.at/umwelt/gewaesser/schutz/hydrografie/pdf/schichtenplan-21-22-mittlere.pdf (accessed: 2019-09-18)

SCHNABEL, W. (Red.), FUCHS, G., MATURA, A., BRYDA, G., EGGER, J., KRENMAYR, H.G., MANDL, G.W., NOWOTNY, A., ROETZEL, R., SCHNABEL, W. & SCHARBERT, S. (2002): Geologische Karte von Niederösterreich 1:200.000 mit Legende und Kurzerläuterung. – 47 S., 2 Karten, Geologische Bundesanstalt/Land Niederösterreich, Wien.

SCHREILECHNER, M., KEGLOVIC, P., REZANIA, R., PRODINGER, C., GADERMEIER, G., RUPPRECHT, D. & GARDEN, M. (in press): The GeoTief EXPLORE 3D Project – an Integrative Approach for the Exploration and Exploitation of Hydrogeothermal Energy in the Vienna Basin. – To be published in the Proceedings of the World Geothermal Congress, 2020, Reykjavik, Iceland.

SCHUBERT, G. (2015): Hydrogeologie der trinkbaren Tiefengrundwässer in Österreich. – In: SCHUBERT, G. (Red.): Trinkbare Tiefengrundwässer in Österreich. – Abhandlungen der Geologischen Bundesanstalt, **64**, 11–70, Wien.

SCHUCH, M. (1980): Beitrag zur Hydrogeologie des Marchfeldes. – Wiener Mitteilungen, Wasser – Abwasser – Gewässer, **32**, J1–J25, Österreichische Wasserwirtschaft, Wien.

SCHÜGERL, W., REZABEK, H.R. & THURNER, G. (1988): Marchfeldkanal – Grundwasserwirtschaftliches Konzept – Hydrogeologische Grundlagen für ein mathematisches Grundwassermodell. – 20 S., Errichtungsgesellschaft Marchfeldkanal, Wien.

STEINER, C., GÖTZL, G. & WEILBOLD, J. (2017): GeoPLASMA-CE in Österreich. – In: WIMMER-FREY, I., RÖMER, A. & JANDA, C.: Arbeitstagung der Geologischen Bundesanstalt: Angewandte Geowissenschaften an der GBA, Tagungsband, 19.–22. Juni 2017, 237–238, Wien.

VAN HUSEN, D. (1990): Gutachterliche Stellungnahme zur geologisch-hydrogeologischen Situation im Areal der geplanten Versickerungsanlage Stallingerfeld. – 6 S., 5 Beilagen, Marchfeldkanalgesellschaft, Wien.

WESSELY, G. (1983): Zur Geologie und Hydrodynamik im südlichen Wiener Becken und seiner Randzone. – Mitteilungen der Österreichischen Geologischen Gesellschaft, **76**, 27–68, Wien.

Law materials

TRINKWASSERVERORDNUNG 2001, BGBl. II Nr. 304/2001 idgF. Verordnung des Bundesministers für soziale Sicherheit und Generationen über die Qualität von Wasser für den menschlichen Gebrauch (Trinkwasserverordnung – TWV).
https://www.ris.bka.gv.at/GeltendeFassung.wxe?Abfrage=Bundesnormen&Gesetzesnummer=20001483 (accessed: 2019-09-18).

WASSERRECHTSGESETZ 1959 – WRG 1959, BGBl. Nr. 215/1959 idgF.
https://www.ris.bka.gv.at/GeltendeFassung.wxe?Abfrage=Bundesnormen&Gesetzesnummer=10010290 (accessed: 2019-09-18).

Received: 21. August 2019, accepted: 19. September 2019

JAHRBUCH DER GEOLOGISCHEN BUNDESANSTALT
Jb. Geol. B.-A. | ISSN 0016–7800 | Band 159 | Heft 1–4 | S. 67–130 | Wien, Dezember 2019

Carbonates in natural and geotechnical settings – chemical sediments as environmental archives

Ronny Boch*

19 Text-Figures

Österreichische Karte 1:50.000
BMN / UTM
101 Eisenerz / NL 33-02-15 Eisenerz
104 Mürzzuschlag / NL 33-02-12 Mürzzuschlag
105 Neunkirchen / NL 33-02-18 Vorau
134 Passail / NL 33-02-23 Weiz

Calcium carbonate
Erzberg
Geothermal energy
Karst caves
Environmental monitoring
Clumped isotopes

Contents

Abstract

The diverse geoscientific topics of this publication are centered around the carbonate system and in particular on anhydrous and hydrous calcium carbonates and the distinct polymorphs of $CaCO_3$. A broad range of physicochemical processes from sub-microscopic to regional scale opens the discussion on fundamental and applied research aspects connecting modern geochemistry with geology. The deposition of carbonate minerals in various natural and (geo)technical settings represents a chemical-sedimentary archive capturing site-specific natural and human-made environmental conditions. Different environmental parameters – changing temporally and spatially – can be reconstructed from the evolving mineral deposits. An in-depth process understanding of fluid-solid (e.g. water-rock) interaction is a key to manifold applications. This involves an advanced understanding of carbonate precipitation (growth) dynamics, inorganic or microbially-mediated crystallization mechanisms and the resulting material characteristics and their environmental dependencies. State-of-the-art and mostly high spatial resolution laboratory analytical geochemical and imaging techniques are utilized. This includes computer-controlled micromill and laser ablation based solid material sampling strategies in combination with mass

* Ronny Boch: Graz University of Technology, Institute of Applied Geosciences, Rechbauerstraße 12, 8010 Graz, Austria. ronny.boch@tugraz.at

spectrometric, electron and X-ray interactive analyses of elemental concentrations and isotopic ratios and fractionation, as well as of variable crystal growth and fabrics. Radiometric uranium-thorium age and rate determination and multiply-substituted isotopologue (clumped isotopes) measurements yielded valuable information. Field-based periodical or on-site and online environmental monitoring mainly of fluid phases applying automated data loggers constitutes an integral part in some of the studies presented.

Applying geochemical approaches and tools to geotechnical settings is focused on unwanted mineral deposits – dominantly carbonate scaling – impairing geothermal energy production from deep aquifers or artificial water channels of different settings. This includes reduced (thermal) water and energy transfers from deep wells, in pipelines and heat exchangers, as well as in tunnel and surface drainages. The concept of 'Scaling Forensics' represents a multi-proxy high-resolution analytical approach of the carbonate scale materials and was developed and applied in order to evaluate and adapt unfavourable site-specific production conditions. Scale depositing geogenic and operational environmental processes determining the scaling progress and scale material characteristics (e.g. growth rate, consistency) are investigated. Specific environmental conditions such as production cessations/restarts, the problem of scale-fragment formation or the distinct role of solid/fluid phase interfaces (e.g. corrosion layers, growth surfaces) and related processes (e.g. crystal nucleation, CO_2/H_2O outgassing, particle mobilization) are highlighted. The formation mechanisms of geologically young veins filling fractures of the Austrian 'Erzberg' iron ore deposit in Styria and their possible relation to gravitational or tectonic mass movements, as well as to variable regional climate conditions in a sensitive Alpine setting are discussed. Karst areas, caves and speleothems were investigated in the context of stalagmite growth dynamics and the reconstruction of past changes in air temperature and meteoric precipitation. Using selected and environmentally well-constrained natural and technical Ca-carbonate materials established as well as newly developed isotope tracers (e.g. clumped isotope thermometer and fluid provenance tracer) can be evaluated and calibrated.

Karbonate in natürlichen und geotechnischen Umfeldern – Chemische Sedimente als Umweltarchiv

Zusammenfassung

Die verschiedenen geowissenschaftlichen Themen dieser Publikation zentrieren sich auf das Karbonatsystem und besonders auf wasserfreie wie wasserhaltige Kalziumkarbonate und die Polymorphe von $CaCO_3$. Ein breites Spektrum physikochemischer Prozesse von submikroskopischer bis regionaler Größenskala eröffnet einen Zugang zu Grundlagen- wie angewandten Forschungsfragen und verbindet Aspekte der modernen Geochemie mit solchen der Geologie. Die Bildung von Karbonatmineralen in natürlichen und (geo)technischen Umfeldern begründet ein chemisch-sedimentäres Archiv, welches ortsspezifische geogen und anthropogen beeinflusste Umweltbedingungen aufzeichnen kann. Verschiedene sich räumlich und zeitlich ändernde Umweltparameter können aus den in-situ und sukzessiv gebildeten mineralischen Ablagerungen rekonstruiert werden. Ein detailliertes Prozessverständnis der Fluid-Solid (z.B. Wasser-Gestein) Wechselwirkung ermöglicht systematische Einsichten und Anwendungen. Dies beinhaltet ein besseres Verständnis der Karbonatfällung (Wachstumsdynamik) aus wässrigen Lösungen, anorganischer oder mikrobiell beeinflusster Kristallisationsmechanismen und von resultierenden Materialcharakteristika und deren Abhängigkeiten von bestimmten Umweltbedingungen. Zu diesem Zweck werden zumeist räumlich hochauflösende geochemische und bildgebende Analysetechniken und Laborverfahren angewandt. Involviert sind etwa Computer gesteuertes Mikrofräsen und Laserablation mit variablen Beprobungsstrategien von Festphasen in Kombination mit massenspektrometrischen Methoden oder Elektronen- und Röntgenstrahlen basierten Analysen zur Bestimmung von Elementkonzentrationen wie auch der Isotopenverhältnisse und -fraktionierung oder des Kristallwachstums und daraus entstehende Materialtexturen. Radiometrische Uran-Thorium basierte Alter und Raten sowie Messungen mehrfach substituierter Isotopologe (Clumped Isotopes) erbrachten spannende Ergebnisse. Geländebasiertes Umwelt-Monitoring, hauptsächlich von Fluidphasen (Lösungen, Atmosphäre) mittels automatischer Datenlogger, ist ein wesentlicher Bestandteil in manchen der präsentierten Studien.

Die Anwendung geochemischer Ansätze und Werkzeuge auf geotechnische Umfelder fokussiert in der vorliegenden Arbeit auf unerwünschte Mineralablagerungen – vor allem Karbonat-Scaling (Sinterkrusten i.w.S.) – welche die geothermische Energieproduktion aus tiefen Aquiferen oder die Wasserführung in künstlichen Gerinnen behindern. Gemeint sind reduzierte (Thermal-)Wasser- und Energie-Transfers aus Tiefbohrungen, in Pipelines und Wärmetauschern, wie auch in Tunnel- und Oberflächendrainagen. Diesbezüglich stellt das Konzept der „Scaling Forensik" einen Multiparameter- und analytisch räumlich-zeitlich hochauflösenden Ansatz der Untersuchung von karbonatischem Scale-Material dar, das zur Evaluierung und Adaption von ungünstigen Orts- (Anlagen-) spezifischen Umwelt- und Betriebsbedingungen herangezogen werden kann. Die maßgeblichen natürlichen und operativen Prozesse und Bedingungen betreffend das variable Fortschreiten und die Materialeigenschaften (z.B. Wachstumsrate, Konsistenz) der Mineralablagerungen werden im Detail untersucht. Rahmenbedingungen im Zusammenhang mit Betriebs-/Förderunterbrechungen, das Problem der Scale-Fragment-Bildung oder die besondere Rolle von Fluid-/Festphasen-Grenzflächen (z.B. Korrosionslagen, Wachstumsoberflächen) und damit einhergehende Prozesse (Kristallnukleation, CO_2/H_2O Entgasen, Partikelmobilisierung) werden diskutiert. Weiters werden die Bildungsmechanismen von geologisch jungen mineralischen Ausfällungen in vertikalen Brüchen der bekannten österreichischen Lagerstätte „Erzberg" in der Steiermark, sowie die Abhängigkeit solcher Kluftverheilungen von gravitativen oder tektonischen Gesteinsbewegungen und auch von sich verändernden regionalen Klimabedingungen im sensitiven alpinen Raum eruiert. Karstgebiete, Höhlen und Tropfsteine sind mit Blick auf die Stalagmiten-Wachstumsdynamik und die daraus mögliche zeitlich hochaufgelöste Rekonstruktion vergangener Änderungen der Lufttemperatur und des meteorischen Niederschlags ein Untersuchungsgegenstand. Unter Verwendung von ausgewählten und gut charakterisierten Kalziumkarbonaten aus natürlichen oder (geo)technischen Bildungsmilieus können etablierte wie neu entwickelte Isotopen-Tracer (z.B. „Clumped Isotope" Thermometer und Fluid-Herkunft Tracer) evaluiert und kalibriert werden.

Preface

Carbonate research and its associated technological developments over the last few decades have highlighted the importance of this comprehensive functional and mineral group in various environmental settings on Earth. The wide range of material characteristics of carbonates depend on variable physicochemical conditions during formation. Considering this broad range of settings and conditions, related research and development activities comprise of fundamental scientific as well as applied objectives, e.g. focusing on natural, laboratory experimental, (geo)technical and material science topics. Relying on an evolving spectrum of field and laboratory analytics, as well as computer modelling techniques utilized to investigate carbonates and their environments, the modern field of carbonate research is highly interdisciplinary. Another principal anchor of carbonate research consists of the detailed examination of fluid-solid interaction, i.e. the intimate association of solid, liquid, and gaseous phases such as carbonate minerals, carbon dioxide, and carbonate alkalinity in aqueous solutions.

Consequently, considering the intention of this piece of work a strong focus is devoted to the advancement in the process understanding of chemical-sedimentary carbonate formation in natural and human-made environmental settings. This means a detailed and site-specific understanding of the distinct mechanisms and parameters controlling mineralogical, elemental and isotopic compositions. These aims are closely related to carbonate crystallization behaviour, material characteristics, and wanted or unwanted natural as well as technical constraints on highly diverse spatial and temporal scales. Elaborated sampling procedures, state-of-the-art and mostly high-resolution laboratory based analytical techniques, field based environmental monitoring campaigns and experimental setups constitute major building blocks of the carbonate research approach presented here. The recognition of widespread analogies in the determining processes and the transfer of knowledge and analytical skills between the more fundamental (e.g. caves and speleothem formation) and the more applied (e.g. carbonate scale deposition during geothermal energy production) geoscientific topics is exemplified and discussed.

The development of this broad yet selective manuscript is founded on the accompanying chapters of my cumulative habilitation thesis. It is mainly based on an accumulation of selected publications generated during the last few years with own contributions as a first author or as a co-author. I hope that this circumstance can provide some excuse for the occasionally pronounced self-citation. The interested reader, however, might pay attention to the comprehensive reference list provided at the end of this publication.

Ronny Boch
April 2019, Graz, Austria

Introduction

From a principal point of view, various carbonate mineral formation is the expression of an acid-base reaction in different environmental conditions, i.e. the salt resulting from the chemical reaction of a weak acid (H_2CO_3) providing the carbonate anion and a base (e.g. $Ca(OH)_2$) providing the variable cation. Regarding carbonic acid, the widespread occurrence and dissolution of **carbon dioxide** (CO_2) in aqueous solutions is of major importance. The solubility of CO_2 compared to many other gas phases is relatively high, i.e. the equilibrium (Henry's Law) constant $K_H = 10^{-1.47}$ (at 25° C) depends on the partial pressure (fugacity) of the gaseous phase, as well as on temperature and ionic strength (salinity) of the aqueous solution (Carroll et al., 1991; Truche et al., 2016). In particular, a higher gaseous carbon dioxide partial pressure ($pCO_{2[g]}$) results in higher CO_2 contents in equilibrium with the aqueous solution ($CO_{2[aq]}$). CO_2 solubility decreases with increasing temperature and decreases with increasing ionic strength (Duan & Sun, 2003; Millero et al., 2006). At high-pressures (> 100 bar), the solubility of CO_2 reverses, i.e. increases with temperature (Duan & Sun, 2003). In solution, the hydrated CO_2, as well as the minor molecular species of carbonic acid (H_2CO_3) possess a strong tendency of partial dissociation towards bicarbonate (HCO_3^-) and the carbonate anion (CO_3^{2-}) assessed by equilibrium dissociation constants (e.g. Millero et al., 2006). These interrelated dissociation equilibria and more generally the **carbonate chemical equilibrium** can be summarized by the following set of equations:

1a) $CO_{2(g)} \leftrightarrow CO_{2(aq)}$

1b) $CO_{2(aq)} + H_2O \leftrightarrow H_2CO_3$

1c) $H_2CO_3 \leftrightarrow HCO_3^- + H^+$

1d) $HCO_3^- \leftrightarrow CO_3^{2-} + H^+$

The different carbonate species concentrations in aqueous solution can be summarized by the content of **dissolved inorganic carbon** (DIC):

2) $[DIC] = [CO_{2(aq)}] + [H_2CO_3] + [HCO_3^-] + [CO_3^{2-}]$

From the fundamental equations noted above, it becomes obvious that the prevailing **pH** conditions in the carbonate chemical system are intimately connected to the dissociation equilibria of the carbonate species, i.e. an acid-base system typically involving the transfer of protons (H^+) in its partial reactions. The proportion of the individual carbonate species in aqueous solution is strongly dependent on the prevailing pH and in turn the content of DIC has a primary effect on the overall solution pH (e.g. in carbonate dominated aquifers, streams and springs; Ford & Williams, 2007; Boch et al., 2015; Kluge et al., 2018). At typical pH ranges in most natural waters (~6.5–8.5), the bicarbonate anion (HCO_3^-) represents the dominant inorganic carbon species in aqueous solution. At lower (acidic) pH conditions, dissolved CO_2 and small fractions of carbonic acid are the main molecular carbon species while at higher (alkaline) pH the carbonate anion prevails (Text-Fig. 1). The latter species is of crucial relevance with regard to the formation of carbonate minerals. Bicarbonate, however, can also be incorporated into the carbonate crystal lattice during rapid carbonate mineral precipitation and favourable kinetic processes (Michaelis et al., 1985; Mickler et al., 2004; Eiler et al., 2014). Regarding the carbonate system pH dependencies, the preferred formation of carbonate minerals at increased pH results in a directly coupled pH decrease, while the dissolution of carbonate minerals (salt) results in an overall pH increase, i.e. the carbonate system is also characterized by a pronounced **pH buffering capacity**. Such behaviour is of major importance in various natural as well as human-made environmental settings of carbonate occurrence.

Carbonate mineral formation involves a wide spectrum of possible **cations** combining with the carbonate functional group in a crystal lattice (or a few known amorphous phases). Owing to the divalent negative charge (2-) of the carbonate anion an arrangement with divalent cations (2+) of the earth alkaline and transition metals is most common in the carbonate mineral group. Carbonate minerals, however, involve ionic and covalent bonding of the atoms. The electric charge and structural prevalence results in carbonate minerals such as $CaCO_3$ (three anhydrous polymorphs: calcite, aragonite, vaterite), $MgCO_3$ (magnesite), $SrCO_3$ (strontianite), $BaCO_3$ (witherite), $FeCO_3$ (siderite), $MnCO_3$ (rhodochrosite), $ZnCO_3$ (smithsonite), $PbCO_3$ (cerussite), $CaMg(CO_3)_2$ (dolomite), $Ca(Fe,Mg)(CO_3)_2$ (an-

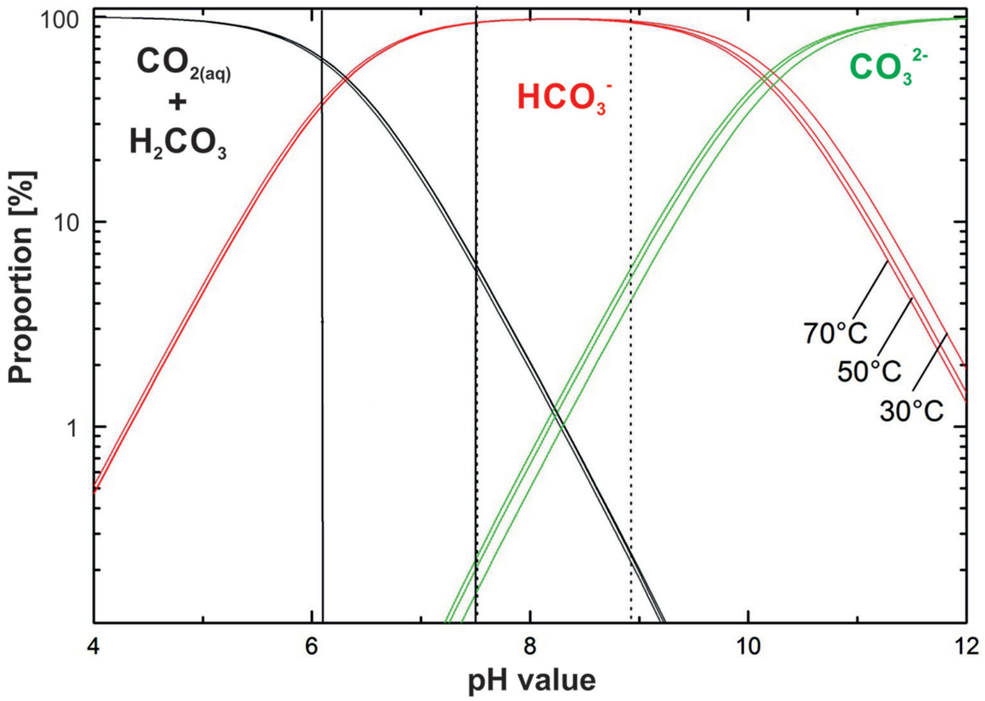

Text-Fig. 1.
Proportion of different inorganic carbonate species in aqueous solution depending on pH and a set of temperatures (adapted from KLUGE et al., 2018).

kerite), $Cu_2CO_3(OH)_2$ (malachite), $Cu_3(CO_3)_2(OH)_2$ (azurite), and several others. Amongst these, calcite and dolomite are the most widespread on Earth accounting for extensive sediment deposits in the ocean basins (e.g. carbonate muds and biogenic compounds) or forming the mass of entire mountain ranges (e.g. the Northern Calcareous Alps and the Dolomites of the Alps; CHANG et al., 1998).

Most of the carbonate minerals mentioned above possess recurrent **structural similarities** (symmetry elements) regarding their atomic bonding and crystallography. A group consists of minerals crystallizing in the **trigonal** (rhombohedral) system (e.g. calcite, magnesite, siderite) in contrast to the **orthorhombic** carbonate group (e.g. aragonite, strontianite, witherite). The former is characterized by a 6-fold coordination of the cation site in the crystal lattice, while orthorhombic carbonates have 9-fold coordinated cation sites. This structural discrepancy results in a significantly different behaviour with regards to the incorporation of cations mostly depending on their respective ionic radius, i.e. divalent cations smaller than Ca (Mg, Zn, Fe, Cu, Mn) are preferred in the rhombohedral crystal lattice while those larger than Ca (Sr, Pb, Ba) show higher average element contents in the orthorhombic ion arrangement (MORSE & MACKENZIE, 1990). The double carbonate dolomite is trigonal-rhombohedral and characterized by a well-ordered and kinetically restricted arrangement of Ca and Mg cations in the crystal lattice. Although there are many similarities and phase relations compared to calcite, the formation of dolomite from direct precipitation or successive dolomitization is a subject of ongoing scientific debate and research activities (MORSE et al., 2007; BALDERMANN et al., 2015). Further considering monovalent alkali metal containing carbonates such as the Na-carbonates natronite ($Na_2CO_3.10H_2O$) and nahcolite ($NaHCO_3$), their formation also strongly relies on the criteria of ionic radius and ionic charge balance in the crystal lattice according to the prevailing hydrochemical conditions. More specifically, their occurrence is frequently associated with mixing or evaporation in the context of highly saline aqueous solutions (MONNIN & SCHOTT, 1984; COUNCIL & BENNETT, 1993). Carbonates can be further classified as **anhydrous and hydrous minerals**, i.e. those lacking a stoichiometric water component and those comprising water molecules and hydroxyl functional groups (crystal water) as part of their crystal lattice. Relatively common representatives are hydrous carbonates such as monohydrocalcite ($CaCO_3.H_2O$), ikaite ($CaCO_3.6H_2O$), nesquehonite ($MgCO_3.3H_2O$), hydromagnesite ($Mg_5[CO_3]_4[OH]_2.4H_2O$) and basic calcium carbonate (BCC; $Ca_3[CO_3]_2[OH]_2.H_2O$). Recently, ZOU et al. (2019) reported the existence of monoclinic Ca-carbonate hemihydrate (CCHH; $CaCO_3.½H_2O$). These minerals typically form under restricted environmental conditions, e.g. low temperatures, elevated (hydrostatic) pressure or high pH, high saturation states and increased Mg concentrations (KRALJ & BREČEVIĆ, 1995; LANGMUIR, 1997; RODRIGUEZ-RUIZ et al., 2014; RIPKEN et al., 2018). Most of these hydrous carbonates are more or less metastable and show partial or complete dehydration (loss of crystal water) in the event of temperature increase. Consequently, individual idiomorphic crystals or mineral aggregates transform and disintegrate into carbonate minerals of more stable configuration at ambient environmental conditions (BOCH et al., 2015; PURGSTALLER et al., 2017a). For example, the calcium carbonates ikaite and monohydrocalcite are known to destabilize towards calcite or other anhydrous carbonate phases. Regarding the thermal stability of anhydrous carbonates, a critical limit consists in the volatilization of CO_2 at higher temperatures of several hundred degrees centigrade, e.g. thermal decomposition (decarbonation) of calcite at > 825° C resulting in the formation of calcium oxide (CaO; burnt lime).

Addressing the general physicochemical characteristics of carbonate minerals, their **solubility** is another parameter of crucial environmental relevance. Compared to other mineral groups (e.g. chlorides, sulphates, sulphides, oxides, silicates) carbonates are of intermediate solubility in aqueous solution. The solubility behaviour is mostly described by the solubility product (equilibrium constant):

3a) $K_{SP} = [X]^a [Y]^b$

based on the educt vs. product chemical equilibrium reaction:

3b) $X_aY_{b(s)} \leftrightarrow aX_{(aq)} + bY_{(aq)}$

The solubility products of the various carbonate minerals differ significantly, e.g. the log_K_{SP} values for selected phases at 25° C and 1 bar are: calcite = -8.5 and aragonite = -8.3 (both from PLUMMER & BUSENBERG, 1982), ikaite = -6.6 (BISCHOFF et al., 1993), monohydrocalcite = -7.2 (KRALJ & BREČEVIĆ, 1995), amorphous calcium carbonate = -6.0 (CLARKSON et al., 1992), siderite = -10.9 (REITERER et al., 1981), magnesite = -7.9 (LANGMUIR, 1997) or the double carbonates dolomite ~ -17.1/2 = -8.6 and ankerite: ~ -19.9/2 = -10.0 (both from MORSE & MACKENZIE, 1990 and depending on stoichiometry). Similar to carbon dioxide and considering moderate environmental conditions, the solubility decreases significantly with increasing temperature (retrograde solubility), increases with increasing pressure, and is further dependent on the ionic strength, specific ion pair and aqueous complex formation with some tendency of increased solubility at higher salinity (LANGMUIR, 1997; MORSE et al., 2007). Based on the solubility of carbonates, the mineral-specific **saturation state** represents another hydrochemical parameter of major environmental relevance. Saturation of an aqueous solution is typically expressed as saturation index defined as the ion activity product of the relevant constituents (mineral assembling ions) versus the solubility product on a logarithmic scale:

4) $SI = \log [IAP/K_{SP}]$

where SI = 0 indicates saturation (mineral vs. solution in equilibrium), SI < 0 indicates undersaturation (mineral dissolution), and SI > 0 indicates supersaturation (mineral precipitation) from a thermodynamic (intrinsic energetic) point of view and thus also strongly depending on the prevailing ambient physicochemical conditions. In nature, waters at the surface or underground are typically saturated with respect to $CaCO_3$ and therefore a change in the prevailing environmental conditions results in mineral precipitation or dissolution. The actual mineral precipitation or dissolution behaviour, however, also depends on the reaction kinetics of a particular mineral phase, i.e. the precipitation or dissolution in a specific environmental setting might be promoted or inhibited apart from the thermodynamic saturation state in aqueous solution. Well known examples of such reaction kinetic control on carbonate mineral formation are the restricted crystallization of well-ordered dolomite or the kinetically preferred precipitation of higher soluble Mg-calcite and aragonite instead of thermodynamically more stable low-Mg calcite in the oceans (MORSE & ARVIDSON, 2002; SARKAR et al., 2013). Regarding dolomite formation and the dolomitization of limestones, the precipitation of less ordered and Ca-excess protodolomite constitutes a specific and intensely studied case mostly associated with conditions of high ionic strength solutions, pronounced evaporation or a mediating (catalytic) contribution of bacteria (MORSE et al., 2007; BALDERMANN et al., 2015).

Biological processes are known as major controls of physicochemical reactions during carbonate biomineralization in marine and continental settings (MORSE & MACKENZIE, 1990; MORSE, 2004). Examples are the various types of **exo- and endoskeletons** dominantly consisting of (calcium) carbonate and characterizing organisms such as corals, bivalves, gastropods, echinoderms and foraminifers. Biogenic carbonate mineralization is increasingly recognized in the context of microbial activity represented by numerous species of bacteria, cyanobacteria, algae and fungi. The **microbial communities** are typically present as biofilms or sophisticated networks consisting of distinct organic tissues, precipitated carbonate minerals, and connecting extracellular polymeric substances (EPS; ARP et al., 1999; PEDLEY, 2013; DIAZ et al., 2017). Micrometre- to millimetre-sized filaments, dendritic structures and delicate fibres are common structural elements of such biocenosis (GUO & RIDING, 1992; LANNELUC et al., 2015; JONES, 2017a). The microbes exert either an **active or a passive role** with regard to carbonate mineral formation. A passive role consists in providing a (high specific surface area) substrate for initial mineral nucleation and ongoing crystal growth. In contrast, an active role means the physicochemical alteration of aqueous solution and thus carbonate precipitation conditions in the course of different organism-specific and mostly catalytic (e.g. reduction of activation energies) processes (RIDING, 2000; FOUKE, 2011; LYONS et al., 2015). With respect to the carbonate chemical system, microbial metabolic processes such as photosynthesis and chemoautotroph energy transfers are the most common manifestation of hydrochemical alteration promoting carbonate mineral deposition or dissolution. Photosynthesis utilized by many microbes existing in a diversity of settings on the Earth's surface can be described by the simplified expression:

5) $CO_2 + H_2O \rightarrow 1/6\ C_6H_{12}O_6 + O_2$

Consequently, various algae or cyanobacteria being common representatives of **photosynthetic microbes** can actively influence the CO_2 budget of their environment and may ultimately trigger carbonate mineral nucleation, or accelerate or reduce local mineral growth (LANGMUIR, 1997; ROGERSON et al., 2008). **Chemoautotroph** life cycles producing their own nutrition and energy gains from selected chemical components and reactions involving aqueous solutions and gases are characteristic of more or less extreme environmental conditions (e.g. thermophile or halophile organisms; TAKAI et al., 2008; LERM et al., 2013). In most cases, the particular energy transfers are based on redox reactions, i.e. redox sensitive chemical constituents being processed in the metabolism of the specialized microbial organism. Examples are the oxidation of organic matter in sediments of the ocean floors or in deep continental reservoirs (sedimentary basins) which liberates CO_2 and therefore provides dissolved carbonate species (alkalinity) in solution and for minerals (MORSE, 2004; VARSÁNYI & KOVÁCS, 2006). Other redox reactions frequently associated with microbial activity are bacterial sulphate reduction (BALDERMANN et al., 2015), sulfide oxidation (LYONS et al., 2015) or iron reduction and oxidation (ZAMMIT et al., 2015). All of these aerobic (e.g. oxidic) or anaerobic (e.g. sulfidic) reaction schemes can have a major influence on carbonate mineral precipitation or dissolution. In this context, the comprehensive topic of burial and maturing carbonate diagenesis and its close interrelation of dissolution and re-precipitation processes should be mentioned.

Microbial processes are further relevant both in natural and human-made (geotechnical) settings of carbonate occurrence (e.g. aquifers; VARSÁNYI et al., 1997; MAYRHOFER et al., 2014), alteration and precipitation (GRENGG et al., 2015; DIAZ et al., 2017; BOCH et al., 2017b).

Calcium carbonate – Precipitation and polymorphs

Amongst the numerous carbonate minerals, the Ca-carbonates constitute a division of overwhelming importance, mainly due to their widespread occurrence in natural and human-made environmental settings, their rich chemical and crystallographic variability, and properties depending on distinct environmental conditions, as well as regarding their potential in diverse material scientific and industrial applications. The diverse settings addressing fluid-solid interaction of various planetary hydrogeochemical cycles and Ca-carbonate formation in geotechnical and laboratory synthetic environments will be the subject of a subsequent chapter. Ca-carbonates are involved in purely inorganic, as well as organically mediated processes on different spatial and temporal scales. As for carbonates in general, anhydrous and hydrous phases can be found within the Ca-carbonate division depending on specific and sometimes rare conditions prevailing. Typically, Ca-carbonate mineral formation follows the overall reaction scheme:

6) $Ca^{2+}_{[aq]} + 2HCO_3^-{}_{[aq]} \leftrightarrow CaCO_{3[s]} + CO_{2[g]} + H_2O$

This **Ca-carbonate chemical equilibrium** displays the forward reaction of dissolved calcium cations and bicarbonate anions towards anhydrous Ca-carbonate precipitating from aqueous solution, gaseous, or partially dissolved carbon dioxide and water. Examples of this forward directed reaction are the formation of speleothems (dripstones) in caves (FAIRCHILD et al., 2006; BOCH et al., 2011a; DENNISTON & LUETSCHER, 2017), synthetic Ca-carbonate precipitation in laboratory experiments (DIETZEL et al., 2004; TANG et al., 2008a, b; PURGSTALLER et al., 2017b), or unwanted Ca-carbonate precipitation affecting geotechnical and water supply infrastructure (HASSON et al., 2010; SÜRMELIHINDI et al., 2013; BOCH et al., 2017a). The inverse reaction (from right to left in equation 6) describes the dissolution of Ca-carbonate via CO_2 and water (carbonic acid) resulting in increased calcium and carbonate species in solution. Typical examples of the latter reaction are the karstification of limestone (FORD & WILLIAMS, 2007; MATTEY et al., 2016), the dissolutional alteration of Ca-carbonate aquifers (HANSHAW & BACK, 1979; SMART & FRIEDERICH, 1986; OTT et al., 2015), or dissolution (vs. re-precipitation) processes during carbonate diagenesis (MORSE & ARVIDSON, 2002; MOORE & WADE, 2013; DE BOEVER et al., 2017). Considering the individual stoichiometric constituents and their equilibrium relation, Ca-carbonate precipitation is promoted by increased initial calcium concentrations and carbonate alkalinity, increased CO_2 outgassing, and/or evaporation of the aqueous solution. The ionic supply strongly depends on site-specific fluid-solid (water-rock) interaction in the case of natural or geotechnical settings (e.g. water residence time and ion exchange in aquifers; LANGMUIR, 1997), or the parent solution ionic compositions in laboratory experiments (e.g. NIEDERMAYR et al., 2013). In addition, the availability of water constitutes a fundamental prerequisite in this chemical equilibrium, next to the prevailing temperature, pressure, and overall hydrochemical composition (ionic strength and ion association) in line with the principle physicochemical dependencies of carbonates in general. The internal (aqueous solution) versus external (atmospheric) **CO_2 partial pressure** and thus effective gradient is of crucial relevance with regard to either CO_2 outgassing and intimately related Ca-carbonate precipitation or enhanced carbonic acid based Ca-carbonate dissolution. A higher solution CO_2 partial pressure, as well as a higher surface area (e.g. water film or stream surface) results in increased CO_2 diffusion and outgassing to the atmosphere, which in turn controls the amount and rate of CO_2 exchange and carbonate precipitation (DANDURAND et al., 1982; BOCH & SPÖTL, 2011; YAN et al., 2017). The role and variable rate of **CO_2 degassing** are frequently discussed in the context of variable Ca-carbonate precipitation in caves, natural streams, fractures, aqueducts, or thermal water wells and transport pipes (MICKLER et al., 2004; SÜRMELIHINDI et al., 2013; BOCH et al., 2017b; JONES, 2017b). In contrast, Ca-carbonate precipitation can also be induced by the **absorption of CO_2** in alkaline (elevated pH) aqueous solutions. The respective set of chemical equilibrium reactions might be summarized as follows:

7a) $Ca(OH)_{2[s]} \leftrightarrow Ca^{2+}_{[aq]} + 2OH^-_{[aq]}$

7b) $CO_{2[g]} \leftrightarrow CO_{2[aq]}$

7c) $CO_{2[aq]} + OH^-_{[aq]} \leftrightarrow HCO_3^-{}_{[aq]}$

7d) $HCO_3^-{}_{[aq]} \leftrightarrow CO_3^{2-}{}_{[aq]} + H^+_{[aq]}$

7e) $Ca^{2+}_{[aq]} + CO_3^{2-}{}_{[aq]} \rightarrow CaCO_{3[s]}$

---

7) $Ca(OH)_{2[s]} + H_2O + CO_{2[g]} \rightarrow CaCO_{3[s]} + 2H_2O$

or alternatively

$Ca(OH)_{2[s]} + 5H_2O + CO_{2[g]} \rightarrow CaCO_3.6H_2O_{[s]}$

This mechanism of Ca-carbonate mineral formation is often based on the dissolution of a Ca-rich phase and the simultaneous occurrence of significantly increased pH values. Both conditions can arise from the dissolution of highly soluble portlandite ($Ca(OH)_2$; equation 7a), e.g. from fresh concrete components (KOSEDNAR-LEGENSTEIN et al., 2008; RINDER et al., 2013; BOCH et al., 2015). The high aqueous solution pH (increased OH^- concentration) results in the predominance of a low internal CO_2 partial pressure (Text-Fig. 1) triggering the absorption of gaseous CO_2 from the surrounding atmosphere. Consequently, the hydroxylation of dissolved CO_2 results in an immediate transformation towards dissolved inorganic carbon species such as bicarbonate (equ. 7c) and the further dissociation towards the carbonate anion (equ. 7d). The latter combines with dissolved calcium ions in order to form Ca-carbonate minerals (equ. 7e). Depending on the specific environmental conditions, anhydrous or hydrous Ca-carbonates may precipitate (equ. 7). For example, the formation of ikaite ($CaCO_3.6H_2O$) is frequently associated with near-freezing temperatures, particularly high pH, and carbonate supersaturation, and eventually with specific $CaCO_3$ inhibiting elemental and molecular constituents (DIECKMANN et al., 2008; HU et al., 2014; BOCH et al., 2015; FIELD et al., 2017). In essence, the CO_2 absorption based Ca-carbonate formation mechanism often results in prominently high precipitation rates and associated crystal growth and fabrics.

Examining the anhydrous $CaCO_3$ minerals, **three polymorphs** of significantly different crystallography and geochemistry can be distinguished: **calcite, aragonite and vaterite** (Text-Fig. 2). Their close environmental and material scientific relations are subject of intense research activities (GEBAUER et al., 2009; RODRIGUEZ-NAVARRO & BENNING, 2013; KONRAD et al., 2016). Amongst the most striking differences, the three polymorphs possess different crystal systems, i.e. calcite is trigonal, aragonite is orthorhombic, and vaterite is hexagonal (CHANG et al., 1998; MORSE et al., 2007). Calcite is known as a mineral of extraordinarily rich crystal shapes (over 400 different forms) based on its rhombohedral unit cell in principal related to the NaCl crystal structure (triangular CO_3^{2-} anions instead of Cl^-). The perfect cleavage (10–11 faces) and typical cleavage rhombohedra of calcite are a direct expression of this structure. Amongst the many forms, rhombohedral and prismatic-scalenohedral calcite habits are characteristic (Text-Figs. 2A–C, E). Aragonite also shows a prominent spectrum of different crystal shapes including radiating-spherical, columnar-pseudohexagonal, acicular (needle) and divergent (wheat-sheaf) forms (Text-Figs. 2B, D). In contrast to calcite, its cleavage is imperfect. Vaterite crystals are rare in nature but typically show spherulitic, tabular and fibrous habits or might occur in the form of aggregates consisting of much smaller crystallites (Text-Figs. 2A, F). In these structures, the cationic lattice site is 6-fold coordinated in calcite, 9-fold coordinated in aragonite and 6- to 8-fold coordinated in vaterite (VAN DRIESSCHE et al., 2017). This variable ionic bonding environment substantiates a significantly different physical and chemical behaviour of these polymorphs. The larger cation site makes aragonite a slightly denser, higher pressure, and temperature resistant polymorph, while calcite is typically the stable form at lower temperature and pressure conditions in aqueous systems. Furthermore, the different cation sites entail a significantly different substitutive incorporation of various (mostly alkaline earth) cations instead of intermediate-sized calcium ions. Aragonite favours the incorporation of relatively large cations (with regard to ionic radius), such as Sr, Ba, Pb, and U as uranyl cation, while the smaller Mg cation is strongly avoided in the aragonite crystal lattice. In contrast, Mg is readily substituted into calcite and $MgCO_3$ proportions of up to 30 mol.% occur in Mg-calcite (CHANG et al., 1998). Fe, Mn, Sr and Ba are also common but minor elemental substitutes in calcites.

In terms of their **thermodynamical stability**, aragonite and vaterite exist as metastable crystalline phases under surface ambient environmental conditions and therefore transform into thermodynamically more stable calcite via dissolution-re-precipitation reactions (BRAND, 1994; VAN DRIESSCHE et al., 2017). For example, aragonite to calcite transformation was investigated in speleothems (FRISIA et al., 2002; PERRIN et al., 2014) and in corals (YOSHIOKA et al., 1986), as well as during ductile deformation processes (SNOW & YUND, 1987) or quasi solid-state transformations based on thermal dehydration of small amounts of fluid inclusions (KOGA et al., 2013). SARKAR et al. (2013) studied the transformation of vaterite to aragonite in a setting potentially relevant for biomineralization. The issue of (meta)stability gets even more obvious for the **hydrous Ca-carbonates** such as **ikaite and amorphous calcium carbonate (ACC)**. Ikaite has a monoclinic crystal structure and typically occurs as aggregates of multi-directional, euhedral and square-prismatic, sigmoidal-bended pyramidal crystals (SWAINSON & HAMMOND, 2001; BOCH et al., 2015; Text-Fig. 2G). ACC ($CaCO_3.nH_2O$) is largely non-crystalline and hydrated and frequently occurs in the form of aggregates assembled from nano-sized and globular shaped crystals (e.g. DEMÉNY et al., 2016a). However, diverse and complex varieties of ACC probably exist (BOTS et al., 2012). For example, GEBAUER et al. (2009) reported a transient form referred to as ACC I, which favoured calcite nucleation, while ACC II resulted in vaterite precipitation. The transformation of ikaite, as well as ACC to more stable and anhydrous forms of $CaCO_3$ is characterized by more or less complete **dehydration** of the structural water. Various conditions and reaction paths of natural and synthetic ikaite transformation towards calcite (GREINERT & DERKACHEV, 2004), vaterite (TANG et al., 2009) or various Ca-carbonate polymorphs (ITO, 1998; PURGSTALLER et al., 2017a) were studied. Similarly, the transformation of ACC towards aragonite (ZHANG et al., 2012) or vaterite (BOTS et al., 2012) was the subject of laboratory experiments. KONRAD et al. (2016) investigated the transformation of additive-free ACC in air and found a strong dependence of ACC metastability on the physisorption of critical H_2O levels, i.e. relative humidity and thin water films adsorbed around ACC particles. Different experimental H_2O exposure conditions resulted in partial dissolution–re-precipitation of the ACC particles and consequently in different and simultaneously formed anhydrous crystalline Ca-carbonate polymorphs of distinct proportions (KONRAD et al., 2016).

The precipitation of the various Ca-carbonates and the polymorphism of anhydrous $CaCO_3$ also strongly depend on their respective **solubility and saturation state** in aqueous solution (Text-Fig. 3). Aragonite and vaterite possess a higher solubility compared to calcite and the hydrous Ca-carbonates monohydrocalcite, ikaite and ACC are even more soluble at widespread ambient environmental conditions. In contrast to the other Ca-carbonates, ikaite shows a prograde solubility behaviour, i.e. an increasing solubility with increasing temperature (Text-Fig. 3). Regarding calcite, its solubility also depends on the available and incorporated Mg concentration, i.e. solid solutions of $CaCO_3$ and $MgCO_3$ resulting in low- or high Mg-calcite (MORSE et al., 2007). Above 5 to 10 mol.% $MgCO_3$ in the crystal lattice, the Mg-calcite solubility exceeds the aragonite solubility (e.g. MORSE et al., 2007; ROSSI & LOZANO, 2016). Ikaite, monohydrocalcite and ACC are often the precipitation products of solutions with prominently high Ca-carbonate supersaturation and other related environmental constraints (KRALJ & BREČEVIĆ, 1995; BOCH et al., 2015; PURGSTALLER et al., 2017a).

In addition to the thermodynamic determination on the occurrence of different Ca-carbonates, **reaction kinetic effects** play a crucial role during mineral precipitation or dissolution. The nucleation or inhibition of a particular Ca-carbonate mineral might also rely on the transgression of thermodynamic, as well as kinetic, barriers. For example, initial calcite nucleation (e.g. on substrates) is well known to require aqueous solution $SI_{calcite}$ values above ~0.3 (multiple supersaturation), depending on additional physicochemical conditions (GEBAUER et al., 2009; VAN DRIESSCHE et al., 2017). Also, the carbonate chemical equilibria consist of several **partial reactions** determining the overall mineral precipitation or dissolution prog-

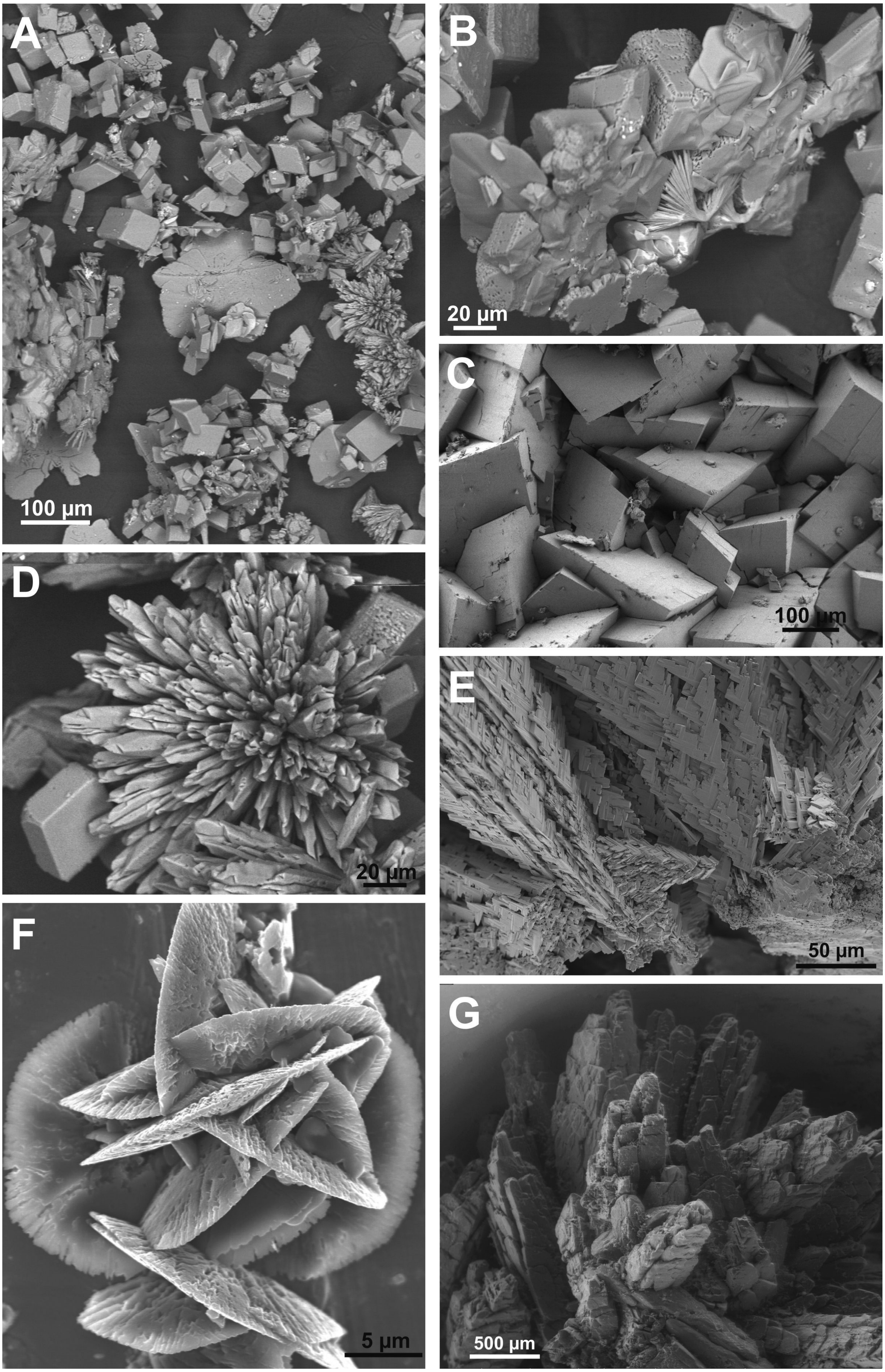
A
100 µm
B
20 µm
C
100 µm
D
20 µm
E
50 µm
F
5 µm
G
500 µm

◀ Text-Fig. 2.
Electron microscopic (SEM) images of different Ca-carbonates. A) The polymorphs calcite (rhombohedral), aragonite (radiating-spherical) and vaterite (hexagonal discs) in close relation during a laboratory precipitation experiment). B) Microporous rhombohedral calcite, wheat-sheaf aragonite and tabular vaterite. C) Dense calcite rhombohedra forming on a corroded steel substrate (from Boch et al., 2017a). D) Synthetic radiating-spherical aragonite crystals and E) relatively large hydrothermal dendritic calcite crystals. F) Association of tabular, hexagonal vaterite crystals and G) aggregate of sigmoidal-bended, pyramidal monoclinic ikaite crystals (from Boch et al., 2015). Note the major differences in crystal shapes and sizes of these Ca-carbonates.

ress. In this context, transport- versus surface-controlled processes, such as diffusional gradients and adsorption or desorption of dissolved species on crystal growth surfaces, might be key (Reddy & Nancollas, 1971; van Zuilen et al., 2016; Mavromatis et al., 2017). Dehydration and dehydroxylation partial reactions of different reaction rate might also control the overall reaction progress (Dietzel et al., 1992; Scholz et al., 2009). The actual precipitation rate of different Ca-carbonate minerals is intimately coupled to these partial chemical reactions, e.g. vaterite nucleation can be promoted by enhanced overall precipitation rates (Langmuir, 1997). The occurrence of different Ca-carbonate polymorphs has also been shown to reflect the prevailing pH conditions (Spanos & Koutsoukos, 1998; Hu et al., 2015). Variable pH determines the prevailing carbonate chemical equilibrium and aqueous species distribution (e.g. of DIC), and thus the thermodynamic and kinetic potential of specific carbonate mineral nucleation mechanisms (Wolthers et al., 2012). Considering the pH dependency, the aqueous solution CO_2 dynamics (outgassing vs. absorption) are of major relevance with respect to variable Ca-carbonate precipitation. The CO_2 gradients, diffusion, and transfer between phases (e.g. solution vs. atmosphere) may additionally rely on the prevailing water flow or water film thickness (Deines et al., 1974; Boch & Spötl, 2011; Dreybrodt & Romanov, 2016).

The precipitation and polymorphism of Ca-carbonates are further influenced by the occurrence and effects of specific **chemical additives** in aqueous solution. Numerous laboratory experiments and empirical observations clearly support the potential of different molecular species to act as nucleation and crystal growth **inhibitors or stabilizers** of particular mineral phases and different actions and types of additives are distinguished (Gebauer et al., 2009; Kumar et al., 2018). In most cases, moderate to very small concentrations of these additives are sufficient to exert a major effect on the resulting mineral formation. With respect to Ca-carbonates, the influence of increased Mg concentrations and Mg/Ca ratios is well established to promote aragonite over calcite nucleation (Berner, 1975; Rossi & Lozano, 2016; Fermani et al., 2017). The co-occurrence and genetic relationship of aragonite and calcite in various natural settings frequently relies on spatiotemporally variable aqueous Mg contents (Spötl et al., 2016; Boch et al., 2019). Different organic constituents can also affect the crystallization behaviour and thus determine resulting carbonate mineral phases. In this context, effects of humic and fulvic acids, polyaspartic and other amino acids, polyacrylic acid, citric acid, EDTA, aloe vera, olive, fig, and gambier extracts from leaves have been studied (Hoch et al., 2000; Ouhenia et al., 2008; Suharso et al., 2011; Gopi & Subramanian, 2012; Chausse-

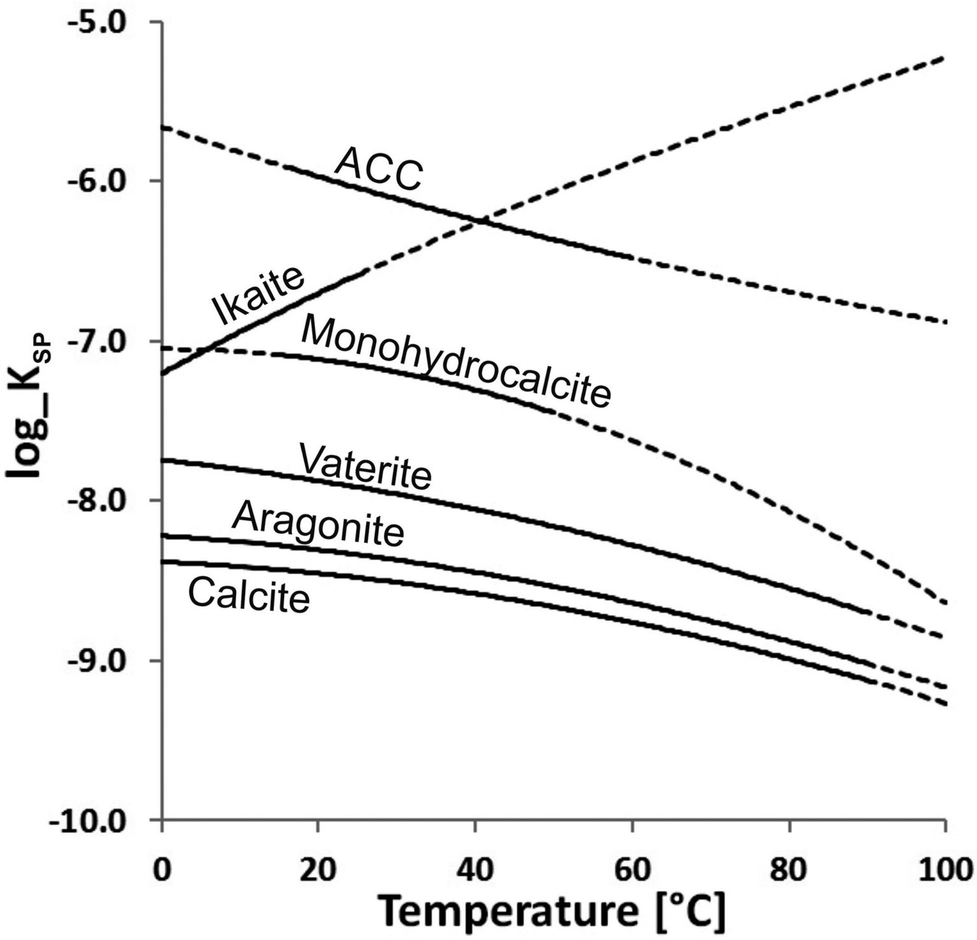

Text-Fig. 3.
Solubility product (log_K_{SP}) of various Ca-carbonates for temperatures ranging from 0 to 100° C (adapted from Boch et al., 2015 and references therein). The continuous curves represent intervals defined by the underlying experimental works, while the dashed sections are extrapolated values. Most Ca-carbonates display a retrograde solubility behaviour, i.e. being less soluble with increasing temperature.

MIER et al., 2015; JIMOH et al., 2017). For example, NIEDERMAYR et al. (2013) studied the influence of polyaspartic acid and found a prevalence of vaterite over aragonite at certain concentrations of this amino acid. MAVROMATIS et al. (2017) showed that different organic ligands have variable effects on aqueous complexation, Mg incorporation and growth of calcite. Similarly, effects of sulphate, phosphate, and phosphonates with regard to Ca-carbonate precipitation in natural and geotechnical settings have been investigated (BUSENBERG & PLUMMER, 1985; GEBAUER et al., 2009; RODRIGUEZ-NAVARRO & BENNING, 2013). HU et al. (2015) found that significant phosphate concentrations favour ikaite over vaterite nucleation at near-freezing temperatures. Considering geotechnical and industrial applications, inorganic and organic additives play a primary role as carbonate scale inhibitors in the course of geothermal energy production from deep aquifers, petroleum production, or drinking- and wastewater treatment (PARLAKTUNA & OKANDAN, 1989; KETRANE et al., 2009; KUMAR et al., 2018; MPELWA & TANG, 2019). LI et al. (2015), for example, tested six different chemical additives commercially available with regard to their effects on Ca-carbonate scale inhibition and reported a distinct control of aragonite versus calcite precipitation, as well as modifications of crystal shapes and fabrics. In essence, the chemical additives influence critical reaction steps and interfaces during fluid-solid interaction on atomic scale, e.g. the stability, kinetics, and prevalence of aqueous complexes, the hydration shell and potential dehydration of dissolved ionic and molecular constituents, as well as the adsorption and eventual blockage of further ion attachment and step propagation at crystal growth sites. For example, Ca-carbonate precipitation is inhibited due to adsorption of soluble prenucleation clusters to polyacrylic acid or other polycarboxylates in aqueous solution resulting in suppressed aggregation (GEBAUER et al., 2009). In some cases, crystal nucleation might be inhibited even under very high supersaturation conditions.

Aside from specific chemical constituents, Ca-carbonate precipitation and different polymorphs might also be affected by physical and biological triggers. Strong **magnetic fields** are long known to have potential to modify the nucleation behaviour and material characteristics of carbonate precipitates and are frequently used for scale mitigation during geothermal energy and oil production from deep boreholes or during desalination of waters (GABRIELLI et al., 2001; WARSINGER et al., 2015). Magnetic treatment of aqueous solutions was shown to influence the proportions of calcite, aragonite, and vaterite crystals mostly depending on the field strength, flow rate and exposure time (KOBE et al., 2002; KNEZ & POHAR, 2005). FATHI et al. (2006) discussed the impact of magnetic forces on homogeneous versus heterogeneous crystal nucleation and variable nucleation rates resulting in different particle sizes, distinct crystal shapes, and a preventable or modifiable adhesion to a substrate (e.g. transport pipe, heat exchanger surface). Regarding ionic interaction and the potential of carbonate precipitation, a magnetic field could manipulate the hydration shell thickness around relevant ions via a rearrangement of polar water molecules during magnetic exposure (AL HELAL et al., 2018). Alternatively, **ultrasonic treatment** was reported to increase $CaCO_3$ precipitation rates in favour of vaterite as a polymorph (SU et al., 2015; VASYLIEV et al., 2018). A major control on mineral precipitation and polymorphism can further result from various **substrate effects**, i.e. the nucleation of different Ca-carbonates on different solid substrates (D'SOUZA et al., 1999; HASSON et al., 2010). This includes studies of carbonate nucleation on surfaces and seeds of different materials and topography, such as steels and silica (WANG et al., 2013), glass (RIECHELMANN et al., 2014), or plastics (WANNER et al., 2017). For example, recent experimental work revealed preferential vaterite nucleation on polyamide (WEDENIG et al., 2016). Moreover, a variable degree of corrosion of conventional (low-alloy) steel surfaces also affects the morphology and rates of Ca-carbonate crystal growth (BOCH et al., 2017a; LI et al., 2019). In essence, the availability of a substrate (surface) can significantly change crystallization mechanisms and associated nucleation barriers, surface- and crystal lattice energies (DE YOREO et al., 2015). The metastable and hydrated Ca-carbonate phases ikaite and monohydrocalcite were unexpectedly found to be stabilized at room temperature and without chemical additives in experiments investigating Ca-carbonate supersaturation in tiny (nano-/picoliter) droplet volumes (RODRIGUEZ-RUIZ et al., 2014). Thus, **volume confinement** of aqueous solutions might also be a parameter of interest regarding the occurrence of the different Ca-carbonates in nature and technical settings. The relevance of micro-domains and associated hydrochemical conditions is further increasingly recognized in the context of microbial activity in biofilms (PEDLEY, 2013; DIAZ et al., 2017) or during crystallization of carbonate **endo- and exoskeletal hard parts** (e.g. corals; VAN DRIESSCHE et al., 2017). Considering biomineralization, the widespread occurrence of metastable aragonite next to (Mg-)calcite at ambient (e.g. shallow marine bivalve shells) environmental conditions has long been a subject of research involving Ca-carbonate polymorphism related to vital effects and hydrochemical modification in micro-domains. During formation of skeletal parts, the initial nucleation and subsequent rapid transformation of metastable amorphous calcium carbonate (ACC) towards vaterite, calcite, and aragonite becomes evident by applying high spatial and/or temporal resolution analytical tools (BOTS et al., 2012; DE YOREO et al., 2015). Nano-sized, globular ACC precipitation and its role for the ripening of Ca-carbonate crystals is also manifested in **biofilms** and carbonate crusts of hot springs (JONES & PENG, 2012), as well as during microbially-mediated and relatively rare ooid deposition on carbonate platforms (e.g. Bahamas; DIAZ et al., 2017). In fact, microbial communities possess a broad array of possible metabolic effects in order to sustain their nutrition and to adapt to local physicochemical conditions (TEMPLETON & BENZERARA, 2015). Several of these metabolic pathways can also promote or retard Ca-carbonate crystallization and microbial relicts. Rod-shaped, globular, filamentous, dendritic, or rosette forms are typical expressions of microbial presence during carbonate deposition.

Another topic that reflects the diverse nature of Ca-carbonate precipitation includes the rich variety of **crystal shapes and fabrics,** even when considering individual Ca-carbonate phases. Distinct crystallization mechanisms that describe nucleation and crystal growth have emerged and in recent years the **classical monomer attachment** approach of crystal growth has been challenged by new models including the nucleation of **amorphous precursors** and the (re)arrangement of **clusters** (VAN DRIESSCHE et al., 2017). In essence, the classical crystallization mechanism interprets crystal growth as an initial nucleus augmentation via successive attachment of ions and molecules on the growing crystal surfaces and defects, kinks, and steps are of major relevance regarding oriented growth progression (e.g. spiral-growth mechanism; Teng, 2013). The state-of-the-art crystallization models consider a variable sequence of ions forming ion clusters (e.g. aqueous complexes), liquid precursors, amorphous intermediates (e.g. ACC), metastable (e.g. vaterite) and stable crystals (e.g. calcite) following the impetus of successive free energy (ΔG) reduction and stepwise transgression of energy barriers and associated phase transformations, i.e. thermodynamic and kinetic constraints (Rao & Cölfen, 2017). Multiple pathways from atoms/molecules to euhedral crystals are currently being evaluated and **particle-based mineral formation** mechanisms, e.g. via nanoparticles and amorphous precursors, are the subject of intense research efforts and increasing recognition (De Yoreo et al., 2015). Gebauer et al. (2008) emphasize the role of pre-nucleation clusters in aqueous solution in the assembly of different types of amorphous Ca-carbonate (ACC) phases subsequently transforming and ripening towards calcite, aragonite, or vaterite. These soluble pre-nucleation clusters are of crucial relevance in a multistep crystal nucleation process. The amorphous particulate carbonate phases are also considered to precede all of the possible crystalline Ca-carbonate polymorphs (Gebauer et al., 2009). Importantly, the initial aggregation of nano-sized clusters is more or less random and the rearrangement of these basic modules results in an increasing order from amorphous to crystalline and a further reduction of surface and lattice energies during ripening from multiple crystallites to larger euhedral crystals (Teng, 2013). The successive order involves dehydration of the less ordered amorphous phases, dissolution versus re-precipitation, and in some cases also biologically mediated reactions (e.g. in marine organisms; Bots et al., 2012). The formation and morphologies of the well-ordered anhydrous Ca-carbonate polymorphs obviously depends on different and variable hydro-physicochemical conditions (Van Driessche et al., 2017). However, these phases as well as ACC are frequently observed to nucleate and coexist next to each other (Nielsen & De Yoreo, 2017; Text-Fig. 2). Such observations suggest only subtle differences in the pre-nucleation and clustering of partial reactions to exert a major control on most of the subsequent Ca-carbonate precipitation and final polymorphism.

Regarding the Ca-carbonate mineral- and polymorph-specific **petrography and morphology**, distinct differences in the overall material appearance and consistency arise. Macroscopic **material characteristics**, such as (an)isotropy, intra- and intercrystalline porosity, colouring (e.g. from light scattering), and durability are directly related to crystal nucleation, crystal growth, and dominant crystal faces, and the resulting Ca-carbonate fabrics. In the case of calcite, columnar, palisade, dendritic, or micritic fabrics can result due to variable crystallization preconditions (Freytet & Verrechia, 1999; Frisia, 2015). Aragonite precipitates typically occur as acicular and radiating, (hemi) spherulitic to botryoidal crystal aggregates and vaterite is mostly tabular or spherulitic (Sand et al., 2012; Jones, 2017a). Importantly, these underlying micro- to macroscopic features affect the visual expression and Ca-carbonate material characteristics of higher order, e.g. brittle consistency or various forms of layering based on crystallite orientation and associated pore spaces (Chafetz & Guidry, 1999; Boch et al., 2011a). Such hierarchical order based on successive deposition of Ca-carbonate is also expressed in the speleothem architectural analysis proposed recently (Martín-Chivelet et al., 2017). In this context, the extensive topic of **carbonate diagenesis** should be addressed. Following deposition from aqueous solution, pristine Ca-carbonate precipitates are frequently transformed or altered, i.e. mineralogical, chemical, and petrographic changes occur spatially and with time during early diagenesis and meteoric alteration or burial diagenesis towards metamorphosis (Morse, 2004; De Boever et al., 2017). Recrystallization often results in the transformation of aragonite to calcite (Domínguez-Villar et al., 2017; Pederson et al., 2019) or metastable ikaite to more-stable calcite (Purgstaller et al., 2017a). A major mechanism of such diagenetic recrystallization consists in the dissolution and subsequent re-precipitation of solid phases (Hanshaw & Back, 1979; Casella et al., 2017; Pederson et al., 2019). During such reactions, the fabrics of recrystallized Ca-carbonate precipitates typically become mosaic and sparry, and thus exhibit larger crystal sizes and more homogeneous fabrics (Frisia, 2015; Boch et al., 2019). This evolution is obviously related to processes such as re-nucleation (e.g. number of nuclei) and particular crystal growth mechanisms (e.g. ionic supply). In most cases, the overall intra- and intercrystalline porosity of the altered carbonate precipitates decreases, although it might also increase in cases of significant volume changes (Casella et al., 2017). The specific progress of such ripening and recrystallization again depends on multiple physicochemical, as well as metabolic (microbial) conditions, e.g. temperature and pressure, and the effect of specific constituents (e.g. inhibitors) in aqueous solution (Brand, 1994; Moore & Wade, 2013). Moreover, the availability of water either in the form of fluid inclusions, fluids associated with organic matter or as later-stage percolating (vadose or phreatic) waters mostly constitutes a crucial prerequisite for dissolution and re-precipitation (De Boever et al., 2017; Pederson et al., 2019).

Calcium carbonate – Element and isotope fractionation

Variable Ca-carbonate precipitation conditions and polymorphism are also manifested in distinct chemical and isotopic compositions depending on equilibrium and/or kinetic fractionation patterns. **Minor and trace elemental fractionation** into Ca-carbonates under physicochemical equilibrium conditions can be expressed quantitatively as specific (molar) elemental ratios (e.g. Mg/Ca, Sr/Ca) and related distribution (partition) coefficients, in which particular elements are more compatible in the different Ca-carbonate crystal lattices, i.e. they are readily substituted instead of calcium cations or carbonate anions (Böttcher & Dietzel, 2010). Apart from structural sites, elemental incorporation is associated with interstitial positions or defect sites in the crystal lattice (Morse et al., 2007). The knowledge of elemental fractionation behaviour and element-specific partition coefficients is either based on laboratory experiments, thermodynamic-kinetic modelling, or empirical (field) related studies. Next to ionic electric charge and ionic radius, primary environmental conditions, such as temperature and pressure, determine the variable elemental incorporation. In general, low temperatures (e.g. high latitude or altitude) hamper the equilibration of aqueous solution versus solid phase elemental partitioning (BÖTTCHER & DIETZEL, 2010). The aqueous speciation – specific constituents, pH, and ionic strength – also exert major effects on minor and trace elemental distributions (MAVROMATIS et al., 2015). Similarly, the precipitation rate, mineral-specific saturation states, and crystal growth mechanisms have shown distinct influences on different elements. Considering the anhydrous $CaCO_3$ polymorphism, pronounced differences between aragonite, vaterite, and calcite are well known, as the concentration of most elements strongly depends on the coordination of available ionic lattice sites and the ionic radius of the substitutes (WASSENBURG et al., 2016). For example, the incorporation of **Mg in calcite and aragonite** constitutes a subject of long-lived research (BERNER, 1975; MAVROMATIS et al., 2013). The distinction of low- and high magnesium calcite and the occurrence of $CaCO_3$-$MgCO_3$ solid solutions rely on the potential of highly variable Mg contents. The calcite Mg concentrations were also shown to increase with increasing temperature, as well as increasing ionic strength, which is particularly evident in marine settings of Ca-carbonate precipitation (BÖTTCHER & DIETZEL, 2010). In addition, Mg concentrations in calcite have been shown to increase with increasing precipitation rate (MAVROMATIS et al., 2013). Investigations have further focused on the alkaline earth elements **Sr and Ba**. These two elements largely display similar behaviour and their incorporation into calcite revealed some weak to ambiguous temperature dependence, but a strong positive relationship with precipitation rate and also pH (LORENS, 1981; TESORIERO & PANKOW, 1996). This is usually explained by the favoured incorporation of the relatively large Sr and Ba cations during rapid, and therefore less selective, calcite crystal growth, e.g. at higher pH and $SI_{calcite}$. Sr and Ba concentrations in aragonite also revealed some significant temperature dependence (DIETZEL et al., 2004). New results, however, support a dominant control of Ba incorporation in aragonite and calcite by the precipitation rate, which in turn is mostly related to ionic radii size effects (MAVROMATIS et al., 2018). Regarding the relationship of Mg, Sr, and Ba, some Ca-carbonate precipitates (e.g. speleothems) show a positive co-variation of their concentrations, mainly reflecting a corresponding hydrochemical evolution (e.g. prior $CaCO_3$ precipitation in the aquifer; MCMILLAN et al., 2005). Alternatively, an inverse correlation of Mg versus Sr and Ba primarily depending on precipitation rate and aqueous solution composition can be observed (BOCH et al., 2011a). A dominant role of increased precipitation rate was also inferred with regards to higher **sodium** and **sulphate** contents in calcite (BUSENBERG & PLUMMER, 1985). Conversely, the concentrations of **manganese, cobalt, and cadmium** in calcite decreased at higher precipitation rate (LORENS, 1981). In recent years, the fractionation and varying incorporation of **numerous other elements** (B, P, S, Fe, Cu, Zn, Br, Y, Pb, U) in Ca-carbonate have been studied and implications on aqueous speciation, pH, sorption and transport processes and overall soil and aquifer hydrological conditions have been drawn (BORSATO et al., 2007; LANGER et al., 2018). In particular, the highly variable incorporation of **uranium** in the dominant form of uranyl cations (UO_2^{2+}) into calcite and aragonite has gained some attention related to (paleo) hydrological process understanding and radiometric U-Th dating of Ca-carbonates (REEDER et al., 2000; LACHNIET et al., 2012). Applications of minor and trace elemental fractionation include paleo- and modern environmental (hydrological and climate) studies of diverse natural settings of carbonate precipitation (FAIRCHILD & TREBLE, 2009; BOCH et al., 2011a), anthropogenic settings (SÜRMELIHINDI et al., 2013; BOCH et al., 2017a), inorganic vs. biotic relationships during water-rock interaction (SAUNDERS et al., 2014), or the removal (co-precipitation) of problematic (e.g. heavy metal contaminants such as Cd) or wanted (e.g. Li) elements with Ca-carbonate (KÖHLER et al., 2007).

Varying environmental conditions of Ca-carbonate formation from aqueous solutions are further reflected in distinct **isotope fractionation** patterns of different elements primarily based on physicochemical transitions between gaseous, liquid, and solid phases of the relevant partial reactions. More specifically, isotopes can be fractionated during mineral precipitation and dissolution, evaporation, sorption, diffusion, redox, and aqueous complexation reactions. In many of the chemical reactions an **isotopic equilibrium** between individual phases is attained, which can be described by fractionation factors determined from experimental, modelling, or empirical approaches (FRIEDMAN & O'NEIL, 1977). At ambient environmental conditions, typical stable isotopic fractionation is sensitive to the prevailing temperature, i.e. the partitioning of the relatively light and heavy isotope(s) of a chemical element reflects the thermodynamic conditions during phase transitions (EPSTEIN et al., 1953). Apart from equilibrium conditions, isotopic fractionation can also be controlled by dominant kinetic influences determining the direction and extent of the resulting isotope separation (MICKLER et al., 2004; DAËRON et al., 2019). These **kinetic effects** are mainly based on the different vibrational frequencies and chemical bonding characteristics between isotopes of distinct masses resulting in different reaction rates during isotope exchange (HOEFS, 2015; GUSSONE et al., 2016). The relatively light and heavy isotopes of an element behave kinetically different during chemical reactions, e.g. light isotopes being kinetically favoured during transition from the liquid to the gaseous state. The latter is manifested in the enrichment of the relatively light stable ^{12}C and ^{16}O isotopes in the course of CO_2 outgassing of dissolved inorganic carbon and evaporation of water (SCHOLZ et al., 2009). **Metabolic (vital) effects** during biological cycles and biomineralization of carbonates are also known as potential fractionation mechanism, e.g. the preferential enrichment of light C isotopes during photosynthesis and associated Ca-carbonate and organic tissue formation (GUO et al., 1996; LIU et al., 2015). Isotope fractionation processes can be further affected by **mixing** of isotopic compositions from different reservoirs (sources). The fractions of the endmembers and resulting isotopic signature might then be described by a mixing model (WIEDERHOLD, 2015). Alternatively, the isotopic evolution of a reservoir in which a fraction of isotopes is physically removed from the reservoir during a directed reaction can follow a **Rayleigh fractionation** model, i.e. light or heavy isotopes are preferentially removed from the reservoir and isotopic re-equilibration is prevented (WIEDERHOLD, 2015). Based on the underlying mechanisms and models of isotope fractionation and evolution, various isotope systems open the door for tracing the sources of constituents, as well as numerous inorganic and biotic processes. Importantly, the isotopic compositions contain both qualitative (provenance signature) and quantitative (extent of chemical/isotopic reaction) environmental information. Typical applications of isotopic fractionation therefore include mineral and fluid provenance studies (RINDER et al., 2013), paleo(geo)thermometry in natural (KLUGE et al., 2014) and geotechnical settings (BOCH et al., 2017a), mineral alteration (GRENGG et al., 2015) and diagenesis (CASELLA et al., 2017), origin and trajectories of air masses (LUETSCHER et al., 2015; HAGER & FOELSCHE, 2015), seasonal and multi-annual climate evolution (FAIRCHILD et al., 2006; BOCH et al., 2011b), and other processes sensitive to isotope fractionation that occur in a variety of natural and anthropogenic environmental settings.

In the context of Ca-carbonate precipitates, diverse **traditional** (light elements, relatively large mass discrimination) and **non-traditional** (heavier metals, subtle mass differences) **isotope systems** have been measured by various techniques of mass spectrometry and have been evaluated for their systematic fractionation behaviour. Considering the carbonate functional group, valuable environmental information is captured in the **oxygen** isotopic composition. The **$^{18}O/^{16}O$** isotope ratio in carbonate minerals depends on factors such as the temperature of crystallization, the source and isotopic evolution of the precipitating fluid, and eventually kinetic (e.g. evaporation), catalytic (e.g. microbial), and diagenetic effects (e.g. recrystallization). An established utilization consists in the oxygen isotope thermometer of carbonate formation (EPSTEIN et al., 1953) relying on equilibrium O isotope fractionation factors derived from laboratory experiments (KIM & O'NEIL, 1997; DIETZEL et al., 2009) or empirical observations (COPLEN, 2007; TREMAINE et al., 2011). This isotopic thermometer was applied in various natural (BOCH et al., 2009; KELE et al., 2015) and human-made settings (BOCH et al., 2017a). The carbonate O isotope signature can further reflect the source and trajectories of meteoric precipitation and related groundwater, e.g. Atlantic versus Mediterranean sources of moisture advected to the Alps (LUETSCHER et al., 2015). Systematic differences also depend on the $CaCO_3$ polymorph formed, e.g. aragonite is enriched in ^{18}O vs. ^{16}O by ~0.5–1 ‰ relative to calcite at similar conditions (CLARK & FRITZ, 1997; BOCH et al., 2005). Another traditional isotope system with respect to environmental process understanding and reconstruction consists in the stable **carbon** isotope composition of carbonate minerals. The **$^{13}C/^{12}C$** isotope ratio primarily depends on the source(s) and (hydro)chemical evolution of the relevant carbon species (e.g. dissolved inorganic carbon) in conjunction with parameters and processes determining CO_2 exchange reactions (temperature, pH) and related C isotopic fractionation. Major contributions to C isotope variation might therefore derive from the interaction of atmospheric, biogenic, pedogenic, and host rock carbon sources (DEINES et al., 1974), vadose and phreatic aquifer dynamics (e.g. dissolution vs. prior $CaCO_3$ precipitation; BAJO et al., 2017), dynamic CO_2 exchange during CO_2 outgassing or absorption (RINDER et al., 2013; DREYBRODT & ROMANOV, 2016), the crystallization temperature and precipitation rate (CLARK & FRITZ, 1997). At similar environmental conditions, aragonite is relatively enriched in ^{13}C vs. ^{12}C by 1.5–2.5 ‰ compared to calcite supporting a major effect of crystal structure (MOOK, 1986; BOCH et al., 2005). Amongst the non-traditional stable isotopes, **$^{44}Ca/^{40}Ca$** ratios of calcite, vaterite, and ikaite showed some positive correlation to precipitation rate, i.e. increased ^{44}Ca vs. ^{40}Ca fractionation at increased precipitation rate (TANG et al., 2008b; GUSSONE et al., 2011, 2016). The **calcium** isotopes further revealed an ambiguous (insignificant) relation to formation temperature with a tendency of decreased ^{44}Ca vs. ^{40}Ca fractionation at higher temperatures (GUSSONE et al., 2003; TANG et al., 2008b). **$^{44}Ca/^{42}Ca$** ratios can be used as a proxy for meteoric paleo-precipitation based on variable prior calcite precipitation in the course of increased recharge or aridity (OWEN et al., 2016). Monitoring of different **magnesium** reservoirs associated with a cave system revealed a dominant relationship of **$^{26}Mg/^{24}Mg$** isotope ratios to speleothem calcite precipitation (growth) rate (IMMENHAUSER et al., 2010). Likewise, laboratory experiments yielded favoured ^{24}Mg concentration in calcite and a decreasing fractionation at higher precipitation rate (MAVROMATIS et al., 2013). This atypical behaviour might be explained by a kinetically inhibited dehydration of aqueous Mg^{2+} in combination with crystal surface entrapment (IMMENHAUSER et al., 2010). SAENGER & WANG (2014) found a major influence on Mg isotope fractionation related to different carbonate minerals (aragonite, dolomite, magnesite, calcite) and growth mechanisms. Moreover, temperature has a primary influence at higher Mg/Ca ratios and respective SI values, while precipitation rate was dominant with regard to Mg isotope fractionation at low Mg/Ca ratios and SI values. Radiogenic **$^{87}Sr/^{86}Sr$** isotope ratios in carbonate constitute a more established isotope system frequently applied in material provenance studies (rocks, artefacts), seawater carbonate-based Sr chronostratigraphy over extended geological time intervals, and in connection with the stable **strontium** isotopes **$^{88}Sr/^{86}Sr$** can also provide information on weathering and orogenic processes (NEBEL & STAMMEIER, 2016). The focused application of **boron** isotopes (**$^{11}B/^{10}B$**) as a promising proxy of (sea)water pH and coupled variation of atmospheric CO_2 concentrations is based on the pH dependent fixation of $B(OH)_4^-$ (borate anion) and isotopically heavier $B(OH)_3$ (boric acid) from aqueous solution into carbonate (BALAN et al., 2018). Further regarding non-traditional (higher atomic mass) Ca-carbonate relevant isotope systems, stable **barium** isotopes (**$^{137}Ba/^{134}Ba$**) have been used as a geochemical parameter reflecting oceanic circulation, weathering, and paleoproductivity in which carbonates preferentially incorporate the lighter Ba isotopes (VAN ZUILEN et al., 2016). However, MAVROMATIS et al. (2016) have shown that Ba isotopic equilibria are subject to dynamic re-equilibration after mineral formation and thus their paleoenvironmental interpretation should be considered with caution. **Iron** isotopes (**$^{56}Fe/^{54}Fe$**) in carbonates and various other minerals are strongly influenced by kinetic fractionation at lower temperatures and are most sensitive to distinct redox conditions (Fe[II]–Fe[III]), inorganic vs. microbial processes (e.g. bacterial iron and sulphate reduction), as well as diagenesis (HOEFS, 2015). **Zinc** isotope fractionation (**$^{66}Zn/^{64}Zn$**) between aqueous solutions and calcite was recently proposed as a non-traditional pH-sensitive isotope system and paleo-proxy based on experiments using mixed-flow reactors under controlled laboratory conditions (MAVROMATIS et al., 2019). Considering unstable isotopes, **uranium** (**$^{234}U/^{238}U$**) isotopic compositions of Ca-carbonates were used as a tracer of hydrological processes, such as differentiated water infiltration areas, aqueous solute provenance, rock weathering, and groundwater flow and evolution (Riotte & Chabaux, 1999). U isotope ratios are primarily sensitive to the prevailing aqueous speciation and redox state, as well as strongly dependent on isotopic disequilibrium during α-recoil processes (preferential leaching of ^{234}U; Paces et al., 2002). The application of U isotopes in carbonate precipitates in the context of radiometric age determination will be discussed in a separate chapter (Shen et al., 2012; Spötl & Boch, 2012). Finally, recent developments of Ca-carbonate isotope analysis include stable **hydrogen (^{2}H/^{1}H)** isotope ratios of tiny fluid inclusions trapped in the mineral precipitates (e.g. speleothems; Dublyansky & Spötl, 2009). These can be liberated, chemically separated and purified via thermal decrepitation or mechanical vacuum crushing (Demény & Siklósy, 2008). In connection with the carbonate oxygen isotopes and established H vs. O isotope relationships such as the Global Meteoric Water Line (Craig, 1961), valuable information regarding formation temperature and water source can be inferred.

Another major progress in isotope analysis includes the recent measurement and interpretation of rare **multiply-substituted isotopologues** (**clumped isotopes**) in various carbonates (Eiler, 2007; Eiler et al., 2014). The clumped isotopic composition of carbonates relies on the determination of relatively rare and heavy stable ^{13}C and ^{18}O isotopes bound together in the carbonate functional group ($^{13}C^{18}O^{16}O_2^{2-}$; Text-Fig. 4). This quantity mainly depends on kinetic and molecular bonding (binding energy) differences of the isotopes involved and thus on the prevailing temperature during mineral (e.g. Ca-carbonate) formation. In particular, more ^{13}C and ^{18}O isotopes are clumped in the carbonate crystal lattice at lower temperature in comparison to a fully stochastic distribution (Schauble et al., 2006). Consequently, **formation (crystallization) temperatures** can be derived from analysis of the clumped isotopic composition of a carbonate mineral without the necessity of knowing the associated (original) aqueous solution stable isotopic composition. The temperature dependence is captured in a single-phase equilibrium (Text-Fig. 4), in contrast to two-phase equilibria, e.g. the established carbonate/solution oxygen isotope thermometer (Daëron et al., 2019).

Technically, clumped isotopes are measured by **multi-collector gas source isotope ratio mass spectrometry** involving state-of-the-art high sensitivity (high electric resistance) Faraday detectors (Eiler et al., 2013). More specifically, CO_2 is extracted from the carbonate mineral via phosphoric acid digestion, further separated, and purified in a multi-step laboratory procedure (Kluge et al., 2015). Based on the relevant isotope ratios measured simultaneously, the deviation of the measured δ^{47} value – mainly represented by the rare clumped $^{13}C^{18}O^{16}O$ molecule – from a stochastic δ^{47} distribution (in a ~1,000° C CO_2 reference gas) results in a characteristic Δ_{47} value (big delta). The latter decreases with increasing temperature. Next to Δ_{47}, the mass spectrometric

$$\mathrm{Ca}\boxed{^{13}\mathrm{C}}^{16}\mathrm{O}_3 + \mathrm{Ca}^{12}\mathrm{C}\boxed{^{18}\mathrm{O}}^{16}\mathrm{O}_2 = \mathrm{Ca}\boxed{^{13}\mathrm{C}^{18}\mathrm{O}}^{16}\mathrm{O}_2 + \mathrm{Ca}^{12}\mathrm{C}^{16}\mathrm{O}_3$$

Text-Fig. 4.
Single-phase equilibrium describing the temperature dependent “clumping” of relatively rare and heavy ^{13}C and ^{18}O isotopes during Ca-carbonate precipitation.

analysis determines the carbonate $\delta^{13}C$ and $\delta^{18}O$ values. In connection with the Δ_{47}-based temperature, the mineral stable O isotopic composition allows for a calculation of the mineral forming fluid (aqueous solution) $\delta^{18}O$ value based on the application of established temperature dependent O isotope fractionation factors (e.g. Kim & O’Neil, 1997; Coplen, 2007). Thus, apart from (paleo)thermometry, clumped isotope analyses constitute a promising tool with regard to the **provenance of (paleo)fluids** (Luetkemeyer et al., 2016; Boch et al., 2019). Considering the **accuracy and precision** of the temperature estimates, unaltered sample materials, the absolute mineralization temperature, the calibration function of Δ_{47} vs. temperature used, the laboratory and analytical protocols applied, and the number of replicate (sub)sample measurements are probably most relevant. The carbonate minerals should not have undergone reordering of their (clumped) isotopes, e.g. during diagenetic or metamorphic recrystallization processes and subsequent cooling below a mineral-specific blocking temperature (Shenton et al., 2015; Lloyd et al., 2017). Moreover, at higher absolute temperatures (> 150–200° C) the precision of the temperature estimates decreases rapidly due to the intrinsically decreasing differences in the Δ_{47} values vs. temperature changes (Kluge et al., 2015). Regarding the numerical calibration functions of the geothermometer, a multitude of existing and ongoing efforts are based on experimental, empirical, and modelling studies and the clumped isotope community seeks for universal (broad temperature range, mineral (in)dependent) and laboratory independent calibrations (Ghosh et al., 2006; Tang et al., 2014; Bonifacie et al., 2017). This also includes critical analytical steps such as the phosphoric acid digestion temperature (e.g. 25 vs. 90° C), statistical procedures, and correction terms applied (Daëron et al., 2016; Kelson et al., 2017). An accurate implementation further involves the investigation of potentially relevant effects influencing clumped isotope fractionation during variable carbonate mineral precipitation. This comprises an evaluation of equilibrium vs. kinetic fractionation effects (Daëron et al., 2011; Levitt et al., 2018), and more specifically temperature, precipitation rate, pH and DIC speciation effects (Tripati et al., 2015; Kluge & John, 2015). For example, Kluge et al. (2018) used natural travertine and geotechnical scale samples from geothermal facilities to investigate the role of pH and DIC speciation effects on calcite formation. Their results revealed a possible underestimation of Δ_{47}-based formation temperatures from true formation temperatures under environmental conditions that include very high mineral precipitation rates, high pH, and/or low temperatures (slow equilibration), i.e. only relevant quantitatively in specific environmental settings. More generally, however, observational evidence suggests that most Earth-surface calcite precipitates form out of oxygen and clumped isotopic equilibrium to a variable degree (Daëron et al., 2019), i.e. potential (kinetic) isotope fractionation effects have to be evaluated with caution for specific environmental settings and applications. Most recent analytical developments further involve the utilization of **laser absorption spectroscopy** for determining the relevant multiply-substituted isotopologues (e.g. of CO_2; Prokhorov et al., 2019). This optical method of clumped isotope thermometry facilitates a simplified sample preparation, more rapid sample throughput and the circumvention of some isobaric interference problems. Further, considering the overall lower instrumentation costs and reduced space requirements, the laser spectroscopic technique might outcompete mass spectrometric analysis in a foreseeable future.

Diverse environmental settings

Carbonates constitute a major **carbon reservoir** participating in the Earth's carbon cycle, i.e. the largest carbon reservoir of the lithosphere (MORSE et al., 2007). In the relation of CO_2 and carbonate minerals, the lithosphere (and mantle), hydrosphere (and cryosphere), pedosphere, biosphere, and atmosphere are coupled in an array of complex albeit few dominant physico-bio-chemical processes determining carbon exchange and carbonate occurrence. The latter processes **spatially** extend from the macroscale (e.g. mountain ranges/landscapes and marine platforms) to the microscale (e.g. crystal nucleation and diagenesis) and **temporally** extend from geological timescales to nearly instantaneous mineral formation. Carbonates in general and Ca-carbonates in particular shape paleo- and modern environmental settings, natural (geogenic), and human-made (anthropogenic, e.g. geotechnical) environments. In addition, Ca-carbonate minerals represent the most abundant mineral group with regard to biomineralization (GEBAUER et al., 2009).

Sedimentary carbonates form from cycles and events of autochthonous and allochthonous carbonate deposition depending on tectonic, climate, and various other environmental factors. Limestones, marls, calcareous sandstones, and dolomite rocks are voluminous manifestations of such foregoing sedimentation. In the **marine realm**, deep and shallow water carbonates are of frequent occurrence including oceanic basin muds (MORSE & MACKENZIE, 1990) and lagoonal sands (e.g. ooids; DIAZ et al., 2017), as well as different types of platform carbonate and coral reefs (DUNBAR, 2000). In this context, coccolithophores, foraminifera, mollusks, red algae, and echinoderms are the most important organisms precipitating Ca-carbonate skeletal parts in the oceans (MORSE, 2004). These sedimentary components of variable fragment- and grain sizes typically undergo burial, hydrothermal, and microbial **diagenetic processes** including the precipitation of carbonate cements in pore spaces (MOORE & WADE, 2013) and/or dolomitization (BALDERMANN et al., 2015). Considering the diverse environmental settings and temporal evolution of sedimentary carbonates, many of these mineral deposits can serve as a valuable chemical-sedimentary archive. Pristine **corals**, for example, are of interest with respect to inorganic versus biochemical carbonate nucleation and as an environmental archive capturing past global sea-level variations affecting coastal areas (SIDDALL et al., 2003). Similarly, **bivalves and brachiopods** are studied in the light of Ca-carbonate polymorphism and biomineralization, and to decipher paleoclimate information from their exoskeletal chemical composition (DETTMAN et al., 1999). In the marine and freshwater sedimentary environment, **stromatolites and microbial mats** constitute a shallow water and mostly laminated mineral formation that is organically-mediated (cyanobacteria, algae) and results in Ca-carbonate precipitation, particle entrapment, and cementation (FREYTET & VERRECCHIA, 1998; RIDING, 2000). Ca-carbonates of micritic to structurally complex growth morphology are also of frequent occurrence in **lake sediments** of different regions and hydrochemistry and in some cases display rhythmic (seasonal, varve) successions (COUNCIL & BENNETT, 1993; OEHLERICH et al., 2013). Freshwater Ca-carbonates such as typically compact and well-laminated **travertines** and porous, more heterogeneous **calcareous tufa** are either associated with thermal or ambient temperature water streams in connection with strongly localized (neo)tectonic or volcanic activity, or other specific sedimentary settings influenced by deep water circulation and carbonate mobilization (BOCH et al., 2005; BROGI et al., 2012). Similar freshwater Ca-carbonate growth successions were also investigated in **historic** (e.g. Roman) **aqueducts and water cisterns** (PASSCHIER et al., 2016a, b). The interplay of Ca-carbonate dissolution (mobilization) and precipitation additionally characterizes the widely distributed **karst areas and caves** involving karstification processes and **speleothem** mineralization (FAIRCHILD & BAKER, 2012). The latter carbonate formations have shown to provide a spatiotemporally attractive chemical-sedimentary archive of diverse (multi-proxy) paleoenvironmental information anchored with precise radiometric (uranium-series) chronologies (BOCH et al., 2011b; CHENG et al., 2016). Similar capabilities can be attributed to the investigation and environmental interpretation of carbonate precipitates in **fractures and faults**, i.e. these deposits might capture chemical and petrographic information on paleoclimate conditions, as well as (neo)tectonic or gravitational mass movements (HAUSEGGER et al., 2010; BOCH et al., 2019). Secondary **carbonate cements** consolidating limestone and dolomite fragments (e.g. boulders) from major mass movements have been used to provide absolute radiometric age constraints (minimum ages) of **rock falls** (OSTERMANN et al., 2007). **Concretions and nodules** in (paleo)**soils** consisting of Ca-carbonate have also been utilized in (paleo)environmental studies targeting meteoric conditions (e.g. loess dolls; BARTA, 2014) or uplift of mountainous terranes (GHOSH et al., 2006). The diverse settings of carbonate occurrence further include **cryogenic precipitates in sea ice** (e.g. ikaite; FISCHER et al., 2013) or **cave ice** (COLUCCI et al., 2017). Such ice-hosted carbonates are indicators of distinct and often extreme hydrochemical and atmospheric conditions.

Considering **natural environmental settings** of carbonate occurrence, some **magmatic rocks** can contain carbonate minerals, i.e. mostly calcite (OKRUSCH & MATTHES, 2010). Typical host rocks are alkaline or ultramafic igneous rocks, such as **carbonatites and kimberlites**. For example, the lava and explosive ejection materials of volcano Lengai located in the East African Rift Zone are known for their Ca-(Na)-carbonate mineral content (WEIDENDORFER et al., 2017). In association with regional magmatic processes, carbonates may also precipitate in **hydrothermal veins**, i.e. mostly calcite and iron and magnesium carbonates deriving from deep and hot water circulation (PIRAJNO, 2009). These carbonates are of interest with regard to their source and evolution and in particular regarding their formation temperature, thermal fluid composition (e.g. brines), and absolute and relative (vs. host rock) age distributions (MASKENSKAYA et al., 2014). For example, LUETKEMEYER et al. (2016) studied calcite veins in the San Andreas Fault system focusing on stable C, O, and clumped isotope signatures in order to trace fluid sources, specific fluid-rock interactions and related mechanisms of frequent seismic events. Networks of calcite veins in connection with fractures and faults in the Oman mountains were elaborated focusing on variable fluid pathways and hydraulic connectivity (ARNDT et al., 2014). A detailed geochemical investigation of vein carbonates is further of interest regarding prospective nuclear waste disposal sites (YARDLEY et al., 2016). Fluid inclusions captured in calcite at Yucca Mountain (Nevada) revealed hypogene hydrothermal activity during the young geological past (DUBLYANSKY & SPÖTL, 2010). Some carbonate minerals characterize regional settings of relevance with regard to economic **raw material** production. **Siderite** has Fe concentrations high enough to be explored as an iron ore for the steel industry, e.g. the major siderite-ankerite iron ore deposit at Erzberg, Austria (PROCHASKA, 2016; BOCH et al., 2019). Similarly, **magnesite** constitutes a (hydrothermal) carbonate of material-specific relevance, e.g. as an ore of refractory Mg sinters (Breitenau, Austria; HENJES-KUNST et al., 2014). In the context of natural carbonate settings, **metamorphic rocks** should also be considered. **Marbles** represent recrystallized Ca-carbonates of variable metamorphic overprint (anchimetamorphous to blueschist facies) and resulting petrography (SEATON et al., 2009). **Carbonate-rich (calcareous) shales** are widespread metamorphic rocks in the Alps (e.g. Bündnerschiefer Formation; SCHMID et al., 2004) and might even host caves and speleothem carbonate precipitation (BOCH & SPÖTL, 2011). Interestingly, carbonate concretions that have formed at relatively low temperature and with chemical zonation were also found in **meteorites** from Mars (VALLEY et al., 1997). Hydrous carbonates such as ikaite and monohydrocalcite are considered prospective minerals of high scientific interest on the **Mars** surface (HARNER & GILMORE, 2015). In this regard, the natural occurrence of carbonates might even be expected from other (exo)planets.

The diverse environmental settings further comprise of **synthetic carbonate** formation in the **laboratory** targeting fundamental, as well as material scientific and industrial applications. This includes **precipitation and alteration experiments** of various carbonate minerals under controlled physicochemical conditions in order to study basic mechanisms of crystal (re)nucleation and growth, and elemental and isotopic fractionation (DIETZEL et al., 2009). The experimental setup might either consist of more or less static steel autoclaves (CASELLA et al., 2017) or various adaptations of dynamic flow reactors (MAVROMATIS et al., 2017). Further, carbonate precipitation from an aqueous reaction solution can be triggered by simple mixing of parent solutions or by the membrane CO_2 diffusion technique (DIETZEL et al., 2004; TANG et al., 2012). In addition, some experimental setups mimic specific chemical-sedimentary environmental conditions, e.g. inorganic stalagmite growth (DAY & HENDERSON, 2013) or biologically mediated freshwater travertine and calcareous tufa deposition (PEDLEY, 2013). Experiments and laboratory based analyses were further dedicated to **historic building materials** involving carbonate mineralization, e.g. **lime mortar**, **plaster, or concrete** of ancient Greek, Roman, or Medieval times (KOSEDNAR-LEGENSTEIN et al., 2008). The archaeological carbonate utilization also includes geochemical and archaeometrical investigations of ancient artefacts by laser ablation mass spectrometry (LA-ICP-MS; DEGRYSE & VANHAECKE, 2016), as well as radiocarbon dating of calcite formed from atmospheric CO_2 absorption in concrete (DIETZEL & BOCH, in press). Likewise, complex fluid-solid interaction involving various carbonates amongst other curing and/or dissolving phases is intensely studied in **modern concrete constructional settings** (MITTERMAYR et al., 2017; GRENGG et al., 2018; GALAN et al., 2019).

Settings of (Ca-)carbonate mineralization also include chemical-sedimentary environments strongly influenced both by **natural and human-made** (operational) conditions. In principal, however, most natural environments involving carbonate (oceans, lakes, rivers, mountain territories, soils, sea ice, etc.) might be more or less affected by human impacts (e.g. global warming, pollution). More specifically, carbonate formation and mobilization in **geotechnical settings** strongly rely on a geogenic versus anthropogenic relationship. For example, Ca-carbonates precipitated from saline (thermal) waters produced from deep reservoirs and boreholes often constitute a major challenge in the course of **geothermal energy production**, as well as in the **oil and gas industry** (BJØRNSTAD & STAMATAKIS, 2006; ZARROUK & MOON, 2014). The occurrence of unwanted **carbonate scaling** mostly depends on the natural reservoir rock and water chemical preconditions in combination with the human-made disturbance of natural physicochemical equilibrium conditions (e.g. pressure/temperature changes; HAKLIDIR & HAKLIDIR, 2017). Typical expressions of these carbonate scale deposits are reduced inner diameters and clogging of **well casings and transport pipelines** (DEMIR et al., 2014; BOCH et al., 2016) or an ongoing blockage and reduced heat and energy transfers in thermal water **heat exchangers** (HASSON et al., 1968; BOCH et al., 2017a). Various forms of scaling and fouling including Ca-carbonates are also major obstacles in many cases of **water treatment**, such as **desalination** during potable or industrial water production (WARSINGER et al., 2015). Unwanted carbonate scales are also common mineral precipitates at low temperature ambient conditions in **artificial channels**, such as **drainages in tunnels** (DIETZEL et al., 2013; CHEN et al., 2019) or bypassing concrete stream beds (BOCH et al., 2015). However, selected geotechnical carbonate scale materials of well constrained environmental conditions have also shown attractive hydro- and geochemical characteristics with regards to fundamental research on isotope (and element) fractionation mechanisms, i.e. a benefit from the otherwise unwanted deposits (KLUGE et al., 2018). Last but not least, considering that $\mathbf{CO_2}$ as a major and increasingly problematic greenhouse gas, its **geotechnical and industrial sequestration**, i.e. CO_2 capture and storage by dissolution in deep sedimentary basin formation waters and/or by solid-phase carbonation are also a subject of modern carbonate research (SANNA et al., 2014). In this context, complex gas-water-rock interactions and mineral dissolution versus precipitation reactions in carbonate, sandstone, or ophiolite reservoirs are evaluated by laboratory experimental, modelling, and field based approaches (KHARAKA et al., 2006; TUTOLO et al., 2015). KELEMEN & MATTER (2008), as an example, investigated geologically young carbonate veins in ophiolites hosting peridotite and found high reaction rates, and therefore geochemical potential, for in-situ conversion of CO_2 and peridotite (weathering) to Ca-Mg-carbonate minerals. More generally, the uptake and conversion of CO_2 exerts a primary role in global **silicate weathering** and in the transformation of silicates (e.g. feldspars, pyroxenes) into clay minerals in association with dissolved inorganic carbon or carbonate minerals (DEPAOLO et al., 2013).

Caves, Speleothems and Climate Reconstruction

Speleothems (dripstones, cave decoration) – in particular stalagmites and flowstones – have emerged as an attractive, and therefore intensely investigated, chemical-sedimentary archive that captures environmental information in diverse ways. The closely related research fields and topics constitute a **multidisciplinary approach** primarily focused around the geoscientific disciplines of geochemistry and Quaternary geology, but further including specialized knowledge from mineralogy, hydro(geo)logy, speleology, climate research and meteorology, material sciences, and (micro)biology. Speleothem formations consisting of Ca-carbonate (dominantly calcite) can form in different caves. **Karst caves** in limestone and dolomite host rocks (aquifers), however, clearly outnumber cave settings of metamorphic (e.g. marbles, calcareous schists) or magmatic (e.g. hydrothermal fractures, lava tunnels) provenance. Regarding their geographic and climate regime **distribution**, caves are a widespread natural phenomenon within the geological wealth of landforms. Consequently, caves represent a (paleo)environmental archive located in areas populated by humans, as well as in remote karst areas (FORD & WILLIAMS, 2007). This circumstance is a spatial advantage compared to other established but locally less diverse environmental (climate) archives, such as ice cores from Greenland and Antarctica (KAWAMURA et al., 2007; BARKER et al., 2011) or sediment cores from the deep ocean basins (LISIECKI & RAYMO, 2005). Another spatial advantage consists in the location of cave settings **underground**, i.e. the environmentally sensitive but fragile speleothem formations are protected from most of the destructive atmospheric, sedimentary, and diagenetic processes shaping the Earth's surface and sedimentary spaces (environmental archives) in particular. Considering the **temporal extension** of caves and speleothems, the time interval associated with the **Quaternary** period (the last ~2.6 millions of years) can be easily covered, although major cave systems and chambers do not constitute a landform of high stability in geological time and space, i.e. caves undergo maturity processes and stages from initial pores and mostly through partly dissolution enlarged fractures in the carbonate host rock towards the phreatic evolution of cave chambers, vadose water percolation, and speleothem deposition, and finally undergo gravitational collapse or erosion at the Earth's surface. Older cave systems may date back to the younger or perhaps middle Tertiary period. In this regard, speleothems constitute an environmental archive of the more recent geological past and its prevailing climate conditions. Importantly, typical speleothem carbonate material of variable age has shown to be well suited for absolute **radiometric age determination** based on uranium-series geochemistry (EDWARDS et al., 1987; RICHARDS & DORALE, 2003; SPÖTL & BOCH, 2012). This potential of establishing precise and accurate **chronologies and growth models** for individual speleothem samples and related environmental information constitutes another prominent strength of this mineral archive in relation to other (bio) chemical sediments susceptible to environmental variability. Although situated underground, caves and successively growing speleothems possess several **interconnections** to the prevailing climate and atmospheric conditions at the **Earth's surface** (FAIRCHILD et al., 2006). The most important are chemical, isotopic, and particle composition signatures transferred by the seepage water (dripwater), a variable cave air exchange (ventilation) influencing air- and hydrochemical gradients and compositions and the multiannual thermal assimilation (equilibration) of the cave interior versus outer atmosphere. **Stalagmites and flowstones** are of primary importance as paleoenvironmental mineral archives owing to their relatively simple growth geometries compared to other forms of speleothems, such as stalactites, stalagnates (columns), curtains, pool formations, and helictites (WHITE & CULVER, 2012). During ongoing speleothem precipitation from aqueous solution, variable environmental parameters have an influence on the chemical and petrographic dripstone composition, and this variability that is captured in the solid carbonate can be reconstructed in a **multi-proxy** (representative variables) approach (BOCH, 2008; FAIRCHILD & BAKER, 2012). In this context, **cave monitoring** programs have shown of great value regarding the fundamental, as well as site-specific, understanding of speleothem growth dynamics and its environmental dependencies (MATTEY et al., 2008; BOCH et al., 2011a). In the following sections, some of the major speleothem based and climate research dedicated requirements will be presented focusing on the author's own scientific experiences.

Uranium-Thorium based speleothem chronologies

The reliable age determination of speleothem carbonates constitute the backbone of this field's rapid scientific development and increasing value in the context of (paleo) climate research. The extraordinary dating capability of typical speleothems is based on selected **uranium-series isotopes** incorporated and evolving in the speleothem Ca-carbonate. Radiometric radiocarbon (^{14}C) dating was applied in the early history of speleothem based paleoclimate research – and still can be of additional value – but suffers from several geochemical restrictions (FOHLMEISTER et al., 2017). The time (age) elapsed after speleothem carbonate (calcite) deposition is reflected in the isotope (and activity) ratios of unstable uranium and thorium parent (^{238}U) and daughter nuclides (^{234}U, ^{230}Th) establishing over time in the speleothem carbonate based on the natural ^{238}U decay chain (IVANOVICH & HARMON, 1992; CHENG et al., 2013). Importantly, the radiogenic ^{230}Th is exclusively derived from the decay of the preceding ^{238}U and ^{234}U isotopes and its relative amount in the carbonate (sub)sample is therefore a precise measure of time depending on well-known half-lives of the relevant unstable nuclides. In principle, the U in the carbonate precipitates available for radioactive decay with time, results from specific dissolved U species (mainly aqueous uranyl – UO_2^{2+} complexes), while Th species are virtually insoluble and expelled from the aqueous solution (adsorbed to solids) and thus not incorporated into the speleothem calcite crystal lattice. An efficient hydrochemical separation of U and Th is essential with regard to the radiometric clock in speleothems. Minor amounts of detrital ^{230}Th (not from in-situ decay) being incorporated in the carbonate precipitated from aqueous solution (seepage water) are corrected for using the measured ^{232}Th isotope ($^{230}Th/^{232}Th$ ratio). In general, the potential and achievable precision of the U-Th ages and chronologies strongly depend on the local **geochemistry and geology** associated with the particular cave setting and speleothem formation (SPÖTL & BOCH, 2012). Depending on the local carbonate host rocks (e.g. marble vs. dolomite vs. pure limestone), the karst processes (fluid-solid interaction), available U concentrations, detrital (Th) contributions, and speleothem growth are significantly different. Also, carbonate host rock mobilization from carbonic acid based dissolution reacts different from sulfide oxidation and sulfuric acid based carbonate dissolution and subsequent Ca-carbonate precipitation (HOLZKÄMPER et al., 2005; BOCH et al., 2009; BAJO et al., 2017). Consequently, some speleothem and other Ca-carbonate precipitate **^{238}U-^{234}U-^{230}Th dating** efforts and dating precisions might suffer from low initial U concentrations (also very young samples), heavy detrital contamination, or later-stage (diagenetic) alteration (RICHARDS & DORALE, 2003). In most cases, however, absolute ages of speleothem formation can be inferred up to a dating limit of ~700,000 years based on U-Th. Select uranium and lead (^{204,205,206,207,208}Pb) isotopes of the natural ^{238}U and ^{235}U decay chains measured against synthetic isotope tracers (technical spikes) allow speleothems to be dated millions of years in age, in the case of favourable geochemical preconditions (WOODHEAD et al., 2006; MEYER et al., 2011). Critical issues with regard to **U-Pb dating** are the initial (common) Pb concentrations (contamination), very low radiogenic Pb concentrations (relatively young samples), and disturbed mineral closed system and therefore secular equilibrium conditions (volatile daughter nuclides).

Regarding the age determination of stalagmites, a first classification might be based on some direct observations, e.g. location in the cave system, and stalagmite size and colouring. Ahead of collecting the entire **stalagmite** sample, it might also be reasonable to extract a small drillcore from the thicker stalagmite base in order to constrain its growth inception and potential time interval of scientific interest based on U-Th (or U-Pb). In the case of massive **flowstones**, the **sampling** is mostly restricted to surface samples or multiple and distributed drillcores of variable diameter (cm-range) and length (meter-range; BOCH & SPÖTL, 2011). The collected stalagmites and flowstone drillcores are typically cut and polished (to enhance visual contrast) for multiple extractions of subsamples across the speleothem growth axis using band- or circular saws or handheld drills. These chunks and powders are then acid digested and processed in a multi-step wet-chemical procedure in a high-level clean laboratory using ion exchange columns and organic resins (chromatography) and various chemicals (SHEN et al., 2012). This multi-step process includes the **separation and enrichment** of tiny amounts of U and Th from the sample carbonate. Subsequently, the separate U and Th fractions and their isotopic compositions are analysed applying thermal-ionization **mass-spectrometry** (TIMS) or, more commonly, multi-collector inductively-coupled-plasma mass-spectrometry (MC-ICP-MS). Due to the small isotope concentrations and resulting ion beams, the ionization efficiency and magnet-optical transfers, and therefore the instrument setup, calibration, tuning and backgrounds, are all critical issues. The relevant isotope mass ranges, resolution, and interferences depend on the measurement protocol and machine setup (e.g. electron multiplier vs. faraday ion detectors), as well as the clean laboratory procedure (e.g. control spikes added) and – based on personal experience – these analytical conditions are significantly different in several aspects between dating laboratories. High-resolution subsampling for U-Th and U-Pb age determination can also be performed by laser ablation coupled to multi-collector mass-spectrometry and the ages might then be calculated online (EGGINS et al., 2005; SMITH, 2014). The precision (age errors) of these measurements, however, is typically significantly lower. Depending on the geochemical preconditions and absolute age of a speleothem sample, relative **age uncertainties** (2-sigma) of 0.2 to 2 % are state-of-the-art for most U-Th dating laboratories, i.e. a radiometric dating technique of high precision in the context of paleoenvironmental studies. Considering very young samples (up to few thousands of years), as well as old samples (half a million years and older), the achievable precision decreases significantly (several percent) and in the case of detritally contaminated sample material the mandatory ^{232}Th correction applied during isotope data processing results in major measured versus corrected age corrections and thus larger age uncertainties (sometimes tens of percent; BOCH et al., 2019). The accuracy of the absolute ages is primarily related to the reliability of the established, but continuously improved, radioactive **decay constants** (half-lives) of the unstable U and Th isotopes (CHENG et al., 2013). SPÖTL & BOCH (2012) provide a compact introduction to uranium-series dating of speleothems.

Interconnecting radiometric ages measured from the speleothem bottom (oldest part) to the top (youngest) or multiple ages distributed across the speleothem growth axis, can be accomplished using sample-specific **age (growth) models**. These **numerical** models interpolate and eventually extrapolate trends inferred from the individual data points (ages) of the radiometric datasets, thereby constituting an integral part of speleothem based **chronologies** that allows for paleoenvironmental information to be tightened to their temporal evolution. Moreover, the particular **speleothem growth rate** (carbonate precipitation rate) is a direct numerical result of such age models. The preferred numerical approach of a specific age dataset strongly depends on the number and distribution of the individual age data points, the overall and variable age uncertainties (error bars), as well as complicating features such as age inversions (within monotonic stratigraphic order), outliers, abrupt growth rate variations, and growth interruptions (hiatuses). These age versus depth characteristics are often evaluated in close connection with available petrographic information from the speleothem sample (e.g. visual indication of growth interruptions, (ir)regular lamination). In any case, the age-depth relationship has to satisfy the criterion of a monotonic slope (e.g. steadily decreasing age with increasing distance from stalagmite base). In the case of a simple stalagmite or flowstone drillcore bottom-top relationship, or an even distribution of multiple ages measured across the respective growth axis, a **simple linear function** might be applied as a numerical age model reflecting the speleothem growth evolution (Text-Fig. 5A; BOCH et al., 2009). These simple models, however, can oversimplify the real growth pattern and minor but environmentally meaningful variations are not reflected. In the case of numerous and closely spaced age data points, these could also be **straightly connected**, i.e. a form of simple linear pointwise interpolation characterizing a more variable but spatially well constrained age model (DYKOSKI et al., 2005). Unfortunately, the latter age models entail somewhat artificial growth rate variations resulting from the sharp changes of slopes at the anchoring age data points, i.e. in nature changes in speleothem growth might be more gradual and not be characterized by partially sampling-dependent kinks. Age-depth distributions of limited complexity can also be represented by various **polynomial functions** of least-squares (SPÖTL & MANGINI, 2002). More detailed growth variations are to be expected in natural speleothem specimen, and are again neglected in such age models. With respect to high temporal resolution paleoclimate records, this deficiency has to be considered. In some cases, however, these numerical solutions might be reasonable within the analytical age uncertainties (Text-Fig. 5B). A more fluent approach supporting the occurrence of significant growth variations consists in various regressions by **smoothing cubic spline functions** (HEEGAARD et al., 2005; SPÖTL et al., 2006). Most spline functions and associated statistics underlying speleothem chronologies are calculated using the open-source programming package "R" (R DEVELOPMENT CORE TEAM, 2018). Utilizing predefined keywords, selected parameters (e.g. degree of freedom) can be modified by the user, and the age and spline-dependent confidence limits (e.g. 2σ) can easily be calculated (Text-Fig. 5C). The manipulation, however, is still of some subjective decision and a combination of trial-and-error and best-case scenario might define the final speleothem chronology. In order to counteract such manipulation, SCHOLZ & HOFFMANN (2011) developed the **StalAge algorithm** based on a Monte-Carlo simulation successively fitting ensembles of linears with variable slopes to subsets of age data points and their respective uncertainties, while also including basic stratigraphic information. This approach of age-depth modelling, including the calculation of confidence intervals (2σ), is suitable for challenging datasets and the lack of adjustable parameters ensures high reproducibility (Text-Fig. 5D). An increasing number of paleoclimate records are temporally constrained by StalAge calculations (BOCH et al., 2011b; PEREZ-MEJIAS et al., 2017). **OxCal** is another **algorithm** of high acceptance and mostly used in radiocarbon dating (BRONK RAMSEY & LEE, 2013). This approach is based on random Poisson processing and only some rigidity parameters of the age model can be modified by the user. Owing to its satisfying flexibility of tracing the age data, automatic calculation of associated age uncertainties (2σ), and user-friendly implementation, it is increasingly used in paleoclimate studies (MOSELEY et al., 2016; PEREZ-MEJIAS et al., 2017). A **comparison** of different speleothem age modelling approaches that considers typical as well as challenging U-Th age datasets is provided by SCHOLZ et al. (2012).

Importantly, the **selected numerical approach** of age-depth modelling has a major influence on the final speleothem chronology, which temporally constrains the captured environmental information. The influence is particularly large for those paleoenvironmental records that are less constrained by the available U-Th data, i.e. being characterized by higher age uncertainties (lower precision), few data points, potential growth interruptions, distributions suggesting unreasonable growth rate variations, outliers and/or age inversions. More specifically, the absolute and relative **timing, duration, and temporal progress** of archived rare or recurrent climate events and cycles on

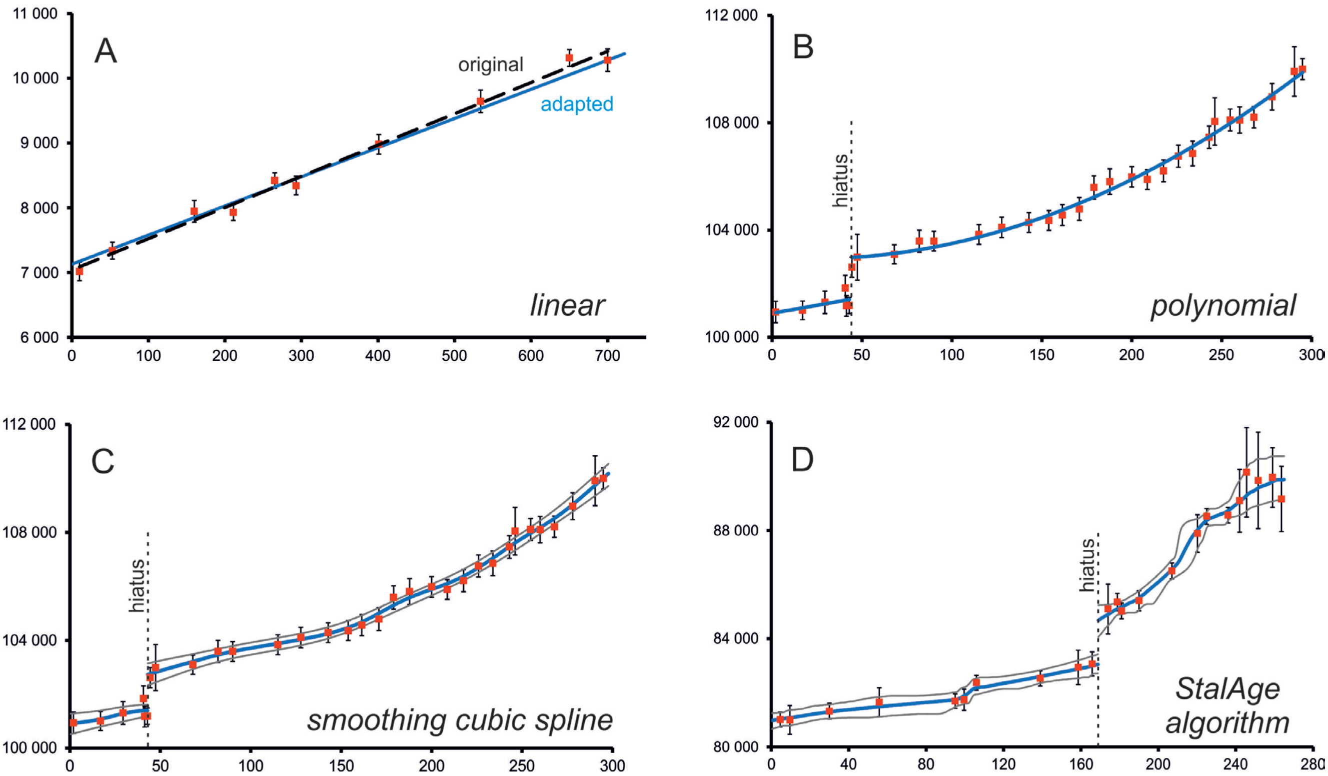

Text-Fig. 5.
Different age (growth) modelling approaches applied to typical U-Th based data points and their respective age uncertainties (2σ error bars). A) Simple linear function proposed by software (e.g. MS Excel) inherent statistics and adapted manually within the age errors. B) Least-squares polynomial fit to relatively evenly distributed age data points including a speleothem growth interruption (hiatus). C) Same dataset as in B but applying a smoothing cubic spline function calculated in the programming software "R" for the two separate growth sections. D) StalAge algorithm developed by SCHOLZ & HOFFMANN (2011) based on approximate Monte-Carlo simulation of piecewise linear fits to age data subsets. Note the variable flexibility of the resulting age models in tracing the measured age data (blue curves) and the variable 95 % (2σ) confidence limits (thin grey curves). The age-depth models also differ in terms of their reproducibility.

short- and longer-term timescales are directly inferred from the calculated age models (BOCH et al., 2011b; CHENG et al., 2016). Consequently, the temporal expression and scientific interpretation of environmental variation is strongly dependent on the – more or less objective – chronology of the individual paleoclimate records and their relation to other absolutely dated chronologies. For example, speleothem U-Th based chronologies are related to ice core based (lamina counting and ice flow modelling) chronologies, which in turn may reveal rapid spatiotemporal variations that include socio-politically critical variables such as air temperature, meteoric precipitation, mean sea level, and greenhouse gas concentrations (KAWAMURA et al., 2007; BARKER et al., 2011). In this context, testing the analytical precision, reliability, and reproducibility of the radiometric ages and superimposed age models is of highest relevance in order to minimize **subjective constraints**. In addition to a comprehensive disclosure of the measurement and data evaluation procedures performed, a favourable speleothem sample geochemistry allowing of precise age data is critical with regards to reliable, and perhaps internationally relevant, chronologies. Additional temporal constraints from detailed petrographic inspection of growth segments or regular minor/trace element variations can be of value, e.g. refining age models between measured U-Th data points by annual lamina counts and/or element cycles (ASRAT et al., 2007; BOCH et al., 2011a).

Speleothem stable oxygen isotope records

Regarding the paleoenvironmental information captured in speleothem carbonates, the stable O isotopic composition constitutes a proxy (representative parameter) of particular relevance. This is manifested in the numerous research publications reporting variable O isotope values in the course of speleothem growth, i.e. mostly isotope curves across the growth axis of a speleothem sample reflecting **spatiotemporal variations** of different origin and magnitude (FAIRCHILD & BAKER, 2012). The stable O isotopes are most relevant considering their occurrence in water and (carbonate) minerals, their often well-known fractionation processes, and their sensitivity to environmental variation on different spatial and temporal scales (HOEFS, 2015). These attributes and resulting potential in the light of paleoclimate investigation are not restricted to speleothems, but to several environmental archives involving stable O isotope analyses, e.g. ice cores, corals, marine and lake carbonate sediments and others. In all of these cases, identifying the variable **reservoirs and isotope fractionation processes** of oxygen are crucial, as they differ significantly between terrestrial and marine settings (CLARK & FRITZ, 1997). Further considering the widespread terrestrial speleothem archive, the carbonate O isotopic compositions capture **environmental information** related to the source and transport routes (trajectories) of air masses and moisture, time and space of meteoric precipitation, the prevailing air temperature, meteoric and carbonate precipitation conditions, and other isotope reservoir specific alterative processes. In particular, the O isotopic signature of atmospheric moisture depends on the source region (e.g. Atlantic vs. Mediterranean), as well as sea surface temperature, and evaporation conditions. The transport distances (advection of moisture), variable latitude (climate zonation) and altitude (ascent/descent of moisture), as well as (re) evaporative and condensation processes affect the specific rainout, O isotopic evolution and signature. Further, the regional climate, meteorological conditions, and season of the year determine the O isotope compositions, while the respective air temperature and meteoric precipitation amounts have a strong effect on condensation and associated O isotopic fractionation (CRAIG, 1961). At the surface and underground, the O isotopic signatures are altered by evapo(transpi)ration from plants and storage reservoirs (lakes, rivers) and various effects from water-rock interaction in soils and aquifers. Finally, equilibrium and kinetic effects control O isotope fractionation between aqueous solutions (e.g. seepage water) and related carbonate precipitates (e.g. speleothems; MICKLER et al., 2004; DAËRON et al., 2019).

Based on this multitude of dominantly physicochemical processes and effects that determine O isotopic compositions, specific **environmental relationships** can be studied qualitatively and quantitatively. In the realm of (paleo) climate research, the O isotope signatures are mainly a proxy parameter for variable air- and water temperatures and meteoric precipitation amounts and sources (FAIRCHILD et al., 2006; HOEFS, 2015). These principal meteorological and climate variables differ significantly on regional and temporal scales and such variability can be archived in the speleothem carbonate at variable degrees of signal to noise. This is expressed in the increasingly available stable O isotope curves of variable timing and **temporal resolution**, resulting from speleothem carbonate subsample transects extracted at variable **spatial resolution**. Depending on spatiotemporal resolution (e.g. high-resolution micromilling) and the overall time interval and growth rates of a particular speleothem, environmental information of diverse implication and detail might be reconstructed. Critically, the environmental and related O isotopic signals are **transferred and altered** between the different reservoirs of relevance, i.e. atmosphere, hydrosphere, pedosphere, aquifer, and cave system. Next to the atmospheric fractionation processes (CRAIG, 1961; HAGER & FOELSCHE, 2015), the stable O isotope processing involves soil water and CO_2 isotope exchanges, as well as typical fluid-solid reactions in the karst aquifers influencing the hydrochemistry of the seepage- and subsequent drip waters (e.g. water mixing from different flow routes, outgassing, prior $CaCO_3$ precipitation; SMART & FRIEDERICH, 1986; MATTEY et al., 2016). Conditions within the cave, particularly atmospheric conditions, can affect the hydrochemistry, including O isotopic compositions, of the water and dissolved inorganic carbonate due to variable gradients, e.g. temperatures and partial pressure differences promoting outgassing of CO_2 and H_2O (MATTEY et al., 2008; BOCH et al., 2011a). The speleothem carbonate O isotope compositions reflect this **cascade** of dominant processes and consequently constitute some **filtering**, **attenuating, and amplifying** variable (TREMAINE et al., 2011).

The stable O isotope records from speleothems therefore often reflect the prevailing meteorological conditions and principal **atmospheric circulation patterns** on different timescales at the cave site. In this context, the existence of pronounced **seasons** in the mid and high latitudes, or lack thereof in tropical low-latitude climate zones, have a strong effect on speleothem growth and O isotope compositions. Some regions and speleothem O isotope records show a distinct sensitivity to variable **monsoonal winds**

and rains and related shifts in the Inter-Tropical Convergence Zone (CRUZ et al., 2005; CHENG et al., 2016). Likewise, O isotopes in stalagmites have recorded variations of the **El Niño Southern Oscillation** (WANG et al., 2017). **Storm events**, such as tropical cyclones (FRAPPIER et al., 2007) or influences of Mediterranean cyclone activity (DEMÉNY et al., 2017), might also be recorded. For major parts of Europe, the positioning and strength of the **westerlies** and seasonal atmospheric circulation patterns such as the **North Atlantic Oscillation** can exert a major influence on the recorded O isotope values (BOCH & SPÖTL, 2011; FOHLMEISTER et al., 2017). In this respect, the extent of **snow** precipitation and subsequent **snowmelt** can significantly impact the karst aquifer recharge and water mixing, and thus the annually averaged isotopic composition of speleothems (FORD & WILLIAMS, 2007). Importantly, the recurrent (cycles) or irregular (events) environmental conditions operate from daily, seasonal, multi-annual to millennial timescales, which strongly affect the final captured isotopic compositions, as well as their magnitude (e.g. weighing of seasonal contributions; BOCH et al., 2011a; DOMÍNGUEZ-VILLAR et al., 2018). For example, in investigating two selected stalagmites from the Swiss Alps, LUETSCHER et al. (2015) found major **storm track and advective moisture transport** changes during the **Last Glacial Maximum** (LGM) dated to 26.5–23.5 kyr BP. Based on a precise U-Th chronology and high-resolution O isotope records, LUETSCHER et al. (2015) built a conceptual model of isotope fractionation derived from meteoric precipitation trajectories and associated O isotopic depletion during a Rayleigh fractionation process. Their results revealed a strongly enhanced advection of moisture from the South towards the Alps. This southward shift is interpreted to be the result of ice sheet expansion in the Atlantic Ocean, which, consequently, precluded common (e.g. modern) advection of moisture from the north-western Atlantic Ocean. The implications from the conceptual model are in line with field evidence of prominent glacier advances in the southern part of the Alps during that time, and an O isotope-based mixing model allowed quantifying S-Alps meteoric precipitation amounts being two or three times higher during LGM compared to today (LUETSCHER et al., 2015). In some places and for some speleothem samples, **quantitative environmental information** might be derived. Relying on long-term meteorological data and cave monitoring observations, BOCH et al. (2009) calculated relative air temperature decreases of ~ -3° C for an abrupt decadal-scale climate event at 8.2 kyr BP, and slightly less cooling for another prominent event at 9.1 kyr BP. These temperature variation determinations are again based on O isotope fractionation, i.e. the positively correlated O isotopic composition of meteoric precipitation with air temperature, as well as O isotope equilibrium fractionation between drip water and speleothem calcite. While the quantitative paleoclimate reconstructions of temperature and meteoric precipitation are the aim of some speleothem studies (e.g. LACHNIET, 2009), overall these studies are relatively scarce.

Broadly, the qualitative interpretation of high-resolution speleothem O isotope profiles are used in combination with precisely dated U-Th data in order to improve our process understanding of principal and often global climate relationships, such as the influence of the North Atlantic realm on Asian monsoon patterns (CHENG et al., 2016). In particular, the speleothem (mostly stalagmite) isotope signals and chronologies can be used to **improve the chronology and timing** of proxy signals from other climate archives, e.g. ice cores or marine sediment cores (BARKER et al., 2011; LISIECKI & STERN, 2016). For example, BOCH et al. (2011b) published a stable O isotope record of the Last Glacial period covering the time interval from 120 to 60 kyr BP at a temporal resolution of 2 to 22 years and typical U-Th based age uncertainties (2σ) of 200 to 500 years. **The NALPS record** is a composite isotope record from several geochemically selected stalagmites from different caves located at the northern rim of the Alps. The record consist of a relatively long time interval at high temporal resolution, and reveals pronounced and detailed paleoclimate variations including the prominent Last Glacial **Dansgaard-Oeschger (D-O) cycles**, as well as recurrent short-lived climate events (precursor-, rebound-, intermittent-type events). The latter climate anomalies were not reported outside Greenland (ice cores) before. D-O oscillations and probably also the minor climate anomalies are mostly explained by rapid (decadal-scale) **air temperature increases and decreases** in connection with the reorganization of major oceanic (e.g. thermo-haline circulation) and atmospheric (e.g. wind fields) variables in the North Atlantic region (JOHNSEN et al., 2001; WUNSCH, 2006). Considering the large amplitudes (up to 4.5 ‰) of the stable O isotope signals recorded in the NALPS curves, temperature control alone seems unlikely (BOCH et al., 2011b). Instead, these stalagmites capture an O isotopic composition strongly influenced by the **seasonal variation of meteoric precipitation** and infiltration next to air temperature. In the Alps, typical seasonal amplitudes in $\delta^{18}O$ of precipitation amount to ~10 ‰ between summer and winter (HAGER & FOELSCHE, 2015), and the timing and amounts therefore strongly affect the overall seepage/drip water compositions. Changes in the timing and duration of seasonal temperature amplitudes, rainfall amounts, and snow cover are thus archived in the speleothems from the N-Alps. Moreover, the observed cycles and events clearly demonstrate regional versus global teleconnections, which can be utilized to compare and refine existing Greenland ice core chronologies by corresponding Greenland versus NALPS stable O isotope signals and the more precise and accurate speleothem U-Th chronology (RASMUSSEN et al., 2014; BARKER et al., 2015; LISIECKI & STERN, 2016). In particular, the absolute and relative timing, durations, temporal progress, and spatial amplitudes can be evaluated in many details. The principal teleconnections in the Earth's climate system can also be reflected in stable O isotope curves on much **longer timescales**, e.g. Quaternary glacial (ice age) and interglacial (warm epochs) cycles. Several drill cores were extracted from subaqueous calcite precipitated over hundred thousands of years in an extensional fracture of **Devils Hole** in Nevada, USA (MOSELEY et al., 2016). Stable O isotopic compositions measured from the drill cores of different length and depth in the fracture reflect the major warm-cold transitions of the last ~200,000 years. In addition, the well constrained U-Th time series strongly supports a tight connection of **ice age terminations** and variable **atmospheric CO_2** concentrations to **northern hemispheric summer insolation,** and thus, **orbital forcing** from the Earth's elliptical orbit (eccentricity), as well as tilt (obliquity), and unstable orientation (precession) of the axis of the Earth (BERGER & LOUTRE, 2002; SARNTHEIN et al., 2009; MOSELEY et al., 2016).

Multi-proxy approach of climate parameters

Speleothems provide many ways of archiving variable environmental – and in particular climate – conditions **in the carbonate material** they consist of. The different ways and chemical-sedimentary mechanisms are reflected in distinct **proxy variables** representing major climate parameters, such as air temperature, the seasonal distribution and amounts of meteoric precipitation, as well as climate related changes of the vegetation above the cave. The availability of multiple proxy parameters enabling more diverse but also more concise constraints on past environmental conditions constitutes another strength of speleothems within the variety of paleoclimate archives. Regarding the reconstruction of climate parameters from the speleothem carbonate, the general but also cave site-specific **transfer mechanisms of the climate signals** to the speleothems depend on the coupling of the cave interior versus exterior environmental conditions. In this context, the translating mechanisms and their partial reactions provide different sensitivities underground with respect to climate changes at the surface, i.e. some proxy parameters might reflect seasonal or even daily changes while others capture a smoothed multi-annual trend (Fairchild & Baker, 2012). Consequently, the temporal resolution of the climate proxy parameter, as well as the spatial resolution and **sampling strategy applied** are critical ingredients in a speleothem based climate reconstruction. For example, proxy measurements applying modern imaging techniques, computer-controlled micromilling, and electron microprobe or laser ablation provide significantly higher resolution paleoclimate information compared to pointwise and handheld sampling tools (Spötl & Mattey, 2006; Boch, 2008). Also, some speleothem proxies are of **indicative** character regarding a specific environmental parameter reflected while others rely on more **complex** environmental controls and transfer relationships.

A principal climate proxy consists in the **occurrence or absence of speleothem growth** during a particular time (climate) interval or region (cave system). Radiometric age constraints and in particular the determination of the growth inception (e.g. stalagmite base), growth cessation (stalagmite top) and eventually growth interruptions (hiatus within stalagmite) of an individual or multiple speleothem samples therefore constitute indicative climate information concerning the **availability of (drip) water** (Text-Fig. 6A). The latter could be restricted by pronounced aridity (drought) conditions (Vaks et al., 2006) or temperatures below freezing (Spötl & Mangini, 2007). Furthermore, a hydrochemistry favourable of speleothem deposition constitutes an essential requirement, i.e. soil and karst processes resulting in vadose waters of sufficient Ca-carbonate supersaturation. Alternatively, speleothem growth might be periodically restricted by excess water availability, e.g. flooding of cave chambers in the course of sea-level oscillations or storm events (Denniston & Luetscher, 2017). Distinct and variable speleothem growth intervals were used as a climate proxy in different regions hosting karst caves (Fleitmann et al., 2007; Boch et al., 2010). Another macroscopic climate proxy consists in the variable **morphology of speleothems** and in particular of stalagmites (Text-Figs. 6B, C). Changing **diameters** along the growth axis and the resulting **shapes** are mainly dependent on water discharge (drip rate), as well as the actual CO_2 gradients (outgassing, growth kinetics) and hydrochemistry ($CaCO_3$ supersaturation; Boch et al., 2011a and references therein). For example, an increased vadose water supply from higher meteoric precipitation amounts can be manifested in overall broader stalagmites and the evolution of increasing diameters and conical shapes. In contrast, reduced drip rates and a hydrochemistry favourable of speleothem growth might result in slim carbonate formations, such as the widespread candle-stick type stalagmites (Martín-Chivelet et al., 2017). The vertical versus horizontal growth of stalagmites depending on the prevailing physicochemical conditions was also investigated based on conceptual models and mathematical approaches (Mühlinghaus et al., 2007). Strongly variable atmospheric and cave climate conditions can further be reflected in a changing speleothem **mineralogy** (Text-Fig. 6E). Typical examples are variable proportions of the Ca-carbonate polymorphs calcite and aragonite in speleothems of different age or within individual samples (Wassenburg et al., 2016), as well as the occurrence of Ca-sulphates such as gypsum (Plan et al., 2012). The latter is frequently associated with hypogenic cave formation in the course of sulphide oxidation and sulphuric acid based carbonate dissolution, mobilization and subsequent Ca-carbonate and Ca-sulphate precipitation in characteristic hypogenic cave chambers (Dublyansky, 2012). Apart from diagenetic transformations, mineralogical changes often reflect extreme environmental conditions, e.g. dryness promoting increased evaporation, mineral-specific supersaturation and increased prior $CaCO_3$ precipitation during vadose water flow (McMillan et al., 2005). For example, Boch et al. (2019) reported a principal control of variable aragonite versus calcite in flowstone-like precipitates of vertical fractures (veins) from variable water flow routes and a hydrochemical evolution involving irregular variations in the Mg/Ca ratio and Ca-carbonate supersaturation in the fissured carbonate aquifer. Often pronounced climate sensitivity is further ascribed to the **speleothem petrography** (Text-Figs. 6D, F). This includes spatiotemporal changes of the fabrics (oriented crystal growth, porosity) and various rhythmic (e.g. annual) or event lamination and zonation patterns along the speleothem growth axis (Frisia, 2015; Martín-Chivelet et al., 2017). Importantly, changes in the speleothem growth rate are reflected in the variable fabrics and layer thicknesses depending on (un)favourable climate and speleothem growth conditions (Baker et al., 2008; Boch & Spötl, 2011). In other words, the seasonally and longer-term variable temperatures and meteoric precipitation amounts translate into drip water and ion supply and consequently into mass, volume (density depending on calcite fabric) and cave site-specific progress of speleothem build-up.

High-resolution climate information is further archived in the variable speleothem carbonate **minor and trace elemental compositions** (Text-Fig. 6H). Mg, Sr and Ba might be considered of particular relevance due to their common occurrence in calcite and/or aragonite and the elements P, S, Mn, Fe, Y, U and the rare earth elements (REE) were also investigated in some detail (Fairchild & Treble, 2009; Boch et al., 2011a; Tremaine & Froelich, 2013). The elemental concentrations reflect numerous underlying mechanisms of fluid-solid interaction including the aquifer host rock, seepage water infiltration and residence time, mixing and phase separation, as well as specific elemental fractionation mainly depending on temperature and speleothem growth rate. BORSATO et al. (2015) studied sulphate concentrations in drip water and speleothems as a proxy of volcanic eruptions, soil and aquifer processes, as well as anthropogenic atmospheric SO_2 emissions. Incorporation of selected elements was also investigated by cave-analogue experiments in the laboratory (DAY & HENDERSON, 2013). Environmental changes of variable complexity are also captured in distinct **isotope ratios** of O, C, S, Mg, Ca, Sr, U and several other (trace) elements (Text-Fig. 6G). The stable and unstable isotopes of typically rare versus more common nuclides reflect even subtle variations in the karst water cycle and related processes of speleothem formation. Stable C and O isotope signals represent the most applied isotope proxies in speleothem carbonate and are mainly sensitive to temperature, meteoric precipitation composition, as well as dissolved vs. gaseous CO_2 dynamics (TREMAINE et al., 2011; DEMÉNY et al., 2017). In this context, **equilibrium and kinetic** C and O isotope fractionation processes have gained special attention (MICKLER et al., 2006; DREYBRODT & ROMANOV, 2016) and clumped isotope values (Δ_{47}) might be particularly sensitive proxies of these processes during speleothem growth (DAËRON et al., 2011, 2019; AFFEK et al., 2014). Stable isotopic compositions of the common elements Ca and Mg are increasingly

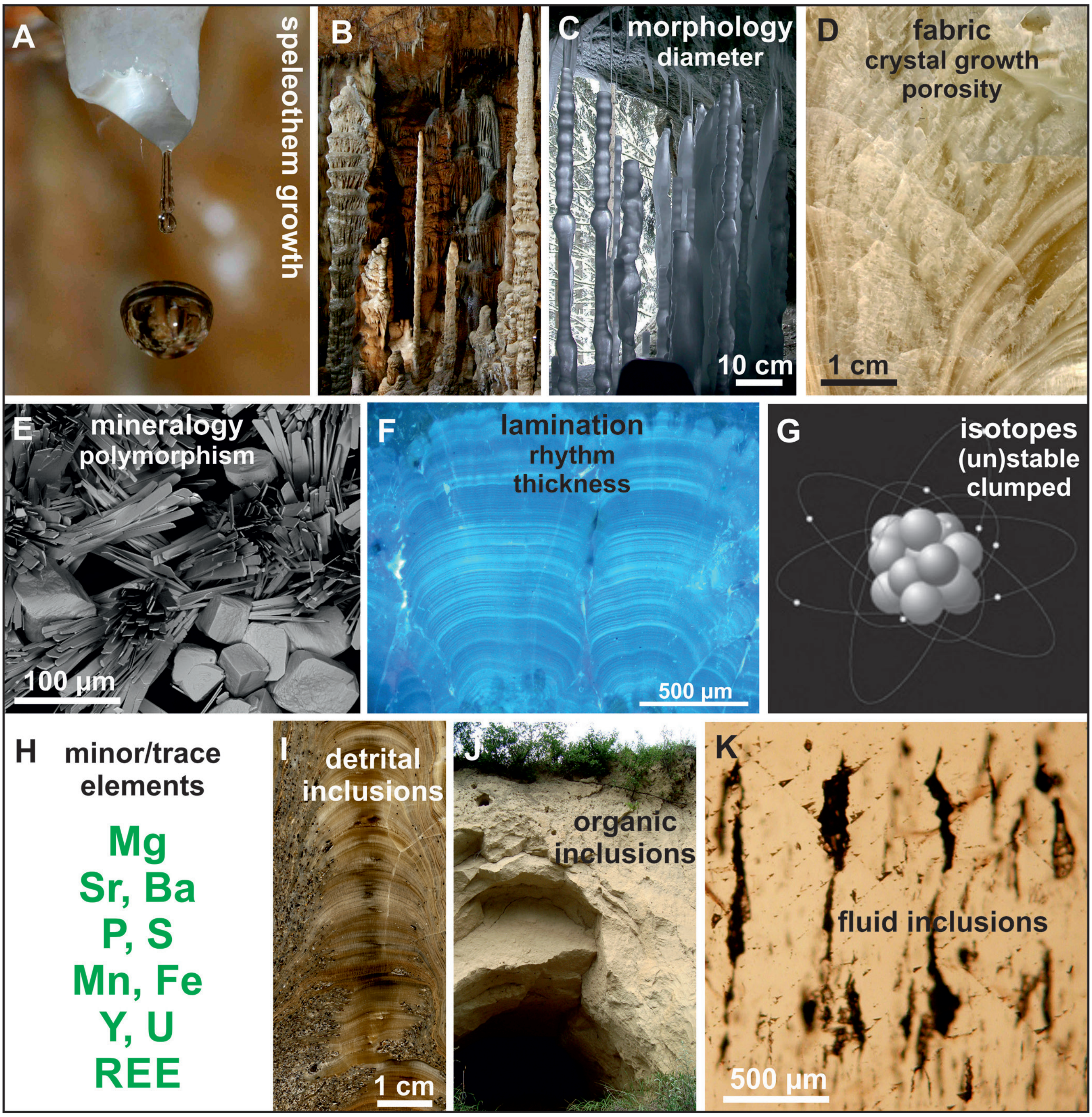

Text-Fig. 6.
Variable environmental (climate) conditions can be reconstructed from multiple proxies archived in speleothems including the occurrence or absence of speleothem growth (A, B), the growth morphologies (shapes) of stalagmites (B, C), speleothem petrography and mineralogy (D, E), rhythmic or event layering (F), various Ca-carbonate (un)stable isotopic (G) and minor/trace elemental compositions (H), as well as detrital (siliciclastic; I), organic (acids or pollen; J) and fluid (water/air, K) inclusions.

studied in speleothems and are mostly related to variable carbonate precipitation rates and aridity (Immenhauser et al., 2010; Owen et al., 2016). Unstable Pb and U isotope systematics were repeatedly discussed as a hydrological proxy of water recharge vs. discharge and thus past meteoric precipitation (Zhou et al., 2005; Yang et al., 2015).

A climate proxy of indicative character consists in various forms of **inclusions** eventually being incorporated in the speleothem carbonate (Text-Figs. 6I–K). **Detrital inclusions** such as sand grains or clay minerals of variable chemistry might be transported to the speleothem surface in the course of major discharge (flushing) from the soil zone and karst aquifer or alternatively from unconsolidated sediment mobilization during major water level rises, i.e. phreatic flooding of otherwise vadose cave sections (Text-Fig. 6I). In this regard, detrital layers are typically a proxy of extreme meteorological events, such as periodical flood waters (Spötl et al., 2011; Denniston & Luetscher, 2017). **Organic inclusions** of highly variable size typically reflect the vegetation cover in the cave area (above the cave; Text-Fig. 6J). In few cases, strongly indicative pollen might be captured in the speleothem carbonate (Meyer et al., 2009). More commonly, allochthonous organic compounds from progressive degradation processes in the soil zone, as well as autochthonous organic matter from microbial communities in the aquifer and cave constitute variable organic contributions (Blyth et al., 2016). Many of these organic inclusions show fluorescence in UV-microscopy (Boch & Spötl, 2011). Finally, **fluid inclusions** comprising of variable amounts of drip water and cave air reflect the prevailing environmental conditions in a rather direct fashion (Text-Fig. 6K). More specifically, the stable H and O isotopic compositions of the water inclusions represent an attractive proxy of the seepage- and meteoric water source and evolution (Dublyansky & Spötl, 2009). Their measurement, however, is highly challenging due to the small sample amounts and potential alteration effects (Demény et al., 2016b). For example, Johnston et al. (2018) conducted fluid inclusion stable H and O isotope analyses of stalagmite and flowstone samples in comparison with the respective calcite O isotope values and known equilibrium fractionation factors in order to calculate the climate dependent past speleothem formation temperatures.

The actual benefit of a multi-proxy approach from speleothems in comparison to other climate archives strongly relies on the scientific development of an **in-depth process understanding** of the different **proxy dependencies** in relation to often highly variable environmental conditions on different spatial and temporal scales. An increased understanding of elemental and isotopic fractionation processes during phase transitions in the atmosphere, soil zone and karst aquifer, as well as during speleothem crystal growth and potential diagenetic alteration might be of particular relevance (Wassenburg et al., 2016). The critical question of qualitative versus quantitative climate reconstruction from the proxies also gains in importance, in particular with regard to numerical (computer) models processing and delivering numbers of past and future climate change (NOAA, 2018). Considering that most speleothem based paleoclimate records provide **qualitative** environmental information in principal (warmer/colder, wetter/drier), a replication of the proxy variability in multiple speleothem samples from a particular location (cave) or even different places in a region should be envisaged. Thus, temporally well constrained coeval and composite speleothem stable isotope and elemental records can be of reliable value regarding pronounced climate variations, e.g. the prominent 8.2 kyr cooling event (Boch et al., 2009; Mischel et al., 2016). Regarding the target of more **quantitative** speleothem based climate reconstructions, O isotopes in the carbonate and in fluid inclusions are promising proxies, e.g. for calculating absolute calcite formation temperatures and temperature changes (Johnston et al., 2018). Clumped isotopic compositions should also be mentioned in this context of absolute temperature constraints (Meckler et al., 2015). Major efforts, however, have to be pursued in order to establish more reliable **proxy calibrations and site-specific transfer functions** of the external climate parameters to the speleothem proxy parameters, i.e. numerical relationships of the prevailing temperature (in ° C) and meteoric precipitation amounts (in mm) being captured in the respective values of the proxy parameters. In this respect, an increasing number of speleothem paleoclimate studies provide selected and calibrated proxy records of (semi) quantitative information. Owen et al. (2016), for example, utilized **stable Ca isotope fractionation** measured in the host rock, drip water and calcite on artificial substrates, as well as in stalagmites from Heshang Cave, China. Based on relatively simple calibration functions and an aquifer model, they inferred a dominant control of the $^{44}Ca/^{42}Ca$ isotope ratios by variable prior calcite precipitation and directly related Ca removal. During the 8.2 kyr cooling event archived in a stalagmite sample, increased prior calcite precipitation and Ca removal were determined to reflect a mean annual **rainfall decrease** of ca. 30 %, i.e. a drop to **~700 mm/yr** for ~80 years duration. In Postojna Cave (Slovenia), a high-resolution stable O isotope record of a young stalagmite measured by ion microprobe was calibrated against the O isotope composition of regional meteoric precipitation (Domínguez-Villar et al., 2018). The calibrated stalagmite proxy $\delta^{18}O$ record allowed to **reproduce the variable $\delta^{18}O$ signature of cave drip waters** collected and further to reconstruct the regional inter-annual precipitation variability filtered by the aquifer. In addition, the proxy calibration revealed average karst aquifer **water residence times of ~11 months** and growth of the analysed stalagmite interval in the years 1984 to 2003. Importantly, these more or less quantitative environmental reconstructions from caves and speleothems are mostly based on multi-annual **cave monitoring** programs of different extent and resolution in combination with various **instrumental meteorological data**.

Environmental Monitoring

In principle, all kinds of environments can be the subject of some physical, chemical or biological monitoring activities applying appropriate analytical techniques in order to understand specific environmental relationships and their implications. Thus, environmental monitoring is also conducted in the attempt of an **increased process understanding** of widespread **carbonate formation and alteration** depending on strongly variable environmental conditions. The variations occur within a broad spatial and temporal range and consequently the monitoring approaches and associated analytical techniques differ significantly. Amongst the great variety of natural and human-made environmental settings to be monitored, the **human to regional scale** systems represent typical subjects of environmental monitoring. Examples are monitoring efforts of various natural and geotechnical springs and streams, cave systems, geothermal and hydrocarbon production wells and deep aquifers or drainages of different implementation in railway and motorway tunnels (Text-Fig. 7). Depending on the particular setting and the **natural site- or installation-specific** characteristics, geologically and anthropogenically influenced (e.g. operational) environmental conditions determine the relevance and magnitude of related processes on different spatiotemporal scales in a system, e.g. effects from global warming, industrial pollution, water recharge and discharge, variable (water, energy) production or mineral formation conditions. In essence, environmental monitoring approaches target an evaluation and more or less detailed

Text-Fig. 7.
Impressions from natural and geotechnical settings of environmental monitoring. A, B) Regular monthly monitoring and process understanding of unwanted Ca-carbonate precipitation and associated hydrochemical alteration in a human-made stream bed. C, D, E) Multi-annual bi-monthly (cave visits) and continuous (data loggers) cave monitoring including cave air, seepage waters and solid precipitates (speleothems) in different cave chambers. F, G) Observation of fluid-solid interaction targeting scaling and corrosion processes impairing deep wells for geothermal energy production. H, I) Monitoring of site-specific mineral precipitates clogging drainages in different tunnels.

classification of the dominant relationships. More specifically, the environmental monitoring programs on macroscopic (living) scale can be distinguished from the typically **laboratory based** monitoring of specific processes in **confined environments**, e.g. monitoring of experimental conditions of fluid-solid interaction on a microscopic scale. The in-situ Raman spectroscopic monitoring of Ca-carbonate transformation reactions in the context of natural biomineralization or industrial material development could be mentioned here (PURGSTALLER et al., 2016). In all of these cases, the **monitoring strategies** applied depend on multiple factors and basic vs. comprehensive, partial vs. holistic approaches might be considered. However, environmental monitoring always involves expert knowledge and various physical-chemical-biological analytical techniques are a key element in order to investigate the complex relationships of natural and/or technical parameters (Text-Fig. 7). In this respect, the broad field of environmental monitoring is clearly an **analytical technology driven undertaking** within the geosciences and other disciplines. This comprises methods and tools applied in the field, in the laboratory and eventually also in computer simulations. In view of the rapid technological development in that area, the state-of-the-art is difficult to define and a combination of established and very new monitoring tools and approaches characterizes environmental monitoring studies providing new insights, e.g. regarding meteorological/climate parameter vs. proxy relationships in the course of Ca-carbonate precipitation dynamics. Also, monitoring of particular parameters and processes is always based on **data acquisition of limited spatial and temporal extension**, e.g. more or less continuous in selected sections within a few hours or years. The interpolation and/or extrapolation of numerical relationships is common practice during the envisaged environmental interpretation and implications inferred. Accordingly, this raises the question on the reliability and detail of the process understanding gained in the course of a monitoring approach. Nevertheless, next to experimental and modelling approaches environmental monitoring constitutes a serious attempt of a more comprehensive and in-depth knowledge on carbonate formation and its various dependencies. Only considering the recent geoscientific literature on this topic would easily exceed the intention of this chapter and the settings discussed in this publication.

Periodical sampling and data loggers

Monitoring of environmental processes in specific settings and over time is intrinsically tied to the spatial and temporal **resolution of the measurements** performed during a monitoring campaign. The analyses of environmental parameters (e.g. temperature, water discharge, mass concentration) can be done in regular or irregular time intervals at one or multiple sampling points of the system observed (e.g. cave; Text-Fig. 8). In most cases, punctual one-time or repeated measurements result in datasets of different spatiotemporal extent and their significance with regard to specific process understanding strongly depends on the spatial and temporal extension of the environmental processes of interest. Consequently, the selective distribution

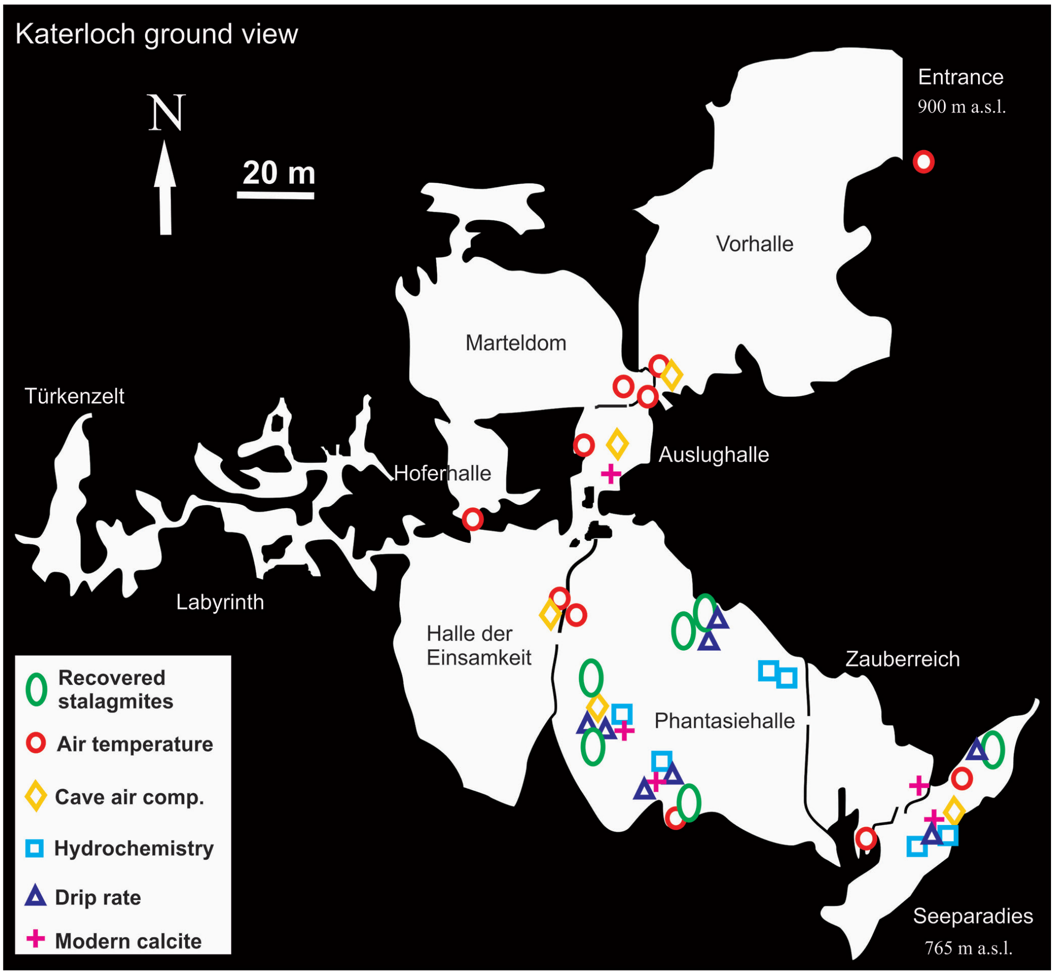

Text-Fig. 8.
Location of cave air, seepage water and Ca-carbonate sampling sites in Katerloch Cave, Styria. The selected positions and technical infrastructure (data loggers) constitute an ongoing multi-annual (since 2005) and partially high temporal resolution (hourly) cave monitoring program in order to investigate the variable cave climate and speleothem growth dynamics in relation to meteorological/climate changes.

and density (spacing) of the sampling sites (e.g. in different cave sections; Text-Fig. 8) and the frequency of the sampling intervals (e.g. seconds to annual) has to be arranged in compliance with the carbonate precipitation dynamics and associated fluid-chemical reactions of interest independent of monitoring natural or human-made (e.g. geotechnical) environmental settings. More importantly, the **timing, duration, progress** and therefore shifts and delays of the relevant environmental variables determining carbonate formation should be captured by the monitoring efforts. For example, an investigation of the prevailing weather conditions (e.g. low air pressure fields and storms) in relation to a karst aquifer and cave system and its short-term effects on speleothem growth should be based on a relatively high temporal (and spatial) resolution monitoring approach, i.e. daily, hourly or less (Celle-Jeanton et al., 2001; Baldini et al., 2008). Likewise, the evolution of longer-term environmental trends (e.g. global warming) affecting a particular system of fluid-solid interaction might not necessarily require a high-resolution monitoring approach, i.e. resolving seasonal or inter-annual differences is sufficient. The latter could be the case for monitoring water recharge and discharge of aquifers in sedimentary basins or crystalline rock formations (Strauhal et al., 2016; Mechal et al., 2017). Karst aquifers, in contrast, are typically highly dynamic and responsive with regard to changing atmospheric and meteoric precipitation conditions and a higher resolution monitoring might therefore be necessary inherently (Ozyurt et al., 2014). The monitoring should further be adapted in the light of more **cyclic** (e.g. seasons, snowmelt) versus **event-like** (e.g. storms, flooding, drought) recurrent variations, i.e. the nature and expression of the environmental trigger motivates irregular or regular observation intervals and the overall resolution recommended. However, the distinction of causes versus effects controlling various Ca-carbonate precipitation mechanisms and occurring either in strictly periodical cycles or irregular (e.g. stochastic) events is obviously a floating transition. In essence, the spatiotemporal strategy has to be well balanced with regard to the environmental processes targeted. A coarse resolution monitoring program runs the risk of an oversimplification or even misguided process understanding. A very high resolution monitoring approach can suffer from an unfavourable signal to noise detection of environmental information, i.e. the relevant processes of a particular research question could be masked in the overwhelming data acquisition. Apart from the critical specialist area constraints, the extension – resolution and duration – of an environmental monitoring program in the course of scientific and applied (e.g. consulting) activities is often restricted by the available time, costs, human resources and overall conditions at the setting (e.g. danger, construction progress; Boch et al., 2015).

Regarding environmental **data acquisition** widespread **punctual sampling** at selected spots of a specific setting (e.g. stream, tunnel, cave, well; Text-Fig. 7) during visits of the site typically requires the field based deployment of specific and mostly handheld analytical instruments in combination with different sampling procedures and preparation techniques for later laboratory based measurements. This comprises analyses of aqueous solutions such as various types of fresh and contaminated waters or brines, gases of variable partial pressure in a confined soil air, cave, well, pipeline or the free atmosphere volume, as well as solid phases forming under very different conditions at distinct rates and being accessible to punctual sampling. The latter includes a multitude of minerals in the context of natural chemical-sedimentary archives (e.g. Ca-carbonate and accessory minerals in speleothems, travertine, lake and marine sediments, veins), unwanted scale deposits in technical settings (e.g. geothermal and oil producing wells and pipelines, tunnel and processing water drainages, drinking water treatment) or corrosion products of various steel components in industrial or geotechnical applications. Common electronic instrumentation for hydrochemical analysis in the field includes pH-, electric conductivity-, redox- and oxi-meters and might be combined with a broad range of physical environmental analyses (e.g. thermometer, flow meter, distance meter, anemometer). For all of these instruments, the achievable analytical accuracy, precision, and resolution of the measurements have to be considered and careful calibration in method-specific intervals constitutes an integral part of professional data acquisition. An **adequate sampling procedure** further involves flexibilities and constraints regarding sample amounts and sample preparation. In some settings, the available sample volumes are strongly restricted, e.g. slow drip water supply in a cave or little mineral precipitate collected on an artificial substrate. The sample amount often determines the possible utilization of laboratory analytical techniques, as well as possible replicate measurements and consequently the reliability of the results and process understanding inferred. A wide range of sample vessels – bottles of various materials for liquids or different bags for gases – are used and play a critical role with regard to sample transport, practical storage life and alteration. Potential sample alteration concerns partial mineral precipitation from altered saturation states due to temperature changes or outgassing, as well as element specific leaching or adsorption effects related to the storage medium. Sample preparation further includes filtering (e.g. using 0.45 µm mesh size cellulose acetate filters), aqueous solution acidification for conservation (e.g. adding nitric acid for ICP-OES based elemental analysis) or permanent cooling during sample transport (cf. Boch et al., 2015). The various avenues of chemical or biological sample contamination should also be considered and avoided. An immediate sample analysis after sampling (e.g. same day) is recommended whenever feasible.

Environmental data acquisition at different spatial and temporal resolution can also be executed by various types of **automated data loggers**. These mostly electronic instruments typically consist of one or more specific sensors connected to a data processing and data storage unit and some power supply. The **sensor** might be based on an electrochemical reaction, such as a pair of electrodes wired to a voltmeter, e.g. measuring electric conductivity, pH or redox potential. Sensors can also be based on optical (e.g. measuring gas concentrations) or acoustic (e.g. drip counting) signals. **Data processing** strongly relies on the particular environmental parameter monitored and data loggers of different complexity range from established and commercially available to scientific prototypes. Considering **data storage** units, such as memory cards the rapid development and miniaturization in recent years is clearly tied to the ongoing evolution in the computer electronic realm, e.g. increased data storage capacities with concurrently decreased storage medium size. Likewise, the **power supply** requirements strongly benefit from recent developments, such as partially decreased energy consumption of more efficient sensors, the rapid evolution of various kinds of (Li-)batteries, and the general public interest in mobile electronics, i.e. independent of a wired power supply. Many data loggers, however, are still in need of a higher voltage energy source and their flexibility might therefore be restricted, e.g. mobile instruments measuring stable isotopic compositions. The **data transfer** from the logger data storage unit is achieved in different ways including shuttle components typically provided with the data logger, USB and memory card based transfers or plug-in connections for laptops and smartphones. Modern developments further comprise the **wireless** and mostly **online** data transfer from local monitoring stations to the user via telecommunication networks, e.g. meteorological stations or hydrochemical and scaling monitoring in geotechnical settings. As for conventional punctual and mostly manual environmental measurements – for example using handheld analytical instruments – the spatial distribution and spacing, as well as temporal resolution of the data logging is of crucial importance and strongly depends on the technical specification and adaptable measurement protocols of the monitoring instrument. Many data loggers stay online and a more or less continuous monitoring of one or more dedicated environmental variables is possible, resulting in numerical environmental records of narrow time intervals (e.g. minute-range datasets).

Continuous monitoring and data storage in distinct short-term intervals are logging tasks implemented in a growing number of **air- and water-temperature loggers** applied in a broad range of different settings including water streams and stagnant bodies, caves, tunnels, deep wells and industrial environments. State-of-the-art temperature loggers cover an attractive range of negative to high temperatures allowing for a multi-annual autonomous registration of higher amplitude temperature changes, while also providing high accuracy and precision of the measurements. Some of these loggers provide a high sensitivity and temperature resolution for capturing even subtle variations (e.g. 0.02° C; Onset HOBO Water Temp Pro v2 data logger used by Boch et al., 2011a). Text-Figure 9 (upper diagram) shows atmospheric (outside) versus cave interior air temperature variation at a high temporal resolution (two-hour intervals) for a one year monitoring period. The temperature logging revealed distinct warm versus cold seasonal modes of cave air exchange (ventilation), as well as changes from daily fluctuation and the prevailing weather conditions. Moreover, the air temperatures increase with depth underground and distance from the cave entrance and the deepest chambers show stable temperatures, although small seasonal amplitudes (~0.1° C) can still be resolved owing to this monitoring approach. In comparison to, e.g. monthly or even weekly measurements, such data clearly promote a more detailed understanding of environmental relationships (exterior/interior climate) and processes (speleothem growth). Recent developments in autonomous and continuous data logging further comprise of different **gas analysers**, e.g. for CO_2 and CH_4 concentrations. These loggers differ significantly in terms of their measurement range, resolution, accuracy and applicability to demanding natural environments, but most are based on nondispersive infrared absorption of the gases analysed (e.g. instruments of the LI-COR company). Luetscher & Ziegler (2012) developed a logger (CORA) for longer-term monitoring of variable **CO_2 concentration**, **air pressure** and temperature even in cold and humid environments (e.g. caves). The hand-sized logger (Text-Fig. 7C) is powered by an internal and additional external battery pack and air CO_2 contents up to 2 vol.% can be measured at high temporal resolution (e.g. every 10 min) with relatively high accuracy (± 3 %). Depending on the selected measurement interval, the mobile power supply lasts for a few months up to several years. CO_2 measurements in four-hour intervals conducted in a major chamber of Katerloch Cave (Austria) over a year (Text-Fig. 9, middle diagram) revealed significantly increased cave air CO_2 concentrations compared to average atmospheric values. The contents further display pronounced seasonal, as well as small daily fluctuations and are commonly related to larger outside vs. inside air temperature changes and eventually to some transient impact from small sized groups of cave visitors (exhaling CO_2). Importantly, the variable CO_2 fluxes are a sensitive record of the variable cave ventilation mainly depending on the prevailing meteorological conditions and further affecting physicochemical processes of fluid-solid interaction in this cave (Boch et al., 2011a). Considering overall **water discharge monitoring**, several techniques including mechanical measurements (e.g. propeller), radar, ultrasound, tipping buckets and acoustic detection are available and their application often depends on the dimension and expected variability of water discharge. Vadose seepage (drip) water supply, for example, can be measured by acoustic counting, e.g. STALAGMATE data logger (Collister & Mattey, 2008; Text-Figs. 7D, E). The latter small sized (~5 x 5 cm, 300 g), Li-battery powered and thus autonomous monitoring instrument is based on the registration of falling water drops by a sealed microphone and ongoing (multi-annual) counting and periodical data storage (e.g. logging intervals of hours to seconds). These highly sensitive monitoring tools provide information on variable **drip rates** (e.g. in caves, tunnels, buildings) in relation to the prevailing (meteoric) environmental conditions. Text-Figure 9 (lower diagram) shows about one year of continuous and high temporal resolution (30 min intervals) monitoring of drip water supply at three different sites in Katerloch Cave. The selected drip sites revealed many similarities regarding their response to meteoric precipitation (recharge) conditions, i.e. contemporaneous rapid increases and more gradual decreases. Regarding their absolute rates and degree of variability, however, the sites react differently and represent markedly different flow regimes in the overlying karst aquifer. The site-specific water discharge thus depends on inter-annual, seasonal (e.g. snowmelt in spring) to daily (e.g. storm events) meteoric and karst aquifer saturation conditions. Next to gaseous and liquid phases, solid materials such as mineral precipitates can be monitored continuously by placing **artificial substrates** in the fluid flow. For example, active speleothem growth can be studied by mounting convex or plain, smooth or roughened **glass** substrates on the top of different stalagmites and drip sites distributed in a cave (Boch, 2008; Tremaine et al., 2011). These glass slides are then recovered regularly (e.g. bimonthly) or after some definite time interval (e.g. eight years in Katerloch Cave). The collected Ca-carbonate can be analysed at high spatiotemporal resolution across the growth axis similar to a stalagmite. Additional environmental information from punctual or continuous monitoring of the drip water and cave air in combination with meteorological data is of high value. Alternatively, round glass substrates can be mounted at the upper end of boreholes drilled from an actively growing flowstone or travertine deposit or short drill cores capturing modern precipitation conditions might be extracted after some time of site-specific monitoring (Boch & Spötl, 2011). Comparable approaches might also be conducted in more applied settings of monitoring mineral precipitation, e.g. various geotechnical drainages, wells and pipelines. Likewise, corrosion and material alteration processes are monitored by placing **coupons** of different material (carbon steel, alloys, plastics) in the fluid flow and their mass loss and later visual inspection can help in the understanding of critical fluid-solid interaction (Nogara & Zarrouk, 2014).

New developments of on-site and online environmental data logging comprise the measurement of different **stable isotopes** of common gases and aqueous solutions. This includes the analysis of stable C isotope ratios and gas concentrations of carbon dioxide and methane, stable H and O ($\delta^{18}O$, $\delta^{17}O$) in water and vapour, and stable N ($\delta^{15}N$) isotopic compositions and gas concentrations of nitrous oxide in the atmosphere (Maher et al., 2014; Erler et al., 2015). These traditional isotope systems provide valuable insights regarding sources and transfer processes of the major water, carbon and nitrogen cycles. Companies such as Thermo Scientific and Picarro develop instruments that are based on mid-infrared absorption of the respective gas phases, i.e. **isotope ratio infrared spectrometry** (IRIS; Thermo Scientific) or laser-light interactive **cavity ring-down spectroscopy** (CRDS; Picarro). Importantly, these techniques are

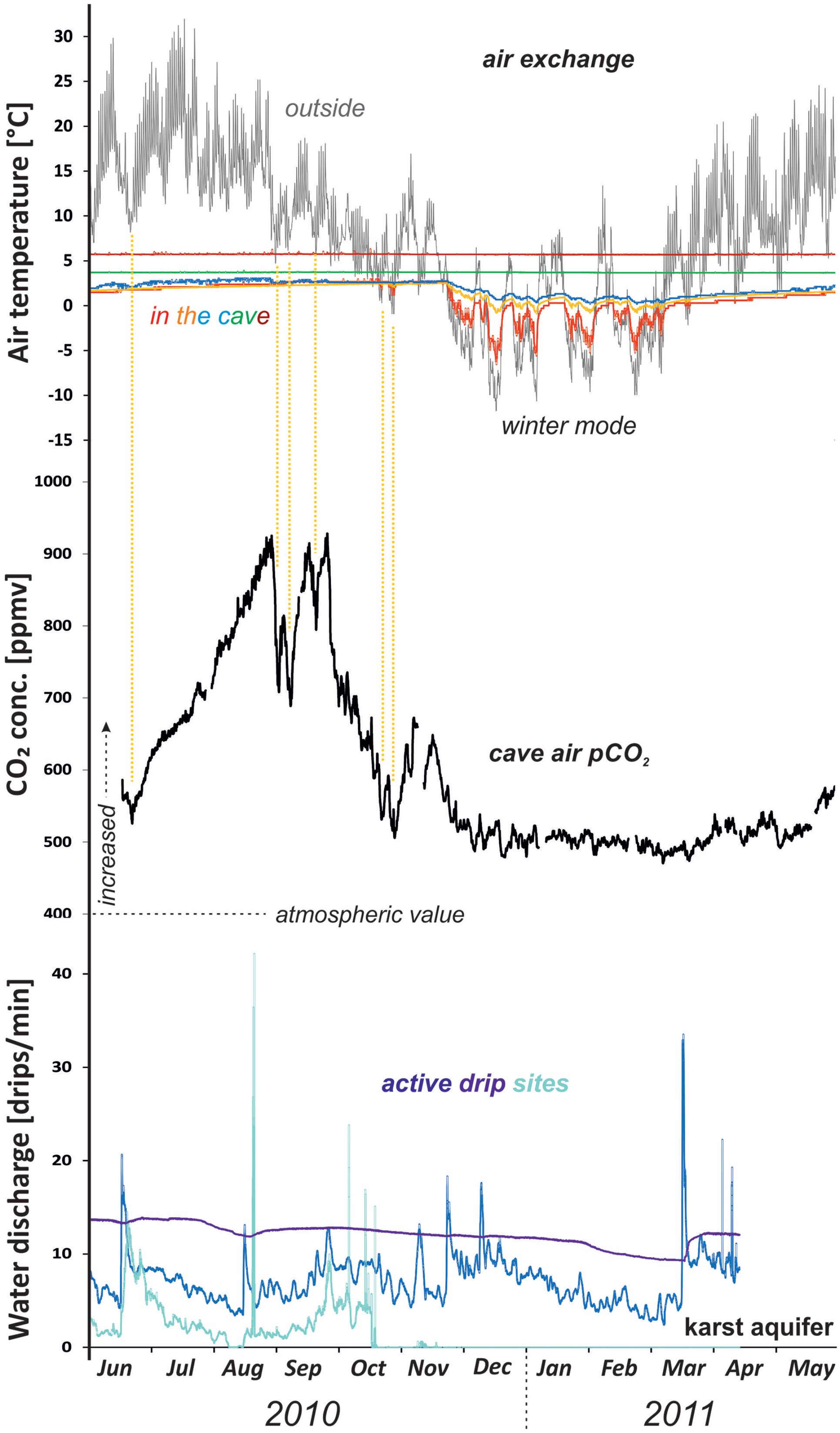

Text-Fig. 9.
Example of environmental monitoring in a cave system (Katerloch, Styria) at high temporal resolution over one year duration using data loggers. Exterior and cave interior air temperature (2 h intervals), CO_2 partial pressure (4 h) and water discharge (sum of drips every 30 min) show pronounced daily to seasonal variations. A cold season mode of enhanced cave air exchange (ventilation) can be distinguished from a warm season mode with higher pCO_2 and little temperature fluctuation. Cave air compositions are affected by major atmospheric (outside) temperature changes (yellow lines). Deeper cave sections show higher and stable temperatures although the small seasonal amplitudes can still be resolved (~0.1° C). Rapid increases in seepage water discharge are observed after several days of rainy weather and during snowmelt in spring. The drip sites reflect different karst aquifer flow regimes of variable sensitivity to meteoric precipitation and karst aquifer recharge.

increasingly sensitive to different stable isotope compositions of the fluids analysed and enable an online (real-time) and local monitoring of the isotope signals. This implies significantly reduced size and weight compared to conventional isotope ratio mass spectrometers and consequently a portable and robust construction scheme with regard to an anticipated application in the field. Also, some of these instruments facilitate multiple input channels in order to monitor isotopic compositions from several sampling sites in a natural or geotechnical environmental setting simultaneously. Most instruments further provide a possible connection to laboratory or field based peripheral instruments for measuring isotope ratios of, e.g. dissolved inorganic and organic carbon or carbonate minerals. Typical applications in the modern environmental realm include the high-resolution analysis of variable **greenhouse gas fluxes**, e.g. spatial and temporal variations of CO_2 and CH_4 concentrations and the respective stable C isotopic compositions emitted from natural gas production wells to the atmosphere (Maher et al., 2014). Online and on-site stable C and O isotope and gas concentration monitoring of ambient air CO_2 was conducted in cave systems in order to trace transient environmental conditions and associated processes at minute-range temporal resolution over a whole year (Töchterle et al., 2017).

Monitoring carbonate precipitation dynamics

Extended and detailed environmental observation of various natural and human-made settings hosting **modern carbonate formation** promotes an understanding of the dominant processes and parameters and implications of major environmental or material related relevance might be inferred from such monitoring efforts. The approaches of clarifying environmental controls on mineral precipitation are highly site-specific. However, increasing scientific and practical knowledge on the (un)favourable (pre)conditions of (un)wanted precipitation of minerals, as well as the associated evolution of fluids, result in an advanced process understanding of the **precipitation mechanisms** and potential **controlling measures**. The latter includes natural and technical possibilities of environmental parameter variation. For example, an environmental monitoring campaign conducted recently targeted the process understanding of unwanted, rapidly precipitated and several centimeter thick **mineral deposits in a human-made concrete river bed** (~1.5 km length) bypassing a repository of excavation materials from a major infrastructure project in Austria (Boch et al., 2015). The periodical on-site sampling and measurements in combination with laboratory and modelling based data enabled to constrain the prominent but rare precipitation of ikaite ($CaCO_3.6H_2O$) crusts in the upper and middle stream sections and more compact but thinner calcite crusts covering the refilled river sediments (colluvium) of the lower stream. Also, the highly anomalous hydrochemical conditions and evolution were evaluated in space (along the stream and tributary inlets) and time (over a year). The hydrochemical analyses revealed pH values up to 12.9 (instead of natural 7.5–8.5), calcium concentrations up to 200 mg/l (instead of 10–20 mg/l) and calcite supersaturation (SI values) up to 2.5 in the otherwise low ionic strength waters at this location (metamorphic host rocks). Ikaite could only be measured in the laboratory (by XRD, FT-IR and ESEM) after solid sample recovery from the river bed in its ambient aqueous solution, transport in refrigerated boxes and careful handling during analysis. The first ikaite samples recovered in plastic bags disintegrated into a loose powder consisting of microscopic calcite crystals within hours to few days. Mainly based on distinct relationships of hydrochemical parameters monitored, e.g. pH, electric conductivity, CO_2 partial pressure and concentrations of dissolved ions, the environmental conditions favourable of ikaite nucleation and rapid crystal growth could be constrained. In essence, enhanced portlandite ($Ca[OH]_2$) dissolution from the human-made concrete river bed resulted in a strong increase of Ca concentrations and pH and concomitantly decreased aqueous solution pCO_2. This in turn facilitated an efficient Ca-carbonate precipitation mechanism relying on the continuous absorption of CO_2 from the atmosphere and persistently increased dissolved inorganic carbon and Ca-carbonate (ikaite) supersaturation (Rinder et al., 2013; Boch et al., 2015). The **concrete leaching** and associated anomalous water chemistry were promoted by a restricted compaction and hardening of the river concrete basement in the course of cold (winter) water temperatures and time pressure, i.e. a higher porosity than usual, slower reaction kinetics during cement hydration and carbonation, as well as increased reactive surfaces and water access in the concrete. Owing to the efficiency of the determining Ca-carbonate precipitation mechanism and the sizes of the principal chemical reservoirs involved (concrete bed, atmosphere, streaming water), up to 2 $kg/m^2/d$ of ikaite deposition were calculated for the early stage of the aqueous solution monitoring. Importantly, the spatiotemporal monitoring in this "**field-based laboratory**" allowed for a better understanding of ikaite versus calcite formation. The few preconditions favouring ikaite include the prevailing cold water temperatures and prominently high Ca-carbonate supersaturation due to high pH, Ca contents and carbonate alkalinity supplied from large reservoirs. A major influence of calcite nucleation inhibitors (e.g. phosphate, organic constituents), strongly elevated ionic strength (saline conditions) or water mixing discussed in the scientific literature (e.g. Hu et al., 2015) could not be confirmed. However, based on the observed spatial and temporal relationships of ikaite and calcite also expressed in the different river sections, the **occurrence of metastable ikaite** could be restricted to temperatures ≤ 6° C, highly alkaline pH > 11, elevated Ca concentrations > 30 mg/l and Ca-carbonate saturation states clearly exceeding the solubility of ikaite. Regarding the temporal evolution of the ikaite precipitates, the monthly monitoring campaign showed a rapid vanishing of the ikaite crusts during a pronounced temperature rise > 6° C in springtime, i.e. most likely thermal decomposition and mobilization of metastable ikaite in the turbulent water flow occurred. In contrast, some hydrochemical parameters showed a more gradual change (e.g. decreasing pH and elemental concentrations) indicative of diminishing concrete leaching. In this respect, the monitoring also allowed some forecasting with regard to the return to geogenic hydrochemical conditions after a limited time of anthropogenic (construction related) impact. It should also be noted, that anomalously altered water chemistries hold the potential of leaching critical constituents (e.g. heavy metals) and thus of an environmental hazard, which was also evaluated in this particular case study.

Environmental monitoring further comprises **cave monitoring of speleothem growth dynamics** in order to utilize these mineral precipitates as paleoclimate archives (Mattey et al., 2008; Boch et al., 2011a; Riechelmann et al., 2013). These monitoring approaches of a natural system are of diverse complexity with regard to their spatial and temporal extent in the particular cave system and also regarding the application of automated in-situ instrumentation in combination with periodical cave visits. The majority of the case studies target a site-specific and detailed understanding of short- and long-term fluid-solid interaction determining the growth and composition of the speleothems. Consequently, aqueous solutions, gases and solid phases are typically monitored as well as the interrelated subsystems comprising of the cave atmosphere, seepage water, carbonate precipitates, soil zone and karst aquifer in relation to the prevailing regional meteorological and climate conditions on different timescales. In this respect, the daily to inter-annual variable hydrochemistry, water discharge, outside vs. inside temperature and air exchange, as well as the extent of modern Ca-carbonate precipitation are of principal interest. Temperature and meteoric precipitation amounts are the meteorological/climate parameters of major relevance regarding speleothem deposition and paleoenvironmental information archived. In many caves, the outside mean annual air temperature is reflected in a very similar average cave air temperature. However, exterior versus interior temperature gradients of variable spatial and temporal extent control the **cave air exchange** ranging from subtle cave breathing to pronounced cave winds (Fairchild & Baker, 2012). This cave ventilation is mostly relevant in regions possessing distinct seasons of the year and further strongly depends on the specific geometry of a cave system, i.e. the number, size and relative position of cave entrances and chambers. Based on these few preconditions, many caves exhibit some distinct cave ventilation dynamics, which can be traced by continuous measurements of air temperature, CO_2 and radon gas concentrations or air pressure (Fernandez-Cortes et al., 2009; Vieten et al., 2016). The ventilation pattern might either be constrained by some seasonally changing bidirectional chimney effect in the case of two or more cave openings (Spötl et al., 2005) or by intermittent trapping of cold (dense) and descending air (Boch et al., 2011a) or warm and ascending air (Boch & Spötl, 2011) through a single upper or lower entrance. Importantly, the air exchange has a strong effect on the cave air composition and the prevailing CO_2 partial pressure and gradients. This in turn affects the intensity of CO_2 outgassing and the hydrochemistry (e.g. pH) of the cave drip waters (Spötl et al., 2005; Mattey et al., 2016; Mickler et al., 2019). In **Katerloch Cave** (Styria), multi-annual cave monitoring revealed a dominant control of the common stalagmite fabrics (lamination), stable C isotopes and minor elements (Mg, Sr, Ba) in the calcite by seasonal contrasts in air temperature determining the intensity of unidirectional cave ventilation and further the rate of CO_2 degassing and the chemistry of the drip waters (e.g. Ca-carbonate saturation state) and finally the amount, geometry and porosity of the precipitated calcite on the growing speleothems (Boch et al., 2011a). In other words: "The air forms the rock" in Katerloch Cave. Interestingly, all of the investigated stalagmites in Katerloch (n = 22) show the same binary lamination pattern consisting of white, porous, fluid inclusion-rich layers with some tendency of enhanced (thicker) calcite deposition on the stalagmite central growth axis versus thinning towards the flank, as well as translucent, compact (dense) layers and more equally distributed calcite deposition across the growing stalagmite top. The recurrent pattern is intimately connected to distinct **warm and cold season modes** in this cave, which also affect other environmental proxies recorded in the stalagmite next to its petrography (Text-Fig. 10). These implications are mainly based on periodical hydrochemical analyses, as well as automated and highly-resolved temperature and CO_2 concentration data logging in comparison to meteorological data from weather stations nearby. Meteoric precipitation in the form of rainfall or snow acts as the principal atmospheric parameter controlling **water recharge** to the karst aquifer and thus **discharge** (drip rate) in Katerloch Cave has shown to exert an additional amplifying or attenuating influence on the seasonally prevailing and mainly temperature dependent speleothem growth mechanism. This is based on hourly drip logger and daily meteorological data in comparison to the periodically monitored hydrochemistry. Available multi-annual drip logger measurements from two active stalagmite precipitating drip sites in combination with petrographic evidence from these samples and older stalagmites support two major types of stalagmites in Katerloch, i.e. those of more regular seasonal lamination forming from more rhythmic (conservative) drip sites and those of more irregular inter-annual fabrics (high variability in lamina thickness) from sites of more individual sensitivity to karst water excess (Sakoparnig et al., 2016). Some **amplifying vs. attenuating effects** of variable drip water supply in relation to more

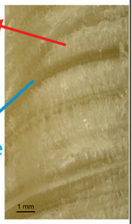

Environmental Proxies Layer type, $\delta^{13}C$, minor elements	Season	Ventilation	Cave air pCO_2	Cave air $\delta^{13}C$	Drip water chemistry SI_{Cc}	pH	$\delta^{13}C_{DIC}$	EC	Drip rate	CO_2 outgassing
white, porous inclusion-rich calcite low $\delta^{13}C$ low Mg, high Sr, Ba	warm (late spring - early autumn)	reduced	high	low	rel. low	low	low	high	typ. high	reduced
translucent, dense compact calcite high $\delta^{13}C$ high Mg, low Sr, Ba	cold (late autumn - early spring)	intensified	low	high	rel. high	high	high	low	typ. low	enhanced

Text-Fig. 10.
Based on multi-annual cave monitoring, the origin of layer formation and principal environmental dependencies of minor elemental and carbon isotope incorporation in stalagmite calcite could be constrained. These proxies revealed a distinct site-specific relation to seasonally prevailing physicochemical conditions reflected in variable cave air and drip water parameters. The process understanding of cave climate and speleothem growth allows for a reconstruction of paleoenvironmental information from the measured stalagmite carbonate proxies (adapted after Boch et al., 2011a).

rhythmic cave air exchange has also been observed for lamination, zonation and stable C and O isotope patterns archived in an active flowstone in the past (drillcores) and during a dedicated cave monitoring campaign (Boch & Spötl, 2011). In both cases, meteoric precipitation and typically related water discharge result in a variable water film thickness on the actively growing stalagmite or flowstone growth surface, which partially controls the effective CO_2 diffusion and outgassing rates from the water to the cave atmosphere. As mentioned earlier, this is further controlled by the prevailing CO_2 partial pressures and gradients in the course of a variable soil zone, karst aquifer and cave atmospheric state and evolution of free vs. dissolved CO_2 (Mattey et al., 2016; Mickler et al., 2019).

From the detailed monitoring of site-specific and in many cases widely distributed carbonate precipitation dynamics, distinct environmental proxy dependencies can be inferred. These constitute a promising starting point for qualitative and quantitative paleoenvironmental reconstructions from the mineral precipitates. In Katerloch Cave, the process understanding of lamina development and selected elemental and isotopic compositions in relation to the prevailing atmospheric conditions promotes an array of possible investigations with regard to climate change of the recent to ancient past (Text-Fig. 10). Based on a **multi-proxy approach**, this includes potential regional reconstructions and overall implications on air temperatures, as well as meteoric precipitation amounts and distributions. Even in the case of comprehensive monitoring efforts, a modern calibration of temperature and precipitation dependencies is challenging, although key to numerical environmental transfer functions (Tremaine et al., 2011; Mickler et al., 2019). Nevertheless, valuable insights into fundamental processes of carbonate crystallization, equilibrium vs. kinetically influenced elemental and isotope fractionation can result from the periodical or high spatiotemporal resolution monitoring in different settings.

Next to more or less purely inorganic hydrochemical variations and related carbonate mineralization, high-resolution environmental monitoring also includes **biological** and mostly **microbial processes** in diverse natural and man-made settings. For example, using a **CO_2-flux monitoring chamber**, the states of dissolved CO_2 and O_2 in connection with variable aquatic photosynthesis, dissolved inorganic carbon contents and autochthonous organic matter were monitored in 15 min intervals over a daily cycle (Liu et al., 2015). Sevilgen et al. (2019) monitored coral calcification in vivo applying microsensors and fluorescent dyeing tracers in order to spatiotemporally constrain the vital Ca-carbonate chemical constituents during biomineralization. Microbial metabolic processes were further monitored with regard to unwanted scaling and corrosion impairing geothermal wells and heat exchangers (Würdemann et al., 2014). In this context, site-specific biofilm formation and in particular microbes of the sulphur, nitrogen and iron redox-chemical cycles can be monitored by connecting a **mobile bypass system** to the hydrothermal fluid flow. Regarding geothermal installations, intermittent stagnant conditions in the course of production cessations have shown to be of major relevance due to microbial activity enhancing temperature effects and unfavourable oxygen ingress (Würdemann et al., 2014). Further considering anthropogenic settings, on-site and online monitoring of dominant carbonate precipitation affecting technical (e.g. tunnel) drainages constitutes a field of interesting developments. For example, the concept and prototype of a "**Sinterwächter**" (scale guard) seeks for an automatization in monitoring hydrochemical scaling potentials based on principal and reliable parameters (e.g. EC, pH; Dietzel et al., 2013). This high temporal resolution and spatially flexible monitoring approach includes a telecommunication based data transfer from the geotechnical infrastructure and new field- and laboratory based test environments (e.g. Koralmtunnel) and technical improvements constitute some promising work in progress. The latter also involves an increased process understanding of scale material characteristics deriving from complex fluid-solid interaction (see respective chapter), as well as the inclusion of efficient and automated countermeasures.

Carbonates from the 'Erzberg' Iron Ore Mine (Austria)

The **iron ore deposit** "Erzberg" might be Austria's most prominent geo-site based on its historic, socio-economic and geoscientific standing. It represents the largest siderite ($FeCO_3$) occurrence worldwide and the conspicuous pyramid shape of the iron-rich mountain range (1,532 m a.s.l. originally; 1,466 m today) and current open pit mine results from 30 successive stages of 24 meters height (Text-Fig. 11). Up to now, ~245 million tons of iron ore carbonate were processed by the VOEST-Alpine steel industry at Erzberg (up to 3 million tons/year) and ~150 million tons future reserves are available for delivery to the manufacturing sites in Linz and Donawitz (Prochaska, 2012). Erzberg hosts **various carbonate minerals** including widespread siderite, ankerite, dolomite, calcite, aragonite and several others, which make it an interesting location for carbonate research. Aside from the dominant Ca-carbonates (calcitic limestone) and Fe-carbonates (siderite, ankerite) a broad range of accessory sulfide minerals (pyrite, chalco- and arsenopyrite, sphalerite, galenite, fahlore, cinnabar), as well as silica minerals (muscovite, quartz) are characteristic of the local rocks (Thalmann, 1979; Schulz et al., 1997). Geologically, the iron ore deposit belongs to the Greywacke zone at the base of the Northern Calcareous Alps and was involved in Variscan nappe stacking of dominant Devonian limestones and Carboniferous dark siliceous schists followed by a Permo-Triassic transgressional phase and Alpine synclinal tectonic deformation during Cretaceous times (Bryda et al., 2013). Silurian/Devonian limestones and dolostones host the closely related siderite and ankerite ($[Ca,Fe,Mg]_2[CO_3]_2$) iron concentrating mineralization, which was further (partially) overprinted during Alpine metamorphism. The **source of the iron** and genetic evolution of the ore deposit constitute a subject of ongoing geoscientific debate involving the two principal ideas of a marine-volcanic-exhalative-synsedimentary formation versus a metasomatic-epigenetic origin (Schulz et al., 1997; Prochaska, 2012). In recent times, a later-stage metasomatic-epigenetic alteration of the original Silurian/Devonian host rock carbonate (Sauberger Kalk) by buried hypersaline (evaporitic) brines and Late Triassic (based on Sm/Nd radiometric dating) hydrothermal fluid mobilization under redox reductive and acidic hydrogeochemical condi-

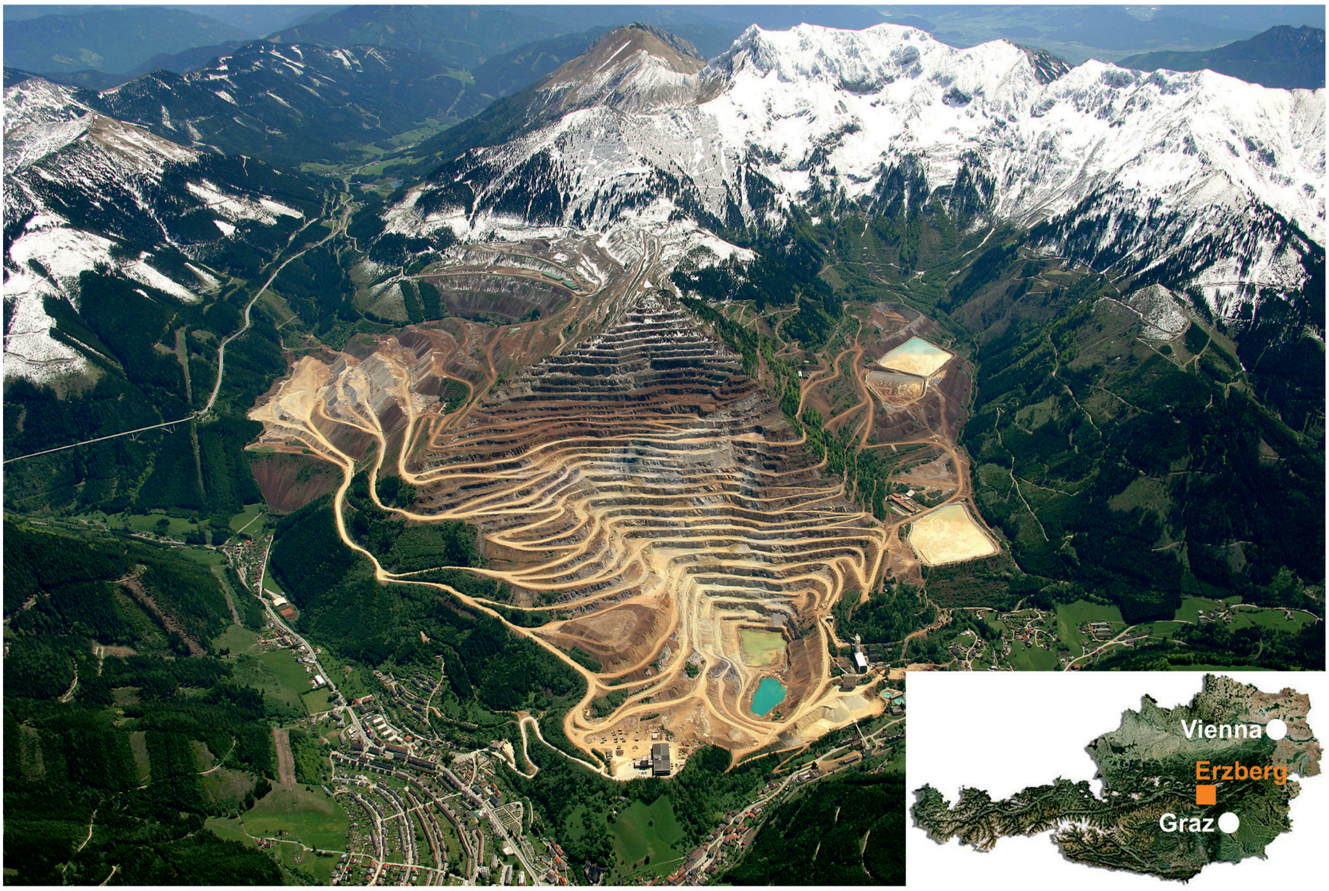

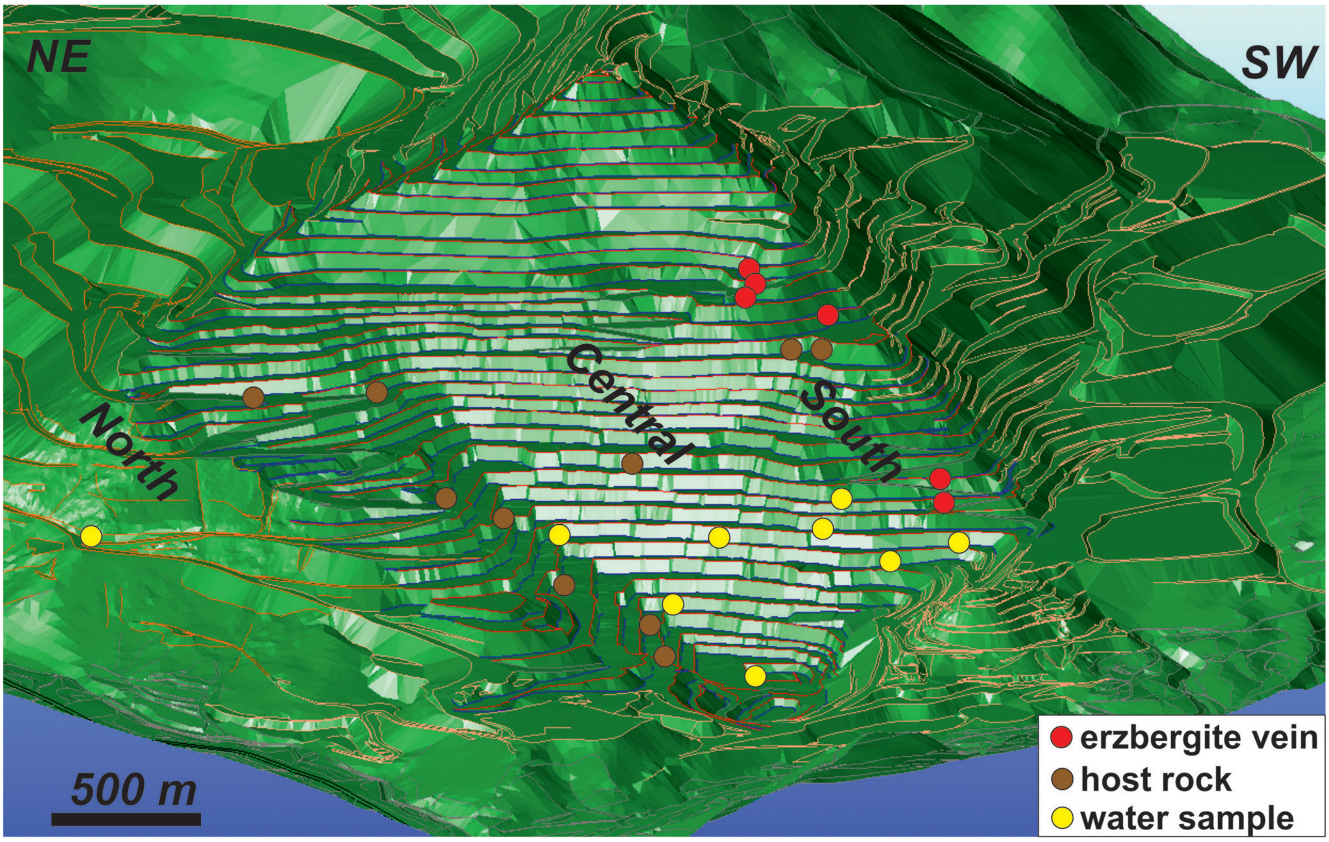

Text-Fig. 11.
Overview and sample locations at Erzberg. Upper image: Aerial impression of the Erzberg open pit iron ore mine and the surrounding Alpine area located in Austria between Graz and Vienna (small map). Lower image: Digital terrain model of Erzberg showing the sampling positions of erzbergite veins, various host rock carbonates, as well as water from small fracture and surface streams (adapted from Boch et al., 2019). Note the preferred occurrence of the $CaCO_3$ vein samples in the more southern Erzberg section.

tions is promoted as the most plausible explanation (Prochaska, 2016). Erzberg carbonate host rocks further allow for the local mineralization of prominent $CaCO_3$ (aragonite, calcite) **veins filling vertical fractures** of centimeter to several decimeters width and often tens of meters length (Hatle, 1892; Boch et al., 2019). The mostly layered (laminated) and visually outstanding precipitates are addressed as "**Erzbergite**" in private and museum mineral collections, some decorative contexts and the sparse scientific literature (Angel, 1939). In the vast majority of erzbergite material encountered on-site, the respective fractures are completely filled (sealed) by these mineral precipitates and their thickness typically reflects the local fracture extension (Text-Figs. 12A–C). In a study published recently, their origin and depositional dynamics, ages and temperatures of formation, as well as related environmental preconditions and implications have been evaluated in detail based on state-of-the-art geochemical and petrographic analytical tools (Boch et al., 2019). In addition, the so-called "**Eisenblüte**" (iron flower) carbonate precipitates represent fragile dendritic and aragonitic mineral formations in rare open fractures and are often closely associated with the flowstone-like erzbergite veins (Hatle, 1892; Angel, 1939). These prominent and wanted mineral formations resemble helictites (eccentriques) forming under specific conditions in some karst caves (Onuk et al., 2014). Interestingly, these aragonite dendrites have not been studied in detail, i.e. they might hold some promising scientific potential regarding an increased understanding of aragonite nucleation during purely inorganic versus possible microbially mediated processes.

In an attempt of **(re)evaluation and increased process understanding** of the carbonate occurrences at Erzberg, new sampling campaigns, field- and laboratory based and often high-resolution and sensitive analytical techniques were recently applied and further work is currently in progress. The sampling included the **major carbonate host rocks**, such as siderite and ankerite dominated sections of the iron ore body, as well as variably altered limestone and dolostone samples recovered on-site from different levels of the open pit mine (Text-Fig. 11). In addition, reworked and partially iron-rich basal breccia material (Permian age; Schulz et al., 1997) was sampled, as well as some specimens of localized pyrite mineralization. The investigation of these samples was mainly focused on genetic and geochemical aspects of the local iron enrichment at Erzberg and also regarding their role as source rocks of the prominent erzbergite vein formation in fractures. **Selected representative erzbergite samples** (n = 25) were collected on-site from the rare veins currently accessible and being mostly located in the southern part of Erzberg (Text-Fig. 11). Interestingly, some of the fractures filled with erzbergite also showed slickenside striations and distinct cataclastic rocks and the latter were also sampled in oriented fashion for further microstructural and chemical analysis. In addition, erzbergite samples from our university collection and private collectors were analysed. The detailed evaluation was mainly focused on the origin and spatiotemporal growth dynamics of the aragonite-calcite veins and their potential value as a chemical-sedimentary environmental archive. In this context, radiometric U-Th dating, high-resolution electron microprobe elemental mapping, as well as stable (C, O) and clumped isotope measurements were conducted for the first time (Boch et al., 2019). In order to better constrain the site-specific water-rock interaction at Erzberg, **modern waters** were collected and analysed in July 2015 and April 2016 from fracture and surface flows of different sections (Text-Fig. 11). The analyses included a broad range of hydrochemical and stable isotopic (H, C, O, S) parameters, as well as aqueous solution modelling (Boch et al., 2019).

Considering the principal research questions, scientific approach and new insights envisaged, the **current research activities at Erzberg** can provide contributions to different geoscientific aspects of regional to fundamental relevance. A detailed evaluation of the prominent erzbergite veins contributes to a better understanding of **vein mineralization** and of associated (brittle) fracture formation and filling and further of the widespread aragonite-calcite relationship. In the realm of vein formation, a growing interest is mainly boosted by the investigation of wanted as well as unwanted carbonate precipitation in deep porous sediment or fissured rock reservoirs (aquifers). For example, the fostered precipitation of long-lasting carbonate minerals in the course of geotechnical CO_2 sequestration (CCS – carbon capture and storage, e.g. in peridotite or basaltic rocks; Kelemen & Matter, 2008; Matter et al., 2016), CO_2-based geothermal energy production (Randolph & Saar, 2011; Buschek et al., 2014), reinjection of saline fluids (Rivera Diaz et al., 2016) or the determination of paleofluid sources and effects in fault zones and Earthquake areas (Luetkemeyer et al., 2016; Pagel et al., 2018) constitute major research fields interested in vein mineralization. Also, genetic aspects of layering (lamination) and carbonate diagenesis can be targeted next to an application of the spatiotemporally evolving veins as a regional chemical-sedimentary archive capturing paleoenvironmental information and the timing and progress of past or recent (neo)tectonic and gravitational mass movements dissecting the Erzberg mountain range. Similarly, new geochemical information based on non-traditional isotopic techniques, could shed light into genetic aspects of the **iron ore formation**. This involves the regional source and concentration of iron and other metals, the potential role and chemistry of paleofluids, the timing of the processes and the metasomatic or metamorphic alteration of the ore deposit. Further, a reliable connection to other locations and episodes of Alpine ore formation (e.g. magnesite deposits) might be established.

Growth dynamics of aragonite-calcite veins ("Erzbergite")

The principal hydrogeochemical mechanisms and environmental dependencies of erzbergite vein formation were analysed in a comprehensive field- and laboratory based investigation (Boch et al., 2019). In particular, new and detailed insights have arisen from the application of high-resolution petrographic and elemental imaging, as well as non-traditional (clumped, U-Th) isotopic techniques. Mineralogical and chemical characterization of different erzbergite veins revealed a clear **dominance of aragonite precipitation** in comparison to pristine **calcite**, i.e. initial calcite crystallization is typically restricted and in fact relatively rare in the fractures at Erzberg. Rather, most of the calcite observed in several of the samples is obviously of **diagenetic origin** following the replacement of former aragonite and the later-stage diagenetic alteration pref-

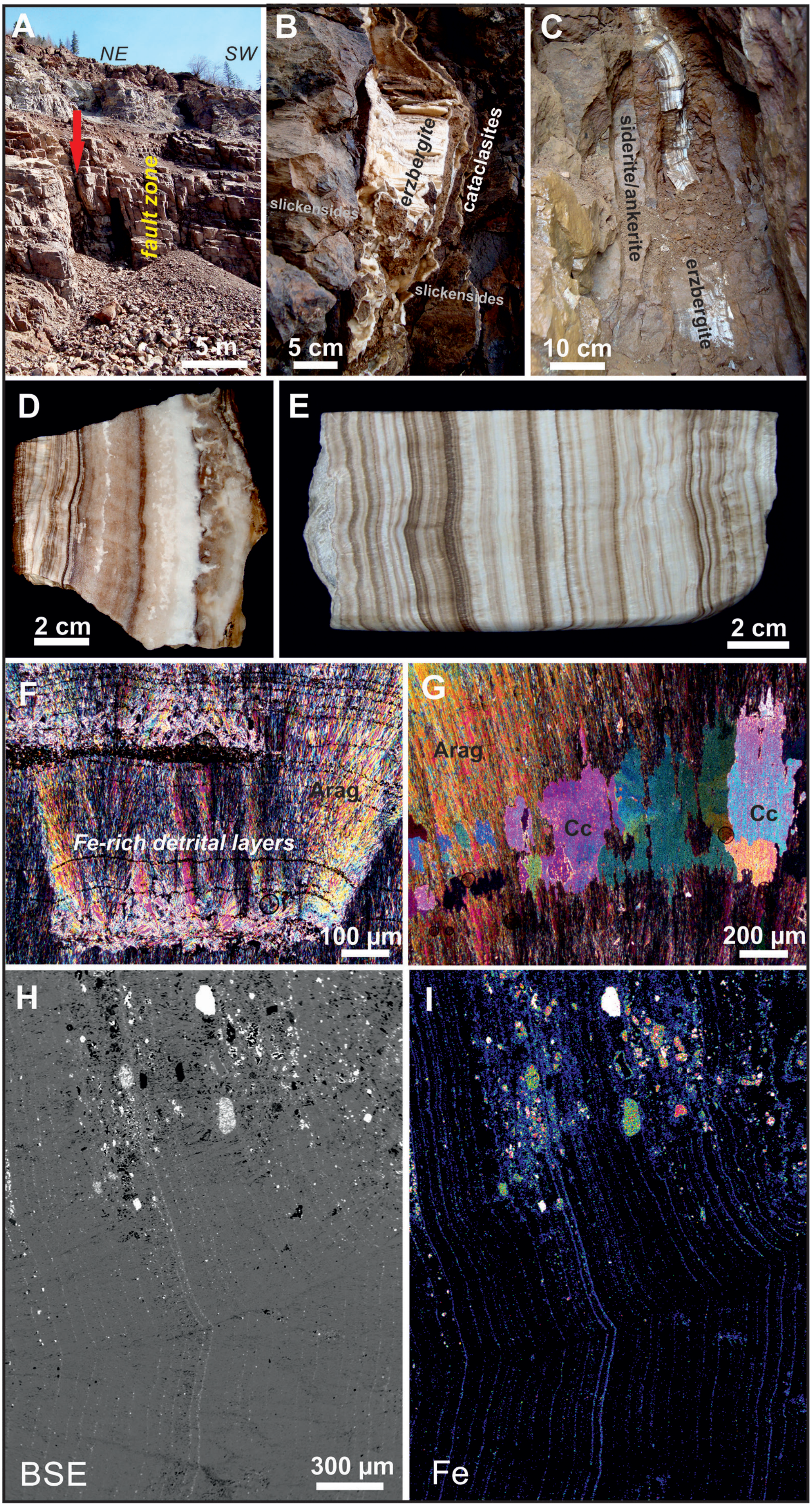

erentially occurs across layers of different thickness and lateral extension (Text-Fig. 12D). Elemental distribution mapping of selected erzbergite sample sections in combination with hydrochemical analysis of modern fracture and surface waters at Erzberg strongly support a major control of the aragonite-calcite polymorphism by conspicuously high aqueous molar **Mg/Ca ratios** (2 up to 26 measured) – inhibiting calcite nucleation – as well as overall high $CaCO_3$ supersaturation (SI_{Arag} up to 1.3; Boch et al., 2019). Only few of the samples showed some indication of scarce microbial presence, i.e. playing an ac-

Text-Fig. 12.
Characteristics of erzbergite veins precipitating in fractures at Erzberg. A) Brittle fault zone of the southern section including two major vertical fractures filled with erzbergite and cataclasite (position of image B marked by red arrow). Slickensides indicate a sinistral strike-slip movement. C) Typical Ca-carbonate vein entirely sealing a formerly open fracture of the surrounding Fe(Ca,Mg)-carbonate host rocks. D) Erzbergite sample collected on-site showing characteristic layering comprising of a mm-scale lamination, broader (cm) zonation, recurrent brownish stained layers and localized carbonate fabrics indicative of partial diagenetic alteration (Arag → Cc). E) Nicely laminated sample from a mineral collection. F) Thin section transmitted-light image (crossed polars) displaying a typical radial fascicular aragonite section in erzbergite interrupted by multiple thinner but variable intra-crystalline particle layers. G) Common diagenetic replacement of pristine and dominant acicular/fascicular aragonite towards mosaic calcite crystals. The diagenetic alteration starts as patches and progresses preferentially across layers. Note the horizontal (vs. in-situ) orientation of erzbergite in the images F) and G). H) Back-scattered electron microprobe image supporting the detrital particulate character of the brownish stained layers within erzbergite. In most vein samples, these detrital layers show more irregular recurrence intervals and thicknesses. I) Electron microprobe based iron concentration distribution indicative of Fe-rich (Fe-carbonates, Fe-[hydr]oxides) detrital particle layers.

tive or passive role in the course of erzbergite deposition. Regarding the mineralogy, the iron mineral goethite and the siliciclastic minerals muscovite and quartz were detected in the brownish-stained layers. Further considering their particulate (different grain sizes) and variably thick character, these stained layers can be interpreted as detrital and **Fe-rich particle layers** within the aragonite-calcite succession. They are sourced by the oxidative corrosion of the widespread Fe-carbonate host rocks (siderite, ankerite) and accessory Fe-sulfides (pyrite) and subsequent detrital mobilization and local sedimentation in the vertical fractures. Regarding the erzbergite petrography, **layering** is a widespread textural feature, which can be differentiated into a narrow (mm-scale) lamination and a broader zonation (cm-scale banding) pattern (Text-Figs. 12D, E). The laminae represent an original growth feature primarily based on the visually outstanding and repeated deposition of the brownish-stained Fe-rich detrital particle layers and the zonation mainly depends on the predominance of either snow-white aragonite or more beige coloured and mostly diagenetic calcite. A regular (e.g. seasonal) alternation of aragonite and calcite proposed in earlier studies (Hatle, 1892; Angel, 1939) could not be confirmed from the vein samples studied (Boch et al., 2019). Additionally, high-resolution petrographic and chemical analysis in combination with radiometric U-Th dating revealed a typically **irregular (episodic) nature of the layering**, i.e. only few erzbergite sample sections showed some closely spaced and most likely periodical deposition of thin detrital particle layers (e.g. from snowmelt; Text-Figs. 12F–I).

Considering the driving mechanism of carbonate dissolution, mobilization and erzbergite vein mineralization, analyses of modern waters at Erzberg in connection with solid-phase mineralogical and stable isotopic analyses strongly support **sulfide oxidation** of the widespread accessory sulfide minerals in the host rocks as a major geochemical precondition. Increased dissolved sulphate concentrations (up to 226 mg/l) in the modern waters, sulphate $\delta^{34}S$ values ranging from -4.9 to +2.5 ‰ (VCDT), increased $\delta^{13}C$ values of dissolved inorganic carbon (DIC; +2.4 to +3.8 ‰ VPDB), as well as persistently high erzbergite $\delta^{13}C$ compositions (up to +6.8 ‰ VPDB) are the most striking features of common sulfide oxidation and related **sulfur acidic** carbonate host rock and accessory mineral dissolution, i.e. an efficient aqueous mechanism involving a relatively strong acid. Stable C and O isotope analyses of the principal host rock carbonates at Erzberg and of numerous erzbergite aragonite-calcite samples yielded limestone/dolostone (Sauberger Kalk), as well as ankerite being the **main source rocks** of vein mineralization in fractures, i.e. the local lithology is reflected in the erzbergite isotopic composition to a variable degree (Boch et al., 2019). In addition, the spatially and temporally variable **hydrochemical evolution** in the dominantly fissured carbonate aquifer results in significant local differences with regard to the aqueous solution chemistry and directly related potential for erzbergite formation. Based on a limited number (n = 10) of modern water analyses, systematic **local differences** between the more **southern, central and northern Erzberg sections** could be claimed. More specifically, from a modern hydrochemical point of view, $CaCO_3$ precipitation should be more pronounced in the southern part and this is in line with the majority of erzbergite samples encountered on-site in the southern Erzberg section today (Text-Fig. 11). These findings are probably related to spatially distinct sources and flow paths of the vein precipitating aqueous solutions. In this context, the hydrogeochemical analyses conducted revealed the occurrence of some characteristic mechanisms of fluid-solid interaction at Erzberg. This includes the prevalence of **prior $CaCO_3$ precipitation** mostly for water flows in the southern section, i.e. the hydrochemical evolution strongly depends on the successive loss (precipitation) of Ca-Carbonate (aragonite or calcite) during water percolation. Such a fractionating mechanism is indicated by the prominently enriched molar Mg/Ca ratios, the Mg/Ca vs. Ca concentration distribution (inverse relationship), strongly increased $\delta^{13}C$ of DIC and erzbergite, and the preferred depletion of Sr, Ba and U concentrations in aqueous solution in the case of prior aragonite precipitation. Furthermore, hydrochemical processes such as **evolving CO_2 outgassing** and pH buffering are of major relevance at Erzberg and are intimately connected to prior and vein $CaCO_3$ precipitation. An enhanced potential of CO_2 degassing arising from principal chemical reactions, such as siderite/ankerite oxidation, sulfur acidic dissolution of limestone/dolostone or ankerite and the different forms of Ca-carbonate precipitation at Erzberg is supported by increased CO_2 partial pressures calculated for the aqueous solutions (log_P_{CO2} of -3.2 to -2.3), compared to the overall prominently elevated C isotopic signatures (Boch et al., 2019). Pronounced **pH buffering** of the evolving waters imprinted by sulfide oxidation and sulfur acidic dissolution, is strongly suggested by the overall high pH values (8.1–8.8) measured and further by the high $CaCO_3$ supersaturation (SI_{Arag} of 0.7 to 1.3; SI_{Cc} of 0.8 to 1.4) calculated based on the local water analyses from different sections at Erzberg. This can be explained by the dominance of various and in principal alkaline carbonate host rocks constituting the fissured carbonate aquifer and thus interacting with the variably acidic solutions. Based on distinct aqueous speciation plots (e.g. Mg vs. Ca. vs. sulphate), the occurrence of some **incongruent dissolution** (e.g. dedolomitization) is suggested with focus on the more central Erzberg section. This hydrochemical mechanism well known from carbonate aquifers relies on the different solubility behaviour and the counteracting crystallization potential of the involved carbonate minerals, e.g. slow dissolution of ankerite or dolomite and the concurrent supersaturation and kinetically-favoured precipitation of aragonite or calcite in fissures and fractures of the Erzberg aquifer.

The first clumped isotope measurements conducted at Erzberg, as well as the typical stable O isotope compositions of the vein carbonates (-11.5 to -5.1 ‰ VPDB) support a **meteoric origin of the erzbergite precipitating aqueous solutions**, i.e. the waters evolving in the fissured aquifer originate from a spatiotemporally variable infiltration of rain or snow. The $\delta^{18}O$ signatures of the original fluids calculated from the Ca-carbonate clumped isotope analyses (Δ_{47} based temperature vs. $\delta^{18}O_{carb}$) range from -11.8 to -8.7 ‰ (VSMOW) and are thus similar to values measured in modern waters at Erzberg ($\delta^{18}O$: -11.2 to -7.7 ‰; Boch et al., 2019) and values based on the Austrian Network of Isotopes in Precipitation (observation station Wildalpen; altitude corrected mean annual $\delta^{18}O$ values of -13.1 ‰ and warm season values of -10.7 ‰; Hager & Foelsche, 2015). Stable H and O isotope measurements of the modern waters further suggest a different meteoric water infiltration area for the southern vs. central and northern sections, i.e. the latter might be sourced from an infiltration area of higher altitude and a higher proportion of cold season precipitation (overall lower δ^2H and δ^{18}O values). Along with the O isotopic paleofluid composition, the clumped isotope analyses also provided reliable and relatively precise constraints on the **formation temperatures of the erzbergite vein precipitates**. Replicated measurements from multiple samples (n = 7) yielded crystallization temperatures from +2 to +9° C (~5° C on average) involving uncertainties of ± 2–8° C based on the temperature calibration of KLUGE et al. (2015). Therefore, the erzbergite veins represent a rare case of dominant aragonite nucleation at cool to near-freezing temperatures and the elevated altitude Alpine setting is reflected in these meteoric (in contrast to hydrothermal hypogenic) carbonate precipitates. These mineral deposits also show some systematic variation depending on their timing of formation (BOCH et al., 2019). Regarding the site-specific formation conditions, the initial **opening of fractures** constitutes an essential prerequisite providing preferential water flow routes and fresh chemical reaction surfaces for pronounced fluid-solid interaction involving sulphide oxidation and the various hydrochemical mechanisms mentioned before (Text-Fig. 13). The dominantly vadose flow regime in the fissured carbonate aquifer results in a uni- or bidirectional growth of erzbergite in the vertical fractures, i.e. vein mineralization progressing from one or both adjacent fracture walls towards complete sealing (Text-Figs. 12A–C). Based on a rich dataset of radiometric **^{238}U-^{234}U-^{230}Th age determination** of erzbergite samples, the typical **growth rates of these veins** can be constrained to some tens of micrometres per year. For example, considering a typical fracture of 10 cm width and a conservative growth rate of 0.02 mm/year in combination with progressive unidirectional erzbergite deposition, it would only take ~5,000 years to entirely seal the void. This corresponds well to the U-Th dating results obtained for many of the samples analysed and a bidirectional growth evident in some erzbergite samples might even proceed more rapidly. Regarding the **absolute ages and their distribution in time**, the erzbergite samples dated so far (n = 20) yielded ages from 285.1 ± 3.9 to 1.03 ± 0.04 kyr BP (thousands of years before 1950 A.D.), i.e. a relatively broad range during the late Pleistocene with some samples as new as the historical age (BOCH et al., 2019). In most cases, the relative age uncertainties (2σ) are of high precision and range within 0.5 to 1 % of the absolute age and thus within ± few hundreds of years mostly depending on the highly variable initial U concentrations (^{238}U from 7 to 3,120 ppb) and detrital Th contamination (^{232}Th from 20 to 96,180 ppt). Most samples revealed a rather continuous growth from their base(s) to top(s) and consequently represented a relatively narrow time interval of deposition (some thousands of years). Only few erzbergite samples showed longer-term growth interruptions and thus captured a large time range. Interestingly, all of the erzbergite samples recovered from currently accessible fractures on-site yielded U-Th ages younger than the Last Glacial Maximum (< ~20 kyr BP) in the Alps, i.e. these carbonate veins are of unexpectedly young geological age. Furthermore, the age distribution strongly supports a preferred erzbergite vein formation during favourable – warm and wet – environmental conditions (Text-Figs. 14, 15). This prominent environmental dependency is clearly related to the hydrogeochemical mechanisms and elevated altitude Alpine setting of erzbergite formation. A conceptual model of the spatiotemporally variable vein growth dynamics at Erzberg is summarized in Text-Figure 13.

Environmental implications on fracture formation and paleoclimate

Based on the new **geochemical investigations** at Erzberg and the more detailed process understanding gained (e.g. erzbergite growth dynamics), various modern and past **environmental dependencies** can be inferred. In particular, implications and potentials with regard to studies on fracture formation and distribution, paleoclimate information from the erzbergite chemical-sedimentary archive and genetic aspects of the iron ore carbonates arise in the context of the recent and ongoing research activities.

The **opening of fractures** constitutes an essential prerequisite with regard to water flow in the fissured carbonate aquifer and related erzbergite vein deposition at Erzberg. Importantly, the open fractures of different width and ver-

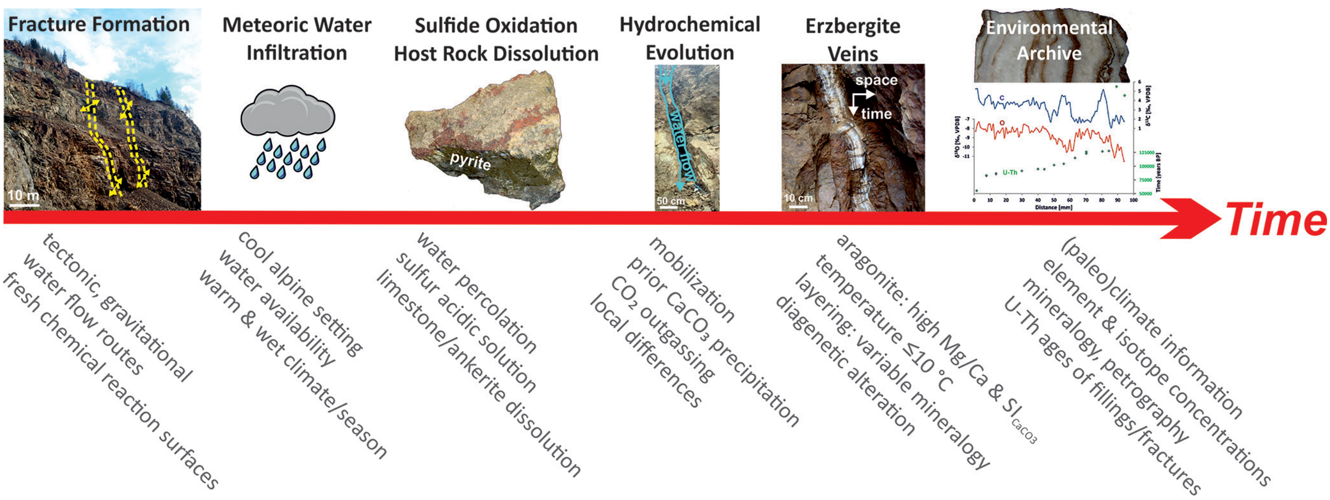

Text-Fig. 13.
Conceptual model of spatiotemporal erzbergite vein formation at Erzberg. The growth dynamics can be illustrated by an essentially stepwise evolution starting with the opening of fractures and associated fresh chemical reaction surfaces towards a potential application of the chemical-sedimentary deposits as a (paleo)environmental archive.

tical extension provide fresh chemical reaction surfaces of the various host rock carbonates and accessory sulphides promoting a distinct hydrochemical evolution of the infiltrating meteoric waters. As seen in the previous chapter, this involves an array of chemical reactions, such as sulphide oxidation and Fe^{2+}-carbonate corrosion, sulphur acidic vs. pH buffered aqueous solutions, (incongruent) carbonate host rock dissolution and mobilization, prior $CaCO_3$ precipitation and CO_2 outgassing, and finally Ca-carbonate vein precipitation and **sealing of the fractures** (BOCH et al., 2019). An overall high efficiency and rapid rates of these physicochemical processes is supported by the radiometric U-Th dating results from erzbergite samples, i.e. the aragonite-calcite veins typically represent relatively short time intervals (some thousands of years) of complete fracture filling and average growth rates of a few tens of micrometres per year were inferred. Analyses of modern waters collected at Erzberg clearly showed a high potential for ongoing Ca-carbonate vein precipitation, i.e. high total dissolved solid contents, high aragonite and calcite supersaturation states, high aqueous solution pCO_2 and thus outgassing and pH increasing tendencies (BOCH et al., 2019). In principle, the mechanism of erzbergite vein mineralization in fractures at Erzberg is still at work based on the modern hydrochemistry, however, the open pit mining activities and in particular the frequent mobilization of dust might exert some disturbing (inhibiting) effect on currently precipitating carbonates in fractures near the surface (dust coatings observed by the author). In essence, these observations and underlying mechanisms of fluid-solid interaction, the consistently young age (< 20 kyr BP) of erzbergite sampled on-site and the typically rapid and complete sealing of the fractures strongly support a **geologically young age of the fractures**. It seems highly unlikely that the vertical fractures have remained open over extended geological time intervals (e.g. hundred thousands or millions of years) and were then filled more or less instantaneously in the recent past. More likely, the opening of a fracture, as well as the occurrence of relatively warm and wet environmental conditions promoting erzbergite growth in this overall cool Alpine Erzberg climate setting, marks the initiation and often rapid progress of fracture sealing.

Evaluating the principal **origin of the fractures** filled with young erzbergite veins, the associated rock movements could either be the expression of gravitational or (neo) tectonic and seismic forces. Regarding a **gravitationally induced** rock failure and displacement, the repeated occurrence of warm climate intervals (interglacials) versus ice ages and related ice cover of mountain ranges and ice streams in valleys should be considered in the Alpine realm during the Late Pleistocene, i.e. the time interval represented by erzbergite samples dated so far (VAN HUSEN, 2009; LUETSCHER et al., 2015). In particular, rock movements could be initiated in the course of glacier and permafrost ice melting and eventually by some regional isostatic rebound after relief of strain or by oversteepened mountain flanks after glacier retreat. The last glaciation (Würm) and its glacial maximum (LGM) in the Erzberg area, however, only featured a relatively minor ice cover, i.e. patches of ice on high mountain tops east of the major connected ice-stream network and the basin of Eisenerz has not been glaciated (VAN HUSEN, 2009; BRYDA et al., 2013). In principal, the aforementioned possible gravitational mass movements should be characterized by dominantly **vertical rock movements**. In some of the fractures filled with erzbergite, however, indications of **lateral movements** including slickensides, cataclasites, kakirite and adjacent damage zones were encountered and these fractures can thus be classified as **fault zones** (Text-Fig. 14). The cataclastic rocks appear mostly in original position (on vertical fracture walls) and can be traced for several meters. Thin section inspection revealed a matrix supported fabric hosting radially disrupted and displaced fragments, elongated and rotated clasts, as well as mm-scale secondary carbonate veins. Importantly, the cataclastics are also cemented by the erzbergite Ca-carbonate precipitates. The orientation of the sinistral slickenside striations on the fracture walls hosting the cataclasites strongly supports directed **strike-slip faulting** and therefore a potential **tectonic origin** (Text-Fig. 14). In connection with the consistently young U-Th ages of erzbergite veins sampled in the field, this raises the principal question of a correspondingly young age of the cataclastic rocks and the slickensides, i.e. a possible origin from some neotectonic activity. These unexpected findings are further supported by the hydrogeochemical mechanism of typically rapid erzbergite infilling and the comparatively soft (immature) material consistency of the formerly more or less uncemented cataclastic rocks adhering to the vertical fracture walls makes it unlikely for these rocks to be spatially stable in an open fracture over extended time intervals. From a regional tectonic and structural geology point of view, the Erzberg area is encircled by major and minor Alpine fault systems, e.g. the two major and sinistral SEMP (Salzach-Ennstal-Mariazell-Puchberg; main strand ~10 km from Erzberg) and Mur-Mürz fault systems, the Trofaiach fault, Palten-Liesingtal fault and Gesäuse fault (BRYDA et al., 2013). Some evidence for potential neotectonic activity also comes from the displacement of relatively young speleothems constrained to Last Glacial times in Hirschgruben Cave (Hochschwab mountain range; PLAN et al., 2010). In a recent publication, BAROŇ et al. (2019) report the registration of active displacements in selected cave systems of that region based on two years of monitoring applying Moiré extensometers. The nearby "Rockslide of Wildalpen" event was dated to ~5800 yr BP and a minor local earthquake or major regional earthquake associated with the fault systems listed before was discussed as a trigger (VAN HUSEN & FRITSCH, 2007). Further, modern earthquakes are relatively frequent in the wider Erzberg area, e.g. a major earthquake in Leoben in 1794 or a minor seismic event in Eisenerz in 1964 (magnitude 2.7; LENHARDT et al., 2007). In principle, the fractures/faults at Erzberg could be part of a conjugated system, i.e. sub-faults of the dominant – mostly sinistral and strike-slip – regional fault regimes not recognized as such at Erzberg so far. For example, brittle tectonic conjugated faults involving cataclasites and affecting carbonate host rocks were reported from three locations relatively close to Erzberg and were related to the major SEMP fault system (HAUSEGGER & KURZ, 2013). First measurements of the principal orientations of vertical faces and slickenside striations in some of the prominent erzbergite filled fractures/faults also support a possible connection to the SEMP fault system. In this tectonic context, these fractures could therefore be another expression of an ongoing uplift and eastward lateral extrusion of the Eastern Alps (DECKER et al., 2005; PLAN et al., 2010; Baroň et al., 2019). Moreover, some fractures and associated erzbergite vein samples show indications of a possible **reactivation of the faults** (episodic slip). Sample EB9 from a fracture accessible in the southern Erzberg section on level Schuchart (~1,110 m a.s.l.; Text-Fig. 14) precipitated in close spatial relation to two different generations of cataclastic rocks, which are probably the expression of two distinct tectonic events. Multiple and precise radiometric U-Th measurements of the adjacent erzbergite aragonite yielded ages ranging from 19.21 ± 0.10 to 13.11 ± 0.09 kyr BP (Text-Fig. 14). Interestingly, the oldest ages (orange in Text-Fig. 14) came from aragonite closest to the fracture wall hosting the cataclasites, while another group of subsamples (red in Text-Fig. 14) shows systematically younger ages towards complete sealing. Possible reactivation and associated opening of fractures is also supported by sample EB2 (cf. Boch et al., 2019 and Text-Fig. 15). The vein sample shows an older interval dated to 285.1 ± 3.9 and 229.6 ± 2.1 kyr BP characterized by bidirectional growth towards complete filling of the void and a much younger interval starting from ~128.16 ± 0.66 to 55.54 ± 0.27 kyr BP and being characterized by unidirectional growth (on one fracture wall) towards complete fracture sealing. These observations are supported by the

Text-Fig. 14.
Brittle fault (damage) zone hosting two major vertical fractures in the southern part of Erzberg both entirely sealed with erzbergite carbonate (level Schuchart, ~1,110 m a.s.l.). The northern (left) fracture features slickensides and two generations of cataclastic rocks. Multiple and precise ^{238}U-^{234}U-^{230}Th age data of the aragonite precipitates support young ages (< 20 kyr BP) and rapid deposition of the $CaCO_3$ filling the fracture and cementing the cataclasites. The latter are mostly in original position and can be traced for several meters in the downwards narrowing fracture. The petrographic and structural characteristics of this place in combination with the radiometric dating results raise questions on a geologically young age of the fractures/faults and cataclastic rocks, as well as the possible reactivation of directed rock movements.

dating results, as well as by detailed petrographic analysis. In principle, the recurrent opening of fractures and closely related erzbergite deposition at Erzberg within the recent geological past could also result from preferential gravitational movements across much older brittle tectonic structures (e.g. strike-slip faults), i.e. a **reactivation of the damaged and weakened zones** in some relation to specific (paleo)environmental conditions. In essence, the origin of the fractures/faults hosting relatively young erzbergite seems a promising field of ongoing research activities and more field- and microstructural data of the faults and its cataclastic rocks in combination with petrographic and geochemical constraints should be targeted.

Apart from fracture formation and structural geology, the vein mineralizations at Erzberg can further contribute to research activities in the field of **Quaternary geology** and paleoclimate reconstruction in the Alps. Based on their timing of formation (Text-Fig. 15) and distinct environmental dependencies (Boch et al., 2019), the spatiotemporally variable deposition of the erzbergite veins represents a **chemical-sedimentary environmental archive** of potentially high temporal resolution in a climatically sensitive Alpine setting. In the context of modern climate change and more specifically global warming, the Alps have shown to be a region of increased sensitivity regarding the magnitude and rate of climate variation (Auer et al., 2007). Considering the preservation of environmental changes in the past and the potential for paleoclimate reconstruction, the erzbergite deposits are comparable to other continental Ca-carbonate precipitates, such as stalagmites and flowstones in karst caves (Boch & Spötl, 2011; Fairchild & Baker, 2012), travertines and calcareous tufa (Capezzuoli et al., 2014; Toker et al., 2015) and lake deposits (Brauer et al., 2007; Oehlerich et al., 2013). In all of these cases, the capability of precise ^{238}U-^{234}U-^{230}Th radiometric dating constitutes a major prerequisite in order to reliably constrain the specific time intervals, rates and progress of carbonate growth and related paleoenvironmental changes manifested in the carbonate mineral deposits. In the first instance, the **presence or absence of erzbergite** forming during a particular time interval has shown to provide some valuable paleoclimate information. Aragonite-calcite precipitation in fractures at Erzberg is clearly favoured during relatively warm and wet climate intervals and is virtually absent during cold and dry periods (Text-Fig. 15). In other words, erzbergite growth is strongly focused on the warm/wet interglacials (e.g. Holocene, Eemian; red labels in Text-Figure 15) and interstadials (orange labels in Text-Figure 15) and did not occur during pronounced cold and dry ice ages (e.g. Marine Isotope Stages 2 and 6; blue labels in Text-Figure 15) and cool stadials (e.g. MIS 4). This can be explained by the cool formation (water) temperatures inferred from the erzbergite aragonite clumped- and stable oxygen isotope measurements, i.e. formation conditions restricted by recurrent freezing and/or dryness in

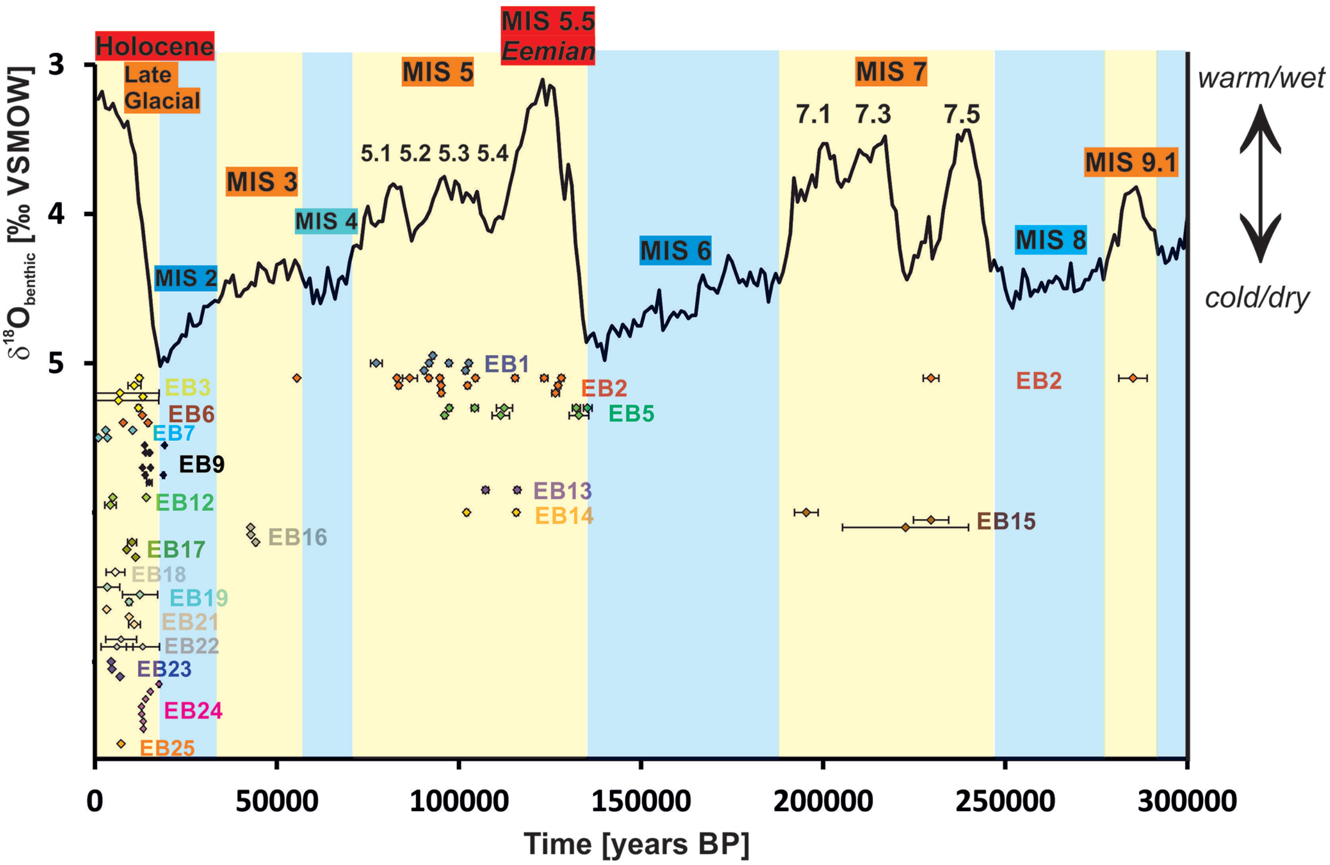

Text-Fig. 15.
Timing of erzbergite formation based on precise radiometric U-Th dating of numerous individual vein samples (n = 20; selection from EB1 to EB25) in comparison to the marine oxygen isotope evolution of the past 300 kyr (after Lisiecki & Raymo, 2005). Erzbergite deposition is clearly favoured during warm and wet climate intervals (yellow bars; MIS – marine isotope stages of low $\delta^{18}O$; interglacials and interstadials) and restricted or absent (freezing) during cold and dry intervals (blue bars; high $\delta^{18}O$; ice ages and cool stadials) at Erzberg. For most erzbergite samples basal (growth initiation), top (growth cessation – fracture filled) and intermittent U-Th ages were measured and the small age uncertainties (2σ errors) are commonly lower than the symbol size. The majority of erzbergite veins is younger than the last glacial maximum (MIS 2) and most samples represent short time intervals, i.e. rapid fracture sealing.

the higher elevation Alpine setting of the Erzberg meteoric water infiltration area and aquifer (Boch et al., 2019). Thus, water recharge and discharge and a hydrochemical evolution supporting erzbergite vein mineralization were repeatedly suppressed during the last ~300 kyr BP (Text-Fig. 15) and probably much longer. The occurrence of erzbergite obviously represents a robust indication of overall favourable (mild) regional climate conditions, i.e. more or less comparable to today. It might therefore serve as a promising paleoclimate proxy of such environmental conditions over time and its full potential could be elaborated in future investigations at Erzberg.

Regarding further paleoclimate information from the erzbergite veins and more specifically from the relatively warm and humid time intervals covered, several other **proxy parameters** can be analysed from this mineral archive in fractures. Multiple and replicated measurements of clumped isotopic compositions of erzbergite subsamples from different age dated growth intervals could provide valuable constraints on the **absolute temperatures** prevailing during specific periods in the past, i.e. erzbergite constitutes an interesting target for the clumped isotope geothermometer. In combination with the Ca-carbonate stable O isotope values and established temperature dependent O isotope fractionation factors (e.g. Coplen, 2007), the clumped isotope measurements can further provide a calculation of the original erzbergite precipitating aqueous solution stable O isotopic composition. The latter strongly reflects **genetic aspects of the vein depositing waters**, e.g. the source and eventual altering effects. At Erzberg, both past and modern waters in the fractures revealed a distinct meteoric origin and their locally differentiated isotopic signatures and hydrochemical evolution reflected seasonal and spatial variations of water infiltration and flow in the fissured carbonate aquifer (Boch et al., 2019). Likewise, the $CaCO_3$ stable O isotope values capture environmental information on the **timing** (e.g. warm vs. cold climate period or season) and **source** (e.g. trajectories of moist air masses) of the carbonate forming aqueous solutions. Importantly, state-of-the-art micro-sampling (e.g. micromilling) and mass spectrometric analytical techniques (see respective chapter) facilitate **high-resolution O isotope transects** reflecting longer- and short-term trends or rare events of the variable paleoclimate conditions. A similar approach might also be chosen with regard to environmental information from the $CaCO_3$ stable C isotopic compositions. The **erzbergite carbon isotope values** were found to mainly reflect the carbonate source rock (Fe-carbonates vs. Ca-Mg-carbonates), as well as site-specific processes of fluid-solid interaction determining the hydrochemical evolution of the aqueous solutions. The latter comprises of processes such as sulfide oxidation, incongruent carbonate dissolution, prior $CaCO_3$ precipitation and CO_2 outgassing in the aquifer (Boch et al., 2019). In this context, the C isotopes represent a sensitive proxy to water recharge and discharge and in particular to differentiated flow routes and associated erzbergite formation. This is also the case with respect to the spatiotemporally variable vein petrography, i.e. the **lamination and zonation patterns** based on a variable mineralogy. The occurrence of aragonite, (Mg)-calcite and brownish stained detrital particle layers during specific time (climate) intervals can also be interpreted in a high-resolution analytical approach. Most likely, the mineralogy and petrography strongly rely on meteoric precipitation and the directly related water saturation conditions in the fissured aquifer. Extreme seasonal and/or climate variations might result in varying water residence times ranging from **nearly complete drying to pronounced flushing events**, which are then further expressed in a more variable erzbergite appearance. In conclusion, the erzbergite vein fillings constitute a potential high-resolution paleoclimate archive of changing air- and related water temperatures, as well as of varying amounts and seasonal distributions of regional meteoric precipitation. Key to this paleoenvironmental application is the climate sensitive Alpine setting, the geochemically favourable material characteristics (pristine aragonite) allowing for precise radiometric (U-Th) age determination and the multi-proxy approach of major atmospheric (climate) variables.

Carbonate Scales forming during Geothermal Energy Production

The **knowledge** of fluid-solid interaction and variable mineral growth dynamics in the carbonate system gained from the detailed investigation of selected natural settings (e.g. speleothems in caves, veins at Erzberg) can be **transferred** to carbonate mineralization occurring in human-made (geotechnical) settings, e.g. geothermal power plants, railway and motorway tunnels. Importantly, the same underlying physicochemical mechanisms determine the carbonate crystallization pathways, their dominant environmental dependencies and consequently the spatiotemporal progress of mineral growth and the closely related material characteristics (e.g. consistency, anisotropy). In contrast to the diverse natural settings of carbonate precipitation, the technical settings primarily consider the **current (modern) and shorter-term state** of chemical-sedimentary deposition instead of longer-term paleoenvironmental considerations. In most geotechnical settings carbonate formation is typically undesired and highly problematic as it impairs fluid flow (e.g. thermal waters) and energy (e.g. heat) transfers in the technical components.

Scaling – unwanted mineral deposits

Unwanted mineral deposition (scaling) constitutes a **common obstacle** during geothermal heat and electric power production from deep thermal water reservoirs. The production of aqueous fluids from depth is typically associated with increased gas and total dissolved solid contents in equilibrium with the surrounding aquifer and more specifically its host rocks and elevated temperature and pressure conditions. In this context, deep geothermal wells (e.g. production and reinjection wells of hydrothermal doublet systems) tapping an aquifer of typically high water residence times lead to a major **disturbance** of the naturally prevailing physicochemical conditions. The pressure, temperature and chemical gradient changes introduced consequently entail an increased potential of mineral precipitation, as well as frequently related material corrosion processes deriving from the saline aqueous fluids. Depending on the natural geological and hydrogeochemical preconditions, the mineral precipitates include various carbonates, sulphates, sulphides, (hydr)oxides, chlorides and silica phases (Corsi, 1986; Finster et al., 2015).

These minerals depositing from the thermal fluid can lead to problematic inner-diameter reductions, disturbed flow regimes and clogging of the deep wells, pumps, pipelines, filters, valves, heat exchangers and other components of geothermal installations (Text-Fig. 16). Regarding mineral formation and material alteration from corrosive mechanisms, sulfidic and oxidic phases of various heavy metals – e.g. Fe, Cu and Zn supplied from steel – are the most common minerals encountered and strongly depend on the locally prevailing redox- and temperature conditions (Valdez et al., 2009; Nogara & Zarrouk, 2017). Important constituents of enhanced corrosion are elevated H_2S, CO_2, O_2 and H_2 gas concentrations, chloride and sulphate contents, and a high constituent supply (flow rate). The particular manifestation and scaling and/or corrosion progress depends both on natural and human-made (operational) environmental conditions. Thus, next to the local natural hydrogeological setting **multiple operational parameters** are involved, such as variable physicochemical gradients, flow rates, flow geometries, mixing, materials used and other technical regulations. Importantly, the natural conditions encountered and operational parameters applied are distinct **site- (installation-) specific** prerequisites but adaptable to variable degrees. The unique appearance of (Ca-)carbonate scale materials found in different geothermal installations is an expression of the site-specific character of geothermal scaling and corrosion processes (Text-Fig. 16; Boch et al., 2017b). Further, these processes are highly variable within an individual installation, i.e. they vary in space and time and different sections of the thermal fluid circuit might be affected constantly or temporarily (e.g. during production cessations). In essence, a better **process understanding of scaling and corrosion** related mineral deposition, as well as economically feasible **strategies and countermeasures** are the subject of major efforts within the deep geothermal energy exploration community. Key elements in this complex field of interdisciplinary and applied research might be more elaborate approaches of resolving fluid-solid interactions and the variable scale material characteristics, the development of new construction materials being in contact with the demanding thermal fluids, the realistic monitoring of scaling and corrosion processes at high spatial and temporal resolution (on-site, online), and sophisticated approaches involving site-specific computer based modelling of multiple engineering and chemical components.

Scaling Forensics – Reconstructing site-specific production conditions

Based on the fact that scale deposits forming in different technical components of geothermal installations with time capture site-specific natural and operational production conditions in their chemical and petrographic (fabric) compositions, these chemical-sedimentary archives can be interpreted in a **scaling forensic approach** (Boch et al., 2017b). In other words, these bodies evolving in pipes and on other substrates represent solid records of favourable vs. unfavourable production conditions with regard to variable effects on the aqueous solution chemistry resulting in variable scaling and corrosion processes. In contrast to the purely natural settings of mineral deposition in paleoenvironmental studies, the geothermal scale materials reflect a combination of natural as well as technical (operational) environmental conditions determining their **site-specific growth dynamics**. In particular, the natural physical and hydrochemical conditions of thermal fluids produced from major deep aquifers are often relatively stable on the relevant timescales (years to few decades), i.e. the extended fluid residence times and enhanced fluid-solid interaction underground provides a well equilibrated

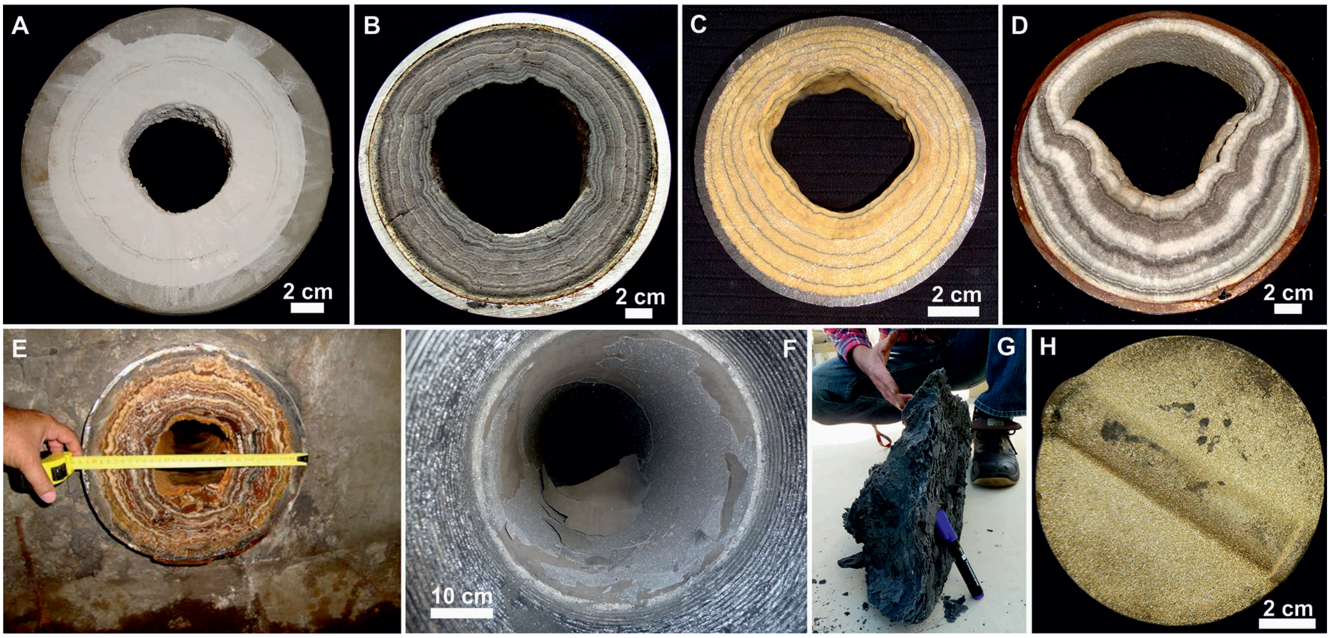

Text-Fig. 16.
Unwanted mineral precipitates impairing energy extraction from deep thermal waters. A) to D) Ca-carbonate scales of different site-specific appearance (colour, layering, consistency, growth progress, substrate material). Scale D) resulted from a separate two-phase (water + gas) thermal fluid streaming in a horizontal steel pipeline. E) Prominent scale sample (calcite, aragonite and Fe-oxyhydroxides) deposited over 45 years in a pipeline draining a storage tank of a thermal spa in Hungary. F) Scale-fragments made of Mg-calcite and accessory sulphide minerals evolving in conventional steel pipes of a geothermal power plant in Germany and further resulting in G) highly problematic massive blocks of accumulated and cemented flakes clogging tube bundle heat exchangers (cf. Boch et al., 2017a). H) Pyrite (FeS_2) mineralization on a valve flap impairing its functionality with time.

and therefore rather stable temperature, pressure, hydrochemical and hydraulic regime. In this regard, the possible short-term variation of human-made operational conditions might exert a stronger control on unwanted scaling and corrosion processes and their progress in most geothermal installations facing such problems. Nevertheless, the natural preconditions encountered are often decisive with respect to the overall potential, rates and volumes of scale deposits or material alterations to be expected and in some cases, the local handicaps might remain challenging for a given site of geothermal energy exploitation. Considering the **frequency of maintenance intervals** and the established **mechanical and chemical cleaning procedures** which can be applied for removing the scale deposits from different components and positions (CANDIDO & ZARROUK, 2017), the scales might be distinguished based on more wanted vs. unwanted material characteristics. Amongst the many possible distinctions mostly depending on genetic aspects of scale formation and fluid-solid interaction (see subsequent chapter), the scale material consistency and resulting durability with regard to its removal constitute a critical parameter. For example, compact and brittle carbonate scales strongly adhering to the underlying substrate material over longer distances (e.g. across pipes; Text-Fig. 16) are more difficult to remove mechanically (and chemically) compared to loose carbonate mud from nucleation in suspension being locally accumulated at obstacles (e.g. filter, heat exchanger). The latter might be removed regularly (e.g. daily) using a pressurized water hose, while the former has to be handled by workers in a time consuming laborious procedure (e.g. with a hammer and chisel or other exhausting mechanical means). Scales with increased porosity (lower density) typically result in a more rapid scaling progress compared to compact (dense) and relatively thinner scales, i.e. inner diameters of wells and pipelines are narrowed more rapidly impairing fluid flow and geothermal energy extraction and the frequency of maintenance intervals must be increased adequately. Importantly, the relevant scale material characteristics and growth dynamics are clearly site-specific and can vary extensively depending on the technical and operational conditions prescribed during thermal water production (BOCH et al., 2017a; HAKLIDIR & HAKLIDIR, 2017). The latter, however, represent an interesting subject for ongoing research activities and for potential site-specific adaptations, i.e. the scale material characteristics and progress could be controlled (operated) in a favourable manner (reduced growth and easy to remove).

The concept of Scaling Forensics is based on the application of a **broad laboratory analytical approach** involving state-of-the-art and mostly high spatial – and consequently temporal – resolution mineralogical/geochemical and imaging techniques (Text-Fig. 17). A **detailed reconstruction** of the spatiotemporally variable **carbonate scale growth dynamics** depending on the site-specific and longer- vs. shorter-term prevailing natural and technical (operational) geothermal production conditions is targeted. This includes an in-depth physicochemical process understanding of favourable (reduced scale deposition) vs. unfavourable (increased scale deposition) thermal water production conditions with regard to the site-specific scaling (and corrosion) progress. Essentially, the scaling forensic approach constitutes a **multi-proxy approach** combining multiple analytical techniques in order to gain environmental information on multiple physical and chemical parameters during thermal water production and consequently geothermal energy extraction. This involves environmental parameters and processes such as temperature and pressure changes, fluid flow rate, CO_2 and H_2O (steam) outgassing, pH and pe (redox) changes, the mobilization of specific elements and particles, mixing of fluids, the role of production cessations and restarts, material specific (e.g. steels, plastics) observations, and others. All of these variables can exert a major or minor, continuous or intermittent effect on the scale growth dynamics and the intimately related scale material characteristics. The laboratory analytical methods of choice include **powder- or micro-X-ray diffraction** measurements of selected subsamples (drilled powders) or spots in order to determine variable mineralogical compositions of the scale deposits (Text-Fig. 17). XRD analyses might also be performed on remaining mineral residua (e.g. sulphide and silica minerals) extracted from the bulk (carbonate) scale materials after chemically-selective procedures of **acid digestion** (e.g. BOCH et al., 2016). Detailed **petrographic information** including mineralogical and textural (fabric) changes can be derived by applying various **light microscopic techniques** to thin-sections prepared from the scales. This includes transmitted-, reflected- and epifluorescence (e.g. UV-activated) microscopy, as well as cathodoluminescence. A higher spatial resolution (µm size) can be achieved by **scanning electron microscopic techniques** (SEM) utilizing secondary electron (SE) or back-scattered electron (BSE) imaging. The latter has shown to be of particular value in evaluating the local presence of microbes (e.g. bacteria, fungi) in scale materials. In the **BSE images**, organic tissues appear in prominently blackish colour compared to the surrounding carbonate matrix or accessory minerals based on their distinct low-density contrast. The occurrence and distribution of microbial communities can further be studied by **fluorescence staining and imaging** of fresh scale material surfaces. This method uses mixed dyes resulting in fluorescence of the stained material when they are bound to nucleic acids (DNA, RNA) eventually being present. The scale surfaces of interest are investigated before and after staining and fluorescent signals can be detected by an epifluorescence microscope or other imaging systems (cf. GRENGG et al., 2017). Significant scale material contrasts mainly comprising of changes in **porosity and fabrics** can also be distinguished based on **micro-computer tomography** (µ-CT; Text-Fig. 17). This high spatial resolution method is typically focused on small volumes (cm^3 size) represented in cylinders of sample material extracted from the bulk samples (e.g. rocks, scales; cf. OTT et al., 2012). High-resolution petrographic insights and simultaneous **major and minor element chemical distribution mapping** (µm-scale) is facilitated by **electron probe microanalysis** (EPMA). This tool is of particular value for resolving distinct mineralogical and material specific contrasts, for example across interfaces (substrate vs. scale) or in layered sample sections (BOCH et al., 2017a). In addition, precise quantitative elemental compositions of selected constituents can be determined by spot analysis of energy-dispersive X-ray spectra (EDX; MITTERMAYR et al., 2017). Regarding the measurement of **minor and trace elemental compositions** in the solid scale materials, **laser ablation coupled to mass spectrometry** (LA-ICP-MS) can provide highly-resolved (10s of µm spot size) and sensitive (ppb range) chemical information (Jochum et al., 2009). Typical **sampling strategies** include pointwise or continuous transects across the spatiotemporally evolving sample materials, as well as more sophisticated sampling grids. In the context of carbonate scales, high-resolution LA-ICP-MS based concentration profiles of the elements **Mg, Sr and Ba** can provide valuable proxy information on the variable scale growth dynamics and therefore progress. In particular, the incorporation of the relatively large cations Sr^{2+} and Ba^{2+} into $CaCO_3$ is well known to strongly depend on the prevailing precipitation rate and varying Mg concentrations often reflect spatial changes of dominant Ca-carbonate (scale) deposition as a result of prior $CaCO_3$ precipitation and related Mg fractionation (enrichment) along the flow path (see Erzberg chapter). Different spatial but mostly high-resolution sampling strategies are further applied for **stable C and O isotope analyses** of the scale carbonate. This is typically accomplished by the extraction of tiny sample powders (~0.3 mg) from the scale material using a **computer-controlled micromill device** in combination with subsequent **mass spectrometric analysis** (CF-IR-MS; Text-Fig. 17). The C and O isotope signatures have shown to be a sensitive proxy for outgassing of CO_2 and H_2O (bubbling/steam formation) from the thermal water (Boch et al., 2017a). More specifically, the isotopically relatively light $^{12}C^{16}O_2$ and $^{1}H_2{}^{16}O$ molecules are preferentially enriched (Rayleigh fractionation) in the separating gas phases and therefore the related **$\delta^{13}C$** and **$\delta^{18}O$** values of the concomitantly precipitating $CaCO_3$ are relatively enriched in the heavier and rare ^{13}C and ^{18}O isotopes. Importantly, the **magnitude and rate of CO_2 and H_2O outgassing** are directly related to the **amount and rate of Ca-carbonate precipitation** based on the carbonate chemical equilibrium (equation 6) and thus the overall scaling progress in a pipeline or other components. The multi-proxy scaling forensic approach of the solid mineral deposits can further be extended by process oriented hydrogeochemical computer modelling, e.g. using the thermodynamic and aqueous speciation based numerical calculations provided in the software PHREEQC (Parkhurst & Appelo, 2013; Akin & Kargi, 2019).

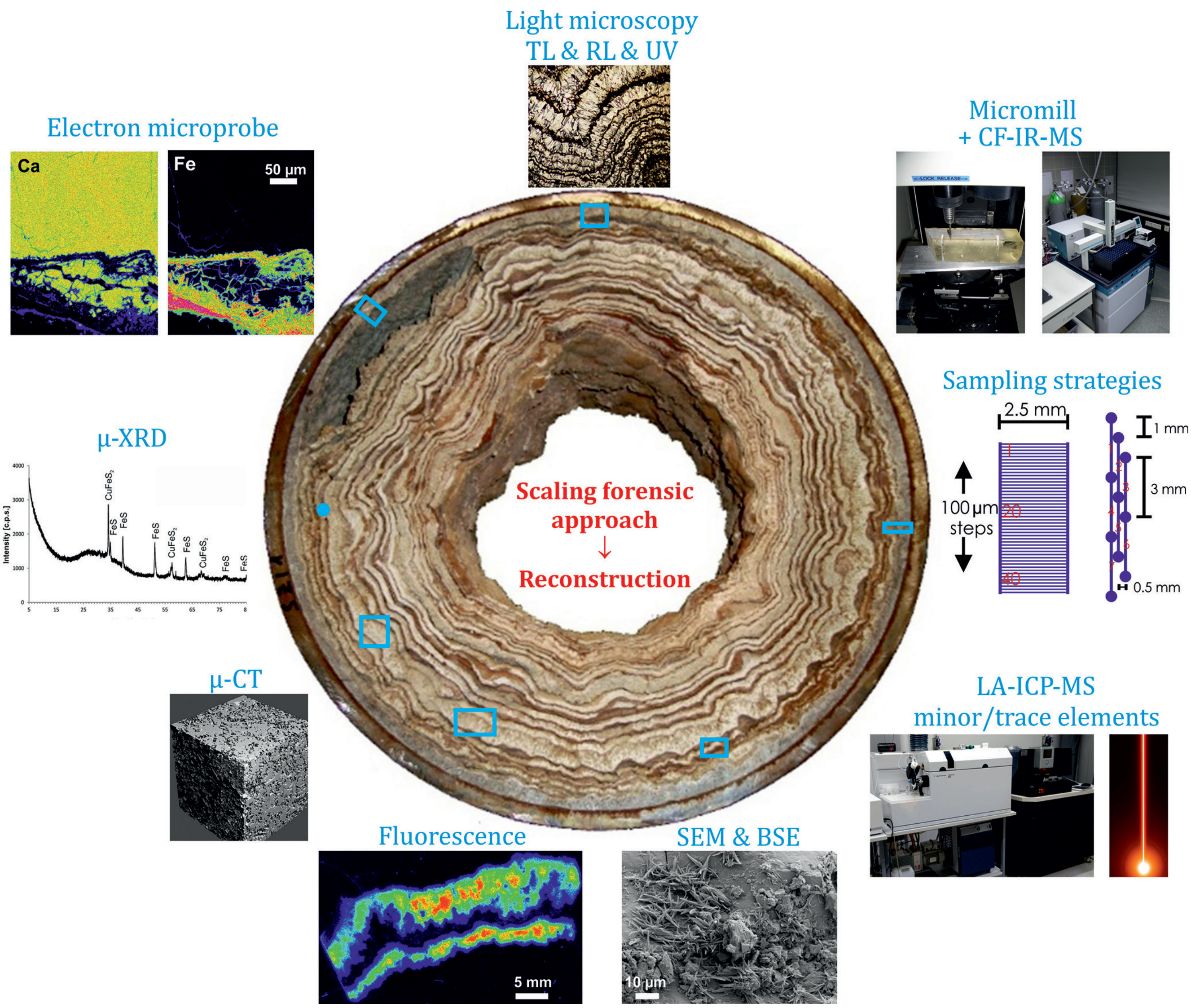

Text-Fig. 17.
Concept of Scaling Forensics based on the application of various high spatiotemporal resolution geochemical and imaging analytical techniques. Carbonate scale deposits constitute an evolving chemical-sedimentary environmental archive capturing site-specific natural and technical (operational) thermal water production conditions in their chemical and petrographic compositions. A reconstruction of favourable vs. unfavourable production conditions and process understanding of the variable scaling progress is targeted.

In a **recent case study**, a **scaling forensic approach** of unwanted mineral deposits increased the site-specific process understanding significantly (BOCH et al., 2017a). Two geothermal facilities for district heating and electric power production with similar construction schemes and located close to each other in S-Germany showed rapid deposition (within weeks to few months) of scale-fragments resulting in massive clogging of the tube bundle heat exchangers which consequently disturbed energy transfers and caused repeated shutdowns of the power plants. A detailed – high-resolution scaling forensic – investigation of solid scale materials from different sections of the plants in combination with comprehensive hydrochemical and technical data revealed the occurrence of partially unfavourable natural as well as human-made physicochemical conditions. This included an intimate connection of H_2S (sulfidic) based steel corrosion and enhanced $CaCO_3$ crystal growth, a critical role of thermal water production cessations and restarts, and the relevance of increased CO_2 concentrations that might be associated with fault zones frequently targeted for hydrogeothermal energy exploitation (BOCH et al., 2017a). The specific character and progress of carbonate scaling and problematic **scale-fragment mobilization** strongly relied on the presence and effects of distinct interfaces (substrate vs. scale vs. fluid flow), the materials used (conventional steel pipes), the scale material consistency (euhedral crystalline, brittle), as well as self-reinforcing feedback mechanisms. It is therefore an example of site-specific fluid-solid interaction. Some of the most relevant processes and effects promoting carbonate scaling will be discussed in the next chapter.

Considering an **application of Scaling Forensics in practice**, this might not be limited to a **late stage clarification** of critical and unwanted processes leading to major scaling and corrosion problems. Rather, it could be implemented in an **early stage evaluation** of potential geogenic and human-made problems and a concomitant site-specific optimization of technical/operational parameters with regard to the most efficient thermal water and energy production. In the future, it could be implemented as a part of a **site-specific testing program** comparable to the well-established hydraulic pumping tests. More specifically, the high spatiotemporal resolution (micrometre range) forensic approach presented facilitates a detailed investigation of even relatively **thin scale coatings** (e.g. millimetre thickness) precipitated within **few days or weeks** only (test phase). These mineral deposits, however, still represent a valuable chemical-sedimentary archive capturing the variable and potentially (un)favourable physicochemical production conditions. The latter could be tested and optimized in a dedicated test series also involving **on-site and online monitoring** of select relevant environmental parameters (e.g. temperature, pressure, flow rate, electric conductivity, pH, pe, pCO_2, particle load, etc.). Importantly, intentionally varied production parameters will be reflected in the precipitated scales, which will effectively allow for a better assessment of site-specific issues (e.g. how the scaling is affected by changes in the aforementioned parameters) and hence allow for optimization of the operating conditions by establishing systematic **countermeasures** to reduce the impact of scaling.

Processes determining carbonate scale material characteristics

Multiple physicochemical processes and related environmental conditions determine the character and extent of mineral deposition in the context of hydrogeothermal scaling and the alteration of materials (e.g. steel corrosion). Focusing on carbonate scaling, the temporally and spatially variable scaling progress and resulting consistencies of the scale materials determine the frequency at which maintenance should be conducted, as well as on the mechanical and chemical cleaning or material treatment procedures that are practical for resolving scaling and/or corrosion problems. Moreover, **different crystallization and depositional mechanisms** yield a broad range of scale materials with different consistencies, from hard and compact to soft and porous. Rhythmic growth successions (layering) and variable material consistencies are a common feature in many scale deposits (Text-Fig. 18; BOCH et al., 2017b).

Carbonate scales can be placed into three major groups based on the dominant depositional mechanism that produced them, these are i) inorganic crystallization, ii) microbially mediated deposition, and iii) particle/fragment mobilization and accumulation. Scale production via **inorganic crystallization** mainly depends on the prevailing hydrochemical production conditions, as well as the chemical and physical properties of the substrate in contact with the thermal water. Inorganic scale formation can be further separated into two sub-groups: i) wall crystallization (heterogeneous scale growth) and ii) suspended particulate nucleation (homogeneous crystallization). **Wall crystallization** refers to crystal nucleation and scale growth on some substrate material (e.g. pipe or heat exchanger surface), whilst **suspended particulate nucleation** of solid phases occurs rather spontaneously in highly supersaturated, gas-rich (bubbling) and/or turbulent water flows (Text-Figs. 18A, B; BRAMSON et al., 1995; BOCH et al., 2016). Regarding inorganic carbonate precipitation in hydrogeothermal settings, the process of variable **CO_2 outgassing** was recognized as highly relevant for scale deposition (ALT-EPPING et al., 2013; WANNER et al., 2017). In principle, CO_2 absorption constitutes another process of potential dissolved inorganic carbonate evolution and subsequent carbonate mineral formation (see equation 7). The latter, however, is restricted to strongly elevated pH (ca. > 10) and strongly reduced CO_2 partial pressure conditions (much lower than atmospheric) of the aqueous solution and is therefore irrelevant for geothermal scaling.

Apart from inorganic controls on crystal growth and fabrics, **microbially mediated processes** can exert a major influence on scale deposition (Text-Figs. 18C, D). These influences comprise of either i) passive or ii) active contributions from the microbial species and communities involved. Typically, extensive microbial presence results in relatively porous fabrics and consequently softer scale consistencies. In various tempered geothermal settings, different bacteria and fungi might be most common (TEMPLETON & BENZERARA, 2015; OSVALD et al., 2017). The distinction and relevance of more passive and more active roles, however, is not strict. **Passive functions of microbial presence** include the availability of an attractive substrate for initial crystal nucleation or particle entrapment owed to the typically large specific surface area and irregularly shaped topography of the filamentous and high-

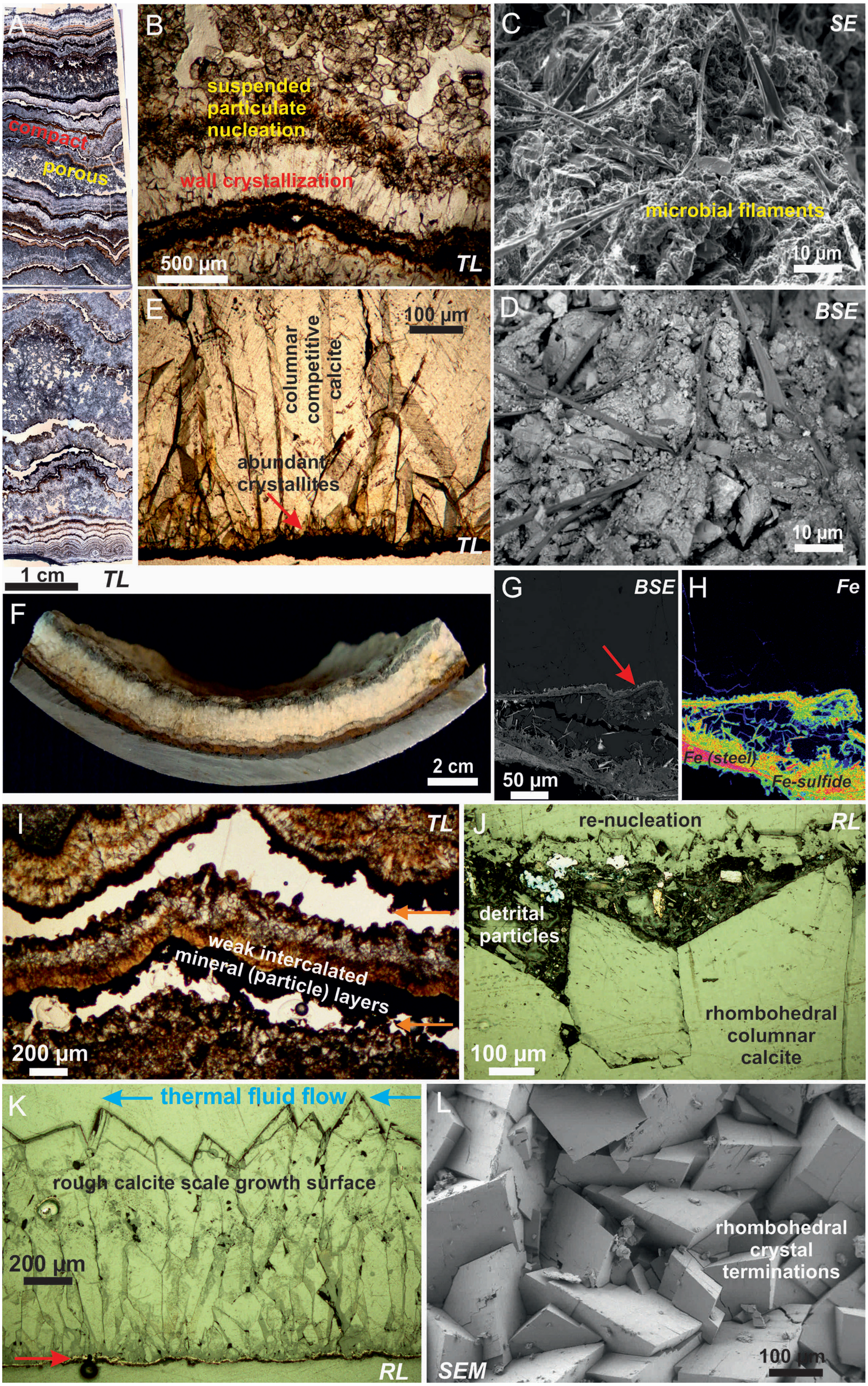
A
compact
porous
1 cm
TL
B
suspended
particulate
nucleation
wall crystallization
500 µm
TL
C
SE
microbial filaments
10 µm
D
BSE
10 µm
E
100 µm
columnar
competitive
calcite
abundant
crystallites
TL
F
2 cm
G
BSE
50 µm
H
Fe
Fe (steel)
Fe-sulfide
I
TL
weak intercalated
mineral (particle) layers
200 µm
J
re-nucleation
RL
detrital
particles
rhombohedral
columnar
calcite
100 µm
K
thermal fluid flow
rough calcite scale growth surface
200 µm
RL
L
rhombohedral
crystal
terminations
100 µm
SEM

◀ Text-Fig. 18.
Overview on principal depositional mechanisms and specific interfaces affecting the carbonate scale growth dynamics, fabrics and material consistency. A) Transmitted-light (TL) thin section composite image showing a multi-annual Ca-carbonate scale sample comprised of compact vs. porous layers of highly variable thickness reflecting different depositional (growth) mechanisms. B) Compact and brittle calcite scale fabric resulting from wall crystallization (on a substrate) vs. porous and softer fabric resulting from $CaCO_3$ (calcite and aragonite) crystallite nucleation in suspension preceding agglomeration and cementation. C) Secondary electron (SE) and D) back-scattered electron (BSE) images of microbial communities (biofilms) influencing scale deposition and consistencies in some geothermal facilities. Note the indicative colour contrast in BSE mode based on the relatively low density of the preserved organic tissue. E) Distinct iron-rich mineral layer (red arrows) resulting from steel corrosion at the base of a carbonate scale and constituting an attractive substrate for abundant crystallite nucleation and ongoing columnar and competitive (dense) calcite crystal growth. F) Prominent corroded interface between a conventional steel pipe and the overgrowing calcite scale material. G) Electron microprobe based BSE image and H) Fe concentration distribution at the base of a carbonate scale-fragment (from Boch et al., 2017a). Progressive H_2S based steel corrosion promotes Fe-sulfidic mineral layers of reduced mechanical strength (cracks, exfoliation). I) Recurrent intercalated (Fe- and Si-rich) loose particle layers within a scale affecting Ca-carbonate crystal growth and the overall mechanical strength (scale consistency). J) Reflected-light (RL) image of intercalated detrital particles flushed onto an euhedral calcite scale growth surface and having an effect on subsequent calcite (re)nucleation. K) RL and L) scanning electron microscope (SEM) images of a rough calcite scale growth surface influencing the streaming thermal fluid (blue arrows) flow resistance and favouring the local occurrence of (micro)turbulences. This interface therefore affects the extent of potential CO_2 and H_2O (steam) outgassing and directly related $CaCO_3$ precipitation (scaling progress).

ly porous biofilms which they form (Riding, 2000; Jones & Renaut, 2010). The nature of these biofilms further influences ongoing crystal growth and possible cementation of trapped particles. The most important **active roles of microbes** regarding scale deposition are their ability to significantly alter chemical gradients in the reactive solution and to catalyse scaling and/or corrosion processes. The former involves hydrochemical adjustments of pH gradients and carbonate alkalinity or the channeling and gradation of specific ionic constituents (e.g. Ca^{2+}) in aqueous solution (Pedley, 2013; Diaz et al., 2017). Concerning catalytic processes, distinct microbes can enable or accelerate carbonate scale growth or corrosive and mostly redox state related reactions (Würdemann et al., 2016; Westphal et al., 2019). In geothermal installations, chemoautotroph sulphur, iron, manganese, carbon or nitrogen cycling bacterial species dominate the microbial activity and communities and these redox sensitive elements are either oxidized or reduced during specific energy delivering redox reactions (Lanneluc et al., 2015; Nogara & Zarrouk, 2017). It should be noted, that the occurrence, extent and speciation of microbial influences might not be accurately reflected in the recovered carbonate scale samples, as in many cases only sparse microbial remnants are preserved. Further, scale deposition can occur in the form of **particle/fragment mobilization and accumulation** (Text-Figs. 16F, G, 18J). Based on the high and often turbulent thermal fluid flow conditions, components of diverse sizes – micrometre crystals to centimetre scale-fragments – can be mobilized and subsequently deposited in wells, pipelines or at obstacles (e.g. filter, heat exchanger, pump). The solid particulate components originate from the corrosion of steel pipes, displacement from the aquifer host rocks, defect well casings, homogeneous particle (crystal) nucleation in suspension or the exfoliation of scale-fragments (Wolfgramm et al., 2011; Boch et al., 2017b). Thus, the well sorted or variably sized particles/fragments typically occur as a loose agglomeration in layers or in local traps but might undergo massive (carbonate) cementation in the course of ongoing thermal fluid flow (Text-Fig. 16G). Processes favouring particle/fragment mobilization are obviously strongly dependent on the geogenic and operational production conditions and are often episodic in their contribution to scale deposits (e.g. after production cessations and restarts).

The forensic approach of geothermal production and scaling conditions presented in this chapter further strongly supports **major effects of distinct interfaces** with regard to carbonate scale initiation, growth and related material characteristics. The interfaces primarily addressed comprise of i) the layer or zone between carbonate scale and the underlying substrate material, ii) intercalated mineral (particle) or biofilm layers within the carbonate scales and iii) the scale growth surface versus thermal fluid flow (Text-Fig. 19). Starting with the **interface between carbonate scale and its substrate** (Text-Figs. 18E–H), the initial scale deposition and ongoing crystal growth is strongly affected by the substrate material, i.e. different types of steel (conventional, alloyed) or plastics (PVC, PE, PP) forming the pipes, heat exchangers and other components and surfaces being exposed to the thermal fluid. In particular, distinct mineral layers between steel substrates and scale deposit are of common occurrence and represent mineral formation in the course of different **sulfidic or oxidic steel corrosion mechanisms** (Choi et al., 2011; Liu et al., 2014). Next to the substrate materials used, the occurrence and character of these **corrosion layers** thus mainly depends on the inorganic – and mostly redox state related – hydrochemical conditions, as well as on potential microbially induced (catalytic) processes enhancing steel corrosion (Valdez et al., 2009; Nogara & Zarrouk, 2017; Westphal et al., 2019). The phenomena of carbonate scaling and steel corrosion have already been recognized as closely interrelated physicochemical processes (Stáhl et al., 2000; Mundhenk et al., 2013; Li et al., 2019). More specifically, detailed investigations of carbonate scales from Germany and Hungary revealed favoured calcite scale nucleation and crystal growth on the basal corrosion layers (Boch et al., 2017a, b). This can be explained by the low degree of crystallinity, numerous defect sites, high specific surface area and possible electric charges of typical corroded steel surfaces. Consequently, they constitute an attractive substrate favouring abundant initial crystallite nucleation and crystal growth. Furthermore, the corrosion derived mineral layers made of iron- and other metal (Cu, Zn, Ni) sulphides and (hydr)oxides at the base of the variably thick Ca-carbonate scale deposits provide an interface of reduced mechanical strength. This in turn promotes the evolution of material deteriorating processes such as pitting, cracking, flaking and eventually local scale fragmentation and mobilization (Text-Figs. 18G, H). Considering different substrate materials in contact with the aqueous solution and hosting the scale deposits, **selective leaching of compounds** from fresh or corroded steel components or different types of plastic pipes and coatings, as well as concrete casings could also have an effect on the hydrochemistry and resultant carbonate scaling (Hewitt, 1989; Boch et al., 2015; Galan et al., 2019).

In some scale deposits, **recurrent intercalated mineral (particle) or biofilm layers** constitute another distinct interface which can exert some influence on progressive scale growth and the scale material characteristics (Text-Figs. 18I, J). These layers within the scales are of variable thickness and particle sizes and the mostly iron-rich or siliceous minerals assemble a loose agglomeration of crystals without preferred orientation. Considering their origin, they can be an episodic expression of **allochthonous input** from corroded steel components or of particle displacement from deep aquifer host rocks and through defect borehole casings. Detrital flushing in the course of major production cessations and restarts was observed to be of particular relevance for particle transport (Wolfgramm et al., 2011). Alternatively, intercalated layers can also result from **autochthonous microbial activity**, e.g. specific (e.g. iron sulphides/(hydr)oxides) mineral precipitation within temporary biofilms on the scale surface in contact with the thermal fluid (Lerm et al., 2013; Würdemann et al., 2016). The often microbially induced mineral precipitates forming during chemoautotroph redox reactions might remain after the decay of the local biofilms. Regarding the scaling progress and consistency, these intercalated mineral layers have a similar effect compared to the basal corrosion layers: an overall reduced mechanical strength and thus a potential of enhanced scale fragmentation and mobilization, providing an attractive substrate for carbonate scale (re)nucleation and growth, and the release of abrasive particles harming smooth material surfaces (e.g. heat exchangers), coatings (e.g. protective plastic layers) and functional components (e.g. pumps).

Last but not least, the critical interface represented by the **carbonate scale growth surface versus streaming thermal fluid flow** also determines a variable scaling progress, as well as the resulting scale material character (Text-Figs. 18K, L, 19). Depending on the site-specific production conditions and fluid-solid interaction, some scale deposits possess prominently rough growth surfaces as a result of distinct crystal nucleation, competitive crystal growth and ultimately euhedral (e.g. rhombohedral) and oriented crystal terminations and relatively large crystal sizes (Text-Fig. 18K). Importantly, the rough scale growth surface entails an increased flow resistance and the occurrence of (micro)turbulences at this interface, which consequently favours significant CO_2 and H_2O outgassing (bubble/steam formation) and directly related enhanced carbonate ($CaCO_3$) precipitation (cf. equation 6). This constitutes an in-situ (local small spatial scale turbulences) self-reinforcing mechanism and under conditions of elevated aqueous solution pCO_2 interrelated carbonate (super)saturation and scale formation can be promoted even at elevated operational pressures (e.g. 18 bar) during thermal water production (Boch et al., 2017a). Moreover, the increased flow-resistance and accompanying shearing forces favour the exfoliation and mobilization of scale-fragments damaging and clogging critical components of the thermal fluid circuit (e.g. filters, heat exchangers). In some geothermal wells and pipelines exhibiting a high gas to water ratio, a two-phase fluid flow might occur, i.e. thermal water and gases (CO_2, H_2O, N_2, CH_4, etc.) as separate but closely related streams (Text-Fig. 19). This typically results in pulsating flow conditions and enhanced turbu-

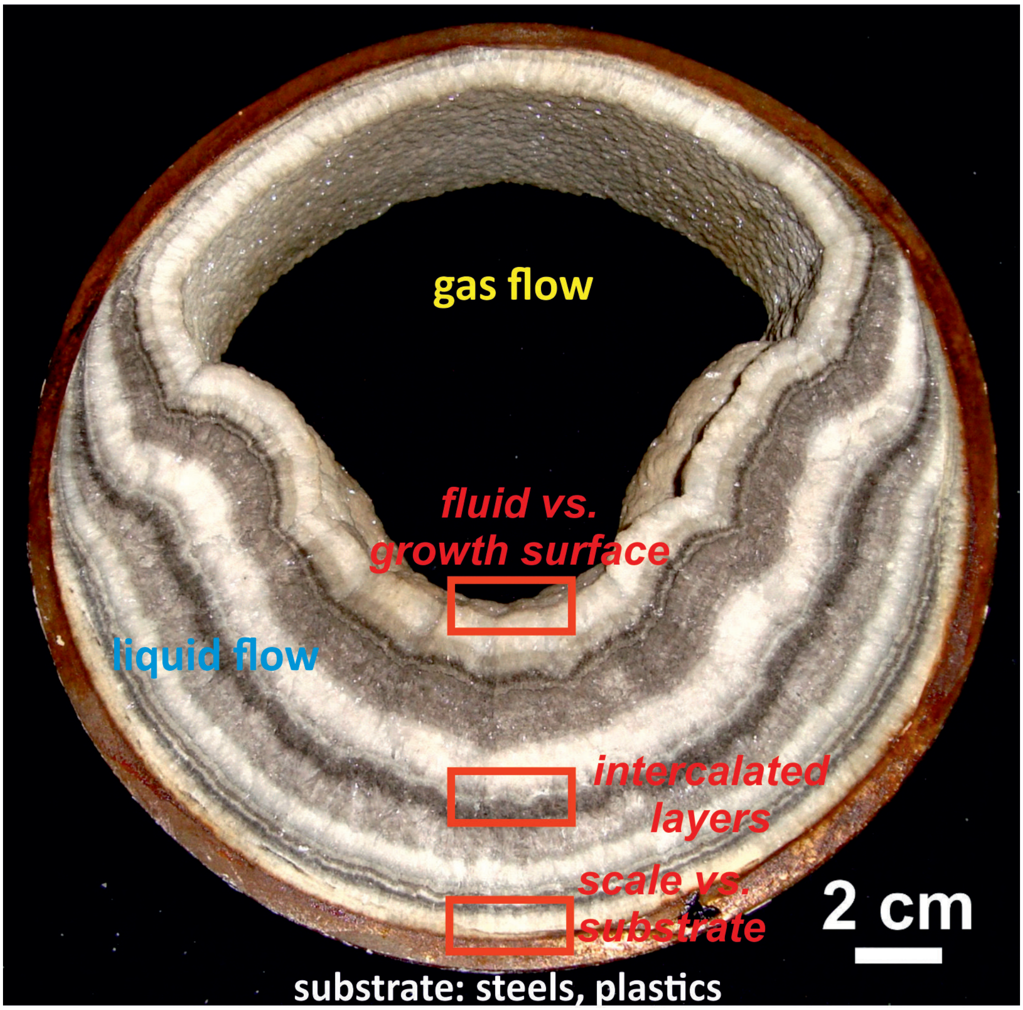

Text-Fig. 19.
Distinct interfaces exerting a major control on carbonate scale initiation, growth and related material characteristics. This involves different substrate (pipe) materials, intercalated mineral (particle) and biofilm layers, as well as the scale growth surface versus fluid flow. In some cases, separated two-phase fluid flows (thermal water + gases) occur and strongly influence the locations and rates of variable scale deposition.

lences. Own investigations on diverse carbonate scales from the Hungarian Pannonian Basin have revealed prominently high average growth rates of such scale materials forming during two-phase pulsating flow conditions. Consequently, these unfavourable geogenic as well as operational conditions should be reduced or avoided, e.g. by increasing the overall working pressures and adjusted flow geometries.

In essence, the distinct scale depositional mechanisms and the specific roles of interfaces contrasting adjacent materials, growth layers and phase transitions strongly influence the overall scaling progress and scale material consistency (durability) and thus the necessary maintenance intervals and cleaning procedures. For example, heterogeneous wall crystallization mostly results in densely packed parallel crystal formation, compact fabrics and a **brittle carbonate scale consistency**, while homogeneous crystallization in suspension is typically manifested in the accumulation of a **loose carbonate mud** (Text-Figs. 18A, B). In some cases, the randomly oriented crystals (c-axis) of the latter might undergo some further compaction and cementation. However, the suspended particulate depositional mechanism typically produces **porous scale fabrics** and a comparatively **rapid scaling progress** (e.g. inner diameter reduction in pipes; Text-Fig. 16). This is also the common case, when extensive microbial biofilms participate in scale deposition, i.e. the resulting scales are often porous and sometimes soft. Nevertheless, the thicker carbonate scales from transport in suspension and subsequent agglomeration or from microbial interaction, might be much easier to **remove mechanically or chemically**. This includes the utilization of a simple or pressurized water hose or the better ingress and interaction of acidified cleaning solutions with regard to softer and more porous scale deposits.

Further, considering the site-specific fluid-solid interaction determining the scale material characteristics, the occurrence and relevance of **interrelated processes** becomes obvious. As an example, a case study on scale-fragment formation in pipelines severely and recurrently clogging the heat exchangers of two major geothermal power plants in Germany revealed the close interrelation of H_2S based steel corrosion and enhanced $CaCO_3$ crystal growth (Boch et al., 2017a). The **complex cascade** of interacting processes comprises of various substrate effects on scale nucleation, ongoing crystal growth and fabric development, and the morphology of the scale growth surface mechanically and chemically interacting with the circulating thermal fluid. More specifically, distinct corrosion layers at the scale base have shown to provide an attractive substrate for abundant Ca-carbonate crystallite nucleation and rapid crystal growth but are also the place of preferred mechanical failure and particle/fragment mobilization. In this context, the site-specific role of thermal water **production cessations and abrupt restarts** should be elaborated more critically. This mainly concerns the temporary physicochemical (e.g. redox states) changes accompanying stagnant fluids in the wells and other technical components, the thermal contraction of materials (e.g. steel → cracking and subsequent exfoliation) and potential microbial (re)settlement (habitable environment) during cooling, and the cumulative mobilization of erosive particles, scale- and steel fragments.

Summary and Outlook

The chapters presented in this publication discuss broad, although still select aspects within the extensive field of **modern carbonate research**. Its focus is constrained to a closely related interaction of research questions and methodological approaches situated between **geochemistry and geology**. On several occasions wider interdisciplinary connections to other geoscientific fields (e.g. mineralogy), as well as adjacent scientific and technical fields (e.g. climate research, construction engineering) are established. Considering the carbonate chemical system, the **Ca-carbonates** and more specifically the anhydrous polymorphs calcite and aragonite ($CaCO_3$), as well as the rarely documented hydrous form ikaite ($CaCO_3.6H_2O$) constitute mineral formations of primary relevance. Further, Fe-carbonates such as siderite ($FeCO_3$) and ankerite ($[Ca,Fe,Mg]_2[CO_3]_2$) are involved in the chapter presenting new investigations of the Erzberg iron ore mine. These carbonate minerals are associated with a highly diverse range of **natural and (geo)technical environmental settings** being exemplified in different chapters. Another principle focus of this work is the critical reflection on the variable **environmental conditions and dependencies** and an advanced **process understanding** of fluid-solid interaction in the course of carbonate precipitation and alteration. The wanted (e.g. speleothem growth in caves) or unwanted (e.g. calcite scaling in geothermal wells) processes are evaluated on strongly **differentiated spatial and temporal scales**. Some of the major conclusions inferred from the selected chapters include:

- The rapid modern development of **in-situ and high-resolution laboratory analytical techniques** (e.g. imaging, chemical composition, isotopic analyses), material- and site-specific **sampling strategies** and field based **on-site and online environmental monitoring** campaigns (e.g. using data loggers) have emerged as important knowledge pacemakers regarding carbonate growth dynamics in natural and human-made environmental settings.
- **Fundamental and applied research** questions and approaches are often closely related and benefit from each other. Regarding distinct chemical-sedimentary processes of carbonate occurrence and characteristics, **widespread analogies** can be recognized. A promising **transfer of knowledge and analytical skills** from fundamental research (e.g. carbonate climate archives) to more applied problems and settings (e.g. carbonate deposition affecting geotechnical infrastructure) is currently evolving. For example, geochemical knowledge and analytical tools associated with natural and site-specific stalagmite growth and cave monitoring have been applied to unwanted and installation-specific carbonate mineralization and its determining natural as well as operational environmental conditions in deep geothermal wells, concrete beds, tunnel drainages and other human-made settings.
- An advanced understanding of **element and isotope fractionation** mechanisms during carbonate precipitation based on laboratory experimental, computer modelled and empirical studies and the utilization of

new (trace) element/isotope chemical systems and analytical techniques increases our knowledge on carbonate mineral-specific crystal nucleation and growth, fabric types and the resulting material consistencies on (geo)technically relevant spatial and temporal scales.

- **Speleothems** made of Ca-carbonate and of diverse age forming in various caves of the Central European Alps constitute a successively deposited archive of the variable **regional climate conditions**. Based on a multi-proxy and mostly high spatial resolution sampling approach of the speleothem carbonate and the cave site-specific growth conditions, valuable paleoclimate information has been extracted, e.g. from the geochemically selected NALPS (northern Alps) stalagmites presented. Precise radiometric **uranium-thorium isotope based chronologies** and high temporal resolution **stable oxygen isotope records** have shown their particular value with regard to distinct climate changes in the past.
- The detailed investigation of typically layered **aragonite-calcite veins** ("Erzbergite") sealing vertical fractures of the **Erzberg iron ore mine** (Austria) revealed the controlling chemical-sedimentary processes and environmental dependencies of these secondary mineral deposits. This included their formation ages and temperature, precipitation rates, carbonate source rocks, origin and hydrochemical evolution of parent waters, their episodic layering and Ca-carbonate polymorphism, as well as their relation and possible constraints on local fracture formation and their application as a climate archive in an environmentally-sensitive Alpine region. Seemingly well-known rock forming minerals and sediments of the Alps (e.g. at Erzberg) are still **worth to be (re)evaluated**.
- **Unwanted carbonate scaling** frequently impairs hydrogeothermal heat and electric energy exploitation from deep reservoirs relying on natural and human-made (operational) thermal water production conditions. In a **scaling forensic approach** the dominant physicochemical processes determining the **scaling progress** and **scale material characteristics** can be evaluated and adapted. This involves a detailed process understanding of various mineral formation in relation to the local (hydro)geological and technical conditions. **Specific interfaces** within and between solid and fluid phases (e.g. corrosion layers vs. carbonate scale) as well as **production cessations** are of particular relevance. "Scaling Forensics" helped to elucidate facility-specific problems such as ongoing scale-fragment formation and severe blockage of heat exchangers.

Based on the geoscientific topics investigated and discussed in this publication, a large variety of **consecutive and extending research questions** arise. A somewhat subjective outlook with regard to possible fundamental and applied research activities includes the following topics:

- The rapid development of high spatial resolution, in-situ and increased sensitivity laboratory analytical techniques for fluid and solid phase measurements advances our process understanding of **Ca-carbonate nucleation and growth dynamics**. Ongoing research on the **crystallization mechanisms** of amorphous versus crystalline carbonate phases therefore constitutes a promising field, e.g. investigating controls of the manifold calcite morphologies. This also includes the relevance of **substrate effects** for Ca-carbonate precipitation, e.g. different substrate materials such as various steels, plastics, corrosion layers and coatings and their effects on scaling progress and (un)wanted material consistencies in technical settings.
- Ongoing research efforts further comprise of process-oriented investigations on various **trace element and isotope fractionation behaviours** based on different approaches. This includes the increased understanding of **equilibrium versus kinetic fractionation** with regard to traditional stable isotopes (e.g. C, O), as well as clumped isotopes measured in carbonates. Considering the fundamental **evaluation and calibration** of element and isotope systems, carbonate scale materials deposited in technical settings have shown some attractive potential based on their diverse formational characteristics. In applied settings such as geothermal energy extraction, stable carbon and oxygen isotopes might be used as a **quantitative proxy** for significant changes in fluid temperature, CO_2 and H_2O outgassing and the closely related precipitation (scaling) rate.
- Next to an increased understanding of the depositional dynamics and advanced hydrogeochemical computer modelling, **efficient and sustainable countermeasures** to reduce unwanted carbonate scaling in geotechnical settings are targeted. This includes the preventive future deployment of **field based and automated environmental monitoring tools**, i.e. on-site and online sensors, data loggers and scale guards operating in geothermal wells and pipelines or technical drainages (e.g. in motorway and railway tunnels). The site-specific application and foregoing laboratory based testing of different kinds (additives) of promising "**green inhibitors**" constitute a more intervening although (bio)degradable and environmentally friendly chemical measure suppressing carbonate scale deposition. This also includes the development of systematic and compact (spatial requirements, short duration) field based testing procedures of different commercial and/or blended products and optimized dosages.
- **Scaling Forensics** could be implemented in a **site-specific test phase and procedure** lasting a few days or weeks in the case of thermal water production from deep wells, depending on the local hydrochemistry and rates of scale deposition. In combination with in-situ fluid and operational monitoring this would contribute to a valuable **early stage evaluation** of the specific production conditions in contrast to later stage clarification and problem solving strategies. Thus, it serves major socio-economic interests, i.e. regarding the time, labour input, costs and technical problems associated with maintenance intervals and cleaning procedures in geotechnical infrastructure.
- Considering further fundamental research activities at the **Erzberg iron ore mine**, the application of **new geochemical and mostly isotopic techniques** in-

cluding clumped isotopes (multiply-substituted isotopologues) and non-traditional isotope systems (e.g. $^{56}Fe/^{54}Fe$, $^{26}Mg/^{24}Mg$) would advance our knowledge on **genetic aspects of the iron ore carbonate**, which still is an ongoing subject of debate. Based on the new and partially unexpected results from the erzbergite veins, the proposed **fracture and fault formation** during young geological times should be assessed critically and a continuation of this work is suggested. Moreover, modern aqueous solutions (e.g. water flows in fractures) encountered at Erzberg revealed an unexpected hydrochemical diversity which could be evaluated in the context of this specific carbonate aquifer and the temporally restrictive (Alpine) hydrogeological and climate conditions.

- **Caves and speleothems** have established as valuable chemical-sedimentary archives mainly relying on their multiple ways of recording paleoenvironmental information, their wide geographical distribution and their geochemical potential for precise chronologies. In most studies published, however, they still suffer from providing only **qualitative climate information** and their compatibility with the **quantitative demand of computer models** calculating past and future climate scenarios is therefore limited. Regardless of the natural complexity and labour intense realization, cave-specific and sophisticated monitoring programs, atmospheric parameter to carbonate **proxy transfer functions and calibrations** might be an obvious way to go.

Acknowledgements

I would like to express my deep gratitude to Martin Dietzel (Graz University of Technology) for the numerous and extensive discussions and invaluable mentoring time on diverse fundamental and applied scientific and interdisciplinary topics. Many thanks to Werner E. Piller (Karl-Franzens-University, Graz) for promoting the publication of this manuscript and for being the chairman during my habilitation process. In the latter context, I would like to thank the habilitation committee at TU Graz represented by Daniel Scott Kieffer, Dorothee Hippler, Michael Wedenig, Martin Dietzel, and the dean of the faculty of construction engineering, Gerald Zenz. The reviewers of my cumulative habilitation thesis (involving chapters of this publication), Anton Eisenhauer (Geomar, Kiel), Ingrid Stober (Karlsruhe Institute of Technology) and Adrian Immenhauser (Ruhr-University Bochum), are also acknowledged accordingly. Christoph Spötl (University of Innsbruck) is acknowledged for his guidance during my PhD studies and earlier scientific career at the Institute of Geology in Innsbruck. Albrecht Leis (JR-AquaConSol GmbH, Graz) helped in providing his expert knowledge and state-of-the-art stable isotope analyses of carbonates and water samples on many occasions. Richard Lawrence Edwards (University of Minnesota, USA) and Hai Cheng (now at Xi´an Jiaotong University, China) facilitated and guided my Postdoc research activities focusing on uranium-thorium isotope geochemistry at the Department of Earth Sciences in Minneapolis. My sincerest appreciation to Jan Kramers (University of Bern, Switzerland; now at University of Johannesburg, South Africa) for his advice during multiple research stays with the isotope geology group in Bern. Michael Sarnthein (Christian-Albrechts-University in Kiel) supported my earlier scientific development and provided access to a scientific ocean cruise for drilling sediment cores between Australia and Indonesia (SO-185 VITAL, research vessel SONNE). Further, I would like to thank my professional collaborators in diverse research projects and analytical techniques of the last years, namely Tobias Kluge (University of Heidelberg, Germany), Xianfeng Wang and Lin Ke (both at Earth Observatory of Singapore), Andrea Mindszenty (Eötvös Loránd University, Hungary), János Szanyi (University of Szeged, Hungary), József Deák (GWIS Ltd., Hungary), Edith Haslinger (Austrian Institute of Technology, Vienna) and Johann E. Goldbrunner (Geoteam GmbH, Graz). Gina E. Moseley and Marc Luetscher (both at University of Innsbruck) and Silvia Frisia (University of Newcastle, Australia) cooperated on cave and speleothem based paleoclimate research partially reported in this publication. Further thanks go to my Institute of Applied Geosciences (IAG) colleagues and collaborators Andre Baldermann, Dorothee Hippler, Cyrill Grengg, Stefanie Eichinger and to Florian Mittermayr (Institute of Technology & Testing of Building Materials, Graz), Walter Kurz and Christoph A. Hauzenberger (both at Karl-Franzens-University in Graz). Daniel Scott Kieffer and Dietmar Klammer, as well as their team consisting of Peter Schreiber, Daniela Sobian, Anna Maria Pendl and Evelyn Reiterer are acknowledged for their support in various IAG organizational skills and works. Special thanks to Judith Jernej, Maria Hierz, Andrea Wolf and Sylvia Perchthold considering their dedicated and often prompt analytical work in our institute's laboratories. Othmar Nestroy and Hans Zojer (both at IAG) provided experienced and friendly advice on scientific and other topics. Ralf Benischke (IAG) and Peter Reichl (Amt der Steirischen Landesregierung, Graz) are acknowledged for their help during several field operations. My best thanks to Fritz Geissler (Katerloch Cave, Weiz) and Hannes M. Pluch (VA Erzberg GmbH) for providing access and operational skills at the respective study sites. Many thanks also to Kathleen A. Wendt (University of Innsbruck) and Isaac J. Kell Duivestein for English language proofreading of selected chapters. Finally, I would like to thank my partner in life Alexandra Kilarski for many great moments and experiences living in Innsbruck, Graz and Vienna.

References

Affek, H.P., Matthews, A., Ayalon, A., Bar-Matthews, M., Burstyn, Y., Zaarur, S. & Zilberman, T. (2014): Accounting for kinetic isotope effects in Soreq Cave (Israel) speleothems. – Geochimica et Cosmochimica Acta, **143**, 303–318, New York.

Akin, T. & Kargi, H. (2019): Modeling the geochemical evolution of fluids in geothermal wells and its implication for sustainable energy production. – Geothermics, **77**, 115–129, Amsterdam.

Al Helal, A., Soames, A., Gubner, R., Iglauer, S. & Barifcani, A. (2018): Influence of magnetic fields on calcium carbonate scaling in aqueous solutions at 150°C and 1bar. – Journal of Colloid and Interface Science, **509**, 472–484, Amsterdam.

Alt-Epping, P., Waber, H.N., Diamond, L.W. & Eichinger, L. (2013): Reactive transport modeling of the geothermal system at Bad Blumau, Austria: Implications of the combined extraction of heat and CO_2. – Geothermics, **45**, 18–30, Amsterdam.

Angel, F. (1939): Unser Erzberg. – Mitteilungen des Naturwissenschaftlichen Vereines für Steiermark, **75**, 227–321, Graz.

Arndt, M., Virgo, S., Cox, S.F. & Urai, J.L. (2014): Changes in fluid pathways in a calcite vein mesh (Natih Formation, Oman Mountains): insights from stable isotopes. – Geofluids, **14**, 391–418, Oxford.

Arp, G., Thiel, V., Reimer, A., Michaelis, W. & Reitner, J. (1999): Biofilm exopolymers control microbialite formation at thermal springs discharging into the alkaline Pyramid Lake, Nevada, USA. – Sedimentary Geology, **126**, 159–176, Amsterdam.

Asrat, A., Baker, A., Mohammed, M.U., Leng, M.J., Calsteren, P.V. & Smith, C. (2007): A high-resolution multi-proxy stalagmite record from Mechara, Southeastern Ethiopia: palaeohydrological implications for speleothem palaeoclimate reconstruction. – Journal of Quaternary Science, **22**, 53–63, Chichester.

Auer, I., Böhm, R., Jurkovic, A., Lipa, W., Orlik, A., Potzmann, R., Schöner, W., Ungersböck, M., Matulla, C., Briffa, K., Jones, P., Efthymiadis, D., Brunetti, M., Nanni, T., Maugeri, M., Mercalli, L., Mestre, O., Moisselin, J.-M., Begert, M., Müller-Westermeier, G., Kveton, V., Bochnicek, O., Stastny, P., Lapin, M., Szalai, S., Szentimrey, T., Cegnar, T., Dolinar, M., Gajic-Capka, M., Zaninovic, K., Majstorovic, Z. & Nieplova, E. (2007): HISTALP – historical instrumental climatological surface time series of the Greater Alpine Region. – International Journal of Climatology, **27**, 17–46, Chichester.

Bajo, P., Borsato, A., Drysdale, R., Hua, Q., Frisia, S., Zanchetta, G., Hellstrom, J. & Woodhead, J. (2017): Stalagmite carbon isotopes and dead carbon proportion (DCP) in a near-closed-system situation: An interplay between sulphuric and carbonic acid dissolution. – Geochimica et Cosmochimica Acta, **210**, 208–227, New York.

Baker, A., Smith, C.L., Jex, C., Fairchild, I.J., Genty, D. & Fuller, L. (2008): Annually Laminated Speleothems: a Review. – International Journal of Speleology, **37**, 193–206, Tampa.

Balan, E., Noireaux, J., Mavromatis, V., Saldi, G., Montouillout, V., Blanchard, M., Pietrucci, F., Gervais, C., Rustad, J.R., Schott, J. & Gaillardet, J. (2018): Theoretical isotopic fractionation between structural boron in carbonates and aqueous boric acid and borate ion. – Geochimica et Cosmochimica Acta, **222**, 117–129, New York.

Baldermann, A., Deditius, A.P., Dietzel, M., Fichtner, V., Fischer, C., Hippler, D., Leis, A., Baldermann, C., Mavromatis, V., Stickler, C.P. & Strauss, H. (2015): The role of bacterial sulfate reduction during dolomite precipitation: Implications from Upper Jurassic platform carbonates. – Chemical Geology, **412**, 1–14, Amsterdam.

Baldini, J.U.L., McDermott, F., Hoffmann, D.L., Richards, D.A. & Clipson, N. (2008): Very high-frequency and seasonal cave atmosphere PCO_2 variability: Implications for stalagmite growth and oxygen isotope-based paleoclimate records. – Earth and Planetary Science Letters, **272**, 118–129, Amsterdam.

Barker, S., Knorr, G., Edwards, R.L., Parrenin, F., Putnam, A.E., Skinner, L.C., Wolff, E. & Ziegler, M. (2011): 800,000 Years of Abrupt Climate Variability. – Science, **334**, 347–351, Washington, D.C.

Barker, S., Chen, J., Gong, X., Jonkers, L., Knorr, G. & Thornalley, D. (2015): Icebergs not the trigger for North Atlantic cold events. – Nature, **520**, 333–336, London.

Baroň, I., Plan, L., Sokol, L., Grasemann, B., Melichar, R., Mitrovic, I. & Stemberk, J. (2019): Present-day kinematic behaviour of active faults in the Eastern Alps. – Tectonophysics, **752**, 1–23, Amsterdam.

Barta, G. (2014): Paleoenvironmental reconstruction based on the morphology and distribution of secondary carbonates of the loess-paleosol sequence at Süttő, Hungary. – Quaternary International, **319**, 64–75, Oxford.

Berger, A. & Loutre, M.F. (2002): An Exceptionally Long Interglacial Ahead? – Science, **297**, 1287–1288, Washington, D.C.

Berner, R.A. (1975): The role of magnesium in the crystal growth of calcite and aragonite from sea water. – Geochimica et Cosmochimica Acta, **39**, 489–504, New York.

Bischoff, J.L., Fitzpatrick, J.A. & Rosenbauer, R.J. (1993): The Solubility and Stabilization of ikaite ($CaCO_3.6H_2O$) from 0 °C to 25 °C: Environmental and Paleoclimatic Implications for Thinolite Tufa. – The Journal of Geology, **101**, 21–33, London.

Bjørnstad, T. & Stamatakis, E. (2006): Mechanisms of mineral scaling in oil and geothermal wells studied in laboratory experiments by nuclear techniques. – Czechoslovak Journal of Physics, **56**, 405–416, Prague.

Blyth, A.J., Hartland, A. & Baker, A. (2016): Organic proxies in speleothems – New developments, advantages and limitations. – Quaternary Science Reviews, **149**, 1–17, Amsterdam.

Boch, R. (2008): Stalagmites from Katerloch Cave, Austria: Growth dynamics and high-resolution records of climate change. – PhD thesis, University of Innsbruck, 223 pp., Innsbruck.

Boch, R. & Spötl, C. (2011): Reconstructing palaeoprecipitation from an active cave flowstone. – Journal of Quaternary Science, **26**, 675–687, Chichester.

Boch, R., Spötl, C., Reitner, J.M. & Kramers, J. (2005): A Lateglacial travertine deposit in Eastern Tyrol (Austria). – Austrian Journal of Earth Sciences, **98**, 78–91, Wien.

Boch, R., Spötl, C. & Kramers, J. (2009): High-resolution isotope records of early Holocene rapid climate change from two coeval stalagmites of Katerloch Cave, Austria. – Quaternary Science Reviews, **28**, 2527–2538, Amsterdam.

Boch, R., Spötl, C. & Kramers, J. (2010): Wachstumsphasen von Stalagmiten im Katerloch (2833/59). – Die Höhle, **61**, 48–56, Wien.

Boch, R., Spötl, C. & Frisia, S. (2011a): Origin and palaeoenvironmental significance of lamination in stalagmites from Katerloch Cave, Austria. – Sedimentology, **58**, 508–531, Amsterdam.

Boch, R., Cheng, H., Spötl, C., Edwards, R.L., Wang, X. & Häuselmann, P. (2011b): NALPS: a precisely dated European climate record 120–60 ka. – Climate of the Past, **7**, 1247–1259, Göttingen.

Boch, R., Dietzel, M., Reichl, P., Leis, A., Baldermann, A., Mittermayr, F. & Pölt, P. (2015): Rapid ikaite ($CaCO_3 \cdot 6H_2O$) crystallization in a man-made river bed: Hydrogeochemical monitoring of a rarely documented mineral formation. – Applied Geochemistry, **63**, 366–379, Amsterdam.

Boch, R., Szanyi, J., Leis, A., Mindszenty, A., Deák, J., Kluge, T., Hippler, D., Demény, A. & Dietzel, M. (2016): Geothermal Carbonate Scaling: Forensic Studies Applying High-Resolution Geochemical Methods. – Proceedings of the European Geothermal Congress, paper #111, 1–10, Strasbourg.

Boch, R., Leis, A., Haslinger, E., Goldbrunner, J.E., Mittermayr, F., Fröschl, H., Hippler, D. & Dietzel, M. (2017a): Scale-fragment formation impairing geothermal energy production: interacting H_2S corrosion and $CaCO_3$ crystal growth. – Geothermal Energy, **5**: 4, https://dx.doi.org/10.1186/s40517-017-0062-3

Boch, R., Leis, A., Mindszenty, A., Goldbrunner, J.E., Szanyi, J., Deák, J., Haslinger, E., Virág, M., Mittermayr, F. & Dietzel, M. (2017b): Scaling Forensics: Evaluating geothermal production conditions from scales as chemical-sedimentary archives. – Proceedings of the German Geothermal Congress 2017, paper #P6, 1–12, Munich.

Boch, R., Wang, X., Kluge, T., Leis, A., Lin, K., Pluch, H., Mittermayr, F., Baldermann, A., Böttcher, M.E. & Dietzel, M. (2019): Aragonite–calcite veins of the 'Erzberg' iron ore deposit (Austria): Environmental implications from young fractures. – Sedimentology, **66**, 604–635, Amsterdam.

Bonifacie, M., Calmels, D., Eiler, J.M., Horita, J., Chaduteau, C., Vasconcelos, C., Agrinier, P., Katz, A., Passey, B.H., Ferry, J.M. & Bourrand, J.-J. (2017): Calibration of the dolomite clumped isotope thermometer from 25 to 350°C, and implications for a universal calibration for all (Ca, Mg, Fe)CO_3 carbonates. – Geochimica et Cosmochimica Acta, **200**, 255–279, New York.

Borsato, A., Frisia, S., Fairchild, I.J., Somogyi, A. & Susini, J. (2007): Trace element distribution in annual stalagmite laminae mapped by micrometer-resolution X-ray fluorescence: Implications for incorporation of environmentally significant species. – Geochimica et Cosmochimica Acta, **71**, 1494–1512, New York.

Borsato, A., Frisia, S., Wynn, P.M., Fairchild, I.J. & Miorandi, R. (2015): Sulphate concentration in cave dripwater and speleothems: long-term trends and overview of its significance as proxy for environmental processes and climate changes. – Quaternary Science Reviews, **127**, 48–60, Amsterdam.

Bots, P., Benning, L.G., Rodriguez-Blanco, J.-D., Roncal-Herrero, T. & Shaw, S. (2012): Mechanistic Insights into the Crystallization of Amorphous Calcium Carbonate (ACC). – Crystal Growth and Design, **12**, 3806–3814, Washington, D.C.

Böttcher, M.E. & Dietzel, M. (2010): Metal-ion partitioning during low-temperature precipitation and dissolution of anhydrous carbonates and sulphates. – EMU Notes in Mineralogy, **10**, 139–187.

Bramson, D., Hasson, D. & Semiat, R. (1995): The roles of gas bubbling, wall crystallization and particulate deposition in $CaSO_4$ scale formation. – Desalination, **100**, 105–113, Amsterdam.

Brand, U. (1994): Morphochemical and replacement diagenesis of biogenic carbonates. – Developments in Sedimentology, **51**, 217–282, Amsterdam.

Brauer, A., Allen, J.R.M., Mingram, J., Dulski, P., Wulf, S. & Huntley, B. (2007): Evidence for last interglacial chronology and environmental change from Southern Europe. – Proceedings of the National Academy of Sciences, **104**, 450–455, Allahabad.

Brogi, A., Capezzuoli, E., Buracchi, E. & Branca, M. (2012): Tectonic control on travertine and calcareous tufa deposition in a low-temperature geothermal system (Sarteano, Central Italy). – Journal of the Geological Society, **169**, 461–476, London.

Bronk Ramsey, C. & Lee, S. (2013): Recent and planned developments of the program OxCal. – Radiocarbon, **55**, 720–730, Cambridge.

Bryda, G., van Husen, D., Kreuss, O., Koukal, V., Moser, M., Pavlik, W., Schönlaub, H.P. & Wagreich, M. (2013): Erläuterungen zu Blatt 101 Eisenerz. – 223 pp., Geologische Bundesanstalt, Wien.

Buschek, T.A., Bielicki, J.M., Chen, M., Sun, Y., Hao, Y., Edmunds, T.A., Saar, M.O. & Randolph, J.B. (2014): Integrating CO_2 Storage with Geothermal Resources for Dispatchable Renewable Electricity. – Energy Procedia, **63**, 7619–7630, Amsterdam.

Busenberg, E. & Plummer, L.N. (1985): Kinetic and thermodynamic factors controlling the distribution of SO_4^{2-} and Na^+ in calcites and selected aragonites. – Geochimica et Cosmochimica Acta, **49**, 713–725, New York.

Candido, C.A.S. & Zarrouk, S.J. (2017): Scaling Mitigations for the Binary Plant Vaporizer: Upper Mahiao, the Philippines. – Proceedings 39th New Zealand Geothermal Workshop, Rotorua, 1–8, Rotorua, New Zealand.

Capezzuoli, E., Gandin, A. & Pedley, M. (2014): Decoding tufa and travertine (fresh water carbonates) in the sedimentary record: The state of the art. – Sedimentology, **61**, 1–21, Amsterdam.

Carroll, J.J., Slupsky, J.D. & Mather, A.E. (1991): The Solubility of Carbon Dioxide in Water at Low Pressure. – Journal of Physical and Chemical Reference Data, **20**, 1201–1209, Melville, N.Y.

Casella, L.A., Griesshaber, E., Yin, X., Ziegler, A., Mavromatis, V., Müller, D., Ritter, A.C., Hippler, D., Harper, E.M., Dietzel, M., Immenhauser, A., Schöne, B.R., Angiolini, L. & Schmahl, W.W. (2017): Experimental diagenesis: insights into aragonite to calcite transformation of Arctica islandica shells by hydrothermal treatment. – Biogeosciences, **14**, 1461–1492, Washington, D.C.

Celle-Jeanton, H., Travi, Y. & Blavoux, B. (2001): Isotopic typology of the precipitation in the Western Mediterranean Region at three different time scales. – Geophysical Research Letters, **28**, 1215–1218, Washington, D.C.

Chafetz, H.S. & Guidry, S.A. (1999): Bacterial shrubs, crystal shrubs, and ray-crystal shrubs: bacterial vs. abiotic precipitation. – Sedimentary Geology, **126**, 57–74, Amsterdam.

Chang, L.L.Y., Deer, W.A., Howie, R.A. & Zussman, J. (1998): Rock-Forming Minerals – Non-silicates: Sulphates, Carbonates, Phosphates and Halides. – 2nd edition, 383 pp., Geological Society of London, London.

Chaussemier, M., Pourmohtasham, E., Gelus, D., Pécoul, N., Perrot, H., Lédion, J., Cheap-Charpentier, H. & Horner, O. (2015): State of art of natural inhibitors of calcium carbonate scaling – A review article. – Desalination, **356**, 47–55, Amsterdam.

Chen, Y., Cui, Y., Guimond Barrett, A., Chille, F. & Lassalle, S. (2019): Investigation of calcite precipitation in the drainage system of railway tunnels. – Tunnelling and Underground Space Technology, **84**, 45–55, Oxford.

Cheng, H., Lawrence Edwards, R., Shen, C.-C., Polyak, V.J., Asmerom, Y., Woodhead, J., Hellstrom, J., Wang, Y., Kong, X., Spötl, C., Wang, X. & Calvin Alexander Jr, E. (2013): Improvements in ^{230}Th dating, ^{230}Th and ^{234}U half-life values, and U–Th isotopic measurements by multi-collector inductively coupled plasma mass spectrometry. – Earth and Planetary Science Letters, **371/372**, 82–91, Amsterdam.

Cheng, H., Edwards, R.L., Sinha, A., Spötl, C., Yi, L., Chen, S., Kelly, M., Kathayat, G., Wang, X., Li, X., Kong, X., Wang, Y., Ning, Y. & Zhang, H. (2016): The Asian monsoon over the past 640,000 years and ice age terminations. – Nature, **534**, 640–646, London.

Choi, Y.-S., Nesic, S. & Ling, S. (2011): Effect of H_2S on the CO_2 corrosion of carbon steel in acidic solutions. – Electrochimica Acta, **56**, 1752–1760, Kidlington.

Clark, I.D. & Fritz, P. (1997): Environmental Isotopes in Hydrogeology. – CRC Press LLC, 1st ed., 352 pp., Boca Raton.

CLARKSON, J.R., PRICE, T.J. & ADAMS, C.J. (1992): Role of metastable phases in the spontaneous precipitation of calcium carbonate. – Journal of the Chemical Society, Faraday Transactions, **88**, 243–249, London.

COLLISTER, C. & MATTEY, D. (2008): Controls on water drop volume and speleothem drip sites: An experimental study. – Journal of Hydrology, **358**, 259–267, Amsterdam.

COLUCCI, R.R., LUETSCHER, M., FORTE, E., GUGLIELMIN, M., LENAZ, D., PRINCIVALLE, F. & VITA, F. (2017): First alpine evidence of in situ coarse cryogenic cave carbonates (CCC_{coarse}). – Geografia Fisica e Dinamica Quaternaria, **40**, 53–59, Torino.

COPLEN, T.B. (2007): Calibration of the calcite–water oxygen-isotope geothermometer at Devils Hole, Nevada, a natural laboratory. – Geochimica et Cosmochimica Acta, **71**, 3948–3957, New York.

CORSI, R. (1986): Scaling and corrosion in geothermal equipment: problems and preventive measures. – Geothermics, **15**, 839–856, Amsterdam.

COUNCIL, T.C. & BENNETT, P.C. (1993): Geochemistry of ikaite formation at Mono Lake, California: Implications for the origin of tufa mounds. – Geology, **21**, 971–974, Washington, D.C.

CRAIG, H. (1961): Isotopic variations in meteoric waters. – Science, **133**, 1702–1703, Washington, D.C.

CRUZ, F.W., BURNS, S.J., KARMANN, I., SHARP, W.D., VUILLE, M., CARDOSO, A.O., FERRARI, J.A., DIAS, P.L.S. & VIANA, O. (2005): Insolation-driven changes in atmospheric circulation over the past 116,000 years in subtropical Brazil. – Nature, **434**, 63–66, London.

DAËRON, M., GUO, W., EILER, J., GENTY, D., BLAMART, D., BOCH, R., DRYSDALE, R., MAIRE, R., WAINER, K. & ZANCHETTA, G. (2011): $^{13}C^{18}O$ clumping in speleothems: Observations from natural caves and precipitation experiments. – Geochimica et Cosmochimica Acta, **75**, 3303–3317, New York.

DAËRON, M., BLAMART, D., PERAL, M. & AFFEK, H.P. (2016): Absolute isotopic abundance ratios and the accuracy of Δ_{47} measurements. – Chemical Geology, **442**, 83–96, Amsterdam.

DAËRON, M., DRYSDALE, R.N., PERAL, M., HUYGHE, D., BLAMART, D., COPLEN, T.B., LARTAUD, F. & ZANCHETTA, G. (2019): Most Earth-surface calcites precipitate out of isotopic equilibrium. – Nature Communications, **10**: 429, London. https://dx.doi.org/10.1038/s41467-019-08336-5

DANDURAND, J.L., GOUT, R., HOEFS, J., MENSCHEL, G., SCHOTT, J. & USDOWSKI, E. (1982): Kinetically controlled variations of major components and carbon and oxygen isotopes in a calcite-precipitating spring. – Chemical Geology, **36**, 299–315, Amsterdam.

DAY, C.C. & HENDERSON, G.M. (2013): Controls on trace-element partitioning in cave-analogue calcite. – Geochimica et Cosmochimica Acta, **120**, 612–627, New York.

DE BOEVER, E., BRASIER, A.T., FOUBERT, A. & KELE, S. (2017): What do we really know about early diagenesis of non-marine carbonates? – Sedimentary Geology, **361**, 25–51, Amsterdam.

DECKER, K., PERESSON, H. & HINSCH, R. (2005): Active tectonics and Quaternary basin formation along the Vienna Basin Transform fault. – Quaternary Science Reviews, **24**, 305–320, Amsterdam.

DEGRYSE, P. & VANHAECKE, F. (2016): Status and prospects for quasi-non-destructive analysis of ancient artefacts via LA-ICP-MS. – Elements, **12**, 341–346, Québec.

DEINES, P., LANGMUIR, D. & HARMON, R.S. (1974): Stable carbon isotope ratios and the existence of a gas phase in the evolution of carbonate ground waters. – Geochimica et Cosmochimica Acta, **38**, 1147–1164, New York.

DEMÉNY, A. & SIKLÓSY, Z. (2008): Combination of off-line preparation and continuous flow mass spectrometry: D/H analyses of inclusion waters. – Rapid Communications in Mass Spectrometry, **22**, 1329–1334, Chichester.

DEMÉNY, A., NÉMETH, P., CZUPPON, G., LEÉL-ŐSSY, S., SZABÓ, M., JUDIK, K., NÉMETH, T. & STIEBER, J. (2016a): Formation of amorphous calcium carbonate in caves and its implications for speleothem research. – Scientific Reports, **6**: 39602, London. https://dx.doi.org/10.1038/srep39602

DEMÉNY, A., CZUPPON, G., KERN, Z., LEÉL-ŐSSY, S., NÉMETH, A., SZABÓ, M., TÓTH, M., WU, C.-C., SHEN, C.-C., MOLNÁR, M., NÉMETH, T., NÉMETH, P. & ÓVÁRI, M. (2016b): Recrystallization-induced oxygen isotope changes in inclusion-hosted water of speleothems – Paleoclimatological implications. – Quaternary International, **415**, 25–32, Oxford.

DEMÉNY, A., KERN, Z., CZUPPON, G., NÉMETH, A., LEÉL-ŐSSY, S., SIKLÓSY, Z., LIN, K., HU, H.-M., SHEN, C.-C., VENNEMANN, T.W. & HASZPRA, L. (2017): Stable isotope compositions of speleothems from the last interglacial – Spatial patterns of climate fluctuations in Europe. – Quaternary Science Reviews, **161**, 68–80, Amsterdam.

DEMIR, M.M., BABA, A., ATILLA, V. & INANLI, M. (2014): Types of the scaling in hyper saline geothermal system in northwest Turkey. – Geothermics, **50**, 1–9, Amsterdam.

DENNISTON, R.F. & LUETSCHER, M. (2017): Speleothems as high-resolution paleoflood archives. – Quaternary Science Reviews, **170**, 1–13, Amsterdam.

DEPAOLO, D.J., COLE, D.R., NAVROTSKY, A. & BOURG, I.C. (2013): Geochemistry of Geologic Carbon Sequestration: An Overview. – Reviews in Mineralogy and Geochemistry, **77**, 1–14, Washington, D.C.

DETTMAN, D.L., REISCHE, A.K. & LOHMANN, K.C. (1999): Controls on the stable isotope composition of seasonal growth bands in aragonitic fresh-water bivalves (unioniëe). – Geochimica et Cosmochimica Acta, **63**, 1049–1057, New York.

DE YOREO, J.J., GILBERT, P.U.P.A., SOMMERDIJK, N.A.J.M., PENN, R.L., WHITELAM, S., JOESTER, D., ZHANG, H., RIMER, J.D., NAVROTSKY, A., BANFIELD, J.F., WALLACE, A.F., MICHEL, F.M., MELDRUM, F.C., CÖLFEN, H. & DOVE, P.M. (2015): Crystallization by particle attachment in synthetic, biogenic, and geologic environments. – Science, **349**, 6247, aaa6760.

DIAZ, M.R., EBERLI, G.P., BLACKWELDER, P., PHILLIPS, B. & SWART, P.K. (2017): Microbially mediated organomineralization in the formation of ooids. – Geology, **45**, 771–774, Washington, D.C.

DIECKMANN, G.S., NEHRKE, G., PAPADIMITRIOU, S., GÖTTLICHER, J., STEININGER, R., KENNEDY, H., WOLF-GLADROW, D. & THOMAS, D.N. (2008): Calcium carbonate as ikaite crystals in Antarctic sea ice. – Geophysical Research Letters, **35**: L08501, Washington, D.C. https://dx.doi.org/10.1029/2008GL033540

DIETZEL, M. & BOCH, R. (2018): Radiometrische Altersdatierung von historischem Kalkmörtel – Geochemische Voraussetzungen und Ansätze zur Interpretation. – in press.

DIETZEL, M., USDOWSKI, E. & HOEFS, J. (1992): Chemical and $^{13}C/^{12}C$- and $^{18}O/^{16}O$-isotope evolution of alkaline drainage waters and the precipitation of calcite. – Applied Geochemistry, **7**, 177–184, Amsterdam.

DIETZEL, M., GUSSONE, N. & EISENHAUER, A. (2004): Co-precipitation of Sr^{2+} and Ba^{2+} with aragonite by membrane diffusion of CO_2 between 10 and 50 °C. – Chemical Geology, **203**, 139–151, Amsterdam.

DIETZEL, M., TANG, J., LEIS, A. & KÖHLER, S.J. (2009): Oxygen isotopic fractionation during inorganic calcite precipitation. – Effects of temperature, precipitation rate and pH. – Chemical Geology, **268**, 107–115, Amsterdam.

DIETZEL, M., PURGSTALLER, B., LEIS, A., REICHL, P., STADLER, H., NIEDERMAYR, A., RINDER, T. & WAGNER, H. (2013): Current challenges for scaling of tunnel drainage systems – Modelling approaches, monitoring tools and prevention strategies. – Geomechanics and Tunnelling, **6**, 743–753, Berlin.

Domínguez-Villar, D., Krklec, K., Pelicon, P., Fairchild, I.J., Cheng, H. & Edwards, L.R. (2017): Geochemistry of speleothems affected by aragonite to calcite recrystallization. – Potential inheritance from the precursor mineral. – Geochimica et Cosmochimica Acta, **200**, 310–329, New York.

Domínguez-Villar, D., Lojen, S., Krklec, K., Kozdon, R., Edwards, R.L. & Cheng, H. (2018): Ion microprobe $\delta^{18}O$ analyses to calibrate slow growth rate speleothem records with regional $\delta^{18}O$ records of precipitation. – Earth and Planetary Science Letters, **482**, 367–376, Amsterdam.

Dreybrodt, W. & Romanov, D. (2016): The evolution of ^{13}C and ^{18}O isotope composition of DIC in a calcite depositing film of water with isotope exchange between the DIC and a CO_2 containing atmosphere, and simultaneous evaporation of the water. Implication to climate proxies from stalagmites: A theoretical model. – Geochimica et Cosmochimica Acta, **195**, 323–338, New York.

D'Souza, S.M., Alexander, C., Carr, S.W., Waller, A.M., Whitcombe, M.J. & Vulfson, E.N. (1999): Directed nucleation of calcite at a crystal-imprinted polymer surface. – Nature, **398**, 312–316, London.

Duan, Z. & Sun, R. (2003): An improved model calculating CO_2 solubility in pure water and aqueous NaCl solutions from 273 to 533 K and from 0 to 2000 bar. – Chemical Geology, **193**, 257–271, Amsterdam.

Dublyansky, Y.V. (2012): Hydrothermal Caves. – In: White, W.B. & Culver, D.C. (Eds.): Encyclopedia of Caves, Chennai Academic Press, 2nd ed., 391–397, Amsterdam.

Dublyansky, Y.V. & Spötl, C. (2009): Hydrogen and oxygen isotopes of water from inclusions in minerals: design of a new crushing system and on-line continuous-flow isotope ratio mass spectrometric analysis. – Rapid Communications in Mass Spectrometry, **23**, 2605–2613, Chichester.

Dublyansky, Y.V. & Spötl, C. (2010): Evidence for a hypogene paleohydrogeological event at the prospective nuclear waste disposal site Yucca Mountain, Nevada, USA, revealed by the isotope composition of fluid-inclusion water. – Earth and Planetary Science Letters, **289**, 583–594, Amsterdam.

Dunbar, R.B. (2000): Clues from corals. – Nature, **407**, 956–958, London.

Dykoski, C.A., Edwards, R.L., Cheng, H., Yuan, D., Cai, Y., Zhang, M., Lin, Y., Qing, J., An, Z. & Revenaugh, J. (2005): A high-resolution, absolute-dated Holocene and deglacial Asian monsoon record from Dongge Cave, China. – Earth and Planetary Science Letters, **233**, 71–86, Amsterdam.

Edwards, R.L., Chen, J.H. & Wasserburg, G.J. (1987): ^{238}U- ^{234}U- ^{230}Th- ^{232}Th systematics and the precise measurement of time over the past 500,000 years. – Earth and Planetary Science Letters, **81**, 175–192, Amsterdam.

Eggins, S.M., Grün, R., McCulloch, M.T., Pike, A.W.G., Chappell, J., Kinsley, L., Mortimer, G., Shelley, M., Murray-Wallace, C.V., Spötl, C. & Taylor, L. (2005): In situ U-series dating by laser-ablation multi-collector ICPMS: new prospects for Quaternary geochronology. – Quaternary Science Reviews, **24**, 2523–2538, Amsterdam.

Eiler, J.M. (2007): "Clumped-isotope" geochemistry – The study of naturally-occurring, multiply-substituted isotopologues. – Earth and Planetary Science Letters, **262**, 309–327, Amsterdam.

Eiler, J.M., Clog, M., Magyar, P., Piasecki, A., Sessions, A., Stolper, D., Deerberg, M., Schlueter, H.-J. & Schwieters, J. (2013): A high-resolution gas-source isotope ratio mass spectrometer. – International Journal of Mass Spectrometry, **335**, 45–56, Amsterdam.

Eiler, J.M., Bergquist, B., Bourg, I., Cartigny, P., Farquhar, J., Gagnon, A., Guo, W., Halevy, I., Hofmann, A., Larson, T.E., Levin, N., Schauble, E.A. & Stolper, D. (2014): Frontiers of stable isotope geoscience. – Chemical Geology, **372**, 119–143, Amsterdam.

Epstein, S., Buchsbaum, R., Lowenstam, H. & Urey, H.C. (1953): Revised carbonate-water isotopic temperature scale. – Geological Society of America Bulletin, **64**, 1315–1326, Boulder.

Erler, D.V., Duncan, T.M., Murray, R., Maher, D.T., Santos, I.R., Gatland, J.R., Mangion, P. & Eyre, B.D. (2015): Applying cavity ring-down spectroscopy for the measurement of dissolved nitrous oxide concentrations and bulk nitrogen isotopic composition in aquatic systems: Correcting for interferences and field application. – Limnology and Oceanography: Methods, **13**, 391–401, Oxford.

Fairchild, I.J. & Baker, A. (2012): Speleothem Science – From Process to Past Environments. – 1st ed., 450 pp., Chichester (Wiley-Blackwell).

Fairchild, I.J. & Treble, P.C. (2009): Trace elements in speleothems as recorders of environmental change. – Quaternary Science Reviews, **28**, 449–468, Amsterdam.

Fairchild, I.J., Smith, C. L., Baker, A., Fuller, L., Spötl, C., Mattey, D., McDermott, F. & E.I.M.F. (2006): Modification and preservation of environmental signals in speleothems. – Earth-Science Reviews, **75**, 105–153, Amsterdam.

Fathi, A., Mohamed, T., Claude, G., Maurin, G. & Mohamed, B.A. (2006): Effect of a magnetic water treatment on homogeneous and heterogeneous precipitation of calcium carbonate. – Water Research, **40**, 1941–1950, Amsterdam.

Fermani, S., Njegic Dzakula, B., Reggi, M., Falini, G. & Kralj, D. (2017): Effects of magnesium and temperature control on aragonite crystal aggregation and morphology. – CrystEngComm, **19**, 2451–2455, London.

Fernandez-Cortes, A., Sanchez-Moral, S., Cuezva, S., Canaveras, J.C. & Abella, R. (2009): Annual and transient signatures of gas exchange and transport in the Castanar de Ibor cave (Spain). – International Journal of Speleology, **38**, 153–162, Tampa.

Field, L.P., Milodowski, A.E., Shaw, R.P., Stevens, L.A., Hall, M.R., Kilpatrick, A., Gunn, J., Kemp, S.J. & Ellis, M.A. (2017): Unusual morphologies and the occurrence of pseudomorphs after ikaite ($CaCO_3.6H_2O$) in fast growing, hyperalkaline speleothems. – Mineralogical Magazine, **81**, 565–589, London.

Finster, M., Clark, C., Schroeder, J. & Martino, L. (2015): Geothermal produced fluids: Characteristics, treatment technologies, and management options. – Renewable and Sustainable Energy Reviews, **50**, 952–966, Oxford.

Fischer, M., Thomas, D.N., Krell, A., Nehrke, G., Göttlicher, J., Norman, L., Meiners, K.M., Riaux-Gobin, C. & Dieckmann, G.S. (2013): Quantification of ikaite in Antarctic sea ice. – Antarctic Science, **25**, 421–432, Cambridge.

Fleitmann, D., Burns, S.J., Mangini, A., Mudelsee, M., Kramers, J., Villa, I., Neff, U., Al-Subbary, A.A., Buettner, A., Hippler, D. & Matter, A. (2007): Holocene ITCZ and Indian monsoon dynamics recorded in stalagmites from Oman and Yemen (Socotra). – Quaternary Science Reviews, **26**, 170–188, Amsterdam.

Fohlmeister, J., Plessen, B., Dudashvili, A.S., Tjallingii, R., Wolff, C., Gafurov, A. & Cheng, H. (2017): Winter precipitation changes during the Medieval Climate Anomaly and the Little Ice Age in arid Central Asia. – Quaternary Science Reviews, **178**, 24–36, Amsterdam.

Ford, D. & Williams, P. (2007): Karst Hydrogeology and Geomorphology. – 2nd ed., 562 pp., Chichester (John Wiley & Sons Ltd, UK).

FOUKE, B.W. (2011): Hot-spring Systems Geobiology: abiotic and biotic influences on travertine formation at Mammoth Hot Springs, Yellowstone National Park, USA. – Sedimentology, **58**, 170–219, Amsterdam.

FRAPPIER, A.B., SAHAGIAN, D., CARPENTER, S.J., GONZALEZ, L.A. & FRAPPIER, B.R. (2007): Stalagmite stable isotope record of recent tropical cyclone events. – Geology, **35**, 111–114, Washington, D.C.

FREYTET, P. & VERRECCHIA, E.P. (1998): Freshwater organisms that build stromatolites: a synopsis of biocrystallization by prokaryotic and eukaryotic algae. – Sedimentology, **45**, 535–563, Amsterdam.

FREYTET, P. & VERRECCHIA, E.P. (1999): Calcitic radial palisadic fabric in freshwater stromatolites: diagenetic and recrystallized feature or physicochemical sinter crust? – Sedimentary Geology, **126**, 97–102, Amsterdam.

FRIEDMAN, I. & O'NEIL, J.R. (1977): Compilation of stable isotope fractionation factors of geochemical interest. – In: FLEISCHER, M. (Ed.): Data of Geochemistry, 6th ed. – Geological Survey Professional Paper, 440–KK, Washington.

FRISIA, S. (2015): Microstratigraphic logging of calcite fabrics in speleothems as tool for palaeoclimate studies. – International Journal of Speleology, **44**, 1–16, Tampa.

FRISIA, S., BORSATO, A., FAIRCHILD, I.J., MCDERMOTT, F. & SELMO, E.M. (2002): Aragonite-calcite relationships in speleothems (Grotte De Clamouse, France): Environment, fabrics, and carbonate geochemistry. – Journal of Sedimentary Research, **72**, 687–699, Tulsa.

GABRIELLI, C., JAOUHARI, R., MAURIN, G. & KEDDAM, M. (2001): Magnetic water treatment for scale prevention. – Water Research, **35**, 3249–3259, Amsterdam.

GALAN, I., BALDERMANN, A., KUSTERLE, W., DIETZEL, M. & MITTERMAYR, F. (2019): Durability of shotcrete for underground support–Review and update. – Construction and Building Materials, **202**, 465–493, Oxford.

GEBAUER, D., VÖLKEL, A. & CÖLFEN, H. (2008): Stable prenucleation calcium carbonate clusters. – Science, **322**, 1819–1822, Washington, D.C.

GEBAUER, D., CÖLFEN, H., VERCH, A. & ANTONIETTI, M. (2009): The multiple roles of additives in $CaCO_3$ crystallization: A quantitative case study. – Advanced Materials, **21**, 435–439, Weinheim.

GHOSH, P., ADKINS, J., AFFEK, H., BALTA, B., GUO, W., SCHAUBLE, E.A., SCHRAG, D. & EILER, J.M. (2006): ^{13}C–^{18}O bonds in carbonate minerals: A new kind of paleothermometer. – Geochimica et Cosmochimica Acta, **70**, 1439–1456, New York.

GOPI, S.P. & SUBRAMANIAN, V.K. (2012): Polymorphism in $CaCO_3$ – Effect of temperature under the influence of EDTA (di sodium salt). – Desalination, **297**, 38–47, Amsterdam.

GREINERT, J. & DERKACHEV, A. (2004): Glendonites and methane-derived Mg-calcites in the Sea of Okhotsk, Eastern Siberia: implications of a venting-related ikaite/glendonite formation. – Marine Geology, **204**, 129–144, Amsterdam.

GRENGG, C., MITTERMAYR, F., BALDERMANN, A., BÖTTCHER, M.E., LEIS, A., KORAIMANN, G., GRUNERT, P. & DIETZEL, M. (2015): Microbiologically induced concrete corrosion: A case study from a combined sewer network. – Cement and Concrete Research, **77**, 16–25, Oxford.

GRENGG, C., MITTERMAYR, F., KORAIMANN, G., KONRAD, F., SZABÓ, M., DEMENY, A. & DIETZEL, M. (2017): The decisive role of acidophilic bacteria in concrete sewer networks: A new model for fast progressing microbial concrete corrosion. – Cement and Concrete Research, **101**, 93–101, Oxford.

GRENGG, C., MITTERMAYR, F., UKRAINCZYK, N., KORAIMANN, G., KIENESBERGER, S. & DIETZEL, M. (2018): Advances in concrete materials for sewer systems affected by microbial induced concrete corrosion: A review. – Water Research, **134**, 341–352, Amsterdam.

GUO, L.I. & RIDING, R. (1992): Microbial micritic carbonates in uppermost Permian reefs, Sichuan Basin, southern China: some similarities with recent travertines. – Sedimentology, **39**, 37–53, Amsterdam.

GUO, L., ANDREWS, J., RIDING, R., DENNIS, P. & DRESSER, Q. (1996): Possible microbial effects on stable carbon isotopes in hot-spring travertines. – Journal of Sedimentary Research, **66**, 468–473, Tulsa.

GUSSONE, N., EISENHAUER, A., HEUSER, A., DIETZEL, M., BOCK, B., BÖHM, F., SPERO, H.J., LEA, D.W., BIJMA, J. & NÄGLER, T.F. (2003): Model for kinetic effects on calcium isotope fractionation ($\delta^{44}Ca$) in inorganic aragonite and cultured planktonic foraminifera. – Geochimica et Cosmochimica Acta, **67**, 1375–1382, New York.

GUSSONE, N., NEHRKE, G. & TEICHERT, B.M.A. (2011): Calcium isotope fractionation in ikaite and vaterite. – Chemical Geology, **285**, 194–202, Amsterdam.

GUSSONE, N., SCHMITT, A.-D., HEUSER, A., WOMBACHER, F., DIETZEL, M., TIPPER, E. & SCHILLER, M. (2016): Calcium Stable Isotope Geochemistry. – 1st ed., 260 pp., Berlin–Heidelberg (Springer).

HAGER, B. & FOELSCHE, U. (2015): Stable isotope composition of precipitation in Austria. – Austrian Journal of Earth Sciences, **108**, 2–13, Wien.

HAKLIDIR, F.T. & HAKLIDIR, M. (2017): Fuzzy control of calcium carbonate and silica scales in geothermal systems. – Geothermics, **70**, 230–238, Amsterdam.

HANSHAW, B.B. & BACK, W. (1979): Major geochemical processes in the evolution of carbonate – Aquifer systems. – Journal of Hydrology, **43**, 287–312, Amsterdam.

HARNER, P.L. & GILMORE, M.S. (2015): Visible-near infrared spectra of hydrous carbonates, with implications for the detection of carbonates in hyperspectral data of Mars. – Icarus, **250**, 204–214, New York.

HASSON, D., AVRIEL, M., RESNICK, W., ROZENMAN, T. & WINDREICH, S. (1968): Calcium carbonate scale deposition on heat transfer surfaces. – Desalination, **5**, 107–119, Amsterdam.

HASSON, D., SIDORENKO, G. & SEMIAT, R. (2010): Calcium carbonate hardness removal by a novel electrochemical seeds system. – Desalination, **263**, 285–289, Amsterdam.

HATLE, E. (1892): Fünfter Beitrag zur mineralogischen Topographie der Steiermark. – Mitteilungen des Naturwissenschaftlichen Vereines für Steiermark, **28**, 294–308, Graz.

HAUSEGGER, S. & KURZ, W. (2013): Cataclastic faults along the SEMP fault system (Eastern Alps, Austria) – A contribution to fault zone evolution, internal structure and paleo-stresses. – Tectonophysics, **608**, 237–251, Amsterdam.

HAUSEGGER, S., KURZ, W., RABITSCH, R., KIECHL, E. & BROSCH, F.-J. (2010): Analysis of the internal structure of a carbonate damage zone: Implications for the mechanisms of fault breccia formation and fluid flow. – Journal of Structural Geology, **32**, 1349–1362, Oxford.

HEEGAARD, E., BIRKS, H.J.B. & TELFORD, R.J. (2005): Relationships between calibrated ages and depth in stratigraphical sequences: an estimation procedure by mixed-effect regression. – The Holocene, **15**, 612–618, Los Angeles.

HENJES-KUNST, F., PROCHASKA, W., NIEDERMAYR, A., SULLIVAN, N. & BAXTER, E. (2014): Sm-Nd dating of hydrothermal carbonate formation: An example from the Breitenau magnesite deposit (Styria, Austria). – Chemical Geology, **387**, 184–201, Amsterdam.

HEWITT, A.D. (1989): Leaching of metal pollutants from four well casings used for ground-water monitoring. – CRREL Special Report 89–32, US Army Corps of Engineers, 11 pp., Hannover.

HOCH, A.R., REDDY, M.M. & AIKEN, G.R. (2000): Calcite crystal growth inhibition by humic substances with emphasis on hydrophobic acids from the Florida Everglades. – Geochimica et Cosmochimica Acta, **64**, 61–72, New York.

HOEFS, J. (2015): Stable Isotope Geochemistry. – 7th ed., 389 pp., Berlin–Heidelberg (Springer).

HOLZKÄMPER, S., SPÖTL, C. & MANGINI, A. (2005): High-precision constraints on timing of Alpine warm periods during the middle to late Pleistocene using speleothem growth periods. – Earth and Planetary Science Letters, **236**, 751–764, Amsterdam.

HU, Y.-B., WOLF-GLADROW, D.A., DIECKMANN, G.S., VÖLKER, C. & NEHRKE, G. (2014): A laboratory study of ikaite ($CaCO_3 \cdot 6H_2O$) precipitation as a function of pH, salinity, temperature and phosphate concentration. – Marine Chemistry, **162**, 10–18, Miami.

HU, Y.-B., WOLTHERS, M., WOLF-GLADROW, D.A. & NEHRKE, G. (2015): Effect of pH and phosphate on calcium carbonate polymorphs precipitated at near-freezing temperature. – Crystal Growth and Design, **15**, 1596–1601, Washington, D.C.

IMMENHAUSER, A., BUHL, D., RICHTER, D., NIEDERMAYR, A., RIECHELMANN, D., DIETZEL, M. & SCHULTE, U. (2010): Magnesium-isotope fractionation during low-Mg calcite precipitation in a limestone cave. – Field study and experiments. – Geochimica et Cosmochimica Acta, **74**, 4346–4364, New York.

ITO, T. (1998): Factors controlling the transformation of natural ikaite from Shiowakka, Japan. – Geochemical Journal, **32**, 267–273, Tokyo.

IVANOVICH, M. & HARMON, R.S. (1992): Uranium-series Disequilibrium: Applications to Earth, Marine Environmental Sciences. – 910 pp., Oxford (Clarendon Press).

JIMOH, O.A., OKOYE, P.U., ARIFFIN, K.S., HUSSIN, H.B. & BAHARUN, N. (2017): Continuous synthesis of precipitated calcium carbonate using a tubular reactor with the aid of aloe vera (Aloe barbadensis Miller) extract as a green morphological modifier. – Journal of Cleaner Production, **150**, 104–111, Amsterdam.

JOCHUM, K.P., STOLL, B., FRIEDRICH, J.M., AMINI, M., BECKER, S., DÜCKING, M., EBEL, D.S., ENZWEILER, J., HU, M., KUZMIN, D., MERTZ-KRAUS, R., MÜLLER, W.E.G., REGNERY, J., SOBOLEV, A., WANG, X. & ZHAN, X. (2009): Laser ablation-inductively coupled plasma-mass spectrometry and its application in geochemistry, cosmochemistry and environmental research. – Rock and Mineral Analysis, **28**, 53–68.

JOHNSEN, S.J., DAHL-JENSEN, D., GUNDESTRUP, N., STEFFENSEN, J.P., CLAUSEN, H.B., MILLER, H., MASSON-DELMOTTE, V., SVEINBJÖRNSDOTTIR, A.E. & WHITE, J. (2001): Oxygen isotope and palaeotemperature records from six Greenland ice-core stations: Camp Century, Dye-3, GRIP, GISP2, Renland and NorthGRIP. – Journal of Quaternary Science, **16**, 299–307, Chichester.

JOHNSTON, V.E., BORSATO, A., FRISIA, S., SPÖTL, C., DUBLYANSKY, Y., TÖCHTERLE, P., HELLSTROM, J.C., BAJO, P., EDWARDS, R.L. & CHENG, H. (2018): Evidence of thermophilisation and elevation-dependent warming during the Last Interglacial in the Italian Alps. – Scientific Reports, **8**: 2680, London. https://dx.doi.org/10.1038/s41598-018-21027-3

JONES, B. (2017a): Review of calcium carbonate polymorph precipitation in spring systems. – Sedimentary Geology, **353**, 64–75, Amsterdam.

JONES, B. (2017b): Review of aragonite and calcite crystal morphogenesis in thermal spring systems. – Sedimentary Geology, **354**, 9–23, Amsterdam.

JONES, B. & PENG, X. (2012): Amorphous calcium carbonate associated with biofilms in hot spring deposits. – Sedimentary Geology, **269–270**, 58–68, Amsterdam.

JONES, B. & RENAUT, R.W. (2010): Calcareous spring deposits in continental settings. – Developments in Sedimentology, **61**, 177–224, Amsterdam.

KAWAMURA, K., PARRENIN, F., LISIECKI, L., UEMURA, R., VIMEUX, F., SEVERINGHAUS, J.P., HUTTERLI, M.A., NAKAZAWA, T., AOKI, S., JOUZEL, J., RAYMO, M.E., MATSUMOTO, K., NAKATA, H., MOTOYAMA, H., FUJITA, S., GOTO-AZUMA, K., FUJII, Y. & WATANABE, O. (2007): Northern Hemisphere forcing of climatic cycles in Antarctica over the past 360,000 years. – Nature, **448**, 912–916, London.

KELE, S., BREITENBACH, S.F.M., CAPEZZUOLI, E., NELE MECKLER, A., ZIEGLER, M., MILLAN, I.M., KLUGE, T., DEÁK, J., HANSELMANN, K., JOHN, C.M., YAN, H., LIU, Z. & BERNASCONI, S.M. (2015): Temperature dependence of oxygen- and clumped isotope fractionation in carbonates: a study of travertines and tufas in the 6–95°C temperature range. – Geochimica et Cosmochimica Acta, **168**, 172–192, New York.

KELEMEN, P.B. & MATTER, J. (2008): In situ carbonation of peridotite for CO_2 storage. – Proceedings of the National Academy of Sciences, **105**, 17295–17300, Allahabad.

KELSON, J.R., HUNTINGTON, K.W., SCHAUER, A.J., SAENGER, C. & LECHLER, A.R. (2017): Toward a universal carbonate clumped isotope calibration: Diverse synthesis and preparatory methods suggest a single temperature relationship. – Geochimica et Cosmochimica Acta, **197**, 104–131, New York.

KETRANE, R., SAIDANI, B., GIL, O., LELEYTER, L. & BARAUD, F. (2009): Efficiency of five scale inhibitors on calcium carbonate precipitation from hard water: Effect of temperature and concentration. – Desalination, **249**, 1397–1404, Amsterdam.

KHARAKA, Y.K., COLE, D.R., HOVORKA, S.D., GUNTER, W.D., KNAUSS, K.G. & FREIFELD, B.M. (2006): Gas-water-rock interactions in Frio Formation following CO_2 injection: Implications for the storage of greenhouse gases in sedimentary basins. – Geology, **34**, 577–580, Washington, D.C.

KIM, S.-T. & O'NEIL, J.R. (1997): Equilibrium and nonequilibrium oxygen isotope effects in synthetic carbonates. – Geochimica et Cosmochimica Acta, **61**, 3461–3475, New York.

KLUGE, T. & JOHN, C.M. (2015): Effects of brine chemistry and polymorphism on clumped isotopes revealed by laboratory precipitation of mono- and multiphase calcium carbonates. – Geochimica et Cosmochimica Acta, **160**, 155–168, New York.

KLUGE, T., AFFEK, H.P., DUBLYANSKY, Y. & SPÖTL, C. (2014): Devils Hole paleotemperatures and implications for oxygen isotope equilibrium fractionation. – Earth and Planetary Science Letters, **400**, 251–260, Amsterdam.

KLUGE, T., JOHN, C.M., JOURDAN, A.-L., DAVIS, S. & CRAWSHAW, J. (2015): Laboratory calibration of the calcium carbonate clumped isotope thermometer in the 25–250 °C temperature range. – Geochimica et Cosmochimica Acta, **157**, 213–227, New York.

KLUGE, T., JOHN, C.M., BOCH, R. & KELE, S. (2018): Assessment of Factors Controlling Clumped Isotopes and $\delta^{18}O$ Values of Hydrothermal Vent Calcites. – Geochemistry, Geophysics, Geosystems, **19**/6, 1844–1858, Washington, D.C.

KNEZ, S. & POHAR, C. (2005): The magnetic field influence on the polymorph composition of $CaCO_3$ precipitated from carbonized aqueous solutions. – Journal of Colloid and Interface Science, **281**, 377–388, Amsterdam.

KOBE, S., DRAZIC, G., CEFALAS, A.C., SARANTOPOULOU, E. & STRAZISAR, J. (2002): Nucleation and crystallization of $CaCO_3$ in applied magnetic fields. – Crystal Engineering, **5**, 243–253, Oxford.

KOGA, N., KASAHARA, D. & KIMURA, T. (2013): Aragonite crystal growth and solid-state aragonite-calcite transformation: A physico-geometrical relationship via thermal dehydration of included water. – Crystal Growth and Design, **13**, 2238–2246, Washington, D.C.

KÖHLER, S.J., CUBILLAS, P., RODRIGUEZ-BLANCO, J.D., BAUER, C. & PRIETO, M. (2007): Removal of cadmium from wastewaters by aragonite shells and the influence of other divalent cations. – Environmental Science and Technology, **41**, 112–118, Washington, D.C.

KONRAD, F., GALLIEN, F., GERARD, D.E. & DIETZEL, M. (2016): Transformation of amorphous calcium carbonate in air. – Crystal Growth and Design, **16**, 6310–6317, Washington, D.C.

KOSEDNAR-LEGENSTEIN, B., DIETZEL, M., LEIS, A. & STINGL, K. (2008): Stable carbon and oxygen isotope investigation in historical lime mortar and plaster. – Results from field and experimental study. – Applied Geochemistry, **23**, 2425–2437, Amsterdam.

KRALJ, D. & BREČEVIĆ, L. (1995): Dissolution kinetics and solubility of calcium carbonate monohydrate. – Colloids and Surfaces A: Physicochemical and Engineering Aspects, **96**, 287–293, Amsterdam.

KUMAR, S., NAIYA, T.K. & KUMAR, T. (2018): Developments in oilfield scale handling towards green technology – A review. – Journal of Petroleum Science and Engineering, **169**, 428–444, Amsterdam.

LACHNIET, M.S. (2009): Climatic and environmental controls on speleothem oxygen-isotope values. – Quaternary Science Reviews, **28**, 412–432, Amsterdam.

LACHNIET, M.S., BERNAL, J.P., ASMEROM, Y. & POLYAK, V. (2012): Uranium loss and aragonite-calcite age discordance in a calcitized aragonite stalagmite. – Quaternary Geochronology, **14**, 26–37, Amsterdam.

LANGER, G., SADEKOV, A., NEHRKE, G., BAGGINI, C., RODOLFO-METALPA, R., HALL-SPENCER, J.M., CUOCO, E., BIJMA, J. & ELDERFIELD, H. (2018): Relationship between mineralogy and minor element partitioning in limpets from an Ischia CO_2 vent site provides new insights into their biomineralization pathway. – Geochimica et Cosmochimica Acta, **236**, 218–229, New York.

LANGMUIR, D. (1997): Carbonate Chemistry. – In: LANGMUIR, D.: Aqueous Environmental Geochemistry, 193–230, Upper Saddle River (Prentice Hall).

LANNELUC, I., LANGUMIER, M., SABOT, R., JEANNIN, M., REFAIT, P. & SABLÉ, S. (2015): On the bacterial communities associated with the corrosion product layer during the early stages of marine corrosion of carbon steel. – International Biodeterioration and Biodegradation, **99**, 55–65, Barking.

LENHARDT, W.A., FREUDENTHALER, C., LIPPITSCH, R. & FIEGWEIL, E. (2007): Focal-depth distributions in the Eastern Alps based on macroseismic data. – Austrian Journal of Earth Sciences, **100**, 66–79, Wien.

LERM, S., WESTPHAL, A., MIETHLING-GRAFF, R., ALAWI, M., SEIBT, A., WOLFGRAMM, M. & WÜRDEMANN, H. (2013): Thermal effects on microbial composition and microbiologically induced corrosion and mineral precipitation affecting operation of a geothermal plant in a deep saline aquifer. – Extremophiles, **17**, 311–327, Tokyo.

LEVITT, N.P., EILER, J.M., ROMANEK, C.S., BEARD, B.L., XU, H. & JOHNSON, C.M. (2018): Near equilibrium ^{13}C-^{18}O bonding during inorganic calcite precipitation under chemo-stat conditions. – Geochemistry, Geophysics, Geosystems, **19/3**, 901–920, Washington, D.C.

LI, H., YANG, J., ZHANG, L., ZOU, H., LI, D., WANG, Q., MENG, D. & LU, M. (2019): Influence of thermophilic sulfate-reducing bacteria and deposited $CaCO_3$ on the corrosion of water injection system. – Engineering Failure Analysis, **95**, 359–370, Oxford.

LI, X., GAO, B., YUE, Q., MA, D., RONG, H., ZHAO, P. & TENG, P. (2015): Effect of six kinds of scale inhibitors on calcium carbonate precipitation in high salinity wastewater at high temperatures. – Journal of Environmental Sciences, **29**, 124–130, Amsterdam.

LISIECKI, L.E. & RAYMO, M.E. (2005): A Pliocene-Pleistocene stack of 57 globally distributed benthic $\delta^{18}O$ records. – Paleoceanography, **20**: PA1003, Washington, D.C. https://dx.doi.org/10.1029/2004PA001071

LISIECKI, L.E. & STERN, J.V. (2016): Regional and global benthic $\delta^{18}O$ stacks for the last glacial cycle. – Paleoceanography, **31**, 1368–1394, Washington, D.C.

LIU, H., LIU, Z., MACPHERSON, G.L., YANG, R., CHEN, B. & SUN, H. (2015): Diurnal hydrochemical variations in a karst spring and two ponds, Maolan Karst Experimental Site, China: Biological pump effects. – Journal of Hydrology, **522**, 407–417, Amsterdam.

LIU, Z.Y., WANG, X.Z., LIU, R.K., DU, C.W. & LI, X.G. (2014): Electrochemical and sulfide stress corrosion cracking behaviors of tubing steels in a H_2S/CO_2 annular environment. – Journal of Materials Engineering and Performance, **23**, 1279–1287, New York.

LLOYD, M.K., EILER, J.M. & NABELEK, P.I. (2017): Clumped isotope thermometry of calcite and dolomite in a contact metamorphic environment. – Geochimica et Cosmochimica Acta, **197**, 323–344, New York.

LORENS, R.B. (1981): Sr, Cd, Mn and Co distribution coefficients in calcite as a function of calcite precipitation rate. – Geochimica et Cosmochimica Acta, **45**, 553–561, New York.

LUETKEMEYER, P.B., KIRSCHNER, D.L., HUNTINGTON, K.W., CHESTER, J.S., CHESTER, F.M. & EVANS, J.P. (2016): Constraints on paleofluid sources using the clumped-isotope thermometry of carbonate veins from the SAFOD (San Andreas Fault Observatory at Depth) borehole. – Tectonophysics, **690**, Part A, 174–189, Amsterdam.

LUETSCHER, M. & ZIEGLER, F. (2012): CORA – a dedicated device for carbon dioxide monitoring in cave environments. – International Journal of Speleology, **41**, 275–283, Tampa.

LUETSCHER, M., BOCH, R., SODEMANN, H., SPÖTL, C., CHENG, H., EDWARDS, R.L., FRISIA, S., HOF, F. & MÜLLER, W. (2015): North Atlantic storm track changes during the Last Glacial Maximum recorded by Alpine speleothems. – Nature Communications, **6**: 6344, London. https://dx.doi.org/10.1038/ncomms7344

LYONS, T.W., FIKE, D.A. & ZERKLE, A. (2015): Emerging biogeochemical views of Earth's ancient microbial worlds. – Elements, **11**, 415–421, Québec.

MAHER, T.D., SANTOS, I.R. & TAIT, D.R. (2014): Mapping methane and carbon dioxide concentrations and $\delta^{13}C$ values in the atmosphere of two Australian coal seam gas fields. – Water, Air and Soil Pollution, **225**: 2216, Dordrecht. https://dx.doi.org/10.1007/s11270-014-2216-2

MARTÍN-CHIVELET, J., MUÑOZ-GARCÍA, M.B., CRUZ, J.A., ORTEGA, A.I. & TURRERO, M.J. (2017): Speleothem Architectural Analysis: Integrated approach for stalagmite-based paleoclimate research. – Sedimentary Geology, **353**, 28–45, Amsterdam.

MASKENSKAYA, O.M., DRAKE, H., BROMAN, C., HOGMALM, J.K., CZUPPON, G. & ÅSTRÖM, M.E. (2014): Source and character of syntaxial hydrothermal calcite veins in Paleoproterozoic crystalline rocks revealed by fine-scale investigations. – Geofluids, **14**, 495–511, Oxford.

MATTER, J.M., STUTE, M., SNÆBJÖRNSDOTTIR, S.Ó., OELKERS, E.H., GISLASON, S.R., ARADOTTIR, E.S., SIGFUSSON, B., GUNNARSSON, I., SIGURDARDOTTIR, H., GUNNLAUGSSON, E., AXELSSON, G., ALFREDSSON, H.A., WOLFF-BOENISCH, D., MESFIN, K., TAYA, D.F.D.L.R., HALL, J., DIDERIKSEN, K. & BROECKER, W.S. (2016): Rapid carbon mineralization for permanent disposal of anthropogenic carbon dioxide emissions. – Science, **352**, 1312–1314, Washington, D.C.

MATTEY, D., LOWRY, D., DUFFET, J., FISHER, R., HODGE, E. & FRISIA, S. (2008): A 53 year seasonally resolved oxygen and carbon isotope record from a modern Gibraltar speleothem: Reconstructed drip water and relationship to local precipitation. – Earth and Planetary Science Letters, **269**, 80–95, Amsterdam.

MATTEY, D.P., ATKINSON, T.C., BARKER, J.A., FISHER, R., LATIN, J.P., DURELL, R. & AINSWORTH, M. (2016): Carbon dioxide, ground air and carbon cycling in Gibraltar karst. – Geochimica et Cosmochimica Acta, **184**, 88–113, New York.

MAVROMATIS, V., GAUTIER, Q., BOSC, O. & SCHOTT, J. (2013): Kinetics of Mg partition and Mg stable isotope fractionation during its incorporation in calcite. – Geochimica et Cosmochimica Acta, **114**, 188–203, New York.

MAVROMATIS, V., MONTOUILLOUT, V., NOIREAUX, J., GAILLARDET, J. & SCHOTT, J. (2015): Characterization of boron incorporation and speciation in calcite and aragonite from co-precipitation experiments under controlled pH, temperature and precipitation rate. – Geochimica et Cosmochimica Acta, **150**, 299–313, New York.

MAVROMATIS, V., VAN ZUILEN, K., PURGSTALLER, B., BALDERMANN, A., NÄGLER, T.F. & DIETZEL, M. (2016): Barium isotope fractionation during witherite ($BaCO_3$) dissolution, precipitation and at equilibrium. – Geochimica et Cosmochimica Acta, **190**, 72–84, New York.

MAVROMATIS, V., IMMENHAUSER, A., BUHL, D., PURGSTALLER, B., BALDERMANN, A. & DIETZEL, M. (2017): Effect of organic ligands on Mg partitioning and Mg isotope fractionation during low-temperature precipitation of calcite in the absence of growth rate effects. – Geochimica et Cosmochimica Acta, **207**, 139–153, New York.

MAVROMATIS, V., GOETSCHL, K.E., GRENGG, C., KONRAD, F., PURGSTALLER, B. & DIETZEL, M. (2018): Barium partitioning in calcite and aragonite as a function of growth rate. – Geochimica et Cosmochimica Acta, **237**, 65–78, New York.

MAVROMATIS, V., GONZÁLEZ, A.G., DIETZEL, M. & SCHOTT, J. (2019): Zinc isotope fractionation during the inorganic precipitation of calcite – Towards a new pH proxy. – Geochimica et Cosmochimica Acta, **244**, 99–112, New York.

MAYRHOFER, C., NIESSNER, R. & BAUMANN, T. (2014): Hydrochemistry and hydrogen sulfide generating processes in the Malm aquifer, Bavarian Molasse Basin, Germany. – Hydrogeology Journal, **22**, 151–162, Berlin–Heidelberg.

MCMILLAN, E.A., FAIRCHILD, I.J., FRISIA, S., BORSATO, A. & MCDERMOTT, F. (2005): Annual trace element cycles in calcite–aragonite speleothems: evidence of drought in the western Mediterranean 1200-1100 yr BP. – Journal of Quaternary Science, **20**, 423–433, Chichester.

MECHAL, A., BIRK, S., DIETZEL, M., LEIS, A., WINKLER, G., MOGESSIE, A. & KEBEDE, S. (2017): Groundwater flow dynamics in the complex aquifer system of Gidabo River Basin (Ethiopian Rift): a multi-proxy approach. – Hydrogeology Journal, **25**, 519–538, Berlin–Heidelberg.

MECKLER, A.N., AFFOLTER, S., DUBLYANSKY, Y.V., KRÜGER, Y., VOGEL, N., BERNASCONI, S.M., FRENZ, M., KIPFER, R., LEUENBERGER, M., SPÖTL, C., CAROLIN, S., COBB, K.M., MOERMAN, J., ADKINS, J.F. & FLEITMANN, D. (2015): Glacial-interglacial temperature change in the tropical West Pacific: A comparison of stalagmite-based paleo-thermometers. – Quaternary Science Reviews, **127**, 90–116, Amsterdam.

MEYER, M.C., CLIFF, R.A., SPÖTL, C., KNIPPING, M. & MANGINI, A. (2009): Speleothems from the earliest Quaternary: Snapshots of paleoclimate and landscape evolution at the northern rim of the Alps. – Quaternary Science Reviews, **28**, 1374–1391, Amsterdam.

MEYER, M.C., CLIFF, R.A. & SPÖTL, C. (2011): Speleothems and mountain uplift. – Geology, **39**, 447–450, Washington, D.C.

MICHAELIS, J., USDOWSKI, E. & MENSCHEL, G. (1985): Partitioning of ^{13}C and ^{12}C on the degassing of CO_2 and the precipitation of calcite. – Rayleigh type fractionation and a kinetic model. – American Journal of Science, **285**, 318–327, New Haven.

MICKLER, P.J., BANNER, J.L., STERN, L., ASMEROM, Y., EDWARDS, R.L. & ITO, E. (2004): Stable isotope variations in modern tropical speleothems: Evaluating equilibrium vs. kinetic isotope effects. – Geochimica et Cosmochimica Acta, **68**, 4381–4393, New York.

MICKLER, P.J., STERN, L.A. & BANNER, J.L. (2006): Large kinetic isotope effects in modern speleothems. – Geological Society of America Bulletin, **118**, 65–81, Boulder.

MICKLER, P.J., CARLSON, P., BANNER, J.L., BREECKER, D.O., STERN, L. & GUILFOYLE, A. (2019): Quantifying carbon isotope disequilibrium during in-cave evolution of drip water along discreet flow paths. – Geochimica et Cosmochimica Acta, **244**, 182–196, New York.

MILLERO, F.J., GRAHAM, T.B., HUANG, F., BUSTOS-SERRANO, H. & PIERROT, D. (2006): Dissociation constants of carbonic acid in seawater as a function of salinity and temperature. – Marine Chemistry, **100**, 80–94, Miami.

MISCHEL, S.A., SCHOLZ, D., SPÖTL, C., JOCHUM, K.P., SCHRÖDER-RITZRAU, A. & FIEDLER, S. (2016): Holocene climate variability in Central Germany and a potential link to the polar North Atlantic: A replicated record from three coeval speleothems. – The Holocene, **27**, 509–525, Los Angeles.

MITTERMAYR, F., BALDERMANN, A., BALDERMANN, C., GRATHOFF, G.H., KLAMMER, D., KÖHLER, S.J., LEIS, A., WARR, L.N. & DIETZEL, M. (2017): Environmental controls and reaction pathways of coupled de-dolomitization and thaumasite formation. – Cement and Concrete Research, **95**, 282–293, Oxford.

MONNIN, C. & SCHOTT, J. (1984): Determination of the solubility products of sodium carbonate minerals and an application to trona deposition in Lake Magadi (Kenya). – Geochimica et Cosmochimica Acta, **48**, 571–581, New York.

MOOK, W.G. (1986): ^{13}C in atmospheric CO_2. – Netherlands Journal of Sea Research, **20**, 211–223, Amsterdam.

MOORE, C.H. & WADE, W.J. (2013): Carbonate diagenesis: Introduction and tools. – Developments in Sedimentology, **67**, 67–89, Amsterdam.

MORSE, J.W. (2004): Formation and diagenesis of carbonate sediments. – In: MACKENZIE, F.T. (Ed.): Sediments, Diagenesis and Sedimentary Rocks, **7**, Treatise on Geochemistry, 67–85, Oxford.

MORSE, J.W. & ARVIDSON, R.S. (2002): The dissolution kinetics of major sedimentary carbonate minerals. – Earth-Science Reviews, **58**, 51–84, Amsterdam.

MORSE, J.W. & MACKENZIE, F.T. (1990): Geochemistry of Sedimentary Carbonates. – Developments in Sedimentology, **48**, 707 pp., Amsterdam.

MORSE, J.W., ARVIDSON, R.S. & LÜTTGE, A. (2007): Calcium carbonate formation and dissolution. – Chemical Reviews, **107**, 342–381, Washington, D.C.

MOSELEY, G.E., EDWARDS, R.L., WENDT, K.A., CHENG, H., DUBLYANSKY, Y., LU, Y., BOCH, R. & SPÖTL, C. (2016): Reconciliation of the Devils Hole climate record with orbital forcing. – Science, **351**, 165–168, Washington, D.C.

MPELWA, M. & TANG, S.F. (2019): State of the art of synthetic threshold scale inhibitors for mineral scaling in the petroleum industry: a review. – Petroleum Science, **16**/4, 830–849. https://dx.doi.org/10.1007/s12182-019-0299-5

MÜHLINGHAUS, C., SCHOLZ, D. & MANGINI, A. (2007): Modelling stalagmite growth and $\delta^{13}C$ as a function of drip interval and temperature. – Geochimica et Cosmochimica Acta, **71**, 2780–2790, New York.

MUNDHENK, N., HUTTENLOCH, P., SANJUAN, B., KOHL, T., STEGER, H. & ZORN, R. (2013): Corrosion and scaling as interrelated phenomena in an operating geothermal power plant. – Corrosion Science, **70**, 17–28, Amsterdam.

NEBEL, O. & STAMMEIER, A. (2016): Strontium Isotopes. – In: WHITE, W.M. (Ed.): Encyclopedia of Geochemistry, 6 p., Cham. https://dx.doi.org/10.1007/978-3-319-39193-9_137-1

Niedermayr, A., Köhler, S.J. & Dietzel, M. (2013): Impacts of aqueous carbonate accumulation rate, magnesium and polyaspartic acid on calcium carbonate formation (6–40 °C). – Chemical Geology, **340**, 105–120, Amsterdam.

Nielsen, M.H. & De Yoreo, J.J. (2017): Liquid phase TEM investigations of crystal nucleation, growth, and transformation. – In: Van Driessche, A.E.S., Kellermeier, M., Benning, L.G. & Gebauer, D. (Eds.): New Perspectives on Mineral Nucleation and Growth. – From Solution Precursors to Solid Materials, 353–374, Cham.

NOAA – National Centers for Environmental Information: https://www.ncdc.noaa.gov/data-access (last visited: 19.08.2018).

Nogara, J. & Zarrouk, S.J. (2014): Evaluation of corrosion resistant alloys as construction material for acidic geothermal wells. – Proceedings of the 36th New Zealand Geothermal Workshop, 14 pp., Auckland.

Nogara, J. & Zarrouk, S.J. (2017): Corrosion in geothermal environment: Part 1: Fluids and their impact. – Renewable and Sustainable Energy Reviews, **82**, 1333–1346, Oxford.

Oehlerich, M., Mayr, C., Griesshaber, E., Lücke, A., Oeckler, O.M., Ohlendorf, C., Schmahl, W.W. & Zolitschka, B. (2013): Ikaite precipitation in a lacustrine environment – implications for palaeoclimatic studies using carbonates from Laguna Potrok Aike (Patagonia, Argetina). – Quaternary Science Reviews, **71**, 46–53, Amsterdam.

Okrusch, M. & Matthes, S. (2010): Mineralogie – Eine Einführung in die spezielle Mineralogie, Petrologie und Lagerstättenkunde, 8th ed., 658 pp., Berlin–Heidelberg (Springer).

Onuk, P., Dietzel, M. & Hauzenberger, C.A. (2014): Formation of helictite in the cave Dragon Belly (Sardinia, Italy) – Microstructure and incorporation of Mg, Sr, and Ba. – Chemie der Erde. – Geochemistry, **74**, 443–452, Washington, D.C.

Ostermann, M., Sanders, D., Prager, C. & Kramers, J. (2007): Aragonite and calcite cementation in “boulder-controlled” meteoric environments on the Fern Pass rockslide (Austria): implications for radiometric age dating of catastrophic mass movements. – Facies, **53**, 189–208, Berlin–Heidelberg.

Osvald, M., Marótti, G., Pap, B. & Szanyi, J. (2017): Biofilm forming bacteria during thermal water reinjection. – Geofluids, **2017**, 7 p., Oxford. https://dx.doi.org/10.1155/2017/9231056

Ott, H., De Kloe, K., van Bakel, M., Vos, F., van Pelt, A., Legerstee, P., Bauer, A., Eide, K., van der Linden, A., Berg, S. & Makurat, A. (2012): Core-flood experiment for transport of reactive fluids in rocks. – Review of Scientific Instruments, **83**: 084501, New York. https://dx.doi.org/10.1063/1.4746997

Ott, H., Pentland, C.H. & Oedai, S. (2015): CO_2-brine displacement in heterogeneous carbonates. – International Journal of Greenhouse Gas Control, **33**, 135–144, New York.

Ouhenia, S., Chateigner, D., Belkhir, M.A., Guilmeau, E. & Krauss, C. (2008): Synthesis of calcium carbonate polymorphs in the presence of polyacrylic acid. – Journal of Crystal Growth, **310**, 2832–2841, Amsterdam.

Owen, R.A., Day, C.C., Hu, C.Y., Liu, Y.H., Pointing, M.D., Blättler, C.L. & Henderson, G.M. (2016): Calcium isotopes in caves as a proxy for aridity: Modern calibration and application to the 8.2 kyr event. – Earth and Planetary Science Letters, **443**, 129–138, Amsterdam.

Ozyurt, N.N., Lutz, H.O., Hunjak, T., Mance, D. & Roller-Lutz, Z. (2014): Characterization of the Gacka River basin karst aquifer (Croatia): Hydrochemistry, stable isotopes and tritium-based mean residence times. – Science of the total Environment, **487**, 245–254, Amsterdam.

Paces, J.B., Ludwig, K.R., Peterman, Z.E. & Neymark, L.A. (2002): $^{234}U/^{238}U$ evidence for local recharge and patterns of groundwater flow in the vicinity of Yucca Mountain, Nevada, USA. – Applied Geochemistry, **17**, 751–779, Amsterdam.

Pagel, M., Bonifacie, M., Schneider, D.A., Gautheron, C., Brigaud, B., Calmels, D., Cros, A., Saint-Bezar, B., Landrein, P., Sutcliffe, C., Davis, D. & Chaduteau, C. (2018): Improving paleohydrological and diagenetic reconstructions in calcite veins and breccia of a sedimentary basin by combining Δ_{47} temperature, $\delta_{18}O_{water}$ and U-Pb age. – Chemical Geology, **481**, 1–17, Amsterdam.

Parkhurst, D.L. & Appelo, C.A.J. (2013): Description of input and examples for PHREEQC version 3. – A computer program for speciation, batch-reaction, one-dimensional transport, and inverse geochemical calculations. – U.S. Geological Survey Techniques and Methods, book 6, chapter A43, 497 pp., Denver.

Parlaktuna, M. & Okandan, E. (1989): The use of chemical inhibitors for prevention of calcium carbonate scaling. – Geothermics, **18**, 241–248, Amsterdam.

Passchier, C., Sürmelihindi, G. & Spötl, C. (2016a): A high-resolution palaeoenvironmental record from carbonate deposits in the Roman aqueduct of Patara, SW Turkey, from the time of Nero. – Scientific Reports, **6**: 28704, London. https://dx.doi.org/10.1038/srep28704

Passchier, C., Sürmelihindi, G., Spötl, C., Mertz-Kraus, R. & Scholz, D. (2016b): Carbonate deposits from the ancient aqueduct of Béziers, France – A high-resolution palaeoenvironmental archive for the Roman Empire. – Palaeogeography, Palaeoclimatology, Palaeoecology, **461**, 328–340, Amsterdam.

Pederson, C., Mavromatis, V., Dietzel, M., Rollion-Bard, C., Nehrke, G., Jöns, N., Jochum, K.P. & Immenhauser, A. (2019): Diagenesis of mollusc aragonite and the role of fluid reservoirs. – Earth and Planetary Science Letters, **514**, 130–142, Amsterdam.

Pedley, M. (2013): The morphology and function of thrombolitic calcite precipitating biofilms: A universal model derived from freshwater mesocosm experiments. – Sedimentology, **61**, 22–40, Amsterdam.

Pérez-Mejias, C., Moreno, A., Sancho, C., Bartolomé, M., Stoll, H., Cacho, I., Cheng, H. & Edwards, R.L. (2017): Abrupt climate changes during Termination III in Southern Europe. – Proceedings of the National Academy of Sciences, **114**, 10047–10052, Washington, D.C.

Perrin, C., Prestimonaco, L., Servelle, G., Tilhac, R., Maury, M. & Cabrol, P. (2014): Aragonite-calcite speleothems: Identifying original and diagenetic features. – Journal of Sedimentary Research, **84**, 245–269, Tulsa.

Pirajno, F. (2009): Hydrothermal Processes and Mineral Systems. – 1250 pp., Berlin (Springer).

Plan, L., Grasemann, B., Spötl, C., Decker, K., Boch, R. & Kramers, J. (2010): Neotectonic extrusion of the Eastern Alps: Constraints from U/Th dating of tectonically damaged speleothems. – Geology, **38**, 483–486, Washington, D.C.

Plan, L., Tschegg, C., de Waele, J. & Spötl, C. (2012): Corrosion morphology and cave wall alteration in an Alpine sulfuric acid cave (Kraushöhle, Austria). – Geomorphology, **169–170**, 45–54, Amsterdam.

Plummer, L.N. & Busenberg, E. (1982): The solubilities of calcite, aragonite and vaterite in CO_2-H_2O solutions between 0 and 90° C, and an evaluation of the aqueous model for the system $CaCO_3$-CO_2-H_2O. – Geochimica et Cosmochimica Acta, **46**, 1011–1040, New York.

Prochaska, W. (2012): Siderite and magnesite mineralizations in Palaeozoic strata of the Eastern Alps (Austria). – Journal of Alpine Geology, **54**, 309–322, Wien.

Prochaska, W. (2016): Genetic concepts on the formation of the Austrian magnesite and siderite mineralizations in the Eastern Alps of Austria. – Geologia Croatica, **69**, 31–38, Zagreb.

Prokhorov, I., Kluge, T. & Janssen, C. (2019): Optical clumped isotope thermometry of carbon dioxide. – Scientific Reports, **9**: 4765, London. https://dx.doi.org/10.1038/s41598-019-40750-z

Purgstaller, B., Mavromatis, V., Immenhauser, A. & Dietzel, M. (2016): Transformation of Mg-bearing amorphous calcium carbonate to Mg-calcite – In situ monitoring. – Geochimica et Cosmochimica Acta, **174**, 180–195, New York.

Purgstaller, B., Dietzel, M., Baldermann, A. & Mavromatis, V. (2017a): Control of temperature and aqueous Mg^{2+}/Ca^{2+} ratio on the (trans-)formation of ikaite. – Geochimica et Cosmochimica Acta, **217**, 128–143, New York.

Purgstaller, B., Konrad, F., Dietzel, M., Immenhauser, A. & Mavromatis, V. (2017b): Control of Mg^{2+}/Ca^{2+} activity ratio on the formation of crystalline carbonate minerals via an amorphous precursor. – Crystal Growth and Design, **17**/3, 1069–1078, Washington, D.C.

R Development Core Team (2018): A language and environment for statistical computing. – R Foundation for Statistical Computing, Vienna, Austria. http://www.R-project.org (last visited: 19.08.2018).

Randolph, J.B. & Saar, M.O. (2011): Combining geothermal energy capture with geologic carbon dioxide sequestration. – Geophysical Research Letters, **38**: L10401, Washington, D.C. https://dx.doi.org/10.1029/2011GL047265

Rao, A. & Cölfen, H. (2017): Mineralization schemes in the living world: Mesocrystals. – In: Van Driessche, A.E.S., Kellermeier, M., Benning, L.G. & Gebauer, D. (Eds.): New Perspectives on Mineral Nucleation and Growth. – From Solution Precursors to Solid Materials, 155–183, Cham.

Rasmussen, S.O., Bigler, M., Blockley, S.P., Blunier, T., Buchardt, S.L., Clausen, H.B., Cvijanovic, I., Dahl-Jensen, D., Johnsen, S.J., Fischer, H., Gkinis, V., Guillevic, M., Hoek, W.Z., Lowe, J.J., Pedro, J.B., Popp, T., Seierstad, I.K., Steffensen, J.P., Svensson, A.M., Vallelonga, P., Vinther, B.M., Walker, M.J.C., Wheatley, J.J. & Winstrup, M. (2014): A stratigraphic framework for abrupt climatic changes during the Last Glacial period based on three synchronized Greenland ice-core records: refining and extending the INTIMATE event stratigraphy. – Quaternary Science Reviews, **106**, 14–28, Amsterdam.

Reddy, M.M. & Nancollas, G.H. (1971): The crystallization of calcium carbonate: I. Isotopic exchange and kinetics. – Journal of Colloid and Interface Science, **36**, 166–172, Amsterdam.

Reeder, R.J., Nugent, M., Lamble, G.M., Tait, C.D. & Morris, D.E. (2000): Uranyl incorporation into calcite and aragonite: XAFS and luminescence studies. – Environmental Science and Technology, **34**, 638–644, Washington, D.C.

Reiterer, F., Johannes, W. & Gamsjager, H. (1981): Semimicro determination of solubility constants: Copper (II) carbonate and iron (II) carbonate. – Mikrochimica Acta, **1**, 63–72, Wien.

Richards, D.A. & Dorale, J.A. (2003): Uranium-series chronology and environmental applications of speleothems. – Reviews in Mineralogy and Geochemistry, **52**, 407–460, Washington, D.C.

Riding, R. (2000): Microbial carbonates: the geological record of calcified bacterial-algal mats and biofilms. – Sedimentology, **47**, 179–214, Amsterdam.

Riechelmann, D.F.C., Deininger, M., Scholz, D., Riechelmann, S., Schröder-Ritzrau, A., Spötl, C., Richter, D.K., Mangini, A. & Immenhauser, A. (2013): Disequilibrium carbon and oxygen isotope fractionation in recent cave calcite: Comparison of cave precipitates and model data. – Geochimica et Cosmochimica Acta, **103**, 232–244, New York.

Riechelmann, S., Schröder-Ritzrau, A., Wassenburg, J.A., Schreuer, J., Richter, D.K., Riechelmann, D.F.C., Terente, M., Constantin, S., Mangini, A. & Immenhauser, A. (2014): Physicochemical characteristics of drip waters: Influence on mineralogy and crystal morphology of recent cave carbonate precipitates. – Geochimica et Cosmochimica Acta, **145**, 13–29, New York.

Rinder, T., Dietzel, M. & Leis, A. (2013): Calcium carbonate scaling under alkaline conditions – Case studies and hydrochemical modelling. – Applied Geochemistry, **35**, 132–141, Amsterdam.

Riotte, J. & Chabaux, F. (1999): ($^{234}U/^{238}U$) activity ratios in freshwaters as tracers of hydrological processes: the Strengbach watershed (Vosges, France). – Geochimica et Cosmochimica Acta, **63**, 1263–1275, New York.

Ripken, M., Gallien, F., Schlotterbach, T. & Lengauer, C.L. (2018): Structural and physicochemical characterization of basic calcium carbonate (BCC), $Ca_3(CO_3)_2(OH)_2.H_2O$. – European Journal of Mineralogy, **30**, 85–96, Stuttgart.

Rivera Diaz, A., Kaya, E. & Zarrouk, S.J. (2016): Reinjection in geothermal fields. – A worldwide review update. – Renewable and Sustainable Energy Reviews, **53**, 105–162, Oxford.

Rodriguez-Navarro, C. & Benning, L.G. (2013): Control of crystal nucleation and growth by additives. – Elements, **9**, 203–209, Québec.

Rodríguez-Ruiz, I., Veesler, S., Gómez-Morales, J., Delgado-López, J.M., Grauby, O., Hammadi, Z., Candoni, N. & García-Ruiz, J.M. (2014): Transient calcium carbonate hexahydrate (ikaite) nucleated and stabilized in confined nano- and picovolumes. – Crystal Growth and Design, **14**, 792–802, Washington, D.C.

Rogerson, M., Pedley, H.M., Wadhawan, J.D. & Middleton, R. (2008): New insights into biological influence on the geochemistry of freshwater carbonate deposits. – Geochimica et Cosmochimica Acta, **72**, 4976–4987, New York.

Rossi, C. & Lozano, R.P. (2016): Hydrochemical controls on aragonite versus calcite precipitation in cave dripwaters. – Geochimica et Cosmochimica Acta, **192**, 70–96, New York.

Saenger, C. & Wang, Z. (2014): Magnesium isotope fractionation in biogenic and abiogenic carbonates: implications for paleoenvironmental proxies. – Quaternary Science Reviews, **90**, 1–21, Amsterdam.

Sakoparnig, M., Boch, R., Wang, X., Lin, K., Spötl, C., Leis, A., Gollowitsch, A. & Dietzel, M. (2016): Calcite precipitation on glass substrates and active stalagmites in Katerloch Cave (Austria): Constraints from environmental monitoring. – Geophysical Research Abstracts, **18**, EGU2016-17458, Katlenburg-Lindau.

Sand, K.K., Rodriguez-Blanco, J.D., Makovicky, E., Benning, L.G. & Stipp, S.L.S. (2012): Crystallization of $CaCO_3$ in water-alcohol mixtures: Spherulitic growth, polymorph stabilization, and morphology change. – Crystal Growth and Design, **12**, 842–853, Washington, D.C.

Sanna, A., Uibu, M., Caramanna, G., Kuusik, R. & Maroto-Valer, M.M. (2014): A review of mineral carbonation technologies to sequester CO_2. – Chemical Society Reviews, **43**, 8049–8080, London.

Sarkar, A., Dutta, K. & Mahapatra, S. (2013): Polymorph control of calcium carbonate using insoluble layered double hydroxide. – Crystal Growth and Design, **13**, 204–211, Washington, D.C.

Sarnthein, M., Bartoli, G., Prange, M., Schmittner, A., Schneider, B., Weinelt, M., Andersen, N. & Garbe-Schönberg, D. (2009): Mid-Pliocene shifts in ocean overturning circulation and the onset of Quaternary-style climates. – Climate of the Past, **5**, 269–283, Göttingen.

Saunders, P., Rogerson, M., Wadhawan, J.D., Greenway, G. & Pedley, H.M. (2014): Mg/Ca ratios in freshwater microbial carbonates: Thermodynamic, kinetic and vital effects. – Geochimica et Cosmochimica Acta, **147**, 107–118, New York.

SCHAUBLE, E.A., GHOSH, P. & EILER, J.M. (2006): Preferential formation of ^{13}C-^{18}O bonds in carbonate minerals, estimated using first-principles lattice dynamics. – Geochimica et Cosmochimica Acta, **70**, 2510–2529, New York.

SCHMID, S.M., FÜGENSCHUH, B., KISSLING, E. & SCHUSTER, R. (2004): Tectonic map and overall architecture of the Alpine orogeny. – Eclogae Geologicae Helvetiae, **97**, 93–117, Basel.

SCHOLZ, D. & HOFFMANN, D.L. (2011): StalAge – An algorithm designed for construction of speleothem age models. – Quaternary Geochronology, **6**, 369–382, Amsterdam.

SCHOLZ, D., MÜHLINGHAUS, C. & MANGINI, A. (2009): Modelling $\delta^{13}C$ and $\delta^{18}O$ in the solution layer on stalagmite surfaces. – Geochimica et Cosmochimica Acta, **73**, 2592–2602, New York.

SCHOLZ, D., HOFFMANN, D.L., HELLSTROM, J. & BRONK RAMSEY, C. (2012): A comparison of different methods for speleothem age modelling. – Quaternary Geochronology, **14**, 94–104, Amsterdam.

SCHULZ, O., VAVTAR, F. & DIEBER, K. (1997): Die Siderit-Erzlagerstätte Steirischer Erzberg: Eine geowissenschaftliche Studie, mit wirtschaftlicher und geschichtlicher Betrachtung. – Archiv für Lagerstättenforschung der Geologischen Bundesanstalt, **20**, 65–178, Wien.

SEATON, N.C.A., WHITNEY, D.L., TEYSSIER, C., TORAMAN, E. & HEIZLER, M.T. (2009): Recrystallization of high-pressure marble (Sivrihisar, Turkey). – Tectonophysics, **479**, 241–253, Amsterdam.

SEVILGEN, D.S., VENN, A.A., HU, M.Y., TAMBUTTÉ, E., DE BEER, D., PLANAS-BIELSA, V. & TAMBUTTÉ, S. (2019): Full in vivo characterization of carbonate chemistry at the site of calcification in corals. – Science Advances, **5**, eaau7447, Washington, D.C.

SHEN, C.-C., WU, C.-C., CHENG, H., LAWRENCE EDWARDS, R., HSIEH, Y.-T., GALLET, S., CHANG, C.-C., LI, T.-Y., LAM, D.D., KANO, A., HORI, M. & SPÖTL, C. (2012): High-precision and high-resolution carbonate ^{230}Th dating by MC-ICP-MS with SEM protocols. – Geochimica et Cosmochimica Acta, **99**, 71–86, New York.

SHENTON, B.J., GROSSMAN, E.L., PASSEY, B.H., HENKES, G.A., BECKER, T.P., LAYA, J.C., PEREZ-HUERTA, A., BECKER, S.P. & LAWSON, M. (2015): Clumped isotope thermometry in deeply buried sedimentary carbonates: The effects of bond reordering and recrystallization. – Geological Society of America Bulletin, **127**, 1036–1051, Boulder.

SIDDALL, M., ROHLING, E.J., ALMOGI-LABIN, A., HEMLEBEN, C., MEISCHNER, D., SCHMELZER, I. & SMEED, D.A. (2003): Sea-level fluctuations during the last glacial cycle. – Nature, **423**, 853–858, London.

SMART, P.L. & FRIEDERICH, H. (1986): Water movement and storage in the unsaturated zone of a maturely karstified carbonate aquifer, Mendip Hills, England. – Proceedings of the Conference on Environmental Problems in Karst Terrains and their Solutions, National Water Well Association, Ohio, 59–87, Columbus.

SMITH, C.J.M. (2014): Laser ablation: A new approach to U-Pb speleothem dating. – Talk at 25th BCRA Cave Science Symposium 2014, Birmingham.

SNOW, E. & YUND, R.A. (1987): The effect of ductile deformation on the kinetics and mechanisms of the aragonite-calcite transformation. – Journal of Metamorphic Geology, **5**, 141–153, Oxford.

SPANOS, N. & KOUTSOUKOS, P.G. (1998): Kinetics of precipitation of calcium carbonate in alkaline pH at constant supersaturation. Spontaneous and seeded growth. – The Journal of Physical Chemistry B, **102**, 6679–6684, Washington, D.C.

SPÖTL, C. & BOCH, R. (2012): Uranium Series Dating of Speleothems. – In: WHITE, W.B. & CULVER, D.C. (Eds.): Encyclopedia of Caves, 2nd ed., 838–844, Amsterdam.

SPÖTL, C. & MANGINI, A. (2002): Stalagmite from the Austrian Alps reveals Dansgaard–Oeschger events during isotope stage 3: Implications for the absolute chronology of Greenland ice cores. – Earth and Planetary Science Letters, **203**, 507–518, Amsterdam.

SPÖTL, C. & MANGINI, A. (2007): Speleothems and paleoglaciers. – Earth and Planetary Science Letters, **254**, 323–331, Amsterdam.

SPÖTL, C. & MATTEY, D. (2006): Stable isotope microsampling of speleothems for palaeoenvironmental studies: A comparison of microdrill, micromill and laser ablation techniques. – Chemical Geology, **235**, 48–58, Amsterdam.

SPÖTL, C., FAIRCHILD, I.J. & TOOTH, A.F. (2005): Cave air control on dripwater geochemistry, Obir Caves (Austria): Implications for speleothem deposition in dynamically ventilated caves. – Geochimica et Cosmochimica Acta, **69**, 2451–2468, New York.

SPÖTL, C., MANGINI, A. & RICHARDS, D.A. (2006): Chronology and paleoenvironment of Marine Isotope Stage 3 from two high-elevation speleothems, Austrian Alps. – Quaternary Science Reviews, **25**, 1127–1136, Amsterdam.

SPÖTL, C., BOCH, R. & WOLF, A. (2011): Eiszeitliche Klimadynamik im Spiegel eines Stalagmiten aus dem Hölloch (Bayern/Vorarlberg). – Die Höhle, **62**, 46–53, Wien.

SPÖTL, C., FOHLMEISTER, J., CHENG, H. & BOCH, R. (2016): Modern aragonite formation at near-freezing conditions in an alpine cave, Carnic Alps, Austria. – Chemical Geology, **435**, 60–70, Amsterdam.

STÁHL, G., PÁTZAY, G., WEISER, L. & KÁLMÁN, E. (2000): Study of calcite scaling and corrosion processes in geothermal systems. – Geothermics, **29**, 105–119, Amsterdam.

STRAUHAL, T., PRAGER, C., MILLEN, B., SPÖTL, C., ZANGERL, C. & BRANDNER, R. (2016): Aquifer geochemistry of crystalline rocks and Quaternary deposits in a high altitude alpine environment (Kauner Valley, Austria). – Austrian Journal of Earth Sciences, **109**, 29–44, Wien.

SU, M., HAN, J., LI, Y., CHEN, J., ZHAO, Y. & CHADWICK, K. (2015): Ultrasonic crystallization of calcium carbonate in presence of seawater ions. – Desalination, **369**, 85–90, Amsterdam.

SUHARSO, BUHANI, BAHRI, S. & ENDARYANTO, T. (2011): Gambier extracts as an inhibitor of calcium carbonate ($CaCO_3$) scale formation. – Desalination, **265**, 102–106, Amsterdam.

SÜRMELIHINDI, G., PASSCHIER, C.W., BAYKAN, O.N., SPÖTL, C. & KESSENER, P. (2013): Environmental and depositional controls on laminated freshwater carbonates: An example from the Roman aqueduct of Patara, Turkey. – Palaeogeography, Palaeoclimatology, Palaeoecology, **386**, 321–335, Amsterdam.

SWAINSON, I.P. & HAMMOND, R.P. (2001): Ikaite, $CaCO_3.6H_2O$: Cold comfort for glendonites as paleothermometers. – American Mineralogist, **86**, 1530–1533, Washington, D.C.

TAKAI, K., NAKAMURA, K., TOKI, T., TSUNOGAI, U., MIYAZAKI, M., MIYAZAKI, J., HIRAYAMA, H., NAKAGAWA, S., NUNOURA, T. & HORIKOSHI, K. (2008): Cell proliferation at 122° C and isotopically heavy CH_4 production by a hyperthermophilic methanogen under high-pressure cultivation. – Proceedings of the National Academy of Sciences, **105**, 10949–10954, Washington, D.C.

TANG, C.C., THOMPSON, S.P., PARKER, J.E., LENNIE, A.R., AZOUGH, F. & KATO, K. (2009): The ikaite-to-vaterite transformation: new evidence from diffraction and imaging. – Journal of Applied Crystallography, **42**, 225–233, Oxford.

TANG, J., KÖHLER, S.J. & DIETZEL, M. (2008a): Sr^{2+}/Ca^{2+} and $^{44}Ca/^{40}Ca$ fractionation during inorganic calcite formation: I. Sr incorporation. – Geochimica et Cosmochimica Acta, **72**, 3718–3732, New York.

TANG, J., DIETZEL, M., BÖHM, F., KÖHLER, S.J. & EISENHAUER, A. (2008b): Sr^{2+}/Ca^{2+} and $^{44}Ca/^{40}Ca$ fractionation during inorganic calcite formation: II. Ca isotopes. – Geochimica et Cosmochimica Acta, **72**, 3733–3745, New York.

TANG, J., NIEDERMAYR, A., KÖHLER, S.J., BÖHM, F., KISAKÜREK, B., EISENHAUER, A. & DIETZEL, M. (2012): Sr^{2+}/Ca^{2+} and $^{44}Ca/^{40}Ca$ fractionation during inorganic calcite formation: III. Impact of salinity/ionic strength. – Geochimica et Cosmochimica Acta, **77**, 432–443, New York.

TANG, J., DIETZEL, M., FERNANDEZ, A., TRIPATI, A.K. & ROSENHEIM, B.E. (2014): Evaluation of kinetic effects on clumped isotope fractionation (Δ_{47}) during inorganic calcite precipitation. – Geochimica et Cosmochimica Acta, **134**, 120–136, New York.

TEMPLETON, A. & BENZERARA, K. (2015): Emerging frontiers in geomicrobiology. – Elements, **11**, 423–429, Québec.

TENG, H.H. (2013): How ions and molecules organize to form crystals. – Elements, **9**, 189–194, Québec.

TESORIERO, A.J. & PANKOW, J.F. (1996): Solid solution partitioning of Sr^{2+}, Ba^{2+}, and Cd^{2+} to calcite. – Geochimica et Cosmochimica Acta, **60**, 1053–1063, New York.

THALMANN, F. (1979): Zur Eisenspatvererzung in der nördlichen Grauwackenzone am Beispiel des Erzberges bei Eisenerz und Radmer/Bucheck. – Verhandlungen der Geologischen Bundesanstalt, **1978**/3, 479–489, Wien.

TÖCHTERLE, P., DUBLYANSKY, Y., STÖBENER, N., MANDIĆ, M. & SPÖTL, C. (2017): High-resolution isotopic monitoring of cave air CO_2. – Rapid Communications in Mass Spectrometry, **31**, 895–900, Chichester.

TOKER, E., KAYSERI-ÖZER, M.S., ÖZKUL, M. & KELE, S. (2015): Depositional system and palaeoclimatic interpretations of Middle to Late Pleistocene travertines: Kocabaş, Denizli, south-west Turkey. – Sedimentology, **62**, 1360–1383, Amsterdam.

TREMAINE, D.M. & FROELICH, P.N. (2013): Speleothem trace element signatures: A hydrologic geochemical study of modern cave dripwaters and farmed calcite. – Geochimica et Cosmochimica Acta, **121**, 522–545, New York.

TREMAINE, D.M., FROELICH, P.N. & WANG, Y. (2011): Speleothem calcite farmed in situ: Modern calibration of $\delta^{18}O$ and $\delta^{13}C$ paleoclimate proxies in a continuously-monitored natural cave system. – Geochimica et Cosmochimica Acta, **75**, 4929–4950, New York.

TRIPATI, A.K., HILL, P.S., EAGLE, R.A., MOSENFELDER, J.L., TANG, J., SCHAUBLE, E.A., EILER, J.M., ZEEBE, R.E., UCHIKAWA, J., COPLEN, T.B., RIES, J.B. & HENRY, D. (2015): Beyond temperature: Clumped isotope signatures in dissolved inorganic carbon species and the influence of solution chemistry on carbonate mineral composition. – Geochimica et Cosmochimica Acta, **166**, 344–371, New York.

TRUCHE, L., BAZARKINA, E.F., BERGER, G., CAUMON, M.-C., BESSAQUE, G. & DUBESSY, J. (2016): Direct measurement of CO_2 solubility and pH in NaCl hydrothermal solutions by combining in-situ potentiometry and Raman spectroscopy up to 280 °C and 150 bar. – Geochimica et Cosmochimica Acta, **177**, 238–253, New York.

TUTOLO, B.M., LUHMANN, A.J., KONG, X.-Z., SAAR, M.O. & SEYFRIED JR, W.E. (2015): CO_2 sequestration in feldspar-rich sandstone: Coupled evolution of fluid chemistry, mineral reaction rates, and hydrogeochemical properties. – Geochimica et Cosmochimica Acta, **160**, 132–154, New York.

VAKS, A., BAR-MATTHEWS, M., AYALON, A., MATTHEWS, A., FRUMKIN, A., DAYAN, U., HALICZ, L., ALMOGI-LABIN, A. & SCHILMAN, B. (2006): Paleoclimate and location of the border between Mediterranean climate region and the Saharo–Arabian Desert as revealed by speleothems from the northern Negev Desert, Israel. – Earth and Planetary Science Letters, **249**, 384–399, Amsterdam.

VALDEZ, B., SCHORR, M., QUINTERO, M., CARRILLO, M., ZLATEV, R., STOYTCHEVA, M. & DE DIOS OCAMPO, J. (2009): Corrosion and scaling at Cerro Prieto geothermal field. – Anti-Corrosion Methods and Materials, **56**, 28–34, Bradford.

VALLEY, J.W., EILER, J.M., GRAHAM, C.M., GIBSON, E.K., ROMANEK, C.S. & STOLPER, E.M. (1997): Low-temperature carbonate concretions in the Martian meteorite ALH84001: Evidence from stable isotopes and mineralogy. – Science, **275**, 1633–1638, Washington, D.C.

VAN DRIESSCHE, A.E.S., KELLERMEIER, M., BENNING, L.G. & GEBAUER, D. (2017): New Perspectives on Mineral Nucleation and Growth – From Solution Precursors to Solid Materials. – 380 pp., Switzerland (Springer International Publishing).

VAN HUSEN, D. (2009): Zusammenfassender Überblick über die quartäre Entwicklung um das westliche Hochschwabmassiv (Blatt 101 Eisenerz). – Tagungsband zur Arbeitstagung der Geologischen Bundesanstalt 2009, Leoben, 106–117, Wien.

VAN HUSEN, D. & FRITSCH, A. (2007): Der Bergsturz von Wildalpen (Steiermark). – Jahrbuch der Geologischen Bundesanstalt, **147**, 201–213, Wien.

VAN ZUILEN, K., MÜLLER, T., NÄGLER, T.F., DIETZEL, M. & KÜSTERS, T. (2016): Experimental determination of barium isotope fractionation during diffusion and adsorption processes at low temperatures. – Geochimica et Cosmochimica Acta, **186**, 226–241, New York.

VARSÁNYI, I. & KOVÁCS, L.Ó. (2006): Arsenic, iron and organic matter in sediments and groundwater in the Pannonian Basin, Hungary. – Applied Geochemistry, **21**, 949–963, Amsterdam.

VARSÁNYI, I., MATRAY, J.-M. & KOVÁCS, L.Ó. (1997): Geochemistry of formation waters in the Pannonian Basin (southeast Hungary). – Chemical Geology, **140**, 89–106, Amsterdam.

VASYLIEV, G., VASYLIEVA, S., NOVOSAD, A. & GERASYMENKO, Y. (2018): Ultrasonic modification of carbonate scale electrochemically deposited in tap water. – Ultrasonics Sonochemistry, **48**, 57–63, Amsterdam.

VIETEN, R., WINTER, A., WARKEN, S.F., SCHRÖDER-RITZRAU, A., MILLER, T.E. & SCHOLZ, D. (2016): Seasonal temperature variations controlling cave ventilation processes in Cueva Larga, Puerto Rico. – International Journal of Speleology, **45**, 259–273, Tampa.

WANG, H., ALFREDSSON, V., TROPSCH, J., ETTL, R. & NYLANDER, T. (2013): Formation of $CaCO_3$ deposits on hard surfaces – Effect of bulk solution conditions and surface properties. – ACS Applied Materials and Interfaces, **5**, 4035–4045, Washington, D.C.

WANG, X., EDWARDS, R.L., AULER, A.S., CHENG, H., KONG, X., WANG, Y., CRUZ, F.W., DORALE, J.A. & CHIANG, H.-W. (2017): Hydroclimate changes across the Amazon lowlands over the past 45,000 years. – Nature, **541**, 204–207, London.

WANNER, C., EICHINGER, F., JAHRFELD, T. & DIAMOND, L.W. (2017): Causes of abundant calcite scaling in geothermal wells in the Bavarian Molasse Basin, Southern Germany. – Geothermics, **70**, 324–338, Amsterdam.

WARSINGER, D.M., SWAMINATHAN, J., GUILLEN-BURRIEZA, E., ARAFAT, H.A. & LIENHARD, J.H. (2015): Scaling and fouling in membrane distillation for desalination applications: A review. – Desalination, **356**, 294–313, Amsterdam.

WASSENBURG, J.A., SCHOLZ, D., JOCHUM, K.P., CHENG, H., OSTER, J., IMMENHAUSER, A., RICHTER, D.K., HÄGER, T., JAMIESON, R.A., BALDINI, J.U.L., HOFFMANN, D. & BREITENBACH, S.F.M. (2016): Determination of aragonite trace element distribution coefficients from speleothem calcite-aragonite transitions. – Geochimica et Cosmochimica Acta, **190**, 347–367, New York.

WEDENIG, M., DIETZEL, M., BOCH, R. & HIPPLER, D. (2016): Experiments on different materials (polyamide, stainless & galvanized steel) influencing geothermal $CaCO_3$ scaling formation: Polymorphs & elemental incorporation. – Geophysical Research Abstracts, **18**, EGU2016-10056, Katlenburg-Lindau.

WEIDENDORFER, D., SCHMIDT, M.W. & MATTSSON, H.B. (2017): A common origin of carbonatite magmas. – Geology, **45**, 507–510, Washington, D.C.

Westphal, A., Eichinger, F., Eichinger, L. & Würdemann, H. (2019): Change in the microbial community of saline geothermal fluids amended with a scaling inhibitor: effects of heat extraction and nitrate dosage. – Extremophiles, **23**/3, 283–304, Tokyo. https://dx.doi.org/10.1007/s00792-019-01080-0

Wiederhold, J.G. (2015): Metal stable isotope signatures as tracers in environmental geochemistry. – Environmental Science and Technology, **49**, 2606–2624, Washington, D.C.

White, W.B. & Culver, D.C. (2012): Encyclopedia of Caves. – 2nd ed., 945 pp., Amsterdam (Chennai Academic Press).

Wolfgramm, M., Rauppach, K. & Thorwart, K. (2011): New mineral formations and transport of particles in the thermal water loop of geothermal plants in Germany. – Zeitschrift für Geologische Wissenschaften, **39**, 213–239, Berlin.

Wolthers, M., Nehrke, G., Gustafsson, J.P. & van Cappellen, P. (2012): Calcite growth kinetics: Modeling the effect of solution stoichiometry. – Geochimica et Cosmochimica Acta, **77**, 121–134, New York.

Woodhead, J., Hellstrom, J., Maas, R., Drysdale, R., Zanchetta, G., Devine, P. & Taylor, E. (2006): U-Pb geochronology of speleothems by MC-ICPMS. – Quaternary Geochronology, **1**, 208–221, Amsterdam.

Wunsch, C. (2006): Abrupt climate change: An alternative view. – Quaternary Research, **65**, 191–203, Amsterdam.

Würdemann, H., Westphal, A., Lerm, S., Kleyböcker, A., Teitz, S., Kasina, M., Miethling-Graff, R., Seibt, A. & Wolfgramm, M. (2014): Influence of microbial processes on the operational reliability in a geothermal heat store – Results of long-term monitoring at a full scale plant and first studies in a bypass system. – Energy Procedia, **59**, 412–417, Amsterdam.

Würdemann, H., Westphal, A., Kleyböcker, A., Miethling-Graff, R., Teitz, S., Kasina, M., Seibt, A., Wolfgramm, M., Eichinger, F. & Lerm, S. (2016): Microbial metabolic processes affect the operation of geothermal plants and the success of countermeasures. – Grundwasser, **21**, 93–106, Berlin–Heidelberg.

Yan, H., Liu, Z. & Sun, H. (2017): Effect of in-stream physicochemical processes on the seasonal variations in $\delta^{13}C$ and $\delta^{18}O$ values in laminated travertine deposits in a mountain stream channel. – Geochimica et Cosmochimica Acta, **202**, 179–189, New York.

Yang, Q., Scholz, D., Jochum, K.P., Hoffmann, D.L., Stoll, B., Weis, U., Schwager, B. & Andreae, M.O. (2015): Lead isotope variability in speleothems – A promising new proxy for hydrological change? First results from a stalagmite from western Germany. – Chemical Geology, **396**, 143–151, Amsterdam.

Yardley, B.W.D., Ewing, R.C. & Whittleston, R.A. (2016): Deep-mined geological disposal of radioactive waste. – Elements, **12**, 225–296, Québec.

Yoshioka, S., Ohde, S., Kitano, Y. & Kanamori, N. (1986): Behaviour of magnesium and strontium during the transformation of coral aragonite to calcite in aquatic environments. – Marine Chemistry, **18**, 35–48.

Zammit, C.M., Shuster, J.P., Gagen, E.J. & Southam, G. (2015): The geomicrobiology of supergene metal deposits. – Elements, **11**, 337–342, Québec.

Zarrouk, S.J. & Moon, H. (2014): Efficiency of geothermal power plants: A worldwide review. – Geothermics, **51**, 142–153, Amsterdam.

Zhang, Z., Xie, Y., Xu, X., Pan, H. & Tang, R. (2012): Transformation of amorphous calcium carbonate into aragonite. – Journal of Crystal Growth, **343**, 62–67, Amsterdam.

Zhou, J., Lundstrom, C.C., Fouke, B., Panno, S., Hackley, K. & Curry, B. (2005): Geochemistry of speleothem records from southern Illinois: Development of (^{234}U)/(^{238}U) as a proxy for paleoprecipitation. – Chemical Geology, **221**, 1–20, Amsterdam.

Zou, Z., Habraken, W.J.E.M., Matveeva, G., Jensen, A.C.S., Bertinetti, L., Hood, M.A., Sun, C.-Y., Gilbert, P.U.P.A., Polishchuk, I., Pokroy, B., Mahamid, J., Politi, Y., Weiner, S., Werner, P., Bette, S., Dinnebier, R., Kolb, U., Zolotoyabko, E. & Fratzl, P. (2019): A hydrated crystalline calcium carbonate phase: Calcium carbonate hemihydrate. – Science, **363**, 396–400, Washington, D.C.

Received: 3. April 2019, accepted: 28. August 2019

JAHRBUCH DER GEOLOGISCHEN BUNDESANSTALT

Jb. Geol. B.-A.	ISSN 0016–7800	Band 159	Heft 1–4	S. 131–143	Wien, Dezember 2019

Geologische Aufnahmen im Gratal (Kreuzeck, Kärnten, Österreich)

Gerit Griesmeier*

5 Abbildungen, 1 Tafel

Österreichische Karte 1:50.000
BMN / UTM
181 Obervellach / NL 33-04-04 Obervellach
/ NL 33-04-10 Kötschach-Mauthen

Geologische Kartierung
Strukturgeologie
Quartärgeologie
Kreuzeckgruppe
Leßnigbach-Scherzone

Inhalt

Zusammenfassung

Aufgrund der geringen eoalpidischen (kretazischen) Überprägung bietet das Gratal (auch Rottensteintal) die Möglichkeit, pre-Alpidische Ereignisse zu untersuchen. Zudem kann durch eine Vielzahl verschiedener glazigener Ablagerungen die jüngste geologische Vergangenheit rekonstruiert werden.

Das untersuchte Gebiet befindet sich auf dem Kartenblatt ÖK50 Blatt 181 Obervellach und umfasst das Gratal in der südöstlichen Kreuzeckgruppe. Tektonisch befindet sich das Untersuchungsgebiet im Drauzug-Gurktal-Deckensystem und wird lithostratigrafisch vom Liegenden in das Hangende vom Strieden- und Gaugen-Komplex aufgebaut.

Im Strieden-Komplex gibt es eine Abfolge aus Granat-Glimmerschiefern, Glimmerschiefern und Paragneisen. Die Gesteine wurden gemeinsam offen verfaltet und von der Grenze zum überlagernden Gaugen-Komplex diskordant abgeschnitten. Diese Grenze ist eine bis zu 300 m mächtige Mylonit/Phyllonitzone, an der die Gesteine beider angrenzender Einheiten stark überprägt wurden. Der Gaugen-Komplex besteht hauptsächlich aus Paragneisen und Glimmerschiefern, welche durch den Hellglimmerreichtum ein charakteristisches Erscheinungsbild aufweisen. Beide Einheiten wurden polyphas verfaltet, wodurch das Einfallen der Schieferungen und Lineationen stark variiert. Neben der Scherzone zwischen Strieden- und Gaugen-Komplex gibt es eine weitere markante Phyllonitzone (Leßnigbach-Scherzone), die den Gaugen-Komplex von Ost nach West durchschneidet.

* Gerit Griesmeier: Geologische Bundesanstalt, Neulinggasse 38, 1030 Wien. gerit.griesmeier@geologie.ac.at

Während des Würm-Hochglazials (Last Glacial Maximum, LGM) war das Gebiet Teil eines großen Eisstromnetzes, das weite Teile der Ostalpen bedeckte. Schliffgrenzen deuten darauf hin, dass die Eisoberfläche im Drautal 2.100 m Seehöhe erreichte. Nur die höchsten Gipfel ragten als Nunataker heraus. In nicht vergletscherten Bereichen herrschte Frostsprengung vor, wodurch heute in oberen Hangbereichen periglazialer Verwitterungsschutt vorliegt. Großflächige Ablagerungen von Grund- und Ablationsmoränen zeugen vom LGM und späteren Glazialen. Als älteste Ablagerungen liegen Eisrandsedimente vor, die an Rändern des zurückschmelzenden Gletschers in Eisstauseen geschüttet wurden. End- und Seitenmoränen zeigen, dass es während des alpinen Spätglazials kleinere Kargletscher gegeben hat, die während einzelner Stadiale unterschiedliche Ausdehnung erreichten. Mit dem Zusammenbruch des Eisstromnetzes kam es infolge der Instabilität der übersteilten Hänge zu tiefgreifenden Massenbewegungen und Hangzerreißungen, wie Zerrgräben vielerorts zeigen.
Verlassene und zum Teil versperrte Stollenlöcher bilden heute noch stumme Zeugen des Gold- und Silberabbaus in der Kreuzeckgruppe.

Geological investigations in the Gra valley (Kreuzeck mountain, Carinthia, Austria)

Abstract

Due to a minor eoalpine (cretaceous) overprint, the Gra valley (also Rottenstein valley) provides the possibility to investigate pre-Alpine events. Additionally, the youngest geological past can be reconstructed due to a variety of sediments of glacial origin.
The studied area can be found on the Austrian 1:50,000 map sheet BMN 181 Obervellach and covers the Gra valley in the southeastern Kreuzeck Mountains. Tectonically, the study area is part of the Drauzug-Gurktal Nappe System and is formed lithostratigraphically by the Strieden and Gaugen complexes from base to top.
In the Strieden Complex there is a sequence of garnet-micaschist, micaschist and paragneiss. These lithologies were open folded together and cut discordantly by the border to the overlying Gaugen Complex. This border is an up to 300 m thick shear zone, were rocks of both adjacent units have been heavily phyllonitized/mylonitized. The Gaugen Complex mainly consists of paragneiss and micaschist with a characteristic appearance due to the abundance of white mica. Both units were folded polyphasely resulting in a great variation of the dip of the schistosity and lineation. Besides the shear zone between the Strieden and Gaugen complexes, there is another prominent phyllonite zone (Leßnigbach Shearzone), which intersects the Gaugen Complex from East to West.
During the Würmian Pleniglacial (= Last Glacial Maximum, LGM) most parts of the area were part of the transection glacier complex covering large parts of the Eastern Alps. Trimlines indicate the ice surface in the Drau valley in c. 2,100 m a.s.l. Only the highest peaks were nunataks. In these areas, which were not covered by glaciers, congelifraction prevailed as documented by a cover of periglacial weathering debris. Large areas covered by subglacial till and ablation till are the legacy of the LGM but also of the following Alpine Lateglacial. The oldest lateglacial deposits are ice-marginal sediments that were deposited during the Phase of ice-decay in ice-dammed lakes along the margin of the rapidly downmelting glaciers, just after the LGM. Latero-frontal moraines are indications of the presence of small cirque glaciers during different stadials of the Alpine Lateglacial. With the collapse of the transection glacier complex of the LGM, glacially oversteepened slopes reacted with deep-seated mass movements as shown by tension cracks in many locations.
Abandoned and partly locked galleries serve as silent witnesses to the gold and silver mining in the Kreuzeck Mountains.

Geologischer Überblick

Geologisch umfasst das bearbeitete Gebiet (Taf. 1) die Kreuzeck-Gailtaler Alpen-Decke des Drauzug-Gurktal-Deckensystems. Diese Decke wird vom Liegenden in das Hangende vom Strieden- und Gaugen-Komplex aufgebaut, wobei der Strieden-Komplex im Norden und der Gaugen-Komplex, der den größten Teil des Gebietes einnimmt, im Süden auftritt. Diese Einheiten sind durch eine markante, mylonitische/phyllonitische Scherzone begrenzt. Der Gaugen-Komplex ist intern von einer mächtigen Phyllonitzone (Leßnigbach-Scherzone; Griesmeier et al., 2019) in E–W-Richtung durchschnitten.

Lithostratigrafische Einheiten und Lithologien

Strieden-Komplex (Drauzug-Gurktal-Deckensystem/Kreuzeck-Gailtaler Alpen-Decke)

Die Hauptlithologie des Strieden-Komplexes ist Glimmerschiefer. Aufgrund der großflächigen Überlagerung von quartären Sedimenten gibt es im Aufnahmegebiet nur wenige Aufschlüsse. Granat-Glimmerschiefer finden sich allerdings in großer Zahl als gerundete Steine in den quartären Ablagerungen. Seltene, wenige Meter mächtige Quarzit- und Amphibolit-Lagen sind in die Granat-Glimmerschiefer eingeschaltet.

Die **Granat-Glimmerschiefer** (Abb. 1a) sind graublau gefärbt und brechen groblockig zu unregelmäßigen, wenige Kubikdezimeter großen Blöcken. Oft sind Quarz-Lagen und Quarz-Klasten in die Schieferung eingeregelt und isoklinal verfaltet. Die prägende Schieferung ist ebenso stark verfaltet und auf den Schieferungsflächen sind feinkörnige, silberige Hellglimmer und grüngrauer Chlorit zu erkennen. Auffallend ist, dass Biotit zumeist vollständig abwesend ist. Granat erreicht eine Größe von bis zu 15 mm und ist zumeist homogen im Gestein verteilt. Er ist gut erhalten, lediglich etwas zerbrochen.

Diese Granat-Glimmerschiefer werden im Nordosten des kartierten Gebietes von **Glimmerschiefern mit weitgehend abgebautem Granat** unterlagert. Die Granate erreichen ebenfalls bis 1 cm Größe, wurden jedoch größtenteils in Eisenoxide/-hydroxide umgewandelt (Abb. 1b). Die Glimmerschiefer beinhalten graue Quarzmobilisate, sind reich an Biotit und weisen eine rote Verwitterungsfarbe auf. Bemerkenswert ist, dass die umgewandelten Granate oft dieselbe dunkelrote Farbe aufweisen. In manchen

Abb. 1. ►
Gesteine aus dem untersuchten Gebiet. a) Granat-Glimmerschiefer des Strieden-Komplexes. b) Glimmerschiefer des Strieden-Komplexes aus dem Bereich der Scherzone zwischen dem Strieden- und Gaugen-Komplex. Typisch sind Granate, die zu Eisenoxiden/-hydroxiden abgebaut wurden. Durch den Einfluss der Scherzone weisen die abgebauten Granate eine sigmoidale Form auf. c) Gebänderter Amphibolit aus dem Strieden-Komplex. Die Bänderung wird durch Wechsellagerung hellgrüner Epidot, dunkelgrüner Amphibol- und weißer Plagioklas-/Quarz-Lagen verursacht. d) Typischer, ockerfarbener, hellglimmerreicher Glimmerschiefer des Gaugen-Komplexes. e) In besonders quarzitischen Paragneisen des Gaugen-Komplexes ist das Auftreten dieser Amphibol-Chlorit-Granat-Quarz-Lagen häufig. f) Granat-Staurolith-Glimmerschiefer des Gaugen-Komplexes. Die Staurolithe erreichen eine Länge von 1 cm. Diese Gesteine sind äußerst selten im Gaugen-Komplex. g) Orthogneis-Lage im Gaugen-Komplex. Große Feldspatkristalle bilden typischerweise sigmoidale Klasten in einer Glimmer-reichen Matrix. h) Grakofel-Dioritgneis mit dunkelgrünen Amphibolen und hellgrünen Klinozoisiten aus dem Gaugen-Komplex. Auffallend ist, dass diese Gesteine selten eine Schieferung ausbilden.

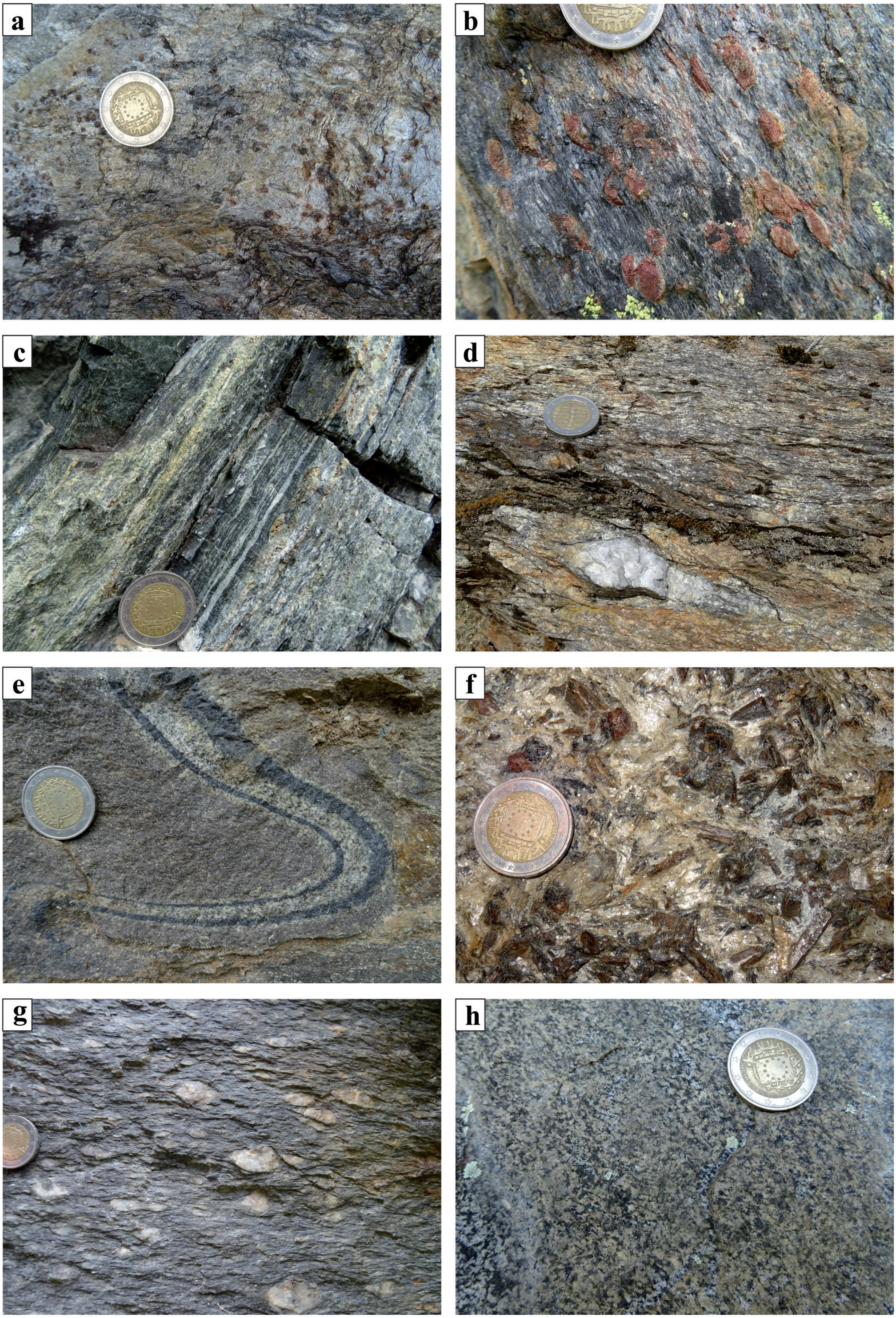
a
b
c
d
e
f
g
h

Typen sind die Granate nicht auffallend rot, sondern – im Schliff erkennbar – fast vollständig in Chlorit umgewandelt, wobei die Umwandlung unter statischen Bedingungen stattgefunden hat. In Annäherung an die Hangendgrenze sind diese Glimmerschiefer phyllonitisch überprägt, wodurch sie fast schwarz erscheinen und die kaputten Granate weisen eine sigmoidale Form auf. Die Abfolge der Granat-Glimmerschiefer und Glimmerschiefer mit den umgewandelten Granaten wurde gemeinsam offen verfaltet und wird von der Grenze zum überlagernden Gaugen-Komplex diskordant abgeschnitten.

In beiden Lithologien finden sich wenige Meter mächtige **Quarzit**-Lagen. Sie sind weiß-gelblich und führen zumeist Hellglimmer, selten auch Biotit.

Neben den Quarziten gibt es auch dunkelgrüne **Amphibolit**-Lagen in den Granat-Glimmerschiefern. Diese brechen auffallend blockig, sind zumeist feinkörnig und deutlich geschiefert. Nicht selten lässt sich ein Lagenbau aus dunkelgrünen Amphibol-, weißen Plagioklas- und hellgrünen Epidot-Lagen erkennen (Abb. 1c). Außerdem führen die Amphibolite häufig Kalzit und Rutil.

Gaugen-Komplex (Drauzug-Gurktal-Deckensystem/ Kreuzeck-Gailtaler Alpen-Decke)

Typischerweise ockerfarbene, monotone Paragneise mit fließenden Übergängen zu Glimmerschiefern bilden die Hauptlithologie des Gaugen-Komplexes (Abb. 1d). Vor allem im Bereich südlich der Leßnigbach-Scherzone sind die Glimmerschiefer und Paragneise quarzitisch ausgebildet. Selten sind Lagen von Augengneisen, hellen Orthogneisen, Granat-Glimmerschiefern, Quarziten und Amphiboliten in die Hauptlithologie eingelagert.

Genaue Beschreibungen der **Paragneise** und **Glimmerschiefer** finden sich in Griesmeier & Schuster (2017).

Markant, vor allem in massigen, quarzitischen Paragneisen, ist das Auftreten geringmächtiger (bis zu wenigen dm) verfalteter Lagen mit chloritisierten Amphibolen und wenige Millimeter großen Granat-Porphyroblasten (Abb. 1e). Oft sind die dunklen Lagen, die vor allem aus Amphibol und Chlorit bestehen, vom Nebengestein durch Anreicherungen felsischer Minerale begrenzt. Granat ist zumeist außerhalb dieser Lagen ebenfalls erkennbar. Diese Lagen finden sich ausschließlich südlich der Leßnigbach-Scherzone.

Granat-Glimmerschiefer führen häufig Biotit und Hellglimmer und die Granate sind zumeist etwa 3–5 mm im Durchmesser. Am Lenkenspitz (2.298 m) erreichen die Granate bis 1 cm Größe und sind lokal mit Staurolith (1 cm Länge) vergesellschaftet (Abb. 1f). Weitere Vorkommen befinden sich bei der Oberen Orteralm (1.886 m), am Kreuzkofel (1.842 m) und nördlich von Flattachberg.

Etwa 200 m nordwestlich der Karlhöhe (2.232 m) befindet sich ein mehrere Meter mächtiger **Orthogneis**körper. Dieser ist hell, mittelkörnig, verwittert bräunlich und bricht blockig. Bereichsweise treten zahlreiche Quarz-Lagen und Quarz-Mobilisate auf. Biotit ist nicht vorhanden, allerdings große Mengen an Hellglimmern, die etwa 2 mm Größe erreichen. Eine weitere, etwa 3 m mächtige, biotitreiche Orthogneis-Lage mit Feldspat-Porphyroklasten findet sich auf der Straße nach Rottenstein auf einer Seehöhe von 1.000 m (Abb. 1g). Die Schieferung des Orthogneises ist subparallel zur Schieferung der umliegenden Glimmerschiefer orientiert. In der Orthogneis-Lage treten Quarz-Gänge auf, die senkrecht zur Schieferung des Gneises orientiert sind und eine Länge von etwa 20 cm erreichen. Ein weiterer mehrere Meter mächtiger Orthogneiskörper mit Feldspat-Porphyroklasten findet sich im Grabach auf einer Seehöhe von etwa 940 m.

Quarzitische Paragneise und Glimmerschiefer sind sehr häufig im Gaugen-Komplex, doch nur selten gibt es **Quarzite** als wenige Meter mächtige Lagen in diese Lithologien eingeschaltet. Sie sind zumeist hellgrau, feinkörnig und brechen auffallend polygonal zu wenigen Kubikdezimeter großen Stücken.

Feinkörnige, dunkelgrüne **Amphibolite** wurden lediglich südlich der Leßnigbach-Scherzone aufgefunden. Sie sind zumeist mittel- bis feinkörnig und besitzen neben dunkelgrünem Amphibol und häufigem Biotit und Kalzit wenige Millimeter dicke Lagen, die von Plagioklas aufgebaut werden. Selten tritt auch Chlorit auf.

Der Grakofel (2.551 m) wird von einem hellgrauen **Dioritgneis (Grakofel-Dioritgneis)** mit grünen Amphibol- und Klinozoisit-Kristallen aufgebaut (Abb. 1h). Der Gneis ist typischerweise sehr massig und bricht regellos zu wenige Kubikdezimeter großen, unregelmäßig geformten Stücken. Schieferung ist zumeist keine erkennbar. Auch die Klüftung weist keine bevorzugte Orientierung auf. Im Dünnschliff ist erkennbar, dass häufig auftretender Plagioklas saussuritisiert ist, also zu Klinozoisit und Serizit umgewandelt wurde. Geochemische Untersuchungen des Dioritkörpers zeigen, dass er peraluminös ist und Signaturen aufweist, die besonders für Inselbögen typisch sind. Dies steht in Einklang mit Untersuchungen von Reche (1981).

Chlorit-Serizit-Schiefer treten in Randbereichen des Grakofel-Dioritgneises intensiv verfaltet auf. Auch der Dioritgneiskörper ist deformiert, die Deformation scheint allerdings schwächer zu sein, als in den Chlorit-Serizit-Schiefern. Entweder war die Deformation tatsächlich schwächer oder sie ist, durch den Mineralbestand bedingt, nicht so gut ersichtlich.

Strukturgeologie und Lagerungsverhältnisse

Im Folgenden werden interne Strukturen und Lagerungsverhältnisse der auftretenden Komplexe näher beschrieben. Außerdem wird auf geologische Trennstrukturen eingegangen.

Strieden-Komplex

Das allgemeine Streichen der (Granat-)Glimmerschiefer des Strieden-Komplexes ist im Westen zumeist NW–SE gerichtet bei steilem Einfallen und ändert sich in östlicher Richtung in NE–SW-Streichen. Eine offene Verfaltung mit flach einfallenden, E–W streichenden Faltenachsenflächen sorgt für eine unstete Einfallsrichtung der Gesteine. Die Orientierung der Streckungslineation und Krenulation variiert zwischen SE- und NE-Fallen (Abb. 2a). Die Änderung der Einfallsrichtung von NW–SE- auf NE–SW-Streichen wird durch eine Großfalte erzeugt, die von der Grenze zum überlagernden Gaugen-Komplex diskordant abgeschnitten wird. In Annäherung an die Hangendgrenze überprägt diese das Schichteinfallen und die Streckungslineare in den aufgeschlossenen Bereichen. Die Schieferung und Streckungslineare fallen in diesem Bereich nach Südost (Abb. 3a, Taf. 1).

Gaugen-Komplex südlich der Leßnigbach-Scherzone

Die Einfallsrichtung der Schieferungsflächen im Gaugen-Komplex südlich der Leßnigbach-Scherzone schwankt hauptsächlich zwischen Nord und Südwest mit relativ flachen Winkeln unter ca. 45°. Das Nordfallen ist vor allem in Annäherung an die Leßnigbach-Scherzone zu beobachten. Auf den Schieferungsflächen ist neben einem etwa N–S streichenden, allerdings zwischen Nordwest und Nordost schwankenden Streckungslinear auch eine subparallel dazu ausgebildete Krenulation vorhanden (Abb. 2b). Die Lineation und Krenulation könnten gleichzeitig entstanden sein. Verantwortlich für das uneinheitliche Einfallen der Schieferung und die Schwankungen im Streichen der Lineare und Krenulationen sind mehrere Faltungsphasen. Auffallend sind Isoklinalfalten mit Nordwest-streichenden, flach einfallenden Faltenachsen. Diese Isoklinalfalten werden oft durch Quarzmobilisat- und Chlorit-Amphibol-Granat führende Lagen sichtbar. Die Faltenachsenflächen dieser Faltung entsprechen zumeist der heutigen, prägenden Schieferung. Wie bereits erwähnt, ist die Schieferung und somit auch diese erste Faltungsphase wiederum verfaltet. Es gibt zum einen etwa moderat bis steil nordfallende Faltenachsenflächen und weitere, die ein NE–SW-Streichen bei moderatem Einfallen aufweisen. Bei allen Faltungen handelt es sich vermutlich um asymmetrische Falten, wodurch das komplexe Einfallen der Schieferungen und Faltungen erzeugt wird.

Gaugen-Komplex nördlich der Leßnigbach-Scherzone

Nördlich der Leßnigbach-Scherzone ist das Einfallen der Schieferung noch komplexer als südlich der Scherzone. Es können alle Einfallsrichtungen beobachtet werden, vorherrschend ist allerdings ein moderates bis flaches Einfallen der Schieferungsflächen gegen Südwesten und Norden. Die Lineare fallen hauptsächlich Richtung Südwesten und Norden, allerdings mit großen Schwankungen sowohl in Einfallswinkel, als auch Einfallsrichtung. Krenulationen und Faltenachsen fallen vorranging nach Westen bis Südwesten bei flachem bis moderatem Einfallen. Wie die Schieferungsflächen sind auch die Faltenachsenflächen stark variierend orientiert. Es können allerdings zwei Systeme ausgemacht werden, ein NW–SE streichendes und ein NE–SW streichendes System, wobei in jedem Fall beide möglichen Einfallsrichtungen vorkommen (Abb. 2c). Aufgrund der polyphasen Verfaltung ist es oft nicht möglich, eine Alterseinstufung der verschiedenen Faltungsphasen zu machen.

Grenze zwischen Strieden- und Gaugen-Komplex

An der Grenze zwischen Strieden- und Gaugen-Komplex treten Mylonite und Phyllonite in einer Mächtigkeit von bis zu 300 m auf. Die Scherzone fällt moderat nach Südosten und ist um subhorizontale, NW–SE streichende Faltenachsen mit vertikalen Achsenebenen offen verfaltet.

Die Streckungslineation fällt moderat nach Südosten (Abb. 3a). Die Richtung der Scherung ist nicht ganz eindeutig. SC-Gefüge und (Quarz-)Klastgeometrien geben Hinweise darauf, dass die Scherzone nach Süden abschiebend bewegt wurde, dies ist allerdings bei kalten Temperaturen um 300° C passiert. Aufgrund der Texturen in Quarz und dem Chloritreichtum werden jedoch grünschieferfazielle Bedingungen für die Scherung angenommen. Der Schersinn dieses duktilen Ereignisses ist unbekannt.

Die Gesteine sind sehr dunkel und brechen grobblockig. Nicht selten ist eine vor allem an Quarzmobilisat-Lagen ersichtliche, starke Verfaltung erkennbar, die nicht von der Scherung, sondern von vorherigen Deformationsereignissen im Strieden-/Gaugen-Komplex stammt (Abb. 3b). Die Gesteine, vor allem die Phyllonite, sind sowohl reich an Hellglimmer, als auch an Chlorit und Grafit, sodass das Gestein schwarz erscheint (Abb. 3c). In manchen Berei-

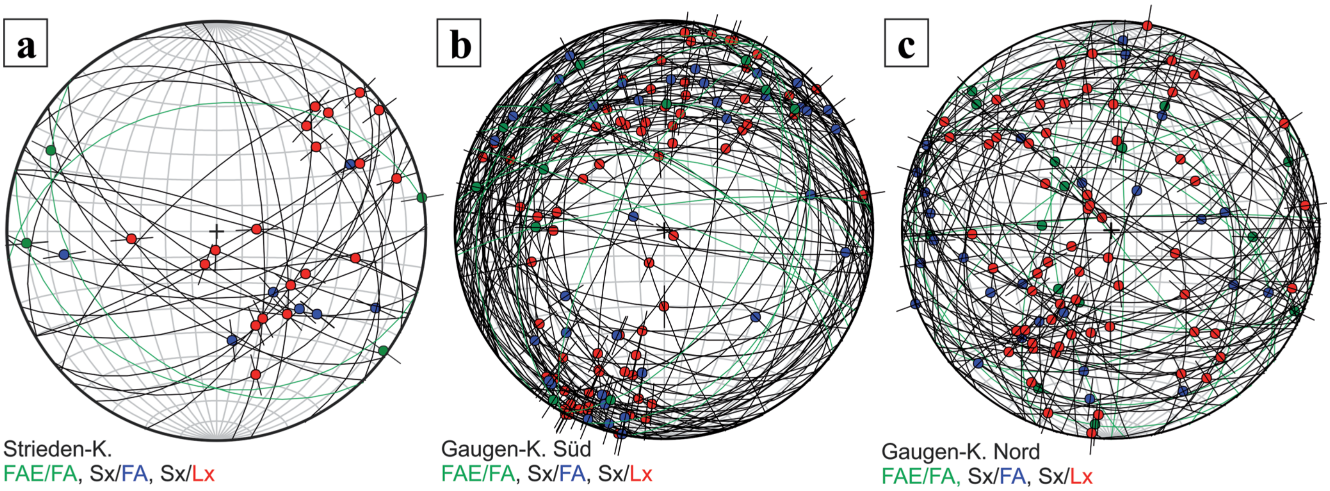

Abb. 2.
Flächentreue Stereoplots der unteren Hemisphäre. Es sind jeweils das Einfallen der Schieferung (Sx; schwarz) und Faltenachsenflächen (FAE; grün) sowie das Streichen der Lineationen (Lx; rot) und Krenulationen (FA; blau) dargestellt. a) Orientierung der Flächen und Lineare im Strieden-Komplex. b) Orientierung der Flächen und Lineare im Gaugen-Komplex südlich der Leßnigbach-Scherzone. c) Orientierung der Flächen und Lineare im Gaugen-Komplex nördlich der Leßnigbach-Scherzone. Für Details, siehe Text.

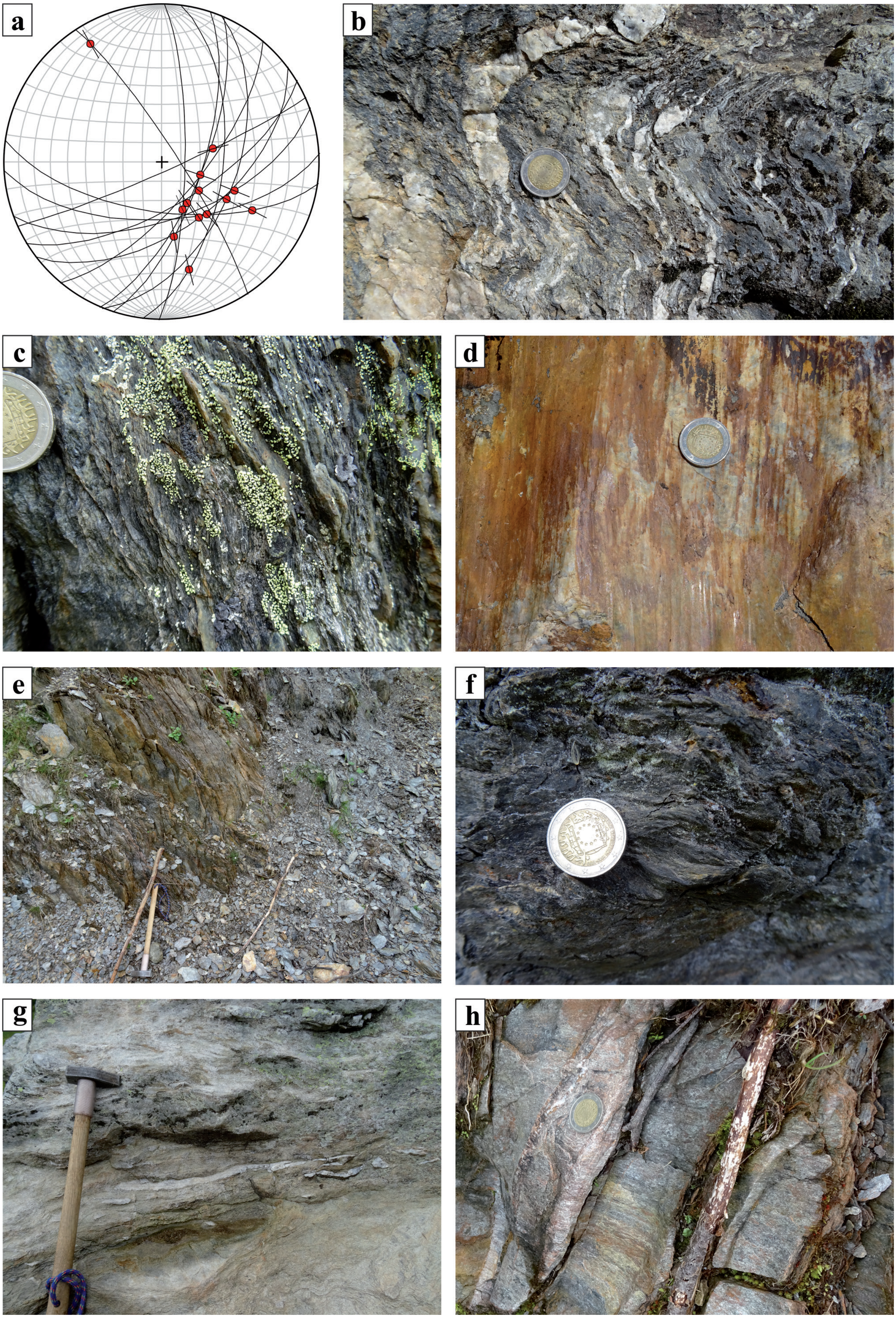
a
b
c
d
e
f
g
h

◀ Abb. 3.
Gesteine in der Scherzone zwischen Strieden- und Gaugen-Komplex (a–d) sowie in der Leßnigbach-Scherzone (e–h). a) Flächentreuer Stereoplot der unteren Hemisphäre. Das Einfallen der Schieferung und Streichen der Lineation (rot) ist dargestellt. b) Glimmerschiefer mit verfalteten Quarz-Lagen. Die Verfaltung stammt vermutlich von älterer Deformation. c) Dunkelgrauer Phyllonit. Die dunkle Farbe wird durch Grafit verursacht. d) Spiegelharnisch in einem Quarzitmylonit. e) Phyllonite der Leßnigbach-Scherzone. Der feinschuppige Bruch ist typisch. f) Auffallend schwarzer Ultrakataklasit. g, h) Grün-weiße Phyllonite der Leßnigbach Scherzone mit einigen Quarz-Lagen. Die grüne Farbe wird von Chlorit verursacht.

chen sind bis zu 1 cm große Granate vorhanden, die eine längliche, sigmoidale Form aufweisen. Sie sind allerdings zumeist zu Eisenoxiden/-hydroxiden zersetzt (Abb. 1b). Vermutlich stellen die Glimmerschiefer mit den abgebauten Granaten (siehe Kap. Strieden-Komplex), die im Strieden-Komplex auftreten, das Ausgangsprodukt dieser Phyllonite dar. Neben den schwarzen Phylloniten treten selten auch karbonatreiche Grünschiefer auf. Ein Vorkommen wurde im Graben, der vom Schanitzentörl in östlicher Richtung in das Gratal führt, auf einer Seehöhe von 1.900 m angetroffen. Zusätzlich treten am Rand der Scherzone auch weiß-gelbliche Quarzmylonite auf, die teilweise Spiegelharnische ausbilden (Abb. 3d). Am südöstlichen Rand der Scherzone treten phyllonitisierte Gesteine des Gaugen-Komplexes auf, die vor allem an ihrem feinstückigen Bruch und der helleren Färbung von den anderen Phylloniten unterscheidbar sind.

Leßnigbach-Scherzone

Die Leßnigbach-Scherzone ist eine ca. 200 m breite, sehr steil (ca. 80°) nordfallende Zone mit (sub)vertikalem Streckungslinear und nach Süden gerichtetem Schersinn, die den Gaugen-Komplex in E–W-Richtung durchtrennt. Die Schieferung wird von einer Faltung mit ESE fallenden Faltenachsen und flach SE fallenden Achsenebenen überprägt. Für nähere Details, siehe GRIESMEIER et al. (2019).

Die Gesteine des Gaugen-Komplexes sind durch den Einfluss der Scherzone stark phyllonitisch überprägt, was sich in Fältelung mit Wellenlängen von wenigen Zentimetern und Feinkörnigkeit zeigt. Die Gesteine brechen zudem zumeist feinschuppiger als in ungestörten Bereichen und zerbröseln in seltenen Fällen regelrecht (Abb. 3e). Durch kataklastische Überprägung sind massigere Gesteine oft stark zerbrochen, wie es vor allem im Bach südlich des Greinwaldgrabens sichtbar ist. In diesem Bereich wurde die Straße durch Rutschungen und kleinere Felsstürze gefährdet und teilweise zerstört. Südlich des Greinwaldgrabens sind Störungsgesteine aufgeschlossen, die stark von Eisenhydroxiden bedeckt sind. Einzelne Minerale können nicht ausgemacht werden und es herrscht ein C-Typ-Gefüge vor. Im Bereich der Mündung des Neubergbaches in den Grabach treten Ultrakataklasite auf, die mehrere Meter Mächtigkeit erreichen können (Abb. 3f). Im oberen Bereich des Neuberggrabens gibt es hellgrüne, silberige Phyllonite des Gaugen-Komplexes. Chlorit, der aus dem Zerfall von Biotit entstand, und Hellglimmer prägen diese Gesteine und eine (Kink)faltung kann beobachtet werden (Abb. 3g, h).

Quartäre Ablagerungen und Formen

Schliffgrenze

Im nördlichen Drautal, im Gebiet des Talausganges des Gratals, wurde die Eisgrenze zurzeit des Würm-Hochglazials von VAN HUSEN (1987) auf etwa 1.900 m geschätzt. Eigene morphologische Beobachtungen am Stagor legen jedoch nahe, dass die Eishöhe bis auf 2.100 m reichte.

Moränenablagerungen

Das kartierte Gebiet beinhaltet große Bereiche, die großflächig von glazigenen Ablagerungen bedeckt sind. Vor allem in den oberen Talbereichen und in Karen befinden sich Grund- und Ablationsmoränenablagerungen (Abb. 4b, c). Es handelt sich dabei um massive korn- oder matrixgestützte Diamikte mit Komponenten diverser Herkunft. Die Matrix ist zumeist siltig bis tonig und weist oft eine rötliche Färbung auf, die durch den Eisenreichtum der Gesteine des Gaugen-Komplexes verursacht wird. Die Größe der Komponenten schwankt je nach Material von wenigen cm^3 bis mehreren dm^3, vor allem abhängig von der Lithologie. Zumeist finden sich in den Ablagerungen lokalere, eckige, kleinere Steine aus dem Gaugen-Komplex und gerundete, größere Steine aus dem Strieden-Komplex. Die Komponenten in Ablationsmoränenablagerungen sind immer eckig. Vor allem in den hinteren Talbereichen und in den Karen sind Grundmoränenablagerungen durch Vernässungszonen charakterisiert, welche die Kompaktheit der Ablagerung widerspiegeln (Abb. 4a). End- und Seitenmoränenablagerungen sind durch Wallformen charakterisiert und finden sich vor allem in Karen. Sie markieren den äußeren Rand ehemaliger Gletscherzungen.

Ablagerungen periglazialer Verwitterung

Es ist auffallend, dass in oberen Hangbereichen, die nicht zu Karen überformt wurden, selten Aufschlüsse zu finden sind und stattdessen nur eckiges, loses Material vorliegt. Diese Bereiche unterlagen vermutlich periglazialer Verwitterung. Es handelt sich dabei um Bereiche, die nicht direkt vergletschert waren, in denen allerdings Permafrost dazu führte, dass der Gesteinsverband vor allem durch Frostsprengung großflächig aufgewittert vorliegt. Stark von periglazialer Verwitterung geprägte Bereiche finden sich zum Beispiel oberhalb der Oberen Orteralm auf etwa 1.800 bis 2.200 m.

Ein weiteres Phänomen (ehemaligen) Permafrosts sind Blockgletscher. Eine besonders imposante Blockgletscherablagerung (Abb. 4e, f) befindet sich südwestlich des Grakofels (2.551 m). Diese liegt auf der östlichen Talseite und reicht bis auf eine Höhe von 2.060 m herab. Weitere derartige Körper treten unterhalb des Lenkenspitzes (2.298 m) auf. Diese sind ebenfalls westschauend und die Untergrenze befindet sich auf etwa 1.900 m. Die Blockgletscherablagerungen besitzen zumeist mehrere Wälle. An der Oberfläche sind neben den namensgebenden großen Blöcken auch weniger große Komponenten im Größenbereich von Kubikdezimeter bis Kubikzentimeter zu beobachten.

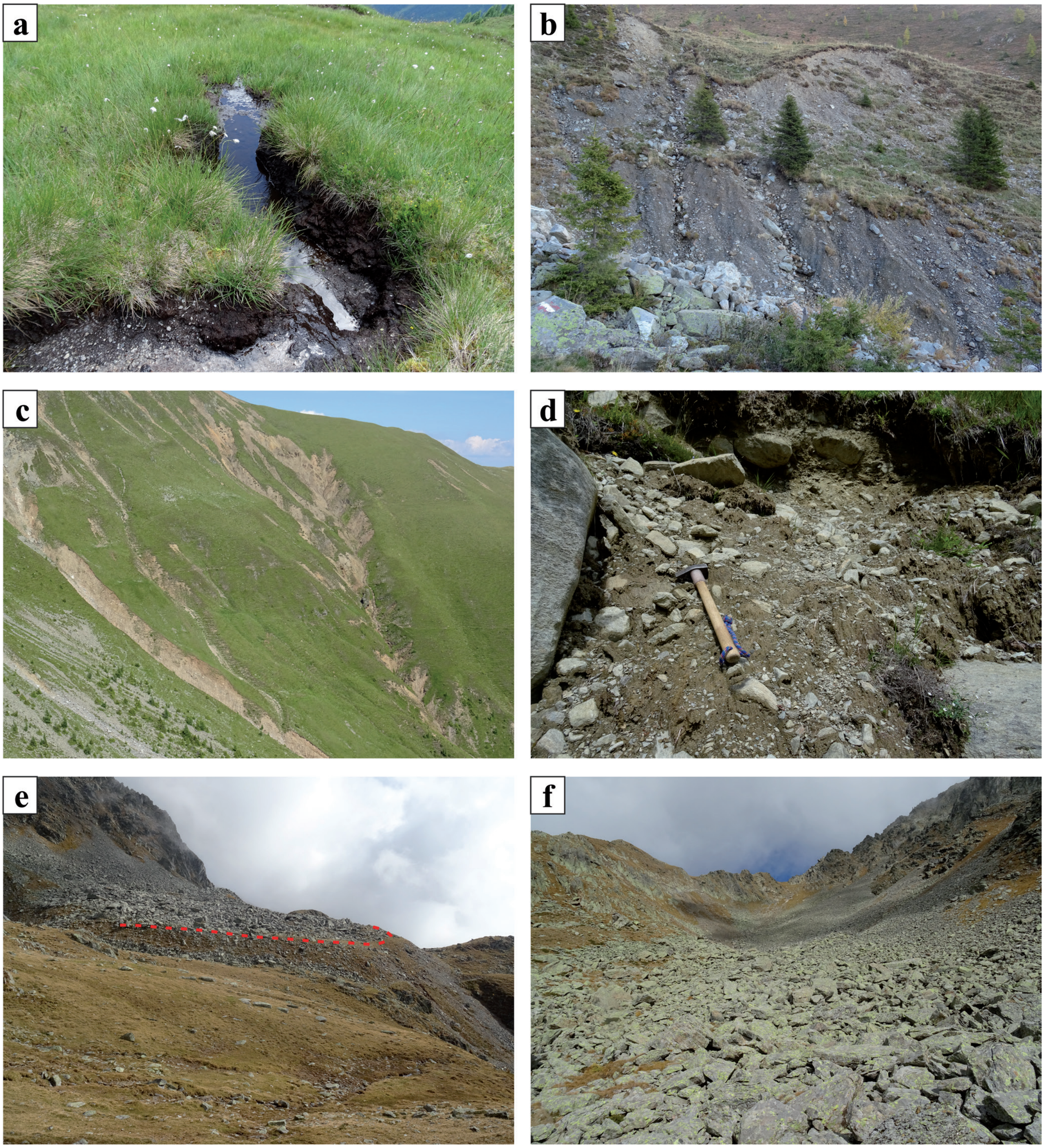

Abb. 4.
Quartärgeologische Phänomene. a) Großflächige Vernässung auf Grundmoräne. b) Grund- und Ablationsmoränenablagerung im Bereich des oberen Grabaches. Die Sedimente wurden fluviatil umgearbeitet. c) Anrisse in Grund- und Ablationsmoränenablagerungen unterhalb des Grakofels (2.551 m). d) Eisrandsediment mit gerundeten Komponenten in sandiger Matrix. e, f) Blockgletscher unterhalb des Grakofels (2.551 m). Der äußere Wall ist rot nachgezeichnet (e).

Eisrandablagerungen

An den Hängen im Drautal finden sich Eisrandsedimente vom Talboden bis auf eine Höhe von etwa 800 m. Diese Sedimente beinhalten gut gerundete Komponenten variabler Größe in sandiger Matrix (Abb. 4d). Da oberflächlich umgelagerte Moränenablagerungen mit bis zu etwa 2 m Mächtigkeit eine ähnliche Fazies aufweisen, wurden für die Zuordnung auch morphologische Charakteristika herangezogen. Typischerweise finden sich in den Eisrandablagerungen eng beieinanderliegende, in Falllinie verlaufende Gräben, die nur zeitweise Wasser führen. Häufig sind auch Abrisskanten ausgebildet, an denen die Lockersedimente abrutschen.

Zumeist sind die erhaltenen Sedimente im Drautal lediglich wenige Meter bis Zehnermeter mächtig. In manchen Bereichen erreichen die Eisrandsedimente jedoch an die hundert Meter Mächtigkeit, wie zum Beispiel bei Radlach. Vor allem bei Radlach und Flattachberg sind Terrassen aus

Eisrandsediment erhalten, die einen deutlichen Geländeknick im Hangprofil markieren. Im Bereich westlich des Talausganges des Gratals gibt es nur lokale, geringmächtige Ablagerungen von Eisrandsedimenten. Allerdings liegen hier einige Gletscherschliffe auf Rundhöckern sowie Grundmoränenablagerungen, die vermutlich aus dem Würm-Hochglazial stammen, vor.

Im Gratal sind unterhalb von etwa 1.200 m nur kleinere Eisrandkörper erhalten. Sie reichen nicht bis zum Talboden, da der Grabach mit der Zeit in anstehendes Gestein eingeschnitten hat. Großflächige Eisrandablagerungen finden sich in oberen Bereichen des Gratals (1.200–1.500 m Seehöhe). In Seitenbächen, die in den Grabach münden, erstrecken sich diese Sedimente bis in Höhen von 1.800 m.

Massenbewegungen

In den Kamm- und oberen Hangbereichen sind vielerorts, vor allem zwischen Lenkenspitz (2.298 m) und Hochbichl (2.275 m), Zerrgräben und antithetische Brüche ausgebildet. Der Hang zwischen der Oberen und Unteren Orteralm ist großflächig aufgelockert. Eine tiefgreifende, komplexe Massenbewegung ist am Osthang oberhalb von Rottenstein ausgebildet. Die oberste Abrisskante befindet sich am Gipfels des Kreuzkofels (1.842 m) und zieht nördlich unterhalb des Kammes entlang. Östlich davon ist der gesamte Hangbereich großflächig aufgelockert. Intern befindet sich eine weitere Abrisskante auf einer Höhe von etwa 1.700 m. Nördlich dieser komplexen Massenbewegung gibt es weitere Abrisskanten auf etwa 1.600 m und 1.500 m. Östlich von Rottenstein befindet sich eine weitere Abrisskante entlang des Kammes, wobei der östliche Hang wiederum stark aufgelöst ist. In diesem Gebiet ist der Gesteinsverband aufgelockert und das Einfallen lokal gestört. Vor allem in Eisrandsedimenten gibt es häufig Massenbewegungen von wenigen Kubikmetern Ausdehnung, wie oben erwähnt. Eine solche ist zum Beispiel im Greinwaldgraben ausgebildet, wo eine kleine Hütte etwas abgerutscht ist.

Abschätzung verschiedener Gletscherstände

Es folgt eine Interpretation der Entwicklung der Landschaft zur Zeit des Quartärs. Die spätglaziale Chronologie orientiert sich an Reitner et al. (2016).

Würm-Hochglazial (~30–20 ka)

Während des letztens glazialen Maximums – dem Würm-Hochglazial – war vermutlich das gesamte Gebiet bis auf eine Höhe von etwa 2.100 m von Eis bedeckt. In den Karen ging die Gletscherbedeckung weiter nach oben bis an die Basis der Felswände, die sich in den obersten Bereichen auf etwa 2.500 m befindet. An der Basis des Gletschers wurden Grundmoränensedimente gebildet, die noch heute vor allem an ostfallenden Hängen im Gratal großflächig vorhanden sind. Von den höher gelegenen Felsen fielen große Schuttmengen auf das Eis, die heute zum Teil noch in Form von Ablationsmoränenablagerungen vorliegen. Bereiche, die nicht vergletschert waren, wurden von periglazialer Verwitterung geprägt. Der vorherrschende Prozess war dabei vermutlich Frostsprengung. Auffallend ist, dass periglazialer Verwitterungsschutt vor allem an den westfallenden Hängen auftritt. Vermutlich waren die Sonneneinstrahlung und dadurch die tageszeitlichen Temperaturschwankungen auf den westfallenden Hängen größer und es kam dadurch vermehrt zu Frostsprengung, während die ostfallenden Hänge weniger davon betroffen waren. Interessant ist, dass dieser Schutt nicht nur oberhalb von 2.100 m auftritt, sondern auch mehrere hundert Meter darunter. Dafür könnte es mehrere Erklärungen geben. Denkbar wäre, dass es sich bei den Ablagerungen nicht um periglazialen Verwitterungsschutt, sondern um Ablationsmoränenablagerungen, also supraglazial transportierten Schutt handelt. Eine weitere und vermutlich sehr plausible Möglichkeit ist, dass der Schutt auch erst nach dem Höhepunkt der Vergletscherung entstand, als sich die Gletscher bereits zurückgezogen hatten.

Eiszerfallsphase (Beginn Würm-Spätglazial; ~20–19 ka)

Als der Gletscher im Gratal mit Beginn der Erwärmung zurückwich und der mächtige Draugletscher das Gratal aufstaute, wurde Material aus Seitenbächen und aus dem Vorfeld des zurückweichenden Gragletschers von Schmelzwasserflüssen in die eisfrei gewordene Landschaft geschüttet. Dabei bildeten sich Staukörper am Eisrand. Auch am Rand des abschmelzenden Draugletschers bildeten sich diese Staukörper. Nach dem vollständigen Abschmelzen des Eises wurden diese Sedimente größtenteils erodiert und in das über zweihundert Meter übertiefte Drautal geschüttet, wie eine bei Kleblach-Lind abgeteufte Bohrung zeigt, die in 200 m Tiefe das Festgestein noch nicht erreichte (Schuster et al., 2006 und Referenzen darin). Auch der Grabach begann die Sedimente anzugraben. In tiefer gelegenen Bereichen (< 1.200 m) des Gratals wurden Sedimente weitgehend ausgeräumt und der Bach schnitt in das Festgestein ein. Durch die fehlende Stabilisation des Eises wurden die teils übersteilten Hänge instabil und es bildeten sich vielerorts Zerrgräben und großflächige Massenbewegungen.

Weitere spätglaziale Ablagerungen

Im Kartierungsgebiet gibt es eine Reihe von glazialen wie auch periglazialen Ablagerungen, die dem Würm-Spätglazial (~20–11,7 ka) zuzurechnen sind, ohne dass gegenwärtig eine konkretere Zuordnung zu Stadialen (wie zum Beispiel in Reitner et al., 2016) möglich ist. Im Folgenden werden Beispiele hierfür gegeben: In den Karen unterhalb des Schanitzentörls (2.188 m), Stawipfels (2.514 m), Karlkopfes (2.502 m), östlich des Schronecks (2.459 m) und unterhalb des Kleinen Kreuzecks (2.505 m) gab es vermutlich mehrere Gletscherzungen, die sich in tieferen Talbereichen, auf etwa 2.000 m, zu einem Gletscher vereinigten. Dieser erstreckte sich vermutlich etwa bis knapp oberhalb der Unteren Hasleralm. Er erreichte also etwa eine Länge von 3 km. Viel weiter ist der Gletscher vermutlich nicht geflossen, da sich unterhalb dieser Höhe Eisrandsedimente befinden, die nicht von Grundmoräne überlagert werden. Es wird interpretiert, dass der Kamm vom Kleinriegel

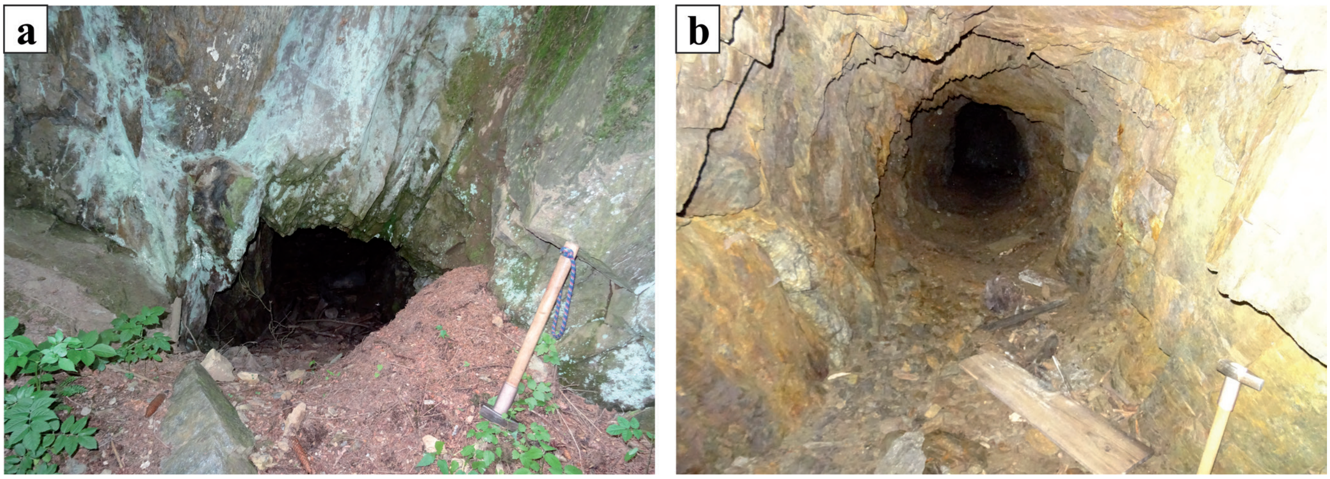

Abb. 5.
a) Stolleneingang beim Campingplatz Rottenstein. b) Der Stollen ist etwa 10 bis 20 m lang und etwa 2 m hoch. Das Umgebungsgestein ist quarzitischer Paragneis mit wenigen kataklastischen Zonen.

(2.163 m) und eine Fortsetzung dessen bis zur Gratalhütte eine Seitenmoräne zwischen zwei dieser Gletscherzungen darstellt. Weitere Kämme zwischen den oben erwähnten Karen bildeten vermutlich ebenfalls seitliche Begrenzungswälle zwischen den einzelnen Gletscherzungen.

Im Kar nordwestlich des Stagors (2.289 m) fehlen trotz der eindeutigen Morphologie direkte Anhaltspunkte für einen Gletscherstand im Würm-Spätglazial.

Vermutlich waren die oberen Kammbereiche des Gratals nach einer ersten Vergletscherungsphase nochmals von kleineren Gletschern bedeckt. Hinweise darauf liefert eine Vielzahl an wenige Meter hohen Wällen zwischen den großen Festgesteinswällen, die oben erwähnt wurden. Es handelt sich dabei zumeist um Seitenmoränen. Es werden drei Gletscherzungen interpretiert, die sich in den Karen unterhalb des Karlkopfes (2.502 m), östlich des Schronecks (2.459 m) und unterhalb des Kleinen Kreuzecks (2.505 m) befanden. Der westlichste war vermutlich der kürzeste und reichte etwa bis auf 2.100 m herab, der mittlere auf etwa 2.000 m und der östlichste auf etwa 1.900 m. Zusätzlich zu den Seitenmoränenwällen gibt es einige Solifluktionswälle, die vermutlich etwas später entstanden sind. In der Nähe großer Felswände bildeten sich in nicht vergletscherten Bereichen Blockgletscher. Die Blockgletscher entstanden wahrscheinlich zur Zeit des Egesen-Stadials (~12,8 ka; Reitner et al., 2016).

Lagerstätten

Die Kreuzeckgruppe ist bekannt für zahlreiche kleine Lagerstätten von Gold, Silber und Antimon, aber auch für Blei, Kupfer und Eisen (Friedrich, 1963). Im kartierten Bereich liegen die historischen Abbaue südwestlich des Kleinen Grakofels (2.459 m) und südlich des Grakofels (2.551 m). Hier wurde bereits im 15. und 16. sowie im 18. Jahrhundert Bergbau betrieben und hunderte Meter lange Stollen in den Berg getrieben, um vorrangig Gold und Silber, aber auch Blei, Arsen, Kupfer und Eisen zu fördern. Manche der Stollen können heute noch gefunden werden, die Halden sind vielerorts von Vegetation bedeckt. Ein Stolleneingang, der sich an der Basis der Felswände des Grakofels befindet (Koordinaten: 13°13‘42,111‘‘E, 46°49‘48,478‘‘N WGS84), wurde aufgefunden. Er befindet sich in massivem Dioritgneis und große Steine wurden vor den Eingang gelegt, sodass ein Betreten nicht möglich ist. Beschreibungen der Vererzungen finden sich in Reche (1981) und Friedrich (1963).

Auch im Bereich der Goldgrubenscharte (2.448 m) wurde nach Erz, vor allem nach Gold und Silber, gesucht.

Bei Rottenstein wurden zwei Stollenlöcher gefunden, wobei ein Stollen begangen wurde. Dieser Stollen befindet sich an der Straße nach Rottenstein neben dem Campingplatz (Koordinaten: 13°14‘34,493“E, 46°45‘45,919“N WGS84) und wurde in Glimmerschiefer des Gaugen-Komplexes geschlagen (Abb. 5a, b). Kataklastische Zonen befinden sich in unmittelbarer Nähe zum Stolleneingang. Der Stollen ist etwa 10 bis 20 m lang, verläuft in westlicher Richtung mehr oder weniger geradlinig und beinhaltet im hinteren Abschnitt einen etwa 4 bis 5 m hohen Schacht, der vertikal nach oben geschlagen wurde. Es konnte nicht erkannt werden, was abgebaut wurde.

Das andere Stollenloch (Koordinaten: 13°14‘21,029“E, 46°46‘38,694“N WGS84) befindet sich an der Straße in das Gratal, etwa 1 km nach Ende der asphaltierten Straße in Glimmerschiefern des Gaugen-Komplexes und verläuft in westlicher Richtung etwa 8 m. Eine kurze Beschreibung findet sich in Pichler (2009).

Literatur

FRIEDRICH, O.M. (1963): Die Lagerstätten der Kreuzeckgruppe. Monographien kärntner Lagerstätten, 3. Teil. – Archiv für Lagerstättenforschung in den Ostalpen, 1. Band, 222 S., Leoben.

GRIESMEIER, G.E.U. & SCHUSTER, R. (2017): Bericht 2016 über geologische Aufnahmen auf Blatt 181 Obervellach. – Jahrbuch der Geologischen Bundesanstalt, **157**, 369–373, Wien.

GRIESMEIER, G.E.U., SCHUSTER, R. & GRASEMANN, B. (2019): Major fault zones in the Austroalpine units of the Kreuzeck Mountains south of the Tauern Window (Eastern Alps, Austria). – Swiss Journal of Geosciences, **112**/1, 39–53, Basel. http://dx.doi.org/10.1007/s00015-018-0328-1

PICHLER, A. (2009): Bergbau in Westkärnten: eine Bestandsaufnahme der noch sichtbaren Merkmale der historischen Bergbaue in Westkärnten. – Carinthia II: Sonderheft, **63**, 416 S., Klagenfurt.

RECHE, R. (1981): Zur petrographischen, erzmineralogischen und geochemischen Untersuchung der Gesteine des Grakfofel (Kreuzeckgruppe, Österreich). – Diplomarbeit, Mineralogisch-Petrographisches Institut der Universität Hamburg, VI + 124 S., Hamburg.

REITNER, J.M., IVY-OCHS, S., DRESCHER-SCHNEIDER, R., HAJDAS, I. & LINNER, M. (2016): Reconsidering the current stratigraphy of the Alpine Lateglacial: Implications of the sedimentary and morphological record of the Lienz area (Tyrol/Austria). – E&G Quaternary Science Journal, **65**/2, 113–144, Göttingen.

SCHUSTER, R., PESTAL, G. & REITNER, J.M. (2006): Erläuterungen zur Geologischen Karte der Republik Österreich 1:50.000, Blatt 182 Spittal an der Drau. – 115 S., Geologische Bundesanstalt, Wien.

VAN HUSEN, D. (1987): Die Eiszeiten in den Ostalpen. – 24 S., Geologische Bundesanstalt, Wien.

Eingelangt: 23. Mai 2019, angenommen: 25. Oktober 2019

Tafel 1

Geologische Karte des Gratals. In der rechten unteren Ecke befindet sich eine lithostratigrafische Übersicht über das Gebiet.

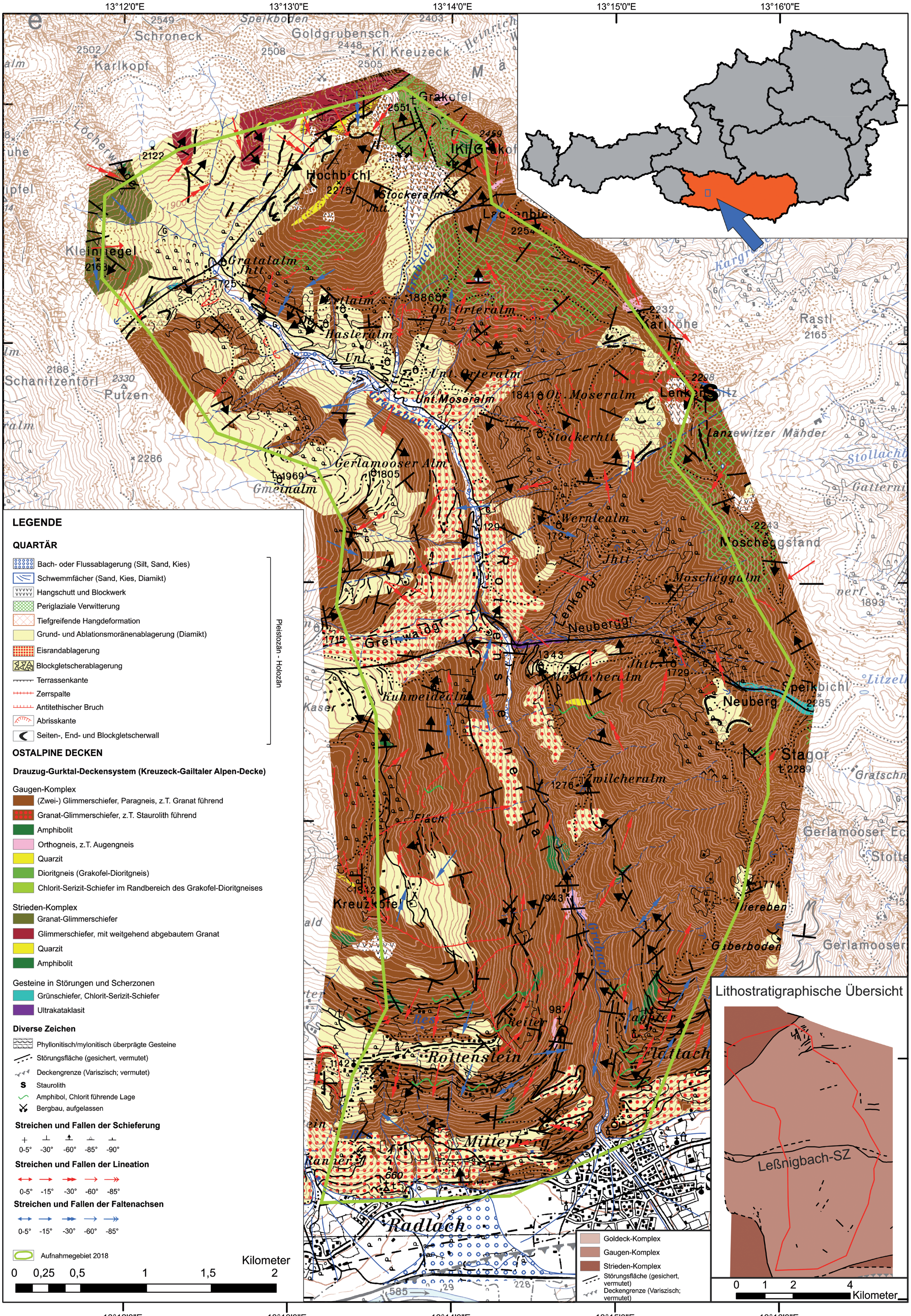

LEGENDE
QUARTÄR
Bach- oder Flussablagerung (Silt, Sand, Kies)
Schwemmfächer (Sand, Kies, Diamikt)
Hangschutt und Blockwerk
Periglaziale Verwitterung
Tiefgreifende Hangdeformation
Grund- und Ablationsmoränenablagerung (Diamikt)
Eisrandablagerung
Blockgletscherablagerung
Terrassenkante
Zerrspalte
Antitethischer Bruch
Abrisskante
Seiten-, End- und Blockgletscherwall
Pleistozän - Holozän
OSTALPINE DECKEN
Drauzug-Gurktal-Deckensystem (Kreuzeck-Gailtaler Alpen-Decke)
Gaugen-Komplex
(Zwei-) Glimmerschiefer, Paragneis, z.T. Granat führend
Granat-Glimmerschiefer, z.T. Staurolith führend
Amphibolit
Orthogneis, z.T. Augengneis
Quarzit
Dioritgneis (Grakofel-Dioritgneis)
Chlorit-Serizit-Schiefer im Randbereich des Grakofel-Dioritgneises
Strieden-Komplex
Granat-Glimmerschiefer
Glimmerschiefer, mit weitgehend abgebautem Granat
Quarzit
Amphibolit
Gesteine in Störungen und Scherzonen
Grünschiefer, Chlorit-Serizit-Schiefer
Ultrakataklasit
Diverse Zeichen
Phyllonitisch/mylonitisch überprägte Gesteine
Störungsfläche (gesichert, vermutet)
Deckengrenze (Variszisch; vermutet)
Staurolith
Amphibol, Chlorit führende Lage
Bergbau, aufgelassen
Streichen und Fallen der Schieferung
0-5° -30° -60° -85° -90°
Streichen und Fallen der Lineation
0-5° -15° -30° -60° -85°
Streichen und Fallen der Faltenachsen
0-5° -15° -30° -60° -85°
Aufnahmegebiet 2018
Kilometer
0 0,25 0,5 1 1,5 2
Goldeck-Komplex
Gaugen-Komplex
Strieden-Komplex
Störungsfläche (gesichert, vermutet)
Deckengrenze (Variszisch; vermutet)
Lithostratigraphische Übersicht
Leßnigbach-SZ
0 1 2 4 Kilometer
13°12'0"E
13°13'0"E
13°14'0"E
13°15'0"E
13°16'0"E
46°45'0"N
46°46'0"N
46°47'0"N
46°48'0"N
46°49'0"N
46°50'0"N
Schroneck
Goldgrubensch
Kl. Kreuzeck
Karlkopf
Grakofel
Kl. Grakofel
Hochbichl
Stockeralm
Kleinegel
Gratalalm
Ob. Orteralm
Haslealm
Unt. Orteralm
Unt. Moseralm
Ob. Moseralm
Schanitzentörl
Putzen
Gerlamooser Alm
Gmeinalm
Wernleralm
Moscheggstand
Moscheggalm
Greimwaldgr
Neuberggr.
Kuhmeidealm
Neuberg
Speikbichl
Stagor
Zwilcheralm
Kreuzkofel
Rottenstein
Mitterberg
Radlach
Rastl
Lanzewitzer Mähder
Gerlamooser

JAHRBUCH DER GEOLOGISCHEN BUNDESANSTALT

Jb. Geol. B.-A. | ISSN 0016–7800 | Band 159 | Heft 1–4 | S. 145–154 | Wien, Dezember 2019

Ergebnisse der Neukartierung des neogenen Oberwölz-Beckens (Steiermark/Österreich)

Ralf Schuster*

3 Abbildungen

Österreichische Karte 1:50.000
BMN / UTM
159 Murau / NL 33-02-19 Oberwölz
/ NL 33-02-25 Murau

Oberwölz-Becken
Neogen
Geologische Kartierung
Steiermark

Inhalt

Zusammenfassung

In diesem Bericht werden die Ergebnisse einer Kartierung des neogenen Oberwölz-Beckens und dessen Untergrund dargestellt. Der Untergrund baut sich aus Glimmerschiefern, Kalkschiefern, Marmoren, Quarziten und verschiedenen Metabasiten auf, die der Murau-Decke und den „Basalen Glimmerschiefer-Decken“ des Drauzug-Gurktal-Deckensystems zugeordnet werden. Die erhaltenen Reste des Oberwölz-Beckens sind in Ost–West-Richtung über mindestens 8 km und in Nord–Süd-Richtung etwa 2 km kartierbar. Über einer basalen Brekzie, die zumeist aus Dolomit-Komponenten besteht, folgen Karbonat-Konglomerate. Das Liefergebiet beider Lithologien ist der unmittelbar darunterliegende, hangende Anteil der Murau-Decke, der sich im Wesentlichen aus Kalkmarmoren, Dolomiten und Kalkschiefern aufbaut. In den Konglomeraten konnten an jeweils einer Stelle eine Mergellage beziehungsweise ein Tuffit angetroffen werden. Gegen das Hangende verschiebt sich das Komponentenspektrum zu Gesteinen aus dem liegenden Anteil der Murau-Decke, welche aus Glimmerschiefern mit Marmorlagen aufgebaut ist. Diese Glimmerschiefer-Marmor-Konglomerate sind bei hohem Anteil an Glimmerschiefer-Material nur wenig zementiert und daher zum Teil als Kiese anzusprechen. Die sedimentäre Schichtung zeigt ein Einfallen zwischen Nordnordwest über West bis Südsüdwest. Transgressionskontakte der basalen Brekzie auf die Gesteine des Drauzug-Gurktal-Deckensystems sind vor allem im Norden des Verbreitungsgebietes der neogenen Sedimente vorhanden, während am Südrand die hangenden Glimmerschiefer-Marmor-Konglomerate dominieren. Dementsprechend ist zu vermuten, dass es sich beim Oberwölz-Becken um einen Halbgraben mit einer steil einfallenden Abschiebung am Südrand handelt. Eine detaillierte strukturelle Kartierung des Südrandes und eine sedimentologische Bearbeitung der Beckensedimente wäre wünschenswert.

A new geological map of the Oberwölz Basin (Styria/Austria)

Abstract

This report summarizes results from geological mapping of the Neogene Oberwölz Basin (Styria/Austria) and its immediately underlying basement. Micaschist, calcareous schist, marble, quartzite and different types of metabasites belonging to the Murau Nappe and “Basal Micaschist Nappes” form the basement. Both nappes are part of the Drauzug-Gurktal Nappe System. The Neogene sediments extend for 8 km in east-west and about 2 km in north-south direction. The basal part consists of

* Ralf Schuster: Geologische Bundesanstalt, Neulinggasse 38, 1030 Wien. ralf.schuster@geologie.ac.at

a dolomite breccia. It is overlain by a conglomerate dominated by carbonate clasts. The source area of both lithologies is the upper part of the Murau Nappe, which is predominantly composed of calcite marble, dolomite (marble) and calcareous schist. Within the conglomerate, a marl layer and a tuffitic layer appear. Upwards the pebble spectrum of the conglomerates shifts to dark grey micaschist and marble from the lower part of the Murau Nappe. If micaschist is dominating, the matrix is only weakly cemented and the rock behaves like gravel. The sedimentary layering of the basin sediments is dipping towards the North-north-west, West and South-south-west. Transgressive contacts of the basal breccia and the basement rocks are frequent in the northern part of the area, whereas the micaschist-rich conglomerate forming the upper part of the sedimentary succession is exposed in the southern part. Due to this distribution, the Oberwölz Basin seems to represent a half-graben with a steep fault along the southern margin. However, detailed mapping and a structural investigation along the southern margin of the basin as well as a sedimentological study focusing on the depositional environment and the formalization of lithostratigraphic units is missing.

Einleitung

Ab den 1990er Jahren wurde an der Geologischen Bundesanstalt unter der Leitung von Hauptabteilungsleiter Wolfgang Schnabel die Erstellung von geologischen Bundesland-Karten im Maßstab 1:200.000 vorangetrieben. Im Zuge der Arbeiten an den geologischen Karten von Salzburg (Braunstingl et al., 2005) und Oberösterreich (Krenmayr et al., 2006) wurde klar, dass die vorhandenen Unterlagen zum Gebiet der Niederen Tauern in vielerlei Hinsicht nicht mehr dem inhaltlichen Wissensstand entsprachen. So war beispielsweise bekannt, dass die in der geologischen Karte der Steiermark (Flügel & Neubauer, 1984) noch sehr einheitlich dargestellten, großflächigen Glimmerschieferareale verschiedenen Decken und Komplexen angehören, oder dass es am Südrand der Niederen Tauern bedeutende Störungszonen gibt (Eder & Neubauer, 2000). Außerdem bedurften die quartären Ablagerungen und Formen dringend einer Bearbeitung. Aus diesen Gründen fanden ab dem Jahr 2004 geologische Kartierungen im Maßstab 1:10.000 entlang des Südrandes der Niederen Tauern statt. 2016 wurde das Kartierungsprojekt ruhend gestellt, beziehungsweise abgeschlossen. Die bis dahin erzielten Ergebnisse konnten bisher nur bruchstückhaft veröffentlicht werden (Kollmann & Schuster, 2014; Schuster, 2014).

Der vorliegende Artikel fasst die Ergebnisse dieses Kartierungsprojektes zusammen, soweit sie die neogenen Sedimente des Oberwölz-Beckens und dessen unmittelbaren Untergrund betreffen. Er enthält Beschreibungen des Beckenuntergrundes, des stratigrafischen Aufbaus der Beckensedimente und der darin auftretenden Lithologien sowie einzelne Dünnschliffbeschreibungen dazu. Des Weiteren sind Hinweise auf die Struktur des Beckens und eine geologische Karte (Abb. 1) enthalten. Der Kartenausschnitt liegt auf dem Kartenblatt ÖK 159 Murau bzw. auf den UTM-Kartenblättern NL 33-02-19 Oberwölz und NL 33-02-25 Murau.

Eine erste Aufnahme des Oberwölz-Beckens ist in der Karte GÖK 158-159 Stadl-Murau (Thurner, 1958) festgehalten. Die Neukartierung ergab eine etwas andere räumliche Verbreitung sowie eine Differenzierung verschiedener Lithologien innerhalb der erhaltenen Reste des ehemaligen Ablagerungsraumes.

Stratigrafie und Gesteinsbeschreibungen

Das Oberwölz-Becken zeigt in Ost–West-Richtung eine Verbreitung von mindestens 8 km, von Oberwölz im Osten bis in die Vordere Pöllau im Westen. In der Vorderen Pöllau verschwinden die neogenen Sedimente unter quartären Moränenablagerungen, sodass die Erstreckung des Beckens gegen Westen schwer abzuschätzen ist. Die Nord–Süd-Erstreckung erreicht bis zu 2 km.

Im Folgenden wird zunächst der unmittelbare Untergrund und danach die stratigrafische Abfolge in den neogenen Sedimenten sowie die einzelnen auftretenden Lithologien beschrieben.

Untergrund

Die neogenen Sedimente transgredieren größtenteils über karbonatische Gesteine der Murau-Decke (von Gosen et al., 1985). Unter diesen folgen Glimmerschiefer der Murau-Decke und in tektonischem Kontakt verschiedene kristalline Gesteine, die hier unter dem Ausdruck „Basale Glimmerschiefer-Decken“ (Iglseder, 2019) zusammengefasst werden. Alle diese Einheiten werden dem Drauzug-Gurktal-Deckensystem (Schmid et al., 2004) zugerechnet.

„Basale Glimmerschiefer-Decken“

Bei den im bearbeiteten Gebiet auftretenden Gesteinen der „Basalen Glimmerschiefer-Decken“ handelt es sich um Granat-Glimmerschiefer mit Einschaltungen von Marmoren, Quarziten und Grünschiefern bzw. Hornblendeschiefern. Diese Gesteine wurden von Maierhofer & Egger (2015) petrologisch untersucht und als Buchen-Komplex beschrieben. Die Gesteine des Buchen-Komplexes zeigen eine einphasige Metamorphoseentwicklung, die während des eoalpidischen Ereignisses in der Kreide stattfand und Bedingungen der Epidot-Amphibolitfazies erreichte.

Die Granat-Glimmerschiefer sind oft quarzitisch und brechen meist plattig. Sie sind fast immer hell, silberig bis grünlich gefärbt. Bis zu 4 mm großer Granat ist manchmal idiomorph ausgebildet. Die Marmore sind typischerweise im dm- bis cm-Bereich gebankt, grau bis dunkelgrau gefärbt und zum Teil gebändert. Bereichsweise sind Zwischenlagen aus zumeist dunkelgrauen, grafitischen Glimmerschiefern vorhanden. Seltener finden sich weiße bis blass rosa gefärbte, etwas grobkörnigere (0,5–2 mm) Kalkmarmore. In diesen sind 0,5 mm große Hellglimmer- und Chloritblättchen zu erkennen. Weiters sind hellgraue, feinkörnige Dolomitmarmore, die eine gelbliche Verwitterungsfarbe zeigen, vorhanden. Die Quarzite sind hellgrau bis gelblich, feinkörnig und im cm-Bereich gebankt. Ein variables Erscheinungsbild zeigen die Metabasite. Es reicht von chloritreichen Grünschiefern bis zu Hellglimmer führenden Hornblendeschiefern, die bis zu 5 mm großen Granat und 1,5 cm lange Amphibolkristalle enthalten. Immer wieder ist auch Biotit und Plagioklas makroskopisch erkennbar. Die Gesteine des Buchen-Komplexes bauen den Buchen (1.350 m) und Kirchberg (1.230 m) nördlich des Wölzer Bach-Tales auf.

Murau-Decke

Die Murau-Decke besteht aus einem liegenden Teil, der sich aus Glimmerschiefern mit darin eingeschalteten Marmorlagen aufbaut und einem hangenden, von karbonatischen Gesteinen dominierten Anteil. Basierend auf dem Mineralbestand und den Strukturen erfuhren diese Gesteine eine eoalpidische (kretazische) Metamorphose, welche zumindest grünschieferfazielle Bedingungen (> 400° C) erreichte. Die Einheit zeigt eine intensive spröde Deformation, welche insbesondere in den Dolomiten weit verbreitet zur Bildung von tektonischen Brekzien geführt hat.

Die Granat-Glimmerschiefer sind recht homogen, dunkelgrau gefärbt und manchmal etwas karbonatisch. Die Schieferungsflächen sind, bedingt durch eine Krenulation, zumeist fein wellig. Bei der Verwitterung zerfallen die Gesteine feinstückig, wobei sie bevorzugt nach den Schieferungsflächen aufblättern. Auf den Verwitterungsoberflächen sind oft dickere, rostrote Eisenoxid/-hydroxid-Beläge vorhanden. Granat misst bis zu 3 mm, selten auch 5 mm im Durchmesser. Er ist meist xenomorph, in einzelnen Lagen aber auch idiomorph entwickelt. Die eingeschalteten kalzitischen Marmore sind grau bis dunkel(blau)grau, selten auch weiß gefärbt, zum Teil gebändert und meist im cm-Bereich gebankt. Bedingt durch eine engständige Klüftung zerfallen sie feinstückig. Der liegende Anteil der Murau-Decke ist auf dem Bergzug südlich des Wölzer Bach-Tales weit verbreitet.

Der hangende Anteil umfasst Kalkschiefer, Kalkmarmore und Dolomite. Die Kalkschiefer sind grau gefärbt, zeigen einen dünnen Lagenbau mit einzelnen Lagen aus gelblich verwitternden, unreinen Marmoren. Zumeist zeigen sie eine isoklinale Verfaltung, die von einer offenen, welligen Faltung überprägt wird. Die grauen, häufig gebänderten Kalkmarmore entsprechen dem „Grebenzen-“ bzw. „Murauer Kalk“ und die hellgrau anwitternden Dolomite bzw. Dolomitmarmore dem „Oberwölzer Dolomit“ aus Flügel & Neubauer (1984). Die karbonatischen Gesteine bauen große Teile des Kirchberges (1.481 m), des Gastrumer Ofens (1.199 m) und des Ofens (1.256 m) auf der Nordseite des Wölzer Bach-Tales auf.

Neogene Sedimente des Oberwölz-Beckens

Innerhalb der neogenen Ablagerungen lässt sich folgende prinzipielle Stratigrafie erkennen. Mehr oder weniger gut aufgeschlossene Transgressionskontakte der neogenen Sedimente auf die Gesteine des Drauzug-Gurktal-Deckensystems befinden sich bei Oberwölz, südöstlich der Burg Rothenfels und südöstlich der St. Pankraziuskirche sowie bei Winklern, südlich von Moar im Lercher. Bei den basalen Ablagerungen handelt es sich um Brekzien aus Karbonatmaterial der unmittelbar angrenzenden Murau-Decke. Diese sind nicht immer eindeutig vom Untergrund abzutrennen, wenn dieser tektonisch brekziert ist. Darüber folgen Konglomerate und Brekzien aus Karbonatkomponenten mit karbonatischer Matrix, die häufig rötlich gefärbt ist. Der hangende Teil besteht aus Brekzien und Konglomeraten, die sich aus grauen Marmoren und dunkelgrauen Granat-Glimmerschiefern zusammensetzen. Innerhalb dieser drei Gesteinseinheiten lassen sich lokal weitere Lithologien differenzieren, welche im Folgenden ebenfalls beschrieben werden.

Basale Brekzie: Bei den basalen Ablagerungen handelt es sich um monomikte Karbonatbrekzien, die aus dem direkt unterlagernden Material bestehen. Bei den Karbonaten handelt es sich zumeist um hellgrau anwitternde Dolomite. Die Brekzie zeigt keine oder nur andeutungsweise eine Schichtung, sie ist schlecht sortiert, matrixarm und daher korngestützt. Die Komponenten sind eckig, zumeist bis zu 10 cm im Durchmesser, einzelne Stücke erreichen aber Blockgröße. Obzwar nirgendwo ein über weite Strecken zusammenhängendes Profil vorhanden ist, lässt sich die Mächtigkeit der basalen Brekzie mit einigen Metern bis etwas über 10 m angeben.

Südlich vom Moar im Lercher ist die basale Brekzie über einige 10er Meter über brekziierten Dolomiten anzutreffen. Der Untergrund zeigt über größere Bereiche zusammenhängende Schichtflächen, die etwas verfaltet sind, aber ein generelles Einfallen gegen Osten zeigen. Direkt über der Transgressionsfläche ist die basale Brekzie lokal stärker herausgewittert und es finden sich einige Höhlungen von denen die tiefsten etwa 1,5 m weit in den Fels reichen (Aufschluss RS-11-159-610, Abb. 2A).

Karbonat-Konglomerat: Gegen das Hangende gehen die basalen Brekzien in Konglomerate und untergeordnete Brekzien mit höherem Matrixgehalt über. Diese zeigen mehr oder weniger deutlich eine sedimentäre Schichtung, welche sich durch das Vorherrschen unterschiedlich großer Komponenten und eine Ausrichtung der plattigen Komponenten manifestiert. So entsteht manchmal auch eine undeutliche Bankung, wobei die einzelnen Lagen einige Dezimeter bis etliche Meter mächtig werden können. Schon aus der Entfernung ist diese Bankung an den Felsen unterhalb der Burg Rothenfels zu erkennen (Abb. 2B). Die Konglomerate sind sehr schlecht sortiert, die größten Komponenten sind zumeist 25 cm bis 40 cm im Durchmesser, einzelne können aber auch bis zu 1,5 m erreichen. Oft sind sie gerundet oder gut gerundet. Im Komponentenspektrum finden sich graue Dolomite, dunkelgraue Bänderkalkmarmore und unreine, gelblich anwitternde Marmore mit wenige Zentimeter großen Flatschen aus silbergrauem Phyllit bzw. Kalkschiefer. Nur sehr selten ist an einigen Stellen ein Glimmerschiefer- oder Gneisgeröll zu beobachten. Die karbonatische Matrix ist grau bis gelblich oder bei einem größeren Tongehalt rötlich gefärbt. Sie ist in unterschiedlicher Menge vorhanden, wobei die Konglomerate zumeist korngestützt sind. Manchmal ist die rötliche Matrix an den Bankflächen angereichert. Die in diesem Bereich eingebetteten Komponenten zeigen keine Anzeichen einer scherenden Deformation und demnach handelt es sich bei den rötlichen Lagen nicht um Scherzonen.

Innerhalb der Konglomerate finden sich an einigen Stellen Bänke von Brekzien, welche einerseits eine bessere Sortierung mit Korngrößen bis zu 10 cm und andererseits eine durch einen höheren Matrixgehalt bedingte stärkere Rotfärbung zeigen. Als Komponenten finden sich dunkelgraue Marmore und rot gefärbte Karbonate (Aufschluss RS-11-159-612, Abb. 2C, 2D), Diese verwittern leichter als die stärker karbonatisch zementierten Konglomerate. An mehreren Stellen unterlagern die Brekzien mächtig Konglomeratbänke, wodurch zum Teil leicht überhängende Felsbauten entstehen. Derartige Felsbauten ziehen, gut von Oberwölz aus sichtbar, südöstlich der St. Pankraziuskirche den Hang hinauf, sie sind aber auch auf einer Felsnase südlich vom Moar im Lercher (Aufschluss RS-11-159-613)

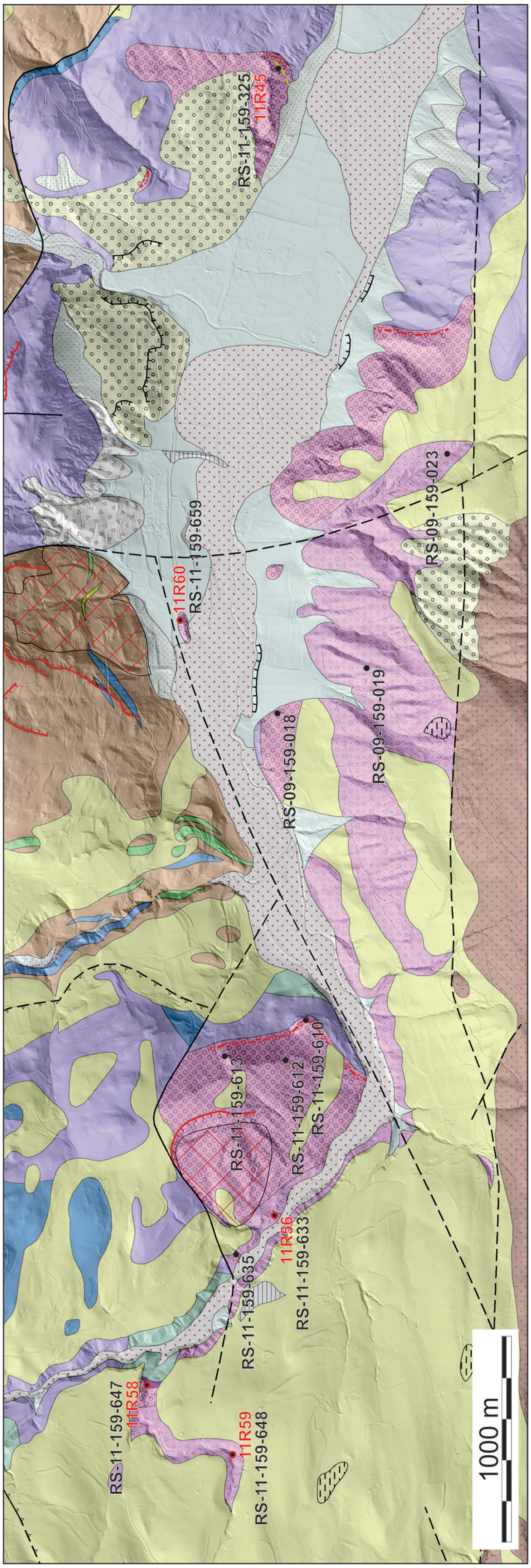
RS-11-159-325
11R45
RS-11-159-659
11R60
RS-09-159-023
RS-09-159-018
RS-09-159-019
RS-11-159-613
RS-11-159-612
RS-11-159-610
11R56
RS-11-159-633
RS-11-159-635
RS-11-159-647
11R58
11R59
RS-11-159-648
1000 m

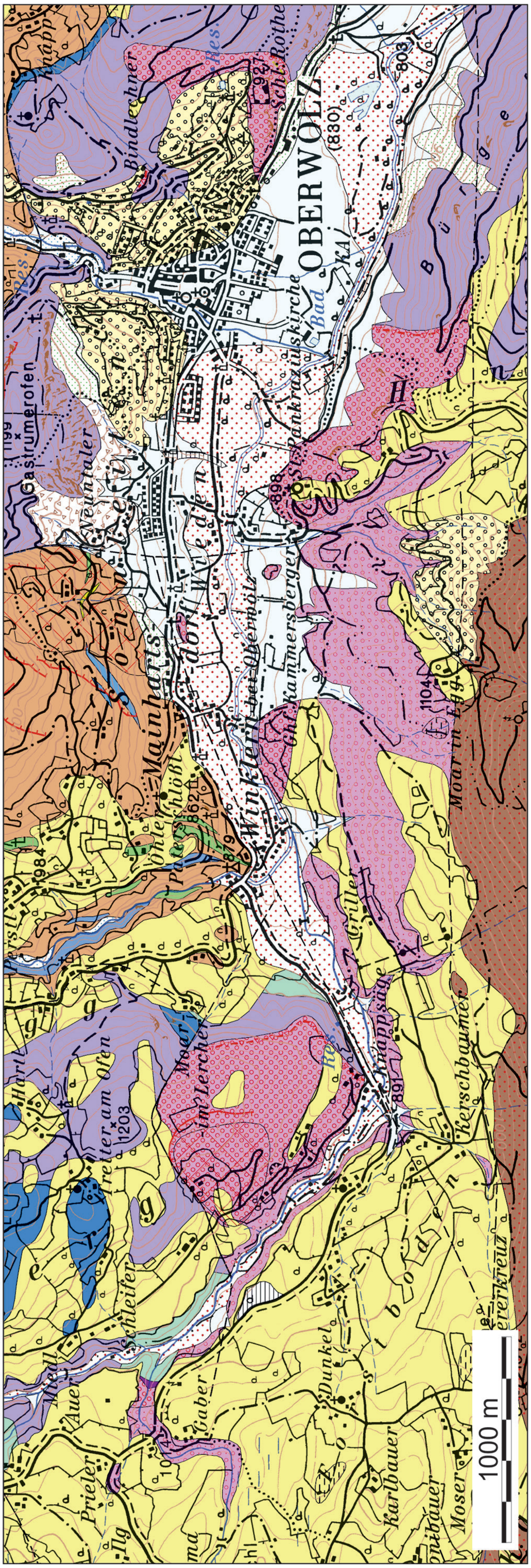
OBERWÖLZ
Kerschbaumer
Karlbauer
Moser
Dunkel
1000 m

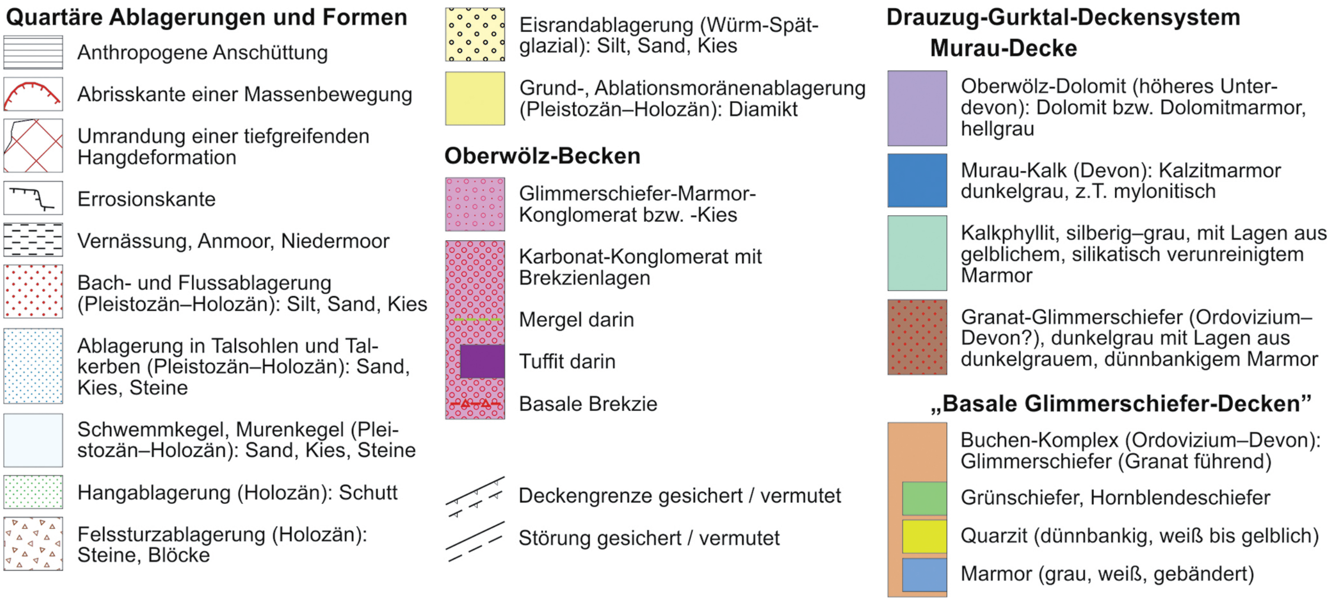

Abb. 1.
Geologische Karte des Oberwölz-Beckens und seiner unmittelbaren Umgebung in Kombination mit einer Reliefschummerung (oben) und der topografischen Karte 1:50.000 (unten). Eingetragen sind im Text erwähnte Aufschlüsse (schwarz) und untersuchte Dünnschliffe (rot).

entwickelt. Ein weiterer derartiger Aufschluss befindet sich im Bereich der Massenbewegung südwestlich vom Moar im Lercher (Abb. 2E).

Auch in schlecht aufgeschlossenen Bereichen lässt sich die Verbreitung der Karbonat-Konglomerate und ihre Abgrenzung gegenüber den unterlagernden Gesteinen der Murau-Decke gut durchführen, da die aus den Konglomeraten herauswitternden Karbonatgerölle sehr auffällig sind. Ein besonders gut erreichbarer Aufschluss befindet sich am Drumlin, der östlich von Mainhartsdorf als Kalvarienberg genutzt wird (Aufschluss RS-11-159-659). Die maximale Größe der Komponenten erreicht hier bis zu 70 cm und die Lage der Schichtung ist schlecht bestimmbar. Im Dünnschliff (Probe 11R60, Abb. 2F) sind verschiedene, gut gerundete Marmorkomponenten mit unterschiedlich starker Schieferung und unterschiedlichem Quarzgehalt zu sehen. Zwischen den größeren Komponenten finden sich vereinzelt kleinere Gerölle aus polykristallinem, metamorphem Quarz und aus Phyllit. Die nicht überall vorhandene Matrix enthält Quarzkörner und einzelne Hellglimmer. Ist keine Matrix vorhanden, sind die Zwickel mit verschiedenen Karbonatzementen verfüllt.

In den liegenden Anteilen der Karbonat-Konglomerate sind an zwei Stellen verschiedene feinkörnige Gesteine als einige Meter mächtige Lagen vorhanden. Südlich der Burg Rothenfels (Aufschluss RS-11-159-325) finden sich am „Sagenweg" im cm-Bereich gebankte, stückig brechende und auffällig gelb gefärbte **Mergelsteine** (Probe 11R45, Abb. 2G). Diese sind sehr feinkörnig und im Handstück intern nicht strukturiert. Im Dünnschliff erkennt man einen undeutlichen Lagenbau, der durch etwas höheren Quarzgehalt in dem ansonsten hauptsächlich aus Karbonat aufgebauten Gestein entsteht. Ansonsten sind nur einzelne opake Körner und braune Verfärbungen durch Eisenhydroxide zu erkennen. Die Korngröße liegt bei 10 bis 100 µm.

Im Graben, der aus dem unteren Eselsberggraben in die Vordere Pöllau zieht, sind bei Seehöhe 980 m (Aufschluss RS-11-159-647, Abb. 3A) ziegelrot gefärbte, feinkörnige Gesteine anzutreffen, die im Gelände als **Tuffite** angesprochen wurden. Die relativ weichen Gesteine sind strukturlos und brechen schalig. Sie enthalten lose verteilt verschiedene, bis zu 1 cm große Komponenten, die zum Teil als Gesteinsbruchstücke zu identifizieren sind. Als Einschaltungen und im Hangenden sind ockerfarbene Karbonat-Konglomerate vorhanden. Im Dünnschliff (Probe 11R58, Abb. 3B) sind in einer sehr feinkörnigen, völlig von rotem Hämatit durchtränkten Matrix eckige Komponenten aus Quarz, einzelne größere Hellglimmer und lithische Fragmente zu erkennen. Letztere umfassen polykristalline, metamorphe Quarzaggregate, sehr feinkörnige Karbonatgesteine und Phyllite.

Glimmerschiefer-Marmor-Konglomerat bzw. -Kies: Die überlagernden Glimmerschiefer-Marmor-Konglomerate entwickeln sich aus den Karbonat-Konglomeraten. Bei einer stetigen Zunahme von Geröllen aus dem liegenden Anteil der Murau-Decke nehmen die Komponenten aus dem Hangenden zusehends ab, bis sie nahezu völlig verschwunden sind. Als Komponenten lassen sich nun dunkelgraue Granat-Glimmerschiefer und Marmore identifizieren (Aufschluss RS-09-159-19, Abb. 3C). Die Marmore sind grau, selten auch weiß und zeigen auffällige, gelbliche Verwitterungsoberflächen. Häufig sieht man auch lagig aufgebaute Marmortypen, die eine in den einzelnen Lagen unterschiedlich starke Anwitterung zeigen.

Die Konglomerate weisen einen sedimentären Lagenbau auf, der durch unterschiedliche Korngrößen und eine Einregelung der plattigen Komponenten nachgezeichnet wird. Sie sind sehr schlecht sortiert und die Größe der Komponenten erreicht bis zu 50 cm im Durchmesser. Der Matrixanteil ist schwankend, sodass sowohl matrix-, als auch korngestützte Lagen vorhanden sind. Bei höherem Anteil an Karbonat ist die Matrix gelblich und gut zementiert, während sie bei hohem Glimmerschieferanteil in grobe Sande übergeht. In diesem Fall fehlt die Zementation und es handelt sich um Kiese. Bisweilen finden sich auch einige Zentimeter bis wenige Dezimeter mächtige Lagen aus Grobsandsteinen und aus sandigen, roten

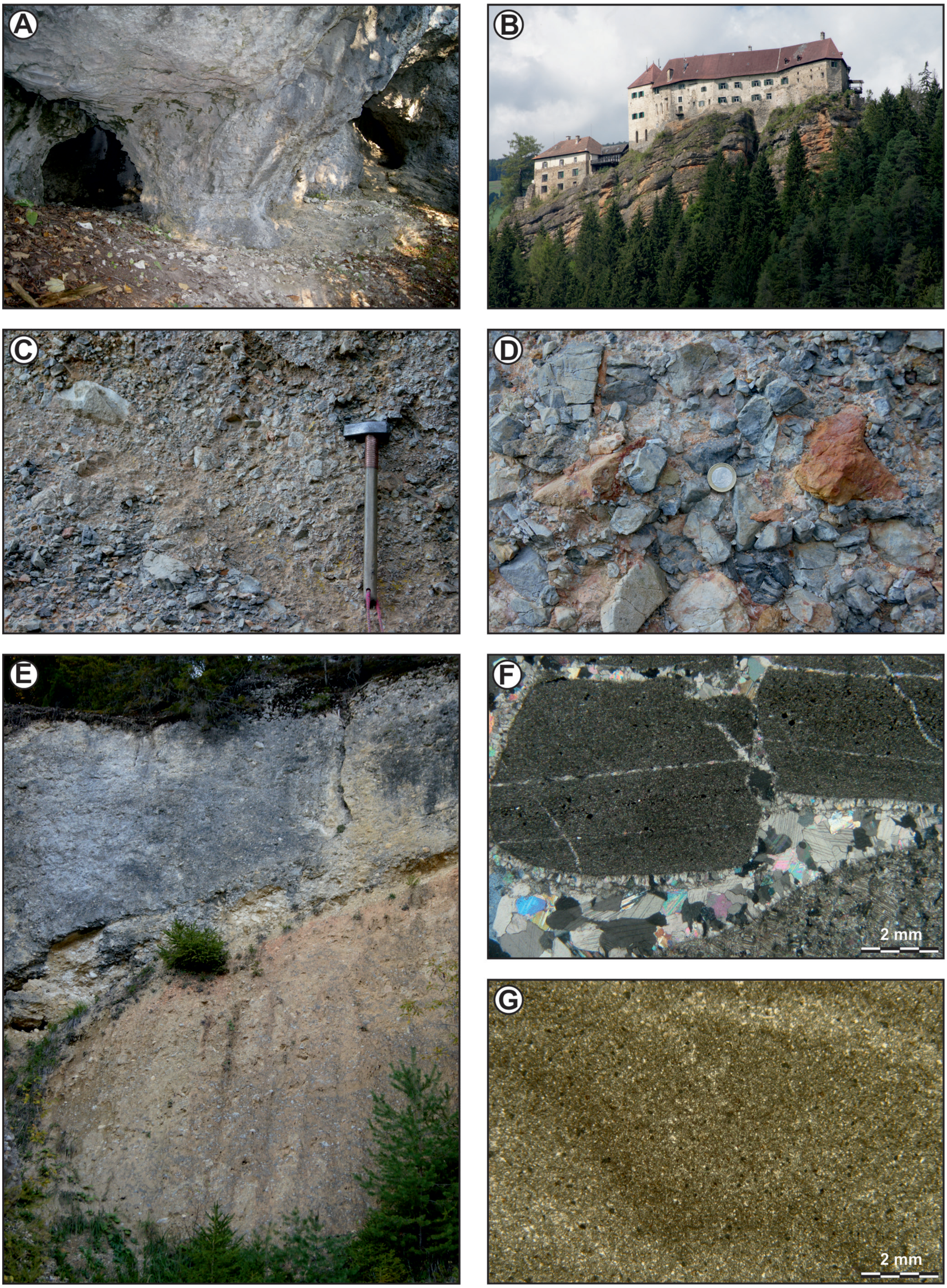

Abb. 2.
A) Basale Brekzie mit Höhlen nördlich der Knappsäge (Aufschluss RS-11-159-610). B) Burg Rothenfels auf rot gefärbtem, gebanktem Karbonat-Konglomerat. C) Brekzienlage in den Karbonat-Konglomeraten mit Komponenten aus dunkelgrauem Marmor und rot gefärbtem Karbonat (Aufschluss RS-11-159-612). D) Brekzienlage aus Karbonat-Konglomerat im Detail (Aufschluss RS-11-159-612). E) Karbonat-Konglomerat über Brekzie südlich-westlich vom Moar im Lercher. F) Dünnschliffbild eines Karbonat-Konglomerats mit Kalzitzementen zwischen den Komponenten (Probe 11R60). G) Dünnschliffbild eines feinkörnigen Mergelsteins mit sedimentärer Internstruktur (Probe 11R45). Lokalitäten der Aufschlüsse in Abbildung 1.

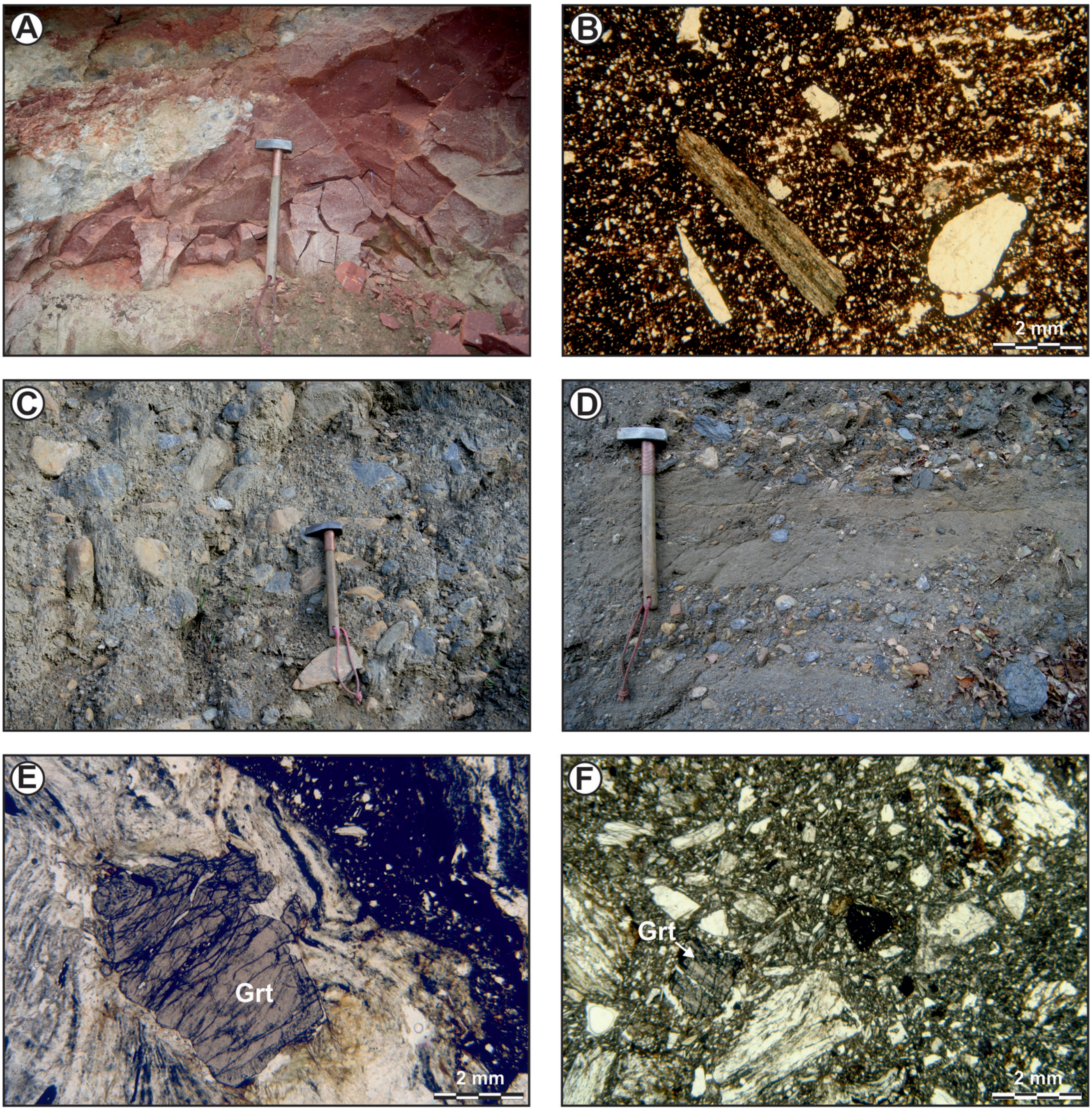

Abb. 3.
A) Roter Tuffit aus dem liegenden Anteil der Karbonat-Konglomerate (Aufschluss RS-11-159-647). B) Dünnschliffbild eines roten Tuffites mit lithischen Fragmenten von polykristallinem, metamorphem Quarz und Phyllit (Probe 11R58). C) Wenig verfestigtes Glimmerschiefer-Marmor-Konglomerat mit dunkelgrauen Glimmerschiefer- und gelblich anwitternden Karbonatkomponenten (Aufschluss 09-159-19). D) Glimmerschiefer-Marmor-Kies mit sandigen Lagen (Aufschluss RS-11-159-635). E) Dünnschliffbild eines Glimmerschiefer-Marmor-Konglomerats mit zweiphasig gewachsenem Granat in einer Glimmerschiefer-Komponente (Probe 11R59). F) Dünnschliffbild der Matrix eines Glimmerschiefer-Marmor-Konglomerats mit eckigen Komponenten aus lithischen Fragmenten, Quarz und Granat (Probe 11R56). Lokalitäten der Aufschlüsse in Abbildung 1.

Tonen (Aufschluss RS-11-159-635, Abb. 3D). Aufschlüsse aus Gesteinstypen mit sandiger Matrix neigen dazu, zu verrutschen. Im Dünnschliff sieht man in den Glimmerschiefer-Marmor-Konglomeraten Komponenten aus verschiedenen Glimmerschiefern, Phylliten, karbonatischen Glimmerschiefern und silikatisch verunreinigten Marmoren. Besonders hervorzuheben sind grafitische Glimmerschiefer mit bis zu 4 mm großem, zweiphasigem Granat (Aufschluss RS-11-159-648, Probe 11R59, Abb. 3E). Die sandige Matrix zeigt eckige Komponenten aus verschiedenen Gesteinsbruchstücken, Quarz, Granat, Glimmer und einzelne opake Körner (Aufschluss RS-11-159-633, Probe 11R56, Abb. 3F).

Verbreitung

Im Allgemeinen muss festhalten werden, dass die Verbreitung der neogenen Gesteine um Oberwölz in der Karte von Thurner (1958) sehr gut dargestellt ist. Im genauen Vergleich ergeben sich aber Abweichungen zur hier vorliegenden Kartierung, die im Folgenden erläutert werden.

Eine gute Übereinstimmung der Flächen ist im Norden am Kirchberg, am Ofen und im Bereich des unteren Eselsberggrabens gegeben. Auch der aus Karbonat-Konglomerat bestehende Drumlin östlich von Mainhartsdorf ist übereinstimmend dargestellt. Die in der Karte von Thurner (1958) ausgeschiedenen, kleinen Vorkommen von neogenen Sedimenten südöstlich der Burg Rothenfels, jenes östlich des Gipfels am Ofen und das bei der Hubertuskapelle nördlich vom Ofen wurden in der hier vorliegenden Bearbeitung als tektonisch brekziierte Karbonate der Murau-Decke interpretiert. Dafür wurde auf der Südseite des Wölzer Bach-Tales zwischen Knappsäge und Oberwölz und im Bereich der Vorderen Pöllau die Verbreitung der neogenen Gesteine erweitert. Diese Gebiete werden von den Glimmerschiefer-Marmor-Konglomeraten aufgebaut, welche bei schlechter Aufschlusssituation und in Verbindung mit quartären Ablagerungen oft nur schwer zu identifizieren sind. Auf der Südseite des Wölzer Bach-Tales sind die Glimmerschiefer-Marmor-Konglomerate nicht wie in der Karte von Thurner (1958) nur bis unter 1.000 m, sondern durchwegs bis knapp unterhalb 1.100 m Seehöhe zu finden. Sie waren zur Zeit der Kartierung in Gräben und an neuen Forststraßen sehr gut aufgeschlossen. In der Vorderen Pöllau bilden sie an der Straße beim Prieler einen markanten Aufschluss und sie sind im Graben südlich davon bis 1.050 m Seehöhe zu verfolgen. Es ist auch anzunehmen, dass sich diese Konglomerate unter den Grundmoränenablagerungen noch weiter gegen Westen erstrecken.

Struktur

Die sedimentäre Schichtung (ss) bzw. die Bankung der basalen Brekzie und der überlagernden Konglomerate fällt im Bereich um Oberwölz sowohl auf der Nordseite bei der Burg Rothenfels, als auch auf der Südseite oberhalb der St. Pankraziuskirche mittelsteil gegen Nordnordwest bis West (ss 342/40, Ss 332/31 bzw. ss 335/16, Ss 301/14, ss 268/51) und in den Aufschlüssen im Tal zwischen Mainhardsdorf und Winklern mittelsteil gegen Westen (ss 268/30) ein. Südlich vom Moar im Lercher ist ein Einfallen gegen Südsüdwest (ss 210/37, ss 200/34) zu verzeichnen. Im unteren Teil des Eselsberggrabens fallen die Schichtflächen mittelsteil gegen Südsüdwesten bis Westen (ss 200/20, ss 273/56) ein.

In den Aufschlüssen im Tal östlich von Winklern (Aufschluss RS-09-159-18) sind in großem Winkel auf die Bankung einzelne, mit Kalzit verfüllte Extensionsklüfte zu beobachten. In Hohlräumen sind bis zu 1 cm große, blättrige Kalzitkristalle vorhanden. Diese Kristalle sprechen dafür, dass die Klüfte bei erhöhten Temperaturen (hydrothermal) verfüllt wurden. Aussagen über die erreichte Temperatur können aber nicht getroffen werden.

In den Glimmerschiefer-Marmor-Konglomeraten sind südlich von Winklern beim Moar im Egg einige Störungszonen vorhanden. Eine der beobachteten Störungen (Aufschluss RS-09-159-23) fällt steil gegen Nordnordost (030/83), wobei die Gerölle in der Störung zerbrochen sind. Eine weitere etwa 1 m breite und aus ockerfarbigem Ton mit Gesteinsbruchstücken bestehende Störungszone (Aufschluss RS-09-159-19) fällt mittelsteil gegen Nordwesten (331/59) ein.

Eine sehr markante Störung ist im südlichen Teil des Tretter am Ofen zu kartieren. An dieser mittelsteil gegen Süden einfallenden Störung wurde die südliche Scholle, bestehend aus Gesteinen der Murau-Decke mit auflagerndem Neogen, mehr als 100 m gegenüber der nördlich gelegenen Scholle, welche aus der gleichen Abfolge besteht, abgesenkt. Obwohl die Störungsfläche nirgendwo aufgeschlossen ist, muss es sich, basierend auf der Verteilung der Lithologien, um eine Abschiebung handeln. Da sich keine Beeinflussung der südgerichteten Abschiebung auf die Sedimentation und damit auf die Verteilung der Lithotypen in den neogenen Sedimenten erkennen lässt, kann angenommen werden, dass es sich um eine postsedimentäre Bewegungszone handelt. Bedingt durch die Abschiebung und ein hangparalleles Einfallen der sedimentären Schichtung sind die neogenen Sedimente am Südwesthang vom Tretter am Ofen von einer Massenbewegung betroffen. Auf etwa 1.060 m Seehöhe verläuft die Abrisskante und darunter ist in 1.030 m Seehöhe eine bis über 20 m tiefe, langgestreckte Senke entwickelt. Die Senke wird unterirdisch entwässert. Der darunterliegende Hang ist stark strukturiert.

Entlang der südlichen Begrenzung der neogenen Sedimente konnte bisher kein direkter Kontakt zu den Glimmerschiefern der Murau-Decke beobachtet werden. Aus morphologischen Gründen scheint hier eher ein tektonischer als ein transgressiver Kontakt der Beckensedimente zu den Gesteinen der Murau-Decke vorzuliegen. In der Karte (Abb. 1) wurde eine steilstehende Störung eingezeichnet.

Zusammenfassung, Interpretation und Ausblick

Auch wenn in diesem Beitrag neue Erkenntnisse zur Geologie des neogenen Oberwölz-Beckens präsentiert werden können, sind durch die Einstellung des Kartierungsprojektes noch zahlreiche Fragen offengeblieben. In diesem Kapitel werden daher zunächst die bisherigen Ergebnisse zusammengefasst und interpretiert, danach werden offene Fragen angesprochen und ein Ausblick auf wünschenswerte weitere Untersuchungen gegeben.

Zusammenfassung der Ergebnisse

Fasst man die sedimentologischen und strukturellen Daten des Oberwölz-Beckens zusammen, so ergibt sich folgendes Bild:

- Alle gemessenen, sedimentären Schichtflächen fallen etwa gegen Westen (NNW–SSW) ein.
- Die basalen Brekzien und die überlagernden Karbonat-Konglomerate enthalten so gut wie ausschließlich Material aus dem im Norden bzw. Osten anstehenden hangenden Anteil der Murau-Decke, während die überlagernden Glimmerschiefer-Marmor-Konglomerate ihr Material vornehmlich aus dem im Süden anstehenden, hangenden Anteil der Murau-Decke beziehen.
- Die gemessenen und aus dem Kartenbild bestimmten Störungen streichen mehr oder weniger Ost–West, sie fallen im nördlichen Verbreitungsgebiet der neogenen Sedimente mittelsteil gegen Süden ein, während der Südrand wahrscheinlich durch eine steilstehende Störung gebildet wird.

Interpretation

Auch wenn es keine Altersinformationen aus den Sedimenten des Oberwölz-Beckens gibt, kann man davon ausgehen, dass es sich im Zuge der lateralen Extrusion der Ostalpen (Ratschbacher, 1986) im frühen Miozän (20–15 Ma) entwickelt hat. Es gehört zu den Norischen Becken, die sich vom Tamsweg-Becken über das Becken von Schöder, das Fohnsdorf-, Leoben-, und Trofaiach-Becken bis in das Mürztal verfolgen lassen.

Basierend auf den vorhandenen Daten lässt sich die Entwicklung des Oberwölz-Beckens wie folgt skizzieren. Im frühen Miozän (Karpatium) muss die Landschaft um das heutige Oberwölz deutlich anders ausgesehen haben als heute. Der heute die Landschaft bestimmende Kamm der Niederen Tauern, welcher durch kreidezeitlich amphibolitfazielle Gesteine aufgebaut ist, war noch nicht vorhanden, da derartige kristalline Gesteine im Geröllspektrum der Beckensedimente völlig fehlen und damit im Hinterland nicht vorhanden waren. Eine weitaus größere Verbreitung hatten hingegen die grünschieferfaziell metamorphen paläozoischen Karbonatgesteine und Glimmerschiefer der Murau-Decke. Im Zuge der Ausbildung des miozänen Störungssystems entstand ab etwa 17 Ma im Bereich des heutigen Oberwölz ein Becken. Wahrscheinlich bildete sich zunächst ein Halbgraben an einer steil gegen Norden einfallenden Störung, die heute die Südbegrenzung der Beckensedimente bildet. Wegen des dadurch geschaffenen Reliefs kam es zur Abtragung der in der unmittelbaren Umgebung anstehenden Karbonate der Murau-Decke. In weiterer Folge kam es zur Freilegung und Erosion der darunterliegenden Glimmerschiefer mit den darin eingeschalteten Marmorlagen. Nach Beendigung der Sedimentation erfolgte die Hauptphase der Bewegungen an den gegen Süden einfallenden Abschiebungen am Südrand der Niederen Tauern. Dadurch kam es einerseits zur Exhumation der tektonisch tieferen, kreidezeitlich metamorphen Kristallineinheiten, welche den Hauptkamm der Niederen Tauern bilden und andererseits zur Einsenkung des Neogenbeckens. Weiter bildeten sich Nord–Süd streichende Störungen und einzelne Blöcke wurden möglicherweise etwas gegen Westen verkippt.

Offene Fragen und Ausblick

Die vorliegenden Ausführungen entstanden im Zuge der geologischen Landesaufnahme. Dabei wurde das Augenmerk auf die Verbreitung der Lithologien und auf die mit dem Becken in Zusammenhang stehenden Strukturelemente gelegt. Durch die Ruhendstellung der Arbeiten sind jedoch noch einige Fragen offen geblieben.

Bezüglich der Kartierung wäre es notwendig, die in der Karte (Abb. 1) als südliche Begrenzung der neogenen Sedimente postulierte Störung zu verifizieren. Das könnte im Bürgerwald oder bei Moar in Egg möglich sein. Betrachtet man die Morphologie nördlich von St. Peter am Kammersberg, so könnte auch in diesem Gebiet die postulierte Südrandstörung und nördlich davon neogene Sedimente unter den quartären Moränen- und Eisrandsedimenten aufgeschlossen sein. Bei weiter Bearbeitung dieser Fragen sollte in jedem Fall auf die Information aus den archivierten Aufschlusskartierungen im Maßstab 1:10.000 zurückgegriffen werden.

Sollte sich die Vermutung bestätigen, dass es sich bei den feinkörnigen Gesteinen im basalen Teil der Karbonat-Konglomerate um ehemalige Tuffe oder Tuffite handelt, könnte man durch die Datierung von Zirkon aus diesen Gesteinen eine genauere zeitliche Einstufung des Oberwölz-Beckens erhalten.

Gänzlich ausständig ist eine sedimentologische Bearbeitung der neogenen Gesteine. Die Aufschlusssituation scheint ausreichend, um deren Genese zu bearbeiten und die auftretenden Lithologien in lithostratigrafische Einheiten zu gliedern. Die bereits kartierten lithologischen Einheiten wären wahrscheinlich in zwei Formationen zu fassen. Für den liegenden Teil, bestehend aus der basalen Brekzie und den Karbonat-Konglomeraten, wären geeignete Typusprofile bei der Burg Rothenfels oder beim Moar im Lercher vorhanden. Eine geeignete Typlokalität für die hangenden Glimmerschiefer-Marmor-Konglomerate ist beim Moar in Egg gegeben.

Dank

Für die Durchsicht des Manuskripts und wertvolle Anregungen möchte sich der Autor bei Gerit Griesmeier, Hans-Georg Krenmayr, Christian Cermak und Christoph Janda bedanken.

Literatur

Braunstingl, R., Pestal, G., Hejl, E., Egger, H., van Husen, D., Linner, M., Mandl, G.W., Reitner, J.M., Rupp, C. & Schuster, R. (2005): Geologische Karte von Salzburg 1:200.000. – Geologische Bundesanstalt, Wien.

Eder, N. & Neubauer, F. (2000): On the edge of the extruding wedge: Neogene kinematics and geomorphology along the southern Niedere Tauern, Eastern Alps. – Eclogae Geologicae Helvetiae, **93**, 81–92, Basel.

Flügel, H.W. & Neubauer, F.R. (1984): Geologische Karte der Steiermark 1:200.000. – Geologische Bundesanstalt, Wien.

Iglseder, C. (2019): Geologische und tektonische Karte der Gurktaler Alpen 1:250.000. – In: Griesmeier, G.E.U. & Iglseder, C. (Red.): Arbeitstagung der Geologischen Bundesanstalt 2019, Geologie des Kartenblattes GK25 Radenthein-Ost, Murau, 24.–27. Juni 2019, 48–54, Geologische Bundesanstalt, Wien.

Kollmann, C. & Schuster, R. (2014): Bericht 2012–2013 über geologische Aufnahmen auf Blatt 158 Stadl an der Mur. – Jahrbuch der Geologischen Bundesanstalt, **154**/1–4, 308–310, Wien.

Krenmayr, H.-J., Pestal, G., Egger, H., van Husen, D., Linner, M., Mandl, G.W., Reitner, J.M., Rupp, C. & Schuster, R. (2006): Geologische Karte von Oberösterreich 1:200.000. – Geologische Bundesanstalt, Wien.

Maierhofer, K. & Egger, W. (2015): Petrologische Untersuchungen an Gesteinskomplexen im Liegenden der Murauer-Decke. – Bakkalaureatsarbeit, Karl-Franzens-Universität Graz, 143 S., Graz.

Ratschbacher, L. (1986): Kinematics of Austro-Alpine cover nappes: changing translation path due to transpression. – Tectonophysics, **125**, 335–356, Amsterdam.

Schmid, S.M., Fügenschuh, B., Kissling, E. & Schuster, R. (2004): Tectonic map and overall architecture of the Alpine orogen. – Eclogae Geologicae Helvetiae, **97**/1, 93–117, Basel.

Schuster, R. (2014): Bericht 2010 über geologische Aufnahmen auf Blatt 158 Stadl an der Mur. – Jahrbuch der Geologischen Bundesanstalt, **154**/1–4, 53–54, Wien.

Thurner, A. (1958): Erläuterungen zur geologischen Karte Stadl-Murau 1:50.000. – 106 S., Geologische Bundesanstalt, Wien.

von Gosen, W., Haiges, K.-H., Neubauer, F., Pistotnik, F. & Thiedig, F. (1985): Die tektonischen Baueinheiten am Nord- und Westrand der Gurktaler Decke (Österreich). – Jahrbuch der Geologischen Bundesanstalt, **127**/4, 693–699, Wien.

Eingelangt: 16. Dezember 2019, angenommen: 17. Dezember 2019

JAHRBUCH DER GEOLOGISCHEN BUNDESANSTALT
Jb. Geol. B.-A. | ISSN 0016–7800 | Band 159 | Heft 1–4 | S. 155–162 | Wien, Dezember 2019

Die Kartierung der Überschiebungsfront der Dachstein-Decke im Bereich des Nussensees (Oberösterreich/Salzburg) mittels hydrogeologischer Detailaufnahme

Hans Jörg Laimer*

5 Abbildungen, 1 Tabelle

Österreichische Karte 1:50.000
BMN / UTM
95 Sankt Wolfgang im Salzkammergut
96 Bad Ischl / NL 33-01-11 Bad Ischl

Nördliche Kalkalpen
Dachstein-Decke
Nussensee
Haselgebirge
Quellen

Inhalt

Zusammenfassung

Strukturgeologische Elemente wie Störungen und Deckengrenzen haben für die hydrogeologische Karteninterpretation große Bedeutung, da sie die Wasserwegigkeit des Gebirges maßgeblich beeinflussen. Für ein hydrogeologisches Projekt war es daher notwendig, den bislang nicht kartierten Verlauf der Überschiebung der Dachstein-Decke im Bereich des Nussensees (Katergebirge) zu lokalisieren. Es war anzunehmen, dass diese über weite Strecken von Haselgebirge begleitet wird. Aufgrund der schlechten Aufschlussverhältnisse wurde eine detaillierte Quellaufnahme durchgeführt, um über evaporitisch beeinflusste Quellen indirekte Hinweise auf Haselgebirge zu erhalten. Mit dieser Methode konnte der Verlauf der Deckengrenze sehr gut eingegrenzt werden. Sämtliche wichtige Quellen der Nordseite des Katergebirges sind an die Überschiebungsfront gebunden.

Mapping of the overthrust boundary of the Dachstein Nappe in the Lake Nussensee area (Upper Austria/Salzburg) by means of a detailed hydrogeological survey

Abstract

Structural geological features as faults and nappe boundaries play an important role in hydrogeological map interpretation since they have a significant influence on the hydraulic conductivity of a rock mass. Within the framework of a hydrogeological project, it was therefore necessary to localise the overthrust boundary of the Dachstein Nappe in the Lake Nussensee area (Katergebirge), whose course was unknown so far. It was assumed, that the boundary is accompanied by evaporites of the Haselgebirge Formation over long distances. Because of bad outcrop conditions, a detailed spring mapping was carried out in order to detect indirect indications of evaporites by tracking down evaporitic waters. With this approach, the course of the nappe boundary could be localised quite well. All the important springs in the northern Katergebirge are bound to the overthrust fault.

* Hans Jörg Laimer: Weinbach 15, 5360 St. Wolfgang im Salzkammergut. hans-joerg.laimer@oebb.at

Einleitung

Bei der Bearbeitung angewandt-hydrogeologischer Fragestellungen zählen geologische Detailkarten, wie sie im Rahmen der geologischen Landesaufnahme im Maßstab 1:25.000 und 1:50.000 erstellt werden, zu den wichtigsten Grundlagendaten. Neben der lithostratigrafischen Gliederung kommt vor allem strukturgeologischen Kartenelementen bei der hydrogeologischen Interpretation eine große Bedeutung zu, da neben Schichtgrenzen auch Störungen und Deckengrenzen häufig Austrittspunkte für Quellen darstellen. Im gegenständlichen Fall war es im Rahmen eines hydrogeologischen Vorprojekts zur Wiedernutzung einer Karstquelle im Katergebirge erforderlich, den bislang nicht kartierten Verlauf einer Deckengrenze mittels einer detaillierten Quellaufnahme zu lokalisieren, um diese als Austrittsursache zu verifizieren.

Die Quellkartierung wurde schließlich auf den gesamten Bereich mit unklarem Deckengrenzverlauf ausgedehnt, um mit diesem tektonischen Detail die geologische Karte ergänzen zu können. Auf das ursprüngliche Projektziel, die Erfassung der hydrogeologischen Verhältnisse der westlich des Nussensees entspringenden Tobiasquellen zur Ausweisung eines Wasserschutzgebietes, wird nicht weiter eingegangen.

Geologische Übersicht

Schichtfolge

Das Katergebirge erstreckt sich als nördlichster Teil der Dachstein-Decke auf die Blätter 95 Sankt Wolfgang im Salzkammergut (Plöchinger, 1982a) und 96 Bad Ischl (Schäffer, 1982) der geologischen Karte 1:50.000. Die Schichtfolge wird von triassischen Plattformsedimenten der Wetterstein- und Dachstein-Formation dominiert, denen am Nordabhang bunte Liaskalke, Megabrekzien der Tauglboden-Formation und Gesteine der Gosau-Gruppe auflagern. Das Auftreten von Brekzien mit oberjurassischen Komponenten am Nussensee haben bereits Leischner (1959) und Schäffer (1982) angedeutet, doch die großflächige Verbreitung wurde erst von Auer et al. (2006) dokumentiert. Eine flächendeckende Neukartierung steht noch aus. Die Gosau-Gruppe hat Wagreich (1998) bearbeitet und dabei starke fazielle Unterschiede zwischen der Fahrnberg-Gosau (Beckenrandsedimente) und der Nussensee-Gosau (Beckensedimente) festgestellt.

Tektonische Situation

Nach Mandl (2012) wurde die Dachstein-Decke in der Unterkreide der Hallstätter Zone von Ischl-Aussee aufgeschoben, wobei auch die von ihm neu definierten Ischl-Schollen der Hallstätter Zone (Abb. 1) abgeschert und zwischen Formationen der „Neoautochthonen Hülle“ und die Dachstein-Decke transportiert wurden. Aus Ha-

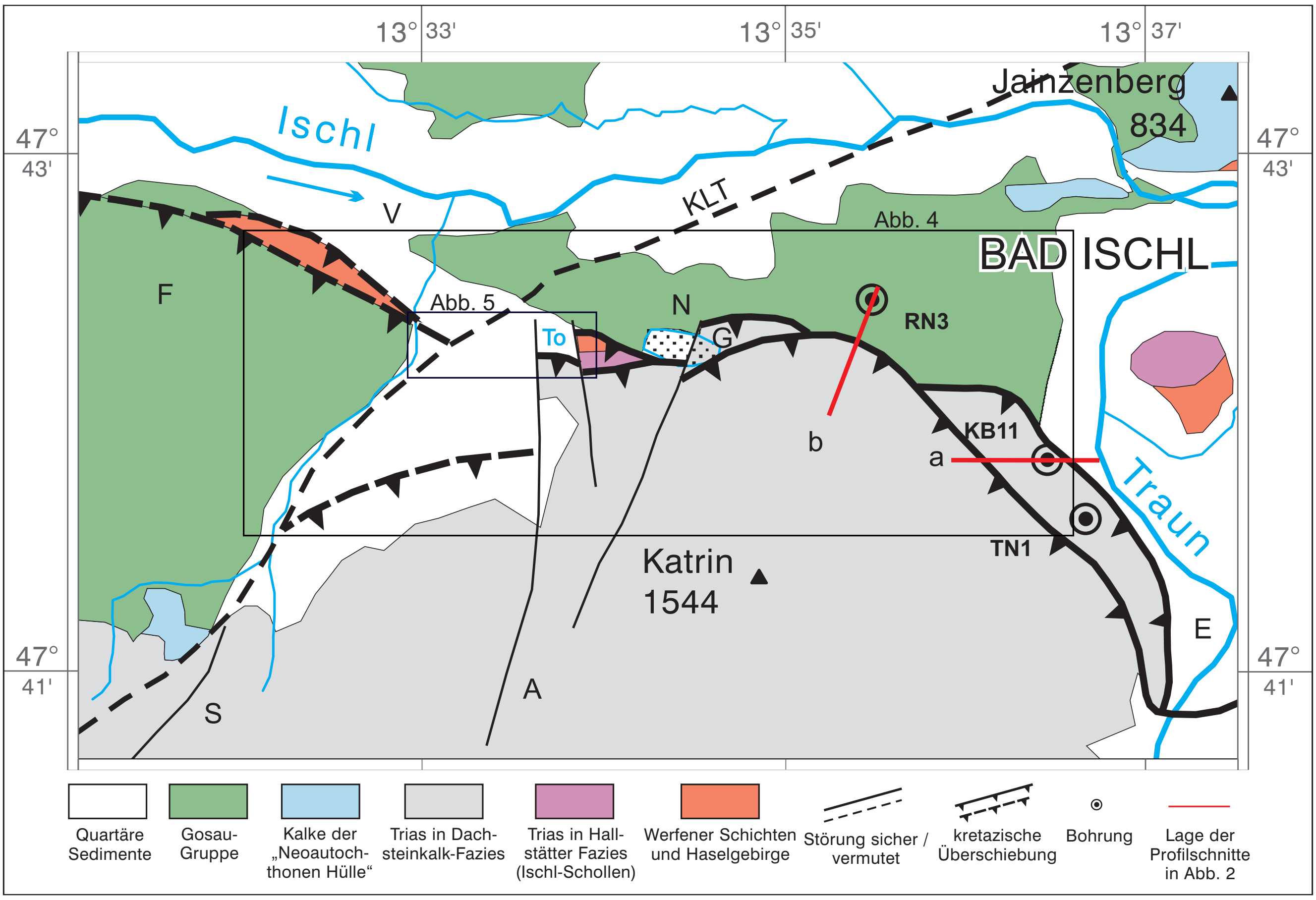

Abb. 1.
Tektonische Übersicht (verändert aus Mandl et al., 2012: Tafel 1). Abkürzungen: A = Ahornzwieselstörung, E = Engleithen, F = Fahrnberg, G = Gawanzerstein, KB11 = Bohrung in Kaltenbach, KLT = Königssee-Lammertal-Traunsee-Störung, N = Nussensee, RN 3 = Bohrung im Rabennest, S = Schöffaustörung, TN 1 = Bohrung am Römerweg, To = Tobiasquelle, V = Voglhub. Die Insert-Kästchen zeigen die Lage der Abbildungen 4 und 5 an.

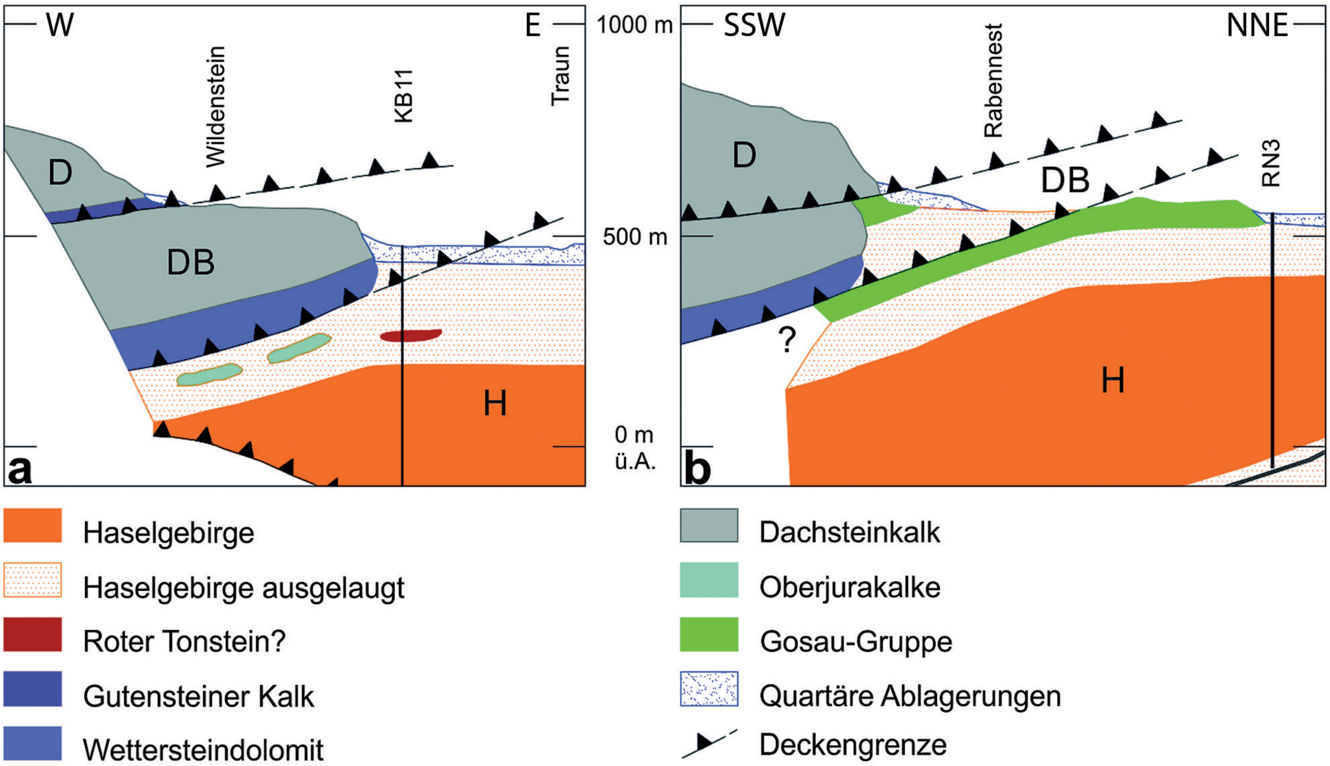

Abb. 2.
Geologische Profile durch die Stirn der Dachstein-Decke im Bereich des Trauntaler (a) und Ischltaler (b) Salzlagers (nach Mayr, 2003). Abkürzungen: D = Dachstein-Decke, DB = Basisschuppe der Dachstein-Decke, H = Hallstätter Zone.

selgebirgsaufschlüssen in Gräben am Nordfuß des Katergebirges schloss Schauberger (1979) auf dessen randliche Aufschiebung auf das Hallstätter Salinar. Bohrungen der Salinen Austria AG (Abb. 2) haben die Unterlagerung mit mächtigem Haselgebirge des Traun- und Ischltaler Salzlagers bestätigt (Mayr, 2003). Während der miozänen ostgerichteten lateralen Extrusion der Ostalpen kam es zur Reaktivierung der Überschiebungsfläche der Dachstein-Decke. Im Nordabschnitt des sinistralen Königssee-Lammertal-Traunsee-Blattverschiebungssystems (KLT-System) nehmen Decker et al. (1994) eine ursprünglich vom Lammertal zum Traunsee durchlaufende Störung an. Der Südteil der Traunsee-Störung wurde von der nördlichen Dachstein-Decke rund 3 km gegen Nordosten überschoben, wobei die Fahrnberg-Gosau auf die Nussensee-Gosau aufgeschoben wurde. Die Fahrnbergüberschiebung ist demnach im KLT-System die kinematische Verbindung von Rigaus- und Traunsee-Störung (Decker & Jarnik, 1992).

Plöchinger (1982a) hat auf Blatt 95 die Überschiebungsfront am Fuß des Fahrnberges vom Strobler Weißenbach bis zur Ortschaft Voglhub kartiert (Abb. 1). In diesem Bereich ist die Überschiebung der beiden Gosauvorkommen durch mehrere kleine Haselgebirgsaufschlüsse markiert, welche Mandl et al. (2017) den Ischl-Schollen zuordnen. Im östlich anschließenden 3 km langen Abschnitt zwischen Schöffaubach und Nussensee, in dem die Tobiasquelle liegt, ist die Deckengrenze nicht ausgewiesen, da quartäre Ablagerungen das Anstehende fast vollständig bedecken. Ihr ungefährer Verlauf ist lediglich auf geologischen Übersichtskarten dargestellt. Spengler (1912: Tafel I) sieht sie unmittelbar an die Südgrenze der aufgeschlossenen Nussensee-Gosau gebunden. Bei Wagreich (1998) liegt sie südlich des Nussensees, bei Mandl et al. (2012) verläuft sie durch den See und ist zwischen Ahornzwiesel-Störung und Schöffau-Störung etwa 600 bis 1.500 m nach Süden versetzt (Abb. 1), ehe sie weiter westlich von der Fahrnbergüberschiebung gebildet wird. Da östlich des Schöffaubaches bislang nur ein kleiner Aufschluss der Fahrnberg-Gosau in 700 m Seehöhe bekannt war, nahm Mandl (persönliche Mitteilung) deren Versatz entlang der NE–SW streichenden Schöffau-Störung an.

Schäffer (1982) hat die Deckengrenze auf Blatt 96 als vermutete Überschiebungsgrenze wieder durchgehend kartiert und dabei noch eine tektonisch isolierte Schuppe zwischen Engleithen und Kaltenbach ausgeschieden. Diese trägt als hangendstes Schichtglied Jurarotkalke und liegt nach Schäffer (1977) bis zur Ruine Wildenstein (südwestlich der Bohrung KB 11) auf Haselgebirge bzw. weiter im Westen auf Gosau-Formationen. Die Existenz dieser Basisschuppe wurde durch die Salinenbohrung TN 1 am Ischler Römerweg nachgewiesen, welche unter geringmächtigem, tektonisch stark beanspruchtem ? Gutensteiner Kalk (Mayr, persönliche Mitteilung) an der Basis der Dachstein-Decke Dachsteinkalk und Wettersteindolomit der Basisschuppe durchörterte, bis sie auf Gipstongebirge stieß. Wie weit diese Basisschuppe nach Westen reicht, ist nicht bekannt. Mayr (2003) rechnet ihr in seinem N–S-Schnitt durch das Ischltaler Salzlager (Abb. 2b) das Haselgebirgsvorkommen im Rabennest zu und vermutet hier auch Schürflinge der Hallstätter Zone. Als solch ein Schürfling ist die von Plöchinger (1982a) kartierte „Hallstätter Deckscholle“ am Nussensee interpretierbar, die von Haselgebirge begleitet wird. Mandl et al. (2012) ordnen den bunten Liaskalk des Gawanzersteins ebenfalls der Basisschuppe zu (Abb. 1). Analog dazu wird in Abbildung 5 die Liaskalkscholle, aus welcher die Tobiasquelle entspringt, als westlichster Ausläufer der Schuppe verstanden.

Hydrogeologische Situation

Die nordvergente Tektonik der Dachstein-Decke hat im Katergebirge zur Bildung einer Stirnfalte geführt, welche die Entwässerung maßgeblich beeinflusst. Am stark verkarsteten Plateau versickern die Niederschlagswässer in den steil nordfallenden gebankten Dachsteinkalk und treten größtenteils an der Nordseite wieder zu Tage. Die beiden wichtigsten gefassten Quellen sind dort an die Grenze der Basisschuppe (Hauseckquelle-Te6, Q: 9 bis mindestens 40 l/s) bzw. die eigentliche Deckengrenze (Wildensteinquelle-K1, Q: 18 bis mindestens 400 l/s) gebunden. Hydrochemie, Q_{max}/Q_{min}-Verhältnis und Tracer-Verweilzeiten zwischen 7 und ~ 21 Monaten weisen bei diesen Quellen auf eine Anspeisung aus einem Kalk-Dolomitaquifer hin (LAIMER, 2010). An der Nordseite existieren im Bereich des Nussensees, der ein typischer Quellenbeckensee ist, mit Teichtbach-Ursprung (Te1, Q: 0 bis mindestens 6 l/s), Hirschbrunn (N4, Q: 5 bis mindestens 1.000 l/s) und den Tobiasquellen (To4–To6, Q: 3 bis mindestens 80 l/s) noch drei weitere Quellen, bei denen die Deckengrenze als Austrittsursache vermutet werden kann.

Angewandte Methoden

Folgt man dem N–S-Schnitt aus MAYR (2003), so markiert an der Basis der Dachstein-Decke hochgeschupptes Haselgebirge deren Überschiebungsfront (Abb. 2b). Auf Blatt 96 tritt dieses am Unterlauf des Teichtbaches gemeinsam mit Werfener Schichten und Gutensteiner Kalk an der Deckengrenze auf (Abb. 5). Am Fuß des Fahrnberges und westlich des Nussensees ist es auf Blatt 95 verzeichnet. Dazwischen sind zwar keine Haselgebirgsaufschlüsse kartiert, doch bei zwei Einzelwasserversorgungsanlagen nördlich (A15) und östlich (Te2) des Nussensees wurden vom Autor bereits früher erhöhte SO_4-Werte dokumentiert (LAIMER, 2010), die auf Kontakt mit Haselgebirge hinweisen. Die Quelle Te2 liegt bei SCHÄFFER (1982) an der Deckengrenze. Für die Primäraustritte von A15 kommt diese Position ebenfalls in Betracht.

Auf Basis dieser Ergebnisse wurde eine flächendeckende Kartierung sämtlicher Quellen und Vernässungsstellen in jenem Korridor durchgeführt, in dem die Überschiebungsfront vermutet wurde. Die Messung der elektrischen Leitfähigkeit (LF) sollte dabei zur Detektion neuer, unter Quartärbedeckung liegender Haselgebirgsvorkommen in den Einzugsgebieten von Ischler Ache, Teicht-, Auer-, Nussen-, Tobias- und Schöffaubach führen. Erfahrungsgemäß sind im weiteren Untersuchungsgebiet bereits LF-Werte > 500 µS/cm ein verlässliches Indiz für evaporitisch beeinflusstes Wasser. An der Quelle Te2 liegen bei LF-Werten zwischen 490–521 µS/cm die Konzentrationen von Na, Cl und SO_4 bei 0,7–0,95 meq/l. Bei A15 ergab sich bei einem LF-Wert von 431 µS/cm ein erhöhter SO_4-Wert von 0,52 meq/l (Abb. 3).

Die Geländearbeit erfolgte nach einer langen Trockenperiode im Frühwinter 2018/2019, um eine Verdünnung der Quellwässer durch Niederschlagswasser ausschließen zu können. Zuvor wurde vor allem die ältere geologische Literatur hinsichtlich bekannter, aber bei PLÖCHINGER (1982a) und SCHÄFFER (1982) nicht dargestellter Haselgebirgsaufschlüsse ausgewertet, um entsprechende Bereiche gezielt hydrogeologisch beproben zu können.

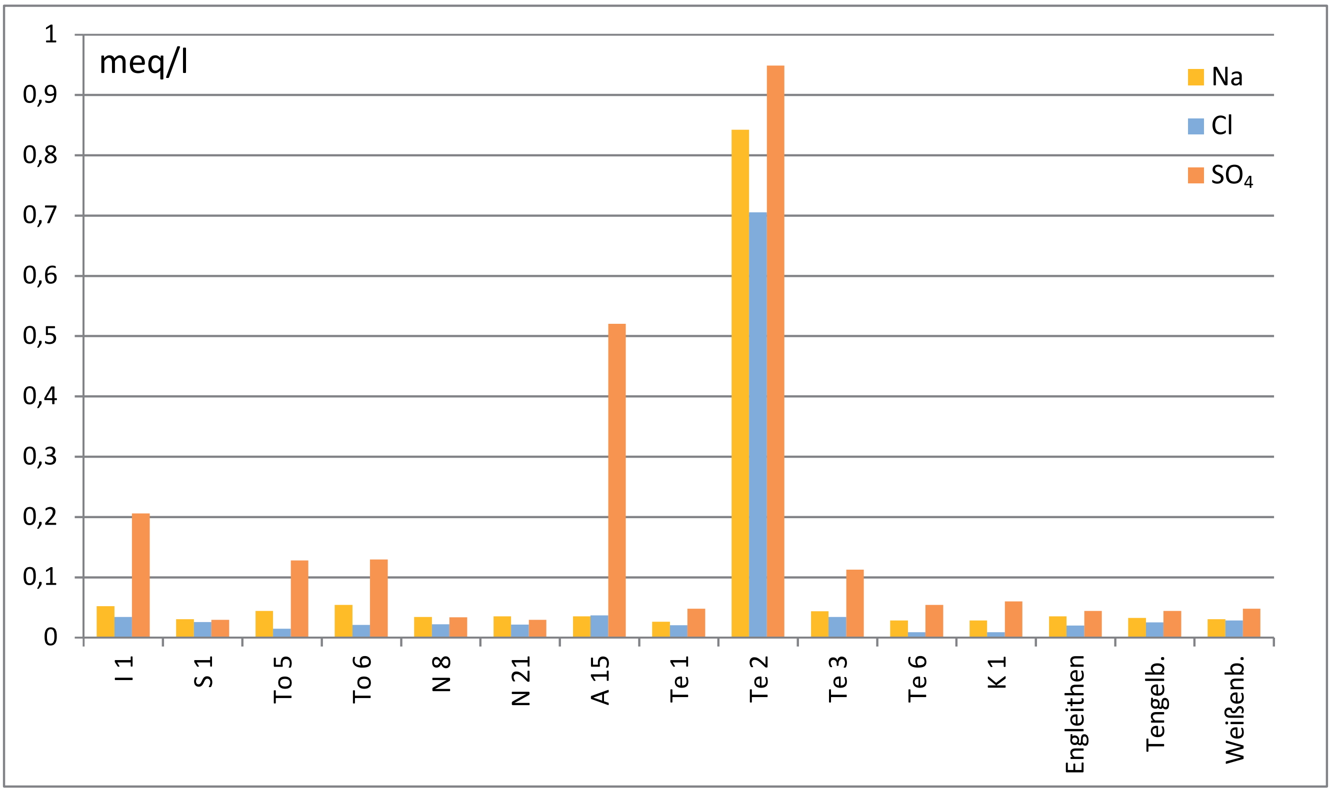

Abb. 3.
Na-, Cl- und SO_4-Konzentrationen an ausgewählten Quellen und Bächen des Katergebirges. Mit Ausnahme von Tengel- und Weißenbach liegen alle Wasseraustritte an der Nord- bzw. Nordost-Seite des Gebirges (Daten: Wasseranalysen der Stadtgemeinde Bad Ischl aus 2008).

Zusätzlich wurden online verfügbare digitale Geländemodelle (DGM aus DORIS bzw. SAGIS) auf das Vorhandensein tiefgreifender Massenbewegungen überprüft, die im Salzkammergut sehr oft auf eine evaporitische Unterlagerung zurückzuführen sind. Auch im Gelände wurde nach dem Auffinden höher mineralisierter Wässer nach geomorphologischen Hinweisen auf Haselgebirge in deren Umgebung gesucht (Dolinen, Gräben, Kriechhänge etc.).

Ergebnisse

Angaben in der Literatur

In der Literatur beschränkt sich die Erwähnung von Haselgebirge an der Basis der Dachstein-Decke auf die Bereiche Kaltenbach–Rabennest und Nussensee. Bereits SPENGLER (1912) beschreibt die bekannten Aufschlüsse von Haselgebirge, Werfener Schichten und Gutensteiner Kalk in Kaltenbach bzw. das Haselgebirge westlich vom Nussensee. In beiden Bereichen weist er auf eine Unterlagerung mit Sedimenten der Ischl-Nussensee-Gosau hin.

Im westlich anschließenden Rabennest hat MAYR (2003) drei bestehende Bohrungen verortet, von denen nur RN3 eine aktuelle Salinenbohrung ist. Die exakte Lage bzw. Zuordnung der alten Bohrungen RN1 und RN2 konnte aufgrund widersprüchlicher Ortsangaben (MAYR, persönliche Mitteilung) nicht geklärt werden. In der ersten Bohrung hat TIETZE (1918) salzhaltige Mergellagen dokumentiert. Die zweite Bohrung erfolgte 1919 und traf ebenfalls Haselgebirge an. 1972 wurde nach SCHAUBERGER (1979) nahe der Liegenschaft Kaltenbach 1 bei einer Brunnenbohrung in 26 m Tiefe eine Kochsalzquelle erschlossen. Diese wird später auch von AUBELL (1991) bzw. ZÖTL & GOLDBRUNNER (1993) erwähnt.

Am Nussensee schließt MÜLLNER (1931) aus den Karten von MOJSISOVICS & BITTNER (1905) sowie SPENGLER (1912) auf eine durch den See verlaufende Deckengrenze, welche von Haselgebirge begleitet wird. Er weist aber keine zusätzlichen Vorkommen nach. Erst PLÖCHINGER (1949) führt einen wenige Meter breiten Haselgebirgsaufschluss westlich des Gawanzersteins an und interpretiert diesen als Fortsetzung seiner späteren „Hallstätter Deckscholle“ am Nussensee. Bei deren Detaildarstellung (PLÖCHINGER, 1982b: Abb. 15) hat er zusätzlich ein kleines Vorkommen direkt am Ausfluss des Nussenbaches kartiert. Beide Aufschlüsse sind jedoch auf Blatt 95 nicht berücksichtigt.

Hydrogeologische Detailaufnahme

Während der hydrogeologischen Kartierung wurden 101 Wasseraustritte (Tab. 1) verortet und die Feldparameter Schüttung, Temperatur und Leitfähigkeit gemessen. Bei 66 Quellen bzw. Vernässungszonen liegt die Schüttung unter 0,1 l/s. Mit Ausnahme der sublimnisch im Nussensee austretenden Quelle N4 sind alle perennierend aktiven Quellen mit Schüttungen > 5 l/s gefasst. Sie liegen in der Gruppe mit den geringsten LF-Werten und wiesen im Jänner Temperaturen zwischen 6,6° C und 8,0° C auf.

67 Quellen im mittleren LF-Bereich und mit witterungsbedingt stark schwankenden Temperaturen repräsentieren überwiegend oberflächennahe Hangwässer und Schuttquellen innerhalb der Gosau-Gruppe bzw. glazialer Ablagerungen. Diese Quellen sind zwischen Ahornzwieselund Schöffau-Störung weit verbreitet, obwohl hier nach der geologischen Karte eher gering mineralisierte Karstwasseraustritte im schuttbedeckten Dachsteinkalk zu erwarten wären. Bei geologischen Übersichtsbegehungen zeigte sich, dass die Sedimente der Gosau-Gruppe am Nordwesthang des Katergebirges wesentlich weiter verbreitet sind, als auf Blatt 95 dargestellt. Sie reichen am Wanderweg zum Ahornfeld bis 1.250 m Seehöhe und nehmen den gesamten Bereich unterhalb des Zwieselstüberls ein, der über Gräben oberirdisch entwässert wird (Abb. 5). Da sich auch am Unterhang unter Schuttbedeckung immer wieder kleine Konglomerat-Aufschlüsse finden, kann eine Fortsetzung der Fahrnberg-Gosau östlich des Schöffautales und somit ein talnaher Verlauf der Deckengrenze angenommen werden.

Einzugsgebiet	Anzahl Quellen	Elektrische Leitfähigkeit (µS/cm)		
		190–290	290–480	> 480
Kaltenbach (K)	1	1	–	–
Teichtbach (Te)	6	4	1	1
Auerbach (A)	15	–	13	2
Nussenbach (N)	24	7	14	3
Tobiasbach (To)	26	3	16	7
Schöffaubach (S)	10	2	8	–
Ischler Ache (I)	19	–	15	4

Tab. 1.
Übersicht der Quellaufnahme. Jeder Wasseraustritt wurde einem der drei Leitfähigkeitsbereiche zugeordnet, wobei die sicher salinar beeinflussten Wässer im Bereich > 480 µS/cm liegen.

Bei 13 Quellen des LF-Bereiches 290–480 µS/cm, an welchen LF-Werte zwischen 418 und 477 µS/cm gemessen wurden, ist ein Kontakt mit Haselgebirge möglich und aufgrund ihrer Nachbarschaft zu sicher salinar beeinflussten Quellen auch plausibel. In diese letzte Gruppe fallen 17 Wasseraustritte (Tab. 1), deren Lage (Abb. 5) im Folgenden von Ost nach West beschrieben wird.

Da das Haselgebirge bis zum Mittellauf des Teichtbaches durch Bohrungen nachgewiesen ist, wurde erst an dessen Oberlauf mit der Quellaufnahme begonnen. Außer der bereits bekannten Quelle Te2, welche etwa 300 m westlich der Bohrung ? RN1 entspringt, fanden sich keine weiteren salinar beeinflussten Wasseraustritte.

Nachdem der LF-Wert von 431 µS/cm bei der Sekundärquelle A15 auf eine erhöhte SO_4-Konzentration zurückgeführt werden konnte, wurde ihr Einzugsgebiet sehr detailliert kartiert. Dabei fanden sich in einem Graben, der die bunten Liaskalke des Gawanzersteins von der Nussensee-Gosau trennt, die Wasseraustritte A3 (LF: 739 µS/cm) und A4 (LF: 635 µS/cm). Sie bilden eine leicht gewölbte Vernässungszone nahe der Grabensohle, die anstehendes Haselgebirge andeutet.

An der Südwestseite des Gawanzersteins tritt in einer Mulde mit unruhiger Morphologie die kleine Quelle N17 (LF: 509 µS/cm) aus. Die NE–SW streichende Hohlform reicht bis zum Nussensee und formt dort eine kleine Bucht im Nordufer. Es handelt sich hier um den bei PLÖCHINGER (1949) erwähnten Haselgebirgsaufschluss. Auch das bei PLÖCHINGER (1982b: Abb. 15) dargestellte Vorkommen am Nussenbach lässt sich hydrogeologisch nachweisen. Hier tritt aus der quartären Bedeckung des Bacheinhanges

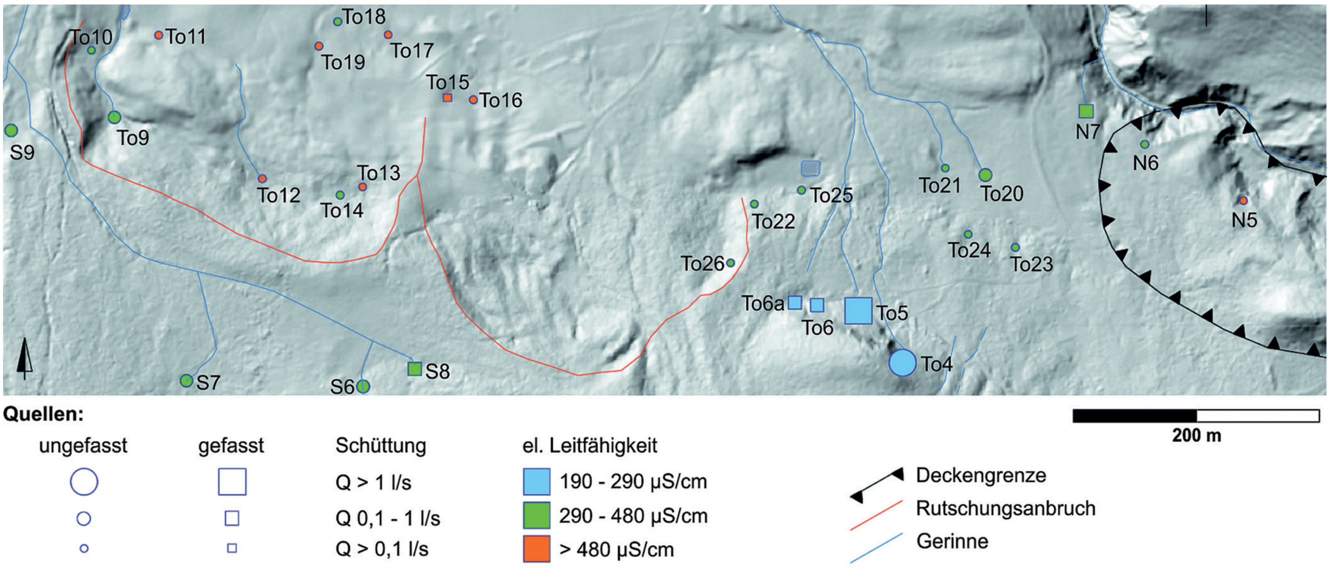

Abb. 4.
Detailansicht der Rutschung zwischen Tobias-Quellgruppe und Schöffaubach mit Lage und Information (gefasst/ungefasst, Schüttung, elektrische Leitfähigkeit) ausgewählter Quellen. Das Quellgewässernetz wurde im Rahmen der Quellaufnahme kartiert. Als topografische Grundlage dient ein digitales Geländemodell mit 1 m Auflösung. © basemap.at (Gelände).

die evaporitisch beeinflusste Quelle N9 (LF: 763 µS/cm) aus. Innerhalb des kartierten Haselgebirges der Nussensee-Deckscholle wurde an der Quelle N5 mit 2 mS/cm der höchste LF-Wert gemessen.

Rund 400 m westlich der Deckscholle ist auf Blatt 95 eine Rutschung kartiert, die in Hangschutt und Grundmoräne abgegangen ist und in ihrem östlichen Teil von fluviatil umgelagertem Schutt überprägt wird. Das tatsächliche Ausmaß der relikten Rutschmasse wird erst im digitalen Geländemodell (Abb. 4) ersichtlich. Sie weist eine bis zu 8 m hohe Abrisskante auf und erstreckt sich auf 700 m Breite zwischen der Tobias-Quellgruppe und dem Schöffaubach. Innerhalb der Rutschmasse weisen sieben Wasseraustritte mit erhöhten LF-Werten auf einen basalen Gleithorizont im Haselgebirge hin. Die höchsten Werte wurden bei den Quellen To15 (LF: 734 µS/cm) und To16 (LF: 756 µS/cm) gemessen.

Westlich der Rutschung wird die Deckengrenze vom 300 m breiten Schwemmkegelhals des Schöffaubaches bedeckt. Wasserproben des hier abgeteuften Brunnens

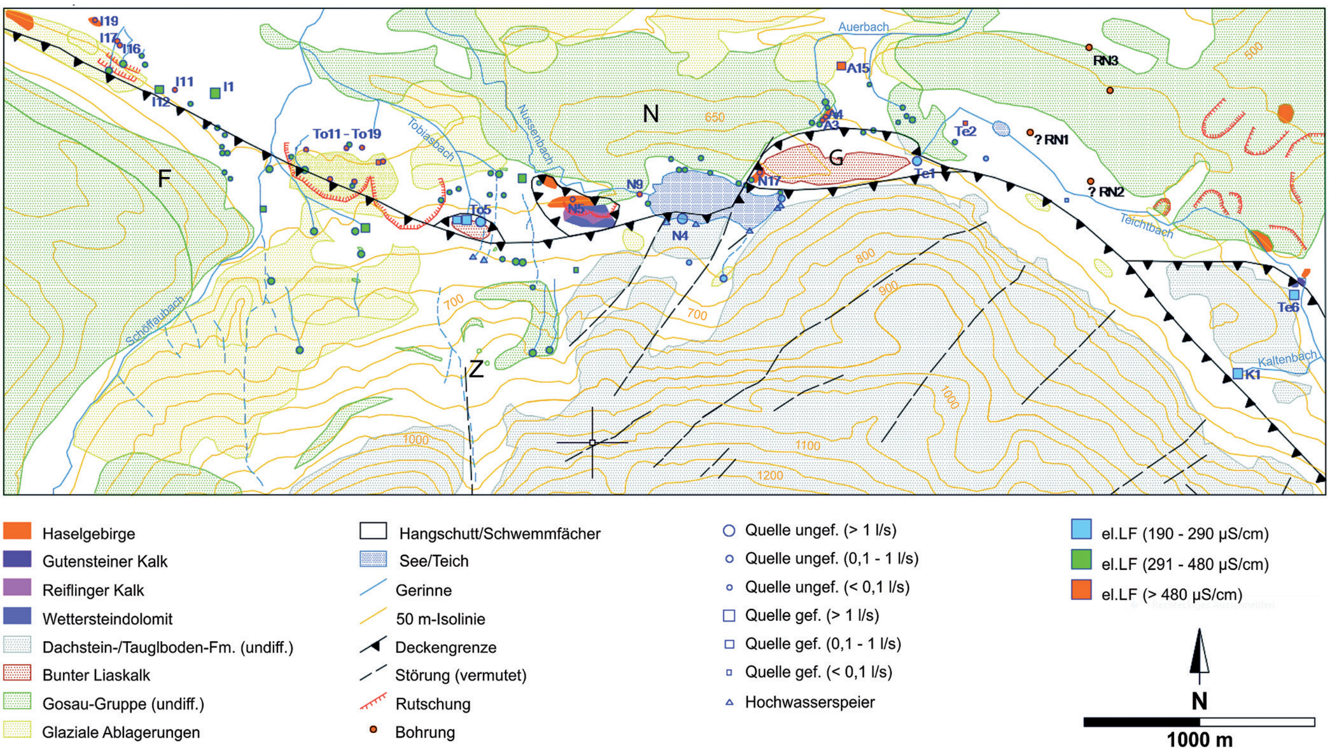

Abb. 5.
Quellkartierung und daraus abgeleiteter Verlauf der Deckengrenze der Dachstein-Decke im Blattschnittbereich 95/96. Das Gewässernetz wurde im Rahmen der Quellaufnahme kartiert. Abkürzungen: F = Fahrnberg, G = Gawanzerstein, N = Nussensee, Z = Zwieselstüberl.

der Wassergenossenschaft Aigen-Voglhub (I1) zeigen mit leicht erhöhten $S0_4$-Werten den Kontakt mit Haselgebirge an (Abb. 3, 5). Der Hangwasseraustritt I11 (LF: 630 µS/cm) leitet zu den ebenfalls auf Blatt 95 kartierten Abrisskanten in der Grundmoräne des Fahrnberges über. Auch hier treten innerhalb einer Rutschmasse evaporitisch beeinflusste Hangwässer (I16, LF: 775 µS/cm und I17, LF: 678 µS/cm) aus. Sie bilden den Lückenschluss zum kartierten Verlauf der Deckengrenze entlang der Fahrnbergüberschiebung (Plöchinger, 1982b).

Schlussfolgerung – Konsequenzen für die Hydrogeologie

Die Deckengrenze der Dachstein-Decke verläuft somit vom Rabennest entlang der Nord- und Westseite des Gawanzersteins zum Nussensee und durch diesen zur dortigen „Hallstätter Deckscholle“. Letztere erstreckt sich an ihrem Ostende zumindest bis zur Quelle N9 und damit 100 m weiter Richtung Seeufer als bei Plöchinger (1982b) dargestellt. Bis hierher entspricht der Verlauf genau jenem der Tafel 1 aus Mandl et al. (2012). Westlich der „Deckscholle“ markieren Massenbewegungen die Überschiebungsfront, deren Lokalisierung bereits Spengler (1912) sehr nahe kam. Die hydrogeologischen Daten lassen vermuten, dass das Haselgebirge zwischen Fahrnberg und Nussensee unter der quartären Bedeckung oberflächennah ansteht. Die „Hallstätter Deckscholle“ wäre damit kein isoliertes Haselgebirgsvorkommen, sondern Teil einer langgestreckten, an der Überschiebung hochgeschürften Ischl-Scholle.

Die Deckengrenze ist somit die Austrittsursache für alle größeren Quellen der Katergebirge-Nordseite: Teichtbach-Ursprung (Te1), Hirschbrunn (N4), Tobiasquellen (To4–To6) und die Quelle I12 am Fahrnberg sind an sie gebunden; die unterirdischen Abflusswege von den Estavellen des Nussensees zu den Hauseck- und Wildensteinquellen (Te6, K1) ebenfalls. An der Deckenbasis hochgeschuppte Mitteltriasgesteine und Haselgebirge bzw. randlich überfahrene Formationen der Ischl-Nussensee-Gosau bilden die Stauer. Mit dem von Ost nach West bis in den Bereich um den Nussensee flach ansteigenden Verlauf der Überschiebung könnte auch das Austreten der beiden schüttungsstärksten Quellen des Gebirges in Kaltenbach erklärt werden. Die Höhenlage eines 100 bis 150 m über dem rezenten Vorflutniveau gelegenen Karstwasserspiegels ist für das Katergebirge somit tektonisch fundierter begründbar, als mit der vermuteten Einstellung auf ein präpleistozänes Talbodenniveau (Laimer, 2005).

Durch die Ausdehnung der schlecht durchlässigen Formationen der Fahrnberg-Gosau auf den Bereich vom Schöffaubach bis zum Zwieselstüberl ergibt sich für das vermutete Einzugsgebiet der Tobiasquellen zumindest am forstwirtschaftlich genutzten Mittelhang ein besserer Wasserschutz, als aus Blatt 95 zu schließen ist.

Dank

Gerhard W. Mandl (ehemals Geologische Bundesanstalt) verdanke ich eine ausführliche Darlegung seiner in die Erläuterungen zu Blatt 96 Bad Ischl eingeflossenen tektonischen Überlegungen. Michael Mayr (Salinen Austria AG) konnte Fragen zu den Salinenbohrungen aufklären. Die Wassergenossenschaft Aigen-Voglhub und die Stadtgemeinde Bad Ischl stellten chemische Wasserbefunde zur Verfügung. Renate Klima übernahm dankenswerterweise die grafische Überarbeitung der Abbildungen.

Literatur

Aubell, W. (1991): Lagerstättenkunde des Bezirkes Gmunden. – In: Hufnagl, F. & Marchetti, H. (Hrsg.): Der Bezirk Gmunden und seine Gemeinden, 53–60, Gmunden (Eigenverlag).

Auer, M., Gawlick, H.-J. & Suzuki, H. (2006): Die Unter-Oxford-Radiolarit-Megabrekzie am Nordrand des Dachstein-Blockes (Nördliche Kalkalpen, Österreich): Radiolarienfaunen, Mikrofazies des Komponentenbestandes und tektonische Bedeutung. – Jahrbuch der Geologischen Bundesanstalt, **146**, 33–51, Wien.

Decker, K. & Jarnik, M. (1992): Structural analysis of the Late Cretaceous Gosau Group of Rigaus, Fahrenberg and Nussensee (Northern Calcareous Alps, Salzburg – Upper Austria): Tertiary deformation during lateral extrusion illustrated. – Mitteilungen der Gesellschaft der Geologie- und Bergbaustudenten Österreichs, **38**, 93–106, Wien.

Decker, K., Peresson, H. & Faupl, P. (1994): Die miozäne Tektonik der östlichen Kalkalpen: Kinematik, Paläospannungen und Deformationsaufteilung während der „lateralen Extrusion“ der Zentralalpen. – Jahrbuch der Geologischen Bundesanstalt, **137**/1, 5–18, Wien.

Laimer, H.J. (2005): Karsthydrogeologisch-speläologische Untersuchungen in der Hallstätter Zone von Ischl-Aussee (Oberösterreich, Steiermark). – Die Höhle, **56**, 12–19, Wien.

Laimer, H.J. (2010): Partielle Karstökosystemanalyse als flankierende Schutzmaßnahme in der kommunalen Wasserversorgung (Salzkammergut, Oberösterreich). – Geo-Öko, **31**/3–4, 198–222, Göttingen.

Leischner, W. (1959): Geologische Neuaufnahme in der Umgebung von Bad Ischl (Ischl- und unteres Rettenbachtal). – Mitteilungen der Gesellschaft der Geologie- und Bergbaustudenten Wien, **10**, 63–94, Wien.

Mandl, G.W. (2012): Geologischer Bau. – In: Mandl, G.W. (Red.), van Husen, D. (Red.) & Lobitzer, H. (Red.): Erläuterungen zur Geologischen Karte der Republik Österreich 1:50.000, Blatt 96 Bad Ischl, 22–32, Geologische Bundesanstalt, Wien.

Mandl, G.W. (Red.), van Husen, D. (Red.) & Lobitzer, H. (Red.) (2012): Erläuterungen zur Geologischen Karte der Republik Österreich 1:50.000, Blatt 96 Bad Ischl. – 215 S., Geologische Bundesanstalt, Wien.

Mandl, G.W., Brandner, R. & Gruber, A. (2017): Zur Abgrenzung und Definition der Kalkalpinen Deckensysteme (Ostalpen, Österreich). – In: Wimmer-Frey, I. (Red.), Römer, A. (Red.) & Janda, C. (Red.): Arbeitstagung 2017 – Angewandte Geowissenschaften an der GBA, 254–255, Geologische Bundesanstalt, Wien.

MAYR, M. (2003): Die Salinen Austria AG und die Geologie ihrer Salzlagerstätten im Salzkammergut. – Mitteilungen IAG BOKU, **13**, 53–97, Wien.

MOJSISOVICS, E. & BITTNER, A. (1905): Geologische Spezialkarte der im Reichsrate vertretenen Königreiche und Länder der österreichisch-ungarischen Monarchie, SW.-Gruppe Nr. 19, 1:75.000, Ischl und Hallstatt. – 1 Bl., k. k. Geologische Reichsanstalt, Wien.

MÜLLNER, J. (1931): Zur Speisung der Seen. – Archiv für Hydrobiologie, **22**, 348–362, Stuttgart.

PLÖCHINGER, B. (1949): Ein Beitrag zur Geologie des Salzkammergutes im Bereich von Strobl am Wolfgangsee bis zum Hang der Zwieselalm. – Jahrbuch der Geologischen Bundesanstalt, **93**, 1–35, Wien.

PLÖCHINGER, B. (1982a): Geologische Karte der Republik Österreich 1:50.000, Blatt 95 Sankt Wolfgang im Salzkammergut. – 1 Bl., Geologische Bundesanstalt, Wien.

PLÖCHINGER, B. (1982b): Erläuterungen zur Geologischen Karte der Republik Österreich 1:50.000, Blatt 95 Sankt Wolfgang im Salzkammergut. – 74 S., Geologische Bundesanstalt, Wien.

SCHÄFFER, G. (1977): Bericht 1976 über Neuaufnahmen im Mesozoikum des Salzkammergutes auf Blatt 96, Bad Ischl. – Verhandlungen der Geologischen Bundesanstalt, **1977**/1, A90–A91, Wien.

SCHÄFFER, G. (1982): Geologische Karte der Republik Österreich 1:50.000, Blatt 96 Bad Ischl. – 1 Bl., Geologische Bundesanstalt, Wien.

SCHAUBERGER, O. (1979): Die Mineral- und Thermalquellen im Bereich des ostalpinen Salinars zwischen Salzach und Enns. – Schriftenreihe des Oberösterreichischen Musealvereins, **9**, 120 S., Linz.

SPENGLER, E. (1912): Untersuchungen über die tektonische Stellung der Gosauschichten. I. Teil. Die Gosauzone Ischl – Strobl – Abtenau. – Sitzungsberichte der mathematisch-naturwissenschaftlichen Klasse der kaiserlichen Akademie der Wissenschaften in Wien, Abteilung I, **121**, 1039–1086, Wien.

TIETZE, E. (1918): Jahresbericht für 1917. – Verhandlungen der k. k. Geologischen Reichsanstalt, **1918**/1, 1–36, Wien.

WAGREICH, M. (1998): Lithostratigraphie, Fazies und Sequenzstratigraphie der Gosau Gruppe von Bad Ischl und Strobl am Wolfgangsee (Oberturon–Maastricht, Nördliche Kalkalpen, Österreich). – Jahrbuch der Geologischen Bundesanstalt, **141**/2, 209–234, Wien.

ZÖTL, J.G. & GOLDBRUNNER, J. (1993): Die Mineral- und Heilwässer Österreichs. – 324 S., Wien (Springer).

Eingelangt: 21. März 2019, angenommen: 18. September 2019

JAHRBUCH DER GEOLOGISCHEN BUNDESANSTALT

Jb. Geol. B.-A.	ISSN 0016–7800	Band 159	Heft 1–4	S. 163–173	Wien, Dezember 2019

The gastropod fauna from the opalite of the late Miocene Lake Tschaterberg (Austria)

Mathias Harzhauser[1], Thomas A. Neubauer[2] & Oliver Schmitsberger[3]

4 Text-Figures

Österreichische Karte 1:50.000
BMN / UTM
168 Eberau / NL 33-03-26 Kohfidisch

Freshwater
Gastropoda
Miocene
Opalite

Contents

Abstract

The mollusk fauna of the opalite of the Tschaterberg region close to Kohfidisch in Burgenland (Austria) is re-evaluated. The assemblage is low diverse, comprising only lymnaeids, planorbids and four parautochthonous helicid gastropod species. The ecological requirements of the genera indicate a pure freshwater setting in a short-lived, shallow lake or pond with rich reed vegetation and peat formation. Stratigraphically, a correlation with the upper Pannonian (upper Miocene) is most likely, excluding any chemical influence on opalite formation by Dacian volcanism. Thus, the opalite-lake existed contemporaneously with the famous early Turolian mammal fauna from Kohfidisch, which is correlated with the European Mammal Zone MN 11.

Die Gastropoden Fauna des Opalits vom spätmiozänen Tschaterberg-See (Österreich)

Zusammenfassung

Die Molluskenfauna des Opalits der Tschaterberg Region nahe Kohfidisch im Burgenland (Österreich) wird neu evaluiert. Die Vergesellschaftung ist gering divers und umfasst lediglich lymnaeide und planorbide Gastropoden neben vier parautochthonen heliciden Schneckenarten. Die ökologischen Erfordernisse der Gastropoden verweisen auf ein reines Süßwasserhabitat eines kurzlebigen, seichten Sees oder Tümpels mit reicher Schilfvegetation und Torfbildung. Stratigrafisch ist eine Korrelation mit dem oberen Pannonium (spätes Miozän) sehr wahrscheinlich, was einen chemischen Einfluss auf die Opalitbildung durch dazischen Vulkanismus im Pliozän ausschließt. Der Opalit-See existierte daher zeitgleich mit der berühmten Turolium-Säugetierfauna von Kohfidisch, die mit der europäischen Säugetierzone MN 11 korreliert wird.

1 Mathias Harzhauser: Natural History Museum Vienna, Geological-Paleontological Department, Burgring 7, 1010 Vienna, Austria. mathias.harzhauser@nhm-wien.ac.at
2 Thomas A. Neubauer: Justus Liebig University, Department of Animal Ecology & Systematics, Heinrich-Buff-Ring 26–32 IFZ, 35392 Giessen, Germany, and Naturalis Biodiversity Center, PO Box 9517, 2300 RA Leiden, The Netherlands. tneub@zo.jlug.de
3 Oliver Schmitsberger: OREA – Institute for Oriental and European Archaeology, Austrian Academy of Sciences, Hollandstraße 11–13, 1020 Vienna, Austria. oliver.schmitsberger@oeaw.ac.at

Introduction

The locality Tschaterberg (Csaterberg, Csartherberg = Tschater Mountain) in the vicinity of Kohfidisch in Burgenland Province (SE-Austria), close to the Hungarian border, is famous for its opalite occurrences. Although the rock is largely unusable for jewellery production, the silicified wood found in the opalite is very well preserved, of high quality and has attracted collectors already in the Early Modern Period. First scientific descriptions date back even to the 16th century when CAROLUS CLUSIUS (1526–1609) described fossil wood from Tschaterberg in his *Rariorum aliquot Stirpium per Pannoniam* (CLUSIUS, 1583: 10). Eighteen years later, he repeated the description in his *Rariorum Plantarum Historia* (CLUSIUS, 1601: 20), adding 1580 as year of collecting. His surprisingly modern descriptions represent the first explicit references to fossils from the territory of modern Austria. The geological setting was investigated much later by HOFFMANN (1877). In his geological survey, BENDA (1929) already tried to interpret the genesis of the opalite as result of geysers. First modern investigations of the silicified wood from the Tschaterberg region were published by FELIX (1884) and HOFMANN (1928, 1929). Additional paleobotanical data were provided by KÜMEL (1957), MÜLLER-STOLL & MÄDEL (1957, 1959) and PAVLICEK (2009). A comprehensive paper discussing the geological setting, mineralogy and genesis of the opalite and its fossils was published by KÜMEL (1957). KÜMEL (1957) rejected the "geysers-hypothesis" of BENDA (1929) and suggested that the opalite formed as precipitation from an acidic spring, chemically fed by the underlying serpentinite. Thereafter, only small guidebook notes were published by SAUERZOPF et al. (1990) and PAHR (2000), more or less repeating the results of KÜMEL (1957). The last synthesis summarizing also the recent (mainly collectors) literature dealing with the mineralogy of the Tschaterberg opalite was published by GÖTZINGER & PRISTACZ (2009), who provided powder X-ray diffraction data on the chemical composition of the various opalite types. A detailed overview about the history of research of the Tschaterberg opalite was compiled by HORVÁTH (1973).

Whilst the plant fossils have been repeatedly investigated, the associated mollusk fauna was only cursorily men-

Text-Fig. 1.
Geographic setting of the investigation area; map generated with Google Earth, Image © 2017; image taken in 6/9/2017).

tioned by Benda (1929) and Kümel (1957). Benda (1929) mentioned *Helix, Pupa* and *Planorbis* and Kümel (1957) listed *Cepaea* (*Megalotachea*) sp., *Planorbis* (*Anisus*) cf. *confusus* Soós and *Limnaea* sp. Most probably, both authors referred to the same taxa: *Helix* sensu Benda (1929) = *Cepaea* (*Megalotachea*) sp., *Pupa* sensu Benda (1929) = *Stagnicola* sp. and *Planorbis* sensu Benda (1929) = *Anisus* cf. *confusus* Soós. The age of the opalite is difficult to assess. Benda (1929) assumed a Pleistocene age, whereas Kümel (1957) interpreted a Miocene age based on the mollusk fauna and the presence of taxodiacean wood. More recently, Sauerzopf et al. (1990) and Pahr (2000) speculated about a relation with Dacian volcanic activity during the Pliocene.

Herein, we try to re-evaluate the taxonomic composition and paleoecology of the mollusk fauna of the opalite and try to achieve more precise age constraints.

Geological setting and structure of the opalite

The Kohfidisch-Tschaterberg region is part of the Penninic Rechnitz Unit, which is represented here mainly by serpentinite and greenschist of the Eisenberg crystalline (Gratzer, 1985). These are surrounded and partly overlain by Neogene clay, silt and sand of late Miocene age (Kümel, 1957). The opalite forms three isolated occurrences, resting on the serpentinite, arranged along a c. 2 km long, roughly W–E trending line (see map in Kümel, 1957). The two main occurrences are found on the Klein Tschater (365 m a.s.l.) and the Hoch Tschater (341 m a.s.l.) (Text-Fig. 1). These two hills are the southwestern foothills of the Eisenberg (= Eisenberg Mountain).

Kümel (1957) identified four types of opalite within the Tschaterberg occurrence, which were mineralogically analysed by Götzinger & Pristacz (2009). The spatial relation of these opalite types, however, was unknown (Kümel, 1957; Götzinger & Pristacz, 2009). Similarly, the thickness of the opalite layer was unclear. To shed light on these problems, several large opalite blocks were excavated during a sampling campaign in 2018. The blocks were cut perpendicular to the bedding plane in the laboratory of the Natural History Museum Vienna (NHMW). The largest block is about 40 cm thick and displays a succession of opalite types (Text-Fig. 2), which was also found in other blocks from the Hoch Tschater (although the thickness of the layers is highly variable). The original orientation of the blocks was reconstructed based on internal erosive boundaries and on cavities of roots and stems crossing the observed layers. The basal layer of the illustrated block represents an about 15 cm thick, whitish, glossy and dense opalite composed of up to 70 % C-T-Opal and various amounts of quartz (Götzinger & Pristacz, 2009) (Text-Fig. 2A). Numerous tube-like cavities, which represent dissolved stalks of reed or comparable plants, characterize this layer. Kümel (1957) classified it as "silicified moss-peat". Locally, the layer passes into brownish, glossy and dense opalite with dissolved stalks. Mineralogically this opalite type is dominated by C-T-Opal (75–100 %) (Götzinger & Pristacz, 2009). This type was classified by Kümel (1957) as "silicified gyttja". A sharp erosive boundary with relief of up to 5 cm separated the lower opalite layer from an about 10 cm thick, granulose-porous, brownish, lustreless layer of goethite and quartz (Text-Fig. 2B). This type was classified by Kümel (1957) as "silica-iron gel". This layer passes without sharp boundary into another, about 10 cm thick layer of granulose-porous, brownish, lustreless opalite with lenses of porcelaneous opalite composed of about 40 % C-T-Opal and large amounts of quartz (Götzinger & Pristacz, 2009) (Text-Fig. 2C). These intercalations were classified as silicified leave-moss-peat by Kümel (1957) occurring within a gyttja matrix. Although mollusks are found in all layers, the basal part of the third layer is especially rich in lymnaeids and planorbids, which lie parallel to the bedding plane. The described thicknesses are variable and the described opalite succession may be a rather local phenomenon.

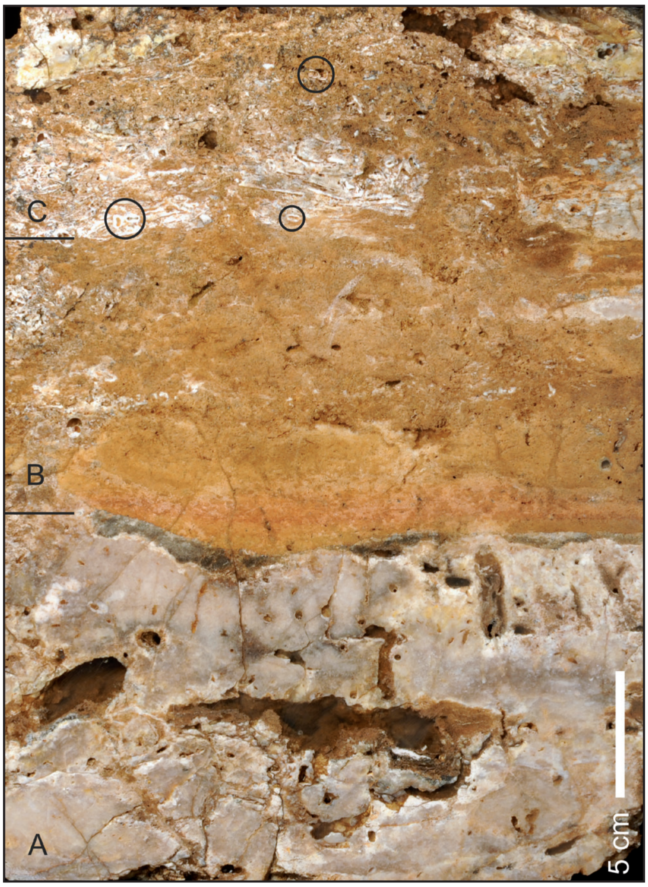

Text-Fig. 2.
Cross-section of the opalite, showing three different layers of opalite type (NHMW 2019/0031/0005). Note the cavities in the lower layer, which represent dissolved stalks preserved *in situ*. Circles indicate lymnaeid and planorbid gastropods.

Material

The herein analysed samples were collected in 2018 at the Tschaterberg in the forest area west of the small chapel around the position 47°10'31.30" N, 16°23'38.32" E. None of the samples occurred in-situ but as isolated blocks in the forest soil. In addition, the private collectors Peter Schebeczek (Pellendorf, NÖ) and Josef Kroiher (St. Florian, OÖ) provided samples from their private collections. Aragonite shells of the gastropods are completely dissolved and usually only partly replaced by silica. Typically, only the internal surface of the shells is preserved, which lack any sculptural details. Partial internal moulds are frequent as well. In rare cases, casts of the external shell surface are available. These cavities were filled by a two-component dental-silicone to allow identification. All material is stored in the paleontological collection of the Natural History Museum Vienna.

Systematics

Subclass Heterobranchia BURMEISTER, 1837

Superorder Hygrophila FÉRUSSAC, 1822

Superfamily Lymnaeoidea RAFINESQUE, 1815

Family Planorbidae RAFINESQUE, 1815

Genus *Anisus* STUDER, 1820

Type species: *Helix spirorbis* LINNAEUS, 1758. Recent, Europe.

Anisus confusus SOÓS, 1934

Text-Fig. 3: Figs. 1–4, 9

1929 *Planorbis* sp. – BENDA, p. 38.

*1934 *Anisus* (*Anisus*) *confusus* n. sp. – SOÓS, p. 194, Fig. 5.

1955 *Planorbis* (*Anisus*) *confusus* SOÓS – BARTHA & SOÓS, p. 64, Pl. 5, Figs. 1–4.

1957 *Planorbis* (*Anisus*) cf. *confusus* SOÓS – PAPP in KÜMEL, p. 8.

non 1953 *Planorbis* (*Anisus*) *confusus* SOÓS – SAUERZOPF, p. 53, Pl. 2, Figs. 1a–c.

non 2004 *Anisus confusus* SOÓS 1934 – HARZHAUSER & BINDER, p. 12, Pl. 4, Figs. 7–10.

Material: One opalite slab with numerous specimens (NHMW 2019/0054/0002).

Discussion: This is the most frequent gastropod in the opalite from Tschaterberg. *Anisus confusus* is characterized by its tightly coiled whorls, convex periphery and prominent growth lines. The largest specimen at Tschaterberg attains a diameter of about 8.5 mm, which is smaller than fully grown specimens from the type locality Öcs (12 mm) and from Balatonszentgyörgy in Hungary as described by SOÓS (1934) and BARTHA & SOÓS (1955). A comparison of whorl diameter increase during ontogeny between *A. confusus* from Tschaterberg with a fully-grown specimen described by BARTHA & SOÓS (1955) from Balatonszentgyörgy reveals a nearly identical mode of growth. Other alleged occurrences of *Anisus confusus*, mentioned by SAUERZOPF (1953) and HARZHAUSER & BINDER (2004) from Eichkogel (Vienna Basin, Austria) and Königsberg-Hannersdorf (Burgenland, Austria), differ in their distinctly smaller size and wider coiling. These differences were already discussed by WENZ & EDLAUER (1942), who nevertheless identified the Eichkogel specimens as *A. confusus*. Especially the erroneous identification of specimens from Königsberg-Hannersdorf by SAUERZOPF (1953) might have led PAPP in KÜMEL (1957) to identify the Tschaterberg specimens as *A.* cf. *confusus*, because the upper Pannonian marl and limestone of Königsberg-Hannersdorf occurs only 5 km north of Tschaterberg. As the Königsberg-Hannerdorf and Eichkogel planorbids are most probably not conspecific with *Anisus confusus*, the correlation of the Tschaterberg opalite with the Eichkogel fauna by PAPP in KÜMEL (1957) was based on a misidentification.

Only a small number of late Miocene to Recent *Anisus* species have been described so far. A morphologically similar species is the late Pannonian *Anisus krambergeri* (HALAVÁTS, 1903), which differs in its distinctly angulated periphery (see BARTHA, 1954, 1959; SCHLICKUM, 1978; FORDINÁL, 1998; HARZHAUSER & BINDER, 2004). The middle Pannonian *Anisus brunnensis* SAUERZOPF, 1953 attains 9 mm in diameter and might be closely related to *A. confusus.* Based on the description in SAUERZOPF (1953), it seems to differ only in its slightly tighter coiling and less convex whorl tops. The Tortonian *A. falsani* (LOCARD, 1883) from the Bresse-Valence Basin in France is smaller (max. diameter = 5 mm) and whorls widen faster. *Anisus komarovae* PRYSJAZHNJUK, 1974 and *A. bondartchuki* PRYSJAZHNJUK, 1974, from the Tortonian (Bessarabian–Khersonian) of Ukraine, are even smaller and differ in their relatively narrower whorls. The extant *A. vortex* (LINNAEUS, 1758) and *A. leucostoma* (MILLET, 1813) and the Pliocene *A. mariae* (MICHAUD, 1862) all differ in their flattened whorl tops on the apical side. The extant *A. spirorbis* (LINNAEUS, 1758) is distinctly smaller (< 6 mm in diameter), and *A. septemgyratus* (ROSSMÄSSLER, 1835) is much more narrowly coiled with hardly widening last whorl.

Ecology: *Anisus* species are obligate freshwater dwellers, which can build up a large population size within a year. The animals live in standing and slowly running waters of periodical and very small water bodies, in periodic swamps and even in moist meadows with rich vegetation; most species tolerate periods of drought (GLÖER & GROH 2007; WELTER-SCHULTES, 2012). The genus displays a wide range of pH-tolerance; e.g., *Anisus spirorbis* occurs in acidic ponds, whereas *A. vortex* appears also in alkaline waters (SPYRA, 2017).

Stratigraphic and geographic distribution: *Anisus confusus* is restricted to the lower part of the upper Pannonian Transdanubian substage sensu SACCHI & HORVÁTH (2002), roughly spanning an interval from 8.9–8.0 Ma. Geographically, it is recorded from the Balaton region in the Pannonian Basin (localities Öcs, Balatonszentgyörgy). The records from Orešany and Čel'adince in the Danube Basin (Slovakia) described by FORDINÁL (1998) might need verification.

Genus *Planorbarius* DUMÉRIL, 1805

Type species: *Helix cornea* LINNAEUS, 1758. Recent, Europe,

Planorbarius cf. *halavatsi* NEUBAUER, HARZHAUSER, KROH, GEORGOPOULOU & MANDIC, 2014

Text-Fig. 3: Fig. 5

cf. 1903 *Planorbis grandis* n. sp. – HALAVÁTS, p. 57, Pl. 3, Fig. 5 [non *Planorbis grandis* DUNKER in KÜSTER et al., 1850].

cf. 1953 *Planorbarius grandis* (HALAVÁTS) – SAUERZOPF, p. 50, Pl. 1, Figs. 3–4.

cf. 1955 *Planorbarius grandis* (HALAVÁTS) – BARTHA & SOÓS, p. 63, Pl. 5, Figs. 15–17.

cf. 2004 *Planorbarius grandis* (HALAVATS) – HARZHAUSER & TEMPFER, p. 60, Fig. 5/3.

cf. 2014 *Planorbarius halavatsi* nom. n. – NEUBAUER et al., p. 26.

Material: One natural cast (NHMW 2019/0054/0003).

Discussion: A single cast is available showing the umbilical side of a large planorbid of about 16 mm diameter and 4.8 mm height. The specimen has a deeply sunken umbilicus and consists of only three slightly flattened teleoconch whorls; the last whorl is missing. The fragmentary preservation does not allow a clear identification. Nevertheless, the available specimen fits well to sub-adult specimens of *Planorbarius halavatsi* from the upper Pannonian of Götzendorf (Austria). This species is characterised by its very large size and flattened whorls (SAUERZOPF, 1953; BARTHA & SOÓS, 1955). However, the type material shows a higher whorl expansion rate, which is why we only tentatively affiliate the present material with *P. halavatsi*. The flattened whorls allow a separation from the extant *Planorbarius corneus* (LINNAEUS, 1758) and the superficially similar Miocene *P. mantelli* (DUNKER, 1848). Specimens of *P. mantelli* (sensu HARZHAUSER & BINDER, 2004) from the upper Pannonian Eichkogel section attain a much larger whorl height at the same growth stage. *Planorbarius margoi* (LÖRENTHEY, 1894) from the late Pannonian of Kurd (Hungary), *P. philippei* (LOCARD, 1883) from the Tortonian of the Bresse-Valence Basin, *P. praecorneus* (FISCHER & TOURNOUËR, 1873) from the Tortonian of the Lower Rhône Basin, as well as the early Pliocene *P. thiollieri* (MICHAUD, 1855) from the same region all differ from the present species in exposing higher whorl expansion rates and relatively higher whorls. *Planorbarius margoi* moreover has a distinct angulation at the transition of whorl flank and umbilical side.

The present species was originally established by HALAVÁTS (1903) as *Planorbis grandis*. That name is preoccupied by *Planorbis grandis* DUNKER in KÜSTER et al. (1850) and therefore, NEUBAUER et al. (2014) introduced *Planorbarius halavatsi* as replacement name.

Ecology: The extant *Planorbarius corneus* (LINNAEUS, 1758) settles standing or slowly moving waters with rich vegetation in wetlands and floodplains and may tolerate periodical droughts. It prefers pH values around 6–9 (all data from WELTER-SCHULTES, 2012). In the Vienna Basin, *Planorbarius halavatsi* was exclusively found in assemblages indicating freshwater wetland lakes (HARZHAUSER & TEMPFER, 2004). The scarceness of *Planorbarius* cf. *halavatsi* in the opalite from Tschaterberg may indicate suboptimal ecological conditions.

Stratigraphic and geographic distribution: The oldest record of this species derives from the upper Pannonian of Götzendorf/Sandberg (southern Vienna Basin). The locality is correlated with the Mammal Zone MN 9 and the Pannonian Zone F sensu PAPP (1951), roughly corresponding to an age of 10.0–9.5 Ma (HARZHAUSER & TEMPFER, 2004). Younger occurrences in the Vienna Basin (Rauchenwarth, Schwadorf) are correlated with the Zone H of PAPP (1951). Coeval occurrences from the Pannonian Basin in Hungary were described by HALAVÁTS (1903), STRAUSZ (1942) and BARTHA & SOÓS (1955) from several localities in the Pannonian Basin (Balatonfőkajár, Balatonszentgyörgy, Borsosgyőr, Nyárád, Tihany, Tüskevár). These can be correlated with the lower part of the Transdanubian substage sensu SACCHI & HORVÁTH (2002). Thus, the temporal range of *P. halavatsi* is c. from 10.9–8.0 Ma.

Family Lymnaeidae RAFINESQUE, 1815

Genus *Stagnicola* JEFFREYS, 1830

Type species: *Buccinum palustre* MÜLLER, 1774. Recent, Europe.

Stagnicola sp.

Text-Fig. 3: Figs. 6–7

1929 *Pupa* sp. – BENDA, p. 38.

1957 *Limnaea* sp. – PAPP in KÜMEL, p. 8.

Material: Six silicone casts (NHMW 2019/0054/0001).

Discussion: Lymnaeids are very abundant in the opalite deposits. Usually only fragments of the spire whorls are preserved, whereas the last whorls are rarely preserved. The species from the opalite is a small lymnaeid of about 14 mm height and 5.5 mm diameter. It is very slender, has a high spire and high whorls with oblique suture. Early spire whorls are relatively convex with distinct suture. These features are reminiscent of the extraordinarily slender *Stagnicola bouilleti* (MICHAUD, 1855) as reviewed by SCHLICKUM (1970). Already KÜMEL (1957) discussed in a footnote the similarity of the Tschaterberg lymnaeids with *Stagnicola bouilleti* from the Eichkogel section in the Vienna Basin. *Stagnicola bouilleti*, however, is larger attaining more than 30 mm in height and has a straight columella and very wide basal margin, whereas the most complete Tschaterberg specimen displays a concave and twisted columella. Due to the convexity of early spire whorls, BENDA (1929) seems to have misidentified spire fragments as "*Pupa*", an outdated name often used in old literature for pupilloid terrestrial gastropods.

Ecology: Extant *Stagnicola* species prefer silent waters with rich vegetation and are found in ponds, swamps, temporary water bodies and periodically flooded areas. Some species may also stand periodical droughts (WELTER-SCHULTES, 2012). *Stagnicola* species are found in alkaline and acidic waters but are most abundant under neutral pH-conditions (SPYRA, 2017).

Stratigraphic and geographic distribution: The presence of *Stagnicola* has no stratigraphic significance.

Superorder Eupulmonata HASZPRUNAR & HUBER, 1990

Superfamily Helicoidea RAFINESQUE, 1815

Family Elonidae GITTENBERGER, 1979

Genus *Apula* BOETTGER, 1909

Type species: *Helix devexa* REUSS, 1861. Early Miocene, Czech Republic.

Apula sp.

Text-Fig. 4: Fig. 10

Material: One spire fragment in opalite, diameter: 9.1 mm (note that the last whorl is missing); collection STEFAN RAIMANN (stored in the Steinmuseum Csaterberg).

Discussion: The single available spire fragment is an internal cast with impressions of the surface sculpture con-

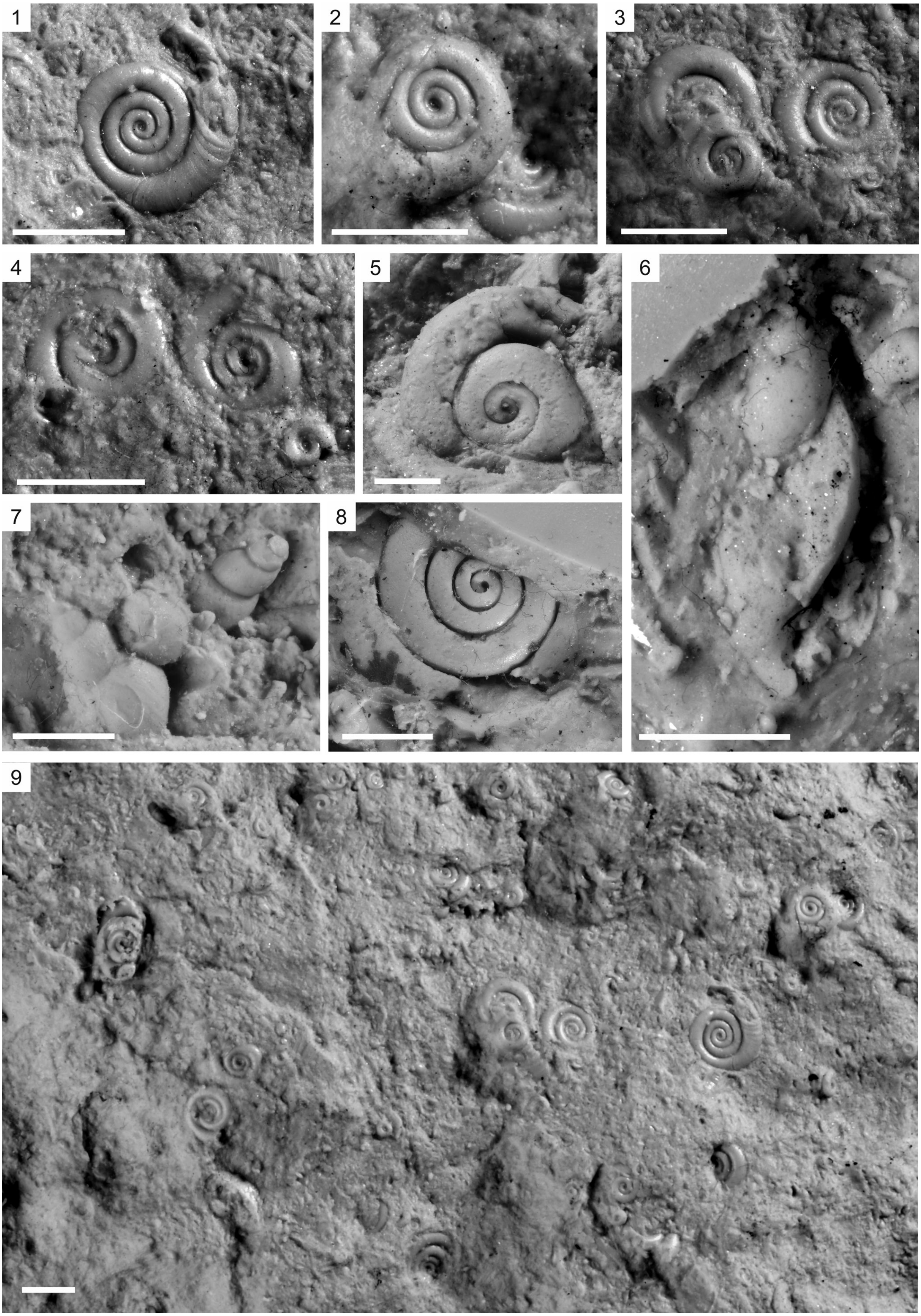
1
2
3
4
5
6
7
8
9

◀ Text-Fig. 3.
Silicone casts of gastropods from the Tschaterberg opalite. Figs. 1–4: *Anisus confusus* Soós, 1934 (NHMW 2019/0054/0002); Fig. 5: *Planorbarius* cf. *halavatsi* Neubauer, Harzhauser, Kroh, Georgopoulou & Mandic, 2014 (NHMW 2019/0054/0003); Figs. 6–7: *Stagnicola* sp. (NHMW 2019/0054/0001); Fig. 8: *Pseudochloritis* cf. *mollonensis* Truc, 1971 (NHMW 2019/0054/0004); Fig. 9: opalite surface showing several *Anisus* specimens parallel to the bedding plane (NHMW 2019/0054/0002); scale bars = 5 mm.

sisting of delicate papillae. This sculpture and the general shape of the narrowly coiled and low conical spire are reminiscent of *Apula goniostoma* (Sandberger, 1872) and *Apula vindobonensis* Harzhauser & Binder, 2004, which were both described from the late Pannonian of the Vienna Basin. These species are mainly distinguished by their peristome morphology and the width of the umbilicus. As both features are missing in the available specimen, an identification is impossible.

Ecology: *Apula* is an extinct genus. The Miocene species are generally associated with assemblages indicating forested wetlands (Harzhauser & Binder, 2004; Harzhauser et al., 2014a, b).

Stratigraphic and geographic distribution: *Apula* species occur throughout the Miocene. The specimen from the Tschaterberg is most probably conspecific with either *Apula goniostoma* (Sandberger, 1872) or *Apula vindobonensis* Harzhauser & Binder, 2004, which indicate a Pannonian age.

Genus *Pseudochloritis* Boettger, 1909

Type species: *Helix inflexa* Zieten, 1832. Miocene, Germany.

Pseudochloritis cf. *mollonensis* Truc, 1971

Text-Fig. 3: Fig. 8; Text-Fig. 4: Figs. 1–3

cf. *1971 *Tropidomphalus* (*Pseudochloritis*) *mollonensis* n. sp. – Truc, p. 275, Pl. 17, Figs. 1–7, 11–14, Pl. 18, Fig. 1.

cf. 1981 *Tropidomphalus* (*Pseudochloritis*) *zelli depressus* Wenz – Lueger, p. 59, Pl. 11, Figs. 1a–b (non Wenz, 1927).

cf. 2017 *Pseudochloritis mollensis* [sic] (Truc, 1971) – Binder, p. 220, Pl. 6, Figs. 1–6.

Material: One natural cast of a spire fragment (NHMW 2019/0054/0004) and one more complete natural internal cast, diameter: 21.3 mm, height: 13.7 mm; collection Günter Baumann (stored in the Steinmuseum Csaterberg).

Discussion: Only internal casts are available showing a medium-sized helicoid of about 22 mm in diameter. One cast shows remnants of a strongly reflected inner lip and a moderately wide umbilicus. The low conical spire consists of five moderately convex whorls, slowly increasing in width, suggesting a relatively tight coiling. The coiling of the Tschaterberg species is reminiscent of *Pseudochloritis* species, such as the Sarmatian/Pannonian *P. gigas* (Pfeffer, 1930) and the Pannonian *P. mollonensis* Truc, 1971 sensu Binder (2017). *Pseudochloritis gigas* differs in its much larger size, whereas specimens of *Pseudochloritis mollonensis* from Götzendorf an der Leitha (Austria) agree in size, outline and umbilical features. Despite this similarity, a clear identification is impossible due to the poor preservation.

Recently, Binder (2017) established *Papillotopsis* as new genus for some species formerly placed in *Pseudochloritis* based on their higher spire and typical papillae. Of these, the only Pannonian species, *Papillotopsis richarzi* (Schlosser, 1907), differs from the Tschaterberg species in its higher spire and its last two whorls are broader (see Harzhauser & Binder, 2004; Binder, 2017). *Mesodontopsis* Pilsbry, 1895 is much larger, has less convex whorls, an even flatter spire and the whorls increase rapidly in width (see also Binder, 2016). Some Miocene species of *Megalotachea* Pfeffer, 1930, such as *M. etelkae* (Halaváts, 1923) and *M. bulla* (Lueger, 1981), display a comparable type of coiling but differ in their higher spire.

Ecology: *Pseudochloritis* is an extinct genus. According to Binder (2017), all known species are bound to moist and warm woodland.

Stratigraphic and geographic distribution: *Pseudochloritis mollonensis* was described from the late Miocene (MN 9) of Mollon in France (Truc, 1971). *Pseudochloritis mollonensis* Truc, 1971 sensu Binder (2017) is documented from the late Pannonian of Götzendorf an der Leitha (MN 9), Stixneusiedl (MN 9) and Neusiedl (MN 10) (Binder, 2017).

Family Helicidae Rafinesque, 1815

Subfamily Ariantinae Mörch, 1864

Genus *Agalactochilus* Kadolsky, Binder & Neubauer, 2016

Type species: *Helix leobersdorfensis* Troll, 1907. Late Miocene, Austria.

?*Agalactochilus* sp.

Text-Fig. 4: Figs. 7–9

Material: One natural internal cast, diameter: 27.6 mm, height: 17.7 mm; collection Günter Baumann (stored in the Steinmuseum Csaterberg).

Discussion: The largest gastropod cast represents a stocky species with wide spire whorls, a high last whorl, which increases in height distinctly towards the aperture, a reflected inner lip and a moderately wide and deep umbilicus. The resulting sub-globose outline is reminiscent of *Agalactochilus* as defined by Kadolsky et al. (2016). Especially the late Miocene *A. leobersdorfensis* (Troll, 1907) agrees in size and outline, but the poor preservation does not allow a clear identification.

Ecology: *Agalactochilus* is an extinct genus. Most species seem to have preferred humid habitats along lakeshores and flood plains (Kadolsky et al., 2016).

Stratigraphic and geographic distribution: The genus is restricted to the Miocene of Europe and becomes extinct during the late Miocene (Kadolsky et al., 2016). Reliable records of *Agalactochilus leobersdorfensis* (Troll, 1907) are described from the middle and late Pannonian of the Vienna Basin (MN 9) (Kadolsky et al., 2016).

Text-Fig. 4.
Internal casts of casts of gastropods from the Tschaterberg opalite. Figs. 1–3: *Pseudochloritis* cf. *mollonensis* TRUC, 1971; Figs. 4–6: *Megalotachea* cf. *etelkae* (HALAVÁTS, 1923); Figs. 7–9: ?*Agalactochilus* sp.; Fig. 10: *Apula* sp.; all specimens stored in the Steinmuseum Csaterberg); scale bars = 5 mm.

Subfamily Helicinae RAFINESQUE, 1815

Genus *Megalotachea* PFEFFER, 1930

Type species: *Helix turonensis* DESHAYES, 1832. Miocene, France.

Megalotachea cf. _etelkae_ (HALAVÁTS, 1923)

Text-Fig. 4: Figs. 4–6

cf. *1923 *Helix* (*Tachaea*) *Etelkae* HALAVÁTS, p. 403, Pl. 14, Figs. 7a–b.

1957 *Cepaea* (*Megalotachea*) sp. – PAPP in KÜMEL, p. 8.

cf. 1981 *Cepaea* (*Cepaea*) *etelkae* (HALAVATS) – LUEGER, p. 72, Pl. 13, Figs. 1–2, Pl. 14, Figs. 1–7.

cf. 2004 *Cepaea etelkae* (HALAVÁTS 1923) – HARZHAUSER & BINDER, p. 27, Pl. 11, Figs. 20–21 (cum syn.).

Material: One natural internal cast, diameter: 18.5 mm, height; 12.8 mm; collection GÜNTER BAUMANN (stored in the Steinmuseum Csaterberg). A second internal cast is stored in the Steinmuseum Csaterberg.

Discussion: The two available specimens are characterized by their relatively high, conical spire and a faint angulation of the last whorl. A narrow but deep impression behind the peristome indicates a prominent inner lip. Size and shape agree well with high-spired specimens of *M. etelkae* from the Vienna Basin and from Öcs (Hungary) stored in the NHMW collections (see also LUEGER, 1981: Pl. 14, Figs. 4, 6, 7). Nevertheless, a reliable identification is impossible due to the poor preservation.

Ecology: *Megalotachea* is an extinct genus. According to LUEGER (1981), *M. etelkae* was a euryoecious species, which preferred moist habitats.

Stratigraphic and geographic distribution: *Megalotachea etelkae* appeared during the early Pannonian and was a common species in the Vienna and Pannonian basins. Its last records in the Vienna Basin derive from "Pannonian H" localities (e.g., Eichkogel, Velm, Schwechat) and from the Transdanubian substage in the Pannonian Basin (LUEGER, 1981; HARZHAUSER & BINDER, 2004).

Discussion

The formation of the opalite was interpreted by KÜMEL (1957) as precipitation from acidic spring water, which attained its silica by dissolution from the underlying serpentinite. Extant *Anisus* and *Stagnicola* both tolerate a wide range of pH-values, ranging from acidic to alkaline lake waters (SPYRA, 2017), whereas *Planorbarius* prefers neutral to slightly alkaline waters (WELTER-SCHULTES, 2012). Thus, the rare occurrence of *Planorbarius* would fit to slightly acidic conditions. All taxa are bound to freshwater conditions and avoid brackish waters. Therefore, we reject the interpretation of KÜMEL (1957), who assumed that the region was a marginal part of brackish Lake Pannon. Instead, the Tschaterberg opalite likely formed in a small pond or lake. Moreover, the western margin of Lake Pannon has already shifted to the Danube Basin at that time (MAGYAR et al., 2013). Similarly, the mollusk faunas mentioned by KÜMEL (1957) from the close-by upper Pannonian outcrops at Hannersdorf, lack any Lake Pannon species. The terrestrial mollusks of Tschaterberg are represented by few species of genera, which are all indicative for moist woodland, which is supported by the paleobotanical record comprising Taxodiaceae, Ulmaceae, Betulaceae, Oleaceae, Tilioideae and *Quercus* (KÜMEL, 1957).

The internal structure of a herein studied block of Tschaterberg opalite suggests at least three different phases with slightly differing ecological conditions. The first phase is represented by a peat bog with moss and reed vegetation. Numerous *in situ* stalks indicate that the silicification took place rapidly, preserving a geological snapshot. Locally, the moss-peat passes into areas in which gyttja accumulated. Planorbids and lymnaeids are found especially in samples with reed vegetation, indicating an autochthonous assemblage with minor time averaging. An interruption of the sedimentation is reflected by an erosional relief separating this first peat bog phase from the overlying layer. This "silica-iron gel" layer is poor in plant fossils and gastropods. Thus, this layer may represent a slightly deeper part of the peat bog at some distance of the reed belt. The increasing amount of leaves and other plant debris in the uppermost layer might indicate a shallowing trend. Especially, the leaf litter is rich in planorbids and lymnaeids. The erosional phase between layer 1 and 2 may either represent a short drying up phase or a change in water chemistry during a water level rise. As no indications for weathering can be found, the latter hypothesis seems to be more realistic. Due to the restricted data availability, however, it remains unclear if this succession is representative for the entire opalite occurrence or a local phenomenon at the Hoch Tschater.

The preservation and low diversity of the mollusk fauna make a reliable dating of the opalite difficult. In the Pannonian Basin, *Anisus confusus* is restricted to the lower part of the Transdanubian substage of the Pannonian, spanning an interval of ~8.9 to ~8.0 Ma (Sacchi & Horváth, 2002). *Planorbarius halavatsi* has a slightly longer range from ~10.0 to ~8.0 Ma. The *Pseudochloritis* group became extinct around the Miocene/Pliocene boundary. Therefore, a late Miocene age of the Tschaterberg opalite is most likely. The opalite lake would thus have been contemporaneous with the famous vertebrate fauna from the close-by Kohfidisch/Kirchfidisch locality, situated about 4 km southwest of the Tschaterberg. That locality represents fossiliferous marly clay in a karstic cave and fissure fillings in Paleozoic limestones and is correlated with the lower Turolian European Mammal Zone MN 11 (Daxner-Höck & Höck, 2015). The late Miocene age clearly excludes any influence of the much younger Dacian volcanism, as hypothesized by Sauerzopf et al. (1990) and Pahr (2000).

Conclusions

The opalite from the Tschaterberg region close to Kohfidisch formed in a small freshwater lake or pond, which was settled by a low-diversity mollusk fauna of planorbids and lymnaeids. Likely, all taxa were adapted to periodic droughts and preferred the vegetated zone of the lake. The opalite displays a threefold internal succession, which might indicate a sequence of establishment of reed vegetation in a very shallow peat bog, a slight increase of the water level coinciding with a decrease in plant fossils and gastropods and a subsequent shallowing with gyttja and peat formation and the development of large populations of lymnaeids and planorbids. The rare terrestrial gastropods indicate a moist and warm forest surrounding the lake.

The fauna suggests a late Miocene age corresponding to the Pannonian Zone H of Papp (1951) and the Transdanubian substage of Sacchi & Horváth (2002). During that time, the western coast of Lake Pannon had already shifted towards the Danube Basin and, therefore, the freshwater lakes that formed in the Tschaterberg, Kohfidisch and Hannersdorf area were hydrologically disconnected from Lake Pannon.

Acknowledgements

We thank Herbert Binder (NHMW) for his valuable comments and suggestions concerning the terrestrial taxa. We are grateful to Pfarrer Stefan Raimann (Hornstein) who provided access to the collection of the Steinmuseum Csaterberg (Klein Csater 10, 7512 Kohfidisch). Many thanks to Peter Schebeczek (Pellendorf, NÖ) and Josef Kroiher (St. Florian, OÖ) who provided material from the studied locality. Thomas Hofmann (Geological Survey of Austria), Sonja Herzog-Gutsch (NHMW), Christa Riedl-Dorn (NHMW) and Peter Huber (Wien) helped with rare literature. Photos were taken by Alice Schumacher (NHMW) and Alexander Lukeneder (NHMW). Many thanks go to Imre Magyar (MOL, Hungary) and Lajos Katona (Natural History Museum of the Bakony Mountains, Hungary) for discussions and pictures of syntypes of *Anisus confusus*. Thomas A. Neubauer was supported by an Alexander-von-Humboldt scholarship.

References

Bartha, F. (1954): Die pliozäne Molluskenfauna von Öcs. – A Magyar Állami Földtani Intézet Évkönyve, **42**, 167–207, Budapest.

Bartha, F. (1959): Finomrétegtani vizsgálatok a Balaton környéki felsö-pannon képzödményeken [Feinstratigraphische Untersuchungsmethoden am Oberpannon der Balatongegend]. – A Magyar Állami Földtani Intézet Évkönyve, **48**/1, 1–239, Budapest.

Bartha, F. & Soós, L. (1955): Die pliozäne Molluskenfauna von Balatonszentgyörgy. – Annales historico-naturales Musei Nationalis Hungarici, **47** (series nova **6**), 51–72, Budapest.

Benda, L. (1929): A Vashegy-Csoport geológiája (Geologie der Eisenberg-Gruppe). – Acta Savariensia, **1**, 1–62, Szombathely.

Binder, H. (2016): Die fossile Gattung *Mesodontopsis* Pilsbry 1894–1895 in Mitteleuropa. – Jahrbuch der Geologischen Bundesanstalt, **156**/1–4, 109–126, Wien.

Binder, H. (2017): *Pseudochloritis* und *Papillotopsis* (nov. gen.) im Miozän Zentraleuropas. – Jahrbuch der Geologischen Bundesanstalt, **157**/1–4, 215–239, Wien.

Boettger, C.R. (1909): Ein Beitrag zur Erforschung der europäischen Heliciden. – Nachrichtsblatt der deutschen Malakozoologischen Gesellschaft, **41**/1, 1–19, Frankfurt am Main.

Burmeister, H. (1837): Handbuch der Naturgeschichte, **2**, xii + pp. 369–858, Berlin (Enslin).

Clusius, C. (1583): Rariorum aliquot Stirpium per Pannoniam, Austriam, & vicinas quasdam Prouincias obseruatarum Historia. – 766 pp. + unnumbered appendix and index, Christophori Plantini, Antverpiae.

CLUSIUS, C. (1601): Rariorum Plantarum Historia. Quae acceßerint, proxima pagina docebit. – 364 + cccxlvii pp. + unnumbered index, Plantiniana, Antverpiae.

DAXNER-HÖCK, G. & HÖCK, E. (2015): Rodentia neogenica. – Catalogus Fossilium Austriae, **4**, XXVI + 158 pp., 77 Pls., Österreichische Akademie der Wissenschaften, Wien.

DESHAYES, G.P. (1832): Encyclopédie méthodique ou par ordre de matières. Histoire naturelle des Vers et Mollusques, **2**, 145–594, Agasse, Paris.

DUMÉRIL, A.M.C. (1805): Zoologie analytique, ou méthode naturelle de classification des animaux, rendue plus facile à l'aide de tableaux synoptiques. – xxxiii + 344 pp., Allais, Paris.

DUNKER, W. (1848): Über die in der Molasse bei Günzberg unfern Ulm vorkommenden Conchylien und Pflanzenreste. – Palaeontographica, **1**, 155–168, Cassel.

FELIX, J. (1884): Die Holzopale Ungarns in palaeophytologischer Hinsicht. – Mittheilungen aus dem Jahrbuche der königlichen ungarischen Geologischen Anstalt, **7**, 1–43, Budapest.

FÉRUSSAC, A.E.J.P.J.F. D'AUDEBARD DE (1821–1822): Tableaux systématiques des animaux mollusques classés en familles naturelles, dans lesquels on a établi la concordance de tous les systèmes; suivis d'un prodrome général pour tous les mollusques terrestres ou fluviatiles, vivants ou fossiles. – 110 pp., Paris–Londres (Bertrand, Sowerby).

FISCHER, P. & TOURNOUËR, R. (1873): Invertebrés fossiles du Mont Léberon. – In: GAUDRY, A., FISCHER, P. & TOURNOUËR, R.: Animaux fossiles du Mont Léberon (Vaucluse), 113–172, Paris (F. Savy).

FORDINÁL, K. (1998): Freshwater gastropods of the Upper Pannonian age in the northern part of the Danube basin. – Slovak Geological Magazine, **4**, 293–300, Bratislava.

GITTENBERGER, E. (1979): On *Elona* (Pulmonata, Elonidae fam. nov.). – Malacologia, **18**, 139–145, Ann Arbor, Michigan.

GLÖER, P. & GROH, K. (2007): A contribution to the biology and ecology of the threatened species *Anisus vorticulus* (TROSCHEL, 1834) (Gastropoda: Pulmonata: Planorbidae). – Mollusca, **25**, 33–40, Dresden.

GÖTZINGER, M.A. & PRISTACZ, H. (2009): Die Opale von Kohfidisch – Csaterberg. – In: GÖTZINGER, M.A. (Ed.): Die Mineralien des Burgenlandes: Geologie, Mineralogie und mineralische Rohstoffe, 162–169, Amt der Burgenländischen Landesregierung, Eisenstadt.

GRATZER, R. (1985): Vergleichende Untersuchungen an Metabasiten im Raum Hannersdorf, Burgenland. – Sitzungsberichte der mathematisch-naturwissenschaftlichen Klasse der Akademie der Wissenschaften, **194**, 131–148, Wien.

HALAVÁTS, G. VON (1903): Die Fauna der pontischen Schichten in der Umgebung des Balatonsees. – Resultate der wissenschaftlichen Erforschung des Balatonsees, **1**/1, 1–80, Budapest.

HALAVÁTS, G. VON (1923): A baltavarsi felsöpontusi koru Molluszkafauna. – A Magyar Állami Földtani Intézet Évkönyve, **24**, 395–407, Budapest.

HARZHAUSER, M. & BINDER, H. (2004): Synopsis of the Late Miocene mollusc fauna of the classical sections Richardhof and Eichkogel in the Vienna Basin. – Archiv für Molluskenkunde, **133**/1–2, 109–165, Frankfurt am Main.

HARZHAUSER, M. & TEMPFER, P.M. (2004): Late Pannonian Wetland ecology of the Vienna Basin based on Molluscs and Lower Vertebrate assemblages (Late Miocene, MN 9, Austria). – Courier Forschungsinstitut Senckenberg (CFS), **246**, 55–68, Stuttgart.

HARZHAUSER, M., NEUBAUER, T.A., GEORGOPOULOU, E. & HARL, J. (2014a): The Early Miocene (Burdigalian) mollusc fauna of the North Bohemian Lake (Most Basin). – Bulletin of Geosciences, **89**, 819–908, Prague.

HARZHAUSER, M., NEUBAUER, T.A., GROSS, M. & BINDER, H. (2014b): The early Middle Miocene mollusc fauna of Lake Rein (Eastern Alps, Austria). – Palaeontographica A, **302**, 1–71, Stuttgart.

HASZPRUNAR, G. & HUBER, G. (1990): On the central nervous system of Smeagolidae and Rhodopidae, two families questionably allied with the Gymnomorpha (Gastropoda, Euthyneura). – Journal of Zoology, **220**, 185–199, London.

HOFFMANN, K. (1877): Mittheilungen der Geologen der k. ungarischen Anstalt über ihre Aufnahmsarbeiten im Jahre 1876. – Verhandlungen der k. k. Geologischen Reichsanstalt, **1877**, 14–24, Wien.

HOFMANN, E. (1928): Verkieselte Hölzer aus dem Museum Szombathely. – Annales Musei comitatus Castriferrei, Sectio Hist. Nat., 9–11, Szombathely.

HOFMANN, E. (1929): Kövült fák a Vashegy csoportjából. Verkieselte Hölzer von der Vashegy (Eisenberg)-Gruppe. – Acta Savariensia, **3**, 81–87, Szombathely.

HORVÁTH, E. (1973): Vom *Lithoxylon* des Clusius und dessen Fundort in der späteren Fachliteratur. – Burgenländische Forschungen, Clusius Festschrift, Sonderheft, **5**, 182–195, Eisenstadt.

JEFFREYS, J.G. (1830): A synopsis on the testaceous pneumonobranchous Mollusca of Great Britain. – Transactions of the Linnean Society of London, **16**, 323–392, London.

KADOLSKY, D., BINDER, H. & NEUBAUER, T.A. (2016): Taxonomic review of the fossil land gastropod species hitherto placed in the genus *Galactochilus* SANDBERGER 1875, with the description of a new genus (Gastropoda: Helicoidea). – Archiv für Molluskenkunde, **145**, 151–188, Frankfurt am Main.

KÜMEL, F. (1957): Der Süßwasseropal der Csatherberge im Burgenlande: zur Geologie, Paläobotanik und Geochemie seltener Quellabsätze. – Jahrbuch der Geologischen Bundesanstalt, **100**, 1–66, Wien.

KÜSTER, H.C., DUNKER, W. & CLESSIN, S. (1841–1886): Die Familie der Limnaeiden enthaltend die Genera *Planorbis, Limnaeus, Physa* und *Amphipeplea*. – Systematisches Conchylien Cabinet (Ed. 2), **1**/17, 1–28, Nürnberg (Bauer & Raspe).

LINNAEUS, C. (1758): Systema naturae per regna tria naturae, secundum classes, ordines, genera, species, cum characteribus, differentiis, synonymis locis. Tomus 1. – 10th edition, 824 pp., Holmia (Laurentius Salvius).

LOCARD, A. (1883): Recherches paléontologiques sur les dépôts tertiaires à *Milne-Edwardsia* et *Vivipara* du Pliocène inférieur du département de l'Ain. – Annales de l'Académie de Mâcon, IIe Série, **6**, 2–166, Mâcon.

LÖRENTHEY, E. (1894): Die Pontische Fauna von Kurd im Comitate Tolna. – Földtani Közlöny, **24**, 73–88, 148–161, Budapest.

LUEGER, J.P. (1981): Die Landschnecken im Pannon und Pont des Wiener Beckens I. Systematik, II. Fundorte, Stratigraphie, Faunenprovinzen. – Denkschriften der mathematisch-naturwissenschaftlichen Klasse der Akademie der Wissenschaften, **120**, 1–124, Wien.

MAGYAR, I., RADIVOJEVIĆ, D., SZTANÓ, O., SYNAK, R., UJSZÁSZI, K. & PÓCSIK, M. (2013): Progradation of the paleo-Danube shelf margin across the Pannonian Basin during the Late Miocene and Early Pliocene. – Global and Planetary Change, **103**, 168–173, Amsterdam.

MICHAUD, G. (1855): Descriptions de coquilles fossiles découvertes dans les environs de Hauterive (Drôme). – Annales de la Societé Linnéenne de Lyon, N.S., **2**, 33–64, Lyon.

MICHAUD, G. (1862): Description des Coquilles fossiles des environs de Hauterive (Drôme). – Journal de Conchyliologie, **10**, 58–84, Paris.

MILLET, P.A. (1813): Mollusques terrestres et fluviatiles, observés dans le Département de Maine et Loire. – 11 + 82 pp., Angers (Pavie).

MÖRCH, O.A.L. (1864): Fortegnelse over de i Danmark forekommende land- og ferskvandsblöddyr. – Videnskabelige Meddelelser fra den Naturhistoriske Forening i Kjöbenhavn, **1863**, 265–367, Kjöbenhavn.

MÜLLER, O.F. (1773–1774): Vermivm terrestrium et fluviatilium, seu animalium infusoriorum, helminthicorum et testaceorum, non marinorum, succincta historia. – xxxiii + 135, xxxvi + 214 pp., Heineck & Faber, Havniae & Lipsiae.

MÜLLER-STOLL, W.R. & MÄDEL, E. (1957): Über tertiäre Eichenhölzer aus dem pannonischen Becken. – Senckenbergiana Lethaea, **38**, 121–168, Frankfurt am Main.

MÜLLER-STOLL, W.R. & MÄDEL, E. (1959): Betulaceen-Hölzer aus dem Tertiär des pannonischen Beckens. – Senckenbergiana Lethaea, **40**, 159–209, Frankfurt am Main.

NEUBAUER, T.A., HARZHAUSER, M., KROH, A., GEORGOPOULOU, E. & MANDIC, O. (2014): Replacement names and nomenclatural comments for problematic species-group names in Europe's Neogene freshwater Gastropoda. Part 2. – Zookeys, **429**, 13–46, Sofia.

PAHR, A. (2000): Kohfidisch Csaterberg. – In: SCHÖNLAUB, H.P. (Ed.): Erläuterungen zur Geologischen Karte des Burgenlandes 1:200.000. Geologie der Österreichischen Bundesländer, 116, Geologische Bundesanstalt, Wien.

PAPP, A. (1951): Das Pannon des Wiener Beckens. – Mitteilungen der Geologischen Gesellschaft in Wien, **39–41** (1946–1948), 99–193, Wien.

PAVLICEK, P. (2009): Korrektur der Beschreinbung eines fossilen Platanen-Wurzelholzes vom Csatherberg bei Kohfidisch im Süd-Burgenland Österreich. – Mitteilungsblatt der Mikroskopischen Gesellschaft Wien, **1/2009**, 8–18, Wien.

PFEFFER, G. (1930): Zur Kenntnis tertiärer Landschnecken. – Geologische und Paläontologische Abhandlungen, **21** (N.F. **17**), 151–380, Jena.

PILSBRY, H.A. (1894–1895): Manual of Conchology: Structural and Systematic, with illustrations of the species. Second series: Pulmonata. Vol. IX. (Helicidae Vol. 7). Guide to the study of Helices. – 366 pp., Academy of Natural Sciences of Philadelphia, Philadelphia.

PRYSJAZHNJUK, V.A. (1974): Pervaya v SSSR nakhodka planorbid podroda *Odontogyrorbis*. – Paleontologicheskiy zbornik, **10**, 51–56, Lviv.

RAFINESQUE, C.S. (1815): Analyse de la nature ou tableau de l'univers et des corps organisés. – 223 pp., Palermo (privately published).

REUSS, A.E. (1861): Die fossilen Mollusken der tertiären Süsswasserkalke Bohmens. – Sitzungsberichte der mathematisch-naturwissenschaftlichen Klasse der kaiserlichen Akademie der Wissenschaften, **42**, 55–84, Wien.

ROSSMÄSSLER, E.A. (1835–1837): Iconographie der Land- und Süßwasser-Mollusken, mit vorzüglicher Berücksichtigung der europäischen noch nicht abgebildeten Arten. – Erster Band: 1 (1): VI + 1–132, Pls. 1–5 [1835]; (1) 1 (2): 6 + 1–26, Pls. 6–10 [1835]; (1) 1 (3): 4 + 1–33, Pls. 11–15 [1836]; (1) 1 (4): 4 + 1–27, Pls. 16–20 [1836]; (1) 1 (5/6): 4 + 1–70, Pls. 21–30 [1837], Dresden–Leipzig (Arnold).

SACCHI, M. & HORVÁTH, F. (2002): Towards a new time scale for the Upper Miocene continental series of the Pannonian basin (Central Paratethys). – EGU Stephan Mueller Special Publication Series, **3**, 79–94, Göttingen.

SANDBERGER, F. (1872): Die Land- und Süsswasser-Conchylien der Vorwelt. – Heft 6–8, 161–256, Pls. 21–32, Wiesbaden (C.W. Kreidel).

SAUERZOPF, F. (1953): Die Planorbidae aus dem Pannon des Alpenostrandes. – Burgenländische Heimatblätter, **15**/2, 49–66, Eisenstadt.

SAUERZOPF, F., SCHÖNLAUB, H-P., GRATZER, R.W. & ZETTER, R. (1990): Exkursion B3. Wandertagung 1990 der Österreichischen Geologischen Gesellschaft in Bernstein: mit Exkursionen in das Kristallin und das Tertiär am Alpenostrand Österreichs und im ungarischen Grenzgebiet, 120–125, Geologische Bundesanstalt, Wien.

SCHLICKUM, W.R. (1970): Zur Molluskenfauna der Brackwassermolasse Niederbayerns. 3. Was ist *Lymnaea bouilleti* MICHAUD? – Archiv für Molluskenkunde, **100**, 89–94, Frankfurt am Main.

SCHLICKUM, W.R. (1978): Zur oberpannonen Molluskenfauna von Öcs, I. – Archiv für Molluskenkunde, **108**, 245–261, Frankfurt am Main.

SCHLOSSER, M. (1907): Die Land- und Süsswassergastropoden vom Eichkogel bei Mödling. Nebst einer Besprechung der Gastropoden aus dem Miocän von Rein in Steiermark. – Jahrbuch der k. k. Geologischen Reichsanstalt, **57**, 753–792, Wien.

SOÓS, L. (1934): Az Öcsi felső-pontusi Mollusca-fauna. – Állattani Közlemények, **31**/3–4, 183–210, Budapest.

SPYRA, A. (2017): Acidic, neutral and alkaline forest ponds as a landscape element affecting the biodiversity of freshwater snails. – The Science of Nature, **104**, 73 (12 pp.), Berlin–Heidelberg.

STRAUSZ, L. (1942): Das Pannon des mittleren Westungarns. – Annales historico-naturales musei nationalis Hungarici, pars mineralogica, geologica et palaeontologica, **35**, 1–102, Budapest.

STUDER, S. (1820): Kurzes Verzeichniss der bis jetzt in unserm Vaterlande entdeckten Conchylien. – Naturwissenschaftlicher Anzeiger der Allgemeinen Schweizerischen Gesellschaft für die Gesammten Naturwissenschaften, **3**/11, 83–90, 91–94, Bern.

TROLL, O.R. VON (1907): Die pontischen Ablagerungen von Leobersdorf und ihre Fauna. – Jahrbuch der k. k. Geologischen Reichsanstalt, **57**, 33–90, Wien.

TRUC, G. (1971): Helicidae nouveaux du Miocene superieur bressan; reflexions sur le genre *Tropidomphalus* (Gastropoda: Euthyneura). – Archiv für Molluskenkunde, **101**/5–6, 275–287, Frankfurt am Main.

WELTER-SCHULTES, F. (2012): European non-marine molluscs, a guide for species identification. – 674 pp, Göttingen (Planet Poster Editions).

WENZ, W. (1927): Weitere Beiträge zur Fauna der pontischen Schichten von Leobersdorf. – Senckenbergiana, **9**, 41–48, Frankfurt am Main.

WENZ, W. & EDLAUER, A. (1942): Die Molluskenfauna der oberpontischen Süßwassermergel vom Eichkogel bei Mödling, Wien. – Archiv für Molluskenkunde, **74**/2–3, 82–98, Frankfurt am Main.

ZIETEN, C.H. VON (1830–1833): Die Versteinerungen Württembergs, oder naturgetreue Abbildungen der in den vollständigsten Sammlungen, namentlich der in dem Kabinet des Oberamts-Arzt Dr. Hartmann befindlichen Petrefacten, mit Angabe der Gebirgs-Formationen, in welchen dieselben vorkommen und der Fundorte. – i–viii + 1–16, Taf. 1–12 (1830); 17–32, Taf. 13–24 (1831); 33–64, Taf. 25–48 (1832); 65–102, Taf. 49–72 (1833), Stuttgart (Verlag & Lithographie der Expedition des Werkes unserer Zeit).

Received: 12. April 2019, accepted: 17. September 2019

JAHRBUCH DER GEOLOGISCHEN BUNDESANSTALT
Jb. Geol. B.-A. | ISSN 0016–7800 | Band 159 | Heft 1–4 | S. 175–201 | Wien, Dezember 2019

Facies changes of the Upper Triassic–Lower Cretaceous Hödl-Kritsch quarry (Lunz Nappe, Northern Calcareous Alps, Austria)

Alexander Lukeneder[1], Petra Lukeneder[1], Luka Gale[2], Ágnes Görög[3] & Daniela Reháková[4]

2 Text-Figures, 6 Plates

Österreichische Karte 1:50.000
BMN / UTM
58 Baden / NM 33-12-25 Baden

Facies change
Carbonate sedimentology
Upper Triassic to Lower Cretaceous
Rhaetian to Berriasian
Lunz Nappe
Northern Calcareous Alps

Contents

Abstract

Detailed palaeontological, lithological and facies studies of a Mesozoic succession within the Lunz Nappe (Hödl-Kritsch section, Northern Calcareous Alps, Lower Austria) uncovered new details on the facies of the Upper Triassic to Lower Cretaceous. The outcrop is situated in an abandoned quarry within the easternmost Flössel Syncline (northern part of the Lunz Nappe, High Bajuvaric Unit), which is formed of Upper Triassic dolomites, the Kössen Formation and Rhaetian limestone, followed by a reduced Jurassic sequence with Klaus Formation, Tegernsee limestone, and Ammergau Formation. The core of the Flössel Syncline consists of the Lower Cretaceous Schrambach Formation. The outcrop provides Upper Triassic (Rhaetian) to Lower Cretaceous (Berriasian) formations and lithologies. The detailed investigation of

1 Alexander Lukeneder, Petra Lukeneder: Museum of Natural History Vienna, Burgring 7, 1010 Vienna, Austria. alexander.lukeneder@nhm-wien.ac.at, petra.lukeneder@gmx.at
2 Luka Gale: Faculty of Natural Sciences and Engineering, Department of Geology, Aškerčeva 12, SI-1000 Ljubljana, Slovenia, and Geological Survey of Slovenia, Dimičeva 14, SI-1000 Ljubljana, Slovenia. luka.gale@geo.ntf.uni-lj.si
3 Ágnes Görög: Eötvös Loránd University, Palaeontological Department; Pázmány Péter sétány 1/c, 1117 Budapest, Hungary. gorog@ludens.elte.hu
4 Daniela Reháková: Comenius University, Faculty of Natural Sciences, Department of Paleontology, Ilkovičova 6, SK-842 15 Bratislava, Slovakia. daniela.rehakova@uniba.sk

microfacies and fossil content is new for the Hödl-Kritsch quarry and for the first time allows precise biostratigraphy of the Triassic to Cretaceous succession. Two main hiati can be recognized in the succession: one marked by a stromatolitic layer at the top of the reefal Upper Triassic limestones (uppermost Rhaetian to Bajocian), and a second one in the upper Lower Tithonian (between the *Parastomiosphaera malmica* and the *Chitinoidella* Zone) marked by intense reworking at the erosive base of the red limestones in the Lower Tithonian.

Fazieswechsel in der Obertrias- bis Unterkreide-Schichtfolge des Hödl-Kritsch Steinbruchs (Lunz-Decke, Nördliche Kalkalpen, Österreich)

Zusammenfassung

Detaillierte paläontologische, lithologische and fazielle Untersuchungen einer Mesozoischen Abfolge aus der Lunz-Decke (Lokalität Hödl-Kritsch, Nördliche Kalkalpen, Niederösterreich) enthüllten neue Details zur Fazies der späten Trias bis zur jüngeren Kreide. Der Aufschluss liegt in einem aufgelassenen Steinbruch innerhalb der östlichsten Flössel Mulde (nördlicher Teil der Lunz-Decke, Hochbajuvarikum). Die Mulde wird aus Dolomiten, der Kössen-Formation und rhätischen Kalken der späten Trias aufgebaut, gefolgt von einer reduzierten jurassischen Abfolge der Klaus-Formation, der Tegernseer Kalke und der Ammergau-Formation. Der Kern der Flössel Mulde besteht aus der unterkretazischen Schrambach-Formation. Der Aufschluss bietet Formationen und Lithologien der Obertrias (Rhätium) bis Unterkreide (Berriasium). Die detaillierte Untersuchung der Mikrofazies und des Fossilinhalts ist neu für den Steinbruch Hödl-Kritsch und erlaubt erstmals eine exakte biostratigrafische Einstufung der Trias- bis Kreideabfolge. Zwei große biostratigrafische Lücken können dabei beobachtet werden: eine wird dabei durch eine markante Stromatolithenlage am Top der triassischen Riffkalke gekennzeichnet (spätes Rhätium bis Bajocium), eine zweite Lücke markiert den Kontakt zwischen dem grauen Top der Klaus-Formation im frühen Tithonium und der erosiven Basis der roten Tegernsee Kalke im späten Tithonium (zwischen *Parastomiosphaera malmica*- und der *Chitinoidella*-Zone).

Introduction

Upper Triassic, Jurassic, and Lower Cretaceous shallow-water limestones and pelagic to hemipelagic sediments are known to form a significant element of the northernmost tectonic units of the Northern Calcareous Alps (e.g., Ternberg-, Reichraming-, Frankenfels-, and Lunz nappes; TOLLMANN, 1976, 1985; EGGER, 1988; EGGER & FAUPL, 1999; VAŠÍČEK & FAUPL, 1999; see also PILLER et al., 2004). However, sections with well-preserved and documented transitions from the Upper Triassic to the Jurassic and to the Lower Cretaceous sequences are rare in the Northern Calcareous Alps. The Hödl-Kritsch locality (northern Lunz Nappe, Lower Austria; Text-Fig. 1) comprises Hauptdolomit (Norian), “Plattenkalk” (Norian), Kössen Formation (Rhaetian), Rhaetian limestones (Rhaetian), Klaus Formation (Bajocian–lower Oxfordian), Ruhpolding Radiolarite Group (Oxfordian), Tegernsee limestones (Late Tithonian), Ammergau Formation (Tithonian–Berriasian), and the Schrambach Formation (Berriasian–Valanginian). Lithologies and formations of the area and distinct parts of the Hödl-Kritsch quarry (Neumühle quarry) were previously described by TOULA (1871, 1879), SPITZ (1910), ROSENBERG (1965), KRYSTYN (1970, 1971, 1972), PLÖCHINGER &

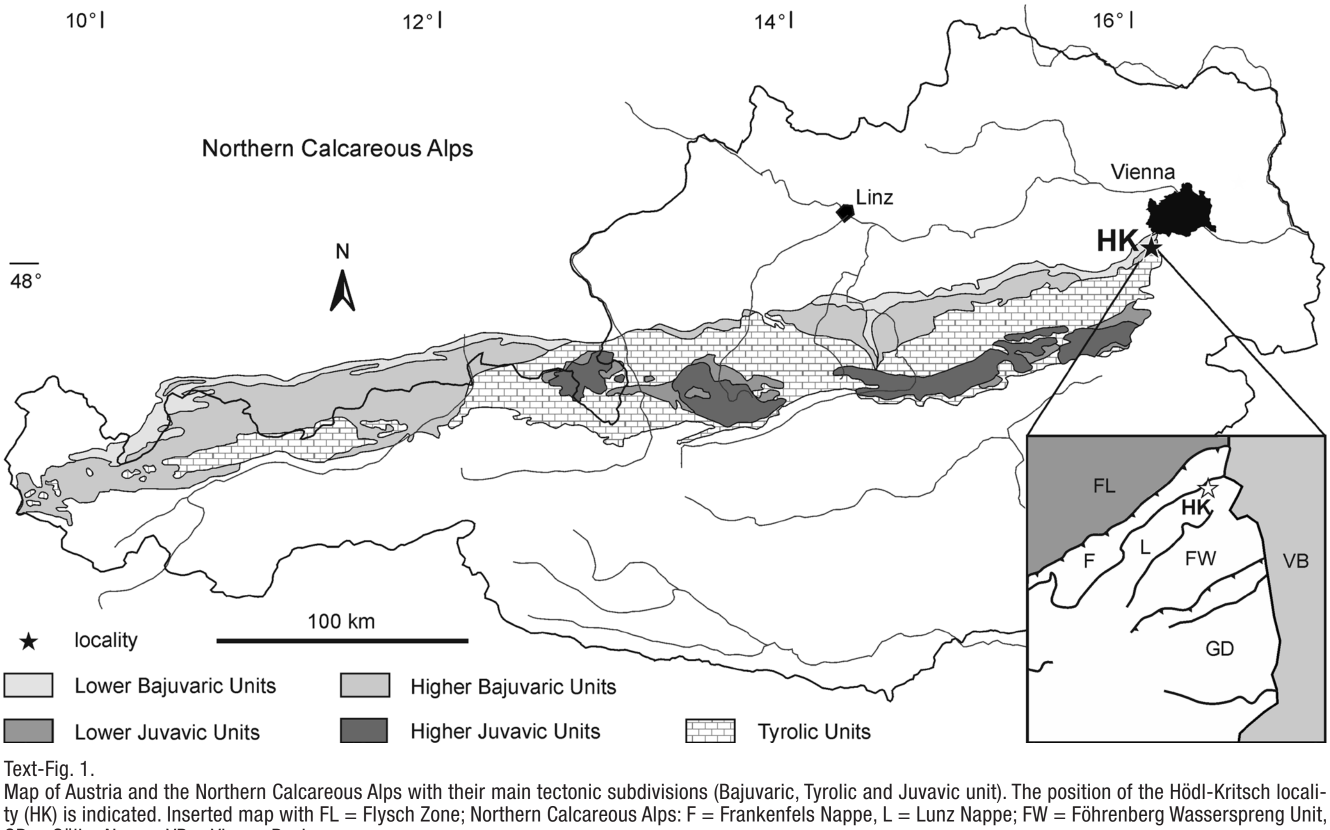

Text-Fig. 1.
Map of Austria and the Northern Calcareous Alps with their main tectonic subdivisions (Bajuvaric, Tyrolic and Juvavic unit). The position of the Hödl-Kritsch locality (HK) is indicated. Inserted map with FL = Flysch Zone; Northern Calcareous Alps: F = Frankenfels Nappe, L = Lunz Nappe; FW = Föhrenberg Wasserspreng Unit, GD = Göller Nappe; VB = Vienna Basin.

Prey (1993), Plöchinger & Karanitsch (2002), Wessely (2006) and Egger & Wessely (2014). Comparable occurrences of similar sequences and sections were described from various regions in Austria (Tollmann, 1976; Wessely, 2006). No microfacies and foraminifera transitions were described in detail or figured until now from the classic Hödl-Kritsch quarry of the Lunz Nappe.

In this paper, we present a detailed study of the Hödl-Kritsch quarry succession comprising marly limestones and limestones of the Kössen Formation, the Rhaetian Limestone Unit, Klaus-, Tegernsee-, and Ammergau formations (Text-Fig. 2). Micro- and macrofossils are determined herein to provide biostratigraphic framework. Three main stratigraphical and lithological units can be subsequently observed: A, the transition from Triassic (Rhaetian) shallow-water limestones into, after a gap, the condensed limestones of the Klaus Formation (Bajocian–lower Oxfordian); B, the transition from the Klaus Formation into deep water radiolaria-rich limestones of the Tegernsee limestone (Kimmeridgian–Tithonian); C, the transition from the red condensed limestones into hemipelagic to pelagic red to grey limestones of the Ammergau Formation (Tithonian–Berriasian). The latter in turn passes to Schrambach Formation (Berriasian–Valanginian), which, however, was not logged in this study. The new faunal record increases the knowledge on the Triassic/Jurassic and Jurassic/Cretaceous transitions from the Northern Calcareous Alps, especially aiding in better understanding of the Mesozoic environments and facies zonation in the Bajuvaric units. The Hödl-Kritsch section may be a standard reference for the Upper Triassic to Jurassic drowning of Alpine carbonate platforms.

Geographic setting

The outcrop Hödl-Kritsch (340 m above sea level) is located in the municipality Perchtoldsdorf (postcode A 2380) 3 km northwest of Kaltenleutgeben within the Lunz Nappe in Lower Austria, at the border to Vienna, south of the Dürre Liesing creek (Schnabel et al., 1997: 1:50,000, sheet 58 Baden; Austromap Online, 2019; Text-Fig. 1). The steep walls of the abandoned quarry are exposed on the northern flank of Mount Bierhäuslberg (488 m). The exact position of the ammonite locality (Klaus Formation) was determined by GPS (global positioning system): N 48°7'44.50" and E 16°14'29.10". The site can only be accessed with the permission of the owner, the Ökotechna – Entsorgungs- und Umwelt GmbH in Perchtoldsdorf (manager Bernd Hajek).

Geological situation

Classically, the Northern Calcareous Alps (NCA) are subdivided from north to south into the Lower and Upper Bajuvaric units, the Tyrolic Unit, and the Lower and Upper Juvavic units (Text-Fig. 1; Wagreich et al., 2008). The northernmost tectonic elements of the NCA are the Ternberg and Frankenfels nappes, followed subsequently to the south by the Reichraming and Lunz nappes. The Weyrer arcs ("Weyerer Bögen") at the Upper Austrian/Lower Austrian boundary separate the Ternberg and Reichraming nappes to the west from the eastern tectonic equivalents with the Frankenfels and Lunz nappes (Tollmann, 1964, 1976; Steiner, 1968; Oberhauser, 1980; Ehrendorfer, 1988; Decker et al., 1994; Egger & Faupl, 1999; Janda, 2000; Faupl et al., 2003). Upper Triassic to Lower Cretaceous pelagic sediments are known to form a significant element of the Ternberg, Reichraming, Frankenfels, and Lunz nappes (Lukeneder, 2003, 2005).

The Upper Triassic to Lower Cretaceous Hödl-Kritsch section is located in the westernmost part of the Flössel Syncline (Höllenstein Unit, Geological map 1:50,000, sheet 58 Baden, Schnabel et al., 1997; Text-Fig. 1). The Flössel Syncline is the northernmost Jurassic/Cretaceous Syncline of the Lunz Nappe followed by the Höllenstein Anticline in the north and the Teufels Anticline to the south. The Lunz Nappe (High-Bajuvaric Unit of the Northern Calcareous Alps) is bordered to the north by the Frankenfels Nappe, and to the south by the Upper Cretaceous Giesshübel Syncline and the Tyrolic units of the Göller Nappe (Schnabel et al., 1997). The complete succession within the Flössel Syncline (see Schnabel et al., 1997; Lukeneder, 2003, 2005; Lukeneder & Schlagintweit, 2005; Lukeneder & Smrecková, 2006; Wessely, 2006) includes a Mesozoic succession from the Norian up to the Barremian.

Previous biostratigraphic research

The investigated succession was previously researched only for ammonites. Biostratigraphic ammonite data from the area around the Hödl-Kritsch quarry ("Öder Saugraben") were already given by Štúr (1860), and more detailed reported by Toula (1871, 1879), later reproduced by Spitz (1910). The most prominent outcrop with abundant ammonites was the "Öder Saugraben" quarry. Toula (1871) noted that the locality was described as the "Klauslokalität bei Kaltenleutgeben" or erroneously from the wrong local description as "Öder Saugraben". In this outcrop Upper Triassic (Rhaetian), Middle Jurassic ("Dogger") and Upper Jurassic ("Malm") formations occur. There is no doubt that the ammonite layer from this outcrop, described as "Doggerian" ammonite bed with abundant ammonite specimens, coated by limonitic crusts, is identical with the ammonite layers described by Krystyn (1971, 1972) from the nearby Hödl-Kritsch quarry. Indeed, the expansion of the quarry from Hödl-Kritsch in the 1960s "absorbed" the classic "Öder Saugraben" locality which since then does not exist. The fauna from the "Öder Saugraben" quarry was assumed to be of Bathonian in age (Toula, 1871). All described specimens from Krystyn (1971, 1972) derive from the boundary zone (30 cm thick interval with layers H1–H4) at the base of the Klaus Formation, immediately overlying the Rhaetian coraline limestone (= limestone with *Rhetiophyllia*, former "Thecosmilien Kalk"). Reinvestigation of the collection, housed in the Natural History Museum Vienna (NHMW) shows, that most ammonites are in contact with the stromatolitic bed (Hkrstromatolite) described herein. Krystyn (1971) reported very dense packings of approximately 30 ammonite specimens per square metre. The condensed layers show uppermost Bajocian (H1 and H2, *Parkinsonia parkinsoni* Zone) to uppermost Bathonian (H2 and H3, *Zigzagiceras zigzag* Zone; H4, middle to upper Bathonian). According to Krystyn (1972), the upper Bathonian *Oxycerites aspidoides* and the *Prohecticoceras retrocostatum* zones could be detected. The filamentous Klaus Formation (layer b in Krystyn, 1970; renamed as layer c in Krystyn, 1972), following the ammonite and stromatolite layer, appears to be lower Callovian, while the top of the Klaus Formation with the grey *Protoglobigerina* limestones (layer c in Krystyn, 1970; renamed as layer d and "Reitmauerkalk" in Krystyn, 1972) is already of Oxfordian age (Krystyn, 1971, 1972).

Material and methods

The now abandoned Hödl-Kritsch quarry was sampled in two sections, and a combined section of almost 50 m thickness was reconstructed (Text-Fig. 2). Sedimentologic and lithologic features were described and specimens were collected bed-by-bed, prepared and photographed. Thin section sampling has been obtained from significant beds in metre distant intervals. Sampling was denser near lithological boundaries, with samples taken in intervals of 20 cm, or even in cm-intervals. Three thin sections were additionally made from an ammonite cast with the surrounding sediment, extracted from the top stromatolite layer (NHMW collection).

Digital high-quality photomicrographs of the thin sections were performed on a Discovery.V20 Stereo Zeiss microscope. Specific magnifications were x 4.7, x 10.5 and x 40 in transmitted light mode. Data from the AxioCam MRc5 Zeiss were processed and documented by using the AxioVision SE64 Rel. 4.9 imaging system. Additional photomicrographs were made from surfaces of the samples cut for the thin sections. The images of the microfossils from the samples HKr-7-R to HKr-7 Base were made with the Nikon Eclipse 800 microscope and AxioCam 3.1 camera of the Palaeontological Department, Eötvös Loránd University and Hantken Foundation, Budapest. Classification of Dunham (1962), Embry & Klovan (1972), Böhm (1992) and Tomašových (2004) was used for description of standard microfacies types (SMF types, Wilson, 1975; Flügel, 2004).

For the determination of calpionellids and calcareous dinoflagellates, sampling in the Steinmühl and Ammergau formations was realized in every one-and-a-half and later every one-meter interval. Beds have been numbered by prefixes of HKr. In total 45 samples were selected for thin sections. Thin sections were studied under the LEICA DM 2500 polarizing microscope. The Axiocam ERc 5s camera was used for documentation of microfacies and biomarkers. Calpionellid zonal scheme sensu Reháková & Michalík (1997), combined with the cyst zonation of Reháková (2000) were adopted. The material is stored at the Natural History Museum in Vienna (NHMW 2019/0162/0001–0110). Ammonite material has been studied within collections of the NHMW from the same locality.

The Hödl-Kritsch section – lithology and lithostratigraphy

The Hödl-Kritsch section (HKr) is located in the steep walls on the mountain side in the abandoned quarry. The section is separated in the lower part A (sample numbers HKr7A to HKr7St450; Text-Fig. 2, Pl. 1), and the upper part B (samples from HKr2 to HKr6), approximately 100 m to the west. Beds are in normal position, dipping to the south (azimuth 190°) at 40° angle. The lower part (N 48°7'44.50" and E 16°14'29.10") ranges from the basal Rhaetian Kössen Formation to the Middle to Upper Jurassic Klaus Formation to the Tithonian Tegernsee limestones. The Rhaetian Kössen Formation comprises fossiliferous (bivalves, brachiopods, corals) grey to black marls and limestones (6.5 m). The Kössen Formation is overlain by the Rhaetian limestone formed by grey coral limestones (4 m) with orange interbeddings of residual layers. After a sedimentological gap, marked by stromatolite occurrences and manganese crusts, the Klaus Formation appears with grey and red filamentous *Bositra*-like limestones (2 m), followed by protoglobigerinid limestones and micritic ooids on top. These are overlain by red saccocomid/radiolaria limestones of the Tegernsee limestones, that contain reworked nodules in dark red limestones at the bottom (4.5 m). As recorded in the second section (N 48°7'43.3" and E 16°14'24.6"), the red saccocomid/radiolaria limestones of the Tegernsee limestones are followed by pink limestones (2 m), light grey limestones (5 m) and whitish limestones (5 m) of the Tithonian to Berriasian Ammergau Formation (Text-Fig. 2).

Microfacies analyses

A brief description of samples, taken along the logged succession, is given below. For the position of samples, see Text-Figure 2. A detailed biostratigraphy with microfossil ranges and figures is in preparation (Lukeneder et al., in prep.), hence the given biostratigraphic data are preliminary. Facies zones and standard microfacies types (FZ types and SMF types, Wilson, 1975; Flügel, 2004).

Kössen Formation – Hochalm Member

from HKr7A–HKr7D (SMF 15 of FZ 7–8; Text-Fig. 2, Pl. 2)

HKr7A bivalve-brachiopod grainstone, with oosparitic layers, most shells preserved with micritisation seams (micrite envelopes), numerous gastropods, rare foraminifera.

HKr7B bivalve-brachiopod grainstone, most shells preserved with micritisation seams, numerous gastropods, frequent foraminifera.

HKr7C crinoidal grainstone, well laminated, crinoids and echinoids, graded bedding.

HKr7D coral boundstone, corals with preserved septa, frequent brachiopod shells, most shells preserved with micritisation seams, crinoids and echinoids.

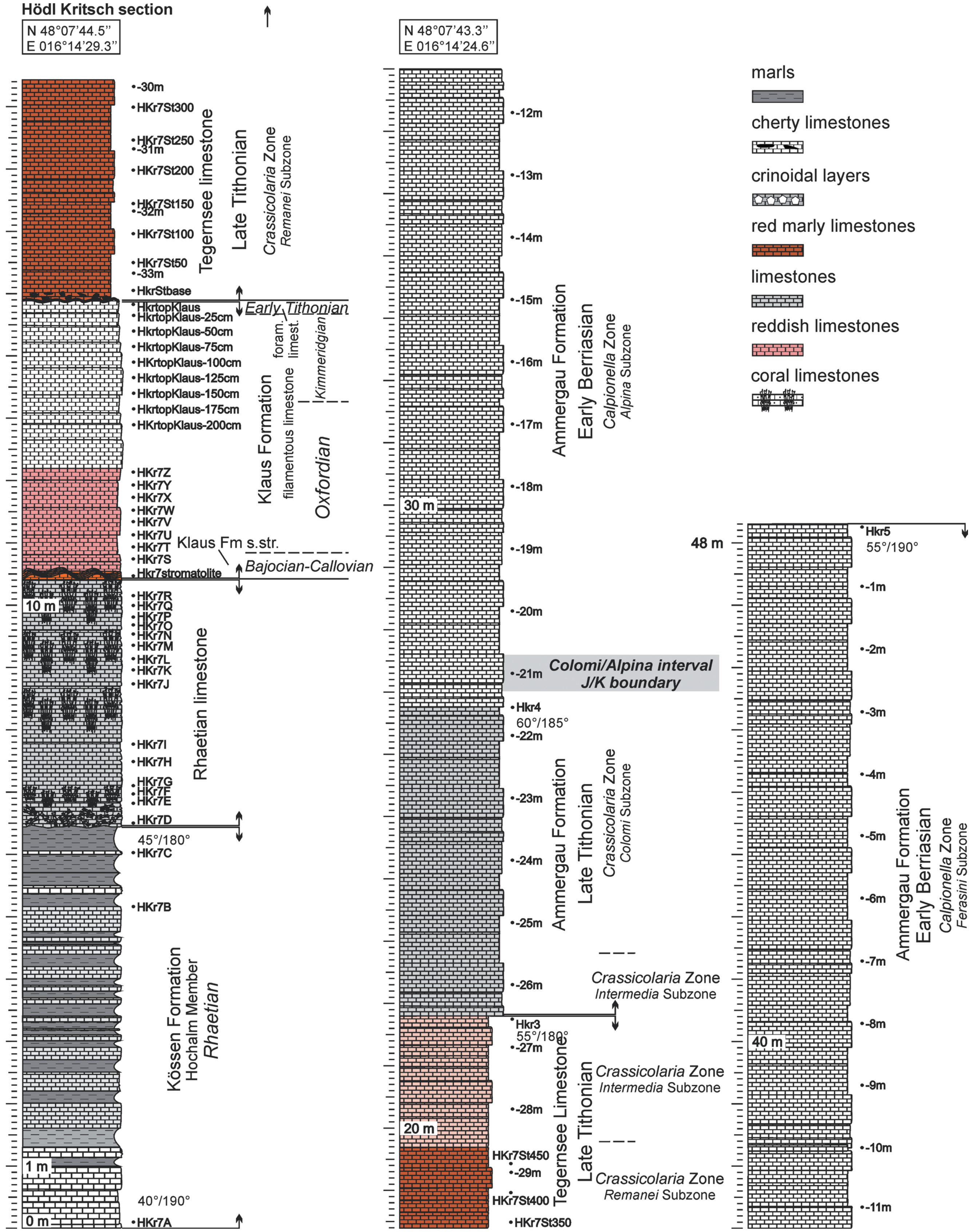

Text-Fig. 2.
Composite vertical section of the Hödl-Kritsch outcrop with the stratigraphic position of the corresponding formations and sample numbers.

Rhaetian limestone member

HKr7E–HKr7R (SMF 7, 11, 12, 13 of FZ 5–6; Text-Fig. 2, Pl. 3)

HKr7E crinoid-brachiopod packstone, encrusting foraminifera, residual layers with "algae", dissolution seams, crinoids and echinoids, rare foraminifera.

HKr7F brachiopod-coral packstone, encrusting foraminifera, brachiopods, corals.

HKr7G crinoidal-brachiopod wacke- to packstone, residual layer.

HKr7H coral boundstone, corals recrystallized, interspace filled by brachiopod coral packstone, rare crinoids, rare foraminifera.

HKr7I coral brachiopod packstone, rare corals with partly recrystallized septa, frequent crinoids and echinoids, rare foraminifera.

HKr7J crinoidal-brachiopod wacke- to packstone, rare echinoids, residual layer.

HKr7K crinoidal-brachiopod packstone, most shells preserved with micritisation seam, encrusting foraminifera, crinoids and echinoids, rare foraminifera.

HKr7L brachiopod packstone to grainstone, most shells preserved with micritisation seam, encrusting foraminifera, crinoids and echinoids, rare foraminifera.

HKr7M packstone, most shells preserved with micritisation seam, encrusting foraminifera, crinoids and echinoids, frequent ostracods, frequent foraminifera.

HKr7N *Bacinella* packstone, with graded filled cracks, most shells preserved with micritisation seam, encrusting foraminifera, *Bacinella irregularis*, brachiopods, corals fragments, gastropods, crinoids and echinoids, frequent ostracods, frequent foraminifera.

HKr7O to HKr7Q coral-*Bacinella* packstone, most shells preserved with micritisation seam, encrusting foraminifera, *B. irregularis*, brachiopods, coral fragments, gastropods, rare crinoids, frequent ostracods, frequent foraminifera.

HKr7R brachiopod-gastropod packstone, most shells preserved with micritisation seam, encrusting foraminifera, *B. irregularis*, brachiopods, coral fragments, gastropods, rare crinoids and echinoids, frequent ostracods, frequent foraminifera.

Stromatolite boundary

HKr7stromatolite (SMF 20 of FZ 7–9; Text-Fig. 2, Pl. 4)

HKr7stromatolite boundstone, *Frutexites*, reworked base with lithoclasts, well laminated, oncoids and cortoids, frequent foraminifera, residual crusts, condensed, with crinoid layers. Stromatolite layer can be up to 40 cm thick. As reported in the 1970s (KRYSTYN, 1971, 1972) the thick stromatolites grow on the abundant ammonite shells, which cannot be observed at the present state of the outcrop situation. Ammonites are mostly orientated parallel to bedding plane. In most specimens, the upper part of the shell is dissolved and eroded. Bioerosional traces occur frequently, reflecting a transgressive, shallow subtidal depositional environment (FLÜGEL, 2004). The fabric is dominantly a packstone exhibiting rounded wackestone intraclasts. The microfossil content of the rock mainly consists of *Bositra*-like shell-fragments. Additionally, echinoids, planktic and benthic foraminifera, *Globochaete alpina*, radiolaria, ostracods, gastropods brachiopods and calcareous dinoflagellate cysts occur. Foraminifera are often limonitized (especially agglutinated groups), and filled with limonitic or glauconitic sediments.

Klaus Formation

HKr7S–HKrtopKlaus (SMF 3–5 of FZ 3, 4 Text-Fig. 2, Pl. 5)

HKr7S to HKr7Z filamentous packstone, mass occurrences of the *Bositra*-like shell-fragments, bioturbation, frequent peloids, rare crinoids, rare foraminifera.

HKrtopKlaus-200cm to HKrtopKlaus-25cm filamentous grainstone, mass occurrences of the *Bositra*-like shell-fragments, bioturbation, frequent peloids, rare radiolaria, rare crinoids, rare foraminifera.

HKrtopKlaus foraminiferal packstone, *Protoglobigerina* mass occurrences, bioturbation, rare benthic foraminifera.

Tegernsee limestone

HKr7baseSt–HKrSt450–HKr3; base Steinmühl, -33 m to -27 m; two separate sections are correlated in that formations, samples St50 to St450 with the part -33 m to -29 m (SMF 3 of FZ 2, 3; Text-Fig. 2, Pl. 6).

HKr7baseSt radiolaria-*Saccocoma* packstone, with clayey residual lamination, with radiolarians and protoglobigerinid lithoclasts from reworked older formations (i.e. top Klaus Formation and Ruhpolding Formation). Clasts of type A: *Protoglobigerina*-radiolarian wackestone – calcified radiolarians and planktonic foraminifera are accompanied by less frequent crinoids, ostracods, aptychi, *Saccoccoma* sp., bivalves and spores of *Globochaete alpina*, cyst of *Colomisphaera fibrata*. Fragments of type B: radiolarian wackestone. Slightly recrystallized matrix with calcified or partially silicified radiolarians and less common sponge spicule. Clasts of type C: *Sacoccoma* wackestone – with *Sacoccoma* sp. fragments dominated.

HKr7St50 to HKr7St400 radiolarian-*Saccocoma* packstone, frequent radiolaria and *Saccocoma* sp., *Laevaptychus* sp., bivalves, ostracods, nodular fabric.

HKr7-33 m to -27 m radiolarian packstone, nodular, frequent *Saccocoma*, bivalves, ostracods, *Laevaptychus* sp. calpionellids start at 32 m.

Ammergau Formation

HKr3+5cm–HKr5; -26 m to -0 m = HKr5 (SMF 3 of FZ 2, 3; Text.-Fig. 2, Pl. 6), -26 m to -0 m = HKr5 radiolaria-calpionellid wackestone, foraminifera, laevaptychi.

HKr5-26m *Saccocoma*-*Globochaeta*-*Calpionella* wackestone.

HKr5-25m *Globochaeta*-*Calpionella* wackestone.

HKr5-24m *Calpionella*-radiolarian wackestone.

HKr5-23m *Saccocoma*-*Globochaeta*-*Calpionella* wackestone.

HKr5-22m up to HKr5 *Calpionella*-radiolarian wackestone.

Preliminary biostratigraphy of the Hödl-Kritsch section

The Triassic Kössen Formation and Rhaetian limestones

Foraminiferal assemblages from the Hödl-Kritsch section were investigated in the upper 10 m of the Kössen Formation. Special attention was given to the stromatolite level representing the unconformity at top of the Rhaetian limestone (Text-Fig. 2). The assemblages are not particularly rich in species but nevertheless, display notably different characters. The number of specimens in sampled beds of the Kössen Formation is low. The erosional discordance between the Upper Triassic light coloured limestone and the Jurassic red marly limestone could be studied in the sample HKr7R. The Triassic limestone of the sample is a packstone with calcite veins (microcracks with offsets) and cortoids, small-sized (up to 5 mm) gastropods, fragments of echinoderms, brachiopods, algae and foraminifers. The microfacies and the fossils indicate a shallow marine environment, with constantly agitated water, at or above the wave base.

The Jurassic Klaus Formation

Two types of fabric could be observed in the Jurassic limestone. The first is a partially dolomitized wackestone. The recrystallisation fabric is nearly equigranular porphyrotropic, the floating rhombs are idiotropic. The dolomitization of the sediment probably took place at shallow burial setting. Molluscs, echinoderms and the epilithic *Lithocodium aggregatum* are the usually present fossils. Following the interpretation of SCHLAGINTWEIT et al. (2009), a shallow, but transgressive, normal marine palaeoenvironment is the most plausible, which is in accordance coincides with the erosional surface and the fabrics. The second type of the fabric is also partly dolomitized limestone (mudstone to wackestone), but dolomite crystals are in porphyritic contact fabric and the shape of the crystals is planar-e (euhedral). This could indicate a near surface, early meteoric dedolomitization (FLÜGEL, 2004). In this microfacies, few ostracod shells and foraminifera could be recognised.

From the thick basal stromatolite layer, an ammonite cast with the surrounding sediment was studied in detail. In a chamber of the phragmocone, a bed-parallel geopetal structure could be observed. The fabric, microfacies and microfossil content are nearly the same outside and inside of the ammonite shell. The main difference can be found in the grain sizes.

The living chamber of the ammonite is filled with packstone with rounded wackestone intraclasts, oncoids and various bioclasts. Oncoids are of centimetre-size. The cores of the oncoids are aggregates with stromatolites and/or cortoidal surface, or micritic intraclasts. The microfossil content of the rock in the order of the frequency, shell-fragments of *Bositra*-like bivalves, echinoids, planktonic foraminifera, benthic ones, *Globochaete alpina*, radiolarians, ostracods, gastropods, brachiopods and calcareous dinoflagellate cysts. The infill of the second and third chambers of the ammonite shell is almost identical to the first chamber. The largest bioclast, a gastropod shell about 800 µm in size, is visible in the second chamber, while in the innermost visible chamber, the lengths of the *Bositra*-like fragments are only about 300 µm.

The determined protoglobigerinid fauna is very similar to the one from the Callovian of Hungary (GÖRÖG et al., 2012). The most common forms are the middle-sized (150–200 µm) tests with low spire and four chambers on the last whorls, the group of *Globuligerina oxfordiana.* The foraminiferal fauna is characteristic for the outer platform-slope environment. Based on the ranges of the benthic forms, the most probable age is Bathonian to lowermost Callovian, which coincidences well with the ammonite age determination (KRYSTYN, 1970, 1972).

Above the stromatolite layer, in the 4.5 m thick succession (the samples HKr7S–Z and HKr7topKlaus-200cm to -25cm), the rocks have relatively similar fabrics: packstone (sensu DUNHAM, 1962) or poorly washed biosparite (sensu FOLK, 1962) with microcracks and sometimes irregular stylolites. The majority (up to 98 %) of the fossil content are fragments of thin-shelled *Bositra*-like bivalves (filaments). These are arranged randomly, except at the margins of common bioturbations. Based on the ratio of bioclasts, two types of the microfacies (MF 1 and MF 2) can be distinguished.

In the MF 1, in the samples HKr7S-U, X and Z, and HKr7topKlaus-75cm to -25cm, the filaments account for ~95 % of the rock volume. The shells are partly recrystallized. Fibrous cement can regularly be observed between the valves. In this microfacies, the second most common bioclasts after the bivalve shells are the foraminifers. Besides them are a few echinoid fragments, calcareous dinoflagellate cysts, *Globochaete* specimens, ostracods, juvenile gastropods (HKr7topKlaus-75cm), sponge spicules (HKr7topKlaus-75cm), and a few calcified radiolaria (only in samples HKr7X and HKr7topKlaus-25cm). Among the benthic foraminifera, the most common group are the lagenids, namely large sized (up to 800 µm), bioeroded *Lenticulina*, *Nodosaria*, *Dentalina* and *Lingulina*. Few specimens of spirillinids also occur in most samples, while agglutinated *Glomospira* sp., *Verneuilina* sp. and porcellanous ophthalmids are very rare. Protoglobigerinids are rare and occur only in the samples HKr7S and HKr7topKlaus-75cm. They could be classified into the morphogroup of *Globuligerina oxfordiana* and *Favusella hoterivica*. These species differ only in the ornamentation of the surface of the shell, which only can be studied in isolated specimens.

In two samples (HKr7X and HKr7Z) small-sized (up to 250 µm), limonitic grain aggregates built up oncoids in relatively large quantities. There is no fibrous cement between the bivalve shells. Dark layers could be observed on both sides of the shells, sometimes showing fibrous structure, perpendicular to the surface of the shells.

In the second microfacies type (MF 2, samples HKr7sV, HKr7sW, HKr7sY, HKr7topKlaus-200cm, -175cm, 150cm, -125cm, -100cm) the amount of fragments of thin bivalve shells drops to only about 40 % of the rock volume. At the same time, the volume of the micritic matrix increases. Moreover, these samples are characterized by the existence of spherical (up to 150 µm) peloids – with micrite content – up to 5 % of the rock volume, calcified spumellarian radiolaria, and the globochaets also occur in each sample of MF 2. Similarly to the MF 1, foraminifers are rare. Other fossils, described in MF 1, are present in this microfacies as well, except for a few sclerites of holothuroids and a brachiopod shell. All foraminiferal taxa of the MF 1 appear sporadically in the MF 2, e.g., protoglobigerinids *(Globuligerina oxfordiana-Favusella hoterivica* group) only in the samples HKr7V and HKr7topKlaus-100cm. Besides them, there are one or two specimens of agglutinated genera, *Textularia* sp., *Valvulina* sp. and *Trochammina* sp., and encrusting, porcellanous forms, tentatively classified to cf. *Nubecularia mazoviensis*. This latter foraminifer appears on the surface of some intraclasts. It was originally described from the residue of the upper Kimmeridgian to lower Tithonian. Gradziński et al. (2004) documented similar forms from the same palaeoenvironment, from the succession built up *Bositra*-like bivalve shells of the Toarcian–Aalenian part of the Krízńa Unit in the Western Tatra Mountains.

At the top of this succession, in the sample HKr7topKlaus, the microfacies significantly changes. The fabric of MF 3 is packstone with intraclasts and bioclasts. More than 90 % of the latter are protoglobigerinid shells, forming nearly 70 % of the rock volume. The other microfossils, in order to their frequency, are fragments of *Bositra*-like bivalves, benthic foraminifers, ostracods (with articulated or disarticulated valves), *Globochaete alpina,* calcareous dinoflagellate cysts and radiolarians. The protoglobigerinid assemblage is relatively homogenous, seems to be oligospecific, consisting of medium-sized (largest diameter 200 µm), dominantly low-trochospiral and a few high trochospiral groups. Usually, the tests are filled with micrite, but sometimes the older part of the shell is filled with sparry calcite. The low trochospiral foraminifers with a lobated outline and four chambers on the final whorls can be assigned to the *Globuligerina oxfordiana-Favusella hoterivica* group, while the high-trochospiral ones belong to cf. *Globuligerina bathoniana*. Within the benthic foraminifers, the most common group are the porcellanous miliolinids, followed by the lagenids and spirillinids. *Ophthalmidium strumosum* is the most common species within the miliolinids. Additionally, a few strongly keeled specimens of *Ophthalmidium* mg. *marginatum* occur. Large, even giant-sized (up to 1.6 mm), lenticulinids, different nodosarids, *Spirillina* sp. and *Radiospirillina* sp. could be identified in this sample.

The most important diagnostic fossils for the detailed biostratigraphy of this succession (HKr7S – HKr7topKlaus-25cm and HKr7topKlaus) are the calcareous dinoflagellate cysts. In the *Bositra*-like shells packstone facies (MF 1 and MF 2) the range of the occurring dinoflagellate cysts are the following: *Cadosina semiradiata fusca*: Oxfordian–Berriasian; *Colomisphaera carpathica*: Oxfordian–upper Berriasian; *Stomiosphaera moluccana* lower part of the upper Kimmeridgian–Valanginian (e.g., Reháková, 2000; Olszewska et al., 2012; Ivanova & Kietzmann, 2017). Based on these data, the Oxfordian starts with the sample HKr7T. Since the lowest occurrence of *S. moluccana* firstly is in the sample HKr7topKlaus-175cm, from this level on the age of the unit is upper Kimmeridgian or younger. The age of the uppermost sample (HKr7topKlaus) is most probably lower Tithonian (based on the relatively frequent *S. moluccana,* the upper Oxfordian–lower Valanginian *Col. lapidosa* and the lower Tithonian *Committosphaera pulla*; Ivanova & Kietzmann, 2017). It coincides with the protoglobigerinids, as the monospecific *Globuligerina* gr. *oxfordiana* fauna characterises the lower Tithonian (Görög & Wernli, 2004; Görög et al., 2010). This, however, seems to contradict the age given by the miliolid foraminifers of this sample. Namely, according to the literature (e.g., Clerc, 2005; Ivanova et al., 2008; Olszewska et al., 2012), the range of the *Ophthalmidium strumosum* is late Oxfordian–lower Kimmeridgian, and *O.* gr. *marginatum* is upper Bajocian–Kimmeridgian. Thus, most probably the range of the *O. strumosum* was longer, extending into the upper Kimmeridgian.

According to the microfacies study, MF 1 represents an unfavourable environment on the sea floor where almost exclusively the benthic, opportunistic and r-strategist *Bositra*-like bivalves could live. The disarticulated, broken, tiny and thin shells, the calcitic cement between them and the bioturbations indicate oxic and moderately agitated bottom water (e.g., Jach, 2007; Molina et al., 2018). This microfacies was characteristic for the lower and the upper part of this interval. In the middle part of the succession (approx. HKr7topKlaus-200cm–100cm), the appearance of the peloids and the radiolarians signifies a higher nutrient availability. During the time when the sediment of the uppermost sample deposited, the environment has changed drastically. Since aragonitic shells of the protoglobigerinids are preserved, the water depth was probably lower, above the aragonitic lysocline.

Jurassic–Cretaceous Tegernsee limestone and Ammergau Formation

Late Tithonian *Crassicollaria* Zone, *Tintinnopsella remanei* Subzone (Remane et al., 1986); samples HKr7–base, HKr7–St200cm, HKr7–St250cm, HKr–St300cm, HKr7–St350cm, HKr7–St400cm, HKr7–St450cm

In the red *Saccocoma*-bearing wackestone different clasts of reworked older rocks a few mm to 1.2 cm in size were recognised (Pl. 6). Several types of clasts can be recognised. Type 1 is protoglobuligerinid-radiolarian wackestone. Calcified radiolarians and planktonic foraminifera are accompanied by less frequent crinoids, ostracods, aptychi, *Saccoccoma* sp., bivalves and spores of *Globochaete alpina*. Cysts of *Colomisphaera fibrata* were determined. Type 2 is radiolarian wackestone. Slightly recrystallized matrix contains calcified or partially silicified radiolarians and less common sponge spicule. Clasts of Type 3 are *Sacoccoma* wackestone. Clasts of Type 4 are small (1–2 mm) fragments of micritic limestone appear with calpionellids and spumellarian radiolarians. Planktonic crinoids *Saccocoma* sp. dominate over less frequent filaments, spores of *Globochaete alpina*, calcified radiolarians, crinoid collumnalia, aptychi, bivalves, cysts of *Colomisphaera*, *Stomiosphaera* and *Cadosina*, and rare calpionellids. The microfossils and the microfacies indicate an open marine environment.

The overlying beds – samples HKr7–St50cm, HKr7–St-100cm belong to biomicritic, slightly bioturbated limestones of *Saccocoma* microfacies (wackestone to packstone; SMF 2) and radiolarian-*Saccocoma* microfacies (wackestone; SMF 2). *Saccocoma* sp. dominate with calcified radiolarians and sponge spicules , being accompanied by less frequent filaments. Additional spores of *Globochaete alpina,* bivalves, aptychi, and cysts of *Parastomiospahera* and *Colomisphaera* occur. Saccocomid skeletal elements of the saccocomid zone Sc 5 prevail. This zone coincides with the *Fallauxi* ammonite zone as proposed by Benzaggagh et al. (2015). Dinoflagellate cysts indicate this interval belongs to lower Tithonian *Malmica* Zone (sensu Nowak, 1968; Reháková, 2000). The latest lower Tithonian *Chitinoidella* Zone, *Dobeni* Subzone was identified in the next sample (HKr7–St-150cm). Here, biomicritic limestone of the radiolarian-*Saccocoma* microfacies (wackestone to packstone; SMF 2) contains *Saccocoma* sp., calcified radiolarians, sponge spicules, ostracods, bivalves, aptychi, calpionellids with *Borziella*, *Carpathella,* spores of *Globochaete*, and cysts of *Colomisphaera* and *Colomisphaera.* Saccocomid skeletal elements of the Sc 6 zone (Benzaggagh et al., 2015) are present. Dissolution seams and stylolites are commonly present.

If the base of the Tegernsee limestones belongs to the *Remanei* Subzone, deposits of the lower Tithonian *Malmica* and the *Chitinoidella* zones, mentioned in HKr7–St50cm, HKr7–St100cm and HKr7–St150cm, represent reworked and resedimented beds incorporated into the sediments of upper Tithonian *Remanei* Subzone of the *Crassicollaria* Zone.

In the HKr7–St200cm and higher, marly limestone (mudstone to wackestone, SMF 3) with rare bioclasts (calcified radiolarians, sponge spicules, spores of *Globochaete alpina, Saccocoma* sp., bivalves), bioturbated radiolarian-*Saccocoma* wackestone to packstone), and radiolarian wackestone predominate. *Saccocoma* sp., calcified radiolarians, and sponge spicules are the most common bioclasts. There are less frequent and rare ostracods, bivalves, aptychi and crinoid fragments, spores of *Globochaete,* and poorly preserved rare hyaline calpionellids with *Tintinnopsella*, and cysts of *Committosphaera, Colomisphaera*, and *Cadosina.* Saccocomid skeletal elements of the higher part of the Sc 6 zone are present. According to Benzaggagh et al. (2015), this zone coincides with the *Microcantum* ammonite zone. Bioclasts are locally chaotically arranged, or concentrated into clusters. The matrix of the sample HKr7–400cm is slightly bioturbated and exhibits some differently orientated geopetal structures. This indicates resedimentation of the lithified sediment. Limestone contains fine silty admixture, mainly clays, less frequent to rare silty quartz grains. Dissolution seams and stylolites are common.

Late Tithonian *Crassicollaria* Zone, *Crassicollaria intermedia* Subzone (Remane et al., 1986); samples 28 m, 27 m, 26 m

The biomicrite is locally slightly laminated and bioturbated limestone of *Saccocoma-Calpionella, Globochaete-Calpionella* and *Calpionella*-radiolarian microfacies (wackestones; SMF 3) occur. Calpionellids occur with *Calpionella*, *Crassicollaria* and *Tintinnopsella,* cysts of *Colomisphaera* and *Stomiosphaerina* forms an assemblage with calcified radiolarians, sponge spicules, rare fragments of bivalves and aptychi. The rock is highly fractured, criss-crossed by calcitic veins. Stylolites locally highlight lamination. Fine silty admixture – mainly clays – is concentrated in dissolution seams. Sample 26 m contains the marks of tectonic breccia.

Late Tithonian *Crassicollaria* Zone, *Crassicollaria colomi* Subzone (Pop, 1994); samples 25 m, 24 m, 23 m, 22 m

Locally slightly bioturbated limestone of *Calpionella*-radiolarian and *Globochaete-Calpionella* microfacies (wackestones, SMF 3). Limestone contains calcified radiolarians, sponge spicules, rare fragments foraminifera (*Spirillina* sp.), bivalves, calpionellids occur with *Calpionella, Crassicollaria* and *Tintinnopsella,* cysts appear with *Colomisphaera* and *Stomiosphaerina*. Limestones show locally signs of resedimentation. Redeposited sediments concentrated in laminae contain microfossils of the older *Intermedia* Subzone with *Crassicollaria*, *Calpionella*; also the angular extraclasts (biomicrite limestone of *Calpionella* microfacies (wackestone) and slightly recrystallized radiolarian wackestone were observed) were observed. Sample 23 m – limestone of *Saccocoma-Globochaete* microfacies (wackestone) with filaments, rare bivalves, aptychi and cysts of *Parastomiosphaera, Stomiosphaera,* and *Colomisphaera* belong probably to the extraclast derived from the lower Tithonian *Malmica* Zone. Matrix of limestones is penetrated by thin fractures and veins filled by calcite. Fine silty admixture, mainly clays, is concentrated in dissolution seams.

Early Berriasian *Calpionella* Zone, *Calpionella alpina* Subzone (sensu Pop, 1974; Remane et al., 1986); samples 21 m, 20 m, 19 m, 18 m, 17 m, 16 m, 15 m, 14 m, 13 m

The *Colomi-Alpina* passing interval or J/K boundary limit was fixed to the sample 21 m. Biomicritic limestones of *Calpionella*-radiolarian microfacies (wackestones; SMF 3) prevails in this interval. Limestones contain calcified radiolarians, sponge spicules, and calpionellid assemblage dominated by small forms of *Calpionella alpina*, rare *Crassicollaria parvula* and *Tintinnopsella carpathica*. There are also rare foraminifer fragments (*Spirillina* sp.), bivalves, crinoids, aptychi, cysts of *Cadosina* and *Colomisphaera*. The rock is fractured. Different infillings of veins – blocky and radiaxial calcite – was observed. Matrix contains also fine silty admixture. Clays are concentrated in dissolution seams. Some of calpionellid loricae appear deformed.

Early Berriasian *Calpionella* Zone, *Remaniella ferasini* Subzone (Pop, 1994); samples 12 m, 11 m, 10 m, 9 m, 8 m, 7 m, 6 m, 5 m, 4 m, 3 m, 2 m, 1 m, HKr5

Biomicrite limestones of *Calpionella*-radiolarian microfacies (wackestones; SMF 3) contain calcified radiolarians, sponge spicules, fragments of aptychi, ostracods, bivalves and foraminifera (*Spirillina* sp., *Patellina* sp.). Calpionellid assemblage consist of *Calpionella, Remaniella, Tintinnopsella*, *Lorenziella* and *Crassicollaria*. Numerous of the loricae are deformed. Cysts are represented by *Colomisphaera*, *Stomiosphaerina*, and *Cadosina*. Calpionellid loricae (and a single fragment of *Sacoccoma* sp.) are concentrated in thin laminae, suggesting redeposition. The matrix is locally penetrated by fractures and veins of different orientation, filled by calcite. Locally (sample 13 m) *Frutextites*, typical for deeper and less oxic environments, were observed in the matrix.

Discussion

The age and biostratigraphy of the limestones, siliceous limestones and marly limestones from the Hödl-Kritsch quarry near Kaltenleutgeben at the western border of Vienna were not known in detail until now. On the geological map of Baden (Geological map 1:50,000, sheet 58; Schnabel et al., 1997) the area is characterized only by the occurrence of the Upper Triassic Kössen Formation, Middle to lower Upper Jurassic Klaus Formation and Lower Cretaceous Schrambach Formation.

For a correlation of Upper Triassic (Rhaetian), Jurassic (Bajocian–Tithonian) to Lower Cretaceous (Berriasian) lithologies and formations observed in the Flössel Syncline with other comparable sections from Upper and Lower Austria see Lukeneder et al. (in prep). It has to be stated, however, that numerous formation names and lithological terms need clarification or still lack formalisation (see also Flügel, 1967; Tollmann, 1976; Piller et al., 2004; Moser et al., 2017). Especially the Upper Jurassic formations are under intense debate and numerous terms are used in literature without any facts and microfacies data.

Klaus Formation

The term Klaus Formation with its type section at the Klausalm in Upper Austria (Suess, 1852; Spengler, 1919; Krystyn, 1971; Gawlick et al., 2009) is in the lower part also used as a synonym of Bathonian Filament limestones. Moser et al. (2017) described this part as Callovian „*Bositra*-Kalk“ (= “*Bositra buchi* Lumachelle“), hence part of the upper Klaus Formation („unterer Reitmauerkalk“; see Trauth, 1922, 1948, 1954; Kunz, 1967; Tollmann, 1976; Janda, 2000). Flügel (1967) used for the lower red to grey part of the Arrach quarry (near Waidhofen an der Ybbs, Lower Austria) the term „Filament Kalke“, equivalent to the Bajocian part of the Klaus Formation. Flügel (1967) introduced four limestone members in that quarry with the basal filamentous red limestone (Filament limestone, ?Callovian). Krystyn (1972) described the red „Mikrolumachellenkalk“ (approx. 1 m) formed of *Bositra buchi* shells from the Hödl-Kritsch quarry (= Neumühle quarry, Abb. 2 in Krystyn, 1972, bed c, Callovian). For the possible mechanisms of the formation of such *Bositra*-like bivalve mass occurrences see Jach (2007).

The term Klaus Formation (upper part) is also used as a synonym of Callovian *Globigerina* limestones. Wessely (2006) used for this lithology of Callovian to Oxfordian limestones in Bajuvaric units the terms „Globigerinen Oolith“ and „Mikro-oolith“, and only for the filamentous limestones („Filament Kalk“ = „*Bositra* Kalk“) in the Middle Jurassic the term „Klauskalk“. Moser et al. (2017) described this part already as lowermost Oxfordian „*Protoglobigerina*-Mikrit“, hence part of the lower part of the Reitbauernmauer Formation (sensu Moser et al., 2017). This recently introduced formation is equivalent to the „Miktitooidkalk“ (= micritic ooid limestone, „Oberer Reitmauerkalk“; see Trauth, 1922; Kunz, 1967; Ehrendorfer, 1988; Janda, 2000). Krystyn (1971) assumed and Oxfordian age for the light grey limestones of the Klaus Formation (e.g „Oberer Reitmauer Kalk“). Trauth (1948) established the term „Obere weisse Reitmauerkalke“ which seems to be equivalent to the Oxfordian micritic ooid limestones (Krystyn, 1971; see also Krystyn, 1972; Moser et al., 2017). The well-defined members of the Middle Jurassic Klaus Formation are well documented for numerous other localities of the Frankenfels Nappe in the Reitbauernmauer section (Lower Austria; Trauth, 1922, 1948; Moser et al., 2017), the Arrach quarry section (Trauth, 1922, 1948, 1954; Flügel, 1967; Tollmann, 1976), and the Lunz Nappe with the Oisberg localities (Oi 1, 2 and 3, Lower Austria; Krystyn, 1971; Lukeneder et al., in prep). The lower filamentous member (with mass occurrence of *Bositra*) and the upper foraminiferal part (with mass occurrence of protoglobigerinid foraminifera) of the Klaus Formation were observed in each of the documented sections. The Klaus Formation clearly needs revision (Lukeneder et al., in prep.), in its present state it is not valid.

Tegernsee limestone

In the near future the Steinmühl Formation („Malm Cephalopodenkalk“ in Tollmann, 1976) should be formalized for all micritic Lower to Upper Jurassic red limestones, with wide occurrences in the Bajuvaric Units. This would result in a range from Kimmeridgian to Berriasian. The Oxfordian red Rotensteiner Kalk is equivalent to the Lower Steinmühl Formation (Trauth, 1948; Tollmann, 1976; see Lukeneder, 2000; Lukeneder & Reháková, 2004).

Today, numerous terms exist for red limestones in the Kimmeridgian with the Tegernsee limestone in the Bavarian Bajuvaric Units (Allgäu Nappe and Lechtal Nappe). Wessely (2006) integrated both, the Kimmeridgian Agatha limestones and the basal part of the Tithonian limestones, in the term „Tegernseer Kalk“. The term „Tegernseer Kalk“ was used by Tollmann (1976) for Kimmeridgian to Lower Tithonian red *Saccocoma* limestones. The term Agatha limestone (= *Acanthicus* beds) derives from the Tyrolic Unit of the Salzkammergut (after St. Agatha near Bad Goisern, Upper Austria), consequently *Aspidoceras acanthicus* after a Kimmeridgian ammonite species, found in Gießhübl (“Tirolerhof”) in the historic “Acanthicus Steinbruch” situated in the Bajuvaric Unit (see Oberhauser, 1980). Wessely (2006) used the term „Agatha Kalk“ and „Saccocomakalk“ for the same Kimmeridgian *Saccocoma* dominated red limestones (e.g. in the Hödl-Kritsch quarry, Lunz Nappe, Lower Austria).

Red Tithonian limestones are often termed as Haselberg limestone (after the Haselberg near Ruhpolding in Bavaria, Germany, see Tollmann, 1976; Janda, 2000), also in the Bajuvaric Unit. After Oberhauser (1980) the “Haselbergkalk” is a variegated Tithonian clayey fibered limestone. In the literature concerning Upper Jurassic lithologies of Lower Austria, the term Tithonflaser limestone is used as a synonym for the Diphyakalk named after the brachiopod *Pygope diphya* in the Bajuvaric units (e.g. Reichraming Nappe, Upper Austria). Oberhauser (1980) separated the Tithonian–Berriasian Ammergau Formation or „Aptychenschichten“ from the variegated „Tithonflaser Kalk“ or coloured Ammergau Formation (see Tollmann, 1976). Oberhauser (1980) used the term “Steinmühlkalk” for the entire ammonite rich Upper Jurassic red facies formed on deepwater swells and submarine highs. At the type locality Arrach quarry, he distinguished the middle Oxfordian Lower Steinmühl limestone, named as the “Rotensteinkalk”, from the Kimmeridgian to Tithonian Upper Steinmühl limestone, named the “Tegernseer Kalk”.

All these terms could/should be linked with different members of the Steinmühl Formation (Kimmeridgian–Berriasian), maybe on the basis of the main fossil groups, as once introduced by Flügel (1967; Steinmühl Limestone Group) for the sequence in the type section Arrach Steinbruch (Lower Austria). Flügel (1967) introduced four members: the basal red Limestone (Filament Limestone, ?Callovian), for the Oxfordian “Radiolaria Siliceous”, the Kimmeridgian *Saccocoma* Limestone, and the Tithonian (“Portlandian”) *Calpionella* Limestone (see Trauth, 1948).

In the Hödl-Kritsch section, the *Saccocoma* limestones contained also the lower Tithonian cysts of calcareous dinoflagellates, and a relatively rich *Saccocoma* microfacies persists into the upper Tithonian part of the succession, bearing calpionellids of the *T. remanei* Subzone of the *Crassicollaria* Zone (Text-Fig. 2). The drop of their abundance began in the *Cr. intermedia* Subzone and prior to the J/K boundary saccocomids practically disappeared. The same was documented in other well documented sections of the Tethyan area (Michalík et al., 2016; Svobodová et al., 2019; Grabowski et al., 2019). The last upper Tithonian *Cr. colomi* Subzone of the *Crassicollaria* Zone was documented in the higher part of the Tegernsee limestone. It is worth to mention that the *Chitinoidella* and *Praetintinnopsella* calpionellid zones were not documented. On the basis of the presence of rare chitinoidellid and ?*Praetintinnopsella* species, which were observed in the *T. remanei* Subzone of the *Crassicollaria* Zone, we suggest redeposition from older strata. The same was documented by Svobodová et al. (2019). The Tegernsee limestone unit needs formalisation (Lukeneder et al., in prep.).

Ammergau Formation

The Ammergau Formation is equivalent to the "Aptychenschichten", representing fine, light grey, well-bedded limestones of Tithonian to Berriasian age (see Tollmann, 1976). Tollmann (1976) used for the type section the exposure in the Arrach quarry (see also Trauth, 1948) the term "Ammergau Schichten" ("Ober Tithon Aptychenkalk") and the term "Schrambach Schichten" ("Neokom Aptychenschichten"). Wessely (2006) used the term Ammergau Formation and "Calpionellenkalk" for upper Tithonian calpionellid-dominated grey limestones in the Bajuvaric units. The term "Aptychenschichten" was also used for the Ammergau Formation of the Hödl-Kritsch quarry. Compared with data, given by Krystyn (1972), the results from the Hödl-Kritsch section show a more detailed stratigraphy of the Ammergau Formation, starting in the higher part of the upper Tithionian *Crassicollaria* Zone (*Cr. intermedia* Subzone) and ending in the lower Berriasian *Calpionella* Zone (*R. ferasini* Subzone, Text-Fig. 2).

By increasing the clay content and the multitude of marly interbeds, the Schrambach Formation develops, ranging from Valanginian to Aptian. The term Ammergau Formation is also used as a synonym for Tithonian *Calpionella* limestones and the term Schrambach Formation unit B is used a synonym for Berriasian limestones, whereas the term Schrambach Formation unit A is also used as a synonym of Valanginian–Aptian limestones and marls.

Conclusions

The so far not precisely described Mesozoic sequence of the Hödl-Kritsch (Lunz Nappe, Northern Calcareous Alps) is presented in detail of microfacies and fossil content. Altogether 100 rock samples for thin sections were collected and analysed for their specific lithological changes and microfacies evolution. The corresponding formations or lithological members are the Rhaetian Kössen Formation, the Rhaetian reefal limestone member, the Middle to Upper Jurassic *Bositra* and protoglobigerinid bearing Klaus Formation (Bajocian to Kimmeridgian filamentous and protoglobigerinid members, topmost bed lower Tithonian), the red Upper Jurassic *Saccocoma* limestones of the Tegernsee limestone (upper Tithonian) and the calpionellid limestones of the red to grey Tithonian to Berriasian Ammergau Formation.

The stromatolite level on top of the Kössen Formation represents the unconformity between the Upper Triassic Kössen Formation and the Middle to Upper Jurassic Klaus Formation. The numerous planktonic foraminifera (protoglobigerina), in addition to thin-shelled bivalve "*Bositra"* and less numerous radiolarians, suggest that the Klaus Formation deposited in a deeper and open marine basin, in contrast to the Kössen Formation, which contains numerous coral boundstone and cortoids, suggestive of deposition within the photic zone. The stromatolite level thus represents a drowning unconformity and a significant time gap. The gap spans at least from the upper Rhaetian to the Bajocian, exhibiting a depositional gap of approximately 30 million years.

The sequence is characterized by the drowning of the platform environment in the Upper Triassic to Middle Jurassic, followed by a continuous deepening in the Upper Jurassic to Lower Cretaceous. The standard microfacies types SMF 2, 3, 4, 5, 7, 11, 12, 13, and 15 were detected. They characterize basin and slope environment of deposition (facies zones FZ 2–8). The deepening is documented by the following shift of microfacies types, subsequently by a change of environmental facies zones. The Kössen Formation is characterized by the SMF 15 type of FZ 7–8 zones restricted to open marine platform interior environments. Rhaetian limestones appear with diversified SMF 7, 11, 12, 13 of FZ 5–6 attributed to platform margin reefal structures and adjacent platform margins. The stromatolite boundary layer represents SMF 20 of FZ 7–9 of the open marine or restricted areas of the platform interior. Klaus Formation shows SMF 3–5 of FZ 3, 4of the middle to deeper slope. The Tegernsee limestone appears with SMF 2 and 3 of FZ 2, 3 of deeper slope and shelf areas. The Ammergau Formation occurs with SMF 3 of FZ 2, 3 characterizing the deeper slope and shelf.

Detail chronostratigraphic calibration of the lower Tithonian to lower Berriasian deposits of the Tegernsee limestone and the Ammergau Formation in the Hödl-Kritsch section was performed using calpionellids and calcareous dinocysts. The top of the Klaus Formation covers one calcareous dinocyst zone of lower Tithonian age (*P. malmica* Zone). It will need to be verified in the future if the top of the formation reaches even younger zones (or deposition lasted longer and the formation top is younger). No complete succession of calpionellid zones and subzones was documented. The *Chitinoidella* and *Praetintinnopsella* zones were not documented. Rare species typical for the *Ch. dobeni* Subzone, as well as few species of *Praetintinnopsella*, were observed in the *T. remanei* Subzone of the *Crassicollaria* Zone. There is a short gap between the *P. malmica* and the *Chitinoidella* Zone. The last known lower Tithonian dinocyst *C. semiradiata* Zone was not confirmed. Further calpionellid succession proved the standard *Crassicollaria* Zone with the *T. remanei*, *Cr. intermedia* and *Cr. colomi* subzones as well as the standard *Calpionella* Zone and its *C. alpina* and *R. ferasini* subzones.

Acknowledgements

We are particularly grateful to Anton Englert, Iris Feichtinger, and Anton Fürst (all Vienna) for the production of thin sections. Thanks go to Godfrid Wessely (Vienna), who reported and communicated important details on the area investigated. The authors wish to thank Bernd Hajek (local manager ÖKOTECHNA Entsorgungs- und Umwelt Ges m.b.H, Perchtoldsdorf) for a driving and digging permit for the Hödl-Kritsch quarry section. The research of Ágnes Görög was supported by the Hungarian Hantken Foundation. Research by Daniela Reháková was supported by the VEGA Project 2/0013/20. The work of Luka Gale is financially supported by the Slovenian Research Agency (programme number P1-0011) This work is dedicated to Lisa Marie Lukeneder (Gablitz), who inspires us every day.

References

Austromap Online (2019): Bundesamt für Eich- und Vermessungswesen, Wien. http://www.austrianmap.at/amap/index.php?SKN=1andXPX=637andYPX=492 (accessed 12. February 2019).

Benzaggagh, M., Homberg, C., Schnyder, J. & Ben Abdesselam-Mahdaoui, S. (2015): Description et biozonation des sections de crinoïdes saccocomidés du Jurassique supérieur (Oxfordien-Tithonien) du domaine téthysien occidental. – Annales de Paléontologie, **101**, 95–117, Paris.

Böhm, F. (1992): Mikrofazies und Ablagerungsmilieu des Lias und Dogger der Nordöstlichen Kalkalpen. – Erlanger Geologische Abhandlungen, **121**, 57–217, Erlangen.

Clerc, C. (2005): Les miliolina (foraminifères porcelanés) du Dogger du Jura méridional (France): systématique, stratigraphie et paléoenvironnement. – Université de Genève, Thèse, 2005, Genève. DOI: https://archive-ouverte.unige.ch/unige:97982

Decker, K., Peresson, H. & Faupl, P. (1994): Die miozäne Tektonik der östlichen Kalkalpen: Kinematik, Paläospannungen und Deformationsaufteilung während der lateralen "Extrusion" der Zentralalpen. – Jahrbuch der Geologischen Bundesanstalt, **137**, 5–18, Wien.

Dunham, R.J. (1962): Classification of carbonate rocks according to depositional texture. – In: Ham, W.E. (Ed.): Classification of carbonate rocks. – The American Association of Petroleum Geologists, Memoirs, **1**, 108–121, Tulsa.

Egger, H. (1988): Zur Geologie der Kalkvoralpen im östlichen Oberösterreich: Austria. – Jahrbuch der Geologischen Bundesanstalt, **131**, 245–254, Wien.

Egger, H. & Faupl, P. (1999): Geologische Karte der Republik Österreich 1:50.000, Blatt 69 Großraming. – 1 Karte, Geologische Bundesanstalt, Wien.

Egger, H. & Wessely, G. (2014): Wienerwald. – Sammlung Geologischer Führer, **59**, 203 pp., Stuttgart (Gebrüder Borntraeger).

Ehrendorfer, T. (1988): Zur Geologie der Weyerer Bögen im Gebiet von Großraming an der Enns (O.Ö.). – Mitteilungen der Gesellschaft der Geologie- und Bergbaustudenten in Österreich, **34/35**, 135–149, Wien.

Embry, A.F. & Klovan, J.E. (1972): Absolute water depth limits of Late Devonian paleoecological zones. – Geologische Rundschau, **61**, 672–686, Stuttgart.

Faupl, P., Skupien, P. & Vašíček, Z. (2003): Biostratigraphische Daten aus der Schrambach- und Tannheim-Formation der Frankenfelser Decke der Weyrer Bögen (Unterkreide, oberösterreichische Kalkalpen). – Mitteilungen der Österreichischen Geologischen Gesellschaft, **93**, 7–13, Wien.

Flügel, E. (1967): Elektromikroskopische Untersuchungen an mikritischen Kalken. – Geologische Rundschau, **56**, 341–358, Stuttgart.

Flügel, E. (2004): Microfacies of Carbonate Rocks: Analysis, Interpretation and Application. – 976 pp., Berlin (Springer).

Folk, R.L. (1962): Spectral subdivision of limestone types. – In: Ham, W.E. (Ed.): Classification of carbonate rocks. – The American Association of Petroleum Geologists, Memoirs, **1**, 62–84, Tulsa.

Gawlick, H.J., Missoni, S., Schlagintweit, F., Suzuki, H., Frisch, W., Krystyn, L., Blau, J. & Lein, R. (2009): Jurassic Tectonostratigraphy of the Austroalpine Domain. – Journal of Alpine Geology, **50**, 1–152, Wien.

Görög, Á. & Wernli, R. (2004): A rare protoglobigerinid association (Foraminifera) from the Tithonian of Gerecse Mts, Hungary. – Hantkeniana, **4**, 37–45, Budapest.

Görög, Á., Szinger, B. & Wernli, R. (2010): Late Jurassic-Early Cretaceous planktonic foraminifera from Tata, Gerecse Mts, N-Hungary. – International Symposium on Foraminifera, FORAMS 2010, Sept. 5–10, University of Bonn, Germany, Abstract, 97–98, Bonn.

Görög, Á., Tóth, E. & Wernli, R. (2012): Foraminifera and Ostracoda of the classic Callovian ammonite-rich bed of the Villány Mountains (Hungary). – Hantkeniana, **7**, 95–123, Budapest.

Grabowski, J., Bakhmutov, V., Kdyr, S., Krobicki, M., Pruner, P., Reháková, D., Schnabl, P., Stoykova, K. & Wierzbowski, H. (2019): Integrated stratigraphy and palaeoenvironmental interpretation of the Upper Kimmeridgian to Lower Berriasian pelagic sequences of the Velykyi Kamianets section (Pieniny Klippen Belt, Ukraine). – Palaeogeography Palaeoclimatology, Palaeoecology, **532**, Amsterdam. https://doi.org/10.1016/j.palaeo.2019.05.038

Gradziński, M., Tyszka, J., Uchman, A. & Jach, R. (2004): Large microbial-foraminiferal oncoids from condensed Lower-Middle Jurassic deposits: A case study from the Tatra Mountains, Poland. – Palaeogeography, Palaeoclimatology, Palaeoecology, **213**, 133–151, Amsterdam.

Ivanova, D.K. & Kietzmann, D.A. (2017): Calcareous dinoflagellate cysts from the Tithonian-Valanginian Vaca Muerta Formation in the southern Mendoza area of the Neuquén Basin, Argentina. – Journal of South American Earth Sciences, **77**, 150–169, Oxford.

Ivanova, D., Kołodziej, B., Koleva-Rekalova, E. & Roniewicz, E. (2008): Oxfordian to Valanginian palaeoenvironmental evolution on the western Moesian Carbonate Platform: a case study from SW Bulgaria. – Annales Societatis Geologorum Poloniae, **78**, 65–90, Krakow.

Jach, R. (2007): *Bositra* limestones – A step towards radiolarites: case study from teh Tatra Mountains. – Annales Societatis Geologorum Poloniae, **77**, 161–170, Krakow.

Janda, C. (2000): Geologisch-fazielle Untersuchungen in der Lunzer Decke südwestlich von Weyer (Oberösterreich). – Unpublished Master thesis, 85 pp., Wien.

KRYSTYN, L. (1970): Stratigraphie und Fauna des Klauskalks (Dogger) im Steinbruch Neumühle, N.Ö. – Anzeiger der mathematisch-naturwissenschaftlichen Klasse der Österreichischen Akademie der Wissenschaften, **107**, 55–59, Wien.

KRYSTYN, L. (1971): Stratigraphie, Fauna und Fazies der Klaus-Schichten (Aalenium-Oxford) in den Östlichen Nordalpen. – Verhandlungen der Geologischen Bundesanstalt, **1971**/3, 486–509, Wien.

KRYSTYN, L. (1972): Die Oberbajocium- und Bathonium-Ammoniten der Klaus-Schichten des Steinbruches Neumühle bei Wien (Österreich). – Annalen des Naturhistorischen Museums in Wien, **76**, 195–310, Wien.

KUNZ, B. (1967): Eine Fauna aus dem oberen Dogger der niederösterreichischen Kalkvoralpen (Unterer Reitmauerkalk, Frankenfelser Decke). – Annalen des Naturhistorischen Museums in Wien, **71**, 263–293, Wien.

LUKENEDER, A. (2000): Bericht 1998 über stratigraphische Untersuchungen eines Faziesüberganges zwischen Steinmühl-Formation und Schrambach-Formation auf Blatt 69 Großraming. – Jahrbuch der Geologischen Bundesanstalt, **142**, 393–394, Wien.

LUKENEDER, A. (2003): Ammonoid stratigraphy of Lower Cretaceous successions within the Vienna Woods (Kaltenleutgeben section, Lunz Nappe, Northern Calcareous Alps, Lower Austria). – In: PILLER, W.E. (Ed.): Stratigraphia Austriaca. – Austrian Academie of Sciences Series, Schriftenreihe der Erdwissenschaftlichen Kommission, **16**, 165–191, Wien.

LUKENEDER, A. (2005): An equivalent of the Karsteniceras Level within the Vienna Woods (Sparbach section, Lunz Nappe, Northern Calcareous Alps, Lower Austria). – Geologica Carpathica, **56**, 307–315, Bratislava.

LUKENEDER, A. & REHÁKOVÁ, D. (2004): Lower Cretaceous section of the Ternberg Nappe (Northern Calcareous Alps, Upper Austria): Facies–changes, biostratigraphy and paleoecology. – Geologica Carpathica, **55**/3, 227–237, Bratislava.

LUKENEDER, A. & SCHLAGINTWEIT, E.F. (2005): Hauterivian allodapic limestones within the Schrambach Formation (Kaltenleutgeben section, Lunz Nappe, Northern Calcareous Alps, Lower Austria). – Geologica Carpathica, **56**, 483–491, Bratislava.

LUKENEDER, A. & SMRECKOVÁ, M. (2006): An Early Cretaceous radiolarian assemblage: palaeoenvironmental and palaeoecological implications for the Northern Calcareous Alps (Barremian, Lunz Nappe, Lower Austria). – Annalen des Naturhistorischen Museums in Wien, **107A**, 23–57, Wien.

MICHALÍK, J., REHÁKOVÁ, D., GRABOWSKI, J., LINTNEROVÁ, O., SVOBODOVÁ, A., SCHLÖGL, J., SOBIEŃ, K. & SCHNABL, P. (2016): Stratigraphy, plankton communities, and magnetic proxies at the Jurassic/Cretaceous boundary in the Pieniny Klippen Belt (Western Carpathians, Slovakia). – Geologica Carpathica, **67**, 303–328, Bratislava.

MOLINA, J.M., REOLID, M. & MATTIOLI, E. (2018): Thin-shelled bivalve buildup of the lower Bajocian, South Iberian paleomargin: development of opportunists after oceanic perturbations. – Facies, **64**, 19, Berlin. https://doi.org/10.1007/s10347-018-0532-5

MOSER, M., MOSHAMMER, B. & GÖRÖG, A. (2017): Reitbauernmauer-Formation: Biostratigrafische und lithostratigrafische Neudefinition des „Mikritooidkalkes“ im Bajuvarischen Deckensystem (Nieder- und Oberösterreich). – Jahrbuch der Geologischen Bundesanstalt, **157**, 173–193, Wien.

NOWAK, W. (1968): Stomiosferidy warstw cieszyńskich (kimeryd – hoteryw) polskiego Śląska Cieszynskiego i ich znaczenie stratygraficzne. – Rocznik Polskiego Towarzystwa Geologicznego, **38**, 275–327, Kraków.

OBERHAUSER, R. (1980): Der Geologische Aufbau Österreichs. – 699 pp., Wien (Springer).

OLSZEWSKA, B., MATYSZKIEWICZ, J., KRÓL, K. & KRAJEWSKI, M. (2012): Correlation of the Upper Jurassic–Cretaceous epicontinental sediments in southern Poland and southwestern Ukraine based on thin sections. – Biuletyn Panstwowego Instytutu Geologicznego, **453**, 29–80, Warszawa.

PILLER, W., EGGER, H., ERHART, C.W., GROSS, M., HARZHAUSER, M., HUBMANN, B., VAN HUSEN, D., KRENMAYR, H.-G., KRYSTYN, L., LEIN, R., LUKENEDER, A., MANDL, G.W., RÖGL, F., ROETZEL, R., RUPP, C., SCHNABEL, W., SCHÖNLAUB, H.P., SUMMESBERGER, H., WAGREICH, M. & WESSELY, G. (2004): Die Stratigraphische Tabelle von Österreich 2004 (sedimentäre Schichtfolgen). – Österreichische Akademie der Wissenschaften und Österreichische Stratigraphische Kommission.

PLÖCHINGER, B. & KARANITSCH, P. (2002): Faszination Erdgeschichte mit Brennbpunkt Mödling am Alpenostrand. – 238 pp., Schwarzach (Heimat Verlag).

PLÖCHINGER, B. & PREY, S. (1993): Der Wienerwald. – Sammlung Geologischer Führer, **59**, 168 pp., Berlin–Stuttgart (Gebrüder Borntraeger).

POP, G. (1974): Les zones des Calpionelles Tithonique-Valanginiens du silon de Resita (Carpates meridionales). – Revue Roumainie de Géologie, Géophysique et Géographie, Série de Géologie, **18**, 109–125, Bucuresti.

POP, G. (1994): Calpionellid evolutive events and their use in biostratigraphy. – Romanian Journal of Stratigraphy, **76**, 7–24, Bucuresti.

REHÁKOVÁ, D. (2000): Evolution and distribution of the Late Jurassic and Early Cretaceous calcareous dinoflagellates recorded in the Western Carpathians pelagic carbonate facies. – Mineralia Slovaca, **32**, 79–88, Bratislava.

REHÁKOVÁ, D. & MICHALÍK, J. (1997): Evolution and distribution of calpionellids – the most characteristic constituents of Lower Cretaceous Tethyan microplankton. – Cretaceous Research, **18**, 493–504, London.

REMANE, J., BORZA, K., NAGY, I., BAKALOVA-IVANOVA, D., KNAUER, J., POP, G. & TARDI-FILÁCZ, E. (1986): Agreement on the subdivision of the standard calpionellid zones defined at the 2nd Planktonic Conference Roma 1970. – Acta Geologica Hungarica, **29**, 5–14, Budapest.

ROSENBERG, G. (1965): Kammerstein (Ruine) – Bierhäuselberg (N.Ö.). – Verhandlungen der Geologischen Bundesanstalt, **1965**, 9–19, Wien.

SCHNABEL, W., BRIX, F., FUCHS, R., PLÖCHINGER, B., PREY, S., WESSELY, G., HOFMANN, T., NOWOTNY, A., PLACHY, H., SCHEDL, A. & VECER, B. (1997): Geologische Karte der Republik Österreich 1:50.000, Blatt 58 Baden. – 1 Karte, Geologische Bundesanstalt, Wien.

SPENGLER, E. (1919): Die Gebirgsgruppe des Plassen und Hallstätter Salzberges im Salkammergut. – Jahrbuch der Geologischen Bundesanstalt, **68**, 285–474, Wien.

SPITZ, A. (1910): Der Höllensteinzug bei Wien. – Mitteilungen der Geologischen Gesellschaft in Wien, **3**, 351–433, Wien.

STEINER, P. (1968): Geologische Studien im Grenzbereich der mittleren und östlichen Kalkalpen (Österreich). – Mitteilungen der Gesellschaft der Geologie- und Bergbaustudenten Österreichs, **18**, 9–88, Wien.

ŠTÚR, D. (1860): J. Cžižek´s geologische Karte der Umgebung Wiens 1:93.000: nach den Arbeiten der k. k. geologischen Reichsanstalt und der Hrn. Dir. Dr. M. Hörnes, Prof. E. Suess, F. Karrer, K.M. Paul u.a. rectificirt und neu aufgenommen. – Wien (Artaria und Comp.).

SUESS, E. (1852): Mitteilung einiger Ergebnisse der Untersuchungen über die Brachiopoden der nordöstlichen Alpen (Hierlatzer Schichten). – Jahrbuch der k. k. Geologischen Reichsanstalt, **3**, 171, Wien.

Svobodová, A., Švábenická, L., Reháková, D., Svobodová, M., Skupien, P., Elbra, T. & Schnabl, P. (2019): The Jurassic/Cretaceous boundary and high resolution biostratigraphy of the pelagic sequences of the Kurovice section (Outer Western Carpathians, the northern Tethyan margin). – Geologica Carpathica, **70**, 153–182, Bratislava.

Tollmann, A. (1964): Analyse der Weyerer Bögen und der Reiflinger Scholle. – Mitteilungen der Gesellschaft der Geologie- und Bergbaustudenten Österreichs, **14**, 89–123, Wien.

Tollmann, A. (1976): Analyse des klassischen nordalpinen Mesozoikums. – 580 pp., Wien (Franz Deuticke).

Tollmann, A. (1985): Geologie von Österreich. Band 2: Außerzentralalpiner Anteil. – 710 pp., Wien (Franz Deuticke).

Tomašových, A. (2004): Microfacies and depositional environment of an Upper Triassic intra-platform carbonate basin: The Fatric Unit of the West Carpathians (Slovakia). – Facies, **50**, 77–105, Erlangen.

Toula, F. (1871): Beiträge zur Kenntnis des Randgebirges der Wienerbucht bei Kalksburg und Rodaun. – Jahrbuch der k. k. Geologischen Reichsanstalt, **21**, 437–450, Wien.

Toula, F. (1879): Kleine Beiträge zur Kenntnis des Randgebirges der Wienerbucht. – Verhandlungen der k. k. Geologischen Reichsanstalt, **1879**/12, 275–280, Wien.

Trauth, F. (1922): Über die Stellung der „Pieninischen Klippenzone“ und die Entwicklung des Jura in den niederösterreichischen Voralpen. – Mitteilungen der Geologischen Gesellschaft, **14** (1921), 105–264, Wien.

Trauth, F. (1948): Die fazielle Ausbildung und Gliederung des Oberjura in den nördlichen Ostalpen. – Verhandlungen der Geologischen Bundesanstalt, **1948**/10–12, 145–218, Wien.

Trauth, F. (1954): Zur Geologie des Voralpengebietes zwischen Waidhofen an der Ybbs und Steinmühl östlich Waidhofen. – Verhandlungen der Geologischen Bundesanstalt, **1954**, 89–142, Wien.

Vašíček, Z. & Faupl, P. (1999): Zur Biostratigraphie der Schrambachschichten in der Reichraminger Decke (Unterkreide, oberösterreichische Kalkalpen). – Abhandlungen der Geologischen Bundesanstalt, **56**, 593–624, Wien.

Wagreich, M., Lukeneder, A. & Egger, H. (2008): Cretaceous History of Austria. – Berichte der Geologischen Bundesanstalt, **74**, 12–27, Wien.

Wessely, G. (2006): Geologie der Österreichischen Bundesländer. Niederösterreich. – 416 pp., Geologische Bundesanstalt, Wien.

Wilson, J.L. (1975): Carbonate Facies in Geologic History. – 971 pp., New York (Springer).

Received: 23. December 2019, accepted: 27. December 2019

Plates

Plate 1

Images from the Upper Triassic to Lower Cretaceous outcrop recorded at the Hödl-Kritsch section.

Fig. A: Rhaetian limestones of the Kössen Formation, HKr7A, metre 0.

Fig. B: Top of the Rhaetian limestones of the Kössen Formation, HKr7D, metre 6.5.

Fig. C: Rhaetian reefal limestones, HKr7H, metre 7.5.

Fig. D: Transition from the Rhaetian reefal limestone to the red condensed limestones of the Middle Jurassic (Bajocian/Bathonian) Klaus Formation, separated by a few cm-thick stromatolitic crust, HKr7Q-S, metre 10.5.

Fig. E: Facies change from the topmost grey protoglobigerinid Klaus Formation to the red *Saccocoma* limestones (Kimmeridgian), HKrtop-Klaus and HKrStbase, metre 13.5.

Fig. F: Red, well bedded flaser like to nodular *Saccocoma* limestones, HKrSt100-350, metre 15–18.

Fig. G: Transition from the light red Tithonian limestone of the Ammergau Formation into the grey to whitish Ammergau Formation, metre 25.5.

Fig. H: Top of the light grey Berriasian Ammergau Formation, HKr5, metre 30.5.

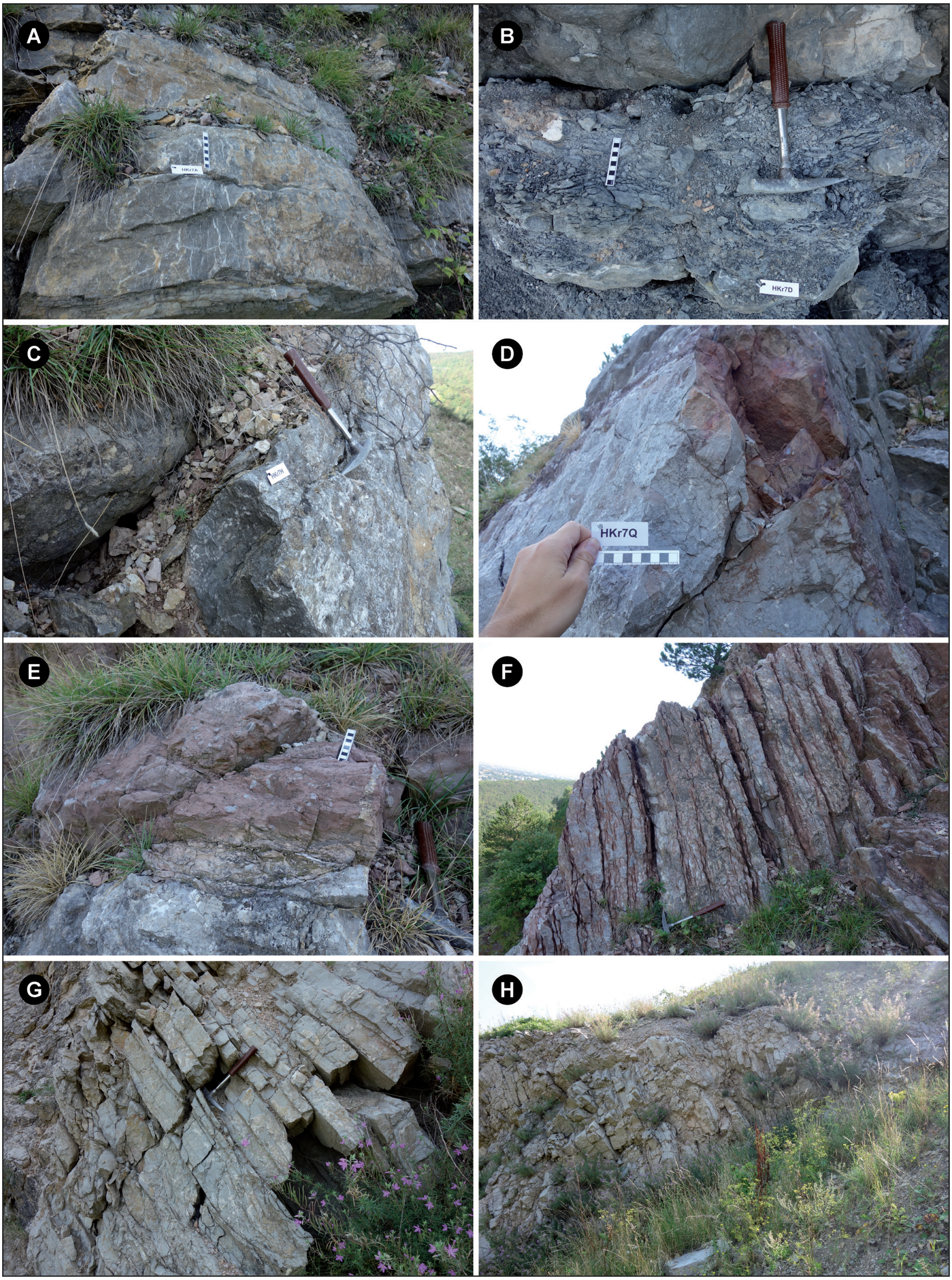
A
B
HKr7D
C
D
HKr7Q
E
F
G
H

Plate 2

Thin sections from the Rhaetian Kössen Formation recorded at the Hödl-Kritsch section.

Fig. A: Bivalve-brachiopod grainstone, with oosparitic layers, most shells preserved with micritisation seams (micrite envelopes), numerous gastropods, rare foraminifera, HKr7A.

Fig. B: Magnification of A with oosparitic layers.

Fig. C: Bivalve-brachiopod grainstone, most shells preserved with micritisation seam, numerous gastropods, frequent foraminifera, HKr7B.

Fig. D: Magnification of C with abundant foraminifera.

Fig. E: Crinoidal grainstone, well laminated, crinoids occurred with echinids, graded bedding, HKr7C.

Fig. F: Magnification of E with crinoids and echinoid spines.

Fig. G: Coral boundstone, corals with preserved septa, frequent brachiopod shells, most shells preserved with micritisation seam, crinoids occurred with echinoids, HKr7D.

Fig. H: Magnification of G with corals and punctated brachiopod shell.

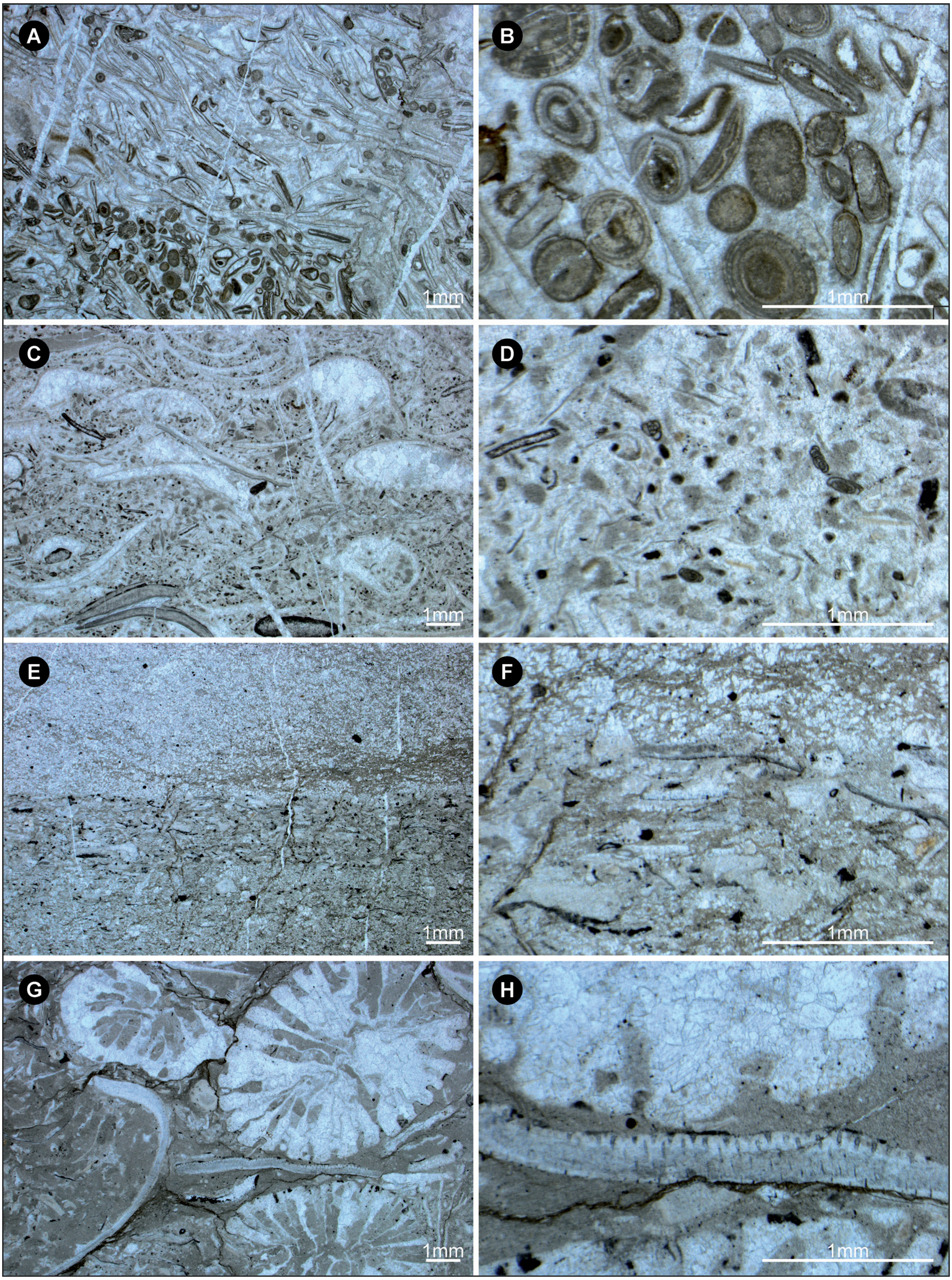
A
1mm
B
1mm
C
1mm
D
1mm
E
1mm
F
1mm
G
1mm
H
1mm

Plate 3

Thin sections from the Rhaetian limestone member recorded at the Hödl-Kritsch section.

Fig. A: Crinoid-brachiopod packstone, encrusting foraminifera, residual layers with “algae”, dissolution seams, crinoids occurred with echinoids, rare foraminifera, HKr7E.

Fig. B: Magnification of A with crinoids and echinoid spine.

Fig. C: Crinoidal-brachiopod wacke- to packstone, rare echinoids, residual layer, HKr7J.

Fig. D: Magnification of C with crinoids in the residual matrix.

Fig. E: Coral-*Bacinella* packstone, most shells preserved with micritisation seam, encrusting foraminifera, *Bacinella irregularis*, brachiopods, corals fragments, gastropods, crinoids occurred with echinoids, frequent ostracods, frequent foraminifera, HKr7O.

Fig. F: Magnification of E with coral septa encrusted by *B. irregularis*.

Fig. G: Brachiopod-gastropod packstone, most shells preserved with micritisation seam, encrusting foraminifera, *B. irregularis*, brachiopods, corals fragments, gastropods, rare crinoids and echinids, frequent ostracods, frequent foraminifera, HKr7R.

Fig. H: Magnification of G with gastropod and brachiopod shells.

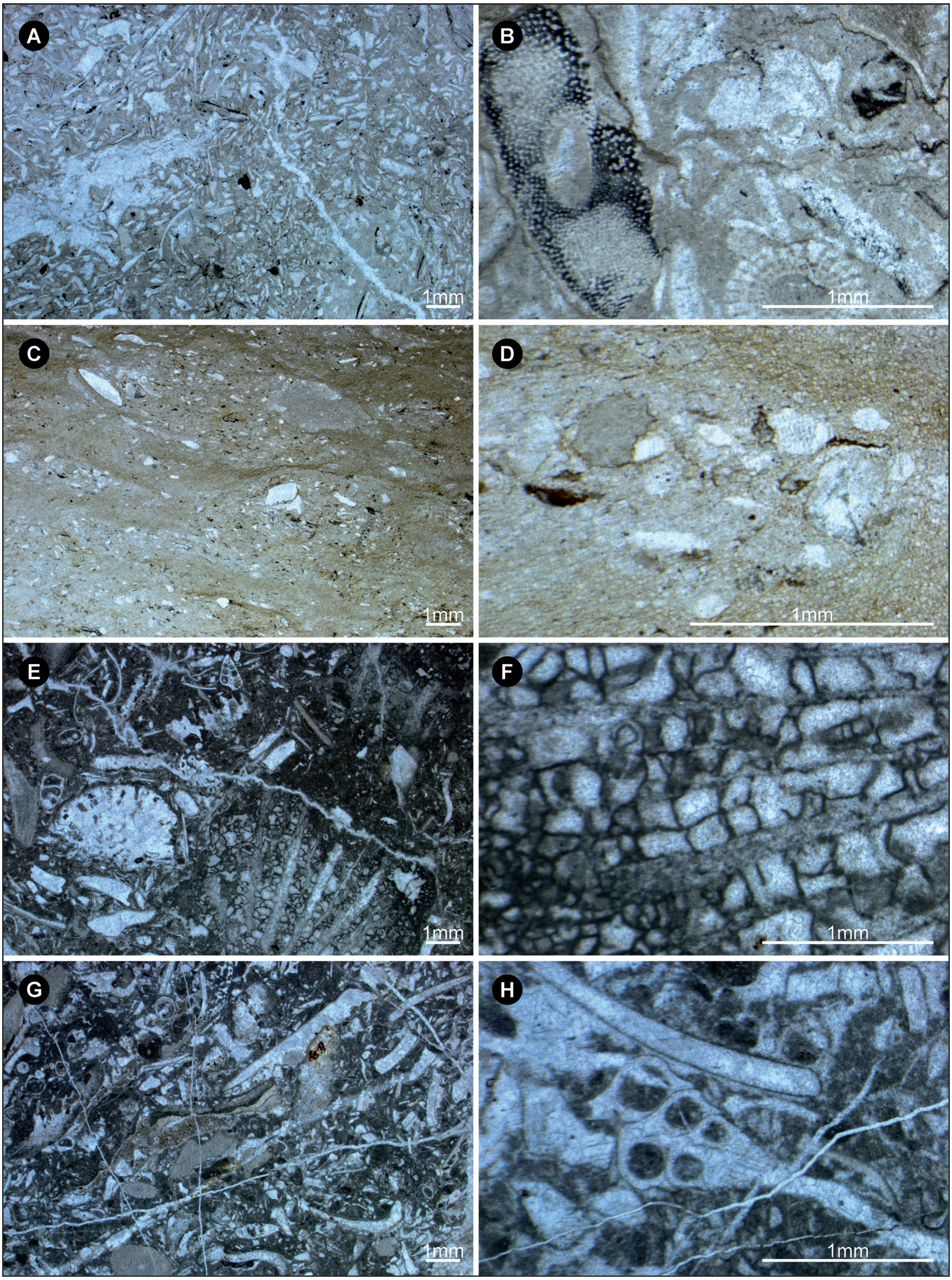
A
1mm
B
1mm
C
1mm
D
1mm
E
1mm
F
1mm
G
1mm
H
1mm

Plate 4

Thin sections from the middle Jurassic stromatolite layer recorded at the Hödl-Kritsch section.

Fig. A: Stromatolite boundstone, *Frutexites*, reworked base with lithoclasts, well laminated, oncoids and cortoids, frequent foraminifera, residual crusts, condensed, with crinoid layers, HKr7stromatolite-10cm.

Fig. B: Magnification of A with crinoids, echinids and filaments.

Fig. C: Multi-layered redeposited fine crinoidal limestone with limonitic crusts impregnation by limonite, note erosive base and top, HKr7stromatolite-5cm.

Fig. D: Magnification of C with the erosive base.

Fig. E: Stromatolite with redeposited and encrusted lithoclasts, filamentous matrix at the top with foraminifera, HKr7stromatolite.

Fig. F: Magnification of E, interspace filled by matrix with foraminifera, bivalves, gastropods and isolated filaments.

Fig. G: Layers of the stromatolite with columnar growth, HKr7stromatolite.

Fig. H: Magnification of G with filled interspaces, note filaments and redeposited foraminifera.

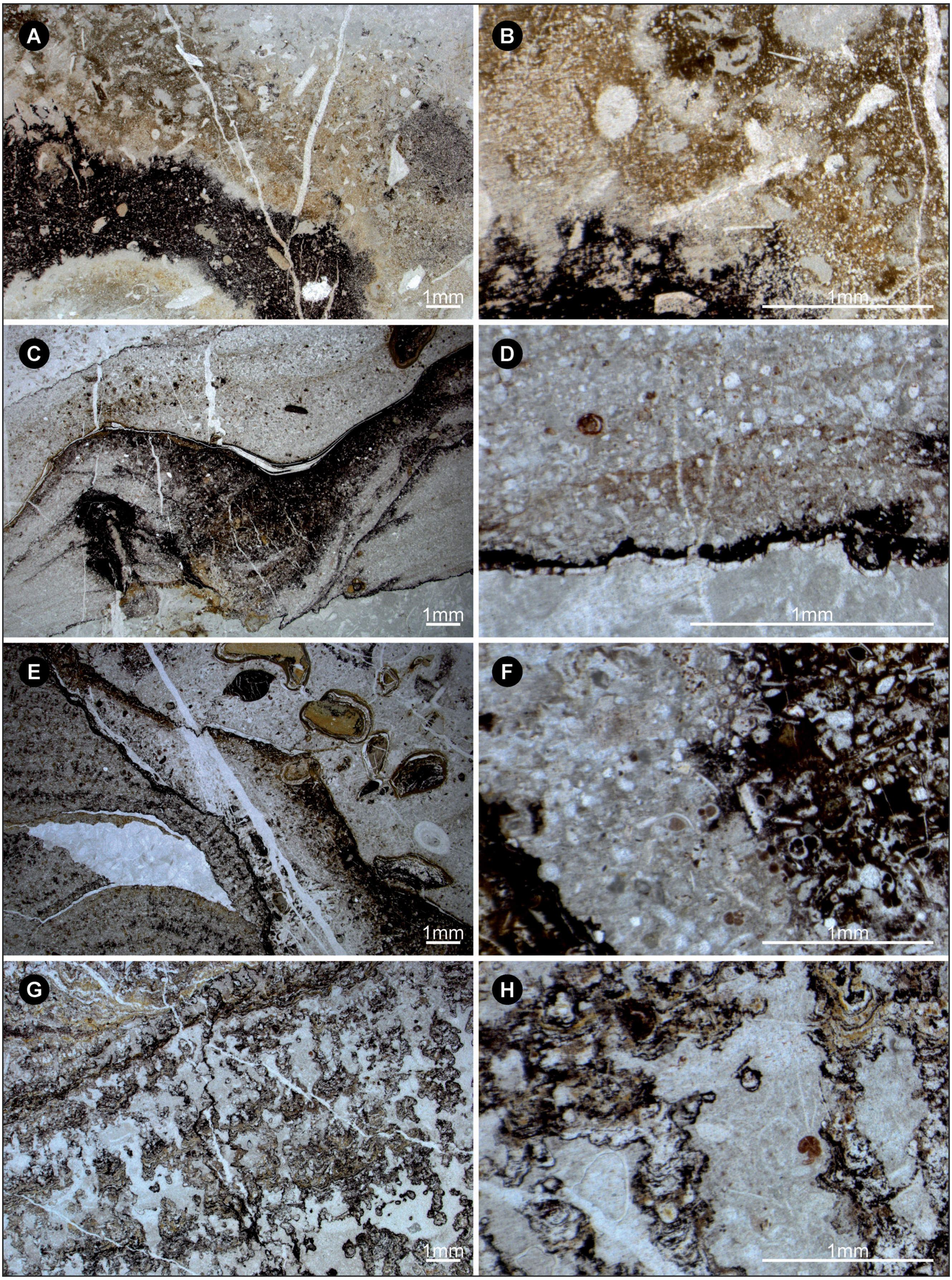
A
1mm
B
1mm
C
1mm
D
1mm
E
1mm
F
1mm
G
1mm
H
1mm

Plate 5

Thin sections from the Bajocian/Bathonian lower Klaus Formation and the Tithonian top of the Klaus Formation recorded at the Hödl-Kritsch section.

Fig. A: Filamentous limestone, mass occurrences of the *Bositra*-like shell-fragments, shells show micritisation seams, HKr7S.

Fig. B: Magnification of A with stacking *Bositra*-like *fragments and* rare peloids.

Fig. C: Filamentous limestone with mass occurrences of the *Bositra*-like shell-fragments, note micritisation seams and bioturbation, HKr7.

Fig. D: Magnification of C with cortoidal mass occurrences of the *Bositra*-like shell-fragments.

Fig. E: Start of foraminiferal limestones with frequent *Bositra*-like shell-fragments, HKr7topKlaus-125cm.

Fig. F: Magnification of E with mass occurrence of filaments.

Fig. G: Foraminiferal limestone with filaments, crinoids and radiolaria, mass occurrence of protoglobigerinids, start of “micritic ooids”, HKr top Klaus.

Fig. H: Magnification of G with mass occurrence of protoglobigerinids and rare filaments.

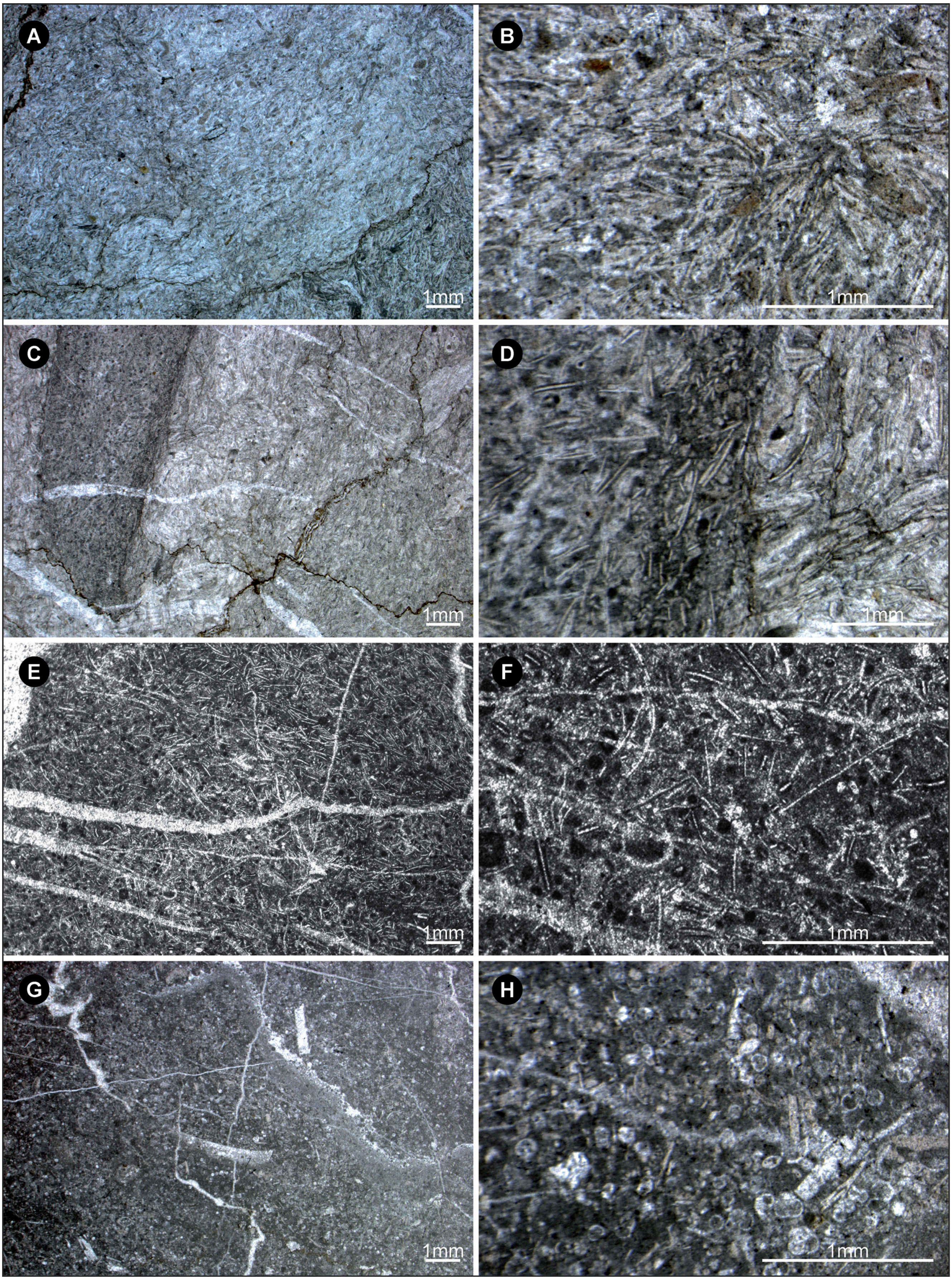
A
1mm
B
1mm
C
1mm
D
1mm
E
1mm
F
1mm
G
1mm
H
1mm

Plate 6

Thin sections from the late Tithonian *Saccocoma* limestones (Tergernsee limestone) and the Tithonian/Berriasian Ammergau Formation recorded at the Hödl-Kritsch section.

Fig. A: Biogenous red limestone with lithoclasts, abundant radiolaria and the start of the crinoidal *Saccocoma* specimens, HKrbaseSt.

Fig. B: Biogenous red limestone with abundant *Saccocoma*, HKr7St50.

Fig. C: Red nodular biogenous limestone bivalves, ostracods and crinoidal fragments, HKr7St450.

Fig. D: Red nodular, radiolarian-*Saccocoma* packstone with frequent *Saccocoma*, bivalves, ostracods and *Laevatychi*, HKr7St350.

Fig. E: Radiolaria-calpionellid wackestone with abundant calpionellids, HKr5-25m.

Fig. F: Grey biogenous limestone, with radiolaria, saccocomids and calpionellids, note resedimentation structures and meshed internal structure of *Laevaptychus*, HKr5-22m.

Fig. G: Grey mudstone with calpionellid laminae and nesting, HKr5-16m.

Fig. H: Top of the radiolaria-calpionellid wackestone with numerous calcite veins, HKr5.

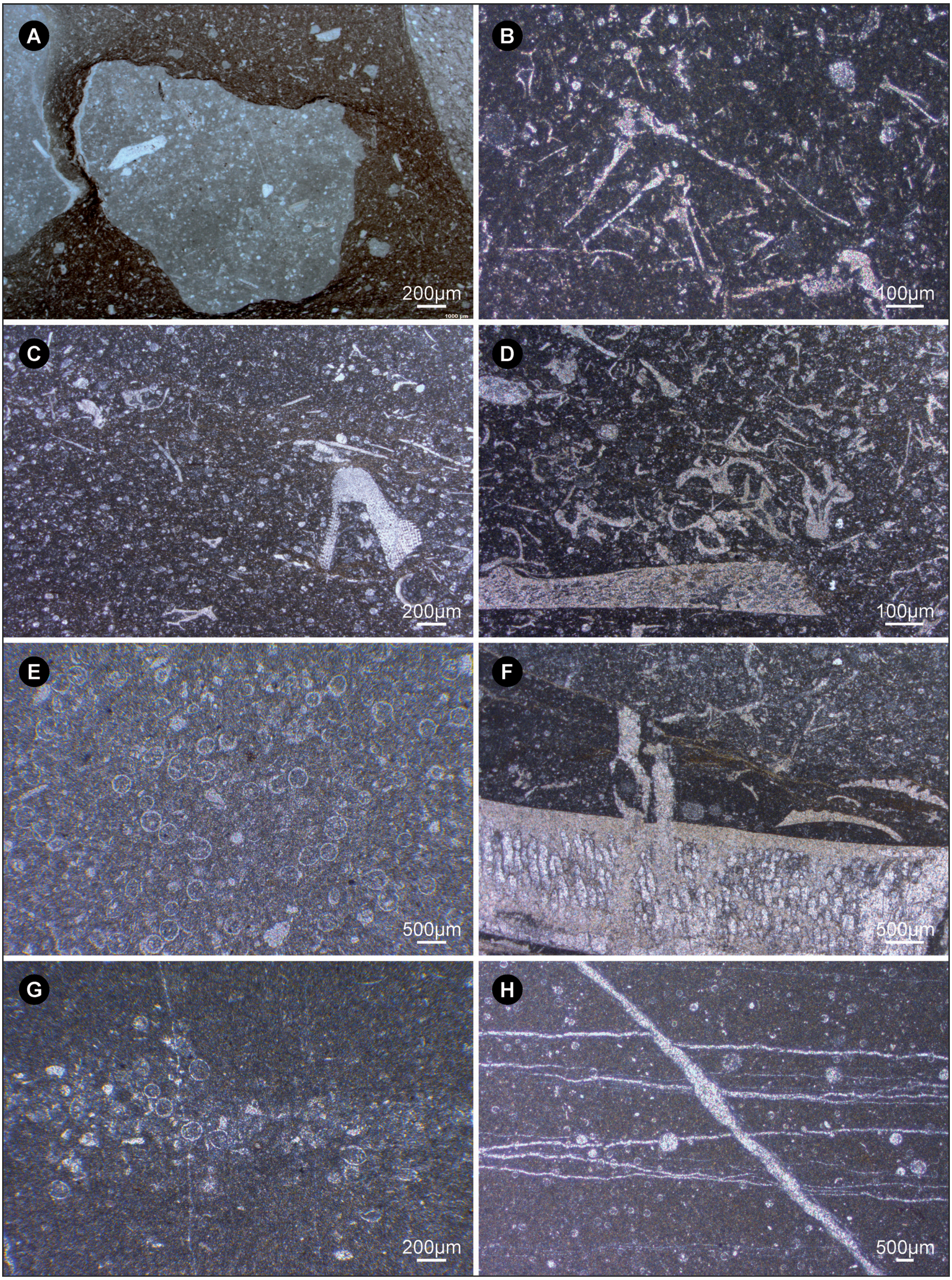
A
200µm
B
100µm
C
200µm
D
100µm
E
500µm
F
500µm
G
200µm
H
500µm

JAHRBUCH DER GEOLOGISCHEN BUNDESANSTALT
Jb. Geol. B.-A. | ISSN 0016–7800 | Band 159 | Heft 1–4 | S. 203–245 | Wien, Dezember 2019

Upper Albian and Lower Cenomanian ammonites from the Mfamosing Quarry, Calabar Flank, Cross River State, south-eastern Nigeria

William J. Kennedy[1] & Harald Lobitzer[2]
With a contribution by Franz Stojaspal (†)

16 Text-Figures, 1 Table, 6 Plates

Ammonites
Albian
Cenomanian
Mfamosing Limestone
Calabar Flank
Cross River State
Nigeria

Contents

Abstract

The Upper Albian and Lower Cenomanian ammonites from the abandoned Mfamosing Limestone Quarry of the Calabar Cement Company (Calcemco) in Cross River State, south-eastern Nigeria, are described. The highly fossiliferous, ferruginous, pyritic and in part nodular phosphatic mineralized hardground at the top of the Mfamosing Formation at this classic locality has yielded a diverse fauna. The index species of the upper Upper Albian *Pervinquieria* (*Subschloenbachia*) *rostrata* Zone, and the succeeding *P.* (*S.*) *perinflata* Zone occur as large limestone moulds. A diverse predominantly phosphatised or pyritic Lower Cenomanian fauna is correlated with the widely recognized lower *Neostlingoceras carcitanense* Subzone of the *Mantelliceras mantelli* Zone, with *Puzosia* (*Anapuzosia*) sp., *Stoliczkaia* (*Lamnayella*) *juigneti* (Wright & Kennedy, 1978), *Salaziceras nigerianum* Förster & Scholz, 1979, *Flickia bullata* sp. nov., *Graysonites wacoense* (Böse, 1928), *Utaturiceras* sp., *Acompsoceras calabarense* Zaborski, 1985, *Acompsoceras* sp. juv., *Mariella* (*M.*) *bicarinata* (Kner, 1852), *Mariella* (*M.*) *essenensis* (Geinitz, 1849), *Mariella* (*M.*) *oehlerti oehlerti* (Pervinquière, 1910), *Mariella* (*M.*) aff. *miliaris* (Pictet & Campiche, 1861), *Mariella* (*M.*) *cenomanensis* (Schlüter, 1876), and *Hypoturrilites betaitraensis* Collignon, 1964.

1 William J. Kennedy: Oxford University Museum of Natural History, Parks Road, Oxford OX1 3PW, and Department of Earth Sciences, South Parks Road, Oxford OX1 3AN, United Kingdom. Jim.Kennedy@oum.ox.ac.uk
2 Harald Lobitzer: Lindaustraße 3, 4820 Bad Ischl, Austria. harald.lobitzer@aon.at

Eine Ammonitenfauna des späten Albiums und frühen Cenomaniums aus dem Mfamosing Steinbruch, Calabar Flank, Cross River State, Südostnigeria

Zusammenfassung

Aus dem fossilreichen Hardground am Top der klassischen Lokalität der Mfamosing-Formation im inzwischen stillgelegten Mfamosing-Kalkstein-Steinbruch der Calabar Cement Company (Calcemco) wird eine diverse, stratigrafisch kondensierte Ammonitenfauna beschrieben. Die Fauna weist sowohl die namensgebende Art der *Pervinquieria* (*Subschloenbachia*) *rostrata*-Zone des obersten Albiums auf, als auch der darüber folgenden *P.* (*S.*) *perinflata*-Zone. Sie kann mit der weithin anerkannten *Neostlingoceras carcitanense*-Subzone der *Mantelliceras mantelli*-Zone des unteren Cenomaniums korreliert werden. Aus letzterer konnten folgende Taxa nachgewiesen werden: *Puzosia* (*Anapuzosia*) sp., *Stoliczkaia* (*Lamnayella*) *juigneti* (Wright & Kennedy, 1978), *Salaziceras nigerianum* Förster & Scholz, 1979, *Flickia bullata* sp. nov., *Graysonites wacoense* (Böse, 1928), *Utaturiceras* sp., *Acompsoceras calabarense* Zaborski, 1985, *Acompsoceras* sp. juv., *Mariella* (*M.*) *bicarinata* (Kner, 1852), *Mariella* (*M.*) *essenensis* (Geinitz, 1849), *Mariella* (*M.*) *oehlerti oehlerti* (Pervinquière, 1910), *Mariella* (*M.*) aff. *miliaris* (Pictet & Campiche, 1861), *Mariella* (*M.*) *cenomanensis* (Schlüter, 1876) und *Hypoturrilites betaitraensis* Collignon, 1964.

Introduction

Unless otherwise stated, the fossils described in this paper were collected in 1976 and 1977 by Lobitzer at the now abandoned Mfamosing limestone quarry of the Calabar Cement Company (Calcemco). The quarry is located close to Mfamosing village on the "Calabar Flank" at latitude 5°04'16'' north, longitude 8°32'20'' east, some 33 km north-east of Calabar, the capital of Cross River State in south-eastern Nigeria (Text-Fig. 1). The Calabar Flank is situated on the southern slopes of the Precambrian crystalline basement complex of the Oban Massif. It constitutes the southernmost part of the Benue Trough, which extends across Nigeria from the south-west to the north-east.

Most of the samples were collected in situ on the bedding plane of the intraformational hardground on top of the Mfamosing Limestone, while some represent loose specimens, collected either on the in situ weathered hardground or from scree after blasting.

Previous research

The limestone potential of south-eastern Nigeria was already recognised in early studies by the Geological Survey of Nigeria (e.g. Raeburn, 1937; Tattam, 1939; Orajaka, 1959a, b), who also published the geological mapsheet 80 Oban Hills in the scale 1:250,000 (Geological Survey of Nigeria, 1957). In addition to the economic evaluation of the limestone and marl occurrences, Reyment (1952, 1955, 1965, 1972, 1980) initiated biostratigraphic investigations on ammonite-bearing localities in the region. Later, Reyment continued this work partly in the frame of IGCP-project 58 "Mid Cretaceous Events" (e.g. Reyment & Dingle, 1987; Reyment & Mörner, 1977; Reyment & Tait, 1983). Reyment was also the first to examine, albeit briefly, the ammonites described below. The late Reinhard Förster (Munich) contacted Lobitzer and published two papers based on the ammonite-fauna described in detail here, as well as additional material he had collected (Förster, 1978; Förster & Scholz, 1979). These contributions already recognized the condensed Upper Albian–Lower Cenomanian character of the hardground faunas on top of the Mfamosing Limestone. The geology of the Calabar Flank also attracted prominent local geoscientists, who contributed essential papers and added greatly to our knowledge of this spectacular region (e.g. Adegoke et al., 1976; Ekwueme et al., 1995; Essien & Ufot, 2010; Fayose & Dessauvagie, 1976; Fayose, 1978; Petters, 1982; Petters & Reijers, 1987; Kogbe, 1989; Nair et al., 1982; Nyong, 1995; Nyong & Ramanathan,1985; Umeji, 2013).

Since the researches of Lobitzer in Nigeria in the years 1976 and 1977, many papers have been published, in particular on the sedimentology, diagenesis and stratigraphy of the Mfamosing Limestone and the overlying Eze-Aku Shale Formation. The main focus of the present paper is the ammonite fauna of the hardground on top of the Mfamosing Limestone. Accordingly, the manyfold studies outside the context of the present paper, as the subdivision of the Asu River Group by various authors, is not discussed here.

According to Reyment & Bengtson (1985), marine sedimentation on the Calabar Flank began with the deposition of the Odukpani Group (sensu Petters et al., 1995) in the mid-Albian linked to the separation of Africa from South America and the development of the South Atlantic Ocean. The Odukpani Group consists of the Albian platform carbonates of the Mfamosing Limestone and the Cenomanian Eze-Aku (Ekenkpon) Shales. Most of the fauna described in this paper was collected from and on the hardground, which separates the Mfamosing Limestone with sharp boundary from the overlying Eze-Aku Shales.

Locality details

As in other south-western African sedimentary basins, and in the Gulf of Guinea, marine sedimentation began in the Albian, associated with the opening of the South Atlantic Ocean and the separation of Africa from South America. The "Calabar Flank-carbonate platform" was established as a result of landward onlap of shallow marine carbonates onto the southern rim of the Oban Hills. Here, the Mfamosing Limestone was deposited on top of the fluvio-deltaic clastic sediments of the Awi Formation of probable Aptian age (Adeleye & Fayose, 1978). The Mfamosing Limestone carbonate platform survived until the Upper Albian, when its existence was abruptly terminated, with the development of a hardground and omission surface from which most of the fauna dealt with in this paper was collected. Upper Albian ammonites are preserved as limestone moulds; Lower Cenomanian elements are phosphatised or pyritised and come from pockets in, and the surface of, the hardground.

In close cooperation with the Calcemco-geologists, Lobitzer carried out extensive field investigations and su-

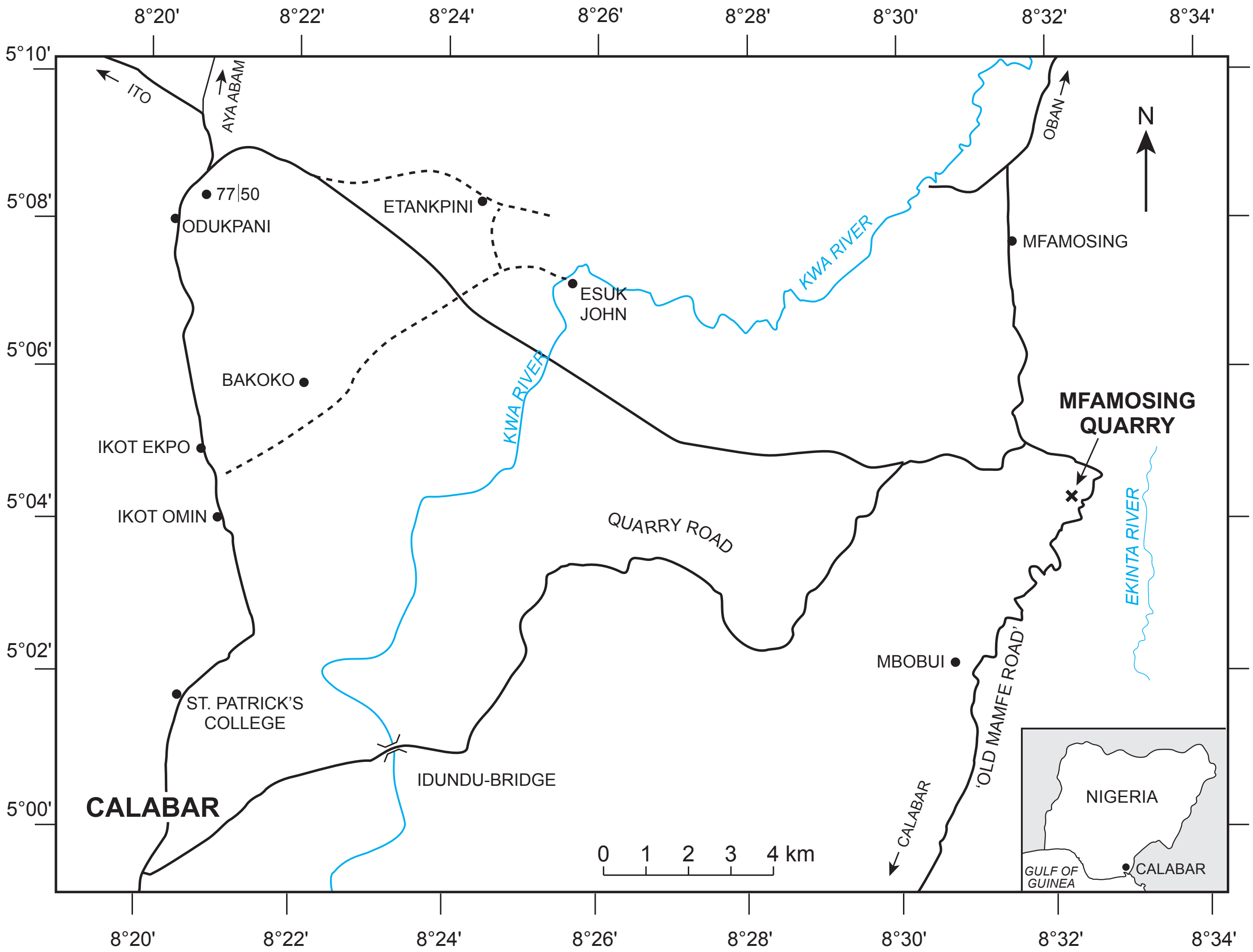

Text-Fig. 1.
Locality map 1976/1977 of the Mfamosing Quarry and outcrop 77/50.

pervised drilling programs for Calcemco in the wider surroundings of the Mfamosing Quarry in order to a better understanding of the spatial facies distribution of the succession. Even the deepest drill hole with approximately 140 m of section did not reach the crystalline basement complex of the Oban Hills. The Mfamosing Limestone, up to 80 m thick, rests on more than 15 m of probably Aptian–Albian cavernous dolomite, chalkified at some levels. From its classic locality the Mfamosing Limestone outcrop extends to the north-west, through Etankpini village (Text-Fig. 1) and beyond, along the southern slope of the Oban Hills. Our studies and those by Agbebia & Egesi (2017) and Reijers & Petters (1997) confirm that karstification increases along strike. Furthermore, terrigenous-clastic input from the exposed hinterland of the Oban Hills becomes increasingly important along strike and landwards to the north. However, during transgressive phases, only minor amounts of siliciclastics accumulated in the Mfamosing Limestone.

The Mfamosing Limestone

The classical locality of the shallow-marine to intertidal Mfamosing Formation sensu Petters (1982) with the hardground at the top is the now abandoned Mfamosing quarry of Calabar Cement Company (Calcemco), (Text-Fig. 2). Here the limestones dip 5–10° to the south-west. Meanwhile, the United Cement Company of Nigeria Ltd. (UniCem) has replaced the historic quarry with a new one.

The Mfamosing Limestone – the “Lower Limestone” sensu Murat (1972a, b) – represents the northernmost carbonate deposit of the South Atlantic Ocean in West Africa. The Middle–Upper Albian stable carbonate platform of the Mfamosing Limestone was established during the initial marine transgression due to landwards onlapping of calcareous sediments on the “Calabar Flank” – the southern slopes of the Precambrian crystalline basement complex of the Oban Hills Massif. Structurally, the Calabar Flank is part of the foundered southeastern Nigerian Continental margin. The formation name “Mfamosing Limestone” has already been used in internal reports of Calcemco since 1976 and finally defined by Petters (1982). The Mfamosing Limestone represents the largest and chemically purest carbonate body in Nigeria, however, Calcemco was using this highest quality limestone for cement production alone. Time-equivalent carbonates occur on either side of the opening South Atlantic Ocean and are also well documented in several DSDP-, respectively ODP-Legs from the South Atlantic (e.g. Pletsch et al., 1996, 2001).

At its classical section – the Mfamosing quarry – the Mfamosing Limestone records a wide variety of shallow ma-

Text-Fig. 2.
The Mfamosing Quarry in February 1976. The photo shows the general dip of the Mfamosing Limestone beds of approximately 9° in a south-westerly direction. A prominent hardground is developed at the top of the Mfamosing Limestone at this classic locality; this is the source of almost all of the Upper Albian and Lower Cenomanian fossils dealt with in this paper. The hardground is overlain by about 5 m of dark-grey to black shales of the Eze-Aku Formation, in turn overlain by about 10 m of coastal plain sands of the Benin Formation.

rine to intertidal depositional environments (Reijers & Petters, 1987). In its upper part a significant influx of siliciclastics from the hinterland of the Oban Hills temporarily suppressed carbonate production. The Mfamosing Limestone is topped by an intraformational hardground (Text-Figs. 3, 4; Förster, 1978; Förster & Scholz, 1979; Oti & Koch, 1990).

Reijers & Petters (1997), Harry et al. (2017) deal with the sequence stratigraphic interpretation of the Mfamosing Limestone and the reason for the hardground on top of it, which they consider as product of a TST (transgressive systems tract), respectively of a MFS (maximum flooding surface). As Reijers (1998) and Petters et al. (1995) pointed out, the influx of siliciclastics and sea-level fluctuations controlled carbonate production. Peritidal, lagoonal and reefal carbonates rim the igneous Oban Massif in the south and southwest and reflect an initial relative sea-level highstand. Maximal carbonate production took place during rising sea-level, when an open-marine carbonate platform and a mixed carbonate-siliciclastic shoal co-existed side by side.

According to Essien & Ufot (2010) the age of the Mfamosing Limestone has been a subject of discussion by several researchers, who ascribed different ages based on different criteria. In his early papers, Reyment (e.g. 1965) assigned a Cenomanian age to the Odukpani Formation, of which the Mfamosing Limestone is the basal unit. Following Reyment, Dessauvagie (1968) erroneously regarded the foraminifer *Trocholina odukpaniensis* as Cenomanian. In the Mfamosing Limestone this characteristic foraminifer predominantly occurs in reef-like environments dominated by encrusting and ramose coralline red algae (Fayose, undated, ?1976; Poignant & Lobitzer, 1982). The latter formed

Text-Fig. 3.
Mfamosing Quarry. Bedding plane surface of the hardground at the top of the Mfamosing Limestone with oyster shells and gastropods.

oncoidal algal packstones with dasycladaceans, stromatolitic and coralline algal boundstones, which point to a tidal flat environment; coralgal boundstones are rather rare. Also *Lithophaga*-borings occur relatively frequent in the coralline algal boundstones in the upper part of the Mfamosing Limestone and also in the hardground.

Akpan (1992) recorded, for the first time, the itierid gastropod *Peruviella dolium* (Römer) from the basal section of the Mfamosing Limestone, and dated it as Mid-Albian on this basis. According to Hanger (1998), communities dominated by *P. dolium* are characteristic for Albian nearshore environments on both sides of the Cretaceous Tethyan seaway.

Oti & Koch (1990) focused on the microfacies and diagenesis of the Mfamosing Limestone, which according to them was deposited during one Albian transgressive cycle. They concluded that the carbonates were deposited in a shallow shelf, characterized by strong lateral facies variations, with high-energy submarine bar carbonate sands, patch reefs, and algal boundstones.

The hardground at the top of the Mfamosing Limestone Formation

A remarkable colour contrast is evident between the top of the bright mud to wackestone of the Mfamosing Limestone and the approximately 30 cm thick, more intensively silicified rusty brown, ferruginous and in the upper part nodular phosphatic and pyritic mineralized hardground (Text-Figs. 3, 4). The stratigraphically condensed fossils on the bedding plane of the hardground – in particular ammonites, gastropods, scarce bivalves and echinoids, *Lithophaga* borings and *Thalassinoides*-burrows (Akpan, 1990) – often show extensive corrosion due to omission and subsolution during the Albian-Cenomanian boundary interval. In contrast to the molluscs, the oyster shells are practically uncorroded, because they were probably growing on the already lithified hardground prior to the onset of sedimentation of the Eze-Aku Shales (Text-Figs. 2, 4). The hardground marks a transgressive event: a distinct sea-level rise during the Upper Albian-Lower Cenomanian interval. With the gradual drowning of the Mfamosing Limestone carbonate platform, an increase of terrigenous influx is evident and carbonate production ceased.

According to Palmer & Wilson (2004), carbonate hardgrounds often formed during calcite sea intervals, which were coincident with times of rapid seafloor spreading and global greenhouse climate conditions (Stanley & Hardie, 1999).

The Eze-Aku Shales

In the Mfamosing Quarry the hardground on top of the Mfamosing limestone is overlain unconformably with a sharp boundary by about five meters of black shales (Text-Fig. 2) of the Eze-Aku Formation sensu Reyment (1965), repectively the Ekenkpon Formation sensu Petters et al. (1995). The Eze-Aku Formation is a sequence of pyritic and organic rich black shales, which locally shows minor intercalations of calcareous mudstones with oyster and inoceramid fragments and variable amounts of organic particles. The Eze-Aku Shales are the result of a second transgression on the Calabar Flank in the late Cenomanian.

Palynological studies by Lawal (1991) demonstrate a Late Cenomanian age (*Triorites africaensis* Zone) for the basal Eze-Aku Formation in the lower Benue Trough. Based on ammonites and planktic foraminifera Nyong & Ramanathan (1985) consider the black organic-carbon-rich Eze-Aku Shales as sediments of a shallow epicontinental sea. It seems very likely that upwelling was responsible for these organic-rich sediments. All our samples of the Eze-Aku Shales analysed by Herbert Stradner (Geological Survey of Austria, Vienna) were barren of calcareous nannofossils.

Text-Fig. 4.
Mfamosing Quarry. The hardground at the top of the Mfamosing Limestone shows pyrite mineralization along vertical fractures and on the bedding plane. The hardground is overlain with sharp boundary by organic-rich black shales of the Eze-Aku Formation. A late Cenomanian age is confirmed by the presence of the arenaceous foraminifer *Thomasinella punica*.

Above the Eze-Aku Formation about 10 m of red lateritic clays and coastal plain sands of the Benin Formation are exposed (Text-Fig. 2).

The Campanian–Maastrichtian Nkporo Shales cap the Cretaceous sequence of the Calabar Flank. They are, however, not exposed in the immediate environs of the Mfamosing quarry.

The first record of the foraminifer *Thomasinella punica* Schlumberger (original description by Schlumberger in Thomas, 1893) in Nigeria – an indicator for a trans-Saharan seaway in the Late Cenomanian

Reyment (1980) initiated the discussion of the timing of the first trans-Saharan transgression in connection with the opening of the South Atlantic Ocean. Ammonite and foraminifer data from the Gulf of Guinea and from adjacent African basins and also of ODP Leg 159 (e.g. Moullade et al., 1998) suggested that mid-or deep-water circulation between the equatorial and South Atlantic existed at least since the late Albian. At this time, faunal exchange along a trans-Saharan Seaway was minimal, if at all (e.g. Bengtson & Koutsoukos, 1992; Courville et al., 1998; Pletsch et al., 1996, 2001). According to Zaborski (2000), an arm of the proto-Atlantic Ocean occupied the lower and middle Benue Trough in the upper Middle Albian, but the Upper Cenomanian transgression was more extensive and reached its acme in the Lower Turonian. During this epicontinental transgression, the sea entered from the Gulf of Guinea via the Calabar Flank into the Benue Trough and flooded the Iullemmeden Basin (e.g. Charrière et al., 1998; Kogbe, 1981; Meister & Abdallah, 1996; Meister et al., 1994,) and subsiding areas of the Sahara East of the Hoggar. Finally, it formed a short-lived connection between the Gulf of Guinea and the Tethys, and a faunal exchange was possible between the South Atlantic and the Tethys Ocean.

In this context an internal report from 1976 of the Geological Survey of Austria by Werner Fuchs (†) is relevent. He described a rich foraminiferan assemblage with hedbergellids, lenticulinids and the Cenomanian arenaceous taxon *Thomasinella punica* from the basal part of the anoxic black shales of the Eze-Aku Formation. It is probably the first record of this characteristic foraminifer from Nigeria. The assemblage indicates a shelf to upper slope depositional setting.

Arnaud-Vanneau & Prestat (1984) report the occurrence of *Thomasinella punica* in other Southwest African coastal basins and in the context of the Congo Basin, Mbani (2008) stated “le Cénomanien est surtout caractérisé par *Thomasinella punica*”. More recently, Igwe et al. (2015) and Harry et al. (2017) dealt with the foraminifera fauna of the Eze-Aku Formation of the Lower Benue Trough.

Thomasinella punica is present in almost all our washed samples from the Eze-Aku Shales from the surroundings of the Mfamosing quarry, however, only in the coarse grain fraction. Therefore the statement by Mbani (2008) is true also for the Calabar Flank.

Age and affinities of the faunas

The faunas described below can be dated in terms of the zonal scheme set out in Table 1, based on the sequence established in Western Europe (Kennedy & Gale, 2015, 2017).

The oldest fauna recognized from the hardground is preserved as limestone moulds comprises *Pervinquieria* (*Subschloenbachia*) *rostrata* (J. Sowerby, 1817) (Text-Figs. 8, 9), and, possibly, *Arestoceras* sp. (Text-Fig. 12). The former indicates the presence of the Upper Albian *rostrata* Zone of the standard sequence, and has a cosmopolitan distribution including Western Europe eastwards to Iran, Japan, Tamil Nadu in South India, Madagascar, and Texas. *Arestoceras* is best known from KwaZulu-Natal in South Africa; records from elsewhere are doubtful.

The presence of the succeeding Upper Albian *perinflata* Zone is indicated by the presence of a single individual (Text-Fig. 10) preserved as limestone internal mould, compared to the index species, which is again cosmopolitan, with records of the species, or close allies, from Western Europe to Ukraine (Crimea), Texas, and KwaZulu-Natal in South Africa and, possibly Iran and Tamil Nadu in south India.

The Lower Cenomanian fauna is:

Puzosia (*Anapuzosia*) sp.

Stoliczkaia (*Lamnayella*) *juigneti* (Wright & Kennedy, 1978)

Salaziceras nigerianum Förster & Scholz, 1979

SUBSTAGE	ZONE	SUBZONE
Lower Cenomanian	*Mantelliceras dixoni*	
	Mantelliceras mantelli	*Mantelliceras saxbii* *Sharpeiceras schlueteri* *Neostlingoceras carcitanense*
	Pleurohoplites briacensis	
Upper Albian (part)	*Pervinquieria* (*S.*) *perinflata*	
	Pervinquieria (*S.*) *rostrata*	
	Pervinquieria (*S.*) *fallax*	
	Pervinquieria (*S.*) *inflata*	

Tab. 1.
Upper Albian and Lower Cenomanian ammonite zonation used in the present study.

Flickia bullata sp. nov.

Graysonites wacoense (BÖSE, 1928)

Utaturiceras sp.

Acompsoceras calabarense ZABORSKI, 1985

Acompsoceras sp. juv.

Mariella (*M.*) *bicarinata* (KNER, 1852)

Mariella (*M.*) *essenensis* (GEINITZ, 1849)

Mariella (*M.*) *oehlerti oehlerti* (PERVINQUIÈRE, 1910)

Mariella (*M.*) aff. *miliaris* (PICTET & CAMPICHE, 1861)

Mariella (*M.*) *cenomanensis* (SCHLÜTER, 1876)

Hypoturrilites betaitraensis COLLIGNON, 1964

The material occurs in three preservations, phosphatic internal moulds, pyritic nuclei, and crushed, unphosphatised material. The last two preservation categories are interpreted as the youngest elements of the fauna. They include *Graysonites wacoense* (unphosphatised) and *Stoliczkaia* (*Lamnayella*) *juigneti* (a pyritic nucleus), the latter a species restricted to the *carcitanense* Subzone of the Lower Cenomanian *mantelli* Zone, which sets an upper age limit for the assemblage. Of other species known from localities other than south-eastern Nigeria, all are restricted to the Lower Cenomanian, and most have wide geographic distributions. Of the remainder, *Flickia bullata* sp. nov. belongs to a genus that is known from the Upper Albian and Lower Cenomanian of Algeria, Tunisia, Texas, KwaZulu-Natal in South Africa, and Madagascar, whilst *bullata* is most closely related to *Flickia quadrata* COLLIGNON, 1964 (23, Pl. 322, Figs. 1428, 1429) known only from the Lower Cenomanian of Madagascar (WRIGHT & KENNEDY, 1979 revise the genus *Flickia* and its constituent species). Its presence is compatible with the Lower Cenomanian assignation of the fauna. *Acompsoceras calabarense* belongs to a genus known from the Lower Cenomanian of Western Europe, Tunisia, Texas, and Madagascar. *Sharpeiceras nigeriense* belongs to an even more widely distributed genus, with records from Western Europe eastwards to Kazakhstan and Iran, Texas and northern Mexico, the Middle East, North Africa, KwaZulu-Natal in South Africa, Madagascar, Tamil Nadu in South India, and Japan.

There remains *Salaziceras nigerianum* FÖRSTER & SCHOLZ (1979: 111) argued for this as an Upper Albian element in the fauna, although the preservation of the types is that of other, unequivocally Lower Cenomanian taxa, rather than the unequivocally Upper Albian taxa present. Furthermore, since the original account of *Salaziceras nigerianum* in 1979, the genus has been recognized in the Upper Albian of Madagascar (KENNEDY & KLINGER, 2008) and Lower Cenomanian of northern KwaZulu-Natal in South Africa (KENNEDY & KLINGER, 2012).

In conclusion, the ammonites faunas from the Mfamosing Quarry belong, predominantly, to cosmopolitan genera and species, suggesting free communication from both north and south during the Upper Albian and Lower Cenomanian.

FÖRSTER & SCHOLZ (1979: 111) argued for the presence of representative elements of the *briacensis* Zone of SCHOLZ (1973) in the Mfamosing faunas, placing special weight on the presence of *Salaziceras*. This is problematic, in that they do not record any of the species upon which Scholz based his *briacensis* Zone, while this zone spans the Albian/Cenomanian boundary in the Global boundary Stratotype Section for the base of the Cenomanian Stage (KENNEDY et al., 2004). The index species is currently referred to the genus *Pleurohoplites* SPATH, 1921 (see KENNEDY, 2015: 409 et seq.), which is restricted to the Old World Boreal Realm. Equally absent from the Mfamosing faunas are elements from the North African equivalent of the *briacensis* Zone, the *Stoliczkaia* (*Shumarinaia*) *africana* Partial Range Zone of ROBASZYNSKI et al. (2008). There is thus no evidence for the presence of unequivocal *briacensis* Zone elements in the faunas from the Mfamosing Quarry.

Conventions

Dimensions are given in millimeters: D = diameter; Wb = whorl breadth; Wh = whorl height; U = umbilicus; c = costal dimension; ic = intercostal dimension. Figures in parentheses are dimensions as a percentage of the diameter. The suture terminology is that of KORN et al. (2003): E = external lobe; A = adventive lobe (= lateral lobe, L, of KULLMANN & WIEDMANN 1970); U = umbilical lobe; I = internal lobe.

Repositories of specimens

BMNH: The Natural History Museum, London.

BSPHG: Bayerische Staatsammlung für Paläontologie und historische Geologie, Munich.

EMP: Collections of the École des Mines, Paris, currently housed in the collections of the Université Claude Bérnard, Lyon.

FSM: Collections of the Faculté des Sciences, Le Mans.

GBA: Geologische Bundesanstalt, Vienna.

MGL: Musée Geologique, Lausanne.

MNHG: Muséum d'Histoire Naturelle, Genève.

MNHN: Laboratoire de Paléontologie of the Muséum nationale d'Histoire Naturelle, Paris.

OUMNH: Oxford University Museum of Natural History.

TMM: Texas Memorial Museum, Austin, Texas.

USNM: US National Museum of Natural History, Washington D.C.

Systematic palaeontology

Order Nautilida DE BLAINVILLE, 1825
Suborder Nautilina DE BLAINVILLE, 1825
Superfamily Nautiloidea DE BLAINVILLE, 1825
Family Cymatoceratidae SPATH, 1927
Genus *Cymatoceras* HYATT, 1884

Type species: *Nautilus pseudoelegans* D'ORBIGNY, 1840: 70, Pl. 8, Figs. 1–4; Pl. 9, Figs. 1, 2, by the original designation of HYATT (1884: 301).

Cymatoceras sakalavum (COLLIGNON, 1949)

(Text-Figs. 5A–D)

1949 *Nautilus* (*Cymatoceras*) *sakalavum* COLLIGNON: 41, Pl. 6, Figs. 1, 2; Pl. 21, Fig. 1.

1979 *Cymatoceras* sp. FÖRSTER & SCHOLZ: 117.

Type: The holotype, by original designation, is the original of COLLIGNON (1949: 41, Pl. 6, Fig. 2) from the Lower Albian of Ambaramaninga, Madagascar, in the collections of the École Nationale Supérieur des Mines, now housed in the collections of the Université de Lyon I, Villeurbanne (EMP).

Material: GBA 2016/003/0001–0003.

Description: GBA 2016/003/0001 (Text-Figs. 5A–B) is an internal mould of a 180° sector of phragmocone with an estimated original diameter of 70 mm approximately. Coiling is very involute, the umbilicus very small and deep. The whorl section is depressed, with a whorl breadth to height ratio of 1.1, the greatest breadth just outside the umbilical shoulder, the flanks feebly convex and converging to the broadly rounded ventrolateral shoulders and venter. The low ribs broaden rapidly across the flanks, and are markedly convex across the ventrolateral shoulders, crossing the venter in a marked concavity.

GBA 2016/003/0003 (Text-Figs. 5C–D) is an internal mould of an incomplete half whorl of body chamber with an estimated original diameter of 120 mm. The original whorl section was depressed, although the original proportions cannot be established. The flanks are convergent and very feebly convex, the venter very broad and feebly convex. The course of the low ribs is clearer than in the previous specimen, straight and rursirdiate on the inner flank, flexing back and broadening markedly on the middle and outer flanks and venter, sweeping back and convex on the outer flank, and markedly concave on the venter, where they are at their broadest.

The siphuncle is in a slightly dorsal position in GBA 2016/003/0002.The suture (Text-Figs. 5A, B) is very feebly concave across the flanks, very feebly convex across the ventrolateral shoulder, and near-straight over the venter.

Discussion: These specimens are referred to *Cymatoceras sakalavum* on the basis of relative proportions, form and course of the low, wide ribs. There are similarities to *Cymatoceras imbricatus* (CRICK, 1907: 220, Pl. 14, Fig. 6), from the presumed Cenomanian of northern KwaZulu-Natal in South Africa in both the width and course of the ribs, but the whorl section is compressed rather than depressed, as in the present species. *Cymatoceras striatocostatus* (CRICK, 1907: 221, Pl. 14, Fig. 7) from the same locality and horizon as *C. imbricatus*, has a depressed whorl section, but the ribs are even broader than those of the present species.

Occurrence: Middle Albian of Madagascar, Lower Cenomanian of Nigeria.

Order Ammonoidea ZITTEL, 1884
Suborder Ammonitina HYATT, 1889
Superfamily Desmoceratoidea ZITTEL, 1895
Family Puzosiinae SPATH, 1922
Subfamily Puzosiinae SPATH, 1922
Genus *Puzosia* BAYLE, 1878

Type species: *Ammonites planulatus* J. DE C. SOWERBY, 1827: 134, Pl. 570, Fig. 5, non SCHLOTHEIM, 1820: 59; = *Ammonites mayorianus* D'ORBIGNY, 1841: 267, Pl. 79, Figs. 1–3, by subsequent designation by H. DOUVILLÉ (1879: 91).

Subgenus *Anapuzosia* MATSUMOTO, 1954

Type species: *Puzosia buenaventura* ANDERSON, 1938: 185, Pl. 40, Fig. 3; Pl. 41, Figs. 1, 2, by the original designation of MATSUMOTO (1954: 71).

Puzosia (*Anapuzosia*) sp.

(Pl. 1, Figs. 6–14; Text-Figs. 6, 7)

Material: GBA 2016/003/0011–0021.

Description: The earliest growth stages seen are represented by GBA 2016/003/0012–0017, which range from 30 to 53 mm in diameter. Coiling is moderately involute, the umbilicus comprising 30 % approximately of the diameter, shallow, with a low, flattened wall and narrowly rounded umbilical shoulder. The whorl section is slightly compressed, with whorl breadth to height ratios of up to 0.9, the inner to mid-flank region feebly convex, the outer flanks converging to broadly rounded ventrolateral shoulders and a feebly convex venter. Ornament is best preserved in GBA 2016/003/0016 (Pl. 1, Figs. 6, 7). Strong collar ribs precede feeble constrictions. The ribs are prorsiradiate, feebly convex on the inner flank, flexed back and concave on the outer flank, and flexed forwards over the ventrolateral shoulder. The collar ribs are separated by much finer ribs that are very weak to obsolete on the inner flank, strengthening at mid-flank and increasing by branching and intercalation. A distinctive feature is that some ribs bifurcate on the ventrolateral shoulder (Pl. 1, Fig. 12). Poor preservations precludes determination of the number of fine ribs between successive constrictions and collar ribs, but there are both coarser (Pl. 1, Figs. 6, 7) and finer and more densely ribbed individuals (Pl. 1, Figs. 8).

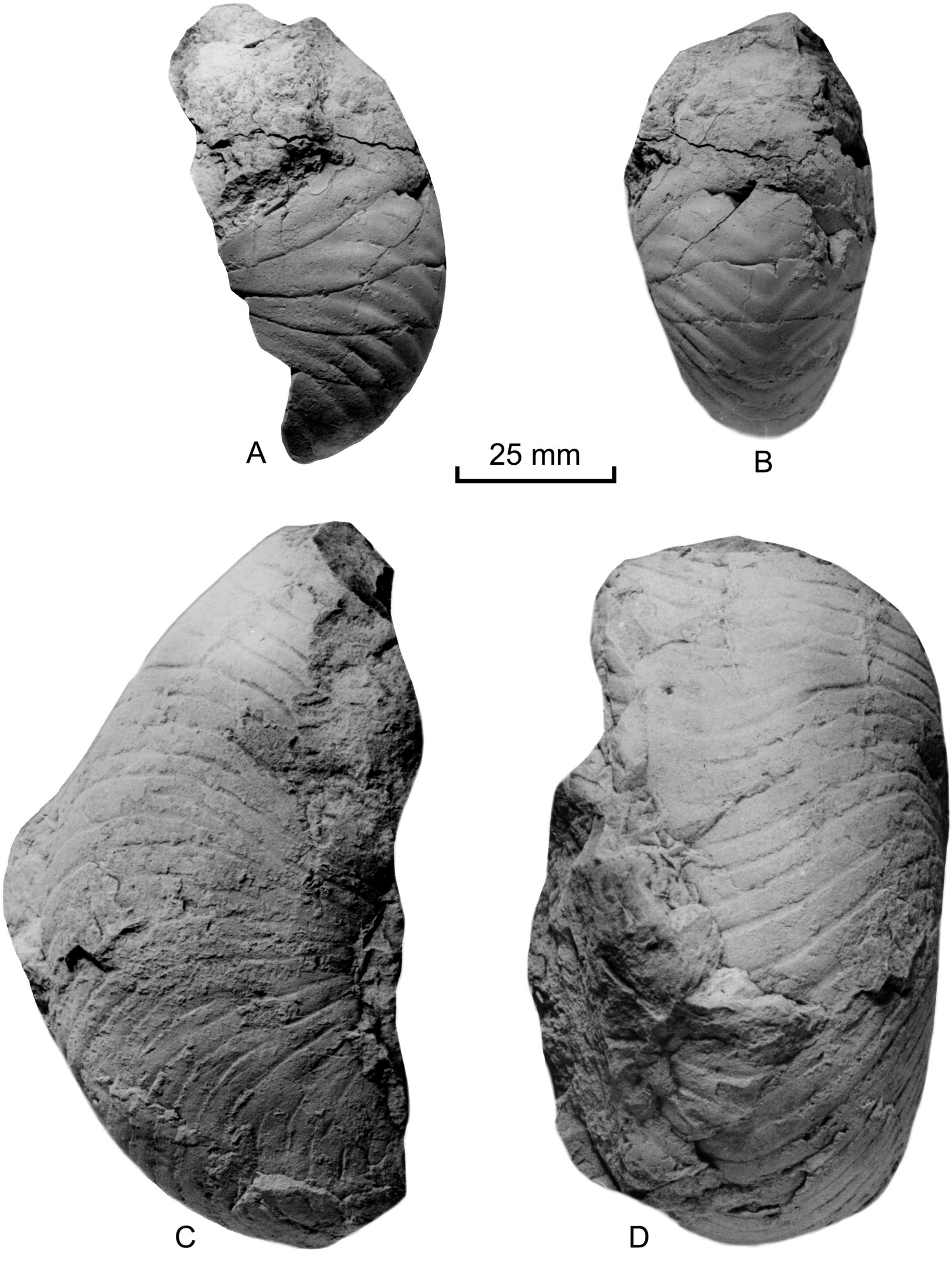

Text-Fig. 5.
Cymatoceras sakalavum (Collignon, 1949), A, B, GBA 2016/003/0001; C, D, GBA 2016/003/0003. Figures are x 1.

There are two much larger specimens. GBA 2016/003/0018 (Pl. 1, Fig. 13) is a crushed individual, 135 mm in diameter. Parts of two collar-ribs, 45° approximately apart, are preserved on the adapical part of the specimen, with an estimated 14 or more weaker ribs between at the ventrolateral shoulder. The ribs are markedly flexuous, and increase by branching and intercalation, in some cases on the ventrolateral shoulder. GBA 2016/003/0019 (Text-Fig. 6) is an undeformed individual retaining extensive areas of replaced shell, the ventrolateral and ventral ornament well preserved. The ribbing is finer than in the previous specimen, with 13 weaker ribs between successive constrictions and collar ribs.

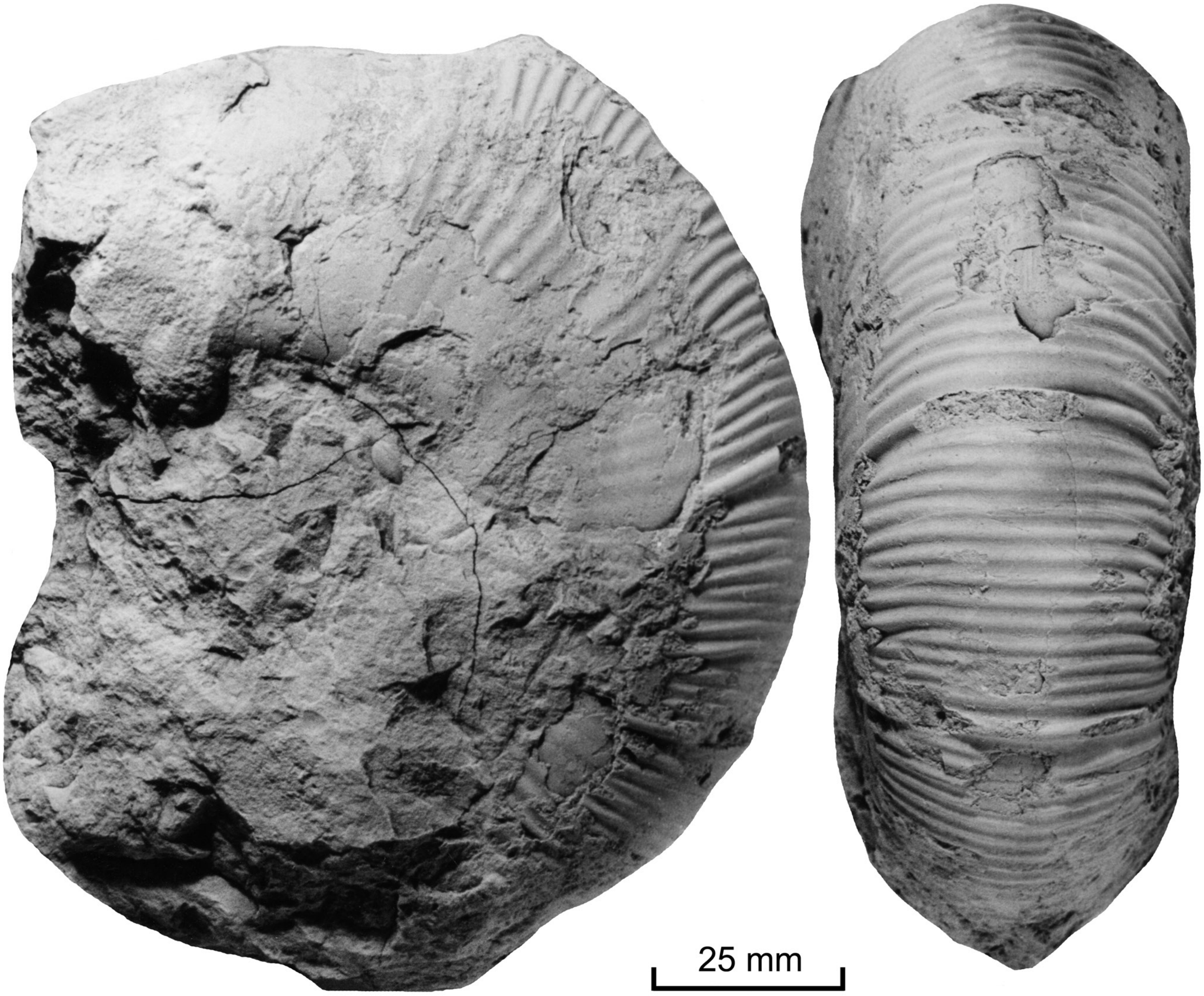

Text-Fig. 6.
Puzosia (*Anapuzosia*) sp. GBA 2016/003/0019. Figures are x 1.

A juvenile suture is shown in Text-Figure 7; E/A and A/U2 are deeply incised, narrow-stemmed, and bifid; A and U2 are deeply incised, and trifid.

Discussion: The present material is interpreted as a variable species with both finer and coarser ribbed individuals. It is referred to *Anapuzosia* in the basis of the whorl section, crowded sinuous ribs and strong collar ribs. Of described species, it most closely resembles *Puzosia* (*Anapuzosia*) *multicostata* Renz, 1972 (707, Pl. 2, Figs. 1, 2; Pl. 3, Fig. 1; Pl. 9, Fig. 4; Text-Figs. 2b, 3) from the Upper Albian of Venezuela, but this has up to 24 ribs between successive collar ribs and constrictions. The present rather poor material is left in open nomenclature.

Occurrence: As for material.

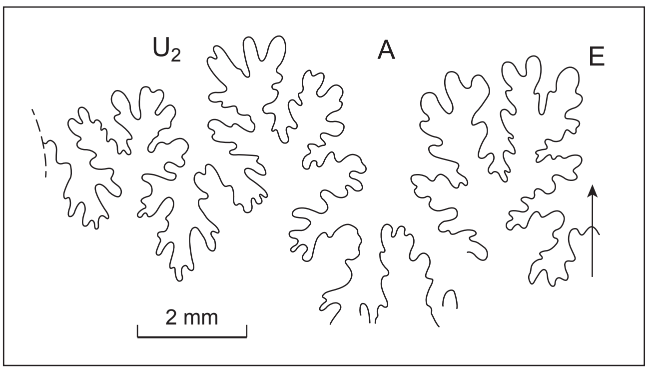

Text-Fig. 7.
Partial external suture of *Puzosia* (*Anapuzosia*) sp. GBA 2016/003/0012.

Superfamily Acanthoceratoidea De Grossouvre, 1894

Family Brancoceratidae Spath, 1934

Subfamily Mortoniceratinae H. Douvillé, 1912

Genus *Pervinquieria* Böhm, 1910

Type species: *Ammonites inflatus* J. Sowerby, 1817: 170, Pl. 178, by the original designation of Böhm (1910: 152).

Subgenus *Subschloenbachia* Spath, 1921 (= *Durnovarites* Spath, 1932: 380)

Type species: *Ammonites rostratus* J. Sowerby, 1817: 163, Pl. 173, by the original designation of Spath (1921: 284).

Pervinquieria (*Subschloenbachia*) *rostrata* (J. Sowerby, 1817)

(Text-Figs. 8, 9)

1817 *Ammonites rostratus* J. Sowerby: 163, Pl. 173.

2018 *Mortoniceras* (*Mortoniceras*) *rostratum* (J. Sowerby, 1817); Klein: 101, 122 (with full synonymy).

2019 *Pervinquieria* (*Subschloenbachia*) *rostrata* (J. Sowerby, 1817); Gale et al.: 214, Pl. 13; Pl. 14, Figs. 1, 2.

Type: The holotype, by monotypy, is OUMNH K.835, the original of *Ammonites rostratus* J. Sowerby, 1817: 163, Pl. 173, from the Upper Greensand of Roke, 1.5 km NNE of Benson, Oxfordshire, refigured by Kennedy et al. (1998: Figs. 9–11).

Material: GBA 2016/003/0004, 0005, 0007.

Text-Fig. 8.
Pervinquieria (*Subschloenbachia*) cf. *rostrata* (J. Sowerby, 1817), GBA 2016/003/0005. Figures reduced x 0.5; the original is 300 mm in diameter.

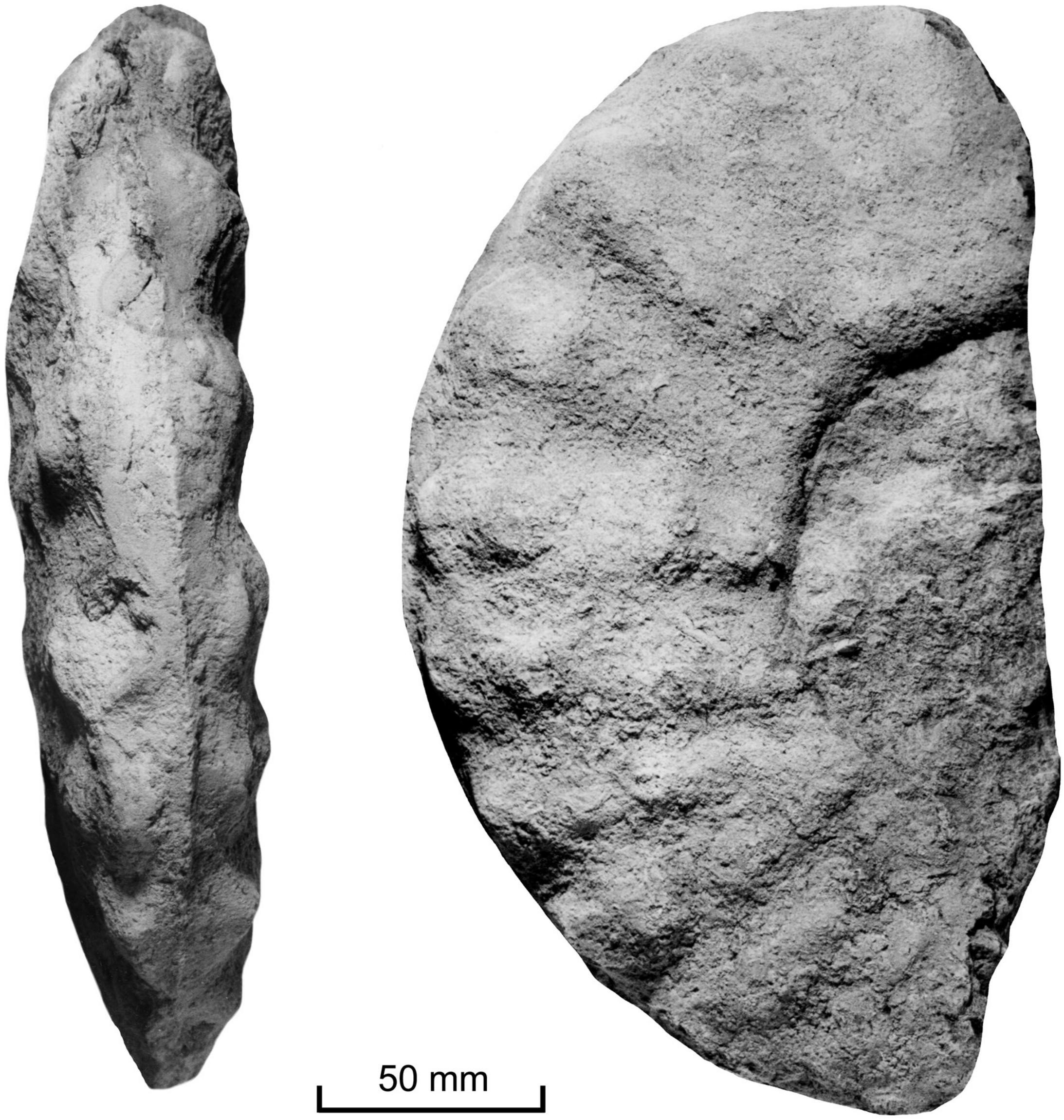

Text-Fig. 9.
Pervinquieria (*Subschloenbachia*) *rostrata* (J. SOWERBY, 1817), GBA 2016/003/0004. Figures are reduced x 0.7; the original is 215 mm in diameter.

Description: The specimens are very poorly preserved, the largest 300 mm in diameter (Text-Fig. 8). The best-preserved fragment is GBA 2016/003/0004 (Text-Fig. 9), a 180° whorl sector with a maximum preserved diameter of 220 mm. Coiling is very evolute, the shallow umbilicus comprising 41 % of the diameter. The original whorl section has been modified by abrasion. The flanks are flattened, the ventrolateral shoulders broadly rounded; there is a strong siphonal keel. There are nine primary ribs on the fragment. Most arise on the umbilical wall and strengthen into a coarse umbilical bulla; others lack a bulla. Most of the bullae give rise to a single rib, with a pair arising from a bulla at the adapical end. The ribs are coarse, broad, straight, prorsirdiate, and bear a coarse outer lateral bulla, coarse rounded inner ventrolateral tubercle and a coarse outer ventrolateral clavus.

Discussion: The coarse ribbing and tuberculation of these poor specimens corresponds to that of the body chamber of the holotype (KENNEDY et al., 1998: Text-Figs. 9–11) and comparable specimens from Texas (KENNEDY et al., 1998: Text-Fig. 13; KENNEDY in KENNEDY et al., 2005: Text-Fig. 12).

Occurrence: Index of the eponymous uppermost Albian zone, the geographic distribution extends from southern England to France, Spain, Germany, Switzerland, Hungary, Serbia, Ukraine (Crimea), Romania, Bulgaria, Turkmenistan, northern Iran, southern Tibet, Texas, Angola, Nigeria, Tamil Nadu in south India, Texas in the United States, and Japan.

Pervinquieria (*Subschloenbachia*) cf. *perinflata* (SPATH, 1921)

(Text-Fig. 10)

Compare:

1860 *Ammonites inflatus* PICTET & CAMPICHE (non J. SOWERBY): Pl. 21, Fig. 5; Pl. 22, Fig. 3.

1921 *Subschloenbachia perinflata* SPATH: 284.

2018 *Mortoniceras* (*Durnovarites*) *adkinsi* (YOUNG, 1957); KLEIN: 137, 138 (with synonymy).

2018 *Mortoniceras* (*Durnovarites*) *depressum* SPATH, 1922; KLEIN: 137, 139 (with synonymy).

2018 *Mortoniceras* (*Durnovarites*) *perinflatum* (SPATH, 1921); KLEIN: 137, 140 (with full synonymy).

2018 *Mortoniceras* (*Durnovarites*) *quadratum* SPATH, 1922; KLEIN: 138, 142 (with synonymy).

2018 *Mortoniceras* (*Durnovarites*) *subquadratum crassicostatum* SPATH, 1933; KLEIN: 138, 143 (with synonymy).

2018 *Mortoniceras* (*Durnovarites*) *subquadratum subquadratum* SPATH, 1933; KLEIN: 138, 145 (with synonymy).

2018 *Mortoniceras* (*Durnovarites*) *subquadratum tumidum* SPATH, 1933; KLEIN: 138, 143 (with synonymy).

2018 *Mortoniceras* (*Durnovarites*) *vraconense* RENZ, 1968; KLEIN: 138, 145 (with synonymy).

Type: The holotype, by monotypy, is the original of PICTET & CAMPICHE 1860 (Pl. 22, Fig. 3), in the collections of the Muséum d'Histoire Naturelle, Geneva, from the Upper Albian of La Vraconne, Saint Croix, Switzerland. It was refigured by RENZ (1968: Pl. 9, Fig. 1), WIEDMANN & DIENI (1968: Pl. 14, Fig. 4) and MEISTER et al. (2011: Text-Figs. 5a, b).

Material: BMNH C83089, collected by P.M.P. Zaborski from the top surface of the main limestone in the Mfamosing Formation of the Mfamosing Quarry.

Description: BMNH C83089 (Text-Fig. 10) is a 180° whorl sector with a maximum preserved diameter of 160 mm, worn on one flank, the umbilicus concealed by matrix. The flattened outer flanks converge to broadly rounded ventrolateral shoulders. The venter is feebly convex in intercostal section, with a coarse siphonal keel. Strong, coarse umbilical bullae give rise to very strong straight prorsiradiate ribs that alternate regularly with single coarse intercalated ribs to give a total of 12 at the ventrolateral shoulder of the fragment. The adapical primary rib has a small lateral tubercle; on the succeeding primary ribs, the tubercle is developed as a low, broad bulla. All ribs bear a strong conical inner ventrolateral tubercle, linked by a broad prorsiradiate rib to a coarse outer ventrolateral clavus, from which a broad rib sweeps forwards and effaces before reaching the siphonal keel.

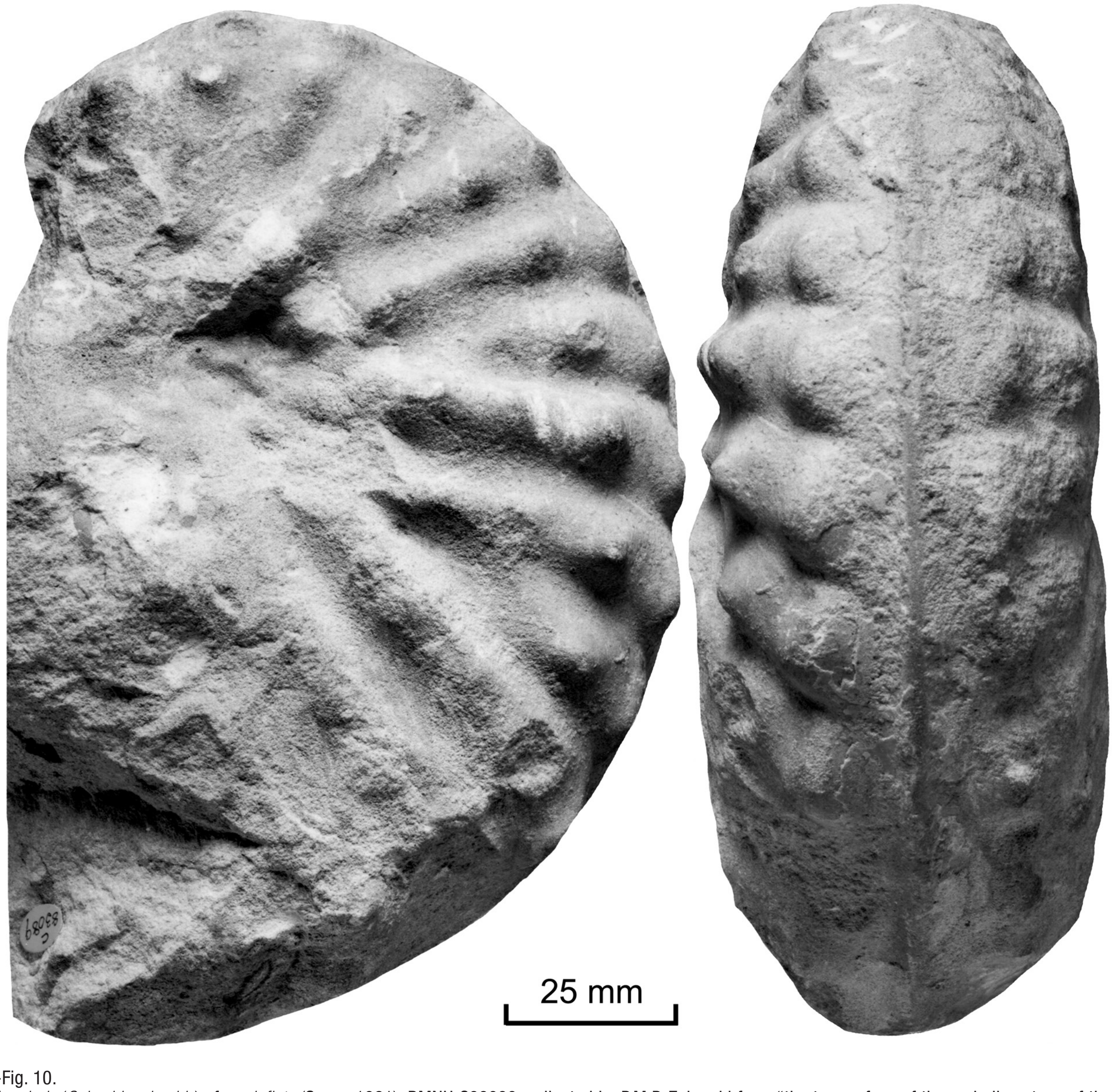

Text-Fig. 10.
Pervinquieria (*Subschloenbachia*) cf. *perinflata* (SPATH, 1921), BMNH C83089, collected by P.M.P. Zaborski from "the top surface of the main limestone of the Upper Albian Mfamosing Formation at the Mfamosing Quarry". Figures are x 1 (photos courtesy of the Natural History Museum, London).

Discussion: The presence of four rows of tubercles in BMNH C83089 indicated in to be a *Mortoniceras* (*Subschloenbachia*). The relatively stout whorl section and coarse tuberculation correspond to that of the holotype of *P.* (*S.*) *perinflata* (see above), which is a phragmocone.

Occurrence: Upper Upper Albian, index of the eponymous zone, with records from southern England, southeastern France, Switzerland, Ukraine (Crimea), Hungary, Texas in the United States, Nigeria, KwaZulu-Natal in South Africa, and, possibly, Iran and Tamil Nadu, south India.

Pervinquieria (*Subschloenbachia*) sp.

(Text-Fig. 11)

Material: GBA 2016/003/0009, collected *ex situ*.

Description: The specimen (Text-Fig. 11) is a 180° sector of body chamber 150 mm in diameter, with one flank and the venter very well preserved. The whorl section is rounded-trapezoidal, with feebly convex convergent flanks and broadly rounded ventrolateral shoulders; there is a strong siphonal keel. Coiling is moderately evolute, the umbilicus quite deep, comprising 31 % of the diameter, with a convex wall and quite narrowly rounded umbilical shoulder. Six well-developed umbilical bullae are preserved on the penultimate half whorl. There are six umbilical bullae of variable strength on the outer half whorl that give rise pairs of ribs, with, in one case, a third rib tenuously attached; there are also long and short ribs, to give a total of 16 ribs at the ventrolateral shoulder. There are faint suggestions of a lateral and inner ventrolateral tubercle, and all ribs bear a well-developed outer ventrolateral clavus.

Discussion: Umbilical and outer ventrolateral tubercles are well defined, but there are only very feeble indications of a lateral and inner ventrolateral row, perhaps a reflection of the specimen being a possibly adult body chamber. Accordingly, it is referred to *Subschloenbachia* with caution.

Occurrence: As for material.

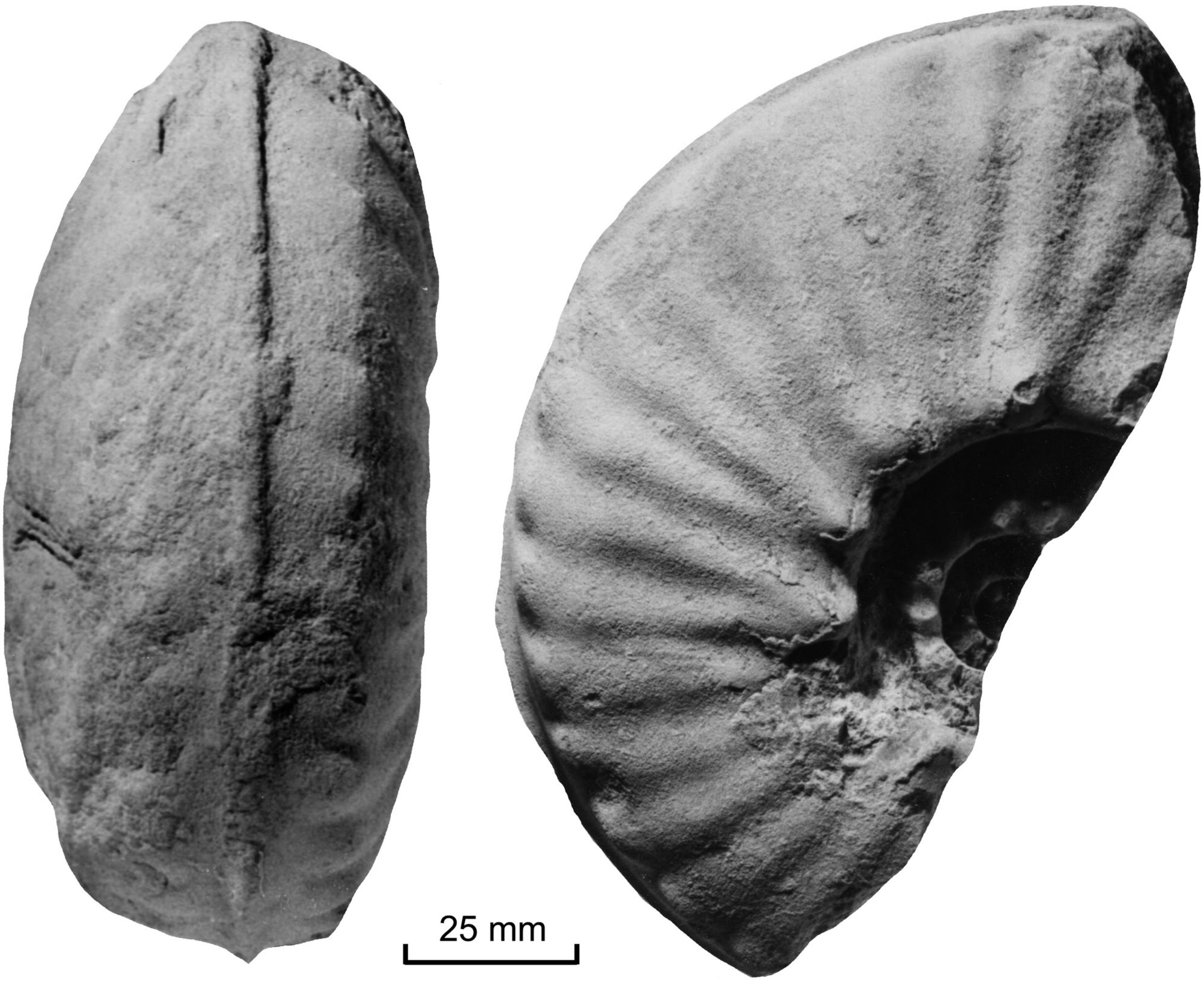

Text-Fig. 11.
Pervinquieria (*Subschloenbachia*) sp., GBA 2016/003/0009, *ex situ* at the Mfamosing Quarry. Figures are x 1.

Genus *Arestoceras* VAN HOEPEN, 1942

Type species: *Arestoceras collinum* VAN HOEPEN, 1942: 118, Text-Figs. 104–109, by original designation.

Arestoceras sp.

(Text-Fig. 12)

Material: GBA 2016/003/0008.

Description: The specimen is a poorly preserved, badly worn internal mould of a 180° sector of phragmocone with a maximum preserved diameter of 126 mm. The whorl section is estimated to have been as wide as high, the inner to mid-flanks feebly convex, the outer flanks converging to broadly rounded ventrolateral shoulders, the venter very feebly convex in intercostal section and broadly fastigiate in costal section, with a coarse siphonal keel. There are estimated 14–17 ribs at the ventral shoulder. The umbilical region is not preserved. The ribs are straight and prorsiradiate on the inner flank, broaden and sweep forwards on the outer flank, and link to blunt, oblique ventrolateral clavi. The clavi give rise to a strongly prorsirsdiate rib that effaces before reaching the siphonal keel.

Discussion: The presence of a single row of ventrolateral tubercles and asbsence of lateral tubercles suggest *Arestoceras*, the specimen most closely resembling the *Arestoceras* sp. nov. of MEISTER et al. (2011: 693, Pl. 6, Fig. 2), from the Upper Albian of the Sumbe region in Cuanza Sul Province, Angola.

Occurrence: As for material.

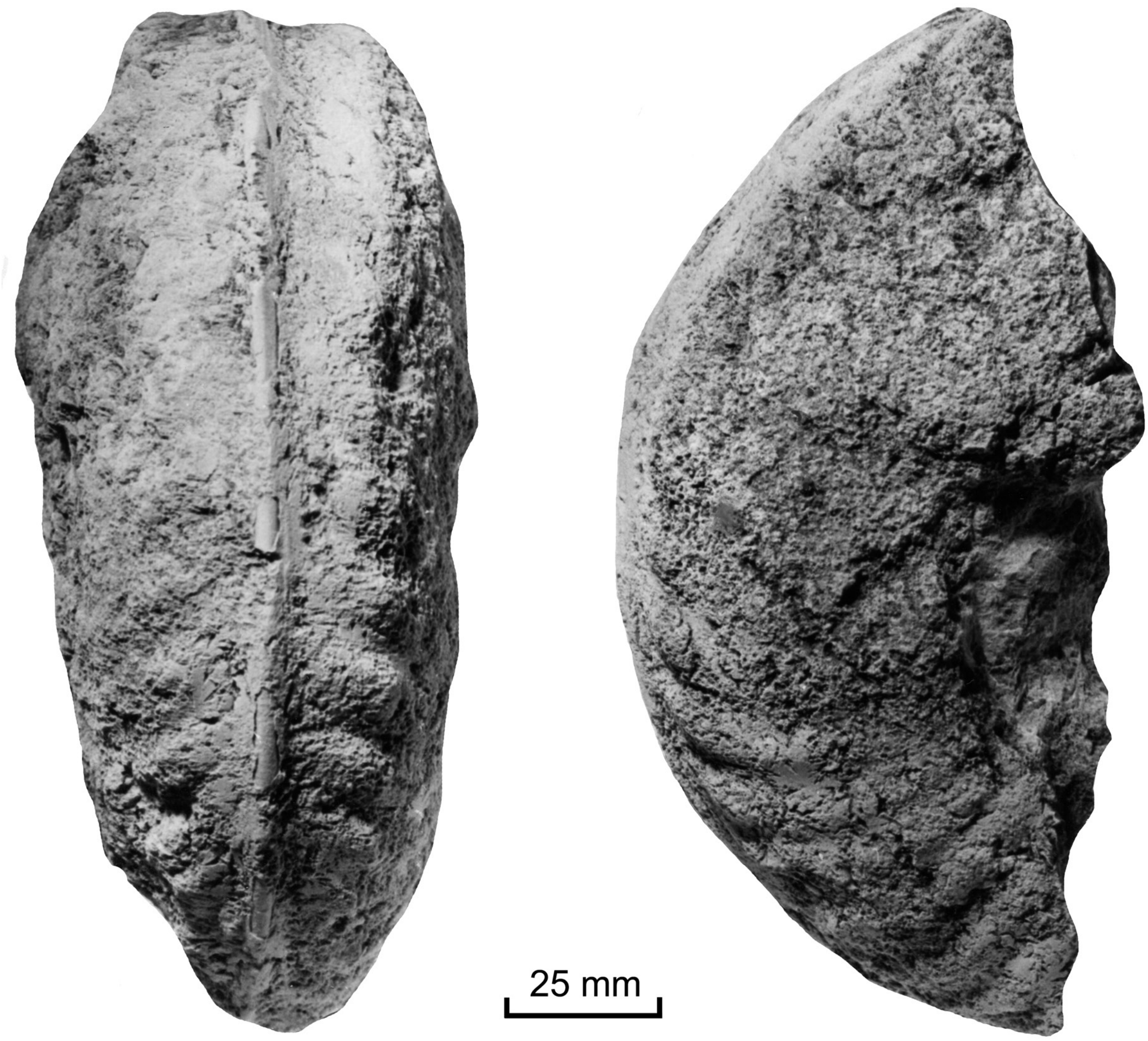

Text-Fig. 12.
Arestoceras sp. GBA 2016/003/0008. Figures are x 1.

Family Lyelliceratidae Spath, 1921
Subfamily Stoliczkaiinae Breistroffer, 1953
Genus *Stoliczkaia* Neumayr, 1875

Type species: *Ammonites dispar* d'Orbigny, 1841: 142, Pl. 45, Figs. 1, 2, by the original designation of Neumayr (1875: 179).

Subgenus *Lamnayella* Wright & Kennedy, 1978

Type species: *Stoliczkaia* (*Lamnayella*) *juigneti* Wright & Kennedy, 1978: 398, Pl. 37, Figs. 1–10, Pl. 38, Figs. 1–12, by the original designation of Wright & Kennedy (1978: 394).

Stoliczkaia (*Lamnayella*) *juigneti* Wright & Kennedy, 1978

(Text-Figs. 13A–D, I)

1978 *Stoliczkaia* (*Lamnayella*) *juigneti* Wright & Kennedy: 398, Pl. 37, Figs. 1–10; Pl. 38, Figs. 1–12; Text-Figs. 4a–c.

2018 *Stoliczkaia* (*Lamnayella*) *juigneti* Wright & Kennedy, 1978; Klein: 235, 237 (with full synonymy).

Types: The holotype, by original designation, is MNHN. F. A27381, the original of Wright & Kennedy (1978: 398, Pl. 37, Figs. 1–4); it and paratypes MNHN. F. A27382–4 and FSM 117 and 173 are from the Lower Cenomanian *Neostlingoceras carcitanense* Subzone of the *Mantelliceras mantelli* Zone, Craie Glauconieuse à *Pecten asper* Lamnay, Sarthe, France. Paratype BMNH C83578 is from the *carcitanense* Subzone fauna of the basement bed of the Wilmington Sands at Hutchin's Pit, Wilmington, Devon.

Material: GBA 2016/003/0022–0026.

Description: The earliest growth stages are represented by GBA 2016/003/0022 (Text-Fig. 13D) and the nucleus of GBA 2016/003/0023 (Text-Figs. 13A, I). The former is a pyritised individual 12 mm in diameter, the umbilicus obscured by pyrite overgrowths. Coiling is very involute, the umbilicus tiny. The whorl section is very compressed, the flanks very feebly convex and subparallel, the ventrolateral shoulders quite narrowly rounded, the narrow venter feebly convex. Delicate falcoid riblets arise on the umbilical shoulder, strengthen across the flanks and develop into relatively broad concave outer flank ribs, 14 on the outer half whorl, that terminate in sharp ventral clavi. The venter is raised into a blunt siphonal ridge. The nucleus of GBA 2016/003/0023 (Text-Figs. 13A, I) has coarse concave ribs on the outer flank. The fragmentary outer whorl of this specimen has an estimated diameter of 43 mm, and retains a short sector of the body chamber. Coiling is only moderately involute, the umbilicus shallow, comprising 20 % of the diameter, the wall low, and outward-inclined in intercostal section. The whorl section is compressed, the intercostal section with feebly convex flanks, broadly rounded ventrolateral shoulders and a feebly convex venter. The costal whorl breadth to height ratio is 0.8 approximately, the greatest breadth at the umbilical bullae. Primary ribs arise at the umbilical seam, and strengthen into prominent bullae that give rise to relatively coarse primary ribs, while up to three long and short ribs intercalate between successive primaries, all ribs strengthening into a feeble ventral bulla that is little more than an an-

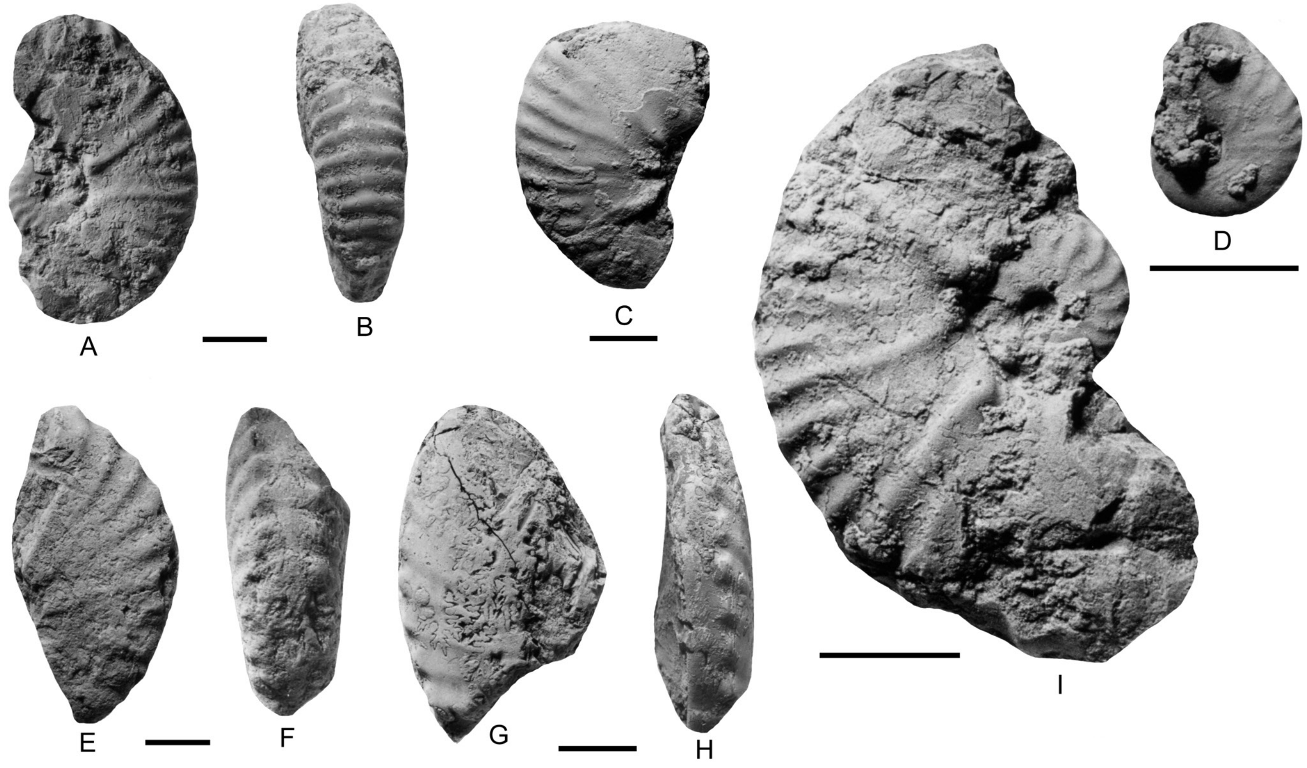

Text-Fig. 13.
A–D, I: *Stoliczkaia* (*Lamnayella*) *juigneti* Wright & Kennedy, 1978. A, B, I: GBA 2016/003/0023; C: GBA 2016/003/0024; D: GBA 2016/003/0022, E–H: *Utaturiceras* sp. E, F: GBA 2016/003/0038; G, H: GBA 2016/003/0039. Figures A–C, E–H are x 1; D and I are x 2.

gulation in the rib profile; the venter is feebly fastigiate in costal section. The largest fragment, GBA 2016/003/0024 (Text-Fig. 13C) has a maximum preserved whorl height of 20 mm and is part body chamber.

Discussion: The species is discussed at length by WRIGHT & KENNEDY (1978: 398; 1984: 77), to whom reference should be made.

Occurrence: Lower Cenomanian of southern England, Sarthe in France, and now Nigeria.

Family Flickiidae ADKINS, 1928

Subfamily Salaziceratinae, KENNEDY & WRIGHT, 1984

Genus *Salaziceras* BREISTROFFER, 1936

Type species: *Ammonites salazacensis* HÉBERT & MUNIER-CHALMAS, 1875: 114, Pl. 5, Fig. 6, by the original designation of BREISTROFFER (1936: 64).

Salaziceras nigerianum FÖRSTER & SCHOLZ, 1979

(Pl. 2, Figs. 14–22)

1979 *Salaziceras nigerianum* FÖRSTER & SCHOLZ: 113, Text-Figs. 1–3.

2018 *Salaziceras* (*Salaziceras*) *nigerianum* FÖRSTER & SCHOLZ, 1979; KLEIN: 246, 247 (with synonymy).

Type: The holotype, by original designation is BSPHG. 1978 X 1, the original of FÖRSTER & SCHOLZ (1979: Text-Figs. 2b, 3, 5) from the Mfamosing Quarry. The specimen was collected by Lobitzer and after the early death of R. Förster, was presented to the Bayerische Staatssammlung für Paläontologie und historische Geologie in Munich.

Material: GBA 2016/003/0027–0033.

Description: Coiling is evolute, the umbilicus comprising an estimated 40 % of the diameter in GBA 2016/003/0030 (Pl. 2, Fig. 19), and of moderate depth. The whorl section is depressed reniform, with costal whorl breadth to height ratios of up to 1.3. On phragmocone fragments, an estimated five coarse primary ribs per half whorl arise at the umbilical seam, sweep forwards across the umbilical wall, and strengthen into prominent umbilical bullae. These give rise to prorsiradiate ribs, either singly or in pairs, with occasional intercalated ribs. The ribs flex forwards on the ventrolateral shoulder, and cross the venter in a feeble convexity. GBA 2016/003/0030 (Pl. 2, Fig. 19), is interpreted as an adult body chamber. Ornament on the adapertural part is as on the phragmocone, but weakens rapidly thereafter to feeble umbilical bullae and flank ribs, the venter near-smooth at the greatest preserved diameter. The suture (FÖRSTER & SCHOLZ, 1979: Text-Fig. 2) is little incised, with bifid A and U_2.

Discussion: The diagnostic feature of *Salaziceras nigerianum* is the prominent umbilical bullae that give rise to pairs of ribs. FÖRSTER & SCHOLZ (1979: 114) discuss differences between the present species and others referred to the genus.

Occurrence: As for material.

Subfamily Flickiinae ADKINS, 1928

Genus *Flickia* PERVINQUIÈRE, 1907

Type species: *Flickia simplex* PERVINQUIÈRE, 1907: 214, Pl. 9, Figs. 2–5; Text-Figs. 80, 82, by monotypy.

Flickia bullata sp. nov.

(Pl. 1, Figs. 1–5)

1986 *Flickia quadrata* ZABORSKI, *non* COLLIGNON: 374, Text-Figs. 1d, e; 2m–q.

Types: The holotype is GBA 2016/003/0010 (Pl. 1, Figs. 3–5); it and paratype GBA 2016/003/0011. Other paratypes are BMNH C90374 and C90375, from the Lower Cenomanian part of the Odukpani Formation in cuttings on the Calabar-Akampka road, 1.5 km north of the junction with the Calabar-Ikot Ekpene road, in Cross River State, Nigeria.

Diagnosis: A *Flickia* with umbilical bullae on the phragmocone.

Description: The holotype (Pl. 1, Figs. 3–5) is a pyritic internal mould of an adult with a maximum preserved diameter of 19.5 mm. Coiling is moderately involute, the umbilicus comprising 30 % approximately of the diameter, shallow, with a flattened wall and broadly rounded umbilical shoulder. The whorl section is compressed, with a whorl breadth to height ratio of 0.8 approximately. The flanks are flattened and subparallel, the ventrolateral shoulders broadly rounded, the venter feebly fastigiate, and feebly convex on either side of the line of the mid-venter. There are six umbilical bullae on the adapertural 90° sector of the penultimate whorl and the adapical 120° sector of the outer whorl. The bullae give rise to low, broad, feeble prorsiradiate ribs that efface on the outer flanks. The bullae are lost on the body chamber, their place taken by low, broad, crowded prorsiradiate ribs that efface on the outermost flanks. There is a single broad, shallow constriction on the ventrolateral shoulders and venter 60° from the apertural end of the body chamber. Paratype GBA 2016/003/0011 (Pl. 1, Figs. 1, 2) is a pyritic internal mould of a 180° whorl sector 14.2 mm in diameter, and almost entirely adult body chamber. Ornament corresponds to that of the holotype. The suture (ZABORSKI, 1986: Text-Figs. 1d, e) has entire elements, as is typical for the genus, with a relatively large E/A and a smaller A/U_2.

The considerable size difference between these two specimens described here may be an indication of dimorphism.

Discussion: The species is clearly closely related to *Flickia quadrata* COLLIGNON, 1964 (23, Pl. 322, Figs. 1428, 1429, refigured by WRIGHT & KENNEDY, 1987: 695, Pl. 88, Figs. 27–37), notably in the presence of a broad constriction on the ventrolateral shoulders and venter of the body chamber, but they differ in the absence of umbilical bullae in *quadrata*.

Occurrence: As for types.

Family Acanthoceratidae De Grossouvre, 1894
Subfamily Mantelliceratinae Hyatt, 1903
Genus *Graysonites* Young, 1958

Type species: *Graysonites lozoi* Young, 1958: 172, Pl. 27, Figs. 1–11, Text-Figs. 1b, c, d, f, by original designation = *Mantelliceras wacoense* Böse, 1928: 215, Pl. 5, Figs. 9–25; Pl. 6, Figs. 1–4.

Graysonites wacoense (Böse, 1928)

(Pl. 4, Figs. 1, 2, 6–8)

1928 *Mantelliceras wacoensis* Böse: 215, Pl. 5, Figs. 9–25; Pl. 6, Figs. 1–4.

2005 *Graysonites wacoense* (Böse, 1928); Kennedy in Kennedy et al.: 390, Text-Figs. 24a, b; 26–32; 33d–f; 34–38 (with full synonymy).

2015 *Graysonites wacoense* (Böse, 1928); Kennedy: 404, Text-Figs. 157g–l.

Types: The holotype is TMM 21610, the original of Böse (1928: Pl. 5, Figs. 9, 10, 23, 24); paratypes are TMM 21611–4. All are from the lower Lower Cenomanian Del Rio Clay on the east side of the Santa Fe track, 7.4 km (4.5 miles) south of McGregor, McLennan County, Texas.

Material: GBA 2016/003/0034–0037.

Description and Discussion: GBA 2016/003/0034–0035 are very crushed fragments. The latter (Pl. 4, Fig. 8), 68 mm in diameter, shows the coiling to have been involute, the umbilicus comprising 22 % approximately of the diameter. Eight primary ribs arise at the umbilical seam, strengthen across the umbilical wall, and develop into elongate umbilical bullae. These give rise to narrow, straight primary ribs, either singly or in pairs, with additional ribs intercalating. The ribs strengthen across the flanks, and link to well-differentiated inner ventrolateral bullae. The ventral region is not preserved on this specimen, which compares well with USNM 520209 (Kennedy in Kennedy et al., 2005: Text-Figs. 29g–i; Kennedy, 2015: Text-Figs. 157i–l). GBA 2016/003/0036 (Pl. 4, Figs. 6, 7) is a phragmocone fragment with a maximum preserved diameter of 115 mm and comparable if worn ornament. The ventrolateral and ventral regions are well preserved, with weak inner ventrolateral bullae linked by a strong prorsiradiate rib to stronger outer ventrolateral clavi. GBA 2016/003/0037 (Pl. 4, Figs. 1, 2) is a phragmocone fragment 101 mm long, lacking the inner flank region. The ornament is comparable in style to that of the previous specimens, but much more subdued, the weak inner ventrolateral bullae progressively effacing to a mere angulation in the rib profile. This specimen corresponds closely to USNM 520210, the original of Kennedy in Kennedy et al. (2005: Text-Fig. 36).

Occurrence: Lower Lower Cenomanian of Texas, California, southern England, and Nigeria.

Genus *Utaturiceras* Wright, 1956

Type species: *Ammonites vicinalis* Stoliczka, 1864: 84, Pl. 44, Figs. 1, 4, 5, 7, 8, non 2, 3, 6, by the original designation of Wright (1956: 392).

Utaturiceras sp.

(Text-Figs. 13E–H)

Material: GBA 2016/003/0038–0039.

Description and Discussion: GBA 2016/003/0038 (Text-Figs. 13E, F) is a 120° whorl sector of phragmocone with a maximum preserved whorl height of 34 mm approximately. Coiling is very involute with a tiny, shallow umbilicus. The whorl section is compressed, with a whorl breadth to height ratio of 0.7 approximately. The umbilical shoulder is quite narrowly rounded, the inner and middle flanks flattened and subparallel, the outer flanks converging to broadly rounded ventrolateral shoulders, the venter flattened, with a feeble siphonal ridge. There are three weak umbilical bullae on the fragment. They give rise to pairs of very feeble ribs, with additional ribs intercalating, to give a total of an estimated 11 ribs at the ventrolateral shoulder. The ribs are straight across the inner and middle flank, strengthening, and feebly concave on the outer flank, where they link to feeble inner ventrolateral bullae, from which a strengthening rib links to stronger outer ventrolateral clavi, the ribs linked across the venter by a low, broad, transverse rib, the ventral ribs separated by narrower interspaces. GBA 2016/003/0039 (Text-Figs. 13G, H) is part of one flank and the venter only of a 90° whorl sector with ornament much better-preserved; the maximum preserved whorl height is 32 mm. The flank ornament is comparable to that of the previous specimen. The inner ventrolateral bullae are very feeble, the outer ventrolateral clavi sharp, the venter with a marked siphonal ridge. These specimens compare well with individuals of like size referred to the type species (Matsumoto & Sarkar, 1966: Pl. 33, Fig. 1; Kennedy et al., 2015: Text-Figs. 8a–f). The specimens differ from the smaller specimens referred to *Graysonites* herein (Pl. 4, Fig. 8), in that their ribs are delicate, crowded, distinctly concave on the outer flank, with very feeble inner ventrolateral bullae.

Occurrence: *Utaturiceras* is restricted to the lower Lower Cenomanian, with records from southern England, south India, Madagascar, KwaZulu-Natal in South Africa, and Nigeria.

Genus *Sharpeiceras* Hyatt, 1903

Type species: *Ammonites laticlavius* Sharpe, 1855: 31, Pl. 14, Fig. 1, by the original designation of Hyatt (1903: 111).

Sharpeiceras nigeriense Zaborski, 1985

(Pl. 2, Fig. 7; Pl. 3, Figs. 1–4, 7–15; Pl. 4, Figs. 3–5; Text-Fig. 14)

1985 *Sharpeiceras laticlavium nigeriense* Zaborski, 26, Text-Figs. 26–28, 31.

1987 *Sharpeiceras laticlavium nigeriense* Zaborski, 1985; Wright & Kennedy: 128, Text-Figs. 32a, b, c, h, i.

Types: The holotype is BMNH C83544, the original of Zaborski, 1985: 26, Text-Figs. 27a, b. There are four paratypes, BMNH C83542, C83543, C83545, together with a specimen in the collections of the University of Ilorin, Nigeria. All are from the Lower Cenomanian part of the Odukpani Formation on the Calabar-Akamkpa road, 1.5 km north of the junction with the Calabar-Ikot Ekpene road, in Cross River State, Nigeria.

Material: GBA 2016/003/0040–0046, and 25 additional fragments.

Description: The earliest growth stages seen are shown by GBA 2016/003/0041–0042 (Pl. 3, Figs. 1, 2, 7–11). Coiling is involute, the umbilicus comprising 20 % of the diameter, of moderate depth, the umbilical wall flattened and subvertical, the umbilical shoulder quite narrowly rounded. The intercostal whorl section is depressed rectangular, the flanks flattened and parallel, the umbilical shoulders broadly rounded, the venter very feebly convex. The costal whorl section is depressed polygonal, with the greatest breadth at the inner ventrolateral spines. Six broad, feeble primary ribs per half whorl arise on the umbilical wall, and strengthen into small conical umbilical bullae. These giver rise to one or two narrow, sharp, widely separate ribs, whilst additional ribs intercalate, to give a total of 11–12 ribs at the ventrolateral shoulder, where they link to conical to feebly bullate inner ventrolateral tubercles that become subspinose as diameter increases. A near-transverse rib links to a strong conical outer ventrolateral tubercle that also becomes subspinose as diameter increases. From a diameter of 17–18 mm, the inner flank part of the ribs strengthens, and a mid-lateral bulla appears, and becomes increasingly prominent as size increases (compare Pl. 3, Figs. 10, 13, 14). GBA 2016/003/0043 (Pl. 3, Figs. 3, 4) shows the continuing strengthening of tuberculation to a diameter of 40 mm approximately, and provides a link to the largest specimen seen, GBA 2016/003/0046 (Pl. 4, Figs. 3–5). This worn individual has a maximum preserved diameter of 78 mm approximately, the umbilicus comprising 25 % approximately of the diameter. The whorl section appears to have been slightly compressed. There are an estimated 14 ribs per whorl at the ventrolateral shoulder.

A juvenile suture is shown in Text-Figure 14; E/A is moderately incised, very broad and bifid, A narrow and also bifid.

Discussion: *Sharpeiceras nigeriense* was regarded as a subspecies of *S. laticlavium* (Sharpe, 1855) (31, Pl. 14, Fig. 1) (see revision in Wright & Kennedy, 1987: 127, Pl. 41, Fig. 4, Text-Figs. 29, 30, 34a). The holotype of *laticlavium* is a much larger phragmocone, with a whorl breadth to height ratio of 0.83 at a diameter of 135 mm, the umbilicus comprising 34.5 % of the diameter with 36 primary ribs per whorl. The earliest whorls, at the same diameter as the holotype of *nigeriense* are not known; the largest paratype of *nigeriense* (Zaborski, 1985: Text-Fig. 26) has ribs that arise in pairs and intercalate, as distinct from the equal, exclusively primary ribs of *laticlavium* at the same diameter. The early growth stage of *nigeriense*, lacking a lateral tubercle is also seen in *Sharpeiceras falloti* (Collignon, 1931) (10, Pl. 8 (4), Figs. 11, 12, non 9, 10), but at this growth stage coiling is very evolute *in falloti*, near serpenticone, with a lower expansion rate, the whorls compressed, with the lateral tubercle, when it does appear, very strong (Kennedy et al., 2015: 12, Text-Figs. 13a–e; 14a–v). *Sharpeiceras minor* Kennedy et al. (2015: 13, Text-Figs. 12a–i, l–o, 13j–m, 15a–l, 16a–e, 17a–e, 18), from the Lower Cenomanian of northern KwaZulu-Natal in South Africa, is a diminutive species with macroconchs reaching only 63 mm in diameter, the ribs coarser and of lower density than in the present species, the inner, conical ventrolateral tubercles stronger than the outer ventrolateral clavi.

Nuclei of *S. nigeriense* prior to the appearance of the lateral tubercle bear a superficial resemblance to juvenile *Acompsoceras calabarense* Zaborski, 1985. They differ in that the umbilical bullae of *calabarense* are coarser, as are the inner

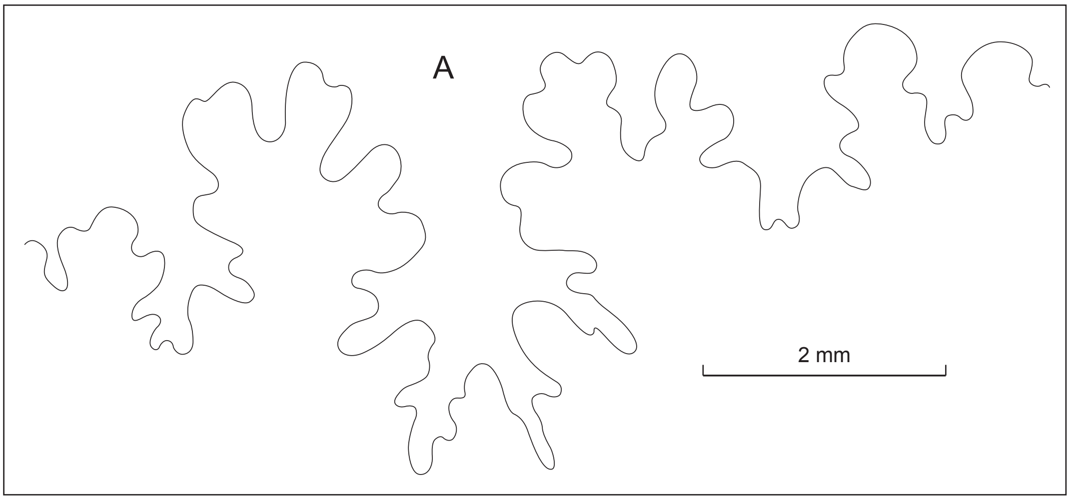

Text-Fig. 14.
Partial external suture of *Sharpeiceras nigeriense* Zaborski, 1985, GBA 2016/003/0041.

flank ribs, which flex back on the outer flank, the inner ventrolateral tubercles are weak, not becoming subspinose, whilst the outer ventrolateral tubercles are clavate rather than conical, do not become subspinose, and there is a blunt siphonal ridge, strengthened into incipient siphonal clavi (compare Pl. 2, Fig. 7; Pl. 3, Figs. 1, 2, 7–11 and Pl. 2, Figs. 3, 4, 8, 9).

Occurrence: Lower Cenomanian of south-eastern Nigeria.

Sharpeiceras florencae Spath, 1925

(Text-Fig. 15)

1925 *Sharpeiceras florencae* Spath: 198, Pl. 37.

2015 *Sharpeiceras florencae* Spath, 1925; Kennedy et al.: 14, Text-Figs. 7g–j, p, q, u, v, w; 12j, k, p, q; 16f–h;17f–l, 19–21, 22c–e (with full synonymy).

Type: The holotype, by monotypy, is the original of Spath (1925: 19, Pl. 37) in the collections of the Ditsong Museum of Natural History (formerly the Transvaal Museum), Pretoria, and from northeastern KwaZulu-Natal [Maputoland] in South Africa.

Material: GBA 2016/003/0047 and 0048, from the Lower Cenomanian part of the Odukpani Formation sample 77/50, an outcrop of about 2 m of hard grey marls in a depression on the eastern side of the main road 900 m north of Odukpani village (Text-Fig. 15).

Description: GBA 2016/003/0047 is a crushed 90° whorl fragment with a maximum preserved whorl height of 54 mm. There are parts of six very coarse straight, prorsiradiate ribs on the fragment. They arise on the umbilical wall, and strengthen into coarse umbilical bullae. There are strong lateral bullae, much stronger conical inner ventrolateral tubercles, and strong outer ventrolateral clavi. The

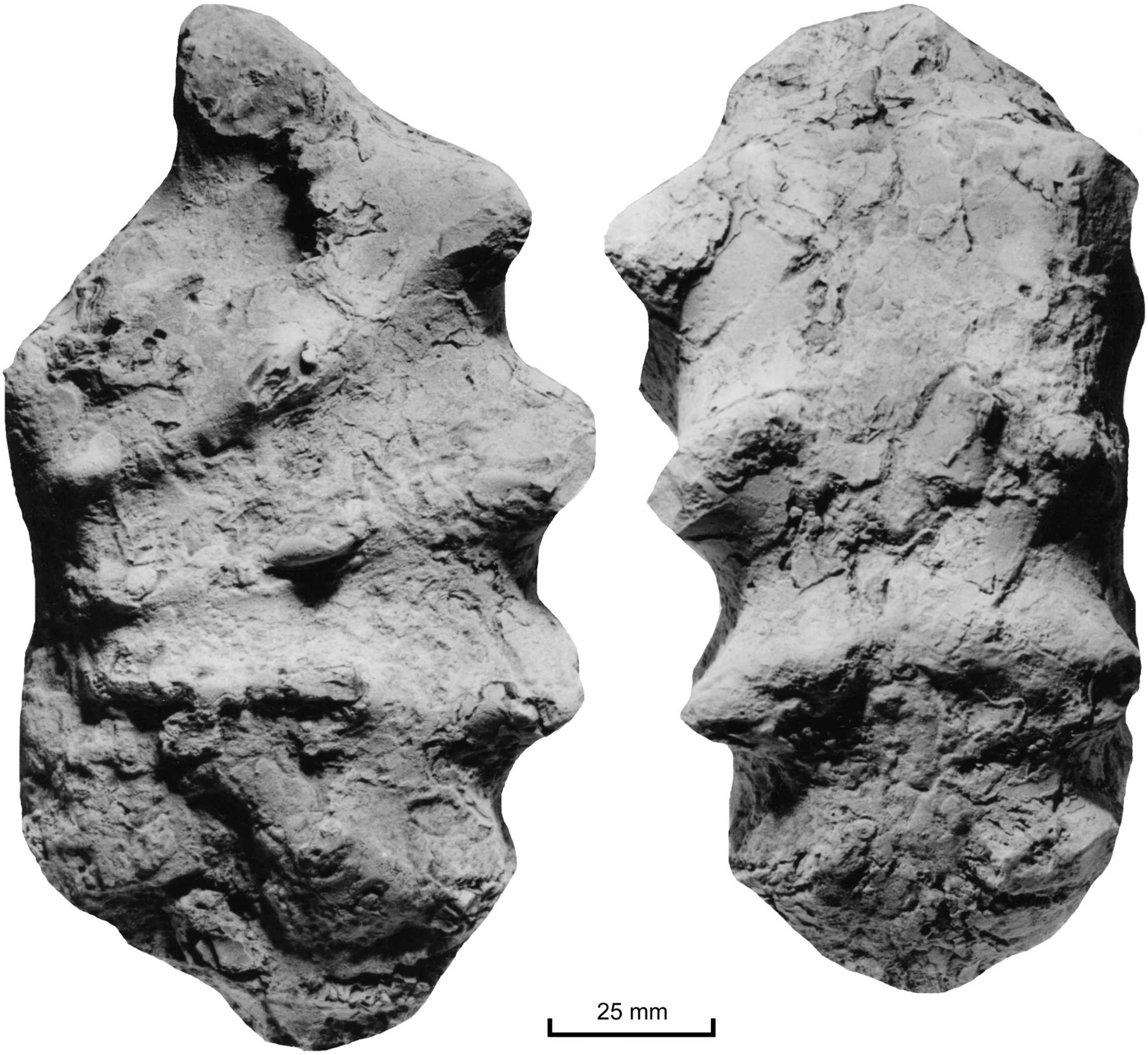

Text-Fig. 15.
Sharpeiceras florencae Spath, 1925. GBA 2016/003/0047, the Lower Cenomanian part of the Odukpani Formation at the 77/50 locality (Text-Fig. 1). Figures are natural size.

umbilical wall is marked by a series of depressions to accommodate the inner ventrolateral tubercles of the preceding whorl.

GBA 2016/003/0047 (Text-Fig. 15) is a 60° whorl sector of the phragmocone of a massive shell. The maximum preserved whorl height is 87 mm. The intercostal whorl section is compressed, with a whorl breadth to height ratio of 0.82, the maximum breadth below mid-flank, the flanks feebly convex, the ventrolateral shoulders broadly rounded, the venter very broad, and very feebly convex. The costal whorl section is as wide as high, polygonal, with the greatest breadth at the ventrolateral horns. The umbilicus is quite deep, the umbilical wall feebly convex. Broad ribs arise at the umbilical seam, and strengthen across the wall to develop into strong umbilical bullae. Single strong, straight, prorsiradiate ribs link to a much stronger mid-lateral bulla, linked by a stronger rib to a laterally compressed ventrolateral horn that has developed by the fusion of inner and outer ventrolateral tubercles, such that only a weakened remnant of the inner ventrolateral is present at the inner end of the horn. The costal profile is concave over the mid-ventral region, the ventral rib connecting the horns on opposite flanks effaced.

Discussion: The change in ornament, notably the change in spacing of the ribs between the two fragments is exactly that shown by the holotype, which is 220 mm approximately in diameter. The differences between the present species and others referred to the genus, is discussed at length by KENNEDY et al. (2015: 15).

Occurrence: Lower Cenomanian of northern KwaZulu-Natal in South Africa, Madagascar, Angola, Nigeria, Peru, and northern Mexico.

Subfamily Acanthoceratinae DE GROSSOUVRE, 1894

Genus *Acompsoceras* HYATT, 1903

Type species: *Ammonites bochumensis* SCHLÜTER, 1871: 1, Pl. 1, Figs. 1–4, by original designation by HYATT, 1903: 111 = *Ammonites renevieri* SHARPE, 1857: 44, Pl. 20, Fig. 2.

Acompsoceras calabarense ZABORSKI, 1985

(Pl. 2, Figs. 3–6, 8, 9, 11–13; Pl. 3, Figs. 5, 6, 16–19; Pl. 5, Figs. 1–13; Text-Fig. 16)

1985 *Acompsoceras calabarense* ZABORSKI: 29, Text-Figs. 30, 32.

Type: The holotype is BMNH C85250, the original of ZABORSKI (1985: 28, Text-Figs. 30, 32); paratypes are BMNH C83552–3, C85249, C85251, from the Lower Cenomanian part of the Odukpani Formation in a cutting on the Calabar–Akamkpa road, 1.5 km north of the junction with the Calabar–Ekpene road in Cross River State, Nigeria.

Material: GBA 2016/003/0048–0055, and 11 additional specimens. GBA 2016/003/0056–0063, from the Lower Cenomanian part of the Odukpani Formation sample 77/50, an outcrop of about 2 m of hard grey marls in a depression on the eastern side of the main road 900 m north of Odukpani village (Text-Fig. 1).

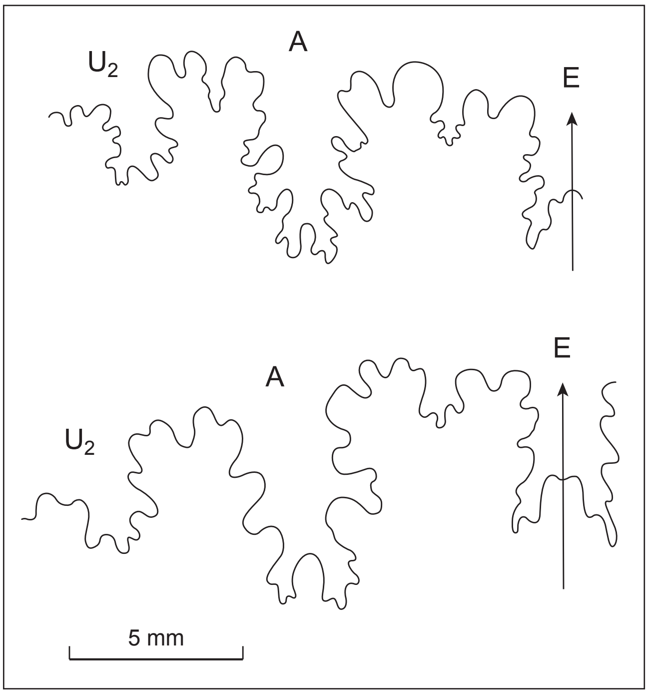

Text-Fig. 16.
External sutures of *Acompsoceras calabarense* ZABORSKI, 1985; A (top): GBA 2016/003/0052; B (bottom): GBA 2016/003/0051.

Description: The earliest growth stages are shown by GBA 2016/003/0048 and 0050 (Pl. 2, Figs. 3, 4, 8, 9). These specimens are up to 15.6 mm in diameter. Coiling is involute, the umbilicus comprising 18 % of the diameter, of moderate depth, with a flattened, outward-inclined umbilical wall. The whorl section is compressed, with a whorl breadth to height ratio of 0.75, the flanks flattened and subparallel, the ventrolateral shoulders broadly rounded, the venter very feebly convex, with a blunt siphonal ridge. There are five to six umbilical bullae of variable strength per half whorl. They give rise to ribs singly or in pairs, the ribs blunt, straight and prorsirsdiate on the inner flank, with some showing a slight backwards flexure on the outer flank, where occasional additional ribs intercalate, to give a total of nine ribs per half whorl at the ventrolateral shoulder, where all link to a small conical inner ventrolateral tubercle, linked by a broad, feebly prorsiradiate rib to a slightly stronger outer ventrolateral clavus. The siphonal ridge is feebly strengthened into incipient clavi in places. GBA 2016/003/0049 (Pl. 2, Figs. 5, 6) is a larger fragment, with a maximum preserved whorl height of 10.5 mm, showing variation in the umbilical bullae from strong to near-effaced, the ribs associated with the stronger bullae weakened and flexed back on the outer flank. The differentiation of the siphonal clavi is better developed than in the previous specimens.

GBA 2016/003/0051–0054 (Pl. 2, Figs. 11–13; Pl. 3, Figs. 5, 6, 16–19) are up to 35 mm in diameter. Coiling remains very involute, with whorl breadth to height ratios of around 0.6, the inner flanks feebly convex and subparallel, the outer flanks flattened and convergent, the ventrolateral shoulders broadly rounded, and the venter very feebly convex, with the feeblest broad siphonal elevation in some but not all. There are five to six umbilical bullae per half whorl, and 13–14 ribs at the ventrolateral shoulder. The strength of the umbilical bullae remains variable, the ribs arising from them either singly or in pairs, with occasional ribs intercalating. The backwards flexure of some of the stronger, bullate primary ribs is well developed in some (GBA 2016/003/0054: Pl. 3, Figs. 6, 16). The inner ventrolateral tubercle are bullate, the outer ventrolateral clavate in these specimens. Adult body chambers (Pl. 5, Figs. 1–13) are up to 112 mm in diameter, and show a range of morphological variation. GBA 2016/003/0060 (Pl. 5, Figs. 9, 10) extends to 180°, and appears to be near-complete. The intercostal section is compressed, with feebly convex inner, and flattened, convergent outer flanks, the ventrolateral shoulders broadly rounded, the venter feebly convex. At the adapical end, coarse, widely separated umbilicolateral bullae give rise to a strong prorsiradiate rib, with a second rib weakly attached in one case. There are also single intercalated ribs, all of the ribs linking to strong, inner ventrolateral tubercles, beyond which the venter is worn. Towards the adapertural end, the bullae and flank ribs weaken and efface. Specimens such as GBA 2016/003/0057 (Pl. 5, Figs. 7, 8) have the ventral region well-preserved, with conical inner, and clavate outer ventrolateral tubercles. GBA 2016/003/0057 (Pl. 5, Figs. 3, 4) shows the outer ventrolateral clavi weakening at the adapertural end, the inner ventrolateral tubercles weakening and changing to a blunt thickening of the ventrolateral part of the ribs, which are low, broad and flat over the venter. A number of specimens show the sutures (Text-Fig. 16); E/A and A/U_2 are only moderately incised and bifid, as are A and U_2.

Discussion: The small adult size and very coarse ribs and tubercles, persisting onto the adult body chamber, distinguish this species from others referred to the genus, as comprehensively discussed by ZABORSKI (1985: 29).

Occurrence: Lower Cenomanian of Cross River State, Nigeria.

Acompsoceras sp. juv.

(Pl. 2, Figs. 1, 2, 10)

Material: GBA 2016/003/0064 and 0065.

Description: GBA 2016/003/0064 (Pl. 2, Figs. 1, 2) is a pyritic nucleus 18 mm in diameter. Coiling is very involute, with a tiny, shallow umbilicus, the low wall flattened, the umbilical shoulder broadly rounded. The whorl section is compressed, with a whorl breadth to height ratio of 0.67, the flanks flat and subparallel, the ventrolateral shoulders broadly rounded, the narrow venter very feebly convex, with a low, blunt median ridge. Six low, coarse ribs arise on the umbilical wall, and strengthen into small bullae of variable strength. These give rise to one or two ribs, with additional ribs intercalating, to give a total of 13 to14 ribs at the ventrolateral shoulder. The ribs strengthen markedly on the outer flank and ventrolateral shoulder and link to small conical inner ventrolateral tubercles, linked in turn by a prorsiradiate rib to slightly larger outer ventrolateral clavi. The siphonal ridge is undulose, and strengthened into feeble clavi that are aligned with the outer ventrolateral rows. GBA 2016/003/0065 (Pl. 2, Fig. 10) is a larger fragment, with a maximum preserved whorl height of 14 mm. The adapertural 120° sector is body chamber. Four feeble umbilical bullae are preserved on the fragment. They give rise to single feeble, straight, prorsiradiate ribs with a second rib feebly linked in some cases, together with single intercalated ribs to give a total of 10 ribs at the ventrolateral shoulder. The ribs bear tiny conical inner ventrolateral tubercles and stronger outer ventrolateral clavi. The venter is poorly preserved.

Discussion: These specimens are referred to *Acompsoceras* on the basis of the presence of a siphonal ridge with feeble siphonal clavi in the smalller specimen. They differ from *Acompsoceras calabarense* of the same size in their greater compression, and much higher rib density (compare Pl. 2, Figs. 1, 2, 10; Pl. 2, Figs. 8, 12).

Occurrence: As for material.

Suborder Ancyloceratina WIEDMANN, 1966
Superfamily Turrilitoidea GILL, 1871
Family Turrilitidae GILL, 1871
Genus and subgenus *Mariella* NOWAK, 1916

Type species: *Turrilites bergeri* BRONGNIART, 1822 (395, Pl. 7, Fig. 3), by the original designation of NOWAK (1916: 10).

Mariella (*Mariella*) *bicarinata* (KNER, 1852)

(Pl. 6, Figs. 10, 11)

1852 *Turrilites bicarinatus* KNER: 9, Pl. 1, Fig. 14, 14a, ? non 14b.

2015 *Mesoturrilites* (*Klingerella*) *bicarinata* (KNER, 1852); KLEIN: 173, 174 (with synonymy).

Types: The lectotype, by the subsequent designation of ATABEKIAN (1985: 40) is the original of KNER (1852: Pl. 9, Figs. 14, 14a) from “Mikalince und Czartorya” in what is now Ukraine. The figures were reproduced by WRIGHT & KENNEDY (1996: Text-Figs. 135a, b).

Material: GBA 2016/003/0066–0067.

Description: The fragments consist of a half a whorl only. The maximum preserved whorl height 14.5 mm. The upper whorl face is feebly concave, with shallow radial grooves to accommodate the ribs on the base of the previous whorl. The narrowly rounded junction between upper and outer whorl faces is crenulated, the crenulations corresponding to depressions that housed the lowest row of tubercles on the preceding whorl. The outer whorl face has a feebly convex upper part, the remainder flattened. The lower whorl face is very feebly convex. There are an estimated 10 rows of tubercles per half whorl. The tubercles of the upper row are rounded-conical, and linked to the junction of the outer and upper whorl faces by a low, broad rib. A second row of tubercles is situated on the lower part of the outer whorl face. A third row of much smaller, spirally elongated tubercles lies at the junction of outer and lower whorl faces, sited on a low protuberance that supports a fourth row of very feeble rounded to feebly spirally elongated tubercles. The protuberance gives rise to a low, broad, radial rib on the lower whorl face that effaces progressively across the face.

Discussion: The diagnostic features of *Mariella* (*M.*) *bicarinata* is the conical shape of the tubercles in the upper row, the spiral elongation of the tubercles in the lower rows, and the close juxtaposition of the third and fourth rows of tubercles. Of other species in the Mfamosing fauna, *M.* (*M.*) *essenensis* (GEINITZ, 1849) (Pl. 6, Fig. 8) has only three rows of tubercles. *M.* (*M.*) aff. *miliaris* (PICTET & CAMPICHE, 1861) has many more and finer tubercles per whorl, with a well-developed narrow rib linking the upper row of tubercles to the junction of outer and upper whorl surfaces (Pl. 6, Figs. 15, 16, 18).

Occurrence: Lower Lower Cenomanian of southern England, Poland, Turkmenistan, and Nigeria.

Mariella (*Mariella*) *essenensis* (GEINITZ, 1849)

(Pl. 6, Fig. 8)

1849 *Turrilites essenensis* GEINITZ: 122, Pl. 6, Figs. 1, 2.

2015 *Mariella essenensis* (GEINITZ, 1849); KLEIN: 132, 143 (with synonymy).

Material: GBA 2016/003/0068.

Description: The specimen consists of one and a half whorls, apparently body chamber, with a maximum preserved whorl height of 10 mm. The upper whorl face is concave, the narrowly rounded junction of the upper and outer whorl faces strongly crenulated to accommodate the lowest row of tubercles. The upper part of the outer whorl face is feebly convex, the remainder flattened. There are 15 rows of tubercles per whorl. Those in the upper row are conical. Those in the second row are displaced adaperturally of those in the upper row, only slightly smaller, and spirally elongate. The tubercles in the third row are displaced adaperturally of those in the second row, and conical, lying at the junction of outer and lower whorl faces. They give rise to a coarse radial rib that extends across all of the lower whorl face.

Discussion: The specimen is assigned to *Mariella* (*M.*) *essenensis* on the basis of the presence of only three rows of tubercles, which distinguishes in from other *Mariella* in the present fauna. Of previously described specimens that have been referred to the species, it most closely resembles the original of ATABEKIAN (1985: Pl. 10, Fig. 12).

Occurrence: Lower Cenomanian, Southern England, northern France, Germany, Poland, Romania, Iran, Turkmenistan, Mozambique (?), Madagascar, and Nigeria.

Mariella (*Mariella*) *oehlerti oehlerti* (PERVINQUIÈRE, 1910)

(Pl. 6, Fig. 17)

1910 *Turrilites oehlerti* PERVINQUIÈRE: 53, Pl. 14 (5), Figs. 14–17.

2015 *Cenomariella oehlerti oehlerti* (PERVINQUIÈRE, 1910); KLEIN: 152, 154 (with synonymy).

Type: The holotype, by original designation is MNHN. F. J13735, the original of PERVINQUIÈRE (1910: Pl. 14, Fig. 16), from Sour El-Ghoslane (formerly Aumale), Algeria. It was refigured by WRIGHT & KENNEDY (1996: Text-Fig. 138j).

Material: GBA 2016/003/0069–0070, 0076, and six additional specimens.

Description: GBA 2016/003/0069 (Pl. 6, Fig. 17) is a fragment of parts of four successive whorls, with a maximum preserved whorl height of 14 mm. Only the largest whorl preserves all of the ornament. The upper part of the outer whorl face is feebly convex, the remainder flattened. There are four rows of tubercles, the tubercles in successive rows displaced slightly adaperturaly of those in the preceding rows. The conical tubercles in the upper row are the largest, and are borne at the end of a short rib that extends across the upper part of the outer whorl face; there are three in a distance equal to the whorl height. The tubercles of the second row are only slightly smaller, and conical to feebly spirally elongated. The tubercles of the third row are weaker and distinctly spirally elongated, and lie at the base of the outer, exposed whorl face. The tubercles of the fourth row are smaller than those in the third row, spirally elongated, and lie at the junction of the outer and lower whorl faces. They give rise to a low radial rib that effaces across the lower whorl face.

GBA 2016/003/0076 is the largest well-preserved specimen in the present material, with a whorl height of 17 mm, and 25–26 ribs per whorl.

Discussion: The present specimens are referred to *Mariella* (*M.*) *oehlerti oehlerti* on the basis of the subequal conical tubercles in the upper two rows, and the smaller, spirally elongated tubercles in the lower two rows. These features distinguish the species from others in the Mfamosing fauna. *Mariella* (*M.*) *oehlerti sulcata* KLINGER & KENNEDY, 1978 (33, Pl. 3, Fig. d; Pl. 8, Fig. d; Pl. 8, Fig. d;Text-Figs. 3d, e; 8h) differs from the nominate subspecies in having a distinctive spiral groove between the second and third rows of tubercles.

Occurrence: Lower Lower Cenomanian, Algeria, Central Tunisia, Nigeria, KwaZulu-Natal in South Africa, Madagascar, Angola, Japan, and, possibly, northern Mexico.

Mariella (*Mariella*) aff. *miliaris* (PICTET & CAMPICHE, 1861)

(Pl. 6, Figs. 15, 16, 18)

Compare:

1861 *Turrilites bergeri* BRONGNIART, var. *miliaris* PICTET & CAMPICHE: 136, Pl. 58, Fig. 5.

2015 *Mariella* (*Mariella*) *miliaris* (PICTET & CAMPICHE, 1861); KLEIN: 132, 146 (with synonymy).

Type: The holotype, by monotypy, is no. 40041 in the collections of the Musée Geologique, Lausanne, the original of PICTET & CAMPICHE (1861: 136, Pl. 58, Fig. 5), from the condensed Upper Albian of Saint Croix, Kanton Waadt, Switzerland. It was refigured by RENZ (1968: Pl. 18, Fig. 10).

Material: GBA 2016/003/0071–0074.

Description: GBA 2016/003/0072 (Pl. 6, Fig. 16) is a fragment of two successive whorls, the maximum preserved whorl height 15 mm approximately. The upper part of the outer, exposed whorl face is feebly convex, the remainder flattened. Weak ribs arise at the junction of upper and outer whorl faces; there are five to six ribs in a distance equal to the whorl height. The ribs are very feebly prorsiradiate and have the same width as the interspaces. They strengthen across the whorl face, and link to small, transversely elongated tubercles just above the mid-point of the face. A relatively wide, near-smooth zone is crossed by the feeblest of ribs, arising from the tubercles of the first row, developing into a barely detectable swelling at the mid-point between the first row and the second row of well-developed, transversely elongated tubercles. A well-developed rib extends to a third row of tubercles at the junction of outer and lower whorl faces. These tubercles give rise to a relatively coarse rib that extends across the lower whorl face. GBA 2016/003/0074 (Pl. 6, Fig. 18) consists of three successive whorls. The greatest measurable whorl height is 14 mm approximately. The density and strength of the ribbing and tuberculation is as in the previous specimen, but here the second row of tubercles is well developed. There are 27–28 ribs per whorl.

GBA 2016/003/0071 (Pl. 6, Fig. 15) consists of a half whorl with a maximum preserved whorl height of 14 mm. There are five ribs in a distance equal to the whorl height, slightly prorsirsdiate, and linking to a well developed transversely elongated tubercle a little above the mid-point of the outer, exposed whorl face. These are separated by a narrow, near-smooth zone from a second row of conical to feebly transversely elongated tubercles, linked by a blunt rib to a close-spaced third and fourth rows of smaller tubercles, the fourth row at the junction of outer and lower whorl faces, and giving rise to a coarse radial rib that weakens progressively across the lower and inner whorl faces.

Discussion: These specimens are linked together by the well-developed tuberculate rib on the upper part of the outer whorl face and the succeeding near-smooth zone where the ribs near-efface. GBA 2016/003/0074 (Pl. 6, Fig. 18) appears to have only three rows tubercles, but this is interpreted as a pathological condition, the fourth row represented by a very weak development in the near-smooth zone below the first row. The well developed rib on the upper part of the outer whorl face distinguishes these specimens from the other *Mariella* recognized in the Mfamosing fauna. The qualified determination given here is based on the rib density of the present material, 27–28 per whorl, substantially lower than that of the holotype of *miliaris*, where they number 54 per whorl. Lower rib densities of 25–35 are seen in specimens from the Upper Albian of Turkmenistan assigned to *miliaris* by Atabekian (1985: 29, Pl. 6, Figs. 1– 3; Pl. 5, Figs. 5–12).

Occurrence: As for material. *Mariella* (*M.*) *miliaris* is typically an Upper Albian species, with records from southern and eastern England, France, Switzerland, Hungary, Romania, Sardinia, Turkmenistan, and KwaZulu-Natal in South Africa. There are Lower Cenomanian records from Mozambique and southern England.

Mariella (*Mariella*) *cenomanensis* (Schlüter, 1876)

(Pl. 6, Fig. 6)

1876 *Turrilites cenomanensis* Schlüter: 131, Pl. 37, Figs. 6–8.

2015 *Mariella cenomanensis* (Schlüter, 1876); Klein: 132, 139 (with synonymy).

Type: The lectotype, by the subsequent designation of Kennedy (1971: 29), is the original of Schlüter (1876: 131, Pl. 37, Fig. 6), allegedly no. 74 in the collections of the Paläontologisches Institut of Bonn University, and from the rotomagensis-Pläner of Lichtenau, Westphalia. It was figured by Wright & Kennedy (1996: Text-Fig. 141b); the specimen bears little relationship to Schlüter's illustration, while the horizon of the lectotype is Lower Cenomanian (Kaplan et al., 1998: 208).

Material: GBA 2016/003/0075.

Description: The specimen consists of two whorls; the greatest preserved whorl height is 10 mm approximately. The junction between upper and outer whorl faces is markedly crenulated to accommodate the lowest row of tubercles of the previous whorl. 17 to 18 strong ribs per whorl arise at the junction of the upper and outer whorl faces, and are feebly prorsiradiate, linking to a transversely elongated tubercle above the mid-point of the outer whorl face. A smooth zone separates this row of tubercles from a second row of smaller adaperturally displaced conical tubercles, with a third row, adaperturally displaced and just above the inter-whorl suture. A fourth row of much smaller tubercles is situated on the outermost part of the lower whorl face. They give rise to well-developed radial ribs on the lower whorl face.

Discussion: This specimen differs from other *Mariella* in the present collection in having coarse ribs and stronger tubercles in the upper row. It compares closely with *Mariella* of comparable size from southern England that were referred to *cenomanensis* by Wright & Kennedy (1996: Pl. 100, Fig. 11).

Occurrence: Lower Cenomanian, Germany, France, southern England, Poland, Romania, northeastern Russia, Turkmenistan, Kazakhstan, Iran, Algeria, Nigeria, and Madagascar.

Genus *Hypoturrilites* Dubourdieu, 1953

Type species: *Turrilites gravesianus* d'Orbigny, 1842: 596, Pl. 144, Figs. 3–5, by original designation by Dubourdieu (1953: 123).

Hypoturrilites betaitraensis Collignon, 1964

(Pl. 6, Figs. 1–5, 7, 9, 12–14)

1964 *Hypoturrilites betaitraensis* Collignon: 13, Pl. 320, Figs. 1837–1838.

2015 *Hypoturrilites betaitraensis* Collignon, 1964; Klein: 156, 158 (with synonymy).

Type: The holotype, by original designation is the original of Collignon (1964: 13, Pl. 320, Fig. 1387) from the Lower

Cenomanian of the 'Vallée de la Betaitra, Fontaine Tunisienne', Madagascar. It was refigured by WRIGHT & KENNEDY (1996: Text-Fig. 134f).

Material: GBA 2016/003/0077–0086, plus nine additional fragments.

Description: Fragments comprise up to three whorls, with whorl heights of up to 13 mm. The upper whorl face is concave, with radial grooves to accommodate the ribs on the base of the previous whorl. The junction between upper and outer whorl faces is markedly crenulated to accommodate the lowest row of tubercles of the previous whorl. The outer whorl face is feebly convex. There are four rows of tubercles. Those in the upper row are the largest and number six per half whorl. They are conical, and positioned on the upper part of the face, and are linked to the junction of the outer and upper whorl faces by one or two variably developed ribs (Pl. 6, Fig. 2), with a single weak rib intercalating between successive tubercles (Pl. 6, Figs. 13, 14). The second row of conical tubercles are smaller than those in the upper row, are displaced adaperturally, and twice as numerous, corresponding to the tubercles and intercalated ribs in the upper row. The tubercles of the third row lie at the junction of the outer and lower whorl faces, and are feebly spirally elongated. The tubercles of the fourth row are situated on the outer part of the lower whorl face, close to those of the third row, and give rise to blunt radial ribs that efface across the lower whorl face.

GBA 2016/003/0081 (Pl. 6, Fig. 7) has ornament of this type on the penultimate whorl. On the final whorl, the differentiation of tubercles and intercalated ribs in the upper row is lost, being replaced by equal ribs that extend across the upper part of the outer whorl face, strengthening into weak transversely elongated tubercles at their lower end. The tubercles of the second row are also transversely elongated.

Discussion: The ribs linking the upper row of tubercles to the junction between outer and upper whorl faces, with ribs between the tubercles, is immediately distinctive. A combination of ribs and tubercles is also seen in species known only from much larger specimens. Of these, *Hypoturrilites laevigatus* (COQUAND, 1862: 175, Pl. 2, Fig. 6) (of which *Turrilites tenouklensis* PERVINQUIÈRE, 1910: 57, Pl. 14 (5), Fig. 31 is a synonym) is revised by WRIGHT & KENNEDY (1996: 373, Pl. 102, Fig. 2; Text-Figs. 146k–m, p, q) and KENNEDY in KENNEDY & GALE (2015: 312, Pl. 24, Fig. 18; Text-Figs. 34a–d), has many more and finer ribs on the outer whorl face, and only three rows of tubercles. *Hypoturrilites tuberculatoplicatus* (SEGUENZA, 1882: 115, Pl. 5, Fig. 3 (see revision in WRIGHT & KENNEDY, 1996: 374, Pl. 108, Fig. 7; Pl. 113, Figs. 3, 4, 6, 8, 9) has four rows of tubercles, as in the present species, but the outer whorl face is covered in far more numerous delicate ribs.

The striking changes of ornament between the penultimate and final whorl of GBA 2016/003/0081 (Pl. 6, Fig. 7) are interpreted as those the adult body chamber of a microconch.

Occurrence: Lower Lower Cenomanian where well dated. The geographic distribution extends from Madagascar to KwaZulu-Natal in South Africa, Nigeria, Brazil, Algeria, Turkmenistan, Haute-Savoie in France, and southern England.

Appendix: Macrofossils (excluding ammonites) from the hardground on top of the Mfamosing Limestone

FRANZ STOJASPAL (†)

The hardground faunas include a range of other organisms in addition to the ammonites described above, notably internal moulds of bivalves and gastropods, oysters, *Holaster* sp. and trace fossils: *Lithophaga* borings and *Thalassinoides* burrows. The material is kept in the GBA collections under the acquisition number GBA 1980/004. The following list comes from an internal GBA report by the late Franz Stojaspal:

Bivalves

1980/004/0001	*Nuculana* (? cf. *cultellus* KOENEN)
1980/004/0002	*Trigonarca* cf. *diceras* (Seguenza)
1980/004/0003	?*Phelopteria* sp. [specimen missing]
1980/004/0004	*Camptonectes* cf. *cretosus* (DEFRANCE)
1980/004/0005	*Neithea aequicostata* (LAMARCK): worldwide distribution from Albian–Senonian
1980/004/0006	*Plicatula auressensis* Coquand: Upper Albian–Senonian of Africa
1980/004/0007	*Lima* sp.
1980/004/0008	*Lopha lombardi* DARTEVILLE & FRENEIX: known only from the Santonian–Campanian of West Africa
1980/004/0009	*Pycnodonta vesicularis* (LAMARCK): worldwide distribution from Aptian–Senonian
1980/004/0010	*Astarte* sp.
1980/004/0011	*Martesia cylindrica* RIEDEL, known only from the Coniacian of Bombe (Cameroon)
1980/004/0012	*Goniomya* cf. *beyrichi* CHOFFAT
1980/004/0021	*Trigonia crenulata* LAMARCK

Gastropods

1980/004/0013	*Turritella* sp.
1980/004/0014	*Nerinea* sp.
1980/004/0015	*Helicaulax* sp.
1980/004/0016	*Rostellaria* sp.
1980/004/0017	*Tylostoma* sp.
1980/004/0018	*Volutilithes* sp.
1980/004/0019	*Avellana incrassata* (SOWERBY)

Echinoidea

1980/004/0020	*Holaster* sp.

Acknowledgements

We are grateful to David Sansom (Oxford) and Marek Plosch (Warsaw) for their assistance in the preparation of the figures and to Wolfgang E. Schollnberger (Potomac, USA) for critical reading of the geological part of the manuscript. Irene Zorn (GBA) created the inventory list for the specimens kept in the GBA collections and Monika Brüggemann-Ledolter (GBA) scanned the slides from Mfamosing quarry. Thanks to Holger Gebhardt (GBA) for his comments on the foraminifer *Thomasinella punica*. During his stay with the Calabar Cement Company (Calcemco) in the years 1976 and 1977 Lobitzer enjoyed the hospitality and friendship of the following esteemed gentlemen, respectively colleagues, for which he is still very grateful. In Calabar: B.O. Edet, General Manager of Calcemco, U.L. Adie, E.O. Esu and U.O. Usen, geologists of Calcemco and K. König, manager of Mfamosing quarry; in Ibadan: D.R. Adeleye, E.A. Fayose, Ivan De Klasz and M.O. Oyawoye, together with cordial thanks to many local helpers, field guides, drivers, and others, not mentioned by name here.

References

Adegoke, O.S., Dessauvagie, T.F.J., Fayose, E.A., Jan du Chene, R.E., Kogbe, C.A., Ogbe, F.G.A., Ebi Omatsola, M., Petters, S.W., Salami, M.B. & Yoloye, V.L.A. (1976): Geological Guide to some Nigerian Cretaceous – Recent localities. – 7th African Micropaleontological Colloquium Ile-Ife, March 16–29, 95 pp., Ile-Ife.

Adeleye, D.R. & Fayose, E.A. (1978): Stratigraphy of the Type Section of Awi Formation, Odukpani Area, Southeastern Nigeria. – Nigerian Journal of Mining and Geology, **15**, 33–37, Ibadan.

Agbebia, M.A. & Egesi, N. (2017): Formation and features of Mfamosing karst topography, South-Eastern Nigeria. – International Journal of Science Inventions Today (IJSIT), **6**/4, 349–360, Port Blair Andaman.

Adkins, W.S. (1928): Handbook of Texas Cretaceous fossils. – University of Texas Bulletin, **2838**, 385 pp., Austin.

Akpan, E.B. (1990): Trace fossils and the depositional elements of the Mfamosing limestone, Calabar Flank S.E. Nigeria. – In: Ofoegbu, C.O. (Ed.): The Benue Trough. Structure and Evolution, 271–286, Braunschweig/Wiesbaden (F. Vieweg & Sohn).

Akpan, E.B. (1992): *Peruviella dolium* (Roemer) and the age of the Mfamosing Limestone, S.E. Nigeria. – Nigerian Journal of Mining and Geology, **51**, 191–196, Ibadan.

Anderson, F.M. (1938): Lower Cretaceous deposits in California and Oregon. – Geological Society of America Special Paper, **16**, x + 340 pp., Baltimore.

Arnaud-Vanneau, A. & Prestat, B. (1984): *Thomasinella* and Co. – In: Oertli, H.J. (Ed.): Benthos ´83, 2nd International Symposium on Benthic Foraminifera, Pau (France), 11–15, Pau–Bordeaux.

Atabekian, A.A. (1985): [Turrilitids of the late Albian and Cenomanian of the southern part of the USSR]. – NAUKA, **14**, 112 pp., Leningrad. [in Russian]

Bayle, É. (1878): Fossiles principaux des terrains. – Explication de la Carte Géologique de France, **4**/1 (Atlas), 158 pls., Service de la Carte Géologique detailée, Paris.

Bengtson, P. & Koutsoukos, E.A.M. (1992): Ammonite and foraminiferal dating of the first marine connection between the Central and South Atlantic. – In: Curnelle, R. (Ed.): Géologie Africaine (Recueil des Communications: 1er. Colloque de Stratigraphie et de Paléogéographie des bassins sédimentaires Ouest-Africains / 2e. Colloque Africain de Micropaléontologie, Libreville, Gabon, 6–8 mai 1991). – Boussens, Elf Aquitaine Edition, 403 (Elf Aquitaine Mémoire, v.**13**).

Blainville, H.M.D. de (1825–1827): Manuel de malacologie et de conchyliologie. – 664 pp. (1825), 87 pls. (1827), Paris–Strasbourg.

Böhm, J. (1910): (Review of 'Études de Paléontologie Tunisienne' by L. Pervinquière). – Neues Jahrbuch für Mineralogie, Geologie und Paläontologie, **1910**, 149–155, Stuttgart.

Böse, E. (1928): Cretaceous ammonites from Texas and northern Mexico. – University of Texas Bulletin, **2748**, 143–357, Austin (misdated 1927).

Breistroffer, M. (1936): Les subdivisions du Vraconien dans le Sud-Est de la France. – Bulletin de la Société Géologique de France, Série 5, Volume **6**, 63–68, Paris.

Breistroffer, M. (1953): L'évolution des Turrilitidés Albiens et Cénomaniens. – Compte Rendu Hebdomadaire des Séances de l'Academie des Sciences, Paris, (D), **237**, 1349–1351, Paris.

Brongniart, A. (1822) : Sur quelques terrains de Craie hors du Bassin de Paris. – In: Cuvier, G. & Brongniart, A. (Eds): Description géologique des environs de Paris, 3rd edn., 80–101, Paris (Dufour & D'Ocagne).

Charrière, A., Andreu, B., Ciszaka, R., Kennedy, W.J., Rossic, A. & Vila, J.-M. (1998): La transgression du Cénomanien supérieur dans la Haute Moulouya et le Moyen Atlas méridional, Maroc. The Upper Cenomanian transgression in the High Moulouya and Southern Middle Atlas, Morocco. – Géobios, **31**, 551–569, Lyon.

Collignon, M. (1931): Paléontologie de Madagascar, XVI. La faune du Cénomanien à fossiles pyriteux du nord de Madagascar. – Annales de Paléontologie, **20**, 43–104 (1–64), Paris.

Collignon, M. (1949): Recherches sur les faunes Albiennes de Madagascar. 1. L'Albien d'Ambarimaninga. – Annales géologiques du Service des Mines, Madagascar, **6**, 1–128, Tananarive.

Collignon, M. (1964): Atlas des fossiles caracteristiques de Madagascar (Ammonites), XI Cenomanien. – xi + 152 pp., Service géologique, Tananarive.

Coquand, H. (1862): Géologie et paléontologie de la région de la Province de Constantine. – Mémoires de la Société d'Émulation de la Provence, **2**, 341 pp., Marseille.

Courville, P., Thierry, J. & Lang, J. (1998): Ammonite faunal exchanges between South Tethyan platforms and South Atlantic during the uppermost Cenomanian – lowermost Middle Turonian in the Benue Trough (Nigeria). – Géobios, **31**/2, 187–214, Lyon.

Crick, G.C. (1907): Cretaceous fossils of Natal. – In: Anderson, W.: Third and final report of the Geological Survey of Natal and Zululand, 161–250, London.

Dessauvagie, T.F.J. (1968): Cenomanian Trocholinas from Nigeria. – Micropaleontology, **14**/1, 64–72, New York.

Douvillé, H. (1879): (Note accompagnant la présentation de l´Atlas de t.iv de l'explication de la carte géologique de France de E. Bayle and R. Zeiller). – Bulletin de la Société Géologique de France, Série 3, Volume **7**, 91–92, Paris.

Douvillé, H. (1912): Evolution et classification des Pulchelliides. – Bulletin de la Société Géologique de France, Série 4, Volume **11**, 285–320, Paris.

Dubourdieu, G. (1953): Ammonites nouvelles des Monts du Mellègue. – Bulletin du Service de la Carte Géologique de l'Algerie, 1e série, Paléontologie, **16**, 76 pp., Algiers.

Ekwueme, B.N., Nyong, E.E. & Petters, S.W. (1995): Geological excursion guidebook to Oban Massif, Calabar Flank and Mamfe Embayment, southeastern Nigeria. – iv + 36 pp., published in commemoration of the 31st annual Conference of the Nigerian Mining and Geosciences Society, Calabar, March 12–16, 1995.

Essien, N.U. & Ufot, D.O. (2010): Age of the Mfamosing Limestone, Calabar Flank, South Eastern, Nigeria. – International Journal of Basic & Applied Sciences, **10**/5, 8–19. https://pdfs.semanticscholar.org/a894/b4b4b5d0a1bb0efc49d42835356c039d7e0f.pdf?_ga=2.49049313.63451396.1571657506-1842199311.1571657506

Fayose, E.A. (undated, ?1976): Upper Cretaceous algae from Calabar area, Cross-River State of Nigeria. – 8 pp., typewritten manuscript.

Fayose, E.A. (1978): Depositional Environments of Carbonates of Calabar Flank, Southeastern Nigeria. – Nigerian Mining Geology, **15**, 1–13, Lagos.

Fayose, E.A. & Dessauvagie, T.F.J. (1976): Excursion 3: Upper Cretaceous and Tertiary sediments of eastern states of Nigeria. – 7th African Micropaleontological Colloquium Ile-Ife March 16–29, 1976, Geological guide to some Nigerian Cretaceous – Recent localities, 35–52, Ibadan.

Förster, R. (1978): Evidence for an open seaway between northern and southern proto-Atlantic in Albian times. – Nature, **272**, 158–159, London.

Förster, R. & Scholz, G. (1979): *Salaziceras nigerianum* n. sp. from southeast Nigeria: Faunal evidence for an open seaway between the northern and southern Atlantic in Late Albian times. – Neues Jahrbuch fur Geologie und Paläontologie, Monatshefte, **1979**, 109–119, Stuttgart.

Gale, A.S., Kennedy, W.J. & Walaszczyk, I. (2019): Upper Albian, Cenomanian and Lower Turonian stratigraphy, ammonite and inoceramid bivalve faunas from the Cauvery Basin, Tamil Nadu. – Acta Geologica Polonica, **69**, 161–338, Warsaw.

Geinitz, H.B. (1849): Das Quadersandsteingebirge oder Kreidegebirge in Deutschland. – 292 pp., Freiberg.

Geological Survey of Nigeria (1957): Nigeria 1:250,000 Geological Series, Sheet 80 Oban Hills. – Compiled by SHELL-BP Nigeria, printed in the Netherlands.

Gill, T. (1871): Arrangement of the Families of Mollusks. – Smithsonian Miscellaneous Collections, **227**, xvi + 49 pp., Washington, D.C.

Grossouvre, A. de (1894): Recherches sur la craie supérieure, 2, Paléontologie. Les ammonites de la craie supérieure. – Mémoires pour servir à l'expication du Service de la Carte Géologique détaillée de la France, 264 pp., Paris (misdated 1893).

Hanger, R.A. (1998): Nearshore *Peruviella dolium* (Roemer, 1849) paleocommunity, Cretaceous (Albian) Walnut Formation, Coryell County, Texas. – Texas Journal of Science, **50**/4, 333–336, Edinburgh, Texas.

Harry, T.A., Bassey, C.E. & Petters, S.W. (2017): Sequence Stratigraphy and Biostratigraphic Characterization of the System Tracts in the Calabar Flank, Lower Benue Trough, Nigeria. – International Journal of Scientific & Engineering Research, **8**/7, 1787–1799. https://www.ijser.org/researchpaper/Sequence-Stratigraphy-and-Biostratigraphic-Characterization-of-the-System-Tracts-in-the-Calabar-Flank-Lower-Benue-Trough-Nigeria.pdf

Hébert, E. & Munier-Chalmas, E.P.A. (1875): Fossiles du Basin d'Uchaux. – Annales des Sciences Géologiques, Paris, **6**, 113–132, Paris.

Hyatt, A. (1884): Genera of Fossil Cephalopods. – Proceedings of the Boston Society of Natural History, **22**, 273–320, Boston.

Hyatt, A. (1889): Genesis of the Arietidae. – Smithsonian Contributions to Knowledge, **673**, xi + 239 pp., Washington, D.C.

Hyatt, A. (1903): Pseudoceratites of the Cretaceous. – United States Geological Survey Monograph, **44**, 351 pp., Washington, D.C.

Igwe, E.O., Okoro, A.U. & Obasi, A.I. (2015): Foraminiferal Biostratigraphic Analysis of the Late Cenomanian–Turonian Eze-Aku Shale in the Afikpo Synclinorium, Lower Benue Trough, Nigeria. – American Journal of Science and Technology, **2**/6, 274–282, Wilmington, New Castle, DE.

Kaplan, U., Kennedy, W.J., Lehmann, J. & Marcinowski, R. (1998): Stratigraphie und Ammonitenfaunen des westfälischen Cenoman. – Geologie und Paläontologie in Westfalen, **51**, 236 pp., Münster.

Kennedy, W.J. (1971): Cenomanian ammonites from southern England. – Special Papers in Palaeontology, **8**, 133 pp., London.

Kennedy, W.J. (2015): The Ammonoidea of the Lower Chalk Part 6. – Monograph of the Palaeontographical Society, 404–459, London.

Kennedy, W.J. & Gale, A.S. (2015): Upper Albian and Cenomanian ammonites from Djebel Mrhila, Central Tunisia. – Révue de Paléobiologie, **34**, 235–361, Geneva.

Kennedy, W.J. & Gale, A.S. (2017): The Ammonoidea of the Lower Chalk Part 7. – Monograph of the Palaeontographical Society, 461–561, London.

Kennedy, W.J. & Klinger, H.C. (2008): Hypermorphosis in *Salaziceras*, a Cretaceous ammonite, from Madagascar. – African Natural History, **4**, 113–116, Cape Town.

Kennedy, W.J. & Klinger, H.C. (2012): Cretaceous faunas from Zululand and Natal. A new species of the ammonite genus *Salaziceras* Breistroffer, 1936, from the Lower Cenomanian Mzinene Formation. – Palaeontologica Africana, **47**, 15–17, Witwatersrand.

Kennedy, W.J. & Wright, C.W. (1984): The affinities of the Cretaceous ammonite *Neosaynoceras* Breistroffer, 1947. – Palaeontology, **27**, 159–167, London.

Kennedy, W.J., Cobban, W.A., Gale, A.S., Hancock, J.M. & Landman, N.H. (1998): Ammonites from the Weno Limestone (Albian) in northeast Texas. – American Museum of Natural History Novitates, **3236**, 46 pp., New York.

Kennedy, W.J., Gale, A.S., Lees, J.A. & Caron, M. (2004): The Global Boundary Stratotype Section and Point for the base of the Cenomanian Stage, Mont Risou, Hautes-Alpes, France. – Episodes, **27**, 21–32, Bangalore.

Kennedy, W.J., Cobban, W.A., Hancock, J.M. & Gale, A.S. (2005): Upper Albian and Lower Cenomanian ammonites from the Main Street Limestone, Grayson Marl and Del Rio Clay in northeast Texas. – Cretaceous Research, **26**, 349–428, London.

Kennedy, W.J., Klinger, H.C. & Lehmann, J. (2015): Cretaceous faunas from Zululand and Natal, South Africa. – The ammonite Subfamily Mantelliceratinae Hyatt, 1903. – African Natural History, **11**, 1–42, Cape Town.

Klein, J. (2015): Lower Cretaceous Ammonites VIII Turrilitoidea – Anisoceratidae, Hamitidae, Turrilitidae, including representatives of the Upper Cretaceous species. – Fossilium Catalogus I: Animalia, **154** *(pars)*, 265 pp., Weikersheim.

Klein, J. (2018): Lower Cretaceous Ammonites XI Acanthoceratoidea: Leymeriellidae, Brancoceratidae, Lyelliceratidae, Flickiidae, Forbesiceratidae, including Upper Cretaceous representatives. – Fossilium Catalogus I: Animalia), **158**, 333 pp., Weikersheim.

Klinger, H.C. & Kennedy, W.J. (1978): Turrilitidae (Cretaceous Ammonoidea) from South Africa, with a discussion of the evolution and limits of the family. – Journal of Molluscan Studies, **4**, 1–48, London.

Kner, R. (1852): Neue Beiträge zur Kenntniss der Kreideversteinerungen von Ost-Galizien. – Denkschriften der mathematisch-naturwissenschaftlichen Classe der kaiserlichen Akademie der Wissenschaften, **3**, 293–334, Wien.

Kogbe, C.A. (1981): Cretaceous and Tertiary of the Iullemmeden Basin in Nigeria (West Africa). – Cretaceous Research, **2**/2, 129–186, London.

Kogbe, C.A. (1989): The Cretaceous and Paleogene Sediments of Southern Nigeria. – In: Kogbe, C.A. (Ed.): Geology of Nigeria, 2nd revised edition, 273–282, Jos.

Korn, D., Ebbighausen, V., Bockwinkel J. & Klug, C. (2003): The A-mode ontogeny in prolecanitid ammonites. – Palaeontology, **46**, 1123–1132, London.

Kullmann, J. & Wiedmann, J. (1970): Significance of sutures in phylogeny of Ammonoidea. – University of Kansas, Paleontological Contributions, **42**, 1–32, Lawrence.

Lawal, O. (1991): Palynological age and correlation of a black shale section in the Eze-Aku Formation, Lower Benue Trough, Nigeria. – Journal of African Earth Sciences, **12**, 473–482, Oxford.

Matsumoto, T. (Ed.) (1954): The Cretaceous System in the Japanese Islands. – 324 pp., Japan Society for the Promotion of Science, Tokyo.

Matsumoto, T. & Sarkar, S.S. (1966): *Utaturiceras vicinale* (Stoliczka) from Southern India. – In: Matsumoto, T., Sastry, M.V.A. & Sarkar, S.S.: Notes on some Cretaceous ammonites from southern India. – Memoirs of the Faculty of Science, Kyushu University, Series D, Geology, **17**, 295–309, Fukuoka.

Mbani, J.-N. (2008): Micropaléontologie et géochimie organique du bassin côtier congolais au Crétacé supérieur: paléoécologie des foraminifères, espèces et associations indicatrices des paléoenvironnements des roches mères pétrolières. – Sciences de la Terre. Thèse de doctorat de l'Université Pierre et Marie Curie, Paris VI, 473 pp., Paris.

Meister, C. & Abdallah, H. (1996): Les ammonites du Cénomanien supérieur et du Turonien inférieur de la région de Gafsa-Chotts, Tunisie du Centre-Sud. Upper Cenomanian-Lower Turonian ammonites of the Gafsa-Chotts area, southern part of Central Tunisia. – Géobios, **29**/5, Supplement 1, 3–49, Lyon.

Meister, C., Alzouma, K., Lang, J., Mathey, B. & Pascal, A. (1994): Nouvelles données sur les ammonites du Niger oriental (Ténéré, Afrique occidentale) dans le cadre de la transgression du Cénomanien-Turonien. New data on the ammonite faunas from eastern Niger (Tenere, Western Africa) during the Cenomanian-Turonian marine transgression. – Géobios, **27**/2, 189–219, Lyon.

Meister, C., Buta, A., David, B. & Tavares, T. (2011): Les ammonites de la limite Albien – Cénomanian dans la région de Sumbe (Bassin de la Kwanza, Angola). – Revue de Paléobiologie, **30**, 685–781, Geneva.

Moullade, M., Watkins, D.K., Oboh-Ikuenobe, F.E., Bellier, J.-P., Masure, E., Holbourn, A.E.L., Erbacher, J., Kuhnt, W., Pletsch, T., Kaminski, M.A., Rauscher, R., Shafik, S., Yepes, O., Dejax, J., Gregg, J.M., Shin, I.C. & Schuler, M. (1998): ODP Leg 159, Equatorial Atlantic: Mesozoic biostratigraphic, paleoenvironmental and paleobiogeographic synthesis. – In: Mascle, J., Lohmann, G.P. & Moullade, M. (Eds.): Proceedings of the Ocean Drilling Program, Scientific Results, **159**, 481–490, College Station, Texas.

Murat, R.C. (1972a): Stratigraphy and Palaeogeography of the Cretaceous and Lower Tertiary in Southern Nigeria. – Geological Magazine, **109**, 411–419, London.

Murat, R. (1972b): Stratigraphy and paleogeography of the Cretaceous and lower Tertiary in Southern Nigeria. – In: Dessauvagie, T.F.J. & Whiteman, A.J.: Proceedings of the Conference on African Geology. Held at the University of Ibadan from 7–14 December 1970 in Commemoration of the Tenth Anniversary, Ibadan.

Nair, K.M., Ramanathan, R.M. & Ukpong, E.E. (1982): Sedimentology and stratigraphy of Cretaceous carbonates and associated rocks of Calabar Flank, Nigeria. – Nigerian Journal of Mining Geology, **18**, 120–129, Ibadan.

Neumayr, M. (1875): Die Ammoniten der Kreide und die Systematik der Ammonitiden. – Zeitschrift der Deutschen Geologischen Gesellschaft, **27**, 854–942, Berlin.

Nowak, J. (1916): Über die bifiden Loben der oberkretazischen Ammoniten und ihre Bedeutung für die Systematik. – Bulletin International de l'Académie des Sciences de Cracovie, Classe des Sciences Mathématiques et Naturelles, Série B: Sciences Naturelles, **1915**, 1–13, Cracow.

Nyong, E.E. (1995): Geological Excursion Guide book to Calabar Flank and Oban Massif. – 31st Annual conference of the Nigerian Mining and Geosciences Society, Calabar, 12–16, Jos.

Nyong, E.E. & Ramanathan, R.M. (1985): A record of oxygen-deficient paleoenvironments in the Cretaceous of the Calabar Flank, SE Nigeria. – Journal of African Earth Sciences, **3**/4, 455–460, Amsterdam.

Orajaka, S. (1959a): Interim report on the limestone reconnaissance in the Odukpani-Mfamosing area North of Calabar. – Geological Survey of Nigeria, Report **1304**, 5 pp., Kaduna.

Orajaka, S. (undated, ?1959b): 2nd interim report on the limestone reconnaissance in the Mfamosing region, North of Calabar. – Geological Survey of Nigeria, Report **1304** A, 1 p., Kaduna.

d'Orbigny, A. (1840–1842): Paléontologie française: Terrains crétacés. 1. Céphalopodes. – 1–120 (1840), 121–430 (1841), 431–662 (1842), Paris.

Oti, M.N. & Koch, R. (1990): Mid-Cretaceous Shelf Carbonates: The Mfamosing Limestone, Lower Benue Trough (Nigeria). – Facies, **22**, 87–102, Erlangen.

Palmer, T.J. & Wilson, M.A. (2004): Calcite precipitation and dissolution of biogenic aragonite in shallow Ordovician calcite seas. – Lethaia, **37**/4, 417–427, London.

Pervinquière, L. (1907): Études de paléontologie tunisienne. 1. Céphalopodes des terrains secondaires. – Carte Géologique de la Tunisie, v + 438 pp., Paris.

Pervinquière, L. (1910): Sur quelques ammonites du Crétacé algérien. – Mémoires de la Société Géologique de France. – Paléontologie, **17**/2–3, 86 pp., Paris.

PETTERS, S.W. (1982): Central West African Cretaceous – Tertiary Benthic Foraminifera and Stratigraphy. – Palaeontographica Abteilung A, **A179**, Lieferung 1–3, 1–104, Stuttgart.

PETTERS, S.W. (2014): Regional Geology of Africa, 2nd edition. – Lecture Notes in Earth Sciences, **40**, 748 pp., Berlin.

PETTERS, S.W. & EKWEOZOR, C.M. (1982): Origin of Mid-Cretaceous black shales in the Benue Trough, Nigeria. – Palaeogeography, Palaeoclimatology, Palaeoecology, **40**, 311–314, Amsterdam.

PETTERS, S.W. & REIJERS, T.J.A. (1987): Cretaceous carbonates on the Calabar Flank. – In: MATHEIS, G. & SCHANDELMEIER, H. (Eds.): Current Research in African Earth Sciences. – Extended Abstracts, 14th Colloquium on African Geology Berlin (West), 155–158, Rotterdam (Balkema).

PETTERS, S.W., NYONG, E.E., AKPAN, E.B. & ESSIEN, N.U. (1995): Lithostratigraphic revision for the Calabar Flank, S.E. Nigeria. – Proceedings of the 31st Anniversary conference of Nigeria Mining and Geosciences Society, 54 pp., Calabar.

PICTET, F.J. & CAMPICHE, G. (1860): Description des fossiles du terrain crétacé des environs de Ste Croix, part 1. Description des fossiles. – Matériaux pour la Paléontologie Suisse, series 2, 209–380, Geneva.

PICTET, F.J. & CAMPICHE, G. (1861): Description des fossiles du terrain crétacé des environs de Ste Croix, part 2. Description des fossiles. – Matériaux pour la Paléontologie Suisse, series 3, 1–144, Geneva.

PLETSCH, T., ERBACHER, J., HOLBOURN, A.E.L., KAMINSKI, M.A., DE KLASZ, S., KUHNT, W. & MOULLADE, M. (1996): The Cretaceous of the Gulf of Guinea (Leg 159) and adjacent coastal basins: implications for the opening of the Equatorial Atlantic Gateway. – Berichte-Reports, Geologisch-Paläontologisches Institut der Universität Kiel, **76**, 201–205, Kiel.

PLETSCH, T., ERBACHER, J., HOLBOURN, A.E.L., KUHNT, W., MOULLADE, M., OBOH-IKUENOBEDE, F.E., SÖDING, E. & WAGNER, T. (2001): Cretaceous separation of Africa and South America: the view from the West African margin (ODP Leg 159). – Journal of South American Earth Sciences, **14**, 147–174, Amsterdam.

POIGNANT, A.-F. & LOBITZER, H. (1982): Les algues de l'Albien supérieur du Nigéria. – Cahiers de Micropaléontologie, **2**, 35–40, Paris.

RAEBURN, C. (1937): Limestone resources of Nigeria. – Geological Survey of Nigeria, Report **771**, 11 pp., Kaduna.

REIJERS, T.J.A. (1998): The Mfamosing Limestone in SE Nigeria: Outcrop-Subsurface Correlation and Reservoir Development. – Journal of Petroleum Geology, **21**, 467–481, London.

REIJERS, T.J.A. & PETTERS, S.W. (1987): Depositional environment and diagenesis of Albian carbonates in Calabar Flank, SE Nigeria. – Journal of Petroleum Geology, **10**/3 283–294, London. https://doi.org/10.1111/j.1747-5457.1987.tb00947.x

REIJERS, T.J.A. & PETTERS, S.W. (1997): Sequence stratigraphy based on microfacies analysis: Mfamosing Limestone, Calabar Flank, Nigeria. – Geologie en Mijnbouw, **76**/3, 197–215, Utrecht. https://doi.org/10.1023/A:1003089529914

RENZ, O. (1968): Die Ammonoidea im Stratotyp des Vraconnien bei Sainte–Croix (Kanton Waadt). – Schweizerische Paläontologische Abhandlungen, **87**, 99 pp., Basel.

RENZ, O. (1972): Die Gattung *Puzosia* BAYLE, *Bhimaites* MATSUMOTO und *Desmoceras* ZITTEL (Ammonoidea) im Oberen Albien Venezuelas. – Eclogae Geologicae Helvetiae, **65**, 701–724, Basel.

REYMENT, R.A. (1952): Explanation of the map of fossil localities. – Geological Survey of Nigeria, Report, **993**, 1–6, Kaduna Junction.

REYMENT, R.A. (1955): The Cretaceous ammonoidea of southern Nigeria and the southern Cameroons. – Geological Survey of Nigeria, Bulletin, **25**, 112 pp., Kaduna Junction.

REYMENT, R.A. (1965). Aspects of the geology of Nigeria. The Stratigraphy of the Cretaceous and Cenozoic deposits. – 133 pp., Ibadan University Press, Ibadan.

REYMENT, R.A. (1972): Cretaceous (Albian-Turonian) geology of the South Atlantic. – In: DESSAUVAGIE, T.F.J. & WHITEMAN, A.J.: Proceedings of the Conference on African Geology. Held at the University of Ibadan from 7–14 December 1970 in Commemoration of the Tenth Anniversary of the Founding of the Geology Department, 505–512, Ibadan.

REYMENT, R.A. (1980): Biogeography of the Saharan Cretaceous and Paleocene epicontinental transgressions. – Cretaceous Research, **1**, 299–327, London.

REYMENT, R.A. & BENGTSON, P. (1985): Nigeria. – Mid Cretaceous Events report on results obtained 1974–1983 by IGCP Project No. 58. – Publications from the Palaeontological Institution of the University of Uppsala, Special Volume, **5**, 71–74, Uppsala.

REYMENT, R.A. & DINGLE, R.V. (1987): Palaeogeography of Africa during the Cretaceous Period. – Paleogeography, Palaeoclimatology, Palaeoecology, **59**, 93–116, Amsterdam.

REYMENT, R.A. & MÖRNER, N.A. (1977): Cretaceous transgressions and regressions exemplified by the South Atlantic. – Special Papers, Paleontological Society of Japan, **21**, 247–261, Tokyo.

REYMENT, R.A. & TAIT, E.A. (1983): Resume of the geology of Nigeria. – In: FABRE, J. (Ed.): Lexique Stratigraphique International, Nouvelle Série, **1**, Afrique de l'Ouest, 127–135, Oxford.

ROBASZYNSKI, F., AMÉDRO, F., GONZÀLEZ-DONOSO, J.M. & LINARES, D. (2008): The Albian (Vraconnian) boundary at the western Tethyan margin (central Tunisia and southeastern France). – Bulletin de la Société geologique de France, **179**, 245–266, Paris.

SCHLOTHEIM, E.F. VON (1820): Die Petrefactenkunde: auf ihrem jetzigen Standpunkte durch die Beschreibung seiner Sammlung versteinerter und fossiler Überreste des Thier- und Pflanzenreichs der Vorwelt erläutert. – LXII + 437 pp., Gotha.

SCHLÜTER, C. (1871–1876): Cephalopoden der oberen deutschen Kreide. – Palaeontographica, **21**, 1–24 (1871), **21**, 25–120, (1872), **24**, 1–144 (121–264) + X (1876), Stuttgart.

SCHOLZ, G. (1973): Sur l'âge de la faune d'Ammonites au Château près de St.-Martin-en-Vercours (Drôme) et quelques considerations sur l'évolution des Turrilitidés et des Hoplitides vracono-cénomaniens. – Geologie Alpine, **49**, 119–129, Grenoble.

SEGUENZA, G. (1881–1882): Studii geologici e paleontologici sul cretaceo medio dell'Italia meridionale. – Memorie Atti della Reale Academia dei Lincei, **12** (for 1879), 65–214 (1–152), Rome.

SHARPE, D. (1853–57): Description of the fossil remains of Mollusca found in the Chalk of England. I, Cephalopoda. – Monograph of the Palaeontographical Society, **68**, 1–26 (1853), 27–36 (1855), 37–68 (1857), London.

SOWERBY, J. (1817): The Mineral Conchology of Great Britain, **2**, Pls. 151–186, London.

SOWERBY, J. (1827): The Mineral Conchology of Great Britain (continued), **6**, Pls. 545–580, London.

SPATH, L.F. (1921): On Cretaceous Cephalopoda from Zululand. – Annals of the South African Museum, **12**, 217–321, Cape Town.

SPATH, L.F. (1922): On the Senonian ammonite fauna of Pondoland. – Transactions of the Royal Society of South Africa, **10**, 113–147, Cape Town. https://doi.org/10.1080/00359192209519274

SPATH, L.F. (1925): On Upper Albian Ammonoidea from Portuguese East Africa, with an appendix on Upper Cretaceous ammonites from Maputoland. – Annals of the Transvaal Museum, **11**, 179–200, Pretoria.

SPATH, L.F. (1927): Revision of the Jurassic fauna of Kach (Cutch). – Memoirs of the Geological Survey of India, Palaeontologica Indica, N.S., **9**, memoir 2, part 1, 1–71, Calcutta.

SPATH, L.F. (1932): A Monograph of the Ammonoidea of the Gault, part 9. – Monograph of the Palaeontographical Society, 379–410, London.

SPATH, L.F. (1934): A Monograph of the Ammonoidea of the Gault, part 11. – Monograph of the Palaeontographical Society, 443–496, London.

STANLEY, S.M. & HARDIE, L.A. (1999): Hypercalcification: Paleontology Links Plate Tectonics and Geochemistry to Sedimentology. – GSA Today, **9**/2, 1–7, Boulder, Colorado.

STOLICZKA, F. (1864): The fossil cephalopoda of the Cretaceous rocks of Southern India. Ammonitidae with revision of the Nautilidae etc. – Memoirs of the Geological Survey of India, Palaeontologica Indica, **3**, 57–106, Calcutta.

TATTAM, C.M. (1939): Preliminary notes on the revision of the sedimentary rocks of the south-eastern provinces. – Geological Survey of Nigeria, Report, **844**, 3 pp., Kaduna Junction.

THOMAS, P. (1893): Description de quelques fossiles nouveaux et critiques des terrains tertiaires et secondaires de la Tunisie recueillis en 1885 et 1886. – Exploration scientifique de la Tunisie, 1–46, Paris.

UMEJI, O.P. (2013): The south and central Benue Trough: Stratigraphic revisions. – In: ASHANO, E.C. & OGEZI, A.E. (Eds.): Proceedings of University of Jos PTDF Chair Endowment Fund Seminar, April 2012, 145–181, University of Jos.

VAN HOEPEN, E.C.N. (1942): Die gekielde ammonite van die Suid-Afrikaanse Gault. II. Drepanoceratidae, Pervinquieridae, Arestoceratidae, Cainoceratidae. – Paleontologiese Navorsing van die Nasionale Museum, Bloemfontein, **1**, 91–157, Bloemfontein.

WIEDMANN, J. (1966): Stammesgeschichte und System der posttriadischen Ammonoideen. Ein Überblick. – Neues Jahrbuch für Geologie und Paläontologie – Abhandlungen, **125**, 49–79; **127**, 13–81, Stuttgart.

WIEDMANN, J. & DIENI, I. (1968): Die Kreide Sardiniens und ihre Cephalopoden. – Palaeontographia Italica, **64**, 1–171, Pisa.

WRIGHT, C.W. (1956): Notes on Cretaceous ammonites. III. *Utaturiceras* gen. nov. and the Metoicoceratinae. – Annals and Magazine of Natural History, **12**/9, 391–393, London.

WRIGHT, C.W. & KENNEDY, W.J. (1978): The Ammonite *Stoliczkaia* from the Cenomanian of England and northern France. – Palaeontology, **21**, 393–409, London.

WRIGHT, C.W. & KENNEDY, W.J. (1979): Origin and evolution of the Cretaceous micromorph ammonite family Flickiidae. – Palaeontology, **22**, 685–704, London.

WRIGHT, C.W. & KENNEDY, W.J. (1984): The Ammonoidea of the Lower Chalk. Part 1. – Monograph of the Palaeontographical Society, 1–126, London.

WRIGHT, C.W. & KENNEDY, W.J. (1987): The Ammonoidea of the Lower Chalk. Part 2. – Monograph of the Palaeontographical Society, 127–218, London.

WRIGHT, C.W. & KENNEDY, W.J. (1996): The Ammonoidea of the Lower Chalk. Part 5. – Monograph of the Palaeontographical Society, 320–403, London.

YOUNG, K. (1958): *Graysonites*, a Cretaceous ammonite in Texas. – Journal of Paleontology, **32**, 171–182, Tulsa.

ZABORSKI, P.M.P. (1985): Upper Cretaceous ammonites from the Calabar region, southeast Nigeria. – Bulletin of the British Museum (Natural History) Geology, **39**, 1–72, London.

ZABORSKI, P.M.P. (1986): Lower Cenomanian (Mid-Cretaceous) ammonites from south-east Nigeria. – Journal of African Earth Sciences, **5**, 371–380, Oxford.

ZABORSKI, P.M. (2000): The Cretaceous and Paleocene transgressions in Nigeria and Niger. – Journal of Mining and Geology, **36**/2, 153–173, Ibadan.

ZITTEL, K.A. VON (1884): Handbuch der Palaeontologie. 1, Abteilung 2, Lieferung 3, Cephalopoda, 329–522, Munich–Leipzig.

ZITTEL, K.A. VON (1895): Grundzüge der Palaeontologie (Palaeozoologie). – vii + 972 pp., Munich–Leipzig.

Received: 29. July 2019, accepted: 21. October 2019

Plates

Plate 1

Figs. 1–5: ***Flickia bullata*** **sp. nov.**

1, 2: paratype GBA 2016/003/0011; 3–5: the holotype, GBA 2016/003/0010.

Figs. 6–14: ***Puzosia*** **(*****Anapuzosia*****) sp.**

6, 7: GBA 2016/003/0016; 8: GBA 2016/003/0014; 9–11: GBA 2016/003/0012; 12: GBA 2016/003/0015; 13: GBA 2016/003/0018; 14: GBA 2016/003/0017.

Figures 1–5, 9–11 are x 2, Figures 6–8, 12–14 are natural size.

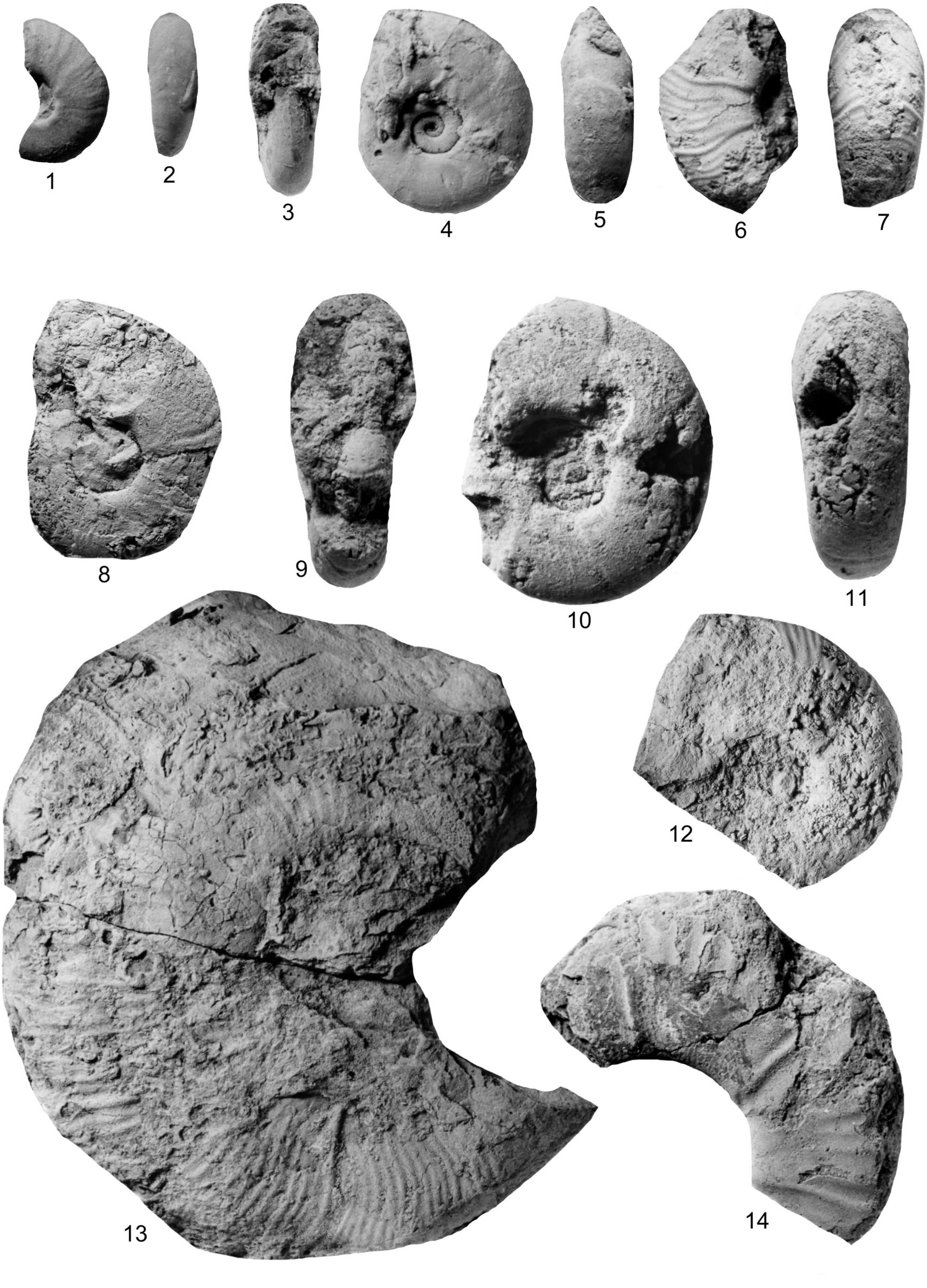
1
2
3
4
5
6
7
7
8
9
10
11
12
13
14

Plate 2

Figs. 1, 2, 10: ***Acompsoceras*** **sp. juv.**

1, 2: GBA 2016/003/0064; 10: GBA 2016/003/0065.

Figs. 3–6, 8, 9, 11–13: ***Acompsoceras calabarense*** **ZABORSKI, 1985.**

3, 4: GBA 2016/003/0048; 5, 6: GBA 2016/003/0049; 8, 9: GBA 2016/003/0050; 11: GBA 2016/003/0051; 12, 13: GBA 2016/003/0052.

Fig. 7: ***Sharpeiceras nigeriense*** **ZABORSKI, 1985**, GBA 2016/003/0040.

Figs. 14–22: ***Salaziceras nigerianum*** **FÖRSTER & SCHOLZ, 1979.**

14: GBA 2016/003/0027; 15, 16: GBA 2016/003/0028; 17, 18: GBA 2016/003/0029; 19, 20: GBA 2016/003/0030; 21, 22: GBA 2016/003/0031.

All Figures are x 2.

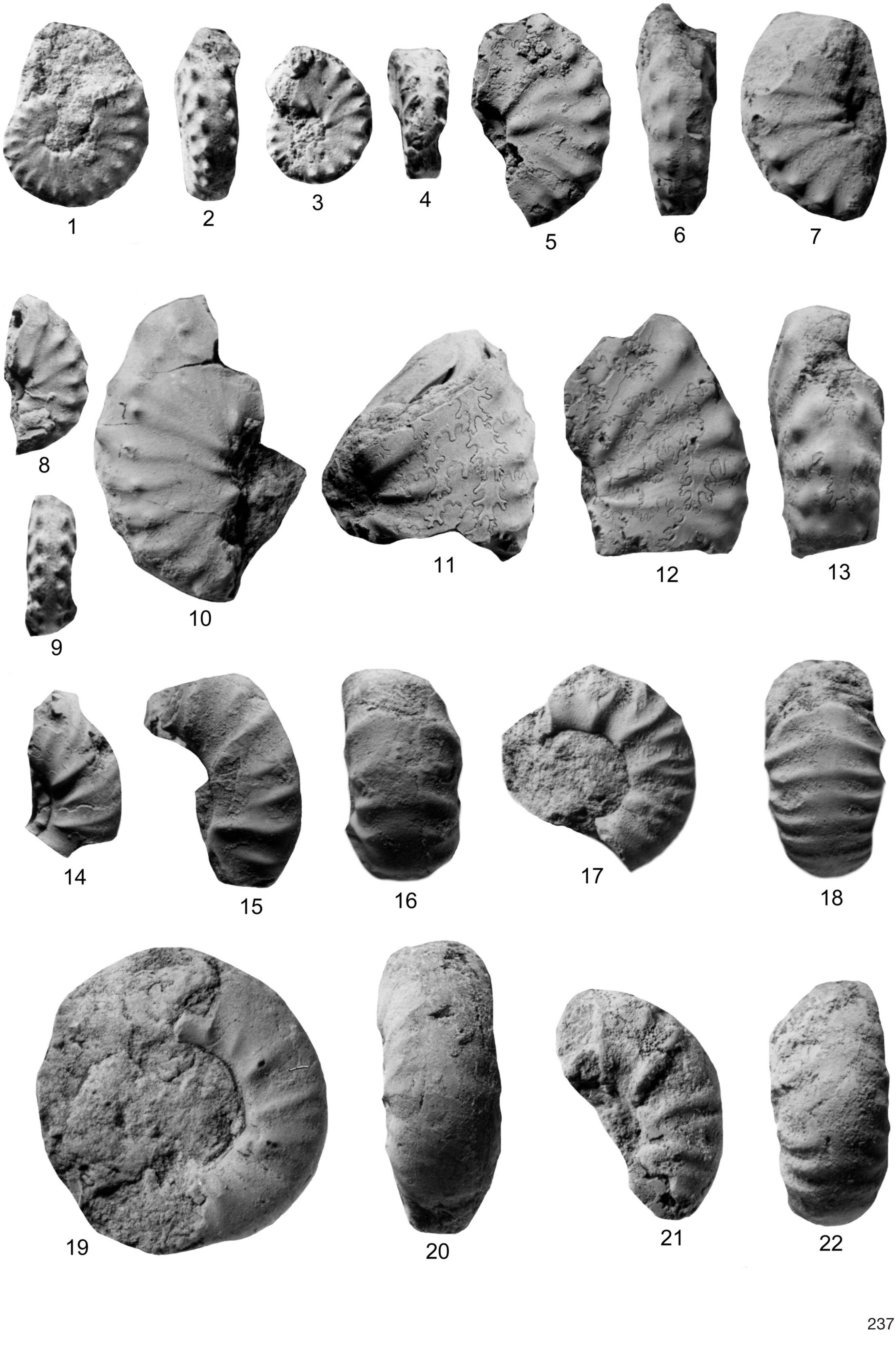
1
2
3
4
5
6
7
8
9
10
11
12
13
14
15
16
17
18
19
20
21
22

Plate 3

Figs. 1–4, 7–15: ***Sharpeiceras nigeriense*** **ZABORSKI, 1985.**

1, 7–9: GBA 2016/003/0041; 2, 10, 11: GBA 2016/003/0042; 3, 4: GBA 2016/003/0043; 12, 13: GBA 2016/003/0044; 14, 15: GBA 2016/003/0045.

Figs. 5, 6, 16–19: ***Acompsoceras calabarense*** **ZABORSKI, 1985.**

5, 18, 19: GBA 2016/003/0053; 6, 16, 17: GBA 2016/003/0054.

Figures 1–6 are natural size, Figures 7–19 are x 2.

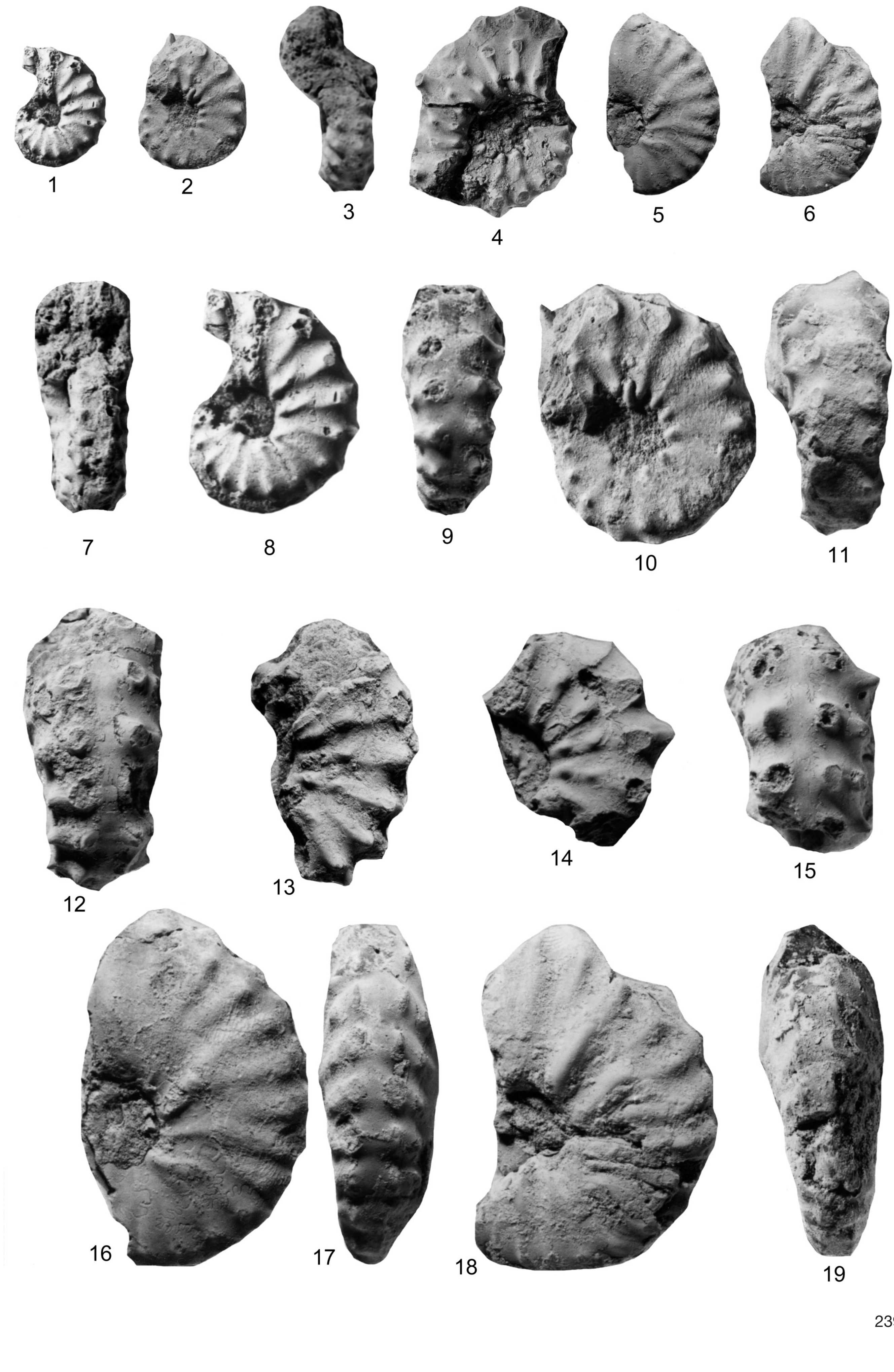
1
2
3
4
5
6
7
8
9
10
11
12
13
14
15
16
17
18
19

Plate 4

Figs. 1, 2, 6–8: ***Graysonites wacoense*** **(Böse, 1928).**
1, 2: GBA 2016/003/0037; 6, 7: GBA 2016/003/0036; 8: GBA 2016/003/0035.

Figs. 3–5: ***Sharpeiceras nigeriense*** **Zaborski, 1985**, GBA 2016/003/0046.

All Figures are natural size.

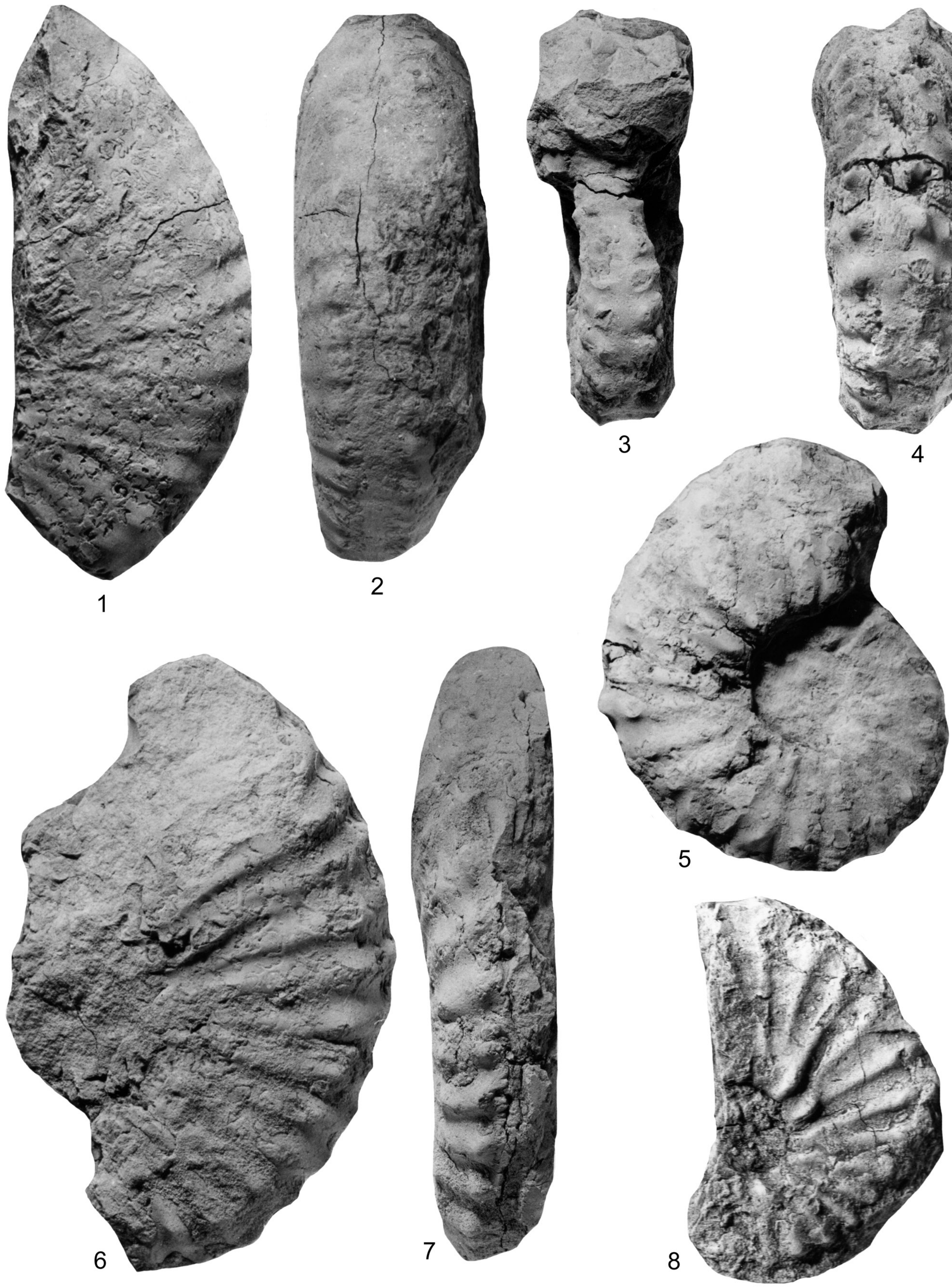
1
2
3
4
5
6
7
8

Plate 5

Figs. 1–13: ***Acompsoceras calabarense*** **Zaborski, 1985.**

1, 2: GBA 2016/003/0056; 3, 4: GBA 2016/003/0057; 5, 6: GBA 2016/003/0058; 7, 8: GBA 2016/003/0059; 9, 10: GBA 2016/003/0060; 11: GBA 2016/003/0055; 12, 13: GBA 2016/003/0061.

The originals of Figures 1–8, 9–13 are from the Lower Cenomanian part of the Odukpani Formation at locality 77/50, North of Odukpani; the original of Figure 11 is from the Mfamosing Quarry.

All Figures are natural size.

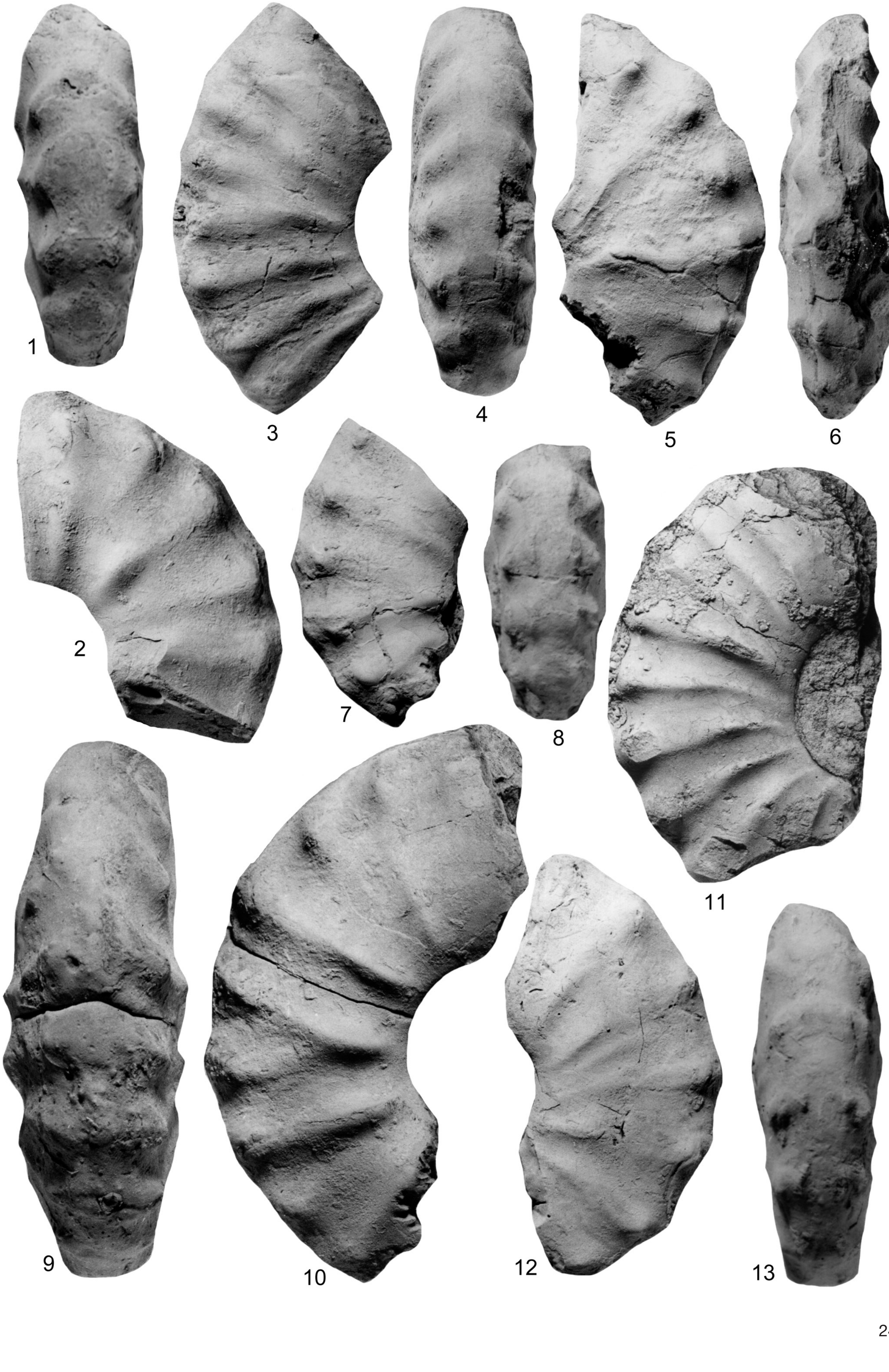
1
2
3
4
5
6
7
8
9
10
11
12
13

Plate 6

Figs. 1–5, 7, 9, 12–14: ***Hypoturrilites betaitraensis*** **(Collignon, 1964).**

1: GBA 2016/003/0083; 2: GBA 2016/003/0077; 3: GBA 2016/003/0078; 4: GBA 2016/003/0079; 5: GBA 2016/003/0080; 7: GBA 2016/003/0081; 9: GBA 2016/003/0082; 12: GBA 2016/003/0084; 13: GBA 2016/003/0085; 14: GBA 2016/003/0086.

All of these figures are natural size.

Fig. 6: ***Mariella*** **(*Mariella*)** ***cenomanensis*** **(Schlüter, 1876)**, GBA 2016/003/0075.

Fig. 8: ***Mariella*** **(*Mariella*)** ***essenensis*** **(Geintz, 1849)**, GBA 2016/003/0068.

Figs. 10, 11: ***Mariella*** **(*Mariella*)** ***bicarinata*** **(Kner, 1852).**

10: GBA 2016/003/0066; 11: GBA 2016/003/0067.

Figs. 15, 16, 18: ***Mariella*** **(*Mariella*) aff.** ***miliaris*** **(Pictet & Campiche, 1861).**

15: GBA 2016/003/0071; 16: GBA 2016/003/0072; 18: GBA 2016/003/0074.

Fig. 17: ***Mariella*** **(*Mariella*)** ***oehlerti oehlerti*** **(Pervinquière, 1910)**, GBA 2016/003/0069.

All of these figures are x 2.

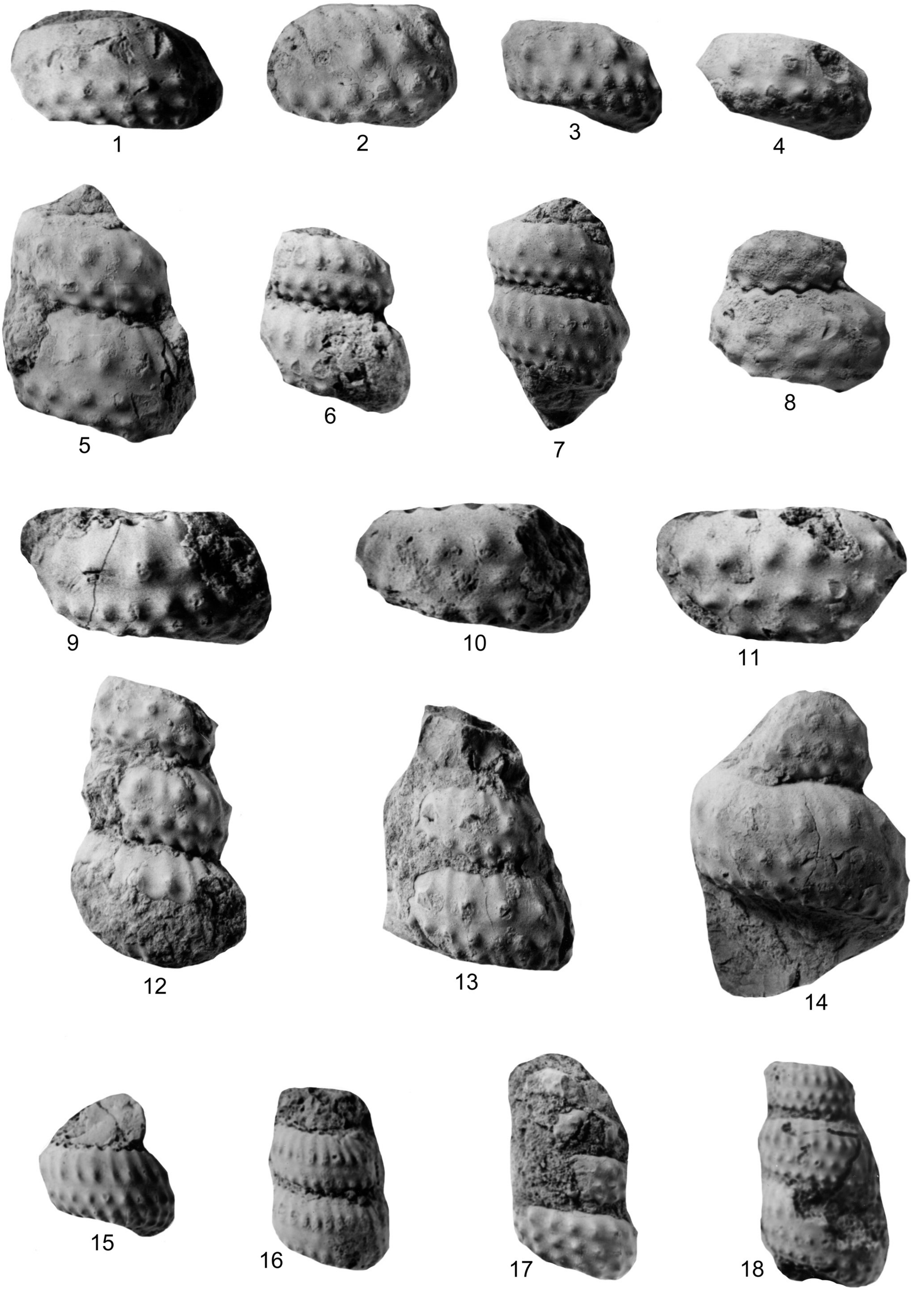
1
2
3
4
5
6
7
8
9
10
11
12
13
14
15
16
17
18

JAHRBUCH DER GEOLOGISCHEN BUNDESANSTALT

Jb. Geol. B.-A. | ISSN 0016–7800 | Band 159 | Heft 1–4 | S. 247–287 | Wien, Dezember 2019

Middle Cenomanian ammonites from the Odukpani Formation, Calabar Flank, Cross River State, southeastern Nigeria

William J. Kennedy[1] & Harald Lobitzer[2]

10 Text-Figures, 1 Table, 13 Plates

Ammonites
Cenomanian
Odukpani Formation
Calabar Flank
Cross River State
Nigeria

Contents

Abstract

The Middle Cenomanian part of the Odukpani Formation in exposures between Odukpani and Itu, Calabar Flank, Cross River State, Nigeria, yielded abundant ammonites. The faunas can be correlated with the *Turrilites costatus* and *Turrilites acutus* subzones of the widely recognized *Acanthoceras rhotomagense* Zone, and are dominated by species of *Cunningtoniceras*. The taxa that are present, in additional to the index *Turrilites*, are: *Damesites africanus* sp. nov., *Forbesiceras obtectum* (Sharpe, 1855), *Forbesiceras* sp., *Cunningtoniceras meridionale* (Stoliczka, 1864), *C. alatum* (Zaborski, 1985), and *Calycoceras* (*Gentoniceras*) group of *gentoni* (Brongniart, 1822).

Eine Ammonitenfauna des mittleren Cenomaniums der Odukpani-Formation, Calabar Flank, Cross River State, Südostnigeria

Zusammenfassung

Eine individuenreiche Ammonitenfauna des mittleren Cenomaniums wird von Aufschlüssen der 1976 und 1977 im Bau befindlichen Straße zwischen Odukpani und Itu, Calabar Flank, Cross River State, Nigeria, beschrieben. Die von *Cunningtoniceras* div. sp. dominierte Fauna kann mit der *Turrilites costatus*- und der *Turrilites acutus*-Subzone der weithin anerkannten *Acanthoceras rhotomagense*-Zone korreliert werden. Zusätzlich zu den erwähnten *Turrilites* sp. konnten folgende Taxa nachgewiesen werden: *Damesites africanus* sp. nov., *Forbesiceras obtectum* (Sharpe, 1855), *Forbesiceras* sp., *Cunningtoniceras meridionale* (Stoliczka, 1864), *C. alatum* (Zaborski, 1985) und *Calycoceras* (*Gentoniceras*) ex gr. *gentoni* (Brongniart, 1822).

1 William J. Kennedy: Oxford University Museum of Natural History, Parks Road, Oxford OX1 3PW, and Department of Earth Sciences, South Parks Road, Oxford OX1 3AN, United Kingdom. jim.kennedy@oum.ox.ac.uk
2 Harald Lobitzer: Lindaustraße 3, 4820 Bad Ischl, Austria. harald.lobitzer@aon.at

Introduction

In 1976 and 1977 Harald Lobitzer, working in close cooperation with the geologists of Calabar Cement Company (Calcemco), carried out extensive fieldwork on the "Calabar Flank" (Murat, 1972) in the wider environs of the Mfamosing limestone quarry. The goal of these investigations was prospecting for raw material commodities suitable for cement production. Special focus was put not only on limestone, but also on supplementary materials such as sand, clay, marl, shale, bauxite and lateritic soils. They supply the bulk of the silica, alumina and ferric oxide for blending the desired cement-clinker composition, which in practice is determined by the locally available raw materials making up the bulk of the cement raw meal. Haulage costs are also a significant factor in view of the large quantities of materials used in cement production.

At the time of the stay of Harald Lobitzer with Calcemco, a new road with excellent fossiliferous roadcuts was in construction. This A4-1 road branches off from the A4 highway about 25 km North of Calabar, respectively north of New Netim village (about 7 km north of Odukpani) to Itu and Ikot Ekpene in western direction (Text-Fig. 1). The distances to the fossiliferous exposures on the A4-1 in direction to the A342 highway were measured from this junction.

During construction the A4-1 road was informally designated as the "Odukpani-Itu road" or "RCC-road" the latter named after the "Reynolds Construction Company". For several kilometers along the route, a highly fossiliferous, but stratigraphically incomplete sequence was well exposed in the embankments on both sides of the road (Text-Fig. 2). Up to about road-km 5,5 the exposures yielded Cenomanian macrofaunas of the Odukpani Formation. Further to the West, progressively younger exposures in the Nkporo Formation yielded rich Campanian–Maastrichtian faunas (Zaborski, 1982, 1983, 1985; López et al., 2004). Macro- and microfossil samples were obtained during sampling for technological investigations in connection with appraisal of the sequence as a potential source of raw materials for the production of cement.

The Odukpani Formation

The term "Odukpani Formation" was coined by Reyment (1955a). In this and several following papers (e.g. Reyment, 1955b, 1965), he recorded Cenomanian and Turonian ammonites from the formation. Subsequently several papers dealt with the micropalaeontology of the Odukpani Formation, and a type section was described by Dessauvagie (1972). It consists predominantly of grey shales and (sandy) marls, with numerous thin limestone and/or (arkosic) sandstone intercalations. Besides molluscs, vertebrate bones (? mosasaurids) occur in some outcrops; they have not been collected. Reyment (1965) considers the sediments of the Odukpani Formation as typical nearshore deposits, Kogbe (1989a, b) follows his opinion, while Fayose & Dessauvagie (1976) wrote about a "*shallow water open marine depositional environment*".

As in the Eze-Aku Shales from the surroundings of the Mfamosing quarry, all our samples of the Odukpani Formation were barren of calcareous nannofossils (Herbert Stradner, Geologische Bundesanstalt, Vienna). However, as in the coarse grain residues of our washed samples from the Eze-Aku Shales from the surroundings of the Mfamosing quarry, the characteristic foraminifer *Thomasinella punica* is also omnipresent in the Odukpani Formation.

In a previous contribution (Kennedy & Lobitzer, 2019), we demonstrated that the hardground at the top of the Mfamosing Limestone yielded an ammonite fauna indicative of the lower Lower Cenomanian *Neostlingoceras carcitanense* Subzone fauna of the widely recognised *Mantellliceras mantelli* Zone. Zaborski (1985) had previously demonstrated the presence of Lower Cenomanian to Lower Turonian ammonite faunas in the Odukpani Formation in cuttings on the Calabar-Ikot Ekpene road. The Middle Cenomanian faunas he described have elements in common with what is described below, but 30 years on from his account, the material before us provides additional information on species present, including new records that reflect the progress made on Cenomanian stratigraphy and ammonite fau-

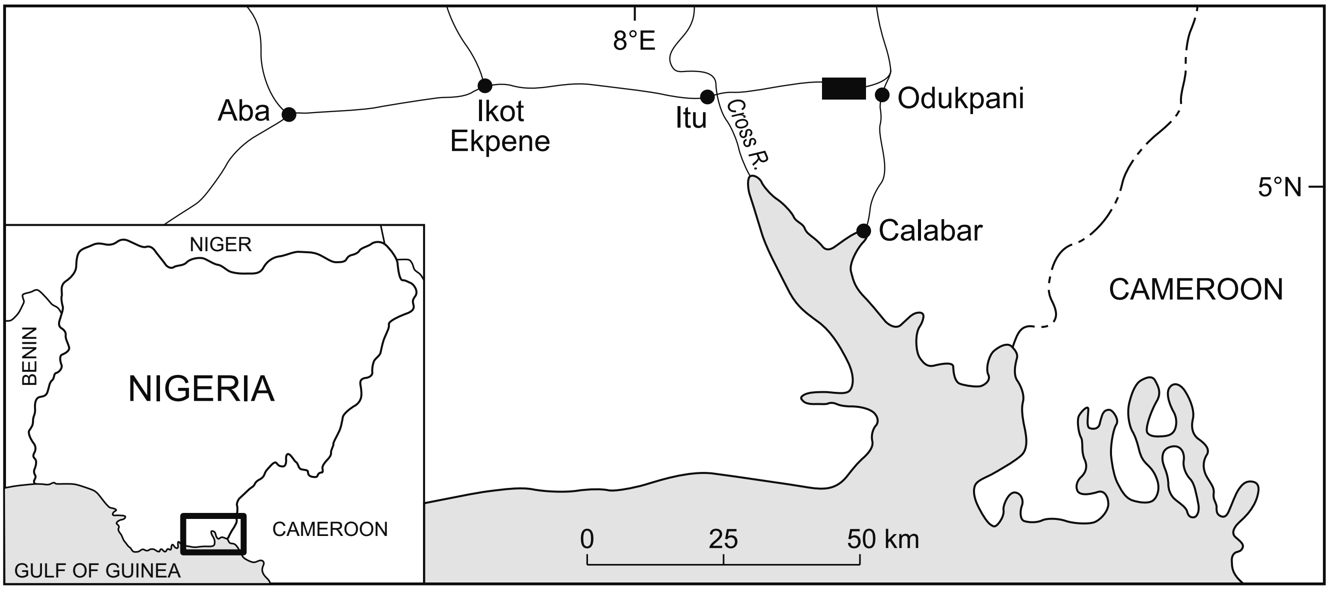

Text-Fig. 1.
Locality map, after López et al. (2004). Black rectangle indicates area of examined road outcrops.

Text-Fig. 2.
Outcrop on Odukpani-Itu-Road, km 4.

nas in the intervening years. The material, from cuttings on the Odukpani-Itu road (Text-Fig. 1–3), becomes progressively younger from east to west, and can be correlated with the standard zonation recognized in Western Europe and across the north side of the Tethys (Tab. 1). The faunas correspond to the lower Middle Cenomanian *Acanthoceras rhotomagense* Zone, the critical markers being the first occurrences of subzonal indices *Turrilites costatus* LAMARCK, 1801, and its successor, *Turrilites acutus* PASSY, 1832. The sequence of faunas and localities are dated in these terms below.

The faunas from km 3.8 (south side), km 3.8–4.2 (loose specimen), km 4 (north side), km 4 (south side), km 4.5 and km 6.1 correspond to faunas 3, 4, 5 and ?6 in ZABORSKI (1985: Fig. 2), and are as follows:

Km 2.8: *Damesites africanus* sp. nov: not dated.

Km 3.8: *Forbesiceras* sp. indet, group of *largilliertianum* (D'ORBIGNY, 1841), *D. africanus* sp. nov., *Cunningtoniceras meridionale* (STOLICZKA, 1864), *Turrilites costatus* LAMARCK, 1801. Middle Cenomanian, *costatus* Subzone.

Km 4.0: *D. africanus*, *Forbesiceras beaumontianum* (SHARPE, 1853), *Cunningtoniceras meridionale*, *Cunningtoniceras alatum* (ZABORSKI, 1985), *Turriites acutus*. Middle Cenomanian, *acutus* Subzone.

Km 4.5: *Cunningtoniceras alatum*, *Calycoceras* (*Gentoniceras*) sp., group of *gentoni* (BRONGNIART, 1822). Middle Cenomanian, *acutus* Subzone inferred.

Km 5.5: *Forbesiceras* sp., Middle or lower Upper Cenomanian.

Text-Fig. 3.
? Mosasaurid bones on Odukpani-Itu-Road, km 4.

SUBSTAGE	ZONE	SUBZONE
Middle Cenomanian	*Acanthoceras jukesbrownei*	
	Acanthoceras rhotomagense	*Turrilites acutus*
		Turrilites costatus
	Cunningtoniceras inerme	

Tab. 1.
Middle Cenomanian ammonite zones and subzones recognized in Western Europe.

Conventions

Dimensions are given in millimeters: D = diameter; Wb = whorl breadth; Wh = whorl height; U = umbilicus; c = costal dimension; ic = intercostal dimension. Figures in parentheses are dimensions as a percentage of the diameter. The suture terminology is that of KORN et al. (2003): E = external lobe; A = adventive lobe (= lateral lobe, L, of KULLMANN & WIEDMANN, 1970); U = umbilical lobe; I = internal lobe.

Repositories of specimens

BMNH: The Natural History Museum, London.

GBA: Geologische Bundesanstalt, Vienna.

MNHP: Laboratoire de Paléontologie of the Muséum Nationale d'Histoire Naturelle, Paris.

Systematic Palaeontology

Order Ammonoidea ZITTEL, 1884
Suborder Ammonitina HYATT, 1889
Superfamily Desmoceratoidea ZITTEL, 1895
Family Desmoceratidae ZITTEL, 1895
Subfamily Desmoceratinae ZITTEL, 1895
Genus *Damesites* MATSUMOTO, 1942

(ICZN name no. 1349)

Type species: *Desmoceras damesi* JIMBO, 1894: 172, Pl. 1, Figs. 2, 3: ICZN Opinion 555, 1959.

Damesites africanus sp. nov.

(Pl. 1, Figs. 1–15; Pl. 2, Figs. 1–4)

Types: The holotype is GBA 2016/004/0001, from the levelled surface at the top of the 4 km section (Pl. 2, Figs. 1–4). Paratypes GBA 2016/004/0002–0003 are from the 4 km, section; paratype GBA 2016/004/0004 is from the 4 km section, south side, all *acutus* Subzone; paratypes GBA 2016/004/0005–0007 are from the 2.8 km section, lower Middle Cenomanian.

Additional material: 2.8 km: 3 specimens, lower Middle Cenomanian. 4 km, north side, 9 specimens; 4 km, from the levelled surface at the top of the north side, 2 specimens; 4 km, south side, top of section, 3 specimens, all *acutus* Subzone.

Diagnosis: A large, slightly involute, compressed species of *Damesites*, with three constrictions per half whorl, the constrictions near-straight across the inner and middle flank, concave on the outer flank, and projected strongly forwards on the ventrolateral shoulders and venter, marking the outline of a long apertural ventral rostrum. Venter rounded to feebly fastigiate on internal mould of phragmocone, with a coarse ventral keel on the internal mould of the body chamber.

Dimensions:

	D	Wb	Wh	Wb:Wh	U
GBA 2016/004/0004	39.1 (100)	12.9 (33.0)	17.9 (45.8)	0.72	9.5 (24.3)
GBA 2016/004/0005	44.4 (100)	14.6 (32.9)	19.0 (42.8)	0.77	10.8 (24.3)
GBA 2016/004/0006	56.8 (100)	19.2 (33.8)	26.0 (45.8)	0.74	14.0 (24.6)
GBA 2016/004/0002	59.2 (100)	20.8 (35.1)	27.7 (46.8)	0.75	13.9 (23.5)
GBA 2016/004/0007	64.5 (100)	21.5 (33.3)	27.4 (42.5)	0.78	18.1 (28.0)
GBA 2016/004/0003	66.9 (100)	22.2 (33.2)	30.1 (44.9)	0.74	18.6 (27.9)

Description: All of the specimens described below are internal moulds. Phragmocones (Pl. 1, Figs. 1–15) are slightly involute, with over half of the previous whorl covered. The umbilicus is of moderate width, shallow, with a low, flattened wall, and quite narrowly rounded umbilical shoulder. The whorl section is compressed, the whorl breadth to height ratio varying between 0.72 and 0.78, the greatest breadth below mid-flank, the inner to middle flanks very feebly convex, and subparallel. The convex ventrolateral shoulders converge to an incipiently to feebly fastigiate venter. There are three narrow rectiradiate constrictions per half whorl. They are feebly concave on the umbilical wall and shoulder in some specimens (Pl. 1, Fig. 2), straight (Pl. 1, Fig. 13) to very slightly convex (Pl. 1, Fig. 8) on the inner to middle flank, convex on the outer flank and ventrolateral shoulder, and projected strongly forwards into a long, narrow, acute ventral chevron.

The holotype (Pl. 2, Figs. 1–4) consists of a phragmocone with a maximum preserved diameter of 78 mm, and a 120° sector of body chamber with a maximum preserved whorl height of 56 mm, corresponding to an estimated diameter of 120–130 mm when complete. The umbilical wall is flattened and outward-inclined, the umbilical shoulder narrowly rounded. The whorl section is compressed, with a whorl breadth to height ratio of 0.67, the greatest breadth below mid-flank. The flanks are very feebly convex and subparallel, the rounded ventrolateral shoulders converging to a coarse, strong siphonal keel. There are two constrictions on the body chamber fragment. They are rectiradiate, very feebly convex on the innermost flank, very feebly convex at mid-flank, and strongly concave on the outermost flank, projecting forwards to form a long, narrow, very acute chevron with the siphonal keel at the apex. The constrictions are markedly asymmetric in cross section, with a wide gently inclined adapical side and a narrow, subvertical adapertural side.

The suture is deeply and intricately subdivided, with narrow-stemmed, bifid E/A and A/U2, and trifid A.

Discussion: The species currently assigned to *Damesites* are comprehensively reviewed by NISHIMURA et al. (2010). The present species differs from all of these in its much wider umbilicus and fewer constrictions per whorl. In *Damesites damesi*, the umbilicus comprises 11 % or less of the diameter (MATSUMOTO, 1954: 268); in *Damesite sugata* (FORBES, 1846) the figure is 11.5 % or less (KENNEDY & HENDERSON 1991), compared to up to 28 % in *D. africanus*. The present species is the largest assigned to the genus; the maximum diameter for previously described species is 90–100 mm according to NISHIMURA et al. (2010). It is also one of, if not the earliest species of this typically Turonian to Maastrichtian genus. The only other Cenomanian species described to date is *Damesites laticarinatus* SAITO & MATSUMOTO, 1956 (192, Text-Fig. 1), from Japan (better figures of the holotype, a half whorl fragment, are provided by NISHIMURA et al., 2010: Text-Figs. 6e–g). This species has longitudinal striations, and lacks constrictions.

Occurrence: As for types.

Superfamily Acanthoceratoidea DE GROSSOUVRE, 1894

Family Forbesiceratidae WRIGHT, 1952

Genus *Forbesiceras* KOSSMAT, 1897

Type species: *Ammonites largilliertianus* D'ORBIGNY, 1841: 320, Pl. 95, by the subsequent designation of DIENER (1925: 180).

Forbesiceras obtectum (SHARPE, 1853)

(Pl. 3, Figs. 1–4)

1853 *Forbesiceras obtectum* SHARPE, 1853: 20, Pl. 7, Fig. 4.

1984 *Forbesiceras obtectum* (SHARPE, 1853); WRIGHT & KENNEDY: 94, Pl. 12, Fig. 4; Pl. 14, Figs. 1, 2; Pl. 15, Fig. 4; Text-Figs. 16g–j, 18 (with full synonymy).

1985 *Forbesiceras obtectum* (SHARPE, 1853); ZABORSKI: 22, Text-Figs. 22–25, 29.

2018 *Forbesiceras obtectum* (SHARPE, 1853); KLEIN: 256, 263 (with synonymy).

Type: The holotype, by monotypy, is the original of SHARPE (1853: Pl. 7, Fig. 4), from the 'chalk with siliceous grains' of Chardstock, Devon. It has not been traced.

Material: GBA 2016/004/0008, from the 4 km section, *acutus* Subzone.

Dimensions:

D	Wb	Wh	Wb:Wh	U
104.3 (100)	26.5 (25.5)	61.6 (59.2)	0.43	4.8 (4.6)
125.3 (100)	– (–)	62.1 (49.6)	–	11.9 (9.5)

Description: The specimen retains areas of replaced shell, and a short sector of body chamber. To a diameter of 110 mm approximately the coiling is very involute, the tiny, shallow umbilicus comprising less than 5 % of the diameter. The whorl section is very compressed, with a whorl breadth to height ratio of 0.43, the flanks very feebly convex, with the greatest breadth around mid-flank. The venter is narrow, with crenulated keels at the junction of flank and venter, and a blunt siphonal ridge. To this diameter, ornament consists of delicate crowded prorsiradiate riblets that arise on the umbilical shoulder and are straight and prorsiradiate on the inner to middle flank. They flex back around mid-flank, and may branch. They are at their greatest strength on the adapical part of the outer whorl, and form an obtuse angle with the inner to mid-flank part of the rib. On the outer part of the flank they are strongly rursiradiate, straight to feebly convex, convexity increasing on the outermost flank, where they sweep back and link to minute clavi on the ventral ridges. Delicate transverse riblets on the venter are more numerous than the clavi. The ribbing weakens on the succeeding 90° whorl sector, and on the final adapertural sector, there are widely spaced low riblets on the inner to mid-flank and numerous barely detectable rursirdiate ribs on the outer flank. The umbilical seam egresses markedly on the final sector, the umbilical diameter increasing to 9.5 %

Discussion: The change in strength of flank ornament and increase in umbilical diameter on the adapertural part of the outer whorl shown by this specimen suggests it is an incomplete adult, and by comparison with previously described *Forbesiceras obtectum* from the Odukpani Formation (the second group of ZABORSKI, 1985: 24) is a microconch. The specimen differs from the missing holotype (SHARPE, 1853: Pl. 7, Fig. 4) in lacking a mid-lateral tubercle at the point where rib direction changes; similar individuals, regarded as intraspecific variants of *obtectum*, are known from southern England (KENNEDY, 1971: Pl. 46, Fig. 1), central Tunisia (KENNEDY in KENNEDY & GALE, 2015: Pl. 1, Fig. 9) and elsewhere. Differences from other species are discussed by WRIGHT & KENNEDY (1984: 95).

Occurrence: The species is lower Middle Cenomanian where well dated, but may appear already in the Lower Cenomanian. Specimens from central Tunisia referred to as *F.* cf. *obtectum* by KENNEDY in KENNEDY & GALE (2015: 262) may indicate an extension of range into the lower Upper Cenomanian. The geographic distribution extends from southern England to France, Turkmenistan, Algeria, Tunisia, Lebanon, Nigeria and Madagascar.

Forbesiceras sp.

(Text-Fig. 4)

Material: GBA 2016/004/0009, from the 5.5 km exposure, Odukpani Formation, Middle or lower Upper Cenomanian.

Description: The specimen is a well-preserved 180° whorl sector of phragmocone 67 mm in diameter, retaining recrystallized shell. Coiling is very involute, the umbilicus minute. The whorl section is very compressed, with a whorl breadth to height ratio of 0.42, the greatest breadth below mid-flank, the inner flanks very feebly convex, the outer flanks flattened and convergent, the venter narrow, the junction of flanks and venter marked by an incipiently crenulated ridge. There is a blunt siphonal ridge. The inner half of the flanks is ornamented by straight prorsiradiate growth lines only. A blunt spiral ridge separates this area

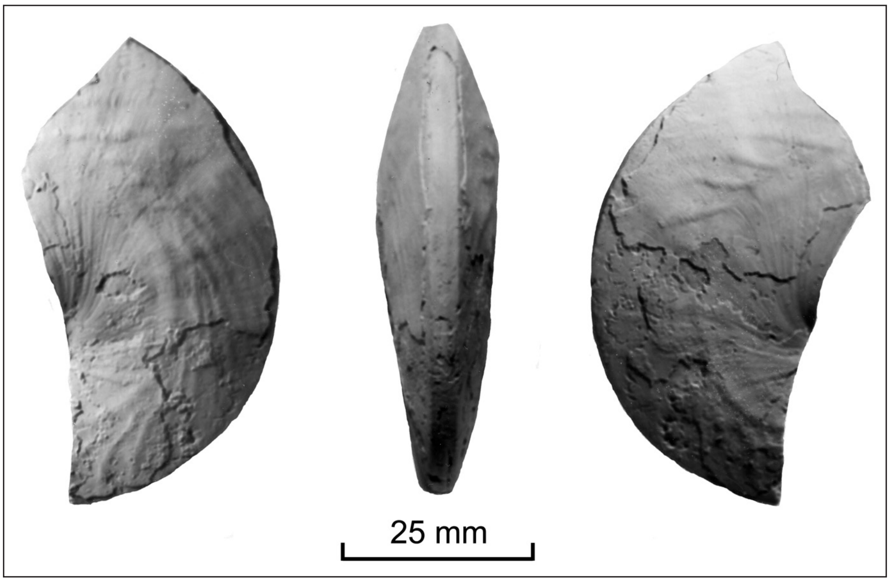

Text-Fig. 4.
Forbesiceras sp. GBA 2016/004/0009, km 5.4, from the Middle or lower Upper Cenomanian part of the Odukpani Formation between Odukpani and Itu, Cross River State, Nigeria.
All figures are natural size.

from the outer flank, which is ornamented by low, blunt, narrow ribs. At the adapical end of the fragment they are very strongly rursirsdiate and concave, becoming feebly convex and very strongly rursiradiate over the remainder. Some appear to bifurcate.

Discussion: Irregular ornament and the presence of a spiral ridge separating the markedly different inner and outer flank ornament are distinctive. There are some similarities to *Forbesiceras bicarinatum* Szász, (1976: 170, Pls. 1, 2, Pl. 3, Figs. 1, 2; Text-Figs. 1, 2) some specimens of which have a comparable spiral ridge (Wright & Kennedy, 1984: Pl. 14, Fig. 5). Alternatively, it may be no more than an aberrant *F. obtectum*. It is left in open nomenclature here.

Occurrence: As for material.

Family Acanthoceratidae De Grossouvre, 1894

Subfamily Acanthoceratinae De Grossouvre, 1894

Genus *Cunningtoniceras* Collignon, 1937

Type species: *Ammonites cunningtoni* Sharpe, 1855: 35, Pl. 15, Fig. 2, by the original designation of Collignon (1937: 64).

Discussion: This is the most abundant ammonite genus in the present material, with over 150 specimens, most of them fragments. They provide a basis for a development of the analysis of the genus put forward elsewhere (Kennedy in Kennedy & Gale, 2015: 284). Two groups were recognised within the genus: The group of *C. cunningtoni sensu stricto*, where there are fewer outer ventrolateral than siphonal tubercles, and the group of *C. meridionale* (Stoliczka, 1864) where there are equal numbers of outer ventrolateral and siphonal tubercles. This is a very different view from that of previous authors, as noted there: Kennedy (1971) regarded *meridionale* as a variety of *cunningtoni*; Cooper (1973) as a subspecies; Howarth (1985) as a variety; Wright & Kennedy (1987) as a synonym; Matsumoto et al. (1969) as a separate species.

In Western Europe, *Cunningtoniceras inerme* (Pervinquière, 1907) is the index species of the lowest zone of the Middle Cenomanian. Above this level, the *Cunningtoniceras* record is minimal. Wright & Kennedy (1990: 193) writing before the recognition that *Cunningtoniceras* preceded *Acanthoceras* in the record (Robaszynski et al., 1994; Gale, 1995) derived *Cunningtoniceras* from *Acanthoceras*; the reverse is the case (Kennedy in Kennedy & Gale, 2015: 284). Subsequent studies in North Africa (Central Tunisia; Kennedy & Gale, 2015; north-west Algeria: Kennedy & Gale, 2017; South India: Kennedy in Gale et al., 2019) demonstrated that *Cunningtoniceras* flourished in these areas after it had disappeared (temporarily at least) from the north side of the Tethys; the present material, with *Cunningtoniceras* abundant in association with the index species of the *costatus* and *acutus* Subzones of the *rhotomagense* Zone, confirm this.

Cunningtoniceras meridionale (Stoliczka, 1864)

(Pls. 4–7; Text-Figs. 5, 6)

1864 *Ammonites meridionalis* Stoliczka: 76, Pl. 41, Fig. 1.

1985 *Euomphaloceras cunningtoni meridionale* (Stoliczka); Zaborski: 43, Figs. 45, 46 (non Fig. 43 = *C. inerme*).

1985 *Euomphaloceras cunningtoni cunningtoni* (Sharpe); Zaborski: 45, Figs. 47–52.

2015 *Cunningtoniceras meridionale* (Stoliczka, 1864; Kennedy in Kennedy & Gale: 286, Pl. 15, Fig. 3; Pl. 16, Figs. 1, 5; Text-Fig. 22a (with additional synonymy).

Type: The lectotype, by the subsequent designation of Matsumoto et al. (1969: 272), is the original of Stoliczka (1864: 76, Pl. 41, Fig. 1, no. 175) in the collections of the Indian Geological Survey, Kolkata, from the Uttatur Group of Odium, South India.

Material: GBA 2016/004/0010–0012, 0014–0016, from the south side of the 3.8 km section, *costatus* Subzone GBA 2016/004/0013, from the top of the km 4 section, *acutus* Subzone.

Dimensions:

	D	Wb	Wh	Wb:Wh	U
GBA 2016/004/0010 (costal)	170 (100)	91.3 (53.7)	73.9 (43.5)	1.24	61.4 (36.1)

Description: GBA 2016/004/0010 (Pl. 4, Pl. 5, Figs. 1, 2) is an internal mould of a phragmocone 170 mm in diameter. Coiling is very evolute, the umbilical wall feebly notched to accommodate the inner ventrolateral spines of the preceding whorl. The umbilicus comprises 36.1 % of the diameter, and is of moderate depth, with a feebly convex wall and broadly rounded umbilical shoulder. At the greatest preserved diameter, the intercostal whorl section is depressed trapezoidal, with a whorl breadth to height ratio of 1.27, the greatest breadth just outside the umbilical shoulder. The flanks are flattened and convergent, the ventrolateral shoulders broadly rounded, the broad venter very feebly convex. The costal whorl section is trapezoidal-polygonal, with the greatest breadth at the umbilical tubercles, the whorl breadth to height ratio 1.24. There are fifteen primary ribs on the penultimate whorl. They arise at the umbilical seam, and strengthen across the umbilical wall and shoulder, where they develop into strong, narrow bullae. A broad, straight, prorsiradiate rib links to laterally compressed, outwards and upwards directed inner ventrolateral horns. There are 19–20 primary ribs on the outer whorl. They are initially of comparable development on the flank as on the penultimate whorl, with prominent inner ventrolateral horns, but as diameter increases, the horns are transformed into a strengthened angulation on the rib. At the beginning of the outer whorl, the inner ventrolateral horns are linked across the venter by two ribs. A strong transverse rib bears equal, rounded to very feebly clavate outer ventrolateral and siphonal tubercles (Pl. 5, Fig. 1). A second, adapertural rib projects forwards from the inner ventrolateral horn, and then flexes back into a transverse rib with outer ventrolateral and siphonal clavi. This pattern of ventral ornament extends to a diameter of 135 mm (Pl. 5, Fig. 2), beyond which only a single double rib of this type is developed, the pattern at this stage being of predominantly regularly alternating primary ribs and single short intercalated ventral ribs. The siphonal clavi decline progressively and are lost on the adapertural 60° sector of the outer whorl, and the outer ventrolateral tubercles are transformed into an angulation in the rib profile (Pl. 5, Fig. 2).

GBA 2016/004/0016 (Pl. 7, Figs. 3, 4) is a body chamber fragment with a maximum preserved whorl height of 69 mm, with comparable ornament to the later growth stages of the previous specimen.

GBA 2016/004/0015 (Pl. 7, Figs. 1, 2) has a maximum measurable whorl height of 60 mm, with stronger inner ventrolateral tuberculation than the previous specimens at the same size.

GBA 2016/004/0011 (Pl. 6) is a 60° whorl sector from the adapical end of an adult body chamber, with a maximum preserved whorl height of 86 mm, corresponding to an estimated diameter of over 200 mm. The convex umbilical wall is inclined outwards. There are four coarse, strong, widely separated primary ribs on the fragment. They are weak on the umbilical wall, but strengthen into feeble bullae, displaced out onto the inner flank. There are well-developed inner ventrolateral tubercles, but the outer ventrolaterals are weak, the venter concave in costal section.

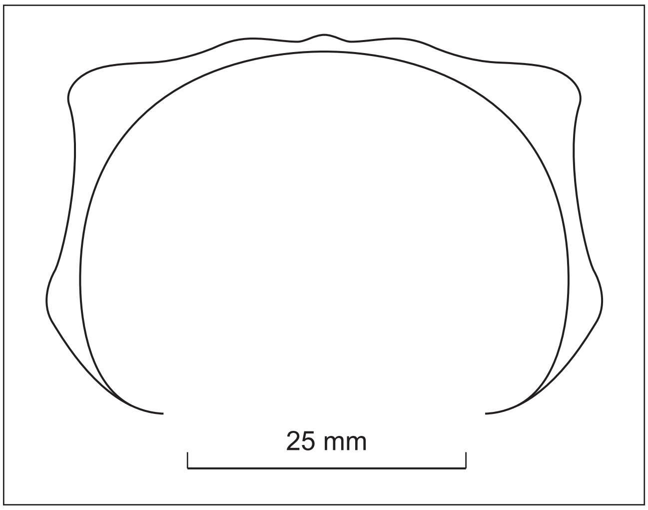

Text-Fig. 5.
Cunningtoniceras meridionale (Stoliczka, 1864), whorl section of GBA 2016/004/0013.

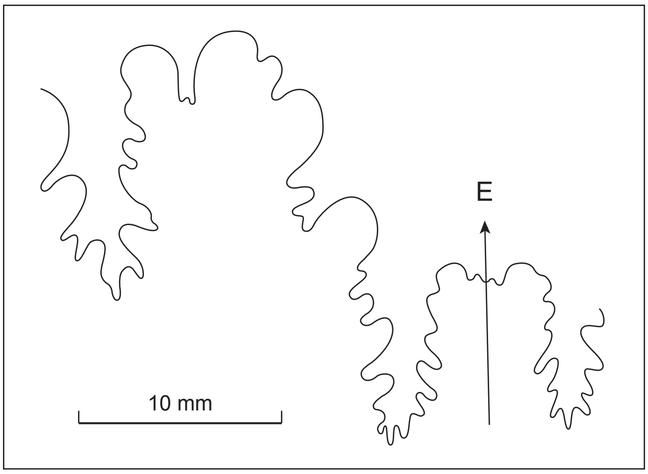

Text-Fig. 6.
Cunningtoniceras meridionale (Stoliczka, 1864), external suture of GBA 2016/004/0013.

GBA 2016/004/0014 (not figured) is a fragment of venter in which the outer ventrolateral tubercles are lost, the ventral development of the ribs flat in costal profile. With an estimated whorl breadth of over 120 mm, the fragment suggests adults of the species may have reached over 220 mm in diameter. All of the above specimens are interpreted as macroconchs.

GBA 2016/004/0012 (Pl. 5 Fig. 3) is the adapical 120° sector of a body chamber. Whereas GBA 2016/004/0010 (Pl. 4) has prominent inner ventrolateral horns at the same whorl height, this specimen has much weaker tubercles in this position, as does phragmocone fragment GBA 2016/004/0013 (Pl. 5, Figs. 4, 5). This latter specimen also shows weakening ventral tuberculation. It is possible that these are fragments of microconchs, but firm evidence is lacking.

A composite partial suture taken from GBA 2016/004/0013 (Text-Fig. 6) shows moderate incision. E/A is very broad and asymmetrically bifid, A is small and bifid.

Discussion: As noted above, *C. meridionale* has equal numbers of outer ventrolateral and siphonal tubercles, whereas in *C. cunningtoni* there are fewer outer ventrolateral than siphonal tubercles. *Cunningtoniceras inerme* (Pervinquière, 1907) (see revisions in Wright & Kennedy, 1987: 194, Pl. 52, Fig. 1; Pl. 53, Fig. 6; Text-Figs. 74, 75, 79; Kennedy in Kennedy & Gale, 2015: 284, Pl. 14, Fig. 4; Pl. 15, Fig. 4; Pl. 16, Fig. 7; Pl. 17, Fig. 1; Pl. 20, Fig. 1; Kennedy in Kennedy & Gale, 2017: 92, Pl. 6, Figs. 4–7; Pl. 7, Figs. 1–11; Pl. 8, Figs. 1, 2, 5, 6; Pl. 9, Figs. 1, 2, 5, 6) has a ribbed body chamber and does not develop ventrolateral horns. *Cunningtoniceras alatum* (Zaborski, 1985), described below, develops a distinctive adult ornament, with enormous compressed ventrolateral horns.

Occurrence: Lower Middle Cenomanian, south India, Hokkaido, Japan, Iran, Morocco, Central Tunisia, Nigeria, Angola, and Bathurst Island, northern Australia.

Cunningtoniceras cunningtoni (Sharpe, 1855)

(Pl. 9, Figs. 9, 10; Pl. 10, Figs. 3, 4)

1855 *Ammonites cunningtoni* Sharpe: 35, Pl. 15, Fig. 2.

non 1985 *Euomphaloceras cunningtoni cunningtoni* (Sharpe); Zaborski: 45, Figs. 47–52 (= *C. meridionale*).

2019 *Euomphaloceras cunningtoni* (Sharpe, 1855); Kennedy in Gale et al.: 229, Pls. 25, 26; Pl. 27, Figs. 1–4; Pl. 37, Figs. 5, 6 (with full synonymy).

Type: The holotype, by monotypy, is BMNH 88704, the original of Sharpe (1855: 35, Pl. 15, Fig. 2), from the Lower Chalk of Upton Scudamore, Wiltshire. It was refigured by Wright & Kennedy (1987: Text-Figs. 76–77).

Material: GBA 2016/004/0017–0018, *ex situ*, from the Middle Cenomanian part of the Odukpani Formation between Odukpani and Itu.

Description: GBA 2016/004/0017 (Pl. 9, Figs. 9, 10) is 120° whorl sector of an internal mould of a phragmocone with a maximum preserved whorl height of 49 mm. Coiling is evolute, the umbilicus deep, the high umbilical wall very feebly convex, the umbilical shoulder very broadly rounded. The whorl section is depressed, rounded-rectangular in intercostal section, the whorl breadth to height ratio 1.19, with the greatest breadth around mid-flank. The flanks are feebly convex, the ventrolateral shoulders broadly rounded, the venter broad and very feebly convex. There are three primary ribs on the fragment. They arise at the umbilical seam, and are low and broad on the umbilical wall, strengthening progressively and linking to a large umbilicolateral bulla, from which a broad, weak, straight rectiradiate rib links to a massive dorsoventrally flattened inner ventrolateral horn. This is wedge-shaped in ventral view, and links to a weak, blunt, outer ventrolateral clavus. A pair of feeble to near-effaced transverse ribs link the clavi across the venter, and bear a siphonal clavus. Short ventral ribs intercalate between successive primary ribs, and bear feeble siphonal tubercles; there are thus more siphonal than outer ventrolateral tubercles. GBA 2016/004/0018 (Pl. 10, Figs. 3, 4) is a much larger fragment, of body chamber, with a maximum preserved whorl height of 51 mm and a whorl breadth to height ratio of 1.3, the greatest breadth at mid-flank. Two ribs are preserved on the fragment. They are very widely separated, and are broad and coarse, developing into large umbilicolateral bullae. These are linked by a broad, strong, feebly prorsiradiate rib to very large ventrolateral horns. These are directed outwards in a direction normal to the median plane of the body chamber, and have a distinct median groove. The venter is feebly concave between in costal section.

Discussion: Differences from *C. meridionale*, and *C. alatum* are noted above.

Occurrence: Lower Middle Cenomanian, southern England, France, Spain, Germany, Switzerland, Nigeria, Madagascar, Tamil Nadu in south India.

Cunningtoniceras alatum (Zaborski, 1985)

(Pl. 8, Figs. 1–28; Pl. 9, Figs. 1–8, 11; Pl. 10, Figs. 1, 2; Pl. 11, Figs. 1–9; Text-Figs. 7–9)

1985 *Euomphaloceras cunningtoni alatum* Zaborski, 49, Text-Figs. 53–56.

Type: The holotype, by original designation, is BMNH C83479, the original of Zaborski (1985: 49, Text-Figs. 53–56), from the Middle Cenomanian part of the Odukpani Formation 30.3 km from Calabar, Cross River State, Nigeria. There are 16 paratypes, BMNH C83108–12, C83480–5, and UIN 485.1–5 in the collections of the Department of Geology of Ilorin University, Nigeria.

Material: GBA 2016/004/0019, km 4; GBA 2016/004/0020, 0021, 0038, 0039, km 4, top of section; GBA 2016/004/0022, 0024–0028, 0030, 0033, km 4, north side; GBA 2016/004/0023, 0029, 0031, 0032, 0035, 0066; GBA 2016/004/0036, south side, top of section; GBA 2016/004/0037, 4.5 km; GBA 2016/004/0040–0041, collected *ex situ*, and numerous additional fragments, all *acutus* Subzone.

Dimensions:

	D	Wb	Wh	Wb:Wh	U
GBA 2016/004/0037 at c	37.7 (100)	22.7 (60.2)	15.8 (41.9)	1.43	12.2 (32.4)
GBA 2016/004/0034 ic	56.6 (100)	25.1 (44.3)	21.6 (38.1)	1.16	17.5 (30.9)
GBA 2016/004/0027 ic	63.8 (100)	30.3 (47.5)	25.8 (40.4)	1.17	22.3 (34.9)
GBA 2016/004/0041 ic	90.6 (100)	40.6 (44.8)	36.0 (39.7)	1.13	33.2 (36.6)
GBA 2016/004/0019 ic	102 (100)	36.1 (35.3)	31.1 (30.5)	1.16	41.8 (41.0)
GBA 2016/004/0019 c	106.5 (100)	51.5 (48.3)	37.4 (35.2)	1.37	41.8 (41.0)

Description: At the smallest diameters seen (34–46 mm: Pl. 8, Figs. 1–13, 16, 17), coiling is very evolute, the umbilicus comprising around 30 % of the diameter, of moderate depth, with a feebly convex, outward-incline wall and broadly rounded umbilical shoulder. The whorl section is slightly depressed in intercostal section, rectangular, with feebly convex flanks, broadly rounded ventrolateral shoulders and a broad, feebly convex venter. There are 6–8 primary ribs per half whorl. They arise at the umbilical seam,

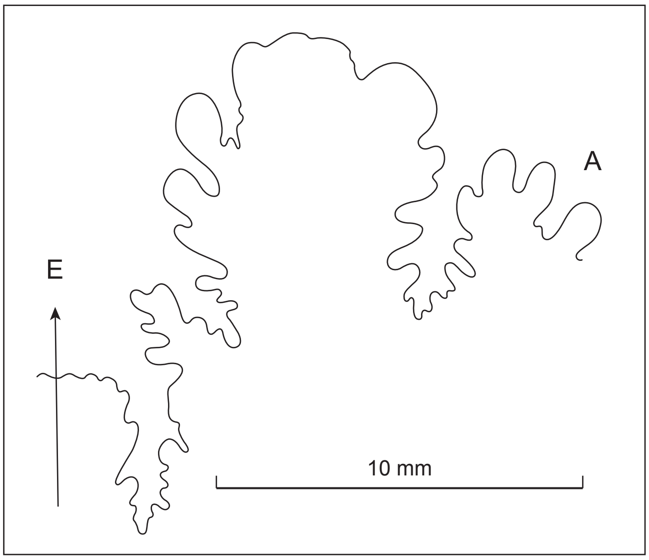

Text-Fig. 7.
Cunningtoniceras meridionale (Stoliczka, 1864), external suture of GBA 2016/004/0036.

strengthen across the umbilical wall, and develop into strong umbilical bullae. These give rise to single straight, coarse, prorsiradiate ribs that link to strong conical inner ventrolateral tubercles. A strong, feebly prorsiradiate rib links to a strong conical to feebly clavate outer ventrolateral tubercle, the tubercles linked across the venter by a low, broad, transverse rib that bears a subequal feebly clavate siphonal tubercle. The primary ribs are separated by single intercalated ribs that arise on the outer flank, strengthen progressively, and link to outer ventrolateral tubercles with a development similar to that seen on the primary ribs. Larger specimens such as GBA 2016/004/0034 (Pl. 8, Figs. 21, 22), show the intercalated ribs confined to the ventrolateral shoulders and venter, and the beginning of a link developing between the outer ends of the intercalated ribs and the inner ventrolateral tubercles of the primary ribs. This arrangement appears irregularly, and at variable whorl heights, typically around 20 mm.

GBA 2016/004/0027 (Pl. 8, Figs. 25, 26), a phragmocone 64 mm in diameter, has 12 very coarse primary ribs on the outer whorl, the ribs becoming progressively more widely-space on the adapertural half of the outer whorl, the primary and secondary ribs looping across the venter from the inner ventrolateral tubercles. GBA 2016/004/0066 (Pl. 8. Figs. 27, 28) also shows the primary ribs becoming more widely spaced on the adapertural half of the outer whorl, the inner ventrolateral tubercle becoming increasingly prominent. They point outwards, normal to the median section of the shell, a feature well-seen in GBA 2016/004/0038 (Pl. 8, Fig. 14; Text-Fig. 9A) and GBA 2016/004/0039 (Pl. 8, Figs. 18, 19), on most of the outer whorl, but on the adapertural two ribs, they strengthen, and their orientation changes to pointing outwards and upwards (Pl. 8, Fig. 28).

GBA 2016/004/0021 (Pl. 11, Figs. 3, 6) is the adapical 120° sector of an adult body chamber with a whorl height of 25 mm at the adapical end. Three primary ribs are very widely separated, intercalated ribs and siphonal tubercles weaken and efface, leaving primary ribs only on the adapertutral part of the fragment, separated by feeble flank ribs. The primaries have much weaker to effaced umbilical bullae compared to the phragmocone, and the profile of their ventrolateral development changes to a wide, compressed flange, with a deep ventral concavity in the rib profile (Text-Fig. 8C), that is lost on the final rib on the fragment. GBA 2016/004/0036 (Pl. 11, Figs. 5, 9) is a complete adult, 98 mm in diameter, with a 120° sector of body chamber. Intercalated ribs are effaced and lost, and the form of the ventrolateral tubercles is as in the previous specimens on two of the ribs. The final three ribs have progressively weakening and effacing umbilical bullae, and lack ventrolateral tubercles, indicating the specimen to be complete, and a microconch. GBA 2016/004/0019 (Pl. 11, Figs. 1, 7, 8) is a larger specimen, the body chamber 105 mm in diameter. There are six primary ribs on the adapertural half of the penultimate whorl, becoming increasingly wider spaced. On the body chamber, intercalated ribs, present at the adapical end, are lost, and the distinctive ventral ornament develops, as in in GBA 2016/004/0040 (Pl. 10, Figs. 1, 2). These specimens may be incomplete macroconchs. The largest fragments in the present collection

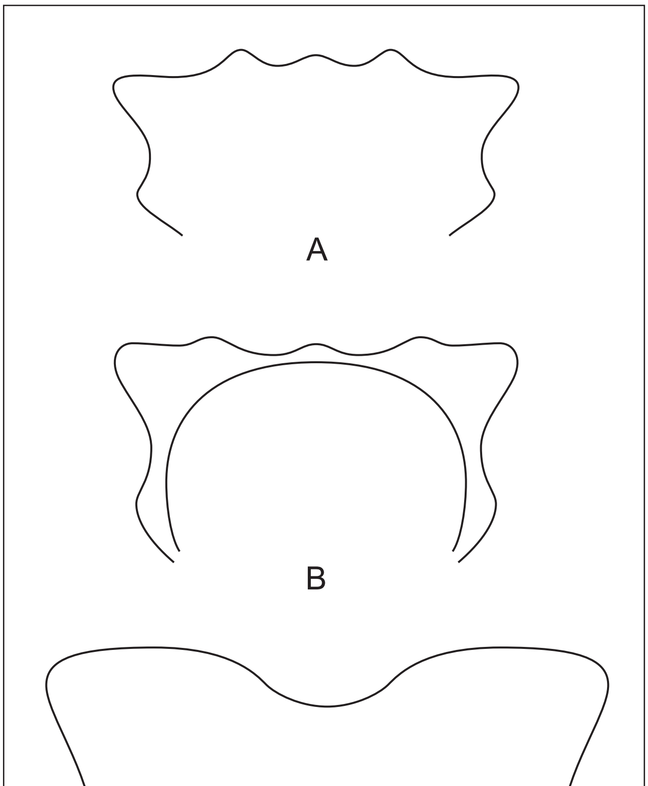

Text-Fig. 8.
Cunningtoniceras alatum (Zaborski, 1985). Whorl sections of A: GBA 2016/004/0038; B: GBA 2016/004/0070; C: GBA 2016/004/0071.

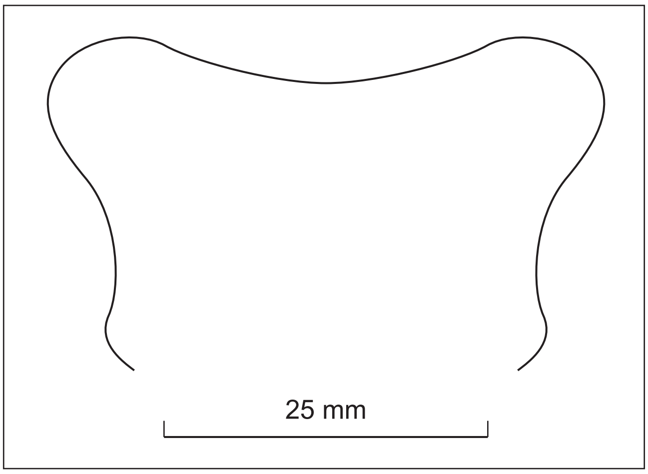

Text-Fig. 9.
Cunningtoniceras alatum (ZABORSKI, 1985). Whorl section of GBA 2016/004/0072.

(GBA 2016/004/0068–0069) have whorl heights of up to 46 mm at the adapertural end, and differ in no significant respects from the holotype body chamber fragment (ZABORSKI, 1985: Text-Figs. 53a, b).

GBA 2016/004/0029 (Pl. 11, Fig. 4) is a fragment from the adapical end of a very small body chamber of a pathological individual, with markedly asymmetric ventral ornament, having suffered non-lethal damage to the mid-ventral region.

The suture (Text-Fig. 7) is moderately incised, with a massive, asymmetrically bifid E/A.

Genus and Subgenus *Calycoceras* HYATT, 1900

(ICZN Generic Name No. 1352)

Type species: By designation under the Plenary Powers (ICZN Opinion No. 557) *Ammonites navicularis* MANTELL, 1822: 198, Pl. 22, Fig. 5 (ICZN Specific Name No. 1633).

Subgenus *Calycoceras* (*Gentoniceras*) THOMEL, 1972

Type species: *Ammonites gentoni* BRONGNIART, 1822: 83, 392, Pl. 6, Fig. 6 from the lower Middle Cenomanian of Rouen, Seine-Maritime, France, by original designation by THOMEL (1972: 65).

Calycoceras (*Gentoniceras*) sp. group of *gentoni* (BRONGNIART, 1822)

(Text-Figs. 10A–D)

Material: GBA 2016/004/0042–0043, from km 4.5, *acutus* Subzone inferred.

Description: GBA 2016/004/0042 (Text-Figs. 10A, B) is a 120° fragment of body chamber with a maximum preserved costal whorl height of 28 mm. Coiling is moderately evolute, the umbilicus of moderated depth, with a feebly convex umbilical wall and broadly round umbilical shoulder. The costal and intercostal whorl sections are reniform, the costal whorl breadth to height ratio 1.1, the greatest breadth at the umbilicolateral bullae. On the outer whorl fragment, six ribs arise at the umbilical seam, strengthen across the umbilical wall and shoulder and strengthen further into a small umbilicolateral bulla. The primary ribs

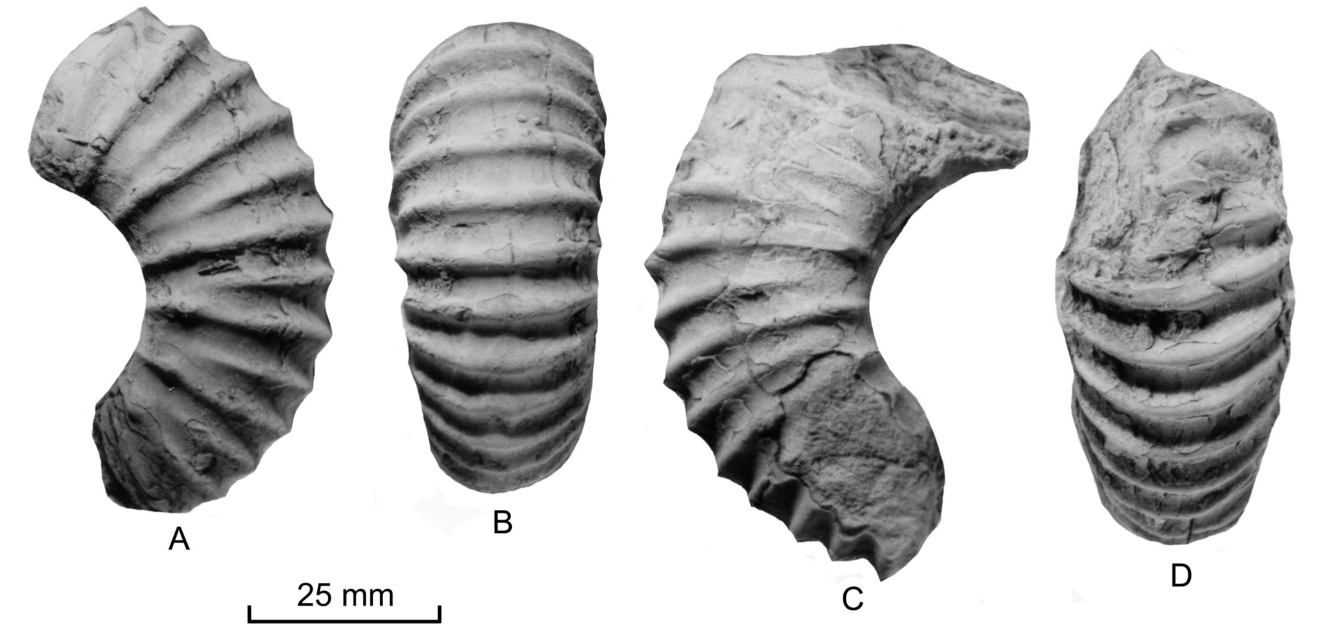

Text-Fig. 10.
Calycoceras (*Gentoniceras*) sp., group of *gentoni* (BRONGNIART, 1822). A, B: GBA 2016/004/0042; C, D: GBA 2016/004/0043.
Both specimens are from the Odukpani Formation at km 4.5, between Odukpani and Itu, Cross River State, Nigeria.
All figures are natural size.

alternate with long intercalated ribs. The ribs are strong, narrow, straight and prorsiradiate, narrower than the interspaces, and pass straight across the venter without any indication of tubercles. The dorsum preserves an external mould of the venter of the preceding whorl; there are indications of possible inner and definite outer ventrolateral tubercles, but the siphonal area is obscured by matrix.

GBA 2016/004/0043 (Text-Figs. 10C, D) is a further 120° body chamber fragment, with a maximum preserved whorl height of 33 mm. Parts of 12 ribs are preserved, the ribbing differing from that of the previous specimen in being slightly rursiradiate.

Discussion: The ribbing style, lack of ventrolateral and siphonal tubercles on what are interpreted as adult body chambers indicate these specimens to be *Calycoceras* (*Gentoniceras*) of the *gentoni* group, revised by WRIGHT & KENNEDY (1987: 128; 1990: 219 et seq.). In that revision, *gentoni* of Brongniart and *subgentoni* of Spath were kept separate. Subsequent study indicates that the latter is no more than a variant of the former (KENNEDY & JUIGNET, 1994: 30, Text-Figs. 1a; 2d, e; 6d, e, j, k; 8a–e; 22a, b). The present slight material most closely resembles that from southern England (WRIGHT & KENNEDY, 1990: Pl. 59, Fig. 2).

Occurrence: The *gentoni* group range from lower Middle to lower Upper Cenomanian, *rhotomagense* to *guerangeri* Zones in Western Europe. The geographic distribution extends from southern England to France, Spain, Germany, Iran, Algeria, Tunisia, northern KwaZulu-Natal in South Africa, Madagascar, and Nigeria.

Suborder Ancyloceratina WIEDMANN, 1966
Superfamily Turrilitoidea GILL, 1871
Genus *Turrilites* LAMARCK, 1801

Type species: *Turrilites costatus* LAMARCK, 1801: 102, by original designation by LAMARCK (1801: 102).

Turrilites costatus LAMARCK, 1801

(Pl. 12, Figs. 1–12; Pl. 13, Fig. 11)

1801 *Turrilites costata* LAMARCK: 102 (*pars*).

1985 *Turrilites scheuchzerianus* BOSC, 1801; ZABORSKI: 10, Text-Figs. 7, 8.

1985 *Turrilites costatus* LAMARCK, 1801; ZABORSKI: 10 (pars), Fig. 10 only.

1996 *Turrilites costatus* LAMARCK, 1801; WRIGHT & KENNEDY: 354, Pl. 103, Figs. 1, 2, 5, Pl. 104, Figs. 1–4, 6, 8–10, Pl. 105, Figs. 1, 5, 6, 10, 12, 13, 16, 17, 19, Pl. 106, Figs. 1–6, 9, 10, Text-Figs. 137c, 139a–c, 142a, f, g, 143a–g, i–p (with full synonymy).

2015 *Turrilites costatus* LAMARCK, 1801; KLEIN: 176, 179 (with synonymy).

2019 *Turrilites costatus* LAMARCK, 1801; KENNEDY in GALE et al.:127, Pl. 58, Figs. 20, 22–25.

Type: The lectotype, by the subsequent designation of DOUVILLÉ (1904: fiche 54a, Fig. 1), is the specimen from Rouen, France, no. F. A25610 in the Lamarck collection, housed in the Muséum national d'Histoire naturelle in Paris that was figured by DOUVILLÉ (1904: fiche 54a, Fig. 1), of which a cast is figured here (Pl. 12, Fig. 2).

Material: GBA 2016/004/0046–0048, 0054, 0067, km 3.8, *costatus* Subzone; GBA 2016/004/0049–0053, 3.8–4.2 km, *ex situ*; GBA 2016/004/0055, km 4, top of section, *acutus* Subzone.

Description: The best-preserved specimen (Pl. 12, Fig. 4) has an apical angle of 20°. The earliest growth stage seen (Pl. 12, Fig. 6) has a minimum whorl height of 9 mm. The whorls are in tight contact, the inter-whorl suture deeply incised, the outer whorl face rounded in intercostal section. There are 19–20 ribs per whorl. They arise at the junction of upper and outer whorl faces, and are strong, straight, and feebly prorsiradiate, strengthening into a sharp, transversely elongated tubercle in the middle of the outer whorl face. The ribs weaken markedly below this, producing a distinctive impressed band that separates the upper row of tubercles from a second, smaller row of transversely elongated tubercles on the lower part of the outer whorl face. There is a much smaller, adaperturally displaced row at the junction of the outer and lower whorl faces. GBA 2016/004/0067 (Pl. 12, Fig. 4) consists of six whorls, in part body chamber, although the position of the final septum cannot be established. The maximum preserved whorl height at the beginning of the final whorl is 28 mm. There are 18–19 ribs on the smallest whorl. They are coarse and straight, and link to a strong, transversely elongated tubercle in the middle of the whorl face, separated by a zone of weakened ornament from a smaller conical tubercle, with a third tubercle partially concealed in the strongly crenulated inter-whorl suture. As size increases, the ribs lengthen, and the final part of the largest whorl elongates, suggesting it to be a near-complete adult.

A series of larger body chamber fragments (Pl. 12, Figs. 8, 9, 11, 12; Pl. 13, Fig. 11) have whorl heights of up to 28 mm. There are up to 25 ribs per whorl that extend across the upper half of the exposed whorl face, and strengthen into a feeble transversely elongated tubercle, much weaker than on the phragmocones, the succeeding zone of weakened ornament less pronounced, and sometimes lost, being replaced by an indentation in the rib, below which a weak transversely elongated tubercle develops. The third and lower row of tubercles is weak to efface in these specimens.

Discussion: GBA 2016/004/0051 (Pl. 12, Fig. 4) differs in no significant respects from the lectotype (Pl. 12, Fig. 2). The ornament of larger body chamber fragments with ribs longer than in the lectotype and the tubercles in the upper row weaker, so that the whorl profile is less angular, corresponds to that of both juvenile and adult specimens from South India figured by STOLICZKA (1866: Pl. 87, Figs. 9, 10), Germany (SCHLÜTER, 1876: Pl. 38, Figs. 1, 2) and Sarthe in France (KENNEDY & JUIGNET, 1983: Text-Figs. 25m–o, 27h, 28a). These variants have a superficial resemblance to *Turrilites scheuchzerianus* BOSC, 1801 (see revision in WRIGHT & KENNEDY, 1996: 349, Pl. 106, Figs. 7, 8, 11, 12, Pl. 107, Figs. 1–7, Text-Figs. 137g, j, 138c, d, f–i, n, 139d–l, 140a, d, e–i, 143h, 147a, b), but this species never develops tubercles, the ribs interrupted or weakened around mid-flank in the early growth stages, but entire thereafter. The upper and lower whorl faces are smooth, and the inter-whorl suture entire, rather than crenulated. The *Turrilites scheuchzerianus* of ZABORSKI (1985: 10, Text-Figs. 7, 8) are *Turriites costatus* body chambers of this type. *Turrilites costatus* gives rise to *Turrilites acutus* PASSY, 1832 (Atlas: 9, Pl. 16, Figs. 3, 4), described below. They differ in that *acutus* is trituberculate rather than ribbed and tuberculate, the whorl section lower in the lectotype and corresponding specimens. There are, however, transitions between the two.

Occurrence: *Turrilites costatus* is index of the widely recognized lower Subzone of the lower Middle Cenomanian *Acanthoceras rhotomagense* Zone, extending as a rarity into the upper Middle and lower Upper Cenomanian, although records from condensed basement beds in Western Europe may be remanié individuals. The geographic distribution extends to England, France, Germany, Switzerland, Poland, Spain, Portugal, Romania, Ukraine (Crimea), Russia, Kazakstan and Kopet Dag in Turkmenia, Iran, Algeria, Central Tunisia, the Middle East, Nigeria, Angola, KwaZulu-Natal in South Africa, Mozambique, Madagascar, South India, Tibet, northern Australia, Mexico, the U.S. Gulf Coast and California.

Turrilites acutus PASSY, 1832

(Pl. 13, Figs. 1–10, 12, 13)

1832 *Turrilites acutus* PASSY: Atlas, 9, Pl. 16, Figs. 3, 4.

1985 *Turrilites costatus* LAMARCK, 1801; ZABORSKI: 10 (pars), Fig. 9 only.

1996 *Turrilites acutus* PASSY, 1832; WRIGHT & KENNEDY: 358, Pl. 103, Fig. 3; Pl. 104, Figs. 5, 7, 11; Pl. 105, Fig. 21; Pl. 108, Figs. 1–4, 8, 11, 12; Text–Figs. 138m, 141a, 146n–o (with full synonymy).

2015 *Turrilites acutus* PASSY, 1832; KENNEDY in KENNEDY & GALE: 318.

2015 *Turrilites acutus* PASSY, 1832; KLEIN: 175, 177.

2017 *Turrilites acutus* PASSY, 1832; KENNEDY in KENNEDY & GALE: 105, Pl. 17, Figs. 9, 11, 15, 17.

2019 *Turrilites acutus* PASSY, 1832; KENNEDY in GALE et al.: 128.

Type: The lectotype, by the subsequent designation of JUIGNET & KENNEDY (1976: 65), is the original of PASSY (1832: Pl. 16, Fig. 3, no. F. RO3993) in the collections of the Muséum national d'Histoire naturelle, Paris, and from Rouen, Seine-Maritime, France. It is figured here as Plate 13, Figures 3, 4.

Material: GBA 2016/004/0056–0061, km 4, north side; GBA 2016/004/0062, 0063, km 4, north side, top of section; GBA 2016/004/0064–0065, km 4, south side, all *acutus* Subzone.

Description: The apical angle of the most complete fragments is 25–27°. The inter-whorl suture is deeply impressed, and strongly crenulated. The outer whorl face has a convex profile in intercostal section and a markedly angular costal section. Eighteen short, coarse, very feebly prorsiradiate ribs arise at the junction of the upper and outer whorl faces and strengthen into strong conical tubercles in the middle of the outer whorl face. A weakened to effaced rib links to second row of weaker, adaperturally displaced conical tubercles on the lower part of the outer whorl face, with a third, much weaker row partially concealed in the crenulations in the inter-whorl suture. Ornament of this type occurs in fragments with whorl heights of up to 36 mm (Pl. 13, Fig. 9). The larger specimens (Pl. 13, Figs. 12, 13) have whorl heights of up to 41 mm, and are interpreted as adult body chambers. The ornament weakens, but the three rows of tubercles persist. The largest specimen (Pl. 13, Fig. 13) has 22 ribs on the final whorl; the lower two rows of tubercles are elongated and distinctly prorsiadiate.

Discussion: The smaller specimens differ in no significant respects from the lectotype (compare Pl. 13, Figs. 1, 2, 5 and Figs. 3 and 4). Differences from *Turrilites costatus* are described above. The *Turrilites costatus* from the Odukpani Formation of ZABORSKI (1985: 10, Fig. 9, non Fig. 10) are in part *Turrilites acutus*.

Occurrence: Middle Cenomanian, index of the upper subzone of the widely recognized *Acanthoceras rhotomagense* Zone to lower Upper Cenomanian *Calycoceras guerangeri* Zone. The geographic distribution extends from England to France, Germany, Poland, Spain, northern Russia, Kazakhstan, Turkmenia, Iran, Algeria, Central Tunisia, Nigeria, South India, Tibet, Texas, the U.S. Western Interior and California.

Acknowledgements

We are grateful to DAVID SANSOM (Oxford) and MAREK PLOSCH (Warsaw) for their assistance in the preparation of the figures. Harald Lobitzer is grateful to the management of CALABAR CEMENT COMPANY (Calcemco) for providing him and his colleagues from Calcemco with a car with driver (including weekends), thus giving us the opportunity to learn more about the geology of the "Calabar Flank". Thanks also to the management of REYNOLDS CONSTRUCTION COMPANY (RCC) for permission to carry out geological research during the construction of the Odukpani-Itu Highway.

References

BOSC, L.A.G. (1801): (An. 13). – In: ROISSY, F.: Histoire Naturelle générale et particulière, des Mollusques, Animaux sans vertèbres et a sang blanc. Ouvrage faisant suite aux Œuvres de Leclerc de Buffon, et partie du Cours complet d'Histoire naturelle, rédigé par C.S. Sonnini, membre de plusieurs sociétés savants. Continué par. F. de Roissy, viii + 448 + 3 pp., Paris.

BRONGNIART, A. (1822): Sur quelques terrains de Craie hors du Bassin de Paris. – In: CUVIER, G. & BRONGNIART, A.: Description géologique des environs de Paris, 3rd ed., 80–101, Paris.

COLLIGNON, M. (1937): Ammonites Cénomaniennes du sud-ouest de Madagascar. – Annales géologiques du Service des Mines Madagascar, **8**, 31–69, Tananarive.

COOPER, M.R. (1973): Cenomanian ammonites from Novo Redondo, Angola. – Annals of the South African Museum, **62**, 41–67, Cape Town.

DESSAUVAGIE, T.F.J. (1972): Biostratigraphy of the Odukpani (Cretaceous) type section, Nigeria. – In: DESSAUVAGIE, T.F.J. & WHITEMAN, A.J.: Proceedings of the Conference on African Geology. Held at the University of Ibadan from 7–14 December 1970 in Commemoration of the Tenth Anniversary of the Founding of the Geology Department, 207–218, Ibadan.

DIENER, C. (1925): Ammonoidea neocretacea. – Fossilium Catalogus I: Animalia, **29**, 244 pp., Berlin.

DOUVILLÉ, R. (1904): *Turrilites costatus* LAMARCK. – *Palaeontologia Universalis*, Fiche **54**, 3 pp., Paris.

FAYOSE, E.A. & DESSAUVAGIE, T.F.J. (1976): Excursion 3: Upper Cretaceous and Tertiary sediments of eastern states of Nigeria. – 7th African Micropaleontological Colloquium Ile-Ife March 16–29, 1976, Geological guide to some Nigerian Cretaceous – Recent localities, 35–52, Ibadan.

FORBES, E. (1846): Report on the Fossil Invertebrata from southern India, collected by Mr. Kaye and Mr. Cunliffe. – Transactions of the Geological Society of London, Second series, **7**/3, 85–174, London.

GALE, A.S. (1995): Cyclostratigraphy and correlation of the Cenomanian Stage in Western Europe. – Special Publications of the Geological Society of London, **85**, 177–197, London.

GALE, A.S., KENNEDY, W.J. & WALASZCZYK, I. (2019) : Upper Albian, Cenomanian and Lower Turonian ammonite and inoceramid bivalve faunas from the Cauvery Basin, Tamil Nadu, South India. – Acta Geologica Polonica, **69**, 161– 338, London.

GILL, T. (1871): Arrangement of the Families of Mollusks. – Smithsonian Miscellaneous Collections, **227**, xvi + 49 pp., Washington, D.C.

GROSSOUVRE, A. DE (1894): Recherches sur la craie supérieure, 2, Paléontologie. Les ammonites de la craie supérieure. – Mémoires du Service de la Carte Géologique détaillée de la France, 264 pp., Paris (misdated 1893).

HOWARTH, M.K. (1985): Cenomanian–Turonian ammonites from the Novo Redondo area, Angola. – Bulletin of the British Museum (Natural History), Geology, **39**, 73–105, London.

HYATT, A. (1889): Genesis of the Arietidae. – Smithsonian Contributions to Knowledge, **673**, xi + 239 pp., Washington, D.C.

HYATT, A. (1900): Cephalopoda. – In: ZITTEL, K.A. VON (1896–1900): Textbook of Palaeontology, 502–604, transl. Eastman, C.R., London–New York.

JIMBO, K. (1894): Beiträge zur Kenntniss der Fauna der Kreideformation von Hokkaido. – Paläontologische Abhandlungen, N.S., **2**/3, 147–194, Jena.

JUIGNET, P. & KENNEDY, W.J. (1976): Faunes d'ammonites et biostratigraphie compareé du Cénomanien du nord-ouest de la France (Normandie) et du sud d'Angleterre. – Bulletin trimestrielle de la Société Géologique de Normandie, **63**, 1–193, Le Havre.

KENNEDY, W.J. (1971): Cenomanian ammonites from southern England. – Special Papers in Palaeontology, **8**, v + 133 pp., London

KENNEDY, W.J. & GALE, A.S. (2015): Upper Albian and Cenomanian ammonites from Djebel Mrhila, Central Tunisia. – Révue de Paléobiologie, **34**, 235–361, Genève.

KENNEDY, W.J. & GALE, A.S. (2017): Trans-Tethyan correlation of the Lower–Middle Cenomanian boundary interval: southern England (Southerham, near Lewes, Sussex) and Douar el Khiana, northeastern Algeria. – Acta Geologica Polonica, **67**, 75–108, Warsawa.

KENNEDY, W.J. & HENDERSON, R.A. (1991): A note on *Ammonites Sugata* FORBES, 1846. – Neues Jahrbuch für Geologie und Paläontologie, Monatshefte, **1991**, 470–476, Stuttgart.

KENNEDY, W.J. & JUIGNET, P. (1983): A revision of the ammonite faunas of the type Cenomanian. 1. Introduction, Ancyloceratina. – Cretaceous Research, **4**, 3–83, London.

KENNEDY, W.J. & JUIGNET, P. (1994): A revision of the ammonite faunas of the type Cenomanian. 6. Acanthoceratinae (*Calycoceras* (*Proeucalycoceras*), *Eucalycoceras*, *Pseudocalycoceras*, *Neocardioceras*), Euomphaloceratinae, Mammitinae and Vascoceratidae. – Cretaceous Research, **15**, 17–57, London.

KENNEDY, W.J. & LOBITZER, H. (2019): Upper Albian and Lower Cenomanian ammonites from the Mfamosing Quarry, Calabar Flank, Cross River State, southeastern Nigeria. – Jahrbuch der Geologischen Bundesanstalt, **159**, 203–245, Vienna.

KLEIN, J. (2015): Lower Cretaceous Ammonites VIII Turrilitoidea. – Anisoceratidae, Hamitidae, Turrilitidae, including representatives of the Upper Cretaceous species. – Fossilium Catalogus I: Animalia, **154** (*pars*), 265 pp., Weikersheim.

KLEIN, J. (2018): Lower Cretaceous Ammonites XI Acanthoceratoidea: Leymerielidae, Brancoceratidae, Flickiidae, Forbesiceratidae, including the Upper Cretaceous representatives. – Fossilium Catalogus, **158** (*pars*), 333 pp., Weikersheim.

KOGBE, C.A. (1989a): Palaeogeographic History of Nigeria from Albian Times. – In: KOGBE, C.A. (Ed.): Geology of Nigeria, 2nd revised edition, 237–252, Jos.

KOGBE, C.A. (1989b): The Cretaceous and Paleogene Sediments of Southern Nigeria. – In: KOGBE, C.A. (Ed.): Geology of Nigeria, 2nd revised edition, 273–282, Jos.

KORN, D., EBBIGHAUSEN, V., BOCKWINKEL J. & KLUG, C. (2003): The A-mode ontogeny in prolecanitid ammonites. – Palaeontology, **46**, 1123–1132, London.

KOSSMAT, F. (1895–1898): Untersuchungen über die südindische Kreideformation. – Beiträge zur Paläontologie Österreich-Ungarns und des Orients, **9** (1895): 97–203 (1–107); **11** (1897): 1–46 (108–153); **11** (1898): 89–152 (154–217), Vienna.

KULLMANN, J. & WIEDMANN, J. (1970): Significance of sutures in phylogeny of Ammonoidea. – University of Kansas, Paleontological Contributions, **42**, 1–32, Lawrence.

Lamarck, J.P.B.A. de M. de (1801): Système des Animaux sans vertebrès. – vii + 432 pp., Paris.

López, G., Dhondt, A.V., Lobitzer, H. & Tröger, K.-A. (2004): Lower Maastrichtian inoceramids from Nigeria. – Kollmann-Festschrift herausgegeben zum 65. Geburtstag von Dr. Heinz A. Kollmann. – Annalen des Naturhistorischen Museums in Wien, **106A**, 227–257, Wien.

Mantell, G.A. (1822): The fossils of the South Downs; or illustrations of the geology of Sussex. – xvi + 327 pp., London.

Matsumoto, T. (1942): A note on the Japanese Cretaceous ammonites belonging to the subfamily Desmoceratinae. – Proceedings of the Imperial Academy of Japan, **18**, 24–29, Tokyo.

Matsumoto, T. (Ed.) (1954): The Cretaceous System in the Japanese Islands. – 324 pp., Japan Society for the Promotion of Science, Tokyo.

Matsumoto, T., Muramoto, T. & Takahashi, T. (1969): Selected Acanthoceratids from Hokkaido. – Memoirs of the Faculty of Science, Kyushu University, Series D, Geology, **19**, 251–296, Fukuoka.

Murat, R.C. (1972): Stratigraphy and Palaeogeography of the Cretaceous and Lower Tertiary in Southern Nigeria. – Geological Magazine, **109**, 411–419, London.

Nishimura, T., Maeda, H., Tanaka, G. & Ohno, T. (2010): Taxonomic evaluation of various morphological characters in the Late Cretaceous desmoceratine polyphyletic genus "*Damesites*" from the Yezo Group of Hokkaido and Sakhalin. – Paleontological Research, **14**, 33–55, Tokyo.

d'Orbigny, A. (1840 –1842): Paléontologie française: Terrains crétacés. 1. Céphalopodes. – 1–120 (1840); 121–430 (1841); 431–662 (1842), Paris.

Passy, A. (1832): Description géologique du département de la Seine–Inférieure. – xvi + 371 pp., Rouen.

Pervinquière, L. (1907): Sur quelques ammonites du Crétacé algérien. – Mémoires de la Société Géologique de France. – Paléontologie, **17**/2–3, 86 pp., Paris.

Reyment, R.A. (1955a): The Cretaceous ammonoidea of southern Nigeria and the southern Cameroons. – Geological Survey Nigeria Bulletin, **25**, 112 pp., Kaduna.

Reyment, R.A. (1955b): Upper Cretaceous Mollusca (Lamellibranchia and Gastropoda) from Nigeria. – Colonial Geology and Mineral Resources, **5**/2, 127–155, London.

Reyment, R.A. (1965). Aspects of the geology of Nigeria. The Stratigraphy of the Cretaceous and Cenozoic deposits. – 133 pp., Ibadan University Press, Ibadan.

Robaszynski, F., Caron, M., Amédro, F., Dupuis, C., Hardenbol, J., Gonzáles Donoso, J.M., Linares, D. & Gartner, S. (1994): Le Cénomanien de la région de Kalaat Senan (Tunisie Centrale). – Révue de Paléobiologie, **12**, 351–505, Geneva.

Saito, R. & Matsumoto, T. (1956): A new species of *Damesites* from the Cenomanian of Hokkaido, Japan. – Transactions and Proceedings of the Palaeontological Society of Japan, New Series, **22**, 191–194, Tokyo.

Schlüter, C. (1871–1876): Cephalopoden der oberen deutschen Kreide. – Palaeontographica, **21**, 1–24 (1871); **21**, 25–120 (1872); **24**, 1–144 (121–264) + x (1876), Stuttgart.

Sharpe, D. (1853–1857): Description of the fossil remains of Mollusca found in the Chalk of England. I, Cephalopoda. – Monograph of the Palaeontographical Society, 1–26 (1853); 27–36 (1855); 37–68 (1857), London.

Stoliczka, F. (1863–1866): The fossil cephalopoda of the Cretaceous rocks of Southern India. Ammonitidae with revision of the Nautilidae etc. – Memoirs of the Geological Survey of India. Palaeontologica Indica, **3** (1), 41–56 (1863); (2–5), 57–106 (1864); (6–9), 107–154 (1865); (10–13), 155–216 (1866), Calcutta.

Szász, L. (1976): Nouvelles espèces d'ammonites dans le Cénomanien de la region de Hateg (Carpates méridionales). – Dări de seamă ale *şedinţelor* (3. Paléontologie), **9**, 53–82, Bucarest.

Thomel, G. (1972): Les Acanthoceratidae Cénomaniens des châines subalpines méridionales. – Mémoires de la Société Géologique de France, Nouvelle Série, **116**, 204 pp., Paris.

Wiedmann, J. (1966): Stammesgeschichte und System der posttriadischen Ammonoideen; ein Überblick. – Neues Jahrbuch für Geologie und Paläontologie Abhandlungen, **125**, 49–79; **127**, 13–81, Stuttgart.

Wright, C.W. (1952): A classification of the Cretaceous Ammonites. – Journal of Paleontology, **26**, 213–222, Chicago.

Wright, C.W. & Kennedy, W.J. (1984): The Ammonoidea of the Lower Chalk. Part 1. – Monograph of the Palaeontographical Society, 1–126, London.

Wright, C.W. & Kennedy, W.J. (1987): The Ammonoidea of the Lower Chalk. Part 2. – Monograph of the Palaeontographical Society, 127–218, London.

Wright, C.W. & Kennedy, W.J. (1990): The Ammonoidea of the Lower Chalk. Part 3. – Monograph of the Palaeontographical Society, 219–294, London.

Wright, C.W. & Kennedy, W.J. (1996): The Ammonoidea of the Lower Chalk. Part 5. – Monograph of the Palaeontographical Society, 320–403, London.

Zaborski, P.M.P. (1982). Campanian and Maastrichtian Sphenodiscid ammonites from Southern Nigeria. – Bulletin of the British Museum (Natural History), Geology, **36**/4, 302–332, London.

Zaborski, P.M.P. (1983): Campano-Maastrichtian ammonites, correlation and paleogeography in Nigeria. – Journal of African Earth Sciences, **1**, 59–63, London.

Zaborski, P.M.P. (1985): Upper Cretaceous ammonites from the Calabar region, southeast Nigeria. – Bulletin of the British Museum (Natural History), Geology, **39**, 1–72, London.

Zittel, K.A. von (1884): Handbuch der Paläontologie. 1, Abteilung 2, Lieferung 3, Cephalopoda, 329–522, Munich–Leipzig.

Zittel, K.A. von (1895): Grundzüge der Paläontologie (Paläozoologie). – vii + 972 pp., Munich–Leipzig.

Received: 2. August 2019, accepted: 21. October, 2019

Plates

Plate 1

Damesites africanus **sp. nov.**

Figs. 1–3: paratype, GBA 2016/004/0004, km 4, south side.
Figs. 4–6: paratype, GBA 2016/004/0005, km 2.8.
Figs. 7–9: paratype, GBA 2016/004/0002, km 4.
Figs. 10, 11: paratype, GBA 2016/004/0006, km 2.8.
Figs. 12, 13: paratype, GBA 2016/004/0003, km 4.
Figs. 14, 15: paratype, GBA 2016/004/0007, km 2.8.

All specimens are from the Middle Cenomanian part of the Odukpani Formation between Odukpani and Itu, Cross River State, south-eastern Nigeria.

All figures are natural size.

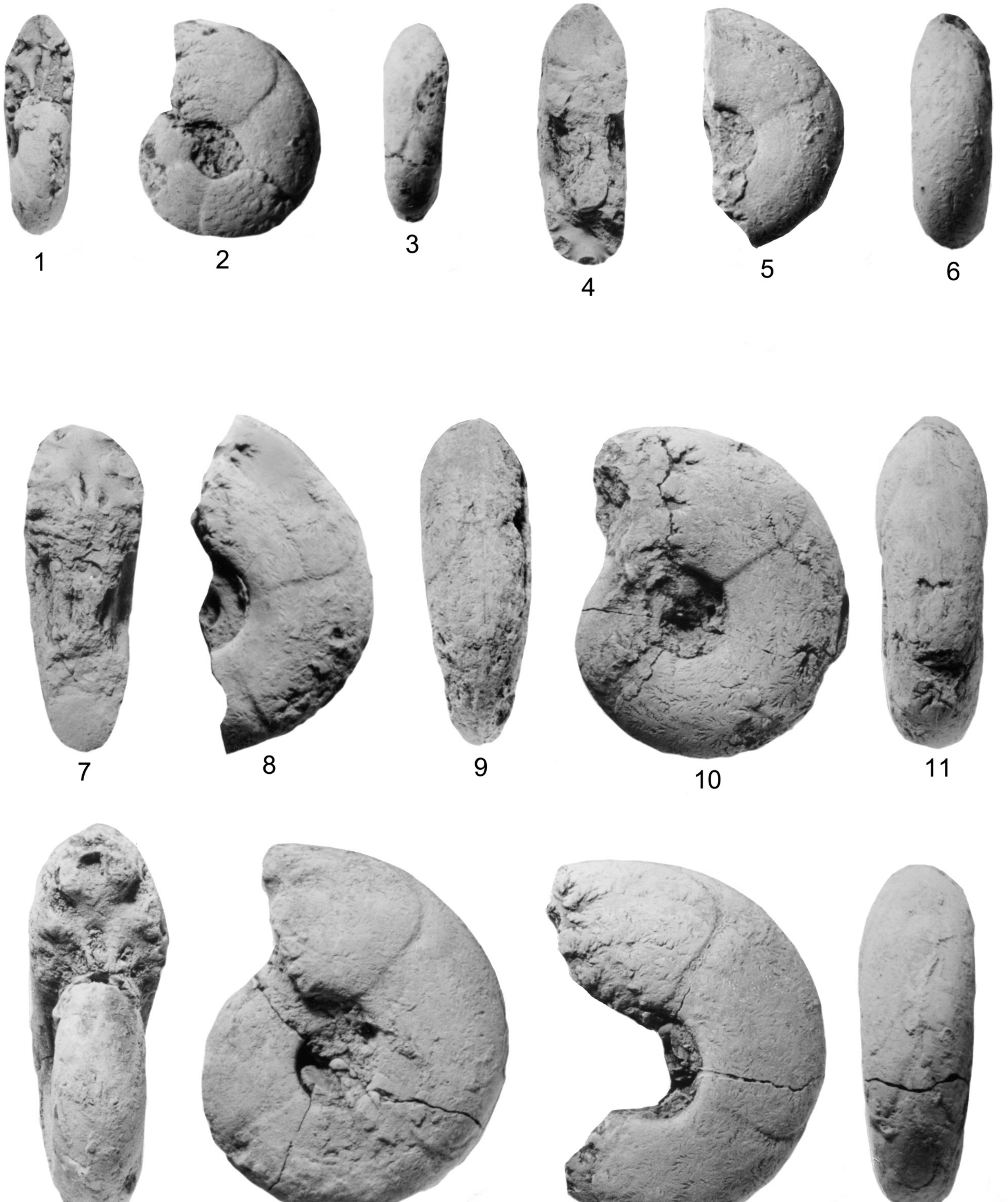
1
2
3
4
5
6
7
8
9
10
11
12
13
14
15

Plate 2

Figs. 1–4: ***Damesites africanus*** **sp. nov.**

The holotype, GBA 2016/004/0001, km 4, upper part of section.

The specimen is from the Middle Cenomanian *acutus* Subzone part of the Odukpani Formation between Odukpani and Itu, Cross River State, southeastern Nigeria.

All figures are natural size.

1

2

3

4

Plate 3

Figs. 1–4: ***Forbesiceras obtectum*** **(Sharpe, 1853).**

GBA 2016/004/0008, km 4, from the Middle Cenomanian *acutus* Subzone part of the Odukpani Formation between Odukpani and Itu, Cross River State, southeastern Nigeria.

All figures are natural size.

1

2

3

4

Plate 4

Cunningtoniceras meridionale **(Stoliczka, 1864).**

GBA 2016/004/0010, km 3.8, south side, from the Middle Cenomanian *costatus* Subzone part of the Odukpani Formation between Odukpani and Itu, Cross River State, southeastern Nigeria.

The figure is natural size.

Plate 5

Cunningtoniceras meridionale (STOLICZKA, 1864).

Figs. 1, 2: GBA 2016/004/0010, km 3.8, south side, *costatus* Subzone.

Fig. 3: GBA 2016/004/0012, km 3.8–4.2, *ex situ*.

Figs. 4, 5: GBA 2016/004/0013 km 4, south side, top of section, *acutus* Subzone.

All specimens are from the Middle Cenomanian part of the Odukpani Formation between Odukpani and Itu, Cross River State, south-eastern Nigeria.

The figures are natural size.

1

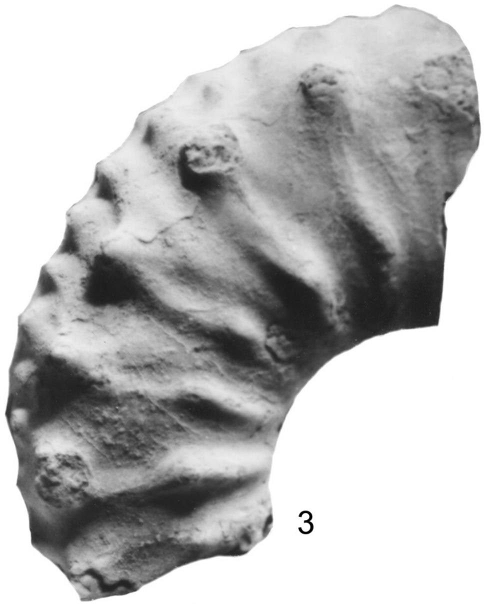

3

2

4

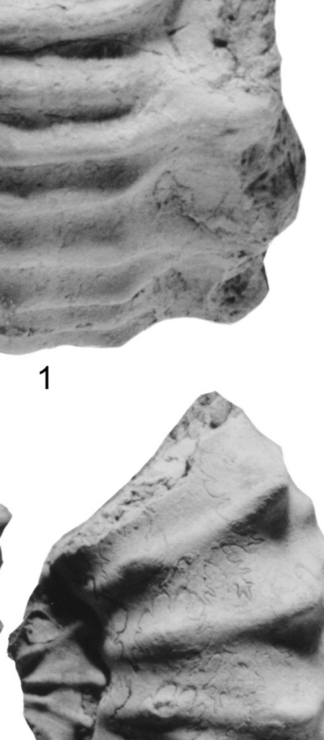

5

Plate 6

Cunningtoniceras meridionale **(Stoliczka, 1864).**

GBA 2016/004/0011, km 3.8, south side, from the Middle Cenomanian *costatus* Subzone part of the Odukpani Formation between Odukpani and Itu, Cross River State, southeastern Nigeria.

The figures are natural size.

Plate 7

Cunningtoniceras meridionale (Stoliczka, 1864).

Figs. 1, 2: GBA 2016/004/0015.

Figs. 3, 4: GBA 2016/004/0016.

Both specimens are from km 3.8, south side, the Middle Cenomanian *costatus* Subzone part of the Odukpani Formation between Odukpani and Itu, Cross River State, southeastern Nigeria.

The figures are natural size.

1

2

3

4

Plate 8

Cunningtoniceras alatum Zaborski, 1985.

Figs. 1, 2: GBA 2016/004/0022, km 4, north side.
Figs. 3, 4: GBA 2016/004/0023, km 4, south side.
Figs. 5, 6: GBA 2016/004/0031, km 4, south side.
Figs. 7, 8: GBA 2016/004/0032, km 4, south side.
Figs. 9–11: GBA 2016/004/0037, km 4.5.
Figs. 12, 13: GBA 2016/004/0020, km 4, north side, upper part of section.
Fig. 14: GBA 2016/004/0038, km 4, upper part of section.
Figs. 15, 20: GBA 2016/004/0035, km 4, south side.
Figs. 16, 17: GBA 2016/004/0024, km 4, north side.
Figs. 18, 19: GBA 2016/004/0039, km 4, upper part of section.
Figs. 21, 22: GBA 2016/004/0034, km 4, south side.
Figs. 23, 24: GBA 2016/004/0026, km 4, north side.
Figs. 25, 26: GBA 2016/004/0027, km 4, north side.
Figs. 27, 28: GBA 2016/004/0066, km 4, south side.

All specimens are from the Middle Cenomanian *acutus* Subzone part of the Odukpani Formation between Odukpani and Itu, Cross River State, southeastern Nigeria.

The figures are natural size.

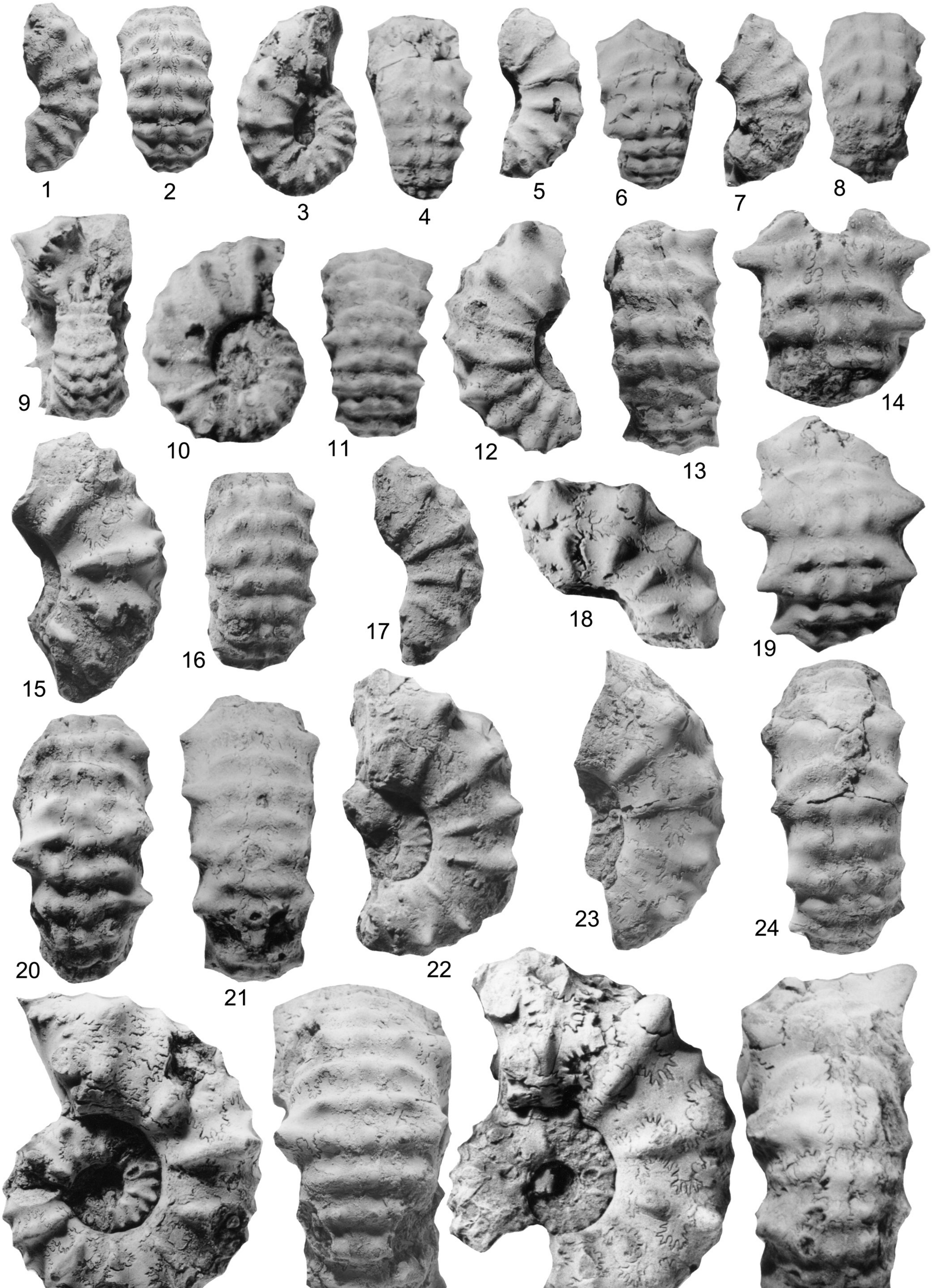
1
2
3
4
5
6
7
8
9
10
11
12
13
14
15
16
17
18
19
20
21
22
23
24
25
26
27
28

Plate 9

Figs. 1–8, 11: ***Cunningtoniceras alatum*** **Zaborski, 1985.**

Figs. 1, 2: GBA 2016/004/0033, km 4, north side, *acutus* Subzone.
Figs. 3, 4: GBA 2016/004/0035, km 4, north side, *acutus* Subzone.
Figs. 5, 6: GBA 2016/004/0030, km 4, north side, *acutus* Subzone.
Figs. 7, 8, 11: GBA 2016/004/0041, *ex situ*.

Figs. 9, 10: ***Cunningtoniceras cunningtoni*** **(Sharpe, 1855)**, GBA 2016/004/0017, *ex situ*.

All specimens are from the Middle Cenomanian part of the Odukpani Formation between Odukpani and Itu, Cross River State, south-eastern Nigeria.

The figures are natural size.

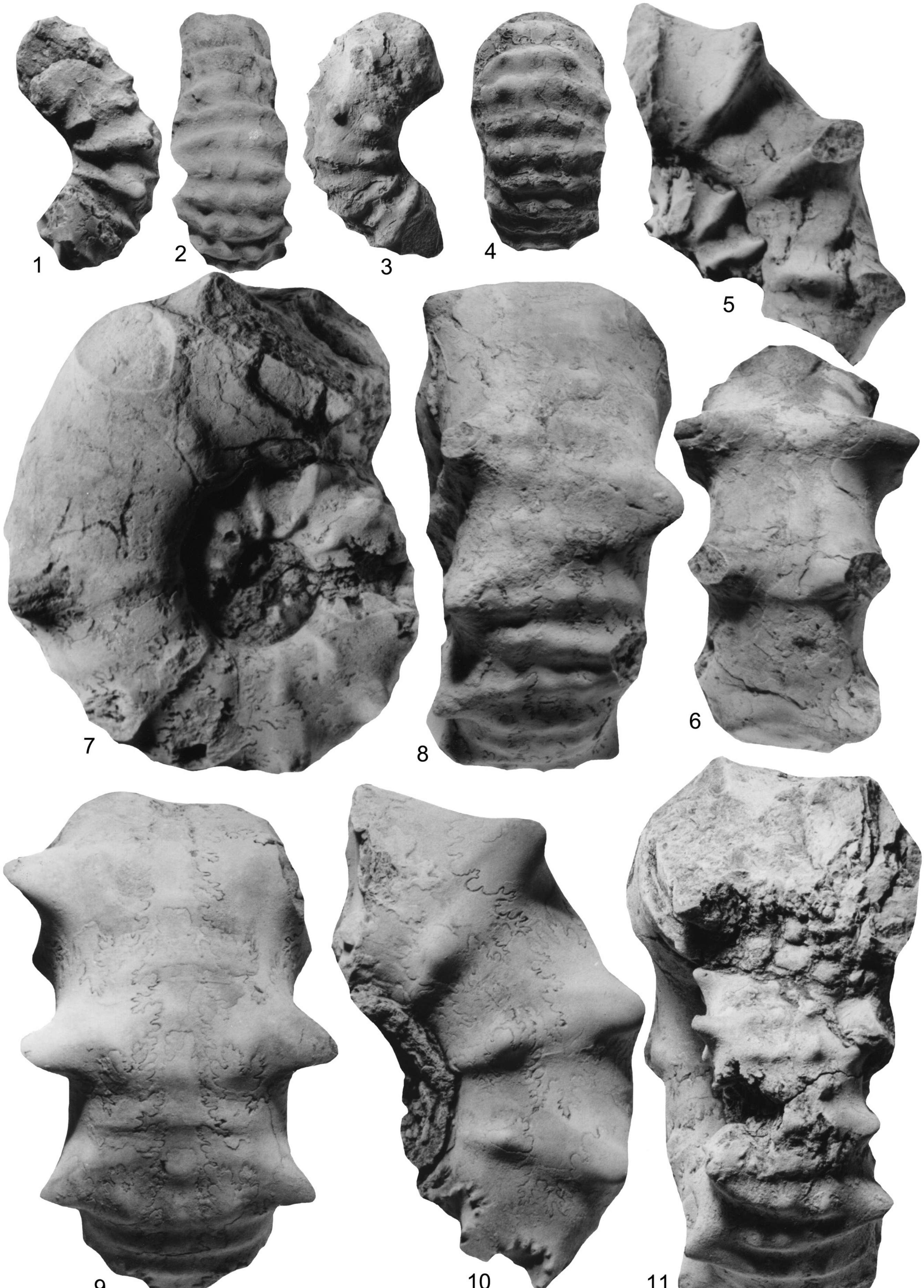
1
2
3
4
5
6
7
8
9
10
11

Plate 10

Figs. 1, 2: *Cunningtoniceras alatum* **Zaborski, 1985**, GBA 2016/004/0040, *ex situ*.

Figs. 3, 4: *Cunningtoniceras cunningtoni* **(Sharpe, 1855)**, GBA 2016/004/0018, *ex situ*.

Both specimens are from the Middle Cenomanian part of the Odukpani Formation between Odukpani and Itu, Cross River State, south-eastern Nigeria.

The figures are natural size.

1

3

2

4

Plate 11

Cunningtoniceras alatum Zaborski, 1985.

Figs. 1, 7, 8: GBA 2016/004/0019, km 4, *ex situ*.
Fig. 2: GBA 2016/004/0028, km 4, north side, *acutus* Subzone.
Figs. 3, 6: GBA 2016/004/0021, km 4, top of section, *acutus* Subzone.
Fig. 4: GBA 2016/004/0029, km 4, south side, *acutus* Subzone.
Figs. 5, 9: GBA 2016/004/0036, km 4, south side, top of section, *acutus* Subzone.

All specimens are from the Middle Cenomanian part of the Odukpani Formation between Odukpani and Itu, Cross River State, south-eastern Nigeria.

The figures are natural size.

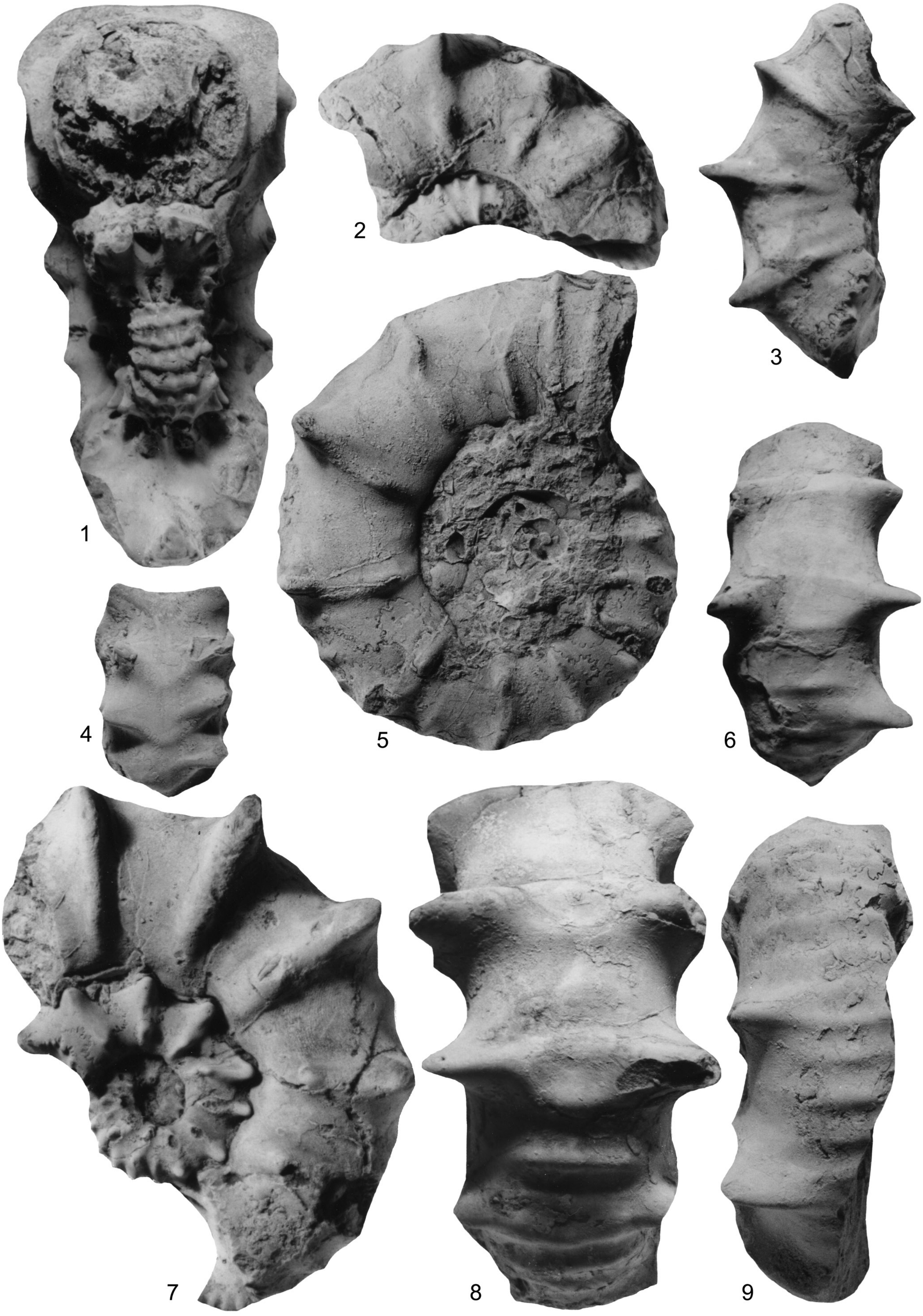
1
2
3
4
5
6
7
8
9

Plate 12

Figs. 1–12: ***Turrilites costatus* LAMARCK, 1801.**

Fig. 1: GBA 2016/004/0046, km 3.8, south side, *costatus* Subzone.

Fig. 2: The lectotype, from Rouen, France, no. F. A25610 in the Lamarck collection, housed in the Muséum National d'Histoire Naturelle, Paris.

Fig. 3: GBA 2016/004/0049, km 3.8–4.2, *ex situ*.

Fig. 4: GBA 2016/004/0067, km 3.8, south side, *costatus* Subzone.

Fig. 5: GBA 2016/004/0051, km 3.8–4.2, *ex situ*.

Fig. 6: GBA 2016/004/0050, km 3.8–4.2, *ex situ*.

Fig. 7: GBA 2016/004/0047, km 3.8, south side, *ex situ*.

Fig. 8: GBA 2016/004/0054, km 4, *acutus* Subzone.

Fig. 9: GBA 2016/004/0054, km 4, *acutus* Subzone.

Fig. 10: GBA 2016/004/0048, km 3.8, south side, *costatus* Subzone.

Fig. 11: GBA 2016/004/0052, km 3.8–4.2, *ex situ*.

Fig. 12: GBA 2016/004/0053, km 3.8–4.2, *ex situ*.

Figures 1 and 3–12 are from the Middle Cenomanian part of the Odukpani Formation between Odukpani and Itu, Cross River State, southeastern Nigeria.

The figures are natural size.

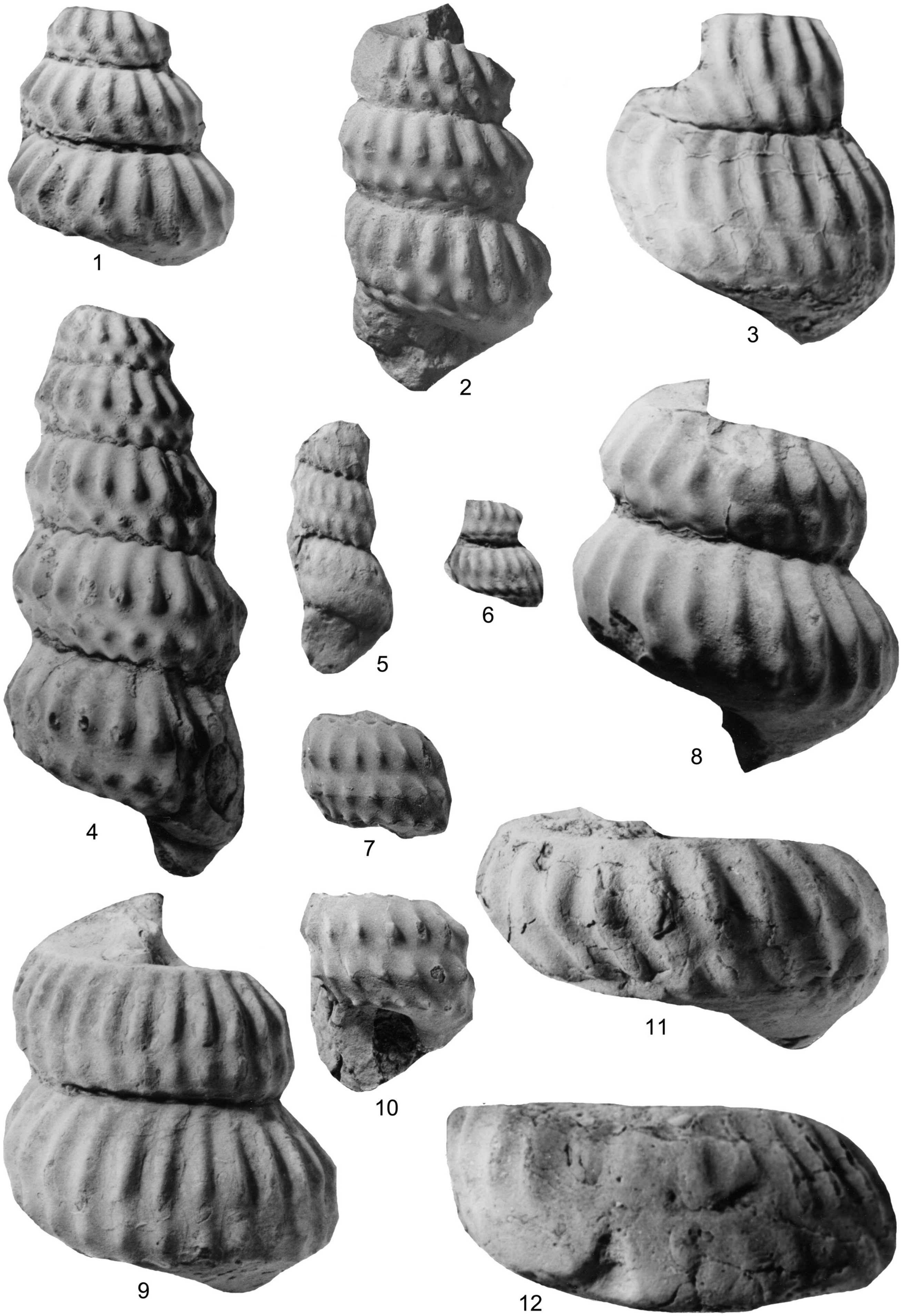
1
2
3
4
5
6
7
8
9
10
11
12

Plate 13

Figs. 1–10, 12, 13: ***Turrilites acutus*** **PASSY, 1832**

Fig. 1: GBA 2016/004/0056, km 4, north side.
Fig. 2: GBA 2016/004/0057, km 4, north side.
Fig. 3: a cast of the lectotype, the original of PASSY (1832: Pl. 16, Fig. 3), no. F. RO3993 in the collections of the Muséum national d'Histoire naturelle, Paris, and from Rouen, Seine-Maritime, France.
Fig. 4: GBA 2016/004/0065, km 4, south side.
Fig. 5: GBA 2016/004/0058, km 4, north side.
Fig. 6: GBA 2016/004/0060, km 4, north side.
Fig. 7: GBA 2016/004/0063, km 4, south side, top of section.
Fig. 8: GBA 2016/004/0059, km 4, north side.
Fig. 9: GBA 2016/004/0064, km 4, south side.
Fig. 10: GBA 2016/004/0061, km 4, north side.
Fig. 12: GBA 2016/004/0065, km 4, south side.
Fig. 13: GBA 2016/004/0062, km 4, north side, top of section.

Fig. 11: ***Turrilites costatus*** LAMARCK, 1801, GBA 2016/004/0055, km 4, south side, top of section.

Figures 1, 2 and 5–13 are from the Middle Cenomanian *acutus* Subzone part of the Odukpani Formation between Odukpani and Itu, Cross River State, southeastern Nigeria.

The figures are natural size.

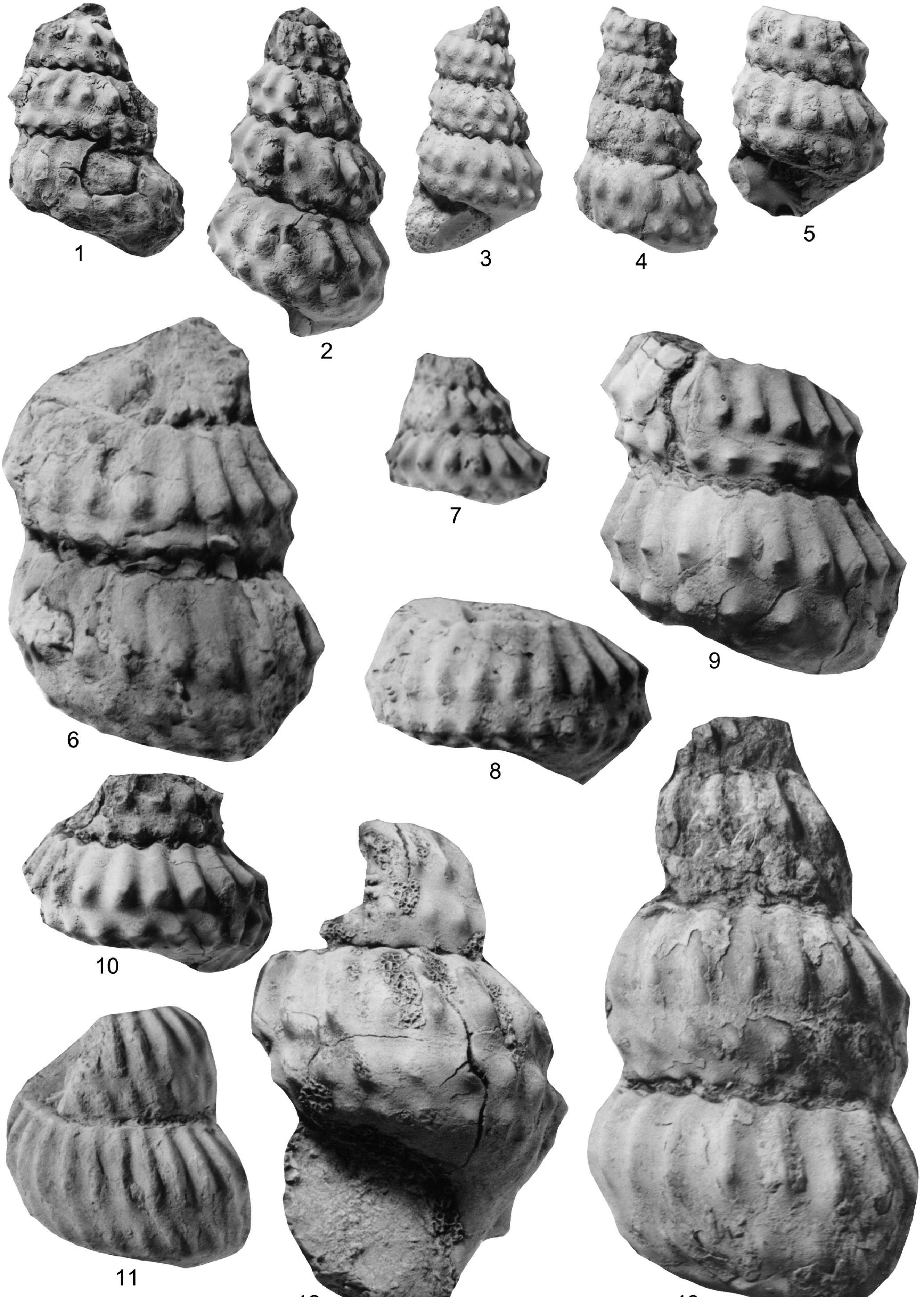
1
2
3
4
5
6
7
8
9
10
11
12
13

JAHRBUCH DER GEOLOGISCHEN BUNDESANSTALT
Jb. Geol. B.-A. | ISSN 0016–7800 | Band 159 | Heft 1–4 | S. 289–313 | Wien, Dezember 2019

Paläobotanische Kostbarkeiten aus den Versteinerten Wäldern von Nová Paka (Tschechien) und Chemnitz (Deutschland) – Originale zu Stenzel (1889, 1906) und Rudolph (1906) in der paläobotanischen Sammlung der Geologischen Bundesanstalt in Wien

Frank Löcse[1], Irene Zorn[2], Lutz Kunzmann[3] & Ronny Rößler[4]

19 Abbildungen, 1 Tabelle

Asterochlaena laxa
Asterochlaena ramosa
Ankyropteris brongniartii
Psaronius
Taeniopteris abnormis
Sammlungshistorie

Inhalt

Zusammenfassung

Paläontologische Sammlungen sind gleichermaßen Quelle und Resultat von Wissen. Als Archive der Erd- und Lebensgeschichte dokumentieren sie nicht nur räumlich-zeitliche Gegebenheiten, die heute nicht mehr existieren, sondern summieren oft den Beitrag mehrerer Forschergenerationen. Im Zuge der Revision fossiler Farnstämme des Karbons und Perms konnten Abbildungsoriginale der Paläobotaniker Stenzel (1889, 1906) und Rudolph (1906) in der Geologischen Bundesanstalt (GBA) in Wien wiederentdeckt werden. Aus diesem Anlass wurde die bewegte Forschungshistorie der wenigen Exemplare von *Asterochlaena laxa* nachgezeichnet, einer seltenen Art silifizierter Baumfarne aus dem Oberkarbon von Flöha und dem Unterperm von Chemnitz. In der GBA konnte das ebenfalls verschollen geglaubte Typusmaterial zu dem Kletterfarn *Zygopteris scandens* (heute unter *Ankyropteris brongniartii* synonymisiert) aufgefunden werden. *Psaronius*-Baumfarne und *Medullosa*-Farnsamer im Bestand der GBA, die aus den versteinerten Wäldern von Nová Paka (Tschechien) und Chemnitz (Deutschland) stammen, wurden katalogisiert und werden hier erstmals vorgestellt. Recherchen in der Bayerischen Staatssammlung für Paläontologie und Geologie in München brachten ein bislang unbekanntes Stammstück des unikaten Baumfarns *Asterochlaena ramosa* zum Vorschein, das hier im Kontext seiner Sammlungsgeschichte abgebildet wird. Historische Katalogeinträge in den Senckenberg Naturhistorischen Sammlungen Dresden belegen nunmehr, dass dieser einzige Fund von *A. ramosa*, dessen Fundort seit der Erstbeschreibung durch Cotta (1832) als unbekannt galt, aus dem Unterperm von Chemnitz stammt.

1 Frank Löcse: Mineralien- und Lagerstättenkabinett St. Egidien, Achatstraße 1, 09356 St. Egidien. frank@loecse.de
2 Irene Zorn: Geologische Bundesanstalt, Neulinggasse 38, 1030 Wien. irene.zorn@geologie.ac.at
3 Lutz Kunzmann: Senckenberg Naturhistorische Sammlungen Dresden, Königsbrücker Landstraße 159, 01109 Dresden. lutz.kunzmann@senckenberg.de
4 Ronny Rößler: Museum für Naturkunde Chemnitz, Moritzstraße 20, 09111 Chemnitz und TU Bergakademie Freiberg, Institut für Geologie, Bernhard-von-Cotta-Straße 2, 09599 Freiberg. roessler@naturkunde-chemnitz.de

Palaeobotanical treasures from the petrified forests of Nová Paka (Czech Republic) and Chemnitz (Germany) – originals of Stenzel (1889, 1906) and Rudolph (1906) in the palaeobotanical collection of the Geological Survey of Austria in Vienna

Abstract

Palaeontological collections are likewise source and result of knowledge. As archives of Earth's and life's history, they do not only record spatio-temporal circumstances that do not exist anymore but accumulate the scientific contributions of several generations of researchers. By revising fossil fern stems from the Carboniferous and Permian, figured specimens of the palaeobotanists Stenzel (1889, 1906) and Rudolph (1906) have been re-discovered in the collection of the Geological Survey of Austria (GBA) in Vienna. In this context, the turbulent collection history has been tracked for the few specimens of the rare petrified tree fern *Asterochlaena laxa* known from the Upper Carboniferous of Flöha and the lower Permian of Chemnitz. Additionally, at GBA the type material of the climbing fern *Zygopteris scandens* (now synonymised as *Ankyropteris brongniartii*), previously believed to be lost, has been recently traced. *Psaronius* tree ferns and *Medullosa* seed ferns from the petrified forests of Nová Paka (Czech Republic) and Chemnitz (Germany) have been indexed in the GBA collection, and they are presented for the first time. Latest inquiries in the Bavarian State Collection of Palaeontology and Geology in Munich revealed a so far unknown stem fragment of the unique tree fern *Asterochlaena ramosa*. The latter is figured here within the scope of its collection history. Only now, a witness is provided of the locality of this single *A. ramosa* specimen. Previously regarded as unknown, we demonstrate the lower Permian of Chemnitz to be the locality and age for the unique *A. ramosa* specimen confirmed from historical catalogue entries at the Senckenberg Natural History Collections Dresden.

Einführung

Seit Beginn der systematischen paläobotanischen Forschung im frühen 19. Jahrhundert begleiten paläobotanische Sammlungen den vergleichsweise jungen Wissenschaftszweig. Die überwiegend privat initiierten frühen Aufsammlungen standen in der Tradition der naturkundlichen Kabinette des 18. Jahrhunderts (Barthel, 1994; Kunzmann, 2006). Sie gingen später nicht selten in öffentlichen Sammlungen auf und gestatten somit auch heute noch den Gewinn neuer paläobotanischer Erkenntnisse (Rößler, 1999). Sammlungen, die dagegen in Privathand verblieben, wurden meist zerstreut und sind für die Wissenschaft verloren.

Doch auch in öffentlichen Sammlungen befinden sich nicht mehr alle Objekte an ihrem ursprünglichen Platz. Ursache hierfür ist nicht nur die bewegte Geschichte des 19. und 20. Jahrhunderts, sondern auch das mehr oder weniger gut dokumentierte Tauschen und Verleihen einzelner Objekte (Löcse et al., 2017). Auch sind nicht alle Objekte, die Eingang in die Magazine gefunden haben, bereits adäquat erfasst. Es ist daher eine lohnende Aufgabe, in den Depots verschollen geglaubte Stücke zu identifizieren und der Forschung erneut zugänglich zu machen bzw. historische Stücke aufzufinden, die dank einer heute breiteren und fortgeschritteneren physikalisch-chemischen Methodik neue Erkenntnisse preisgeben. Besonders lohnenswert erscheint die gezielte Durchsicht der Sammlungen im Hinblick auf versteinerte Hölzer Mitteleuropas, da die frühen Funde den Gang der Paläobotanik als Wissenschaft maßgeblich beeinflusst haben. Insofern ist der Dokumentation, Pflege und dem Erhalt historischer Sammlungen eine große Bedeutung beizumessen.

Die Geologische Bundesanstalt (GBA) beherbergt mit etwa 300.000 Objekten eine paläontologisch-geologische Sammlung von internationalem Rang. Die bis auf das Jahr 1835 zurückgehenden Bestände umfassen überwiegend Belege aus den Ländern der ehemaligen kaiserlich-königlichen Monarchie (Meller, 2005; Zorn et al., 2007). Vor allem die zweite Hälfte des 19. und der Beginn des 20. Jahrhunderts brachten reichen Zuwachs an paläozoologischen wie paläobotanischen Objekten, darunter zahlreiche Makrofossilien aus dem Oberkarbon und Unterperm Böhmens, Deutschlands und Österreichs. Unter den Originalen im Bestand der GBA befinden sich unter anderem die Typen zu den von Krasser (1909, 1919) bearbeiteten triassischen Pflanzenfossilien, der oberkarbonischen Flora Štúrs (1885, 1887) und dem paläo- und neogenen Material zu von Ettingshausen (1851, 1852, 1854) (Meller, 2005; Zorn et al., 2007).

Abb. 1.
Die paläobotanische Sammlung der GBA ist seit der Neuaufstellung in der Neulinggasse 38 in einem Rollschranksystem untergebracht und für paläobotanische Forschungen zugänglich.

Das Interesse an der paläontologischen Sammlung ging im 20. Jahrhundert stark zurück, vor allem in den Jahren nach dem Zweiten Weltkrieg. Das änderte sich ab 1959 mit der kustodialen Tätigkeit des Paläontologen Rudolf Sieber (1905–1988), der mit einer Revision und Neuordnung der Bestände begann (Sieber, 1984; Hofmann, 2009). Nach dessen Pensionierung führte der Zoologe und Paläontologe Franz Josef Stojaspal (1946–2012) die Neuordnung in den Sammlungen der GBA fort (Zorn, 2012). Seinen Schwerpunkt legte Stojaspal auf die Typensammlung, die heute etwa 1.676 verifizierte Holotypen und 270 Lectotypen für Vergleichs- und Revisionsarbeiten zur Verfügung stellt (Zorn et al., 2007). Einen detaillierten Überblick über die wechselvolle Geschichte der Sammlungen der GBA geben Stojaspal (1999) und Steininger et al. (2018). Ab 2004 wurden die bis dahin verstreut gelagerten unterschiedlichen Sammlungsteile im Gebäudekomplex an der Neulinggasse 38 zusammengeführt (Abb. 1). Seitdem läuft der Aufbau einer objektbezogenen Datenbank, um zukünftig den geowissenschaftlichen Gesamtbestand der Sammlungen der GBA abzubilden (Meller, 2005).

Die Suche nach den europaweit versprengten silifizierten Stammresten der seltenen fossilen Farngattung *Asterochlaena* aus dem Jungpaläophytikum, zugehörige Beblätterung und Fruktifikation sind bislang nicht gefunden worden, führte im Sommer 2018 an die GBA. Die wenigen bekannten Bruchstücke des Farns wurden, wie im 19. Jahrhundert üblich, mehrfach geschnitten und bereits frühzeitig auf verschiedene paläobotanische Sammlungen in Europa verteilt. Erschwert diese Praxis bereits eine Bearbeitung der häufiger in den Sammlungen vertretenen Kieselhölzer wie Psaronien, Calamiten oder Koniferen, so stellt das frühere Verteilen der Stücke für die Neubearbeitung der selteneren, oft nur auf wenigen Funden basierenden Arten ein gravierendes Hindernis dar. Das verschafft ihnen zwar einen interessanten sammlungshistorischen Kontext, erfordert aber auch ein erhebliches Maß an finanziellen und personellen Ressourcen, um sie in zeitaufwändigen Recherchen aufzuspüren.

Welchen Umfang ein derartiges Unterfangen annehmen kann, illustrieren die Arbeiten von Sahni (1932) und Löcse et al. (2015, 2017), die jeweils den Verbleib der bislang nur am Gückelsberg bei Flöha (Deutschland) gefundenen verkieselten Stammreste der unikaten Farnarten *Zygopteris primaria* (Cotta, 1832) Stenzel, 1889 und *Tubicaulis solenites* (Sprengel, 1828) Cotta, 1832 recherchierten.

Der vorliegende Beitrag befasst sich vor allem mit der Sammlungshistorie seltener Farne der fossilen Gattungen *Asterochlaena* und *Ankyropteris* aus den versteinerten Wäldern von Nová Paka und Chemnitz, insbesondere mit den verschollen geglaubten Originalen zu Stenzel (1889, 1906) und Rudolph (1905) aus dem Bestand der GBA.

Carl Gustav Wilhelm Stenzel (1826–1905), Oberlehrer am Realgymnasium am Zwinger in Breslau (heute Wrocław, Polen), bearbeitete mit den Psaronien (Stenzel, 1854, 1906) und einer Reihe seltener Baum- und Kletterfarne (Stenzel, 1889) wiederholt Kieselhölzer der klassischen Fundstellen um Nová Paka und Chemnitz. Der junge Paläobotaniker Karl Rudolph (1881–1937) wandte sich bereits mit seiner Dissertation über die Psaronien (Rudolph, 1905) den paläophytischen Kieselhölzern zu.

Auch die wenigen in der Sammlung der GBA vorhandenen Medullosen werden angeführt. Zu ihnen ist ein historischer Gipsabguss zu stellen, der als mögliche Beblätterung von *Medullosa leuckartii* als *Taeniopteris schenkii* in die Literatur Eingang fand (Sterzel, 1876).

Neben besagten Originalen befinden sich an der GBA weitere Kieselhölzer, darunter solche aus dem tschechischen Radvanice (Radowenz) und Trutnov (Trautenau), Psaronien und zahlreiche Calamiten von Nová Paka und Chemnitz, auch Koniferen- und Cordaitenhölzer unterschiedlicher Lokalitäten. Vor allem die umfangreiche, weitgehend unbearbeitete Calamiten-Suite dürfte ein lohnendes Untersuchungsobjekt für zukünftige Arbeiten darstellen. Der Bearbeitungsgrad der Psaronien und einer der Medullosen legt eine zumindest beabsichtigte paläobotanische Untersuchung nahe. Die wenigen beiliegenden Etiketten stammen aus der Feder des Geologen, Paläontologen und späteren Direktors der k. k. Geologischen Reichsanstalt, Dionýs Rudolf Josef Štúr (1827–1893, Abb. 2).

Die Durchsicht der Sammlung ergab, dass einige der historischen Etiketten durcheinander, auch einzelne zum selben Fossil gehörige Teile in unterschiedliche Schubladen geraten waren. Soweit möglich, wurden die betreffenden Stücke und Etiketten wieder zusammengeführt. Nicht alle der beiliegenden Etiketten gestatten jedoch eine sichere Zuordnung der bezeichneten Stücke zu einem der beiden prominenten Fundorte Nová Paka und Chemnitz, da auf den Etiketten Neu Paka gelegentlich in die Nähe von Chemnitz gerückt wird, bzw. in der Vergangenheit zwischen Neu Paka und Chemnitz überhaupt keine Trennung vorgenommen wurde (Abb. 3).

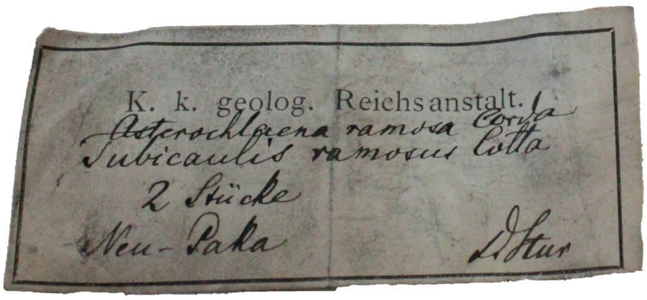

Abb. 2.
Historisches Etikett aus der Feder Štúrs. Das Etikett bezieht sich auf die beiden einzigen bekannten, heute zu *A. laxa* gestellten verkieselten Farnfragmente aus Nová Paka. Alle weiteren zu *A. laxa* gehörigen Funde stammen aus Chemnitz und Flöha. Bis zur Wiederentdeckung im Sommer 2018 galt die *A. laxa* aus Nová Paka nicht nur als verschollen, es war darüber hinaus nicht einmal bekannt, dass es sich um zwei Stücke handelt, da Stenzel (1889), der bislang einzige Bearbeiter der *A. laxa* von Nová Paka, nur ein Fragment erwähnt.

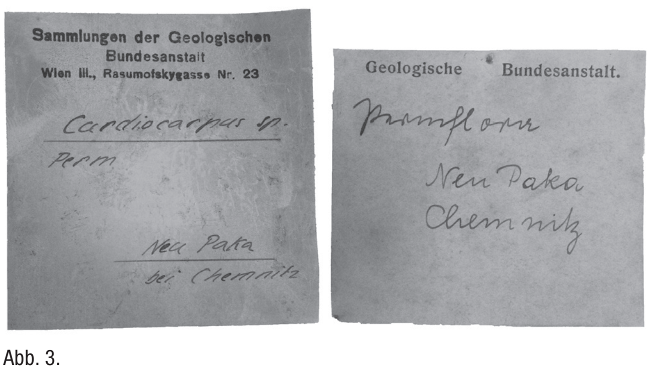

Abb. 3.
Die Fundorte Nová Paka und Chemnitz sind anhand der Etiketten nicht immer sauber voneinander getrennt worden.

Anhand einer Reihe von Merkmalskombinationen, beispielsweise der Fluoriterhaltung, die bislang nur von Chemnitz bekannt ist, oder der für zahlreiche Fossilien aus Nová Paka typischen Sedimentkruste und der markanten hellrötlichen Färbung der petrifizierten Hölzer, kann eine nachträgliche Zuordnung zu einem der beiden Fundorte meist zuverlässig erfolgen. Vielversprechende, in Kooperation zwischen der TU Bergakademie Freiberg und dem Museum für Naturkunde in Chemnitz weiterentwickelte Methoden, lassen, basierend auf der Untersuchung der Silifizierung mittels Kathodolumineszenz, zukünftig eine Zuordnung verkieselter Hölzer zu unterschiedlichen Fundorten und taphonomischen Gegebenheiten erwarten (Götze & Rößler, 2000; Trümper et al., 2018).

Fossile Farne des Oberkarbons und Perms

Farne sind eine überaus erfolgreiche, stratigrafisch weit verbreitete Pflanzengruppe. Sie erreichten im Oberkarbon und Unterperm eine besondere Vielfalt und Variabilität. Seit den Anfängen der Paläobotanik standen paläozoische Farne im Fokus der Wissenschaft (Cotta, 1832). In jüngerer Zeit haben Phillips (1974), DiMichele & Phillips (2002), Phillips & Galtier (2005, 2011) und Galtier & Phillips (1996, 2014) den Kenntnisstand zu Anatomie, Ontogenie, Phylogenie und Ökologie zahlreicher fossiler Farne zusammengefasst und durch erkenntnisreiche eigene Studien bereichert.

Morphologisch erreichen die Farne im Laufe ihrer Stammesentwicklung ein vielfältiges Formenspektrum, wobei ihr grundsätzlicher Bau bis heute unverändert geblieben ist (Stewart & Rothwell, 1993). Bei dem Farn-Sporophyten handelt es sich um eine phototrophe Pflanze mit großen mehr oder weniger stark gefiederten, ausladenden Wedeln, einer rhizom- bis baumartigen Sprossachse und Adventivwurzeln. Aufgrund seines unipolaren Wachstums bildet der Sporophyt keine primäre Wurzel aus. Sekundäres Dickenwachstum und Holz fehlen den Farnen bis auf wenige Ausnahmen. Neben kleinwüchsigen Formen, Kletterfarnen und Epiphyten gab es auch hoch aufragende imposante Baumfarne (DiMichele & Phillips, 2002).

Farne besetzten im Laufe des Devons mit kleinwüchsigen Formen neue ökologische Nischen. Häufig als Erstbesiedler vegetationsfreier Areale kam ihnen eine wichtige ökologische Rolle zu. Zum ausgehenden Oberkarbon hin entwickelten sie sich mit den stattlichen Baumfarnen zu einem bestandsbildenden Florenelement der tropischen Tiefland- und Feuchtwälder (Pfefferkorn & Thomson, 1982). Noch im unteren Perm dominieren sie die saisonal trockenen Feuchtoasen (Phillips, 1974; DiMichele & Phillips, 2002; Falcon-Lang, 2006).

Im Bestand der GBA befinden sich mit dem kleinen Baumfarn *Asterochlaena laxa* Stenzel (1889), dem Kletterfarn *Ankyropteris brongniartii* (Renault 1869) Bertrand 1907 und verschiedenen *Psaronius*-Baumfarnen jeweils strukturbietende Quer- und Längsschnitte von Farnen unterschiedlicher ökologischer Funktion und Anpassung.

Ökologisch bedeutsam sind unter anderem Unterschiede in ihrer Sporenentwicklung. Die fossilen Farne der GBA repräsentieren verschiedene Ordnungen, die sich im Reproduktionsmechanismus voneinander unterscheiden. Die Psaronien, die zu den eusporangiaten Marattiales gehören (Rudolph, 1905; Morgan, 1959; Stewart & Rothwell, 1993; DiMichele & Phillips, 2002), zeichnen sich durch eine enorme Sporenzahl aus, ein Vorteil bei der Besiedlung neuer Standorte. Das macht sie auch für palynologische Fragestellungen interessant (Juncal et al., 2019). Ähnlich hohe Sporenzahlen erreichen die Zygopteridales, zu denen *A. laxa* gehört. Deren Sporangien ähneln im Aufbau den leptosporangiaten Filicales (Stewart & Rothwell, 1993). Die Filicales des Paläophytikums, zu denen der Kletterfarn *A. brongniartii* gestellt wird, bilden deutlich weniger Sporen pro Sporangium aus (Mickle, 1980; Stewart & Rothwell, 1993; Phillips & Galtier, 2011).

Die Sporophyten sind in unterschiedlichen Erhaltungsformen überliefert, die Organzusammenhänge nur ausnahmsweise abbilden. Eine Zuordnung der unterschiedlich fossilisierten Pflanzenteile zu einer fossilen Art gelingt daher nur selten. Während in der historischen Literatur die Beschreibung einzelner Arten und damit im Zusammenhang stehende taxonomische Fragen im Mittelpunkt standen, rückt heute verstärkt die Entschlüsselung ökologischer und evolutionärer Zusammenhänge permokarbonischer Lebensgemeinschaften in den Vordergrund (Rößler, 2000; Krings et al., 2010, 2017).

Asterochlaena laxa Stenzel 1889 – Verworrene Wege eines seltenen fossilen Farns

Ausgangspunkt der Recherchen an der GBA war der bei Stenzel (1889: Taf. IV, Fig. 37) abgebildete unvollständige Querschnitt einer *A. laxa* aus Nová Paka, der sich einst „*im Museum der K. K. geolog. Reichsanstalt zu Wien*“ (Stenzel, 1889: 48) befand (Abb. 4). Noch vor einiger Zeit war die Anfrage nach dem Stück negativ beschieden worden: „*The Nová Paka fragmentary specimen must be regarded as lost (Dr. Stojaspal, Vienna, personal communication). Unfortunately, it was not possible to trace the specimen at its published depository, the collection of the former ‘kaiserlich-königlich geologische Reichsanstalt’, now Geologische Bundesanstalt of Austria at Vienna.*“ (Rößler & Galtier, 2002: 255). Die Recherche im „Catalogue of Palaeontological Types in Austrian Collections“ (www.oeaw.ac.at/oetyp/palhome.htm) ergab ebenso wenig einen Treffer, wie die in der hausinternen Datenbank. Im Vertrauen auf die Angaben von Stenzel (1889) wurde die paläobotanische Sammlung der GBA von uns schließlich von Hand durchmustert. Vor allem zwei Holzkisten aus der Kisten-Sammlung mit Kieselhölzern von Nová Paka erregten unsere Aufmerksamkeit. Das Material lagerte in den verschlossenen Kisten mindestens seit 1945. Eine der Kisten enthielt das gesuchte Fossil.

A. laxa ist ein kleinwüchsiger Baumfarn mit einer zentralen Aktinostele (Bertrand, 1907, 1911). Der Stele entspringen spiralig angeordnete, nach innen konkave, C-förmige Blattstielbasen. Zwischen ihnen gehen zahlreich Adventivwurzeln ab. Eine detaillierte Studie zur Anatomie des Farns legte Bertrand (1911) vor. Zuletzt referierten Rößler (2001a) und Rößler & Galtier (2002) über Anatomie, Verwandtschaftsverhältnisse, Fund- und Forschungsgeschichte der *A. laxa*. Bedeutsam ist das Stück aus Nová

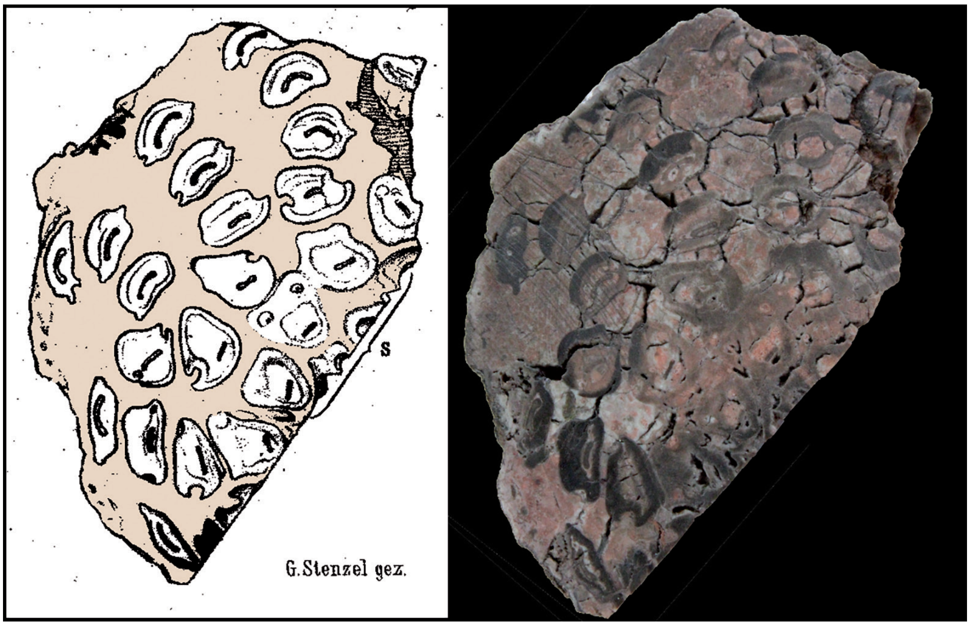

Abb. 4.
A. laxa aus Nová Paka in der für diesen Fundort typischen rötlichen Färbung. Links: Zeichnung aus Stenzel (1889: Taf. IV, Fig. 37). Rechts: Original zur Zeichnung im Bestand der GBA in Wien (GBA 1889/004/0001). Das Stück war lediglich geschnitten, nicht geschliffen oder poliert. Maßstab: 2 cm.

Paka vor allem seiner Herkunft wegen, denn alle anderen Exemplare stammen aus Sachsen.

Neuerliches Interesse an dem Farn flammte mit der Revision der Geologie und Paläontologie des oberkarbonischen Flöha-Beckens auf. Hierbei war der früher mit dem unterpermischen Zeisigwald-Tuff (Luthardt et al., 2018) unzutreffend parallelisierte Schweddey-Ignimbrit, eine der angegebenen Fundschichten der *A. laxa*, als oberkarbonisch erkannt worden (Löcse et al., 2013, 2015, 2019). Damit existierte der bislang ausschließlich mit dem Perm assoziierte Farn über einen Zeitraum von fast 20 Ma. Auch die stratigrafische Einstufung weiterer, im 19. Jahrhundert in Flöha gefundener seltener Taxa, wie *T. solenites* oder *Asterochlaena (Menopteris) dubia* (Cotta, 1832) Stenzel, 1889 war nun zu revidieren (Löcse et al., 2017).

Obgleich Stenzel (1889) von nur einem Stück aus der Sammlung der k. k. Geologischen Reichsanstalt in Wien berichtet, sind es tatsächlich zwei zusammengehörige Fragmente, die sich heute in der Sammlung der GBA befinden (Abb. 5). Das Stenzelsche Stück wurde geschnitten,

Abb. 5.
Überraschend stellte sich heraus, dass es nicht nur ein, sondern zwei Fragmente zur *A. laxa* aus Nová Paka in der Sammlung der GBA gibt (GBA 1889/004/0001–0002). Ein drittes Fragment, ein Längsschnitt, muss offenbar von den beiden zusammengehörigen Querschnitten zuvor abgetrennt worden sein. Maßstab: 2 cm.

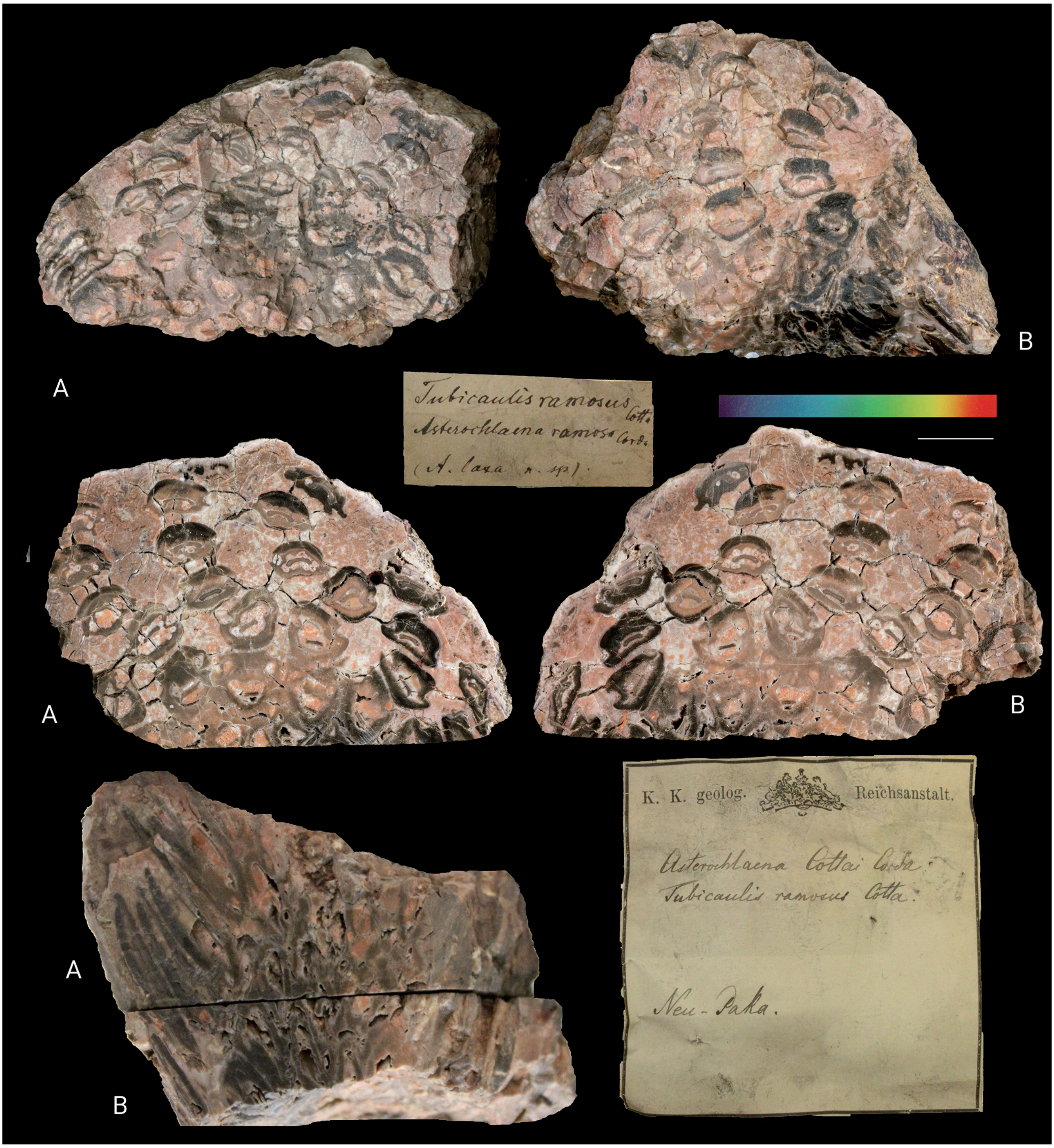

Abb. 6.
Übersicht über die in der GBA befindlichen Stücke der *A. laxa* aus Nová Paka. Die Quer- und Längsschnitte wurden neu geschliffen und poliert. Die Aktinostele fehlt. Die beiden Fragmente zeigen lediglich zahlreiche C-förmige Blattspurabgänge (A–GBA 1889/004/0001, B–GBA 1889/004/0002). Maßstab: 2 cm.

ohne die Schnittflächen anzuschleifen. Letzteres wurde erst nachträglich im Rahmen der vorliegenden Arbeit veranlasst. Bevor der historische Querschnitt angefertigt wurde, war von dem Stück, knapp entlang des äußeren Randes der Stele, ein Längsschnitt abgetrennt worden. Dieser Längsschnitt fehlt. Ein in Klammern gesetzter Hinweis „*A. laxa* n. sp.“ auf einem kleineren, später hinzugefügten Etikett verweist auf die durch STENZEL (1889) beschriebene Art (Abb. 6). Die ursprünglich durch Štúr dem Stück beigegebenen Etiketten geben noch *Asterochlaena ramosa* CORDA und *Tubicaulis ramosus* COTTA an (Abb. 2, 6).

Von COTTA (1832) bis BERTRAND (1911)

Die Geschichte der durch STENZEL (1889) etablierten Art *A. laxa* ist verworren und eng mit der auf COTTA zurückgehenden *A. ramosa* verknüpft. Sie beginnt mit der Dissertation des jungen Carl Bernhard Cotta (1808–1879; COTTA, 1832), der die Kieselhölzer aus der Sammlung seines Vaters, des Tharandter Forstgelehrten Johann Heinrich Cotta (1763–1844; SÜSS & RANGNOW, 1984), beschreibt. Cotta errichtet die neue Art *Tubicaulis* (?) *ramosus* basierend auf einem Einzelfund, der ausnahmsweise nicht der Sammlung seines Vaters entstammt. Die zwei bislang bekannten dünnen Scheiben befinden sich seither in der paläobotanischen Sammlung der TU Bergakademie Freiberg bzw. in den Senckenberg Naturhistorischen Sammlungen Dresden (ehemalige Staatliche Naturhistorische Sammlungen Dresden mit dem Museum für Mineralogie und Geologie). Die Dresdner Scheibe gelangte in den Jahren 1805/1806 über die Mineraliensammlung des Freiherrn Joseph Friedrich von Racknitz (1744–1818) in den Bestand des Königlichen Mineralienkabinetts im Zwinger zu Dresden (THALHEIM, 2006). Zur Herkunft der Freiberger Scheibe gibt es keine Unterlagen mehr. Den extrem dünnen Scheiben geschuldet, war sich Cotta der Zugehörigkeit des Fundes zu seiner neu errichteten Gattung *Tubicaulis* nicht sicher, was er mit dem Fragezeichen zum Ausdruck brachte (COTTA, 1832). Der Fundort der beiden Scheiben war Cotta unbekannt.

Da es Cottas Beschreibung an Tiefe fehlte, sah sich der aus dem böhmischen Reichenberg (heute Liberec, Tschechien) stammende Prager Botaniker und Paläobotaniker August Karl Joseph Corda (1809–1849) veranlasst, den Farn neu als *Asterochlaena Cottai* zu beschreiben (CORDA, 1845). Nomenklatorisch war das nicht korrekt, wurde dennoch durch einige Autoren übernommen (u.a. UNGER, 1850: 200; SCHIMPER, 1869: 697).

Bereits 1864 beschreibt STENZEL in GÖPPERT (1864: 41, Taf. VIII, Fig. 1, Taf. IX, Fig. 1a, b) zwei weitere Exemplare, die er nomenklatorisch zwar noch bei *T.* (?) *ramosus* belässt, aber bereits Unterschiede zum Cottaschen Exemplar aufzeigt: „*Im Thonstein bei Chemnitz in Sachsen. Wir besitzen von dieser Art nur zwei Stücke, ein grosses aus der Cotta'schen Sammlung im K. Mineralogischen Museum zu Berlin* [...] *und ein kleines in meiner Sammlung, auf unserer Taf. VIII in natürlicher Größe abgebildet. Beide sind Platten, quer aus einer cylindrischen Stammmasse herausgeschnitten*.“ (GÖPPERT, 1864: 41). Wie bereits BERTRAND (1911: 43) bemerkt, stellen beide Abbildungen bei GÖPPERT (1864) aber dasselbe Stück aus Göpperts Sammlung dar.

Auf Vermittlung von Alexander von Humboldt (1769–1859) wurde 1845 ein Teil der Cotta-Sammlung an die Friedrich-Wilhelms-Universität Berlin (heute Humboldt-Universität zu Berlin) verkauft (SÜSS & RANGNOW, 1984). Im zugehörigen handschriftlichen Verkaufskatalog, von B. Cotta am 27. Januar 1845 unterzeichnet, wird unter der Position 2994 „Tubicaulis ramosus wahrscheinlich aus Chemnitz“ angeführt, das Berliner Stück.

Die Sammlung H. Cottas war bereits 1839 zu Teilen durch B. Cotta an das British Museum (Natural History) London (Natural History Museum) verkauft worden (SÜSS & RANGNOW, 1984). Der Verkauf kam auf Vermittlung des Schottischen Botanikers Robert Brown (1773–1858) zustande: „*During a short visit to London, he* (Anm.: B. Cotta) *made the acquaintance of the botanist Robert Brown, and, on his return to Saxony to assume the post of teacher at the forestry institute in Tharandt, became the intermediary between the British Museum and his father, with the result that, in 1839, half of the latter's collection, containing several of the figured specimens* (Anm.: in COTTA, 1832), *was bought by the Trustees.*“ (LANKESTER, 1904: 280). So ist es nicht verwunderlich, dass neben dem bei GÖPPERT (1864) erwähnten, in Berlin befindlichen Exemplar der in Göttingen (Deutschland) und Strasbourg (Frankreich) wirkende Paläobotaniker Hermann Graf zu Solms-Laubach (1842–1915) ein weiteres Stück, „*eine von Cotta herstammende Querschnittsplatte im geol. Dep. des British Museum […] zu sehen Gelegenheit hatte*“ (SOLMS-LAUBACH, 1887: 177). Das Stück ist auch bei KIDSTON (1886: 11) aufgelistet: „*A portion of the specimen figured by Cotta as Tubicaulis (?) ramosus, […], is in the Collection*.“. Da COTTA (1832) ausdrücklich darauf hinweist, nur die beiden eingangs erwähnten, heute zu *A. ramosa* gestellten Scheiben aus den Sammlungen in Dresden (Deutschland) und Freiberg (Deutschland) zu kennen, gelangten die von Göppert im Berliner und die durch Solms-Laubach im Londoner Teil der Cotta-Sammlung ausfindig gemachten Scheiben wohl erst nach 1832 in die Sammlung seines Vaters.

Schließlich war es STENZEL (1889), der im Rahmen seiner *Tubicaulis*-Revision innerhalb der Cordaschen Gattung *Asterochlaena* die drei Untergattungen *Menopteris*, *Asterochlaena* und *Clepsydropsis* etablierte. Zu *Asterochlaena* stellte Stenzel seine neue Art *A. laxa* und die Cottasche *A. ramosa*. Bei letzterer beließ Stenzel lediglich die beiden Cottaschen Stücke. In seiner *A. laxa* vereinte er alle anderen Stücke, die bislang unter *T.* (?) *ramosus* bzw. *A. Cottai* versammelt waren (GÖPPERT, 1864).

Die Mehrzahl der damals bekannten Funde von *A. laxa* und *A. ramosa* konnte Stenzel selbst vergleichen. Das sind zwei Scheiben aus der Sammlung Schreckenbach und eine Scheibe aus der Sammlung Leuckart, heute zur Gänze im Museum für Naturkunde in Chemnitz (*A. laxa*), von den Stücken aus der Cotta-Sammlung dasjenige aus Berlin (*A. laxa*), die Scheiben aus Freiberg (*A. ramosa*) und Dresden (*A. ramosa*), die Scheibe aus der Göppertschen Sammlung im Mineralogischen Museum Breslau (*A. laxa*) „*und endlich das in der k. k. geologischen Reichsanstalt in Wien befindliche, neuerdings bei Neu-Paka in Böhmen aufgefundene* (Anm.: Stück *A. laxa*)*, dessen Versteinerungsmasse der für viele Pflanzenreste dieses Fundorts bezeichnende rötliche-graue Kiesel ist.*“ (STENZEL, 1889: 18). Von den Stücken, die STENZEL (1889) vorlagen, befinden sich bis auf das Exemplar aus der Sammlung Göppert alle an ihrem ursprünglichen Platz. Die Londoner Scheibe, auf die SOLMS-LAUBACH (1887) und KIDSTON (1886) verweisen, lag Stenzel nicht vor.

Das Göppertsche Stück muss derzeit als verschollen gelten. Stenzel schreibt dazu: „*Schon vor vielen Jahren übergab mir Göppert sein Exemplar des Tubicaulis ramosus (Asterochlaena laxa m.) zur Untersuchung*“ (STENZEL, 1889: 1). Allerdings ist davon auszugehen, dass Stenzel das Stück zurückgab, denn es lässt sich bis zu Paul Charles Édouard Bertrand (1879–1944) verfolgen, der es im Rahmen seiner umfangreichen Bearbeitung zygopteridér Farne beschreibt und auch zeichnet (BERTRAND, 1911: 43–44, Fig. 5). Er fotografierte es 1907 während eines Breslau-Aufenthaltes: „*J'ai pu étudier l'échantillon original lors d'un voyage à Breslau en 1907 et J'adresse ici mes remerciments à MM. les Professeurs Frech et Gurich, qui ont bien voulu m'autoriser à en prendre une photographie.*“ (BERTRAND, 1911: 43). Eine bebilderte Dokumentation, die Bertrand nach Abschluss seiner Arbeiten Johann Traugott Sterzel (1841–1914), dem Bürgerschullehrer, Paläontologen und erstem Direktor der Städtischen Naturwissenschaftlichen Sammlungen Chemnitz übergab, enthält ein Foto des Göppertschen Exemplars.

Schließlich stellen TANSLEY (1907) und SCOTT (1909) *Asterochlaena* in die Nähe der Zygopteridales. Aber erst BERTRAND (1907, 1909a, b) klärt den Zusammenhang anhand der Struktur der Blattspurbündel auf. Einen gewissen Schlusspunkt liefert die Bearbeitung durch BERTRAND (1911). Ihm lag für seine Untersuchungen neben der Scheibe aus der Sammlung Göppert eines der beiden Abbildungsoriginale zu Stenzels neuer Art aus Chemnitz vor (STENZEL, 1889: Taf. IV, Figs. 33, 34), Material aus der Sammlung Solms-Laubach und eine Scheibe aus dem „Musée géologique de Fribourg en Brisgau". Von der Chemnitzer Scheibe fertigte Bertrand zahlreiche Dünnschliffe an, die er auch abbildet (BERTRAND, 1911: Figs. 1, 2, Pl. I, Fig. 1, Pl. II, Figs. 1–10, Pl. III, Figs. 11–21, Pl. IV, Figs. 22, 27–28). Er gibt für das Stück die alte Objektnummer T2 an. Mit Verweis auf diese Nummer ist die Scheibe im historischen handschriftlichen „Katalog der Kieselhölzer und Tuffabdrücke" (Bestand des Museums für Naturkunde in Chemnitz) unter der Nummer 519 verzeichnet mit den ergänzenden Bemerkungen: „*Schreckenbach, Flöha, Original zu Stenzel Tubicaulis 1889*".

Den letzten Nachweis für das verschollene Stück aus der Göppertschen Sammlung liefert ebenfalls BERTRAND (1911). Eine Durchmusterung der Sammlung am heutigen Instytut Nauk Geologicznych/Muzeum Geologiczne „Henryk Teisseye" in Wrocław, Polen, im Jahr 2005 blieb bezüglich *A. laxa* ergebnislos. Auch das Material aus der Sammlung Solms-Laubach muss derzeit als verschollen gelten. In Strasbourg sind heute keine Stücke mehr auffindbar. In den 1960er Jahren gab es in Strasbourg einen größeren Brand, dem wohl auch die Sammlung Solms-Laubach zum Opfer fiel (freundl. Mitteilung von Jean-Pierre Laveine, Lille, Frankreich). Ein ähnlich ungünstiges Schicksal ereilte die Scheibe in der Freiburger Sammlung. Die geowissenschaftliche Sammlung der Universität Freiburg im Breisgau (Deutschland), auf die sich die Bezeichnung „Musée géologique de Fribourg en Brisgau" bei BERTRAND (1911) und anderen bezieht, wurde am 27. November 1944 beim alliierten Bombenangriff auf Freiburg komplett zerstört (freundl. Mitteilung von Norbert Wiedemann, Museum Natur und Mensch, Freiburg im Breisgau). In London sind heute am British Museum (Natural History Museum) zwei zusammengehörige Scheiben von *A. laxa* nachweisbar. Das Stück aus der Cotta-Sammlung wurde offenbar geteilt.

Die Sammlung Güldner, ein Flohmarktfund, wiederentdeckte Stücke in Wien und München

In der Folgezeit gelangten weitere Exemplare von *A. laxa* über private Sammler in öffentliche Sammlungen, vor allem nach Chemnitz. Ein mehrfach abgebildetes längeres Stammstück befindet sich im Besitz eines Erben der Max Güldner-Sammlung und ist derzeit nicht zugänglich (BARTHEL, 1976: Taf. 11, Fig. 15; RÖßLER, 2001a: 95; 2002: Abb. 11; RÖßLER & GALTIER, 2002: Pl. VI, Fig. 2). Im Jahr 1997 entdeckte der damalige Vorstandsvorsitzende des Freundeskreises des Museums für Naturkunde Chemnitz e.V., Dr. Karl-Heinz Müller, auf einem Thüringer Flohmarkt ein Endstück von *A. laxa*. Er erwarb es für ein Taschengeld und übergab es dem Museum für Naturkunde in Chemnitz (RÖßLER, 2001a). Die jüngste Wiederentdeckung stellt das zweite Fragment von *A. laxa* aus Nová Paka im Bestand der GBA dar.

Eine weniger rühmliche Rolle spielt dagegen der aus Bärwalde bei Zwickau (Deutschland) stammende Apotheker und Sammler Friedrich Nindel (1887–1960). Seine 1961 durch die Humboldt-Universität zu Berlin angekaufte Sammlung (SÜSS & RANGNOW, 1984) enthält zwei Fragmente von *A. laxa*, ein dem Etikett nach zu urteilen 1914 gefundenes Stück mit der Nindel-Nr. 538 und ein dünnes Endstück mit der Nindel-Nr. 681. Das Endstück ist vom Stenzelschen Original (STENZEL, 1889: Taf. IV, Figs. 35, 36) abgeschnitten worden, das sich Stenzel zufolge in der Chemnitzer Sammlung befinden sollte. In dem oben erwähnten „Katalog der Kieselhölzer und Tuffabdrücke" wird das Stämmchen auch unter der Nr. 194 geführt mit Verweis auf „*Schreckenbach, Orig. zu Stenzel Tubicaulis IV, Fig. 35*". Aber in Chemnitz ist das Stenzelsche Original nicht mehr nachweisbar. Es befindet sich heute in der Berliner Sammlung. Unter welchen Umständen es dorthin gelangte, ist ungeklärt. Den Nindel-Nummern nach zu urteilen, gelangte das dünne, vom Original abgetrennte Endstück aus der Nindel-Sammlung erst nach 1914 in Nindels Besitz. Das war nach dem Tod Sterzels. Nindel hatte zu dieser Zeit freien Zugang zur Chemnitzer Sammlung. Auch von dem seltenen Baumfarn *T. solenites* hatte Nindel mehrere Fragmente in seinen Besitz gebracht, um sie in seiner eigenen Sammlung vertreten zu sehen und ferner, um damit andere seltene/wertvolle Belege im Tausch zu erlangen (LÖCSE et al., 2015). Auch befanden sich in seinem Nachlass Sammlungsstücke und Literatur aus dem Eigentum der Städtischen Naturwissenschaftlichen Sammlungen Chemnitz.

Bei einem Besuch der Bayerischen Staatssammlung für Paläontologie und Geologie in München konnte unerwartet ein drittes, zu *A. ramosa* gehörendes Stück aufgefunden werden, das bislang noch nie in der Sammlungs- und Forschungsgeschichte erwähnt worden war. Es handelt sich um ein Endstück, das unmittelbar an die Dresdner Scheibe anschließt, aber nicht nachträglich von dieser abgeschnitten worden sein kann, da bereits COTTA (1832), Bezug nehmend auf die Stücke aus Freiberg und Dresden, von Scheiben berichtet „*beide [...] so dünn geschnitten, dass man nicht beurtheilen kann, ob die Gefässbündel parallel oder convergirend stehen*." (COTTA, 1832: 23). Auf der Rückseite eines Etiketts zum Münchner Stück notiert am 16. Februar 2002 Walter Jung (1931–2018), Paläobotaniker und langjähriger Kustos der Münchner Sammlung, dass es sich bei dem Stück um eine „*Scheibe mit Ende*" handelt, die an die Dresdner Scheibe anschließt (Abb. 7). Auf der Vorderseite findet sich ein Hinweis „ehedem Slg. Deutsches Museum" (Abb. 7). Dieses dritte Stück birgt einiges Potenzial, denn „*ob die erkannten Merkmale der A. ramosa und A. laxa wirklich natürliche Taxa trennen oder nur verschiedene ontogenetische Stadien bzw. zufällige Schnittlagen aus unterschiedlichen Positionen am Stamm repräsentieren, kann hier nicht mit Sicherheit gesagt werden. Leider gibt es zu wenig Material.*" (RÖßLER, 2001a: 95). Ein zweites Etikett, geschrieben am 1. Februar 2005, suggeriert, dass im Rahmen einer Sonderschau am Jura-Museum in Eichstätt (Deutschland) das Endstück der *A. ramosa* der Öffentlichkeit gemeinsam mit anderen Kieselhölzern aus der Münchner Sammlung präsentiert worden war (Abb. 7). Von dort gelangte es zurück nach München, war aber zunächst nicht auffindbar. Eine intensive Suche im Februar 2019 förderte das an anderer Stelle einsortierte Stück zu Tage (Abb. 7). Neben den beiden dünnen Scheiben in Freiberg

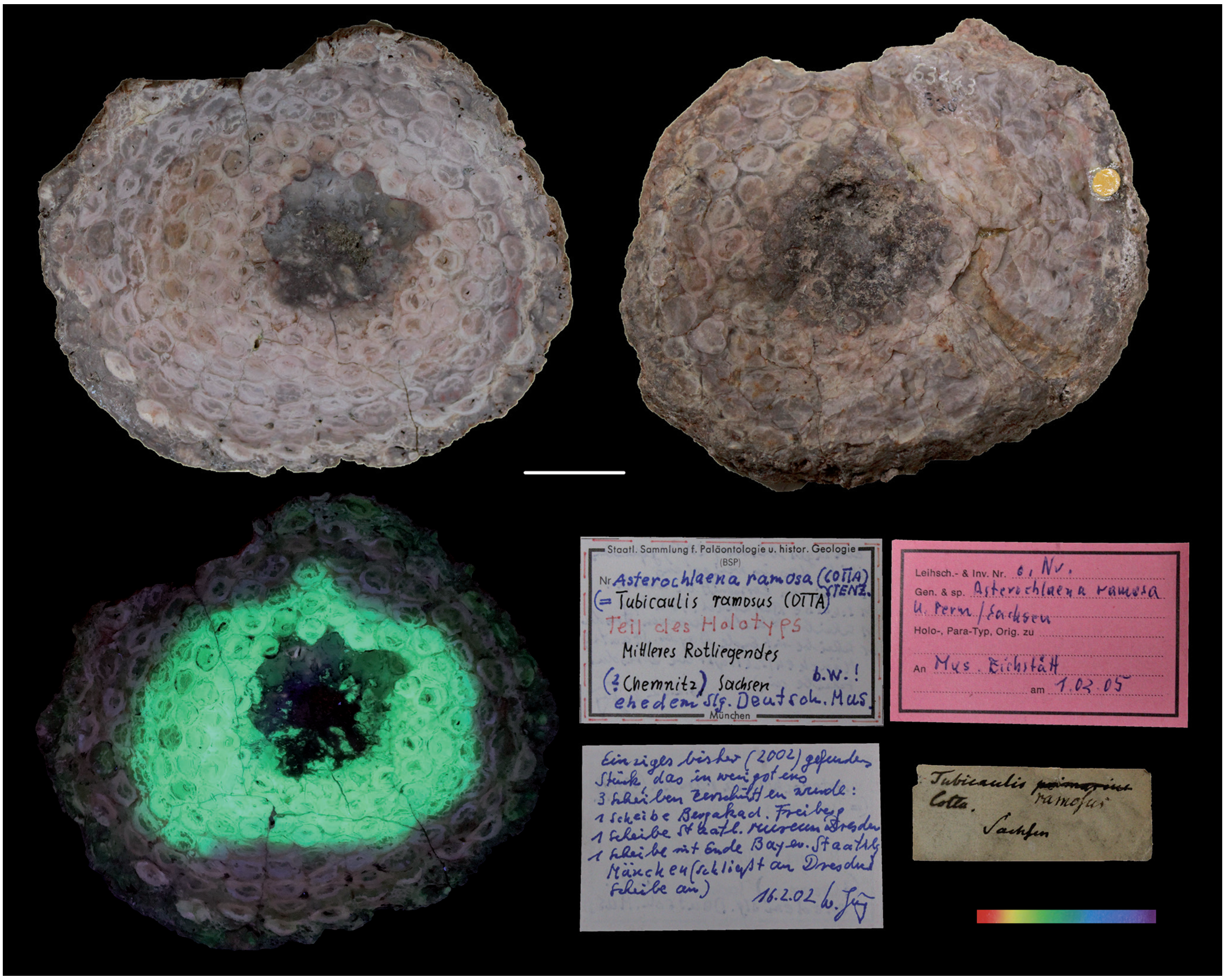

Abb. 7.
Neu aufgefundenes Endstück zur *A. ramosa* in der Bayerischen Staatssammlung für Paläontologie und Geologie in München (SNSB-BPSG 1950 XXXV 506). Die Scheibe fluoresziert unter UV-Licht (254 nm). Das Originaletikett (unten rechts) verweist auf Sachsen als Fundort. Zwischenzeitlich war das Stück im Rahmen der Sonderschau „Steinerne Pflanzenstrukturen" ausgeliehen worden (rotes Etikett).

und Dresden steht damit ein drittes Stück *A. ramosa* für paläobotanische Untersuchungen zur Verfügung, alle von ein und demselben Individuum. Das Endstück war am 30. Juli 1930 durch den in Halle/Saale (Deutschland) geborenen Physiker Oskar Knoblauch (1862–1946), seit 1910 mit Lehrstuhl an der Technischen Universität München tätig, dem Deutschen Museum gestiftet worden. Unter UV-Licht (254 nm) zeigt das Stück im zentralen Teil eine markante grüne Fluoreszenz (Abb. 7), deren Ursache im Kristallgitter des Versteinerungsmediums SiO_2 liegt und Gegenstand weiterer Untersuchungen ist.

Fundortnachweise

Die Fundortangaben legen nahe, dass der Farn *A. laxa* sowohl in oberkarbonischen, als auch in unterpermischen Schichten vorkommt und somit eine bemerkenswerte stratigrafische Reichweite aufweist. Die zwei Schreckenbachschen Scheiben stammen Sterzel zufolge aus den oberkarbonischen Schichten vom Gückelsberg in Flöha: *„In der städtischen Mineraliensammlung zu Chemnitz (Schreckenbachsche Sammlung) befinden sich zwei Exemplare hiervon, das eine von Oberforstrath Cotta, das andere vom Oberförster Steeger in Chemnitz. Beide sind von Gückelsberg."* (Sterzel, 1875: 104). Die Stücke gelangten nach 1830 in den Besitz Schreckenbachs: *„Diese Sammlung* (Anm.: Sammlung Schreckenbach) *wurde 1830 zum grössten Theile bei einem Brande zerstört, später aber wieder derartig ergänzt, dass sie zu den vollständigsten und reichhaltigsten bezüglich der Chemnitzer Holzversteinerungen gehört. Im Juni 1875 ist sie für die hiesige städtische Mineraliensammlung angekauft worden. … Es sind ferner darin vertreten die seltenen Tubicaulis-Arten (1 Zyg. prim., 1 Selenochl. Reichi, 2 Asterochl. Cottai), ..."* Sterzel (1875: 127). Es sind diese beiden Stücke aus der Sammlung Schreckenbach, die Stenzel abbildet. Damit machte Stenzel ungewollt die beiden einzigen Funde aus dem Oberkarbon zu Abbildungsoriginalen seiner neuen Art (Tab. 1). Alle weiteren bislang aufgetauchten Fundstücke sind den unterpermischen Schichten bei Chemnitz und Nová Paka zuzuordnen, soweit der Fundort überhaupt bekannt ist. Bezeichnenderweise vermerkt Nindel auf dem Etikett zu seinem dünnen Endstück als Fundort Flöha-Gückelsberg.

Die seit fast 190 Jahren (Cotta, 1832) mit unbekanntem Fundort in der Literatur präsenten Scheiben von *A. ramosa* stammen, wie das neu entdeckte Münchner Endstück, aus Chemnitz. Das belegen historische Aufzeichnungen im Bestand der Senckenberg Naturhistorische Sammlungen Dresden. Die Dresdner Scheibe ist unter der Nr. 2703 im Katalog zur Racknitz-Sammlung unter „Versteinertes Holz, Sachsen, 1 Taler 12 Groschen“, verzeichnet. Der Racknitz-Katalog enthielt keine genaueren Fundortangaben. Diese waren auf den zugehörigen Etiketten notiert (freundl. Mitteilung Klaus Thalheim, Kustos der mineralogischen Sammlungen SNSD). Die Originaletiketten zur Dresdner Scheibe sind nicht erhalten. Dem Mineralogen Johann Heinrich Gottlieb Gössel (1780–1846) verdankt die mineralogisch-geologische Sammlung in Dresden einen handschriftlich verfassten, vierbändigen „Katalog der Königlich Saechsischen mineralogischen Sammlung“ (KÜHNE et al., 2006). Der Katalog befindet sich noch heute im Besitz der Dresdner Sammlung. Gössel listet akribisch den Bestand einschließlich der Neuzugänge auf und übernimmt auch Informationen von den Etiketten der einzelnen Stücke. Der Eintrag unter Nr. 94 „*Holzstein, graulichweiß und röthlich, mit dicht aneinander liegenden runden Röhren, bräunlichgrauer Rinde und aschgrauen mit Quarz ausgefüllten Kern, eine besondere Abänderung des Starsteins als dünne polierte Platte; von Chemnitz, 4 1/4 ... 3* 1/2 [Zoll; 1 Zoll = 2,35 cm] *R. no. 2703.*“ (GÖSSEL, 1846, Bd. 2: 377) bezieht sich auf *A. ramosa*. Es kann nicht davon ausgegangen werden, dass zu Beginn des 19. Jahrhunderts die nah beieinanderliegenden Fundorte Chemnitz und Flöha zuverlässig auseinandergehalten wurden. Für Chemnitz als Fundort spricht neben der Notiz bei Gössel aber die Tatsache, dass vor 1805 am Gückelsberg bei Flöha praktisch keine Fossilfunde gemacht worden sind (LÖCSE & RÖßLER, 2018a).

Von den wenigen Funden zu *A. laxa* und *A. ramosa* gelangten vermutlich mehrere Stücke in Privatsammlungen, denn die nachweisbaren Fragmente passen trotz Berücksichtigung etwaiger Schnittverluste nicht lückenlos aneinander. Es ist nicht ausgeschlossen, dass von dort weitere Stücke unbeachtet Eingang in öffentliche Sammlungen fanden. Auch zukünftig lohnt sich daher ein kritischer Blick in die Depots.

Nach Fertigstellung des Manuskriptes wurde bekannt, dass in Lucknow (Uttar Pradesh, Indien) in einem Gedenkstein anlässlich der Gründung des ehemaligen Birbal Sahni Instituts für Paläobotanik neben weiteren seltenen Chemnitzer und Flöhaer Kieselhölzern eine *A. laxa* eingemauert worden ist.

In Tabelle 1 sind die aktuellen Aufbewahrungsorte der wenigen bekannt gewordenen Stücke von *A. laxa* und *A. ramosa* einschließlich historischer wie aktueller Objektnummern zusammengestellt.

Nachweis	**Nummer/Status**	**Herkunft**	**Fundort**
Asterochlaena laxa			
MfNC	K1052 **(Lectotypus)**	Slg. Schreckenbach (T2, 519 Kieselholzkatalog)	Flöha
MB	MB.Pb.2014/0246(H/681)	Slg. Schreckenbach (194 Kieselholzkatalog)	Flöha
MfNC	K5229	Hilbersdorf (201 Kieselholzkatalog)	Chemnitz
MfNC	K5228	O. Weber/Hilbersdorf (478 Kieselholzkatalog)	Chemnitz
MfNC	K6762	von Dr. K.-H. Müller auf Flohmarkt erworben	?Chemnitz
MfNC	K4799	B. Winkler/Chemnitz (1772 Kieselholzkatalog)	Chemnitz
MB	MB.Pb.2005/1215(H/678)	Slg. Cotta (2994 Cotta-Katalog)	Chemnitz
MB	MB.Pb.2014/0250(H/679)	Slg. Nindel (538)	Chemnitz
MB	MB.Pb.2014/0251(H/680)	Slg. Nindel (681), abgeschnitten von MB.Pb.2014/0246(H/681)	Flöha
GBA	GBA 1889/004/0001		Nová Paka
GBA	GBA 1889/004/0002		Nová Paka
NHM	13605a	Slg. Cotta	Chemnitz
NHM	13605b	Slg. Cotta	Chemnitz
BSI	Foundation Stone		?Chemnitz
Privatbesitz	ohne Nummer	Slg. Güldner	Chemnitz
–	verschollen	Slg. Solms-Laubach	Chemnitz
–	verschollen	Slg. Freiburg im Breisgau	Chemnitz
–	verschollen	Slg. Göppert	Chemnitz
–	verschollen	Slg. Leuckart (No. 98, 195a Kieselholzkatalog)	Chemnitz
–	verschollen	Slg. Leuckart (No. 99, 195b Kieselholzkatalog)	Chemnitz
Asterochlaena ramosa			
BAF	BAF 175/2 **(Lectotypus)**		Chemnitz
SNSD	SaP 1898	Slg. Racknitz (2703 Racknitz-Katalog, 94 Gössel-Katalog)	Chemnitz
BSPG	SNSB-BPSG 1950 XXXV 506	Slg. Knoblauch (63443, E36)	Chemnitz

Tab. 1.
Überblick über Herkunft und Verbleib der einzelnen Fragmente von *A. laxa* und *A. ramosa*. Von *A. laxa* sind heute Stücke im Museum für Naturkunde in Chemnitz (MfNC), der paläobotanischen Sammlung der Humboldt-Universität Berlin (MB), dem Natural History Museum London (NHM), Birbal Sahni Institute of Palaeosciences (BSI) und der Geologischen Bundesanstalt in Wien (GBA) nachweisbar. Von *A. ramosa* befinden sich heute Stücke in der Bayerischen Staatssammlung für Paläontologie und Geologie (BSPG), den Senckenberg Naturhistorischen Sammlungen Dresden (SNSD) und der paläobotanischen Sammlung der TU Bergakademie Freiberg (BAF). In der zweiten Spalte sind historische Objektnummern angegeben. Sie entstammen entweder beiliegenden Etiketten oder historischen handschriftlichen Katalogen: MfNC – Katalog der Kieselhölzer und Tuffabdrücke (Kieselholzkatalog), MB – Allgemeiner Katalog der Cottaischen Versteinerungssammlung (Cotta-Katalog), SNSD – Katalog zur Racknitz-Sammlung (Racknitz-Katalog), Katalog der Königlich Saechsischen mineralogischen Sammlungen in Dresden. A – Katalog der oryktognostischen Sammlung (Gössel-Katalog).

Psaronien – landschaftsprägende Florenelemente jungpaläophytischer Ökosysteme

Die wissenschaftliche Erstbeschreibung der imposanten Baumfarne geht auf Cotta (1832) zurück, der ursprünglich zwei Arten, *Psaronius asterolithus* und *P. helmintholithus*, aufstellte. Bereits ein reichliches halbes Jahrhundert später führt Stenzel (1906) nicht weniger als 32 Arten an, zusätzlich in Formen untergliedert. Mittlerweile existiert eine kaum zu überblickende taxonomische Vielfalt (Corsin, 1955). Die Zahl der natürlichen Arten dürfte dagegen deutlich geringer gewesen sein. Und obgleich auch mehr als 100 Jahre später eine Revision der Gattung nicht in Sicht ist, haben zahlreiche Studien den Kenntnisstand zu Morphologie und Anatomie enorm vermehrt (Stewart & Rothwell, 1993; Taylor et al., 2009), was neben den frühen Bearbeitern vor allem der Untersuchung neuer Funde in den nordamerikanischen Steinkohlevorkommen zu verdanken ist (vgl. u.a. Morgan, 1959; Stidd, 1971; Mickle, 1984).

Die zwei Holzkisten aus der Kisten-Sammlung der GBA enthielten zahlreiche Psaronien aus dem Unterperm von Nová Paka, die neu in die paläobotanische Sammlung der GBA eingeordnet werden konnten. Die der Sammlung beiliegenden Etiketten tragen die Handschrift Štúrs (Abb. 2). Mit ihr versehen sind schmale Streifen bzw. rechteckige kleine Zettel aufgeklebt. Die Psaronien aus den Holzkisten entstammen ursprünglich einer umfangreicheren Suite, wie aus der fortlaufenden Nummerierung zahlreicher Stücke hervorgeht. Die gleiche Nummerierung tragen einige der Psaronien, die bereits in den Schubladen eingeordnet waren. Da dort oft Etiketten fehlen, geben die Nummern einen Hinweis auf Nová Paka als Fundort im Unterschied zu Chemnitzer Stücken, die vereinzelt ebenfalls in den Schubladen vertreten sind. Bei mehreren Psaronien in den Schubladen sind die Etiketten im Lauf der Jahre verloren gegangen, worauf bereits Meller (2005) hingewiesen hat. Einige der Stücke mit fehlendem Etikett, sowohl in den Schubladen, als auch den Holzkisten, fügen sich nach Art und Umfang der Bearbeitung in die historische Sammlung ein und könnten einigen fehlenden Nummern entsprechen. Zu etlichen Stücken, insbesondere denen aus Nová Paka, konnten passende Gegenstücke aufgefunden werden. Der überwiegende Teil der Stücke ist mit einem historischen Schliff versehen.

Eine Notiz bei Stenzel (1889: 31) legt nahe, dass ihm die Psaronien-Sammlung durch Štúr zur Bearbeitung vorgelegt worden war: „*Die Conglomerate des Rothliegenden von Neu-Paka haben früher Corda einen großen Theil der schönen von ihm beschriebenen Psaronien geliefert; in neuerer Zeit sind seine Schätze verkieselter Pflanzen durch die Bemühungen von Štúr wieder erschlossen worden. Die dort neu aufgefundenen, z. Th. prachtvollen Psaronien, welche mir von demselben zur Untersuchung und Bestimmung übergeben worden sind, gedenke ich in einer neuen Bearbeitung dieser Gattung zu behandeln.*“ Tatsächlich abgebildet hat Stenzel in der angekündigten Arbeit dann allerdings nicht das aufbereitete Material aus der k. k. Geologischen Reichsanstalt, sondern überwiegend Chemnitzer Material, vorwiegend aus der Sammlung des Chemnitzer Fabrikanten Leuckart.

Abb. 8.
Vorder- und Rückseite eines *P. helmintholithus* (links, GBA 2019/008/0001) und *P. infarctus* (rechts, GBA 2019/008/0005) aus der Sammlung der GBA. Bei *P. infarctus* liegt ein kompletter, aus vermutlich taphonomischen Gründen abgeplatteter Querschnitt aus einem mittleren Stammabschnitt vor. Die zentralen Leitbündel sind von einem Luftwurzelmantel umgeben, dem randlich Sediment anhaftet. Maßstab: 2 cm.

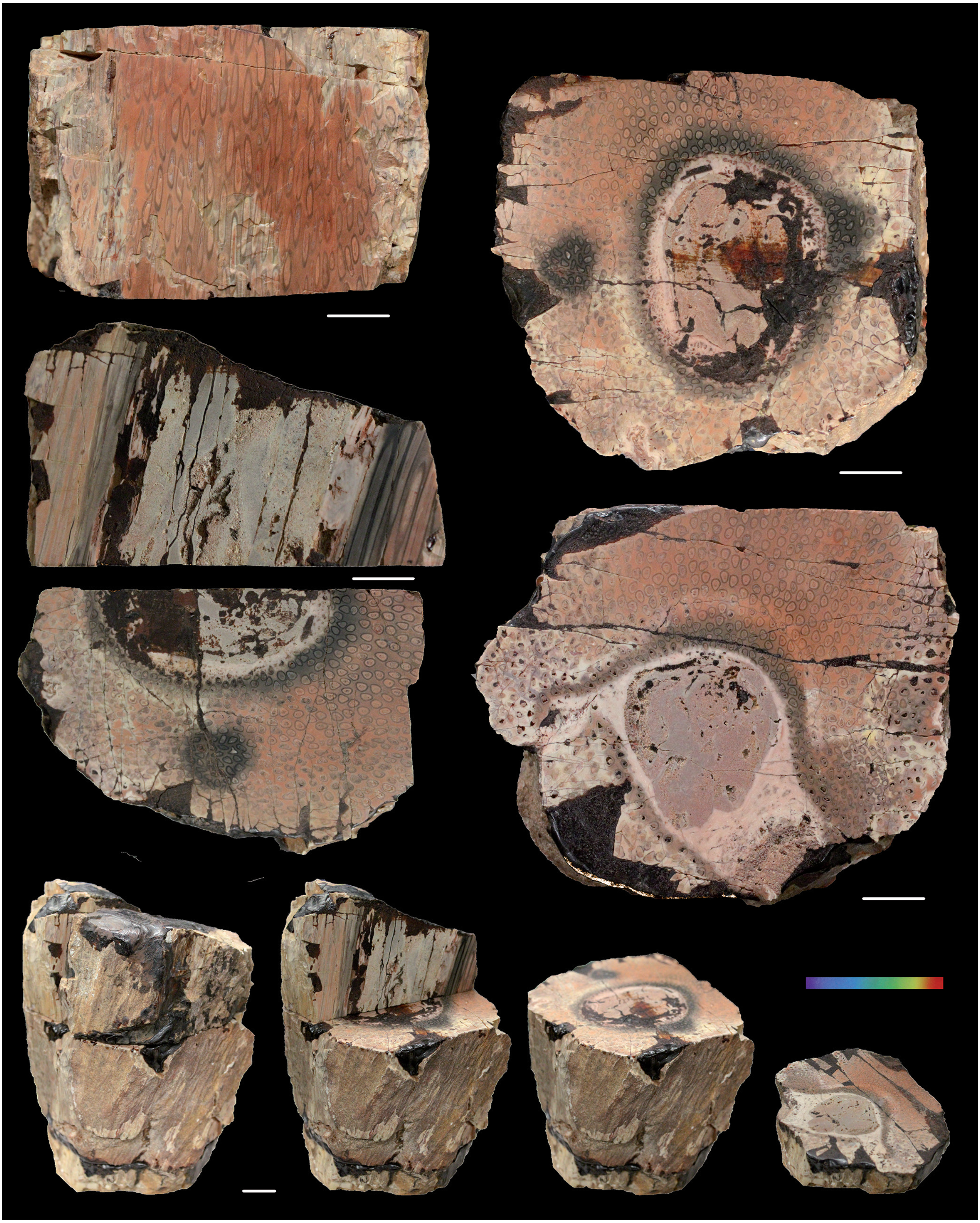

Abb. 9.
Vollständiger Querschnitt eines in vier größere Fragmente zersägten *Psaronius asterolithus* aus Nová Paka (GBA 2019/008/0008–0010). Die Längs- und Querschnitte sind geschliffen und poliert. Der eigentliche Stamm besteht aus sehr dünnen Leitbündeln, die von einem Luftwurzelmantel umgeben sind.

Aus der historischen Psaronien-Sammlung der k. k. Geologischen Reichsanstalt erhalten geblieben sind die Nummern 15, 32, 35, 60–61, 66–67, 70–74 und 77–78. Sie umfassen die historischen unrevidierten Taxa *P. asterolithus*, *P. haidingeri*, *P. helmintholithus*, *P. infarctus* und mehrere nicht näher bestimmte *Psaronius* sp. (Abb. 8–11). Die vorliegenden Stücke, zumal oft nur vom Wurzelmantel stammend, können nicht näher bestimmt werden.

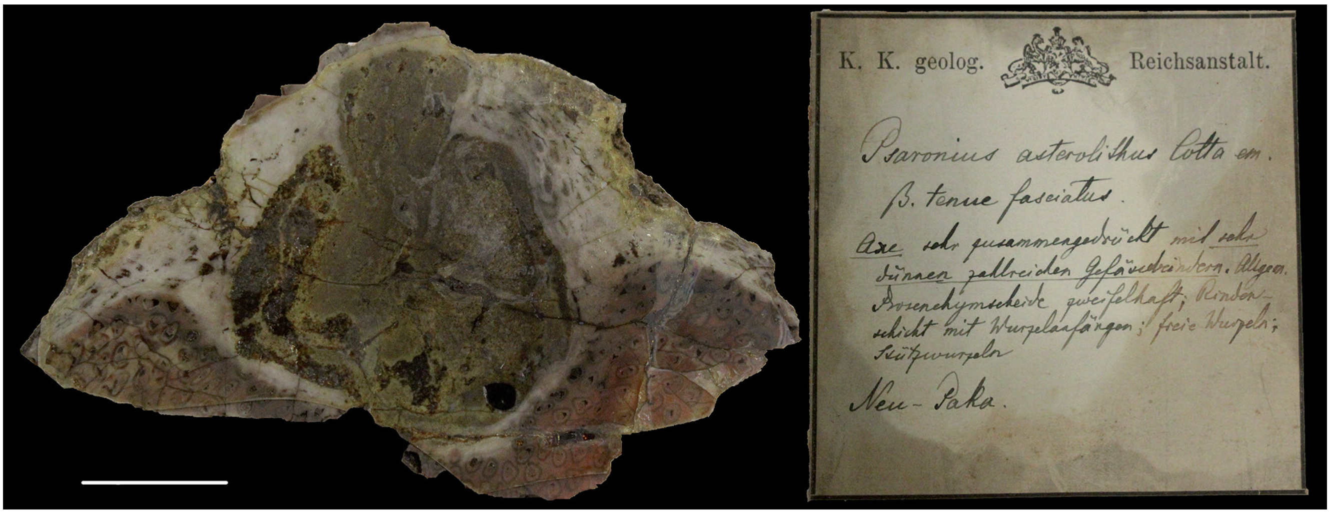

Abb. 10.
Dünnschliff zu dem *P. asterolithus* (GBA 2019/008/0011) aus Abbildung 13. Auf dem Etikett ist eine Kurzbeschreibung des Schliffes vermerkt: „*Axe sehr zusammengedrückt mit sehr dünnen zahlreichen Gefässbündern. Allgem. Parenchymscheide zweifelhaft; Rindenschicht mit Wurzelanfängen; freie Wurzeln; Stützwurzeln. Neu-Paka*“. Maßstab: 2 cm.

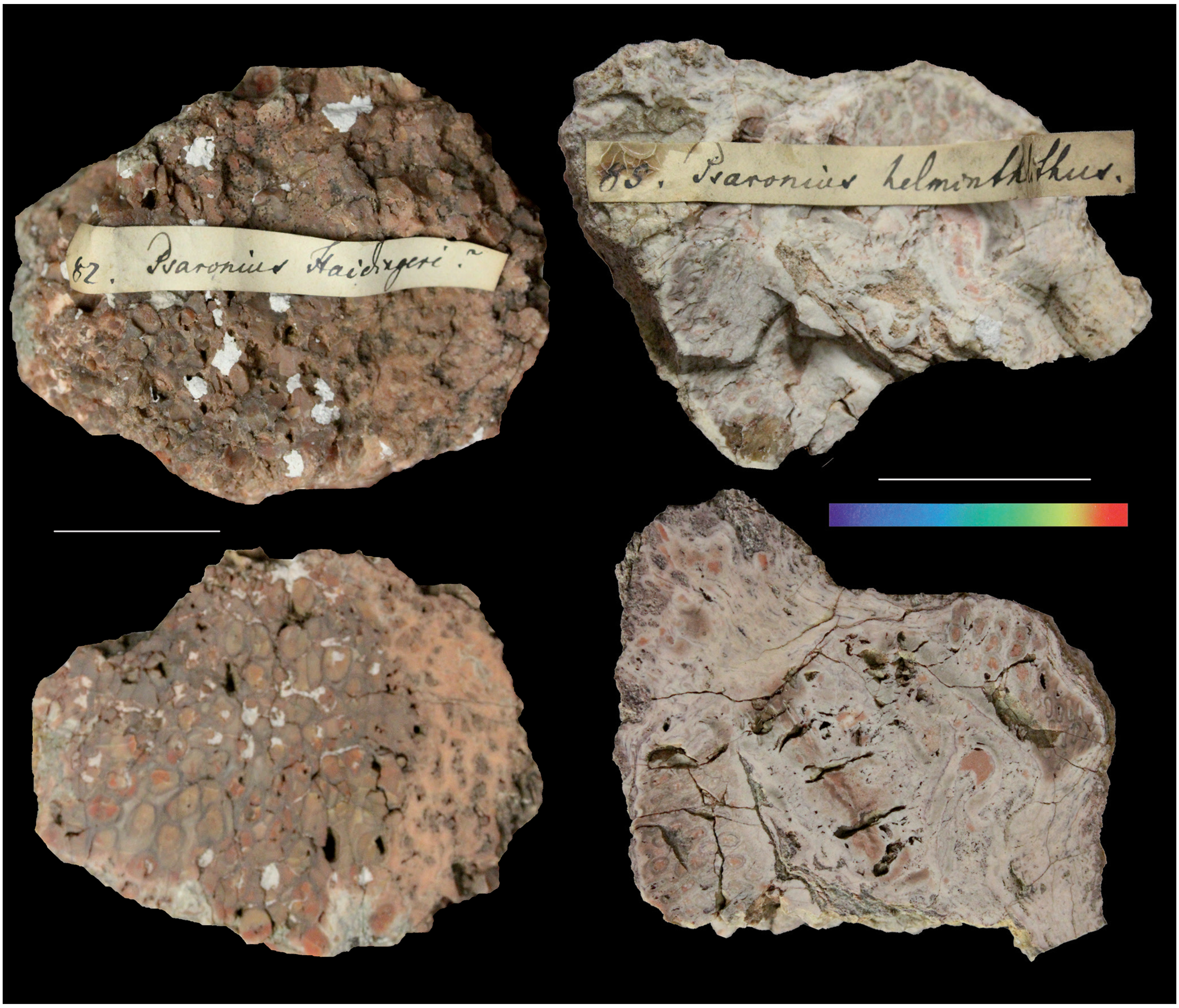

Abb. 11.
Kleinere Bruchstücke von *P. haidingeri* (links, GBA 2019/008/0012) und *P. helmintholithus* (rechts, GBA 2019/008/0014–0015). Nach heutigen Maßstäben ist eine Bestimmung auf Artebene, wie auf den Etiketten angegeben, zweifelhaft. Maßstab: 2 cm.

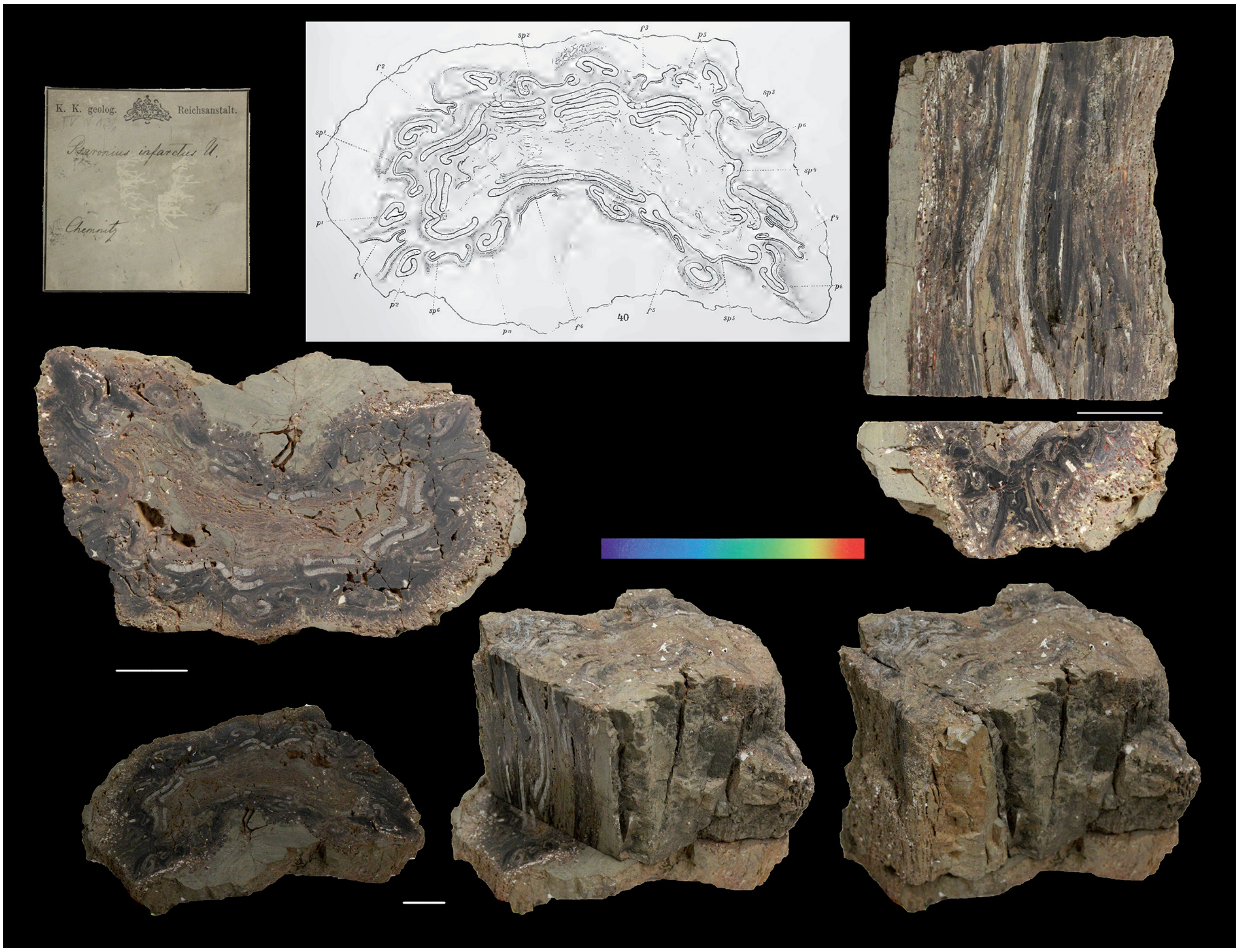

Abb. 12.
Ein in mehrere Längs- und Querschnitte zerteilter *P. infarctus* (GBA 1906/007/0001–0003). Der unter dem historischen Etikett abgebildete Querschnitt ist Abbildungsoriginal zu Stenzel (1906: Taf. IX (V), Fig. 40). Bei Stenzel (1906) ist Böhmen als Fundort angegeben, was nicht stimmen kann, denn dem *Psaronius* haftet der für Chemnitz typische Zeisigwald-Tuff an. Maßstab: 2 cm.

Eine besondere Überraschung boten die aus unterschiedlichen Schubladen zusammengetragenen Fragmente eines *Psaronius*, der dem anhaftenden Gestein nach zu urteilen, aus Chemnitz stammt (Abb. 12). Dem beiliegenden Etikett nach handelt es sich um einen *P. infarctus*. Einer der Querschnitte der insgesamt drei jeweils längs und quer geschnittenen Teile ist Abbildungsoriginal zu Stenzel (1906: Taf. IX (V), Fig. 40), der das Stück jedoch als *P. bibractensis* aus Böhmen beschreibt (Stenzel, 1906: 100). Zumindest der angegebene Fundort ist unzutreffend. Die Ursache für das Missverständnis ist wohl nicht Stenzel anzulasten, der bei Drucklegung bereits verstorben war, als vielmehr einem Missgeschick in der Redaktion geschuldet. In einer Fußnote zu Tafel V (I) heißt es: „*Durch einen unglücklichen Zufall ist das Manuskript der Tafelerklärungen in Verstoß geraten. Leider ließen sich dieselben nur mangelhaft nach dem Texte wieder herstellen, so daß nur bei einzelnen Arten die Sammlungen, aus denen die Originale stammten, angegeben werden konnten. Auch die Autorennamen nach dem Texte anzugeben war nur stellenweise möglich.*“ (Stenzel, 1906).

Ein weiterer, basaler bis mittlerer kompletter Stammquerschnitt ist zugleich Abbildungsoriginal zu Rudolph (1905: Taf. I, Fig. 1) und zu Stenzel (1906: Taf. VI (II), Fig. 18). Allerdings wird bei Stenzel (1906) der Querschnitt seitenverkehrt wiedergegeben (Abb. 13). Auf dem beiliegenden Etikett ist neben Chemnitz als Fundort *P. scolecolithus* Unger vermerkt. Da das bereits Rudolph (1905: 2) feststellt, scheinen Etikett und Stück tatsächlich zusammenzugehören. Da Rudolph an dem Stück neben Ähnlichkeiten mit *P. scolecolithus* auch solche zu *P. musaeformis* Corda und *P. Ungeri* Corda sieht, belässt er es schließlich mit einem *P. spec*. Stenzel (1906) dagegen legt sich fest und stellt das Stück zu *P. musaeformis*, ergänzt um *P. musaeformis* f. *scolecolithus*.

Einige der größeren Psaronien sind in mehrere Längs- und Querschnitte zersägt und poliert worden, was eine beabsichtigte paläobotanische Bearbeitung oder Präsentation nahelegt (Abb. 14). Eine Annahme, die durch das Vorhandensein mehrerer Dünnschliffe untermauert wird. Bei genauerem Betrachten zeigen einige dieser aufwändig hergerichteten Psaronien mehrere, in ihrem Wurzelmantel kletternde Farne der Art *A. brongniartii*, unter ihnen die verschwunden geglaubten Typen zu *Z. scandens*, wie ein Teil der heute unter *A. brongniartii* vereinten Formen ursprünglich bezeichnet wurde.

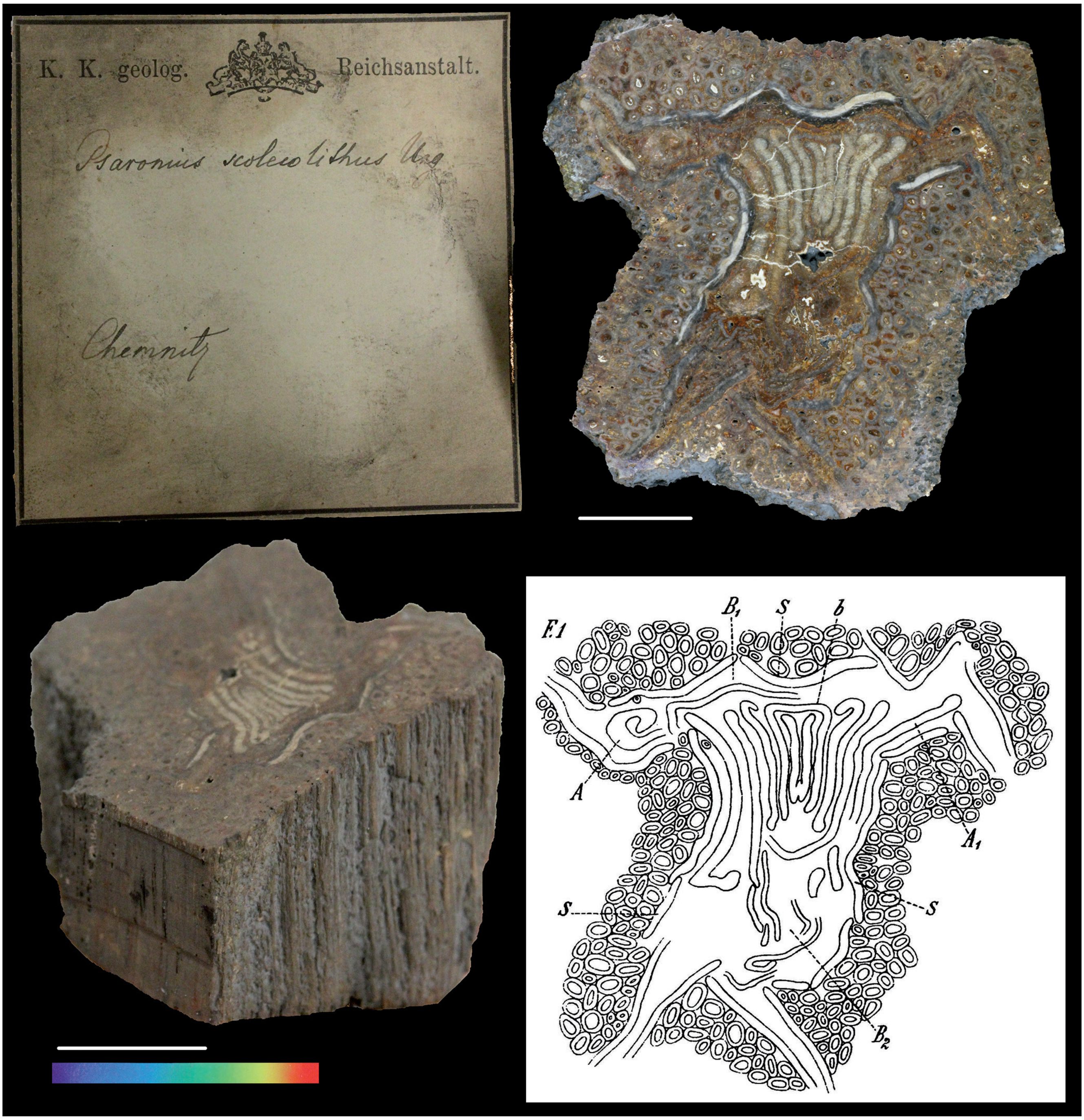

Abb. 13.
Der *Psaronius scolecolithus* (GBA 1905/006/0001) ist Abbildungsoriginal sowohl bei Rudolph (1905: Taf. I, Fig. 1) als auch bei Stenzel (1906: Taf. VI (II), Fig. 18). Stenzel bildet den *Psaronius* seitenverkehrt ab. Rudolph und Stenzel sind sich in der Benennung des Stückes durchaus uneins. Maßstab: 2 cm.

Ankyropteris brongniartii (Renault, 1869) Mickle, 1980 – Kletterfarn des Paläophytikums

Wie sich herausstellte, enthielten die robusten Holzkisten neben der gesuchten *A. laxa* weitere Originale, darunter das Typusmaterial zu dem permokarbonischen Kletterfarn *Zygopteris (Ankyropteris) scandens* Stenzel, 1889, nach Mickle (1980) Synonym zu *Ankyropteris brongniartii* (Renault, 1869) Mickle, 1980.

Sterzel (1887) war es, der erstmals zwischen den Luftwurzeln des großen *Psaronius weberi* aus dem Versteinerten Wald von Chemnitz die schmalen Achsen eines Kletterfarns erkannte. Unabhängig davon beschrieb bereits Renault (1869) an dem reichhaltigen Material aus dem französischen Autun den ebenfalls im Wurzelmantel der Psaronien emporklimmenden Farn *Zygopteris brongniarti* Renault 1869. Wenige Jahre später etablierte Stenzel (1889) in einer umfangreichen Studie innerhalb der Gattung *Zygopteris* die Untergattung *Ankyropteris*, der er unter anderem Renaults *Z. brongniarti* einverleibte, zu der er aber auch seine neue Art *Zygopteris (Ankyropteris) scandens* Stenzel (1889) stellte. Dazu lag ihm Material aus Nová Paka vor. Bertrand (1907) schließlich erhob die Untergattung *Ankyropteris* zur Gattung, was den Namen des neuen Stenzelschen Kletterfarns auf


AX
X
AS
R
P
A
X
AX
LR
cf. Psaronius sp.
vermutlich
Nova Paka, Böhmen,
Perm
(Möller 2009)

◀ Abb. 14.
Psaronius sp., vermutlich aus Nová Paka. Das große, zweiteilige Stammstück mit der Sammlungsnummer GBA 2001/218/0001–0002 enthält mehrere Achsen des Kletterfarns *Ankyropteris brongniartii* mit axillärer Verzweigung (AX), Abgänge von Aphlebien, Wedelstiele mit dem markanten H-förmigen Blattspur-Xylem (X) und mehrere laterale Wurzelquerschnitte (LR). Die Achse setzt sich zusammen aus der Aktionostele (AS), die von einer Parenchymscheide (P) und der Rinde (R) umgeben ist. Das beiliegende Etikett stammt aus der Feder der Wiener Paläontologin Barbara Meller. Maßstab: 2 cm.

A. scandens verkürzte. Seit dieser Zeit sind weitere Kletterfarne in enger Lebensgemeinschaft mit Psaronien gefunden worden. Einen Überblick gibt Rößler (2000, 2001b), der bei der Durchmusterung des historischen Chemnitzer Materials zahlreiche Achsen des Kletterfarns neu nachweisen konnte. Ob es sich dabei um eine Symbiose handelt oder die Kletterer eher parasitär vom Wirtsbaum profitierten, ist Gegenstand aktueller Forschung. Den Kenntnisstand zu Evolution und Ökologie des Kletterfarns fassen zuletzt Phillips & Galtier (2011) zusammen.

Die Gattung *Ankyropteris* umfasst axillär verzweigte Farne mit fünf- bis sechslobiger Aktinostele und markantem H-förmigem Blattspur-Leitbündel. Die Achsen der schlanken, spiralig an den Psaronien rankenden Kletterfarne sind von einem dichten Netz aus kleinen diarchen Adventivwurzeln umgeben (Abb. 14). Spiralig angeordnete Blattnarben an den Sprossachsen rühren von Aphlebien her.

Basierend auf nordamerikanischem Material aus den Coal Balls von Lewis Creek (Kentucky, USA) unterzog Mickle (1980) die Gattung *Ankyropteris* einer Revision. Das von ihm untersuchte Material stammt von einem räumlich wie stratigrafisch eng umgrenzten Ausschnitt, zeigt aber eine Variabilität, die mehrere der bis dato unter *Ankyropteris* vereinten Spezies umfasst. Mickle zog den Schluss, dass zahlreiche der bislang aus Europa und Nordamerika beschriebenen Arten lediglich unterschiedliche ontogenetische Stadien ein- und derselben Art repräsentieren: „*The similarity of features of A. brongniartii, A. grayi, A. glabra, A. scandens, A. bibractensis, Anachoropteris decaisnei, and T. glabra, as shown in the Kentucky specimens, demonstrate that these species are occurrences of a single taxon and are thus to be considered taxonomically synonymous.*“ (Mickle,

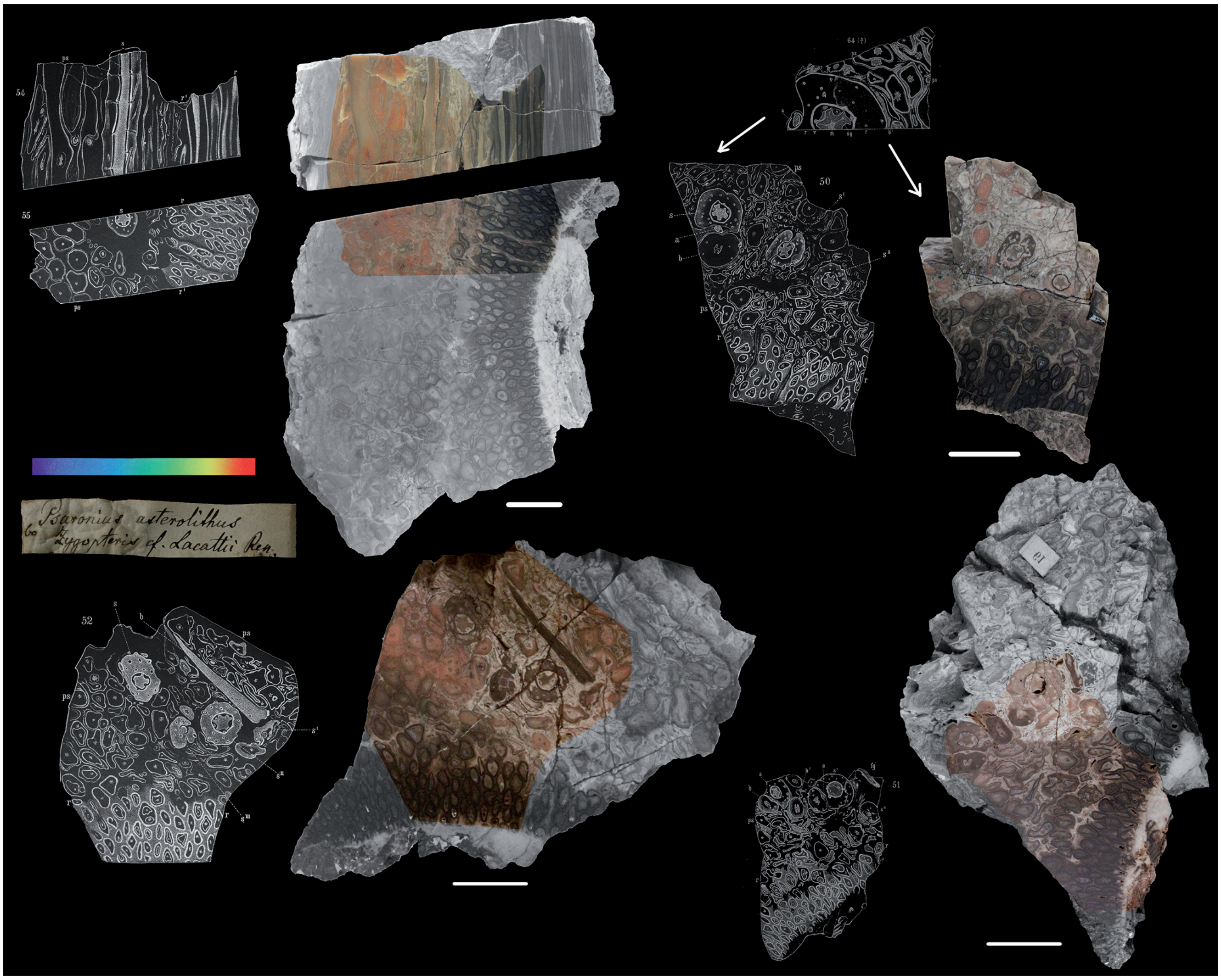

Abb. 15.
Abbildungsoriginale zu Stenzel (1889: Taf. VI, Figs. 50–55, Taf. VII, Fig. 64) (GBA 1889/004/0003, 0004, 0006). Stenzel hat nur jeweils Teile der *A. brongniartii* gezeichnet. Die den Originalabbildungen bei Stenzel (1889) entsprechenden Partien sind farbig belassen; darüber hinaus gehende Bereiche der Abbildungsoriginale sind in Grautönen gehalten. Von dem Stück zu Tafel VI, Figure 51 (oben rechts, GBA 1889/004/0003) wurde ein kleineres Fragment herausgesägt, nachdem Stenzel es abgezeichnet hat. Der herausgetrennte Block diente zur Herstellung von Dünnschliffen. Das dazu passende Detail ist bei Stenzel (1889) auf Tafel VII, Figure 64 abgebildet. Die Stenzelsche Abbildung Tafel VI, Figure 61 ist offenbar seitenverkehrt dargestellt. Für einen direkten Vergleich wurde das Typusmaterial (unten rechts) ausnahmsweise seitenverkehrt und passend gedreht abgebildet, kenntlich an der spiegelverkehrten Sammlungsnummer. Stenzel (1889) bildet mit Tafel VI, Figure 51 die weitestgehend unbearbeitete Rückseite des Gegenstückes zu Tafel VI, Figure 52 ab. Maßstab: 2 cm.


Zygopteris scandens
(R. Fuess, Berlin)
Siehe Stenzels Brief vom 28/2 1886
Zygopteris scandens
Siehe Stenzels Brief vom 1/9 1886
59

◀ Abb. 16.
Notizzettel mit Bleistiftzeichnungen zu den Abbildungen auf den Tafeln VI und VII bei Stenzel (1889). Auf beiden Zetteln findet sich ein Hinweis auf Stenzelsche Korrespondenz, die leider nicht mehr ausfindig gemacht werden konnte. Das kleine Fragment unten rechts (GBA 1889/004/0007) ist das Original zu Stenzel (1889: Taf. VII, Fig. 59). Stenzel fertigte auch von diesem Block einen Dünnschliff, was den seitenverkehrten Abdruck im Vergleich zum Original erklärt. Bild unten: Zwei der angefertigten Dünnschliffe.

1980: 240). Mickle fasste die Synonyme zu der heute gültigen Art *A. brongniartii* zusammen. Das Material aus dem französischen Autun, dem sächsischen Chemnitz und dem böhmischen Nová Paka lag ihm bei seiner Studie nicht vor. Erst später, im Jahr 1988, fand Mickle „*während eines Forschungsaufenthaltes im damaligen Karl-Marx-Stadt seine Auffassung am reichen Material überzeugend bestätigt.*“ (Rössler, 2001b: 140). Das Typusmaterial zu Stenzel (1889) galt zu dieser Zeit bereits als verschollen.

Die Tafeln VI und VII zu Stenzel (1889) zeigen 15 Zeichnungen seiner *Z. scandens*, die er sämtlich nach Stücken und Dünnschliffen aus der k. k. Geologischen Reichsanstalt in Wien angefertigt hatte. Heute wissen wir, dass die Abbildungsoriginale erhalten sind (Abb. 15, 17). Ebenso die Dünnschliffe, nach denen Stenzel den überwiegenden Teil seiner Detailzeichnungen anfertigte und die er vor allem auf Tafel VII zusammenstellte. Es überrascht, dass Stenzel nur jeweils kleinere Bereiche der meist sehr viel größeren Stücke zeichnete, teilweise seitenverkehrt, ohne darauf hinzuweisen. Vielleicht ist das Stenzelsche Typusmaterial deshalb nicht eher als solches erkannt worden. In Abbildung 15 sind Bereiche, die Stenzel nicht zeichnete, in Grautönen abgesetzt. In einem Fall (Abb. 15, oben rechts) waren die Stücke nach Anfertigung der Zeichnung weiter zerschnitten worden, um Material für Dünnschliffe zu gewinnen. Zwei der Dünnschliffe sind bei R. Fuess in Berlin und drei Dünnschliffe bei Voigt & Hochgesang in Göttingen angefertigt worden (Abb. 16).

Teile der Abbildungsoriginale lassen sich zu einem größeren Exemplar zusammensetzen (Abb. 17). Neben den bei Stenzel abgebildeten Exemplaren gibt es im Bestand der GBA weiteres Material, dass zu *A. brongniartii* gehört (Abb. 14, 17). In einer der beiden Holzkisten mit dem Stenzelschen Typus befanden sich zwei vergilbte Zettel, auf denen mit dünnem Bleistift zahlreiche Details zur Stenzelschen *Z. scandens* wiedergegeben sind (Abb. 16). Es dürfte sich um die Originalzeichnungen handeln, nach denen später die Feinzeichnungen für den Druck der Tafeln VI und VII ausgeführt worden sind. Die diesbezügliche Korrespondenz Stenzels, auf die mit schwarzer Tinte am unteren Rand der Bleistiftzeichnungen hingewiesen wird (Abb. 16), ist nicht überliefert.

Medullosen – farnblättrige Gymnospermen des Paläophytikum

In der Sammlung der GBA finden sich einige wenige Medullosen. Diese Farnsamer gehörten zu einer heute ausgestorbenen paläophytischen Entwicklungslinie, die Merkmale sowohl der Farne, als auch der Samenpflanzen in sich vereint. Von dem vollständigsten Stück, dem Etikett nach einer *Medullosa porosa* Cotta (1832), sind Längs- und Querschnitte angefertigt, die Schnittflächen auch ange-

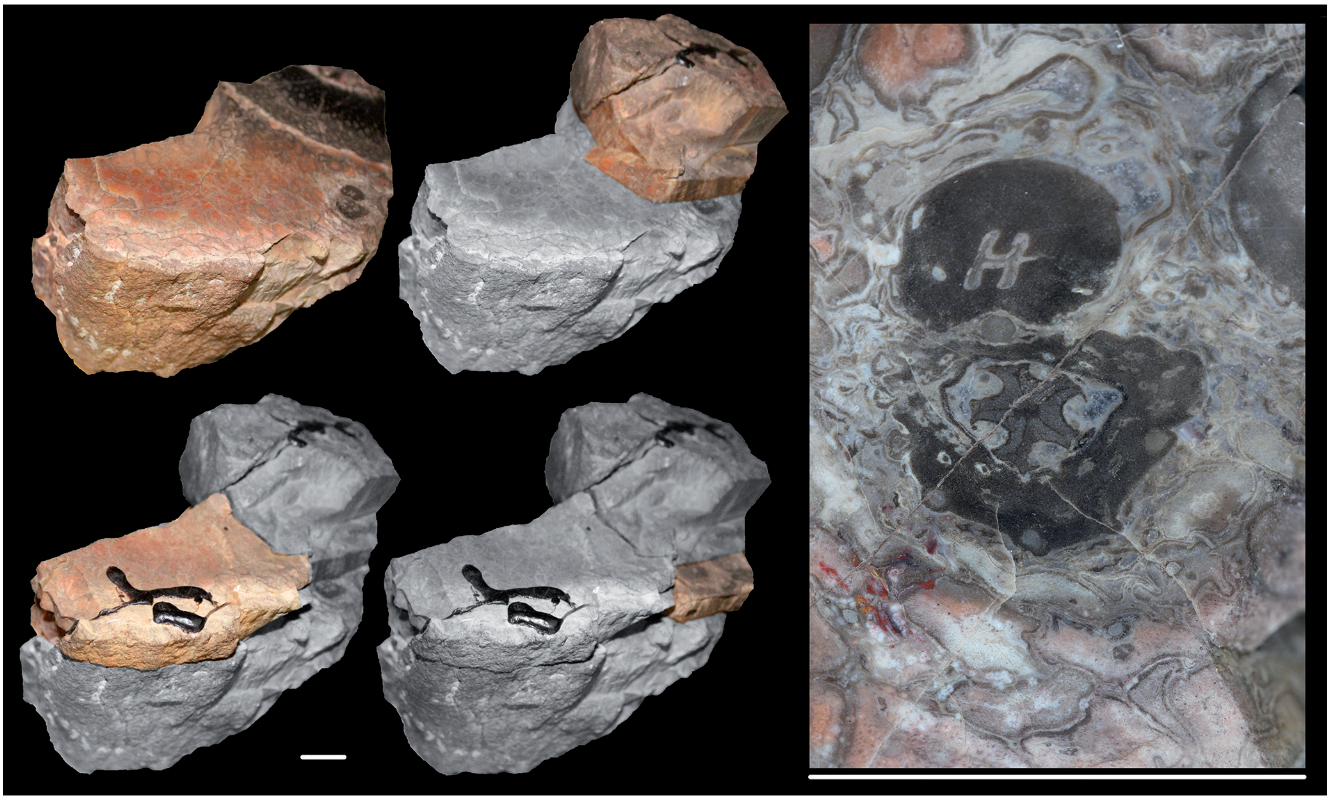

Abb. 17.
Ein Teil der Abbildungsoriginale zu Stenzel (1889: Taf. VI, Figs. 50–55; Taf. VII, Figs. 56–65) erwies sich als zu einem Exemplar gehörig, da einige der Fragmente zu einem größeren Stück zusammengesetzt werden konnten (links, mitte, GBA 1889/004/0007–0010). Neben den bei Stenzel abgebildeten Details enthält das Exemplar weitere polierte Anschliffe, die Achsen mit axillärem Verzweigungsmuster und Blattspurabgängen der *A. brongniartii* zeigen (rechts). Maßstab: 2 cm.

Abb. 18.
Quer- und Längsschnitt einer *M. porosa* aus dem Bestand der GBA. Die *Medullose* stammt aus Chemnitz, was der im Markraum enthaltene Zeisigwald-Tuff zeigt. Längsschnitte wurden selten, meist nicht ohne paläobotanischen Beweggrund, angefertigt. Maßstab: 2 cm.

schliffen worden (Abb. 4). Das Stück stammt aus Chemnitz. Der Markraum ist teilweise mit dem für Chemnitz typischen Zeisigwald-Tuff verfüllt (Abb. 18). Ein kleineres (etwa 5 x 3 x 1 cm) angeschliffenes Bruchstück einer *M. stellata* lässt sich anhand der Fluoriterhaltung ebenfalls eindeutig Chemnitz zuordnen. In derselben Schublade befinden sich außerdem zwei kleinere angeschliffene Bruchstücke von *Myeloxylon elegans*, den Wedelstielen der Medullosen. Auf den beiliegenden Etiketten sind nur die auf COTTA (1832)

Abb. 19. ▶
Der Gipsabguss einer Einzelfieder von *T. schenkii* wurde vom Holotypus zu STERZEL (1876) angefertigt: (a) Gipsabguss der *T. schenkii* aus der GBA mit historischem Etikett, (b) Gipsabguss mit Etikett aus dem Sächsischen Landesamt für Umwelt, Landwirtschaft und Geologie in Freiberg (RS 1984/161), (c) Holotypus der *T. schenkii* aus der Sammlung des Museums für Naturkunde in Chemnitz mit Sterzelschem Originaletikett (MfNC 1690), (d) Chemnitzer Gipsabguss mit Sterzelschem Originaletikett (MfNC 2337), (e) historische Detailzeichnung der Nervatur aus dem Museum für Naturkunde Chemnitz als Vorlage für die Detailabbildungen bei STERZEL (1876) und (e) Auszug aus dem handschriftlichen Katalog von Geinitz, der die *T. schenkii* neben den Originalen der *T. abnormis* als Bestand des Königlich Mineralogischen Museums in Dresden ausweist. Maßstab: 2 cm.

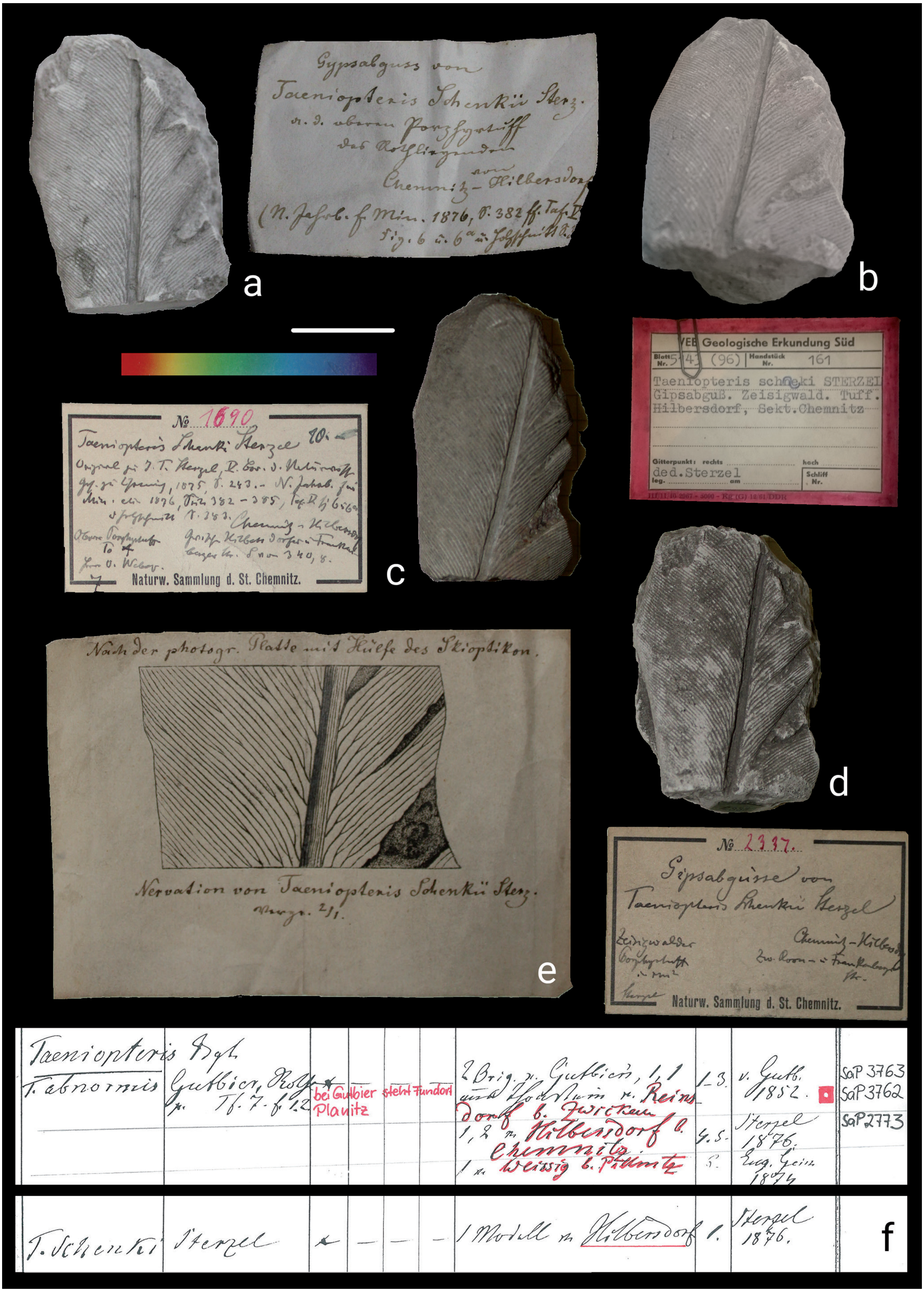
a
b
c
d
e
f
Gypsabguss von Taeniopteris Schenkii Sterz.
VEB Geologische Erkundung Süd
Blatt Nr.
Handstück Nr. 161
Taeniopteris schenki STERZEL
Gipsabguß. Zeisigwald. Tuff.
Hilbersdorf, Sekt.Chemnitz
Gitterpunkt: rechts
hoch
ded.Sterzel
leg.
am
Schliff Nr.
№ 1690
Taeniopteris Schenkii Sterzel
Naturw. Sammlung d. St. Chemnitz.
Nach der photogr. Platte mit Hülfe des Skioptikon.
Nervation von Taeniopteris Schenkii Sterz.
№ 2337.
Gipsabgüsse von Taeniopteris Schenkii Sterzel
Naturw. Sammlung d. St. Chemnitz.
Taeniopteris
T. abnormis
bei Gutbier steht Fundort Planitz
SaP 3763
SaP 3762
SaP 2773
T. Schenki
Sterzel
1 Modell
Hilbersdorf
Sterzel 1876.

und Göppert (1864) zurückgehenden frühen Bezeichnungen *Medullosa elegans* bzw. *Stenzelia elegans* vermerkt. Die systematische Bearbeitung der Chemnitzer Medullosen in der 2. Hälfte des 19. Jahrhunderts fand bis heute leider keine Fortsetzung. Chemnitzer Grabungsfunde aus den Jahren 2008 bis 2011 lassen in Verbindung mit einer Neubearbeitung des historischen Typusmaterials für die Zukunft neue Erkenntnisse zu Wuchsform, Vermehrungsstrategie und Taxonomie der Medullosen erwarten (Rößler et al., 2012). Als bedeutsam erweist sich hierfür auch das Auffinden historischen Materials, wie jenes der GBA (Abb. 18) oder in Museum und Kunstsammlung Schloss Hinterglauchau, wo jüngst eine umfangreiche Suite vorzüglich präparierter Medullosen wiederentdeckt wurde, unter ihnen verschollen geglaubte Originale zu Rudolph (1922) und Gegenstücke zu den Medullosen der Chemnitzer Sammlung (Löcse & Rößler, 2018b).

Von historischem Interesse ist ein Gipsabguss des vermutlich mittleren Teils einer Einzelfieder von *Taeniopteris schenkii* Sterzel (1876), die von Sterzel beschrieben und mit den Medullosen in Zusammenhang gebracht worden war (Sterzel, 1876; Abb. 19). Heute wird *T. schenkii* zu *Taeniopteris abnormis* Gutbier (1835) gestellt (Barthel, 1976). Sterzel ließ, seinen Angaben zufolge, vom Holotypus drei Gipsabgüsse anfertigen, je einen für die „Städtische Mineraliensammlung zu Chemnitz“, heute Museum für Naturkunde Chemnitz, das „Königlich mineralogische Museum in Dresden“, heute Senckenberg Naturhistorische Sammlungen Dresden, und das „Museum der geologischen Landesuntersuchung in Leipzig“, heute Landesamt für Umwelt, Landwirtschaft und Geologie, Abteilung Geologie mit Sammlungen am Standort Freiberg/Sachsen (Sterzel, 1876: 381, 385). Die Gipsabgüsse in den Sammlungen in Chemnitz und Freiberg lassen sich nachweisen (Abb. 19). Der Dresdner Abguss fehlt. Er war gemeinsam mit einigen fossilen Abdrücken von *T. abnormis* bereits 1876 von Sterzel nach Dresden gegeben worden, wie aus einer Notiz im handschriftlichen Sammlungskatalog „Dyas“ der Dresdner Sammlung hervorgeht (Abb. 19). Der Katalog ist 1885 von dem Paläontologen, Geologen und langjährigen Direktor der Sammlung, Hanns Bruno Geinitz (1814–1900), verfasst worden. Das Etikett zu dem Wiener Gipsabguss trägt die Handschrift von Johannes Victor Deichmüller (1854–1944), seit 1877 Assistent bei Geinitz (Abb. 19). Zwischen der k. k. Geologischen Reichsanstalt in Wien und dem Königlich Mineralogischen Museum in Dresden gab es Mitte des 19. Jahrhunderts einen regen wissenschaftlichen Austausch. Štúr war wiederholt bei Geinitz zu Gast, so in den Jahren 1874, 1876 und 1883 (Štúr, 1874, 1876, 1883, 1885). Štúr erwähnt wiederholt, dass er aus Dresden fossile Schätze zur wissenschaftlichen Bearbeitung ausgeliehen hatte und auch zum dauerhaften Verbleib überlassen bekam (Štúr, 1874: 138, 225f., 1885: 160, 163, 201, 405f.). Den Gipsabguss führt der für seine Akribie in Sammlungsangelegenheiten bekannte Geinitz noch 1885 auf, hinterlässt auch keinen Ausgangsvermerk zu dem Stück. Die Herkunft des Gipsabgusses von *T. schenkii* an der GBA bleibt damit ungeklärt. Das durch Sterzel (1876: Taf. V, Figs. 6, 6a) abgebildete Original zum Gipsabguss wird heute im Museum für Naturkunde in Chemnitz verwahrt (Abb. 19).

Resümee

Im Zuge umfangreicher Recherchen an der GBA in Wien im Juni 2018 konnten zahlreiche Abbildungsoriginale paläophytischer Farne ausfindig gemacht werden. Die Suche galt zunächst dem als verschollen gegoltenen Abbildungsoriginal zu Stenzel (1889: Taf. IV, Fig. 37), einem seltenen kleinwüchsigen Baumfarn, *Asterochlaena laxa*, aus Nová Paka. Nicht nur dieses Stück wurde in der GBA aufgefunden, sondern auch ein passgenau dazugehöriges zweites, bisher in der Literatur nicht erwähntes Fragment. In der Bayerischen Staatssammlung für Paläontologie und Geologie in München wurde ein dritter, bislang nie in der Literatur erwähnter Abschnitt des unikaten, mit *A. laxa* eng verwandten Baumfarns *Asterochlaena ramosa* entdeckt. Die neu- bzw. wiederentdeckten Stücke waren Anlass, die bereits vor einigen Jahren begonnene Recherche zu Herkunft und Verbleib sämtlicher Funde von *A. laxa* und *A. ramosa* abzuschließen. Es stellte sich heraus, dass die beiden anderen Abbildungsoriginale, auf die Stenzel seine neue Art *A. laxa* gründete, heute im Museum für Naturkunde in Chemnitz (Stenzel, 1889: Taf. IV, Figs. 33, 34) und in der paläobotanischen Sammlung des Museums für Naturkunde der Humboldt-Universität Berlin (Stenzel, 1889: Taf. IV, Figs. 35, 36) verwahrt werden. Unsere Recherchen legen nahe, dass Stenzel unbeabsichtigt neben dem einzigen bekannten Fund aus Nová Paka, die beiden einzigen oberkarbonischen Funde vom Gückelsberg (Flöha bei Chemnitz) als Typusmaterial für *A. laxa* wählte. Alle anderen bekannten Stücke stammen aus dem Unterperm von Chemnitz. Unsere Nachforschungen ergaben außerdem, dass der bislang einzige Fund von *A. ramosa* in Chemnitz gemacht worden ist. Seit der Erstbeschreibung durch Cotta (1832) galt der Fundort der *A. ramosa* als unbekannt.

In der GBA konnte das ebenfalls als verschollen geglaubte Typusmaterial zu dem permokarbonischen Kletterfarn *Zygopteris scandens* (heute unter *Ankyropteris brongniartii* synonymisiert), einschließlich der dazugehörigen Dünnschliffe, aufgefunden werden. Weitere in der GBA neu nachgewiesene Abbildungsoriginale (Rudolph, 1905: Taf. I, Fig. 1; Stenzel, 1906: Taf. VI (II), Fig. 18, Taf. IX (V), Fig. 40) betreffen die *Psaronius*-Baumfarne.

Mit *Taeniopteris schenkii*, heute Synonym zu *T. abnormis*, wurde in der GBA einer von vermutlich nur drei Gipsabgüssen des Typusmaterials zu Sterzel (1876: Taf. V, Figs. 6, 6a) aufgefunden. Unsere Recherchen ergaben, dass sich neben dem Original ein weiterer, identischer Gipsabguss im Museum für Naturkunde in Chemnitz und ein weiterer Gipsabguss am Sächsischen Landesamt für Umwelt, Landwirtschaft und Geologie in Freiberg/Sachsen befindet. Der ursprünglich für das Königlich Mineralogische Museum in Dresden bestimmte und dort an Hand historischer Sammlungskataloge nachgewiesene Gipsabguss ist heute in Dresden nicht mehr nachweisbar. Es ist nicht auszuschließen, dass er auf heute nicht mehr nachvollziehbarem Wege nach Wien in die Sammlung der GBA gelangte.

Dank

Unser Dank gilt MICHAEL KRINGS und GERTRUD RÖßNER, Bayerische Staatssammlung für Paläontologie und Geologie, München, die uns Zugang zur Sammlung gewährten und unsere Recherchen mit wertvollen Hinweisen unterstützten. Die Recherchen zu Herkunft und Verbleib einzelner Stücke wurden, teilweise seit mehreren Jahren, von zahlreichen Fachkollegen in dankenswerter Weise unterstützt. Zu ihnen gehören: MANFRED BARTHEL †, STEPHAN SCHULTKA und CATRIN PUFFERT, Museum für Naturkunde Berlin, PAUL KENRICK und PETA HAYES, Natural History Museum London, England, KLAUS THALHEIM, Senckenberg Naturhistorische Sammlungen Dresden, BIRGIT G. GAITZSCH, Paläontologische Sammlung der TU Bergakademie Freiberg, JEAN-PIERRE LAVEINE, Lille, Frankreich, THOMAS SPECK, Botanischer Garten, Universität Freiburg im Breisgau, PHILLIP SCHEITENBERGER, Deutsches Museum München, NORBERT WIEDEMANN, Museum Natur und Mensch, Freiburg im Breisgau, JOHANNES RICHTER und MANUEL LAPP, Sächsisches Landesamt für Umwelt, Landwirtschaft und Geologie, Freiberg/Sachsen. Die Autoren danken ANDREAS WUNDERLICH und MONIKA BRÜGGEMANN-LEDOLTER für das Polieren bzw. Fotografieren ausgewählter Hölzer aus den Sammlungen der Geologischen Bundesanstalt.

Literatur

BARTHEL, M. (1976): Die Rotliegendflora Sachsens. – Abhandlungen des Staatlichen Museums für Mineralogie und Geologie zu Dresden, **24**, 1–190, Dresden.

BARTHEL, M. (1994): Von Mylius bis Schlotheim. Paläobotanische Sammlungen des 18. Jahrhunderts aus Manebach, Thüringer Wald. – In: GROTE, A. (Hrsg.): Macrocosmos in Microcosmo – Die Welt in der Stube – Zur Geschichte des Sammelns 1450 bis 1800, 707–720, Wiesbaden (Springer).

BERTRAND, P. (1907): Classification des Zygoptéridées d'aprés les caractéres de leurs traces foliares. – Compte Rendus Hebdomadaires des Seances de l'Academie des Sciences, **145**, 775–777, Paris.

BERTRAND, P. (1909a): Études sur la Fronde des Zygoptéridées. Thèses. – 307 S., Lille (Imprimerie L. Danel).

BERTRAND, P. (1909b): Études sur la Fronde des Zygoptéridées. Atlas. – 35 S., Lille (Imprimerie L. Danel).

BERTRAND, P. (1911): Structure des Stipes d'*Asterochlœna laxa* STENZEL. – Mémoires de la Société Géologique du Nord, Tome **VII**/I, 1–72, Lille.

CORDA, A.J. (1845): Beiträge zur Flora der Vorwelt. – 128 S., Prag (J.G. Calve'sche Buchhandlung).

CORSIN, P. (1955): Position systematique des *Pécopteris*. – Compte Rendus Hebdomadaires des Seances de l'Academie des Sciences, **240**/6, 661–663, Paris.

COTTA, B. (1832): Die Dendrolithen in Beziehung auf ihren inneren Bau. – 89 S., Dresden–Leipzig (Arnoldische Buchhandlung).

DIMICHELE, W.A. & PHILLIPS, T.L. (2002): The ecology of Paleozoic ferns. – Review of Palaeobotany and Palynology, **119**, 143–159, Amsterdam.

ETTINGSHAUSEN, C. V. (1851): Beiträge zur Flora der Vorwelt. – Haidinger's Naturwissenschaftliche Abhandlungen, **4**/1, 65–100, Wien.

ETTINGSHAUSEN, C. V. (1852): Die Steinkohlenflora von Stradonitz in Böhmen. – Abhandlungen der k. k. Geologischen Reichsanstalt, **1**/3, 1–18, Wien.

ETTINGSHAUSEN, C. V. (1854): Die Steinkohlenflora von Radnitz in Böhmen. – Abhandlungen der k. k. Geologischen Reichsanstalt, **2**/3, 1–74, Wien.

FALCON-LANG, H.J. (2006): Latest Mid-Pennsylvanian tree-fern forests in retrograding coastal plain deposits, Sydney Mines Formation, Nova Scotia, Canada. – Journal of the Geological Society, **163**, 81–93, London.

GALTIER, J. & PHILLIPS, T.L. (1996): Structure and evolutionary significance of Palaeozoic ferns. – In: CAMUS, J.M., GIBBY, M. & JOHNS, R.J. (Eds.): Pteridology in Perspective, 417–433, Royal Botanic Gardens, Kew.

GALTIER, J. & PHILLIPS, T.L. (2014): Evolutionary and ecological perspectives of Late Paleozoic ferns. Part III. Anachoropterid ferns (including *Anachoropteris*, *Tubicaulis*, the Sermayaceae, Kaplanopteridaceae and Psalixochlaenaceae). – Review of Palaeobotany and Palynology, **205**, 31–73, Amsterdam.

GÖPPERT, H.R. (1864): Die fossile Flora der Permischen Formation. – 314 S., Cassel (Verlag von Theodor Fischer).

GÖSSEL, J.H.G. (1832–1846): Katalog der Königlich Saechsischen mineralogischen Sammlungen in Dresden. A. Katalog der oryktognostischen Sammlung. – 4 Bände, Dresden (handschriftlich, Zugangsbuch).

GÖTZE, J. & RÖßLER, R. (2000): Kathodolumineszenz-Untersuchungen an Kieselhölzern – I. Silifizierungen aus dem Versteinerten Wald von Chemnitz (Perm, Chemnitz). – Veröffentlichungen des Museums für Naturkunde Chemnitz, **23**, 35–50, Chemnitz.

GUTBIER, A. v. (1835): Abdrücke und Versteinerungen des Zwickauer Steinkohlengebirges und seiner Umgebung. – 80 S., Zwickau (Richtersche Buchhandlung).

HOFMANN, T. (2009): Erinnerungen an den Paläontologen Rudolf Sieber (1905–1988). – In: ANGETTER, D. & HOFMANN, T. (Hrsg.): Festschrift zum 66. Geburtstag: HR Dr. Tillfried Cernajsek Bibliotheksdirektor i.R. der Geologischen Bundesanstalt, 261–268, Wien.

JUNCAL, M.A., LLORET, J., DIEZ, J.B., LÓPEZ-GÓMEZ, J., RONCHI, A., DE LA HORRA, R., BARRENECHEA, J.F. & ARCHE, A. (2019): New Upper Carboniferous palynofloras from Southern Pyrenees (NE Spain): Implications for palynological zonation of Western Europe. – Palaeogeography, Palaeoclimatology, Palaeoecology, **516**, 307–321, Amsterdam.

KIDSTON, R. (1886): Catalogue of the Palæozoic Plants in the Department of Geology and Palæontology, British Museum (Natural History). – VIII + 288 S., London (Printed by Order of the Trustees).

KRASSER, F. (1909): Die Diagnosen der von Dionysus Stur in der obertriadischen Flora der Lunzerschichten als Marattiaceenarten unterschiedenen Farne. – Sitzungsberichte der mathematisch-naturwissenschaftlichen Klasse der kaiserlichen Akademie der Wissenschaften, **118**, 13–43, Wien.

KRASSER, F. (1919): Studien über die fertile Region der Cycadophyten aus den Lunzer Schichten: Makrosporophylle. – Denkschriften der mathematisch-naturwissenschaftlichen Klasse der kaiserlichen Akademie der Wissenschaften, **97**, 1–32, Wien.

KRINGS, M., DOTZLER, N., TAYLOR, T.N. & GALTIER, J. (2010): A fungal community in plant tissue from the Lower Coal Measures (Langsettian, Lower Pennsyslvanian) of Great Britain. – Bulletin of Geosciences, **85**/4, 679–690, Praha.

KRINGS, M., HARPER, C.J., WHITE, J.F., BARTHEL, M., HEINRICHS, J., TAYLOR, E.L. & TAYLOR, T.N. (2017): Fungi in a *Psaronius* root mantle from the Rotliegend (Asselian, Lower Permian/Cisuralian) of Thuringia, Germany. – Review of Palaeobotany and Palynology, **239**, 14–30, Amsterdam.

KÜHNE, E., LANGE, J.-M. & ERLER, D. (2006): Die Geschichte des Museums für Mineralogie und Geologie Dresden. – In: LANGE, J.-M. & KÜHNE, E. (Hrsg.): Das Museum für Mineralogie und Geologie. Von der kurfürstlichen Kunstkammer zum staatlichen Forschungsmuseum in den Staatlichen Naturhistorischen Sammlungen Dresden, 13–95 (Staatliche Naturhistorische Sammlungen Dresden).

KUNZMANN, L. (2006): Die paläobotanische Sammlung des Museums für Mineralogie und Geologie Dresden. – In: LANGE, J.-M. & KÜHNE, E. (Hrsg.) Das Museum für Mineralogie und Geologie. Von der kurfürstlichen Kunstkammer zum staatlichen Forschungsmuseum in den Staatlichen Naturhistorischen Sammlungen Dresden, 127–136 (Staatliche Naturhistorische Sammlungen Dresden).

LANKESTER, E.R. (1904): The History of the Collections contained in the Natural History Department of the British Museum. – Volume I, 144 S., London (British Museum Natural History).

LÖCSE, F. & RÖßLER, R. (2018a): Zur geologisch-paläontologischen Forschungsgeschichte des Flöha-Beckens. – Ein Mosaikstein zur historischen Entwicklung der Geowissenschaften in Sachsen. – Geohistorische Blätter, **29**, 1–24, Berlin.

LÖCSE, F. & RÖßLER, R. (2018b): Gesammelt, bewahrt, vergessen, wiederentdeckt: Die paläobotanische Sammlung von Prof. Dr. med. Paul Geipel. – Veröffentlichungen des Museums für Naturkunde Chemnitz, **41**, 5–54, Chemnitz.

LÖCSE, F., MEYER, J., KLEIN, R., LINNEMANN, U., WEBER, J. & RÖßLER, R. (2013), Neue Florenfunde in einem Vulkanit des Oberkarbons von Flöha – Querschnitt durch eine ignimbritische Abkühlungseinheit. – Veröffentlichungen des Museums für Naturkunde Chemnitz, **36**, 85–142, Chemnitz.

LÖCSE, F., LINNEMANN, U., SCHNEIDER, G., ANNACKER, V., ZIEROLD, T. & RÖßLER, R. (2015): 200 Jahre *Tubicaulis solenites* (SPRENGEL) COTTA. Sammlungsgeschichte, Paläobotanik & Geologie eines oberkarbonischen Baumfarn-Unikats aus dem Schweddey-Ignimbrit vom Gückelsberg bei Flöha. – Veröffentlichungen des Museums für Naturkunde Chemnitz, **38**, 5–46, Chemnitz.

LÖCSE, F., ZIEROLD, T. & RÖßLER, R. (2017): Provenance and collection history of *Tubicaulis solenites* (SPRENGEL) COTTA. A unique fossil tree fern and its 200-year journey through the international museum landscape. – Journal of the History of Collections, **30**/2, 241–251, Oxford.

LÖCSE, F., LINNEMANN, U., SCHNEIDER, G., MERBITZ, M. & RÖßLER, R. (2019): First U-Pb LA-ICP-MS zircon ages assessed from a volcano-sedimentary complex of the mid-European Variscids (Pennsylvanian, Flöha Basin, SE Germany). – International Journal of Earth Sciences (Geologische Rundschau), **108**/2, 713–733, Heidelberg. https://dx.doi.org/10.1007/s00531-019-01684-z

LUTHARDT, L., HOFMANN, M., LINNEMANN, U., GERDES, A., MARKO, L. & RÖßLER, R. (2018) A new U-Pb zircon age and a volcanogenic model for the early Permian Chemnitz Fossil Forest. – International Journal of Earth Sciences (Geologische Rundschau), **107**/7, 2465–2489, Heidelberg. https://dx.doi.org/10.1007/s00531-018-1608-8

MELLER, B. (2005): Die paläobotanische Sammlung der Geologischen Bundesanstalt Wien: Ein Archiv der mehr als 150jährigen Sammlungstätigkeit und der Entwicklungsgeschichte der Pflanzen auf der Erde. – Berichte des Institutes der Erdwissenschaften der Karl-Franzens-Universität Graz, **10**, 73–75, Graz.

MICKLE, J.E. (1980): *Ankyropteris* from the Pennsylvanian of Eastern Kentucky. – Botanical Gazette, **141**, 230–243, Chicago.

MICKLE, J.E. (1984): Taxonomy of specimens of the Pennsylvanian age marattialean fern *Psaronius* from Ohio and Illinois. – Illinois State Museum Science Paper, **19**, 1–64, Springfield.

MORGAN, J. (1959): The morphology and anatomy of American species of the genus *Psaronius*. – Illinois Biological Monographs, **27**, 1–107, Urbana.

PFEFFERKORN, H.W. & THOMSON, M.C. (1982): Changes in dominance patterns in upper Carboniferous plantfossil assemblages. – Geology, **10**, 641–644, Boulder.

PHILLIPS, T.L. (1974): Evolution of vegetative morphology in coenopterid ferns. – Annals of Missouri Botanical Garden, **61**, 427–461, St. Louis.

PHILLIPS, T.L. & GALTIER, J. (2005): Evolutionary and ecological perspectives of Late Paleozoic ferns: Part I. Zygopteridales. – Review of Palaeobotany and Palynology, **135**, 165–203, Amsterdam.

PHILLIPS, T.L. & GALTIER, J. (2011): Evolutionary and ecological perspectives of late Paleozoic ferns: Part II. The genus *Ankyropteris* and the Tedeleaceae. – Review of Palaeobotany and Palynology, **164**, 1–29, Amsterdam.

RENAULT, B. (1869): Etudes de quelques végétaux silicifiés des environs d'Autun. – Annales des sciences naturelles. Botanique et biologie végétale, 5ème série, **12**, 161–190, Paris.

RÖßLER, R. (1999): Paläontologische Schätze im Naturalienkabinett Waldenburg – Eine Sammlung der ersten Fossilfunde in Mitteleuropa. – Veröffentlichungen des Museums für Naturkunde Chemnitz, **22**, 65–78, Chemnitz.

RÖßLER, R. (2000): The late Palaeozoic tree fern *Psaronius* – an ecosystem unto itself. – Review of Palaeobotany and Palynology, **108**, 55–74, Amsterdam.

RÖßLER, R. (2001a): Vielfalt paläozoischer Baumfarne – eine bis heute lebende Erfindung der Natur. – In: RÖßLER, R. (Hrsg.): Der Versteinerte Wald von Chemnitz. Katalog zur Ausstellung Sterzeleanum, Museum für Naturkunde Chemnitz, 78–99, Chemnitz.

RÖßLER, R. (2001b): Alternative Wuchsformen – die Sieger beim Ringen um Licht, Nahrung und Schutz. – In: RÖßLER, R. (Hrsg.): Der Versteinerte Wald von Chemnitz. Katalog zur Ausstellung Sterzeleanum, Museum für Naturkunde Chemnitz, 138–159, Chemnitz.

RÖßLER, R. (2002): Zwischen kostbarem Erbe und eigenem Erleben – Paläobotanische Forschungen im Perm von Chemnitz, Deutschland. – In: DERNBACH, U. & TIDWELL, W.D.I. (Hrsg.): Geheimnisse Versteinerter Pflanzen, 104–119, Rom (D'ORO Verlag).

RÖßLER, R. & GALTIER, J. (2002): *Dernbachia brasiliensis* gen. nov. et sp. nov. – a new small tree fern from the Permian of NE Brazil. – Review of Palaeobotany and Palynology, **122**, 239–263, Amsterdam.

RÖßLER, R., ZIEROLD, T., FENG, Z., KRETZSCHMAR, R., MERBITZ, M., ANNACKER, V. & SCHNEIDER, J.W. (2012): A snapshot of an early Permian ecosystem preserved by explosive volcanism: New results from the Chemnitz Petrified Forest, Germany. – Palaios, **27**, 814–834, Tulsa.

RUDOLPH, K. (1906): Psaronien und Marattiaceen. Vergleichende anatomische Untersuchungen. – Denkschriften der mathematisch-naturwissenschaftlichen Klasse der kaiserlichen Akademie der Wissenschaften in Wien, **LXXVIII**, 165–201, Wien.

RUDOLPH, K. (1922): Zur Kenntnis des Baus der Medullosen. – Beihefte zum Botanischen Centralblatt, **XXXIX**, 2. Abteilung, 196–222, Dresden.

SAHNI, B. (1932): On the structure of *Zygopteris primaria* (COTTA) and on the relations between the genera *Zygopteris*, *Etapteris* and *Botrychioxylon*. – Philosophical Transactions of the Royal Society of London B, **222**, 29–45, London.

SCHIMPER, W.P. (1869): Traité de paléontologie végétale, ou, La flore du monde primitif dans ses rapports avec les formations géologiques et la flore du monde actuel. – V.1, 738 S., Paris (J.B. Baillière et fils).

SCOTT, D.H. (1909): Studies in fossil botany. – 1683 S., London (Adam and Charles Black).

SIEBER, R. (1984): Bericht über Ordnungsarbeiten in der paläobotanischen Sammlung der Geologischen Bundesanstalt. – Jahrbuch der Geologischen Bundesanstalt, **127**/2, 273–276, Wien.

SOLMS-LAUBACH, H. ZU (1887): Einleitung in die Paläophytologie vom botanischen Standpunkt aus. – 416 S., Leipzig (Verlag von Arthur Felix).

SPRENGEL, D.A. (1828): Commentatio de Psarolithis, ligni fossilis genere. – 42 S., Halle.

STEININGER, F.F., ANGETTER, D. & SEIDL, J. (2018): Zur Entwicklung der Paläontologie in Wien bis 1945. – Abhandlungen der Geologischen Bundesanstalt, **72**, 9–159, Wien.

STENZEL, K.G. (1854): Über die Staarsteine. – Nova acta physico-medica Academiae Caesareae Leopoldino-Carolinae Naturae Curiosum, **24**/2, 1–146, Breslau–Bonn.

STENZEL, G. (1889): Die Gattung *Tubicaulis* COTTA. – Bibliotheca Botanica, Abhandlungen aus dem Gesamtgebiete der Botanik, **12**, 1–50, Cassel.

STENZEL, G. (1906): Die Psaronien, Beobachtungen und Betrachtungen. – Beiträge zur Paläontologie und Geologie Österreich-Ungarns und des Orients, **19**, 85–123, Dresden–Leipzig.

STERZEL, J.T. (1875): Die fossilen Pflanzen des Rothliegenden von Chemnitz in der Geschichte der Palaeontologie. – Fünfter Bericht der Naturwissenschaftlichen Gesellschaft zu Chemnitz, umfassend die Zeit vom 1. Januar 1873 bis 31. Dezember 1874, 71–243, Chemnitz (Carl Brunnersche Buchhandlung).

STERZEL, J.T. (1876): Taeniopterideen aus dem Rothliegenden von Chemnitz-Hilbersdorf. – Neues Jahrbuch für Mineralogie, Geologie und Paläontologie, Jahrgang **1876**, 369–385, Stuttgart (E. Schweizerbart'sche Verlagsbuchhandlung).

STERZEL, J.T. (1887): Über den grossen *Psaronius* in der naturwissenschaftlichen Sammlung der Stadt Chemnitz. – Zehnter Bericht der Naturwissenschaftlichen Gesellschaft zu Chemnitz, umfassend die Zeit vom 1. September 1884 bis 31. Dezember 1886, 144–156, Chemnitz (Carl Brunnersche Buchhandlung).

STEWART, W.N. & ROTHWELL, G.W. (1993): Paleobotany and the Evolution of Plants. – Second edition, 521 S., Cambridge (Cambridge University Press).

STIDD, B.M. (1971): Morphology and Anatomy of the Frond of *Psaronius*. – Palaeontografica, Abteilung B, **134**/4–6, 87–123, Stuttgart.

STOJASPAL, F. (1999): Sammlungen. – In: GEOLOGISCHE BUNDESANSTALT (Hrsg.): Die Geologische Bundesanstalt in Wien. 150 Jahre Geologie im Dienste Österreichs (1849–1999), 189–212, Wien (Böhlau Verlag).

STUR, D. (1874): Reise-Skizzen. I. Dresden, d. 15. März 1874. – Verhandlungen der k. k. Geologischen Reichsanstalt, **1874**, 135–138, Wien.

STUR, D. (1876): Reise-Berichte. – Verhandlungen der k. k. Geologischen Reichsanstalt, **1876**, 261–289, Wien.

STUR, D. (1883): Zur Morphologie und Systematik der Culm- und Carbonfarne. – Sitzungsberichte der mathematisch-naturwissenschaftlichen Klasse der kaiserlichen Akademie der Wissenschaften, **LXXXVIII**, 633–846, Wien.

STUR, D. (1885): Die Carbon-Flora der Schatzlarer Schichten. Abtheilung 1: Die Farne der Carbon-Flora der Schatzlarer Schichten. – Abhandlungen der k. k. Geologischen Reichsanstalt, **11**/1, 418 S., Wien.

STUR, D. (1887): Die Carbon-Flora der Schatzlarer Schichten. Abtheilung 2: Die Calamarien der Carbon-Flora der Schatzlarer Schichten. – Abhandlungen der k. k. Geologischen Reichsanstalt, **11**/2, 240 S., Wien.

SÜSS, H. & RANGNOW, P. (1984): Die Fossiliensammlung Heinrich Cottas im Museum für Naturkunde der Humboldt-Universität zu Berlin. – Neue Museumskunde, **27**, 17–34, Berlin.

TANSLEY, A.G. (1907): Lectures on the evolution of the filicinean vascular system. – The New Phytologist, **VI**/3–4, 53–68, London.

TAYLOR, T.N., TAYLOR, E.L. & KRINGS, M. (2009): Paleobotany. The Biology and Evolution of fossil plants. – 2^{nd} edition, 1230 S., Amsterdam (Elsevier).

THALHEIM, K. (Hrsg.) (2006): Schatzkammer – Museum. Vom Mineralienkabinett zum Museum für Mineralogie und Geologie. 275 Jahre naturwissenschaftliche Sammlungen in Dresden. – Schriften des Staatlichen Museums für Mineralogie und Geologie Dresden, **14**, 160 S., Dresden (Staatliches Museum für Mineralogie und Geologie zu Dresden).

TRÜMPER, S., RÖßLER, R. & GÖTZE, J. (2018): Deciphering Silicification Pathways of Fossil Forests: Case Studies from the Late Paleozoic of Central Europe. – Minerals, **2018**/8, 432, 1–29, Basel. https://dx.doi.org/10.3390/min8100432

UNGER, F. (1850): Genera et Species Plantarum Fossilium. – XL + 627 S., Vindobonae (Wilhelmum Braumüller).

ZORN, I. (2012): In memoriam HR Dr. phil. Franz Stojaspal. 2. April 1946 – 31. August 2012. – Jahrbuch der Geologischen Bundesanstalt, **152**/1, 5–12, Wien.

ZORN, I., MELLER, B., DRAXLER, I., SURENIAN, R. & GEBHARDT, H. (2007): Historische Kostbarkeiten der Sammlungen der Geologischen Bundesanstalt in Wien. – Geo.Alp, Sonderband **1**, 165–173, Innsbruck.

Eingelangt: 12. August 2019, angenommen: 16. Oktober 2019

JAHRBUCH DER GEOLOGISCHEN BUNDESANSTALT
Jb. Geol. B.-A.	ISSN 0016–7800	Band 159	Heft 1–4	S. 315–338	Wien, Dezember 2019

Die Geologische Erforschungsgeschichte des Achensee-Gebietes: Experimentierfeld von stratigrafischen und tektonischen Kontroversen

Ein Beitrag zu den Erläuterungen von Kartenblatt 88 Achenkirch

Alfred Gruber* & Michael Lotter*

11 Abbildungen

Österreichische Karte 1:50.000
BMN / UTM
87 Walchensee / NL 32-03-17 Hinterriß
88 Achenkirch / NL 32-03-18 Kundl
89 Angath
118 Innsbruck / NL 32-03-23 Innsbruck
119 Schwaz / NL 32-03-24 Schwaz
120 Wörgl

Nördliche Kalkalpen
Geologische Kartenwerke
Jurassische Geodynamik
Bächentaler Becken
Achentaler Schubmasse
Karwendel-/Thiersee-Synklinale
Quartärgeologie

Inhalt

Zusammenfassung

Im Zuge der Erstellung der Erläuterungen zur geologischen Karte 1:50.000 Blatt 88 Achenkirch wurde die über 150-jährige geologische Erforschungsgeschichte der Achensee-Region detailliert aufgearbeitet. Rund um den Achensee, im östlichen Karwendel, im Rofan, am Unnutz und Guffert wurden grundlegende geologische Erkenntnisse der westlichen Nördlichen Kalkalpen erarbeitet. Dies betrifft vor allem den Decken-, Überschiebungs- und Faltenbau (Karwendel-Überschiebung, „Achentaler Schubmasse“, Tiefbohrung Vorderriss, TRANSALP-Tiefenseismik-Profil), die geodynamische und fazielle Entwicklung in Obertrias und Jura (GSSP Trias-Jura-Grenze, Jura-Extensions- und Gleittektonik, Resedimente), aber auch Aspekte der Quartärgeologie (Deltasysteme, Achensee-Damm, Begriff der „Bergzerreißung“).

The geological research history of the Achensee area: experimental field of stratigraphic and tectonic controversies

A contribution to the explanations of map sheet 88 Achenkirch

Abstract

In the course of writing the explanatory notes of the geological map 1:50,000 sheet 88 Achenkirch, the more than 150-year geological research history of the Achensee region was reviewed in detail. Around the Achensee, in the eastern Karwendel, in Rofan, at Unnutz and Guffert, fundamental geological knowledge of the western Northern Calcareous Alps was acquired. This concerns the structures of nappes, thrusts and folds (Karwendel thrust, “Achentaler Schubmasse”, deep drilling of Vorderriss, TRANSALP deep seismic profile), the geodynamic and facies development in Upper Triassic and Jurassic (GSSP Triassic-Jurassic boundary, Jurassic extensional and glide tectonics, resediments), but also aspects of Quaternary Geology (delta systems, Achensee dam, the concept of “Bergzerreißung”).

* Alfred Gruber, Michael Lotter: Geologische Bundesanstalt, Neulinggasse 38, 1030 Wien. alfred.gruber@geologie.ac.at, michael.lotter@geologie.ac.at

Einleitung

Die umfangreiche stratigrafische und strukturgeologische Literatur zur geologischen Erforschung der Achensee-Region wird in diesem Beitrag chronologisch und themenbezogen abgehandelt. Die im Text angeführten Legendennummern beziehen sich auf die Schichtfolge der im Jahr 2012 publizierten Geologischen Karte 1:50.000, Blatt 88 Achenkirch (Gruber & Brandner, 2012), deren begleitende Lektüre zur Orientierung empfohlen wird. Weiterführende Informationen finden sich in den im kommenden Jahr erscheinenden zugehörigen Erläuterungen (Gruber et al., in Druck).

Erkundungen und Kartenwerke im 19. Jahrhundert

Die Geologie des Kartenblattes 88 Achenkirch wird erstmals auf der „Geognostischen Karte Tirols" im Maßstab 1:115.200 (Geognostischer Verein für Tirol und Vorarlberg, 1849) dargestellt und von Widmann (1853) erläutert (Abb. 1).

Pichler (1856) veröffentlicht Ergebnisse seiner geologischen Streifzüge durch die Nördlichen Kalkalpen Tirols. Der geologische Aufbau des Gebietes zwischen Seefeld und Kufstein (Karwendel, Brandenberger Alpen) wird anhand von 17 Schichtgliedern detailliert beschrieben. Im Gebiet von Blatt Achenkirch sind „Cardita-Schichten" (Nordalpine Raibler Schichten, **43**), „Gervillien-Schichten" (Kössen-Formation, **39**), „Lithodendronkalk" (Oberrhätkalk, **38**), „Adnether Schichten" (auf dem aktuellen Kartenblatt subsumiert unter Rotkalk-Gruppe, **34**), „Roter Hornstein" (Radiolarit, Ruhpolding-Formation, **31**), „Aptychenkalk" (Ammergau-Formation, **28**) sowie „Neocomien" (Schrambach-Formation, **27**), „Diluvium" und „Neubildungen" (pleistozäne und holozäne Ablagerungen) ausgeschieden. Die Verbreitung der Schichten ist in einer geologischen Manuskriptkarte im Maßstab 1:200.000 dargestellt. Pichler (1856) entwirft Profilschnitte durch die überkippte Schichtfolge an der Unnutz-Westflanke, durch die Thiersee-Synklinale im Bereich Ampelsbach (Abb. 2) und durch den Knick der Karwendel-Synklinale an ihrem Ostende (Seebergspitze, 2.085 m, ÖK 119).

Pichler (1869) beschreibt ein Profil in den „Cardita-Schichten" des Unnutz-Massivs. In deren Kalken und Sandsteinen findet er typische Fossilien wie *Ostrea montis caprilis* und „Lettenkohlen"-Pflanzenreste wie *Equisetites arenaceus* sowie

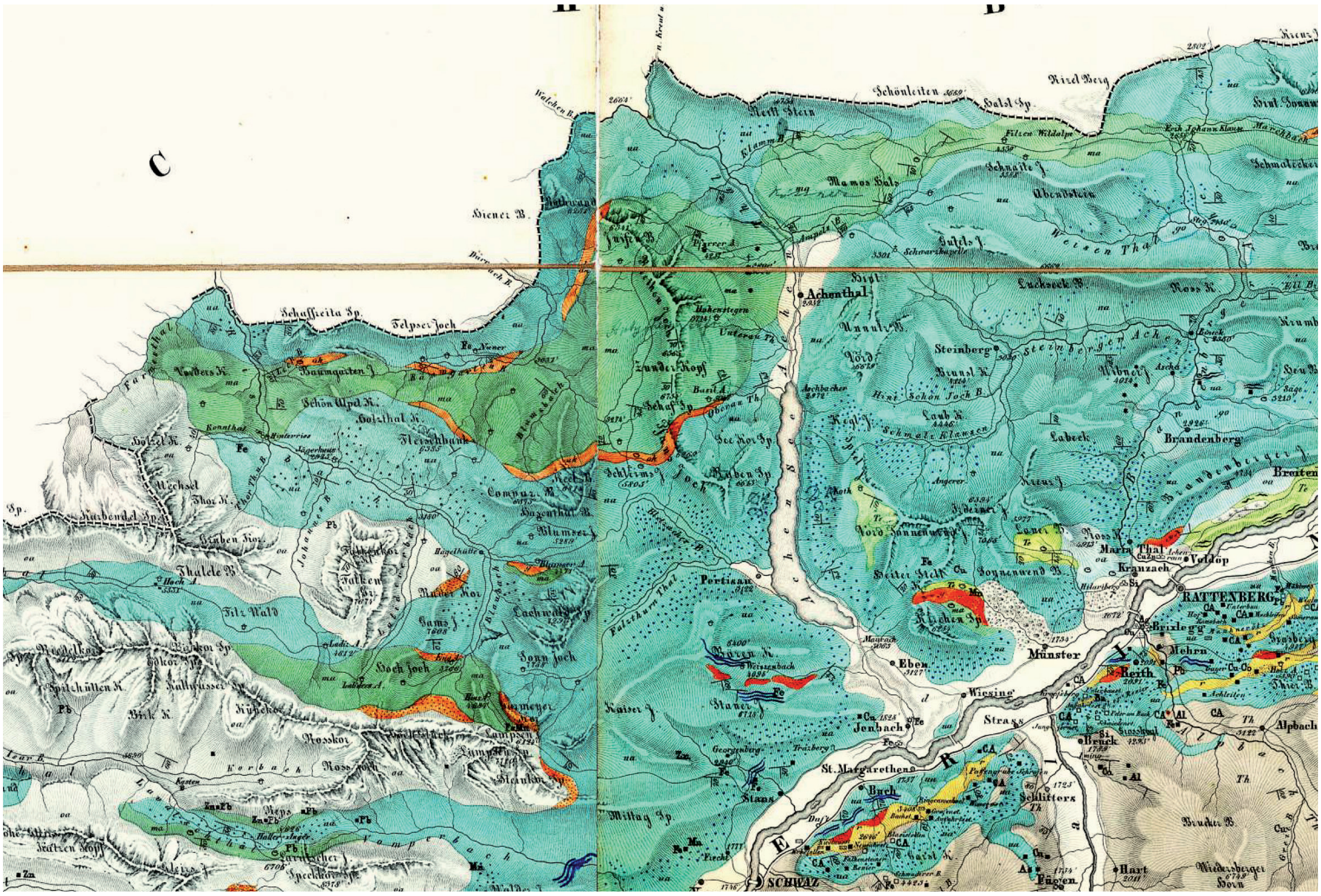

Abb. 1.
Erste geologische Karte mit Darstellung des Achensee-Gebietes: „Geognostische Karte Tirols, aufgenommen und herausgegeben auf Kosten des geognostisch montanistischen Vereins von Tirol und Vorarlberg 1849". Der hier gezeigte Ausschnitt umfasst die damalige Schichtfolge „**Th** Thonglimerschiefer (Übergangsschiefer)" (hellbraungrau), „**r** Rother und grauer Sandstein (Porphyrsandstein)" (gelb), „**g** Gips. Alabaster." (rot), „Rauhwacke" (rot gepunktet), „**ua** Unterer Alpenkalk" (blau), „Dolomit des untern Alpenkalkes" (blau mit Punkten), „Dunkle Kalk Mergelschiefer des untern Alpenkalkes" (blau mit dunklen Streifen), „**ak** Ammonitenkalk" (dunkles Rot), „**ma** Mittlerer Alpenkalk" (grün), „**oa** Oberer Alpenkalk" (hellblau), „**Te** Tertiaere Gebilde" (hellgrün), „**d** Diluvium" (weiß) und „Alluvium" (weiß). Der Verlauf von Karwendel- und Thiersee-Synklinale ist bereits erkennbar.

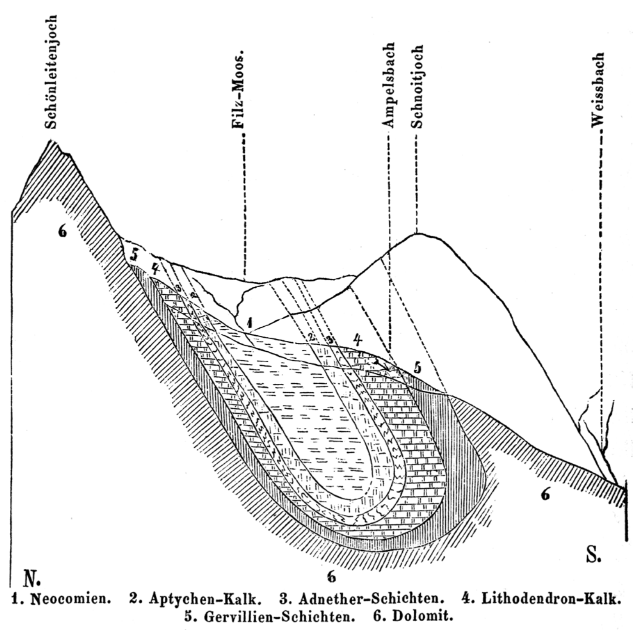

Abb. 2.
Erste Darstellung der überkippten Thiersee-Synklinale im Ampelsbach (PICHLER, 1856).

ein „bernsteinartiges Harz“. In dieser Publikation erfolgt auch eine Beschreibung des Jura-Profils am Fonsjoch (das Profil liegt im Gratabschnitt Juchtenkopf–Hohe Gans, 1.950 m, ÖK 119) und eine Auflistung der reichen Fossilführung aus einem „gelblichen Kalk“ („Enzesfelder Kalk“ – Kendlbach-Formation, subsumiert unter **37** und **32**).

GÜMBEL (1861) veröffentlicht die „Geognostische Karte des Königreichs Bayern“ im Maßstab 1:100.000. Auf Blatt IV Miesbach ist das gesamte Kartenblatt Achenkirch dargestellt. Das Kartenwerk wird in der „Geognostischen Beschreibung des Bayerischen Alpengebirges und seines Vorlandes“ erläutert. GÜMBEL erwähnt darin einige grundlegende stratigrafische und tektonische Details des Kartenblattes. Er zeigt unter anderem Profilschnitte vom Zotenjoch zum Juifen (1.988 m) und von der Großzemmalm zur Hochplatte (1.813 m). In letzterem erkennt er die überkippte Lagerung der Schichten. GÜMBEL (1894) präsentiert ein Nord–Süd-Profil von Bad Tölz bis in das Inntal.

NEUMAYR (1870a–d, 1871) stellt für die Geologische Reichsanstalt die geologischen Verhältnisse des Karwendelgebirges auf handkolorierten Manuskriptkarten im Maßstab 1:28.800 zusammen. Diese Karten dienen als Vorlage für die Geologische Spezialkarte der Österreichisch-Ungarischen Monarchie im Maßstab 1:144.000, die jedoch nie gedruckt wird.

MOJSISOVICS (1870, 1871) bearbeitet für die Blätter „Umgebungen von Kufstein und Schwaz“ dieses Kartenwerkes im Maßstab 1:144.000 den Abschnitt vom Achental ostwärts bis zur Salzburger Grenze. 1870 veröffentlicht er einen Kurzbericht, der „das Kalkalpengebiet zwischen Schwaz und Wörgl im Norden des Inn“ behandelt. Er schreibt: *„Im Jura-Kreide-Becken von Achenkirchen und Ampelsbach wurde als Unterlage der jurassischen Schichten die rhätische Stufe nachgewiesen und durch Petrefactenfunde (Lima gigantea, Avicula sinemuriensis, …) auch der untere Lias in einer an die Schichten […] des Salzkammergutes erinnernden lithologischen Entwicklungsform […] constatirt.“* (MOJSISOVICS, 1870: 183).

1871 legt MOJSISOVICS einen ausführlichen Aufnahmsbericht seines Kartiergebietes vor. Wichtige Aussagen sind z.B.:

„Die Gruppen des Unnutz und des Guffert. Mächtige allseits mit steil gestellten Flügeln abfallende Gewölbe von Wettersteinkalk bilden die Hauptmassen dieser Gruppen. Gegen Süden fallen die Schichten südlich ein; sie unterteufen, von einer schmalen Zone von Torer Schichten überdeckt, in regelmässiger Weise die Hauptdolomit-Massen der Rofan-Gruppe. Gegen Westen neigen sich die Schichten sehr steil gegen das Achenthal zu“ (MOJSISOVICS, 1871: 198).

„Ob man im Westen, wo der Ampelsbach die südliche Wandung quer durchreisst, oder im Osten bei Hinter-Thiersee ein Profil zieht, es bleibt mit geringen Abweichungen das gleiche. Innerhalb dieser langen Strecke ist der südliche Schenkel der Mulde immerfort überkippt und fällt conform mit dem nördlichen Schenkel regelmässig ziemlich flach gegen Süden ein“ (MOJSISOVICS, 1871: 199).

„Am Mamoshals selbst, wo die Abzweigung dieses Zuges eintritt, treten die neocomen Mergel in Contact mit rhätischem Korallenkalk, wohl nur eine Folge von intensiver Pressung und Ueberschiebung über die dazwischen lagernden Bildungen“ (MOJSISOVICS, 1871: 200).

Schon bald kristallisieren sich regionale Schwerpunkte der Forschung heraus: die „Jura-Kreide-Mulde“ im nördlichen Karwendel (Karwendel-Synklinale, ÖK 87, 88, 118, 119) sowie das geologisch vielfältige Rofangebirge östlich des Achensees (ÖK 88, 89, 119).

ROTHPLETZ (1888) erstellt die erste „Geologische Karte des Karwendelgebirges“ im Maßstab 1:50.000 auf Basis der Alpenvereinskarte. Diese Karte ist das Ergebnis systematischer Kartierungen im Rahmen von Dissertationen, die in den Gebieten westlich des Achentales bzw. des Achensees von CLARK (1887), im Umkreis des Juifen (1.988 m) von SAPPER (1888) sowie im westlichen Bächental und im Rißtal (ÖK 87 und 118) von SCHÄFER (1888) durchgeführt werden.

CLARK (1887) erwähnt Details wie bituminöse Einschaltungen im Hauptdolomit (**41**) und die rhätische Riffbildung der „Wilden Kirche“ (Schoberberg, 1.711 m, auf ÖK 119). Er unterteilt den Oberjura in einen „Roten Hornstein“ (Ruhpolding-Formation, **31**), einen „Grauen Hornstein“ (Tauglboden-Formation, **30**) und in einen mächtigen „Aptychenkalk“ (Ammergau-Formation, **28**). Im „Aptychenkalk“ führt er die Rippen aus „Breccien mit Hornstein“ (Rofan-Brekzie, Barmsteinkalk, **29**) an. Das darüber folgende mergelige „Neocom“ (Schrambach-Formation, **27**) erkennt er im Bächental, zwischen Juifen (1.988 m) und Marbichlerspitze (1.898 m) und am Gröbner Hals. CLARK spricht von „der großen Mulde“ (Karwendel-Synklinale) mit „Neocom“ im Kern, die von einem E–W- auf ein N–S-Streichen umbiegt. Weiters notiert er zwei senkrecht aufeinander stehende Faltenrichtungen und hebt „die Überlagerung des Aptychenkalkes durch Hauptdolomit“ im Unterau- und Blaserbachtal hervor.

SAPPER (1888) liefert ein erstes detailliertes Schichtenprofil vom Juifen-Nordgrat. Die Faziesunterschiede und Mächtigkeitsschwankungen der Schichtfolge des Unterjura werden anhand von fünf Detailprofilen (Juifen, Dollmannsbach, Rotwandalm-Hochleger und Rotwandalm-Niederleger sowie Fonsjoch, ÖK 119) herausgearbeitet. SAPPER erkennt Störungen und Faltenstrukturen am Schulterberg (1.686 m), Pitzkopf (1.670 m) und am Demeljoch (1.924 m).

Frühe stratigrafische Studien

Der Paläontologe NEUMAYR (1879) vergleicht die Fauna (Ammoniten, Brachiopoden) der Zone des *Aegoceras Planorbis* vom Profil Fonsjoch im Gratabschnitt Juchtenkopf–Hohe Gans (1.950 m, ÖK 119) mit Lokalitäten im Salzkammergut (Breitenberg und Zlambachgraben). Durch diese Arbeit wird das Fonsjoch als Fossilfundstelle und das Achensee-Gebiet in Geologenkreisen allgemein bekannt gemacht. Die reiche Unterjura-Fauna am Fonsjoch ist später mehrfach Gegenstand paläontologischer und fazieller Untersuchungen (VORTISCH, 1926; LANGE, 1952; BLIND, 1963; KARLE, 1984).

WÄHNER (1886a) baut seinen Beitrag zur litho- und biostratigrafischen Gliederung des tiefsten Unterjura der Nördlichen Kalkalpen unter anderem auf genauen Profilstudien am Fonsjoch und im Rofan auf. In Teil 1 seiner Arbeit vergleicht er gelblich-rote, fossilreiche Kalke mit der Fazies der „Enzesfelder Schichten“ in Niederösterreich. Er schlägt hierfür die Bezeichnung „Bunte Cephalopodenkalke“ vor. In Teil 2 seiner Abhandlung fordert WÄHNER (1886b) für die Fazies der Bunten Cephalopodenkalke, der Adneter Schichten und der Fleckenmergel (Allgäu-Formation, **32**) große Meerestiefen und Küstenferne. „Brauneisenkonkretionen und rote Tone“ im Horizont der *Schlotheimia marmorea* wären mit den rezenten Bildungen der Tiefsee vergleichbar. Laut WÄHNER (1886b) sind die alpinen Unterjura-Bildungen von den Hochzonen (Dachsteinkalk-Plateaus mit Ablagerung des Hierlatzkalks) bis in die Tiefsee alle durch fazielle Übergänge untereinander verbunden. WÄHNER (1886b) führt eine heftige Auseinandersetzung mit GEYER (1886) und DIENER (1885a, b) über die stratigrafischen Beziehungen der unterstjurassischen Horizonte zum Dachsteinkalk. Unter anderem lehnt er deren gemeinsame Verzahnung bzw. eine dazwischenliegende subaerische Erosion strikt ab.

WÄHNER (1903) fasst mit seiner Monografie „Das Sonnwendgebirge im Unterinnthal – Ein Typus alpinen Gebirgsbaues“ (1. Teil) die Ergebnisse von 20 Jahren präziser geologischer Feldforschung im Rofan zusammen. Das gesamte Werk (der zweite Band wird 1935 von Erich Spengler mit Geologischer Karte im Maßstab 1:10.000 herausgegeben – WÄHNER & SPENGLER, 1935, siehe unten) stellt bis heute einen reichen Fundus stratigrafischer, paläontologischer und tektonischer Erkenntnisse über dieses Gebirge hinaus dar.

HAHN (1911) beschreibt das Obertrias-Jura-Profil am unteren Ampelsbach. Er unterstreicht den Fossilreichtum der Kössen-Formation (**39**) und erwähnt darin stellenweise Pyritvorkommen, die der Grund für die Bildung der dortigen Schwefelquelle und in Folge für die Entstehung des Schwefelbades verantwortlich seien. Die sandigen Kalke des untersten Jura setzt er mit den „Grestener Schichten“ (Gresten-Formation des Helvetikums) in Niederösterreich gleich.

Otto Ampferer – Pionier des Deckenbaus der Kalkalpen und moderner Geologischer Kartenwerke

Mit ihrer gemeinsamen Dissertation über das südliche Karwendelgebirge werden die Innsbrucker Geologen Otto Ampferer und Wilhelm Hammer in Geologenkreisen schlagartig bekannt (AMPFERER & HAMMER, 1898, 1899). Die k. k. Geologische Reichsanstalt beauftragt daraufhin Otto Ampferer mit der Neuaufnahme des gesamten Karwendelgebirges und der östlich anschließenden Brandenberger Alpen (AMPFERER, 1902a, b, 1903a, b, 1905a, b, c, 1907, 1914a, b). In den Jahren 1912 bis 1925 erscheinen vier Geologische Spezialkarten im Maßstab 1:75.000 (Aufnahmemaßstab 1:25.000), die das gesamte Gebiet des Achensee-Raumes umfassen. Es handelt sich um die Blätter „Achenkirch und Benedictbeuern“ (Abb. 3), „Innsbruck und Achen-See“, „Kufstein“, sowie „Rattenberg“ (AMPFERER, 1912a, 1925a; AMPFERER & OHNESORGE, 1912, 1918). Das Gebiet des Blattes 88 Achenkirch wird hierbei vollständig von Blatt „Achenkirch und Benedictbeuern“ abgedeckt.

AMPFERER (1902b) gibt einen ersten geologischen Überblick betreffend die Neuaufnahme des Karwendelgebirges und präsentiert ein tektonisches Süd–Nord-Profil vom Halltal bis zum Südrand der Karwendel-Synklinale im Bereich Kompar (2.011 m, Bächen-/Risstal, ÖK 118, 119) (Abb. 4). Auf dem Profil sind überkippte Faltenschenkel und Überschiebungen zu sehen. Erstmals ist von einer großen Karwendel-Überschiebung die Rede. Diese Erkenntnis ist Ausgangspunkt für Ampferers spätere Einteilung der westlichen Nördlichen Kalkalpen in Allgäu-, Lechtal-, Inntal- und Krabachjoch-Decke (AMPFERER, 1912b, 1914c). Das genannte Süd–Nord-Profil durch das Karwendelgebirge wurde später mehrfach von namhaften Kalkalpengeologen zur Veranschaulichung des Deckenbaus herangezogen und erweitert (z.B. SCHMIDT-THOMÉ, 1950; TOLLMANN, 1969; BRANDNER, 1980; BAYERISCHES GEOLOGISCHES LANDESAMT, 1996). HEISSEL (1977, 1978) gab dem kompliziert gebauten Grenzbereich zwischen Inntal-Decke und Lechtal-Decke im nördlichen Karwendel die Bezeichnung Karwendel-Schuppenzone. Die in den letzten Jahren erfolgte Neubearbeitung durch KILIAN & ORTNER (2019) und BRANDNER (2013, 2019) revidiert diese tektonische Situation und definiert den Deckenbau neu. Die Inntal-Decke reicht demnach wesentlich weiter nach Norden bis an den Kalkalpenrand, was im Übrigen schon RICHTER (1937) sehr früh erkannt hat. Eine ausführliche Abhandlung dieser Thematik findet sich in den Erläuterungen zum Kartenblatt (GRUBER et al., in Druck).

In AMPFERER (1902a, 1903a) werden Unterschiede der tektonischen Verformung zwischen Karwendel- und Rofangebirge herausgearbeitet. Ost–West streichende Falten- und Überschiebungsstrukturen beherrschen das tektonische Muster im Karwendelgebirge: Die ursprünglich von Mittenwald bis Kufstein durchgehend West–Ost-streichende Kreidemulde des Karwendel wurde laut Ampferer später von der „Sonnwendjochplatte“ (Rofan) zu einer „Muldenschlinge“ verformt. Im Achental beobachtet der Autor einen Störungskontakt (Unnutz-Überschiebung) zwischen dem Hauptdolomit und dem Wettersteinkalk des Unnutz und Guffert.

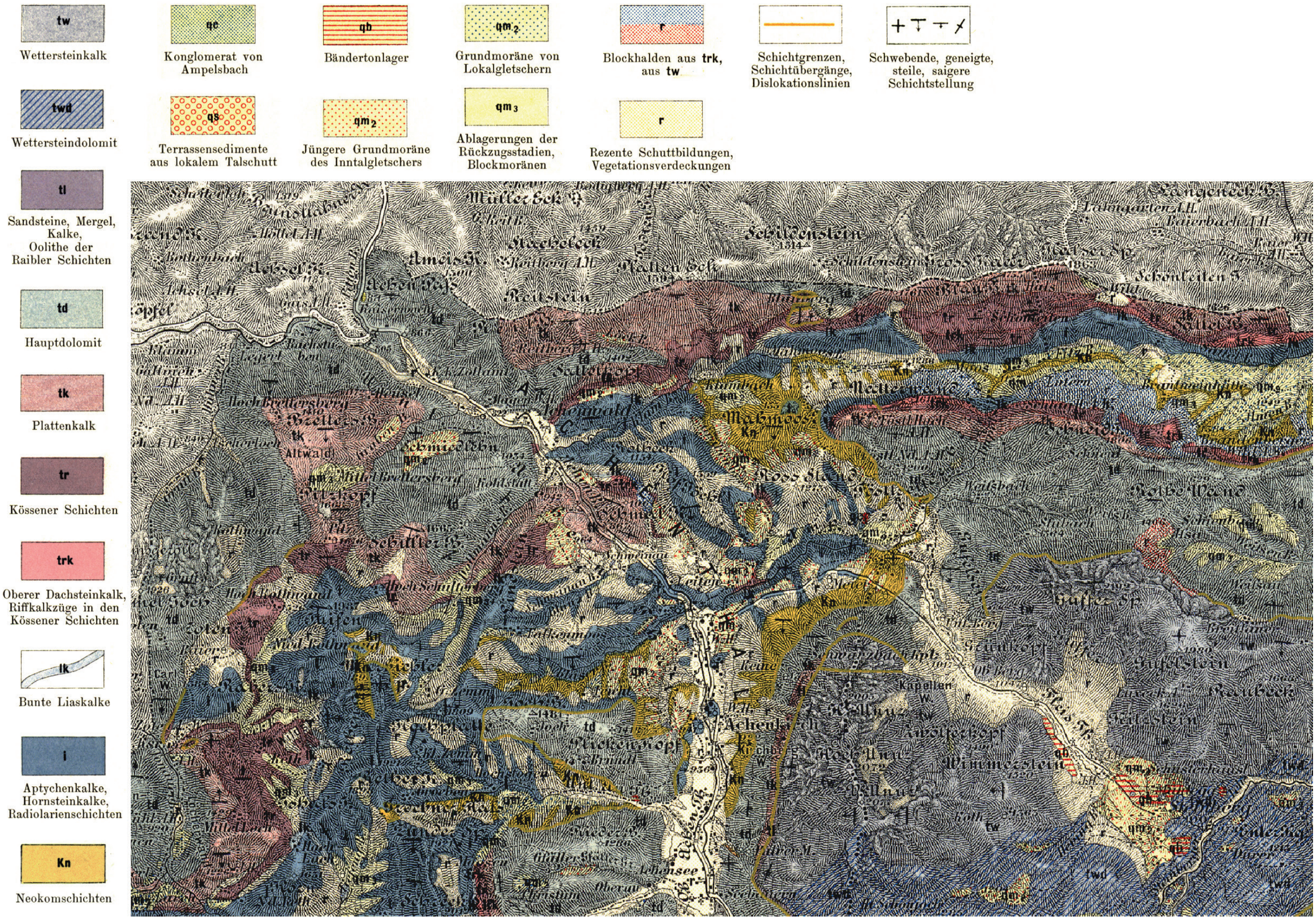

Abb. 3.
Ausschnitt von Blatt 4947 Achenkirch und Benedictbeuern im Maßstab 1:75.000 der Geologischen Spezialkarte Österreich-Ungarns (AMPFERER, 1912a). Diese Karte zeigt erstmalig die Unnutz-Überschiebung und differenziert Festgesteins- und Quartärablagerungen mit „moderner", teils heute noch gültiger Nomenklatur.

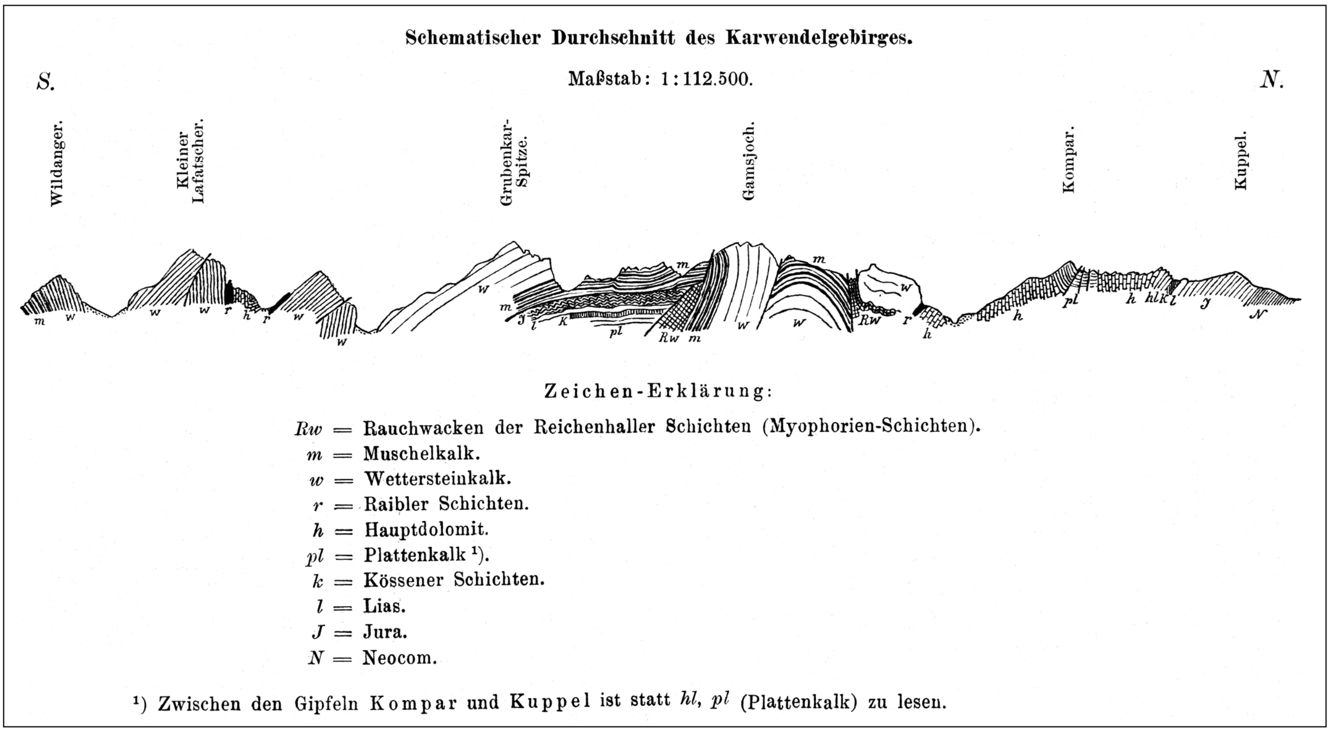

Abb. 4.
Erste Profildarstellung der Karwendel-Überschiebung, Prototyp für die spätere Deckengliederung Inntal-Decke/Lechtal-Decke (AMPFERER, 1903b). Zwischen Grubenkarspitze und Gamsjoch ist eine flache Überschiebungsbahn dargestellt, an der Muschelkalk und Wettersteinkalk (Inntal-Decke) Gesteine der Obertrias und des Jura (Lechtal-Decke) überlagern. Auch in allen späteren Bearbeitungen hat sich der Bereich des Gamsjochs als Schlüsselstelle der Deckengliederung erwiesen.

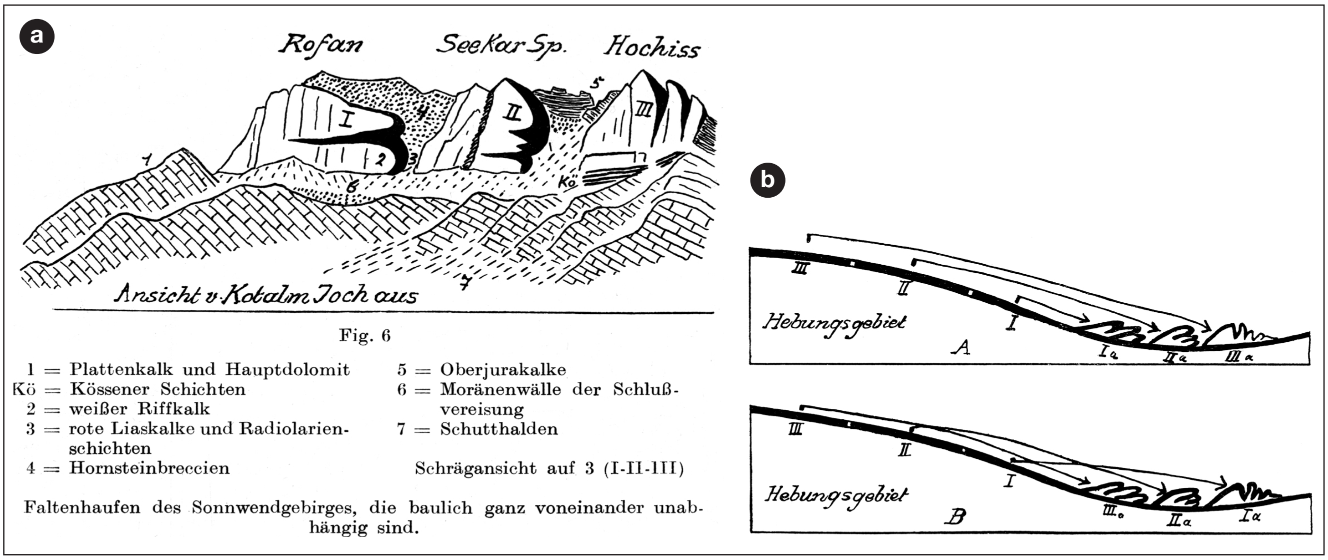

Abb. 5.
a) Ansicht der Nordwand des Rofangebirges (Ampferer, 1941a). Die Faltenstrukturen im weißen Riffkalk (2; Oberrhätkalk) werden hier als Gleitfalten interpretiert, über welche die Hornsteinbreccien (4) transgredieren. b) Modelle der Gleitfalten- und Gleitschollenbildung (Ampferer, 1941a).

Ampferer (1903b) veranschaulicht den Gebirgsbau im Karwendelgebirge mit zahlreichen Profilschnitten. Die quartären Ablagerungen sind bezüglich Aufbau und Genese treffend dargestellt.

Das Erscheinen von Wähners Monografie über das Rofangebirge (Wähner, 1903) nimmt Ampferer (1903a) zum Anlass, Wähners tektonische Deutung der „Hornsteinbreccie des Sonnwendgebirges“ (= Rofan-Brekzie) zu widerlegen und deren sedimentäre Entstehung zu unterstreichen, wobei er das Vorkommen von Störungsbrekzien prinzipiell nicht in Frage stellt. Er erläutert mit Profilschnitten die „Unnutz-Überschiebung“, die er „von Südosten nach Nordwesten vorschreitend“ betrachtet. Ampferer (1903a) bezeichnet das Rofangebirge als „beispielhaft für die Gesetze der alpidischen Gebirgsbildung“ (zu diesem Zeitpunkt hat Ampferer seine Unterströmungstheorie noch nicht formuliert) und geht hierzu näher auf die Faltenstrukturen und die Mehrphasigkeit der Einengung ein.

Bereits 1905 legt Ampferer acht fertige Aufnahmsblätter des riesigen Kartierungsgebietes zwischen dem Fernpass und dem Achensee vor und umreißt in einem Aufsatz die geologischen Grundzüge von Mieminger Gebirge, Wetterstein- und Karwendelgebirge (Ampferer, 1905a, b).

Ampferer (1908) setzt sich eingehend mit dem Thema der „Hornsteinbreccie“ im Rofan (ÖK 119) auseinander und sammelt Argumente für deren sedimentäre Natur. Er betont, dass die Brekzien genauso Tiefseeablagerungen seien wie die mit ihnen wechsellagernden „Radiolarienschichten“. Er zeigt am Profil Vorderes Sonnwendjoch (2.224 m) – Rofanspitze (2.259 m), dass die jurassischen „Hornsteinbreccien“ (Rofan-Brekzie) und der darüber folgende „Hornsteinkalk“ (Barmsteinkalk, **29**) N–S streichende Faltenstrukturen diskordant sedimentär überlagern und plombieren. Die Faltenentstehung erklärt er sich durch „Abgleitungen von einer Hochzone im Osten“ (Gleitfalten) (Abb. 5a, b). In der Folge wird die Bildung der Brekzien ausführlich beschrieben. Am Ende seiner langen produktiven Schaffensphase geht Ampferer nochmals ausführlich auf die vielfältigen Faltenstrukturen und die Genese der „Hornsteinbreccien“ im Rofan ein (Ampferer, 1941a).

Die Erläuterungen zu Blatt „Achenkirchen“ erscheinen 1914, jene zu Blatt „Innsbruck und Achen-See“ im Jahr 1924 (Ampferer, 1914b; Ampferer & Ohnesorge, 1924).

Im Beitrag über „NW-Beanspruchungen in den Nordalpen“ rückt Ampferer (1921) von seiner bis dahin geäußerten Ansicht (Ampferer, 1902a, b, 1903a, 1908) einer zweiphasigen Einengung (zuerst in E–W-, dann in N–S-Richtung) im Bereich der „Achentaler Querstruktur“ ab. Aus seiner Beobachtung vieler NW-schauender Faltenstirnen, wie z.B. der Unnutz-Falte, entwirft er die These von der „Drehscheibe von Achenkirchen“ (Abb. 6): Demnach hätte die „Unnutzmasse“ im Zuge der nordgerichteten Überschiebung eine Drehbewegung um 45° nach Nordwesten vollzogen, mit einem Angelpunkt an der Seebergspitze (2.085 m, ÖK 119). Auch die NE–SW streichenden Faltenstrukturen im Rofan erklärt Ampferer (1921) analog dazu mit einem Verdrehen ursprünglich E–W streichender Strukturen.

Angeregt durch die geologische Gutachtertätigkeit beim Bau des Druckstollens für das Achenseekraftwerk (siehe unten) prägt Ampferer (1924a, b) am Stanser Joch, südlich über dem Achensee (ÖK 119), den Begriff der Reliefüberschiebung (Abb. 7). Er versteht darunter den Vorschub einer Schubmasse nicht mehr über ein flaches „Schichtenland“, sondern über ein vorher gefaltetes und tief erodiertes Untergrundrelief, das überwältigt und unter der Schubmasse begraben wird. Hierbei werden die Talfurchen im Relief mit den durch die Reibung zurückgebliebenen Resten der überfahrenden Schubmasse verstopft und chaotisch verpresst. Mit der Schubmasse ist im konkreten Fall die Inntal-Decke gemeint. Ausgehend vom Stanser Joch wendet Ampferer das Prinzip der Reliefüberschiebung auf zahlreiche ähnlich gebaute Gebiete im Karwendel, in den Nördlichen Kalkalpen und sogar in den Dolomiten an (Ampferer, 1924a, b, 1928, 1929a, 1946; Ampferer & Pinter, 1927). In einer Neuuntersuchung der Typlokalität bestätigt Krauter (1967) Ampferers Reliefüberschiebungstheorie und baut diese sogar noch aus, indem er versucht, *„das Bewegungsbild der Überschiebungsvorgänge und das mechanische Verhalten der Basisgesteine zu rekonstruieren“* (Krauter, 1967: 23).

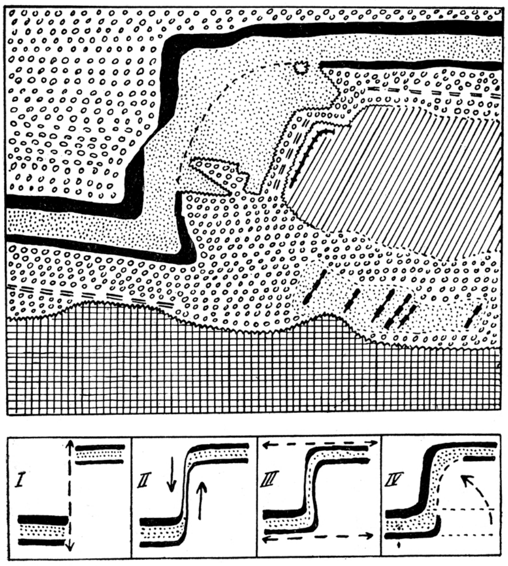

Abb. 6.
Das Modell der „Drehscheibe von Achenkirchen" als Erklärung für die „Knickungen" im Übergangsbereich Karwendel-/Thiersee-Synklinale (Ampferer, 1921).

Der Österreichische Alpenverein gibt Ende der 1930er Jahre den Auftrag, das Gebiet der damals neu erstellten Alpenvereinskartenblätter (Maßstab 1:25.000) „Karwendelgebirge West, Mitte und Ost" geologisch neu zu kartieren. Otto Ampferer bearbeitet das Blatt „Karwendelgebirge Ost". Im Rahmen seiner Kartierung geht er auf die Bedeutung von „Gleitungen" (gravitative Massenbewegungen) ein, die er z.B. an beiden Flanken des Achensees (ÖK 119) und mit Profilschnitten beschreibt (Ampferer, 1939, 1940a, b, 1941b).

Die abgeschlossene Neuaufnahme des östlichen Karwendelgebirges und das Erscheinen der östlich anschließenden „Geologischen Karte 1:10.000 des Sonnwendgebirges" (Wähner & Spengler, 1935) nützt Ampferer (1941a), um großräumige tektonische Zusammenhänge zwischen diesen beiden Gebirgsstöcken aufzuzeigen. Das Karwendelgebirge ist demnach an der Karwendel-Überschiebung auf das Sonnwendgebirge, die Kreide-Mulde (Karwendel-Synklinale) und die Schubmasse des Unnutz-Guffert-Massivs aufgeschoben. Durch die *„mächtige Abbiegung dieser tiefgreifenden Mulde"* aus der Ost–West- in die Nord–Süd-Richtung *„erscheint das Sonnwendgebirge um etwa 10 bis 11 km weiter gegen Norden vorgedrängt"* (Ampferer, 1941a: 182). Dem „Südgelenk" der Kreide-Mulde steht weiter nördlich ein durch Überschiebungen verformtes „Nordgelenk" gegenüber. Dieser Deformationsstil wird auf das „Ost-West-Vorpreschen" der Wettersteinkalk-Masse des Unnutz- und Guffert-Massivs zurückgeführt.

Fuchs (1944), Quenstedt (1951a) und Spengler (1953) widersprechen Ampferer in diesem Punkt und gehen von der Annahme zweier getrennter Synklinalen aus. Laut Fuchs (1944) machten der Kern und der Nordflügel der Karwendel-Synklinale diesen Knick nicht mit (keine „Schlingenbildung"), womit der Knick älter als die Bildung der Synklinale sein muss. Die Wettersteinkalk-Masse (**47**–**50**) bildet laut Ampferer (1941a) ein großes Gewölbe, das im Westen eine gegen das Achental *„schauende Überschiebungsstirne"* zeigt, die *„samt einem überkippten Streifen von Raibler Schichten und Hauptdolomit unvermittelt auf flach lagernde Neokommergel vorgetrieben erscheint"* (Ampferer, 1941a: 184). Im geologischen Profil über die Hochplatte (1.813 m) westlich des Achentals ist die Schubmasse an glatter Störungsfläche völlig vom Untergrund abgeschert. Im Profil über den Christlumkopf (1.758 m) zeigt sich noch eine zusammenhängende Schichtfolge. Ampferer (1941a) folgert aus den Überschiebungsstrukturen am Westabfall des Unnutz-Massivs (Verschiebung nach Westen), am Gröbner Hals und an der Marbichlerspitze (1.898 m) („Süd-Nord-Bewegung") eine zweiphasige Bewegung der Schubmasse. In diesem Artikel beschäftigt sich Ampferer auch mit der strukturell bedingten Entstehung des Achensees. Er postuliert das Vorkommen von, durch den See verdeckten, Nordalpinen Raibler Schichten (**43**) und erklärt sich dadurch *„die Ausschürfung des Sees"*, wie auch *„die Bildung von Großgleitungen"* (Ampferer, 1941a: Fig. 5, E–W-Profil).

Drei Jahre nach Ampferers Tod – er stirbt 1947 – bringt Werner Heissel das geologische Blatt „Karwendelgebirge

1 = Alttrias
2 = Muschelkalk—Wettersteinkalk
3 = Raibler Sch.
4 = Hauptdolomit—Kössener Sch.
5 = Jura-Sch.
I = Erste Reliefüberschiebung der Inntaldecke
II = zweite Reliefüberschiebung von Lechtal- und Inntaldecke
III = engerer Zusammenschub und Hebung des Altreliefs

Zwischen I und II sowie zwischen II und III sind starke Abtragungen eingeschaltet.

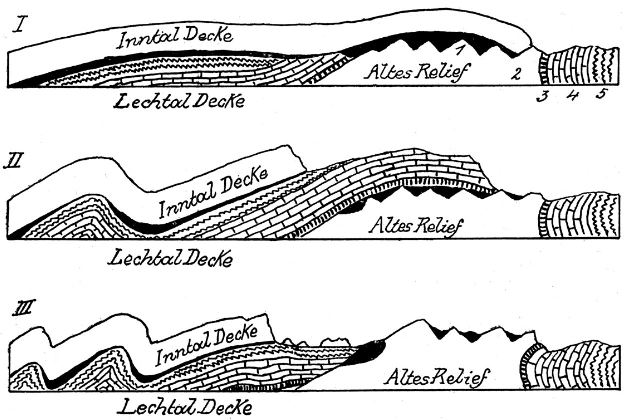

Abb. 7.
Modell der Reliefüberschiebung von Ampferer (1946). Erstmals beschreibt er diese am Stanser Joch südlich des Achensees (Ampferer & Ohnesorge, 1924).

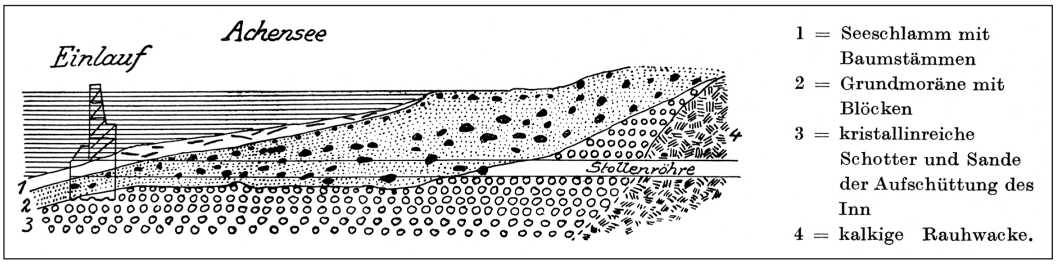

Abb. 8.
Geologisches Profil im Bereich des Einlaufbauwerks für das Achensee-Kraftwerk (AMPFERER, 1946). Fluviatile Kiese und Sande des Inn werden diskordant von Würm-hochglazialer Grundmoräne des Inngletschers überlagert. Zusammen bilden sie den natürlichen „Achensee-Damm“.

Ost“ im Maßstab 1:25.000 mit Erläuterungen heraus (AMPFERER & HEISSEL, 1950a, b). Ein Kapitel befasst sich mit der Entstehung des Achensees und mit den quartärgeologischen Ergebnissen der Bohrungen, die der Botaniker RUDOLF VON SARNTHEIN (1940) in der Bucht von Maurach (ÖK 119) in den Seeschlamm abgeteuft hat. Die eigentlichen Erläuterungen verfasst Ampferer jedoch bereits 1942 in der „Geologischen Formenwelt und Baugeschichte des östlichen Karwendelgebirges“ (AMPFERER, 1946). Er legt anhand zahlreicher Profilschnitte und Kurzbeschreibungen anschaulich den tektonischen Bau dar. Es finden sich Ost–West-Profilschnitte über die Schreckenspitze (2.022 m) zur Christlumalpe (1.231 m) und über die Hochplatte (1.813 m). Quartäre Themen wie die Verbreitung von Lokal- und Fernmoräne (**21**, **22**), von kristallinen Erratikern (**19**) und glazialen Erosionsformen sowie die Auswirkungen der „Schlußvereisung/Schlußeiszeit“ (Bezeichnung Ampferers für die Vorstoßphase der Würm-spätglazialen Gletscher nach dem vollständigen Abschmelzen der Würm-hochglazialen Gletscher; AMPFERER, 1925b, 1929b, 1936) werden breit ausgeführt.

Auch als Baugeologe hat Ampferer sich verdient gemacht. In den 1920er und 1930er Jahren wirkt er bei zwei großen Bauprojekten als geologischer Gutachter mit: bei der Errichtung des Achensee-Kraftwerkes (mit Druckstollen nach Jenbach, ÖK 119) und seinen Zuleitungen aus dem Einzugsgebiet der Seeache und beim Bau der neuen Achenseestraße B 181 von Wiesing im Inntal (566 m) nach Achenkirch (916 m). Die neuen künstlichen Aufschlüsse lieferten wertvolle Einblicke in den Aufbau des quartären Untergrundes des Achensees und des „Achensee-Dammes“ (Abb. 8). Die Ergebnisse sind in mehreren Veröffentlichungen dokumentiert (AMPFERER, 1919, 1940c; AMPFERER & PINTER, 1927; AMPFERER & BERGER, 1929). Neuere Arbeiten zu diesem Thema stammen von POSCHER (1994) und BURGER et al. (2011).

Quartärgeologische Forschung

Die Suche nach erratischen Geschieben, Moränen und glazialen Schliffformen beginnt bereits mit PICHLER (1856, 1859, 1872, 1876), MOJSISOVICS (1870, 1871) und SAPPER (1888), die von ersten Erratika-Funden im Achental berichten. Dieses Tal zählt zu den drei Hauptübertrittstellen von Eis des Inngletscher-Systems in die Nördlichen Kalkalpen und in das bayerische Alpenvorland während des Würm-Hochglazials. STARK (1873) erkennt erstmals diesen Zusammenhang und veröffentlicht eine Karte des Würm-hocheiszeitlichen Eisstromnetzes von Südostbayern im Maßstab 1:250.000 (Abb. 9).

Das durch die glazialgeologischen Arbeiten von PENCK (1882) und BLAAS (1889a, b, 1891) geweckte Interesse an der alpinen Quartärgeologie führt zur intensiven Erforschung des Inntales (Höttinger Brekzie, Inntal-Terrassen; Überblick in PENCK & BRÜCKNER, 1901–1909). Die „Achensee-Schwelle“ bei Maurach (ÖK 119) wird als Teil der Inntal-Terrassen als eine Schlüsselstelle erkannt. Ampferer geht in den ersten Veröffentlichungen über seine geologischen Aufnahmen des Großraumes Karwendelgebirge–Achensee-Gebiet vor allem auf die glazialen Ablagerungen in den Karwendeltälern näher ein (AMPFERER, 1902b, 1903b; siehe oben). Eine ausführliche Zusammenfassung über die quartären Ablagerungen des Achensee-Gebietes und des Steinberger Beckens (Bänderschluffe, **23**, **25**) findet sich im Aufsatz „Aus der geologischen Geschichte des Achensees“ (AMPFERER, 1905c).

KLEBELSBERG (1913) geht davon aus, dass der Inngletscher von den „zentralalpinen Massenerhebungen“ (Ötztaler, Stubaier, Zillertaler Alpen) seine Haupteiszufuhr erhielt. Dieser Gletscher gab über die Fernpass-Talung, das Seefelder Plateau und das Achental wieder Eis in die Nördlichen Kalkalpen ab. Zusammen mit den kalkalpinen Gletschern bildeten sich daraus neue große Gletscherströme (z.B. Loisach- und Isargletscher), die weit in das Alpenvorland vorstießen. Die östlich des Rofangebirges, des Unnutz- und Guffert-Massivs rasch abnehmenden Gebirgshöhen ermöglichten es dem Inngletscher, in großer Breite nordwärts vorzustoßen und Eisströme von Brandenberg in das Achental zu entsenden.

KLEBELSBERG (1914) erläutert in Teil IV der „Glazialgeologischen Notizen vom bayerischen Alpenrande“ die einstigen Wege der Ferneisströme, Eistransfluenzen, Eishöhen etc. im Abschnitt zwischen Loisach und Isar. Eine genaue Karte im Maßstab 1:150.000 stellt die anhand von Findlingen und glazialen Schliffspuren ermittelten Eishöhen am Höhepunkt der Würmvereisung dar. Für die Mündungsbereiche von Bächen- und Achental werden Eishöhen von etwa 1.400 bis 1.500 m angenommen.

WOLF (1922) betreibt eine systematische glazialgeologische Durchforstung des Achensee-Gebietes und des Steinberger Beckens. Er gibt einen umfassenden Überblick über die Verbreitung der glazialen Ablagerungen, die Verteilung der zentralalpinen (kristallinen) Erratika (**19**) und die glazialmorphologischen Phänomene, die von der letzten eiszeitlichen Vergletscherung (Würm-Hochglazial und Würm-Spätglazial) stammen. Der Reichtum der kristallinen Erratika (**19**) im Becken von Steinberg fällt ihm besonders auf, ebenso deren Fehlen nördlich des Guffert-Massivs so-

Abb. 9.
Eiszeitkarte von STARK (1873), die das Würm-hochglaziale Eisstromnetz im Einflussbereich des Inngletschers in bemerkenswerter Genauigkeit erfasst. ▶


MÜNCHEN
Forstinding
Haag
Haus
Pfaffenhofen
Haching
Ebersberg
Kirchseon
Leutstetten
Hanfeld
Starnberg
Neukirn
Hohenschäftlarn
Egmating
Isar
Endmoräne des Inn
Endlhausen
Gr. Helfendorf
Lochen
Holzkirchen
Rosenheim
Loisach
Tölz
Miesbach
Neubeuern
Kochel
Kufstein
Isar
Inn
Rattenberg
Schwaz
Hall
INNSBRUCK

wie im mittleren und hinteren Bächental. Er beobachtet die dichte Streu an den unteren Talhängen sowie die rasche Ausdünnung der Funde mit der Höhe und entlang der ehemaligen Hauptgletscherströme alpenauswärts. Seine systematischen Geländebeobachtungen verarbeitet er in einer paläogeografischen Karte 1:100.000 für den Eishochstand des Würm-Glazials im Achensee-Gebiet. Seine präzisen Beobachtungen haben größtenteils heute noch Gültigkeit. Wolf (1922) stellt eine Gliederung der Moränen für Gebiete auf, in denen „zentralalpine Ferngletscher“ in die Kalkalpen eindrangen. Er scheidet hochglaziale „Fernmoränen mit kristallinen Geschieben“ und hochglaziale und stadiale „Ortsmoränen“ (**22**, **21**) aus. Die Funde von Grundmoräne (**22**, „Ortsmoräne“) hoch oben an den Westhängen des Achentales erachtet er als wichtigen Hinweis für das nordwärtige Abdrängen der lokalen Seitentalgletscher durch den aus dem Inntal vorstoßenden Ferneisstrom (Achental-Gletscher). Wolf (1922) vermutet Eisübertritte aus den östlichen Karwendeltälern (Risstal, Gern- und Falzthurntal) in das Bächental und weiter in das Achental. Er misst dem kristallinen Erratikum (**19**) eine gesonderte Bedeutung bei, da dieses eine Mindesterstreckung des zentralalpinen Eises in den Nördlichen Kalkalpen anzeige. Er beschäftigt sich auch eingehend mit den Seeablagerungen (**23**, **25**) des Ampelsbach-, Unterau- und Hühnersbachtales. Die Bänderschluffe (**25**) im Unterautal und an der Steinberger Ache stuft er – wie damals üblich – in das Riß-Würm-Interglazial ein.

Wolf (1924) dehnt seine glazialgeologischen Studien mit der gleichen Gründlichkeit auf das Gebiet zwischen dem Riss- und dem Bächental („Risser Gebirge“; ÖK 87, 118, 119) aus und entwirft auch für diese Bergregion eine Karte 1:100.000 des Würm-glazialen Eishochstandes.

Für Osswald (1924) ist die Höhenlage und Herkunft der erratischen kristallinen und kalkalpinen Geschiebestreu (**19**) aus „südlicheren Bezirken“ eine Schlüsselfrage. Er beobachtet in den vom Inneisstrom durchflossenen Tälern eine starke Abnahme der kristallinen Geschiebe nördlich der Staatsgrenze Österreich/Deutschland. Die mächtige Abfolge von Bändertonen, Sanden und Kiesen im Weißachtal (Staukörper am Eisrand, **16**) ist nach Osswald (1924) im Zuge des Eiszerfalls des Würm-hochglazialen Eisstromnetzes zwischen Isar und Inn entstanden.

Schreiber (1949) befasst sich in seiner morphologischen Studie über das Gebiet zwischen Brandenberg und Steinberg mit der Entstehungszeit der zahlreichen Klammen und Schluchten sowie mit der „Mechanik der Talverschüttung und Talzerschneidung“. Im Zusammenhang mit den nach seiner Meinung „Riß-Würm-interglazialen Sedimentfüllungen“ der Klammen werden auch Fragen der Genese, der wiederholten Entstehung, des Alters und der zeitlichen Reichweite von Eisstauseen diskutiert.

In den letzten Jahrzehnten wird der Quartärgeologie des betrachteten Raumes wieder neue Beachtung geschenkt: Mit der Verbreitung der Bänderschluffe (**25**) von Steinberg und ihrer Eignung als Zement-, Ziegel- und Keramikrohstoff befassen sich Horvacki (1982) und Czurda & Bertha (1984).

Die Quartärgeologen Diethard Sanders und Lukas Wischounig widmen sich ab der Jahrtausendwende den prä- bis hochglazialen, fluviatilen und lakustrinen Sedimenten (**23**, **25**), die in den Schluchten von Steinberg am Rofan in großer Mächtigkeit aufgeschlossen sind (Ampferer, 1905c; Wolf, 1922; Horvacki, 1982; siehe oben). Neben einer Detailkartierung im Maßstab 1:5.000, Profilaufnahmen, sedimentpetrografischen und sedimentologischen Untersuchungen wird erstmals mittels U-Th-Datierung von Zementen in Konglomeraten (**23**) ein zeitlicher Fixpunkt in der Quartärabfolge gesetzt. Details hierzu finden sich in den Arbeiten von Wischounig (2006), Gruber et al. (2011) und Sanders et al. (2014). In Sanders et al. (2014) und Sanders & Gruber (2016) werden das Nebeneinander von verlassenen, Sediment gefüllten und ausgeräumten Klammabschnitten im Einzugsgebiet der Steinberger Ache, deren Anlage und Alter und die darin ablaufenden Sedimentations- und Erosionsvorgänge im Zuge der Vorstoßphase zum Würm-Hochglazial bis in das Holozän ausführlich diskutiert. Seit mehreren Jahren untersucht die Arbeitsgruppe von Christoph Spötl an der Universität Innsbruck mit modernen sedimentologischen, geophysikalischen und Datiermethoden das vielfältige Würm-Hoch- und Würm-Spätglazial sowie das holozäne Sedimentinventar im Risstal und in den Pertisauer Karwendeltälern. Forschungsergebnisse sind in Spötl (2019), Spötl et al. (2014) und Mair et al. (2016) veröffentlicht.

Regionale stratigrafische und tektonische Arbeiten

Am Beginn des 20. Jahrhunderts werden von Geologen der Münchner Universitäten (Ludwig-Maximilians-Universität und Technische Universität) großangelegte stratigrafische und tektonische Arbeiten im an das Achental angrenzenden bayerischen Alpenraum durchgeführt. Damit sind stets genaue geologische Kartierungen im Maßstab 1:25.000 verbunden. Zu erwähnen sind die Arbeiten von Daqué (1912, auf ÖK 89), Boden (1915, auf ÖK 88 und 89) sowie Osswald (1924, 1928, auf ÖK 88, 89 und 90).

Die Arbeit von Osswald (1924) liefert grundlegende Erkenntnisse zur kalkalpinen Stratigrafie der Obertrias und des Jura, zur Tektonik und zur Quartärgeologie am Blaubergkamm beidseits der Staatsgrenze. Wichtige Informationen stellen die Angaben zum Hauptdolomit (**41**) und Plattenkalk (**40**) an der Halserspitze (1.863 m), die Dreiteilung der Kössen-Formation (**39**), die Untergliederung des Oberrhätkalkes (**38**) in einen Unteren und einen Oberen Thecosmilienkalk (Oberrhätkalk i.e.S.) und die Angaben über oolithische, kieselige und dolomitische Abschnitte in diesem Riffkalk dar. Osswald (1924) scheidet eine Reihe von unter- und mitteljurassischen Schichtgliedern aus, die er vier Faziestypen zuordnet. In der für das Kartenblatt relevanten „Bayrachenfazies“ ist der gesamte Unter- und Mitteljura der Thiersee-Synklinale in Schwellenfazies entwickelt. Er notiert an den drei „Hauptbruchrichtungen“ (NW–SE, N–S und ENE–WSW) horizontale Versätze.

Leuchs (1921) gelingt am Nordrand des „Guffert-Pendling-Zuges“ (ÖK 88, 89, 90) der Nachweis von bis dato unbekannten Vorkommen von Nordalpinen Raibler Schichten (**43**) und beschreibt erstmals Kalke innerhalb des basalen Hauptdolomits (**41**). Er vermerkt die Mehrfachscharniere der Antiklinalstrukturen innerhalb des obersten Wettersteinkalkes (**47**) am Nordabhang des Guffert-Massivs. Er erwägt aufgrund der Auflagerung der Gosau-Gruppe auf gefaltetem Untergrund im Gebiet des Thierseer Tals (ÖK 89, 90) eine prägosauische Anlage der Thiersee-Synklinale.

Vortisch (1926) liefert als erster eine ausführliche lithostratigrafische Beschreibung des berühmten Obertrias-Unterjura-Profils in Beckenfazies am Fonsjoch (das Profil liegt im unteren Drittel des Gratabschnittes Juchtenkopf–Hohe Gans, 1.950 m, ÖK 119). Er beschreibt die lateralen Faziesübergänge vom rhätischen Becken (Kössen-Formation, **39**) in das rhätische Riff (Oberrhätkalk, **38**) der Wilden Kirche (Schoberberg, 1.711 m, ÖK 119) und die dem Riff auflagernden, kondensierten Karbonate des Unterjura (vor allem Rotkalke, **34**). Er konstatiert den strukturellen Zusammenhang mit dem Oberrhät-Riff im Rofangebirge (ÖK 119).

Von Trusheim (1930) stammt eine sehr detaillierte geologische Bearbeitung des Westteiles der Karwendel-Synklinale im Bereich Mittenwald-Risstal (ÖK 87, 118), die überregionale Neuerkenntnisse zur obertriassisch-jurassischen Faziesentwicklung liefert. Ein Fokus liegt auf den bituminösen Einschaltungen im Hauptdolomit (**41**), ein anderer auf den Konglomerat- und Brekzien-Bildungen im „Aptychenkalk“ (Ammergau-Formation, **28**) des Oberjura. Trusheim (1930) widmet sich ausführlich der Sedimentpetrografie und Herkunft der Klasten, den sedimentären Gefügen und der Entstehung der Brekzien. Die Konglomerate und Brekzien des Oberjura unterteilt er in ein tiefer gelegenes, intraformationelles „Boden‘sches Konglomerat“ und in eine höher gelegene „Hornsteinbreccie“. Darin entdeckt er sowohl Aufarbeitungsprodukte älterer Schichtglieder, als auch synsedimentär gebildeten Flachwasserdetritus. Er zieht Vergleiche zur „Hornsteinbreccie“ der östlichen Karwendel-Synklinale (ÖK 88, 119) und des Rofangebirges (ÖK 119) und stellt für beide deren sedimentäre Bildung außer Frage.

Der Münchner Paläontologe und Pionier der Aptychenforschung, Werner Quenstedt, befasst sich intensiv mit der Juraschichtfolge und mit dem geologischen Bau des Achentales. Quenstedt (1951a, b) versucht in zahlreichen stratigrafischen Profilen, hauptsächlich mittels der Biostratigrafie (Aptychen und Rhynchoteuthen), den Mittel- und Oberjura, das heißt die „Hornsteinkalke“ (Allgäu-, Ruhpolding- und Tauglboden-Formation, **32**, **31**, **30**) und die „Aptychenschichten“ (Ammergau-Formation, **28**) zu gliedern. Hierfür verwendet er eine Reihe von lokalen Schichtnamen, die sich jedoch nicht durchsetzen (vgl. Schütz, 1975, 1979; Jaksch, 2003). Hardetert (1985) ordnet die umfangreiche Fossilsammlung Quenstedts (hauptsächlich Material aus dem Achental) an der Universität Tübingen, präpariert und bearbeitet die Rhyncholithen neu (vgl. Hardetert & Riegraf, 1990).

Jaksch (1996), ein Schüler Quenstedts, steuert durch Neuauswertung des bisherigen Belegmaterials und durch neue Aufsammlungen in den Profilen Ampelsbach und Schwendt (ÖK 91) zusätzliche Daten zur Entwicklung der Lamellaptychen, insbesondere zu deren Faunenwandel an der Grenze Unter-/Obertithonium innerhalb der Ammergau-Formation (**28**) bei.

Im Mittelpunkt von Quenstedts tektonischen Studien im Achental stehen die „Achentaler Schubmasse“ und deren Überschiebungsfläche. Bereits in der Arbeit zur „Überschiebungszone von Achenkirch“ kommt Quenstedt (1933) zum bemerkenswerten Schluss, dass entlang der Überschiebung unter dem Hauptdolomit (**41**) „Schubfetzen“ von überkipptem Plattenkalk (**40**), Kössen-Formation (**39**), Rotkalken (**34**) und Ammergau-Formation (**28**) vom Unnutz bis zur Hochplatte und zur Moosenalm verfolgbar seien und daher „*die Schubfläche hervorgeht aus einer großen liegenden Falte*“. „*Ihr Mittelschenkel zerriß unter der Last der überfahrenden Hauptdolomitmassen und wurde zerschoben*“ (Quenstedt, 1933: 460).

In der „Geologischen Exkursion in das Achental-Gebiet“ fasst Quenstedt (1951a) sein stratigrafisches und tektonisches Wissen zusammen. Darin präzisiert er, dass die „Achentaler Schubmasse“ aus dem E–W streichenden Faltenbau des Vorkarwendel (= Karwendel-Synklinale) durch Umbiegen der Falten im Bereich der Pasillalm (ÖK 119) in N–S-Richtung hervorgeht und dass der Stirnrand der „Schubmasse“ zwischen der Hochplatte (1.813 m) und dem Rotmöserkopf (1.522 m) abgetragen ist. Quenstedt (1951a) erkennt, dass das Liegende der „Achentaler Schubmasse“ aus einem kompliziert gebauten, plus/minus W–E streichenden und weitgehend von der „Schubmasse“ beeinflussten Faltenbau besteht, dessen Achsenstreichen und -fallen letztlich erst durch die stratigrafisch-paläontologische Gliederung der Aptychenkalke verständlich werde. Eine logische Folgerung daraus ist, dass die Karwendel-Synklinale sich nicht über einen „Knick“ im Achental („Achentaler Querstruktur“, „Schlingenbildung“ sensu Ampferer) in der nordöstlich gelegenen Thiersee-Synklinale fortsetzt, sondern dass es sich um jeweils verschiedene Synklinalen handelt. Erstere ist die südlichste, letztere die nördlichste einer Reihe von E–W-Falten.

Ende der 1940er Jahre werden von der Technischen Universität München unter der Leitung von Paul Schmidt-Thomé im Zusammenhang mit der Errichtung des Sylvensteinspeichers (Energiewirtschaft, Isar-Hochwasserschutz, ÖK 87) flächenhafte stratigrafische, tektonische und quartärgeologische Kartierungen beidseits des Isartales durchgeführt. In die Erkundungen werden auch das Tal der Walchen (Seeache unterhalb Achenwald), das Demeljoch-Massiv (ÖK 88, 87) und das Einzugsgebiet der Dürrach (Scharfreiter-Massiv, Bächental, ÖK 87, 88, 118) mit einbezogen. Näher behandelt werden die Großfaltenstrukturen (Wamberger Antiklinorium, Bayerisches Synklinorium, Scharfreiter-Antiklinale) und die „Diagonalstörungen“ (Seitenverschiebungen) sowie ein Nord–Süd-Profil durch die gesamten Kalkalpen von Bad Tölz über das Demeljoch (1.924 m) bis Hall in Tirol vorgestellt. Die geophysikalischen und bohrtechnischen Erkundungen des Isar-Talbodens im Gebiet des geplanten Speichersees erbringen Informationen zur Talübertiefung und zum quartären Sedimentaufbau (mächtige Bändertone und Sande in Verzahnung mit Deltasedimenten, siehe auch Knauer, 1952). Die Daten sind in der umfassenden Arbeit von Schmidt-Thomé (1950) zusammengefasst.

Ulrich (1960) studiert im Detail die obertriassische bis unterkretazische, fazielle und paläogeografische Entwicklung in der Karwendel-Synklinale westlich des Kartenblattes. Seine Erkenntnisse gelten größtenteils auch für den auf Blatt Achenkirch gelegenen Ostteil der Synklinale. Er führt für die geringmächtigen siltigen Mergel und kondensierten, fossilreichen Kalke die Bezeichnung „Grauer Lias Basiskalk“ (Kendlbach-Formation, integriert in **32**, **37**) ein. Wie schon Trusheim (1930) zuvor, beschäftigen

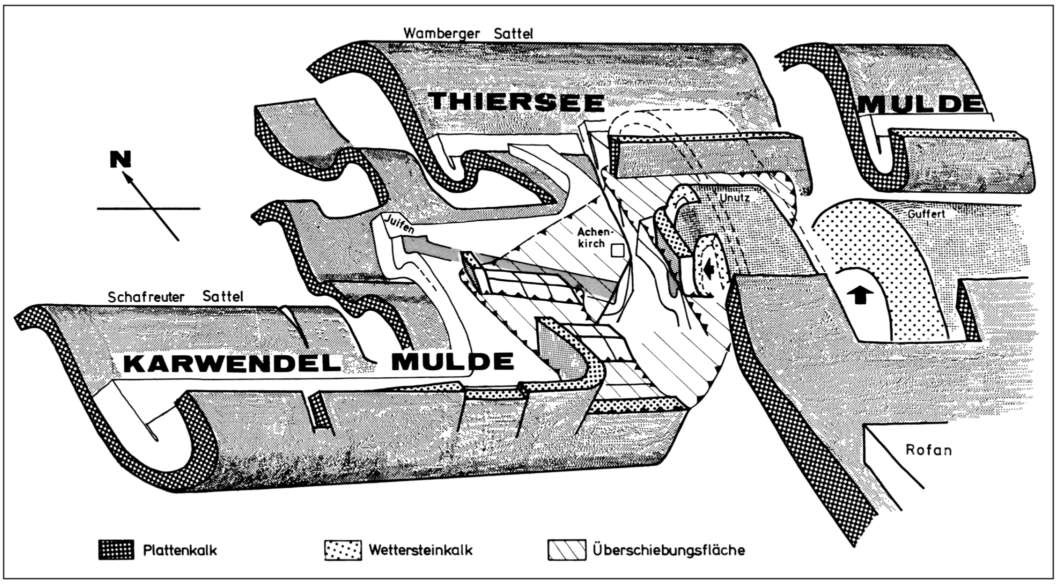

Abb. 10.
Blockmodell der Querstruktur von Achenkirch (NAGEL, 1975). Damit wird der Versuch unternommen, die komplexe tektonische Situation des Achensee-Gebietes aufzulösen. Dabei wird erkannt, dass Karwendel- und Thiersee-Synklinale zwei getrennte Faltenstrukturen darstellen und nicht durch „Knickungen" im Sinne von AMPFERER (1921) verbunden sind.

ihn die „Malm-Konglomerate". Es gibt eine untere, monomikt zusammengesetzte „Aptychenbreccie" und eine obere, polymikte „Hornsteinbreccie" (Rofan-Brekzie, Barmsteinkalk, **29**), die normal sedimentär in beiden Schenkeln der Karwendel-Synklinale eingelagert sind. Die Brekzienbildung führt er auf tektonische Hebungen und nachfolgende Erosion zurück. ULRICH (1960) stellt anhand von Faziesvergleichen in der Karwendel-Synklinale ab dem Sinemurium eine generelle Faziesdifferenzierung in Ost–West- und in Nord–Süd-Richtung fest: Der Westteil wird von einer Schwellen-, der Ostteil von einer Beckenfazies dominiert. Ab dem mittleren Jura zeichnet sich eine Vertiefung des Ablagerungsraumes von Nordwesten nach Südosten ab. Dies drückt sich in der Gesamtmächtigkeit der Jura-Schichtfolge aus, die von 100 m im Westen (Mittenwald) auf 1.100 m im Osten (Bächental) ansteigt.

Die Arbeitsgruppe von Werner Zeil (Technische Universität Berlin) kartierte in den 1960er und 1970er Jahren die Thiersee- und die Karwendel-Synklinale systematisch nach stratigrafischen, biostratigrafischen, faziellen und strukturgeologischen Gesichtspunkten aus.

Grundlegend für das vorliegende Kartenblatt ist die sedimentologische und fazielle Neuuntersuchung der „Aptychen-Schichten" (Ammergau-Formation, **28**) durch SCHÜTZ (1975, 1979) im Westteil der Thiersee- und im Ostteil der Karwendel-Synklinale. Zwei Faziesbereiche unterscheiden sich in der Lithologie und in den Mächtigkeiten: bis 200 m mächtige pelagische „Bianconekalke" in der östlichen Thiersee-Synklinale und bis 800 m mächtige pelagische Kalke und Resedimente (allodapische Kalke; Barmsteinkalk, **29**) in der westlichen Thiersee- und in der Karwendel-Synklinale. Beide Fazieszonen sind durch einen Nord–Süd verlaufenden Übergangsbereich im Achental getrennt. Paläogeografisch bestand demnach im Tithonium und Berriasium eine sich rasch vertiefende, Ost–West ausgerichtete Senke, die von Hochzonen im Norden und Süden (Rofan) episodisch mit Resedimenten beliefert wurde. Der Sedimentationstrog wurde östlich von Achenkirch vermutlich durch eine Störungszone begrenzt. SCHÜTZ (1975, 1979) gelangt mithilfe von Calpionellen-Stratigrafie zu einer lithostratigrafischen Dreiteilung der „Aptychen-Schichten" in „Untere, dünnbankige dunkelgraue Aptychen-Schichten", „Mittlere, unregelmäßig gebankte Aptychen-Schichten mit Resedimenten" und „Obere bianconeähnliche, dünngebankte Aptychen-Schichten".

Jüngst haben ORTNER & KILIAN (2016) Slumping-Strukturen in der überkippten pelagischen Ammergau-Formation (**28**) entlang des oberen Ampelsbaches mit strukturgeologischen Methoden untersucht.

Die strukturgeologische Arbeit von NAGEL (1975) ist darauf ausgelegt, das „alte tektonische Problem" im Raum Achenkirch, die Frage nach dem Umbiegen der Thiersee- in die Karwendel-Synklinale, zu klären. Im Gebiet zwischen Bächental und Brandenberger Ache werden alle größeren Faltenstrukturen und Störungen mithilfe zahlreicher Diplomarbeiten (DIETTRICH, 1970; EHLERS, 1969; FIEDLER-VOLMER, 1968; LÜTKEMEIER, 1972; SCHÜRMANN, 1969; SCHÜTZ, 1971; SCHÜTZ, 1974; WEISTROFFER, 1974; ZÖLLER, 1972) systematisch kartiert und beschrieben sowie die Gefügedaten mittels statistischer Methoden ausgewertet. Die Karwendel-Synklinale endet demnach im Osten an der „Achentaler Schubmasse" und taucht unter diese ein. Die Thiersee-Synklinale hebt bei Achenwald nach Westen in die Luft aus. Beide Synklinalen sind durch den aus mehreren Falten gebildeten „Schafreitersattel" getrennt, der ebenso nach Osten unter die „Achentaler Schubmasse" abtaucht. Diese strukturelle Anordnung der Falten ist somit nach NAGEL (1975) der beste Beweis, dass sich die Karwendel- nicht mit der Thiersee-Synklinale verbinden lässt und damit keine „Muldenschlinge" im Sinne von AMPFERER (1921) vorliegt (Abb. 10). Eine solche manifestiert sich nur in der „Achentaler Schubmasse", die einen zweifachen Knick vollzieht, einen nördlichen an der Sonntagsspitze (1.926 m) und einen südlichen an der Seebergspitze (2.085 m, ÖK 119). NAGEL (1975) betont, dass alle Deformationen im Achensee-Gebiet mit einer kontinuierlichen und konstanten N–S-Einengung einhergehen, wobei die vorgosauische Bildung der E–W-Falten die wichtigste ist und alle anderen Faltenrichtungen aufgrund lithologischer Unterschiede sowie „tektonischer Unebenheiten des Untergrundes" erzwungen worden sind. Die „Achentaler Schubmasse" selbst hat sich aus der Abscherung des Südflügels der Karwendel-Synklinale herausentwickelt und wurde an einer „flachen Überschiebungsbahn" nach

Norden bis Nordwesten geschoben. Die N–S-Achsenrichtung in der „Achentaler Schubmasse“ an der Schreckenspitze (2.022 m) sowie am Unnutz-Massiv ist auf spätere Rotation zurückzuführen. FUCHS (1944), der eine gründliche Aufnahme und statistische Analyse der tektonischen Strukturen beidseits des Achentales durchführt, sieht dies genau umgekehrt: Zuerst erfolgte die Bildung der „Achentaler Schubmasse“ durch E–W-Einengung, nachher jene der Karwendel- und Thiersee-Synklinale durch N–S-Einengung. NAGEL (1975) lässt, auch im Gegensatz zu QUENSTEDT (1933, 1951b) und SPENGLER (1953), die „Achentaler Schubmasse“ am Nordrand des Unnutz-Massivs enden.

NAGEL et al. (1976) betonen, dass während der alpidischen Einengungstektonik im Gebiet um Achenkirch die obertriassischen bis unterkretazischen Beckensedimente der Karwendel- und Thiersee-Synklinale aufgrund ihrer vermuteten Unterlagerung durch Partnach-Schichten (nicht am Kartenblatt) stärker deformiert wurden, als die angrenzenden rigiden Trias-Karbonatplattformen des Guffert- und Unnutz-Massivs sowie die sie überlagernden Jura-Schwellensedimente. Beide Fazieszonen waren im Jura durch eine synsedimentäre Flexur in N–S-Richtung getrennt. Die geringere Mächtigkeit der Jurasedimente in der Thiersee-Synklinale führte zu deren stärkerer Verformung im Vergleich zur Karwendel-Synklinale. Hierzu trug auch der stärkere Nordschub des Wettersteinkalkes östlich von Achenkirch bei. Dieser bewirkte eine seitliche Mitschleppung und Westbewegung des Ostendes der Karwendel-Synklinale.

Das Rofangebirge als Schlüsselregion jurassischer Tektonik

Seit dem späten 19. Jahrhundert inspiriert die vielfältige Geologie des Rofangebirges, unmittelbar im Süden (ÖK 119) an Blatt Achenkirch angrenzend, zahlreiche Wissenschaftler zu umfangreichen geologischen Forschungen (z.B.: Wähner und Ampferer, siehe oben), die für das Verständnis der Geologie auf Blatt 88 Achenkirch sehr wichtig sind. Dies betrifft die blattübergreifenden Faziesverzahnungen zwischen Plattform (Rofan) und Becken (Bächen-/Achental) in der Obertrias und im Oberjura. Heftige wissenschaftliche Dispute finden über die zeitliche Reichweite des oberrhätischen Riffkalkes (**38**), seine Überlagerung durch unterjurassische Rotsedimente (**34**, konkordant vs. diskordant), sowie über die Entstehung der oberjurassischen Hornsteinbrekzie (Rofan-Brekzie) und des darüber liegenden Hornsteinkalkes (Ammergau-Formation, **28** und Barmsteinkalk, **29**) auf stark verfaltetem älterem Untergrund und über die Entstehung dieser Falten durch tektonische Einengung (Rampenfalten) oder durch gravitative Gleitprozesse (Gleitfalten) statt.

Die Genese der Hornsteinbrekzie rückt in den Mittelpunkt der Diskussion: WÄHNER (1903), als bester Kenner dieses Gebirges, hebt deren tektonische Entstehung („Dislokationsbrekzie“) hervor. Dieser Meinung schließen sich VORTISCH (1926, siehe oben), STEINMANN (1925), KÜHN (1935) und SPENGLER (1935) an. Demgegenüber betont AMPFERER (1903a, 1905b, 1908, 1946, etc., siehe oben) die sedimentäre Natur der Brekzie, unterstützt durch TRUSHEIM (1930, siehe oben), SANDER (1941) und WEYNSCHENK (1949). Vor allem SANDER (1941) kann sedimentäre Strukturen bis in den Mikrobereich nachweisen. Eine moderne sedimentologische Bearbeitung der Hornsteinbrekzie stammt von WÄCHTER (1987). Weitere Informationen zur Hornsteinbrekzie des Rofan („Rofan-Brekzie“) und deren unterschiedliche Aussagekraft für die oberjurassische Tektonik finden sich in BRANDNER & GRUBER (2011) sowie GAWLICK et al. (2011). Beide sehen diese Brekzie als synorogenes Sediment im Zusammenhang mit den kompressiven bzw. transpressiven Bewegungen im Vorlandbereich des sich schließenden Meliata-Hallstatt-Ozeans.

Von überregionaler Bedeutung ist auch die Arbeit von WENDT (1969) über die Sedimentpetrografie, Mikrofazies, Paläogeografie und Bathymetrie der Jura-Rotkalke (**34**) im Rofangebirge. Darin werden jurassische Spaltentypen und die Mikrofazies der Eisen-Mangan-Krusten analysiert sowie eine biostratigrafische Einordnung der verschiedenen Rotkalke mithilfe von Ammoniten versucht. An der Trias-Jura-Grenze kommt es demnach zu einer Sedimentationsunterbrechung, wobei Omissionshorizonte durch Eisen-Mangan-Krusten präsent sind und die ältesten Jurasedimente frühestens für das Sinemurium nachgewiesen werden können.

Erstellung der Geologischen Karte von Bayern 1:25.000

Das damalige Bayerische Geologische Landesamt setzt ab Mitte der 1960er Jahre einen Forschungs- und Kartierungsschwerpunkt im Isar- und Tegernseer Tal (Randbereich des Kartenblattes). Dazu zählen geophysikalische Messungen und Bohrungen, die zwischen Vorderriß (ÖK 87) und Lenggries Talübertiefungen von mindestens 350 m ermitteln, die durch die Erosion mehrerer Eiszeiten geschaffen wurden. Deren Becken wurden beim Eiszerfall (Toteisseen) mit mächtigen Delta- und Seesedimenten verfüllt (FRANK, 1979; BADER, 1979). Die Forschungsbohrung Vorderriß 1 (ÖK 87) liefert weitere wichtige Daten zur quartären Abfolge und Übertiefung. Die überregionale Bedeutung dieser Bohrung beruht auf dem endgültigen Nachweis der Deckennatur und des Deckenbaus der Nördlichen Kalkalpen für diesen Abschnitt (BACHMANN & MÜLLER, 1981, 2011; BRANDNER, 1980, 2013, 2019; MÜLLER-WOLFSKEIL, 1981; siehe auch KILIAN & ORTNER, 2019).

In der Folge werden vom Bayerischen Geologischen Landesamt mehrere Blätter im Maßstab 1:25.000 dieses bayerischen Alpenanteiles neu herausgebracht: Die im Nordwesten und Norden an Blatt Achenkirch angrenzenden geologischen Kartenblätter 1:25.000 8434 Vorderriß, 8335 Lenggries und 8336/8436 Rottach-Egern (DOBEN, 1991, 1993, 1995). Die entfernteren Blätter 8533/8633 Mittenwald (JERZ & ULRICH, 1966; ÖK 117) und 8338 Bayrischzell (WOLFF, 1985a, b; ÖK 89, 90) sind wichtige Informationsquellen zur Stratigrafie, Paläontologie und Tektonik der Schichtfolge der Karwendel- und Thiersee-Synklinale.

Faziesstudien zur Riff-Beckenentwicklung im Rhätium

FABRICIUS (1959, 1962, 1966) führt sedimentpetrografische, fazielle und paläogeografische Studien zur Rhätium-Unterjura-Grenze in den Bayerischen und Nordtiroler Kalkalpen zwischen Mittenwald und Kufstein durch. Diese Arbeiten präzisieren für den Achensee-Raum die räumliche Verteilung und die Mächtigkeiten der obertriassischen Beckenfazies der Kössen-Formation (**39**) und der sich mit ihr verzahnenden Plattform(Riff)-Fazies des Oberrhätkalkes (**38**). In der von FABRICIUS (1959) verfassten Arbeit zur Fazies und Nomenklatur der rhätischen Riffkalke wird die Umbenennung des „Oberrätkalkes“ in „Rätolias-Riffkalk“ vorgeschlagen. Dies begründet er damit, dass sich die Rifffazies mit echten Oolithen verzahnt, welche von KOCKEL et al. (1931; „Geiselsteinfazies“) und SÄRCHINGER (1939; „Mauerlias“) zeitlich in den Unterjura gestellt werden. FABRICIUS (1962) beschreibt die Vorkommen rhätischer Riffbildungen, die er in der Thiersee-Synklinale östlich der Gufferthütte (1.465 m), am Ostende der Karwendel-Synklinale (ÖK 119) und im Rofan (ÖK 119) antrifft. Die Diversifizierung des Unterjura in „Rotfazies“ („Roter Bank- und Knollenkalk“, **34**) und „Graufazies“ („Fleckenmergel und -kalke“, **32**) entsteht laut FABRICIUS (1962) durch unterschiedlich starke Absenkungs- und Sedimentationsraten, unabhängig von der zugrundeliegenden Paläogeografie. Diese Thematik wird nochmals in einer Monografie (FABRICIUS, 1966) mit vielfältigem Bezug zur Achensee-Gegend sehr ausführlich behandelt.

KUSS (1983) untersucht die Kössen-Formation (**39**) zwischen Salzburg und Innsbruck unter mikrofaziellen, paläontologischen, sedimentologischen, palökologischen und geochemischen Gesichtspunkten. Er spricht von Intraplattform-Beckensedimenten und ordnet sie drei mehrfach alternierenden Fazieseinheiten zu. In den Untersuchungen wird auf die Profile Fonsjoch, Wilde Kirche (beide auf ÖK 119), Christlumkopf-Kleekopf und oberer Ampelsbach näher eingegangen.

RIEDEL (1988) befasst sich mit der Faziesentwicklung des Wilde Kirche Riff-Komplexes (Oberrhätkalk, **38**; Schoberberg, 1.711 m, ÖK 119), den er in vier übergeordnete Fazieseinheiten gliedert, zwischen denen graduelle Übergänge bestehen. Das Korallenkalk-Niveau (Lithodendronkalk) der Kössen-Formation (**39**) bildete ein sanftes Relief, auf dem die Riffknospen entstanden, die sich zu einem typischen oberrhätischen Riff (mit vier Einzelriffen, **38**) entwickelten. Die Riffentwicklung fand an der Trias-Jura-Grenze ein abruptes Ende.

SATTERLEY et al. (1994) setzen sich am Beispiel des Wilde Kirche Riffes mit dem Thema der subaerischen Exposition an der Trias-Jura-Grenze auseinander. In dem etwa 75 m mächtigen Riff implizieren bis 50 m tiefe Hohlräume mit verschiedenen marinen Zementen und bunten Internsedimenten für die Frühdiagenese eine sehr kurze Auftauchphase mit Verkarstung, auch wenn direkte Belege hierfür fehlen.

Die sedimentologischen, makro- und mikropaläontologischen sowie isotopengeologischen Forschungen zum Rhaetium (Kössen-Formation, **39**; Oberrhätkalk, **38**) und zur Trias-Jura-Grenze im nördlichen Karwendel fruchten in der internationalen Festlegung des Profils am Kuhjoch, einer etwa 1.760 m hohen Scharte 500 m nördlich des Hölzelstaljochs (2.012 m, ÖK 118) als GSSP für die Trias-Jura-Grenze (VON HILLEBRANDT & KMENT, 2009; VON HILLEBRANDT & KMENT, 2011; VON HILLEBRANDT et al., 2013; RICHOZ & KRYSTYN, 2015).

Fazielle und strukturelle Neubearbeitung durch die Universität Innsbruck

In seiner Dissertation befasst sich BUNZA (1971) mit der sedimentologischen und mikropaläontologischen Untersuchung der Nordalpinen Raibler Schichten (**43–46**) des Guffert- und Unnutz-Massivs. Hierzu nimmt er feinstratigrafische Profile entlang des Fahrweges zur Köglalm (1.428 m, ÖK 88/119) auf und arbeitet Mikrofaziestypen von verschiedenen Kalktypen heraus. Außerdem kann er den Wettersteinkalk makro- und mikrofaziell mittels Grünalgen- und Schwammbestimmungen in eine Riff-, Riffschutt- und Lagunenfazies gliedern.

In den 1980er Jahren lenkt Rainer Brandner sein Forschungsinteresse auf die vielfältige Jura-Schichtfolge im Achensee-Gebiet, angeregt durch Vorstudien für das TRANSALP-Tiefenseismik-Projekt. Axel Spieler (Dissertant) führt hierzu eine sehr detaillierte Kartierung im Maßstab 1:10.000 des Bächentales, des westlichen Achentales und des Gebietes nordwestlich Pertisau (ÖK 119) durch. Im Mittelpunkt steht die Detailuntersuchung der kleinräumigen faziellen Diversifizierung im Unterjura, die aus zahlreichen Profilaufnahmen erarbeitet wird.

Eine erste Zusammenfassung dieser Untersuchungen findet sich in SPIELER & BRANDNER (1989): Impulsartige tektonische Ereignisse steuerten demnach die paläoozeanografischen Verhältnisse und damit ruckartige fazielle und sedimentäre Entwicklungen in der Obertrias und im Jura. Ausgangspunkt war das Zerbrechen der obertriassischen Karbonatplattformen im Rhaetium im Bereich des Achentales, das zur Ausbildung einer N–S streichenden Absenkungszone mit Beckensedimenten (Kössen-Formation, **39**) im Westen und oberrhätischen Riffkalken (**38**) im Osten führte. Diese Faziesanordnung pauste sich noch in den Unterjura durch. Die unterjurassische Beckenkonfiguration ist durch Tiefschwellen-, Beckenrand- und Beckenfazies geprägt. Der Beckenbereich mit der stärksten Subsidenz (Bächental) ist durch die Ablagerung bitumenreicher Mergel („Bächentaler Bitumenmergel“, **33**) gekennzeichnet. Diese werden als Bildungen eingeschränkter Zirkulation in Folge eines drastischen übergeordneten Temperaturanstieges im Toarcium (globales „anoxic event“) betrachtet. Das „Bächentaler Becken“ bildete sich durch tektonische Verkippungen innerhalb eines NE–SW verlaufenden pull-apart-Beckens, das sich an E–W streichenden, überspringenden sinistralen Blattverschiebungen entwickelte. Die für das Kartenblatt charakteristischen, mächtigen oberjurassischen Resedimente und Flachwasserschüttungen (Barmsteinkalk, **29**; Rofan-Brekzie) in das pelagische Ammergauer Becken (Ammergau-Formation, **28**) bringen die Autoren ursächlich mit transpressiver Tektonik in Verbindung. In der oberen Unterkreide erfolgte die westvergente Überschiebung der „Achentaler Schubmasse“, damit zusammenhängend die Abscherung und Einengung des Bächentaler Beckens an den vorgegebenen Störungssystemen. Die Herausformung der E–W streichenden Karwendel- und Thiersee-Synklinale erfolgte postgosauisch, zumal die „Achentaler Schubmasse“ ebenso von einem E–W-Faltenbau überprägt ist, der auch die Gosau-Sedimente auf ÖK 89 erfasste.

In den Arbeiten von CHANNELL et al. (1990, 1992) wird die jurassische Beckengeometrie und Subsidenzgeschichte in Abhängigkeit von Dehnungstektonik sowie die alpidische Deformation im Bächen- und Achental ausführlich erörtert. Anlass für die detaillierten Paläomagnetik-Untersuchungen war unter anderem die Frage, inwiefern eine mögliche Rotation zur „Achentaler Querstruktur“ geführt hätte.

SAUSGRUBER (1994a) untersucht im Rahmen seiner Diplomarbeit (Betreuer: Rainer Brandner) den komplexen Übergangsbereich zwischen Karwendel- und Thiersee-Synklinale – die „Achentaler Schubmasse“ und Achental-Überschiebung – nach stratigrafisch-faziellen und strukturgeologischen Gesichtspunkten neu. Er verwendet moderne Methoden der Strukturgeologie mit Auswertung der gemessenen Strukturdaten im Schmidt’schen Netz inklusive einer Paläospannungsanalyse. Damit gelingt ihm die Entflechtung der verschiedenen Faltensysteme und der erstmalige Nachweis, dass der vermeintlich überkippte Südschenkel der Thiersee-Synklinale im Bereich der Natterwand – wie früher schon von QUENSTEDT (1933) und SPENGLER (1953) vermutet – der überkippte Vorderschenkel der großen Unnutz- und Guffert-Antiklinale und damit Bestandteil der „Achentaler Schubmasse“ ist (allerdings ist die „Achentaler Schubmasse“ bis zu dem Zeitpunkt nur unklar definiert bzw. abgegrenzt worden). Diese ist also an der Achental-/Thiersee-Überschiebung auf die Thiersee-Synklinale überschoben. Die strukturgeologischen Erkenntnisse sind in einer tektonischen Detailkarte und in mehreren geologischen Profilschnitten anschaulich dargestellt. An stratigrafischen Details kann SAUSGRUBER (1994a) für den Bereich östlich des Achentales im Unter- und Mitteljura eine durchgehende kieselige Hangfazies (Scheibelberg-Formation, **37**; Chiemgauer Schichten, integriert in Allgäu-Formation, **32**) nachweisen. Für den Oberjura kann er das Einsetzen und das nordwärtige Auskeilen der Barmsteinkalk-Schüttungen (**29**) in der pelagischen Ammergau-Formation (**28**) auskartieren, siehe auch SAUSGRUBER (1994b).

Erkenntnisse aus ausgeglichenen Tiefenprofilkonstruktionen

Die oben genannten Arbeiten der Universität Innsbruck laufen in enger Kooperation mit überregionalen strukturgeologischen Untersuchungen der Arbeitsgruppe von Gerhard H. Eisbacher (Karlsruher Institut für Technologie) in den westlichen Nördlichen Kalkalpen mit dem Ergebnis einer tektonischen Übersichtskarte im Maßstab 1:200.000 (EISBACHER & BRANDNER, 1995, 1996). Die Arbeitsgruppe von Eisbacher beginnt in den späten 1980er Jahren mit der Rekonstruktion ausgeglichener Tiefenprofile durch die Nördlichen Kalkalpen: An ausgesuchten N–S-Profilen werden Strukturdaten von der Oberfläche bis an die Basisüberschiebung der Kalkalpen projiziert und mit Daten von Tiefbohrungen und tiefenseismischen Messungen abgeglichen. Die Hauptstrukturen der Kalkalpen (Falten, Decken- und Schuppengrenzen, Basisüberschiebung) werden nach dem Prinzip der ausgeglichenen Längen (ausgeglichene Profile) in der Tiefe rekonstruiert. Ziel ist es, mittels palinspastischer Rückabwicklung der Decken das Maß der Verkürzung der Kalkalpen während der alpidischen Einengung zu quantifizieren. Die bilanzierten Tiefenprofile dieser Arbeitsgruppe sind in EISBACHER et al. (1990), LINZER et al. (1995), AUER (2001) und AUER & EISBACHER (2003a; Abb. 11) veröffentlicht.

In der Arbeit über die heteroaxiale Deformationsgeschichte der Inntal-Decke gehen EISBACHER & BRANDNER (1990, 1995, 1996) auch auf den besonderen strukturellen Baustil des Achensee-Gebietes näher ein. Die Autoren betonen die Dominanz der nordwestvergenten und nach Südwesten abtauchenden, überkippten Unnutz-Antiklinale, die durch steile NW–SE streichende Transferstörungen (Issalm-, Pertisau-Störung, ÖK 89, 119) segmentiert ist. Die Achental-Überschiebung mit der Unnutz-Antiklinale im Hangenden („Achentaler Schubmasse“) scherte vermutlich im Verzahnungsbereich Wettersteinkalk-Plattform/Partnach-Becken oder an einer NE–SW streichenden synsedimentären jurassischen Abschiebung entlang des Achentales ab und war damit faziell vorgegeben.

AUER & EISBACHER (2003a, b) errechnen entlang der TRANSALP-Trasse durch Auswertung von Oberflächendaten und Interpretation seismischer Profile der OMV im Abschnitt Schliersee–Inntal aus der Rückabwicklung der Deformation mittels Schichtlängenausgleich am Kontakt Nordalpine Raibler Schichten (**43**) zu Hauptdolomit (**41**) eine Verkürzung der Kalkalpen von etwa 80 km (73 %). Die Verkürzung manifestiert sich von Norden nach Süden in vier strukturellen Stapeln (Cenomanium-Randschuppe, Allgäu-Decke, basale Schuppen der Lechtal-Decke und eigentliche Lechtal-Decke), die im Zuge der zweiphasigen Einengung (prägosauische WNW- bis NNW- und paläobis neogene N- bis NNE-Einengung) geformt wurden. Die konstruierten geologischen Profile basieren unter anderem auf den seismischen Profilen der OMV. Die im Tiefenprofil stärksten seismischen Reflektoren (Evaporite und Dolomite der Reichenhall-Formation und der Nordalpinen Raibler Schichten, **43**) sind die prädestinierten Abscherhorizonte. Einer der Hauptreflektoren der für das gegenständliche Kartenblatt relevanten Lechtal-Decke (im Sinne von AUER & EISBACHER, 2003a, b) streicht im Kern der Thiersee-Synklinale aus und wird mit dem Verlauf der großen internen Achental-Überschiebung korreliert. Im extrapolierten geologischen Tiefenprofil wird die Reichweite dieser Überschiebung weit nach Süden bis fast zur Inntal-Störung vermutet. Der Versatz an der Überschiebung wird auf mindestens 5 km errechnet. Das angenommene kristalline Basement der Lechtal-Decke wird bis unter die Guffert-Antiklinale hineingezeichnet. Laut Seismik könnte in dieser Antiklinale eine pop-up-Struktur stecken (Abb. 11).

BEER (2003; Arbeitsgruppe von Hubert Miller, Ludwig-Maximilians-Universität München) stellt in seiner Dissertation tektonische Vergleiche zwischen der „Achentaler Schubmasse“ und der „Salzachstörung“ an. Er scheidet in zeitlicher Reihenfolge fünf Deformationsphasen aus: 1. N–S-Faltung, 2. NW-gerichtete Überschiebung der „Achentaler Schubmasse“, 3. N–S-Faltung der „Achentaler Schubmasse“, 4. SW–NE-Faltung, 5. Querwellung der E–W streichenden Falten. BEER (2003) geht – wie schon NAGEL

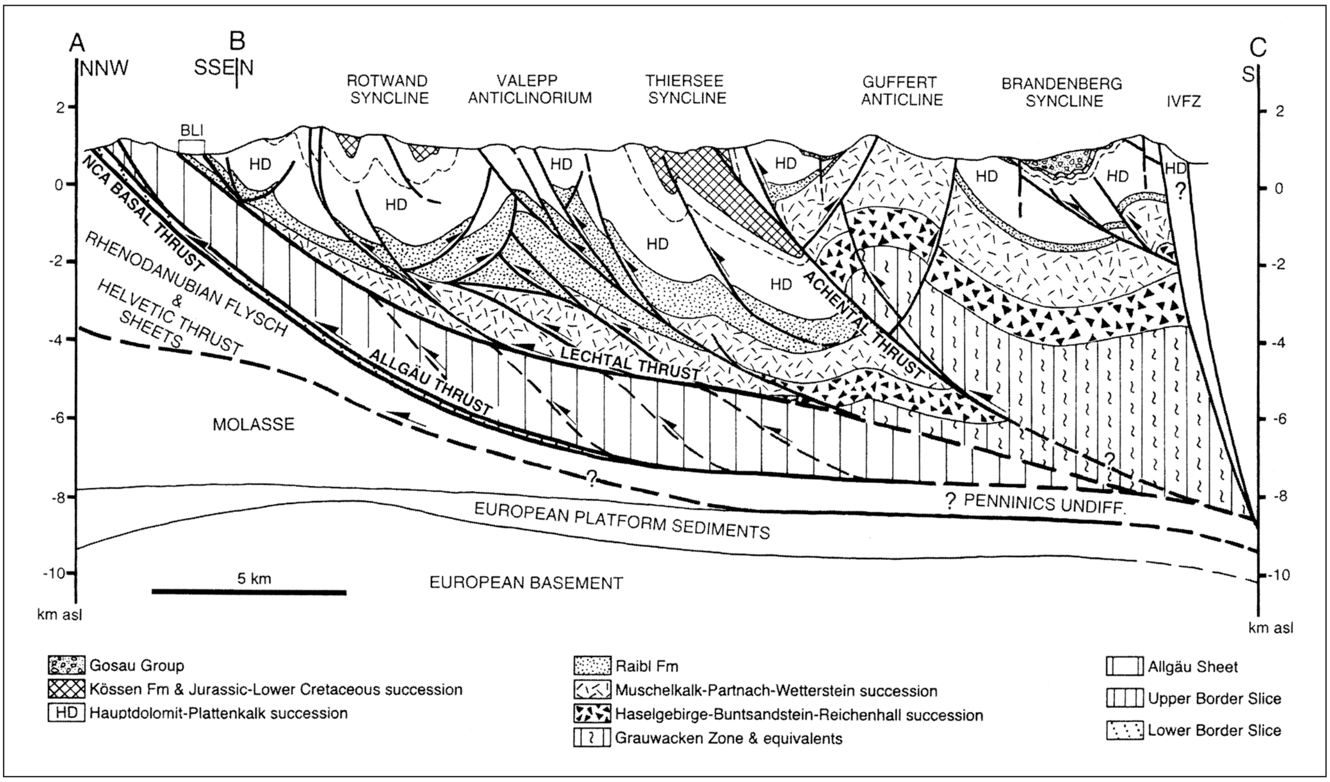

Abb. 11.
Ausgeglichenes Tiefenprofil von AUER & EISBACHER (2003a) entlang der Trans-Alp-Trasse, das durch eine tiefwurzelnde, steile Achental-Überschiebung geprägt ist. Zum einen streicht diese nach Norden in der Thiersee-Synklinale aus, zum anderen ist im Hangendblock die markante, pop-up-artig hochgepresste Guffert-Antiklinale entwickelt.

(1975) – von einer langandauernden, bis in das Oligozän reichenden Kompression in N–S-Richtung aus. Laut BEER (2003) zeigen die Reflektoren unpublizierter Seismikprofile der OMV im Raum Achenkirch–Steinberg keine Tiefenfortsetzung der „Achentaler Schubmasse“. Daher stellt die Achental-Überschiebung für ihn nur eine oberflächennahe, flach südfallende Überschiebung dar. Die Entstehung der „Achentaler Schubmasse“ wird derart erklärt, dass ab der Oberkreide die ursprünglich E–W streichende, überkippte Antiklinale des Unnutz-Massivs im Zwickel zwischen der sinistralen Achensee-Störung und der dextralen Rotmöserkopf-Störung gegen den Uhrzeigersinn nach Nordwesten gedreht und verschoben wurde (vgl. NAGEL, 1975). Die Nordwestüberschiebung der „Achentaler Schubmasse“ erfolgte demnach auf einen bereits älteren E–W streichenden Faltenbau. Im Paläogen und Neogen wurden Liegendes und Hangendes der Achental-Überschiebung zusammen in N–S- und NNE–SSW-Richtung kompressiv überprägt.

ORTNER (2003) versucht eine Synthese des tektonischen Baus und der Deformationsabfolge im Gebiet zwischen den Ostenden der Karwendel- und der Thiersee-Synklinale. Er stellt, ausgehend von der Thiersee-Synklinale, anhand der Thiersee- und Achental-Überschiebung ein Entwicklungsmodell der „Achentaler Schubmasse“ vor. Im Thierseer Tal (ÖK 89, 90) kommen im Liegenden und im Hangenden der E–W streichenden Thiersee-Überschiebung synorogene Gosau-Sedimente vor. Daraus schließt ORTNER (2003) auf ein postgosauisches Alter dieser Überschiebung. Das Hangende der Thiersee-Überschiebung wird im Gebiet des Kartenblattes (Guffert-Schneidjoch) aus der großen liegenden Guffert-Antiklinale gebildet. Da diese ebenso E–W streicht, wird ihre Entstehung zeitgleich mit der Thiersee-Überschiebung angenommen. Die Achental-Überschiebung ist laut dem Autor die direkte Westfortsetzung der Thiersee-Überschiebung ab deren Umbiegen nach Süden am Mahmooskopf. Deren Hangendes („Achentaler Schubmasse“) stellt die NNE–SSW streichende, liegende Unnutz-Antiklinale dar. ORTNER (2003) erklärt sich die Entstehung der „Achentaler Querstruktur“ wie folgt: Zuerst bildete sich eine Antiklinale mit Wettersteinkalk (**47–50**) im Kern und einem basalen Abscherhorizont unterhalb davon („fault propagation fold“) während westgerichteter Überschiebung (= Achental-Überschiebung). Die Faltung wurde von westgerichteter, schichtparalleler Scherung begleitet, die in den Nordalpinen Raibler Schichten (**43**) ablief und zur Bildung der liegenden Isoklinalfalte westlich des Unnutz-Massivs führte. In der nachfolgenden postgosauischen Deformation wurde die Thiersee-Überschiebung aktiviert und die Guffert-Antiklinale angelegt. Gleichzeitig damit wurde die Achental-Überschiebung reaktiviert, indem die liegende Unnutz-Antiklinale schräg abgeschnitten und nach NNW transportiert wurde. Die Achental-Überschiebung und die Unnutz-Antiklinale wurden dadurch selbst wieder verfaltet. Die jüngsten Sedimente im Liegenden der Achental-Überschiebung haben ein Barremium-Alter (Unterkreide) und geben damit das Maximalalter dieser Überschiebung an.

TÖCHTERLE (2005) bearbeitet im Rahmen des TRANSALP-Tiefenseismik-Projektes stratigrafisch und strukturgeologisch einen Nord–Süd-Streifen in der Thiersee-Synklinale des Brandenberger Tales (ÖK 89). Er liefert eine genaue Beschreibung der dort vorkommenden obertriassischen bis oberkretazischen Schichtglieder mit Fokus auf die synorogenen Sedimente der Gosau-Gruppe.

Anhand von N–S verlaufenden bilanzierten Profilen, die verschiedene Entwicklungsstadien zu verschiedenen Zeiten (obere Unterkreide, Oberkreide, heute) zeigen, wird die Deformationsgeschichte entlang der TRANSALP-Trasse rekonstruiert. Dank der Gosau-Sedimente kann er prä- und postgosauische Deformationsstrukturen klar trennen. Töchterle (2005) geht näher auf die Jura-Beckenentwicklung ein, die er – dem Konzept von Spieler & Brandner (1989) folgend – mit N–S streichenden Halbgrabenbildungen in einem Pull-apart-Becken, das sich zwischen sinistralen E–W streichenden Seitenverschiebungen entwickelt, erklärt. Die nördliche dieser Störungen befindet sich im Bereich der späteren Thiersee-Synklinale. Die jurassische Extensionstektonik ist durch Brekzienbildungen dokumentiert. Im Zuge der eoalpidischen Gebirgsbildung (NW-Einengung) entsteht die südliche Thiersee-Überschiebung, welche die Sedimentation beendet und in deren Hangendblock sich bereits in wesentlichen Zügen große Antiklinal- und Synklinalstrukturen wie die Guffert-Pendling-Antiklinale herausformen. In der Folge treten innerhalb des ostalpinen Akkretionskeiles Abschiebungen und starke Erosion auf, die zusammen mit den eoalpidischen Strukturen nachfolgend mit den Sedimenten der Gosau-Gruppe plombiert werden. Im Paläogen werden die Gosau-Sedimente und ihr bereits deformierter Untergrund neuerlich deformiert. Im Bereich der Thiersee-Synklinale bildet sich die bedeutende nordvergente, nördliche Thiersee-Überschiebung heraus, der Nordschenkel der Thiersee-Synklinale wird steil gestellt.

Die von Töchterle (2005) und anderen aus dem Projekt gewonnenen strukturgeologischen Neuergebnisse (Thiersee-Überschiebung, Guffert-Pendling-Antiklinale, Brixlegg-Überschiebung, Subtauern-Rampe, Inntal-Störung) für den Tiroler Raum (Nördliche Kalkalpen-Südrand bis Tauernfenster-Nordrand) sind in der Arbeit von Ortner et al. (2006) und im Exkursionsführer von Lammerer et al. (2011) zusammenfassend dargestellt. Der letzte Stand zur Mechanik und Kinematik und zu den Faltenstrukturen der „Achentaler Schubmasse“ ist in Ortner & Gruber (2011), van Kooten (2018) und Ortner & Thöny (2019) wiedergegeben.

Paläomagnetische Untersuchungen

Channell et al. (1990, 1992) führen paläomagnetische Untersuchungen an Jura-Rotsedimenten der Nördlichen Kalkalpen (auch im Achensee-Gebiet) zwecks Ermittlung von Rotationen im Zuge der alpidischen Gebirgsbildungen durch. Die zentrale Aussage aus den paläomagnetischen Daten ist, dass diese in der Karwendel-Synklinale, in der „Querstruktur von Achenkirch“ und in der Thiersee-Synklinale überall eine konstante Ausrichtung der Magnetisierung anzeigen. Die Autoren sehen darin einen Beweis, dass die vermeintliche S-Form des Übergangs von der Karwendel- in die Thiersee-Synklinale nicht durch Rotation während der alpidischen kompressiven Deformation entstanden ist.

Im Rahmen ihrer paläomagnetischen Untersuchungen zu vermuteten Blockrotationen in den Ostalpen beproben Thöny & Ortner (2001) sowie Thöny et al. (2002, 2006) auch das Schichtenprofil (Obertrias bis Unterkreide) im überkippten Liegendschenkel der „Achentaler Schubmasse“ am oberen Ampelsbach und setzen sich mit der kretazischen bis „tertiären“ Deformationsgeschichte der Thiersee-Überschiebung (siehe auch Ortner, 2003) und der Guffert-Pendling-Antiklinale auseinander, die von der TRANSALP-Trasse durchörtert werden. Am Ampelsbach kann keine primäre Magnetisierung festgestellt werden. Das gesamte Profil zeigt eine überprägende Magnetisierung, die zeitgleich mit der post-unteroligozänen, vermutlich miozänen Faltung erfolgte. Diese Magnetisierung wurde später um etwa 20° im Uhrzeigersinn rotiert (Ortner et al., 2015). Die Rotation fand in den Nördlichen Kalkalpen an großen NE- bis ENE streichenden sinistralen Störungen (z.B. Inntal-Störung) im Dominostil statt (Ortner et al., 2015).

Forschungen zu den „Bächentaler Bitumenmergeln“

Die Bedeutung der „Bächentaler Ölschiefer“ als Rohstoff für Brenn- und Heilzwecke wird schon früh von Müller (1782, zitiert in Mutschlechner, 1980) hervorgehoben, gerät jedoch rasch wieder in Vergessenheit. Mit der Wiederentdeckung und Wiederaufnahme des Abbaus im Jahr 1911 durch die Gebrüder Albrecht aus Pertisau präsentiert Sander (1921, 1922) erstmals eine genaue petrografische und mineralogische Beschreibung der Bitumenmergel, die auch Angaben zu deren stratigrafischen und tektonischen Lagerungsverhältnissen beinhaltet. Funde von *Harpoceras* sp. erlauben ihm die zeitliche Einstufung in den oberen Unterjura. Hradil & Falser (1930) vermuten eine größere Verbreitung der Bitumenmergel bis zum Juifen hin (Boden, 1935, fand die Bitumenmergel auch noch im weiter nördlich gelegenen Roßstein- und Buchsteingebiet) und berichten über physikalische und chemische Eigenschaften, Gewinnungsmethoden (Schweltechniken) und Verwendungszwecke der Ölschiefer im Allgemeinen. Bitterli (1962) steuert Ergebnisse chemischer Analysen bei. Spieler & Brandner (1989) und Spieler (1994, 1995) führen mittels Profilaufnahmen und Mikrofaziesanalysen detaillierte stratigrafische Untersuchungen sowie eine genaue Kartierung der Verbreitung der Bitumenmergel durch und postulieren für den Ablagerungsraum ein lokal begrenztes, aber sedimentologisch dynamisches „Bächentaler Becken“, dessen Entstehung mit pull-apart-Tektonik verbunden wird. Lobitzer et al. (1988, 1994), Kodina et al. (1988), Solti et al. (1987), Solti & Lobitzer (1989), Ebli (1991, 1997) und Ebli et al. (1998) liefern Beiträge zur Stratigrafie, Fazies, Paläontologie und organischen Geochemie.

In jüngster Zeit versuchen Neumeister et al. (2011, 2015) mit einem multidisziplinären Ansatz (Mineralogie, Geochemie, Kohlenstoffisotopie, Kohlenwasserstoffpetrologie etc.) die Redoxbedingungen und die daraus sich ergebenden Anreicherungen von organischem Kohlenstoff im Bächentaler Becken zu klären. Sie führen diese Sonderausbildung auf das Zusammenwirken von globalen (eustatische Meeresspiegelschwankungen, Vulkanismus) und lokalen Einflussfaktoren (Redox- und Salinitätsverhältnisse, Beckenmorphologie) zurück. Aufgrund biostratigrafischer Vergleiche mit den verwandten Bildungen der

Posidonienschiefer in Südwestdeutschland gelangen die Autoren zu einem Beginn der Schwarzschieferbildung im Bächental bereits im oberen Pliensbachium. In NEUMEISTER et al. (2016) wird die Verteilung von Spurenelementen untersucht, die typisch für reduzierende Milieus sind (Molybdän, Uran, Vanadium, Kupfer, Nickel), um Variationen der Redoxbedingungen während der Ablagerung der „Bächentaler Bitumenmergel“ zu ermitteln. Die Anreicherung der Spurenelemente wird dabei direkt durch siliziklastischen Eintrag und die Anreicherung organischen Materials befeuert.

SUAN et al. (2016) setzen sich kritisch mit den bisherigen biostratigrafischen Daten zum „Bächentaler Bitumenmergel“ auseinander, insbesondere mit der Arbeit von NEUMEISTER et al. (2015). Sie nehmen eine Revision der bereits publizierten Ammonitenbestimmungen vor. Zusammen mit neuen Ammonitenfunden und Nannofossilbestimmungen wird der Beginn der Bitumenanreicherung in den Mergeln („anoxic event“) gegenüber NEUMEISTER et al. (2015) auf Unteres Toarcium korrigiert.

ANGERMAIER (2015) stellt in seiner Masterarbeit mit verschiedenen Methoden (Dünnschliff- und Rasterelektronenmikroskopie, Pulverdiffraktometrie, Kohlenstoffisotopie) fazielle Vergleiche zwischen den Beckensedimenten der Bitumenmergel im Steinbruch Bächental und den gleich alten Hang- und Schwellensedimenten am Fohnsjoch an. Er weist darauf hin, dass beide Profile durch komplexe synsedimentäre bis syndiagenetische gravitative Prozesse (Rutschfaltung, Gleitung, submarine Schuttstromablagerung, Turbidite) und spätere tektonische Überprägungen gekennzeichnet sind und dadurch deren chrono- und isotopenstratigrafische Aussagekraft mit Vorsicht zu betrachten seien. Die mineralogische Zusammensetzung, Kohlenstoff- und Karbonatisotopie der Bitumenmergel sowie Kontrollfaktoren der Schwarzschiefergenese und die palinspastische Hangneigungsrekonstruktion zwischen Schwelle und Becken werden im Detail herausgearbeitet. Zuletzt wird ein Sedimentationsmodell des Bächentaler Beckens für den Zeitraum Rhaetium bis Unterkreide entworfen.

Literatur

AMPFERER, O. (1902a): Über den geologischen Zusammenhang des Karwendel- und Sonnwendgebirges. – Verhandlungen der k. k. Geologischen Reichsanstalt, **1902**, 104–113, Wien.

AMPFERER, O. (1902b): Bericht über die Neuaufnahme des Karwendelgebirges. – Verhandlungen der k. k. Geologischen Reichsanstalt, **1902**, 274–276, Wien.

AMPFERER, O. (1903a): Die neueste Erforschung des Sonnwendgebirges im Unterinnthal. – Verhandlungen der k. k. Geologischen Reichsanstalt, **1903**, 41–51, Wien.

AMPFERER, O. (1903b): Geologische Beschreibung des nördlichen Theiles des Karwendelgebirges. – Jahrbuch der k. k. Geologischen Reichsanstalt, **53**, 169–252, Wien.

AMPFERER, O. (1905a): Geologische Beschreibung des Seefelder-Mieminger und südlichen Wettersteingebirges. – Jahrbuch der k. k. Geologischen Reichsanstalt, **55**, 451–562, Wien.

AMPFERER, O. (1905b): Einige allgemeine Ergebnisse der Hochgebirgsaufnahme zwischen Achensee und Fernpaß. – Verhandlungen der k. k. Geologischen Reichsanstalt, **1905**, 118–125, Wien.

AMPFERER, O. (1905c): Aus der geologischen Geschichte des Achensees. – Zeitschrift des Deutschen und Österreichischen Alpenvereins, **XXXVI** (1905), 1–15, Innsbruck.

AMPFERER, O. (1907): Über Gehängebrekzien der Nördlichen Kalkalpen. – Jahrbuch der k. k. Geologischen Reichsanstalt, **57**, 727–752, Wien.

AMPFERER, O. (1908): Studien über die Tektonik des Sonnwendgebirges. – Jahrbuch der k. k. Geologischen Reichsanstalt, **58**, 281–304, Wien.

AMPFERER, O. (1912a): Geologische Spezialkarte der Österreichisch-Ungarischen Monarchie 1:75.000, Blatt 4947 Achenkirch und Benedictbeuern. – 1 Blatt, k. k. Geologische Reichsanstalt, Wien.

AMPFERER, O. (1912b): Gedanken zur Tektonik des Wettersteingebirges. – Verhandlungen der k. k. Geologischen Reichsanstalt, **1912**, 197–212, Wien.

AMPFERER, 0. (1914a): Besprechung mit O. Schlagintweit, K. Ch. v. Loesch und H. Mylius über das Wettersteingebirge. – Verhandlungen der k. k. Geologischen Reichsanstalt, **1914**, 338–352, Wien.

AMPFERER, O. (1914b): Erläuterungen zur geologischen Spezialkarte 1:75.000 Österreich-Ungarns, Blatt Achenkirchen. – 30 S., k. k. Geologische Reichsanstalt, Wien.

AMPFERER, O. (1914c): Über den Bau der westlichen Lechtaler Alpen. – Jahrbuch der k. k. Geologischen Reichsanstalt, **64**, 307–326, Wien.

AMPFERER, O. (1919): Landschaft und Geologie des Achensees. – Die Wasserwirschaft, Sonderheft 2019: Der Achensee und die Ausnützung seiner Wasserkräfte, 1–3, Wien.

AMPFERER, O. (1921): Über NW-Beanspruchungen in den Nordalpen. – Jahrbuch der Geologischen Staatsanstalt, **71**, 198–202, Wien.

AMPFERER, O. (1924a): Beiträge zur Auflösung der Mechanik der Alpen, 1. Fortsetzung. – Jahrbuch der Geologischen Bundesanstalt, **74**, 35–73, Wien.

AMPFERER, O. (1924b): Über die Tektonik der Alpen. – Die Naturwissenschaften, **12**, 1–24, Berlin.

AMPFERER, O. (1925a): Geologische Spezialkarte der Österreichisch-Ungarischen Monarchie 1:75.000, Blatt 4948 Kufstein. – 1 Blatt, Geologische Bundesanstalt, Wien.

AMPFERER, O. (1925b): Über Wachstumsunterschiede zwischen Fern- und Nahgletschern. – Die Eiszeit: Zeitschrift für allgemeine Eiszeitforschung, **2**, 41–49, Wien.

AMPFERER, O. (1928): Die Reliefüberschiebung des Karwendelgebirges. – Jahrbuch der Geologischen Bundesanstalt, **78**, 241–256, Wien.

AMPFERER, O. (1929a): Einige Beispiele von Kerbwirkung und Reliefüberschiebung aus den Südtiroler Dolomiten. – Jahrbuch der Geologischen Bundesanstalt, **79**, 241–256, Wien.

AMPFERER, O. (1929b): Über die Ablagerungen der Schlußeiszeit in der Umgebung des Arlbergpasses. – Jahrbuch der Geologischen Bundesanstalt, **79**, 307–332, Wien.

AMPFERER, O. (1936): Waren die Alpen zwischen Würmeiszeit und Schlußvereisung unvergletschert? – Sitzungsberichte der mathematisch-naturwissenschaftlichen Klasse der Akademie der Wissenschaften Wien, Abteilung I, **145**, 201–208, Wien.

AMPFERER, O. (1939): Über einige Formen der Bergzerreißung. – Sitzungsberichte der mathematisch-naturwissenschaftlichen Klasse der Akademie der Wissenschaften Wien, Abteilung I, **148**, 1–14, Wien.

AMPFERER, O. (1940a): Zum weiteren Ausbau der Lehre von den Bergzerreißungen. – Sitzungsberichte der mathematisch-naturwissenschaftlichen Klasse der Akademie der Wissenschaften in Wien, Abteilung I, **149**, 51–70, Wien.

AMPFERER, O. (1940b): Die Neuaufnahme des Karwendelgebirges. – Mitteilungen des Alpenländischen geologischen Vereines, **32**, 119–123, Wien.

AMPFERER, O. (1940c): Über die geologischen Aufschlüsse beim Bau der neuen Achenseestraße auf der Strecke zwischen Wiesing und Scholastika. – Geologie und Bauwesen, **11**, 12 S., Wien.

AMPFERER, O. (1941a): Tektonische Nachbarschaft Karwendel-Sonnwendgebirge. – Sitzungsberichte der mathematisch-naturwissenschaftlichen Klasse der Akademie der Wissenschaften in Wien, Abteilung I, **150** (1940), 181–199, Wien.

AMPFERER, O. (1941b): Bergzerreißungen im Inntalraume. – Sitzungsberichte der mathematisch-naturwissenschaftlichen Klasse der Akademie der Wissenschaften in Wien, Abteilung I, **150** (1940), 97–114, Wien.

AMPFERER, O. (1946): Geologische Formenwelt und Baugeschichte des östlichen Karwendelgebirges. – Denkschriften der mathematisch-naturwissenschaftlichen Klasse der Akademie der Wissenschaften in Wien, **106**, 1–95, Wien.

AMPFERER, O. & BERGER, J. (1929): Vom geologischen Aufbau der Achenseeufer, seine Auswirkung bei der Spiegelabsenkung. – Schweizerische Bauzeitung, **93–94**/14, 170–174, Zürich.

AMPFERER, O. & HAMMER, W. (1898): Geologische Beschreibung des südlichen Theiles des Karwendelgebirges. – 1 geologische Karte 1:50.000. – k. k. Geologische Reichsanstalt/Militärgeographisches Institut, Wien.

AMPFERER, O. & HAMMER, W. (1899): Geologische Beschreibung des südlichen Theiles des Karwendelgebirges. – Jahrbuch der k. k. Geologischen Reichsanstalt, **48**, 289–374, Wien.

AMPFERER, O. & HEISSEL, W. (1950a): Geologische Karte des östlichen Karwendel und des Achensee-Gebietes 1:25.000. – 1 Blatt, Innsbruck (Universitätsverlag Wagner).

AMPFERER, O. & HEISSEL, W. (1950b): Das östliche Karwendel. Erläuterungen zur geologischen Karte des östlichen Karwendel und des Achensee-Gebietes. – 55 S., 1 Profil, 1 tektonische Übersichtskarte, Innsbruck (Universitätsverlag Wagner).

AMPFERER, O. & OHNESORGE, T. (1912): Geologische Spezialkarte der Österreichisch-Ungarischen Monarchie 1:75.000, Blatt 5047 Innsbruck und Achensee. – 1 Blatt, k. k. Geologische Reichsanstalt, Wien.

AMPFERER, O. & OHNESORGE, T. (1918): Geologische Spezialkarte der Österreichisch-Ungarischen Monarchie 1:75.000, Blatt 5048 Rattenberg. – 1 Blatt, k. k. Geologische Reichsanstalt, Wien.

AMPFERER, O. & OHNESORGE, T. (1924): Erläuterungen zur Geologischen Spezialkarte der Republik Österreich, Blatt Innsbruck-Achensee (5047). – 108 S., Geologische Bundesanstalt, Wien.

AMPFERER, O. & PINTER, K. (1927): Über geologische und technische Erfahrungen beim Bau des Achenseewerkes in Tirol. – Jahrbuch der k. k. Geologischen Reichsanstalt, **77**, 279–332, Wien.

ANGERMAIER, J. (2015): Der Jura zwischen Fonsjoch und Ölschieferabbau im Bächental. – Unveröffentlichte Masterarbeit, Universität Innsbruck, 109 S., Innsbruck.

AUER, M. (2001): Struktur und Kinematik der nördlichen Kalkalpen im TRANSALP-Profil (Südbayern, Nordtirol). – Unveröffentlichte Dissertation, Universität Karlsruhe, 132 S., Karlsruhe.

AUER, M. & EISBACHER, G.H. (2003a): Deep structure and kinematics of the Northern Calcareous Alps (TRANSALP profile). – International Journal of Earth Sciences, **92**, 210–227, Stuttgart.

AUER, M. & EISBACHER, G.H. (2003b): Structure and Kinematics of the Northern Calcareous Alps along the Transalp-Profile. – Geologisch-Paläontologische Mitteilungen Innsbruck, **25**, 19–20, Innsbruck.

BACHMANN, G.H. & MÜLLER, M. (1981): Geologie der Tiefbohrung Vorderriß (Kalkalpen, Bayern). – Geologica Bavarica, **81**, 17–53, München.

BACHMANN, G.H. & MÜLLER, M. (2011): Exkursion E4c – Tiefbohrung Vorderriß I. – In: GRUBER, A. (Red.): Arbeitstagung 2011 der Geologischen Bundesanstalt, Blatt 88 Achenkirch, 255–260, Wien.

BADER, K. (1979): Exarationstiefen würmeiszeitlicher und älterer Gletscher in Südbayern (Trennung eisvorbelasteter und nicht eisvorbelasteter Sedimente aufgrund der seismischen Geschwindigkeiten). – Eiszeitalter & Gegenwart, **29**, 49–62, Hannover.

BAYERISCHES GEOLOGISCHES LANDESAMT (1996): Geologische Karte von Bayern 1:500.000. – 1 Blatt, GLA, München.

BEER, E. (2003): Vergleichende tektonische Untersuchungen an zwei längsalpinen Störungen: der Achentaler Schubmasse und der Salzachstörung. – Unveröffentlichte Dissertation, Universität München, 135 S., München.

BITTERLI, P. (1962): Studien an bituminösen Gesteinen aus Österreich und benachbarten Gebieten. – Erdoel-Zeitschrift, **78**/7, 405–416, Wien–Hamburg (Urban-Verlag).

BLAAS, J. (1889a): Ein Profil durch den Achensee-Dammschotter. – Verhandlungen der k. k. Geologischen Reichsanstalt, **1889**, 232–234, Wien.

BLAAS, J. (1889b): Über sogenannte interglaziale Profile. – Jahrbuch der k. k. Geologischen Reichsanstalt, **39**, 477–482, Wien.

BLAAS, J. (1891): Notizen über diluvioglaziale Ablagerungen im Inntalgebiete. – Berichte des naturwissenschaftlich-medizinischen Vereins Innsbruck, **19**, 92–136, Innsbruck.

BLIND, W. (1963): Die Ammoniten des Lias alpha aus Schwaben, vom Fonsjoch und Breitenberg (Alpen) und ihre Entwicklung. – Palaeontographica (A), **121**, 37–131, Stuttgart.

BODEN, K. (1915): Geologische Aufnahme der Tegernseer Berge im Westen der Weißach. – Geognostische Jahreshefte, **27**, 173–214, Profilschnitte, 1 geologische Karte 1:25.000, München.

BODEN, K. (1935): Die geologische Aufnahme des Roßstein- und Buchstein-Gebietes zwischen der Isar und dem Schwarzenbach. – Abhandlungen der Geologischen Landesuntersuchung am Bayerischen Oberbergamt, **17**, 7–45; **18**, 3–57, München.

BRANDNER, R. (1980): Geologische Übersichtskarte von Tirol 1:300.000. – Tirol Atlas, Institut für Geographie, Abteilung Landeskunde, Innsbruck.

BRANDNER, R. (2013): Alpen-Profil. Geologischer Schnitt von Bad Tölz bis zum Schlern. – https://dx.doi.org/10.13140/RG.2.2.20466.81603

BRANDNER, R. (2019): Spuren von Stein und Eis. Die geologische Entstehung der Landschaft. Außergewöhnliche Landschaft – außergewöhnliche Geologie. – In: SONNTAG, H., STRAUBINGER, F., BRANDNER, R., SPÖTL, C. & VON NICOLAI, C. (Hrsg.): Großer Ahornboden. Eine Landschaft erzählt ihre Geschichte, 2. Auflage, 35–48, Wattens (Berenkamp).

BRANDNER, R. & GRUBER, A. (2011): Exkursion E2a – Rofangebirge. – In: GRUBER, A. (Red.): Arbeitstagung 2011 der Geologischen Bundesanstalt Blatt 88 Achenkirch, 149–167, Wien.

BUNZA, G. (1971): Geologische Kartierung zwischen Achental, Ampelsbach und Grund-Ache (bei Achenthal und Steinberg am Rofan, Sonnwendgebirge, Nordtirol) unter besonderer Berücksichtigung der Trias des Unutz-Guffert-Gewölbes. Ein Beitrag zur Stratigraphie und Fazieskunde der Nördlichen Kalkalpen. – Unveröffentlichte Inaugural-Dissertation, Universität Innsbruck, XI + 130 S., Innsbruck.

BURGER, U., EDER, S. & POSCHER, G. (2011): Exkursion E1 – Faziesmodell der Zentralalpinen Kiese und deren Deckschichten als Grundlage für den Ausbau der wasserwirtschaftlichen Nutzung des Achenseedamms. – In: GRUBER, A. (Red.): Arbeitstagung 2011 der Geologischen Bundesanstalt, Blatt 88 Achenkirch, 141–148, Wien.

CHANNELL, J.E.T., BRANDNER, R., SPIELER, A. & SMATHERS, N.P. (1990): Mesozoic paleogeogra-phy of the Northern Calcareous Alps – evidence from paleomagnetism and facies analysis. – Geology, **18**, 828–831, Boulder.

CHANNELL, J.E.T., BRANDNER, R., SPIELER, A. & STONER, J.S. (1992): Paleomagnetism and paleo-geography of the Northern Calcareous Alps (Austria). – Tectonics, **11**/4, 792–810, Washington, D.C.

CLARK, W.B. (1887): Über die geologischen Verhältnisse der Gegend nordwestlich vom Achensee mit besonderer Berücksichtigung der Bivalven und Gastropoden des unteren Lias. – Unveröffentlichte Dissertation, Universität München, 45 S., München.

CZURDA, K.A. & BERTHA, B. (1984): Verbreitung und rohstoffmäßige Eignung von Tonen und Tongesteinen in Nordtirol. – Archiv für Lagerstättenforschung der Geologischen Bundesanstalt, **5**, 15–28 Wien.

DACQUÉ, E. (1912): Geologische Aufnahme des Gebietes um den Schliersee und Spitzingsee in den oberbayerischen Alpen. – Landeskundliche Forschungen, herausgegeben von der Geographischen Gesellschaft in München, **15**, 1–68, München.

DIENER, C. (1885a): Über das Vorkommen von Hierlatz-Schichten in der Rofangruppe. – Verhandlungen der k. k. Geologischen Reichsanstalt, **1885**, 82, Wien.

DIENER, C. (1885b): Über den Lias der Rofan-Gruppe. – Jahrbuch der k. k. Geologischen Reichsanstalt, **35**, 27–36, Wien.

DIETTRICH, T. (1970): Die Geologie der Thiersee-Mulde zwischen Dollmannsbach und Unterautal. – Unveröffentlichte Diplomarbeit, Technische Universität Berlin, 78 S., Berlin.

DOBEN, K. (1991): Geologische Karte von Bayern 1:25.000, Blatt Nr. 8335 Lenggries. Mit Erläuterungen. – 120 S., Bayerisches Geologisches Landesamt, München.

DOBEN, K. (1993): Geologische Karte von Bayern 1:25.000, Blatt Nr. 8434 Vorderriß. Mit Erläuterungen. – 73 S., Bayerisches Geologisches Landesamt, München.

DOBEN, K. (1995): Geologische Karte von Bayern 1:25.000, Blatt Nr. 8336 u. 8436 Rottach-Egern. – Bayerisches Geologisches Landesamt, München.

EBLI, O. (1991): Fazies, Paläontologie und organische Chemie der Sachranger Schiefer (Untertoarcium) im Mittelabschnitt der nördlichen Kalkalpen zwischen Isar und Saalach. – Jahrbuch der Geologischen Bundesanstalt, **134**, 5–14, Wien.

EBLI, O. (1997): Sedimentation und Biofazies an passiven Kontinentalrändern: Lias und Dogger des Mittelabschnitts der Nördlichen Kalkalpen und des frühen Atlantik (DSDP site 547B, offshore Marokko). – Münchner Geowissenschaftliche Abhandlungen, Reihe A – Geologie und Paläontologie, **32** (1997), 255 S., München (Friedrich Pfeil).

EBLI, O., VETÖ, I., LOBITZER, H., SAJGÓ, C., DEMÉNY, A. & HETÉNYI, M. (1998): Primary productivity and early diagenesis in the Toarcian Tethys on the example of the Mn-rich black shales of the Sachrang-Formation, Northern Calcareous Alps. – Organic Geochemistry, **29**/5–7, 1635–1647, London.

EHLERS, H. (1969): Die Geologie der Thierseemulde zwischen Natterwand und Hofjoch. – Unveröffentlichte Diplomarbeit, Technische Universität Berlin, 77 S., Berlin.

EISBACHER, G. & BRANDNER, R. (1990): Platznahme und Deformation der Inntaldecke, Nördliche Kalkalpen. – TSK III. 3. Symposium für Tektonik, Strukturgeologie, Kristallingeologie im deutschsprachigen Raum Graz, 19.–21.April 1990, Kurzfassungen der Vorträge und Poster (1990), 50–51, Graz.

EISBACHER, G. & BRANDNER, R. (1995): Role of high-angle faults during heteroaxial contraction, Inntal thrust sheet, Northern Calcareous Alps, western Austria. – Geologisch-Paläontologische Mitteilungen Innsbruck, **20**, 389–406, Innsbruck.

EISBACHER, G.H. & BRANDNER, R. (1996): Superposed fold thrust structures and high angle faults, northwestern Calcareous Alps, Austria. – Eclogae Geologicae Helvetiae, **89**, 553–571, Basel.

EISBACHER, G., LINZER, H.-G., MEIER, L. & POLINSKI, R. (1990): A depht-extrapolated structural transect across the Northern Calcareous Alps of western Tirol. – Eclogae Geologicae Helvetiae, **83**/3, 711–722, Basel.

FABRICIUS, F. (1959): Vorschlag zur Umbenennung von „Oberrhätkalk“ in „Rätolias-Riffkalk“ (Nördliche Kalkalpen). – Neues Jahrbuch für Geologie und Paläontologie, Mitteilungshefte, **1959**/12, 546–549, Stuttgart.

FABRICIUS, F. (1962): Faziesentwicklung an der Trias-Jura-Wende in den mittleren Nördlichen Kalkalpen. – Zeitschrift der Deutschen Geologischen Gesellschaft, **113**, 311–319, Hannover.

FABRICIUS, F. (1966): Beckensedimentation und Riffbildung an der Wende Trias/Jura in den Bayrisch-Tiroler Kalkalpen. – International Sedimentary Petrographical Series, **9**, 143 S., Leiden.

FIEDLER-VOLMER, R. (1968): Zur Geologie der Thiersee-Mulde zwischen Guffert-Hütte und Natterwand. – Unveröffentlichte Diplomarbeit, Technische Universität Berlin, 82 S., Berlin.

FRANK, H. (1979): Glazial übertiefte Täler im Bereich des Isar-Loisach-Gletschers: Neue Erkenntnisse über Aufbau und Mächtigkeit des Quartärs in den alpinen Tälern, im Gebiet des „Murnauer Schotters“ und im „Tölzer Lobus“ (erste Mitteilung). – Eiszeitalter & Gegenwart, **29**, 77–100, Hannover.

FUCHS, A. (1944): Untersuchungen am tektonischen Gefüge der Tiroler Alpen. II. Kalkalpen Achensee – Karwendelgebirge. – Neues Jahrbuch für Mineralogie, Geologie und Paläontologie, Abhandlungen, Abteilung B, **88**, 337–373, Stuttgart.

GAWLICK, H.-J., SUZUKI, H. & MISSONI, S. (2011): Neue Radiolarienfaunen aus der Ruhpolding-Formation im Liegenden der Rofan-Brekzie des Rofan-/Sonnwendgebirges: Implikationen zur Deckenneugliederung der westlichen Nördlichen Kalkalpen. – In: GRUBER, A. (Red.): Arbeitstagung 2011 der Geologischen Bundesanstalt, Blatt 88 Achenkirch, 39–50, Wien.

GEOGNOSTISCHER VEREIN FÜR TIROL UND VORARLBERG (Hrsg.) (1849): Geognostische Karte Tirols im Maßstab 1:115.200, Bozen.

GEYER, G. (1886): Ueber die Lagerungsverhältnisse der Hierlatz-Schichten in der südlichen Zone der Nordalpen vom Pass Pyhrn bis zum Achensee. – Jahrbuch der k. k. Geologischen Reichsanstalt, **36**, 215–294, Wien.

GRUBER, A. & BRANDNER, R. (2012): Geologische Karte der Republik Österreich 1:50.000, Blatt 88 Achenkirch. – 1 Bl., Geologische Bundesanstalt, Wien.

GRUBER, A., WISCHOUNIG, L. & SANDERS, D. (2011): Exkursion E4a – Ablagerungs- und Flussgeschichte während des späten Quartärs im Bereich nördlich des Rofan. – In: GRUBER, A. (Red.): Arbeitstagung 2011 der Geologischen Bundesanstalt, Blatt 88 Achenkirch, 226–246, Wien.

GRUBER, A., LOTTER, M. & BRANDNER, R. (in Druck): Erläuterungen zur Geologischen Karte der Republik Österreich 1:50.000 – Blatt 88 Achenkirch. – Geologische Bundesanstalt, Wien.

GÜMBEL, C.W. V. (1861): Geognostische Beschreibung des bayerischen Alpengebirges und seines Vorlandes. – 950 S., 42 Prof.-Taf., 1 Karte, 5 geologische Kartenblätter 1:100.000, u.a. III Werdenfels, IV Miesbach, Gotha, Faksimile-Ausgabe zum 100. Todestag 1998, München (Dr. Friedrich Pfeil).

GÜMBEL, C.W. V. (1894): Geologie von Bayern, II. Band. Geologische Beschreibung von Bayern. – 1184 S., Kassel (T. Fischer).

HAHN, F.F. (1911): Neue Funde in nordalpinem Lias der Achenseegegend und bei Ehrwald. – Neues Jahrbuch für Mineralogie, Geologie und Paläontologie, Beilagen-Band, **32**, 535–577, Stuttgart.

HARDETERT, P. (1985): Cephalopodenkiefer aus dem Mesozoikum des Achentals (Nordtirol/Österreich). – Unveröffentlichte Dissertation, Universität Münster, 195 S., Münster.

HARDETERT, P. & RIEGRAF, W. (1990): The Tübingen fossil collections of WERNER QUENSTEDT (1893–1960): Mesozoic cephalopod jaws (Rhyncholithes, Aptychi) from the Achensee area (Tyrol, Austrian Alps). – Paläontologische Zeitschrift, **64**/1–2, 63–73, Stuttgart.

HEISSEL, G. (1977): Die geologische Neuaufnahme des Karwendelgebirges und seine tektonische Ausdeutung. – Unveröffentlichte Dissertation, Universität Innsbruck, 372 S., 1 geologische Karte 1:20.000, 1 tektonische Karte 1:100.000, 17 Profile 1:25.000, Innsbruck.

HEISSEL, G. (1978): Karwendel – geologischer Bau und Versuch einer tektonischen Rückformung. – Geologisch-Paläontologische Mitteilungen Innsbruck, **8**, Festschrift W. Heissel, 227–288, Innsbruck.

HILLEBRANDT, A. V. & KMENT, K. (2009): Die Trias/Jura-Grenze und der Jura in der Karwendelmulde und dem Bayerischen Synklinorium. – Exkursionsführer, Deutsche Stratigraphische Kommission, Jahrestagung der Subkommission für Jurastratigraphie in Fall vom 10.–13.06.2009, 45 S., Erlangen.

HILLEBRANDT, A. V. & KMENT, K. (2011): Lithologie und Biostratigraphie des Hettangium im Karwendelgebirge. – In: GRUBER, A. (Red.): Arbeitstagung 2011 der Geologischen Bundesanstalt, Blatt 88 Achenkirch, 17–38, Wien.

HILLEBRANDT, A. V., KRYSTYN, L., KÜRSCHNER, W.M., BONIS, N.R., RUHL, M., RICHOZ, S., SCHOBBEN, M.A.N., URLICHS, M., BOWN, P.R., KMENT, K., MCROBERTS, C.A., SIMMS, M. & TOMASOVYCH, A. (2013): The Global Stratotype Sections and Point (GSSP) for the base of the Jurassic System at Kuhjoch (Karwendel Mountains, Northern Calcareous Alps, Tyrol, Austria). – Episodes, **36**/3, 162–198, Ottawa.

HORVACKI, J. (1982): Ablagerungsmodell der Tiroler Bändertone aufgrund sedimentpetrographischer Analysen mit rohstoffkundlicher Bewertung. – Unveröffentlichte Dissertation, Universität Innsbruck, 124 S., Innsbruck.

HRADIL, G.H. & FALSER, V.H. (1930): Die Ölschiefer Tirols. – 122 S., Leipzig (Johann Ambrosius Barth).

JAKSCH, K. (1996): Aptychen aus den Tithonprofilen von Achenkirch und Schwendt (Tirol) mit Einbeziehung von Vergleichsexemplaren von den Ionischen Inseln. – Jahrbuch der Geologischen Bundesanstalt, **139**/4, 453–466, Wien.

JAKSCH, K. (2003): Werner Quenstedt und sein Achentaler Ampelsbachprofil (Tirol) mit einem Beitrag zur frühen Lamellaptychenentwicklung. – Jahrbuch der Geologischen Bundesanstalt, **143**/1, 45–55, Wien.

JERZ, H. & ULRICH, R. (1966): Geologische Karte von Bayern 1:25.000, Blatt Nr. 8533-8633 Mittenwald. Mit Erläuterungen. – 152 S., Bayerisches Geologisches Landesamt, München.

KARLE, U. (1984): Palynostratigraphische Untersuchung eines Rhät-Lias-Profils am Fonsjoch, Achensee (Nördliche Kalkalpen, Österreich). – Mitteilungen der Österreichischen Geologischen Gesellschaft, **77**, 331–353, Wien.

KILIAN, S. & ORTNER, H. (2019): Structural evidence of in-sequence and out-of-sequence thrusting in the Karwendel mountains and the tectonic subdivision of the western Northern Calcareous Alps. – Austrian Journal of Earth Sciences, **112**/1, 62–83, Wien.

KLEBELSBERG, R. V. (1913): Die eiszeitliche Vergletscherung der Alpen unter besonderer Berücksichtigung der Ostalpen. – Zeitschrift des Deutschen und Österreichischen Alpenvereins, **44** (1913), 26–39, Wien.

KLEBELSBERG, R. V. (1914): Glazialgeologische Notizen vom bayrischen Alpenrande, Teil IV. – Zeitschrift für Gletscherkunde, **8**, 226–262, 331–343, Berlin.

KNAUER, J. (1952): Diluviale Talverschüttung und Epigenese im südlichen Bayern. – Geologica Bavarica, **11**, 1–32, München.

KOCKEL, C.W., RICHTER, M. & STEINMANN, H.G. (1931): Geologie der Bayerischen Berge zwischen Lech und Loisach. – Wissenschaftliche Veröffentlichungen des Deutschen und Österreichischen Alpenvereins, **10**, 231 S., Innsbruck.

KODINA, L. A., BOGATCHEVA, M.P. & LOBITZER, H. (1988): An Organic Geochemical Study of Austrian Bituminous Rocks. – Jahrbuch der Geologischen Bundesanstalt, **131**/2, 291–300, Wien.

KRAUTER, E. (1967): Zur Frage der Reliefüberschiebung am Staner-Joch (Östliches Karwendel, Tirol). – Mitteilungen der Geologischen Gesellschaft in Wien, **60**, 23–64, Wien.

KÜHN, O. (1935): Die Hornsteinbreccie des Sonnwendgebirges und ihre Korallenfauna. – Paläontologische Zeitschrift, **17**, 178–204, Stuttgart.

KUSS, J. (1983): Faziesentwicklung in proximalen Intraplattformbecken: Sedimentation, Palökologie und Geochemie der Kössener Schichten (Obertrias, Nördliche Kalkalpen). – Facies, **9**, 61–172, Erlangen.

LAMMERER, B., ORTNER, H. & HEYNG, A. (2011): Field trip to the Northern Alps between Munich and the Inn Valley. – In: CARENA, S., FRIEDRICH, A.M. & LAMMERER, B. (Eds.): Geological Field Trips in Central Western Europe: Fragile Earth International Conference, Munich, September 2011. – Geological Society of America Field Guide, **22**, 75–100. https://dx.doi.org/10.1130/2011.0022(06)

LANGE, W. (1952): Der untere Lias am Fonsjoch (östliches Karwendelgebirge) und seine Ammonitenfauna. – Palaeontographica (A), **102**, 49–162, Stuttgart.

LEUCHS, K. (1921): Tektonische Untersuchungen im Guffert-Pendling-Gebiete (Nordtirol). – Neues Jahrbuch für Mineralogie, Geologie und Paläontologie, **1921**/1, 35–50, Stuttgart.

LINZER, H.-G., RATSCHBACHER, L. & FRISCH, W. (1995): Transpressional collision structures in the upper crust: the fold-thrust belt of the Northern Calcareous Alps. – Tectonophysics, **242**, 41–61, Amsterdam.

LOBITZER, H., KODINA, L.A., SOLTI, G., SCHWAIGHOFER, B. & SURENIAN, R. (1988): Fazies, Geochemie und Stratigraphie ausgewählter Vorkommen österreichischer organisch reicher Gesteine – ein Zwischenbericht. – Geologisch-Paläontologische Mitteilungen Innsbruck, **15**, 85–107, Innsbruck.

LOBITZER, H., SOLTI, G. & RAVASZ, C. (1994): Fazies und Geochemie ausgewählter Vorkommen bituminöser und kerogenreicher Gesteine Österreichs. – Jubiläumsschrift 20 Jahre Geologische Zusammenarbeit Österreich-Ungarn, Teil 2, 465–483, Geologische Bundesanstalt, Wien.

LÜTKEMEIER, S. (1972): Die Geologie zwischen Hochunütz und Ampelsbach (NE vom Achensee/Tirol). – Unveröffentlichte Diplomarbeit, Technische Universität Berlin, 130 S., Berlin.

MAIR, D., CHWATAL, W., REIMER, P.J. & SPÖTL, C. (2016): Quaternary evolution of the inner Riss Valley, Tyrol (Austria) – an integrated sedimentological and geophysical case study. – Austrian Journal of Earth Sciences, **109**/2, 277–288, Wien.

MOJSISOVICS, E. V. (1870): Das Kalkalpengebiet zwischen Schwaz und Wörgl im Norden des Inn. – Verhandlungen der k. k. Geologischen Reichsanstalt, **1870**, 183–185, Wien.

MOJSISOVICS, E. V. (1871): Beiträge zur topischen Geologie der Alpen. – Jahrbuch der k. k. Geologischen Reichsanstalt, **21**, 189–210, Wien.

MÜLLER-WOLFSKEIL, P. (1981): Tektonische Analyse des Wamberger Sattels im Bereich Vorderriß. – Geologica Bavarica, **8**, 235–250, München.

MUTSCHLECHNER, G. (1980): Aus der Geologie des Achentales. – In: STAUDIGL-JAUD, K. (Hrsg.): Achentaler Heimatbuch, 2. Auflage, Schlern-Schriften, **241**, 75–122, Innsbruck (Universitätsverlag Wagner).

Nagel, K.H. (1975): Der Bau der Thiersee- und Karwendel-Mulde (Tirol). – Geotektonische Forschungen, **48**, 136 S., Stuttgart.

Nagel, K.H., Schütz, K.-I., Schütz, S., Wilmers, W. & Zeil, W. (1976): Die geodynamische Entwicklung der Thiersee- und Karwendelmulde (Nördliche Kalkalpen). – Geologische Rundschau, **65**, 536–557, Stuttgart.

Neumayr, M. (1870a): Gefürstete Grafschaft Tyrol, Unter Inn Thaler Kreis Wattens – Volders. – Handkolorierte geologische Manuskriptkarten 1:28.800, Archiv der Geologischen Bundesanstalt, Wien [A 01824-m28/3a/33-3].

Neumayr, M. (1870b): Tirol, Hinterauthal. – Handkolorierte geologische Manuskriptkarten 1:28.800, Archiv der Geologischen Bundesanstalt, Wien [A 01796-m28/3a/21-2].

Neumayr, M. (1870c): Gefürstete Grafschaft Tyrol, Kreis Unter inn Thal Schwaz – Stans. – Handkolorierte geologische Manuskriptkarten 1:28.800, Archiv der Geologischen Bundesanstalt, Wien [A 01797-m28/3a/22-2].

Neumayr, M. (1870d): Tirol, Kohlstatt. – Handkolorierte geologische Manuskriptkarten 1:28.800, Archiv der Geologischen Bundesanstalt, Wien [A 01776-m28/3a/3-2].

Neumayr, M. (1871): Das Karwendelgebirge. – Verhandlungen der k. k. Geologischen Reichsanstalt, **1871**, 235–236, Wien.

Neumayr, M. (1879): Zur Kenntnis der Fauna des untersten Lias in den Nordalpen. – Abhandlungen der k. k. Geologischen Reichsanstalt, **7**/5, 1–46, Wien.

Neumeister, S., Gawlick, H.-J., Gratzer, R. & Bechtel, R. (2011): Muttergesteinspotential und organisch-geochemische Charakteristika der Sachrang-Subformation (Unter-Toarcium, Nördliche Kalkalpen, Unkener Mulde). – In: Gruber, A. (Red.): Arbeitstagung 2011 der Geologischen Bundesanstalt, Blatt 88 Achenkirch, 128–132, Wien.

Neumeister, S., Gratzer, R., Algeo, T.J., Bechtel, A., Gawlick, H.-J., Newtonc, R.J. & Sachsenhofer, R.F. (2015): Oceanic response to Pliensbachian and Toarcian magmatic events: Implications from an organic-rich basinal succession in the NW Tethys. – Global and Planetary Change, **126**, 62–83, Amsterdam.

Neumeister, S., Algeo, T.J., Bechtel, A., Gawlick, H.-J., Gratzer, R. & Sachsenhofer, R.F. (2016): Redox conditions and depositional environment of the Lower Jurassic Bächental bituminous marls (Tyrol, Austria). – Austrian Journal of Earth Sciences, **109**/2, 142–159, Wien.

Ortner, H. (2003): Cretaceous thrusting in the western part of the Northern Calcareous Alps (Austria) – evidences from synorogenic sedimentation and structural data. – Mitteilungen der Österreichischen Geologischen Gesellschaft, **94**, 63–77, Wien.

Ortner, H. & Gruber, A. (2011): 3D-Geometrien der Strukturen zwischen Karwendel-Synklinale und Thiersee-Synklinale. – In: Gruber, A. (Red.): Arbeitstagung 2011 der Geologischen Bundesanstalt, Blatt 88 Achenkirch, 51–67, Wien.

Ortner, H. & Kilian, S. (2016): Sediment creep on slopes in pelagic limestones: Upper Jurassic of Northern Calcareous Alps, Austria. – Sedimentary Geology, **344**, 350–363, Amsterdam.

Ortner, H. & Thöny, W. (2019): Field trip to the western Northern Calcareous Alps (NCA). – Unpublished Field trip Guide, Universität Innsbruck / OMV, 58 S., Appendix, Innsbruck.

Ortner, H., Reiter, F. & Brandner, R. (2006): Kinematics of the Inntal shear zone–sub-Tauern ramp fault system and the interpretation of the TRANSALP seismic section, Eastern Alps, Austria. – Tectonophysics, **414**, 241–258, Amsterdam.

Ortner, H., Aichholzer, S., Zerlauth, M., Pilser, R. & Fügenschuh, B. (2015): Geometry, amount and sequence of thrusting in the Subalpine Molasse of Western Austria and Southern Germany, European Alps. – Tectonics, **34**/1, 1–30, Washington, D.C.

Osswald, K. (1924): Das Risserkogelgebiet. – Geognostische Jahreshefte, **37**, 111–166, mit 1 geologische Karte 1:25.000, München.

Osswald, K. (1928): Die Wendelsteingruppe. Abriß der stratigraphischen, tektonischen und morphologischen Geschichte. – Mitteilungen der Geographischen Gesellschaft München, **21**, 183–304, 1 geologische Karte 1:25.000, München.

Penck, A. (1882): Die Vergletscherung der deutschen Alpen, ihre Ursache, periodische Wiederkehr und ihr Einfluss auf die Bodengestaltung. – 483 S., Leipzig (J.A. Barth).

Penck, A. & Brückner, E. (1901–1909): Die Alpen im Eiszeitalter. – Band I–III, 1199 S., Leipzig (Tauchnitz).

Pichler, A. v. (1856): Zur Geognosie der nordöstlichen Kalkalpen Tirols. – Jahrbuch der k. k. Geologischen Reichsanstalt, **7**/4, 737, Wien.

Pichler, A. v. (1859): Beiträge zur Geognosie Tirols. – Zeitschrift des Ferdinandeums für Tirol und Vorarlberg, **3**/8, 1. Folge, 169, Innsbruck.

Pichler, A. v. (1869): Beiträge zur Geognosie und Mineralogie Tirols. – Verhandlungen der k. k. Geologischen Reichsanstalt, **1869**/6, 101–102, Wien.

Pichler, A. v. (1872): Erratische Blöcke am Achensee, Fossilfunde in Brandenberg und Pertisau. – Neues Jahrbuch für Mineralogie, Geologie und Paläontologie, **1872**, 407, Stuttgart.

Pichler, A. v. (1876): Beiträge zur Geognosie und Mineralogie Tirols. – Neues Jahrbuch für Mineralogie, Geologie und Paläontologie, **1876**, 920, Stuttgart.

Poscher, G. (1994): Fazies und Genese der pleistozänen Terrassensedimente im Tiroler Inntal und seinen Seitentälern – Teil 1: Der Achenseedamm. – Jahrbuch der Geologischen Bundesanstalt, **137**/1, 171–186, Wien.

Quenstedt, W. (1933): Studien in der Überschiebungszone von Achenkirch. – Zeitschrift der Deutschen Geologischen Gesellschaft, **85**, 459–461, Hannover.

Quenstedt, W. (1951a): Geologische Exkursion in das Achentalgebiet (Tirol) am 9. und 10. September 1950. – Geologica Bavarica, **6**, 55–64, München.

Quenstedt, W. (1951b): Geologisch-paläontologische Monographie des Achentales (Tirol). Teil 1: Tabula stratigraphica (geohistorica) Mesozoici Achentalensis (Tirolis). – Biotropia, **1**, 12 S., Innsbruck (Felizian Rauch).

Richoz, S. & Krystyn, L. (2015): The Upper Triassic events recorded in platform and basin of the Austrian Alpsw. The Triassic/Jurassic GSSP and Norian/Rhaetian GSSP candidate. – Berichte der Geologischen Bundesanstalt, **111**, 75–136, Wien.

Richter, M. (1937): Die deutschen Alpen und ihre Entstehung. – 179 S., Berlin (Gebrüder Borntraeger).

Riedel, F. (1988): Facies and development of the “Wilde Kirche” reef complex (Rhaetian, Upper Triassic, Karwendelgebirge, Austria). – Facies, **18**, 205–218, Erlangen.

Rothpletz, A. (1888): Das Karwendelgebirge. – Zeitschrift des Deutschen und Österreichischen Alpenvereins, **1888**, 1–74, topographische und geologische Karte 1:50.000, München.

Sander, B. (1921): Über bituminöse Mergel. – Jahrbuch der Geologischen Staatsanstalt, **71**, 135–148, Wien.

Sander, B. (1922): Über bituminöse und kohlige Gesteine. – Mitteilungen der Geologischen Gesellschaft in Wien, **15**, 1–50, Wien.

Sander, B. (1941): Zum Gesteinscharakter der Hornsteinbreccien des Sonnwendjochgebirges. – Berichte der Reichsstelle für Bodenforschung, Zweigstelle Wien, **1941**, 81–89, Wien.

SANDERS, D. & GRUBER, A. (2016): Inner gorge-slot canyon system produced by repeated major base-level changes (Northern Calcareous Alps). – Field trip 13, GeoTirol 2016 – Annual Meeting DGGV, Geo.Alp, **13**, 277–292, Innsbruck.

SANDERS, D., WISCHOUNIG, L., GRUBER, A. & OSTERMANN, M. (2014): Inner gorge–slot canyon systemproduced by repeated streamincision (eastern Alps): Significance for development of bedrock canyons. – Geomorphology, **214**, 465–484, Amsterdam.

SAPPER, C. (1888): Über die geologischen Verhältnisse des Juifen und seiner Umgebung mit besonderer berücksichtigung der Liasablagerungen. – Inaugural-Dissertation, Universität München, 34 S., geologische Karte, München.

SÄRCHINGER, H. (1939): Geologie des Benediktenwandgebirges zwischen Glaswandscharte und Isar. – Neues Jahrbuch für Mineralogie, Geologie und Paläontologie, Beilagenband, **81**, 347–376, Stuttgart.

SARNTHEIN, R. V. (1940): Moor- und Seeablagerungen aus den Tiroler Alpen in ihrer waldgeschichtlichen Bedeutung: II. Teil: Seen der Nordtiroler Kalkalpen. – Beihefte zum Botanischen Centralblatt, **60B**, 437–492, Dresden.

SATTERLEY, A.K., MARSHALL, J.D. & FAIRCHILD, I.J. (1994): Diagenesis of an Upper Triassic reef complex, Wilde Kirche, Northern Calcareous Alps, Austria. – Sedimentology, **41**, 935–950, Oxford.

SAUSGRUBER, T. (1994a): Jurabeckenentwicklung nördlich vom Achensee und deren Folgen bei der alpidischen Kompressionstektonik. – Unveröffentlichte Diplomarbeit, Universität Innsbruck, 133 S., Innsbruck.

SAUSGRUBER, T. (1994b): Bericht 1993 über geologische Aufnahmen in den Nördlichen Kalkalpen auf Blatt 88 Achenkirch. – Jahrbuch der Geologischen Bundesanstalt, **137**, 469–474, Wien.

SCHÄFER, R. (1888): Über die geologischen Verhältnisse des Karwendels in der Gegend von Hinterriss und um den Scharfreiter. – Unveröffentlichte Dissertation, Ludwig-Maximilians-Universität, 37 S., München.

SCHMIDT-THOMÉ, P. (1950): Geologie des Isartalgebietes im Bereich des Rißbach-Stollens und des geplanten Sylvenstein-Staubeckens. – Geologica Bavarica, **4**, 3–55, München.

SCHREIBER, W. (1949): Über die Klammbildung und Talverschüttung im Brandenberg-Steinberger Gebiet. – Veröffentlichungen des Tiroler Landesmuseums Ferdinandeum, **26–29**, 33–60, Innsbruck.

SCHÜRMANN, W. (1969): Die Geologie der Thiersee-Mulde zwischen Hof-Joch und Schulter-Berg bei Achenwald/Tirol. – Unveröffentlichte Diplomarbeit, Technische Universität Berlin, 73 S., Berlin.

SCHÜTZ, K.-I. (1971): Die Geologie des Juifen und seiner Umgebung (Nordtirol). – Unveröffentlichte Diplomarbeit, Technische Universität Berlin, 93 S., Berlin.

SCHÜTZ, K.-I. (1975): Die Aptychenschichten der Thiersee- und der Karwendel-Mulde (Nordtirol). – Unveröffentlichte Dissertation Technische Universität Berlin, 183 S., Berlin.

SCHÜTZ, K.-I. (1979): Die Aptychenschichten der Thiersee- und der Karwendel-Mulde. – Geotektonische Forschungen, **57**, 1–84, Stuttgart.

SCHÜTZ, S. (1974): Die Geologie der Karwendel-Mulde zwischen Dürrach und Baumgartenjoch (Nordtirol). – Unveröffentlichte Diplomarbeit, Technische Universität Berlin, 160 S., Berlin.

SOLTI, G. & LOBITZER, H. (1989): Aufsuchung von Alginit in Österreich. Endbericht über die Österreichisch-Ungarische Zusammenarbeit in der Ölschiefer-Alginit-Prospektion. – Berichte der Geologischen Bundesanstalt, **17**, 47 S., Wien.

SOLTI, G., LOBITZER, H., CSASZAR, G. & SELMECZI, I. (1987): Bericht von den Ergebnissen der österreichischen-ungarischen Ölschiefer-Alginit-Forschungszusammenarbeit im Jahr 1986. – Unveröffentlichter Bericht, Bund/Bundesländer-Rohstoffprojekt Ü-LG-019/86, 176 S., Budapest–Wien.

SPENGLER, E. (1935): Bemerkungen zum Problem der Hornsteinbreccie im Sonnwendgebirge. – Verhandlungen der Geologischen Bundesanstalt, **1935**, 157–165, Wien.

SPENGLER, E. (1953): Versuch einer Rekonstruktion des Ablagerungsraumes der nördlichen Kalkalpen (1. Teil, Westabschnitt). – Jahrbuch der Geologischen Bundesanstalt, **96**, 1–64, Wien.

SPIELER, A. (1994): Bericht 1993 über geologische Aufnahmen in den Nördlichen Kalkalpen auf Blatt 88 Achenkirch. – Jahrbuch der Geologischen Bundesanstalt, **137**, 474–475, Wien.

SPIELER, A. (1995): Bericht 1994 über geologische Aufnahmen in den Nördlichen Kalkalpen auf Blatt 119 Schwaz. – Jahrbuch der Geologischen Bundesanstalt, **138**, 526–527, Wien.

SPIELER, A. & BRANDNER, R. (1989): Vom jurassischen Pull-Apart Becken zur Westüberschiebung der Achentaler Schubmasse (Tirol, Österreich). – Geologisch-Paläontologische Mitteilungen Innsbruck, **16**, 191–194, Innsbruck.

SPÖTL, C. (2019): Von der Eiszeit zur heutigen Warmzeit. Das Werden der Landschaft am Großen Ahornboden. – In: SONNTAG, H., STRAUBINGER, F., BRANDNER, R., SPÖTL, C. & VON NICOLAI, C. (Hrsg.): Großer Ahornboden. Eine Landschaft erzählt ihre Geschichte, 2. Auflage, 49–59, Wattens (Berenkamp).

SPÖTL, C., MAIR, D. & STARNBERGER, R. (2014): From Vorderriß to Großer Ahornboden: Quaternary geology of the Riss Valley (Karwendel Mountains) – Von Vorderriß bis zum Großen Ahornboden: Quartärgeologie des Risstales (Karwendelgebirge). – In: KERSCHNER, H., KRAINER, K. & SPÖTL, C. (Eds.): From the foreland to the Central Alps – Field trips to selected sites of Quaternary research in the Tyrolean and Bavarian Alps, 32–44, Deuqua Excursions, Berlin (Geozon Science Media).

STARK, F. (1873): Die bayerischen Seen und die alten Moränen. Mit Karte 1:250.000. – Zeitschrift des Deutschen und Österreichischen Alpenvereins, **1873**, 67, Frankfurt am Main.

STEINMANN, G. (1925): Gibt es fossile Tiefseeablagerungen von erdgeschichtlicher Bedeutung? – Geologische Rundschau, **16**, 435–468, Berlin.

SUAN, G., SCHLÖGL, J. & MATTIOLI, E. (2016): Bio- and chemostratigraphy of the Toarcian organic-rich deposits of some key successions of the Alpine Tethys. – Newsletters on Stratigraphy, published online February 2016, 19 S., Stuttgart. https://dx.doi.org/10.1127/nos/2016/0078

THÖNY, W. & ORTNER, H. (2001): Early Cretaceous to Tertiary thrusting in the Thiersee structure: results from stratigraphic and paleomagnetic investigations. – In: BRANDNER, R., KONZETT, J., MIRWALD, P., ORTNER, H., SANDERS, D., SPÖTL, C. & TROPPER, P. (Eds.): 5th Workshop of Alpine Geological Studies, Obergurgl, Abstracts. – Geologisch-Paläontologische Mitteilungen Innsbruck, **25**, 212–213, Innsbruck.

THÖNY, W., ORTNER, H. & SCHOLGER, R. (2002): Differentielle Blockrotationen in den nördlichen Kalkalpen: Ergebnisse paläomagnetischer Untersuchungen. – In: INSTITUT FÜR GEOLOGIE UND PALÄONTOLOGIE SALZBURG (Ed.): PANGEO 2002, Abstracts, 179, Salzburg.

THÖNY, W., ORTNER, H. & SCHOLGER, R. (2006): New paleomagnetic data from syntectonic sediments indicate joined geodynamics of Eastern and Southern Alps in Oligocene to Miocene times. – Geophysical Research Abstracts, **8**, 03940, Katlenburg-Lindau.

TÖCHTERLE, A. (2005): Tektonische Entwicklungsgeschichte des Südteiles der Nördlichen Kalkalpen entlang der TRANSALP-Tiefenseismik anhand bilanzierter Profile. – Unveröffentlichte Diplomarbeit, Universität Innsbruck, 91 S., Innsbruck.

TOLLMANN, A. (1969): Tektonische Karte der Nördlichen Kalkalpen, 3. Teil: der Westabschnitt. – Mitteilungen der Geologischen Gesellschaft in Wien, **62** (1969), 78–170, 1 tektonische Karte 1:100.000, Wien.

TRUSHEIM, F. (1930): Die Mittenwalder Karwendel-Mulde. – Wissenschaftliche Veröffentlichungen des Deutschen und Österreichischen Alpenvereins, **7**, 69 S., 1 geologische Karte 1:25.000, Innsbruck.

ULRICH, R. (1960): Die Entwicklung der ostalpinen Juraformation im Vorkarwendel zwischen Mittenwald und Achensee. – Geologica Bavarica, **41**, 99–151, München.

VAN KOOTEN, W.S.M.T. (2018): Structural evolution of the Achental Jurassic basin and present-day oblique structure in field and analogue model. – Unpublished Master Thesis, Universität Innsbruck, 156 S., Innsbruck.

VORTISCH, W. (1926): Oberrhätischer Riffkalk und Lias in den nordöstlichen Alpen. I. Teil. – Jahrbuch der Geologischen Bundesanstalt, **76**, 1–64, Wien.

WÄCHTER, J. (1987): Jurassische Massflow- und Internbreccien und ihr sedimentär-tektonisches Umfeld im mittleren Abschnitt der Nördlichen Kalkalpen. – Bochumer Geologische und Geotechnische Arbeiten, **27**, 239 S., Bochum.

WÄHNER, F. (1886a): Zur heteropischen Differenzirung des alpinen Lias. – Verhandlungen der k. k. Geologischen Reichsanstalt, **1886**, 168–176, Wien.

WÄHNER, F. (1886b): Zur heteropischen Differenzirung des alpinen Lias (Schluss). – Verhandlungen der k. k. Geologischen Reichsanstalt, **1886**, 190–206, Wien.

WÄHNER, F. (1903): Das Sonnwendgebirge im Unterinntal, 1. Teil. Ein Typus alpinen Gebirgsbaues. – 356 S., Leipzig–Wien (Deuticke).

WÄHNER, F. & SPENGLER, E. (1935): Das Sonnwendgebirge im Unterinntal, 2. Teil, mit geologischer Karte 1:10.000. – 200 S., Leipzig–Wien (Deuticke).

WEISTROFFER, K. (1974): Die Geologie der Karwendel-Mulde im Bereich des östlichen Bächentals, Nordtirol. – Unveröffentlichte Diplomarbeit, Technische Universität Berlin, 152 S., Berlin.

WENDT, J. (1969): Stratigraphie und Paläogeographie des Roten Jurakalks im Sonnwendgebirge (Tirol, Österreich). – Neues Jahrbuch für Geologie und Paläontologie, Abhandlungen, **132**, 219–238, Stuttgart.

WEYNSCHENK, R. (1949): Beiträge zur Geologie und Petrographie des Sonnwendgebirges (Tirol), besonders der Hornsteinbreccien. – Schlern-Schriften, **59**, 1–66, Innsbruck.

WIDMANN, H. V. (1853): Erläuterungen zur Geognostischen Karte Tirols. – 95 S., Innsbruck (Wagner'sche Buchdruckerei).

WISCHOUNIG, L. (2006): Das Quartär bei Steinberg am Rofan (Tirol): Stratigraphie, Sedimentologie und Aspekte der Landschaftsentwicklung. – Unveröffentlichte Diplomarbeit, Universität Innsbruck, 105 S., Innsbruck.

WOLF, H. V. (1922): Beiträge zur Kenntnis der eiszeitlichen Vergletscherung des Achenseegebiets in Tirol. – Mitteilungen der Geographischen Gesellschaft München, **15**, 147–304, München.

WOLF, H. V. (1924): Eiszeitstudien im Risser Gebirge. – Mitteilungen der Geographischen Gesellschaft München, **17**, 255–274, München.

WOLFF, H. (1985a): Geologische Karte von Bayern 1:25.000, Blatt Nr. 8338 Bayrischzell. – Bayerisches Geologisches Landesamt, München.

WOLFF, H. (1985b): Geologische Karte von Bayern 1:25.000. Erläuterungen zu Blatt Nr. 8338 Bayrischzell. – 190 S., Bayerisches Geologisches Landesamt, München.

ZÖLLER, I. (1972): Geologie der Karwendel-Mulde zwischen Achensee und Bächental in Tirol (Österreich). – Unveröffentlichte Diplomarbeit, Technische Universität Berlin, 108 S., Berlin.

Eingelangt: 12. Dezember 2019, angenommen: 18. Dezember 2019

JAHRBUCH DER GEOLOGISCHEN BUNDESANSTALT

Jb. Geol. B.-A.	ISSN 0016-7800	Band 159	Heft 1–4	S. 339–349	Wien, Dezember 2019

Beschreibungen von Salzburger Höhlen aus dem Jahr 1797

Peter Danner*

3 Tafeln

Österreichische Karte 1:50.000
BMN / UTM
94 Hallein / NL 33-01-16 Bischofshofen

Höhlen
Spätaufklärung
Land Salzburg
Bergwerksgeschichte

Inhalt

Zusammenfassung

Unterlagen, welche die Verwaltung des Eisenwerks Werfen (Land Salzburg) 1797 in Erfüllung eines Befehls des Salzburger Erzbischofs zur Sammlung von Materialien für eine Bergwerksgeschichte des Fürsterzbistums Salzburg vorlegte, enthalten auch detaillierte Angaben über zwei Höhlen des Hagengebirges, das Brunnloch und den Scheukofen. Sie können als älteste Dokumente der Höhlenforschung im Land Salzburg angesehen werden.

Descriptions of caves of Salzburg from the year 1797

Abstract

The records, which the administration of the ironworks of Werfen (region of Salzburg) presented in 1797 in fulfilment of an order of the archbishop of Salzburg to collect material about the history of mining in the archbishopric of Salzburg, include detailed informations about two caves in the Hagengebirge, Brunnloch and Scheukofen. They can be considered to be the earliest documents of speleology in the region of Salzburg.

* Peter Danner: Fürstallergasse 33, 5020 Salzburg. pdanner100@gmail.com

Einleitung

Während der Spätaufklärung im Fürsterzbistum Salzburg, die mit der Regierungszeit von Erzbischof Hieronymus Graf Colloredo (1732–1812), die von 1772 bis 1803 dauerte, zusammenfällt, erlangten Höhlen im Zuge von topografischen Forschungen eine größere Beachtung (DANNER, 2017).

Im Zuge der Vorbereitungen zur Abfassung einer vom Salzburger Hofkammerdirektor und Leiter des Münz-, Salz- und Bergwesens, Karl Ehrenbert von Moll (1760–1838), angeregten (SCHALLHAMMER & KÖCHEL, 1865: 34) und vom Erzbischof Graf Colloredo am 2. März 1796 befohlenen Bergwerksgeschichte des Erzstiftes Salzburg (Befehls-Abschrift 1796) legte Conradin Oberreiter, der Leiter der Eisenwerksverwaltung Werfen, am 3. März 1797 Unterlagen vor, in denen neben Bergwerken und Neuschürfen auch zwei Höhlen im Hagengebirge (Land Salzburg, Bezirk St. Johann), das Brunnloch bei Stegenwald (KLAPPACHER & KNAPCZYK, 1979: 135–137, Nr. 1335/3) (Taf. 1, Figs. 1–5) und der Scheukofen bei Sulzau (KLAPPACHER & KNAPCZYK, 1979: 138–157, Nr. 1335/4) (Taf. 2, Figs. 1–4; Taf. 3, Figs. 1–3), erfasst sind (OBERREITER, 1797). Diese Unterlagen umfassen die „Tabelle einer erzstiftlichen Bergwerks-Geschichte und vorzüglichen Nachrichten von alten Bergwerken und Neuschürfen“ (Tabelle 1797), das „Berg-Protokoll Über die auf gnädigste Anbefehlung Einer Hochlöblichen Hofkammer von 2ten März 1796 gesammelte Nachrichten, und schürffend bewerkte Untersuchungen, welche man von alten Bergwerken, Neuschürffen, Schmelz und Hüttenwerken erhalten konnte“ (Berg-Protokoll 1797) und das „Verzeichnis der im Pfleggericht Werfen und Landgericht Bischofshofen in ältern Zeiten bestandenen Berg und Schmelzwerke, so viel davon aus den Akten zu nehnben war“ (Verzeichnis 1797). Da diese Quellen bisher nur in geringen Ausschnitten veröffentlicht und nur in eingeschränktem Ausmaß ausgewertet wurden (POSSELT-CSORICH, 1879: 2; POSSELT-CZORICH, 1880: 266–267; WORLICZEK, 1977), werden die Abschnitte, welche die Höhlen betreffen, im vollen Wortlaut zitiert.

Erläuterungen zu Begriffen und Maßen

In den Texten kommen etliche im Bergbau übliche Ausdrücke vor. Krack bedeutet Höhle (CAMPE, 1808: 1026), Firste die Decke, Sohle der Boden, Ulmen oder Stöße die Wände (KAUFMANN, 1833: 82, § 125) und Teufe die Tiefe.

Weltgegend bedeutet Himmelsrichtung, Abend aufgrund der Richtung des Sonnenuntergangs Westen. Die Angabe „6 Abends“ entspricht genau dem Westen, die Angabe „8 Abends“ der Richtung zwischen Westnordwest und Nordwest. Diese Werte ergeben sich aufgrund des Vergleiches der Windrose mit der Uhrzeit (STEINHAUSER, 1864: 27, Abb. 58).

„Tabelle einer erzstiftlichen Bergwerks-Geschichte“

1. Thales-Nämen und Benennung des Orts mit Weltgegend.	2. Anzahl der alten Gruben und deren allfällige Nämen.	3. Gebirgsarten.	4. Einschiessen des Gesteins.	5. Verschiedene Gesteinsarten.
In dem Steinwänd-Gebirg ober den Lehen gleiches Namen, in dem Steinwänd-Brunnloch an der Filling. Gegen Abend.	Nº 16. Ein offener Krack oder Ofen bey 150 Lachter tief und etliche Lachter hoch in der Öffnung.	Ein gemeiner Kalkstein.	Im schwebenden Blättern gelagertes Kalkgebirg.	Unterschiedlich figurirte Tropfsteine, Kalksinter und deto Schallen.
In der Blientau auf der Steinwändalpen vulgo in Scheickofen. Gegen Abend.	Nº 18. Ein offener Krak oder Ofen, bey 200 Lachter tief, und von verschiedener von ¼ bis mehreren Lachter Höche in der Offnung. Der Scheickofen genannt.	Ein gemeiner Kalkstein, so in etwas der Verwitterung geneigt.	Ein in dick blättrig und auch wellen förmiges Gesteine stockendes Gebirg	Verschiedenlich und besonders figurirte Tropfsteine, Kräusen, Schallen und mehrley Kalksinters-Arten und Rinden, die das ganze Kraksgestein krustieren.
6. Gänge oder Laager.	**7. Streichen nach welcher Weltgegend.**	**8. Fallen derselben.**	**9. Mächtigkeit der Erzlagerstätte und Gesteinslagen.**	**10. Gänge und Erzarten.**
Ein durch den Krak richtig stechender Gang oder ächte Gebirgsscheidung.	6 Abends.	Gänzlich schwebendes Blättergestein.	Ohne alle Erzspuren, in denen Blättern in etwas ablosiges Gebirg.	Eine schmalle Lettenkluft, welche den Gang hin und hin folgend bestimmt, ohne eine merklichen Mineralzeichen.
Ein meistens in ganzen Stockgebirg und auch wohl einigen gang förmigen Nebenkraken in einer verwitterlichen Steinrevier entstandene Gebirgsöffnung, und unterschiedlich absinternnder Schallengesteins-Anhäufungen, die die Verwachsung einiger Kraksorter wiederum bewerken.	Ein in Durchschnitte der abwechslend sich stürzenden Steinblättern bestehendes Gebirgs-Scheidungs-Verhältniß auf 8 Abends.	In der vordern oder Zechhmässig, doch aber auch hin und hin steigende und auch fallenden Kraks-Einfahrte verflächt sich der Krak in 80 Grade. Der donlägige Schachtort senkt sich aber 32 Grade, und ist bey 80 Lachter tief.	Beleuchtet man nichts von einer Mineralspure, indem alle Ulmen die Sohle wie die Firste mit Kalkrannschallen überrunnen, und dick bedeckt sind.	Ein mit mehrer theils offen, theils schon verwachsenden Nebenkraken sehr beträchtlich sehenswürdige Gebirgs-Offnung, welche mit einer Schalle von Tropfstein-Rinde gänzlich überzogen, und ohne einer Erzspure ist.

Nix ist eine der Bezeichnungen für die Bergmilch, ein Speläothem (Höhlenmineral), das sich vor allem aus mikrokristallinem Kalzit oder Hydromagnesit zusammensetzt und in der Volksmedizin Verwendung fand (DANNER, 2017: 117).

Die Längenmaße Klafter oder Lachter entsprechen einem Wert von 1,7802 Metern. Der Metzen ist ein Hohlmaß, das in Salzburg 35,9478 Liter entspricht (WEILMEYR, 1813: 227; SCHWAGER, 1870: 56).

„Berg-Protokoll"

Im „Berg-Protokoll" finden sich ausführlichere Angaben zu den einzelnen Orten. Über das Brunnloch und den Scheukofen wird berichtet:

„N° 16.

Im Blientau Thale auf der Steinwand an der Filling ober den Steinwändlehen in dem Steinwänd-Brunnloch. Ein gegen Abend sehende Berghölle.

Ober den ansteigenden Kalkgebirgsfuße.

Kömmt man auf einen schmallen Steige durch die Wande zu einen von Ferne ersehlich sehr weit und hoch offenen Kracke diesseits des Salza Flußes das Steinwänd-Brunnloch genannt, von dessen tiefesten Orte dieses Lehen ihren Brunn in den gewöhnlich hölzernen Röhren zum Hause führt. Die Strecke dieser Kracksteufe beträgt wenigstens bey 150 Lachter, wobey merkwürdig ist, daß aus diesen Gebirgs-Ofen, wenn die abrinnenden Schneewässer zur Frühlingszeit am heftigsten sind, so vieles Wasser fließet, daß auch sogar die an der Firste dieses Kracks anstehende Brunnröhre an mehrern Orten von dieser unterirdischen Wasserflutte abgehoben und gewaltsam fortgeschwemmt werden: woher einleuchtend ist, daß auch dessen Gebirgsjoch beträchtlich Riesse und große Spaltungen erlitten haben müsse, wodurch diese Wasserkanale reichen, daß ein so namhafter Bach in erwähnten Kracke, oder sogenannten Brunnloch entstehen könne, indessen Stoß oder tiefesten Ort man noch wegen gar zu enger Fahrbarkeit nicht gekommen ist. Dieser Krack ist in der ersten oder Vorhölle wohl mehrere Lachter hoch und eben so viel breit, der so hin und hin bis an Stoß abwechslend bald grösser bald kleiner wird. In dieser Berghölle sind sehr vielle übereinander da liegende Steinbruchstücke von ungemeiner Größe, und auch kleinere von einer sehr großen Menge, die meistens so scharfschneidig sind, daß man über solche nicht ohne Gefahr steigen kann, sogaar, daß es einen oberirdischen Schuttort eines einen gewaltigen Erdstoß erlittenen Berges ganz ähnlich darstellet.

[...]

N° 18.

In dem Blientau Thale an der Steinwand in der Steinwändalpen, vulgo der Scheickofen. Ein gegen Abend zugängige Berghölle.

Auf einen Vorgebirgsthale im Aufsitz des hochen Kalkgebirgs.

Stehet ein offener Krack oder sehr große Berghölle am Fuß der steilen Wande, auf welchen Steinfelsen im anfänglichen Orte das hangend Gestein eine wellenförmige sich weitherunterlassende Firste hat, so auf einen in der Mitte dieses Krackseingang stehenden großen Stein passet, hinter welchen ein groß von Natur künstlich formirte Grotte mit unterschiedlich seltnen Tropfstein-Gehängen und mit Schallen gänzlich überzogen von Tag hell beleuchtet wird. Nicht nur allein die beyden Ulmen oder Wände, und die gerundete Firste, sondern auch die Sohle sind gänzlich mit der abgerunnenen Tropfsteinschalle uberzogen. Ohne von den vielen Figuren und seltenen Abtropfungen genaue Erwähnung beyrücken zu können, ist dieser Krack so wenigst 200 Lachter tief, hin und hin beynahe in gleicher Beschaffenheit des Schallenüberzugs und der Tropfsteine, nur mit dem Unterschiede, daß die wichtigsten und schönsten Tropfsteins-Arten jenseits des Sees und noch mehr in selben, wohin man durch einen bey 80 Lachter tiefen und sehr niedrig, flachen Krack fahren muß, am meisten angetroffen werden. Von den ersten und weitesten Kracks-Orte oder der Grotte und durch den Schacht bis ins tiefeste Ort oder Gebirgsstoß jenseits des Sees, so auch noch eine Strecke von 30 Lachtern der Nebenkracken und Schachten unberechnet beträgt, liegen hin und wieder viele lose Steine, die alle mit einer Schalle überzogen sind. In ältern Jahren hatten die Schatzgräber noch ihren eifrrigsten Zutritt in diese Berghölle, in welch albernen Absichte einer von diesen ob den See in der zu sehr verengten Steinöffnung mit den Kopf sich versteckte und so hängend bleibend darinn verdarb. Der todten Kopf blieb zwischen den sehr engen hangend und liegend Blatt, wo der arme Tropf nicht mehr vorwärts oder zuruck kommen konnte, stecken, wie man solchen auch da vor etlichen Jahren antraff. Der Leib aber fiel nach erfolgter Fäullung des Halsbeins in den See hinunter. Vermuthlich wird dieser neugierige Mensch auf den heilen liegend Blatt gestraucht, und sich den Kopf zwischen das enge schliefens Gestein gewaltig eingeklemmt haben, und da er keinen Stand mehr fassen konnte, so elend hat bleiben müssen."

„Verzeichnis der im Pfleggericht Werfen und Landgericht Bischofshofen in ältern Zeiten bestandenen Berg und Schmelzwerke"

Dieses Verzeichnis enthält einen ausführlichen Bericht über den Scheukofen:

„Scheickofen

So wird nach hierortigen Sprachgebrauch, welchem scheick- oder scheickig so viel als grausen erregend, fürchterlich, und Ofen für Felsen, und Höhle gilt, sonach Scheickofen – eine fürchterliche Höhle bedeutet, eine im Westen des Plientau Thales in der Steinwendalpe an einer Felsenwand befindliche Berghöhle genannt.

Dieser Scheickofen war früher eine Wallfahrt des Aberglaubens; gefundene Todtenschedel bürgen diese Wahrheit.

Ein Hofrathsbefehl vom 30. May 1650 befahl über die Besuche dieser Höhle zu inquirirn.

Des Georg Krack Bauers zu Steinwend ist die Aussage hierüber er sey vor 50 Jahren mittels Hilfe eines Fadens in die Höhle eine Stunde lang herumgegangen, wollte Bergwerk finden, brachte aber nichts heraus, er habe verschiedene Löcher, auch einen 20–30 Schritte langen See und 2 Todtenköpfe gesehen, gehört aber nichts. Er wisse einen Mann von Hallein, der vor einem Jahr in der Höhle gewesen, der bey 5 Metzen Nix heraustrug, die ein Fuhrmann wegführte.

Im Inquisitions Einbegleitungs Bericht vom 1. July wird noch gesagt es sey wissentlich, daß sowohl in als ausländische haim und öffentlich ermeldten Ort aus und eingehen, und bringen weisse Materie wie Schotten heraus, welche sie Nix nennen, und in die Apotheke das Pfund à 4 x [Kreuzer] verkaufen.

Zwey Knappen von Werfen, welche Tropfsteine aus dieser Höhle hohlten, machten den 4: Jäner 1791 die Anzeige: wie sie beylich 200 Klafter tief im Scheikofen waren, kamen sie zu einem kleinen See, welcher 4 Klafter lang, 2 breit und Manns tief wäre. Der Weeg tiefer in diese Höhle sey schmall und sehr schräge. Ober diesem See sey eine Felsen öfnung, auf deren Ranft sie einen Todtenkopf entdeckten, welcher gerade stand und mit Tropfsteinen umgeben war.

Es hat sich hinnach entdeckt, daß dieser Kopf eines 18jährigen Metzgerknechtes von hier sey, der vor 40 Jahren in diese Höhle gerathen und umgekommen ist. Er wird auch seinen Hund bey sich gehabt haben, denn ein Bauers Sohn von Steinwend betheurte hinnach vor einigen Jahren in der Höhle ein Hundsgrippe gefunden zu haben.

In jüngere Zeiten finden sich von einem Nix keine Spurren mehr, wohl aber zeigen sich verschieden gestaltete Tropfsteine."

Analyse

Die systematische Erfassung der Bergwerke und Höhlen unter festgelegten Gesichtspunkten wie Bezeichnung, Lage, Länge, Ausrichtung, Gesteinarten in der „Tabelle einer erzstiftlichen Bergwerks-Geschichte" nahm die systematische Erfassung der Höhlen in Höhlenkatastern voraus, die in Österreich erst ab 1900 einsetzte (Danner, 2015: 108–109).

Die ergänzenden Texte im „Bergprotokoll" und im „Verzeichnis der im Pfleggericht Werfen und Landgericht Bischofshofen in ältern Zeiten bestandenen Berg und Schmelzwerke" enthalten neben ausführlicheren Beschreibungen der Höhlen auch Angaben über die Höhlennutzung und somit über die wirtschaftliche Bedeutung der Höhlen. Beim Brunnloch liegt diese in der Wasserversorgung, beim Scheukofen in der Suche nach Erzen („Bergwerk"), Bergmilch, Tropfsteinen und Schätzen. Beim Scheukofen wird auch die Bedeutung des Namens der Höhle erklärt.

In den Text über das Brunnloch sind hydrologische Überlegungen einbezogen. Aus der im Frühjahr austretenden Wassermenge wurde gefolgert, dass das Wasser aus einem großen Einzugsgebiet durch Risse und Spalten im Berg in die Höhle gelangte.

Die Informationen über die früheren Besuche des Scheukofens wurden Akten des Pfleggerichts Werfen entnommen, dem Hofratsbefehl vom 30. Mai 1650, dem Bericht des Werfener Pflegverwalters Kaspar Glück vom 1. Juli 1650 und dem Protokoll über das Verhör („Examen") vom 6. Juli 1650 (Akten 1650), ferner dem Bericht über die Vernehmung der Bergknappen Martin Gebhart und Matthias Gschwandner aus Werfen vom 4. Jänner 1791 (Summarische Vernehmung 1791). Von den 1650 ermittelten Besuchern des Scheukofens sind nur jene erwähnt, die darin Erze und Nix suchten. Andere, die aus Kurzweil oder aus nicht bekannten Motiven hineingingen (Akten 1650), sind in den 1797 vorgelegten Unterlagen nicht erwähnt, was vielleicht damit zu erklären ist, dass in diesen Fällen kein Zusammenhang mit der Bergwerksgeschichte vorliegt.

Der Inhalt dieser Akten wurde in noch kürzerer Form von Franz Michael Vierthaler in seinem 1801 anonym erschienen Bericht über seinen Besuch der Höhle im Jahr 1799 wiedergegeben (Vierthaler, 1801: 216–217). Dort sind nur Georg Krack um 1600 und die zwei Knappen 1791 als Besucher erwähnt.

Schlussfolgerung

Die in Erfüllung des erzbischöflichen Befehls vom 2. März 1796 von der Eisenwerksverwaltung Werfen eingereichten Unterlagen enthalten die älteste umfassende Dokumentation der Untersuchung von Höhlen im Land Salzburg, die aufgrund der Aufgabenstellung vor allem unter geologischen und montanistischen Gesichtpunkten erfolgt ist. Sie können als älteste Zeugnisse von Höhlenforschung im Land Salzburg angesehen werden. Während über das Brunnloch in den folgenden Jahren keine schriftlichen Quellen bekannt sind, wurde der Scheukofen durch die ausführlichen Berichte von Franz Michael Vierthaler aus dem Jahr 1801 (Vierthaler, 1801) und Joseph August Schultes aus dem Jahr 1804 (Schultes, 1804: 150–156), die von vielen anderen Autoren ohne Nennung der Quelle übernommen wurden, eine der bekanntesten Höhlen des Landes Salzburg. Obwohl Vierthaler und Schultes auch wissenschaftliche Interessen hatten und deren Reisen auch wissenschaftlich motiviert waren, sind deren Berichte nicht als Zeugnisse von Höhlenforschung im engeren Sinn zu bewerten. Diese setzte sich 1801 mit der von Erzherzog Johann angeordneten Vermessung des Scheukofens (Danner, 2017: 116) fort.

Dank

Der Verfasser dankt den Bediensteten des Salzburger Landesarchivs für das Engagement bei der Suche nach den Archivalien, Michael Krebs, Herbert Seidl und Gerhard Zehentner für die Begleitung bei Befahrungen des Brunnloches und Scheukofens, Herbert Seidl auch für die zur Verfügung gestellten Fotos.

Archivalien

Akten (1650): Akten betreffend Scheukofen, 30.05.–07.07.1650. – Salzburger Landesarchiv, Pfleggericht Werfen, HR, Lit. B, Kest IV, 1–3, Ktn. 58, 3. Bund, Nr. 28.

Befehls-Abschrift (1796): Hochlöbliche Hofkammer Befehls-Abschrift, 02.03.1796. – Salzburger Landesarchiv, Pfleg Werfen, 84. Fach / 13–14 / 1794–1798, Karton 549, 14. Bund, Nr. 391.

Berg-Protokoll (1797): Berg-Protokoll Über die auf gnädigste Anbefehlung Einer Hochlöblichen Hofkammer von 2ten März 1796 gesammelte Nachrichten, und schürffend bewerkte Untersuchungen, welche man von alten Bergwerken, Neuschürffen, Schmelz und Hüttenwerken erhalten konnte. – Salzburger Landesarchiv, Bergwesen, Fasz. 9/2, 1800, 2. Teil, causa Domini, Karton 44, Nr. 63.

Oberreiter, C. (1797): Brief an Hofkammer vom 03.03.1797. – Salzburger Landesarchiv, Bergwesen, Fasz. 9/2, 1800, 2. Teil, causa Domini, Karton 44, Nr. 63.

Summarische Vernehmung (1791): Summarische Vernehmung, 04.01.1791. – Salzburger Landesarchiv, Pfleggericht Werfen, 1776–1807, Karton 471, 62. Fach, 3. Bund, Nr. 69.

Tabelle (1797): Tabelle einer erzstiftlichen Bergwerks-Geschichte und vorzüglichen Nachrichten von alten Bergwerken und Neuschürfen. – SLA, Bergwesen, Fasz. 9/2, 1800, 2. Teil, causa Domini, Karton 44, Nr. 63; Salzburger Landesarchiv, Pfleg Werfen, 84. Fach / 13–14 / 1794–1798, Karton 549, 14. Bund, Nr. 391.

Verzeichnis (1797): Verzeichnis der im Pfleggericht Werfen und Landgericht Bischofshofen in ältern Zeiten bestandenen Berg und Schmelzwerke, so viel davon aus den Akten zu nehnben war. – Salzburger Landesarchiv, Pfleg Werfen, 84 / 13–14 / 1794–1798, Karton 549, 14. Bund, Nr. 391.

Literatur

Campe, J.H. (Hrsg.) (1808): Wörterbuch der Deutschen Sprache. Zweiter Theil. F – bis – K. – 1116 S., Braunschweig (Schulbuchhandlung).

Danner, P. (2015): Der Welthöhlenkataster von Gustave Abel und sein Bezug zu Katasterprojekten in Deutschland und Österreich. – Die Höhle, **66**/1–4, 107–125, Wien.

Danner, P. (2017): Höhlenbesuche und Höhlenforschung in Salzburg um 1800. – Mitteilungen aus dem Haus der Natur, **24**, 100–131, Salzburg.

Kaufmann, P. (1833): Propädeutik zur Kameralistik und Politik, ein Handbuch der Encyclopädie, Methodologie und Litteratur der Kameral- und Staatswissenschaften zum Gebrauche für Verwaltungsbeamte, Kameralbeflissene und Juristen. – 367 S., Bonn (T. Habicht).

Klappacher, W. & Knapczyk, H. (Red.) (1979): Salzburger Höhlenbuch, Band 3. – 487 S., Salzburg (Landesverein für Höhlenkunde in Salzburg).

Posselt-Csorich, A. (1879): Der Scheuckofen bei Sulzau. – Salzburger Volksblatt, 14.10.1879, 1–2, Salzburg.

Posselt-Czorich, A. (1880): Höhlenwanderungen im Salzburger Kalkgebirge. Zweite Folge. – Zeitschrift des Deutschen und Oesterreichischen Alpenvereins, **11**, 258–275, München.

Schallhammer, A. von & Köchel, L. von (1865): Karl Maria Ehrenbert von Moll. – Mittheilungen der Gesellschaft für Salzburger Landeskunde, **5**, Anhang, 1–79, Salzburg.

Schultes, J.A. (1804): Reise auf den Glockner. III. Theil. Reise durch Salzburg und Berchtesgaden. I. Theil. – 274 S., Wien (J.V. Degen).

Schwager, H. (1870): Die Neue Maß- und Gewichts-Ordnung für das Königreich Bayern. – 3. Auflage, 134 S., Würzburg (Julius Kellner's Buchhandlung).

Steinhauser, A. (1864): Grundzüge der mathematischen Geographie und der Landkartenprojection. – 138 S., Wien (Friedrich Beck's Universitäts-Buchhandlung).

Vierthaler, F.M. (1801): Aus den Papieren eines Reisenden (Fortsetzung). Der Scheukofen. – Intelligenzblatt von Salzburg, 11.04.1801, Nr. **15**, 214–219, Salzburg.

Weilmeyr, F.X. (1813): Salzburg, die Hauptstadt des Salzach-Kreises. Ein Hand- und Addreß-Buch für Jedermann. – IV + 342 S., Salzburg.

Worliczek, K. (1977): Eine alte Beschreibung des Brunnloches bei Stegenwald. – LVHK Salzburg, VM [Vereinsmitteilungen], Nr. **3**, 21–22, Salzburg.

Worliczek, K. (1979): Historische Arbeiten über den Scheukofen bei Sulzau. – In: Klappacher, W. & Knapczyk, H.: Salzburger Höhlenbuch, 3. Band, 145–153, Salzburg.

Eingelangt: 6. August 2019, angenommen: 4. Dezember 2019

Tafel 1

Fig. 1: Brunnloch, Höhlenportal, „*von Ferne ersehlich sehr weit und hoch offenen Kracke*“ (Foto: Peter Danner).

Fig. 2: Brunnloch, Vorhalle (Foto: Peter Danner).

Fig. 3: Brunnloch, „*unterschiedlich figurierte Tropfsteine* …“ (Foto: Peter Danner).

Fig. 4: Brunnloch, „… *Kalksinter und deto Schallen*“ (Foto: Herbert Seidl).

Fig. 5: Brunnloch, Holzröhren der Wasserleitung (Foto: Herbert Seidl).

1

2

3

4

5

Tafel 2

Fig. 1: Scheukofen, Höhlenportal (Foto: Peter Danner).

Fig. 2: Scheukofen, Vorhalle, „*weitherunterlassende Firste* [...]*, so auf einen in der Mitte dieses Krackseingang stehenden großen Stein passet*“ (Foto: Peter Danner).

Fig. 3: Scheukofen, Versinterungen vor der Riesentreppe, „*gänzlich mit der abgerunnenen Tropfsteinschalle uberzogen*“ (Foto: Peter Danner).

Fig. 4: Scheukofen, Riesentreppe (Foto: Peter Danner).


1


2


3


4

Tafel 3

Fig. 1: Scheukofen, Tropfsteinkluft mit abgeschlagenen Tropfsteinen (Foto: Peter Danner).

Fig. 2: Scheukofen, Tropfsteinkluft mit abgeschlagenen Tropfsteinen (Foto: Peter Danner).

Fig. 3: Scheukofen, Zweiter See (Foto: Peter Danner).

1

2

3

JAHRBUCH DER GEOLOGISCHEN BUNDESANSTALT
Jb. Geol. B.-A. | ISSN 0016-7800 | Band 159 | Heft 1–4 | S. 351–355 | Wien, Dezember 2019

Zur Erinnerung an Dr. phil. Peter Jürgen Müller, Ingenieurkonsulent für Technische Geologie
(4. August 1942 – 11. Dezember 2019)

Peter Jürgen Müller wurde am 4. August 1942 in Villach geboren. Sein Vater, Peter Müller, übte den Beruf eines Kaufmanns aus, seine Mutter Elsa (geborene Kolitscher) war Hausfrau. So konnte Peter in einem wohlbehüteten Elternhaus zusammen mit seiner Schwester Geralda die Kindheit verbringen und in Paternion aufwachsen. Er besuchte hier die Volksschule und in Spittal an der Drau das Bundesrealgymnasium, an dem er 1961 die Matura bestand. Einer seiner Klassenkameraden war Hans Peter Schönlaub, der später als Geologe (Dr. phil., Hofrat und tit. Univ.-Prof.) an der Geologischen Bundesanstalt in Wien, zuletzt von 1993 bis 2009 als deren Direktor, arbeitete.

Von 1961 bis 1962 leistete Peter seinen ordentlichen Präsenzdienst (heute Grundwehrdienst) als Einjährig-Freiwilliger beim Österreichischen Bundesheer ab. Er diente beim damaligen Panzerbataillon 1 (ausgerüstet mit den legendären Jagdpanzern AMX 13) in Wiener Neustadt, avancierte in einem Panzergrenadierzug zum stellvertretenden Gruppenkommandanten und rüstete als Gefreiter ab. Nach einigen Übungen in der Reserve wurde er 1974 zum Korporal befördert.

Unmittelbar nach seinem Wehrdienst begann er im Herbst 1962 in Wien ein Studium der Veterinärmedizin. Nach erfolgreicher Ablegung der ersten Staatsprüfung 1966 erlitt er einen Autounfall und entschloss sich zum Abbruch dieses Studiums. Noch im selben Jahr präzisierten sich die Aspekte auf seine künftige Berufslaufbahn als Geologe, weshalb für Peter ausschließlich Studien der Fächerkombination Geologie, Paläontologie sowie Mineralogie und Petrographie in Frage kamen, zunächst einmal an der Universität Wien. Dieses Studium setzte er 1967 an der Leopold-Franzens-Universität Innsbruck fort, weil sich dort gerade eine Mikrofazies-Arbeitsgruppe mit Schwerpunkt Drauzug bildete. Zu seinen akademischen Lehrern in Innsbruck zählten die Professoren Werner Heißel und Helfried Mostler (Geologie), Josef Ladurner (Mineralogie), Fridolin Purtscheller (Petrographie) und Oskar Schulz (Lagerstättenlehre) sowie die Assistenten Werner Resch, Kurt Czurda, Rainer Brandner, Christine Miller und Stephan Hoernes. Studienkollegen von Peter Jürgen Müller waren unter anderem Toni Aichhorn, Hans Angerer, Günther Bunza, Elmar Colins de Tarsienne, Antonio Donofrio, Erich Enichlmayr, Herbert Fuchs, Christoph Hauser, Gunther Heißel, Georg Hoinkes, Manfred Köhler, Wolfgang Leichtfried, Wolfgang Nachtmann, Jörg Schantl, Josef-Michael Schramm, Ewald Tentschert, Franz Vavtar, Heinrich Wallner und Heinrich Winkler. Wie in dieser Kommilitonen-Liste ersichtlich, gab es zu jener Zeit im Fachstudium (leider) noch keine Kolleg*inn*en!

Peters Vorliebe für gesellige Zusammentreffen mit Studien- und Fachkollegen, aber auch mit Corpsbrüdern seiner farbentragenden und schlagenden Studentenverbindung „Akademisches Corps Saxonia“ sowie mit Jagdfreunden ließ das Ausmaß seiner Studienzeit etwas gedehnt erscheinen. In diesem Zusammenhang darf jedoch nicht vergessen werden, dass Peter für sein Studium auf einen zeitintensiven Zuverdienst angewiesen war, er belieferte u.a. als Chauffeur eines Kühltransporters verschiedene Grünmärkte in Wien mit Schwammerln aus Kärnten. Vor allem forderten seine besonders gründlichen, aber auch wetterabhängigen Geländearbeiten für die Dissertation „Zur Geologie des Raumes zwischen Reißkofel und Jauken, unter besonderer Berücksichtigung der Mikrofazies mitteltriadischer Becken- und Plattformsedimente (westliche Gailtaler Alpen, Kärnten)“ entsprechende Zeit. Hinzu kamen umfangreiche Labortätigkeiten und mikroskopische Analysen an großformatigen Dünnschliffen. Seine Betreuer bzw. „Doktorväter“ waren die Universitätsprofessoren Werner Heißel und Helfried Mostler. Peter Jürgen Müller wurde am 5. November 1977 in der Aula der Universität Innsbruck zum Doktor der Philosophie promoviert.

1975 ehelichte er seine Rosi (Rosina, geborene Tschernutter). Dieser Ehe entsprossen drei Kinder, Peter (1975, in direkter Folge: Peter der Dritte), Arnulf (1977) und Barbara (Babsi, 1982). Nach einem Baustellenbesuch samt Stollenbefahrung (gefräster Triebwasserweg für das Kraftwerk Strubklamm, Land Salzburg) besuchten am Dreikönigstag des Jahres 1982 der Verfasser dieser Zeilen und Peter Jürgen Müller dessen Gattin Rosi im nahe gelegenen Halleiner Krankenhaus. Dort hatte Rosi vor kurzem ihre Tochter Babsi (vom glücklichen Vater Peter Jürgen oftmals und gerne als „Prinzesschen" tituliert) entbunden. Rosi freute sich zwar, zeigte jedoch über unser Erscheinen nicht gerade helle Begeisterung, zumal dieser Besuch in gelber Baustellenmontur samt Schutzhelm mit Geleucht erfolgte. Das entsprach eben einer der so typischen Spontanaktionen von Dr. Müller! Zum anschließenden Mittagessen beim distinguierten Hohlwegwirt wurde uns beiden (nach wie vor im selben Hackler-Outfit) der Eintritt so lange verwehrt, bis der Chef des Hauses die eher unpassend gewandeten Gäste persönlich in Augenschein nahm und mit folgenden Worten begrüßte *„ach sie sind's, meine Herren Doktoren! Aber sooo bekleidet passen sie gar nicht zu meiner Gästeschar. Würden sie doch deshalb bitte im Extrastüberl Platz nehmen wollen"*. Und ob wir beide dies wollten! Speis und Trank mundeten auch im Séparée und wir ließen Rosi mit Babsi oftmals hochleben!

Sohn Peter und Tochter Babsi sind inzwischen selbst verheiratet und bescherten ihren Eltern bislang fünf Enkelkinder. Von Kärnten nach Salzburg übersiedelt, wohnte die Familie zuerst in einer höheren Etage der Hüttenbergstraße (Stadtteil Lehen) in Sichtweite zum ehemaligen Stadion des SV Austria Salzburg. Später zog die Familie Müller nach Henndorf um, wo sie ein schmuckes Reihenhaus am nördlichen Ortsrand samt Jagdhund bevölkerten und in dem von Rosi sehr gepflegten Garten so manche fröhlichen Grillfeste mit Freunden stiegen.

Von 1976 bis 1978 kartierte Peter Jürgen Müller als „Auswärtiger Mitarbeiter" der Geologischen Bundesanstalt in den westlichen Gailtaler Alpen auf den Kartenblättern 197 (Kötschach) und 198 (Weißbriach). Seine hauptberufliche Tätigkeit begann Peter beim Innsbrucker Ingenieurbüro ILF. Dort wurde er ab 1977 beim Pipelinebau in Nigeria für die geotechnischen Untersuchungen und Beurteilungen eingesetzt. Von 1979 bis 1983 war Müller beim Salzburger Ingenieurbüro GEOCONSULT beschäftigt, wo er mit anspruchsvollen Stollen- und Tunnelprojekten im In- und Ausland betraut wurde. Dies erweiterte seine Sprachkenntnisse wesentlich. Dr. Peter Jürgen Müller beherrschte neben seiner Muttersprache auch Englisch (very british), Italienisch, Französisch, Spanisch, etwas Slowenisch, einige Brocken Arabisch und – dies darf keinesfalls unerwähnt bleiben – auch ein sehr gepflegtes Oberkärntnerisch. In dieser *seiner* Mundart plauderte er gerne in geselliger Runde vor allem mit Freunden und beschrieb dann das Gelände seiner Arbeitsgebiete verniedlichend, z.B. die knapp 2.000 m hohen Bergketten westlich des nordostindischen Loktak Sees bei der Stadt Imphal (Manipur) *„des san lei ois Mugale"* [= das sind alles bloß Hügel].

Mehrere Bauvorhaben bedingten wochen- bis monatelange Aufenthalte in Afrika, Asien und Südamerika, z.B. Loktak Hydropower Projekt (Nordost-Indien, nahe der Grenze zu Myanmar, früher Burma), Barrage al Izdihar Projekt (Algerien), Avenida Boyaca Projekt (Caracas, Venezuela), Tailrace Tunnel – Mosul Dam (Gimod JV, Irak), Projekt Metro d´Alger (Algerien), Projekt „Pan Dao Ling" (VR China) und das Staudamm-Projekt Nangbeto (Togo, Westafrika). Für seine beim erwähnten Loktak Hydro Projekt in Indien entstandene, gemeinsam mit Dipl.-Ing. Johann Golser [später Professor an der Montanuniversität Leoben] und Dr. Josef-Michael Schramm 1980 publizierte Arbeit „The NATM, a special tunneling conception and its application in poor rock" zeichnete ihn die Indian Geotechnical Society anlässlich der 23. Jahrestagung in Hyderabad 1981 mit der „HEICO Gold Medal" aus.

Große Bauvorhaben innerhalb von Europa bedingten oftmalige zeitintensive Dienstreisen, wie etwa zum Autobahn-Baulos „Zeitlarn" (Regensburg, Bundesrepublik Deutschland), dem Hydroelectric Project Pigai/Aoos (Ioannina, Nordwest-Griechenland), zum Monte d´Oro Tunnelprojekt (Triest, Italien), dem Tunnelprojekt San Remo (Italien) und dem Tunnel No. 2 Calahonda (Andalusien, Spanien).

Während seiner Tätigkeit bei der GEOCONSULT war Dr. Müller an folgenden österreichischen Untertagebauten beschäftigt: Bosrucktunnel-Süd (A9, Pyhrn-Autobahn), Massenbergtunnel-Weströhre der S6 Semmering Schnellstraße (Leoben/Steiermark) und Wolfsbergtunnel (A10, Tauernautobahn, Kärnten). Wenn sich Dr. Müller über *„Sand im Getriebe"* ärgerte, was ja in einer Ziviltechniker-Kanzlei hin und wieder vorkommen dürfte, dann pflegte er seine beiden Chefs (Dipl.-Ing. Johann Golser und Dipl.-Ing. Erich Hackl) mit *„Yeti und Silberfuchs"* zu titulieren. Dies äußerte er aber nie in despektierlicher Form. Jedenfalls verstand es Dr. Müller – als ein über die Maße engagierter und couragierter Kollege – im Laufe seines Berufslebens Diskussionen und Auseinandersetzungen mit feiner scharfer Klinge zu führen. Seine vornehme Streitkultur perfektionierte er besonders im Umgang mit (bisweilen umständlichen) Behördenvertretern und Bauingenieuren. Er war aber auch fähig, mit schlagkräftigen Argumenten und schwerem Geschütz zu kontern, falls dies wirklich nötig war. Peter ging zeitlebens einen geraden Weg, man könnte ihn umgangssprachlich als „Sturkopf" bezeichnen, gerade das zeichnete ihn jedoch als verlässlichen Partner aus.

Im Rahmen der Bund-Bundesländer-Kooperation leitete er eine Reihe von Rohstoffprojekten im Bundesland Salzburg, z.B. eine geologisch-geotechnische Kartierung im Raum Lofer–Paß Stein (Projekt S-A-016b), Erfassung ausgewählter Schottervorkommen im Flachgau-Nord (Projekt S-A-016f) und später Hydrogeologie der Osterhorngruppe (Projekte S-A-006k und S-A-006u).

1983 erlangte Dr. Müller die Befugnis eines Ingenieurkonsulenten für Technische Geologie und machte sich sukzessive selbständig. Zusammen mit seinem Studienkollegen Dr. Heinrich Wallner gründete er im Herbst 1983 die INTERGEO. Diese Ziviltechniker-Gesellschaft wuchs rasch und entwickelte mit weltweiten Niederlassungen ein dichtes Netz an Experten auf den Fachgebieten Umwelt, Geotechnik, Umweltschutz und Arbeitssicherheit sowie Abfallwirtschaft. Ab Bestehen der INTERGEO begleitete Dr. Müller zahlreiche österreichische Straßenbau-, Bahnbau- sowie Wasserkraftprojekte mit geotechnischen Expertisen vor Ort, z.B. den Haberbergtunnel (A2, Kärnten), die Südröhre des Oswaldibergtunnels (A10, Kärnten), die Ost- und Weströhre des Donnersbergtunnels (A2, Kärnten), die Nordröhre des Kollmanntunnels (A2, Kärnten), die Weströhre des Karawankentunnels (A11, Kärnten), die Umfahrung Lofer (S12 Loferer Schnellstraße, Land Salzburg), den Umfahrungstunnel Unken (B178 Loferer Straße, Land Salzburg), die Teilkollaudierung „Fels A9" Baulos 4 (Ried im Traunkreis, Oberösterreich), den Triebwasserweg des ÖBB-Kraftwerks Uttendorf II (Land Salzburg) usw.

Müller wirkte auch an ausländischen Projekten mit, wie beispielsweise dem Tunnel Santa Caterina (SS13, Malborghetto, Italien), dem Frässtollen San Remo (Italien), der Tunnelkette Monrepos (Nordspanien), dem Thissavros Damm (Griechenland), dem Tunnel Gorges de Kherrata (Algerien, mit etwa 7 km längster Straßentunnel Afrikas), und dem Bewässerungsprojekt Yindaruquin (Gansu-Provinz, VR China, mit insgesamt 17 km Stollensystem).

Das edle Weidwerk war eines seiner Hobbys, welches Dr. Müller auch nach Beendigung seines Studiums gerne ausübte. Ein anderes Steckenpferd Peters waren PS-starke und schnelle Autos, etwa Audi-Modelle höherer Klassen. Der Verfasser dieser Zeilen erinnert sich an eine Mitfahrt (zusammen mit Dipl. Geol. Klaus Reder) von Salzburg nach Saarbrücken gegen Ende der 1980er Jahre. Diese Reise erfolgte zwecks Besichtigung eines Labors für Cerchar-Versuche (Bestimmung der Abrasivität von Gesteinen), was Klaus Reder u.a. für seine Doktorarbeit benötigte, und Befahrung einer knapp über tausend Meter tiefen Steinkohlengrube der Saarbergwerke AG. Die knapp 600 Kilometer lange Hinfahrt wollte Peter in weniger als fünf Stunden bewältigen, was ihm – auf deutschen Autobahnen ohne Geschwindigkeitsbeschränkung – auch beinahe glückte. Allerdings mussten nach einer Vollbremsung bei 200 km/h nahe Saarbrücken (durch einen LKW verschuldet, der die Fahrspur ohne Blinker urplötzlich wechselte!) alle vier Reifen ausgetauscht werden. Der Autobahnbelag hatte nämlich diese bis knapp an die Felgen abradiert. Peter rezitierte spontan ein Lied der steirischen Band „Erste Allgemeine Verunsicherung“ (EAV): *„Die Reifen müssen qualmen wie heißer Leberkäs' …“*. Auf die sehr erleichterte Reaktion seines etwas bleich gewordenen Beifahrers reagierte Peter mit der scherzhaften Bemerkung *„jetzt hat der Pepi derart intensiv beim Mitbremsen geholfen, dass er mit seinem Fuß beinahe das Blech zum Motorraum eingedrückt hat“*.

Nachdem seine Gemahlin Rosi ab 1991 aufgrund eines tragischen und nachhaltig wirkenden Unglücks fortan ein schweres Handicap zu tragen hatte, zog die Familie wieder nach Kärnten. Das Elternhaus Dr. Müllers in Paternion bot sowohl für die Familie, als auch für eine INTERGEO-Niederlassung ausreichend Platz. Dieser Standort lag für die zahlreichen Tunnelbau-Aktivitäten entlang der Südautobahn, Karawankenautobahn und Tauernautobahn sowie der Bahntunnel im Kanaltal (z.B. Camporosso), für welche Dr. Müller verantwortlich zeichnete, wesentlich näher als die Zentrale in Salzburg. Zur fünfzigsten Wiederkehr seines Geburtstages im August 1992 lud Peter zu einem standesgemäßen Fest in das Krastal nordöstlich von Gummern, wo mit seiner Familie, vielen Freunden und Kollegen in einem alten Marmorsteinbruch ober- und untertägig trotz schlechten Wetters ausgiebig und fröhlich gefeiert wurde.

Als der stets apart gekleidete Dr. Peter Müller den Verfasser dieser Zeilen wieder einmal in den Diensträumen der Universität Salzburg aufsuchte, stach eine ungewöhnlich schrille (um nicht zu sagen hässliche) Krawatte ins Auge. Auf die Frage nach diesem Kleidungs-Fauxpas antwortete Müller so: *„Ja weißt du, ich fahre anschließend zur Feier eines Tunneldurchschlags nach Kärnten. Da gibt es einen Lokalpolitiker, so eine Art ‚Hans Dampf in allen Gassen', der bei solchen Festivitäten im beschwipsten Zustand immer wieder versucht, möglichst vielen Anwesenden ihre Krawatten abzuschneiden. Deshalb habe ich mir jetzt ein paar ‚recht schiache' Krawatten zugelegt, um die es mir nicht leidtun muss, wenn sie abgesäbelt werden. Dann hat dieser Kerl wenigstens seine kleine Freude …“*.

Dr. Müller war Mitglied bei folgenden Fachvereinigungen und Fachgesellschaften: Gesellschaft der Geologie- und Bergbaustudenten in Österreich, Naturwissenschaftlicher Verein für Kärnten, Österreichische Geologische Gesellschaft (ÖGG), Arbeitsgruppe Ingenieurgeologie in der ÖGG, Arbeitsgruppe Wehrgeologie in der ÖGG, Österreichische Gesellschaft für Geomechanik, Deutsche Gesellschaft für Erd- und Grundbau, International Society for Rock Mechanics und International Association of Engineering Geology. Peter versuchte ständig auf dem aktuellsten Stand der Fachliteratur zur Angewandten Geologie und Geotechnik zu bleiben. Seine Besuche an der Universität Salzburg oder auch privat führten ihn stets als Erstes zu den Regalen mit Fachbüchern und Fachzeitschriften. Nach der für ihn so typischen Einleitung *„jajajaja …“*, folgte die Feststellung *„was hat denn der Pepi da schon wieder Neues. Das muss ich mir auch gleich bestellen“*. Peter war zeitlebens ein biblio- und kartophiler Mensch, dem es mit Hartnäckigkeit meist gelang, auch längst vergriffene Werke als Desiderata in zahlreichen Antiquariaten Europas aufzustöbern.

Ab den 1990er Jahren bediente Dr. Müller ein Großprojekt in Libyen und musste dazu ansehnliche Investitionen vornehmen, welche er zum größten Teil vorfinanzierte. Dazu zählte neben der Einstellung von qualifiziertem Fachpersonal die Beschaffung spezieller Ausrüstung und vor allem die Installation umfangreicher Infrastruktur vor Ort. Derartige Akquisitionen zählen und zählten zu den oft unwägbaren Risiken freiberuflich tätiger Ingenieurkonsulenten, was Dr. Müller aufgrund seiner jahrelangen Auslandserfahrungen durchaus bewusst war! Das aufgrund ergiebiger Erdöl- und Erdgas-Vorkommen reiche Libyen war bestrebt, seine Gewinne in ambitionierte Bewässerungs- und Tourismusprojekte zu investieren, um das Land zu modernisieren. Jedoch unterstellten mehrere westliche Staaten (unter Führung der USA) Libyen Staatsterrorismus und dämonisierten diese Nation zum „Schurkenstaat“. Mangels juristischer Beweise wurden internationale Embargos zwar nach und nach gelockert und zuletzt aufgehoben. Dennoch betrieb eine Achse etlicher westlicher Geheimdienste auch weiterhin die nachhaltige Destabilisierung dieses nordafrikanischen Landes. Dies alles geschah unter dem Vorwand, den „Arabischen Frühling“ zwecks Demokratisierung zu fördern – mit den für ganz Europa fatalen Auswirkungen. Infolge des politischen Umbruchs und einer Eskalation zum blutigen bis heute tobenden Bürgerkrieg in Libyen wurden die im Auftrag des vormaligen Regimes von Muammar al-Gaddafi (2011 ermordet) erbrachten ingenieurgeologisch-geotechnischen Leistungen leider nicht mehr beglichen. Das Projekt „Neue Eisenbahnstrecke von Sirth nach Benghazi“ enthielt eine 550 km lange zweigleisige Hochgeschwindigkeitsstrecke (250 km/h) mit 850 Durchlässen, 25 Fußgängertunnel, 45 Brücken und 35 Bahnstationen. Die Auftragsarbeiten umfassten die geologisch-geotechnische Planung, baugeologische Kartierung der Eisenbahntrasse sowie Planung und Überwachung der Untergrunderkundung (mit Bohrungen, Baggerschürfen, Laborversuchen, Rammsondierungen, Lastplattenversuchen usw.). Die Projektarbeiten kamen mangels Bezahlung durch die libyschen Auftraggeber zum Erliegen, herbe finanzielle Verluste waren die Folge und trieben Peters Part der INTERGEO völlig unverschuldet in den wirtschaftlichen Ruin. Dieser Schlag belastete den bislang stets korrekt und umsichtig wirtschaftenden Dr. Müller so schwer, dass er sich mit 69 Lebensjahren erstmals mit dem Gedanken eines baldigen Übertritts in den Ruhestand auseinandersetzte. Aber, wie sich leider zeigte, kommt ein Unglück selten allein.

Bei einem verhängnisvollen Sturz erlitt Peter Jürgen Müller 2016 massive Rückenverletzungen, deren Auswirkungen sich nach einem operativen Eingriff sogar verschlechterten. Deshalb musste er aufgrund eingeschränkter Bewegungsfähigkeit sowohl seinem geliebten Beruf, als auch der Jägerei entsagen. Nach einem längeren Rehabilitationsaufenthalt in Bad Häring (südsüdwestlich von Kufstein) wurde er in häusliche Pflege entlassen und ließ einen Teil seines Elternhauses barrierefrei adaptieren. Aufgrund einer kurzfristigen Verschlechterung seines Gesundheitszustandes folgte eine stationäre Aufnahme in das Landeskrankenhaus Villach. Hier entschlief Dr. Peter Jürgen Müller völlig unerwartet am 11. Dezember 2019 im 78. Lebensjahr.

Zur Verabschiedung Dr. Peter Müllers am 21. Dezember 2019, einem wolkenverhangenen regnerischen Tag, fanden sich in der katholischen Pfarrkirche zu Paternion neben seiner großen Familie zahlreiche Freunde, Kollegen, Mitarbeiter und Kameraden ein und füllten das barocke Gebäude bis auf den letzten Platz. Corpsbrüder des „Akademischen Corps Saxonia“ in Trauercouleur gaben ihrem Alten Herrn ein letztes Geleit. Ein Chor der Jägerschaft Paternion umrahmte die Feier stimmig und mehrere Redner, u.a. Peters ehemaliger Mitarbeiter Dr. Dirk Jesinger und GBA-Direktor i.R. Hofrat Univ.-Prof. Dr. Hans Peter Schönlaub, würdigten den Verstorbenen in bewegten Worten. Die Beisetzung der Urne am Friedhof Paternion erfolgte im engsten Familienkreis im Jänner 2020.

Die Geologenschaft zollt der umfangreichen, stets objektiven Expertise von Dr. Peter Jürgen Müller den gebührenden Respekt und vermisst einen großzügigen Freund mit beneidenswerter Schlagfertigkeit sowie verschmitztem Humor. Auf seinem Partezettel steht vollkommen zutreffend „Ich höre auf zu leben, aber ich habe gelebt“. In diesem Sinne bewahren wir Peter in bester Erinnerung.

Josef-Michael Schramm

Werkeverzeichnis von Dr. Peter Jürgen Müller (Auswahl)

(Auswertung des Onlinekatalogs der Geologischen Bundesanstalt, zusammengestellt von Josef-Michael Schramm)

1968

Müller, P.J. & Pongrácz, L. (1968): Geologische Kartierungsübungen im Bergbau. Cu-Lagerstätte Mitterberg. Kartierungsbericht. – 4 S., 3 Beilagen (Rupertistollen: m0-m60 SW, Kartierung mit aufgeklappten Ulmen 1:100), Wien.

1977

Müller, P.J. (1977): Bericht 1976 über Aufnahmen in den westlichen Gailtaler Alpen zwischen Jauken und Reißkofel auf den Blättern 197, Kötschach und 198, Weißbriach. – Verhandlungen der Geologischen Bundesanstalt, **1977**, A 154, Wien.

Müller, P.J. (1977): Zur Geologie des Raumes zwischen Reißkofel und Jauken, unter besonderer Berücksichtigung der Mikrofazies mitteltriadischer Becken- und Plattformsedimente (Westliche Gailtaler Alpen, Kärnten). – Dissertation, Universität Innsbruck, 133 S., 2 Beilagen, 1 Karte, Innsbruck.

Müller, P.J. (1977): Zur Geologie des Raumes zwischen Reißkofel und Jauken, unter besonderer Berücksichtigung der Mikrofazies mitteltriadischer Becken- und Plattformsedimente (Westliche Gailtaler Alpen, Kärnten). – Kurzfassungen von in Innsbruck fertiggestellten Dissertationen (1965–1977): Teil 1. – Geologisch-Paläontologische Mitteilungen Innsbruck, **6**/10, 62–63, Innsbruck.

Müller, P.J. (1977): Geologische Karte zwischen Jauken und Reißkofel 1:10.000 (aufgenommen in den Jahren 1973–77). – 1 Bl. (900 x 600 mm), handkoloriert, Salzburg.

1979

Müller, P.J. (1979): Bericht 1977 über Aufnahmen in den westlichen Gailtaler Alpen auf den Blättern 197, Kötschach und 198, Weißbriach. – Verhandlungen der Geologischen Bundesanstalt, **1978**, A 147–A 148, Wien.

1980

Golser, J., Müller, P.J. & Schramm, J.-M. (1980): The NATM, a special tunneling conception and its application in poor rock. – Proceedings GEOTECH-80, Conference on Geotechnical Engineering, volume **1**, 333–345, Bombay.

1981

Müller, P.J. (1981): Bericht 1978 über geologische Aufnahmen in den westlichen Gailtaler Alpen auf den Blättern 197, Kötschach und 198, Weißbriach. – Verhandlungen der Geologischen Bundesanstalt, **1979**, A 153–A 154, Wien.

Müller, P.J. (1981): Untersuchung der Lockergesteine ausgewählter Salzburger Gebiete: Geologische-Geotechnische Kartierung im Raum Lofer–Paß Stein: Schlussbericht 1980. – Bund-Bundesländer-Rohstoffprojekt S-A-016b/80, 5 S., Salzburg.

Müller, P.J. (1981): [Geologische Manuskriptkarte] Weißbriach 1:25.000. – 1 Bl. (470 x 590 mm), handkoloriert mit Legende, Wien.

Müller, P.J. (1981): [Geologische Manuskriptkarte] Kötschach-Mauthen 1:25.000. – 1 Bl. (470 x 590 mm), handkoloriert mit Legende, Wien.

1982

Müller, P.J. (1982): Erfassung ausgewählter Schottervorkommen im Flachgau-Nord zwischen den Linien Nockstein, Hof bei Salzburg, Schober und Obertrum, Neumarkt am Wallersee: Schlußbericht zur I. Projektstufe (Prospektion) für den Zeitraum 20-2-1981 – 31-12-1981. – Bund-Bundesländer-Rohstoffprojekt S-A-016f/81, 18 S., 1 Karte (Ausgewählte Schotter-Vorkommen im nördlichen Flachgau/Salzburg 1:25.000), Salzburg.

MÜLLER, P.J. (1982): Erfassung ausgewählter Schottervorkommen im Flachgau-Nord zwischen den Linien Nockstein/Hof bei Salzburg/Schober und Obertrum/Neumarkt am Wallersee: Ergebnisbericht zur II. Projektstufe (Exploration) für den Zeitraum 1.02.1982 – 31.10.1983. – Bund-Bundesländer-Rohstoffprojekt S-A-016f/82, 38 S., 32 Anlagen, Salzburg.

MÜLLER, P.J., BECHTOLD, D. & KLEBERGER, J. (1982): Erfassung ausgewählter Schottervorkommen im nördlichen Flachgau (Salzburg). – Archiv für Lagerstättenforschung der Geologischen Bundesanstalt, **2**, 137–142, Wien. [Bund-Bundesländer-Rohstoffprojekt S-A-016/f/81]

MÜLLER, P.J., BECHTOLD, D. & KLEBERGER, J. (1982): Untersuchungen der Lockergesteine ausgewählter Salzburger Gebiete: Geologische-geotechnische Kartierung im Raum Lofer–Paß Stein: Endbericht 1982. – Bund-Bundesländer-Rohstoffprojekt S-A-016b/81, 14 + 10 S., 4 Beilagen, Salzburg.

1983

BECHTOLD, D., KLEBERGER, J. & MÜLLER, P.J. (1983): Untersuchungen der Lockergesteine ausgewählter Salzburger Gebiete: Geologisch-geotechnische Kartierung im Raum Lofer–Paß Stein. – Archiv für Lagerstättenforschung der Geologischen Bundesanstalt, **3**, 7–12, Wien. [Bund-Bundesländer-Rohstoffprojekt S-A-016b/82]

1984

MÜLLER, P.J., WALLNER, H. & MEYER, J.W. (1984): Erfassung ausgewählter Schottervorkommen im Flachgau-Nord zwischen den Linien Nockstein/Hof bei Salzburg/Schober und Obertrum/Neumarkt am Wallersee: Schlußbericht zur 3. Projektstufe (Exploration) für den Zeitraum 1984. – Bund-Bundesländer-Rohstoffprojekt S-A-016f/84, 26 S., 1 Anlage, 10 Karten, Salzburg.

1991

MÜLLER, P.J. (1991): Baugeologische Verhältnisse im Karawankentunnel-Nord. Inzenirsko geoloske razmere v severnem odseku predora Karavanke. – In: KRAJNC, M. (Vorw.), MIKOS, B. (Red.) & ZITTA, W. (Übers.): Karawankentunnel: Geologie und Geotechnik, Predor Karavanke: geologija in geotehnika, 30–35, Ljubljana.

MÜLLER, P.J., WALLNER, H., GAMERITH, W., FANK, J. & HARUM, T. (1991): Hydrogeologie Osterhorngruppe: Detailuntersuchung Postalm (Teil III). – Bund-Bundesländer-Rohstoffprojekt S-A-006k/89F, 35 + 13 S., 4 Anlagen, Salzburg.

1995

LEIN, R., SCHLAF, J., MÜLLER, P.J., KRYSTYN, L. & JESINGER, D. (1995): Neue Daten zur Geologie des Karawanken-Straßentunnels. – Geologisch-Paläontologische Mitteilungen Innsbruck, **20** (Festschrift Helfried Mostler), 371–387, Innsbruck.

1997

MÜLLER, P.J. (1997): Hydrogeologie der Osterhorngruppe: Erkundung des hydrogeologischen Naturraumpotentials Gebiet Kellau – Grubach – Weitenau: Teil 1. – Bund-Bundesländer-Rohstoffprojekt S-A-006u/96, 35 S., 5 Anlagen, Salzburg.

1999

MÜLLER, P.J. (1999): Hydrogeologie der Osterhorngruppe: Erkundung des hydrogeologischen Naturraumpotentials Gebiet Kellau – Grubach – Weitenau: Teil 2. – Bund-Bundesländer-Rohstoffprojekt S-A-006u/96, 28 S., 5 Anlagen (geologische Karte Weitenau 1:10.000), Salzburg.

JAHRBUCH DER GEOLOGISCHEN BUNDESANSTALT
Jb. Geol. B.-A. | ISSN 0016–7800 | Band 159 | Heft 1–4 | S. 357–417 | Wien, Dezember 2019

Berichte über Tätigkeiten zur Erstellung der Geologischen Karte der Republik Österreich 1:50.000 in den Jahren 2016–2019

Im Zuge der Umstellung auf das neue topografische Kartenwerk im UTM-System werden die Kartierungsberichte in einen Abschnitt unterteilt, der sich auf das „alte“ BMN-System bezieht und einen, der sich auf das „neue“ UTM-System bezieht. Details zur Umstellung sind in Krenmayr (Jahrbuch der Geologischen Bundesanstalt, 150/3–4, 2010) erläutert. Die UTM-Kartenblätter werden ab 2016 im internationalen Blattnamenformat aufgelistet.

Kartenwerk im BMN-System

Blatt 21 Horn

Bericht 2017 über geochemische und petrografische Untersuchungen an Orthogneisen und schwach deformierten Graniten des Moravikums auf Blatt 21 Horn

Friedrich Finger (Auswärtiger Mitarbeiter),
Manfred Linner & Gudrun Riegler
(Auswärtige Mitarbeiterin)

Im Berichtsjahr wurde ein vollständiges West–Ost-Profil im südlichen Teil des Moravikums bearbeitet, das vom Bittesch-Gneis bis zur Diendorf-Störung reicht. Die Beprobung erfolgte südöstlich von Fernitz entlang des Tiefenbachtals über die Seewiese bis zum Gebiet zwischen Manhartsberg-Gipfel und Sulzberg (einem südlichen Vorgipfel) und in der östlichen Fortsetzung bis zur Pernersdorferöde. Anhand dieses Profils kann eine vergleichende Charakterisierung der Orthogesteine der tektonisch hangenden Pleißing- und der liegenden Pulkau-Decke (Linner et al., 2019) vorgenommen werden.

Ganz im Westen des Profils, im Hangenden der Pleißing-Decke, wurden im Tiefenbachtal westlich der Pfarrleiten zwei Proben von Bittesch-Gneis genommen (Fi 12/17, Fi 13/17). Es handelt sich um helle, mylonitische bis ultramylonitische Bittesch-Gneise mit relativ wenigen Porphyroklasten reliktischer magmatischer Feldspate. Die Porphyroklasten bestehen zu etwa gleichen Anteilen aus Kalifeldspat und Plagioklas (Fi 13/17) beziehungsweise in der ultramylonitischen Bittesch-Gneis Probe (Fi 12/17) aus überwiegend Kalifeldspat. Bei den sehr stark dynamisch rekristallisierten magmatischen und den feinschuppigen metamorphen Glimmern dominiert Muskovit, und Biotit ist etwas chloritisiert. Mit einem SiO_2-Gehalt von rund 73 Gew.%, einem K_2O/Na_2O-Verhältnis um 1 und Gesamteisengehalten von rund 1,2 Gew.% Fe_2O_3 weisen beide Proben leukogranitische bis -granodioritische Zusammensetzung auf. Die Spurenelementgehalte zeigen hohe Sr/Zr-Verhältnisse (> 4) bei niedrigen Zr-Gehalten (< 100 ppm) und liegen damit in der charakteristischen Bandbreite des Bittesch-Gneises.

Der Buttendorf-Gneis ist im Tiefenbachtal von der Pfarrleiten nach Osten in großer Mächtigkeit aufgeschlossen und wurde daher von hangend gegen liegend mit drei Proben (Fi 14/17 bis Fi 16/17) erfasst. Zusätzlich wurde eine Probe (Fi 11/17) aus einem geringmächtigen Gneiszug direkt aus Buttendorf analysiert, der durch Glimmerschiefer vom mächtigen Buttendorfer Gneiszug im Teichwiesenbachtal abgetrennt ist. Der Buttendorf-Gneis ist ein dunkler Granodioritgneis mit hohen Anteilen an Biotit und einer verbreiteten Augentextur, infolge der mylonitischen bis ultramylonitischen Deformation. Im Dünnschliff zeigen sich als magmatische Relikte Plagioklas, Kalifeldspat, Biotit sowie teilweise Hornblende, Allanit und selten Titanit. Sie treten zugleich als Porphyroklasten bzw. als Aggregate in augenförmigen Domänen auf. Bei den Feldspaten dominiert mengenmäßig Plagioklas, in dem die magmatische Zonierung erhalten sein kann. Der magmatische Biotit ist größtenteils dynamisch rekristallisiert und die olivgrüne Hornblende ist von metamorph gebildetem, blassgrünem Amphibol überwachsen. In der feinkörnig rekristallisierten Matrix aus Biotit, Plagioklas, Kalifeldspat und Quarz ist typischerweise metamorph gebildeter Epidot zu finden und in den ultramylonitischen Proben (Fi 11/17, Fi 15/17) zusätzlich etwas Muskovit.

Der Buttendorf-Gneis des Tiefenbachtals und jener direkt aus Buttendorf weisen geochemisch keine nennenswerten lokalen Besonderheiten auf. Sie sind gut vergleichbar mit der Typlokalität dieser Granodioritgneise im Teichwiesenbachtal (Finger & Riegler, 2012), mit intermediärem SiO_2-Gehalt (62–66 Gew.%), relativ hohem MgO-Gehalt (3–4 Gew.%) und Cr-Gehalt (75–136 ppm), bei gleichzeitig hohen K_2O- (3–5 Gew.%) und Ba-Gehalten (598–1.765 ppm). Diese Kombination geochemischer Parameter verleiht dem cadomischen Buttendorf-Gneis eine bemerkenswerte geochemische Ähnlichkeit mit den variszischen Durbachiten im Moldanubikum (Janoušek & Holub, 2007).

Westlich der Seewiese ist ein bis zu 35 m breiter und 70 m langer heller Orthogneiskörper an der Hangendgrenze des Kriegenreith-Gneises aufgeschlossen. Im hangenden Teil dieses Kriegenreith-Gneises sind weitere geringmächtige Lagen aus hellem Orthogneis eingeschaltet (Schantl, 2018). Der Orthogneis zeigt im Dünnschliff reichlich Plagioklas-Porphyroklasten in einer quarzreichen mylonitischen Matrix. Die Risse der zerbrochenen magmatischen Plagioklase sind quarzgefüllt. In der Matrix ist etwas feinstschuppiger Muskovit beigemengt. Auffällig sind zahlreiche große und idiomorphe akzessorische Zirkone. Eine Probe aus dem größeren Orthogneiskörper (Fi 17/17) weist einen sehr hohen SiO_2-Gehalt von rund 79 Gew.% auf, sowie ein bemerkenswert hohes Na_2O/K_2O-Verhältnis (4,9 Gew.% Na_2O vs. 1,2 Gew.% K_2O). Die Zusammensetzung der Hauptelemente tendiert somit in Richtung Aplit. Im Unterschied zu den meisten anderen Apliten des Moravikums sind in dieser Probe aber auch hohe Zr- (329 ppm), REE- (z.B. 130 ppm Ce) und Y-Gehalte (58 ppm) zu beobachten. Der hohe Zr-Gehalt bei niedrigem Sr-Gehalt verleiht diesem Aplit geochemisch eine A-Typ-Charakteristik. Insgesamt sind die Orthogneislagen im Hangendbereich des Kriegenreith-Gneises westlich der Seewiese als mylonitisch deformierte Aplitgneise zu bezeichnen (Tab. 1).

Ebenfalls in der Umgebung der Seewiese wurden zwei Proben des Kriegenreith-Gneises beprobt (Fi 18/17 und Fi 20/17). Reichlich Biotit und bis zu 3 mm große, rundliche Plagioklas-Porphyroblasten kennzeichnen diesen dunklen, relativ mafischen Granodioritgneis. Wegen seines hohen Plagioklasgehaltes ist das Gestein massiger als der Buttendorf-Gneis und bricht vergleichsweise mehr blockig. Im Dünnschliff erweist sich die Deformation als proto- bis ultramylonitisch. Die Plagioklas-Porphyroklasten, teils mit magmatischer Zonierung und mit quarzgefüllten Rissen, sind von einer feinstkörnigen, quarzdominierten Matrix mit reichlich dynamisch rekristallisiertem Biotit umgeben. Magmatische Biotite sind aber erhalten und sehr untergeordnet finden sich auch Porphyroklasten aus magmatischem Kalifeldspat. Die recht deutliche metamorphe Überprägung äußert sich unter anderem durch feinkörnigen Epidot/Klinozoisit und feinschuppigen Muskovit in schieferungsparallelen Domänen. Die Probe Fi 18/17 zeigt mit einem relativ hohen A/CNK-Wert von 1,28 eine untypische, an CaO verarmte und wahrscheinlich alterierte Hauptelementgeochemie. Mit der Probe Fi 20/17 wurde eine außergewöhnlich mafische und wenig alterierte Variante des Kriegenreith-Gneises erfasst (SiO_2 rund 61 Gew.%, $Fe_2O_{3(tot)}$ 5,7 Gew.%; Tab. 1).

Nördlich der Seewiese treten im Liegenden vom Kriegenreith-Gneis nur kleine Aufschlüsse des Sachsendorf-Gneises zu Tage. Die Proben Fi 19A/17 und Fi 19B/17, beides helle Granodioritgneise, entstammen einer kleinen ehemaligen Steingrube und repräsentieren den Sachsendorfer Gneiszug im untersuchten Profil. Die letztgenannte Probe ist von feinen Aplit- und Quarzgängchen durchsetzt und zeigt im Dünnschliff nur protomylonitische Deformation. Bei den Feldspaten dominiert Plagioklas, magmatischer Biotit ist gut erhalten und selbst Muskovit hat als Einschluss im Plagioklas überdauert. Die Probe Fi 19A/17 zeigt hingegen mylonitisches Gefüge, wobei die feinen Quarzgängchen zu augenförmigen Domänen deformiert und die Schieferungsflächen mit feinschuppigem Biotit und Muskovit belegt sind. Die Quarzgängchen erklären den in beiden Proben für Sachsendorf-Gneis eher hohen SiO_2-Gehalt. In der weniger deformierten Probe Fi 19B/17 kann ein unüblich hoher K_2O- und Rb-Gehalt durch Alteration mit muskovitreichen Adern erklärt werden. Die Probe Fi 19A/17 reiht sich hingegen bei den meisten Elementen gut in die Charakteristik dieses relativ sauren Granodioritgneises ein (Finger & Riegler, 2017), mit Na-Vormacht über K und einem ausgesprochen niedrigen Rb/Sr-Verhältnis (0.25).

Die Proben aus dem Gebiet südlich vom Manhartsberg-Gipfel wurden von Manfred Linner im Rahmen seiner Kartierung 2017 genommen. Der Sachsendorf-Gneis ist auch östlich der Manhartsbergstraße fast nur in Lesesteinen zu finden. Zwischen Silberne Eiche und dem Westfuß vom Manhartsberg-Gipfel zeigt der liegende Teil des Sachsendorf-Gneiszuges mylonitische bis ultramylonitische Deformation, wodurch die Deckengrenze zwischen der Pleißing- und Pulkau-Decke an der Basis vom Sachsendorf-Gneis angezeigt ist. Diese verläuft in N–S-Richtung streichend vom westlichen Hangfuß des Manhartsberg-Gipfels in den Hang westlich vom Sulzberg-Gipfel und dem Dienbachgraben folgend Richtung Jungenberg.

Im Hang westlich vom Sulzberg-Gipfel ist diese Deckengrenze mit Hilfe von Lesesteinen sehr gut zu lokalisieren. Es treten dort Glimmerschiefer auf, begleitet von ultramylonitisch deformierten Orthogneisen. Von beiden Lithologien gelangten Proben zur Analyse, um zu prüfen ob für die Glimmerschiefer sedimentäres Ausgangsmaterial gegeben war oder eine metasomatische Bildung in der Scherzone in Betracht zu ziehen ist beziehungsweise um den ultramylonitischen Orthogneis einzuordnen. Im Dünnschliff zeigen sich die Glimmerschiefer (Proben ML17-21-16A, -16C) ebenfalls mylonitisch deformiert. Biotit und Muskovit sind teils noch schön schuppig erhalten. Die Proben sind quarzbetont und weisen auch metamorph gebildetes Quarzmobilisat auf. Dazu kommen feinkörniger Plagioklas und etwas Turmalin. Die Glimmerschiefer-Probe ML17-21-16B ist weniger stark deformiert, enthält reichlich schuppigen Muskovit und viel körnigen Turmalin. Im Dünnschliff erweist sich dieser Turmalin zoniert mit braun-olivgrünen Kern und olivgrün-blauen Rändern sowie durch die Deformation kataklastisch zerbrochen. Diese Probe ist zusätzlich durch ein 10 cm Boudin aus einem Turmalin-Quarz-Gang charakterisiert.

Geochemisch zeichnen sich die Glimmerschiefer durch einen starken peralumischen Charakter aus (A/CNK 1,5–1,6 bei 62,5–68 Gew. % SiO_2-Gehalt). Erhöhte Cr- und Ni-Gehalte sprechen für ein feinklastisches Sediment als Ausgangsmaterial. Der bei den Hauptelementen stark abweichende turmalinreiche Glimmerschiefer (Probe ML17-21-16B) könnte als Nebengestein des Turmalin-Quarz-Ganges bereits im Zuge der Gangbildung stark metasomatisch verändert worden sein. Einerseits ist seine Modalzusammensetzung bezüglich Muskovit und Turmalin stark abweichend. Andererseits kann die mylonitische Deformation für die Stoffverschiebungen nicht verantwortlich sein, weil gerade dieser Glimmerschiefer deutlich schwächer deformiert ist. Petrografisch und geochemisch betrachtet sind die Glimmerschiefer an der Deckengrenze aus siliziklastischen Sedimenten abzuleiten. Der boudinierte Turmalin-Quarz-Gang verweist bezüglich der tektonischen Zu-

	a	b	c	d	e	f	g	h	i	j	k
Probe	**Fi 11/17**	**Fi 12/17**	**Fi 13/17**	**Fi 14/17**	**Fi 15/17**	**Fi 16/17**	**Fi/ 17/17**	**Fi 18/17**	**Fi 19A/17**	**Fi 19B/17**	**Fi 20/17**
SiO_2	64,46	72,83	72,61	62,17	64,32	65,65	78,95	67,12	73,09	74,26	61,30
TiO_2	0,56	0,11	0,14	0,62	0,55	0,53	0,16	0,49	0,21	0,10	0,72
Al_2O_3	15,36	14,79	14,72	15,10	15,62	14,89	11,76	16,45	15,07	13,77	17,24
Fe_2O_3	4,57	1,18	1,26	5,21	4,23	4,38	1,18	3,71	1,55	0,93	5,68
MnO	0,08	0,03	0,02	0,09	0,07	0,08	0,01	0,10	0,04	0,03	0,10
MgO	3,23	0,47	0,72	3,92	3,52	3,62	0,17	1,36	0,69	0,25	2,39
CaO	1,98	1,05	0,51	3,86	1,71	2,14	0,19	0,87	0,76	0,2	3,71
Na_2O	3,07	3,75	4,52	3,54	3,93	4,33	4,92	3,98	4,99	4,34	3,84
K_2O	4,88	4,34	4,01	3,71	4,25	2,73	1,18	4,41	2,09	4,74	2,78
P_2O_5	0,32	0,07	0,06	0,30	0,32	0,28	0,07	0,17	0,13	0,06	0,20
GV	1,73	1,24	1,26	1,56	1,91	1,05	1,22	1,80	1,55	1,21	2,53
Total	**100,24**	**99,86**	**99,83**	**100,08**	**100,43**	**99,68**	**99,81**	**100,45**	**100,17**	**99,89**	**100,49**
Rb	175	146	91	144	162	119	44	151	63	190	109
Sr	545	295	346	651	545	462	54	228	251	163	409
Ba	1.765	873	1.294	994	1.076	598	235	738	611	555	522
Th	25	4	10	25	21	43	10	8	22	37	9
La	45	19	26	77	78	51	53	34	30	18	35
Ce	109	44	50	138	124	136	130	79	68	43	58
Nd	32	22	26	57	53	42	68	29	30	14	24
Ga	16	17	15	18	18	18	11	18	14	14	19
Nb	17	7	6	19	22	16	17	11	11	10	10
Zr	158	72	86	188	195	182	329	167	131	86	166
Y	15	10	7	23	17	15	58	15	16	15	19
Sc	14	4	4	13	13	13	3	7	0	5	14
Pb	29	12	13	17	10	17	8	17	17	27	8
Zn	60	29	26	70	47	63	17	101	26	28	72
V	116	6	6	124	90	110	3	36	10	6	65
Co	11	2	3	16	11	11	2	4	4	2	11
Cr	126	10	11	136	75	104	6	18	12	6	30
Ni	27	8	7	28	23	26	8	8	8	9	10

Tab. 1., Teil 1.
Röntgenfluoreszenzanalysen (Hauptelemente in Gew.%, Spurenelemente in ppm, GV = Glühverlust, u.d.N. = unter der Nachweisgrenze). Koordinaten der Probenpunkte im Koordinatensystem BMN M34 (R: Rechtswert, H: Hochwert).

a: Buttendorf-Gneis, dunkelgrau, feinkörnig, ultramylonitisch; Felsaufschluss am westlichen Ortsrand von Buttendorf (Probe Fi 11/17; R: 706420, H: 383636).
b: Bittesch-Gneis, hellgrau, feinkörnig, ultramylonitisch, wenige Porphyroklasten; Tiefenbachtal SSE Fernitz, Felsaufschluss westlich Pfarrleiten (Probe Fi 12/17; R: 704027, H: 378525).
c: Bittesch-Gneis, hellgrau, mylonitisch, Feldspat-Porphyroklasten, großer Muskovit; Tiefenbachtal südöstlich Fernitz, Wegaufschluss am Hang oberhalb Tiefenbach, westlich Pfarrleiten, aus Blockschutt (Probe Fi 13/17; R: 704262, H: 378425).
d: Buttendorf-Gneis, dunkelgrau, fein- bis mittelkörnig, feldspatreich, mylonitisch; Tiefenbachtal südöstlich Fernitz, südwestlich Pfarrleiten, Felsaufschluss (Probe Fi 14/17; R: 704370, H: 378109).
e: Buttendorf-Gneis, dunkelgrau, sehr feinkörnig, ultramylonitisch, sehr biotitreich, kleine Feldspat-Porphyroklasten; Tiefenbach südöstlich Fernitz, südlich Pfarrleiten, südlich Kote 394, Felsaufschluss (Probe Fi 15/17; R: 704592, H: 377936).
f: Buttendorf-Gneis, dunkelgrau, feinkörnig, mylonitisch, biotitreich; Tiefenbach südöstlich Fernitz, südöstlich Pfarrleiten, Steingrube am Hang (Probe Fi 16/17; R: 704975, H: 377972).
g: Orthogneis, hell, gelbgrau, mylonitisch; Tiefenbach südöstlich Fernitz, westlich Seewiese, aus Blockschutt (Probe Fi 17/17; R: 705436, H: 378048).
h: Kriegenreith-Gneis, dunkelgrau, fein- bis mittelkörnig, biotitreich, kleine Plagioklas-Porphyroklasten, mylonitisch; Manhartsberg, südlich Seewiese, Steingrube an der Manhartsbergstraße (Probe Fi 18/17; R: 705720, H: 377984).
i: Sachsendorf-Gneis, sehr hell, feinkörnig, feldspatreich; Manhartsberg, nordöstlich Seewiese, Steingrube im Wald nahe der Manhartsbergstraße (Probe Fi 19A/17; R: 706017, H: 378222).
j: Sachsendorf-Gneis, von Aplit- und Quarzgängchen durchsetzt; Manhartsberg, nordöstlich Seewiese, Steingrube im Wald nahe der Manhartsbergstraße (Probe Fi 19B/17; R: 706017, H: 378246).
k: Kriegenreith-Gneis, dunkelgrau, fein- bis mittelkörnig, biotitreich, kleine Feldspat-Zeilen; Manhartsberg, nördlich Seewiese, Wasserauffanggrube direkt an der Manhartsbergstraße (Probe Fi 20/17; R: 705874, H: 378297).

ordnung der Glimmerschiefer auf die Pulkau-Decke, in der in den Paragesteinen nahe der deformierten Granitplutone derartige Turmalinanreicherungen auftreten (Frasl, 1983).

Im ultramylonitischen leukokraten Orthogneis (Probe ML17-21-17) sind im Dünnschliff bis zu einem Millimeter große, teilweise zerbrochene Plagioklas-Porphyroklasten erkennbar. Reichlich feinstschuppiger Muskovit und sehr wenig Biotit belegen die Schieferungsflächen. Eine starke Veränderung der Hauptelemente ist beispielsweise durch einen niedrigen CaO-Gehalt angezeigt und von Stoffverschiebungen sind daher vermutlich auch mobilere Spurenelemente wie Sr betroffen. Die Frage ist, ob dieser ultramylonitische Orthogneis aus einem Sachsendorf-Gneis der hangenden Pleißing-Decke oder einem Manhartsberg-Granit der liegenden Pulkau-Decke entstanden ist. Die Na-Vormacht über K und der hohe Zr-Gehalt deuten eher auf Sachsendorf-Gneis hin. Insofern ist die durch den Hang westlich vom Sulzberg-Gipfel streichende Deckengrenze in das Liegende der leukokraten Orthogneise und in das Hangende der Glimmerschiefer zu legen.

Im Dienbachgraben wurde am Fuß vom Sulzberg ein Aplit (Probe ML17-21-15) im Sachsendorf-Gneis beprobt. Dieses körnige helle Gestein besteht hauptsächlich aus Quarz und Feldspat, wobei der Plagioklas gegenüber Kalifeld-

	l	m	n	o	p	q	r	s	t	u
Probe	**ML 17-21-8**	**ML 17-21-9**	**ML 17-21-10**	**ML 17-21-11A**	**ML 17-21-11B**	**ML 17-21-12A**	**ML 17-21-12B**	**ML 17-21-13**	**ML 17-21-14**	**ML 17-21-15**
SiO_2	72,30	75,76	70,50	71,65	71,58	73,96	73,76	73,74	75,51	74,41
TiO_2	0,21	0,03	0,25	0,21	0,21	0,04	0,05	0,05	0,01	0,06
Al_2O_3	15,16	12,93	15,75	15,31	15,26	14,43	14,55	14,33	12,86	13,66
Fe_2O_3	1,32	0,13	2,08	1,98	2,16	0,48	0,64	0,71	0,20	0,85
MnO	0,01	0,00	0,04	0,10	0,13	0,02	0,01	0,02	0,01	0,05
MgO	0,37	0,01	0,62	0,42	0,52	0,14	0,16	0,13	0,02	0,05
CaO	0,50	0,17	0,42	0,34	0,38	0,34	0,40	0,27	0,13	0,20
Na_2O	3,67	4,89	4,09	3,71	3,73	4,16	4,51	3,99	3,14	6,12
K_2O	5,02	4,81	4,82	4,87	4,60	5,10	4,58	5,43	6,80	3,20
P_2O_5	0,09	0,03	0,10	0,07	0,08	0,05	0,07	0,07	0,06	0,11
GV	1,33	0,41	1,40	1,35	1,36	0,92	0,89	0,88	0,33	0,81
Total	**99,98**	**99,17**	**100,06**	**100,01**	**100,01**	**99,65**	**99,62**	**99,62**	**99,07**	**99,52**
Rb	150	86	149	138	132	255	217	320	290	104
Sr	230	127	261	232	231	104	127	68	58	89
Ba	651	199	858	725	779	186	175	89	128	414
Th	12	9	8	8	7	16	17	19	6	10
La	19	u.d.N.	30	19	20	15	11	11	2	9
Ce	45	17	44	46	43	21	23	18	10	15
Nd	26	7	25	22	19	17	15	13	11	12
Ga	17	13	18	18	17	16	19	21	16	12
Nb	11	6	11	9	10	9	16	18	9	9
Zr	99	41	115	101	94	50	44	42	53	47
Y	19	10	14	12	14	26	22	22	18	19
Sc	3	1	0	2	2	0	1	2	4	2
Pb	18	6	10	18	15	29	31	33	35	11
Zn	64	6	42	62	59	16	18	18	9	9
V	8	3	9	11	12	4	u.d.N.	1	1	4
Co	1	1	3	4	4	2	1	2	1	1
Cr	17	7	14	14	10	14	6	12	13	6
Ni	8	7	11	9	9	9	9	9	8	8

Tab. 1., Teil 2.
Röntgenfluoreszenzanalysen (Hauptelemente in Gew.%, Spurenelemente in ppm, GV = Glühverlust, u.d.N. = unter der Nachweisgrenze). Koordinaten der Probenpunkte im Koordinatensystem BMN M34 (R: Rechtswert, H: Hochwert).

l: Manhartsberg-Granit; Rücken zwischen Jungbrunnenbach und Pernersdorferöde, Wegaufschluss bei der Einfahrt zu Christbaumplantage (Probe ML17-21-8; R: 707189, H: 377732).
m: Aplitschliere im Manhartsberg-Granit; Rücken zwischen Jungbrunnenbach und Pernersdorferöde, Wegaufschluss (Probe ML17-21-9; R: 707706, H: 377654).
n: Manhartsberg-Granit; Aufschluss hinter der Lagerhalle des Wildgatters am Jungbrunnenbach (Probe ML17-21-10; R: 707671, H: 378002).
o: Manhartsberg-Granit; Steinbruch und Grusgrube am Rücken zwischen Jungbrunnenbach und Pernersdorferöde (Probe ML17-21-11A; R: 707463, H: 377892).
p: Manhartsberg-Granit; Steinbruch und Grusgrube am Rücken zwischen Jungbrunnenbach und Pernersdorferöde (Probe ML17-21-11B; R: 707463, H: 377892).
q: Turmalin führender Aplit; Bombentrichter südöstlich vom Manhartsberg-Gipfel (Probe ML17-21-12A; R: 707028, H: 378475).
r: Aplit und Leukogranit; Bombentrichter südöstlich vom Manhartsberg-Gipfel (Probe ML17-21-12B; R: 707028, H: 378475).
s: Turmalin führender Aplit; Lesestein südöstlich vom Manhartsberg-Gipfel (Probe ML17-21-13; R: 706983, H: 378510).
t: Aplit und Leukogranit; Lesestein nordwestlich vom Manhartsberg-Gipfel (Probe ML17-21-14; R: 706731, H: 378692).
u: Aplit; Dienbachgraben westlich Sulzberg (Probe ML17-21-15; R: 706442, H: 378034).

spat dominiert, sowie sehr wenig schuppigem Muskovit. Die Deformation erweist sich im Dünnschliff als stark protomylonitisch bis kataklastisch. Geochemisch ist dieser plagioklasreiche Aplit natriumbetont. Er besitzt einen niedrigen Rb-Gehalt von nur gut 100 ppm und zeigt dadurch eine Ähnlichkeit zum Sachsendorf-Gneis, der auch an anderen Stellen nicht selten von Aplit- und Quarzadern durchzogen ist (siehe Probe Fi 19B/17).

Das gesamte Gebiet südlich vom Manhartsberg-Gipfel, zwischen Jungbrunnenbach, Sulzberg und Pernersdorferöde, wird von hellem, stark von Aplit durchsetztem Granit aufgebaut. Damit besteht die Pulkau-Decke in diesem Bereich lithologisch hauptsächlich aus diesem als Manhartsberg-Granit benannten und geochemisch charakterisierten Granit (Finger et al., 2017). Es handelt sich um einen körnigen biotitarmen Granit, schmutzig weiß bis blass rosa. Die unzähligen feinkörnigen Aplitschlieren weisen keinen scharfen Kontakt zum Granit auf, sind ebenfalls oft blass rosa und sind ihrerseits mitunter von sehr grobkörnigen pegmatoiden Schlieren mit gleichem Mineralbestand durchzogen. Es treten aber auch einige größere Aplitkörper auf, die in sich in gröberen Leukogranit übergehen aber trotzdem vom Manhartsberg-Granit kartierungsmäßig abgrenzbar sind. Lithologisch sind letztere Aplite den dif-

	v	**w**	**x**	**y**	**z**	**aa**	**ab**	**ac**	**ad**	**ae**
Probe	**ML 17-21-16A**	**ML 17-21-16B**	**ML 17-21-16C**	**ML 17-21-17**	**ML 17-21-18**	**ML 17-21-19**	**ML 17-21-20A**	**ML 17-21-20B**	**ML 17-21-21**	**ML 17-21-22**
SiO_2	62,82	70,23	67,49	72,65	87,12	66,33	74,05	76,24	76,64	76,29
TiO_2	1,26	0,88	0,83	0,23	0,15	0,93	0,24	0,61	0,02	0,03
Al_2O_3	16,36	14,82	14,45	15,24	8,07	17,88	13,22	13,40	12,65	12,84
Fe_2O_3	7,40	7,34	6,40	1,83	0,29	4,23	3,11	2,62	0,44	0,11
MnO	0,11	0,05	0,10	0,03	0,00	0,12	0,12	0,03	0,01	0,00
MgO	2,75	2,66	2,38	0,62	0,29	0,96	0,51	0,73	0,06	0,01
CaO	0,43	0,59	0,65	0,20	0,01	0,29	0,08	0,17	0,18	0,11
Na_2O	2,90	0,85	2,74	4,59	0,17	1,80	1,54	0,24	5,38	5,09
K_2O	4,42	0,93	3,45	3,15	2,29	5,43	5,20	4,32	3,28	4,23
P_2O_5	0,17	0,22	0,14	0,10	0,07	0,26	0,24	0,17	0,04	0,03
GV	2,15	2,17	1,86	1,84	0,97	2,27	1,59	1,78	0,55	0,44
Total	**100,77**	**100,74**	**100,50**	**100,49**	**99,44**	**100,50**	**99,90**	**100,31**	**99,25**	**99,18**
Rb	196	53	176	118	81	275	181	175	126	118
Sr	81	111	95	119	27	69	72	19	75	102
Ba	741	117	474	470	269	934	760	719	157	111
Th	21	15	14	16	5	5	u.d.N.	4	17	14
La	27	46	16	39	167	47	71	26	8	2
Ce	58	82	77	79	273	102	118	62	16	2
Nd	16	38	15	31	139	37	6	20	10	8
Ga	25	26	21	19	8	23	29	13	18	16
Nb	19	9	14	8	2	25	12	23	20	11
Zr	281	176	197	191	67	417	150	316	47	52
Y	21	35	18	21	49	36	35	21	34	48
Sc	20	17	12	2	1	16	8	6	4	0
Pb	9	11	11	3	38	10	2.901	47	29	21
Zn	86	161	69	19	8	35	120	43	10	8
V	130	164	87	7	11	46	22	30	2	u.d.N.
Co	14	22	14	4	0	8	15	13	2	1
Cr	164	118	84	12	18	52	17	29	11	8
Ni	33	44	35	9	10	17	29	25	7	7

Tab. 1., Teil 3.
Röntgenfluoreszenzanalysen (Hauptelemente in Gew.%, Spurenelemente in ppm, GV = Glühverlust, u.d.N. = unter der Nachweisgrenze). Koordinaten der Probenpunkte im Koordinatensystem BMN M34 (R: Rechtswert, H: Hochwert).

v: Glimmerschiefer; Hang westlich Sulzberg-Gipfel (Probe ML17-21-16A; R: 706542, H: 378050).
w: Glimmerschiefer mit Boudin aus Turmalin-Quarz-Gang; Hang westlich Sulzberg-Gipfel (Probe ML17-21-16B; R: 706542, H: 378050).
x: Glimmerschiefer; Hang westlich Sulzberg-Gipfel (Probe ML17-21-16C; R: 706542, H: 378050).
y: Ultramylonit aus Sachsendorf-Gneis; Hang westlich Sulzberg-Gipfel (Probe ML17-21-17; R: 706596, H: 377928).
z: Ultramylonit aus Aplit; Sulzberg-Gipfel (Probe ML17-21-18; R: 706767, H: 377984).
aa: Gumping-Gneis, mylonitisch; Sulzberg-Gipfel (Probe ML17-21-19; R: 706745, H: 378022).
ab: Manhartsberg-Granit, mylonitisch; Sulzberg-Gipfel (Probe ML17-21-20A; R: 706823, H: 378035).
ac: Gumping-Gneis, mylonitisch; Sulzberg-Gipfel (Probe ML17-21-20B; R: 706823, H: 378035).
ad: Aplitschliere im Manhartsberg-Granit; Steingrube nordwestlich vom Sulzberg-Gipfel (Probe ML17-21-21; R: 706670, H: 378236).
ae: Aplitschliere im Manhartsberg-Granit; Steingrube westlich Pernersdorferöde (Probe ML17-21-22; R: 706952, H: 377363).

fusen Aplitschlieren recht ähnlich, sie führen aber oftmals feinstängeligen Turmalin und nur selten Granat. Derartige bis zu 100 m große Aplitkörper sind um den Sulzberg und südöstlich vom Manhartsberg-Gipfel aufgeschlossen. Vom Gipfel selbst erstreckt sich der größte dieser Aplitkörper in länglicher Form über 300 m nach Westen bis nahe zur Deckengrenze der Pulkau- zur Pleißing-Decke. Als einzelne Lesesteine finden sich Turmalin führende Aplite praktisch überall im Manhartsberg-Granit, wobei diese Stücke durch ihre Homogenität und orthogonale Kluftflächen leicht ins Auge fallen. Somit erscheinen die teils Turmalin führenden Aplite als kleine diskordante Stöcke beziehungsweise Gänge im Granit zu stecken.

Der Manhartsberg-Granit ist sehr unterschiedlich deformiert. Starke mylonitische Deformation besteht an der Deckengrenze im Hangenden, die westlich vom Manhartsberg-Gipfel über den Hang westlich vom Sulzberg-Gipfel Richtung Olbersdorf streicht. Kühl mylonitische bis kataklastische Deformation ist entlang der Diendorf-Störung, im Gebiet westlich Tobelkreuz–Pernersdorferöde, maßgeblich. Protomylonitische und kataklastische Verformung sind aber sehr wohl auch im Gebiet dazwischen zu beobachten und dem Deckenbau beziehungsweise der Diendorf-Störung genetisch zugehörig.

Vom Manhartsberg-Granit wurden repräsentative Proben genommen, und zwar am Rücken südöstlich vom Sulzberg (Probe ML17-21-8), vom Aufschluss hinter der Lagerhalle des Wildgatters am Jungbrunnenbach (Probe ML17-21-10) sowie aus der Stein- und Grusgrube am Weg vom Jungbrunnenbach zum Sulzberg (Probe ML17-21-11A, -11B). Der Mineralbestand erweist sich im Dünnschliff als ziemlich einheitlich, dominiert von perthitischem Kalifeldspat mit Mikroklingitterung, weniger Plagioklas und reichlich Quarz. Der Glimmeranteil ist sehr gering, wobei grobschuppiger Biotit und Muskoviteinschlüsse im Kalifeldspat als magmatische Relikte gelten können. Alle Proben sind protomylonitisch und überprägend kataklastisch deformiert. Feinster Hellglimmer in der kataklastischen Matrix zeigt eine Alteration im Zuge dieser Deformation an.

Geochemisch zeigen die Proben des Manhartsberg-Granits eine normalgranitische Hauptelementzusammensetzung mit $Fe_2O_{3(tot)}$ zwischen ca. 1 und 2 Gew.%, was laut Mesonorm einem primären Biotitgehalt von etwa 4–6 Vol.% entspricht. Bei rund 5 Gew.% K_2O liegen die normativen Kalifeldspatanteile dieser Proben um 30 %, und egalisieren damit etwa den Plagioklas- (30 %) und Quarzanteil (30 %). Auffällig ist ein niedriger CaO-Gehalt von nur 0,3–0,5 Gew.%, der auf niedrige Anorthitgehalte im primären Plagioklas schließen lässt. Die A/CNK-Werte sind mit 1,2 bis 1,3 deutlich peralumisch und wären im Prinzip für einen S-Typ beziehungsweise einen Zweiglimmergranit typisch, vorausgesetzt das keine signifikanten postmagmatischen Elementverschiebungen stattgefunden haben. Durch seinen deutlichen peralumischen Charakter hebt sich der Manhartsberg-Granit sowohl vom Retz- wie auch vom Eggenburg-Granit ab.

Bei den leukogranitischen bis aplitischen Proben ($Fe_2O_{3(tot)}$ < 1 Gew.%) stehen solche mit hohem Na_2O-Gehalten (5–6 Gew.%) und Plagioklasvormacht solchen mit hohen K_2O-Gehalten (5–6 Gew.%) und Kalifeldspatvormacht gegenüber. Von den quarzreichen Aplitschlieren im Manhartsberg-Granit wurden drei repräsentative Proben genommen. Diese Gesteine verwittern aufgrund des höheren Quarzgehaltes und der Feinkörnigkeit weniger stark als der Granit selbst. Aplitreiche Felsaufschlüsse wurden westlich vom Tobelkreuz (Probe ML17-21-9), am Rücken Burgfrieden nördlich vom Sulzberg (Probe ML17-21-21) und westlich Pernersdorferöde (Probe ML17-21-22) beprobt. Die Aplite bestehen im Allgemeinen nur aus Plagioklas, Kalifeldspat und Quarz, lediglich eine Probe (ML17-21-21) zeigt unter dem Mikroskop Spuren von Biotit und Muskovit. Die zum Teil vorhandenen gröberkörnigen Domänen im Aplit sind im Mineralbestand ganz gleich. Bezüglich der Deformation ist anzumerken, dass die Aplitschlieren protomylonitisch und, im Unterschied zum umgebenden Granit, nicht kataklastisch deformiert sind. Aus geochemischer Sicht sind diese plagioklasreichen Aplitschlieren natriumbetont mit schwach metaalumischem Charakter sowie stets niedrigem Rb-Gehalt von nur rund 100 ppm.

Von den zuvor genannten Turmalin führenden Aplitkörpern und -gängen wurden mehrere Proben rund um den Manhartsberg-Gipfel genommen (ML17-21-12A, -12B, -13, -14). Unter dem Mikroskop zeigt sich ein Gemenge aus Kalifeldspat, Plagioklas und Quarz vorwiegend feinkörnig, aber auch mit gröberen Schlieren und Adern. Dazu kommen sehr wenig schuppiger Muskovit und selten Biotit. Typisch sind bis 3 mm große, feinstängelige Turmalinkristalle, im Dünnschliff olivgrün mit mattblauen Kernen, sowie sehr wenig feinkörniger Granat. Aufgrund erhöhter Rb-Gehalte (200–300 ppm) und reduzierter Sr-, Ba-, LREE- und Zr-Gehalte können diese kaliumreichen Aplite gut als fraktionierte Schmelzen vom Manhartsberg-Granit interpretiert werden. Der größere der Aplitkörper am Manhartsberg-Gipfel ist nur schwach duktil und nicht kataklastisch deformiert.

Vom Sulzberg-Gipfel wurden ungewöhnliche mylonitische Gesteine analysiert. Die Hauptelemente dieser Proben sind offensichtlich stark verändert und lithologische wie genetische Zuordnungen sind dementsprechend schwierig. Die beiden grauen mylonitischen Gneise (Proben ML17-21-19, -20B) zeigen eine augenförmige Textur aus Aggregaten von Kalifeldspat, Plagioklas und Quarz in einer glimmerreichen Matrix mit feinschuppigem Muskovit und wenig Biotit. Geochemisch kann aufgrund hoher Zr-Gehalte Gumping-Gneis als Ausgangsmaterial vermutet werden. Dieser tritt im Manhartsberg-Granit in Form von metergroßen Schollen wiederholt auf (Finger et al., 2017). Bei der Probe ML17-21-20A weist der makro- und mikroskopische Befund auf einen inhomogen, ultramylonitisch deformierten Manhartsberg-Granit, mit Muskovit führender, feinstkörniger Matrix. Die Änderungen bei den Haupt- und Spurenelementen lassen vermuten, dass einerseits Plagioklas zerstört und damit verbunden CaO und Na_2O abgeführt wurden. Der Abbau von Kalifeldspat zu Muskovit hat hingegen keine größeren Stoffverschiebungen bewirkt. Anzumerken bleibt ein unerklärlich hoher Pb-Gehalt von 2.900 ppm in dieser Probe. Ebenfalls außergewöhnlich ist ein weißer Ultramylonit (Probe ML17-21-18) mit serizitbelegten Schieferungsflächen, der durch hohe LREE-Gehalte bei niedrigem Zr-Gehalt auffällt. Im Dünnschliff lassen sich augenförmig deformierte Porphyroklasten aus Quarz in feinstkörniger, von Serizitlagen durchzogener Matrix ausmachen. Wahrscheinlich wurde ein relativ quarzreicher Aplit einer äußerst starken Deformation unterzogen, in Verbindung mit ausgeprägten Stoffverschiebungen.

Literatur

FINGER, F. & RIEGLER, G. (2012): Bericht 2010 über petrografische und geochemische Untersuchungen an Metagranitoiden und Orthogneisen des Moravikums auf Blatt 21 Horn. – Jahrbuch der Geologischen Bundesanstalt, **152**, 216–218, Wien.

FINGER, F. & RIEGLER, G. (2017): Bericht 2016 über petrografische und geochemische Untersuchungen an Orthogneisen und schwach deformierten Graniten des Moravikums auf Blatt 21 Horn. – Jahrbuch der Geologischen Bundesanstalt, **157**, 311–315, Wien.

FINGER, F., LINNER, M. & RIEGLER, G. (2017): Bericht 2015 über petrografische und geochemische Untersuchungen an Orthogneisen und schwach deformierten Graniten des Moravikums auf Blatt 21 Horn. – Jahrbuch der Geologischen Bundesanstalt, **157**, 307–311, Wien.

FRASL, G. (1983): Einführung in die Geologie der Moravischen Zone. – In: HÖCK, V., FRASL, G., STEININGER, F. & VETTERS, W. (1984): Zur Geologie des Kristallins und Tertiärs der weiteren Umgebung von Eggenburg: Exkursion der Österreichischen Geologischen Gesellschaft zum 75 jährigen Bestandsjubiläum am 8. Oktober 1983. – Exkursionsführer der Österreichischen Geologischen Gesellschaft, Nr. **1**, 4–18, Wien.

JANOUŠEK, V. & HOLUB, F.V. (2007): The causal link between HP–HT metamorphism and ultrapotassic magmatism in collisional orogens: case study from the Moldanubian Zone of the Bohemian Massif. – Proceedings of the Geologists' Association, **118**, 75–86, London.

LINNER, M., ROETZEL, R., HUET, B. & HINTERSBERGER, E. (2019): Two nappes in the Austrian part of the Moravian Superunit. – 17th Meeting of the Central European Tectonic Groups, Rozdrojovice, 24–27 April 2019, Abstract Volume, 44, Rozdrojovice.

SCHANTL, P. (2018): Bericht 2017 über geologische Aufnahmen auf Blatt 21 Horn. – Jahrbuch der Geologischen Bundesanstalt, **158**, 110–113, Wien.

Bericht 2016 über strukturelle Aufnahmen im Gebiet Weißer Graben auf Blatt 21 Horn

BENJAMIN HUET

Einleitung

In diesem Bericht sind Ergebnisse und Interpretationen von strukturellen Aufnahmen, die 2016 im Weißen Graben auf Blatt 21 Horn durchgeführt wurden, zusammengefasst. Zwischen Fernitz und der Straße über den Manhartsberg, südwestlich Klein-Burgstall, bietet der Weiße Graben ein fast kontinuierliches Profil in der Pleißing-Decke mit relativ guten Aufschlussbedingungen. Dies ermöglicht die Deformation an der tektonischen Grenze zwischen Moldanubikum und Moravikum als auch innerhalb vom Moravikum zu charakterisieren.

Der Bericht folgt der Nomenklatur von FRASL (1974), die von SCHANTL (2017) erweitert wurde. Die makroskopischen Analysen basieren auf Beobachtungen und Strukturmessungen von 52 Aufschlüssen. Strukturmessungen wurden mit dem Software TectonicsFP 1.7.5 (ORTNER et al., 2002) ausgewertet. Die Mächtigkeit der lithologischen Einheiten wurde mit der scheinbaren Mächtigkeit auf der Karte und dem mittleren Einfallen des planaren Gefüges gerechnet. Für die mikroskopischen Analysen wurden 40 Dünnschliffe, von denen 25 orientiert sind, mit dem optischen Mikroskop ausgewertet. Schersinnindikatoren wurden parallel zur Lineation (Streckungs- bzw. Minerallineation) und senkrecht zum planaren Gefüge (Schieferung bzw. Foliation) makro- sowie mikroskopisch bestimmt. Die gegebenen Korngrößenwerte sind Einschätzung und wurden nicht systematisch und quantitativ gemessen. Aufschluss- bzw. Probenlokalitäten sind in Tabelle 1 zusammengefasst.

Für die mikroskopische Beschreibung der Deformation werden die klassischen Abkürzungen aus PASSCHIER & TROUW (2005) verwendet: BLG („bulging recrystallisation" – Niedertemperatur-Rekristallisation durch Korngrenzenwanderung), SGR („subgrain rotation recrystallisation" – Rekristallisation durch Subkornrotation), GBM („grain boundary migration recrystallisation" – Rekristallisation durch Korngrenzenwanderung), SPO („shape preferred orientation" – bevorzugte Formorientierung) und CPO („crystallographic preferred orientation" – bevorzugte kristallografische Orientierung). Die Terminologie der planaren und linearen Strukturen bzw. Schersinnindikatoren stammt aus HUET et al. (2020).

Strukturelle Beobachtungen

Im Weißen Graben ist eine Abfolge mit Orthogneisen unterschiedlicher chemischer Zusammensetzung und metasedimentären Gesteinen (Glimmerschiefer, Paragneis, Marmor) aufgeschlossen. Sie hat ein konsistentes Einfallen nach Westen bis Westsüdwest. Von Westen bis Osten, i.e. vom Hangenden in das Liegende, sind folgende lithologische Einheiten aufgeschlossen: Metasedimentäre Einheit 1, Bittesch-Gneis, Metasedimentäre Einheit 2, Buttendorf-Gneis, Metasedimentäre Einheit 3, Kriegenreith-Gneis und Sachsendorf-Gneis. Die strukturellen Merkmale dieser Einheiten sind im Folgenden beschrieben. Anschließend wird die Interpretation der Beobachtungen diskutiert.

Metasedimentäre Einheit 1

Makroskopische Beobachtungen: Innerhalb des hangenden Teiles des Bittesch-Gneises sind metasedimentäre Gesteine eingelagert. Diese Einheit ist nicht kontinuierlich, zeigt die Form einer größeren Linse und ihre Mächtigkeit variiert von 0 bis 50 m. Sie entspricht einer Wechsellagerung von phyllonitischem Glimmerschiefer mit Resten von grobschuppigem Hellglimmer und braunem bis dunklem, quarzreichem, mylonitischem Paragneis. Im Kern dieser Einheit tritt eine Lage von hell- bis dunkelgrauem, grobkörnigem und unreinem Marmor auf. Die Mächtigkeit dieser Marmorlage erreicht bis zu circa 10 m. In allen Lithologien sind die Schieferung bzw. Foliation und die Minerallineation gut ausgebildet. Die Foliation bzw. Schieferung schwankt zwischen 253/30 und 278/49. Die Streckungs- bzw. Minerallineation ist subhorizontal und schwankt zwischen 198/18 und 003/06. Es wurden keine makroskopischen Schersinnindikatoren beobachtet.

Mikroskopische Beobachtungen: Der Paragneis besteht aus einer Matrix mit länglichen Aggregaten aus feinkörnigem Quarz und Plagioklas (bis 100 µm groß), die durch feinen Biotit und untergeordnet Hellglimmer getrennt sind. Quarz und Plagioklas sind total rekristallisiert. Die schräge SPO von Quarz und Plagioklas im Vergleich zu den Schichtsilikatlagen zeigt eine Top-nach-N-Scherung an.

Aufschluss	Geologische Einheit	Rechtswert	Hochwert	Probe
BH-16-0025	Metasedimentäre Einheit 1	552933	5378378	BH/16/2
BH-16-0027	Metasedimentäre Einheit 1	552953	5378380	BH/16/4
BH-16-0002	Bittesch-Gneis	552878	5378342	
BH-16-0003	Bittesch-Gneis	552986	5378279	
BH-16-0004	Bittesch-Gneis	553028	5378211	
BH-16-0026	Bittesch-Gneis	552956	5378399	BH/16/3
BH-16-0028	Bittesch-Gneis	553079	5378474	BH/16/5a, BH/16/5b
BH-16-0029	Bittesch-Gneis	553070	5378428	BH/16/6
BH-16-0030	Bittesch-Gneis	552862	5378346	BH/16/7a, BH/16/7b
BH-16-0031	Bittesch-Gneis	553044	5378198	BH/16/8
BH-16-0032	Bittesch-Gneis	553066	5378194	BH/16/9
ML-16-P458	Bittesch-Gneis	552984	5378288	Fi 18-16
ML-16-P459	Bittesch-Gneis	553040	5378207	Fi 19-16
BH-16-0005	Metasedimentäre Einheit 2	553089	5378170	
BH-16-0006	Metasedimentäre Einheit 2	553155	5378183	
BH-16-0033	Metasedimentäre Einheit 2	553105	5378183	BH/16/10a, BH/16/10b
BH-16-0007	Buttendorf-Gneis	553259	5378181	
BH-16-0008	Buttendorf-Gneis	553478	5378119	
BH-16-0009	Buttendorf-Gneis	553571	5378069	
BH-16-0010	Buttendorf-Gneis	553616	5378040	
BH-16-0034	Buttendorf-Gneis	553246	5378184	BH/16/11
BH-16-0035	Buttendorf-Gneis	553376	5378178	BH/16/12
BH-16-0036	Buttendorf-Gneis	553537	5378091	BH/16/13
BH-16-0585	Buttendorf-Gneis	553447	5378127	
BH-16-0586	Buttendorf-Gneis	553805	5378089	
ML-16-P461	Buttendorf-Gneis	553442	5378131	Fi 21-16
ML-16-P462	Buttendorf-Gneis	553617	5378052	Fi 22-16
ML-16-P463	Buttendorf-Gneis	553794	5378097	Fi 23-16
BH-16-0011	Metasedimentäre Einheit 3	553752	5378080	
BH-16-0012	Metasedimentäre Einheit 3	553906	5378133	
BH-16-0013	Metasedimentäre Einheit 3	554032	5378144	
BH-16-0023	Metasedimentäre Einheit 3	554155	5378130	
BH-16-0024	Metasedimentäre Einheit 3	554067	5378126	
BH-16-0037	Metasedimentäre Einheit 3	553757	5378079	BH/16/14
BH-16-0038	Metasedimentäre Einheit 3	553867	5378147	BH/16/15
BH-16-0039	Metasedimentäre Einheit 3	554126	5378130	BH/16/16
BH-16-0040	Metasedimentäre Einheit 3	554316	5378328	BH/16/17
BH-16-0043	Metasedimentäre Einheit 3	554274	5378214	BH/16/20
BH-16-0018	Kriegenreith-Gneis	554560	5378325	
BH-16-0019	Kriegenreith-Gneis	554464	5378318	
BH-16-0020	Kriegenreith-Gneis	554426	5378335	
BH-16-0021	Kriegenreith-Gneis	554352	5378354	
BH-16-0022	Kriegenreith-Gneis	554394	5378324	
BH-16-0041	Kriegenreith-Gneis	554332	5378348	BH/16/18
BH-16-0042	Kriegenreith-Gneis	554279	5378236	BH/16/19
BH-16-0587	Kriegenreith-Gneis	554391	5378328	
BH-16-0588	Kriegenreith-Gneis	554420	5378323	
BH-16-0589	Kriegenreith-Gneis	554552	5378334	
BH-16-0591	Kriegenreith-Gneis	554936	5379208	
ML-16-P464	Kriegenreith-Gneis	554391	5378322	Fi 24/16
ML-16-P465	Kriegenreith-Gneis	554397	5378327	Fi 25/16
ML-16-P466	Kriegenreith-Gneis	554420	5378353	Fi 26/16
ML-16-P467	Kriegenreith-Gneis	554415	5378337	Fi 27/16
ML-16-P470	Kriegenreith-Gneis	554943	5379212	Fi 30/16

Aufschluss	Geologische Einheit	Rechtswert	Hochwert	Probe
BH-16-0016	Sachsendorf-Gneis	554956	5378099	
BH-16-0017	Sachsendorf-Gneis	554728	5378239	
BH-16-0590	Sachsendorf-Gneis	554715	5378236	BH/16/142
BH-16-0592	Sachsendorf-Gneis	554957	5379253	
BH-16-0593	Sachsendorf-Gneis	555172	5379456	
BH-16-0594	Sachsendorf-Gneis	555187	5378384	BH/16/143
ML-16-P468	Sachsendorf-Gneis	554554	5378347	Fi 29/16
ML-16-P471	Sachsendorf-Gneis	554954	5379255	Fi 31/16
ML-16-P472	Sachsendorf-Gneis	555176	5379463	Fi 32/16
ML-16-P053	Sachsendorf-Gneis	554945	5376364	ML17-21-17

Tab. 1.
Aufschluss- bzw. Probenlokalitäten. Koordinaten sind im System UTM 33N, WGS 84 angegeben.

Der Marmor besteht aus länglichen Calcitkörnern, die subparallel zur Schieferung liegen, mit untergeordnet Hellglimmer, Tremolit und kugeligem Quarz. Die Größe der Calcitkörner ist ziemlich homogen (2 × 0,5 mm). Calcit ist total rekristallisiert und hat starke SPO und CPO. Hellglimmer- und Tremolitkörner sind bis 100 µm lang, liegen parallel zur Schieferung und zeigen keinen Reaktionssaum. Die SPO im Calcit zeigt eine Top-nach-N-Scherung an. Der Glimmerschiefer wurde nicht beprobt.

Bittesch-Gneis

Makroskopische Beobachtungen: Die Mächtigkeit des Bittesch-Gneises ist größer als 200 m. Seine Hangendgrenze ist hier unter Lössbedeckung. Der Bittesch-Gneis ist ein relativ heller, mesomylonitischer bis ultramylonitischer Orthogneis mit stark ausgeprägter Foliation und Streckungs- bzw. Minerallineation. Die Matrix besteht aus fein rekristallisiertem Quarz und Hellglimmer, welche die Foliation bilden. Kalifeldspat-Porphyroklasten sind verbreitet, zumeist rund und erreichen einen Durchmesser bis zu 1 cm. Bis zu 5 mm, vereinzelt bis 2 cm große, magmatische Muskovite haben sich erhalten. Magmatischer Biotit wurde nur einmal beobachtet. Quarz-Mobilisate sind durch die starke Deformation in die Foliation eingeschlichtet. Am Kontakt zur metasedimentären Einheit 1 ist der Bittesch-Gneis deutlich stärker deformiert und tritt als heller, feinkörniger ultramylonitischer Orthogneis auf. Die Foliation schwankt zwischen 261/19 und 303/54 mit einem Mittelwert von 284/34 (N = 12). Die Streckungs- bzw. Minerallineation ist subhorizontal und streicht um einen Mittelwert von 197/04 (N = 13). Die Schwankung der Foliation ist konsistent mit einer engen bis isoklinalen Faltung im Zehnermeter-Maßstab mit Faltenachsen subparallel zur Lineation. Solche Strukturen konnten aber nicht beobachtet werden. Top-nach-N-Scherung ist durch Sigmaklasten aus Kalifeldspat, Scherband-Boudins und C-Typ-Gefüge makroskopisch angedeutet.

Mikroskopische Beobachtungen: Die magmatischen Phasen, teilweise als Porphyroklasten erhalten, sind stark deformiert und rekristallisiert. Die Matrix besteht aus feinkörnigem metamorphem Quarz und Plagioklas. Quarz rekristallisiert mit SGR und GBM und formt Quarz „ribbons". Plagioklas ist rekristallisiert und oft saussuritisiert. Die Korngröße von Quarz (200–300 µm) ist größer als die vom Plagioklas (100–150 µm). In mesomylonitischen Proben sind Muskovit und Biotit mit einem feinen rekristallisierten Saum ummantelt. In ultramylonitischen Proben sind sie vollständig rekristallisiert und bilden foliationsparallele, feinkörnige Aggregate. Kalifeldspat tritt als magmatisch zonierter, verzwillingter und gerundeter Porphyroklast auf. Er rekristallisiert mit GBM an Zwillingsgrenzen und am Rand in den Verkürzungsquadranten in Verknüpfung mit Myrmekitisierung. Feinkörniger Plagioklas, möglicherweise Albit und Quarz bilden Deformationsschatten um den Porphyroklasten. Spröde Deformation von Kalifeldspat wurde nur in einem Dünnschliff beobachtet. Sigmaklasten aus Kalifeldspat, Glimmerfische und C-Typ-Gefüge zeigen eine Top-nach-N-Scherung an.

Metasedimentäre Einheit 2

Makroskopische Beobachtungen: Im Liegenden des Bittesch-Gneises tritt ein grobkörniger, dunkelgrauer, unreiner Marmor auf, mit Einschaltungen aus Kalksilikatgestein und untergeordnet Glimmerschiefer und Paragneis an der Basis. Die Mächtigkeit dieser Einheit variiert zwischen 30 und 50 m. Die Foliation bzw. Schieferung und die Streckungs- bzw. Minerallineation sind stark ausgeprägt. Im Marmor schwanken die Strukturen sehr wenig: Foliation um 277/47 und Mineral- bzw. Streckungslineation um 196/11. Zentimetergroße Sigmoide aus Quarz im Marmor zeigen eine Top-nach-N-Scherung an.

Mikroskopische Beobachtungen: Der Marmor besteht aus Calcit, Muskovit, Quarz und Phlogopit. Calcit ist ungleichförmig und die Korngröße variiert zwischen 100 µm und 2 mm. Die Calcitkörner haben eine leichte SPO bzw. CPO. Muskovit und Phlogopit sind kleiner als 200 µm und liegen parallel zur Schieferung. Sie sind oft fein rekristallisiert, zeigen aber keinen Reaktionssaum. Quarz tritt in Form von entweder kleinen, undeformierten, kugeligen Körnern oder sigmoidalen Aggregaten auf. Die Aggregate sind mit einem feinkörnigen Hellglimmersaum ummantelt. In diesem Fall zeigt der Quarz undulöse Auslöschung. Top-nach-N-Scherung ist durch die Sigmoide angedeutet. Der Paragneis ist sehr feinkörnig. Seine Matrix besteht aus Quarz- und Plagioklas (Korngröße kleiner als 100 µm) mit disseminiertem Biotit und untergeordnetem Epidot. Bis zu 1 mm große Hellglimmer sind leicht rekristallisiert. Längliche Calcitkörner (< 500 µm) bilden Aggregate und zeigen eine schräge SPO und eine leichte CPO. Quarz kann auch Aggregate bilden. In diesem Fall rekristallisiert er mit SGR und GBM. Asymmetrische Mikrostrukturen (Glimmerfische, C′-Typ-Gefüge, schräge SPO) zeigen eine Top-nach-N-Scherung an.

Buttendorf-Gneis

Makroskopische Beobachtungen: Der Buttendorf-Gneis ist ein ziemlich inhomogener, dunkler, mesomylonitischer bis ultramylonitischer Orthogneis mit stark ausgeprägter Foliation und Streckungs- bzw. Minerallineation. Seine Mächtigkeit ist ungefähr 400 bis 450 m. Die mesomylonitischen Teile sind durch eine Abfolge im Millimeter-Maßstab mit hellen Quarz-Feldspat-Lagen und dunkleren Lagen mit ferromagnesischen Phasen charakterisiert. Gerundete Kalifeldspat- und/oder Plagioklas-Porphyroklasten bis zu 2 mm sind häufig. In ultramylonitischen Teilen ist der Orthogneis homogener, extrem feinkörnig, deutlich angereichert an Biotit und enthält keine sichtbaren Feldspat-Porphyroklasten. Dieser ultramylonitische Buttendorf-Gneis tritt an der Basis des Zuges auf und ist schwer vom biotitreichen, ultramylonitischen Paragneis zu unterscheiden. Die Foliation ist um einen Mittelwert von 271/41 (N = 11) konzentriert und die Mineral- bzw. Streckungslineation um einen Mittelwert von 197/13 (N = 11). Die Quarzmobilisate sind isoklinal verfaltet, mit einer Faltenachse subparallel zur Lineation und einer Achsenebene subparallel zur mylonitischen Foliation. Top-nach-N-Scherung ist durch C-Typ-Gefüge angedeutet.

Mikroskopische Beobachtungen: Der Buttendorf-Gneis ist wegen der variierenden Mineralogie bzw. Deformation auch im Dünnschliff heterogen. Die magmatischen Mineralphasen (Kalifeldspat, Plagioklas, Biotit, Hornblende) sind stark bis vollständig rekristallisiert und/oder umgewandelt. In mesomylonitischen Proben besteht die Matrix aus feinkörnigem Quarz, Plagioklas, Biotit und Epidot. Quarz rekristallisiert mit SGR und GBM und formt Quarz „ribbons“ mit einer Korngröße von 200 bis 400 µm, die von Biotit begrenzt sind. Plagioklas formt eckige bis gerundete Porphyroklasten, die bis zu 1 mm groß sind, die am Rand rekristallisiert und oft saussuritisiert sind. Kalifeldspat tritt als verzwillingter, gerundeter Porphyroklast auf. Er rekristallisierte mit GBM am Rand und in den Verkürzungsquadranten in Verknüpfung mit Myrmekitisierung. Kalifeldspat- und/oder Plagioklas-Porphyroklasten haben oft Deformationsschatten aus feinkörnigem Feldspat, möglicherweise Albit, und Quarz. Sie können auch spröd deformiert sein. Magmatische Hornblende wurde in zwei Proben beobachtet. Sie ist nicht deformiert aber rotiert und reagierte zu einer zweiten Generation Amphibol sowie Biotit, Epidot und/oder Titanit. In ultramylonitischen Proben sind Porphyroklasten fast nicht mehr zu beobachten und die Matrix besteht aus sehr feinkörnigem Quarz, Feldspat, Biotit und Epidot. Die schräge SPO im Quarz, Sigma- bzw. Deltaklasten aus Kalifeldspat und Plagioklas und C- bzw. C′-Typ Gefüge zeigen eine Top-nach-N-Scherung an.

Metasedimentäre Einheit 3

Makroskopische Beobachtungen: Die metasedimentäre Einheit 3 trennt den Buttendorf-Gneis im Hangenden vom Kriegenreith-Gneis im Liegenden. Sie ist ungefähr 250 bis 300 m mächtig und besteht aus grauem bis silberigem, phyllonitischem, oft quarzreichem Glimmerschiefer und grauem schichtsilikatführendem Marmor. In der metasedimentären Einheit 3 sind auch dunkle, biotitreiche, ultramylonitische Paragneise inkludiert, die gemeinsam mit Quarzgängen in das Liegende des Buttendorf-Gneises eingeschaltet sind. Alle Lithologien zeigen ein gut ausgebildetes planares Gefüge mit Lineation. Die Foliation bzw. Schieferung streut zwischen 281/66 und 202/38 mit einem Mittelwert von 260/46 (N = 13), während die Mineral- bzw. Streckungslineation sich um einen Mittelwert von 189/15 (N = 12) konzentriert. Die Streuung des planaren Gefüges lässt sich mit den beobachteten engen bis isoklinalen Falten mit einer Faltenachse subparallel zur Lineation erklären. Top-nach-N-Scherung ist durch Sigmoide und C′-Typ-Gefüge angedeutet.

Mikroskopische Beobachtungen: Glimmerschiefer und Paragneis sind durch kleine Korngröße und fast totale Rekristallisation charakterisiert. Der Paragneis unterscheidet sich durch die signifikante Menge an Plagioklas-Porphyroklasten. Diese sind rundlich, oft von einem Hellglimmersaum in den Verkürzungsquadranten ummantelt und erreichen eine Größe von 200 µm. Generell ist Biotit sehr fein, kann in Chlorit umgewandelt sein, während Hellglimmer ein breiteres Korngrößenspektrum hat, von feinschuppig total rekristallisiert bis zum 500 µm großen undeformierten Glimmerfisch. Quarz bildet 50 bis 100 µm große Körner und rekristallisierte durch SGR und untergeordnete GBM. Noch kleinere Quarzkörner bildeten sich durch BLG. Große erhaltene Quarzkörner aus Mobilisaten zeigen Deformationslamellen. Sowohl längliche Quarzkörner, die von Hellglimmer parallel zur Schieferung begrenzt sind, als auch ein Glimmersaum, der mit unlöslichen Phasen angereichert ist, zeigen, dass Drucklösung beteiligt war. Schersinnindikatoren wie C- bzw. C′-Typ-Gefüge, Glimmerfische, Sigmaklasten, asymmetrische Deformationsschatten und Sigmoide zeigen eine Top-nach-N-Scherung an.

Kriegenreith-Gneis

Makroskopische Beobachtungen: Der Kriegenreith-Gneis ist ein dunkler, mafischer Orthogneis, charakterisiert durch bis zu 1 mm große Plagioklas-Porphyroklasten. Seine Mächtigkeit erreicht 150 bis 200 m. Die proto- bis ultramylonitische Deformation, die Prägung des planaren Gefüges und der Lineation, sowie die Korngröße sind variabel. Ultramylonitische Typen treten an der Hangendgrenze auf und schauen grünlicher und extrem feinkörnig aus. Die Foliation ist um einen Mittelwert von 268/51 (N = 5) konzentriert. Steileres Einfallen gegen Westen lässt sich mit engen bis isoklinalen Falten mit einer Faltenachse subparallel zur Lineation erklären. Die Mineral- bzw. Streckungslineation konzentriert sich um einen Mittelwert von 268/51 (N = 5). Seltene Sigmaklasten zeigen eine Top-nach-N-Scherung an.

Mikroskopische Beobachtungen: Die Matrix besteht aus Quarz, Biotit, Plagioklas und Hellglimmer. Quarzkörner sind 50 bis 200 µm groß und rekristallisierten durch SGR und BLG. Quarz hat eine klare SPO und CPO. Körner, die nicht zu stark deformiert sind, zeigen erhaltene GBM. Plagioklaskörner sind auch 50 bis 200 µm groß. Biotit und Hellglimmer sind fast total rekristallisiert, wobei Biotit partiell bis total in Chlorit umgewandelt wurde. Plagioklas-Porphyroklasten sind 1 bis 5 mm groß. Sie sind oft eckig und senkrecht zur Foliation gebrochen und in den Rissen ist Quarz und seltener Calcit ausgefällt. Plagioklas ist oft in Albit umgesetzt. Diese zwei Beobachtungen zeigen, dass Drucklösung an der Deformation beteiligt war. Kalifeldspat wurde nicht beobachtet. Die SPO von Quarz, das C-Typ-Gefüge und die Sigmaklasten aus Plagioklas deuten eine Top-nach-N-Scherung an. Trotz der intensiven Deformation gibt es Proben, die gut erhaltene magmatische Merkmale wie equigranulare Mikrostruktur, zonierten Plagioklas und Hornblende zeigen.

Sachsendorf-Gneis

Makroskopische Beobachtungen: Der Sachsendorf-Gneis ist ein hellglimmerarmer, oft verquarzter, heller bis dunkler Orthogneis. Seine Mächtigkeit ist größer als 550 m. Kalifeldspat-Porphyroklasten erreichen eine Größe von 1 cm. Die Deformation ist heterogen und wird nach Osten in das Liegende mehr kataklastisch. Damit sind die Foliation und die Lineation nicht immer klar ausgeprägt. Als Ausnahme dieser Tendenz wurde am Sulzberg südlich vom Manhartsberggipfel eine Probe eines ultramylonitischen Sachsendorf-Gneises als Lesestein gefunden. Dort ist der Orthogneis graubraun, sehr feinkörnig und hat seltene, bis zu 3 mm große Kalifeldspat-Porphyroklasten. Die Foliation und die Streckungslineation sind sehr ausgeprägt. Der Sachsendorf-Gneis ist oft von Pegmatit und Aplit durchsetzt. Wegen der dicken Verwitterungsdecke kann die Mächtigkeit dieser späten Gänge nicht genau bestimmt werden. Aus dem gleichen Grund waren nur wenige Strukturmessungen möglich. Zwei Messungen zeigen, dass die Foliation um 274/56 und die Streckungslineation um 190/08 orientiert sind. Makroskopischen Schersinnindikatoren wurden im Sachsendorf-Gneis nicht beobachtet.

Mikroskopische Beobachtungen: Der kataklastisch deformierte Sachsendorf-Gneis zeigt wenig dynamische Rekristallisation. Dennoch weist er 100 bis 500 µm dicke, spröd-duktile Scherbänder auf, die aus feinem Quarz, Kalifeldspat und Epidot bestehen. Diese Scherbänder können durch Verwachsung von Quarz und Kalifeldspat umschlossen sein und sind nur durch ausgerichtete feine Epidotkörner bemerkbar. Dynamisch rekristallisierte Proben, außer die ultramylonitische Probe, haben eine quarzdominierte Matrix. Die Quarzkörner sind 50 bis 200 µm groß, rekristallisierten durch SGR und haben eine starke SPO und CPO. Sehr kleine Quarzkörner wurden durch BLG gebildet. Hellglimmer und Biotit sind metamorph rekristallisiert und oft zwischen Quarz bzw. Feldspat eingezwängt. Biotit ist teilweise in Chlorit umgewandelt. Die Kalifeldspat- und Plagioklas-Porphyroklasten sind eckig, senkrecht zur Foliation gebrochen und löschen undulös aus. Die Risse sind mit ausgefälltem Quarz gefüllt. Plagioklas ist auch oft von Albit oder Hellglimmer durchsetzt. Diese zwei Beobachtungen zeigen, dass Drucklösung stattgefunden hat. Spröd-duktile Scherbänder schneiden sowohl Matrix wie Porphyroklasten durch. Die SPO von Quarz und spröd-duktile Scherbänder zeigen eine Top-nach-N-Scherung an. In der ultramylonitischen Probe besteht die Matrix aus feinkörnigem (20–50 µm) Quarz, untergeordnet Plagioklas und völlig rekristallisiertem Muskovit und Biotit. Die Quarzkörner zeigen eine undulöse Auslöschung, aus denen noch kleinere Körner (5 µm) durch BLG entstanden. Biotit ist partiell in Chlorit umgewandelt. In dieser Matrix findet man Kalifeldspat- und Plagioklas-Porphyroklasten. Sie erreichen 3 mm, sind oft verzwillingt, etwas serizitisiert und haben völlig rekristallisierte Deformationsschatten.

Interpretation

Das gesamte Profil im Weißen Graben zeigt eine bemerkenswerte Übereinstimmung der planaren und linearen Strukturen als auch der Schersinnindikatoren. Das planare Gefüge ist um dem Mittelwert 270/42 (N = 49) konzentriert und das mittlere Einfallen der Einheiten nimmt vom Hangenden in das Liegende progressiv von ca. 30° bis ca. 55° nach Westen zu. Die Lineation ist stark um den Mittelwert 193/10 (N = 48) konzentriert. Die Streuung des Streichens des planaren Gefüges um einen Großkreis deutet auf eine berechnete „best-fit“ Faltenachse von 209/24 hin. Dieser Wert ist nicht genau parallel zur mittleren Lineation. Die Variation der Orientierung des planaren Gefüges im Maßstab 10 bis 1.000 m ist trotzdem mit engen bis isoklinalen Falten mit einer Faltenachse subparallel zur regionaler Lineation zu interpretieren. Solche Strukturen wurden im 10 cm bis 1 m Maßstab beobachtet. Parallel zur Lineation und senkrecht zur Schieferung wurde makroskopisch und mikroskopisch ein breites Spektrum von einheitlich Top-nach-N-Schersinnindikatoren (C- bzw. C′-Typ-Gefüge, Sigma- bzw. Deltaklasten, Glimmerfische, Scherband-Boudins, schräge SPO, asymmetrische Deformationsschatten und Sigmoide) beobachtet. Diese finden sich in allen lithologischen Einheiten. Die bearbeiteten Gesteine haben deshalb ein Deformationsereignis mit gleichzeitiger Verkürzung und Faltung senkrecht zum planaren Gefüge, N–S-Streckung und Top-nach-N-Scherung erlebt. Detailbeobachtungen weisen aber darauf hin, dass sich die Deformation lokalisiert und unter unterschiedlichen Bedingungen stattgefunden hat.

Mehrere Deformationsgradienten wurden beobachtet. Zwei großräumige Deformationsgradienten mit ultramylonitischen Orthogneisen weisen auf Lokalisierung entlang der Deckengrenzen der Pleißing-Decke hin. Im Bittesch-Gneis nimmt die Deformation in das Hangende zu, dies ist konsistent mit der Position der Moldanubischen Überschiebung an dessen Hangendgrenze. Die extreme Lokalisierung im ultramylonitischen Sachsendorf-Gneis zeigt die Basis der Pleißing-Decke. Scherzonen innerhalb der metasedimentären Einheiten und die begleitenden Gradienten in Orthogneisen sind mit Lokalisierung aufgrund lithologischer und mechanischer Heterogenität zu interpretieren.

Vom Hangenden in das Liegende, also von Westen nach Osten, sind folgende Merkmale der Deformationsmechanismen ausgebildet: (1) Makroskopisch ist die Deformation duktil bis zunehmend spröd. (2) Mikroskopisch ist dynamische Rekristallisation mit intrakristalliner Plastizität dominant und untergeordnet ist zunehmend Drucklösung beteiligt. (3) Die Rekristallisationsmechanismen im Quarz sind SGR und GBM, dann wird GBM dominant und letztendlich tritt BLG auf, begleitet von einer Abnahme der rekristallisierten Korngröße von Quarz. (4) Die Deformationsmechanismen der Feldspäte sind duktil, werden duktil und spröd und letztendlich fast nur spröd. Dies deutet einen Temperatur- und/oder Deformationsratengradienten mit Abnahme der Temperatur bzw. Zunahme der Verformungsrate in das Liegenden während des Deformationsereignisses an.

Basierend auf diesen Beobachtungen ist es möglich, die Temperatur an beiden Enden des Profils abzuschätzen, wenn man eine mehr oder weniger konstante Deformationsrate annimmt. Am Westende im Bittesch-Gneis herrschte dynamische Rekristallisation der Feldspäte und

GBM in Quarz vor, womit die Temperatur der Deformation höher als 450° C war. Die Gesteine am Ostende des Profils zeigen kataklastische Deformation, mit BLG im Quarz und Drucklösung um Plagioklas-Porphyroklasten, womit eine Temperatur im Übergangsbereich der spröd-duktilen Deformation um 300 bis 350° C anzusiedeln ist. Daraus ergibt sich ein Gradient der Deformationstemperatur von 100 bis zu 200° C vom Hangenden in das Liegende, also nach Osten zu. Zusätzliche Beobachtungen deuten an, dass die Hypothese eines Temperaturgradienten zu bevorzugen ist. Die Stabilität von kleinem Granat in Glimmerschiefer aller metasedimentären Einheiten (Schantl, 2017) und Tremolit und Phlogopit im Marmor ist kompatibel mit dem oberen Wert des Temperaturgradienten. Die Umwandlung von Biotit in Chlorit und die Überprägung von BLG-Rekristallisation über GBM-Rekristallisation im östlichen Teil des Profils weisen auf eine Temperaturabnahme. Diese Beobachtungen zeigen auch, dass niedrigtemperierte Deformation höhertemperierte Mikrostrukturen im Liegenden überprägt hat.

Damit zeigt das Profil insgesamt progressive niedrigtemperierte Überprägung der höhertemperierten Strukturen in östliche Richtung und eine Lokalisierung der Deformation durch lithologische Heterogenität. Dies hat sehr wahrscheinlich unter gleichen kinematischen Rahmenbedingungen stattgefunden. Auch wenn die Deformations- und Rekristallisationsmechanismen sowohl von der Temperatur, als auch von der Verformungsrate abhängig sind, nimmt die Intensität der Deformation nach Osten zu. Diese Beobachtungen sind nicht konsistent mit einer einzigen kontinuierlichen Scherzone, von duktil im Hangenden zu spröd-duktil im Liegenden. Während die duktile Deformation im Bittesch-Gneis sicherlich die Deformation an der Deckengrenze zwischen Moldanubikum und Moravikum widerspiegelt, könnte die spröd-duktile Deformation im Osten zur Bildung der Deckengrenze an der Basis der Pleißing-Decke gehören.

Literatur

Frasl, G. (1974): Aufnahmen 1973 auf Blatt 21 (Horn), Moravischer Anteil. – Verhandlungen der Geologischen Bundesanstalt, **1974**, A 37–A 42, Wien.

Ortner, H., Reiter, F. & Ács, P. (2002): Easy handling of tectonic data: the programs TectonicVB for Mac and TectonicsFP for Windows. – Computers & Geosciences, **28,** 1193–1200, Oxford.

Passchier, C.W. & Trouw, R.A.J. (2005): Microtectonics. – 2. Auflage, XVI + 366 S., Berlin.

Schantl, P. (2017): Bericht 2016 über geologische Aufnahmen auf Blatt 21 Horn. – Jahrbuch der Geologischen Bundesanstalt, **157**, 328–330, Wien.

Bericht 2018 über geologische Aufnahmen auf Blatt 21 Horn

Dominik Sorger

(Auswärtiger Mitarbeiter)

Kartierungsgebiet und Aufschlusssituation

Im Rahmen der geologischen Neuaufnahme von Blatt 21 Horn wurde im Jahr 2018 eine geologische Karte im Maßstab 1:10.000 südöstlich von Pernegg, beiderseits des Mödringbaches, aufgenommen. Das Arbeitsgebiet schließt nördlich an das im Jahr 2017 kartierte Gebiet, nördlich vom Mostelgraben und der Flur „Hauersteig", an (Sorger, 2018) und verläuft entlang des Pernegger Grabens (Mödringbach) weiter nach Norden bis zum Kloster Pernegg und zur Straße Pernegg–Posselsdorf. Im Westen wurde es durch die Straße Mödring–Staningersdorf und nördlich fortsetzend durch die großen Ackerflächen östlich von Staningersdorf begrenzt. Im Osten reicht das Aufnahmegebiet bis zu den Ackerflächen westlich von Lehndorf und weiter Richtung Nordwesten bis zum Trampelkreuz sowie Hammerkreuz.

Die Aufschlusssituation im Arbeitsgebiet ist, ähnlich wie im Gebiet 2017, sehr unterschiedlich ausgeprägt und meist von der Morphologie bestimmt. Gute Aufschlussverhältnisse findet man meist nur entlang von Gräben und eingeschnittenen Bachläufen (Mödringbach, Marbach, Aumühlbach, Mostelgraben). Die Lagerungsverhältnisse der metamorphen Gesteine sind meist nur in diesen Bereichen feststellbar. Auf den Verebnungs- beziehungsweise Hochflächen war oft nur eine Kartierung mittels Lesesteinen möglich, da nur vereinzelt Aufschlüsse vorhanden sind.

Die Ergebnisse der Neukartierung sind zwar in weiten Teilen konsistent mit bestehenden Kartierungen von Höck et al. (1987), siehe auch Höck & Vetters (1973, 1979) sowie Waldmann (1926, 1927), es zeigen sich jedoch bei genauerer Betrachtung einige Unterschiede, insbesondere im Verlauf einiger lithologischer Grenzen und in den Bereichen der sedimentären Bedeckung.

Moravikum

Die Gesteine des Moravikums können im Kartierungsgebiet in vier lithostratigrafische Komplexe unterteilt werden. Der Bittesch-Gneis im Südwesten bildet den hangendsten Komplex, der Richtung Norden von einem Komplex aus Marmor und Kalkschiefer unterlagert wird, der vor allem im westlichen Randbereich des Arbeitsgebietes aufgeschlossen ist. Vereinzelt tritt auch Fugnitz-Kalksilikatschiefer an der Liegendgrenze des Bittesch-Gneises auf. Der bei weitem größte Teil des kartierten Gebietes wird von Glimmerschiefern und Paragneisen aufgebaut, die den liegendsten metamorphen Komplex bilden.

Bittesch-Gneis

Bittesch-Gneis tritt nur im Südwesten des Kartierungsgebietes, im Bereich nördlich und nordwestlich Jägerbild, in der Flur „Säbel" und auf den Äckern entlang der Straße nach Staningersdorf, auf. Von der Straße Mödring–Staningersdorf reicht der Orthogneiskörper etwa 250 bis 300 m in Richtung Osten beziehungsweise Norden. Die Kartierung war dabei ausschließlich über Lesesteine auf den Ackerflächen und in angrenzenden Waldgebieten möglich, da in diesem Bereich keine Aufschlüsse von anstehendem Gestein vorhanden sind. Typisch für den meist hellen Orthogneis sind ein dünnplattiger Bruch, eine deutliche Schieferung und bis zu 5 mm große Kalifeldspat-Porphyroklasten. Das Hauptgemenge bildet eine eher feinkörnige Matrix (≤ 0,5 mm) aus Quarz und Plagioklas. Die Schieferung wird von grobem Muskovit (≤ 2 mm) und eher feinschuppigem Biotit (≤ 0,5 mm) ausgebildet. Akzessorisch findet man immer wieder Zirkon als Einschluss im Biotit, weiters Rutil und opake Phasen, vermutlich Eisenoxide oder Eisensulfide.

Fugnitz-Kalksilikatschiefer

Östlich von Staningersdorf, etwa 250 m nördlich der Straße, befindet sich an der Liegendgrenze des Bittesch-Gneises ein etwa 480 m langer Gesteinskörper von Fugnitz-Kalksilikatschiefer, in der Mitte von pleistozäner Bedeckung kurz unterbrochen. Eine weitere Einschaltung befindet sich nordwestlich davon, im Liegenden eines ca. 80 m breiten Bandes aus Marmor, und ist in westliche und nördliche Richtung von quartären Ablagerungen bedeckt. Der Fugnitz-Kalksilikatschiefer zeichnet sich durch eine dunkle Färbung, eine deutliche Schieferung und ein generell dünnplattiges Auftreten aus. Der Mineralbestand wird vor allem von Diopsid und bläulich-grüner bis blassbrauner, nematoblastischer Hornblende (≤ 2 mm) bestimmt. Die eher feinkörnige Matrix (≤ 0,2 mm) wird durch Quarz, Plagioklas, Klinozoisit/Epidot, Calcit und teils idiomorphen Titanit aufgebaut. Der Anteil an Calcit schwankt stark und teilweise ist das Gestein sogar karbonatfrei.

Marmor und Kalkschiefer

Im nordöstlichen und südwestlichen Randbereich des Kartierungsgebietes ist der Komplex aus Marmor und Kalkschiefer aufgeschlossen. Etwa 200 m südlich und 500 m südöstlich des Trampelkreuzes beginnend, zieht ein Körper Richtung Nordwesten bis zur Grenze des Arbeitsgebietes an der Straße Pernegg–Posselsdorf. In einem Seitengraben des Pernegger Grabens, ca. 450 m westlich des Trampelberges, lässt sich ein Marmorzug am Osthang etwa 130 m den Hang hinauf, am Westhang sogar bis auf die Hochfläche verfolgen. Nordwestlich des Klosters Pernegg ist im Graben des Aumühlbaches, an der Grenze des Kartierungsgebietes, die lithologische Grenze von Glimmerschiefer und Paragneis zu Marmor und Kalkschiefer aufgeschlossen. Auch in einem kleinen Seitengraben westlich des Aumühlbaches lässt sich eine Marmorlinse mit 50 bis 100 m Durchmesser auskartieren. Südlich davon, im Bereich der Flur „Teile" befindet sich im Liegenden vom Fugnitz-Kalksilikatschiefer ein weiterer großer Marmor- und Kalkschieferkörper. Ebenso tritt Marmor und Kalkschiefer südöstlich davon in einem ca. 600 m langen und 80 m breiten Gesteinskörper auf, hangend und teilweise auch liegend begleitet von Fugnitz-Kalksilikatschiefer.

Marmor und Kalkschiefer zeichnen sich durch einen hohen Anteil an teilweise recht grobem Calcit (≤ 2 mm) und einem variablen Anteil an silikatischen Mineralen, wie Biotit und Quarz, aus. Je höher dabei der silikatische Anteil ist, desto dunkler ist meist die Färbung des Gesteins und desto deutlicher ist eine vorhandene Schieferung erkennbar. Biotit ist meist feinschuppig (≤ 0,5 mm) und bildet mit sporadisch auftretendem Muskovit die Schieferung aus. Quarz tritt entweder feinkörnig (≤ 0,2 mm) zwischen grobem Calcit auf oder in Form von grobkörnigem Mobilisat. Diese Quarzmobilisate können bis zu mehrere Zentimeter große Quarzknollen ausbilden. Akzessorisch treten vor allem opake Phasen auf, wobei es sich dabei um Eisenoxide oder Eisensulfide handeln dürfte. Eine Besonderheit bilden vereinzelt auftretende Einschaltungen von grobkörnigem Kalksilikatgestein, etwa im Graben des Aumühlbaches oder nordöstlich der Straße Mödring–Staningersdorf im Bereich südlich der Flur „Teile". Charakteristisch sind große, teilweise verzwillingte Diopsid-Porphyroblasten (≤ 1 cm) in einer ebenfalls relativ groben Calcitmatrix (≤ 2 mm). Vereinzelt kann man idiomorphen Titanit zwischen Diopsid und Calcit beobachten.

Glimmerschiefer und Paragneis

Im Allgemeinen kommt es immer wieder zu Mischtypen beziehungsweise zu sehr lokalem Wechsel von Glimmerschiefer und Paragneis. Darüber hinaus ist die Aufschlusssituation vor allem auf den Hochflächen sehr dürftig und das darunterliegende Gestein konnte nur anhand von feinen Glimmerplättchen im Verwitterungsmaterial identifiziert werden. Daher konnten die beiden Lithologien im Kartenmaßstab nicht unterschieden werden und wurden als zusammenhängender Komplex kartiert.

Der weitaus größte Teil des bearbeiteten Gebietes wird von Glimmerschiefer und Paragneis aufgebaut. Abgesehen von der West- und Südwestgrenze setzt sich der Komplex aus diesen Metasedimenten über die Grenzen des Kartierungsgebietes hinaus fort. Westlich des Trampelberges und entlang vom Aumühlbach finden sich Linsen von Marmor und Kalkschiefer in dem ansonsten zusammenhängenden Körper aus Glimmerschiefer und Paragneis.

Die Glimmerschiefer zeichnen sich durch ein lepidoblastisches Gefüge aus feinkörnigem (≤ 0,1 mm) Muskovit und Biotit aus. Immer wieder tritt gröberer (≤ 2 mm), schuppiger Biotit in „Glimmerfischen" auf. Der Gehalt an Quarz und Plagioklas schwankt und ist oft in eher feinkörnigen (≤ 0,2 mm), gneisigen Lagen konzentriert. Immer wieder führen die Gesteine grobe Plagioklasblasten oder sind von Adern aus grobkörnigem Quarzmobilisat durchzogen. Häufig findet man Granat-Staurolith-Glimmerschiefer, wobei die Modalgehalte vor allem an Staurolith schwanken können. Granat bildet Porphyroblasten (≤ 5 mm), die meist poikiloblastisch sind und häufig Abbaureaktionen zu Chlorit zeigen. Manchmal beobachtet man idiomorph angewachsenen Granat im Druckschatten der rotierten und teils resorbierten Porphyroblasten. Lokal, etwa an den steilen Hängen nördlich und südlich vom Marbach, findet man sehr große Granat-Porphyroblasten mit bis zu 4 cm Durchmesser. Der Großteil des Granats ist synkinematisch gewachsen und zeigt immer wieder Kerne mit teils sternförmiger Sektorzonierung. Die Ränder der Granate sind dabei oft klar und einschlussfrei. Staurolith bildet idio- bis hypidiomorphe Porphyroblasten (≤ 3 mm), häufig mit der für dieses Mineral typischen Durchkreuzungs-Verzwillingung. Wie Granat ist auch Staurolith synkinematisch gewachsen, oft poikiloblastisch und randlich resorbiert.

Bei den mengenmäßig untergeordneten Paragneisen dürfte es sich um ehemalige psammitische Lagen in dem ansonsten eher pelitischen Ausgangsmaterial der Glimmerschiefer handeln. Der sedimentär angelegte Lagenbau ist oft noch gut im Millimeter-Bereich erhalten. Obwohl die Gesteine an sich sehr feinkörnig sind und allem voran aus Quarz und Plagioklas bestehen, lassen sich bei den einzelnen Lagen grobkörnigere (≤ 0,5 mm) quarz- und plagioklasreiche, sowie eher feinkörnigere (≤ 0,1 mm) glimmerreichere Lagen unterscheiden. Wie Glimmerschiefer ist auch Paragneis des Öfteren von grobkörnigen Adern aus Quarzmobilisat durchzogen. Teilweise tritt stark resorbierter Granat auf, wobei dieser an die glimmerreicheren Lagen gebunden zu sein scheint. Teilweise kann man wieder groben, schuppigen Biotit in Form von „Glimmerfischen" beobachten. Staurolith konnte in den Paragneisen keiner gefunden werden.

Strukturelle Beobachtungen und Lagerungsverhältnisse

Das generelle Streichen der Schieferung ist annähernd E–W, im Osten des Kartierungsgebietes im Bereich Trampelberg bis Lehndorf eher NW–SE, im Bereich südwestlich des Klosters Pernegg eher SW–NE, mit einem flachen Einfallswinkel (10–35°) Richtung SW–SE. Die dazugehörige Lineation fällt mit annähernd gleichem Winkel Richtung SSW, vereinzelt Richtung Süden ein. Schersinnindikatoren, die vor allem in Glimmerschiefern und stärker deformierten Marmoren bzw. Kalkschiefern zu finden sind, zeigen meist eine Bewegung mit Top Richtung Norden bis Nordosten.

Lokal findet man immer wieder Anzeichen von stärkerer Deformation. Westlich des Pernegger Klosters treten phyllonitische und mylonitische Glimmerschiefer beziehungsweise Paragneise auf, aber auch manche Marmore zeigen zumindest schwache Mylonitisierung. Dies deutet auf partitionierte Deformation in Form lokaler Scherzonen in den Glimmerschiefern und Marmoren westlich beziehungsweise östlich vom Kloster Pernegg hin. Eine an der Liegendgrenze des Bittesch-Gneises lokalisierte durchgehende mylonitische Scherzone ist hingegen nicht gegeben. In manchen Paragneisen lässt sich eine deutliche Verfaltung erkennen, meist jedoch nur im Zentimetermaßstab und aufgrund der Aufschlusssituation nur in Lesesteinen.

Junge Bedeckung

Neogene Ablagerungen

An der Westgrenze des Kartierungsgebietes, auf den Äckern ca. 700 m östlich von Staningersdorf liegen grobkörnige, kantengerundete bis gerundete, quarzreiche Schotter. Der weitere Verlauf der Schotterflächen wird im Rahmen der folgenden Kartierung Richtung Westen erhoben werden. Die Schotter und Sande werden vorläufig in das Neogen (Untermiozän; Eggenburgium–Ottnangium) eingestuft.

Quartäre Ablagerungen

Ebenfalls auf den Äckern östlich von Staningersdorf, im Grenzbereich von Bittesch-Gneis zu Fugnitz-Kalksilikatschiefer beziehungsweise Marmor und Kalkschiefer, werden die metamorphen Gesteine von lehmigem, mit Kristallinkomponenten durchsetztem Sediment überlagert. Südwestlich von Lehndorf liegen am Beginn eines Seitengrabens des Trampelbaches auf ca. 250 m Länge und 50 m Breite bis zu 7 m mächtige Lössablagerungen, in die tiefe Gräben eingeschnitten sind.

In Hangfußlagen und flachen Senken an Bachoberläufen konnten Solifluktions- und Flächenspülungssedimente festgestellt werden. Dabei handelt es sich vorwiegend um Lehme mit unterschiedlichem Anteil an Kristallingrus. Fluviatile Ablagerungen liegen in den Gräben entlang vom Mödringbach, Marbach und Aumühlbach, aber auch entlang von kleinen Seitengräben dieser größeren Bäche.

Literatur

Höck, V. & Vetters, W. (1973): Bericht 1972 über geologische Aufnahmen auf Blatt Horn (21). – Verhandlungen der Geologischen Bundesanstalt, **1973**/4, A 26–A 28, Wien.

Höck, V. & Vetters, W. (1979): Bericht 1977 über geologische Aufnahmen im Kristallin auf Blatt 21, Horn. – Verhandlungen der Geologischen Bundesanstalt, **1978**/1, A 49–A 51, Wien.

Höck, V., Frasl, G. & Vetters, W. (1987): Geologische Manuskriptkarte Blatt 21 Horn 1:25.000. – 1 Blatt, Geologische Bundesanstalt, Wien. [GBA, Wissenschaftliches Archiv, Nr. A 06524-ÖK25V/21-1]

Sorger, D. (2018): Bericht 2017 über geologische Aufnahmen auf Blatt 21 Horn. – Jahrbuch der Geologischen Bundesanstalt, **158**/1–4, 114–116, Wien.

Waldmann, L. (1926): Bericht über die geologische Aufnahme des moravischen Gebietes zwischen Eggenburg – Pernegg – Theras. – Anzeiger der mathematisch-naturwissenschaftlichen Klasse der Akademie der Wissenschaften, **62**/1, 2–7, Wien.

Waldmann, L. (1927): Bericht über die geologische Aufnahme des Moravischen Grundgebirges in Niederösterreich, IV. Teil. – Anzeiger der mathematisch-naturwissenschaftlichen Klasse der Akademie der Wissenschaften, **64**/1, 5–7, Wien.

Bericht 2019 über geologische Aufnahmen auf Blatt 21 Horn

Michal Vachek

(Auswärtiger Mitarbeiter)

Im Jahr 2019 wurde die geologische Kartierung auf Blatt 21 Horn im Gebiet zwischen Altenburg, Burgerwiesen und Mühlfeld sowie östlich und südöstlich von Mühlfeld bis zur Taffa fortgesetzt. Ein weiteres, kleineres Kartiergebiet lag nordöstlich von Wanzenau und nordwestlich von Etzmannsdorf. Die ältesten Gesteine sind moldanubische Metamorphite, wie Gföhl-Gneis, Amphibolit und Paragneis. Über diesen Gesteinen folgen lithologisch unterschiedliche fluviatile Sedimente der St. Marein-Freischling-Formation aus dem Unter- bis Oberoligozän (Kiscellium–Egerium). Die Quartärbedeckung ist bunt und besteht aus äolischen, deluvio-äolischen, deluvialen (solifluidalen), deluvio-fluviatilen und fluviatilen Sedimenten. Die geologische Aufnahme wurde mittels Handbohrsonden bis in 1 m Tiefe durchgeführt.

Kristallines Grundgebirge (Moldanubikum)

Metamorphe moldanubische Gesteine bilden einen großen Teil des kartierten Gebietes. Am verbreitetsten ist Gföhl-Gneis, der zwischen Altenburg und Burgerwiesen, nördlich der Straße Burgerwiesen–Mühlfeld, im Ortsbereich Mühlfeld und östlich davon oberflächennah, häufig in natürliche Felsaufschlüssen, auftritt. Am besten ist der Gföhl-Gneis in einem sehr kleinen, aufgelassenen Steinbruch am südlichen Rand von Altenburg (BMN M34 R: 695861, H: 389855) an einer 2,5 m hohen Wand zu sehen. Daneben finden sich steinige Eluvien von Gföhl-Gneis, das heißt graue, braungraue, rostig-graue oder grüngraue, glimmerige, kalkfreie Sande. Südlich des aus Gföhl-Gneis gebildeten Gebietes überwiegen Amphibolit und Paragneis. Einige Meter hohe Aufschlüsse dieser Gesteine befinden sich im Tal des Stranzlbaches (z.B. R: 697784, H: 389560) und im Wolfsgraben südlich von Mühlfeld (R: 699915, H: 388802). Eluvien von Paragneis sind jenen von Gföhl-Gneis sehr ähnlich. Sandige Eluvien von Amphibolit haben dagegen dunkelgrüngraue oder dunkel rostig-graue Farben. Auf dem Käferbigl zwischen Burgerwiesen und Mühlfeld treten in einem ca. 50 bis 80 m breiten Streifen Kalksilikatgesteine an die Oberfläche. Dieser morphologisch ausgeprägte Horizont setzt sich vom Käferbigl etwa 1 km gegen Westen und 700 m gegen Osten-Südosten fort. Auf der Anhöhe am östlichen Rand von Altenburg ist Serpentinit ausgepflügt, der jedoch vollkommen verwittert und erodiert ist.

In der Verwitterungskruste des Serpentinits tritt in bis zu 25 cm großen Hohlräumen Chalzedon auf (R: 696216, H: 390163; R: 696013, H: 390216). Das Gebiet nordöstlich von Wanzenau und westlich von Etzmannsdorf wird von Paragneis und Granulit gebildet. Granulit verwittert zu hellgrauen und braungrauen Sanden, die glimmerfrei oder nur leicht glimmerig sind.

Paläogen–Neogen

In dem kartierten Gebiet wurden einige neue Lokalitäten der fluviatilen **St. Marein-Freischling-Formation** (Unter bis Oberoligozän, Kiscellium–Egerium) gefunden. Nordöstlich von Altenburg, an den flachen Hängen beiderseits einer flachen Senke, wurden unter Tonen graugrüne, grobsandige Lehme und grüngraue bis rostig-graue, grobkörnige Sande erbohrt. Diese Sedimente sind kalkfrei und beinhalten Quarzgerölle bis zu 1 cm Größe. Südöstlich von Mühlfeld, auf den Anhöhen südlich und nördlich vom Wolfsgraben, treten ebenfalls sandige Schotter auf. Die Gerölle sind vorwiegend wenig gerundet bis kantengerundet und kugelig, seltener plattig. Gut gerundete Quarzgerölle treten selten auf und sind meist nur einige Zentimeter groß. Die Gerölle bestehen überwiegend aus Quarz und in einem geringen Maß auch aus Granitoiden und Gneis und sind meist nicht größer als 15 cm. Die maximal festgestellte Größe beträgt ca. 30 cm. Weitere kleinere Vorkommen von Schotter wurden auch östlich von Mühlfeld (z.B. R: 700368, H: 389407; R: 700686, H: 389572) und südöstlich von Burgerwiesen (R: 697751, H: 390126) registriert. Alle diese Schottervorkommen werden vorläufig der St. Marein-Freischling-Formation zugeordnet, obwohl südöstlich von Mühlfeld auch quartäre Terrassensedimente möglich sind.

Pleistozän

Löss ist auf größeren Flächen südlich und südöstlich von Burgerwiesen und westlich und nordwestlich von Mühlfeld verbreitet. Bei Burgerwiesen sedimentierte er an den östlich und südöstlich exponierten Hängen und bei Mühlfeld an nordöstlich orientierten. Typische Lössanwehungen findet man auch in einem linken Seitengraben des Stranzlbaches und nordöstlich von Wanzenau. In einem aufgelassenen Abbau (Ziegelgrube) beim Stranzlbach (R: 697784, H: 389466) ist Löss mit einer Mächtigkeit von 6 m aufgeschlossen. In der nordöstlichen Wand befindet sich unter 3,5 m Löss ein schräg einfallender, toniger, Schwarzerde-artiger Horizont (Paläoboden) mit bis zu 20 cm großen Kalkkonkretionen. An der Grenze von Löss zu den Tonsedimenten ist ein Horizont mit eckigen Quarzkomponenten bis zur 0,5 cm Größe eingeschaltet. Weitere Lössablagerungen befinden sich entlang des Waldweges südwestlich vom Käferbigl (z.B. R: 698045, H: 389760), am Stranzlbach (z.B. R: 697640, H: 389392) und nordöstlich von Wanzenau (R: 696367, H: 387380). Kleinere Lössvorkommen wurden zum Beispiel auch nordöstlich von Altenburg (R: 696411, H: 390032), nördlich von Burgerwiesen (R: 697445, H: 390737) und in der Umgebung vom Wolfsgraben, südöstlich von Mühlfeld kartiert. Im letztgenannten Gebiet bedeckt Löss an einigen Stellen teilweise Sedimente der St. Marein-Freischling-Formation (z.B. R: 700015, H: 388705). In den Lössen bildeten sich stellenweise Kalkkonkretionen bis zu 15 cm Größe.

Deluvio-äolische Sedimente wurden als Einschaltung in Löss in zwei kleineren Lokalitäten nordöstlich von Wanzenau kartiert (R: 696297, H: 387060; R: 696438, H: 387334). Es handelt sich um an steileren Hängen abgelagerte geschichtete Lösse, die Lagen aus bis zu 3 cm großen eckigen Granulit- und Paragneisstücken beinhalten. Diese kristallinen Komponenten wurden durch solifluidale, gravitative Prozesse aus höher gelegenen Hangbereichen in die äolischen Sedimente eingelagert.

Holozän–Pleistozän

Im Bereich des Hangfußes liegen an vielen Stellen über 1 m mächtige **deluviale (solifluidale) Sedimente**. Am verbreitetsten sind sie entlang der zwischen Burgerwiesen und Mühlfeld verlaufenden Senke. Es handelt sich um braune, kalkfreie bis schwach kalkige, siltige bis sandig-siltige Tone, die stellenweise verwitterte Bruchstücke von metamorphen Gesteinen beinhalten. Ihre Quelle sind vor allem Lösse und Lösslehme, untergeordnet auch Eluvien von metamorphen Gesteinen. Sie treten z.B. am südöstlichen Rand von Burgerwiesen und westlich und südwestlich von Mühlfeld auf. Leicht kalkige, siltige bis lehmig-siltige deluviale Tone wurden auch entlang des zum Elendgraben verlaufenden Baches nordöstlich von Wanzenau kartiert. Ein weiteres Vorkommen von deluvialen Sedimenten befindet sich in der Senke nordwestlich von Etzmannsdorf. Hier treten braune bis dunkelbraune, rostig fleckige, kalkfreie, sandig-lehmige Tone auf, die kleine Bruchstücke von metamorphen Gesteinen beinhalten.

Holozän

Fluviatile Sedimente füllen die schmale Talaue des südöstlich von Wanzenau entspringenden und durch den Elendgraben fließenden Baches. Am linken Ufer des Baches, ca. 350 m östlich bis südöstlich der Kapelle von Wanzenau, wurden unter 50 cm graubraunen, kalkfreien, lehmig-siltigen Tonen rostig-graue, kalkfreie Hochwasserlehme erbohrt.

Deluvio-fluviatile Sedimente wurden in kleineren, zeitweise durchflossenen Tälern abgelagert. Östlich von Altenburg liegen diese Sedimente in einer über 100 m breiten Senke, die in einen Graben zum Försterbach entwässert. Ihr oberer Teil wird von graubraunen, siltigen, kalkfreien Tonen mit einer Mächtigkeit von 35 bis 50 cm gebildet. Die Tone liegen über grauen, rostig-fleckigen, kalkfreien Lehmen. In einem Fall wurde in 0,6 m Tiefe dunkelgrauer, organischer Lehm erbohrt (R: 696454, H: 390125). Deluvio-fluviatile Sedimente füllen auch den Talboden des durch Burgerwiesen gegen Mühlfeld fließenden und bei der Raschmühle in die Taffa mündenden Baches. Es handelt sich vor allem um schwach braune bis braungraue, siltige bis sandig-siltige, kalkfreie bis leicht kalkige, stellenweise glimmerige, rostig fleckige Tone. In einem erweiterten Teil der Senke, nahe der Straße nordwestlich vom Käferbigl, gehen die Tone in 30 bis 75 cm Tiefe in schwach graue, siltige, rostig fleckige Lehme über. Am östlichen Rand von Mühlfeld (R: 699819, H: 389563), südlich von Burgerwiesen (R: 697286, H: 390206) und nördlich vom Käferbigl (R: 698254, H: 390093) wurden in 40 bis 80 cm Tiefe glimmerige, körnige Sande erbohrt. Schließlich fanden sich deluvio-fluviatile Sedimenten auch nordwestlich von Etzmannsdorf. Unter braunen und dunkelbraunen, lehmig-sandigen, kalkfreien Tonen mit einer Mächtigkeit von 30 bis 60 cm wurden hier graue bis dunkelgraue, kalkfreie, sandige Lehme festgestellt.

Anthropogene Sedimente wurden an einigen kleineren Lokalitäten abgelagert. Südlich der Straße Altenburg–Burgerwiesen (R: 696822, H: 390173) wurde auf einem Feld Aushubmaterial aus Bodensediment, verschiedenen metamorphen Gesteinen und Quarzgeröllen sowie Beton und Ziegel angeschüttet. Die Mächtigkeit der Anschüttung übersteigt stellenweise einen Meter. Eine weitere Lokalität befindet sich etwa 700 m nordwestlich der Kapelle Mühlfeld, südlich der Straße nach Burgerwiesen (R: 698922, H: 389917). Die Felder wurden hier an zwei Stellen mit siltigen Tonen und Löss verbessert. Eine kleinere Anschüttung unbekannten Charakters wurde auch bei einem Betrieb östlich des Friedhofes Altenburg festgestellt.

Blatt 68 Kirchdorf an der Krems

Bericht 2019 über geologische Aufnahmen im Gebiet Hirschwaldstein, Großer Landsberg und Schoberstein (Oberösterreichische Voralpen) auf Blatt 68 Kirchdorf an der Krems

Thomas Hornung

(Auswärtiger Mitarbeiter)

Die geologische Kartierung mit der Arbeitsbezeichnung „Hirschwaldstein, Großer Landsberg und Schoberstein“ auf Kartenblatt 68 Kirchdorf an der Krems erfolgte von Mai bis November 2019. Die nördliche Gebietsgrenze ist identisch mit dem Kalkalpen-Nordrand und verläuft von Burg Altpernstein oberhalb Micheldorf in Oberösterreich am Nordwesthang des Hirschwaldsteins entlang über den Rinnerberger Bach nach Hausmanning und weiter zum Großen Landsberg, weiter über das Steyrtal nördlich des Schobersteins zur Teufelskirche und Herndleck bis zur Blattgrenze zu Blatt 69 Großraming. Die Südgrenze des kartierten Gebietes zieht an den Südhängen von Schoberstein und Gaisberg knapp nördlich der Krummen Steyrling in den Mollner Talkessel und folgt dem Verlauf der Steyr und Enns wieder zurück nach Micheldorf.

Zum Zeitpunkt der Aufnahme standen folgende Karten- und Literaturwerke der GBA zur Verfügung:

- Der Kalkalpennordrand zwischen Krems- und Steyrtal in Oberösterreich 1:12.500 (Bauer, 1953).
- Geologische Karte der Flysch-Zone und des Kalkalpenrandes beidseits der Enns 1:25.000 (Braunstingl & Egger, 1985).
- Geologische Manuskriptkarte (handgezeichnet, Maßstab 1:10.000): Oberleonstein, Wienerweg, Hambaum, Rinnerberger Bach, Steyrdurchbruch, Landsberg (Birkenmajer, 1995).
- Geologische Karte von Österreich 1:50.000, Blatt 69 Großraming (Egger & van Husen, 2011).
- Historische Manuskriptkarte von Österreich 1:75.000 (Abel & Geyer, 1910).
- Geologische Karte von Oberösterreich 1:200.000 (Krenmayr et al., 2006).
- Erläuterungen zur Geologischen Karte von Oberösterreich 1:200.000 (Rupp et al., 2011).
- Quartärgeologische Manuskriptkarte am Südrand des Sengsengebirges (Steyr – Teichl – Rettenbach) (van Husen, 2017).
- Geologische Manuskriptkarten des Gebietes (Moser, 2014a, b, 2017a, b).

Naturräumlicher und geologischer Überblick

Das etwa 47 km^2 große Kartiergebiet (inkludiert und überarbeitet sind kleine Teilbereiche von van Husen (2017) im Mollner Talkessel) umfasst die nördlichsten, stark bewaldeten Mittelgebirgskämme der Oberösterreichischen Kalkvoralpen zum offenen, deutlich niedrigeren Vorland mit Rhenodanubischem Flysch und Ultrahelvetikum. Die höchste auf dem Gebiet liegende Erhebung ist der Schoberstein (1.285 m). Weitere markantere Erhebungen des Untersuchungsraumes sind der Gaisberg (1.267 m), der Steinkogel (1.097 m), der Hirschwaldstein (1.095 m), der Große Landsberg (898 m), der Rinnerberg (878 m) sowie der Sonnkogel (828 m). Den tiefsten Punkt des Gebietes definiert die nach Norden fließende Steyr mit etwa

361 m ü. A. zwischen Rieserberg im Osten und Rohregg im Westen.

Die Entwässerung des Gebietes erfolgt ausschließlich über die Steyr. Die beiden größten Zuflüsse des Gebietes sind die Krumme Steyrling und der Schmiedleithner Bach. Die Krumme Steyrling fließt im Tal von Breitenau nach Molln und mündet dort in die Steyr – der Schmiedleithner Bach trennt das kleine bewaldete Massiv des Landsberges vom Hirschwaldstein-Zug ab und mündet nördlich von Leonstein in die Steyr.

Das Klima des Areals wird entscheidend durch die Topografie bestimmt und kann als feucht-gemäßigt charakterisiert werden. Bedingt durch den oftmaligen Wolkenstau am Kalkalpen-Nordrand fällt im bewaldeten Mittelgebirge zwischen Totem Gebirge im Süden und dem Sengsengebirge im Nordosten für die Höhenlage relativ viel Niederschlag und Schnee.

Der Untersuchungsraum erlaubt Einblicke in zwei tektonische Bauelemente der Nördlichen Kalkalpen: beinahe das gesamte Untersuchungsgebiet liegt im Bereich der „hochbajuvarischen“ Reichraming-Decke (nach der klassischen Deckengliederung sensu Tollmann (1976) ein Pendant zur Lechtal-Decke in den westlichen Nördlichen Kalkalpen). Nur ein kleiner Teil unmittelbar am Kalkalpen-Nordrand kann – tektonisch durch kretazische Einheiten abgetrennt – zur „tiefbajuvarischen“ Ternberg-Decke (Pendant zur Allgäu-Decke in den westlichen Nördlichen Kalkalpen) gerechnet werden. Kriterien zur Deckengliederung werden eingehend im Kapitel „Tektonik“ erläutert.

Schichtenfolge

Reichraming-Decke

Trias

Reifling-Formation

Illyrium (Oberes Anisium) bis Julium (Unteres Karnium)

Die Reifling-Formation als tiefstes stratigrafisches Stockwerk des Kartiergebietes zieht in einer E–W streichenden, schmalen Antiklinale von Schmiedleithen südlich des Kleinen Landsberges über das Steyrtal nach Gradau und lässt sich an der Nordwestflanke des Gaisberges bis unter das Dürre Eck verfolgen („Gaisberg-Antiklinale“). Das stratigrafisch Liegende, die Gutenstein- und Steinalm-Kalke, die in Moser (2017a) ohne Fundortbeschreibung aus Bohrkernen beschrieben wurden, konnten nicht beobachtet werden.

Während die Schichtenfolge der Reifling-Formation im Steyrtal zur Gänze mit mächtigen verfestigten Niederterrassenschottern überdeckt ist und an Schmiedleithen an den Hügeln nördlich des Ortskerns nur unzureichend erschlossen ist, sind die Sequenzen auf der anderen Talseite unter dem Gaisberg relativ vollständig erhalten geblieben. Moser (2017a) konnte dabei einen basalen anisischen und einen höheren ladinischen Abschnitt biostratigrafisch unterscheiden (s.u.). Als Gesamt-Mächtigkeit gibt er 60 m an. Detailliertere Beschreibungen zu Lithologie und Altersdatierung finden sich in Moser (2017a), Egger (2007) und Hornung (2007).

Partnach-Formation

Langobardium bis Julium (Unteres Karnium)

Über der Reifling-Formation oder mit dieser faziell verzahnend treten mit der Partnach-Formation dunkelbraune bis dunkelgrüne Tonschiefer auf. Ihre Verbreitung im Kartiergebiet beschränkt sich auf den Kernbereich der Gaisberg-Antiklinale unter dem Kamm Dürres Eck bis Gaisberg und dürfte sich unter mächtiger quartärer Überdeckung bis westwärts bis in den Bereich von Gradau erstrecken. Unterhalb des Wanderweges zum Dürren Eck auf etwa 970 m ü. A. können dunkelgraue, ebenflächige Mergelkalke und braungraue, wellige bis ebenflächige mittelbankige Kalke vom Reiflinger Faziestypus eingeschaltet („Partnach-Kalke“) sein. Moser (2017a) erwähnt ferner dickbankige allodapische Kalkeinschaltungen („Raminger Kalk“). Die erhaltene Mächtigkeit beträgt nur etwas mehr als 30 m, kann durch intensive interne Faltung jedoch scheinbar höher ausfallen.

Üblicherweise ist die Partnach-Formation im Kartiergebiet als dunkelbraune bis dunkel-olivgrünliche Tonschiefer, die zu einer fettglänzenden, schweren Erde verwittern. Von der lithologisch ganz ähnlichen, und ebenfalls in diesem Bereich anstehenden Lunz-Formation unterscheiden sich die Mergel der Partnach-Formation einerseits durch den Farbwechsel von Braungrau auf Dunkelgrau, andererseits durch den höheren Karbonatgehalt (Test mit verdünnter Salzsäure). Ein primärer, das heißt fazieller Übergang oder eine Verzahnung zwischen Partnach- und Lunz-Formation kommt im Kartiergebiet nicht vor.

Die Fossilführung der Partnach-Formation ist ausgesprochen gering: Egger & van Husen (2011) erwähnen von Nachbarblatt 69 Großraming (Hohe Dirn) Conodontenfunde, die auf basales Karnium hinweisen. Moser (2017a) fand am Nordhang des Dürren Ecks die Muschel *Halobia vixaurita* und den Conodonten *Gondolella foliata*, die gleichfalls auf unterkarnisches Alter (Julium 1, *aonoides*-Zone) hindeuten.

Wetterstein-Formation

Illyrium (Oberes Anisium) bis Julium (Unteres Karnium)

Kalke der Wetterstein-Formation treten im Kartiergebiet ausschließlich innerhalb der Gaisberg-Antiklinale auf und ziehen sich als breites Band von Schauderzinken-Außerort (westlich von Schmiedleithen) über das Steyrtal bis in den Pfaffenboden. Sie tritt dabei durch relative Erosionsbeständigkeit gegenüber umgebenden Lithologien wie z.B. dem Hauptdolomit vor allem im Südschenkel der Sattelstruktur als hauptsächlicher Gipfelbildner des Höhenzuges Dürres Deck und Gaisberg auf. Da die Achse der Gaisberg-Antiklinale flexurell gegen Osten abtaucht, ist das Ende der Vorkommen von Wettersteinkalken am Pfaffenboden primär mit umlaufenden Streichen gekennzeichnet und nicht tektonisch reduziert. Westlich der Steyr tritt Wettersteinkalk am Rabenstein sowie an den weithin sichtbaren Kalknadeln des Schauderzinkens zutage. Seine maximale Mächtigkeit beträgt im Kartiergebiet 250 bis 300 m. Detailliertere Beschreibungen zu Lithologie und Altersdatierung finden sich in Hornung (2018).

Lunz-Formation: Tonmergel, Schluffsteine und Sandsteine, Kalke und Dolomite, untergeordnet Rauwacken

Julium (Unteres Karnium)

Stratigrafisch unmittelbar über der Wetterstein-Formation anstehend, konturieren die lithologisch variablen Gesteine der terrigen-siliziklastisch geprägten Lunz-Formation die Gaisberg-Antiklinale in einem in der Regel sehr schlecht aufgeschlossenen schmalen Streifen. Die derzeit besten Aufschlüsse bietet der in Abbau stehende Steinbruch in der Gradau (Fa. Bernegger). Natürliche Aufschlüsse finden sich an der Südwestseite des Dürren Ecks sowie entlang der Forstwege auf der Nordseite des Mittelgebirgskammes. Im Bereich des Schauderzinkens unter dem Landsberg auf der orografisch linken Seite der Steyr stehen Mergel der Lunz-Formation zwar oberflächlich nicht an, wurden jedoch aufgrund von fett dunkelgrau bis schwärzlich gefärbtem, staunassen Boden und der morphologischen Herausbildung flacher terrassenähnlicher Mulden kartiert.

Die vielerorts tektonisch amputierten, und nur wenig mehr als 10 m mächtigen Lunzer Tone stellen hier die Basis der Lunz-Formation dar und haben unverwittert eine ausgeprägt schwarzgraue bis schwarzgrau, teilweise in bläulich- bis stahlgrau gehende Färbung. Der enthaltene Anteil an (Hell)Glimmern ist makroskopisch stets sichtbar, der Karbonatgehalt mit verdünnter Salzsäure im Gelände leicht feststellbar. Letzteres unterscheidet sie von den Reingrabener Schiefern, die gänzlich karbonatfrei, beispielsweise in der Kaltau südlich der Kremsmauer, auftreten (Hornung, 2014). In die metermächtigen Mergelpakete schalten sich gegen das stratigrafisch Hangende immer mächtiger werdende Toneisenstein bzw. Hellglimmer führende Sandsteinbänke ein. Die Toneisensteine zeigen mitunter eine auffallend ockerfarbene bis ockerorangefarbene Tönung, die Sandsteine teilweise orangene Verwitterungsfarben auf den Bruchflächen. Diese Färbungen sind Folge von oxidierendem hohen Eisen- und Pyritgehalt (Limonit).

Im Steinbruch Gradau enthalten die Lunzer Tone und Mergel im oberen Bereich zu den hangenden Kalken der Opponitz-Formation cm-mächtige blendend weiße, lateral rasch auskeilende Gipsfladen. Der Gipsgehalt (stark erhöhter Sulfatanteil) konnte durch großzügig zur Verfügung gestellte Analysedaten des Gesteinslabors der Fa. Bernegger vom Hauptwerk Gradau bestätigt werden.

Obgleich wenig erosiv widerstandsfähig, ist die Lunz-Formation mit Tonen, Mergeln und zwischengeschalteten Feinsandsteinen über dem liegenden Wettersteinkalk im Untersuchungsgebiet stets konkordant zwischen stratigrafisch liegenden und hangenden Einheiten erschlossen.

Aus den Lunzer Schichten ist von Blatt Grünau (Egger, 2007; Egger & van Husen, 2007) eine schlecht erhaltene karnische Sporenflora erhalten – korrelierende multistratigrafische Studien mit einem sequenzstratigrafischen Modell (Hornung, 2007) grenzen die Zeitspanne mit dem Oberen Julium („Mittleres Karnium“) ein.

Opponitz-Formation

Tuvalium (Oberes Karnium)

Die Opponitz-Formation als stratigrafisch Hangendes zur Lunz-Formation besitzt innerhalb der Gaisberg-Synklinale eine ähnliche Verbreitung wie die zuvor beschriebene Lunz-Formation auf der Südseite vom Dürren Eck und Gaisberg sowie am Schauderzinken nördlich von Schmiedleithen. Am Landsberg ist die Opponitz-Formation ferner an der nördlichen Stirn der Reichraming-Decke zwischen Großem und Kleinen Landsberg erschlossen. Des Weiteren bestehen Oberflächen-Vorkommen ganz im Süden des Kartiergebietes bei Roß (nördlich Breitenau) sowie entlang der Oberleonsteiner Überschiebungsbahn südlich des Riedberges. Auch südöstlich von Hambaum nahe Leonstein sind in einem kleinen Kerbtal im Kern der Riedberg-Antiklinale Gesteine der Opponitz-Formation aufgeschlossen. Oftmals sind die Aufschlüsse stark verwachsen und nur schwer zugänglich – die aktuell beste Aufschluss-Situation bietet derzeit der Steinbruch der Fa. Bernegger in Gradau. Trotz der guten Aufschlussbedingungen in Gradau können keine definiten Angaben über die Gesamtmächtigkeit der Opponitz-Formation gegeben werden – sie dürfte sich zwischen 30 und 50 m bewegen.

Im Bereich der Gaisberg-Antiklinale sind die Sequenzen der Opponitz-Formation als in der Regel dünnbankiger, hell- bis mittelgrauer, lokal auch braungrauer Dolomit führender Kalk mit stets ebenen Bankflächen ausgebildet. Die frisch erschlossenen Opponitzer Schichten im Steinbruch Gradau zeigen zudem eine ausgeprägte Schichtung mit schwarzen bis schwarzgrauen, vermutlich organogenreichen stromatolithischen Lagen, die vermutlich von Algen und/oder Mikrobenmatten stammen. Am Hambaum sowie westlich Oberleonstein ist die Opponitz-Formation wieder deutlich kalkiger ausgebildet.

Hauptdolomit-Formation; Hauptdolomit-Formation in kalkiger Ausbildung

Tuvalium (Oberes Karnium) bis Alaunium (Mittleres Norium)

Neben der Wetterstein-Formation ist der Hauptdolomit im Kartiergebiet die dominierende Lithologie der hochbajuvarischen Reichraming-Decke. Seine Verbreitung liegt schwerpunktmäßig im Westteil des Kartiergebietes (westlich der Steyr) in einem Mittelgebirgszug zwischen Ochsenkogel und Plachwitz. Östlich der Steyr ist Hauptdolomit am Nordschenkel der Riedberg-Antiklinale am südexponierten Hang Dürres Eck–Schoberstein im Tal der Krummen Steyrling sowie an den (teilweise tektonisch reduzierten) Schenkeln der Gaisberg-Antiklinale (Gebiet Dorngraben–Pfaffenboden–Hochbuchberg) und der Schreibach-Synklinale flächig erschlossen. Die höhere Verwitterungsanfälligkeit des Hauptdolomits gegenüber der liegenden Wetterstein-Formation bedingt durchschnittlich verringerte Gipfelhöhen und ein flach welliges, kupiertes und zudem stark bewaldetes Oberflächenrelief. Eine Ausnahme bildet der 1.273 m messende Hochbuchberg östlich der Grünburger Hütte, der überwiegend aus Hauptdolomit aufgebaut ist. Sowohl im Liegenden (Mandlmais) als auch in den hangenden Partien der Schichtfolge (Rinnerberg und Plan) können großflächigere Bereiche in kalkiger Ausbildung vorliegen.

Sowohl Monotonie als auch das Fehlen von charakteristischen Leitbänken in den drei untergliederbaren Abschnitten des Hauptdolomits machen Abschätzungen über die erhaltene Maximalmächtigkeit schwierig – auf dem Kartengebiet dürften sich die größten Werte bei etwa 600 bis 700 m bewegen. Detailliertere Beschreibungen zu Lithologie und Altersdatierung finden sich in Hornung (2018).

Plattenkalk und Dachsteinkalk

Alaunium bis Sevatium (Oberes Norium)

In der Regel gehen die obersten Partien des Hauptdolomits im Kartiergebiet lithologisch fließend in den Hangenden Plattenkalk über, so an der Koglerstein-Synklinale und an deren westwärtiger, jenseits der Steyr gelegenen Verlängerung am Sonnstein. Kleinere Vorkommen konturieren die Schreibach-Synklinale und sind im oberen Dorngraben leidlich erschlossen. Die hauptsächlichen Vorkommen im westlichen Abschnitt des Kartiergebietes krönen den Bergkamm vom Ochsenkogel zum Steinkogel und liegen westlich der Burg Altpernstein. Dabei ist der Plattenkalk selten als typisch dünnbankiger reiner Mikrit ausgebildet, sondern vielmehr als mittel- bis dickbankiger Kalk, der in Habitus und Fossilführung (zahlreiche Muscheln) stark einem (lagunären) Dachsteinkalk ähnelt. Darin muss der These von Moser (2017a) widersprochen werden, der einen Plattenkalk postuliert, allerdings auch mittelbankige Partien hier mit einbezieht. Die Typusregion des Plattenkalks – soweit man überhaupt von einer solchen sprechen kann – liegt im Karwendel und ist in durchwegs dünnbankigen Sequenzen in Übergangsfazies zum Dachsteinkalk entwickelt, der sukzessive gegen das Hangende größere Bankdicken aufweist. Aus diesem Grund wird weiterhin der Begriff „Plattenkalk und Dachsteinkalk“ sensu Egger (2007) zu einer lithologischen Kartiereinheit zusammengefasst, verwendet.

Geschuldet den rasch wechselnden faziellen Übergängen und auch internen, oft parasitären Verfaltungen sind Aussagen über die Maximaldicke der Kalke schwierig – sie dürfte in den o.a. Bereichen bei maximal 100 m liegen. Detailliertere Beschreibungen zu Lithologie und Altersdatierung finden sich in Hornung (2018).

Kössen-Formation

Rhaetium

Kalke, Mergelkalke und Mergel der lithologisch heterogenen Kössen-Formation bilden das stratigrafisch Hangende der Plattenkalke und verzahnen als Beckenfazies mit der flachermarin abgelagerten riffogenen Fazies des Oberrhätkalkes. Die Vorkommen typischer Kössen-Formation sind im Kartiergebiet lokal eng begrenzt und werden zumeist von mächtigeren Hangschuttbereichen überdeckt. Ganz im Westen des Untersuchungsgebietes nahe Altpernstein tritt am Südschenkel der Hirschwaldstein-Synklinale ein kleines Vorkommen auf. Weiter östlich sind zieht die mit schätzungsweise 10 bis 20 m recht geringmächtige Schichtenfolge in drei teilweise tektonisch amputierten Synklinalzügen („Rinnerberger Synklinale“ und „Sonnkogel-Synklinale“). Östlich der Steyr konturiert die Kössen-Formation in enger fazieller Bindung zum Oberrhätkalk in nur metermächtigen Bänden die großen Synklinalbereiche zwischen Gaisberg und Schoberstein und ist oberflächennah nur mit Lesesteinen erfasst.

Im Vergleich zum Plattenkalk zeigt die Kössen-Formation einen deutlich erhöhten Mergelanteil, was sich in durchwegs dunkleren Gesteinsfärbungen äußert. Die Abfolge kann als Wechsellagerung von a) dm-gebankten, grauen bis dunkelgrauen, lokal bläulich- bis bräunlichgrauen bituminösen, mikritischen Kalken inklusive sparitverheilten Klüften und b) fossilreichen bioklastischen Kalken ausgebildet sein (nur durch Lesesteine nachgewiesen). Detailliertere Beschreibungen zu Lithologie und Altersdatierung finden sich in Hornung (2018).

Oberrhätkalk

Rhaetium

Je nach diachroner Faziesverzahnung zur Kössen-Formation entwickelt sich der Oberrhätkalk als jüngste erschlossene triassische Einheit im Kartiergebiet fließend aus der Kössen-Formation oder lagert unter Reduktion des Plattenkalks – wie nördlich der Grünburger Hütte sowie am Krennkogel nahe der Stirn der Reichraming-Decke – unmittelbar dem Hauptdolomit auf. Aufgrund der größeren Härte gegenüber dem stratigrafisch Liegenden und Hangenden konturiert er in erosiv herauspräparierten Rippen die Anti- und Synklinalzüge in den Höhenzügen östlich der Steyr. Er tritt aber auch morphologisch westlich der Steyr am Rinnerberg und am Großen Landsberg zutage, kann jedoch dort aufgrund lithologischer Ähnlichkeiten leicht mit dem morphologisch ebenfalls bedeutsamen, allerdings oberjurassischen Mikritooidkalk verwechselt werden. Die Gesamtmächtigkeit des Oberrhätkalks wird mit ca. 100 m angenommen. Detailliertere Beschreibungen zu Lithologie und Altersdatierung finden sich in Hornung (2017a–c).

Wie oben kurz angerissen, zeigt der Oberrhätkalk morphologisch große Ähnlichkeiten zum ebenfalls weitgehend massig ausgebildeten Mikritooidkalk. Erschwerend kommt hinzu, dass sowohl Oberrhätkalk als auch Mikritooidkalk in enger Verzahnung zu Rotkalken stehen – Mikritooidkalke werden oft von karminroten Steinmühlkalken gesäumt. Unterscheidungskriterien können entweder lithologisch gezogen werden: Oberrhätkalk ist in der Regel grau gefärbt, Mikritooidkalke meistens fleischfarben. Zudem können im Oberrhätkalk enthaltene Korallenreste als sicheres Differenzierungsmerkmal herangezogen werden. Allerdings treten diese weitaus weniger häufig auf, als dies Moser (2017a) vermuten ließe. Trotz eingehender Suche wurden nur an zwei Stellen im Kartiergebiet Korallenfragmente (*Thecosmilia* sp.) gefunden. Egger (mündl. Mitteilung) erwähnt ein Vorkommen aus der Rinnerberger Klamm. Am Krennkogel nahe der Stirn der hochbajuvarischen Reichraming-Decke wurden zahlreiche Korallen- und Muschelreste entdeckt.

Jura

Adnet-Formation

Hettangium bis Sinemurium (unterer Jura)

Flächig auskartierbare, nodulare rote Bankkalke der unterjurassischen Adnet-Formation können aufgrund der derzeit schlechten Aufschluss-Situation und der nur kleinräumigen Vorkommen am Top des Oberrhätkalkes nur an drei Positionen des Kartiergebietes gesichert auskartiert werden. Ein kleines Vorkommen besteht am Forstweg vom Sonnkogel zum Rabenstein, ein weiteres zieht sich in einem sehr schmalen, E–W streichenden Band nördlich der Grünburger Hütte am Berghang entlang und wird beim Wanderweg absteigend vom Schutzhaus in Richtung Rieserberg angeschnitten. In diesen beiden Fällen liegen sie eingekeilt zwischen Oberrhätkalken und der nachfolgenden, ebenfalls unterjurassischen Scheibelberg-Formation. Ein unmittelbarer Kontakt zu roten Spatkalken der Hierlatz-Formation – wie in Hornung (2017b) beschrieben, konnte nicht beobachtet werden. Aufgrund der schlechten

Aufschlussbedingungen können Maximalmächtigkeiten nur grob abgeschätzt werden – sie dürften sich im Bereich von nur wenigen Metern bewegen. Detailliertere Beschreibungen zu Lithologie und Altersdatierung finden sich in Hornung (2017a, b).

Hierlatzkalk, Echinodermatenspatkalk

Sinemurium (unterer Jura)

Der Hierlatzkalk bildet in den unterjurassischen, oft kondensierten Abfolgen das bei weitem mächtigste und auch morphologisch augenscheinlichste Schichtglied. Bis auf wenige Ausnahmen (s.o.) liegt die Abfolge aus Crinoiden-Spatkalken auf obertriassischem Oberrhätkalk und bildet im Untersuchungsraum zum Teil mächtige Wandstufen im ansonsten stark bewaldeten Gelände – teilweise zusammen mit dem erosiv ähnlich widerstandsfähigen Oberrhätkalk (Wände an den Gaisbergwiesen, Schwalbensteinmauer über dem Pranzlgraben). Der Hierlatzkalk ist mit dem Oberrhätkalk dort ein wichtiger landschaftsbildender Horizont. Dabei sind die Mächtigkeiten sehr unterschiedlich, maximal betragen sie etwa 75 m – mächtiger scheinende Vorkommen dürften tektonisch dupliziert und/oder intern verfaltet sein. Die Mächtigkeitsschwankungen können auch in der lateralen Verzahnung mit Adnet-Formation über submarinen Schwellenpositionen und mit Scheibelberg-Formation in Lokalbeckenbereichen, aber auch mit der Sedimentation über einem bewegten, von Spalten durchzogenen Oberrhätkalk-Relief, das vermutlich Ende der Trias längere Zeit keine Sedimentation erfahren hatte, bedingt sein.

Das Vorkommen der Hierlatzkalke westlich der Steyr beschränkt sich bis auf ein kleines Vorkommen südwestlich von Altpernstein auf die südexponierte Seite des Gebirgszuges vom Gaisberg bis zum Schoberstein – gegen Norden hin scheinen die Crinoidenspatkalke mit den Hornstein führenden Scheibelbergkalken zu verzahnen und zeigen einen tiefer werdenden Ablagerungsraum an.

Lithologisch betrachtet handelt es sich um einen vorwiegend rötlich bis rötlich-violetten, seltener fleischfarbenen bis hellgrauen, jedoch stets grobspätigen, aufgrund fehlender Schichtung massigen Kalk, dessen Komponenten sich hauptsächlich aus zerfallenen Crinoidenresten (etwa Seelilien) zusammensetzen. Meist ist der Übergang zwischen Oberrhätkalk und Hierlatzkalk scharf gezogen. Dies ist jedoch im Gelände oft an der gleichartigen hellgrauen Verwitterungsfarbe schwer nachzuvollziehen, so dass beide Einheiten oft eine Einheit zu bilden scheinen – im Anschlag mit dem Hammer jedoch wird der Unterschied zwischen beiden offensichtlich. Seltener enthalten die Hierlatzkalke auch Brachiopoden-Schill und komplette Brachiopoden-Gehäuse.

Scheibelberg-Formation

Hettangium (unterer Jura)

Gesteine der Scheibelberg-Formation konturieren im Kartiergebiet westlich der Steyr vor allem die Hirschwaldstein-Synklinale zwischen Altpernstein und Hausmanning. Östlich der Steyr bestehen Vorkommen an den teilweise tektonisch verschuppten Rändern der E–W orientierten Koglerstein-Synklinale, der Schreibach-Synklinale sowie der Brettmaisalm-Synklinale. Auch hier sind Maximal-Mächtigkeiten nur abzuschätzen, dürften sich aber im Bereich zwischen 50 und 100 m bewegen. Östlich der Steyr liegen relativ gute, aber lokal eng begrenzte Aufschlüsse der Abfolge an der Fahrstraße von Mandlmais zur Schobersteinhütte sowie am Fahrweg vom Pfaffenboden von Osten auf den Hochbuchberg. Vielerorts wurden nur Lesesteine gefunden, wie entlang des Wanderweges vom Kogler über die Schwalbensteinmauer nach Mandlmais. Auch westlich der Steyr im Kern der Hirschwaldstein-Synklinale sind entsprechende Schichtfolgen nicht allzu gut erschlossen und wurden im Wesentlichen mittels Lesesteindecken kartiert. Allenfalls am unteren Fahrweg von Tragl in ein nördlich vom Rinnerberger Bach abzweigendes Sekundärtal sind Hornstein führende Kalke der Scheibelberg-Formation leidlich aufgeschlossen. Detailliertere Beschreibungen zu Lithologie, fazieller Stellung sowie Altersdatierung finden sich in Hornung (2017a–c).

Klaus-Formation

?Toarcium bis Callovium (unterer bis mittlerer Jura)

Die Klaus-Formation als relativ geringmächtige spät-unterjurassische bis mitteljurassische Fortsetzung der Schwellenfazies der Adnet-Formation ist nur an wenigen Stellen im Kartiergebiet direkt erschlossen und wurde größtenteils mittels Lesesteinen kartiert. Da die Klaus-Formation eine kondensierte Schichtfolge mit vermutlich zahlreichen Sedimentationslücken aufweist, lateral mit den Vilser Kalken und eventuell auch mit der Chiemgau-Formation verzahnt, ist sie oft primär nicht ausgebildet. Die besten Aufschlüsse finden sich innerhalb der Hirschwaldstein-Synklinale etwa 700 m nordöstlich des Hirschwaldstein-Gipfels an der mittleren Forststraße auf der Ostflanke des Berges. Es handelt sich hierbei um dünn- bis mittelbankige rote Knollenkalke, die jedoch etwas mergelreicher als die liegende Adnet-Formation erscheinen.

Die kleinräumigen Vorkommen könnten mit den Klauskalken auf Nachbarblatt 69 Großraming (Egger & van Husen 2011) korrelieren. Die dort gefundenen Ammoniten deuten auf eine relativ große stratigrafische Breite von Toarcium (höherer Unterjura) bis Callovium (höherer Mitteljura) hin.

Neben den auffallend rötlich gefärbten Jurakalken fanden sich noch seltene Schollen von Hierlatzkalken sowie helle Spatkalke vom Typ „Vilser Kalk". Alle bunten Jurakalke (ausgenommen die liegende, bedeutend mächtigere Scheibelberg-Formation) sind subanstehend und äußerst schlecht aufgeschlossen, am ehesten noch mit Lesefunden nachweisbar. Deutlicher sichtbar sind die roten, mergelreichen Kalke (Adneter Schichten, Klauskalk), die zu einem schmierig-lehmigen, schweren, karminroten Boden verwittern und so leicht gefunden werden können. Die Mächtigkeiten betragen vermutlich nur wenige Meter bis allenfalls Zehnermeter.

Chiemgau-Formation

?mittlerer Jura

Sowohl in den hangenden Partien des Hierlatzkalkes, jedoch auch über den hellen Hornstein führenden Mikriten der Scheibelberg-Formation können überwiegend graue bis bräunlichgraue Hornsteinknollenkalke auftreten – die Vorkommen liegen ausschließlich östlich der Steyr innerhalb der Schoberstein-Synklinale und ziehen in schmalen E–W streichenden Bändern – meist Verebnungsflächen –

südlich der Mollner Hütte über die Gaisbergwiesen sowie in Gipfelnähe am Kamm zwischen Koglerstein zum Schoberstein. Auch hier wurden die Ausbisse zumeist mit Lesesteinen und morphologisch eingegrenzt.

Die Mächtigkeit dürfte nur wenige Zehnermeter betragen – ebenso können keine Aussagen über Bankung gemacht werden. Egger & van Husen (2011) inkludieren in die Chiemgau-Formation Einschaltungen von mikritischen Hornsteinknollenkalken und gebankten bis massigen hellen Echinodermatenspatkalken. Die Hornsteinkalke wurden hier als Scheibelbergkalke auskartiert, die hellen Crinoidenspatkalke als Vilser Kalk.

Die kieseligen Kalke der Chiemgau-Formation verwittern zu einem kleinstückigen Grus mit scharfkantigen Komponenten mit bräunlicher bis braungrauer Färbung. Die Böden sind teilweise intensiv braunrot gefärbt und zeigen viele dieser kleinen Kieselsplitter.

Vilser Kalk

mittlerer Jura

Helle Crinoidenspatkalke vom Typ „Vilser Kalk“ bilden östlich der Steyr quasi das morphologisch hervortretende „Rückgrat“ der Hirschwaldstein-Synklinale und den Höhenzug um den Hirschwaldstein. Auch östlich der Steyr ziehen landschaftsmorphologisch als schmale Kämme hervortretende Vorkommen innerhalb der Schoberstein-Synklinale von den Gaisbergweisen bis zu Koglerstein und Schoberstein. In der Schreibach-Synklinale lassen sich die Vilser Kalke auf beiden Faltenschenkeln vom Hochbuchberg bis zum Schreibach verfolgen, werden allerdings dort durch Störungen gekappt und ziehen nicht bis zur Blattgrenze zu GK 69 Großraming durch. Auch in der Brettmaisalm-Synklinale kontieren die Vilser Kalke den Nordschenkel – der Südschenkel ist tektonisch reduziert.

Die Vilser Kalke sind homogene, relativ harte, massig wirkende Crinoidenspatkalke von auffallend heller, grauer bis ockercremefarbener Tönung, die im Gegensatz zu den stets rötlich bis fleischfarbenen Hierlatzkalken steht. Aus diesem Grund wurden beide Lithologien getrennt voneinander auskartiert.

Die Vilser Kalke scheinen mit Rotkalken der Klaus-Formation und tiefermarin abgelagerten Kieselkalken der Chiemgau-Formation zu verzahnen – diese Beobachtung ist allerdings aufgrund des geologisch komplexen, bereichsweise stark verschuppten Aufbaus der Schoberstein-Synklinale lediglich eine Vermutung und kann an keinem Aufschluss im Gelände direkt nachvollzogen werden. Die Mächtigkeiten dürften nicht mehr als 30 m betragen. Geeignete Fossilien für eine biostratigrafische Altersdatierung wurden nicht gefunden.

Mikritooidkalk

Oxfordium (oberer Jura)

Der bis zu 40 m mächtige Mikritooidkalk sensu Moser (2017a) ist trotz seiner relativ geringen Dicke im Kartiergebiet eine wesentliche landschaftsmorphologisch bedeutsame Lithologie, da er aufgrund seiner relativ großen Widerstandsfähigkeit hinsichtlich Erosion in der Regel wandbildend auftritt. Faziell vertritt der im Stirnbereich der Reichraming-Decke sowohl die oberen Bereiche der Klaus-Formation sowie die Ruhpolding-Formation. Die Vorkommen liegen in den Kernbereichen der Synklinalzüge beidseits der Steyr und fungieren als wichtige Gipfelbildner (Hirschwaldstein, Großer Landsberg, Koglerstein sowie Schoberstein).

Beim Mikritooidkalk handelt es sich um einen meistens blass fleischroten, teilweise auch bräunlichen bis hellcremefarbenen, meist massigen bis allenfalls sehr dickbankigen Peloid-Mikrit (< 0,2 mm), aber auch Mikritooidkalk (0,2–0,5 mm). Zur biostratigrafischen Altersdatierung geeignete Fossilien wurden nicht gefunden.

Die Unterscheidung und Abgrenzung vom lithologisch und landschaftsmorphologisch ganz ähnlich ausgebildeten Oberrhätkalk kann gesichert nur durch die im Mikritooidkalk nicht enthaltenen Korallen erfolgen. Da jedoch auch im Oberrhätkalk gut erhaltene und auch als solche erkennbare (!) Korallen selten sind, bleibt oft nur der stratigrafische Zusammenhang. Das Erkennen desselben ist jedoch durch die lithologisch ganz ähnlich ausgebildeten unter- und überlagernden Rotkalke in beiden Fällen (Adnet-Formation beim Oberrhätkalk und Steinmühlkalk beim Mikritooidkalk) zusätzlich erschwert.

Bunte Oberjura-Kalke

Kimmeridgium bis Tithonium (oberer Jura)

Über den Mikritooidkalken folgt in der Regel in den Synklinalkernen beidseits der Steyr eine tektonisierte und stark verfaltete Melange aus diversen Lithologien, deren Vorkommen jedoch zu kleinflächig sind, als dass sie auskartiert werden könnten. Die Oberflächenausbisse ziehen sich in der Hirschwaldstein-Synklinale von Altpernstein nach Nordosten bis unter den Hirschwaldstein und liegen im Norden des Kartiergebietes zwischen Rinnerberg und Furth. Über den Gipfel des Großen Landsberges zieht sich ebenfalls ein schmaler, E–W streichender Ausbiss. Östlich der Steyr treten sie flächig an der Brettmaisalm („Brettmaisalm-Synklinale“) auf und ziehen sich im Kern dieser teilweise tektonisch amputierten Muldenstruktur bis zum Trattenbach.

Die wesentlichen Lithologien dieser Melange sind Steinmühlkalk, Tegernseer Kalk und Ammergau-Formation. In ersteren beiden Fällen handelt es sich um rot, hellrot, rosa bis teilweise grünlich gefärbte dünnbankige, sowohl ebenflächig als auch knollig auftretende Mikrite, seltener Crinoidenspatkalke. Moser (2017a) fand am Forststraßenprofil zwischen Trattenbach und Buchberghütte Calpionellen, mit denen er das oberste Tithonium und damit einen Bereich nahe der Obergrenze des Jura belegen konnte. Sofern sie nicht wie in den Kernen von Hirschwaldstein- und Schoberstein-Synklinale gesondert auskartiert werden konnten, werden in die Melange auch kleinräumig eingeschuppte Ammergauer Schichten in einer grauen und rötlichen Farbvariante gerechnet.

Ammergau-Formation

Tithonium bis Valanginium (oberer Jura bis untere Kreide)

Die Ammergau-Formation bildet zusammen mit den hangenden kretazischen Einheiten die Kernbereiche der teilweise tektonisch amputierten Synklinalen beidseits der Steyr und hat etwa dasselbe Vorkommen wie die Melange der „Bunten Oberjurassischen Kalke“.

Es handelt sich ausschließlich um stark verfaltete, intern verquetschte und zerwürgte Mergelkalke und Kieselkalke. Typisch sind dm-gebankte, zart beige bis grünlichgrau gefärbte, dichte und splittrig brechende Radiolarienmikrite mit vorwiegend glatten Schichtbegrenzungen. Charakteristisch sind weiterhin graue bis bräunliche Kieselknauer, vereinzelt finden sich Aptychenreste, etwas häufiger erscheinen bioturbate Strukturen (Grab- und Wohnbauten von Annelliden o.ä.). Häufig durchziehen bis 1 cm dicke, sparitverheilte Klüfte das Gestein ähnlich einem Spinnennetz.

Das Alter der Formationen-Gruppe geben Piller et al. (2004) mit dem Zeitbereich von Tithonium bis Valanginium an.

Kreide

Schrambach-Formation

Valanginium bis Aptium (Unterkreide)

Die früher als „Neokom-Aptychenschichten" bezeichnete Abfolge der Schrambach-Formation bildet auf der Reichraming-Decke die Synklinalkerne beidseits der Steyr und damit die jüngste Lithologie des diesjährigen Kartiergebietes. Relativ gut erschlossen stehen die mergelreichen Schrambacher Schichten an der Fahrstraße zum Hirschwaldstein nahe dem Nordkamm an. Ein weiterer kleinräumiger Aufschluss im Zentrum zur Schoberstein-Synklinale liegt am Beginn der Fahrstraße von Mandlmais zur Schobersteinhütte. Besonders hervorzuheben, da tektonisch beeindruckend, ist der tektonische Kontakt der Schrambach-Formation im Kern der Brettmaisalm-Synklinale gegen den Hauptdolomit der Hochbuchberg-Scholle.

Die Mächtigkeit der Schrambach-Formation kann aufgrund intensiver Verfaltung nicht sicher angegeben werden, dürfte sich jedoch nur bei einigen wenigen Zehnermetern bewegen. Detailliertere Beschreibungen zu Lithologie, fazieller Stellung sowie Altersdatierung finden sich in Hornung (2017a, 2017c).

Ternberg-Decke

Trias

Opponitz-Formation

Tuvalium (Oberes Karnium)

Östlich der Steyr bildet die Opponitz-Formation auf der Ternberg-Decke oberflächennah die Nordgrenze des Kalkalpins und den steil stehenden Nordschenkel der Rieserberg-Synklinale. Die Deckengrenze verläuft in diesem Bereich von südlich Steyrleithen zum Rutzelbach, weiter nach Oberbrandl und nachfolgend ziemlich genau in östlicher Richtung gegen den Bäckengraben. Vermutlich dürften im Untergrund im Liegenden zur Opponitz-Formation noch mergelreiche Schichten der Lunz-Formation eingeschuppt sein. Der Südschenkel der Rieserberg-Synklinale ist knapp südlich des Rieserberg-Gipfels tektonisch amputiert und von einer steil nach Süden einfallenden Hauptdolomit-Schuppe überschoben, an deren Basis sich gleichfalls ein schmales, E–W streichendes Vorkommen von Opponitz-Formation erhalten konnte. Dieses reicht vom Rieserberg im Westen über den oberen Rutzelbach bis knapp westlich der Passanhöhe Gscheid.

Vom lithologischen Habitus gleicht die Opponitz-Formation jener der südlich überschobenen Reichraming-Decke.

Hauptdolomit-Formation; Hauptdolomit-Formation in kalkiger Ausbildung

Tuvalium (Oberes Karnium) bis Alaunium (Mittleres Norium)

Der Hauptdolomit ist die dominierende Lithologie der in diesem Bereich recht schmalen und zudem stark verschuppten Ternberg-Decke. Er umfasst sowohl die Rieserberg-Synklinale westlich, als auch die Herndleck-Synklinale im Osten. Zudem bildet er die Stirn der Ternberg-Decke im Bereich des Kleinen Landsberges.

Vom lithologischen Habitus gleicht der Hauptdolomit der tiefbajuvarischen Ternberg-Decke weitgehend den Vorkommen der südlich überschobenen Reichraming-Decke, zeigt jedoch einen auffallend hohen Grad an interner Zerlegung und starker Tektonisierung, wenngleich in den Aufschlüssen das Schichtgefüge weitgehend erhalten geblieben ist.

Plattenkalk und Dachsteinkalk

Alaunium bis Sevatium (Oberes Norium)

Der Platten- und Dachsteinkalk konturiert in schmalen, E–W streichenden Ausbissen die beiden Muldenstrukturen der Ternberg-Decke auf Kartenblatt 68 Kirchdorf an der Krems und zieht zusätzlich dazu als schmales Band von der Steyr am Nordhang des Dorngrabens gegen den P. 903 m und keilt dort offenbar im Hauptdolomit aus. Nördlich des Kleinen Landsberges tritt Plattenkalk in zwei relativ schmalen eingeschuppten, NW–SE streichenden Bändern auf.

Vom lithologischen Habitus gleicht die Einheit den Plattenkalken der südlich überschobenen Reichraming-Decke.

Kössen-Formation

Rhaetium

Die Kössen-Formation in mergelig-toniger und kalkiger Ausbildung steht in den beiden Kernen der Rieserberg- und Herndleck-Synklinale an. Während diese im Süden nahe der Überschiebungsfront der Reichraming-Decke noch weitgehend durch Oberrhätkalk vertreten sind bzw. mit diesem verzahnen, vertreten sie im Norden gegen die Überschiebung auf den Rhenodanubischen Flysch zur Gänze das Rhaetium und damit die Obertrias.

Nördlich des Kleinen Landsberges treten die Kössener Schichten lediglich in einem sehr schlecht erschlossenen und nur durch wenige Lesesteine belegten, schmalen NW–SE streichenden Band auf.

Vom lithologischen Habitus gleicht die Kössen-Formation jener der südlich überschobenen Reichraming-Decke.

Jura

Allgäu-Formation

Unterjura

Mergelreiche und Hornstein führende Allgäu-Formation steht in den beiden Kernen der Rieserberg- und Herndleck-Synklinale an, allerdings sehr schlecht aufgeschlossen und nur mit wenigen Handstücken belegt. Die Allgäu-Formation scheint innerhalb der Ternberg-Decke die Scheibelberg-Formation auf der Reichraming-Decke zu vertreten.

Bunte Jurakalke i.A. (tw. als tektonische Melange)

Unterer und Mittlerer Jura

Die lithologische „Sammeleinheit“ Bunte Jurakalke i.A. wurde innerhalb der Ternberg-Decke kartiert, weil in den stark tektonisierten bzw. verschuppten Arealen eine lithologische Auflösung nach einzelnen Lithologie-Gruppen nicht möglich bzw. für das Kartenbild sinnvoll erschien. In den Kernbereichen der verscherten Synklinale am Kleinen Landsberg, im Dorngraben sowie in den beiden Muldenstrukturen am Rieserberg und zwischen Saugraben und Herndleck am östlichen Blattrand (Rieserberg- und Herndleck-Synklinale) fallen rote Knollenkalke vom Typ „Adnet-Formation“ auf und es treten lokal immer wieder rote Mergelkalke und Mergel vom Typ „Klauskalk“ auf.

Neben den auffallend rötlich gefärbten Jurakalken fand sich bei Rohregg noch eine geringmächtige Bank mit hellen Crinoidenspatkalken vom Typ „Vilser Kalk“ unmittelbar unter darüber anstehenden Mikritooidkalken. Weiterhin zu den Bunten Jurakalken wird ein schmaler Span von grau gefärbten Ammergauer Schichten auf der Südseite des Kleinen Landsberges gerechnet. Diese wird beim steilen, teilweise ausgesetzten Anstieg auf den 834 m hohen Gipfel berührt.

Die Mächtigkeiten der einzelnen Schichtglieder sind aufgrund der starken tektonischen Überprägung allenfalls grob anzuschätzen und betragen vermutlich nur wenige Meter bis allenfalls Zehnermeter.

Mikritooidkalk

Oxfordium (oberer Jura)

Auch auf der Ternberg-Decke ist innerhalb der „Bunten Jurakalke“ die landschaftsmorphologisch bedeutsame Lithologie „Mikritooidkalk“ gut auszukartieren. Sie bildet westlich der Steyr in schmalen, NW–SE streichenden Ausbissen schmale Rippen und Kämme, darunter auch den Gipfelkamm des Kleinen Landsberges. Östlich der Steyr bauen sie den Gipfelkamm des Rieserberges auf.

Vom lithologischen Habitus gleichen die Mikritooidkalke jenen der südlich überschobenen Reichraming-Decke.

Kreide

Losenstein-Formation

Oxfordium (oberer Jura)

Die Losenstein-Formation wurde nach KOLLMANN (1968) in Losenstein (ca. 10 km östlich der Blattrandgrenze zu Kartenblatt 69 Großraming) definiert und von WAGREICH (2003) charakterisiert. Obwohl oberflächlich nur unzureichend und in einem verrutschten Ausbiss erschlossen, zieht das Vorkommen als schmales, von West nach Ost streichendes Band vom Bereich zwischen Großem und Kleinem Landsberg westlich der Streyr über den Dorngraben bis zur Westflanke des Krennkogels. Dort wird es durch eine sinistrale Seitenverschiebung nach Norden verschoben und zieht von der Passanhöhe Gscheid zwischen Teufelskirche und Krennkogel den Trattenbach entlang bis zur östlichen Blattgrenze. Die beiden halbwegs guten Aufschlüsse befinden sich am Fuß des Dorngrabens sowie südlich der Grünburger Hütte.

Es handelt sich um braun verwitternde, im frischen Zustand dunkelgraue bis grünlichgraue, relativ feinkörnige harte Sandsteine mit karbonatischer Matrix. Nördlich der Grünburger Hütte sind der Abfolge grünlichgraue Tonmergel-Lagen zwischengeschaltet. Selten kann eine flyschoide Ausbildung mit charakteristischen Wühlspuren gefunden werden. Gegen Osten scheint die erhaltene Abfolge etwas mächtiger zu werden – dennoch konnten die in EGGER & VAN HUSEN (2011) gemachten weiteren lithologischen Beobachtungen nicht bestätigt werden, was aber an der ungenügenden Aufschluss-Situation liegen mag.

Quartär

Pleistozän & Holozän

Einige der im Untersuchungsgebiet kartierten quartären Ablagerungen lassen sich gesichert dem Pleistozän zuordnen: Vermutlich mindelzeitliches Alter haben isolierte Moränenreste im Bereich des Hirschwaldsteins, risszeitliches Alter besitzen isolierte Vorkommen von einem Moränenflecken sowie das kleinräumige Vorkommen von Eisrandsedimenten knapp nördlich des großen Steinbruches Gradau der Fa. Bernegger. Die vor allem im Mollner Becken weit verbreiteten Niederterrassen-Sedimente datieren in das Hochwürm während des letzten glazialen Vereisungsmaximums. In diese haben sich die heutigen Vorfluter Steyr und Krumme Steyrling canyonartig eingeschnitten. Für weitere Informationen siehe HORNUNG (2017a–c, 2018) sowie MOSER (2014a, b, 2017a, b).

Tektonik

Die bereits in vormaligen Kartierberichten (HORNUNG, 2014, 2016, 2017a–c, 2018) beschriebene, durch die nach Norden gerichtete Kompression mit nordgerichteten und nach Süden einfallenden Überschiebungsbahnen von Tirolikum und bajuvarischem Deckensystem mit einem damit einhergehenden kompressiven strikt E–W streichenden Synklinal-Antiklinal-Muster lässt sich vom Landsberg-Massiv bis zur östlichen Blattgrenze von Blatt 69 Großraming konsistent weiterverfolgen. Eine Ausnahme bildet der Hirschwaldstein-Rinnerberg-Zug, dessen Muldenstruktur einen SW–NE streichenden Verlauf hat und damit Parallelen zu den weiter im Osten liegenden Weyerer Bögen (Blatt 69 Großraming) aufweist. Zu ausführlichen Beschreibungen der lokalen Tektonik sei weiters auf die Aufnahmeberichte von MOSER (2014a, b, 2017a, b) sowie MOSER et al. (2016) verwiesen.

Die Abgrenzung der Ternberg-Decke gegen die Reichraming-Decke

Das diesjährige Kartiergebiet umfasst einen kleinen Ausschnitt des Nordrandes der Nördlichen Kalkalpen (NKA) mit der Überschiebungszone auf den Rhenodanubischen Flysch. Wie im westlichen Bereich dieser großtektonischen Einheiten lassen sich im Sinne des Deckenkonzeptes von TOLLMANN (1976) innerhalb des Bajuvarikums mit der liegenden Allgäu-Decke („Tiefbajuvarikum“) und einer tektonisch hangenden Lechtal-Decke („Hochbajuvarikum“) auch im mittleren Abschnitt der Nördlichen Kalkalpen östlich des Salzachtals zwei Decken-Stockwerke voneinander abgrenzen: die tiefbajuvarische Ternberg-Decke und die hochbajuvarische Reichraming-Decke. Jenseits der Weyerer Bögen im östlichen Abschnitt der Nördlichen Kalkalpen spricht man von der tiefbajuvarischen Frankenfels-Decke und der hochbajuvarischen Lunz-Decke. In diesem klassischen Deckenschema (siehe auch in Oberhauser, 1980) werden im zentralen Abschnitt der NKA beide Deckenkomplexe durch die mittelkretazische Losenstein-Synklinale voneinander getrennt.

Gemäß dem neuen Deckenkonzept von Mandl et al. (2017) wird zwar die räumliche Verteilung der Deckenkomplexe nicht infrage gestellt, sehr wohl aber ihre tektonogenetische Zugehörigkeit. Demnach wird die Reichraming-Decke zu tirolischen Einheiten gerechnet und als unterstes tektonisches Stockwerk gezählt, das von der Staufen-Höllengebirge-Decke – hier in der Region definiert mit dem Sengsengebirge-Südabfall – überschoben wurde. Die Ternberg-Decke verbleibt als einzige bajuvarische Decke – an der Unterscheidung zur Reichraming-Decke mittels der Losenstein-Formation hat sich nach derzeitigem Wissensstand nichts geändert.

Die Grenze zwischen Ternberg- und Reichraming-Decke und – nach dem Modell von Mandl et al. (2017) – gleichbedeutend mit der Deckengrenze zwischen Bajuvarikum und Tirolikum, verläuft demnach im Kartiergebiet von der Mulde zwischen Kleinem und Großem Landsberg über die Steyr in den Dorngraben, verlässt diesen im Mittellauf gegen Osten und erreicht nördlich der Grünburger Hütte den Krennkogel. Durch eine dextrale Seitenverschiebung nach Norden versetzt, verläuft sie knapp südlich der Passanhöhe Gscheid unter der Teufelskirche und den Rehböden zum Trattenbach an der Grenze zu Blatt 69 Großraming.

Die Hirschwaldstein-Synklinale und ihre deckentektonische Stellung

Die Hirschwaldstein-Synklinale und angrenzende kalkalpine Gebiete wurden im Jahr 2014 durch Moser (2014b) geologisch aufgenommen und als Revision der Kartierungen von Birkenmayer (1995) bearbeitet. Trotz der damals durchgeführten Detailkartierungen gibt es jedoch Diskussionspunkte, die hier im Folgenden kurz besprochen werden sollen.

Der stark bewaldete Mittelgebirgszug des Hirschwaldsteins bildet eine SW–NE streichende nordwestvergente Synklinale mit jurassischen Schichten im Zentrum und konturierenden obertriassischen Sequenzen. Sowohl Nord- als auch Südschenkel werden durch nach Südost einfallende Überschiebungsbahnen zumindest teilweise amputiert. Mit seiner SW–NE streichenden Anlage folgt die Hirschwaldstein-Synklinale nicht dem allgemeinen Trend von E–W streichenden tektonischen Mulden und Sätteln, die aus der alpinen N–S-Einengung hervorgegangen sind. Sie erinnert in ihrer Grundstruktur eher an das tektonische Großelement der Weyerer Bögen im Osten des Kartenblattes (GK 69 Großraming bzw. GK 70 Waidhofen an der Ybbs). Auch sie zeigen am Kalkalpen-Nordrand eine SW–NE streichende triassisch-jurassische, (tief)bajuvarische Schichtenfolge der Frankenfels-Decke, die bei Großraming auf ein N–S-Streichen nach Süden umbiegt und auf die westlich davon liegenden Einheiten der Reichraming-Decke überschoben wurde. Warum dieses wichtige nordalpine Bauelement der allgemeinen Kompressionsrichtung nicht folgt, ist bis heute nicht endgültig geklärt (u.a. Janda, 2000) – da im eingedrehten Weyerer Bogen paläozäne Gosau-Sedimente überfahren wurden, ist das Bildungsalter zumindest mit Eozän bis Miozän einzugrenzen.

Weil in den Weyerer Bögen als tiefstes tektonisches Element weiters auch die bajuvarische Frankenfels-Decke in die Deformation miteinbezogen wurde, stellt sich die Frage, ob dies auch für die Hirschwaldstein-Synklinale zutrifft und ob sich in der Hirschwaldstein-Synklinale – eingekeilt zwischen Rhenodanubischem Flysch und Reichraming-Decke – ein Fragment der Ternberg-Decke hat erhalten können. Die Arbeiten von Bauer (1953) lassen vermuten, dass der Südostschenkel der Hirschwaldstein-Synklinale mit Unterjura-Hornsteinkalken (Scheibelberg-Formation) über Kössener Schichten konkordant in den Hauptdolomit übergeht und damit zur Reichraming-Decke zu rechnen ist. Moser (2014b) hingegen spricht durch seine Kartierung des Gebietes der Hirschwaldstein-Muldenstruktur eine tektonische Eigenständigkeit und damit eine Zugehörigkeit zur Ternberg-Decke zu. Sein Hauptargument zu diesem Postulat ist die offenbar fehlende Kössen-Formation und damit eine Diskordanz innerhalb der obersten Trias. Auch bei der diesjährigen Kartierung konnten zwischen dem Schwarzbach (Seitenbach des Rinnerberger Baches) und dem Steinkogel keine rhätischen Kössener Schichten gefunden werden. Allerdings erschließt die Straße von Altpernstein zu einem südöstlich davon gelegenen Anwesen Kalke mit Kössener Habitus. Gegen Osten gehen diese in mittel- bis dickbankigen Kalk (Plattenkalk) und stark tektonisierten Dolomit (Hauptdolomit), nachfolgend abermals Plattenkalk und letztendlich in einer morphologisch herauspräparierten Felsrippe in helle Kalke (Oberrhätkalk) und rötliche bis fleischfarbene Crinoidenspatkalke (Hierlatzkalk) über, so dass hier weitgehend eine vollständige und zudem verfaltete Abfolge von der Obertrias bis in den basalen Lias vorliegt. Der tektonische Kontakt von Hauptdolomit-Sequenzen zu den Unterjura-Hornsteinkalken ist zweifelsfrei gegeben, jedoch kann er mit einer einfachen, im Süden E–W verlaufenden, gegen Norden langsam in nordöstliche Richtung umbiegenden, steil nach Südosten einfallenden, lokalen Überschiebungsbahn erklärt werden, der den Südostschenkel der Hirschwaldstein-Synklinale amputiert bzw. deren weiter im Süden flexurell nach WSW aufwärts gebogene Faltenachse mit hier nur tiefjurassischem Muldenkern in nordöstliche Richtung geschoben hat. Aus heutiger Sicht ist somit die Hirschwaldstein-Synklinale zur Reichraming-Decke zu rechnen, wenngleich die Ausbildung von oberjurassischem Mikritooidkalk (= „Reitbauernmauer-Formation“ in Moser, 2017a) anstelle der Ruhpolding-Formation eher untypisch für die Reichraming-Decke erscheint. Nach Moser (2017a) können Mikritooidkalke jedoch im „Hochbajuvarikum“ durchaus vorkommen. Der Hirschwaldstein erschließt eine extrem stark komprimierte triassisch-jurassische Schichtenfolge in einer Art zerscherten Doppel-Synklinale, die dennoch in ihrem stratigrafischen Zusammenhang weitgehend erhalten geblieben ist.

Nach Norden gegen den Rinnerberger Bach tritt unter dem Nordschenkel der Hirschwaldstein-Synklinale wieder Hauptdolomit zutage. Dass die Überschiebungsbahn zumindest in diesem Bereich relativ flach nach Südosten einfallen muss, zeigen insgesamt vier isolierte Klippen aus Mikritooidkalk, die wurzellos auf Hauptdolomit-Abfolgen „schwimmen“, Zwei dieser Klippen liegen östlich des Schwarzbaches, zwei westlich von diesem. Im Rinnerberger Bach wird eine größere dextrale Seitenverschiebung vermutet – der nach Norden anschließende Rinnerberg stellt einen tektonischen, diesmal wieder nordvergenten

Sattel dar („Rinnerberger Antiklinale“), dessen Südschenkel durch diese Lateralstörung amputiert wurde. Dieser ist seinerseits auf eine nordvergente Doppelsynklinal-Struktur überschoben, deren Kernbereich von oberjurassischen Sequenzen gebildet wird und dessen Nord- und Südschenkel gleichfalls tektonisch stark zerschert bzw. zur Gänze amputiert sind. Damit ergeben sich auffallende Parallelen zur Hirschwaldstein-Synklinale und lassen an eine Fortsetzung dieser nach Norden denken – allerdings mit einem in das klassische E–W-Streichen rotierten Verlauf.

Ob hier die Stellung der Doppelsynklinal-Struktur zu einer tiefergelegenen bajuvarischen Ternberg-Decke gerechtfertigt erscheint, ist aufgrund der Parallelen zur weiter südlichen Hirschwaldstein-Synklinale fragwürdig, obgleich die Muldenfüllung aus jurassischen Schichten „wurzelloser“ erscheint als weiter südlich. Zur tektonischen Stellung diskutieren Moser et al. (2016) für diesen Bereich eine Zugehörigkeit zunächst zur Ternberg-Decke, die jedoch in Moser (2017a) wieder revidiert wird und die Synklinal-Struktur nördlich des Rinnerberges zur Reichraming-Decke gestellt wird.

Die Altpernstein-Scholle

Während der Kartierung wurden Anfang August 2019 bei Leitungsarbeiten knapp südöstlich der Burg Altpernstein graue bis graublaue mergelige Schichten mit zum Teil dezimetermächtigen Kohleflözen erschlossen. Zunächst wurde gemutmaßt, ob es sich hier um ein neogenes Glanz-Braunkohle-Vorkommen handeln könnte, das sich – eingequetscht zwischen mesozoischen Schichtenfolgen – durchaus hätte erhalten können. Die Inaugenscheinnahme vor Ort jedoch ergab, dass die graublauen Mergel mit orangefarbenen Bestegen Ähnlichkeit mit der obertriassischen mergelig-tonig ausgebildeten Lunz-Formation haben, wenngleich diese normalerweise etwas dunkler gefärbt in der Region auftritt. Jedoch sind Kohlevorkommen innerhalb der Lunz-Formation durchaus möglich (Typlokalität in Lunz), jedoch aus der Region noch nicht beschrieben. Zur Sicherheit wurden sowohl aus den Kohleflözen, als auch aus den grauen Mergeln Proben genommen und zur biostratigrafischen Einstufung an die GBA übersandt.

Sollte sich die Vermutung bestätigen, dass die Mergel und die Kohle kein neogenes, sondern ein obertriassisches Alter haben, ist auch die stratigrafische Stellung der Kalkklippe zu überdenken, auf der die Burg Altpernstein steht. Die in Moser (2014b) postulierte Stellung zum Mikritooidkalk erscheint aufgrund des lithologischen Habitus – schlecht gebankt, feinklüftig und von hellgrauer bis weißlichgrauer Färbung – als nicht zwingend erforderlich. Die in dieser Gegend überlieferten Mikritooidkalke zeigen fast durchwegs eine fleischfarbene Färbung. Sollte es sich bei den Mergeln und dem Kohleflöz tatsächlich um Teile der Lunz-Formation handeln, könnte die Kalkklippe von Altpernstein den hangenden Teil der Wetterstein-Formation repräsentieren. Der hohe Tektonisierungsgrad dürfte der Position unmittelbar an der Deckenstirn südöstlich des überschobenen Rhenodanubischen Flyschs geschuldet sein. Interessant ist in diesem Zusammenhang die kurze Notiz in Moser (2014a), der einen Lesestein mit Dasygladaceen, Crinoiden und Gastropoden unweit nördlich der Burg Altpernstein richtig als zum Oberen Abschnitt der Wetterstein-Formation (Alter Julium 1) zugehörig beschreibt. Hier werden die Datierungsergebnisse der GBA abzuwarten sein, um endgültige Aussagen hinsichtlich Stratigrafie und tektonischer Stellung der kleinräumigen Scholle zur Diskussion stellen zu können. Aus heutiger Sicht erscheint eine Zugehörigkeit der Altpernstein-Scholle mit Wetterstein- und Lunz-Formation zumindest tektonisch möglich, da die gegen Norden aufgebogenen Hauptdolomit-Sequenzen im Nordwesten der Hirschwaldstein-Synklinale an deren Basis noch Opponitz- und Lunz-Formation vermuten lassen.

Das Landsberg-Massiv

Das Mittelgebirge-Massiv Großer und Kleiner Landsberg wird durch die Losensteiner Mulde zwischen den beiden Gipfel zweigeteilt. Der Anteil der Ternberg-Decke stellt eine NNE-vergente, teilweise intern verschuppte, intensiv verfaltete Abfolge obertriassischer bis oberjurassische Lithologien dar. Am augenscheinlichsten ist die E–W streichende Rippe aus Mikritooidkalken, die den Gipfelkamm des Kleinen Landsberges aufbauen.

Wie bereits in Moser et al. (2016) beschrieben, ist die Westflanke des Großen Landsberges eine NNW-vergente Antiklinale, wenn auch hier von einer Hauptscherbahn (dextrale Seitenverschiebung südlich des Gipfelkammes) zerlegt und tektonisch amputiert. Am Nordschenkel reicht die Abfolge nur bis zur Opponitz-Formation, während hingegen der Südschenkel teilweise unter vermutlich tektonisch reduziertem Hauptdolomit über erhaltenem Oberrhätkalk bis zur Reifling-Formation im Kern reicht und damit die Gaisberg-Antiklinale übergeht. Während sich dieses wichtige Strukturelement über die Steyr nach Osten fortsetzen lässt, wird die Landsberg-Schuppe ostwärts durch eine lokale Scherbahn und der Grenze zur Ternberg-Decke überfahren und tritt nicht mehr zutage. Interessant ist am Großen Landsberg der schon in Moser et al. (2016) beschriebene Gipfelkamm aus Mikritooidkalken, der wurzellos von Hauptdolomit umgeben ist. Knapp östlich des Großen Landsberg-Hauptgipfels sind noch geringmächtige dünnbankige und Hornstein führende Kalke der Ammergau-Formation sowie Steinmühlkalke erschlossen, die dieser isolierten Oberjura-Scholle die Struktur einer kleinen Synklinale geben. Der Frage der Herkunft der Mikritooidkalke auf Hauptdolomit wird in Moser et al. (2016) leider nicht nachgegangen. Erwähnenswert in diesem Zusammenhang wäre ein schmaler, ebenfalls W–E streichender Kamm aus Mikritooidkalk, der die Stirn der Reichraming-Decke vor der Losenstein-Formation der Ternberg-Decke bildet und der als mögliche „Wurzelzone“ der isolierten Scholle auf dem Landsberg-Gipfel in Frage kommt. Diese wäre dann im Zuge der Deckenüberschiebung als „out-of-sequence-thrust“ auf Hauptdolomit-Folgen abgeschert und sich relikthaft am Großen Landsberg erhalten.

Der Schuppenbau innerhalb des Gaisberg-Schoberstein-Höhenzuges

Das Mittelgebirge nördlich des Tals der Krummen Steyrling lässt sich übersichtsmäßig als eine nordvergent verfaltete Obertrias- bis Oberjura/Unterkreide-Abfolge beschreiben. Die wichtigen Faltenzüge sind die Gaisberg-Antiklinale und die Schreibach-Synklinale. Erstere lässt sich von Schmiedleithen südlich des Großen Landsberges über die Steyr nach Osten verfolgen und endet aufgrund eines gegen Osten wirksamen flexurellen Abtauchens der

Faltenachse östlich des Pfaffenbodens. An diese Flexur gebunden ist der Ausbiss der etwas nördlich gelegenen Schreibach-Synklinale, deren Nordschenkel im Westen und Südschenkel im Osten partiell zerschert sind. Weiter nach Norden werden diese beiden Strukturelemente auf oberjurassische-unterkretazische Jungschichten der Brettmais-Scholle überschoben. Diese stellt ihrerseits eine im Nordschenkel weitgehend erhaltene Synklinalstruktur an der Stirn der Reichraming-Decke in diesem Bereich dar.

Interessant ist der interne Bau dieses Höhenzuges. Die Gaisberg-Antiklinale erscheint mit ihrem Kern aus Wettersteinkalken als ein extrudierter Block, der beidseits von Synklinalen mit Jungschichten umgeben ist.

Dieselbe Beobachtung machte bereits Spengler (1959), der von einer *„steil aus der Tiefe aufsteigenden Schuppe“* sprach, allerdings nicht wirklich von einer Faltenstruktur sprach (siehe auch Moser, 2014b). Während die Brettmaisalm-Synklinale nördlich der Gaisberg-Antiklinale eine verfaltete, aber weitgehend konkordante Schichtenfolge von der Obertrias bis in den Oberjura zeigt, erscheint die südlich lagernde, hier als Koglerstein-Synklinale bezeichnete Struktur stark zerschert bzw. verschuppt. Wie bereits in Moser (2014b) angedeutet, lässt sich der Geländebefund im konstruierten Profil durchaus mit einer im Bereich der Scheibelberg-Formation flach abgescherten Teilschuppe erklären, deren Abfolge – jedoch nur gering disloziert – bis in die Ammergau-Formation reicht. Für weitere, detailliertere Ausführungen zur Tektonik sei auf Moser (2014b) verwiesen.

Literatur

Birkenmajer, K. (1995): Geological Map 1:10.000 Kartenblatt Kirchdorf an der Krems (Oberleonstein, Wienerweg, Hambaum, Rinnerberger Bach, Steyrdurchbruch, Landsberg). – 1 Blatt, Polish Academy of Sciences/Institute of Geological Sciences, Krakau.

Bauer, F. (1953): Der Kalkalpennordrand zwischen Krems- und Steyrtal in Oberösterreich 1:12.500. – 1 Blatt, Wien.

Braunstingl, R. & Egger, J. (1985): Geologische Karte der Flysch-Zone und des Kalkalpenrandes beiderseits der Enns (zwischen Steyrtal und Pechgraben, Oberösterreich). – Unveröffentlichte geologische Karte 1:25.000, Geologische Bundesanstalt, Wien.

Egger, H. (2007): Erläuterungen zur Geologischen Karte der Republik Österreich 1:50.000, Blatt 67 Grünau im Almtal. – 66 S., Geologische Bundesanstalt, Wien.

Egger, H. & van Husen, D. (2007): Geologische Karte der Republik Österreich 1:50.000, Blatt 67 Grünau im Almtal. – Geologische Bundesanstalt, Wien.

Egger, H. & van Husen, D. (2011): Geologische Karte der Republik Österreich 1:50.000, Blatt 69 Großraming. – Geologische Bundesanstalt, Wien.

Hornung, T. (2007): The ‚Carnian Crisis‘ in the Tethys realm – multistratigraphic studies and palaeoclimate constraints. – Dissertation, Universität Innsbruck, 233 S., Innsbruck.

Hornung, T. (2014): Bericht 2013 über geologische Aufnahmen im Gebiet Steyrling–Kremsmauer auf Blatt 4201 Kirchdorf an der Krems. – Jahrbuch der Geologischen Bundesanstalt, **154**, 343–353, Wien.

Hornung, T. (2016): Bericht 2014 über geologische Aufnahmen im Gebiet Kienberg und Klaus (Oberösterreichische Voralpen / Sengsengebirge) auf Blatt NL 33-02-01 Kirchdorf an der Krems. – Jahrbuch der Geologischen Bundesanstalt, **156**, 318–326, Wien.

Hornung, T. (2017a): Bericht 2015 über geologische Aufnahmen im Gebiet Schillereck (Oberösterreichische Voralpen / Sengsengebirge) auf Blatt NL 33-02-01 Kirchdorf an der Krems. – Jahrbuch der Geologischen Bundesanstalt, **157**, 387–400, Wien.

Hornung, T. (2017b): Bericht 2016 über geologische Aufnahmen im Gebiet Breitenau (Oberösterreichische Voralpen / Sengsengebirge) auf Blatt NL 33-02-01 Kirchdorf an der Krems. – Jahrbuch der Geologischen Bundesanstalt, **157**, 401–412, Wien.

Hornung, T. (2017c): Bericht 2017 über geologische Aufnahmen im Gebiet Hoher Nock (Oberösterreichische Voralpen / Sengsengebirge) auf Blatt 68 Kirchdorf an der Krems. – Jahrbuch der Geologischen Bundesanstalt, **157**, 340–353, Wien.

Hornung, T. (2018): Bericht 2018 über geologische Aufnahmen im Gebiet Weißenbach (Oberösterreichische Voralpen / Totes Gebirge) auf Blatt 68 Kirchdorf an der Krems. – Jahrbuch der Geologischen Bundesanstalt, **158**, 120–129, Wien.

Janda, C. (2000): Geologisch-fazielle Untersuchungen in der Lunzer Decke südwestlich von Weyer (Oberösterreich). – Unveröffentlichte Diplomarbeit, Universität Wien, 104 S., Wien.

Kollmann, H.A. (1968): Zur Gliederung der Kreideablagerungen der Weyerer Bögen (OÖ.). – Verhandlungen der Geologischen Bundesanstalt, **1968**, 126–137, Wien.

Krenmayr, H.-G., Schnabel, W. & Reitner, J. (2006): Geologische Karte von Oberösterreich 1:200.000. – Geologische Bundesanstalt, Wien.

Mandl, G., Brandner, R. & Gruber, A. (2017): Zur Abgrenzung und Definition der Kalkalpinen Deckensysteme. – Teilprojekt zu TEKDAT200. – Arbeitstagung 2017 – Angewandte Geowissenschaften an der GBA, 19.–22. Juni 2017, Bad Ischl, Hallstatt, Gmunden, 254–255, Geologische Bundesanstalt, Wien.

Moser, M. (2014a): Bericht 2014 über geologische Aufnahmen im Gebiet Leonstein–Oberleonstein–Hambaum–Riedberg–Plan–Steinkogel–Ochsenkogel auf Blatt 4201 Kirchdorf an der Krems. – Jahrbuch der Geologischen Bundesanstalt, **154**, 353–354, Wien.

Moser, M. (2014b): Bericht 2014 über geologische Aufnahmen des Hirschwaldstein-Zuges der Ternberg-Decke zwischen Micheldorf und Molln auf Blatt 4201 Kirchdorf an der Krems. – Jahrbuch der Geologischen Bundesanstalt, **154**, 354–357, Wien.

Moser, M. (2017a): Bericht 2016 über geologische Aufnahmen im Gebiet Gradau, Dorngraben, Dürres Eck, Gaisberg, Gaisbergwiesen, Pfaffenboden, Mandlmais, Koglerstein, Schoberstein, Sonnseite, Roßberg auf Blatt NL 33-02-01 Kirchdorf an der Krems. – Jahrbuch der Geologischen Bundesanstalt, **157**, 412–423, Wien.

Moser, M. (2017b): Reitbauern-Formation: Biostratigrafische und lithostratigrafische Neudefinition des „Mikritooidkalkes“ im Bajuvarischen Deckensystem (Nieder- und Oberösterreich). – Jahrbuch der Geologischen Bundesanstalt, **157**, 173–193, Wien.

Moser, M., Elster, D., Lukeneder, A., Rehakova, D. & Ćorić, S. (2016): Bericht 2015 über geologische Aufnahmen im Gebiet Kleiner und Großer Landsberg, Schauderzinken, Rabenstein, Sonnkogel, Krautige Eben, Rinnerkogel und Plachwitz auf Blatt NL 33-02-01 Kirchdorf an der Krems. – Jahrbuch der Geologischen Bundesanstalt, **156**, 326–335, Wien.

Oberhauser, R. (1980): Der geologische Aufbau Österreichs. – 695 S., Wien (Springer).

PILLER, W., EGGER, H., ERHART, C.W., GROSS, M., HARZHAUSER, M., HUBMANN, B., VAN HUSEN, D., KRENMAYR, H.-G., KRYSTYN, L., LEIN, R., LUKENEDER, A., MANDL, G.W., RÖGL, F., ROETZEL, R., RUPP, C., SCHNABEL, W., SCHÖNLAUB, H.P., SUMMESBERGER, H., WAGREICH, M. & WESSELY, G. (2004): Die stratigraphische Tabelle von Österreich 2004 (sedimentäre Schichtfolgen). – Österreichische Akademie der Wissenschaften und Österreichische Stratigraphische Kommission, Wien.

RUPP, C., LINNER, M. & MANDL, G.W. (2011): Erläuterungen zur Geologischen Karte von Oberösterreich 1:200.000. – 255 S., Geologische Bundesanstalt, Wien.

SPENGLER, E. (1959): Versuch einer Rekonstruktion des Ablagerungsraumes der Decken der Nördlichen Kalkalpen. III. Teil: Der Ostabschnitt der Kalkalpen. – Jahrbuch der Geologischen Bundesanstalt, **102**, 193–312, Wien.

TOLLMANN, A. (1976): Monographie der Nördlichen Kalkalpen. Teil III: Der Bau der Nördlichen Kalkalpen: Orogene Stellung und regionale Tektonik. – IX + 449 S., Wien (Deutike).

VAN HUSEN, D. (2017): Quartärgeologische Karte von Kirchdorf a.d. Krems. – Unveröffentlichte Geologische Manuskriptkarte 1:25.000, Geologische Bundesanstalt, Wien.

WAGREICH, M. (2003): A slope-apron succession filling a piggyback basin: the Tannheim and Losenstein Formations (Aptian – Cenomanian) of the Eastern part of the Northern Calcareous Alps (Austria). – Mitteilungen der Österreichischen Geologischen Gesellschaft, **93**, 31–54, Wien.

Blatt 90 Kufstein

Bericht 2019 über geologische Aufnahmen in der Grauwackenzone auf den Blättern 90 Kufstein und 121 Neukirchen am Großvenediger

HELMUT HEINISCH & CLAUDIA PANWITZ

(Auswärtiger Mitarbeiter und Auswärtige Mitarbeiterin)

Im Zuge der Fertigstellung von Blatt 121 Neukirchen war es notwendig, Lücken in der Aufnahme im Grenzbereich zu Blatt 90 Kufstein zu schließen. Aus Gründen der Zugänglichkeit bot es sich an, auch die noch nicht kartierten Bereiche von Blatt Kufstein mit zu bearbeiten. Die Aufnahme dieses Bereiches oblag dem verstorbenen GERHARD PESTAL. Der Bearbeitungsstand war uns in Farbkopien zur Verfügung gestellt worden. Für den Anteil von Neukirchen liegt bereits eine digitalisierte Version vor. Die Analyse der Daten zeigte Unstimmigkeiten und geologisch nicht sinnvolle Grenzverläufe im digitalen Datensatz. Dies machte umfangreichere Geländekontrollen notwendig. Ziel war eine in sich kohärente, blattschnittübergreifende Kartendarstellung im Maßstab 1:25.000.

Das zu kontrollierende und in Teilen neu aufzunehmende Gebiet umfasst 50 km^2. Es ist etwa hälftig zwischen den beiden Autoren aufgeteilt. Die Nomenklatur der Gesteine und die Farbwahl folgen der Generallegende, wie sie für die Manuskriptkarten von Blatt 123, 122, 121 und 120 benutzt wurde (HEINISCH et al., 2015). Petrografische Beschreibungen und die Kriterien zur Definition der tektonischen Großeinheiten wurden analog beibehalten (HEINISCH, 1986).

Umgrenzung des Bereichs

Beim Untersuchungsgebiet handelt es sich über weite Strecken um einen eher flachen Gebirgszug, der das Tal von Söll-Ellmau vom Brixental trennt, zuzüglich des Hohe Salve-Stocks. Im Norden folgt die Grenze dem Beginn der quartären Bedeckung, von Stampfanger über Blaiken bis Ellmau-Going. Im Süden liegt die Grenze zunächst am Rand der Talsohle des Hohe-Salve-Gebietes, um dann nach Norden über den Zinsberg zum Hartkaser zu verschwenken.

Das Gebiet wird intensiv forstlich und skitouristisch genutzt. In flachen Bereichen herrschen schlechte Aufschlussverhältnisse. In den Waldgebieten sind die Bedingungen ebenfalls suboptimal, die Bäche sind zum Teil überraschend schwer begehbar (s.u.).

In Zonen mit kleinteiliger Geologie ist das Gebiet daher als anspruchsvoll zu bezeichnen.

Neu gezeichnet wurden auf Blatt Neukirchen, wie vereinbart, nur die Bereiche, in denen Änderungen vorzunehmen sind. Auf Blatt Kufstein wurde der gesamte Festgesteinsanteil neu gezeichnet. Die Quartärpolygone liegen bereits digital vor und wurden entsprechend übernommen.

Probleme bei der Bearbeitung

Es zeigte sich bei der Geländearbeit, dass die Fehlstellen in der Aufnahme vor allem sehr ungünstigen Relief-Verhältnissen geschuldet waren. Diese waren aus dem Kartenbild zunächst nicht unbedingt erkennbar. Die Steilgräben im Bereich Nieringerwald/Hirschenalm und Breuergraben werden in den entscheidenden Bereichen nicht durch Forstwege oder Jagdsteige gequert. Sie mussten daher direkt im Bachlauf angegangen werden, was wiederum durch Wasserfallstufen erschwert wurde.

Bei der Kontrolle der digitalisierten Polygone (Blatt Neukirchen) stellte sich heraus, dass bei der Übertragung aus den Manuskriptkarten offensichtlich Farbverwechslungen aufgetreten sind. Dies bezieht sich zum einen auf Rot/Braun-Töne. Dadurch wurden siliziklastische Gesteine der Löhnersbach-Formation mit Blasseneck-Porphyroid verwechselt. Andererseits gab es Verwirrung innerhalb der zahlreichen Grüntöne der Metabasit-Folgen.

Dies zog sonderbare Grenzziehungen nach sich, wie z.B. geradlinig quer zum Streichen durchtrennende Grenzen, die geologisch eine Störung bedeuten würden, aber Artefakte der Digitalisierung darstellen. Es ist offensichtlich, dass die digitale Version in manchen Bereichen nicht mehr durch den Autor mit geologischem Sachverstand kontrolliert werden konnte.

Beschreibung der Zone zwischen Stampfanger und Modereralm

Das Gebiet ist in zwei verschiedene Bereiche zu untergliedern:

Bereich 1: Im Liegenden und im Ostteil besteht die Lithologie aus monotonen Wechselfolgen von Löhnersbach- und Schattberg-Formation. Diese fallen mittelsteil bis flach gegen den Hang ein und streichen durchschnittlich West–Ost. Die Raumlage schwankt kleinräumig, was einer kleinskaligen Faltung geschuldet ist. Lokal ist mit Verstellungen durch Massenbewegungen zu rechnen.

Bereich 2: Im Hangenden, insbesondere zwischen Köpfing/Nieringerwald und Blaiken/Bromberg tritt ein kleinteiliger Wechsel von Gesteinen auf. In einer Matrix aus Löhnersbach-Formation schwimmen Schollen von Spielbergdolomit, Bankkalken, Kieselschiefern und Dolomit-Kieselschieferkomplex. Hinzu tritt ein in der Mächtigkeit stark schwankender Zug von Blasseneck-Porphyroid. Innerhalb des Porphyroides treten Lagen von Jausern-Formation auf. Der ordovizische Porphyroidkomplex wird streichend von einer Metabasit-Wechselfolge abgelöst. Diese enthält im engen Lagenwechsel Metabasalte, aber auch Metapyroklastika und Tuffite. Aufgrund des Darstellungsmaßstabs von 1.25:000 musste hier stark generalisiert werden.

Aufgrund der Lithologie und der Art der internen Gesteinsgrenzen ist es plausibel, den Bereich 2 der Olistholith-Zone (Hochhörndler Schuppenzone) zuzuordnen, während der monotonere Bereich 1 zur Glemmtal-Einheit Nord zu stellen ist. Grenzkriterium ist der letzte auftretende Olistholith. Grafisch ist zu beachten, dass die Olistholithe mit runden Grenzen in der Schiefermatrix einzutragen sind, während spitzwinkelig auslaufende Grenzen synsedimentäre Verzahnungen symbolisieren.

Dieser im Durchschnitt West–Ost verlaufende Komplex wird durch Nord–Süd bis NNW–SSE verlaufende Sprödstörungen nochmals zerhackt und kulissenartig verschoben. Soweit feststellbar, herrscht ein sinistraler Schersinn vor. Die Verwerfungen spalten in Sekundärstörungen auf und verlaufen nicht notwendigerweise genau im Bachtiefsten.

Beschreibung der Zone um Hochlechen und Oberberg

Der Bereich ist durch weitflächige Grundmoränenbedeckung geprägt. Im Festgestein ist die Grenze zwischen permotriadischen Rotsedimenten und Grauwackenzone aufgeschlossen. Die Grauwackenzone wird durch einen mächtigen Metabasit-Zug repräsentiert, der eine Wasserfallstufe bildet. Es handelt sich durchwegs um Pyroklastika, die eine interne Kleinfaltung zeigen. Basaltlaven treten nicht auf. Die Metabasite sind in Siliziklastika vom Typ Löhnersbach-Formation eingelagert.

Die postvariszischen Rotsedimente bestehen aus feinkörnigen, dm-bankigen Sandsteinen, wechsellagernd mit roten Siltsteinen. Tendenziell ähneln sie eher dem unteren Alpinen Buntsandstein als der Gröden-Formation. Dies sollte in den Manuskriptkarten des Buntsandstein-Kartierers (Volkmar Stingl) nochmals überprüft werden. In der Kompilation ist derzeit die Farbe für Gröden-Formation eingetragen.

Der Kontakt zur Grauwackenzone ist gestört. Die Verwerfung läuft W–E und steht weitgehend senkrecht. Sie ist nirgendwo direkt aufgeschlossen. Aufgrund des Grenzverlaufs ist ein leichtes Südfallen anzunehmen. Jüngere Querstörungen versetzen die Grenze zwischen Breuergraben und Tiefenbach mit sinistralem Versatz von etwa 350 m nach Norden. Der einzige gewinnbare Messwert innerhalb der Rotsedimente zeigt eine Steilstellung und Rotation des Blocks gegen die Störung an.

Damit lässt sich alleine für die alpidische Zeit eine mehrphasige Sprödtektonik herleiten.

Die postvariszischen Decksedimente wurden durch Extension zunächst grabenartig eingesenkt, analog zu Strukturen wie z.B. am Hahnenkamm (Heinisch et al., 2003, 2015). Danach kam es zu einer nordgerichteten Überschiebung der Grauwackenzone auf die Rotsedimente. Dies erklärt das Fehlen der Basisbrekzie und gegebenenfalls der Gröden-Formation. Einen letzten Akt stellen die Sprödstörungen dar. Je nachdem, ob man die roten Sandsteine dem Perm oder der Untertrias zuordnet, variiert die zu fordernde Sprunghöhe an der tektonischen Grenze.

Beschreibung eines Kleinbereichs südlich der Talstation der Hartkaserbahn/Ellmau

Aufgrund unklarer Farbgebung in den verschiedenen Manuskriptkarten-Versionen wurde der Bereich nochmals aufgenommen. Es handelt sich um eine Wechselfolge zwischen Löhnersbach-Formation, Metapyroklastika und Tuffitschiefern. Die Raumlage variiert im Kleinbereich sehr stark. In der Summe kommt ein umlaufendes Streichen um den Hügel südlich der Hartkaserbahn zu Stande. Der kleinräumige Lagenwechsel war selbst im Aufnahmemaßstab 1:10.000 nicht mehr darstellbar. Entsprechend generalisiert ist die Darstellung im Maßstab 1:25.000. Die Privathäuser im Weißachgraben grenzen unmittelbar an schroffe Felsen an, wandbildend sind die Metapyroklastika. In den kleinen Erosionsrinnen am Südrand des Blattes sind Schwarzschiefer sowie eine Gabbro-Intrusion zu vermerken.

Beschreibung der Zone um Hacha/Hopfgarten

In den steilen Bachgräben oberhalb des Zentrums von Hopfgarten am Fuß der Hohen Salve treten komplizierte geologische Verhältnisse zu Tage. Bei weitgehend horizontaler Raumlage wechseln mehrfach Löhnersbach-Formation, basaltische Tuffitschiefer und dünne Porphyroidlagen miteinander ab. In der Schiefermatrix schwimmen zusätzlich Schollen aus Spielbergdolomit. Hangend folgt dann das km-mächtige Paket aus Porphyroid, welches Richtung Gipfel der Hohen Salve von einem ebenso mächtigen Paket aus Spielbergdolomit streichend abgelöst wird.

Wegen der Grenzziehung zur Olistholith-Zone wurden die Details nochmal nachgesehen. Es ist plausibel, hier die Basis der Wildseeloder-Decke festzulegen, welche als Klippe hangend auf der Olistholith-Zone (Hochhörndler Schuppenzone) auflagert. Kennzeichen sind sowohl mächtiger Blasseneck-Porphyroid, als auch mächtiger Spielbergdolomit. Die Wildseeloder-Decke kann intern ebenfalls verschuppt sein, sodass der primär stratigrafische Verband nicht mehr gewährleistet ist. Es wird vorgeschlagen, den Bereich der Hohen Salve als isolierten Deckenrest zu interpretieren, der, unterbrochen von Olistholith-Zone, die tektonische Fortsetzung des Porphyroids vom Rauhen Kopf darstellt.

Weiteres Vorgehen

Da im vorliegenden Datensatz die tektonischen Grenzen fehlen, ist eine Endkontrolle der Konturen nicht möglich. Es wird daher notwendig sein, nach Einpflegen unserer Aufnahmen eine weitere Kontrolle durchzuführen. Da auch immer wieder Farbverwechslungen vorkamen, wird dies recht zeitaufwendig erfolgen müssen. Es wird vorgeschlagen, dies nicht mit Farbkopien, sondern unter Zugrundelegung der Originalmanuskripte von Gerhard Pestal durchzuführen. Eine einheitlich nummerierte Legende ohne Reste von Geofast-Bezeichnungen ist unerlässlich.

Literatur

HEINISCH, H. (1986): Die Geologie der Nördlichen Grauwackenzone zwischen Kitzbühel und Zell am See und ihre Bedeutung für die Rekonstruktion der altpaläozoischen Geodynamik des Ostalpenraumes. – Habilitationsschrift, Universität München, X + 291 S., München.

HEINISCH, H., PESTAL, G., REITNER, J. & STINGL, V. (2003): Geologische Karte der Republik Österreich 1.50.000, Blatt 122 Kitzbühel. – 1 Blatt, Geologische Bundesanstalt, Wien.

HEINISCH, H., PESTAL, G. & REITNER, J. (2015): Geologische Karte der Republik Österreich 1:50.000, Erläuterungen zu Blatt 122 Kitzbühel. – 301 S., Geologische Bundesanstalt, Wien.

Blatt 103 Kindberg

Bericht 2018 über geologische Aufnahmen südlich des Mürztales auf Blatt 103 Kindberg

JOSEF NIEVOLL

(Auswärtiger Mitarbeiter)

In Fortführung der Aufnahmen im Jahr 2017 (NIEVOLL, 2018) wurden die Südostecke des Kartenblattes von Kindberg nach Osten sowie die Gölkschneid neu aufgenommen; die lithologischen Grenzen des 2017 aufgenommenen Gebietes im Bereich der Stuhleck-Kirchberg-Decke wurden nach Dünnschliffuntersuchungen und zusätzlichen Begehungen zum Teil modifiziert.

Rabenwald-Decke: Die Traibachschiefer vom Freßnitzgraben konnten nach Westen bis zum Nordabhang des Fürhauptkogels verfolgt werden. Zunehmende Zerscherung der subhorizontalen Gneistextur durch eine jüngere, steilstehende Schieferung und damit einhergehende Phyllonitisierung ist an der Straße am Ausgang des Freßnitzgrabens zwischen Gölksiedlung und dem ehemaligen Fh. Orgovany zu beobachten. Am südlichen Blattrand treten Traibachschiefer am Geländerücken südöstlich Jh. Schwaighof und in größerer Verbreitung am Nordabfall der Stanglalpe auf; letzteres Vorkommen ist bereits CORNELIUS (1936) aufgefallen und zieht sich bis zum Jahn-Denkmal herunter. Beide Vorkommen führen in Gängen feinnadeligen Turmalin; eine 2017 entnommene Probe vom Rotriegel wurde röntgendiffraktometrisch als Foitit bestimmt.

Mürz-Tachenberg-Decke: Die Grenze der Rabenwald-Decke zur Mürz-Tachenberg-Decke der Gölkschneid verläuft von der Gölksiedlung in ESE-Richtung über das Wetterkreuz zum Gölkbauern (hier mit kräftiger Quelle) und weiter in gerader Linie in den Freßnitzgraben. Am östlichen Blattrand wird der Nordhang des Freßnitzgrabens von Semmeringquarzit aufgebaut, der Südhang von Traibachschiefern; für einen präalpidischen Untergrund der Mürz-Tachenberg-Decke ist hier kein Platz vorhanden. Im Westen wird die Gölkschneid an einer NNW–SSE verlaufenden Störung abgeschnitten, die im ehemaligen Steinbruch Posch oberhalb der Gölksiedlung freigelegt ist. Die Grenze zum Neogen des Mürztales im Norden ist ebenfalls störungsbedingt, wie aus der Höhen- und Reliefkarte des Digitalen Atlas der Steiermark (www.gis.steiermark.at) ersichtlich ist; in streichender Verlängerung war diese Störung 1984 östlich der Alplstraße auf Blatt 104 Mürzzuschlag aufgeschlossen (NIEVOLL, 1985). Die permotriassischen Gesteine der Gölkschneid werden somit im Westen, Norden und Süden durch steilstehende Störungen begrenzt. Der Semmeringquarzit am Südabfall der Gölkschneid ist tektonisch in mehrere Schollen mit unterschiedlicher Lagerung zerlegt. Der Kammbereich der Gölkschneid wurde in den letzten Jahren durch Forstwege aufgeschlossen: Südabfall, Kammbereich und Nordabfall bis etwa 900 bis 1.000 m Seehöhe werden von meist dunkelblaugrauen, plattigen Kalkmarmoren aufgebaut, die lokal hellrosa Lagen und Schlieren, sowie Dolomitknollen führen. Der Nordabfall unterhalb 900 bis 1.000 m Seehöhe besteht überwiegend aus hellgrauen Dolomitmarmoren, in denen nur selten die primäre Lagerung zu messen ist. Die primäre Lagerung in den Karbonaten ist meist flach bis sehr flach, die Achsen streichen ENE–WSW und weichen damit deutlich von den flach nach ESE fallenden Achsen in den südlich angrenzenden Phylloniten der Rabenwald-Decke ab. Die Karbonate werden von zahlreichen Störungen mit zum Teil dm-dicken Reibungsbrekzien durchsetzt, zum Teil sind in offenen Spalten auf den Störungsflächen cm-dicke Kalksinter aufgewachsen. Wie die neuen Forstwege zeigen, ist die löchrige Erscheinung der Rauwacken eine oberflächennahe Verwitterungsbildung, sowohl auf Kalk- als auch auf Dolomitmarmoren. Es handelt sich um tektonische Brekzien und nicht um sedimentäre Bildungen in einer bestimmten stratigrafischen Einheit. Westlich vom Freßnitzgraben sind dunkelblaugraue Kalkmarmore in geringmächtigen Linsen südlich Grund und im Obstgarten vom Zaschenbauer oberflächlich aufgeschlossen; in größerer Mächtigkeit dürften die Karbonate der Mürz-Tachenberg-Decke in der Bohrung Mürztal Thermal 1 (Blatt 134 Passail), die in den Jahren 2002 bis 2003 abgeteuft wurde, in einer Tiefe von 1.285–1.620 m angetroffen worden sein.

Stuhleck-Kirchberg-Decke: Wie eingangs erwähnt wurde die Verbreitung des Pretul-Orthogneises in der Umgebung des Jh. Schwaighof und am Wolfsriegel gegenüber dem Vorjahr verkleinert, da sich die vermeintlichen Orthogneismylonite nach Dünnschliffuntersuchungen als Paragneise herausgestellt haben. In den Orthogneisen ist Granat in den Schliffen selten und Biotit etwas häufiger anzutreffen; polykristalline Kalifeldspatkörner erreichen bis 8 mm Durchmesser; Serizit und Biotit entlang der jüngeren Schieferungsflächen sind meist undeformiert, Quarzkörner in den quarzreichen Lagen weisen gerade Korngrenzen auf.

Mächtigkeiten und Lagerung des Pretul-Orthogneises sind recht unterschiedlich: Im Teschengraben und Überländ bildet er steilstehende, einige Zehnermeter mächtige Züge innerhalb der Hüllschiefer, am Freßnitz- und Fürhauptkogel flachliegende Körper ähnlicher Mächtigkeit; im hinteren Schwaighofgraben, der Wartberger Gmoa und im Bürgerwald flachliegende Körper von über 100 m Mächtigkeit. Südöstlich Friedl, am Rücken westlich Wolfsbach, am Stanglalmweg auf ca. 1.220 m Seehöhe und am Rücken südwestlich Jh. Schwaighof auf 1.280 bis 1.300 m Seehöhe fehlen die typischen Kalifeldspatporphyroblasten, der Orthogneis weist eine mittelkörnige Struktur auf. Geringmächtiger Quarzolit („Rittiser Quarzit") nahe dem Kontakt zu den Hüllschiefern ist im Bürgerwald, im Töschbachgraben, auf der Kuppe westlich Hiasl in der Alm und im Schwaighofgraben zu beobachten.

Die Hüllschiefer erweisen sich bei näherer Betrachtung als keineswegs einförmig. Die Herkunft von Paragneisen ist an zahlreichen Stellen aus grobkörnigem Feldspat und seltenen Relikten grober Muskovitblätter ersichtlich; auch der makroskopisch erkennbare Biotit sowie die < 3 mm großen Granate im Teschengraben, an der alten Zufahrt zum Jh. Schwaighof und am Nordabhang der Gmoa dürften präalpidischer Entstehung sein. Im Steinbachgraben tritt auf etwa 970 m Seehöhe innerhalb der Schiefer ein mehrere Meter mächtiger Quarzit auf, der lateral jedoch nicht verfolgt werden kann. An der Zufahrt vom Töschbachgraben zum Binderbauer sind auf ca. 790 m Seehöhe quarzitische Schiefer aufgeschlossen. Schließlich sind noch die feinkörnigen Paragneise bis Glimmerschiefer auf der Nordseite des Spregnitzgrabens zu erwähnen: sie enthalten in geringer Mächtigkeit Amphibolite, feinkörnige helle Orthogneise und auch helle Orthogneise mit cm-großen, zum Teil idiomorphen Kalifeldspateinsprenglingen, wie sie für den Pretul-Orthogneis bezeichnend sind. Eine weitere Besonderheit sind bis 10 mm große dunkelgraue, prismatische Einschlüsse, die im Dünnschliff aufgrund ihrer Gestalt als Pseudomorphosen nach Staurolith angesprochen werden. Diese Gesteinsgesellschaft kann im Streichen nach Osten nicht über Hiasbauer hinaus, nach Westen nicht in Richtung Überländ verfolgt werden.

Die Faltenachsen innerhalb der Stuhleck-Kirchberg- und auch Rabenwald-Decke beschreiben einen weiträumigen Bogen, von NE–SW südlich Kindberg über E–W südlich Mitterdorf bis NW–SE im Freßnitzgraben. Südostvergenter Faltenbau im m-Bereich kann in den flach Nordwest fallenden Hüllschiefern im Hangenden der Pretul-Orthogneislamelle der Wildfrauengrotte beobachtet werden, eine Generalisierung dieses Faltenbaues, welche die Verbreitung der Orthogneiskörper erklären könnte, drängt sich dem Betrachter jedoch nicht auf. Die Schieferungsflächen fallen südlich Kindberg steil nach Nordwest bis Südost, im Gebiet der Bärenleiten und am Fürhauptkogel sehr flach nach Norden bis Osten, am Freßnitzkogel sehr flach bis mittelsteil nach Süden, im Schwaighofgraben sehr flach nach Nordwesten und am Rotriegel flach nach Norden bzw. auch Süden. Eine zweite, jüngere Schieferung kann fehlen, von geringer Intensität sein oder auch zu einer sehr starken Überprägung (Phyllonitisierung) führen. Eine kartenmäßige Darstellung der Phyllonitisierung war lediglich innerhalb der Rabenwald-Decke möglich.

Neogen: Als Nachtrag zum Kartierungsbericht von 1984 (Nievoll, 1985) wurde am östlichen Blattrand südöstlich vom Magritzerhof eine dick gebankte Karbonatbrekzie mit hellbrauner Matrix abgegrenzt, die flach nach Südosten einfällt, rund 40 m mächtig ist und offenbar von NW–SE streichenden Störungen durchzogen bzw. auch begrenzt wird. Die neogenen Sande und Kiese in der Umgebung vom Magritzerhof liegen dagegen söhlig.

Quartär: Größere Massenbewegungen, zum Teil > 500 m breit, treten am Freßnitzkogel auf, zahlreiche kleinere, zum Teil als Viehweiden genutzte, im Bereich der Bärenleiten, Überländ und Töschbachgraben.

Literatur

Cornelius, H.P. (1936): Geologische Spezialkarte des Bundesstaates Österreich 1:75.000, Blatt Mürzzuschlag. – Geologische Bundesanstalt, Wien.

Nievoll, J. (1985): Bericht 1984 über geologische Aufnahmen im Tertiär und Quartär des mittleren Mürztales auf den Blättern 103 Kindberg und 104 Mürzzuschlag. – Jahrbuch der Geologischen Bundesanstalt, **128**, 269–274, Wien.

Nievoll, J. (2018): Bericht 2017 über geologische Aufnahmen im Koralpe-Wölz-Deckensystem auf Blatt 103 Kindberg. – Jahrbuch der Geologischen Bundesanstalt, **158**, 135–136, Wien.

Blatt 121 Neukirchen am Großvenediger

Siehe Bericht zu Blatt 90 Kufstein von Helmut Heinisch und Claudia Panwitz.

Bericht 2016 über geologische Aufnahmen im Bereich Dösner und Kaponig Tal auf Blatt 181 Obervellach

Michael Schuh

(Auswärtiger Mitarbeiter)

Das Kartierungsgebiet befindet sich im Bundesland Kärnten nördlich bzw. östlich der Gemeinden Obervellach und Mallnitz. Etwa 20 km^2 wurden von Frühsommer bis Spätherbst des Jahres 2016 bearbeitet. Als Kartengrundlage dienten auf 1:10.000 vergrößerte Ausschnitte des ÖK50 Blattes 181 Obervellach. Bei der Bearbeitung des Grundgebirges orientierte man sich an den Kartierungen von Angel & Staber (1950), Marschallinger (1987), Cliff et al. (1971) und Schuh (2010, 2011). Zusätzlich erfolgte die qualitative Erfassung von quartären Formen, Massenbewegungen und anderen Lockergesteinen. Zu deren Abgrenzung wurden mit den Ausschnitten der Kartierungsblätter deckungsgleiche Laserscans herangezogen. Die Reinzeichnung der Karte erfolgte digital.

Das Gebiet wird im Norden vom Kamm, beginnend etwas östlich des Maresenspitzes bis zum Säuleck, abgegrenzt. Ab hier zieht sich die Grenzlinie nach Süden entlang über die markanten Punkte Großer Gößspitz, Mallnitzer Scharte und Dösner Spitz bis zum Kaponig Törl, um von dort nach Südwesten zu biegen und der Furche des Kaponig Tales bis zur Mündung des Wühlschgitzengrabens zu folgen. Die weitere Abgrenzung orientiert sich am Unteren Sickerkopf als westlichsten Eckpunkt, quert das Dösner Tal, um sich östlich des Maresenspitzes zu schließen. Randbereiche wurden mit eingearbeitet, beziehungsweise mit benachbarten Kartierungen abgeglichen.

Die im Kartierungsgebiet vorgefundenen Gesteine werden im Folgenden hinsichtlich ihrer makroskopischen Auffälligkeiten und ihrer Verbreitung beschrieben. Bei der Namensgebung und Unterscheidung der verschiedenen Gesteinstypen waren rein optisch-lithologische Merkmale maßgebend. Die im Text fett unterlegten Ausdrücke dienen als Verweis zur Legende in der archivierten Karte (Schuh, 2016). Grundsätzlich wurden zwei Gruppen von Festgesteinen differenziert, die Gesteine des Alten Daches oder der „Habach-Gruppe“ und die Zentralgneise.

Gesteine des Alten Daches oder der „Habach-Gruppe“

Unter dem Begriff Habach-Gruppe wird eine Suite spätproterozoischer bis paläozoischer Gesteine verstanden, die das prä- bis syn-Zentralgneis-Basement des Tauernfensters darstellen und heute meist als polymetamorphe Gneise bis Schiefer vorliegen. Die größte Verbreitung hat die Gruppe zwischen Krimmler Achental und Kaprunertal in den zentralen Hohen Tauern. Vergleichbare Gesteine befinden sich aber auch im östlichen Tauernfenster zwischen Mallnitz und Maltatal (Seebachmulde) und in der Reisseck-Gruppe (Klötzli et al., 2001).

Als **undifferenzierte Metabasite** (Amphibolite im engeren Sinne) wurden feinkörnige, bisweilen auch mittelkörnige, dunkelgrüne bis schwarze Gesteine mit einem deutlichen Lagenbau bezeichnet. Sie konnten mit Unterbrechungen am gesamten Kamm zwischen Schafleck und Großfeldspitz, im Bereich der Glantschnigalm sowie an der westlichen Begrenzung des Maresenkares verfolgt werden. Das Massiv Lawogge-Zagutnigspitz, teilweise die Sickerköpfe, sowie die Gesteinstypen am Wandfuß südlich der Dösner Hütte (hier, so die Annahme des Autors, verzahnen sie mit Zentralgneisen) wurden ebenfalls als basische Metamorphite klassifiziert.

Untergeordnet zu den Amphiboliten treten seltener basische Metamorphittypen hervor, die ein massig-granoplastisches Gefüge aufweisen und somit auf Gabbros als Ausgangsgesteine hindeuten. Diese grobkörnigen, porzellanweiß-dunkelgrün gesprenkelten Gesteinstypen (Hauptgemengteile sind Plagioklas und Hornblende) wurden in der Kartenlegende als **Metagabbros** klassifiziert. Sie sind stets in mächtigen Amphibolitabfolgen eingelagert, treten also nie isoliert auf. Größere Vorkommen wurden im Ostteil des kleinen Kares südlich der Dösner Hütte sowie nordwestlich der Lawogge vorgefunden. Ein geringmächtiges Auftreten befindet sich am Wandfuß südlich der Konradlacke.

Metabasite mit häufigem aber mengenmäßig untergeordnetem Auftreten von hellen, sauren Gneislagen, wurden als **Bänderamphibolite** ausgeschieden. Solche wurden nördlich der Lawogge und des Zagutnigspitzes, sowie nördlich des Wabnigspitzes kartiert.

Als **undifferenzierte Gneise des Alten Daches** wurden mittelkörnige, variable, gneisartige Gesteine benannt. Diese ähneln gelegentlich den als Biotitgneise bezeichneten Gesteinstypen im Zentralgneis (siehe unten). Gelegentlich weisen sie eine Bänderung infolge von basischen Einschaltungen auf. Ihr Vorkommen konzentriert sich auf das Umfeld des Kleinfeldspitzes.

Als **helle Gneise des Alten Daches** wurden extrem fein- bis mittelkörnige, helle, fast weiße Gesteine bezeichnet. Einerseits gangartig auftretend, andererseits störungsgebunden ist ihre stratigrafische Stellung nicht vollständig geklärt (Meinung des Autors). Ihr Vorkommen verteilt sich – mit Ausnahme der Pfaffenberger Alm – regelmäßig im Arbeitsgebiet.

Eine relativ große Zone mit (basischen) **Migmatiten** wurde in den Felswänden, welche die Seealm im Nordwesten begrenzen, vorgefunden.

Metasedimente mit einem sehr feinen Lagenbau, silbrig glänzenden Schieferungsflächen (hoher Muskovitanteil) und einer sehr auffälligen, rostbraunen Anwitterungsfarbe wurden der Gruppe der **Glimmerschiefer** zugeordnet. Ihr Vorkommen konzentriert sich auf den „Stremsenig“ und die Sickerköpfe. Gelegentlich wurde ein gehäuftes Auftreten von Granatkristallen (Sickerköpfe) beobachtet und gesondert als **Granatglimmerschiefer** in die Karte eingetragen.

In den vorgefundenen Metasedimentabfolgen bezeichnete man grobkörnigere Gesteinstypen (höherer Feldspatanteil) als **Paragneise**. Diese relativ härteren Lithologien bilden typische Geländeaufschwünge wie z.B. im Profil der Sickerköpfe.

Sehr ähnlich den Paragneisen treten, ebenfalls im Profil der Sickerköpfe, Gesteinstypen mit einem vergleichsweise höheren Anteil an dunklen Gemengteilen auf. Sie wurden als basische Metasedimente, **Paraamphibolite** im engeren Sinne angesprochen.

Zentralgneise

Die Namensgebung und Unterscheidung der Zentralgneistypen erfolgte teilweise gemäß der Nomenklatur von Holub & Marschallinger (1989).

Der weit verbreitete **Hochalmporphyrgranit** erstreckt sich im Nordosten des Arbeitsgebietes vom Massiv des Säulecks bis zum Dösner Spitz. Das im Gelände auffälligste Merkmal dieses Zentralgneistyps sind die bis zu 10 cm großen, idiomorphen Kalifeldspateinsprenglinge. Magmatisch gebildeter Plagioklas erreicht eine maximale Größe von durchschnittlich 7 mm (Holub, 1988). Biotit stellt den makroskopisch dominierenden Glimmer dar und ist in undeformierten Bereichen regelmäßig im Gestein verteilt. Rauchgrauer Quarz füllt die Zwickel zwischen den genannten Mineralen.

Leukokrater Zentralgneis, der zum Teil grobkörnig ausgebildet ist, schaltet sich mehrmals in den Hochalmporphyrgranit zwischen Säuleck und Dösner Spitz ein. Ein größeres Vorkommen existiert am Dösner Spitz selbst. Die Farbe dieses Zentralgneistyps schwankt zwischen mittel- und hellgrau, bisweilen auch grünlich infolge flaserig angeordneter Biotitschüppchen (Cliff et al., 1971; Schuh, 2011).

Der **Augengneis**, dessen charakteristisches Merkmal bis zu mehreren Zentimeter große Feldspataugen sind, entspricht dem Hochalmporphyrgranit in dessen westlichen Randbereichen. Die relative Härte dieses Gesteinstyps bedingt die morphologische Ausbildung markanter Gratgendarmen und sehr kompakter, steiler Felswände. Der Augengneis baut einen Großteil des Kammes zwischen Seeschartl und Mitterkeil auf. Weiters umrahmt er das Maresenkar im Süden und Osten.

Ein Zentralgneistyp, dessen besonderes Merkmal in der netzwerkartigen, sperrigen Anordnung seiner Biotitschüppchen, zwischen denen porzellanweiße Plagioklase von bis zu 1 cm Größe und graue Quarznester eingeflochten sind, besteht, wird als **Maltatonalit** bezeichnet. Er kommt im Bereich Ebeneck und im weiten Kessel der Pfaffenberger Alm vor (Cliff et al., 1971; Schuh, 2011).

Biotitgneis (Biotitgranitgneis), der sowohl in fein- als auch in mittel- bis grobkörniger Form vorgefunden wurde, sollte das stärker deformierte Äquivalent des leukokraten Zentralgneises darstellen. Er verzahnt sich zwischen Mitterkeil und Ochenladinspitz mit dem Augengneis.

Struktureller Bau

Der strukturelle Bau des Arbeitsgebietes ist sehr klar und einfach. Das generelle Westfallen (Nordwest bis Südwest) der Schieferung wird von wenigen, markanten Sprödstörungen durchschlagen. Die meisten Verwerfungen konnten im Zuge einer Gratbegehung zwischen Lawogge und Seeschartl nachgewiesen werden. Oft verlaufen diese schieferungsparallel oder schneiden den primären Lagenbau schleifend und sind über deutliche Scharten und Couloirs verfolgbar.

Quartäre Ablagerungen und Formen

Dösner und Kaponig Tal stehen als Musterbeispiele für glazial ausgeschürfte, stark eingetiefte Tröge. Besonders das Dösner Tal weist ein unausgeglichenes, in mehrere Böden gegliedertes Längsprofil auf. In diese Verebnungen sind entweder wasserbedeckte Wannen eingetieft (Dösner See, Konradlacke) oder es akkumulierten sich dort Schutt des verzweigten Hauptwasserlaufes. Ebenso lagern die zahlreichen Nebenbäche ihre Sedimentfracht in großen Schwemmfächern auf den Böden des Haupttales ab und zwingen den Dösenbach zu permanenten Richtungsänderungen.

Der Gletscherrückgang bzw. das nahezu völlige Verschwinden letzter kleiner Wandvereisungen (Wegfall des Widerlagers) bewirkt eine Zerlegung der Grate und Wände. Grobe Blockansammlungen häufen sich an Füßen der Kar- und Trogwände resistenter Lithologien wie Metabasiten und Gneisen. Metasedimente produzieren entsprechend feineren Schutt.

Die Bereitstellung von Blocksturz- und Schuttmaterial sowie das teilweise Vorhandensein von restlichen Kargletschern führten zur Ausbildung von Blockgletschern. Aktive Formen findet man knapp außerhalb des Arbeitsgebietes unmittelbar südlich des Dösner Sees sowie im Mitterkeiltal. Daneben wurden grobblockige inaktive (z.B. Seealm, Kare nördlich des Ochenladinspitzes und westlich des Kleinfeldspitzes) und einige fossile Formen (z.B. Talböden östlich der Dösner Hütte, Glantschnigalm) kartiert.

Eine aus relativ feinerem Material bestehende, fossile Permafrostform befindet sich im Erosionskessel südlich des Oberen Sickerkopfes.

Gut erhaltene Moränenwälle wurden südlich des Schaflecks und südlich des Kleinfeldspitzes vorgefunden. Der Autor vermutet hier ein holozänes Alter. Spätglaziale End- und Seitenmoränenwälle lagern in den meisten, südseitig offenen Karen etwas weiter distal. Die nordseitigen Kare ließen aufgrund der großen Geländesteilheit keine Erhaltung zu. Als stratigrafische Disposition der meisten distalen Wallformen kommt höchstwahrscheinlich Egesen (ca. 10.000 vor heute) in Frage.

Im Südwestteil des Arbeitsgebietes (Bereich Sickerköpfe-Lawogge) sind bei der Geländebegehung Zerrspalten aufgefallen, die sich an den Nord- und Ostabstürzen der Lawogge in Form eindrucksvoller Couloirs manifestieren.

Im Bereich der Kaponig Wiesen, südlich von Lawogge und Zagutnigspitz, konnte eine knapp 3 km^2 große Hangfläche als Rutschmasse ausgewiesen werden. Wenig resistente Gesteine, vor allem Glimmerschiefer, bewirken die Instabilität des Untergrundes.

Literatur

ANGEL, F. & STABER, R. (1950): Geologische Karte des Ankogel-Hochalm-Gebietes 1:50.000. – 1 Blatt, Innsbruck (Wagner).

CLIFF, R.A., NORRIS, R.J., OXBURGH, E.R. & WRIGHT, R.C. (1971): Structural, metamorphic and geochronological studies in the Reisseck and southern Ankogel groups, the Eastern Alps. – Jahrbuch der Geologischen Bundesanstalt, **114**, 121–272, Wien.

HOLUB, B. (1988): Geologie, Petrologie und Intrusionsfolge der Zentralgneise im Großelendtal (Hochalm-Ankogel-Gruppe, Kärnten). – Dissertation, Universität Salzburg, 217 S., Salzburg.

HOLUB, B. & MARSCHALLINGER R. (1989): Die Zentralgneise im Hochalm-Ankogel-Massiv (östliches Tauernfenster). Teil I: petrographische Gliederung und Intrusionsfolge. – Mitteilungen der Österreichischen Geologischen Gesellschaft, **81**, 5–31, Wien.

KLÖTZLI, U., HÖCK, V. & KEBEDE, T. (2001): Die Alterstellung der Habach-Gruppe im zentralen Tauernfenster: eine kurze Diskussion. – In: HUBMANN, B. (Ed.): Paläozoikumforschung in Österreich. – Workshop, 19.–20. Oktober 2001, St. Pankrazen/Stmk., 26–29, Graz.

MARSCHALLINGER, R. (1987): Geologie und Petrologie der Zentralgneise und ihres alten Daches im Bereich des oberen Maltatales (Kärnten). – Dissertation, Universität Salzburg, 257 S., Salzburg.

SCHUH, M. (2010): Kartierungsbericht 2010 ÖK 181 Obervellach, „Hohes Gößkar“. – Unpublizierter Aufnahmebericht, 2 S., 1 Karte mit Legende, Wien. [GBA, Wissenschaftliches Archiv, Nr. A 16595-RA/181/2010]

SCHUH, M. (2011): Bericht 2007, 2008 und 2010 über geologische Aufnahmen im Bereich „Hohes Gößkar“ auf Blatt 181 Obervellach. – Jahrbuch der Geologischen Bundesanstalt, **151**/1–2, 159–160, Wien.

SCHUH, M. (2016): Bericht 2016 über geologische Aufnahmen im Bereich „Dösner und Kaponig Tal“ auf Blatt 181 Obervellach. – Unpublizierter Aufnahmebericht, 10 S., 1 Karte mit Legende, Wien. [GBA, Wissenschaftliches Archiv, Nr. A 19839-RA/181/2016]

Bericht 2017 über geologische Aufnahmen im Bereich Kaponig, Zwenberger und Zandlacher Tal auf Blatt 181 Obervellach

MICHAEL SCHUH

(Auswärtiger Mitarbeiter)

Das Kartierungsgebiet befindet sich im Bundesland Kärnten nördlich bzw. östlich der Gemeinden Unterkolbnitz und Obervellach. Etwa 20 km^2 wurden von Frühsommer bis Spätherbst des Jahres 2016 bearbeitet. Als Kartengrundlage dienten auf 1:10.000 vergrößerte Ausschnitte des ÖK50 Blattes 181 Obervellach. Bei der Bearbeitung des Grundgebirges orientierte man sich an den Kartierungen von ANGEL & STABER (1950), MARSCHALLINGER (1987), CLIFF et al. (1971) und SCHUH (2011). Zusätzlich erfolgte die qualitative Erfassung von quartären Formen, Massenbewegungen und anderen Lockergesteinen. Zu deren Abgrenzung wurden mit den Ausschnitten der Kartierungsblätter deckungsgleiche Laserscans herangezogen. Die Reinzeichnung der Karte erfolgte digital.

Zusätzlich erfolgte die qualitative Erfassung von quartären Formen, Massenbewegungen und anderen Lockergesteinen. Zu deren Abgrenzung wurden mit den Ausschnitten der ÖK 181 deckungsgleiche Laserscans herangezogen. Die Reinzeichnung der Karte erfolgte digital.

Das Gebiet wird im Norden vom Kaponig Tal, beginnend bei der Gaschnighütte bis zum Kaponig Törl, abgegrenzt. Die östliche Gebietsgrenze bildet der Kammverlauf Tristenspitze–Riekenkopf–Zwenberger Scharte–Gamolnigspitz bis zur Karstufe des Zandlacher Grabens. Letzterer bildet den südlichen Rand des bearbeiteten Bereichs bis zum Ende des Talbodens südwestlich der Riekenalm. Eine Linie vom Zandlacher Graben über Kampleck und Groneck bis zum Kaponig Tal schließt das Kartierungsgebiet gegen Südwesten und Westen.

Randbereiche wurden miteingearbeitet beziehungsweise mit benachbarten Kartierungen abgeglichen.

Die im Kartierungsgebiet vorgefundenen Gesteine werden nun hinsichtlich ihrer makroskopischen Auffälligkeiten und ihrer Verbreitung kurz beschrieben. Bei der Namensgebung und Unterscheidung der verschiedenen Gesteinstypen waren rein optisch-lithologische Merkmale maßgebend. Die im Text fett unterlegten Ausdrücke dienen als Verweis zur Legende in der archivierten Karte (SCHUH, 2017). Grundsätzlich wurden zwei Gruppen von Festgesteinen differenziert, die Gesteine des Alten Daches oder der „Habach-Gruppe“ und die Zentralgneise.

Gesteine des Alten Daches oder der „Habach-Gruppe“

Unter dem Begriff Habach-Gruppe wird eine Suite spätproterozoischer bis paläozoischer Gesteine verstanden, die das prä- bis syn-Zentralgneis-Basement des Tauernfensters darstellen und heute meist als polymetamorphe Gneise bis Schiefer vorliegen. Die größte Verbreitung hat die Gruppe zwischen Krimmler Achental und Kaprunertal in den zentralen Hohen Tauern. Vergleichbare Gesteine befinden sich aber auch im östlichen Tauernfenster zwischen Mallnitz und Maltatal (Seebachmulde) und in der Reisseckgruppe (KLÖTZLI et al., 2001).

Gesteine, die als **Metabasite** (meist Amphibolite im engeren Sinne) bezeichnet wurden, sind feinkörnige, bisweilen auch mittelkörnige, seltener grobkörnige, dunkelgrüne bis schwarze Gesteine. Bei den feinkörnigen Varietäten wurde meist ein deutlicher Lagenbau festgestellt, wohingegen die grobkörnigen Ausbildungen mit hohem Plagioklasanteil ein gneisartiges bis granoblastisches Erscheinungsbild aufweisen können. Gelegentlich schalten sich in den Metabasiten mm- bis cm-dicke, saure, quarzreiche Lagen ein. Derartige Typen wurden als **Bänderamphibolite** bezeichnet.

Das Vorkommen der Metabasite beschränkt sich im Vergleich zum benachbarten Arbeitsgebiet des Vorjahres auf einige wenige Lokalitäten. An den Nordwesthängen östlich der Gaschnighütte (Kaponig Tal) wurden feinkörnige Amphibolite sowie lokal Bänderamphibolite kartiert. Diese setzen sich am Südwestrücken des Gronecks sowie in dessen Südostflanke in Forstweganschnitten fort. Weiters treten Metabasite im kleinen Kar nördlich der „Spiegetzn“, hier vergesellschaftet mit hellen, gneisartigen Gängen (siehe helle Gneise des Alten Daches), auf. Mit Unterbrechung setzen sich diese auf der Südseite des Kammes Krachriegel–Kesseleck, dort mit Metasedimenten gemeinsam auftretend und zum Teil als Bänderamphibolite vorliegend, fort. Zusätzlich zu diesen Vorkommen konnten schollenartige, sich über mehrere 100 Meter erstreckende Metabasite in das Kartenblatt aufgenommen werden. Nach Ansicht des Autors stehen diese nicht in Zusammenhang mit den vorher beschriebenen, basischen Gesteinstypen, da sie nur sehr isoliert, also scharf abgegrenzt vom umgebenden Gestein (meist Leukokrater Zentralgneis) auftreten und, entgegen der generellen Raumlage (SW-, W- bis NW-Fallen), steil nach Nordost geneigt sind. An folgenden Lokalitäten konnten solche Metabasitschollen beobachtet werden: zwischen Unterem Zwenberger See und Gamolnigspitz, in der Westflanke des Nordgrates vom Jocheck sowie eine kleine Scholle am höchsten Punkt des Kares nördlich des Dornecks.

Untergeordnet zu den Amphiboliten treten basische Metamorphittypen hervor, die ein massig-granoplastisches Gefüge aufweisen und somit auf Gabbros als Ausgangsgesteine hindeuten. Diese grobkörnigen, porzellanweiß-dunkelgrün gesprenkelten Gesteinstypen mit den Hauptgemengteilen Plagioklas und Hornblende wurden in der Kartenlegende als **Metagabbros** klassifiziert. Ein isoliertes, punktuelles Vorkommen wurde südwestlich unterhalb der Grateinsenkung des Südwestgrates vom Gamolnigspitz vorgefunden.

Als **undifferenzierte Gneise des Alten Daches** wurden mittelkörnige, variable, gneisartige Gesteine benannt. Diese ähneln gelegentlich den als Biotitgneisen bezeichneten Gesteinstypen im Zentralgneis (siehe unten). Oftmals weisen sie eine Bänderung infolge von basischen Einschaltungen auf. Ein lokales Vorkommen wurde nördlich der Zwenberger Alm, etwa 200 Höhenmeter hangaufwärts kartiert.

Die in der Legende mit dem Terminus **helle Gneise des Alten Daches** klassifizierten Lithologien beschreiben extrem fein- bis mittelkörnige, helle, fast weiße Gesteinstypen. Sie können einerseits die Umgebungsgesteine diskordant (gangartig) durchschlagen oder auch konkordant an Bewegungsflächen respektive Störungszonen auftreten. Beide Ausprägungen ähneln sich makroskopisch, können aber im Kartenbild sehr gut voneinander differenziert werden. Die gangartigen Hellen Gneise wurden ausschließlich in Zentralgneistypen, wie Augengneisen und Tonalitgneisen, seltener auch in Vergesellschaftung mit Metabasiten vorgefunden. Hingegen treten störungsgebundene Helle Gneise besonders an Grateinsenkungen wie Sätteln oder Scharten zutage. Ein sehr augenfälliges Merkmal dieser Gesteinstypen sind häufig auftretende, bis zu mehrere Zentimeter große Muskovitblättchen.

Ein relativ breiter Streifen migmatisierter Gesteinstypen zieht in NW–SE-Richtung über den Kamm unmittelbar westlich des Gamolnigspitzes. Zusätzliche Vorkommen entdeckte man in den nach Süden geneigten Hängen des Zandlacher Grabens unmittelbar nördlich der Rieken- und der Zandlacher Alm. Die **Migmatite** erscheinen im Gelände sehr heterogen: einerseits findet man diffuse, „verwaschene" Konturen zwischen den dunklen und hellen Anteilen vor, andererseits beobachtet man scharf abgegrenzte, schollenartige, basische Gesteine von mehreren Metern bis Zehnermetern Größe im umgebenden Leukosom (?).

Metasedimente mit einem sehr feinen Lagenbau, silbrig glänzenden Schieferungsflächen (hoher Muskovitanteil) und einer sehr auffälligen, rostbraunen Anwitterungsfarbe wurden der Gruppe der **Glimmerschiefer** zugeordnet. Vereinzelt wurde ein gehäuftes Auftreten von Granatkristallen beobachtet und gesondert als **Granatglimmerschiefer** in die Karte eingetragen. Grobkörnigere Gesteinstypen mit höherem Feldspatanteil wurden als **Paragneise** ausgeschieden. Das größte Vorkommen von Metasedimenten konzentriert sich auf den nach Norden gerichteten Hang südlich der Gaschnighütte (Kaponig Tal). Innerhalb von Zentralgneisabfolgen findet man Metasedimente am Wandfuß östlich und südlich des Krachriegels sowie am Arlkopf (beides im Zwenberger Tal).

Zentralgneise

Die Namensgebung und Unterscheidung der Zentralgneistypen erfolgte teilweise gemäß der Nomenklatur von Holub & Marschallinger (1989).

Der weit verbreitete **Hochalmporphyrgranit** erstreckt sich im Nordosten, etwas außerhalb des diesjährigen Arbeitsgebietes vom Massiv des Säulecks bis zum Dösner Spitz. Das im Gelände auffälligste Merkmal dieses Zentralgneistyps sind die bis zu 10 cm großen, idiomorphen Kalifeldspateinsprenglinge. Magmatisch gebildeter Plagioklas erreicht eine maximale Größe von durchschnittlich 7 mm (Holub, 1988). Biotit stellt den makroskopisch dominierenden Glimmer dar und ist in undeformierten Bereichen regelmäßig im Gestein verteilt. Rauchgrauer Quarz füllt die Zwickel zwischen den genannten Mineralen.

Der **Augengneis**, dessen charakteristisches Merkmal bis zu mehrere Zentimeter große Feldspataugen sind, entspricht dem Hochalmporphyrgranit in dessen Randbereichen. Die relative Härte dieses Gesteinstyps bedingt die morphologische Ausbildung markanter Gratgendarmen und sehr kompakter, steiler Felswände. Der Augengneis baut folgende Bereiche des Arbeitsgebietes auf: das Groneck, einen Streifen westlich des Kesseleckgipfels, den Bereich Lackenspitz, Abschnitte östlich und südöstlich des Kamplecks sowie südlich des Dornecks.

Eine Gneisvarietät, die unbedingt zu differenzieren ist, findet man am Kampleck: ein sehr dunkler, dem Biotitgneis ähnlicher Gesteinstyp mit wenigen, eher kleinen ausgelinsten Feldspäten und Feldspatleisten. Er hebt sich von den übrigen Zentralgneisen durch seine stratigrafische Stellung ab. Eine radiometrische Datierung ergab für diesen Gesteinstyp ein Alter an der Perm/Trias-Grenze (Ralf Schuster, persönliche Mitteilung).

Ein sehr großer Anteil des Arbeitsgebietes wird von **Leukokratem Zentralgneis** eingenommen. Dieser Zentralgneistyp, der einerseits grobkörnig, andererseits feinkörnig ausgebildet ist, schaltet sich mehrmals im Kamm zwischen Groneck und Kesseleck ein. Das größte Vorkommen füllt den Kessel des Oberen Zwenberger Sees aus. Am Südrand des Arbeitsgebietes sind Dorneck und Gamolnigspitz sowie Teilbereiche dazwischen aus Leukokratem Zentralgneis aufgebaut. Die Farbe dieses Zentralgneistyps schwankt zwischen mittel- und hellgrau, bisweilen auch grünlich infolge flaserig angeordneter Biotitschüppchen (Cliff et al., 1971; Schuh, 2011).

Ein Zentralgneistyp, dessen besonderes Merkmal in der netzwerkartigen, sperrigen Anordnung seiner Biotitschüppchen, zwischen denen porzellanweiße Plagioklase von bis zu 1 cm Größe und graue Quarznester eingeflochten sind, besteht, wird als **Maltatonalit** bezeichnet (CLIFF et al., 1971; SCHUH, 2011). Die Gesteinstypen am SE-Rand der Pfaffenberger Alm, jene am Tristenspitz-Massiv und südlich davon, sowie die Zentralgneise rund um den Unteren Zwenberger See und östlich bzw. südöstlich des Jochecks wurden als Maltatonalit eingestuft. Wo keine eindeutige Identifizierung im Gelände möglich war, wurde der Gesteinstyp als grobkörniger Biotit-Orthogneis (**grobkörniger Biotitgneis**) bezeichnet. Eine Untersuchung der entsprechenden Gesteinsproben im Dünnschliff wird eine feinere Differenzierung ermöglichen.

Biotitgneis (Biotitgranitgneis), der sowohl in fein- als auch in mittel- bis grobkörniger Form vorgefunden wurde, sollte das stärker deformierte Äquivalent des leukokraten Zentralgneises darstellen. Er zieht sich in einem markanten, in etwa NNW–SSE verlaufenden Streifen vom oberen Kaponig Tal über das Kesseleck und das Jocheck bis zum Zandlacher Graben.

Struktureller Bau

Wie das angrenzende Arbeitsgebiet des Vorjahres ist auch das diesjährige strukturell sehr klar und einfach gegliedert. Wiederum liegt eine, von wenigen Ausnahmen abgesehen, generelle, mittelsteile W- (NW- bis SW-) Neigung der Schieferung vor. Wenige, markante Sprödstörungen konnten bei einer Begehung des Kammes zwischen Krachriegel und Krachriegel direkt eingesehen werden. Meist sind die eigentlichen Bewegungsflächen stark schuttbedeckt, also nicht eindeutig messbar. Sie wurden folglich als vermutete Störung eingezeichnet.

Quartäre Ablagerungen und Formen

Die glaziale Prägung des Arbeitsgebietes gleicht jener des Vorjahres. Die drei Täler, Kaponig-, Zwenberger und Zandlacher Tal, wurden stark eingetieft und sind im Längsschnitt in einen oberen (Kar) und einen unteren (eigentliches Tal) Boden unterteilt. In diese Böden oder Verebnungen sind entsprechend wasserbedeckte Wannen eingetieft (Paffenberger und Zwenberger Seen).

Der Gletscherrückgang bzw. das nahezu völlige Verschwinden letzter kleiner Wandvereisungen (Wegfall des Widerlagers) bewirkt eine Zerlegung der Grate und Wände. Grobe Blockansammlungen häufen sich an Füßen der Kar- und Trogwände resistenter Lithologien, wie Metabasiten und Granitgneisen. Metasedimente produzieren entsprechend feineren Schutt.

Die Bereitstellung von Blocksturz- und Schuttmaterial sowie das teilweise Vorhandensein von restlichen Kargletschern führten zur Ausbildung von Blockgletschern. Inaktive Formen findet man – vorausgesetzt, das Gelände ist nicht zu stark geneigt – in nahezu jedem Kar im Arbeitsgebiet. Aktive Blockgletscher konnten nicht festgestellt werden.

Gut erhaltene Moränenwälle wurden nördlich vom Lackenspitz und dem Kesseleck vorgefunden. Diese spätglazialen End- und Seitenmoränenwälle, so die Annahme des Autors, sind stratigrafisch höchstwahrscheinlich dem Egesen-Stadium (ca. 10.000 Jahre vor heute) zuzuordnen. Die Vergesellschaftung mit einem Blockgletscher festigt diese Vermutung. Im Zandlacher Graben konnte am distalen Ende des Talbodens auf der orografisch linken Seite ein endnaher Uferwall identifiziert werden. Seine stratigrafische Disposition könnte in das Gschnitz-Stadium (ca. 15.000 Jahre vor heute) fallen.

Im Zwenberger Tal, nördlich der Jagdhütte westlich der Zwenberger Alm, wurde ein lobenförmiger, mehrere 100 m messender Lockersedimentkörper als Rutschmasse ausgewiesen.

Literatur

ANGEL, F. & STABER, R. (1950): Geologische Karte des Ankogel-Hochalm-Gebietes 1:50.000. – 1 Blatt, Innsbruck (Wagner).

CLIFF, R.A., NORRIS, R.J., OXBURGH, E.R. & WRIGHT, R.C. (1971): Structural, metamorphic and geochronological studies in the Reisseck and southern Ankogel groups, the Eastern Alps. – Jahrbuch der Geologischen Bundesanstalt, **114**, 121–272, Wien.

HOLUB, B. (1988): Geologie, Petrologie und Intrusionsfolge der Zentralgneise im Großelendtal (Hochalm-Ankogel-Gruppe, Kärnten). – Dissertation, Universität Salzburg, 217 S., Salzburg.

HOLUB, B. & MARSCHALLINGER, R. (1989): Die Zentralgneise im Hochalm-Ankogel-Massiv (östliches Tauernfenster). Teil I: petrographische Gliederung und Intrusionsfolge. – Mitteilungen der Österreichischen Geologischen Gesellschaft, **81**, 5–31, Wien.

KLÖTZLI, U., HÖCK, V. & KEBEDE, T. (2001): Die Alterstellung der Habach-Gruppe im zentralen Tauernfenster: eine kurze Diskussion. – In: HUBMANN, B. (Ed.): Paläozoikumforschung in Österreich. – Workshop, 19.–20. Oktober 2001, St. Pankrazen/Stmk., 26–29, Graz.

MARSCHALLINGER, R. (1987): Geologie und Petrologie der Zentralgneise und ihres alten Daches im Bereich des oberen Maltatales (Kärnten). – Dissertation, Universität Salzburg, 257 S., Salzburg.

SCHUH, M. (2011): Bericht 2007, 2008 und 2010 über geologische Aufnahmen im Bereich „Hohes Gößkar" auf Blatt 181 Obervellach. – Jahrbuch der Geologischen Bundesanstalt, **151**/1–2, 159–160, Wien.

SCHUH, M. (2017): Bericht 2017 über geologische Aufnahmen im Bereich „Kaponig, Zwenberger und Zandlacher Tal" auf Blatt 181 Obervellach. – Unpublizierter Aufnahmebericht, 7 S., 1 Karte mit Legende, Wien. [GBA, Wissenschaftliches Archiv, Nr. A 19837-RA/181/2017]

Kartenwerk im UTM-System

Die Blattnamen und Blattnummern beziehen sich auf die Kartenblätter aus der Reihe „Österreichische Karte 1:50.000-UTM" und werden ab 2016 mit den internationalen Blattnamen angegeben.

Blatt NL 32-03-17 Hinterriß

Bericht 2018 über geologische Aufnahmen im Karwendelgebirge auf den Blättern UTM NL 32-03-17 Hinterriß und UTM NL 32-03-23 Innsbruck

Hugo Ortner

(Auswärtiger Mitarbeiter)

Das Karwendelgebirge ist mit dem Beginn der Neuaufnahme des geologischen UTM-Kartenblattes NL 32-03-23 Innsbruck (Viertelblatt NW) wieder in den Fokus interessanter großflächiger fazieller und tektonischer Untersuchungen gerückt. Unmittelbarer Anlass für die Geländeaufnahmen, über die hier berichtet wird, waren einerseits Schichtgeometrien im Wettersteinkalk der Laliderer Wände im Gebiet des Kaltwasserkars, die nicht einfach erklärbar sind, andererseits die Dokumentation der Reifling-Formation im unteren Birkkar und im Rauhkarl (Büsel, 2014; Gruber, 2017). Um die Geometrie der Wettersteinkalk-Plattform besser zu verstehen, wurden Geländebegehungen in der Umgebung des Karwendelhauses (1.771 m) und im Kaltwasserkar, einem nordseitigen Kar in der Hinterautal-Vomper Kette, und in den südseitigen Karen, Großes Kühkar, Moserkar, Rauhkarl und Birkkar, sowie im kleinen Kühkar in der Nördlichen Karwendelkette, nordwestlich des Karwendelhauses durchgeführt (alle Lokalnamen, sofern nicht anders angegeben, sind der ÖK entnommen).

Kaltwasserkar

Das Kaltwasserkar weist an seinem Ausgang einen Felsriegel auf, in dem die Abfolge des Alpinen Muschelkalks aufgeschlossen ist, während weiter südlich in den Karwänden selbst (Laliderer Wände) der Wettersteinkalk ansteht. Eine weitgehend schuttgefüllte Rinne etwas westlich der Karmitte gewährt Zugang zum Kar und erschließt eine stratigrafische Abfolge durch den Alpinen Muschelkalk.

Die Abfolge ist zyklisch aufgebaut und beginnt mit dm-gebankten mikritischen bioturbaten Wurstelkalken der Virgloria-Formation. Diese wechsellagern in einem Abstand von mehreren Zehnermetern mit unregelmäßig 0,5 m gebankten oolithischen oder Crinoiden führenden Schuttkalken. Nach oben wird die Schichtung in den Wurstelkalken dünner sowie unschärfer und es finden sich unter der Lupe manchmal stark gebogene Filamente. Oberhalb zwei solcher Zyklen erscheinen mit dem Übergang zur Steinalm-Formation bei 1.740 m massige Encrinite, die lokal Kieselknauern aufweisen. Auf diesen folgen nach oben wiederum Fossilschuttkalke, die aufgearbeitete, unregelmäßig geformte Fetzen von Mikrit mit reichlich Filamenten darin führen, und somit die Schüttungen von der Wettersteinkalk-Plattform in das Reiflinger Becken repräsentieren. Die damit verzahnenden Reiflinger Knollenkalke sind unter der Schuttbedeckung des Kaltwasserkars verborgen. Bei 1.860 m am Nordrand des Kaltwasserkars sind die Reiflinger Knollenkalke am Fuß der Wettersteinkalkwände erschlossen.

Im Hintergrund des Kaltwasserkars sind parallel zum Talhintergrund verlaufende Störungen vorhanden (ca. Sf. 205/80), welche die lagunäre, gut gebankte Fazies des Wettersteinkalks im Süden gegen die grobgebankte Fazies im Norden versetzen. Diese grobgebankte Fazies wird als Vorrifffazies mit Klinoformen interpretiert, die im östlichen Abschluss des Kaltwasserkars direkt sichtbar sind. Im Aufschluss sind auch Großoolithe und Stromatactis zu erkennen, die meisten der dicken Bänke bestehen aus feinem Riffschutt.

Zwischen der Steinalm-Formation und dem Wettersteinkalk ist am Südostrand des Kaltwasserkars nur eine Schichtfuge vorhanden. An der Ostseite des kleinen Kars zwischen Kaltwasserkarspitze (2.733 m) und dem namenlosen Gipfel Pkt. 2.548 m (nur in der Alpenvereinskarte) ist auch die Verzahnung von Klinoformen mit der Reifling-Formation zu erkennen, der Riffhang muss somit etwa nach Norden bis Nordosten zeigen. Diese Verzahnung ist an einer etwa südfallenden Störung lokal verdoppelt.

Das Riff und die Lagune können anhand des Bankungstyps unterschieden werden. Während die Lagune meist sehr gut gebankte Kalke zeigt, ist das Riff massig (z.B. Ott, 1967). Der Riffabhang ist grobgebankt und im Schnitt rechtwinklig zur Progradationsrichtung schräggeschichtet. Diese Schrägschichtung kann steil sein, wie sie in den mitteltriadischen Riffen der Dolomiten gut dokumentiert ist (z.B. Brandner & Keim, 2011; Keim & Schlager, 2001; Maurer, 2000). Vergleichbares ist im unteren Kaltwasserkar zu sehen, wo im östlichen Abschnitt der nach Norden absteigende Riffhang sichtbar ist. Im Hintergrund des Kares scheinen diese Kalke horizontal gebankt, da der Schnitt dort offensichtlich parallel zum Riffhang liegt.

Sehr auffällig sind die vertikalen Sprünge der Basis der lagunären Kalke. Während das Riff bis fast zum Gipfel von Pkt. 2.548 m reicht, liegt die Grenze Riff-Lagune im Kaltwasserkar nahe am Wandfuß, was einem vertikalen Sprung von mindestens 600 m entspricht. Dieser Sprung findet an zwei Störungen statt, die erste reicht vom kleinen Kar südöstlich des Kaltwasserkars bis in das Rauhkarl und verläuft etwa N–S; sie wird hier als Rauhkarl-Störung bezeichnet; die zweite ist ungefähr E–W orientiert. Zwischen der Kote 2.548 m und der Kaltwasserkarspitze sind in den lagunären Kalken keilförmige Sedimentkörper zu erkennen. Die Mächtigkeitszunahme zur Störung hin legt synsedimentäre, mitteltriassische Abschiebungsaktivität nahe. Die Schichtung in den lagunären Kalken im Hintergrund des Kaltwasserkars ist über die gesamte Breite in etwa parallel zu den untersten Einheiten der keilförmigen Einheiten, was vermuten lässt, dass diese Kalke zu einer Abschiebung hin verkippt sind.

Kühkar

Die nördlich des Hochalmsattels (1.803 m) gelegene Nördliche Karwendelkette wurde im Bereich des südseitigen Kühkars (südöstlich unterhalb des Lackenkarkopfs, 2.416 m) begangen, um Panoramafotos der Nordwände der Hinterautal-Vomper Kette (Laliderer Wände) zu machen. Diese Gegend ist bereits in der Arbeit von Donofrio et al. (1980) in einer geologischen Skizze dargestellt. Die das Kühkar nach Südwesten begrenzende Wand bietet einen guten Einblick in die stratigrafische Abfolge.

Bei 1.960 m reichen von Westen wellig dm-gebankte Riffschuttkalke bis in den Kargrund herunter. Darunter, in einer zurückwitternden Rinne, liegen stark kieselige Knollenkalke der Reifling-Formation. Im Anschlag sind die hellgrau verwitternden Riffschuttkalke fast schwarz, einzelne Bänke bestehen nur aus Crinoidenstielgliedern. Im zweiten Bankpaket, das stellenweise massig wirkt, sind schichtparallele Kieselschnüre vorhanden, im Anschlag handelt es sich wiederum teilweise um Encrinite, oder crinoidenreiche Packstones, in manchen Bänken mit bis zu 5 mm großen Bruchstücken von Brachiopoden (Rynchonelliden). Die zurückwitternde Fuge zwischen den beiden Bankpaketen besteht aus cm- bis dm-gebankten bioturbaten Kalken („Wurstelkalk“). Bankpakete 1 und 2 werden mit der Steinalm-Formation gleichgesetzt. Wurstelkalke sind schließlich die dominierenden Lithologien in Bankpaket 3, welches deshalb der Virgloria-Formation zugeordnet wird.

Karwendelhaus

Die gesamte Schichtfolge der Nördlichen Karwendelkette im Bereich des Hochalmsattels liegt verkehrt. Im Gegensatz dazu liegt dieselbe Abfolge in den Wänden, welche die breite Passlandschaft zwischen Kleinem Ahornboden (Johannestal) und Karwendeltal im Süden flankieren, aufrecht. Die verkehrte Abfolge reicht jedoch noch bis nahe an die Wände beim Karwendelhaus (1.771 m) heran, wo sie an der Ostseite des Personalhauses aufgeschlossen ist. Die Reichenhall-Formation, die aus Dolomiten, Kalken und Rauwacken besteht, bildet die Basis der Sedimentabfoge der Inntal-Decke. Sie steht hier subvertikal, parallel zum Kontakt mit den jurassisch-kretazischen Beckensedimenten (oft auch als „Jungschichten“ bezeichnet) der liegenden Lechtal-Decke. Während die Reichenhall-Formation nur wenig deformiert ist, sind die „Jungschichten“, von denen die Allgäu-, Ruhpolding-(Radiolarit), Ammergau- und Schrambach-Formation, aufgeschlossen sind, intensiv im dm- bis m-Maßstab verfaltet und an subvertikalen Störungen, die in den inkompetenten Gesteinen s-c-Gefüge bilden, zerschert. Die Falten weisen subhorizontale Achsen auf und zeigen dort, wo eine Asymmetrie erkennbar ist, eine Vergenz, die zeigt, dass der nördliche Block an der Scherzone nach oben geht. Damit kann es sich nicht um Strukturen handeln, die mit der Deckenüberschiebung in Zusammenhang stehen, da diese den nördlichen Block nach unten bringen müsste. Man muss annehmen, dass der Aufschluss im nördlichen, subvertikalen Schenkel einer Falte liegt, in der die Deckengrenze versetzt ist.

Wenige Schritte weiter ist direkt beim Karwendelhaus der aufrechte Schenkel dieser Falte aufgeschlossen. Die dm- bis m-gebankten, wellig geschichteten Schuttkalke mit wenigen Filamenten gleichen denen im Kühkar oder Kaltwasserkar im höheren Teil des Alpinen Muschelkalks. Die Schichtung fällt mittelsteil nach Nordost, ist aber, mit erkennbarem Scharnier, nach Norden parallel zur Störung beim Personalhaus aufgeschleppt. Auch in diesem Fall muss sich der südliche Block nach unten bewegt haben, wodurch die Basis der Reichenhall-Formation und die „Jungschichten“ im vertikalen bis überkippten Schenkel der Falte in Kontakt mit dem oberen Alpinen Muschelkalk aus dem aufrechten Schenkel dieser Falte kommen. Subvertikale, WSW-streichende Störungen mit sinistralem und dextralem Bewegungssinn verursachen diesen Kontakt.

Rauhkarl, Moserkar und unteres Kühkar

Diese Kare sind nur von Süden, von der Kastenalm im Hinterautal aus erreichbar. Am östlichen Ast des Moserkarbaches, der aus dem Großen Kühkar zufließt, ist oberhalb der Verzweigung bei 1.540 m Höhe, m-gebankter lagunärer Wettersteinkalk mit stromatolithischer Lamination und großen Grünalgen (*Teutloporella herculea*?) in Wechsellagerung mit Schuttkalken erschlossen. Manche Bänke bestehen aus feinstlaminiertem Kalkschlamm. Diese Bänke sind gelegentlich aufgearbeitet und bilden Plastiklasten, die an Großoolithe erinnern. Auch dm-große Turmschnecken der Gattung *Omphaloptychia* sind manchmal zu beobachten.

Im Anstehenden werden die Schuttkalke nach oben gröber. Zwischen den Algenkalken mit *Teutloporella herculea* treten Hohlraumfüllungen auf (Teepees?) mit wandständigen Zementen, die stark an Großoolithe erinnern. Nachdem *Teutloperella herculaea* nach Ott (1966, 1967) der riffnahen Lagune zugeordnet wird, ist anzunehmen, dass im Kühkar oberhalb von 1.640 m Höhe das Wettersteinkalk-Riff erschlossen ist.

Von 1.590 m bis mindestens 1.640 m Höhe findet man immer wieder Blöcke mit Ammoniten, die aus dem Wettersteinkalk-Riff stammen, die daneben auch groben Riffschutt und Großoolithe enhalten. Bei 1.640 m Höhe ist erkennbar, dass die Blöcke in Grundmoräne stecken. Da die Umrahmung des Großen und Kleinen Kühkars mit der Moserkarspitze (2.533 m), Kühkarlspitze (2.465 m) und der Nördlichen (2.650 m) und Südlichen Sonnenspitze (2.668 m) aus lagunärem Wettersteinkalk besteht, sollte das dazugehörige Riff im Großen Kühkar oberhalb der begangenen Aufschlüsse noch innerhalb des Kars anstehen.

Beim Aufstieg vom Moserkar in das Rauhkarl werden entlang des Jägersteigs lutitische, unregelmäßig dm- bis 0,5 m gebankte bioklastische Kalke, in wenigen Bänken auch mit Muschelschill oder Peloiden, gequert. Auf ca. 1.750 m Höhe treten Schüttungen mit kleinen Kalkalgen und großen Crinoidenstielgliedern hinzu. Auf 1.780 m Höhe quert der Steig eine bedeutende Nordost streichende subvertikale Störung, die hier als Moserkar-Störung bezeichnet wird. Der Block nordwestlich dieser Störung zeigt eine vollkommen von der im unteren Teil des Großen Kühkars abweichende Abfolge.

Die ältesten und tiefsten Anteile der Abfolge sind in dem Bach erschlossen, der vom Großen Heissenkopf (2.437 m) in südöstlicher Richtung das unterste Rauhkarl quert. Oberhalb der bereits erwähnten Störung, die den Bach bei 1.760 m Höhe quert, stehen m-gebankte hellgraue Mikrite an. Diese gehen nach oben in stark bioturbate Kalke über, in denen die Wühlgänge mit Kalklutit bis Kalkarenit gefüllt sind. Die Wühlgänge verwittern heller als die Matrix. Die Formen können vermutlich der Cruziana-Ichnofazies zugeordnet werden, die randmarine Bedingungen anzeigt (z.B. Frey & Pemberton, 1984). Die Bankung liegt zunächst ebenfalls noch im m-Bereich, aber es tauchen schnell weniger stark verwühlte Bankabschnitte mit dm-Schichtung auf. Darüber folgen flachwinkelig schräggeschichtete, ebenflächig gebankte Kalke des Subtidals, die dunkelgrau und schwach bituminös sind. Schließlich tritt ein 20 cm dicker Abschnitt mit papierdünn geschichteten, schwarzen, stark bituminösen Mergeln auf. Oberhalb dieser Einschaltung beginnen wellig bis knollig geschichtete, stark bituminöse Mikrite mit Filamenten und Radiolarien, die klar der Reifling-Formation zugeordnet werden können. Diese Abfolge zeigt das Absinken des Ablagerungsraums vom flachen Subtidal mindestens bis in den neritischen Bereich an.

Nach einer Aufschlusslücke zwischen 1.840 und 1.900 m Höhe geht die Abfolge der Beckensedimente mit bituminösen dm-gebankten Knollenkalken weiter, die aber jetzt umkristallisiert sind, sodass keine Filamente oder Radiolarien mehr erkennbar sind. Die Bankungsdicke nimmt oberhalb von 1.920 m Höhe wieder zu (manche Bänke sind 40 cm dick), die Schichtflächen werden ebenmäßiger. In einigen dickeren Bänken sind Erosionsflächen und Flaserschichtung aufgrund von Bioturbation zu sehen. Das deutet darauf hin, dass der Ablagerungsraum wieder flacher wird. Nach oben wird die Abfolge von hellgrauen, 0,5 m gebankten Schuttkalken abgeschlossen, die bereits zum Wettersteinkalk gehören. Im Profil ist diese Abfolge der Reifling-Formation 200 m dick.

Nach Westen grenzt die Reifling-Formation mit einer steilen, N–S streichenden und steil westfallenden Störung an den Wettersteinkalk. Das Linear an der Störung zeigt eine steile, NNW-gerichtete abschiebende Bewegung des Hangendblocks. Dieser ist direkt westlich der Störung über mehrere Zehnermeter dolomitisiert, die Störung selbst wird von einem 0,5 m dicken Kataklasit gebildet. An der Störung ändert sich die Schichtorientierung von SW-fallend östlich der Störung auf S-fallend westlich davon. Trotz Dolomitisation sind Bankung und Sedimentstrukturen erhalten, in den dm-gebankten löchrigen Dolomiten wurden Algen und Mikrogastropoden herausgelöst, die dem lagunären Wettersteinkalk ein löchriges Erscheinungsbild verleihen.

Die Reifling-Formation kann nach Osten bis in das mittlere Rauhkarl verfolgt werden. Auf dem flachen Rücken bei 1.900 m Höhe in der Mitte des Rauhkarls sind nur mehr die verwühlten Kalke aus dem Liegenden der Reifling-Formation vorhanden. Sie werden direkt von m-gebankten Biogenschuttkalken mit Grünalgen und wenigen Gastropoden der Gattung *Omphaloptychia* überlagert, manche Bänke bestehen zur Gänze aus grobem Biogenschutt. Die Reifling-Formation verzahnt also über wenige Zehnermeter hinweg mit Wettersteinkalk in lagunärer Fazies.

Ähnliche Lithologien des Wettersteinkalks sind auch weiter oben im Rauhkarl vorhanden, oft mit peloidalen Packstones, lokal reich an Gastropoden. Stromatolithische Lamination ist nur westlich der Rauhkarl-Störung zu finden. Im hintersten Kessel des Rauhkarls (unter der Westlichen Moserkarscharte, 2.468 m) ändert sich oberhalb von 2.300 m Höhe die Fazies der Kalke. In den dm- bis 0,5 m gebankten Kalken wechsellagern Biogenschuttkalke, in einigen Abschnitten auch Grainstones aus Onkoiden mit laminierten Mikriten. Die geschütteten Lagen zeigen Belastungsmarken. In den laminierten Lagen findet man vergente Falten, die auch isoklinal sein können. An mehreren Stellen sind allseitig geschlossene Taschenfalten zu sehen. Sie können stellenweise unvermittelt in klastische Gänge übergehen, die in das Überlagernde eindringen oder zwei mikritische Lagen verbinden. Lokal sind solche Gänge an Erosionsflächen gekappt, was zeigt, dass deren Entstehung und Sedimentationsprozesse gleichzeitig stattfanden. Die Vergesellschaftung von Strukturen zeigt, dass es während der Ablagerung dieser Kalke wiederholt zu seismischen Ereignissen gekommen sein muss, die zu Rutschprozessen und Gangbildung führten. Die Strukturen werden daher als Seismite klassifiziert.

Die onkolithische Fazies ist lateral aushaltend und auch im Oberen Moserkar vorhanden. Ob sie sich als deutlich erkennbarer, bei der Kartierung brauchbarer Horizont eignet, müssen erst weitere Untersuchungen zeigen.

Birkkar

Im Birkkar sind entlang des Wanderweges Richtung Karwendelhaus ab 1.500 m Höhe Kalke der Reifling-Formation aufgeschlossen, die denen im Rauhkarl gleichen. Die Abfolge unterscheidet sich in der Mächtigkeit, die hier maximal um 10 m liegt. Die bioturbaten Kalke im stratigrafisch Liegenden sind wesentlich mächtiger entwickelt und zeigen eine größere Vielfalt an Wühlspuren. In diesem Aufschluss sind in einzelnen Lagen schmale Kieselschnüre entwickelt, im oberen Teil der Abfolge mehrere orangefarbene, stark verwitterte Tufflagen eingeschaltet (vgl. Gruber, 2017). Nach Norden, in das Innere des Birkkars, dünnt die Reifling-Formation schnell durch *onlap* auf bioklastische Kalke aus. Es ist anzunehmen, dass die Aufschlüsse im Birkkar Beckensedimente darstellen, die mit den Klinoformen des Vorriffs verzahnen. Dementsprechend ist bei 1.840 m Höhe am Birkkarbach nur mehr eine Schichtfuge vorhanden.

Im östlichen Birkkar ist auf 2.000 m Höhe, 200 m nördlich der Verzweigung des Birkkarbaches, wieder lagunäre Fazies des Wettersteinkalks anstehend. Der Blick nach SSE in die Westflanke des Großen Heissenkopfes (2.437 m) zeigt den Übergang von der Lagune zum Riffgürtel, der bei 2.200 m Höhe den Rücken der Heissenköpfe erreichen sollte und weiter hangabwärts nach Westen in das Vorriff des Wettersteinkalks mit grobgebankten Klinoformen übergeht. Die Reifling-Formation im Birkkar steht somit in Verzahnung mit Klinoformen des Wettersteinkalk-Riffs, die im Wesentlichen aus dickgebankten bioklastischen Kalken bestehen.

Der Blick in die Westflanke des östlichen Birkkars zeigt zwischen 2.140 und 2.500 m Höhe lagunäre Kalke des Wettersteinkalks mit einer komplexen internen Geometrie. An der Basis der Wand fallen die Kalke parallel zum

Karboden mit 20° nach Süden ein. Im unteren Drittel der Wand ist eine Winkeldiskordanz mit Erosionsrelief sichtbar. Direkt über der Diskordanz fallen zwei Bänke flacher nach Süden ein und liegen parallel zur Diskordanz. Oberhalb dieser beiden Bänke folgen im südlichen Teil des Rückens über einer *downlap*-Fläche undeutlich gebankte Kalke, die nunmehr etwas steiler gegen Süden einfallen. Nach Norden verschwinden die *downlap*-Fläche und auch die undeutliche Bankung darüber; letztere taucht erst wieder 150 m weiter nördlich jenseits des ungebankten Abschnitts wieder auf. Im Hangenden der massigen Zone, oberhalb der Oberkante einer senkrechten Wand, bilden die jüngeren Schichten ein *onlap* an einer Winkeldiskordanz. Nach Süden verschwindet diese Winkeldiskordanz oberhalb des *downlap*.

Aus diesen Beobachtungen kann folgendes abgeleitet werden: (1) Die Kalke wurden während der progressiven Verkippung des Untergrundes nach Süden abgelagert und (2) durch die Verkippung über den *base level* gehoben und teilweise abgetragen. Auf den gehobenen Teilen kam es möglicherweise zur Ausbildung von Fleckenriffen, die wiederum Schutt produzierten, der umgelagert und in lokalen Klinoformen abgelagert wurde. Das Fleckenriff bildete ein topografisches Relief, das von den darauffolgenden Einheiten mit einem *onlap* einsedimentiert wurde. Diese Interpretation basiert nur auf Geometrien der Sedimentkörper, lithologische Untersuchungen vor Ort fehlen noch.

Diskussion und Zusammenfassung

Bei den Kartierungsarbeiten konnten zwei Störungssysteme identifiziert werden:

(1) Das **Rauhkarl-Moserkar-Störungssystem**: die Rauhkarl-Störung beginnt im Norden unter der Felsstufe unterhalb des Ostteils des Kaltwasserkars, quert die Hinterautal-Vomper Kette knapp westlich von Pkt. 2.548 m und anschließend das Rauhkarl in Richtung Südwesten, um östlich des Großen Heissenkopfs den Fuß der Wände zu erreichen. Dort ändert die Störung ihre Richtung auf N–S und bleibt am Fuß dieser Wände. Die Rauhkarl-Störung schiebt den westlichen Block schräg nach Nordwesten ab. In einem N–S-Profil durch den Gipfel der Kaltwasserkarspitze ist die Reifling-Formation im Kaltwasserkar gegenüber dem Vorkommen im Rauhkarl um etwa 1.000 m nach unten versetzt. Im Kar östlich des Kaltwasserkars versetzt die Rauhkarl-Störung die Unterkante des lagunären Wettersteinkalks um mindestens 600 m, aber den Alpinen Muschelkalk nur um 200 m. Der Rest des Versatzes muss an der E–W verlaufenden Störung im hinteren Kalkwasserkar stattfinden. Im E–W-Schnitt ist der Versatzbetrag in der Größenordnung von 250 m, wenn man die Lage der Reifling-Formation im Birkkar und im Rauhkarl vergleicht.

Wo die Felsstufe unterhalb des westlichen Rauhkarls mit den Felswänden östlich des Großen Heissenkopfs zusammenwächst, wird die Rauhkarl-Störung von der NE–SW verlaufenden Moserkar-Störung abgeschnitten. Im Unterschied zur Rauhkarl-Störung versetzt die Moserkar-Störung den SE-Block nach unten, sodass die Reifling-Formation auch an dieser Störung an lagunären Wettersteinkalk grenzt. Die beiden Störungen scheinen kinematisch gekoppelt zu sein, da es südöstlich der Moserkar-Störung keine Fortsetzung der Rauhkarl-Störung gibt.

Grundsätzlich sollten die Schichtorientierungen in einem Gebiet, in dem ein Faltenbau mit km-großen, mehr oder weniger zylindrischen, WNW–ESE verlaufenden Falten vorhanden ist (Heissel, 1978; Tollmann, 1970), entweder SSW- oder NNE-fallend sein. Abweichungen von diesem Muster können entweder auf die Schrägschichtung des Riffhangs zurückzuführen sein, oder auf die Verkippungen der Schichtung an Störungen. Dabei gibt es zwei Möglichkeiten: Verkippung zu einer Störung hin, die dann listrische Geometrie haben muss, oder Verkippung von einer Störung weg durch Schleppung.

Im N–S-Profil sind kaum solche Effekte zu beobachten, da die Schichtung, wenn Sie von der oben beschriebenen Orientierung abweicht, entweder nach Westen oder Osten einfällt, somit subparallel zum Profil liegt und dieses schleifend schneidet. Im E–W-Profil ist zur Rauhkarl-Störung hin immer steileres Fallen nach Westen zu beobachten. Das könnte als Schleppung an der Rauhkarl-Störung aufgefasst werden. Alternativ könnte daran gedacht werden, dass es im Untergrund noch eine zweite, zur Moserkar-Störung parallele listrische Abschiebung gibt, welche die nach unten zunehmende Verkippung der Schichtung verursacht.

Durch die Rauhkarl-Störung wird das Riff und Vorriff des Südgratrückens im Bereich der Heissenköpfe abgeschnitten. Die mächtige Reifling-Formation befindet sich, verglichen mit der Progradationsrichtung des Riffs im E–W-Profil nach Westen, hinter dem Riff, und verzahnt mit lagunärem Wettersteinkalk (vgl. Brandner & Krystyn, 2013).

(2) Das unter (1) beschriebene Rauhkarl-Störungssystem setzt sich nicht nach Nordwesten in die überkippte Abfolge der Nördlichen Karwendelkette fort. Der Taleinschnitt des Filztals und Hochalmsattels folgt einer Störung, an der kombinierter Lateralversatz und Abschiebung des südlichen Blocks beobachtet wird (siehe Abschnitt Karwendelhaus) und welche die Rauhkarl-Störung abschneidet. Das **Schafjöchl-Lamsenjoch-Störungssystem** weiter im Osten (Kilian, 2013), das Störungssystem in dessen unmittelbarer Westfortsetzung im Rücken Gamsjoch-Gumpenspitze (Ortner & Kilian, 2018) haben dieselben Eigenschaften. Es ist anzunehmen, dass dieses bis mindestens zum Karwendelhaus und darüber hinaus vorhanden ist. Möglicherweise durchschneidet es den Kamm von der Brunnensteinspitze (2.180 m) zur Westlichen Karwendelspitze (2.372 m) zwischen Mittenwald und Scharnitz, wo an steilen Störungen immer wieder „Jungschichten“ in den Wettersteinkalk hineingeschert worden sind (Ampferer, 1914: Profil in Abbildung 3).

Literatur

Ampferer, O. (1914): Besprechung mit O. Schlagintweit, K.Ch. v. Loesch und H. Mylius über das Wettersteingebirge. – Verhandlungen der k. k. Geologischen Reichsanstalt, **1914**, 338–352, Wien.

Brandner, R. & Keim, L. (2011): A 4-day field trip in the western Dolomites. – Geo.Alp, **8**, 76–118, Innsbruck.

Brandner, R. & Krystyn, L. (2013): Bericht 2012 über Profilaufnahmen und biostratigraphische Probenbearbeitungen in der Mitteltrias der Nördlichen Kalkalpen (Karwendelgebirge) auf UTM-Blatt 2223 Innsbruck. – Jahrbuch der Geologischen Bundesanstalt, **153**, 417–420, Wien.

BÜSEL, K. (2014): Bericht 2013 über quartärgeologische Aufnahmen in den Nördlichen Kalkalpen im Gebiet Hinterautal auf Blatt 2223 Innsbruck. – Jahrbuch der Geologischen Bundesanstalt, **154**, 315–323, Wien.

DONOFRIO, D.A., HEISSEL, G. & MOSTLER, H. (1980): Beiträge zur Kenntnis der Partnachschichten (Trias) des Tor- und Rontales und zum Problem der Abgrenzung der Lechtaldecke im Nordkarwendel. – Mitteilungen der Österreichischen Geologischen Gesellschaft, **73**, 55–94, Wien.

FREY, R.W. & PEMBERTON, S.G. (1984): Trace fossil facies models. – In: WALKER, R.G. (Eds.): Facies models, Geoscience Canada Reprint Series 1, 2nd Edition, 189–208, Toronto.

GRUBER, J. (2017): Bericht 2016 über geologische Aufnahmen im Gebiet Birkkarklamm, Großer Heissenkopf, Reps, Zeigerkopf, Hintere Schwarzenwand (Karwendel) auf Blatt NL 32-03-23 Innsbruck. – Jahrbuch der Geologischen Bundesanstalt, **157**, 380–384, Wien.

HEISSEL, G. (1978): Karwendel – geologischer Bau und Versuch einer tektonischen Rückformung. – Geologisch-Paläontologische Mitteilungen Innsbruck, **8**, 227–288, Innsbruck.

KEIM, L. & SCHLAGER, W. (2001): Quantitative compositional analysis of a Triassic carbonate platform (Southern Alps, Italy). – Sedimentary Geology, **139**, 261–283, Amsterdam.

KILIAN, S. (2013): Bericht 2012 über geologische und strukturgeologische Aufnahmen im Karwendelgebirge auf UTM-Blatt 2223 Innsbruck. – Jahrbuch der Geologischen Bundesanstalt, **153**, 411–417, Wien.

MAURER, F. (2000): Growth mode of Middle Triassic carbonate platforms in the Western Dolomites (Southern Alps, Italy). – Sedimentary Geology, **134**, 275–286, Amsterdam.

MUTSCHLECHNER, G. (1941): Geologische Karte des Karwendelgebirges 1:25.000, westliches und mittleres Blatt. – Unpublizierte Manuskriptkarte, Innsbruck.

ORTNER, H. & KILIAN, S. (2018): Interacting folds, faults and thrusts – the conundrum of the Karwendel zone of slices (“Karwendelschuppenzone”). – In: KOUKAL, V. & WAGREICH, M. (Eds.): PANGEO AUSTRIA 2018 – Abstracts, 24–26 September 2018. – Berichte der Geologischen Bundesanstalt, **128**, 113, Wien.

OTT, E. (1966): Die gesteinsbildenden Kalkalgen im Schlauchkar (Karwendelgebirge). – Jahrbuch des Vereins zum Schutze der Alpenpflanzen und -tiere, **31**, 152–159, München.

OTT, E. (1967): Segmentierte Kalkschwämme (Sphinctozoa) aus der alpinen Mitteltrias und ihre Bedeutung als Riffbildner im Wettersteinkalk. – Abhandlungen der Bayerischen Akademie der Wissenschaften, Mathematisch-Naturwissenschaftliche Abteilung, Neue Folge, **138**, 1–96, München.

TOLLMANN, A. (1970): Tektonische Karte der Nördlichen Kalkalpen, 3. Teil: Der Westabschnitt. – Mitteilungen der Österreichischen Geologischen Gesellschaft, **62** (1969), 78–170, Wien.

Blatt NL 32-03-23 Innsbruck

Siehe Bericht zu Blatt NL 32-03-17 Hinterriß von Hugo Ortner.

Blatt NL 32-03-28 Neustift im Stubaital

Bericht 2018 über quartärgeologische Aufnahmen in den Gebieten Ranalt und Neustift auf Blatt NL 32-03-28 Neustift im Stubaital

ANNE HORMES

(Auswärtige Mitarbeiterin)

Der Bericht präsentiert das Ergebnis der Kartierung in den Gebieten Ranalt und Neustift vom Sommer 2018 für das UTM Kartenblatt NL 32-03-28 Neustift im Stubaital. Die Kartierung beschreibt die quartärgeologischen Ablagerungen und Phänomene inklusive Massenbewegungsablagerungen und beruht auf dem neuen Begriffskatalog der Geologischen Landesaufnahme für Quartär und Massenbewegungen in Österreich (STEINBICHLER et al., 2019). Das Hauptaugenmerk liegt dabei auf der Kartierung der spätglazialen Gletscherablagerungen der Stadien Egesen und Gschnitz. Im Kartiergebiet Ranalt im Langental wurden die End- und Seitenmoränen des Egesenvorstoßes (E2; Jüngere Dryas) auf 1.550–1.600 m erfasst. Südlich von Ranalt auf der Südseite des Mutterbergtales und bei Ebendl im Langental auf 1.700 m wurden Seitenmoränen kartiert (Egesen I), die auf einer tiefgründigen Hangbewegung liegen und deutlich höher liegen als die Inneren Egesenmoränen im Ausgang des Längentales. Im Kartiergebiet Neustift wurden zwei deutlich voneinander abgrenzbare Eisrandablagerungen auf beiden Seiten des Stubaitales kartiert. Die weiter oben an der Talflanke abgelagerten Eisrandsedimente (> 1.050 m) werden dem Spätglazial zugerechnet, während die unteren im Bereich von 950–1.050 m dem Gschnitz-Stadial zugeordnet werden. Endmoränen sind hier nicht vorhanden, da diese durch Schwemmfächer bedeckt sind oder durch glazifluviatile Prozesse ausgeräumt wurden.

Einleitung

Der Bericht präsentiert das Ergebnis der quartärgeologischen Kartierung für das Stubaital bei Ranalt und Neustift. Die Kartierung wurde ausgeführt von Anne Hormes im Maßstab 1:10.000. Die einzelnen Geologischen Einheiten sind für den Auftraggeber auch in digitaler Form zugänglich (QGIS). Das Hauptaugenmerk bei der Kartierung lag vor allem auf Gletscherablagerungen, gravitativen Massenbewegungsablagerungen und Hochwasser-/Wildbachablagerungen.

Auftraggeber für die Quartärgeologische Karte und den vorliegenden Bericht ist die Geologische Bundesanstalt.

Das Gschnitz-Stadium repräsentiert einen präborealen Gletschervorstoß vor ca. 16,8 ± 1,7 ka (1.000 Jahre vor heute = kilo ages). Kosmogene Nukliddatierungen von der Typlokalität Gschnitzmoräne im Gschnitztal bei Trins ergeben im mittleren Durchschnitt Alter von 17 ka (Ivy-Ochs et al., 2006). Das Egesen-Stadium wird in unserem Bericht im Sinne der geochronologischen Einordnung zur Jüngeren Dryas verwendet (12,9–11,7 ka; Ivy-Ochs et al., 2007; Reitner et al., 2016).

Quartärgeologie, Maßstab und Gebrauch der Karte

Die Kartierung, die in diesem Bericht präsentiert wird, fokussiert auf Quartär und Massenbewegungen und verwendet die empfohlenen Begriffe aus dem „Begriffskatalog der Geologischen Landesaufnahme für Quartär und Massenbewegungen in Österreich" (Steinbichler et al., 2019). Die Kartierung im Gelände wurde in einem Maßstab von 1:10.000 durchgeführt und entspricht damit einem Detailgrad der Kommunalen Ebene. Für die Ausarbeitung der Karte wurden auch digitale Höhenmodelle und Orthofotos verwendet.

Übersicht über das Kartierungsgebiet

Lage und Topografie Ranalt

Das Untersuchungsgebiet Ranalt liegt hauptsächlich entlang des Längenbaches im Langental auf einer Höhe von rund 1.700 m und zieht sich bis zum Haupttalboden der Ruetz zwischen 1.700 m und 1.320 m südwestlich von Ranalt im Mutterbergtal. Am Talschluss des Langentals liegt die Unfallspitze (2.805 m) oberhalb der Nürnberger Hütte (2.280 m), die Mairspitze (2.781 m) im Westen und die Innere und Äußere Wetterspitze (3.052 m, 3.068 m) im Osten bilden die höchsten Erhebungen des Tales.

Im mittleren Teil des Langentals liegt die Bsuchalm auf 1.580 m im Talboden des Langentals.

Vor allem die Ostseite des Langentals, unterhalb der Südlichen Rötenspitze (2.980 m), weist viele interessante quartäre Ablagerungen auf, die Aufschluss über lokale spätglaziale Gletschervorstöße geben.

Das Untersuchungsgebiet lässt sich grob in folgende Bereiche aufteilen:

1) Talboden und fluviale Ablagerungen.
2) Hangablagerungen von unterschiedlichen gravitativen Massenbewegungen.
3) Glazigene Ablagerungen des Egesen-Gletschervorstoßes sensu Jüngere Dryas im Ausgang des Langentals auf 1.500 m (E1).
4) Seitenmoränen im Ebendlaswald auf 1.700 m (E2).

Lage und Topografie Neustift

Das Untersuchungsgebiet Neustift zieht sich im Talboden der Ruetz von Schaller im Süden (1.050 m unterhalb der Seblasspitze (2.351 m) und der Zwölferspitze (2.562 m) bis Kampl im Norden (950 m). Der Ausgang des Oberbergtales ist Teil des Kartierungsgebietes zwischen Milders (1.000 m) und 1.100 m oberhalb des Energiewerkes.

Das Untersuchungsgebiet von Neustift lässt sich grob in die folgenden Bereiche aufteilen:

1) Talboden und fluviale Ablagerungen.
2) Hangablagerungen von unterschiedlichen gravitativen Massenbewegungen, insbesondere große Schwemmfächer und tiefgründige Massenbewegungen.
3) Eisrandablagerungen mit stellenweise Grundmoräne des Spätglazials (> 1.050 m) auf beiden Seiten des Stubaitals zwischen Neustift und Kampl, Grundmoränenablagerungen (spätglazial) im Ausgang des Obertals auf beiden Talseiten, zwischen 1.100 m und 1.200 m.
4) Eisrandablagerungen Gschnitz (950–1.050 m) auf beiden Seiten des Stubaitals, teilweise auch Grundmoränenreste im Talgrund südlich des Kampl- Schwemmfächers.
5) Hangablagerungen und Felsstürze auf der Südseite des Hohen Burgstalls (2.611 m).
6) Talzuschub und tiefgründige Massenbewegung auf der Südostseite der Seblasspitze bei Milders.

Untersuchungsgebiet Ranalt

Gletscherablagerungen Ranalt

Grundsätzlich können wir Seiten- und Endmoränen von zwei verschiedenen Gletschervorstoßphasen unterscheiden.

End-/Seitenmoränen Langental – Egesen 2

Es wurden vier deutliche Wallstrukturen auskartiert, die aus ungerundeten, teils gekritzten Geschieben und unsortierter, verfestigter Grundmoräne bestehen. Diese End- bzw. Seitenmoränen wurden von einem Gletscher abgelagert, der nur das Langental bedeckt hat und dessen Gletscherfront hier auf rund 1.500 bis 1.600 m endete. Das Wallmaterial besteht aus verfestigter Grundmoräne mit subkantengerundeten Geschieben und einer tonig-siltigen Matrix mit geringem Sandanteil. Diese Moränenwälle wurden bereits von Penck & Brückner (1909) beschrieben, und als Daun-Lokalität sensu strictu identifiziert. Mit unserem heutigen Verständnis der Geochronologie der spätglazialen Gletscherstände können wir diese Langental-End-/Seitenmoränen dem Egesenstand (Jüngere Dryas) zuordnen. Wir empfehlen eine CN-Datierung (cosmogenic nuclide dating) der Blöcke, die sich auf den deutlichen Wällen befinden (z.B. Hippe et al., 2014). Die Wälle sind sehr blockreich, allerdings ist es eine Herausforderung, passende Blöcke für eine Datierung zu finden, da es wahrscheinlich ist, dass diese Wälle degradiert sind. Die Blöcke könnten ein scheinbar zu junges Alter ergeben, wenn sie bei der Stabilisierung der Moränenwälle noch mit Grundmoräne bedeckt waren.

Seitenmoränen auf Ebendl – Egesen 1

Die höchsten Seitenmoränen bei Ranalt liegen auf Ebendl oberhalb des nordöstlichen Langentalausgangs auf 1.700 m. Die Seitenmoräne liegt parallel zum Langental und hat eine ausgeprägte Wallform mit einigen großen erratischen Blöcken, die potenziell für eine CN-Datierung herangezogen werden können. Weiter östlich liegen zwischen 1.700 und 1.400 m deutlich ausgeprägt drei Seitenmoränen parallel zum Ruetztal. Diese wurden bereits von SENARCLENS-GRANCY (1938) und MAYR & HEUBERGER (1968) dahingehend interpretiert, dass hier die Gletscher aus dem Langental und Mutterbergtal zusammengeflossen sein müssen.

Zwischen der Seitenmoräne bei Ebendl und der dreiwalligen Seitenmoräne ist kein eindeutiger Wall zu kartieren, allerdings liegen auf einer tiefgründigen Massenbewegung mit deutlichen Zerrspalten und antithetischen Grabensystemen viele große erratische Blöcke verstreut, die Ausdruck geben für die einstige Vergletscherung. Die Seitenmoräne Egesen 1 liegt rund 100 m höher als die vier Wälle der Seitenmoräne Egesen 2. Eine Datierung von einigen Blöcken auf diesen Moränenwällen ist daher essenziell für die Alterseinstufung.

Deutliche Endmoränen finden sich von diesem Vorstoß nicht. Die Endmoränen wurden vermutlich vom Schwemmfächer südlich Ranalt ausgeräumt und bedeckt. Die drei Seitenmoränen ziehen hier deutlich bis auf eine Höhe von 1.400 m hinab und sollten gletschergeometrisch ungefähr bei Issebichl enden. Laut SENARCLENS-GRANCY (1938) enden diese Seitenmoränen bei Falbeson, während MAYR & HEUBERGER (1968) das Gletscherende bei Issebichl vermuten.

Eisrand- und Grundmoränenablagerung

Der Osthang im Ausgang des Langentals ist mit Eisrandablagerungen und Grundmoränenablagerungen bedeckt. Auch zwischen den Egesen-Seitenmoränenwällen finden sich Eisrandablagerungen und stellenweise Grundmoräne.

Die Eisrandablagerungen sind unsortiert, es finden sich alle Korngrößen, jedoch keine gekritzten Geschiebe, teilweise ist der Rundungsgrad etwas höher als in den Grundmoränen, oder die Matrix ist nicht verfestigt und nicht konsolidiert. In den Aufschlüssen entlang des Waldrandes finden sich überwiegend Eisrandablagerungen, nur hin und wieder fördern Baumaufschlüsse eindeutige Grundmoränen zu Tage. Daher sind die Ablagerungen als Eisrandsediment in der Karte, obwohl stellenweise Grundmoräne zu kartieren wäre.

Erratische Blöcke

Im gesamten Gebiet unterhalb des Grieplastals zwischen Langental und dem Wildbach unterhalb der Rötenspitze liegen erratische Blöcke, die eindeutige Zerrspalten und antithetische Grabensysteme einer tiefgründigen Massenbewegung im Ebendlwald bedecken.

Glazigene Ablagerungen

In der Ebene bei Spitz im Mutterbergtal unterhalb der deutlichen Seitenmoränen des Egesen 1 liegen sehr viele große (mindestens 1 m^3), kantige und subkantengerundete Blöcke. Die Ablagerung kann entlang der Ruetz in Aufschlüssen beschrieben werden. Die Ablagerung ist unsortiert, jedoch nicht konsolidiert. Es kann sich daher um eine Ablationsmoräne handeln, die supraglazial als debris cover den ehemaligen Mutterbergtal-/Langental-Gletscher bedeckt hat. Der Interpretation von MAYR & HEUBERGER (1968) folgend können die Ablagerungen auch als Bergsturzmasse interpretiert werden, die sich auf dem Gletscher abgelagert hat. Da jedoch der gesamte Nordhang des Mutterbergtales mit Hangschutt bedeckt ist, lässt sich dies nicht eindeutig klären. Sollte es sich um eine Bergsturz-Ablagerung handeln, die auf dem spätglazialen Gletscher zu liegen gekommen ist, dann würde man idealerweise auch noch Ablagerungen der Bergsturzmasse auf der gegenüberliegenden Hangseite erwarten.

Gravitative Massenbewegungsablagerungen Ranalt

Felssturzablagerung und Hangablagerungen

Im oberen Langental dominieren Felssturzprozesse die gesamte westliche Bergflanke unterhalb der Mairspitze (2.780 m). Andere gravitative Prozesse wie Lawinen und Murschuttablagerungen lassen sich ebenfalls beobachten. Letztere bilden den Schuttkegel westlich des Langentals bei Langental auf 1.600 m. Auf der gesamten Ostseite des Langentals bilden Prozesse wie Steinschlag, kleinere Felsstürze, Lawinenabgänge die Hangablagerungen.

Schwemmfächer

Im nördlichen Teil des Langentals sind eher wassergesättigte Prozesse vorherrschend und haben größere Schwemmfächer abgelagert, die aber auch teils durch Lawinen und Hangmuren abgelagert sein können. Ein großer Schwemmfächer unterhalb der Rötenspitze südlich von Ranalt hat die Seitenmoränen Egesen 1 ausgeräumt. Große Schuttfächer mit kantigem, lokalem Material finden sich auch auf der Nordseite der Mairspitze, die sich bis zum Ruetztalboden hinunterziehen und hier hauptsächlich durch Steinschlagprozesse genährt werden.

Fluss- und Wildbachablagerungen

Im Talboden des Langentals und des Mutterbergtals finden sich fluviatile Ablagerungen und Wildbachablagerungen. Vor allem am Talausgang des Langentals sind die fluviatilen Ablagerungen eher als Wildbachablagerungen mit großen Blöcken zu bezeichnen, während die flachen Talböden von Ruetz und dem Langental durch weniger grobes und gerundetes Material gekennzeichnet sind.

Wildbachablagerungen lassen sich sowohl im Griesbachtal, im Norden der tiefgründigen Massenbewegung, als auch südlich der drei Seitenmoränen im Ebendlwald und auf der Westseite des Ruetztals unterhalb der Pfandleralm kartieren.

Anthropogene Phänomene Ranalt

Auf der Ostseite des Langentals wurden mehrere Lawinenverbauungen errichtet, um die landwirtschaftlichen Gebäude zu schützen, ebenso eine Wildbachverbauung unten im Tal der Ruetz bei den Wildwasserfällen.

Untersuchungsgebiet Neustift

Gletscherablagerungen Neustift

Eisrandablagerung

Im südlichen Teil des Kartierungsgebietes, südlich von Milders und dem Oberbergtal, finden sich hauptsächlich Eisrandablagerungen, die mit mehr oder minder geschlossenen Grundmoränenablagerungen verzahnt sind. Auf der Westseite des Stubaitales sind Eisrandablagerungen durch den Talzuschub unterhalb der Seblasspitze gen Tal verschoben.

Zwischen Neustift und Kampl ziehen auf beiden Talseiten des Stubaitales zwei Eisrandterrassen hinab bis zum Schwemmfächer von Kampl. Teilweise findet sich Grundmoräne am Westhang des Stubaitales. Die obere Eisrandlage (> 1.050 m) ist mindestens 100 bis 150 m mächtig und wird der spätglazialen Eiszerfallsphase zugerechnet. Oberhalb Ausserrain, nordöstlich vom Jedlerhof, befindet sich ein sehr blockreicher Wall auf 1.080 m (47°07‘39“ N, 011°19‘28“ E). Dieser kann sowohl als Seitenmoräne interpretiert werden, als auch als Erosionsrest während des Eiszerfalls.

Die untere Eisrandlage wird dem Gschnitz-Stadium zugerechnet und liegt zwischen 1.050 und 950 m. Die Eisrandlagen-Sedimente zeigen ein variables Spektrum von Dgm, Dgc, Dmc.

Glazifluviatile Ablagerung

Südlich von Kampl und nördlich von Neustift wurden aufgrund der, in den Laserscans erkennbaren, braided river (verzweigter Fluss) Morphologie glazifluviatile Terrassen kartiert, die sich aus den Eisrandablagerungen lösen. Glazifluviatile Ablagerungen sind zwischen Bichlweg und Neder im Liegenden des Drumlins aufgeschlossen.

Glaziogene Ablagerung und Grundmoränenablagerung

Eindeutige und zusammenhängende Grundmoränenablagerungen finden sich mit einer unsortierten Geschiebezusammensetzung und allen Korngrößen im Ausgang des Oberbergtals auf beiden Talseiten in den Sediment-Variationen Dmm, Dh, Dms, Dcs, Dcm, Dgc.

Zwischen Bichlweg und Pinisweg in Neder findet sich eine typische Grundmoränenablagerung, die morphologisch als Drumlin ausgeprägt ist. In einem Hausaufschluss am Bichlweg waren glazifluviatile Vorstoßschotter mit einer subglazialen überkonsolidierten Grundmoräne bedeckt.

Auch am Oberberg sind glazifluviatile Vorstoßschotter mit einer subglazialen, konsolidierten Grundmoräne bedeckt. Erratische Blöcke finden sich vor allem auf der rechten Talseite auf der Gschnitz-Eisrandlage.

Gravitative Massenbewegungsablagerungen Neustift

Murablagerungen

In den Grundmoränen und Eisrandsedimenten lösen sich häufig Muren und oberflächennahe Hangmuren, z.B. auf der Südseite von Neustift im Schittertal und Lehnertal. Sicherlich finden sich auch im Frauental Murablagerungen, wir haben uns aber entschieden, den Frauental-Fächer eher als Schwemmfächer zu kartieren. Eine frische Hangmure hat sich im Sommer 2018 oberhalb des Wasserwerks im Oberbergtal ereignet und hat seine Abrisskante in der Grundmoräne.

Felssturzablagerung

Der Bereich des Oberbergtal-Ausganges und die anschließenden Talflanken im Stubaital östlich von Milders werden von Felssturzprozessen dominiert.

Hangablagerungen, Schuttfächer

Der gesamte Osthang des Stubaitals zwischen Schaller und Neustift ist hauptsächlich durch Hangablagerungen und Schuttfächer dominiert. Glazigene Ablagerungen sind komplett bedeckt.

Talzuschub

Der gesamte Südhang der Seblasspitze (Grüblen) westlich von Milders/Oberbergtal ist als tiefgründige Massenbewegung auskartiert. Der Lauf der Ruetz ist hier deutlich nach Süden verschoben und wir finden die engste Talstrecke des gesamten Stubaitals. Um eine mögliche Aktivität des Grüblenhanges zu bestimmen, wäre es von Vorteil, die Interferometric Synthetic Aperture Radar-Methodik (InSAR) mit Sentinel-1 oder TerraSAR-X Satellitendaten zu verwenden. Im unteren Teil gibt es deutliche Hinweise auf eine fortschreitende Deformation des Hangs. Antithetische Täler stellen eindeutige morphologische Parameter für tiefgründige Massenbewegungen dar.

Fluss- und Wildbachablagerungen Neustift

Fluviatile und Wildbach-Ablagerungen

Im oberen Teil des Bachertales sind Wildbachprozesse als Hauptprozess in der Karte hervorgehoben und ebenso in den beiden Tälern östlich vom Bachertal unterhalb des Mahderberges.

Bei einigen großflächigen fluviatilen Ablagerungen östlich von Neustift dürfte es sich um glazifluviatile Ablagerungen handeln, da sich im Laserscan sehr verzweigte Flussverästelungen zeigen (braided river).

Schwemmfächer, Schwemmkegel

Große Schwemmfächer befinden sich im am Fuß des Bacher- und Frauentals.

Landschaftsentwicklung

Nördlich von Neustift wurden Gschnitz-Seitenmoränen niemals in detaillierten Karten präsentiert, die klassische End-/Seitenmoränen des Gschnitz darstellen. Das Gschnitz-Stadium wurde von Penck & Brückner (1909) in einer kleinen Karte des Stubaitals präsentiert, und eindeutig als Gletscherstirnlage bezeichnet, ohne dass es deutliche End-/Seitenmoränen südlich von Mieders/Telfes gibt.

Das klassische Gschnitz wurde im Nachbartal Gschnitz definiert und weist eine Schneeliniendepression von 600 m

(Penck & Brückner, 1909) oder 700 m auf (Kerschner, 2009). Mayr & Heuberger (1968) beschreiben eine Endmoräne rund 4 km südwestlich von Fulpmes bei Kampl ohne Karte (sensu Penck & Richter, 1903) und merken an, dass die Seitenmoränen des Gschnitzstandes von Hangbewegungsmaterial bedeckt seien.

Im Kartiergebiet finden sich zwei Eisrandlagen ohne deutliche Moränen südlich vom Kampl-Schwemmfächer. Die obere Eisrandlage (> 1.050 m) rechnen wir dem spätglazialen Eiszerfall zu. Die untere Eisrandlage (950–1.050 m) rechnen wir dem Gschnitz-Stadium zu. Auf der linken Stubaitalseite beim Jedlerhof könnte man Blöcke des oberen Walles CN datieren, auf der rechten Talseite gibt es sehr große erratische Blöcke im Wald der unteren Gschnitz-Eisrandlage, um eine Altersbestimmung vorzunehmen.

Das Daunstadium wurde erstmals von Penck & Brückner (1909) im Ausgang des Langentals südlich von Ranalt definiert, daher stellen die Moränen im Kartiergebiet Ranalt die Typlokalität für das Daunstadium dar. Laut Schneegrenzdepressionsberechnungen und Kartierungen von End-/und Seitenmoränen soll die Schneegrenzdepression des Daunstadiums rund 400 bis 500 m betragen (Klebelsberg, 1947; Kerschner, 2009; Ivy-Ochs et al., 2007). Bevor bessere Datierungsmöglichkeiten für die Endmoränenstände zur Verfügung standen, wurden in den Alpen Schneelinienendepressionen auf Grundlage der Karte von Klebelsberg (1947) berechnet.

Das Bølling/Allerød Interstadial (14,7–12,9 ka) wird von einem weiteren Gletschervorstoß, dem Egesen, während der Jüngeren Dryas abgelöst. Die zugehörigen Endmoränen liegen am Ausgang des Langentals auf 1.600 m und die berechnete Schneegrenzdepression für diese Moränen wurde auf 200 bis 400 m geschätzt, bzw. 250 bis 400 m (Kerschner, 1979; Ivy-Ochs, 2007). Klassische Egesenmoränen sind deutlicher ausgeprägt im Gegensatz zur runderen Morphologie von Daunmoränen, die von Solifluktion überprägt wurden. Die Egesenmoränen wurden an mehreren Orten in den Alpen mit 13,9 bis 10,6 ka datiert (Ivy-Ochs et al., 2009). Es bleibt die Frage offen, ob es tatsächlich vor dem Bølling/Allerød einen präborealen Gletschervorstoß gegeben hat, oder ob die Daunmoränen eher dem Egesen (Jüngere Dryas) zuzuordnen wären. Solange es keine Altersdatierungen der klassischen Daunmoränen gibt, wird diese Frage nicht zu beantworten sein. International gibt es durchaus Hinweise auf einen zweistufigen Verlauf der Jüngeren Dryas (Ivy-Ochs et al., 2007; Bakke et al., 2009).

Im Raum Lienz konnte eine Endmoräne, die aufgrund der Schneegrenzdepressionsmethode als Daun eingestuft wurde, auf 12,8 ± 0,8 ka datiert werden und muss daher dem Egesenvorstoß in der frühen Jüngeren Dryas (Reitner et al., 2016) zugeordnet werden. Darauf aufbauend, bezeichnen wir in diesem Bericht die Endmoränenwälle auf Ebendl als Egesen I, die wir im Sinne einer chronologischen Zuordnung zur Jüngeren Dryas zurechnen (Mayr & Heuberger, 1968).

Senarclens-Grancy (1938) hat für die beschriebenen Moränen von Penck & Brückner (1909) bei Ranalt eine eigene Terminologie benutzt. Äußere Seitenmoränenwälle (D/g) liegen rund 100 m höher auf der Ebene Ebendl oberhalb der Inneren Egesen-Endmoränen auf 1.600 bis 1.700 m (Senarclens-Grancy, 1938). Er stellt am Ausgang des Langentals fest, dass hier die bestens ausgeformten Inneren Egesen-Wälle liegen (D/d) (Senarclens-Grancy, 1938). Dementsprechend hat er bereits die klassischen Daun-Moränen als Egesen bezeichnet (D/d). Er zählt sieben Stirnwälle des Inneren Egesenstandes im Talgrund des Langentals auf 1.500 bis 1.600 m. Im Zuge der Kartierung konnten nur rund vier Wälle festgestellt werden, wobei diese Wälle so nah beieinanderliegen, dass die Wallstrukturen nicht deutlich voneinander zu trennen sind. Dieser Stand wurde von Penck & Brückner (1909) als Daunwall im unteren Langental bezeichnet, während wir die unteren Egesenwälle als Egesen II bezeichnen.

Literatur

Bakke, J., Lie, Ø., Heegaard, E., Dokken, T., Haug, G.H., Birks, H.H., Dulski, P. & Nilsen, T. (2009). Rapid oceanic and atmospheric changes during the Younger Dryas cold period. – Nature Geoscience, **2**/3, 202–205, London.

Hippe, K., Ivy-Ochs, S., Kober, F., Zasadni, J., Wieler, R., Wacker, L., Kubik, P.W. & Schlüchter, C. (2014). Chronology of Lateglacial ice flow reorganization and deglaciation in the Gotthard Pass area, Central Swiss Alps, based on cosmogenic 10^{Be} and in situ14^{C}. – Quaternary Geochronology, **19**, 14–26, Amsterdam.

Ivy-Ochs, S., Kerschner, H., Kubik, P. & Schlüchter, C. (2006): Glacier response in the European Alps to Heinrich Event 1 cooling: the Gschnitz stadial. – Journal of Quaternary Science, **21**, 115–130, Chichester.

Ivy-Ochs, S., Kerschner, H. & Schlüchter, C. (2007): Cosmogenic nuclides and the dating of Lateglacial and Early Holocene glacier variations: the Alpine perspective. – Quaternary international, **164**, 53–63, Oxford.

Ivy-Ochs, S., Kerschner, H., Maisch, M., Christl, M., Kubik, P. & Schlüchter, C. (2009): Latest Pleistocene and Holocene glacier variations in the European Alps. – In: Thompson Davis, P., Menounos, B. & Osborn, G.: Holocene and Latest Pleistocene Alpine Glacier Fluctuations: A global Perspective, 2137–2149, Amsterdam.

Kerschner, H. (2009): Gletscher und Klima im Alpinen Spätglazial und frühen Holozän. – In: Schmidt, R., Matulla, C. & Psenner, R.: Klimawandel in Österreich: Die letzten 20.000 Jahre ... und ein Blick voraus, 5–26, Innsbruck.

Klebelsberg, R. (1947): Die heutige Schneegrenze in den Ostalpen. – Berichte des Naturwissenschaftlich-Medizinischen Vereins in Innsbruck, **47**, 9–32, Innsbruck.

Mayr, F. & Heuberger, H. (1968): Type Areas of Late Glacial and Post-Glacial Deposits in Tyrol, Eastern Alps. – In: Richmond, G.M.: Glaciation of the Alps: Proceedings of the VII Congress of the International Union for Quaternary Research 1965, 143–165, Boulder.

Penck, A. & Brückner, E. (1909): Die Alpen im Eiszeitalter: 1. Band: Die Eiszeiten in den nördlichen Ostalpen. – XVI + 393 S., Leipzig.

Penck, A. & Richter, E. (1903): Glazialexkursion in die Ostalpen. – In: Teller, F.: IX. Internationaler Geologen-Kongress: Führer für die Exkursionen in Österreich, 97, Wien.

Reitner, J.M., Ivy-Ochs, S., Drescher-Schneider, R., Hajdas, I. & Linner, M. (2016): Reconsidering the current stratigraphy of the Alpine Lateglacial: Implications of the sedimentary and morphological record of the Lienz area (Tyrol/Austria). – E&G Quaternary Science Journal, **65**/2, 113–144, Hannover.

Senarclens-Grancy, W. (1938): Die Gliederung der stadialen Moränen im Stubaital. – Jahrbuch der Geologischen Bundesanstalt, **88**, 13–24, Wien.

Steinbichler, M., Reitner, J.M., Lotter, M. & Steinbichler, A. (2019): Begriffskataloge der Geologischen Landesaufnahme für Quartär und Massenbewegungen in Österreich. – Jahrbuch der Geologischen Bundesanstalt, **159**, 5–49, Wien.

Bericht 2018 über geologische Aufnahmen im östlichen Ötztal-Kristallin östlich der Brennerspitze auf Blatt NL 32-03-28 Neustift im Stubaital

Markus Palzer-Khomenko

(Auswärtiger Mitarbeiter)

Kartierungsgebiet

Das Untersuchungsgebiet erstreckt sich auf 24 km^2 südlich und östliches des Kamms von der Falbesoner Ochsenalm bis zum Taleingang des Oberbergtals und kann grob in zwei Bereiche unterteilt werden. Westlich der „Matzelehnergisse“ ist der Untergrund stabil und die Hänge in das Haupttal sind sehr steil und schwer begehbar. In den höher gelegenen Bereichen haben sich gut begehbare Kare mit hervorragenden Aufschlüssen ausgebildet („Bassler-Rinne“, „Kerrachgrube“, „Hinterm Gemäuer“). Das Gestein wird durch Orthogneise dominiert.

Die „Matzelehnergisse“ markiert einen markanten Wechsel zum östlichen, sehr instabilen Gebiet. Verschiedene Phänomene von Massenbewegungen sind allesamt einem großen Talzuschub zuzuordnen, der die gesamte Südost-Ost-Flanke erfasst und die Kartierung des Festgesteins stark verkompliziert. Gleichzeitig sind die Hänge hier wesentlich sanfter ausgebildet, leichter begehbar und weitestgehend durch Straßen und Wege erschlossen. Vor allem in den unteren Bereichen fehlen Aufschlüsse allerdings völlig. Die besten tiefgelegenen Aufschlüsse konnten im Bereich der Haupt-Abrisskanten der Massenbewegung gefunden werden.

Die vorliegende Kartierung stellt die Fortsetzung der Kartierungsarbeiten aus den Jahren 2014 bis 2017 dar (Palzer, 2015; Palzer-Khomenko, 2017). Das Falbeson westlich des Arbeitsgebietes wurde durch Klötzli-Chowanetz (2016) kartiert. Kleinräumige Kartierungen des Quartärs von Schmidegg (1939, 1944) liegen vor. Eine großräumige geologische Karte gibt es von Hammer (1929). Mineral-Abkürzungen wurden nach Kretz (1983) verwendet (mit Ausnahme von Amphibol = Amph, Klinopyroxen = Cpx, Feldspat = Fsp und Hellglimmer = Hg).

Beschreibung und Verbreitung verwendeter Lithodeme

Im Untersuchungsgebiet wurden eine ganze Reihe von bereits bekannten und (informell) beschriebenen Lithodemen angetroffen. Darüber hinaus ergab sich die Notwendigkeit der Einführung eines zusätzlichen Komplexes. Im Bereich des langen Grats zwischen „Brennerspitze“ und „Seblasspitze“ wurde eine Abfolge aus Staurolit führenden Paragneisen angetroffen, welche durch eher geringmächtige Orthogneise intrudiert und thermisch überprägt wurden. Diese Paragneise lassen sich von jenen des Franz-Senn-Komplexes abgrenzen, der kein solches Intrusionsereignis erfuhr.

Glockturm-Suite

Bassler-Granitgneis

Der relativ einfach zu unterscheidende Bassler-Granitgneis wurde bereits mehrfach beschrieben (Palzer, 2015; Klötzli-Chowanetz, 2016). Er zählt zu den Zwei-Glimmer-Granitgneisen der Glockturm-Suite (Schindlmayr, 1999). Besonders charakteristisch sind die großen Kfs-Augen, welche oft rosa oder weiß gefärbt erscheinen. Der Bassler-Granitgneis liegt in manchen Bereichen auch als stark elongierter Stängelgneis vor. Zu den randlichen Bereichen hin nimmt die Korngröße ab und die charakteristischen Kfs-Augen verschwinden, bis er von einem leukokraten Paragneis kaum noch zu unterscheiden ist. Allerdings enthalten die angrenzenden Paragneise und Schiefer deutlich mehr Glimmer und Eisen, was in einer stärker ausgeprägten Schieferung und Verfärbung resultiert. Anhand dieses Kompetenz- und Farbkontrastes kann der Bassler-Granitgneis gut von seinem Umgebungsgestein unterschieden und abgegrenzt werden. Darüber hinaus kommt es direkt im Kontaktbereich zur Ausfällung einer weißlichen, feinkörnigen Substanz, deren chemische Zusammensetzung noch nicht analysiert werden konnte. Diese Ausfällungen konnten bereits 2014 am Winterweg zur Franz-Senn-Hütte (Long: 11.1837; Lat: 47.0902) sowie am „Schafleger“ (Long: 11.2019; Lat: 47.0609) beobachtet werden. Im Untersuchungsgebiet konnten die Ausfällungen im Ausbruchsgebiet eines frischen Felssturzes nahe Volderau (Long: 11.2452; Lat: 47.0655) angetroffen werden. Ein Zusammenhang zwischen Felssturz und dem strukturell schwachen Kontakt zwischen Paragneisen und Bassler-Granitgneis scheint naheliegend. Außerhalb des Untersuchungsgebietes wurden Ausfällungen auch im Kontaktbereich zwischen den beiden auf der Geofast-Karte verzeichneten Granitgneisen entlang der alten Straße zum „Forchach-Hof“ angetroffen (Long: 11.2790; Lat: 47.1078).

Der Bassler-Granitgneis dominiert den westlichen Teil des Untersuchungsgebietes zwischen Falbesoner Ochsenalm und Milderaunalm. Nur in den höchsten Bereichen zwischen Brennerspitze und Kerrachspitze wurden Paragneise, Glimmerschiefer und Amphibolite angetroffen. Bemerkenswert ist hierbei eine mehrere 100 m mächtige stark verschieferte Paragneis-Septe innerhalb des Bassler-Granitgneis-Körpers, die in der „Kerachgrube“ eine großräumige Faltenstruktur im km-Bereich nachzeichnet. Nach Osten hin nimmt sowohl die Mächtigkeit der Septe, als auch jene des Bassler-Granitgneises zwischen Septe und Paragneisen bis auf wenige Zehnermeter ab, kann aber bis in den Bereich des „Hühnerspiels“ gut nachverfolgt werden.

In Dünnschliffen aus den randlichen Bereichen des Bassler-Granitgneises aus der „Kerachgrube“ sowie zwischen „Die Flecke“ und „Hühnerspiel“ zeigte sich ein Hg-reicher, Czo-führender Gneis mit mittelgroßen Kfs. Die Hg-Leisten sind relativ groß ausgebildet und definieren die Foliation. Ein teilweise chloritisierter, grünlicher Bt kommt seltener vor. Kfs zeigt manchmal schöne Mikroklin-Gitter. Stark verzwillingter Pl zerfällt zu relativ großem Hg und Czo. Auch Aggregate von Grt wurden in einem Schliff gefunden. In einem Schliff wurden große, kantige, teils würfelige Erzminerale beobachtet.

Schrankogel Komplex

Rinnengruben-Lithodem

Das Rinnengruben-Lithodem (Palzer-Khomenko, 2017) konnte nur im westlichsten Teil zwischen Falbesoner Ochsenalm und Regensburger Hütte angetroffen werden. Dort wurden Grt-Amphibolite, Amphibolite, Grt-führende sowie Grt-freie Gneise beobachtet. In den Schuttfächern wurden zahlreiche Grt-Glimmerschiefer entdeckt, die vermutlich vom weiter oben entlangziehenden Höllenrachen-Lithodem stammen. Das Rinnengruben-Lithodem ist im Bereich der Regensburger Hütte mit spektakulären Eklogiten vergesellschaftet. Die Aufschlussverhältnisse ließen eine klare Abgrenzung zum Höllenrachen-Lithodem und zum Sommerwand-Lithodem nicht zu.

Höllenrachen-Lithodem

Das Höllenrachen-Lithodem (Palzer-Khomenko, 2017) konnte nur in einem Aufschluss zwischen Falbesoner Ochsenalm und Regensburger Hütte in Form eines Grt-Glimmerschiefers angetroffen werden. Im Dünnschliff zeigen sich neben großen Granaten und Hellglimmern auch serizitische Nester, die als Pseudomorphosen von Ky und St gedeutet werden. Grt ist stark zerbrochen und teilweise völlig chloritisiert. Manche Grt-Körner zeigen im Kern auch eine ältere Schieferung. Weitere Bestandteile sind ein graugrünlich-pleochroitischer Amph, in Adern vorkommender Cal, Czo, Qtz sowie Erzphasen. Die Aufschlussverhältnisse ließen eine durchgehende Verfolgung des Höllenrachen-Lithodems nicht zu. Daher konnte sein Verlauf nur anhand von Rollstücken und Interpolation ungefähr auf der Karte verzeichnet werden.

Franz-Senn-Komplex

Sommerwand-Lithodem

Das Sommerwand-Lithodem (Palzer-Khomenko, 2017) bildet den Rahmen des Bassler-Granitgneises. Es setzt sich aus Bt-Gneisen, Amphiboliten, Bt-Schiefern und vereinzelt auch Grt-Amphiboliten zusammen. Nahe der Falbesoner Ochsenalm konnte das Sommerwand-Lithodem zwischen Höllenrachen-Lithodem und Bassler-Granitgneis angetroffen werden. Dort zeichnet der Kontakt zum Bassler-Granitgneis eine großräumige Faltenstruktur nach. Dieselben Gneise und Schiefer mit vereinzelten Amphiboliten wurden in den untersten Bereichen entlang des Stubaier-Haupttals angetroffen. Im Bereich „Kerachgrube" – „Hinterm Gemäuer" – „Hühnerspiel" bilden Bt-Schiefer eine Septe innerhalb des Bassler-Granitgneises. Oberhalb des darüber folgenden Bassler-Granitgneis-Bandes finden sich mehrere 100 m mächtige Amphibolite und Bt-Gneise. Ob die Bt-Gneise im Bereich der „Matzelehnergisse", welche dort östlich an den Bassler-Granitgneis anschließen, dem Sommerwand-Lithodem oder doch besser dem Brenner-Komplex zugerechnet werden sollten, bleibt nicht zuletzt aufgrund der schwierigen Aufschlussverhältnisse offen. Da bisher in diesem Bereich keine Phänomene einer T-betonten Überprägung (migmatische Strukturen, Feldspat-Blasten, große Staurolite) beobachtet wurden, werden sie vorerst dem Sommerwand-Lithodem zugerechnet. Die ungewöhnlich große scheinbare Mächtigkeit, im Vergleich zu jener am Hühnerspiel, ist dem Verschnitt mit dem Gelände und der großräumigen Massenbewegung geschuldet. Außerdem musste in diesem Bereich aufgrund fehlender Festgesteinsaufschlüsse besonders stark interpoliert werden.

Bei den Bt-Schiefern der Septe handelt es sich um fein-mittelkörnige, gleichkörnige, stark geschieferte Qtz-reiche Gesteine. Der moderate Anteil an stark hellbraun pleochroitischem und nur schwach chloritisiertem Bt definiert die Schieferung. Hg kommt in Form einzelner, teilweise quer-sprossender Körner sowie als Serizit vor. Pl kann nur selten identifiziert werden uns ist weitestgehend serizitisiert. Stellenweise findet sich auch hypidiomorpher Grt. Der Grt-Amphibolit im Bereich der Falbesoner Ochsenalm ist reich an Ep und großen, idiomorphen und Fe-armen (niedrige Interferenzfarben) Czo. Die großen Grt-Augen enthalten im Kern eine alte Foliation. Bt ist bräunlich stark pleochroitisch mit schwach- bis starkem Grünstich. In manchen Bereichen ist Bt vollständig chloritisiert. Weite Bereiche bestehen aus sehr feinkörnigem Ep, der von flaserigen Qtz-Lagen unterbrochen wird. Pl scheint vollständig abgebaut worden zu sein. Akzessorisch finden sich auch Ttn und Ap. Die Schliffe südlich der Brennerspitze zeigen eine ähnliche Zusammensetzung. In manchen Bereichen konnte auch hier eine sehr feinkörnige Ep-Matrix unterbrochen durch Qz-Lagen beobachtet werden. Allerdings ist der Grt-Gehalt reduziert und größerer Ep und Czo fehlt. Dafür hat sich teilweise ein blaugrünlich-bräunlich-pleochroitischer Amph erhalten. Im selben Bereich haben sich auch viele Erzphasen (Ilmenit?) erhalten, welche randlich zu Ttn zerfallen.

Brenner-Komplex

Im Bereich der Brennerspitze wurden die Paragneise und Amphibolite durch Orthogneise intrudiert, welche im Bereich der Mittergratspitze eine Mächtigkeit von mehreren Zehnermetern erreichen, ohne einen gut abgrenzbaren Orthogneis-Körper zu bilden, wie das etwa beim Bassler-Granitgneis der Fall ist. Die Platznahme dieser geringmächtigen Orthogneis-Lagen führte zur Aufheizung der umgebenden Paragneise des Sommerwand-Lithodems und damit zu einer T-betonten Überprägung, die sich im Wachstum von bis zu 5 cm großem St, Grt und Fsp-Blasten äußerte. Darüber hinaus kam es stellenweise zu kleineren partiellen Aufschmelzungen.

Aufgrund der unterscheidbaren Zusammensetzung und Evolution dieser Gesteine können diese vom Sommerwand-Lithodem abgegrenzt und als eigenständige Lithodeme auf dem Kartenblatt ausgeschieden werden. Da die Ortho- und Paragneise eng miteinander „wechsellagern", was in manchen Bereichen eine Generalisierung notwendig macht, und da diese Gesteine das jüngste prägende Ereignis gemeinsam haben, werden sie zum Brenner-Komplex zusammengefasst. Der Brenner-Komplex wiederum umfasst den Schafgrübler-Orthogneis, die Paragneise des Brenner-Komplexes sowie die Amphibolite des Brenner-Komplexes. Auf der Karte werden vorwiegend und im Zweifel die Paragneise des Brenner-Komplexes ausgeschieden. Nur wo Orthogneise und Amphibolite tatsächlich in ausreichender Mächtigkeit angetroffen wurden, sind sie als eigenständige Lithodeme dargestellt. Geringmächtige Orthogneis-Lagen sowie Dykes sind als lithologische Linien eingetragen.

Schafgrübler-Orthogneis

Palzer-Khomenko (2017) beschrieb bereits das Schafgrübler-Lithodem, interpretierte es jedoch irrtümlich als leukokraten Paragneis. Die Vermutung, dass es sich bei den Orthogneis-Lagen der Mittergratspitze um dieselben Gesteine handelt, die auch im Bereich des „Schafgrübler" vorkommen, liegt aufgrund der petrografischen Zusammensetzung und aufgrund der Lage und Orientierung der Gesteine nahe. Daher werden die hier angetroffenen Orthogneise des Brenner-Komplexes dem Schafgrübler-Lithodem zugerechnet und das Schafgrübler-Lithodem als Ganzes wird zum Schafgrübler-Orthogneis umgedeutet. Hierbei handelt es sich um eine Reihe von Orthogneis-Lagen, welche die umgebenden Paragneise sowie die Amphibolite mit wechselnder Mächtigkeit durchsetzen.

Im Dünnschliff zeigt sich ein relativ gleichkörniges Gestein aus Kfs, Pl, Qtz und Bt. Kfs zeigt häufig gut ausgeprägte Mikroklin-Gitter. Pl ist stark serizitisiert. Bt ist kräftig dunkelbraun gefärbt und scheint sehr frisch. Der Glimmergehalt ist generell sehr niedrig. In einem Schliff wurden große Körner von Hg anstelle von Bt gefunden. Akzessorisch kommen auch Grt, Ttn und Zrn vor. Neben den Kfs-Klasten sind auch Allanite mit Anwachssäumen ein starkes Indiz für den plutonischen Ursprung der Gneise.

Paragneis des Brenner-Komplexes

Die Paragneise des Brenner-Komplexes umfassen alle Gesteine, die von der thermischen Überprägung durch den Schafgrübler-Orthogneis erfasst wurden und nicht eindeutig demselben oder den Amphiboliten zugeordnet werden können. Sie umfassen Bt-reich und arme Gneise, Fsp-Blasten-Gneise, St-Bt-Schiefer, Bt-Schiefer, Bt-Ms-Schiefer, vereinzelt Grt-Glimmerschiefer sowie Gneise mit migmatischen Strukturen. Ob letztere als Migmatite bezeichnet werden können, bleibt offen. Das generelle Fehlen von Kfs sowie das poikiloblastische Überwachsen von Qtz durch Pl deuten jedenfalls auf eine rein metamorphe Überprägung von Paragneisen hin. Der auf Foliationsflächen häufig zufindende St scheint typisch für diese Gneise und erinnert stark an das mylonitische Villergruben-Lithodem, das sich ebenfalls durch quer-sprossenden St auf den Schieferungsflächen auszeichnet. Jedoch bildet das Villergruben-Lithodem eine stark mylonitisierte Glimmerschiefer-Zone, die zwischen Schafgrübler-Orthogneis und den Amphiboliten der Villerspitze leicht abgegrenzt werden kann. Da sich die Paragneise des Brenner-Komplexes aber weniger leicht abgrenzen lassen, bei weitem nicht überall als Mylonit vorliegen und umgekehrt vom Villergruben-Lithodem (noch) keine Fsp-Blastenbildung und keine Orthogneis-Lagen bekannt sind, werden diese beiden Einheiten vorerst getrennt ausgeschieden. Die weitere Bearbeitung des noch ausständigen Gebietes zwischen den beiden bereits kartierten Bereichen sollte in dieser Frage Klarheit bringen.

Im Dünnschliff zeigt sich häufig das Bild eines Pl, welcher Qtz poikiloblastisch umwächst. Pl selbst ist häufig teilweise bis vollständig serizitisiert, was in manchen Fällen das Bild eines Serizit-Nestes erzeugt, welches Qtz poikiloblastisch umgibt. Teilweise lässt sich in den Pl-Blasten noch eine ältere Foliation erkennen. Demzufolge sind die Pl-Blasten metamorphen, und nicht magmatischen Ursprungs. Der häufig in Form kleiner Körner auftretende, teilweise chloritisierte Grt, der laut Ralf Schuster (mündliche Mitteilung, 2019) an Paragneise des Bundschuh-Deckensystems erinnert, ist ein weiteres Indiz, dass es sich um Paragesteine handelt. Auch das Fehlen von Mikroklin-Gittern unterstützt diese These. Grt lässt in manchen Fällen eine Zweiphasigkeit erkennen. Der makroskopisch erkennbare St zeigen sich unter dem Mikroskop zumeist vollständig serizitisiert. Glimmer bilden in den meisten Schliffen einen wesentlichen Bestandteil. Bt ist meistens frisch und liegt in kleinen bis mittelgroßen Leisten vor. Hg bildet in manchen Schliffen mit besonders hohem Hg-Gehalt auch große elongierte Blasten. Generell entsteht der Eindruck, dass mit zunehmender Nähe zu den Orthogneisen sowohl Hg als auch Pl und die Serizit-Nester größer werden. In einem Fall wurde nahe der Seblasspitze ein Gestein mikroskopiert, das als Grt-Glimmerschiefer bezeichnet werden muss. Hier liegt Grt in größeren Augen vor und ist von einem Saum aus Bt und Hg umgeben. Teilweise sind auch reine Hg-Augen vorhanden. Akzessorisch kommen Ap und Zr vor.

Amphibolit des Brenner-Komplexes

An der Straße zwischen Milderaunalm und Brandstattalm wurde im Bereich des „Grüblen" ein 10er-Meter mächtiger Aufschluss von Bänderamphiboliten mit hellen und dunklen Amphibolit-Lagen, Amphibolititen und Bt-reichen, feinkörnigen Gneisen gefunden. Leider konnten vergleichbare Gesteine nur noch als Rollstücke unterhalb der Seblasspitze und im Oberbergtal auf der Höhe von Seduck angetroffen werden. Eine Interpolation zwischen den beiden Fundstellen erscheint allerdings derzeit zu spekulativ, zumal ungeklärt ist, ob es sich überhaupt um denselben Amphibolit-Zug handelt. Das Fehlen eines Grt-Amphibolits in den Bänderamphiboliten kommt erschwerend hinzu. Allerdings wurde einige Meter unterhalb der Seblasspitze ein stark foliierter Mylonit beprobt, der sich im Dünnschliff als Amphibolit darstellte. Möglicherweise handelt es sich dabei um eine mylonitische Variante des Amphibolits vom „Grüblen", der eine Interpolation bis zum Grat nahe der Seblasspitze zulässt.

Im Dünnschliff zeigen sich in den dunklen Lagen des Bänderamphibolits Pl, Amph, Cpx, Czo und Bt. Amph bildet sowohl wesentliche Teile der Matrix, als auch Augen. In manchen Bereichen kam es an Amph-Lagen auch zur Bildung von Scherband-Boudinage. Pl kommt nur in der Matrix vor und ist teilweise serizitisiert bzw. enthält Pl häufig Czo-Nadeln. Der Qtz-Gehalt ist sehr gering. Im Bt kam es zur Ausbildung von Saginitgitter, die auf einen magmatischen Ursprung hindeuten. Die hellen Lagen bestehen überwiegend aus Qtz, Pl und Bt. Pl ist serizitisiert und enthält Czo. Auch hier enthält Bt Saginitgitter. Daneben finden sich auch großer Hg. Der Schliff des mylonitischen Amphibolits zeigt sich fein- und relativ gleichkörnig mit zahlreichen Scherbändern. Er enthält Amph, serizitischen Fsp, Qtz und Bt. Daneben kommen auch feinkörnige Nester, die pseudomorph aus Grt hervorgegangen sein könnten. Akzessorisch finden sich Zr, Ap, Ttn und Rt.

Dykes

Im Bereich der Brennerspitze wurden neben den Orthogneisen auch noch feinkörnige, nahezu undeformierte Dykes entdeckt. Die subvulkanitisch anmutenden Gesteine ähneln jenen Dykes, die in der „Oberen Rinnengrube“ angetroffen wurden. Ein ganz ähnliches Ganggestein wurde auch auf der Straße zur Milderaunalm bei Kehre 5 (Long: 11.2703, Lat: 47.0917) angetroffen. Im Dünnschliff sind aufgrund der extrem feinkörnigen Textur lediglich Phänokristalle von Fsp, Qtz, Bt, kleiner, synkinematisch gewachsener Grt, Cal-Ausscheidungen sowie Turmalin zu erkennen. Der Cal kommt sowohl in Form von Adern, als auch als Zwickel-Füllungen und mitunter als idiomorphe Körner vor. In der Matrix ist auch Czo zu erkennen. Die Intrusionen sind reich an opaken Phasen.

Strukturen

Die Foliation variiert über das gesamte Untersuchungsgebiet hinweg, wobei ein mittelsteiles Einfallen nach Nordost als bevorzugte Richtung erscheint. Im Bereich des Bassler-Granitgneises ist die Foliation zumeist parallel zum Außenrand orientiert. So wurde oberhalb der Falbesoner Ochsenalm zumeist ein mittelsteil bis steiles (40–75°) Einfallen Richtung ENE gemessen. An der Ostflanke des Eingangs zum Falbeson wurde vorwiegend eine Foliation annähernd parallel zum Haupttal mit mittelsteilem (~ 50°) Einfallen nach Nordwest gemessen. Einzelne Flächen waren aber auch parallel zum Falbeson NNW–SSE streichend orientiert. In den „Bassler-Rinnen“ und in der „Kerachgrube“ wurde vorwiegend ein moderates Einfallen nach Nordost gemessen, das im oberhalb liegenden „Hinterm Gemäuer“ auf eine moderat bis steil nach N–NNW einfallende Foliation drehte. Zwischen „Hinterm Gemäuer“ und „Hühnerspiel“ wurden steil nach Norden einfallende Foliationen parallel zum Rand des Bassler-Granitgneises gemessen. Ähnliche Werte lagen auch weiter nördlich zwischen Brennerspitze und Mittergratspitze sowie nördlich der Mittergratspitze vor. Im weiteren Verlauf entlang des Grats zur Seblasspitze wurden die gemessenen Werte sehr viel variabler, wobei das meist steile Einfallen zwischen Süd und Nordost orientiert war. An den subanstehenden Aufschlüssen im Bereich des großen Talzuschubs, der das gesamte Gebiet östlich der Mittergratspitze erfasst, wurden vorwiegend moderat (~ 50°) nach Nordost einfallende Werte ermittelt. Nach Norden hin scheinen diese Werte leicht auf Ost bis Südost zu drehen.

Bei den Faltenachsen scheinen im Untersuchungsgebiet zwei Richtungen vorzuherrschen: Ein Einfallen nach Norden und ein Einfallen nach Nordwesten. Am Taleingang zum Falbeson sowie nahe der Falbesoner Ochsenalm wurden flach nach Norden einfallende Faltenachsen gemessen. Ähnliche Werte wurden im Bereich des Felssturzes nahe Volderau sowie in der „Kerachgrube“ ermittelt. Am Nordrand des Bassler-Granitgneises sowie in den nördlich anschließenden Einheiten wurden flach nach ENE sowie WSW einfallende Faltenachsen gemessen, die erneut parallel zum Rand des Bassler-Granitgneises ausgerichtet waren. Am Grat nahe der Seblasspitze wurden vorwiegend flach nach Nordost einfallende Werte ermittelt, wobei auch E- und ESE-einfallende Faltenachsen und eine Faltenachse mit NW-Orientierung gemessen wurden.

Die Orientierung der Foliation scheint durch die Orientierung des Bassler-Granitgneises und seiner Ränder maßgeblich beeinflusst. Sie zeichnen ebenso wie der lithologische Kontrast zwischen Bassler-Granitgneis und Umgebungsgestein zwei große Faltenstrukturen nach. Eine große Faltenstruktur findet sich im Bereich der „Falbesoner Ochsenalm“ wobei der ENE-orientierte Talverlauf dem Faltenkern zu folgen scheint, bevor er abrupt an der Schrimmennieder-Störung (Palzer, 2015) nach Süden umbiegt. Die zweite große Faltenstruktur wird durch die Bt-Schiefer-Septe innerhalb des Bassler-Granitgneises nachgezeichnet. Der Faltenkern befindet sich in der „Kerachgrube“, beziehungsweise in der Nordost-Wand zum „Hinterm Gemäuer“ unterhalb der Kerachspitze. Messungen an Faltenachsen ergaben in beiden Faltenkernen ein flaches Einfallen nach Norden. Eine dritte Faltenstruktur kann am Grat westlich der Seblasspitze vermutet werden, wo zahlreiche kleinmaßstäbliche Falten und eine stark wechselnde Foliation auf den Bereich eines Faltenkerns hindeuten. Allerdings fehlen in diesem Bereich leicht verfolgbare Lithologie-Kontraste, was eine eindeutige Identifikation einer großen Falte sowie ihrer Orientierung schwierig machen. Hinzu kommen mehrere Störungen und/oder Abrisskanten des großräumigen Talzuschubs, die einerseits ebenfalls für die variablen Messwerte verantwortlich sein könnten, andererseits aber auch eine mögliche Falte verschleiern.

Neben den großen Faltenstrukturen sind auch zwei bedeutende Störungssysteme relevant für die vorliegende Kartierung. Das westliche Störungssystem wurde bereits von Palzer (2015) als Schrimmennieder-Störung beschrieben, die, N–S streichend, steil stehend durch das gleichnamige Joch verläuft und an der der Bassler-Granitgneis ca. 1.500 m dextral versetzt ist. Sie ist an einem Set kleinerer E–W streichender Störungen gestaffelt sinistral versetzt. Diese Störung ist auch für das markante Knie im Bereich der Falbesoner Ochsenalm verantwortlich und legte im Norden die Grundlage für die Entstehung der „Platzengrube“ und das markante, scharf eingeschnittene Ostende der „Villergrube“.

Das zweite Störungsset weiter im Osten bildet zugleich einen Teil der Hauptabrisskante des Talzuschubs bei Milders. Gewaltige, mit ~50° ENE-einfallende Harnische mit Linearen in Fallrichtung entlang und unterhalb des Grates nordöstlich der Mittergratspitze sowie über den gesamten Grat zur Seblasspitze verteilt, lassen aber vermuten, dass es sich hierbei nicht nur um eine Abrisskante, sondern auch um ein bedeutendes System von Abschiebungen handelt. Nördlich des Grates, wo die Massenbewegung nicht aktiv war, setzt sich in der Verlängerung der Abrisskante ein markanter Bruch fort, der sich aufgabelt und in zwei steilen Rinnen in das Oberbergtal abfällt. Eine mögliche Fortsetzung am gegenüberliegenden Hang wird durch mehrere 100 m mächtige Quartär-Ablagerungen verdeckt. Nach Süden hin setzt sich diese Zone in der morphologisch auffälligen „Matzelehnergisse“ in das Stubaital fort. Am gegenüberliegenden Hang des Stubaitals findet sich die langgezogene markante „Innere Mischbachgrube“, die westlich am Habicht vorbeiläuft und in einer Scharte endet. Dass es sich bei der „Inneren Mischbachgrube“ um eine weiter N–S streichende Störung oder Abschiebung handelt, scheint anhand der auffälligen Morphologie naheliegend. Ob es sich dabei aber auch um die südliche Fortsetzung der vorliegenden Abschiebung handelt, muss geprüft werden. Unter anderem muss geklärt werden, ob sich im Stubaital selbst ein NE–SW orientiertes, gegebenenfalls jüngeres Störungssystem befindet. Denkbar ist auch, dass die „Innere Mischbachgrube“ die sinistral nach Nordosten versetzte Fortsetzung der Schrimmennieder-Störung darstellt. Der gerade Verlauf der „Inneren Mischbachgrube“ über die Scharte in ein weiteres, gerades und deutlich eingeschnittenes Tal lassen ein steilstehendes Störungssystem vermuten, demgegenüber die Abschiebungen durch ihr Einfallen von 50° im Verschnitt mit der Topografie keinen geraden Verlauf zeigen.

Quartär

Im unteren Falbeson, rund um die Falbesoner Ochsenalm, finden sich zwischen mächtigen End- und Seitenmoränen des Egesen-Stadials mehrere Terrassenebenen mit großen Blöcken an den vorderen Kanten und feinkörnigen Sedimenten im Rückraum. Die NNW–SSE-Ausrichtung der Terrassenkanten lässt vermuten, dass ein Zusammenhang mit der NNW–SSE orientierten Schrimmennieder-Störung besteht, die sich auch für die scharfe Biegung des Falbeson nach Süden an dieser Stelle verantwortlich zeichnet. Etwa 100 m weiter taleinwärts befindet sich ein markanter Moränenwall, der mutmaßlich den Stand des Hochmoos Ferners um 1850 markiert. Wenn dies zutrifft, war die Stelle, an der heute die Regensburger Hütte steht, vor 150 Jahren noch durch einen Gletscher bedeckt. An der orografisch linken Flanke des Talausgangs haben sich unmittelbar oberhalb der Zufahrtsstraße zur Falbesoner Ochsenalm zahlreiche End- und Seitenmoränenwälle erhalten. Die vielen eng nebeneinander liegenden Wälle sprechen für eine Einordnung in das mehrphasige Egesen-Stadial. Bemerkenswert ist hier auch ein Einschnitt, der als ehemaliger Abfluss gedeutet werden kann. Nachdem sich der Egesen-Gletscher zurückgezogen hatte, bildeten sich mehrere Blockgletscher, die heute unterhalb der Falbesoner Ochsenalm und auch im unteren Bereich der „Schrimmen“ vor allem auf Laserscans gut zu erkennen sind. In jüngster Vergangenheit bedeckten teilweise rezent aktive Schutt- und Schwemmkegel vor allem die südwestlichen Hänge.

Bemerkenswerte quartäre Ablagerungen befinden sich auch in der „Kerachgrube“ und vor allem im darüber gelegenen Kar „Hinterm Gemäuer“, wo ein mächtiges Blockgletscher-System das gesamte Kar ausfüllt. Die „Kerachgrube“ selbst wird durch End- und Seitenmoränen und durch kleinere Blockgletscher beherrscht. Im hintersten Bereich der „Kerachgrube“ kam im Westhang zu einer kleineren Massenbewegung.

Mächtige glazigene Ablagerungen befinden sich westlich und nordwestlich des Hühnerspiels. Die genaue Genese der markanten Wälle, mächtigen Quartärabfolge und der tief eingeschnittenen Abflusskanäle bleibt vorerst unklar.

Der gesamte östliche Teil des Untersuchungsgebietes wird durch ein mächtiges Talzuschub-System geprägt, das den gesamten Berg erfasst. Die Hauptabrisskante beginnt nördlich des „Hühnerspiels“ und zieht sich bis in den Hauptkamm oberhalb der „Kohlgrube“, wo es zu Doppelgrat-Bildungen kommt. Dort dreht sie nach Osten und kann hangabwärts bis nach Milderaun verfolgt werden. In kleinerem Ausmaß wurde auch die Seblasspitze und ihr Nordhang vom Talzuschub erfasst. Hierbei bleibt allerdings offen, ob es sich um ein zusammenhängendes System handelt, oder ob man die Massenbewegungsphänomene im Norden, insbesondere unterhalb (nördlich) der Brandstattalm, als eigenständiges System betrachten sollte. In jedem Fall scheint der Bereich rund um den „Bichl“ eher stabil zu sein. Im oberen Bereich des Talzuschubs kam es zu teils intensiver Zerrspaltenbildung, insbesondere im Bereich der „Kohlgrube“, der „Madlesböden“, im Kammbereich zwischen „Madlesböden“ und „Malgrube“, zwischen Seblasspitze und Brandstattalm, am „Milderer Berg“, zwischen „Hühnerspiel“ und „Auf der Mure“ sowie oberhalb vom Unteregg-Hof. In diesen Bereichen bilden sich auch bedeutende Hohlräume und Höhlen. Innerhalb des Talzuschubs wechseln sich Gebiete mit subanstehendem Fels mit kleineren, oberflächennahen Massenbewegungen ab. Insbesondere am „Milderer Berg“, zwischen Milderaunalm und „Hühnerspiel“ und unterhalb der Brandstattalm haben sich mächtige Kriechmassen gebildet. In den oberen Bereichen befinden sich auch Blockgletscher, die eindeutig älter sind als der Talzuschub. So kann an vielen Stellen beobachtet werden, dass die Abrisskanten des Talzuschubs die Wälle der Blockgletscher zerschneiden. An der Front des Talzuschubs kam es zur Ausbildung von Bulges, welche im Laserscan mit End- und Seitenmoränenwällen verwechselt werden können.

Am Taleingang des Oberberg-Tals wurden an beiden Seiten Eisrand-Terrassen gebildet. Die Tatsache, dass diese Terrassen an der Front des Talzuschubs nach wie vor erhalten sind, spricht dafür, dass der Talzuschub zu diesem Zeitpunkt bereits wieder stabilisiert war. Allerdings widerspricht diese Beobachtung den zerschnittenen Blockgletschern im oberen Bereich, da davon ausgegangen werden kann, dass die Blockgletscher in jedem Fall jünger sind als die Eisrandterrassen.

2017 kam es nahe dem Campingplatz in Volderau zu einem Felssturz. Die Kartierung in diesem Bereich hat gezeigt, dass sich genau dort der Kontakt zwischen Bassler-Granitgneis und seinem Umgebungsgestein befindet. Dieser Kontakt, der auch in anderen Aufschlüssen als strukturell schwach erschien, ist mit Sicherheit als ein wesentlicher Faktor zu nennen, warum es ausgerechnet an jener Stelle zum Felssturz kam. Das Ereignis zeigt auch, dass der Kontakt des Bassler-Granitgneises zum Umgebungsgestein eine Schwächezone darstellt, der auch die Gletscher bevorzugt folgen konnten. Es ist daher kein Zufall, dass der Kontakt im Bereich zwischen Falbeson und „Matzelehnergisse“ parallel zum Stubaital verläuft.

Das Fehlen von Gletschern und aktiven Blockgletschern in diesem Gebiet sorgt für eine in manchen Sommern angespannte Wasserversorgung der höher gelegenen Almen. So kam es im relativ heißen und trockenen Sommer 2018 zu einer beinahe vollständigen Austrocknung von wichtigen Wasserstellen oberhalb der Brandstattalm. Nach Aussage der Hüttenwirtin häufte sich dieses bisher in diesem Bereich eher unbekannte Phänomen in den letzten Jahren. Im Zuge dieser Kartierung wurde deutlich, dass für die Wasserversorgung der Almen und des Viehs im Spätsommer und Herbst vor allem die langlebigen Schneefelder entscheidend sind. Diese befinden sich westlich des Hühnerspiels und östlich der Brennerspitze und Mittergratspitze. Diese Schneefelder versorgen vor allem die Quellen nahe der Milderaunalm. Für die Brandstattalm könnte sich die Situation bei zunehmender Trockenheit und Hitze im Sommer daher zuspitzen.

Literatur

HAMMER, W. (1929): Erläuterungen zur Geologischen Spezialkarte der Republik Österreich, Blatt Ötztal. – Geologische Bundesanstalt, Wien.

KLÖTZLI-CHOWANETZ, E. (2016): Bericht 2014 über geologische Aufnahmen im östlichen Ötztalkristallin auf Blatt 147 Axams. – Jahrbuch der Geologischen Bundesanstalt, **156**, 270–273, Wien.

KRETZ, R. (1983): Symbols for rock-forming minerals. – American Mineralogist, **68**, 277–279, Washington, D.C.

PALZER, M. (2015): Mapping Report 2014 concerning the Crystalline between Franz Senn Hütte and Bassler Joch, Stubaier Alpen, Tyrol. – Aufnahmsbericht, 17 S., 6 Karten, Wien. [GBA, Wissenschaftliches Archiv, Nr. A 18377-RA/147/2014]

PALZER-KHOMENKO, M. (2017): Bericht 2017 über geologische Aufnahmen im östlichen Ötztal-Kristallin im Gebiete der Franz Senn Hütte auf Blatt 147 Axams (GK UTM Neustift im Stubaital). – Jahrbuch der Geologischen Bundesanstalt, **158**, 154–157, Wien.

SCHINDLMAYR, A. (1999): Granitoids and Plutonic Evolution of the Ötztal-Stubai Massifs. – Unveröffentlichte Dissertation, Universität Salzburg, 288 S., Salzburg.

SCHMIDEGG, O. (1939): Ranaltwerk (Stubaiergruppe) – Bemerkungen zu den Geologischen Profilen und Karte. – Aufnahmsbericht, 2 S., 2 Karten, Wien. [GBA, Wissenschaftliches Archiv, Nr. A 00630-RA/147/1939]

SCHMIDEGG, O. (1944): Stubaier Kraftwerke. – 3 Teile, ungezählte Beilagen, Stubaier Kraftwerke, Stubaital. [GBA, Wissenschaftliches Archiv, Nr. A 00428-R]

Bericht 2019 über geologische Aufnahmen im Gschnitztal und Stubaital auf Blatt NL 32-03-28 Neustift im Stubaital

MICHAEL SCHUH

(Auswärtiger Mitarbeiter)

Das Kartierungsgebiet befindet sich im Bundesland Tirol im trennenden Gebirgskamm der beiden zentralalpinen Täler Stubai und Gschnitz.

Etwa 17 km^2 wurden vom Frühsommer bis Herbst des Jahres 2019 bearbeitet. Als Kartengrundlage dienten auf 1:10.000 vergrößerte Ausschnitte des UTM-Blattes NL 32-03-28 Neustift im Stubaital.

Bei der Bearbeitung des Grundgebirges orientierte man sich an folgenden Kartierungen:

HAMMER, W. (1929): Blatt Ötztal (5146) 1:75.000. – Geologische Bundesanstalt, Wien.

MOSER, M. (2008): Geofast – Zusammenstellung ausgewählter Archivunterlagen der Geologischen Bundesanstalt 1:50.000, Blatt 147 Axams, Stand 2011, Ausgabe 2011/07. – Geologische Bundesanstalt, Wien.

Zusätzlich erfolgte die qualitative Erfassung von quartären Formen, Massenbewegungen und anderen Lockergesteinen. Zu deren Abgrenzung wurden deckungsgleiche Laserscans sowie Orthofotos (© TIRIS 2018) herangezogen. Die Reinzeichnung der Karte erfolgte manuell auf Papier.

Das stark zergliederte Gebiet wird im Norden vom Stubaital im Bereich der Gemeinden Volderau und Gasteig begrenzt. Es umfasst nördlich des Hauptkammes (damit ist der trennende Kamm zwischen dem Stubai- und dem Gschnitztal gemeint) die Äußere und die Innere Mischbachgrube sowie deren trennenden und deren begrenzende Kämme.

Der zentrale Bereich des bearbeiteten Gebietes fällt auf die westliche Hälfte des Habichtmassivs und auf den isolierten Gebirgsstock der Glättespitze.

Südlich des Hauptkammes wurden von Nordosten nach Südwesten die Kare Beilgrube, Bockgrube und Plattental aufgenommen. Diese glazialen Einsenkungen münden in den trogförmigen Talkessel der Traulalm, der ebenfalls kartiert wurde.

Zusätzliche Geländearbeiten fanden weiter im Südwesten, im Massiv der Wetterspitze sowie im östlich anschließenden Verbindungskamm „Hohe Burg“, statt. Die südlich angrenzende „Simmingalm“ und der Talschluss des Gschnitztales mit dem anliegenden, orografisch rechten Hang wurden ebenfalls mit eingearbeitet.

Lithologische Beschreibung der kartierten Gesteine

Wie bereits im Vorjahr werden die im Kartierungsgebiet vorgefundenen Gesteine hinsichtlich ihrer makroskopischen Auffälligkeiten und ihrer Verbreitung kurz beschrieben. Bei der Namensgebung und Unterscheidung der verschiedenen Gesteinstypen sind rein optisch-lithologische Merkmale maßgebend.

Grundsätzlich werden zwei große Gruppen von Festgesteinen differenziert:

Orthogesteine: metamorphe Gesteinstypen, die von basischen, intermediären oder sauren magmatischen Edukten abstammen.

Undifferenzierte Gneise magmatischen Ursprungs bauen etwa 10 % des Grundgebirges auf. Die wichtigsten Vorkommen wurden an folgenden Lokalitäten festgestellt:

- Südlich der Gemeinde Gasteig an den ersten Aufschlüssen oberhalb der Talfüllung.
- Am Rotspitzl bzw. nördlich und südöstlich davon.
- Nördlich vom Habichtgipfel (von Geofast übernommen).
- Südlich von P. 3033 (Innere Mischbachgrube).
- Im Nordgrat der Äußeren Wetterspitze (muss noch nachgeprüft werden).
- Gangartiges Vorkommen an der orografisch rechten Seite der Bockgrube (muss noch nachgeprüft werden).
- Im zentralen Bereich der Simmingalm an der orografisch linken Seite.
- Ein Streifen an der orografisch rechten Seite der Hohen Burg.

Was die makroskopische Ausbildung dieser Gneise angeht, so gleicht sie im Großen und Ganzen jener der im Vorjahr als Orthogneise bezeichneten Gesteinstypen. Deren Beschreibung wurde daher teilweise übernommen.

Magmatische Gneise stellen eine variable Gruppe auf und sind überwiegend mittel- bis grobkörnig ausgebildet. Deren charakteristische Mineraleinregelung wird vorwiegend durch nicht isometrisch ausgestaltete Kristalle oder Kristallgruppen akzentuiert. Besonders Schichtsilikate (Biotite) zeichnen eine annähernd parallele Anordnung planarer Gefügeelemente, eine Schieferung, nach. Diese passt sich den nahezu idiomorphen Mineralen – vorwiegend Feldspäte – an. Infolgedessen resultieren unebene bis wellige Flächen. Granoblastische Strukturen und Bänderung wurden ebenfalls nachgewiesen.

Generell bilden Gneise magmatischer Herkunft massige, steile Felsstufen und deutlich hervorwitternde Grate. Bei der Verwitterung lösen sich grobe, annähernd isometrische Blöcke, die sich als charakteristisches Erkennungsmerkmal an den Wandfüßen in Form von Geröllhalden sammeln.

In seltenen Fällen konnten **Augengneise** differenziert werden. Solche wurden in einem kleinen Aufschluss nördlich einer verfallenen Almhütte im Gebiet Traulalm (auf der ÖK als P. 1980 bezeichnet), sowie südöstlich von P. 2749 (Wanderweg Bremer – Innsbrucker Hütte) in das Kartenblatt eingetragen.

Zwei kleine Vorkommen sogenannter „**Grüner Gneise**“ treten unmittelbar südlich der Gemeinde Gasteig zutage (Aufschlusspunkte 2019-125 und 126). Aufgrund der auffälligen Färbung, die eventuell sekundär ist, wurde dieser Gesteinstyp in der Karte gesondert eingezeichnet. Der darin vorkommende Kalifeldspat deutet auf einen magmatischen Ursprung hin. Eine genauere Bestimmung steht noch aus.

Mit dem **Biotit-Granitgneis** konnte eine weitere Variation magmatischer Gneise differenziert werden. Dieser massige Gesteinstyp ist im Gelände unverkennbar und im Aufschluss einfach nachzuweisen. Der namensgebende Biotit ist im Gestein regelmäßig verteilt und hebt sich deutlich vom porzellanweißen Feldspat und dem hellgrauen Quarz ab. Einerseits bildet er diffuse, feinkörnige Wolken, andererseits etwas gröbere Einzelkristalle (< 5 mm). Letztere verleihen dem Gestein ein granitartiges, gesprenkeltes Gefüge. Durchgehende Biotitzeilen kommen nicht vor.

Biotit-Granitgneise treten an folgenden Lokalitäten zutage:

- Am Ausgang der Äußeren Mischbachgrube am Felsriegel östlich der Mischbachalm.
- In der Äußeren Mischbachgrube in der talparallelen Felsstufe orografisch rechts der Hauptrinne (in Letzterer treten auch Aufschlüsse zutage).
- Im nordöstlichen Bereich des Kammes, der die Äußere Mischbachgrube von der Inneren trennt.
- Im Westteil des Habichtmassives bis P. 3033.
- Am Rotspitzl.

Die metabasischen Gesteinstypen (in der Legende als **Metabasite** bezeichnet), die im aktuellen Arbeitsgebiet vorgefunden wurden, gleichen generell jenen des Jahres zuvor (SCHUH, 2018). Es können zwei Haupttypen herausgearbeitet werden: Einerseits stellt man feinkörnige Varietäten, andererseits grobkörnige, Gabbro artige Ausprägungen fest.

Erstere sind durch ihre markante, rostbraune bis rostrote Anwitterungsfarbe im Gelände schon von weitem erkennbar. Im Anschlag stets hell, bilden diese Gesteinstypen in Bezug auf die generelle Raumlage diskordante, intrusionsartige Körper oder durchschlagen gangförmig das Umgebungsgestein. Man findet sie in Vergesellschaftung mit Orthogneisen auf der orografisch rechten Seite der Inneren Mischbachgrube.

Die grobkörnigen Ausbildungen erscheinen dem Betrachter infolge des hohen Plagioklasanteils granoblastisch-gneisartig. An bestimmten Lokalitäten zeigt sich ein Gabbro-ähnliches Erscheinungsbild (grob, dunkelgrün (bis schwarz), weiß sprenkelig). Ein größeres Vorkommen wurde am von P. 3033 nach Westen herunterziehenden Felssporn entdeckt. Punktuelle Aufschlüsse befinden sich im nordöstlichen Arm der Beilgrube (Aufschlusspunkt 2019-160, orografisch links), respektive im nördlichen Gipfelhang der Glättespitze (Aufschlusspunkt 2019-175).

Eine Sonderform, die vom Verfasser ebenfalls den Metabasiten zugerechnet wird, erscheint dem Betrachter im Gelände äußerst markant. Seine dunkelbraune bis schwarz-violett schillernde Anwitterungsfarbe hebt sich deutlich von der Umgebung ab. Der frische Bruch zeigt sich in einem porzellanartigen Weiß (Plagioglas) und wird von dunkelgrünen bis schwarzen, stengel- bis plättchenförmigen Mineralen durchsetzt. Letztere unterstreichen die straffe Schieferung dieser fein- bis mittelkörnigen Gesteinstypen. Die Fundorte befinden sich im südwestlichen Arm der Beilgrube sowie sehr proximal in der Bockgrube zwischen Nördlicher und Südlicher Rötenspitze (Gipfelname ist Hinweis).

Metasedimente: Mit diesem Terminus wurden jene Gesteinstypen bezeichnet, deren Edukte den Sedimentgesteinen angehören. Da meist mehrere, unterschiedliche Ausprägungen vergesellschaftet sind, wurden zwei Hauptvertreter, bei denen entweder Paragneise oder Glimmerschiefer dominieren, unterschieden.

Paragneise sind im Arbeitsgebiet sehr häufig anzutreffen und verteilen sich über die gesamte Fläche. Für eine Beschreibung wird auf SCHUH (2018) verwiesen.

Staurolith führende Paragneise treten im Unterschied zum vorjährigen Arbeitsgebiet relativ häufig auf. Die größten Vorkommen konzentrieren sich auf den Stock der Glättespitze und südlich davon. Die makroskopischen Merkmale dieses Gesteinstyps können im Kartierbericht des Vorjahres (SCHUH, 2018) eingesehen werden.

Glimmerschiefer werden im Arbeitsgebiet nur vereinzelt im Verband mit Paragneisen angetroffen. Morphologisch äußern sie sich in Form von Geländeverflachungen und Grateinschartungen. Letztere entsenden Couloirs in die Gratflanken, die entsprechend feinen Schutt transportieren.

Ein schmaler Glimmerschieferhorizont tritt südöstlich der Gemeinde Volderau, orografisch links des Mischbachwasserfalles zutage (Aufschlusspunkt 2019-194).

Zwei Horizonte konnten bei der Begehung des Südwestgrates der Glättespitze herausgearbeitet werden.

Eine bisher nicht vorgefundene Ausprägung stützt partiell den nördlichsten Felssporn an der orografisch rechten Seite der Inneren Mischbachgrube (Aufschlusspunkt 2019-075). Deren Besonderheit sind die bis mehrere Zentimeter langen Hornblendestengel und -nadeln auf den s-Flächen. Es könnte sich bei diesem Gestein um eine retrograde Bildung handeln.

Struktureller Aufbau

Die tektonischen Strukturen des Kartiergebietes aus dem Jahr 2018 finden in der aktuell bearbeiteten Fläche eine Fortführung. Wie bereits gehabt, liegt eine relativ einheitliche NW–SE orientierte Streichrichtung der Gesteine vor. Planare Gefügeelemente (Foliation) neigen sich demzufolge um diese Streichachse nach Südwesten respektive Nordosten. Lineare Strukturen, wie Faltenachsen und Streckungslineare, sind entsprechend parallel zur Streichrichtung angeordnet. An ausgewählten Lokalitäten kann im Aufschlussbereich eine offenkundige Rotation der Einfallsrichtung eingesehen werden: am Südwestgrat der Glättespitze dreht die Foliation an mehreren Gratabschnitten im 10er- bis 100er-Meterbereich um die Hauptstreichrichtung (Wechsel von Nordost auf Südwest und umgekehrt). Die Flächen fallen mit einem mittelsteilen bis steilen Winkel (nie flacher als 45°) ein und bestätigen die Annahme eines großräumigen Faltenbaus. Diese tektonische Gliederung gibt sich ferner anhand parasitärer Syn- und Antiklinalen im Meterbereich kund.

Die in der Legende eigens ausgehaltenen **Mylonite** deuten ebenfalls die tektonische Beanspruchung an. Sie liegen in mehr oder minder mächtigen Horizonten vor und haben sich aufgrund der Kompetenzunterschiede zwischen Ortho- und Paragesteinen vor allem innerhalb metasedimentärer Sequenzen ausgebildet. Eine derartige Situation ist am Südwestgrat der Glättespitze beachtenswert einsehbar: Abfolgen von Paragneisen, Staurolith führenden Paragneisen und Glimmerschiefern werden immer wieder von Mylonithorizonten unterbrochen. Wo die Feinkörnigkeit der Mylonite keine Rückschlüsse mehr auf das Eduktgestein erlaubt, wurden diese Gesteine im Geländebefund als Ultramylonite eingestuft. Wenn das Ausgangsgestein eindeutig als Ortho- oder Paragneis identifizierbar war, wurde dem Edukt bei der Namensgebung die Erweiterung „mylonitisch überprägt(er)“ vorangestellt.

Sprödstörungen konnten selten direkt gemessen werden. Meist sind die eigentlichen Bewegungsflächen so stark schuttbedeckt, dass sie nicht eindeutig messbar sind. Sie wurden folglich als vermutete Störungen abgelegt.

Quartär

Die generelle glaziale Morphologie des letztjährigen Arbeitsgebietes findet ihren Fortgang im aktuellen Gebiet. Es wird hier nicht näher darauf eingegangen.

Der Hauptanteil der vorgefundenen Moräne könnte – so die Annahme des Verfassers – den letzten großen Eisvorstößen im Spätglazial zugeordnet werden (Egesen I bis III). Jene glazialen Formen, die eventuell dem Gletscherhöchststand von 1850 angehören, wurden in einem dunkleren Gelb gehalten.

Noch nicht geklärt ist die stratigrafische Stellung des großen stirnnahen Uferwalles, der oberhalb der Trogkante östlich der Gemeinde Gasteig abgelagert wurde.

Blockgletscher findet man, wie schon im Jahr zuvor, im gesamten Arbeitsgebiet. Die größten lagern in der Äußeren und der Inneren Mischbachgrube. Es existieren keine aktiven Formen.

Von den auf dem UTM-Blatt NL 32-03-28 innerhalb des Kartierungsgebietes eingezeichneten Gletschern sind der Mischbach- und der Pinnisferner von Bedeutung. Auch am Talschluss der Inneren Mischbachgrube und im Kar nördlich Glättespitze stößt man noch auf Eis. Dieses ist jedoch komplett schuttbedeckt. Die übrigen, in der Landeskarte vermerkten Gletscher sind nicht mehr vorhanden.

Literatur

Schuh, M. (2018): Bericht 2018 über geologische Aufnahmen im Gschnitztal auf Blatt NL 32-03-28 Neustift im Stubaital. – Jahrbuch der Geologischen Bundesanstalt, **158**, 161–163, Wien.

Blatt NL 33-10-29 Vöcklabruck

Bericht 2019 über geologische Aufnahmen auf Blatt NM 33-10-29 Vöcklabruck

Tobias Ibele

(Auswärtiger Mitarbeiter)

Das UTM-Kartenblatt NM 33-10-29 Vöcklabruck folgt dem Blattschnitt des neuen UTM-Kartenwerks. Es wird bereits zu einem großen Teil durch das im alten Blattschnitt publizierte Blatt ÖK 47, Ried im Innkreis (Rupp, 2008a) abgedeckt, so dass nur im Ostteil geologische Neuaufnahmen durchzuführen sind (siehe dazu auch Rupp, 2013). Im Rahmen dieser Neuaufnahmen wurde zwischen November 2016 und April 2018 ein etwa 45 km² großes Gebiet zwischen Eberschwang im Nordwesten, Geboltskirchen im Nordosten und Ottnang am Hausruck im Süden geologisch kartiert (Ibele, 2017, 2018). Ab November 2018 bis März 2019 wurde dann ein nördlich anschließendes, ca. 24 km² großes Gebiet aufgenommen. Die Ergebnisse dieser Kartierung sind im Folgenden dargestellt.

Das Gebiet der Kartierung 2018/19 reicht von Geiersberg und St. Marienkirchen im Westen über Haag am Hausruck bis zu den Weilern Pommersberg (Nordosten) und Grolzham (Südosten) im Osten. Zusammen mit den Kartierungen 2016/17 (Ibele, 2017) und 2017/18 (Ibele, 2018) deckt es einen rechteckigen Perimeter zwischen der Koordinate RW: 394250 / HW: 5339500 im Nordwesten und der Koordinate RW: 400725 / HW: 5328300 im Südosten (alle Koordinaten in UTM 33N) ab und schließt damit insgesamt zwischen Geiersberg im Norden und Ampflwang im Süden, östlich an Blatt ÖK 47 Ried im Innkreis an.

Im genannten Perimeter des Gesamtgebiets 2016–2019 existieren Vorarbeiten in Form dreier Diplomkartierungen

(Deckers, 1988; Kaltbeitzer, 1988; Schläger, 1988). In vielen Fällen haben sich aber die Aufschlussbedingungen geändert. Ehemalige Gruben sind häufig planiert und rekultiviert, neuere Weganschnitte oder Baugruben ergaben hingegen an anderer Stelle Einblicke in den Untergrund. So liegen mit Peresson et al. (2015, 2016, 2017) aus dem nordöstlichen Gebietsteil Aufschlussbeschreibungen von der Erweiterung der Autobahn A8 (Innkreis Autobahn) vor. Im Vergleich zu den Diplomkartierungen wurde bei den aktuellen Aufnahmen ein größeres Augenmerk auf die quartäre Bedeckung gelegt. Aufschlüsse des neogenen Untergrunds sind generell selten und, wenn vorhanden, meist nur wenige Quadratmeter groß. Deshalb wurde bei der Feldarbeit zusätzlich ein Erdbohrstock (Stechbohrer) verwendet, mit dem bei günstigen Bedingungen (wenig steiniger Boden) Proben aus bis zu einem Meter Tiefe entnommen werden konnten. Ergänzt wurde die Kartierung außerdem durch einzelne, bis zu zwei Meter tiefe Handbohrungen.

Landschaftlich gliedert sich das Kartierungsgebiet 2018/19 in die nördlichen Ausläufer der waldbestandenen Höhenzüge des Hausruck, denen westlich, nördlich und östlich offenes Hügelland mit Siedlungs- und Landwirtschaftsflächen vorgelagert ist. Bei Haag am Hausruck sind teilweise größere Bereich durch Wohn- und Gewerbegebiete überbaut. Der Kamm des Hausruck teilt sich in den N–S verlaufenden, eigentlichen „Haager Rücken“ sowie einen im Südteil gegen Westen abzweigenden Seitenast, der sich bis südlich Pilgersham erstreckt („Pilgershamer Rücken“), und einen kurzen, gegen Nordnordwest absinkenden Rücken südlich Schernham. Vom Hausruckkamm gehen im Kartierungsgebiet zwei Wasserscheiden aus. Die Gebiete westlich einer Linie Schernham–Jetzing–Grausgrub entwässern in die Antiesen, die zwischen dieser Linie und einer Linie „Haager Rücken“–Eidenedt–Buchegg gelegenen Gebiete in die Pram, und die östlich anschließenden Gebiete in die Trattnach. Der höchste Punkt des Kartierungsgebiets liegt mit etwas über 720 m über Meer im Bereich Schlossberg. Der tiefste Punkt liegt am Bach westlich Pommersberg auf etwas unter 440 m über Meer.

Untermiozän, Ottnangium: Ottnang-Formation und Ried-Formation

Als untermiozäne Schichtglieder des Ottnangiums der Innviertel-Gruppe (Rupp, 2008b; Piller et al., 2004; Papp et al., 1968) treten im Kartierungsgebiet die ältere Ottnang-Formation und die jüngere Ried-Formation auf. Ihre Grenze fällt mit wenigen Grad gegen Norden bis Nordwesten ein (Aberer, 1957). Sie werden diskordant von der obermiozänen Ampflwang-Formation der Hausruckviertel-Gruppe (Pannonium; Rupp, 2008b) überlagert, deren Basis subhorizontal oder leicht gegen Südosten abfallend verläuft.

Untermiozän, Ottnangium: Ottnang-Formation

Als ältestes Glied wurde die Ottnang-Formation (Rupp, 2008b) ausgeschieden. Sie ist im Gebiet Haag am Hausruck östlich einer Linie Zeißerding–Reischau unterhalb von 540 m über Meer im Süden und 480 m über Meer im Norden verbreitet und wird überall von der Ried-Formation überlagert. Die Ottnang-Formation ist vor allem entlang von Bachläufen aufgeschlossen, so östlich Reischau, südlich Steinpoint, westlich Aubach und südlich Grolzham. Daneben ist sie bei Steinpoint, im Haager Ortsteil um den ehemaligen Bahnhof und südlich Niedernhaag untief anstehend und wurde durch Baumaßnahmen entlang der Autobahntrasse zwischen Reischau und Nidernhaag an mehreren Stellen aufgeschlossen (Peresson et al., 2016, 2017). Im Nordosten reicht die Ottnang-Formation bei Pommersberg bis zum tiefsten Punkt des Kartierungsgebiets auf 440 m Höhe hinab.

Bei den Gesteinen der Ottnang-Formation handelt es sich vorwiegend um graue bis blaue, siltige bis feinsandige, oft weiche Tone und Mergel. In Aufschlüssen beobachtet man teils dünn geschichtete, teils ungeschichtete, einfarbige und einförmig wirkende, sandig-siltige Tone mit dünnen, selten einige Zentimeter mächtigen, zu Mergeln verhärteten Lagen. Hellglimmer ist insgesamt häufig anzutreffen und kann in sandigen Laminä angereichert sein. Bereichsweise kommen stärker mergelige und dann zum Teil harte, zu Platten zerfallende Lagen vor. Weniger häufig können hellere, im trockenen Zustand bis ausgesprochen hellgraue oder gelblich-beige sowie andernorts im Zentimeterbereich geschichtete Partien auftreten, die dann oft durch einen relativ hohen Gehalt an Feinsand gekennzeichnet sind. In Sondierungen mit dem Erdbohrstock und in den Handbohrungen sind eine einheitlich graue bis blaue und selten beige Farbe, sowie eine einheitliche, siltige bis feinsandige Korngröße und kleinblättriger Hellglimmer charakteristisch. Als Lesesteine treten in Äckern und Maulwurfshügeln härtere Mergel-Blättchen auf, die aber von Hand zerbrochen werden können.

Im Gebiet Haag am Hausruck weisen die obersten Zehnermeter der Formation im Feld, bei meist typisch blaugrauer Färbung, häufig Charakteristika der Ried-Formation, wie Feinschichtungen und Feinsandbestege, auf. Proben aus diesem Bereich ergaben allerdings eine mikropaläontologische Zuordnung zur Ottnang-Formation.

Zwischen Reitting und Zeißerding konnte im Bacheinschnitt bei (RW: 398490 / HW: 5335830) der Übergang in die hangende Ried-Formation beobachtet werden (siehe auch Ibele, 2018). Dabei handelt es sich um einen Bereich von wenigen Metern, in dem grau verwitternde, siltige Mergel vom Typus der Ottnang-Formation mit bräunlich verwitternden, feingeschichteten, siltigen Mergeln vom Typus der Ried-Formation wechsellagern. Während innerhalb der Aufschlüsse die bräunlich verwitternden Mergel nach oben rasch zunehmen, fehlen sie in den jeweils nur wenige Metern unterhalb gelegenen, nächst tieferen Aufschlüssen ganz. Allerdings treten in den nächst höheren westlicheren Aufschlüssen, ca. 30–40 m bachaufwärts, zwischen 545 und 550 m über Meer, nochmals graue, entschichtete, sandige Mergel auf, die lithologisch der Ottnang-Formation angehören. Aufgrund der geringen Zahl der Aufschlüsse kann nicht beurteilt werden, ob es sich dabei um eine Fazieswiederholung, eine Faziesverzahnung oder eine tektonische Komplikation handelt. Eine in diesem Bereich beobachtete kleine Faltenstruktur, weist aber auf einen tektonisch bedingten Aufbruch des Liegenden hin (siehe Abschnitt Tektonik).

Die Obergrenze der Ottnang-Formation liegt im Südosten des Kartierungsgebietes bei 540, im Nordosten bei 480 und im Nordwesten sicher tiefer als 505 m über Meer. Ihre Untergrenze ist im Osten sicher tiefer als 440 m über Meer. Die in den Kartierungsgebieten 2016/17 und 2017/18 (Ibele

2017, 2018) bestimmten Mächtigkeiten von rund 60–70 m können, bei Annahme eines Nord- bis Nordwest gerichteten Einfallens von wenigen Grad (Aberer, 1957), auch für den Bereich Haag am Hausruck angenommen werden.

Untermiozän, Ottnangium: Ried-Formation

Nördlich und östlich des „Haager Rückens“ tritt die Ried-Formation unterhalb von 600 bis 630 m über Meer als älteste, an der Oberfläche ausbeißende Einheit auf. Im östlichen Gebietsteil steigt die Untergrenze zur liegenden Ottnang-Formation von 480 m über Meer bei Reischau auf 540 m über Meer südlich Zeißerding an.

In ihrem Verbreitungsgebiet ist die Ried-Formation vereinzelt in ehemaligen Gruben, in Weganschnitten, an den Prallhängen der Bäche und in deren Bachbett aufgeschlossen und oft untief anstehend. So stößt man im westlichen Gebietsteil, außerhalb der Decken kiesiger Hanglehme aus dem Hausruckwald, bei St. Marienkirchen-Hatting, im Bereich Grausgrub–Jetzing–Kruglug und Pramerdorf–Hinteregg–Pramwald auf Feldern, in Waldstücken und bei Sondierungen mit dem Erdohrstock häufig auf Ried-Formation. Im östlichen Gebietsteil bildet sie über der Ottnang-Formation eine Geländestufe, zu der der Anstieg der Rieder Straße (B 141) bei Reischau, der Rücken von Schloss Starhemberg, der Haager Marktplatz und die Kuppen der Weiler Fürt, Letten (Golfklub) und Zeißerding gehören.

Bei den Gesteinen der Ried-Formation handelt es sich um hellgraue bis grau- oder olivgrüne und teils gelblichbraune, siltige bis feinsandige Tone und Mergel sowie selten blaugraue Tone und Mergel. Oft sind die braunen und grünlichen Bereiche stärker feinsandig, die helleren und graueren Bereiche dagegen tonig-mergeliger ausgebildet. Hellglimmer ist in der Regel vorhanden und kann auf den Trennflächen der Feinschichtung langenweise angereichert sein. In Aufschlüssen beobachtet man meist dünn geschichtete, oft feinlaminierte, manchmal schichtweise farblich zwischen hellgrau, braun und graugrün wechselnde, siltige Tone oder plattige, teils harte Mergel. Beispielshaft wurden südlich Pramerdorf (Koordinaten: RW: 396430 / HW: 5338800) fein geschichtete, tonige, an kleinblättrigen Hellglimmern reiche, graue Silte beobachtet, in denen die Hellglimmer alle 1–2 mm in Lagen angereichert sind. Darin eingeschaltet finden sich ca. 10 cm mächtige, härtere und weniger zurückwitternde Bänke, in denen die Hellglimmer-Lagen bis 5 mm auseinander liegen und wellig ausgebildet sind. Während sich die Amplituden um wenige Millimeter bewegen, betragen die Wellenlängen um 10 cm, so dass im Zerfall eine muschelige Struktur entsteht. Selten kann die Ried-Formation eintönig graue, kaum geschichtete, weiche Mergel führen, die dann den Gesteinen der Ottnang-Formation stark ähneln.

In Sondierungen mit dem Erdbohrstock und in den Handbohrungen sind graue bis grüne, siltige Tone und helle mergelige Plättchen charakteristisch. Als Lesesteine treten häufig bis über 10 cm messende, oft nur einige Millimeter dicke, sehr harte hellgraue bis kreidig helle Platten, in Maulwurfshügeln auch typischerweise dünne Mergelplättchen auf, die im Gegensatz zur Ottnang-Formation bei der Ried-Formation eine meist hellere und im frischen Bruch weniger blaugraue Färbung aufweisen sowie tendenziell härter sind.

Im Grenzbereich zur liegenden Ottnang-Formation wurden an einigen Stellen Proben genommen, die durch Felix Hofmayer (Geologische Bundesanstalt) mikropaläontologisch untersucht wurden. Dabei erwiesen sich einzelne der Proben als nicht so leicht einzustufen. So treten in der, makrolithologisch als Ottnang-Formation bestimmten Probe diejenigen Faunen der Ried-Formation auf, die bei geringem Sauerstoffgehalt auch in der Ottnang-Formation gehäuft sein können, während einige typische Formen der Ottnang-Formation fehlen (Mitteilung Felix Hofmayer, 2019). Um nicht eine tektonische Störung annehmen zu müssen und aufgrund der makrolithologischen Kriterien wurde das Gestein auf der Karte als oberste Ottnang-Formation ausgeschieden.

Die Obergrenze der Ried-Formation liegt östlich Kruglug auf gut 630 m über Meer, ihre Untergrenze rund 2 km östlich bei Haag am Hausruck auf ca. 490 m über Meer. Damit beträgt ihre Mächtigkeit in diesem Bereich bis zu 140 m.

Untermiozän, Ottnangium: Ried-Formation, sandige Fazies

Innerhalb der Ried-Formation lässt sich lokal eine sandige Fazies kartieren. In den südlich und westlich anschließenden Gebieten konnte dabei eine im Bereich der Basis der Formation auftretende Variante vom Typus der Reith-Formation (Rupp, 2008b) von einer innerhalb höherer Formationsteile auftretenden Variante unterschieden werden, die eher der Mehrnbach-Formation (Rupp, 2008b) ähnelt (Ibele, 2018). Da die Vorkommen aber stets räumlich begrenzt sind, sich maximal auf einige hundert Quadratmeter erstrecken und seitlich mit der „Normal-Fazies“ verzahnen, wurden sie bei der Kartierung stets zusammengefasst und vereinfachend als Ried-Formation in sandiger Fazies ausgeschieden (Ibele, 2018). In der gleichen Weise konnten gering ausgedehnte Körper der sandigen Fazies der Ried-Formation, meist in der Nähe ihrer Basis, auch bei der Kartierung 2018/19 ausgeschieden werden.

Zur Ried-Formation in sandiger Fazies gestellt wurden im Bereich nordöstlich Fürt (Koordinaten: RW: 399075 / HW: 5337175) an der Basis der Formation auftretende helle, beige bis gelbliche, teils geschichtete, teils ungeschichtete oder durchwühlte Sande mit großen Hellglimmern, die von knorrigen, mergeligen Partien teilweise durchsetzt sind und teilweise mit ihnen wechsellagern. In Bereichen mit Wechsellagerung bildet der Glimmer dünne, die Schichtung hervorrufende Lagen und es kann ein farblicher Wechsel zwischen hellgrau in den mergelreicheren und hellbeige bis gelb in den sandreichen Bänken beobachtet werden. Die mikropaläontologische Untersuchung einer Probe aus diesem Bereich brachte bei auffallender Individuenarmut keine typische Fauna der Ried-Formation. Auch fehlen gewisse indikative Arten der Ottnang-Formation und die vertretenen Lenticulinen zeigen Aufarbeitungserscheinungen. Zusammen mit dem sandigen Detritus spricht dies für eine transgressive Übergangsfazies, die hier an die Basis der Ried-Formation gestellt werden soll.

Im Taleinschnitt nördlich Schloss Starhemberg und am nördlichen Blattrand bei Reischau wurden graugrüne, dickbankig bis massige Sand- und Feinsandsteine mit teilweise großen Glimmern und Muschelschalen als Ried-Formation in sandiger Fazies kartiert. Nördlich Starhemberg bilden sie im Bach kleine Wasserfall-Stufen und stehen wahrscheinlich im Zusammenhang mit einem natürlichen Quellaustritt und einer weiteren gefassten Quelle zwischen 510 und 520 m über Meer.

Obermiozän, Pannonium: Ampflwang-Formation

Über den Sedimenten des Ottnangiums folgt mit einer Schichtlücke die Ampflwang-Formation (Rupp, 2008b). Sie streicht in wechselnder Mächtigkeit in Höhenlagen zwischen 600 und 640 m über Meer an der Oberfläche aus, so dass ihre Verbreitung auf der Karte bandartig den Hängen des Hausruckwaldes folgt. Dieser Bereich fällt meist mit der Grenze zwischen Wald und landwirtschaftlicher Nutzfläche zusammen. Im Gegensatz zu den südlich angrenzenden Gebieten wurde die, in die Ampflwang-Formation eingelagerte Braunkohle, am „Haager Rücken“ nicht bergmännisch abgebaut. Ihr Verbreitungsgebiet ist daher kaum durch anthropogene Überprägung, sondern lediglich durch eine Geländeverflachung mit häufigen Wasseraustritten gekennzeichnet und wird häufig durch gravitative Massenbewegungen mit Material der überlagernden Hausruck-Formation überdeckt.

Lithologisch ist die Ampflwang-Formation im Gegensatz zu den Sedimenten des Ottnangiums vor allem durch ihre Vielfalt gekennzeichnet. Nahe der Basis treten sandige bis grobsandige, weiche und oft nasse, hellgraue bis weiße und kaum verfestigte, karbonatfreie Sande auf. Im oberen Teil der Formation sind meist zwei, jeweils bis mehrere Meter mächtige Braunkohle-Flöze und die diese trennenden und überlagernden, hellgrau- silbrigen bis dunkelgrau-schwarzen, meist reinen Tone entwickelt (Ibele, 2018). Im Gebiet der Kartierung 2018/19 tritt die Ampflwang-Formation in Sondierungen mit dem Erdbohrstock fast überwiegend in Form weißlicher, durch Verwitterung auch gelbbrauner, karbonatfreier, Gries-artiger „Klebsande“ auf, wie sie in den südlich angrenzenden Gebieten häufig die tieferen Anteile der Formation bilden. In den höheren Formationsteilen ist Braunkohle in ein bis zwei dünnen Flözen anzutreffen, die kleine Geländestufen bilden. Dort werden in Wurzelballen oder mit dem Erdbohrstock zahlreiche Bruchstücke der Braunkohle gefördert. Entlang kleiner Bachläufe ist der Horizont der Braunkohle durch Passagen wenige Meter tiefer Einschnitte gekennzeichnet, in denen die Kohle teilweise ansteht oder in größeren, durch Unterspülung aus dem Verband gelösten Blöcken im Bachbett liegt.

Im Pilgershamer Wald (RW: 395680 / HW: 5336530) wurden helle, beige, kaum verfestigte Fein- bis Mittelsande beobachtet, die in zentimetermächtigen Lagen mit millimeterdünnen, hellen Tonen wechsellagern. Die Tone zerfallen zu dünnen Blättchen, die mit der Hand beim Zerdrücken nicht brechen, sondern verschmieren. Die Sande sind karbonatisch, führen dunkle bis schwarze, punktförmige Komponenten, bei denen es sich wahrscheinlich um Pflanzenhäcksel handelt, und unauffällig Hellglimmer. Die Lithologie erinnert stark an die basale Ried-Formation, wie sie im Gebiet Geboltskirchen bei Scheiben und Brunau (Ibele, 2018) als auskeilende Ried-Formation auch direkt unter Ampflwang-Formation kartiert wurde. Die Position im Pilgershamer Wald entspräche aber in Bezug auf die Ried-Formation ihrem Hangenden. Möglicherweise handelt es sich bei diesen Bildungen um eine wiederkehrende Fazies vor allem mergelärmerer und daher weniger zur Verfestigung neigender Sedimente, die aber nicht an die Basis der Ried Formation, sondern eher an die Ampflwang-Formation gebunden ist. Bei der aktuellen Kartierung wurde das Vorkommen im Pilgershamer Wald zur Ampflwang Formation gestellt.

Das Top der Ampflwang-Formation bewegt sich im Kartierungsgebiet recht konstant zwischen 635 und 640 m über Meer. Die Basis verläuft uneben meist auf etwa 600 m über Meer, steigt aber zwischen Kruglug und Eidenedt auf über 630 m über Meer an, wobei es sich klar um ein (prä-?) Pannonisches Relief handelt. Die Mächtigkeit der Ampflwang-Formation kann auf maximal 40 m bestimmt werden, wobei sie zwischen Kruglug und Eidenedt maximal wenige Meter beträgt und möglicherweise sogar ganz fehlt. Aufgrund der schlechten Aufschlussverhältnisse sind die Positionen der Formationsgrenzen auf der Karte und die darauf beruhenden Abschätzungen zu Höhenlagen und Mächtigkeiten mit größeren Unsicherheiten behaftet.

Obermiozän, Pannonium: Ampflwang-Formation, Grimberg-Subformation, Pramquellen-Bank

Die Pramquellen-Bank wird von Rupp (2008b) als Untereinheit der Grimberg-Subformation eingeführt und mit dieser in die basale Ampflwang-Formation gestellt. Ihr gehören primär diejenigen der in der Oberösterreichisch-Niederbayrischen Molasse als Lesesteine weit verbreiteten Quarzitkonglomerate an, die sich im Raum Frankenburg in (sub)anstehender Position in den beschriebenen stratigrafischen Kontext stellen lassen (Roetzel, 1988; Krenmayr, 1995; Rupp, 2008b) und von Aretin (1988) auch an den Pramquellen („Symbrunn-Quelle“) bei Schernham beschrieben wurden. Detailkartierungen im Raum Frankenburg zeigten aber auch, dass sich die Quarzitkonglomerate der Ampflwang-Formation nicht nur auf deren Basis beschränken, sondern ebenso in höheren Niveaus der Formation eingeschaltet sein können (Krenmayr, 1995).

Bei den Quarzitkonglomeraten der Pramquellen-Bank handelt es sich um quarzitisch zementierte, äußerst harte, meist korngestützte Fein- bis Grobkonglomerate, deren gut gerundete weiße, graue und seltener rötliche Komponenten von Quarz und Quarzit in groben Lagen Faust- bis selten Kopfgröße erreichen können. Daneben treten auch massige, praktisch komponentenfreie, weiße oder hellgraue und ebenfalls sehr harte Quarzite auf. Ausgehend von der Matrix zeigt sich oft eine braune bis rötliche oder gelbliche Verwitterungsfarbe und die Oberflächenstruktur kann, aufgrund fehlender Komponenten, löchrig ausgebildet sein.

Das sehr verwitterungsresistente Gestein findet sich in bis mehrere Kubikmeter großen Blöcken in unterschiedlicher Dichte in den Lehm- und Solifluktionsdecken des Kartierungsgebietes, wo es in Äckern und Baugruben auftritt und dann, meist kleinräumig anthropogen umgelagert, an Feldrändern und in Bachgräben zu finden ist. Diese kaum fluviatil transportierten Blöcke stellen in ihrer heutigen Verbreitung wahrscheinlich Residuale einer einstmals im Schichtverband vorhandenen Lage dar, deren Hangendes und Liegendes längst erodiert und abtransportiert wurde. In diesem Sinne markiert das nur bereichsweise gehäufte Auftreten dieser Blöcke wahrscheinlich auch das ungefähre primäre Verbreitungsgebiet der Einheit.

Die Pramquellen-Bank kann nirgends auf größere Distanz im Verband anstehend beobachtet werden. Die in der Karte eingetragenen Aufschlüsse sind Bereiche mit einer großen Dichte an sehr unwahrscheinlich umgelagerten Blöcken, die oft im Bereich von Geländestufen auftreten und leicht talwärts gekippt sind. Wahrscheinlich wird die schon primär möglicherweise wellige und nicht durchgehend zementierte, sehr harte Bank mit ihrem verwitterungsanfälligen Unterlager oberflächennah durch Unterspülung stets in Blöcke zerlegt, die dann als subanstehend bezeichnet werden können.

Als subanstehend wurde die Pramquellen-Bank südlich Schernham, vom Pilgershamer Wald bis zur Pramquelle, an mehreren Stellen flächig auskartiert. An der Typlokalität, der Pramquelle, tritt die oberste Bank aus Quarzitkonglomerat unmittelbar unter der Hausruck-Formation, das heißt am Top der Ampflwang-Formation auf. Darunter folgen über gut 25 Höhenmeter und über eine morphologische Steilstufe ausgebreitet, zahllose bis wohnzimmergroße und in-situ verkippte Blöcke, die insgesamt eine größere Mächtigkeit der Bank implizieren. Die zahllosen Blöcke lassen sich mit der Geländestufe noch ca. 300 m nach Süden bis in den Talgrund verfolgen. Von dort westwärts zeichnet sich auf 620 m über Meer eine obere und auf 600 m über Meer eine untere solche Geländestufe ab. Zusammen mit dem Vorkommen an der Pramquelle und unmittelbar unter der Hausruck-Formation bestätigt diese doppelt auftretende Bankstufe die Befunde von Krenmayr (1995), dass die Quarzitkonglomerate in mehreren Niveaus der Ampflwang-Formation auftreten können. Westlich der Schottergrube Schernham ist im Pilgersahmer Wald nur noch die untere Bank ausgebildet. Sie tritt bei diser Lokalität (RW: 396150 / HW: 5336825) als eine hangparallel mit rund 3° gegen Nordnordwest einfallende Fläche auf, was wahrscheinlich auf Unterspülung und nachfolgendes Absacken zurückzuführen ist.

In auffälliger Dichte treten, wahrscheinlich residuale, blockgroße Lesesteine der Pramquellen-Bank in den Gebiete Pilgersham–Schrenham, Kruglug–Pramerdorf und Eidenedt–Steinpoint–Reischau auf. Dagegen fehlen solche Lesesteine von Steinpoint bis Leithen und im Gebiet Grausgrub weitestgehend.

Die Konglomerate der Pramquellbank werden als Rinnensedimente interpretiert (Rupp, 2008b), wobei der gute Rundungsgrad der Gerölle auf einen größeren Transportweg hinweist. In diesem Zusammenhang ist interessant, dass kaum 200 m nördlich der Pramquelle mit der offensichtlich großen Mächtigkeit der Quarzitkonglomerate, die Ried-Formation bis wenige Meter unter die Hausruck-Formation reicht. Hier vollzieht sich also auf kurze Distanz ein Höhensprung des Prä-Pannonischen Reliefs von rund 30 m, der räumlich mit der hohen Mächtigkeit des Rinnensediments zusammenfällt.

Obermiozän, Pannonium: Hausruck-Formation

Die Hausruck-Formation (Rupp, 2008b) ist das jüngste neogene Schichtglied im Kartierungsgebiet. Sie baut die bewaldeten Hochlagen oberhalb von rund 640 m über Meer auf und ist in diesen Bereichen immer wieder in kleineren Gruben und in Weganschnitten aufgeschlossen. Südlich Scheiben wurde ihr Kies in einer größeren Grube bis vor wenigen Jahren abgebaut. Die Gebiete mit Hausruck-Formation sind durch trockene, steinige Böden sowie die Abwesenheit von Oberflächenwässern gekennzeichnet und werden ausschließlich forstwirtschaftlich genutzt. In Steilhängen sind stellenweise auffällige Flachstufen ausgebildet, die wahrscheinlich auf linsenartige Bereiche mit sandiger Fazies hinweisen. Sie wurden bei der Kartierung nach morphologischen Kriterien andeutungsweise ausgeschieden, sind insgesamt aber etwas weniger deutlich ausgeprägt als in den südwestlich angrenzenden Gebieten (Ibele, 2017, 2018).

Lithologisch handelt es sich um gut gerundete, schlecht sortierte Grobkiese mit einer grobsandigen Matrix und immer wieder eingeschalteten, bis mehrere Meter mächtigen Sandlagen sowie dünnen, schnur- und linsenförmigen Bereichen, in denen die Komponenten gut sortiert und nur wenige Zentimeter groß sind. Als Gerölle überwiegen Quarzit- und Kristallingesteine, Kalksteine und anderen Sedimente kommen untergeordnet vor. Die Korngröße reicht von der Kiesfraktion bis zu Steinen mit einigen Dezimetern Durchmesser. Die Kiese sind korngestützt, in Gruben meist standfest, und fleckenhaft zu Konglomerat verfestigt. Im Gegensatz zu den südwestlich anschließenden Gebieten (Ibele, 2017, 2018) sind solche verfestigten Konglomerate am Haager Rücken und im Gebiet Geboltskirchen häufiger. Sie treten immer wieder als kleine Felswände und in deren Auslaufbereichen als Sturzblöcke auf. Auch die sandigen Lagen können verfestigt sein und bilden dann graue, massige, teilweise auch plattige, glimmerarme Grobsandsteine, die einzelne, bis zentimetergroße Gerölle führen. Die Sandeinschaltungen sind aber am „Haager Rücken“ weniger auffällig als in den südlich anschließenden Gebieten.

Am nördlichen „Haager Rücken“ kann im Bereich des Schlossbergs südlich Schernham zwischen 640 m und etwas über 720 m über Meer eine Mächtigkeit von mindestens 80 m für die Hausruck-Formation angegeben werden.

Pleistozän: Umlagerungskiese der Hausruck-Formation

Während der verschiedenen pleistozänen Kaltzeiten wurden Kiese der Hausruck-Formation erodiert und umgelagert (Rupp, 2008b; Ibele, 2017, 2018). Reste dieser Umlagerungen finden sich vielfach als Kiesstreu in den Äckern und Wiesen der Talflanken, wo sie in den Gebieten Eberschwang, Ottnang und Geboltskirchen als Relikte pleistozäner Terrassen angesprochen wurden (Ibele, 2017, 2018). Dabei handelt es sich in der Regel um Vorkommen steiniger Böden auf Kuppen oder konvexen Hangknicken, oder in Lagen, die so weit von anstehender Hausruck-Formation entfernt liegen, dass eine Entstehung als Hangschutt oder kiesiger Verwitterungslehm unwahrscheinlich ist.

Auch bei der Kartierung 2018/19 im Gebiet Haag am Hausruck wurden Bereiche mit stark steinigen Böden auskartiert, wobei sie hier aber nur schwierig bestimmten Höhenlagen und somit einzelnen Terrassenniveaus zugeordnet werden können. Sie sind deshalb auf der Karte als undifferenzierte Pleistozäne Schotter ausgeschieden. Die flächenmäßig größeren dieser Vorkommen liegen zudem nicht auf Kuppen oder in Hanglagen, sondern bilden talbodenähnliche Decken. Dies ist besonders zwischen Niedernhaag und Bachleithen sowie bei Aubach, aber auch nordöstlich Reischau (Gewerbezone bei der Autobahnauffahrt) oder nördlich Meggenbach zu beobachten. Wahrscheinlich handelt es sich dabei um kaltzeitliche fluviatile

Ablagerungen, die zwar von den rezenten Bachläufen eingeschnitten werden, dabei aber noch weitestgehend erhalten sind. Sowohl an der Böschung der Autobahn bei Reischau (Peresson et al., 2016), als auch am Einschnitt des Rottenbachs bei Bachleithen ist zu beobachten, dass diese Kiesdecken nur wenige Meter mächtig sind. Die Kiese an der Böschung der Autobahn bei Reischau wurden von Peresson et al. (2016) als Hochterrassenkiese angesprochen. Die übrigen, als undifferenzierte Pleistozäne Kiese ausgeschiedenen Vorkommen, markieren meist kleinräumige Bereiche sehr steiniger Ackerböden und unterscheiden sich von den „verschwemmten Kiesen" nur durch einen graduell noch höheren Anteil an Steinen.

Mit der Signatur „verschwemmte Kiese" wurden stärker steinige Lehme belegt, die mit dem steinigen Hanglehm vergleichbar sind, sich von ihm aber dadurch unterscheiden, dass die Hausruck Formation im aktuellen Umfeld nicht oder nicht mehr als Liefergebiet der steinigen Komponenten in Frage kommt. Diese Vorkommen sind wahrscheinlich als mehrfach umgelagerte kiesige Hanglehme oder als Reste pleistozäner Terrassenschotter zu deuten.

Im Nordwestteil des Kartierungsgebietes konnten zwei Vorkommen pleistozäner Umlagerungskiese bestimmten, auf Blatt 47 Ried im Innkreis (Rupp, 2008a, b) ausgeschiedenen Terrassenniveau zugeordnet werden. So reicht bei Geiersberg im äußersten Nordwesteck der Geiersberg-Schotter auf das Blattgebiet, während sich nordöstlich Ötzling ein Vorkommen der Aichberg-Geinberg-Schotter bis in das Kartierungsgebiet erstreckt.

Pleistozän-Holozän: Verwitterungslehm

Lehme und kiesige Lehme bedecken weite Teile der mäßig geneigten Hanglagen. Dabei handelt es sich um Fließerden (Solifluktionsdecken), die sich durch eine Mischung von in-situ Verwitterung und gravitativem Eintrag aus höheren Lagen bildeten und, vor allem während Kaltzeiten, sich langsam kriechend talwärts bewegten und durchmischten. In flachen Lagen überwiegt wahrscheinlich die Bildung aus in-situ Verwitterung. Die so entstandenen pleistozänen–holozänen Überdeckungen wurden bei der Kartierung qualitativ in kiesigen und schwach kiesigen Umlagerungslehm unterschieden, wobei die Grenzen fließend sind. So finden sich über kiesigen Umlagerungslehmen auf Feldern sowie in Bodenaufschlüssen Steine in lockerer Verteilung, während über schwach kiesigem Umlagerungslehm nur ganz vereinzelt Steine auftreten.

Kiesige Verwitterungslehme treten allgemein unterhalb von Hausruck-Formation und pleistozänen Umlagerungskiesen auf. Von diesen Sedimentquellen weitestgehend isolierte kiesige Verwitterungslehme wurden dagegen als verschwemmte Kiese ausgeschieden.

Pleistozän-Holozän: Sackungsgebiete

Sackungsgebiete treten vor allem an steileren, Süd- und West- sowie stellenweise an Ost- und, in kleinerem Umfang, an Nordhängen auf. In der Regel sind dabei die Kiese der Hausruck-Formation als größere Pakete über Wasser stauenden Horizonten der unterlagernden Ampflwang-Formation abgeglitten. Die Hauptaktivität der Sackungen ist wahrscheinlich in das periglaziale Umfeld während des späten Pleistozäns zu stellen.

Pleistozän-Holozän: Rutschgebiete und Hangkriechen

In den Gebieten um den Haager Rücken, in denen kein Braunkohlebergbau stattgefunden hat, gehen die Sackungsmassen der Hausruck-Formation talwärts in größere Rutschgebiete und Gebiete mit Hangkriechen über. Hier sind die teils mächtigen Lockergesteinsbedeckungen aus Umlagerungen der Hausruck-Formation über den Tonen der Ampflwang-Formation, und auch mit ihnen durchmischt, als Rutschmassen in Bewegung. Sie wurden im Gelände anhand ihrer unruhigen Oberflächenformen ausgeschieden, wobei sowohl die Grenzen gegenüber Sackungsmassen, als auch gegenüber kiesigem Verwitterungslehm fließend sind.

Holozän: Alluvionen

Rezente Alluvionen begleiten vielfach die aktuellen Bachläufe. Dabei handelt es sich um wechselnd feinkiesige, sandige oder tonige Ablagerungen episodischer Überschwemmungsereignisse. Daneben wurden bei der Kartierung vereinzelt auch fluviatile Schüttungsfächer am Ausgang von Trockentälchen im Bereich der Hausruck-Formation als kiesige Alluvionen und vernässte oder sumpfige Alluvionen aus überwiegend tonigem Detritus ausgeschieden. Innerhalb der kiesigen Verwitterungslehme sind Kiese und Steine teilweise in Mulden und Tälchen durch oberflächennahe Umlagerung angehäuft. Dabei sind die Übergänge zwischen Alluvionen, kiesigem Verwitterungslehm und verschwemmten Kiesen fließend.

Anthropozän: Halden, Pingen, künstlich gestaltete Geländeform

Am Haager Rücken des Hausruckwalds hat kein nennenswerter Braunkohlebergbau stattgefunden. Somit sind im Kartierungsgebiet 2018/19 die natürlichen Geländeformen im Bereich der Ampflwang-Formation weitestgehend erhalten. Dagegen sind künstlich gestaltete Geländeformen in den landwirtschaftlich genutzten Flächen sowie in den Siedlungen häufig anzutreffen und wurden, wo sie klar als solche zu erkennen sind, auf der Karte ausgeschieden. Dazu zählen künstliche Aufschüttungen wie Straßen- und Bahndämme oder Ausebnungen von Feldern. Südlich und östlich Letten wurde im Gebiet des Golfklubs das Gelände über größere Flächen künstlich gestaltet.

Im Zuge einer Grundzusammenlegung in den späten 1970er Jahren kam es zu größeren Geländekorrekturen, die kaum noch als solche erkannt werden können. Sie müssen aber bei der geologischen Interpretation von Geländeformen und Lesesteinen im Bereich der landwirtschaftlichen Nutzflächen stets berücksichtigt werden.

Tektonik

Die Oberösterreichische Molasse im Gebiet des Hausruck ist tektonisch allgemein ruhig gelagert (Krenmayr & Schnabel, 2006). Durch Bohrungen, tiefe Geophysik und wenige Schichtmessungen bestätigt, kann ein gegen Nord- bis Nordwest gerichtetes Einfallen von wenigen Grad bestimmt werden (z.B. Aberer, 1957; Rupp, 2008a; Ibele, 2017, 2018), das auf die spätorogene Hebung des Alpenkörpers im Süden zurückzuführen ist.

Bei den aktuellen Aufnahmen wurde in Aufschlüssen am Bach südlich Steinpoint sowie nordöstlich Niedernhaag stärker geklüftete Ottnang-Formation kartiert, wobei das Gestein teilweise kataklastisch zerbrochen ist. Zusammen mit Beobachtungen beim Sicherheitsausbau der Inntal Autobahn A8 (Peresson et al., 2016) und am Nordrand von Blatt 47 Ried im Innkreis (Rupp, 2008b) lassen sich die Aufschlüsse bei Steinpoint und Niedernhaag lose zu einer W–E streichenden Störungszone verbinden, die etwa dem Ried-Antitheter der Molassebasis folgt (Rupp, 2008b; Kröll et al., 2006). Aufgrund der Lagen der Aufschlüsse von Ried- und Ottnang-Formation zwischen Hundassing und Niedernhaag ist es wahrscheinlich, dass sich die Störungszone oberflächennah aus mehreren kurzen Einzelstörungen zusammensetzt, die zwischen W–E und WNW–ESE streichen. Sie wurden jeweils als vermutet in der Karte eingezeichnet. Anhand der unterschiedlichen Höhen der Basis der Ried-Formation lässt sich ein, in Bezug auf das südgerichtete Einfallen der Molassebasis antithetischer Versatz vermuten, der die nordöstliche Seite um maximal einige Meter relativ tiefer versetzt.

In einem Aufschluss am Bach südlich Zeißerding fällt die Ottnang-Formation mit 35° gegen Süden (Azimut 195) ein. Fünf bis zehn Meter weiter nördlich wurde ein Einfallen von 48° gegen Norden (Azimut 008) gemessen. Daraus ergibt sich das Bild einer kleinen, W–E streichenden und leicht nordvergenten Faltenstruktur. Dem entspricht auch ein etwa 100 m langer Aufbruch von Ottnang-Formation aus basaler Ried-Formation. Bei Falten dieser Größenordnung kann es sich sowohl um lokale Kompressionsstrukturen, als auch um synsedimentäre Rutschfalten handeln.

Post-mittelmiozäne kompressive Tektonik in der Molassezone ist nur westlich Salzburg bekannt (Ortner et al., 2015). Im oberösterreichischen Abschnitt der Alpenfront endete sie im frühen Miozän (Hinsch, 2013; Beidinger & Decker, 2014) und noch vor der Sedimentation der Ottnang-Formation. Differenzielle Hebung der Vorlandmolasse ab dem Pliozän (Genser et al., 2007; Gusterhuber, 2013) orientierte sich dagegen wahrscheinlich an präexistenten Bruchsystemen, die aus dem mesozoisch-paläozoischen Untergrund und dem angrenzenden Böhmischen Massiv als vorwiegend NW–SE und NE–SW streichende Störungszonen bekannt sind (Kröll et al., 2006). Bei einer Reaktivierung dieses präexistenten Bruchmusters im Untergrund sind einzelne initiale tektonische Erscheinungen auch in der überlagernden Molasse zu erwarten.

Literatur

Aberer, F. (1957): Die Molassezone im westlichen Oberösterreich und in Salzburg. – Mitteilungen der Geologischen Gesellschaft in Wien, **50**, 23–93, Wien.

Aretin, G. (1988): Bericht 1987 über geologische Aufnahmen im Tertiär und Quartär des Hausruckgebietes auf Blatt 48 Vöcklabruck. – Jahrbuch der Geologischen Bundesanstalt, **131**, 404–405, Wien.

Beidinger, A. & Decker, K. (2014): Quantifying Early Miocene in-sequence and out-of-sequence thrusting at the Alpine-Carpathian junction. – Tectonics, **33**, 222–252, Washington, D.C.

Deckers, S. (1988): Geologische Karte des östl. Hausruckgebietes (östl. von Ampflwang) 1:10.000. – Unpublizierte Diplomkarte, Universität München, München.

Genser, J., Cloetingh, S. & Neubauer, F. (2007): Late orogenic rebound and oblique Alpine convergence: New constraints from subsidence analysis of the Austrian Molasse basin. – Global and Planetary Change, **58**, 214–223, Amsterdam.

Gusterhuber, J. (2013): Multidimensional Basin and Petroleum Systems Modeling in the Molasse Basin, Austria. – PhD Thesis, Montanuniversität Leoben, 152 S., Leoben.

Hinsch, R. (2013): Laterally varying structure and kinematics of the Molasse fold and thrust belt of the Central Eastern Alps: Implications for exploration. – American Association of Petroleum Geologists, AAPG, Bulletin, **97**, 1805–1831, Tulsa.

Ibele, T. (2017): Bericht 2017 über geologische Aufnahmen auf Blatt NL 33-10-29 Vöcklabruck. – Jahrbuch der Geologischen Bundesanstalt, **157**, 434–437, Wien.

Ibele, T. (2018): Bericht 2018 über geologische Aufnahmen auf Blatt NL 33-10-29 Vöcklabruck. – Jahrbuch der Geologischen Bundesanstalt, **158**, 176–181, Wien.

Kaltbeitzer, J. (1988): Geologische Karte des Hausruckgebietes östl. von Eberschwang (Oberösterreich) 1:10 000. – Unpublizierte Diplomkarte, Universität München, München.

Krenmayr, H.G. (1995): Bericht 1994 über geologische Aufnahmen im Tertiär auf Blatt 47 Ried im Innkreis. – Jahrbuch der Geologischen Bundesanstalt, **138**, 484–485, Wien.

Krenmayr, H.G. & Schnabel, W. (Red.) (2006): Geologische Karte von Oberösterreich 1:200.000. – Geologische Bundesanstalt, Wien.

Kröll, A., Motschka, K., Meurers, B., Slapansky, P. & Wagner, L. (2006): Erläuterungen zu den Karten über die Molassebasis Salzburg – Oberösterreich. – 24 S., Geologische Bundesanstalt, Wien.

Ortner, H., Aichholzer, S., Zerlauth, M., Pilser, R. & Fügenschuh, B. (2015): Geometry, amount, and sequence of thrusting in the Subalpine Molasse of western Austria and southern Germany, European Alps. – Tectonics, **34**, 1–30, Washington, D.C.

Papp, A., Grill, R., Janoschek, R., Kapounek, J., Kollmann, K. & Turnovsky, K. (1968): Zur Nomenklatur des Neogens in Österreich. – Verhandlungen der Geologischen Bundesanstalt, **1968**, 9–27, Wien.

Peresson, M., Posch-Trözmüller, G., Bieber, G., Hobiger, G., Rabeder, J., Römer, A., Rupp, C. & Supper, R. (2015): Geologische Bearbeitung kurzfristiger Aufschlüsse in Oberösterreich mit Schwerpunkt auf infrastrukturelle Bauten und schlecht aufgeschlossene Regionen sowie auf rohstoffwissenschaftliche, umweltrelevante und grundlagenorientierte Auswertungen. Jahresendbericht 2014. – Neue Bauaufschlüsse – Neues Geowissen: Oberösterreich, 115 S., Geologische Bundesanstalt, Wien. [GBA, Wissenschaftliches Archiv, Nr. A 18399-R]

Peresson, M., Posch-Trözmüller, G., Hobiger, G., Rabeder, J. & Rupp, C. (2016): Geologische Bearbeitung kurzfristiger Aufschlüsse in Oberösterreich mit Schwerpunkt auf infrastrukturelle Bauten und schlecht aufgeschlossene Regionen sowie auf rohstoffwissenschaftliche, umweltrelevante und grundlagenorientierte Auswertungen. Jahresendbericht 2015. – Neue Bauaufschlüsse – Neues Geowissen: Oberösterreich, 132 S., Geologische Bundesanstalt, Wien. [GBA, Wissenschaftliches Archiv, Nr. A 18834-R]

Peresson, M., Posch-Trözmüller, G., Hobiger, G., Rabeder, J. & Rupp, C. (2017): Geologische Bearbeitung kurzfristiger Aufschlüsse in Oberösterreich mit Schwerpunkt auf infrastrukturelle Bauten und schlecht aufgeschlossene Regionen sowie auf rohstoffwissenschaftliche, umweltrelevante und grundlagenorientierte Auswertungen. Jahresendbericht 2016. – Neue Bauaufschlüsse – Neues Geowissen: Oberösterreich, 160 S., Geologische Bundesanstalt, Wien. [GBA, Wissenschaftliches Archiv, Nr. A 19148-R]

PILLER, W., EGGER, H., ERHART, C.W., GROSS, M., HARZHAUSER, M., HUBMANN, B., VAN HUSEN, D., KRENMAYR, H.-G., KRYSTYN, L., LEIN, R., LUKENEDER, A., MANDL, G.W., RÖGL, F., ROETZEL, R., RUPP, C., SCHNABEL, W., SCHÖNLAUB, H.P., SUMMESBERGER, H., WAGREICH, M. & WESSELY, G. (2004): Die stratigraphische Tabelle von Österreich 2004 (sedimentäre Schichtfolgen). – Österreichische Akademie der Wissenschaften und Österreichische Stratigraphische Kommission, Wien.

ROETZEL, R. (1988): Bericht 1987 über geologische Aufnahmen im Tertiär und Quartär nördlich und östlich von Frankenburg auf Blatt 47 Ried im Innkreis. – Jahrbuch der Geologischen Bundesanstalt, **131**, 403–404, Wien.

RUPP, C. (2008a): Geologische Karte der Republik Österreich 1:50.000, Blatt 47 Ried im Innkreis. – Geologische Bundesanstalt, Wien.

RUPP, C. (2008b): Erläuterungen zur Geologischen Karte der Republik Österreich 1:50.000, Blatt 47 Ried im Innkreis. – 100 S., Geologische Bundesanstalt, Wien.

RUPP, C. (2013): Bericht 2012 über geologische Aufnahmen auf Blatt 3329 Vöcklabruck-Ost. – Jahrbuch der Geologischen Bundesanstalt, **153**/1–4, 433–434, Wien.

SCHLÄGER, A. (1988): Geologische Karte des Hausruckgebietes nördlich von Ottnang/OÖ 1:10.000. – Unpublizierte Diplomkarte, Universität München, München.

Blatt NM 33-12-13 Hollabrunn

Bericht 2019 über geologische Aufnahmen im Neogen auf Blatt NM 33-12-13 Hollabrunn

HOLGER GEBHARDT

Arbeitsgebiet

Im Jahr 2019 wurde mit der Kartierung des südwestlichen Viertelblattes von NM 33-12-13 Hollabrunn begonnen. Von diesem wiederum ist die westliche Hälfte vor kurzem von ROETZEL (2015) veröffentlicht worden. Die kartierten Gebiete sind ausschließlich der Autochthonen Molasse zuzurechnen, weitere tektonische Einheiten kommen nicht vor. Zusätzlich wurden die Einheiten der „Jüngeren (quartären) Bedeckung“ geologisch kartiert. Vom Autor wurden zum Auffinden der häufig von geringmächtigem (wenige dm) Löss verdeckten Laa-Formation zahlreiche Handbohrungen bis 1 m Tiefe durchgeführt. Das bearbeitete Gebiet umfasst die nördliche Hälfte der Osthälfte des südwestlichen Viertelblattes. Dieses reicht von Göllersdorf im Norden bis nach Unterhautzental im Süden und von Stranzendorf im Westen bis zum Schloss Schönborn im Osten. Die Unterscheidung und Benennung der pleistozänen und holozänen Einheiten (Junge Bedeckung) erfolgte entsprechend den Vorgaben in KRENMAYR et al. (2012). Die Benennung der übrigen Einheiten erfolgte entsprechend der vorhandenen Literatur (GRILL, 1962; SCHNABEL et al., 2002; ROETZEL et al., 2009; ROETZEL, 2015), bzw. den eigenen Beobachtungen.

Kartierte Einheiten

Autochthone Molasse

Laa-Formation (Karpatium)

Im Arbeitsgebiet kommt die Laa-Formation in drei verschiedenen Faziesvarianten vor, die auch im Kartenbild getrennt dargestellt werden: konglomeratisch, sandig und tonig-mergelig. Laa-Formation tritt vorwiegend entlang der meisten West- und Südhänge der Täler auf, da die Ost- und Nordhänge fast immer von teilweise sehr mächtigen Löss-Schichten überdeckt sind (siehe unten).

Die weitaus häufigste Fazies besteht aus dunkelgrauen Tonmergeln (bzw. Siltsteinen) und untergeordneten dünnbankigen (mm–cm) Sanden und Sandsteinen. In der Ziegelgrube der Fa. Wienerberger in Göllersdorf (Grenzbereich zu Blatt 23 Hadres; ROETZEL et al., 2009) sind im unteren Teil mergelige Ton-Siltsteine mit cm-dicken Sandsteinlagen aufgeschlossen, die im oberen Teil sukzessive in tonig-siltige Sandsteine von bis zu mehreren Meter Mächtigkeit übergehen. Die tonig-siltigen Schichten sind teilweise reich an Mikrofossilien (hauptsächlich planktische und benthische Foraminiferen, Diatomeen), die ein karpatisches Alter anzeigen (oberes Untermiozän, ROETZEL et al., 2009; GEBHARDT, 2018). Im Steinbruch Wienerberger gibt es auch einzelne Lagen mit zerbrochenen dünnschaligen Muscheln. Die feinkörnigen Gesteine verwittern hellgrau bzw. später grünlich (Mergel) bis gelblich (Mergel, Sandsteine). Weitere Vorkommen der tonig mergeligen Fazies befinden sich nordöstlich und südöstlich von Eitzersthal, nordöstlich und südöstlich von Oberparschenbrunn, in Viendorf, nördlich von Stranzendorf, sowie östlich von Unterparschenbrunn.

Die überwiegend sandige Fazies tritt sehr viel seltener auf. Aufgrund der gelben Verwitterungsfarbe können die Sedimente im aufgelockerten Zustand leicht mit dem fast überall auftretenden Löss verwechselt werden. Die Dicke der Sandsteinlaminae bzw. Sandsteinbänke reicht von wenigen Millimetern bis zu mehreren Metern. Auffällige Sedimentstrukturen wurden wegen der Verwitterungsanfälligkeit nicht gefunden. Vereinzelt tritt horizontale Laminierung oder Schrägschichtung auf. Östlich von Oberparschenbrunn wurde ein Vorkommen mit Planzenhäckseln gefunden. Weitere Vorkommen befinden sich nördlich von Oberparschenbrunn und östlich von Unterparschenbrunn.

Die konglomeratische Fazies fällt durch Gerölle von 1 bis 20 cm Durchmesser auf, die auf den abgeernteten Äckern leicht zu finden sind. Einzig in einem Graben nordöstlich der Ziegelgrube Wienerberger wurde die konglomeratische Fazies anstehend gefunden, sodass dort der Schichtaufbau und die Lagerungsverhältnisse studiert werden können. Der Aufschluss befindet sich allerdings bereits auf dem anschließenden Nachbarblatt 23 Hadres. Alle anderen Vorkommen sind Lesesteine. Roetzel et al. (2009) beschreibt diese Fazies im Detail aus dem sich nördlich anschließenden Kartenblatt (matrixgestützte Kiese mit kalkigen Tonsilten, die als debritische Rinnenfüllungen interpretiert werden; siehe auch Gebhardt, 2018). Die kartierten Vorkommen befinden sich im Norden des Arbeitsgebietes nordöstlich von Göllersdorf, nordwestlich von Eitzersthal und südöstlich von Wischathal.

Junge Bedeckung

Fluviatile Schotter (Pliozän/Pleistozän)

Östlich von Stranzendorf am Westrand des hier bearbeiteten Gebiets befindet sich eine große Sandgrube (Fink & Piffl, 1976; heute Sportplatz), in der hauptsächlich Löss für Baumaßnahmen abgebaut wurde. An der östlichen Wand sind stark zementierte fluviatile Schotter (Konglomerate) in 300 m Seehöhe unterhalb von Lössen und Paläoböden aufgeschlossen. Nach Rabeder (1981) sind diese in den Grenzbereich Pliozän/Pleistozän zu stellen. Zumindest sind sie älter als die Säugetierfundschicht G mit einem Alter von etwa 2,14 Ma (in Rabeder, 1981). In der selben Grube wurden jedoch auch wesentlich ältere (spätpliozäne) Lösse und Rotlehme angetroffen. Die Alter wurden durch paläomagnetische Datierungen bestätigt.

Älterer Deckenschotter (Höhere Terrassenschotter, Günz-Eiszeit)

Östlich des Göllersbaches und des Porraubaches werden zwischen den Höhenmetern 210 und 230 große Flächen von Älterem Deckenschotter bedeckt, die auch bei Viendorf in größerem Maßstab und nordöstlich von Schloss Schönborn in kleinerem Maßstab abgebaut wurden. Die Schotter entsprechen den bisherigen Beschreibungen (z.B. Gebhardt, 2016). Westlich des Göllersbaches wurde am östlichen Ortseingang ein kleines Vorkommen in gleicher Höhenlage angetroffen, das auch schon in der Karte von Grill (1957) eingezeichnet ist.

Löss, untergeordnet Lösslehm

Die typischen gelblichen, kalkhaltigen, teilweise feinsandigen Silte mit kurzen Pseudomyzelien, Konkretionen (Lösskindl) und/oder Lössschnecken nehmen weite Flächen auf den Hochebenen und den Ostabhängen der Höhenzüge im gesamten Arbeitsgebiet ein. Lössprofile mit Paläoböden (Rotlehme) sind weit verbreitet. Die Rotlehme treten insbesondere im Kontaktbereich zur unterlagernden Laa-Formation auf. Leicht zugängliche, mehrteilige Lössprofile mit Paläoböden wurden an folgenden Stellen angetroffen: Fußballplatz westlich Göllersdorf nahe der Weinviertler Schnellstraße S3, südlich Unterparschenbrunn entlang der Straße nach Oberhautzental sowie in der oben erwähnten Sandgrube östlich von Stranzendorf. Im Rahmen der Kartierung wurden keine Altersdatierungen der verschiedenen Lössablagerungen getätigt. Aufgrund der Lagerungsverhältnisse reicht das Alter der Lössablagerungen vom obersten Pliozän (Stranzendorf; Rabeder (1981), bis in das Spätpleistozän (z.B. östlich Göllersbach, auf Älterem Deckenschotter (Günz-Eiszeit; Fuchs & Grill, 1984) aufliegend).

Gleit- und Rutschmassen (Würm bis Spätglazial, teilweise rezent)

Vorkommen von Massenbewegungsablagerungen wurden nur an einer Stelle im Arbeitsgebiet angetroffen. Diese liegt in Lössvorkommen mit relativ steilen Hangwinkeln und ist verhältnismäßig kleinräumig (nördlich des Eisenbergs). Große Massenbewegungen mit deutlich im Gelände erkennbaren Abrisskanten wie in Lotter & Gebhardt (2018) beschrieben, wurden im Arbeitsgebiet nicht beobachtet.

Solifluktions- und Flächenspülungssediment

Die braunen, oft kalkfreien Lehme treten regelmäßig im Hangfußbereich rund um Höhenzüge und in vielen Tälern mit geringem Böschungswinkel auf. In vielen kleinen Tälchen zeichnet das Vorkommen dieser Sedimente den Verlauf der ehemaligen Gerinne nach. Der Übergang zu den höher gelegenen Hangarealen mit anstehendem Gestein des Untergrundes ist durch einen Hangknick gekennzeichnet. Eine Ableitung des Lehms aus Löss ist für weite Gebiete anzunehmen.

Bach- oder Flussablagerung

Talfüllungen aus fluviatilen Sedimenten und Böden wurden entlang größerer Gerinne (z.B. Göllersbach, Porraubach, Parschenbrunner Bach) sowie den kleineren Zuflüssen kartiert (ebene Fläche entlang von noch existierenden und ehemaligen Wasserläufen).

Schwämmfächer

Deutliche kegelförmige morphologische Erhebungen in Verbindung mit Einmündungen von Bächen oder Taleinkerbungen wurden südlich von Stranzendorf und nördlich des Eisenbergs kartiert.

Anthropogene Ablagerung/Bedeckung (Anschüttung, Verfüllung, Dämme)

Künstliche Anschüttungen wurden beim Bau der S3 an zahlreichen Stellen vorgenommen. Im Bereich des ehemaligen Abbaus der Grube Wienerberger bei Göllersdorf wurde Abraummaterial wiederverfüllt. Dämme zur Hochwasserabwehr befinden sich im Porraubach östlich Viendorf und westlich der S3 gegenüber dem Golfplatz Schloss Schönborn. Daneben gibt es zahlreiche kleinere Anschüttungen innerhalb von Siedlungen (z.B. westliches Ende von Unterparschenbrunn), die aber nicht in allen Fällen in die Karte eingetragen wurden.

Strukturelle Interpretation

Der gesamte in 2019 kartierte Bereich fällt in die Alpin-Karpatische Vortiefe (Autochthone Molasse). Aufgrund der tiefgründigen Verwitterung und der intensiven landwirtschaftlichen Nutzung des Arbeitsgebietes konnten keine Einfallswerte gemessen werden. Auch die Interpretation der kartierten Ausbisslinien brachte keine Hinweise auf Störungen oder andere Strukturelemente. Das in der Grube Wienerberger bei Göllersdorf messbare Schichteinfallen (generell ca. 25° Richtung NNE) liegt knapp außerhalb des Arbeitsgebietes, wie auch das oben erwähnte Konglomerat der Laa-Formation (Einfallen 245/15). Eine detaillierte tektonische Analyse der dort auftretenden Gesteine der Laa-Formation weist auf listrische Abschiebungen und en-echelon-angeordnete Kippschollen hin (Roetzel et al., 1999, 2009). Eine in der Literatur erwähnte Verwerfung weist auf teilweise sehr junge (pleistozäne) tektonische Aktivitäten hin (Sandgrube Stranzendorf; Rabeder, 1981; Fuchs & Grill, 1984).

Literatur

Fink, J. & Piffl, L. (1976): Stop 6/4: Schottergrube Stranzendorf. – In: Fink, J. (Ed.): Exkursion durch den österreichischen Teil des nördlichen Alpenvorlandes und den Donauraum zwischen Krems und Wiener Pforte, Volume **1**, 102–109, Kommission für Quartärforschung der Österreichischen Akademie der Wissenschaften, Wien.

Fuchs, W. & Grill, R. (1984): Geologische Karte von Wien und Umgebung, 1:200.000. – Geologische Bundesanstalt, Wien

Gebhardt, H. (2016): Bericht 2015 über geologische Aufnahmen im Paläogen/Neogen auf Blatt NM 33-12-13 Hollabrunn. – Jahrbuch der Geologischen Bundesanstalt, **156**, 351–353, Wien.

Gebhardt, H. (2018): Bericht 2018 über geologische Aufnahmen im Paläogen/Neogen auf Blatt NM 33-12-13 Hollabrunn. – Jahrbuch der Geologischen Bundesanstalt, **158**, 190–196, Wien.

Grill, R. (1957): Geologische Karte der Umgebung von Korneuburg und Stockerau 1:50.000. – Geologische Bundesanstalt, Wien.

Grill, R. (1962): Erläuterungen zur geologischen Karte der Umgebung von Korneuburg und Stockerau. – 52 S., Geologische Bundesanstalt, Wien.

Krenmayr, H.-G., Ćorić, S., Gebhardt, H., Iglseder, C., Linner, M., Mandl, G.W., Reitner, J., Rockenschaub, M., Roetzel, R. & Rupp, C. (2012): Generallegende der pleistozänen bis holozänen Sedimente und Verwitterungsprodukte des Periglazialraumes auf den geologischen Spezialkarten (1:50.000, 1:25.000) der Geologischen Bundesanstalt. – Jahrbuch der Geologischen Bundesanstalt, **152**/1–4, 57–66, Wien.

Lotter, M. & Gebhardt, H. (2018): Bericht über geologische Aufnahmen quartärer Sedimente und Formen (Solifluktion, gravitative Massenbewegungen) auf Blatt NM 33-12-13 Hollabrunn. – Jahrbuch der Geologischen Bundesanstalt, **158**, 197–199, Wien.

Rabeder, G. (1981): Die Arvicoliden (Rodentia, Mammalia) aus dem Pliozän und dem älteren Pleistzän von Niederösterreich. – Beiträge zur Paläontologie von Österreich, **8**, 1–373, Wien.

Roetzel, R. (2015): Geologische Karte der Republik Österreich 1:50.000, Blatt 39 Tulln. – Geologische Bundesanstalt, Wien.

Roetzel, R., Cicha, I., Stojaspal, F., Decker, K., Wimmer-Frey, I., Ottner, F. & Papp, H. (1999): C5 Göllersdorf – Ziegelei und Tonbergbau Wienerberger. – In: Roetzel, R. (Ed.): Arbeitstagung der Geologischen Bundesanstalt, Geologische Karten ÖK 9 Retz und ÖK 22 Hollabrunn, Geogenes Naturraumpotential der Bezirke Horn und Hollabrunn, 335–341, Geologische Bundesanstalt, Wien.

Roetzel, R., Ahl, A., Götzinger, M.A., Koçiu, A., Pristacz, H., Schubert, G., Slapansky, P. & Wessely, G. (2009): Geologische Karte der Republik Österreich 1:50.000, Erläuterungen zu Blatt 23 Hadres. – 150 S., Geologische Bundesanstalt, Wien.

Schnabel, W., Krenmayr, H.-G., Mandl, G.W., Nowotny, A., Roetzel, R. & Scharbert, S. (2002): Geologische Karte von Niederösterreich 1:200.000 mit Erläuterungen. – 47 S., 2 Karten, Geologische Bundesanstalt, Wien.

Buchbesprechungen

Johannes Seidl (2019): **Geschichte der Geologie in wissenschaftshistorischer Perspektive – Von der Antike bis ins 20. Jahrhundert.** – 198 S., illustriert, Weißenthurm (CARDAMINA Verlag).

ISBN: 978-3-86424-465-0
Preis: 36,00 €
https://www.cardamina.net/artikeldetails.php?aid=688

Dieses Buch, das der Verfasser als Lehrbuch bezeichnet, hat seinen Schwerpunkt in der Geschichte der Wissenschaften in Österreich und hier wiederum im 19. und 20. Jahrhundert, jener Epoche, wo die Erdwissenschaften mit der Gründung von Geologischen Diensten und Lehrstühlen an Universitäten eine rasante Entwicklung nehmen.

Johannes Seidl, stellvertretender Leiter des Archivs der Universität Wien, beschäftigt sich seit vielen Jahren mit Themen aus der Geschichte der Erdwissenschaften, seine Schwerpunkte sind hier u.a. Forschungen zu Eduard Suess und Ami Boué.

Das Buch ist in neun Kapitel gegliedert. Zeitlich stehen am Beginn „Orientalische Reiche“, gefolgt von der „Griechisch-Römischen Periode“, den „Arabern“ und dem „Mittelalter“ (Kapitel 4). Werden in ersteren Kapiteln so wichtige Proponenten der Naturwissenschaften, wie Aristoteles, Plinius und Avicenna genannt, fällt in letzteres Zeitalter u.a. die Gründung der Universität Wien (1365). Nach weiteren Kapiteln über „Renaissance und Humanismus“ (15. und 16. Jh.), wo wir Leonardo da Vinci und Athanasius Kirchner, der das epochale Werk „Mundus subteranneus“ (1678) verfasste, sowie Georgius Agricola (De re metallica) begegnen, folgt Kapitel 6: „Das 17. Jahrhundert“. Wir finden nicht nur Isaac Newton, sondern auch Johann Jakob Scheuchzer und Nils Stensen, dem wir das Lagerungsgesetz verdanken. Im „18. Jahrhundert“ (Kapitel 7) erweist sich das Montanwesen als großer Motor für die Erdwissenschaften, auch die beiden Theorien Plutonismus (Buffon) versus Neptunismus (Werner) sind zu nennen. In Kapitel 8, „Das frühe 19. und frühe 20. Jahrhundert“ wird die Etablierung der Geologie als Naturwissenschaft dargestellt.

Den verhältnismäßig größten Raum nimmt Kapitel 9 („Zur Entwicklung der Erdwissenschaften in Österreich“) auf den Seiten 121 bis 160 ein. Hier wird unterschieden zwischen der Zeit vor 1848, jener Epoche, wo Rohstoffsuche und Bergbau prägend waren (hier sind insbesondere die Darstellungen der Vereine, der Vereinigungen, der Museen, der Sammlungen, der Akademie der Wissenschaften, der Bergakademien und der Geologischen Reichsanstalt hervorzuheben). In die zweite Hälfte des 19. Jahrhunderts fällt die Gründung der Universitätsinstitute, wo die Lehre institutionalisiert wurde, die bisher an den vorher genannten Institutionen betrieben worden war.

Ein umfangreiches Literaturverzeichnis, gegliedert nach den Kapiteln, sowie ein Personenindex runden das Werk ab.

Fazit: Ein übersichtliches, verständlich geschriebenes Kompendium, auf das viele schon lange gewartet haben und vor allem für den österreichischen Bereich eine Lücke schließt, die es bis zum Erscheinen des Buches bei der Geschichte der Erdwissenschaften gab.

Thomas Hofmann

Arnold Mihatsch (2019): **MinroG – Mineralrohstoffgesetz** (mit Bergbau-Abfall-Verordnung, Bergbau-Unfallverordnung 2015 und VPB-V 2017). – 4. Auflage, 556 S., Wien (MANZ Verlag).

ISBN: 978-3-214-10337-8
Preis: 128,00 €
https://www.manz.at/list.html?isbn=978-3-214-10337-8

Nach nunmehr 12 Jahren seit der letzten Auflage legt der Herausgeber, Dipl.-Ing. Mag. Arnold Mihatsch, der seit Beginn (1999) mit dem MinroG eng verbunden ist, eine Neuauflage vor, die sich insbesondere durch Kommentare auszeichnet, welche die Lektüre des Gesetzestextes wesentlich erleichtern.

Mit inkludiert sind auch die wichtigsten Änderungen von insgesamt acht Novellen der letzten Jahre, wie auch diverse Namensänderungen der zuständigen Behörde, die seit 2017 in Kraft sind. Diese werden im Abschnitt „Hinweise für den Benützer“ vorab erklärt.

Um einen Einblick in das Werk zu geben, sei ein Beispiel aus dem „Anwendungsbereich“ auf Seite 25 zitiert. Hier ist folgendes zu entnehmen:

„§ 2. (1) Dieses Bundesgesetz gilt für das Aufsuchen und Gewinnen[1] der bergfreien, bundeseigenen und grundeigenen mineralischen Rohstoffe, …“

Der Verweis (1) beim Wort „Gewinnen“ liefert Erläuterndes auf Seite 27. Hier wird nicht nur eine Definition („*Das Aufsuchen und Gewinnen ist umfassend im Sinne der vorbereitenden, begleitenden und nachfolgenden Tätigkeiten (vgl § 1 Z 1 und 2) zu verstehen.*“) gegeben, sondern auch klar eine Abgrenzung zu Bereichen dargelegt, wo nicht von „Gewinnen“ gesprochen werden kann („*Hinzuweisen ist, dass Vorhaben des Hoch- und Tiefbaus (etwa Tunnelbau, „Seitenentnahmen“ oder Geländekorrekturen im Rahmen des Straßenbaus, Aushub von Baugruben, Anlegen von Deponien u dgl) vom Geltungsbereich des MinroG nicht erfasst sind, weil es sich gegenständlichenfalls nicht um solche Maßnahmen handelt, die dem „Bergbau“ mit seinen typischerweise verbundenen Gefahren zuzurechnen sind und überdies die genannten Tätigkeiten nicht auf das Gewinnen von mineralischen Rohstoffen ausgerichtet sind*.

Die Entnahme mineralischer Rohstoffe im Rahmen des Nebengewerbes der Land- und Forstwirtschaft, zu dem auch der Abbau der eigenen Bodensubstanz zählt, wird dann nicht dem Geltungsbereich des MinroG unterliegen, wenn diese Tätigkeiten mit typisch land- und forstwirtschaftlichem Gerät vorgenommen werden, der mineralische Rohstoff zur Befriedigung des Eigenbedarfes dient und keine einem Bergbaubetrieb vergleichbare Organisationsform vorliegt (sVfGH 11.12.1996, B 4598/96-8) […].)“.

Ausgenommen vom Wirkungsbereich des MinroG sind im Übrigen auch rein wissenschaftliche Tätigkeiten und das Sammeln von Mineralien.

Dieses Beispiel zeigt in eindrucksvoller Weise, wie praxisnah das Buch, in das mittlerweile 20 Jahre Erfahrung eingeflossen sind, geschrieben ist.

Es verfügt über sechs Anhänge, wobei sich bei Anhang Nr. 6 das Kürzel im Untertitel, „VPB-V 2017“, wie folgt erklärt: „Verordnung des Bundesministers für Wissenschaft, Forschung und Wirtschaft über verantwortliche Personen im Bergbau 2017“.

Ein Stichwortverzeichnis (S. 543–555) rundet das Buch ab, das im handlichen Kleinformat überall Platz findet und in keinem Betrieb fehlen sollte.

Fazit: Die nunmehr 4. Auflage des MinroG stellt auf Grund der zahlreichen Kommentare eine wesentliche Erleichterung in Hinblick auf die Anwendung dar, die sehr zu loben ist. Das Gesetz ist mit den Anforderungen der Realität mitgewachsen. War etwa Geothermie vor 20 Jahren noch nicht derart im Vordergrund wie heute, finden sich auch hier Stellen, die darauf Bezug nehmen.

THOMAS HOFMANN

GERALD MANSBERGER (Koord.) & MARKUS EISL (Red.) (2019): **Wüsten – Lebensraum der Extreme.** – 256 S., 130 Satellitenbilder, Salzburg (eoVision-Media).

ISBN: 978-3-902834-28-7
Preis: 49,95 €
http://www.eovision.at/shop/wuesten-lebensraum-der-extreme/

Die eoVision Gmbh aus Salzburg ist sowohl im Medienbereich mit faszinierenden Bildbänden, als auch im Consultingbereich tätig. Schwerpunkt, da wie dort, ist der Blick von oben, sprich Satellitenbilder, die eine weitere – im wahrsten Sinn des Wortes – Sicht der Dinge ermöglichen.

Bei den Büchern, wie dem im Herbst 2019 erschienenen über Wüsten, fasziniert vor allem der ästhetische Zugang, bei großzügigem Format von 26,5 x 34 cm und höchster Druckqualität.

Wer meint, beim Thema Wüsten geht es nur um Sandwüsten, wie sie allgemein aus der Sahara oder der Wüste Gobi bekannt sind, wird hier eines Besseren belehrt. Nicht alleine nur die 130 Satellitenbilder beeindrucken, sondern auch Beiträge renommierter Autoren, darunter auch Manfred Buchroithner, der beim Thema „Wirtschaftsräume“ die „Rohstoffsuche in der Wüste“ bearbeitet hat.

Die Themen zeigen die Vielfalt der Wüsten, die sich hier als erstaunlich vielfältig, ja sogar lebendig erweisen und damit dem Vorurteil, das hier kein oder kaum Leben sei, zuvorkommen. Alleine die Einleitung, „Lebensraum der Extreme“ führt dies vor Augen. Hier geht es vor allem um Definitionen und Ansätze, diese rund 20 Prozent der Landoberfläche des Planten Erde zu beschreiben. Diese Landschaften der Extreme sind nicht nur als Sand- und Steinwüsten verbreitet, auch Eiswüsten sind ebenso in Betracht zu ziehen, wie jene Gebiete, wo es extreme Trockenheit und besondere Temperaturverhältnisse gibt. Wüsten, damit schließt die Einleitung, haben nicht nur eine lange (geologische) Geschichte, sondern wohl auch eine Zukunft.

Wolf Dieter Blümel (Emeritus des Geographischen Instituts der Universität Stuttgart) widmet sich der steten Veränderung unter dem Thema „Dynamische Lebensräume“. Hier werden neben Wind auch die Kräfte des Wassers thematisiert, die wesentlich zum Relief von Wüsten beitragen. Auch auf die Desertifikation, die anthropogen verursachte Wüstenausweitung, geht Blümel ein.

Manfred Schrenk, Stadtplaner und Direktor des CORP (Competence Center of Urban and Regional Planning) in Wien, geht in seinem Beitrag „Die Stadt in der Wüste“ exemplarisch auf eine Reihe von Städten ein, die rund um den Globus angesiedelt sind und vielfach in Wüsten liegen. Dabei beschreibt er nicht nur den arabischen Raum, sondern auch die weltbekannte Glückspielstadt Las Vegas in der Wüste von Nevada. Ein wesentlicher, wenn nicht DER entscheidende Faktor ist dabei die Versorgung der vielfach künstlich geschaffenen Metropolen mit Trinkwasser.

„Geernteter Regen“ heißt der Beitrag von Abdulmalek A. Al Alshaikh von der King Saud Universität in Riad (Saudi-Arabien). Er geht vor allem auf die Speicherung von Regen ein, der in Wüstengebieten nur höchst selten, dann aber sehr heftig fällt. Dementsprechend hat die Regenwasserspeicherung und Grundwasserauffüllung ein besonderes Augenmerk, vor allem vor dem Szenario des Klimawandels.

Der griffige Titel „Krokodile und Felsbilder“ im Abschnitt Welterbe in der Wüste des Geowissenschaftlers Stefan Kröpelin ist dem Ennedi-Massiv gewidmet, ein Sandsteinplateau im Nordosten des Tschad, das in etwa die Größe der Schweiz hat. Seit 2016 ist es UNESCO Weltkulturerbe für Natur- UND Kultur, eine Kombination, die es unter den 1.121 Welterbestätten nur fünfmal in Afrika gibt. Was den Kulturpart betrifft, so sind es vor allem die Felsbilder, die aus dem 9. (!) Jahrtausend vor Christus stammen. Damit, so schließt Kröpelin, ist Ennedi „*ein magischer Ort, ein Louvre der Vorzeit, eine Arche Noah der Artenvielfalt, ein Garten Eden der Sahara*.“

Fazit: ein höchst faszinierendes Panoptikum zum Thema Wüste, das in der Form einzigartig ist. Die Beiträge und vor allem die Bilder stellen eine Erweiterung des gängigen Wüstenbegriffes auf höchstem ästhetischem Niveau, begleitet von verständlichen wissenschaftlichen Texten, dar.

Thomas Hofmann

Daniela Angetter-Pfeiffer (Hrsg.) & Bernhard Hubmann (Hrsg.) (2020): **Quadrifolium.** – 332 S., Göttingen (V&R Unipress, Vienna University Press).

ISBN: 978-3-8471-1118-4
Preis: 55,00 €
https://www.vandenhoeck-ruprecht-verlage.com/themen-entdecken/geschichte/geschichte-des-20.-jahrhunderts/55537/quadrifolium

Der Titel „Quadrifolium“ lässt einen zunächst im Unklaren; es handelt sich um eine Festschrift für Johannes Seidl, dem stellvertretenden Leiter des Archivs der Universität Wien. Der Titel, so das Herausgeberduo, spielt auf die vierfältigen [sic!] Interessen des Jubilars an, auf „Archivwesen bzw. Sammlungsbestände“, auf „Mediävistik“, auf „Universitätsgeschichte“ und auf „(Natur)Wissenschaftsgeschichte“. Der Jubilar, dies ist der Biografie (S. 11–29) zu entnehmen, ist Jahrgang 1955 und wurde in Wien geboren. Nach seiner universitären Ausbildung war er ab 1991 Archivar der Marktgemeinde Perchtoldsdorf in Niederösterreich. 1997 wechselte er zum Redaktionsteam des Österreichischen Biographischen Lexikons der Österreichischen Akademie der Wissenschaften, mit dem Jahr 2001 kam er an das Archiv der Universität Wien. 2010 habilitierte er sich für Wissenschaftsgeschichte an der Universität Graz.

Der Biografie folgen ab Seite 33 sechs, teils sehr ausführliche Grußbotschaften (bis S. 76), ehe die Fachbeiträge, nach der oben genannten Vierteilung beginnen.

Fritz F. Steininger („Archivwesen bzw. Sammlungsbestände“) schreibt über bedeutende Sammlungen im westlichen Weinviertel und dem östlichen Waldviertel im frühen 19. Jahrhundert, wobei ein Fokus auf Candiz Ponz, Reichsritter von Engelshofen (1803–1866) liegt.

Im Bereich „Mediävistik“ gibt es Beiträge von Martin Georg Enne über prosopographische Schätze der Universität Wien, während Elisabeth Köck über die Marktbücher von Perchtoldsdorf schreibt.

Zur „Universitätsgeschichte“ liegen vier Beiträge vor, darunter einer von Matthias Svojtka zur Naturgeschichte, Zoologie und Paläobiologie an der Universität Wien im Zeitraum 1774 bis 1924. Gregor Gatscher-Riedl beleuchtet die Persönlichkeit des jüdischen Arztes und Bibliothekars Oskar Franz Steuer. Richard Lein erinnert sich an den Herbst 1968 im Geologischen Institut der Universität Wien, während Wolfgang Rohrbach sich dem Thema der Wechselbeziehungen von Universitäten und Versicherungen widmet.

Auch die „(Natur)Wissenschaftsgeschichte“ ist mit vier Beiträgen in der Festschrift vertreten. Günther Bernhard berichtet über „Quinquennium“ – das Erzbistum Salzburg und die Leistung der Fortifikationssteuer. Es folgen die Herausgeberin, Daniela Angetter-Pfeiffer, mit medizinischen Ergebnissen der Novara-Expedition, und dann der Herausgeber, Bernhard Hubmann, zum Themenkreis Lyrik und Geologie. Hier werden literarische Beschreibungen der Alpen-Exkursion 1950 der Universität Graz veröffentlicht, die einmal mehr Kreativität und Humor der Teilnehmenden unter Beweis stellen.

Der letzte Beitrag stammt von Angelika Ende, er widmet sich Franz Strauss und dessen drei Töchtern. Dass hier auch Verbindungen zur Familie von Eduard Suess bestehen, würde man a priori nicht vermuten, der Artikel bildet aber einen schönen Schlusspunkt des Werkes, da der Jubilar ja ein bekannter Forscher zur Vita von Eduard Suess ist und sich über diesen Forscher auch habilitierte.

Ein gelungenes Opus, das in den Beiträgen die vielfältigen Interessen des Jubilars zeigt, dem bei dieser Gelegenheit alles Gute für die nächsten Jahre zu wünschen ist. Ad multos annos!

Thomas Hofmann

ULRICH HAUNER, GERHARD LEHRBERGER & MATTHIAS BRUGGER (2019): **Der Naturraum Bayerischer Wald – Šumava in den Eiszeiten.** – Nationalparkverwaltung Bayerischer Wald: Wissenschaftliche Reihe, Heft **20**, 132 S., 1 Kartenbeilage, Grafenau.

ISBN: 978-3-930977-40-6
Preis: 14,90 €
https://www.bestellen.bayern.de/application/eshop_app000001?SID=904188954&ACTIONxSETVAL(artdtl.htm,APGxNODENR:352992,AARTxNODENR:356383,USERxARTIKEL:artlist1.htm)=Z

In diesem Band wird die jüngste geologische Entwicklung während der letzten beiden Eiszeiten im Bayerischen Wald und Böhmerwald (Šumava) zu beiden Seiten der europäischen Wasserscheide sowie die Goldgewinnung nach der Besiedelung des Raumes umfassend beschrieben. Die beiden Themenkomplexe beinhalten:

1. Die eiszeitliche Überformung der höchsten Erhebungen (Vereisungszentren) des Mittelgebirgszuges, einerseits durch Kryoplanation und Solifluktion der unvergletscherten Hochflächen, andererseits durch die Gletscher mit ihren Karen und glazialen Ablagerungen und den anschließenden fluvioglazialen Sedimenten.

2. Die ehemalige Goldgewinnung aus Seifenlagerstätten im Bereich der eiszeitlichen Ablagerungen. Der Konnex zu den eiszeitlichen Phänomenen ist, einerseits durch die Sedimente, andererseits auch durch die Interpretation der Bergbaulandschaft in einer frühen Phase der Erforschung als glaziale Erscheinungen, hergestellt.

Im ersten Komplex folgt nach einem kurzen Überblick über die Erforschungsgeschichte eine Erläuterung zur Erstellung der Laserscans, die in dem Band, im Gegensatz zu den sonst üblichen Kartendarstellungen, zur Dokumentation einerseits der glazialen Formen und Ablagerungen, andererseits der Strukturen des präquartären Untergrundes, genutzt werden. Dadurch wird die Zusammenschau von Morphologie und geologischen Aussagen sehr gefördert.

Eine kurze Einführung, im Vergleich mit rezenten Beispielen, zur Bildung von Ablagerungen durch Gletscher und periglaziale Vorgänge leitet über zur Zusammenfassung der generellen Entwicklung des kristallinen Mittelgebirges, von einer tiefgreifend verwitterten Rumpfflächenlandschaft des Paläogens über die fluviatile Talbildung im Neogen bis zur Formung der Landschaft durch die Gletscher der beiden jüngsten Eiszeiten.

Die auffälligsten Formen sind die Kare, die im Bereich der großen Gletscher geformt wurden, in denen durch die intensive Frostverwitterung und Glazialerosion das sonst nicht erkennbare örtliche Kluft- und Störungsmuster des präquartären Untergrundes offengelegt wird. Entsprechend ihrer Ausbildung parallel oder orthogonal zur Orientierung der dominanten Schwächezone werden zwei Kartypen unterschieden, die sich in der Übertiefung des Karbodens unterscheiden.

An den drei Gebieten Arbermassiv, Lusen-Rachel-Massiv und Dreisesselberg-Plöckenstein-Gebirgszug werden die örtlichen Muster, in unterschiedlichen Maßstäben, dem regionalen Störungsmuster gegenübergestellt. Dabei wird jeweils ein Laserscan ohne und einer mit Interpretation präsentiert, um den Rezipienten auch eine unbeeinflusste Betrachtung zu ermöglichen.

Anschließend wird noch kurz auf die lokalen und überregionalen klimatischen Einflüsse für die Gletscherbildung eingegangen. Dabei zeigt sich bei der Verteilung der Gletscher im ganzen Untersuchungsgebiet eine deutliche Abhängigkeit von der Exposition nach Norden oder Süden und der Luv- oder Leelage (vorherrschende W/NW-Winde) der Einzugsgebiete (Beilage 1). Diese Faktoren haben sich in den Eiszeiten wohl mit der zunehmenden Ausformung der Kare und Tieferlegung der Talböden verstärkt.

Ein ganz wesentliches Kapitel beschäftigt sich mit der stratigrafischen Zuordnung der Endmoränenzüge. Den Expositionsaltersbestimmungen (^{10}Be-Datierungen) an Blöcken der Moränenfolge um den Kleinen Arbersee folgend, wird eine Zuordnung der Moränenzüge zum Würm-Hochglazial sowie Spätglazial (Gschnitz und Älteste Dryas) vorgenommen. Pollenprofile und ^{14}C-Datierungen belegen die Eisfreiheit der Karseen (Kleiner/Großer Arber- und Plöckensteinsee) seit diesem Zeitraum, was sehr gut in das stratigrafische Bild passt. Die außerhalb der würmzeitlichen Wälle liegenden und durch Solifluktion wesentlich geringer akzentuierten Wallformen werden der Rißeiszeit zugeordnet. Diese stratigrafische Einstufung wird wohl zu Recht auf alle großen Kare übertragen.

Die detaillierte Beschreibung der Vereisungszentren schließt den Komplex der eiszeitlichen Formung ab. Hier wird jeder einzelne Gebirgsstock mit seinen großen und kleinen Karformen sowie den Moränenwällen (mit Höhenlage und stratigrafischer Einordnung) tabellarisch erfasst. Ergänzt wird diese Beschreibung jeweils durch Laserscan-Karten, die eine Auffindung der Wallformen im Gelände gut ermöglichen. Die vielen aussagekräftigen Fotos vermitteln auch eine gute Vorstellung der Landschaft.

Der zweite Komplex ist der Beschreibung der historischen Goldgewinnung aus Seifenlagerstätten gewidmet. Die Bergbautätigkeit ging im Mittelalter und der frühen Neuzeit besonders im Bereich des Grenzgebirgskammes um. Die Arbeit bezieht sich bis auf eine Ausnahme nur auf die Abbaue im Bayerischen Wald. Diese hinterließen die ausgedehnten Spuren z.B. der Grübenfelder, die in der Frühzeit der Eiszeitforschung mit ihren Hügeln und Gruben als glaziale Ablagerungen gedeutet wurden. Durch jüngere Forschung konnte deren anthropogene Bildung belegt, sowie – nicht zuletzt mit Hilfe der Laserscans – ihre Ausdehnung auch in dicht bewaldeten Gebieten besser erfasst werden. Die Goldvorkommen sind an fluvioglaziale Schotter oder tonige Gelifluktionsdecken und groben Frostschutt im periglazialen Raum gebunden.

Eine genaue Beschreibung der einzelnen Abbaugebiete schließt auch diesen Komplex ab. Die Fotografien und die Laserscan-Karten ergeben einen guten Überblick über den beeindruckenden Aufwand, der über die Jahrhunderte getrieben wurde und das Ausmaß der Flächen, die umgestaltet wurden.

Der Band stellt eine klare und ausführliche Zusammenfassung des heutigen Wissensstandes über die glaziale Formung des Gebietes und die ehemalige Goldgewinnung dar, die für Erdwissenschaftlerinnen und Erdwissenschaftler sowie an historischen Bergbauen interessierte Personen von Interesse ist. Die aufwändige Dokumentation durch die Laserscankarten macht das Nachvollziehen auch im Gelände leicht möglich.

Eine Übersichtskarte (Beilage 1) stellt das gesamte Untersuchungsgebiet und die Lage der Vereisungszentren sowie der Stellen der Goldgewinnung dar.

DIRK VAN HUSEN

Inhalt

Contents

www.geologie.ac.at

ISSN 0016-7800